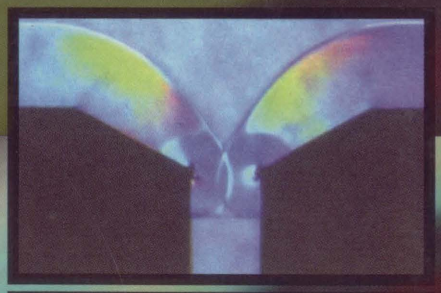

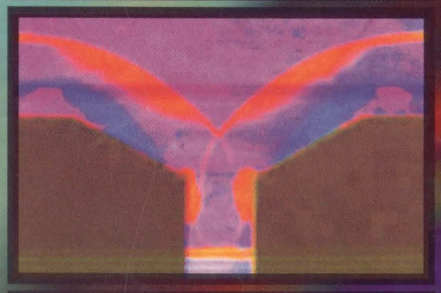

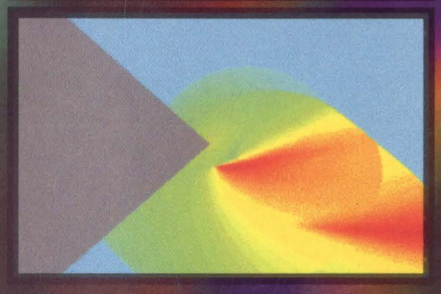

Proceedings of the
First International Conference on

Heat Transfer, Fluid Mechanics and Thermodynamics

Volume 1 ~ Part 2

HEFAT 2002

Skukuza
Kruger National Park
South Africa

8 - 10 April 2002

Editor: JP Meyer

Proceedings of the
First International Conference on

Heat Transfer, Fluid Mechanics and Thermodynamics

Volume 1 ~ Part 2

HEFAT2002

Skukuza
Kruger National Park
South Africa
8 – 10 April 2002

Editor: JP Meyer

The 1st International Conference on Heat Transfer, Fluid Mechanics and Thermodynamics was held in the Skukuza Rest Camp of the Kruger National Park from 8 to 10 April 2002. The conference was organized by HEFAT and sponsored by the South African Institute for Mechanical Engineers (SAIMechE) and the American Society for Mechanical Engineers (ASME).

Published by HEFAT, PO Box 9669, Centurion, 0046, South Africa.

ISBN: 0-86970-536-9

Acknowledgements
Figures on front cover were kindly provided by Professor BW Skews from the University of the Witwatersrand. More information can be obtained from his keynote paper in these Proceedings.

The cover page was designed by Hester Roets from the RAU.

INTERNATIONAL ADVISORY COMMITTEE

P Bansal	University of Auckland, New Zealand
A Barletta	University of Bologna, Italy
M Behnia	University of New South Wales, Australia
AE Bergles	RPI, USA
NG Choon	National University of Singapore, Singapore
G Dumitrascu	University of Iasi, Romania
SJ Eckels	Kansas State University, USA
YA Hassan	University of Texas A&M, USA
B Horbaniuc	University of Iasi, Romania
N Jambunathan	Nottingham Trent University, UK
M Kedzierski	NIST, USA
MS Kim	Seoul National University, Korea
C Machielsen	University of Delft, The Netherlands
S Moeykens	Trane, USA
K Okamoto	University of Tokyo, Japan
AT Prata	Federal University of Santa Catarina, Brazil
RK Shah	Delphi Harrison Thermal Systems, GM, USA
JR Thome	Swiss Federal Inst. of Technology, Switzerland
PS Wei	National Sun Yat-Sen University, Rep. of China

CONTENTS (PART TWO)

PREFACE

The purpose of most conferences and also this conference is to provide a forum for world-wide specialists in heat transfer, fluid mechanics and thermodynamics to present progress of researchers and developments, and to discuss the state of the art, the future directions and priorities in the various areas of heat transfer, fluid mechanics and thermodynamics. The additional purpose of this conference is to introduce Southern Africa to the rest of the world and to initiate research collaboration.

To start with so many papers is indeed a good beginning. More than 350 manuscripts were received and peer-reviewed and approximately 200 were accepted and are collected in these proceedings. I wish to express my sincere thanks to the reviewers whose generous efforts made it possible to select these papers. With this number of papers a meaningful forum has been created to discuss the latest developments and to come abreast with the state of the art in heat transfer, fluid mechanics and thermodynamics. As a result of the many papers received the Organizing Committee has already initiated the organization of the 2nd International Conference on Heat Transfer, Fluid Mechanics and Thermodynamics (HEFAT2003), which will hopefully be presented in June/July 2003.

Thank you to the keynote lecturers and the participants for their invaluable written and oral contributions to HEFAT2002. I also wish to extent my appreciation to the Rand Afrikaans University for hosting the conference and to the South African Institute for Mechanical Engineers (SAIMechE) and to the American Society for Mechanical Engineers (ASME) for sponsoring the conference. I also wish to extend my appreciation to the International Advisory Committee and the Organizing Committee, named and unnamed, who contributed to the success of this conference and the quality of these Proceedings.

On behalf of the Organizing Committee, I would like to welcome you all to HEFAT2002. I trust that this conference will reach the goal of bringing together scientists and engineers and inspire them to gather more knowledge in order to tackle mankind's future problems. Last but not least we would be happy if your stay in the Kruger National Park would be enjoyable, fruitful and pleasant and that you will not only see the Big Five (lion, elephant, rhino, buffalo and leopard) but also some of the best scenery in the world.

JP Meyer
Editor

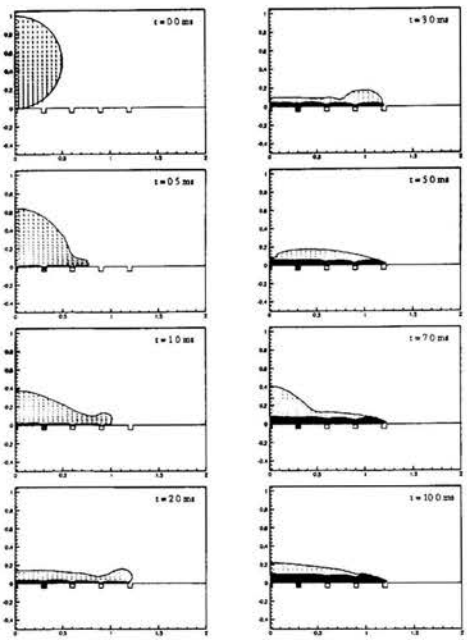

Figure 9: Splashing and solidification sequence of a liquid tin droplet on the stainless steel substrate for surface defects with pitch of 0.3 D_0 at Re = 1.3×10^4.

liquid drop to be decelerated. Hence, the maximum spread factor in most cases is reduced with decreasing pitch of the defect. However, as shown in Fig. 8 (a), the spread factor with pitch of 0.25 D_0 is greater than that with pitch of 0.3 D_0. Splat has its maximum diameter around the sixth defect in the case of 0.25 D_0. However, splat has its maximum diameter around fifth defect for the pitch of 0.3 D_0. This is attributed to the fact that the spread factor with multiple concave surface defects is affected both by the number of the defects and by the distance between the impacting point and defect position. Velocity reduction for the pitch of 0.3 D_0 is larger than that for the pitch of 0.25 D_0 since the distance between the impacting point and each defect position for the pitch of 0.3 D_0 is greater than that for the pitch of 0.25 D_0. Figure 9 shows the behavior of the droplet on the substrate in the case with the defect pitch of 0.25 D_0. It is shown that the cavity near to the impacting point is completely filled with liquid droplet, but the cavity far from the impacting point is not fully filled, similar to the one as shown in Fig. 6(a). Thus, the pores form outside the cavity. This means imperfect deposition of spray material. The thickness of the solidified layer above the pores is thinner than at other position during solidification process.

CONCLUSION

The problem of the impact and solidification of liquid metal droplet onto the substrate either with or without surface defects has been studied. The value of thermal contact resistance between the droplet and substrate is determined by comparing the spread factor from the present work with experimental results [5,6] on the flat substrate. The variations of the maximum spread factor are examined by considering the following factors: various shapes, position and size of the surface defects, and number of surface defects. It is found that the surface defects hinder spreading of the liquid drop and uniform material deposition. The spread factor is reduced more in the case with convex surface defects than concave surface defects. It is also found that the increase of defect size and number of surface defects results in the decrease of the maximum spread factor. Results show that the distance between the impacting point and the location of defect is an important parameter to affect the maximum spread factor on the substrate with multiple surface defects. It is also noted that pores are easily formed outside the cavity in the case with multiple surface defects

REFERENCES

[1] Poulikakos, D. and Waldvogel, J. M., 1996, "Heat Transfer and Fluid Dynamics in the Process of Spray Deposition," Advances in Heat Transfer 28, pp.1-74

[2] Zhang, H., 1999, "Theoretical Analysis of Spreading and Deposition," International Journal of Heat and Mass Transfer, Vol. 42, pp. 2499-2508

[3] Trapaga, G., Matthys, E. F., Valencia, J. J., and Szekely, J., 1992, "Fluid Flow, Heat Transfer, and Solidification of Molten Metal Droplets Impinging on Substrate: Comparison of Numerical and Experimental Results," Metallurgical Transaction B, Vol. 23B, pp. 701-718

[4] Delplanque, J. P., Lavernia, E. J., and Rangel, R. H., 1996, "Multidirectional Solidification Model for the Description of Micropore Formation in Spray Deposition Processes," Numerical Heat Transfer A, Vol. 30A, pp. 1-18

[5] Pasandideh-Fard, M., Bhola, R., Chandra, S. and Mostaghimi, J., 1998, "Deposition of Tin Droplets on a steel plate: Simulations and Experiments," International Journal of Heat and Mass Transfer, Vol. 41, pp. 2929-2945

[6] Aziz, S. D. and Chandra, S., 2000, "Impact, Recoil and Splashing of Molten Metal Droplets," International Journal of Heat and Mass Transfer, Vol. 43, pp. 2841-2857

[7] Tong, A. Y. and Holt, B. R., 1997, "Numerical Study on the Solidification of Liquid Metal Droplets Impacting onto a Substrate," Numerical Heat Transfer A, Vol. 31A, pp. 797-817

[8] Kothe, D. C., and Mjolsness R. C., 1992, "RIPPLE: A Computer Program for Incompressible Flows with Free Surfaces," AIAA Journal, Vol. 30, pp. 2694-2700

[9] Swaminathan, C. R. and Voller, V. R., 1993, "On the Enthalpy Method," International Journal of Numerical Methods in Heat and Fluid Flow, Vol. 3, pp. 233-244

[10] Brackbill, J. U., Kothe, D. B. and Zemach, C., 1992, "A Continuum Method for Modeling Surface Tension," Journal of Computational Physics, Vol. 100, pp. 335-354

HEFAT2002
1st International Conference on Heat Transfer, Fluid Mechanics and Thermodynamics
8-10 April 2002, Kruger Park, South Africa
BJ1

TURBULENT CONVECTIVE HEAT TRANSFER FOR ACCELERATING RADIAL FLOWS WITH SPECIAL EMPHASIS ON BUOYANCY

J.H.M. Beyers, D.G. Kröger and T.M.Harms
Department of Mechanical Engineering
Stellenbosch University
P.O. Box X10
Matieland
7600
South Africa
E-mail: mbeyers@ing.sun.ac.za

ABSTRACT

This paper describes a numerical simulation to predict the thermo-fluid behaviour of an accelerating turbulent radial flow with special emphasis on the effect of buoyancy on the convective heat transfer characteristics. The computational fluid dynamics software suite CFX4.4 was used to obtain the thermo-flow field results by including the effects of buoyancy. These results are compared to earlier results [1],[2] found by employing a newly generated Fortran 77 numerical code. Buoyancy was excluded in the earlier work.

The present research focuses on gaining insight into the thermo-flow field of accelerating radial flows between parallel plates where buoyancy may contribute to the overall heat transfer from the plates into the flow and may influence the rate of development and size of the hydrodynamic and thermal boundary layer. Such flow conditions present themselves inside a circular solar collector of a solar chimney power generating plant. The present work aims to illustrate the behaviour and influence of buoyancy on the local turbulent frictional pressure losses and wall heat transfer coefficient. Apart from the earlier numerical work, extensive analytical work [3][4], has also been carried out to predict these fluid characteristics. The analytical evaluation also excluded buoyancy effects to simplify the governing equations.

INTRODUCTION

The present study evaluates the effect of local buoyancy effects on the thermo-flow field development in the collector of a solar chimney power generating plant. The solar chimney power generating principle is currently under investigation as a potential economical and renewable energy source. A typical solar chimney power generating plant is depicted in figure 1. It consists of mainly three components namely a solar collector and a central chimney with a turbo-generator at its base. The solar collector consists of a circular glass cover supported above the ground surface. The glass cover allows solar radiation to pass through and to be absorbed in the ground.

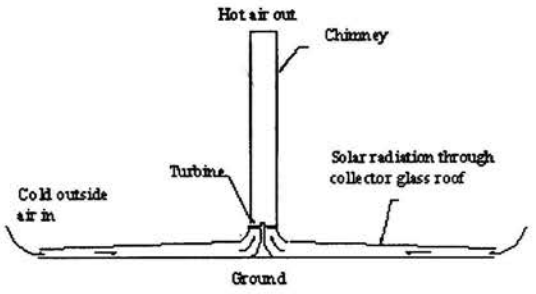

Figure 1: Solar chimney power generating principle

This absorbed solar energy leads to an increased soil temperature, which in turn results in the heating of the surrounding air through convection. The heated air in the collector causes a natural draft effect in the chimney. This draft moves from the outer perimeter of the glass collector, through the collector area and up the chimney, powering the turbo-generator in the process.

From experimental work carried out presently it is evident that very interesting flow conditions are observed for the problem under discussion. When the flow velocity at the entrance of the collector increases, the thermal characteristics of the flow change from natural convection to a combination of natural and forced convection due to buoyancy effects and eventually to forced turbulent convection. The CFD work

presented here intends to complement the experimental observations to further investigate the fundamental flow mechanisms at work. The CFX4.4 software allows us to include the effects of buoyancy and compare the predicted results to earlier numerical work, thereby providing a more complete picture of the flow problem at hand. Results presented here include the new results where buoyancy was included compared to the results from the earlier numerical [1] and analytical work [3][4] where buoyancy was excluded. The comparative results shown here are for highly turbulent axial and radial flows between parallel plates. Results are also shown for radial flows at lower Reynolds numbers where the buoyancy effects become more pronounced. Such conditions may arise for solar chimney operation during periods of low solar radiation.

The results found show good comparison to those found from earlier numerical work and analytical formulations. More importantly, results from new numerical simulations provide important insights into the relevance of including buoyancy effects in the analysis of the solar chimney collector air stream.

NOMENCLATURE

A	Total area
C_p	Specific heat C_p
d	Diameter
h	Heat transfer coefficient $h=Nu^*k/(r_o-r_i)$
H	Height
k	Turbulent kinetic energy, conductivity
m	mass flow rate
P_k	Production of turbulent kinetic energy
p	Pressure
q''	Heat source per unit area
Re	Reynolds number
T	Temperature
u,v,w	Cartesian velocity component
x,y,z	Cartesian coordinate

Greek letters

β	Coefficient of thermal expansion
Γ	Diffusion coefficient
ε	Rate of dissipation
μ	Dynamic viscosity
ρ	Density
Φ	Viscous dissipation function
ϕ	Instantaneous transported scalar

Subscripts

e	Effective
f	Bulk fluid
i	Inner radius, inlet
o	Outer radius, outlet
r	Radial position
s	Static
w	Wall
0	Reference

Superscripts

*	Dimensionless

NUMERICAL PROCEDURE

Governing equations:

The governing equations for steady state, incompressible and turbulent fluid flow are continuity, momentum and energy conservation equations. The continuity equation is given by

$$\vec{\nabla}\cdot\vec{V}=0 \tag{1}$$

and the momentum conservation and energy conservation may be presented as a general transport equation i.e.,

$$\frac{\partial}{\partial t}(\rho\phi)+\vec{\nabla}\cdot\vec{J}(\phi)=S(\phi) \tag{2}$$

$$\vec{J}(\phi)=\rho\vec{V}\phi-\Gamma\vec{\nabla}\phi \tag{3}$$

This general transport equation simplifies the discretisation of these governing equations. Table 1 shows the transported variables and source terms relevant to the applicable governing equations. The numerical method employed to obtain the earlier results compared here, was based upon a finite volume flux split method [5][6], for non-orthogonal control volumes. Furthermore, a flux blended deferred correction interpolation scheme was used as suggested by Péric [7] and Khosla and Rubin [8]. Details of the method may be found in [1][2]. The numerical simulation employs the standard k-ε turbulence model for modeling of the turbulence kinetic energy and dissipation rate. Table 1 shows the terms relevant to the general transport equation variables and source terms for the governing turbulence equations. The eddy viscosity is found from

$$\mu_t=\rho C_\mu\frac{k^2}{\varepsilon} \tag{4}$$

Wall functions were employed to approximate the logarithmic region of the turbulent velocity profile. The earlier numerical work [2] showed that this turbulence model gives accurate predictions for the flow conditions evaluated. Turbulent heat transfer was included by means of a similar Boussinesq analogy for eddy conductivity leading to

	ϕ	Γ	$S(\phi)$
x-Momentum transport	u	$\mu + \mu_t$	$-\frac{\partial p}{\partial x} + \frac{\partial}{\partial x}\left(\mu\frac{\partial \bar{u}}{\partial x}\right) + \frac{\partial}{\partial y}\left(\mu\frac{\partial \bar{v}}{\partial x}\right) + \frac{\partial}{\partial z}\left(\mu\frac{\partial \bar{w}}{\partial x}\right) + \rho g_x$
y-Momentum transport	v	$\mu + \mu_t$	$-\frac{\partial p}{\partial y} + \frac{\partial}{\partial x}\left(\mu\frac{\partial \bar{u}}{\partial y}\right) + \frac{\partial}{\partial y}\left(\mu\frac{\partial \bar{v}}{\partial y}\right) + \frac{\partial}{\partial z}\left(\mu\frac{\partial \bar{w}}{\partial y}\right) + \rho g_y$
z-Momentum transport	w	$\mu + \mu_t$	$-\frac{\partial p}{\partial z} + \frac{\partial}{\partial x}\left(\mu\frac{\partial \bar{u}}{\partial z}\right) + \frac{\partial}{\partial y}\left(\mu\frac{\partial \bar{v}}{\partial z}\right) + \frac{\partial}{\partial z}\left(\mu\frac{\partial \bar{w}}{\partial z}\right) + \rho g_z$
Energy transport equation	T	$\frac{k + k_t}{C_p}$	$\Phi + q''$ $\Phi = \mu\left[2\left(\frac{\partial u}{\partial x}\right)^2 + 2\left(\frac{\partial v}{\partial y}\right)^2 + 2\left(\frac{\partial w}{\partial z}\right)^2 + \left(\frac{\partial v}{\partial x} + \frac{\partial u}{\partial y}\right)^2 + \left(\frac{\partial w}{\partial y} + \frac{\partial v}{\partial z}\right)^2 + \left(\frac{\partial u}{\partial z} + \frac{\partial w}{\partial x}\right)^2\right]$
Turbulent kinetic energy equation	k	$\frac{\mu + \mu_t}{\sigma_t^k}$	$P_k - \rho\varepsilon$ $P_k = \mu_t\left(2\left(\left(\frac{\partial \bar{u}}{\partial x}\right)^2 + \left(\frac{\partial \bar{v}}{\partial y}\right)^2 + \left(\frac{\partial \bar{w}}{\partial z}\right)^2\right) + \left(\frac{\partial \bar{u}}{\partial y} + \frac{\partial \bar{v}}{\partial x}\right)^2 + \left(\frac{\partial \bar{v}}{\partial z} + \frac{\partial \bar{w}}{\partial y}\right)^2 + \left(\frac{\partial \bar{w}}{\partial x} + \frac{\partial \bar{u}}{\partial z}\right)^2\right)$
Turbulent dissipation rate equation	ε	$\frac{\mu + \mu_t}{\sigma_t^\varepsilon}$	$\frac{\varepsilon}{k}(C_{\varepsilon 1}P_k - C_{\varepsilon 2}\rho\varepsilon)$

Table 1: General transport equation variables and source terms

$$k_t = \frac{C_\mu \mu_t}{Pr_t} \tag{5}$$

where $Pr_t = 0.9$ as recommended by White [9]. Buoyancy is included in the present work by means of a modification of the buoyancy terms in the momentum equations [10] i.e.

$$\rho = \rho_0\left(1 - \beta(T - T_0)\right) \tag{6}$$

Additional equations.

The apparent friction factor is found from field solutions calculated from the Darcy-Weisbach relation

$$f_{app}\,Re = \frac{\Delta p}{4\left(\rho\frac{\bar{u}^2}{2}\right)\left(\frac{L}{d_e}\right)}Re \tag{7}$$

Local and mean Nusselt numbers are respectively found from

$$Nu_x = \frac{mC_p(T_o - T_i)}{A_w(T_w - T_f)} \quad \text{and} \quad Nu_m = \frac{1}{L}\int_0^L Nu_x\,dx \tag{8}$$

The static pressure drop along the plates was calculated by subtracting the dynamic pressure from the total average pressure as predicted by the CFD code i.e.

$$\Delta p_s = \left(\bar{p}_o - \bar{p}_r\right) - \frac{1}{2}\rho\left(\bar{u}_o^2 - \bar{u}_r^2\right) \tag{9}$$

The static pressure loss coefficient based on the inlet velocity then becomes

$$K_0 = \Delta p_s / \left(0.5\rho\bar{u}_0^2\right) \tag{10}$$

RESULTS

Axial flow between smooth parallel plates:

The geometry modeled, fluid properties and boundary conditions employed are shown in figure 2. Grid independent results were achieved for a 65x3x17 uniform grid geometry.

Figure 3 shows good comparison for the friction factor distribution along the length of the plates. The results also agree well with the values for the fully developed friction factors for parallel plate flows found from equation (11) from White [9] i.e.

$$\frac{1}{f_D^{0.5}} = 2.0\log_{10}\left(Re\,f_D^{0.5}\right) - 1.19 \;\Rightarrow f_D = 844.14 \tag{11}$$

at the respective fully developed hydrodynamic entrance lengths calculated from the relation given by White [9] namely

$$x/(d_e\,Re) \approx 4.4\,Re^{-5/6} = 0.000171 \qquad (12)$$

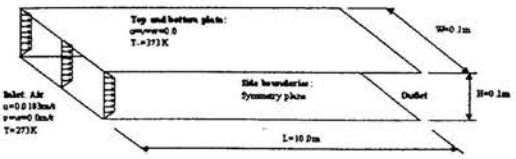

Figure 2: Flow between parallel plates

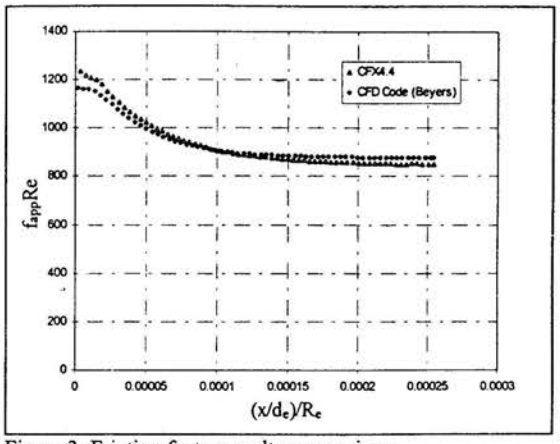

Figure 3: Friction factor results comparison.

Figure 4 shows the comparative code results of the heat transfer characteristics for Re=196721. These are also

compared to the results from an equation proposed by Hausen [11] and as given by Kröger [12] for the Nusselt number for developing flow in ducts i.e.

$$Nu = 0.0235\left(Re^{0.8} - 230\right)\left(1.8\,Pr^{0.3} - 0.8\right)\left[1 + \left(\frac{d}{L}\right)^{0.667}\right]\left(\frac{\mu}{\mu_w}\right)^{0.14} \qquad (13)$$

The above-mentioned results indicate that both the friction factor and heat transfer coefficients are not affected by the inclusion of buoyancy for this high Reynolds number flow. This supports the exclusion of buoyancy in the earlier numerical and analytical work previously based only on the large Grashof numbers involved. From Metais and Eckert [13] we have the relation

$$Gr\,Pr\frac{d_e}{L} = \frac{g\beta(T_w - T_\infty)d_e}{\upsilon^2}\cdot Pr\frac{d_e}{L} = 43.26\cdot 10^6 \qquad (14)$$

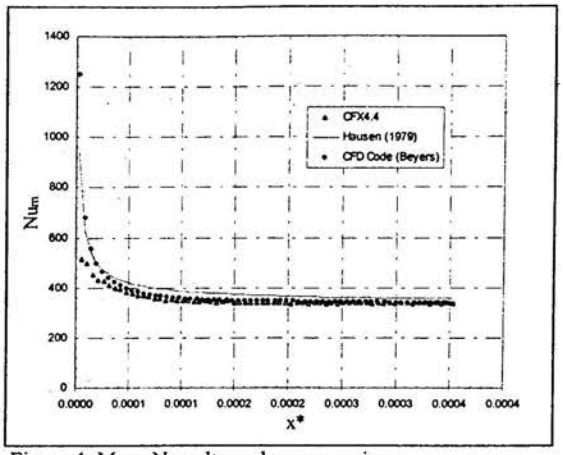

Figure 4: Mean Nusselt number comparison

which suggests that turbulent forced convection would prevail for Re=196721.

Radial flow between smooth parallel plates, Re=196721:

The flow conditions and fluid properties are the same as for the test case for turbulent axial flow between infinite parallel plates. The geometry is also of similar size except that the flow is between two circular plates instead of infinite parallel plates. The plates has an outer radius of r_o=12.5m., inner radius r_i=2.5m. An axi-symmetric wedge was modeled with an included angle of θ=0.1 radians.

Figure 5 shows the comparative frictional pressure loss coefficient results. As expected, the effects of buoyancy in the highly accelerated radial flow are insignificant. The loss coefficient due to wall friction in the entrance region between two surfaces of radial plates and based on the inlet velocity was derived by Kröger and Buys [3] i.e.

$$K_0 = 0.08038\left(\frac{\mu H}{\dot{m}}\right)^{0.1667}\left(\frac{r_o}{H_0}\right)F_s\left(\frac{r}{r_0}\right) \qquad (15)$$

where,

$$F_s = \left(1 - \frac{r}{r_0}\right)^{5/6}\left[1.51 + \left(1.71 - 2.5b\right)\left(1 - \frac{r}{r_0}\right)^{5/6}\right] \qquad (16)$$

The above formulation allows for the variation of the top plate according to the relation

$$H = H_o\left(\frac{r}{r_o}\right)^{-b} \qquad (17)$$

where b=0 for constant plate spacing in the present calculations. The mass flow, $\dot{m}$, in equation (15) is the total

mass flow through the plates, $\dot{m} = 2\pi r_o H \rho \bar{u}_o$. Kröger [4] presents another equation for the pressure loss coefficient for the fully developed region for turbulent radial flows between smooth surfaces and based on the average inlet velocity i.e.

$$K_0 = \frac{1.4633 \cdot 10^{-3} \dot{m}^{1.8} \mu^{0.2} \left[r_{fd}^{(3b-0.8)} - r^{(3b-0.8)} \right]}{\rho \left(H_0 r_0^b \right)^3 (3b - 0.8)} \frac{1}{0.5 \rho u_0^2} \qquad (18)$$

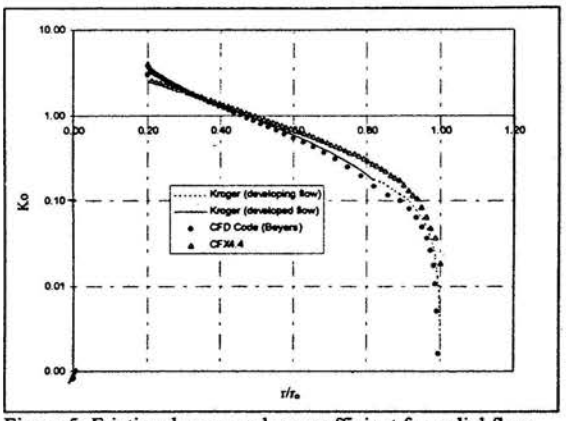

Figure 5: Frictional pressure loss coefficient for radial flow

Figure 6 shows the comparative local heat transfer coefficient predictions. The accelerating radial flow between the parallel plates gives rise to higher turbulent levels along the length of the plates which in turn increase the heat transfer from the walls due to increased eddy conductivity [1][2][3]. Kröger and Buys [3] predicts the local Nusselt number for radial flows within the entrance region between smooth plates as follows

$$Nu_r = 0.003 \, Pr^{0.333} \left(1 - \frac{r}{r_o} \right) \left(\frac{\dot{m}}{\mu H} \right) \left(\frac{r_o}{r} \right)^{0.8(1-b)} \times \left[\frac{6.218 - 15.08b}{\left(\frac{r}{r_o} \right)^{1.2-0.2b} - \left(\frac{r}{r_o} \right)^{2.743-3.943b}} \right] \qquad (19)$$

with the local heat transfer coefficient based on distance from the entrance. Kröger [4] also presents an equation for the fully developed local Nusselt number for radial flows

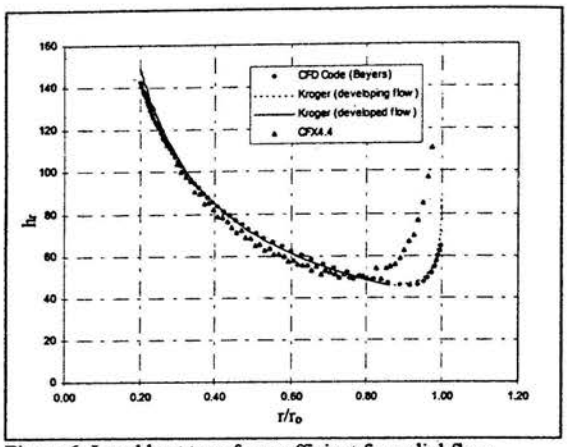

Figure 6: Local heat transfer coefficient for radial flow between smooth parallel plates i.e.

$$Nu_r = \frac{(f_D/8)(Re - 1000)Pr}{\left[1 + 12.7 (f_D/8)^{0.5} \left(Pr^{0.67} - 1 \right) \right]} \qquad (20)$$

where the local heat transfer is based on the hydraulic diameter. The Darcy friction factor for a smooth surface in equation (20) is be given by

$$f_D = \left(1.82 \log_{10} Re - 1.64 \right)^{-2} \qquad (21)$$

For the radially accelerating flow described above the effects of buoyancy is again insignificant for the Reynolds numbers in question.

Radial flow between smooth parallel plates, Re<196721:

Figure 7 shows the fluid temperature rise at the centerline for radial flow similar to the test case mentioned above but for smaller Reynolds numbers. The numerical simulation compares the results found when including buoyancy to numerical results predicted when excluding buoyancy. From figure 7 it is evident that the effects of buoyancy become important at Re<318 which is in line with the theory of Metais and Eckert [13]. They define the approximate regimes for free, forced and mixed convection for horizontal tubes as,

Re>10000	Forced turbulent convection
1000<Re<10000	Mixed turbulent convection
100<Re<1000	Mixed laminar convection
Re<100	Free convection

As seen from figure 7, the difference between the results with and without buoyancy only become significant for Re=327. At this point the steady state CFD simulations also become

unstable, a further indication that the buoyancy effects starts to dominate.

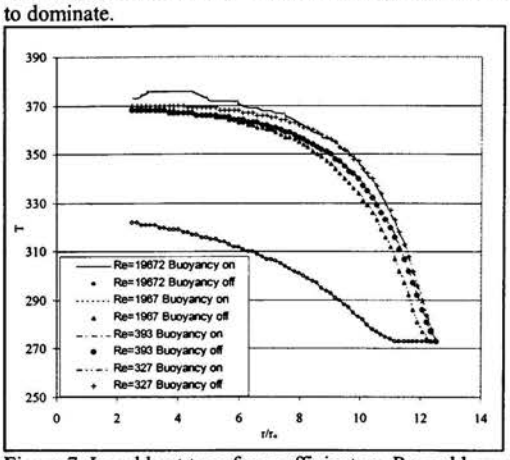

Figure 7: Local heat transfer coefficient vs. Reynolds number

CONCLUSION

The numerical results presented here included the evaluation of the effects of buoyancy at high Reynolds number axial and radial flows between parallel plates. The frictional pressure loss and heat transfer coefficients results were compared to results from earlier numerical and analytical research where buoyancy was excluded. The comparative results suggest that these effects are indeed negligible for the high Reynolds number flows considered earlier. Numerical results are also shown for smaller Reynolds number radial flows. These results illustrate when the effects of buoyancy become relevant. Future work will include similar evaluations at lower Reynolds numbers to numerically study the transient buoyancy effects as well as the influence of different turbulence models on the numerical predictions.

REFERENCES

[1] J.H.M. Beyers, T.M. Harms, D.G. Kröger, A finite volume analysis of turbulent convective heat transfer for accelerating radial flows, Paper accepted for publication in Numerical Heat Transfer, 2001.

[2] J.H.M. Beyers, A finite volume method for the analysis of the thermo-flow field of a solar chimney collector, M.Sc. Thesis, University of Stellenbosch, Stellenbosch, South Africa, 2000.

[3] D.G. Kröger and J.D. Buys, Radial flow boundary layer development analysis, South African Institution for Mechanical Engineers R&D Journal, vol. 9, no. 3, pp. 95-102, 1999.

[4] D.G. Kröger, Unpublished paper, Fully developed radial flow frictional pressure drop and heat transfer correlations, 2000

[5] H. Jasak, Error analysis and estimation for the finite volume method with applications to fluid flows, Ph.D. thesis, University of London, London, United Kingdom, 1996.

[6] O. Ubbink, Numerical prediction of two fluid systems with sharp interfaces, Ph.D. thesis, University of London, London, United Kingdom, 1997.

[7] M. Perić, A finite volume method for the prediction of three-dimensional fluid flow in complex ducts, Ph.D thesis, University of London, London, United Kingdom, 1985.

[8] P.K. Khosla, and S.G. Rubin, A diagonally dominant second-order accurate implicit scheme, Computer and Fluids, vol. 2, pp. 207-209, 1974.

[9] F.M. White, Viscous Fluid Flow, 2nd ed., McGraw-Hill, New York, 1991.

[10] CFX Solver manual, AEA Technology, Harwell

[11] H. Hausen, Extended equation for heat transfer in tubes at turbulent flow, Wärme und stoffübertragung, vol. 7, pp. 222-225, 1979.

[12] D.G. Kröger, Air cooled heat exchangers and cooling towers, 1st ed., Begell House, New York, 1998.

[13] B. Metais and E.R.G. Eckert, Forced, mixed and free convection regimes, Journal of heat transfer, vol. 86, pp. 519-537, 1964.

HEFAT2002
1st International Conference on Heat Transfer, Fluid Mechanics, and Thermodynamics
8-10 April 2002, Kruger Park, South Africa
DD1

IMPROVEMENT OF GAS TURBINE POWER PLANTS

Rodney Scott, Department of Mechanical Engineering, Auburn University, Auburn, Al 36849

David Dyer, Department of Mechanical Engineering, Auburn University, Auburn, Al 36849

ABSTRACT

Gas turbine power plants are increasingly being used to generate electrical power. Tremendous effort has been expended to increase efficiency by use high temperature materials and exotic cooling methods. The objective of this paper is to show that the use of regenerative cycles combined with various modifications of the expansion and compression processes and/or the use bottoming steam cycles allow far greater efficiency improvement than current approaches relying on higher temperature operation. This objective is accomplished by developing thermodynamic models of three physical situations: 1. the standard Brayton cycle, 2. multi-stage Brayton cycle with regeneration, intercooling, and reheat, and 3. The Brayton cycle with the addition of a waste heat boiler and steam injection into the expander. The modeling is accomplished by air standard analysis that incorporates real effects parametrically. Based on a survey of current "state-of-the-art" by the author, values representing this practice are used in the thermodynamic model to determine performance (efficiency and size) of the three cycles.. The same models are used to clearly show that the future direction for gas turbine development is the use of regenerative cycles that approach isothermal expansion and compression rather than improved material performance and sophisticated cooling systems..

INTRODUCTION

Introduction

The concept of a gas turbine and its functionality were conceived way before there were necessary materials to withstand high temperatures [1]. Hero in approximately 150 BC described a turbine driven by rising combustion gases. Real development languished for nearly 2000 years until the dawn of the industrial age in the late 1700's. Materials an inability to understand design of rotating compressors and turbines were major impediments. It was not until the early 1900's that any practical device was developed and demonstrated. Early engineers had to wait for the development of these materials to make this theory become reality [2,3,4].

A gas turbine is a device that converts chemical energy in fuel to shaft and/or jet power. There are some specific characteristics of a gas turbine to differentiate it from other power sources. A gas turbine is a rotary device that utilizes near constant pressure combustion. A simple gas turbine consists of three components: a compressor, a combustion chamber, and a turbine. This simple gas turbine set can be seen in Figure 1. This gas turbine operates on the Brayton cycle which is well documented in numerous references (eg reference [5]).

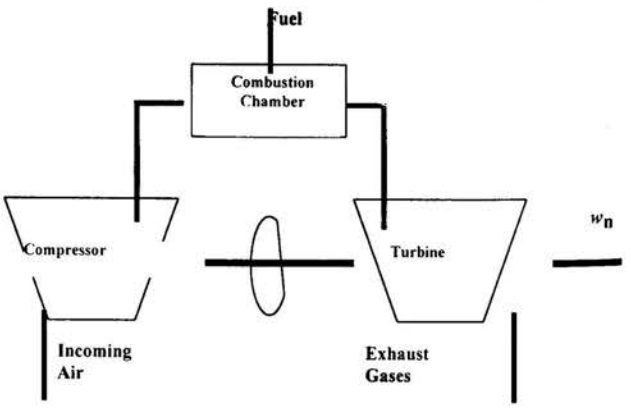

Figure 1 Simple Gas Turbine Set

The directions for technology improvements from the past lie in 4 different approaches. The improvements are as follows:

1. Steam, possibly generated by exhaust gases can be injected into the gas stream entering the expansion turbine. The procedure produces two benefits: reduced temperature protecting the metal from excessive temperature and increased mass flow generating more power.
2. Improve materials so that turbine inlet temperatures can run higher increasing turbine life and efficiency.
3. Various techniques to cool turbine blades with either water or air. This again allows the temperature of the gas entering the turbine to increase that in turn increases turbine efficiency.
4. Use of regeneration to recover exhaust energy otherwise lost.

All of these technology directions have merit today. The factors driving further development in technology of gas turbines include longer life, lower cost, higher efficiency, lower weight (particularly for aerospace derivatives), and higher reliability.

The objective of this paper is to characterize potential stationary gas turbine cycle improvements in succinct categories and to demonstrate which of these cycle improvements portend the greatest practical potential for future improvement. These improvements are then used to specify three different cycles that will allow the benefits of the improvements to be studied. Finally, parametric analysis is performed on each of the cycles to allow a comparison of the performance improvement that the particular improvement will allow. In comparing the various improvements, "state-of-the-art" operating conditions are used. The thesis underlying this work is that current efforts for improving gas turbines is focused on improving efficiency through various techniques to increase turbine inlet temperature and that this effort is misdirected. The authors seek to show that efforts to produce near isothermal compression and expansion in conjunction with regeneration offers far more potential to the development of stationary gas turbine power plants. To accomplish the objective air standard analysis of the three cycles are made. In an air standard cycle the working fluid is considered to be air. The combustion process is replaced with heat transfer and the cycle is "closed" by adding an imaginary heat rejection device. Subsequent discussion and analysis will be with respect to an air standard cycle. Experience has shown that air standard analysis can be used to closely represent reality [5]. In the analysis done in this work variable specific heats and non-ideal compression and expansion are used. Also pressure loss in heat exchange that is less than 100% effective is incorporated in the analysis.

This type analysis is well developed in numerous references [e.g. 5], and, therefore, is not repeated here. The value of this paper is the systematic examination of various categories of potential cycle improvements to determine the direction for future development of stationary gas turbine power plants.

Categorization of Potential Cycle Improvements

For the purpose of this work potential cycle improvements are placed in three categories:

1. Techniques which allow effectively a higher inlet turbine temperature
2. Techniques which combine isothermal expansion/compression with regeneration
3. A hybrid of techniques 1 and 2 in which regeneration is used to effectively allow a higher inlet turbine temperature.

The standard Brayton cycle (B cycle), shown in Figure 1, allows the effect of higher inlet turbine temperatures to be studied individually. The standard Brayton cycle can be modified by use of multistage compression with intercooling and multistage expansion with reheat to approach isothermal compression and expansion. This allows a regenerator to be effectively used. This modified Brayton cycle (MBR cycle) is

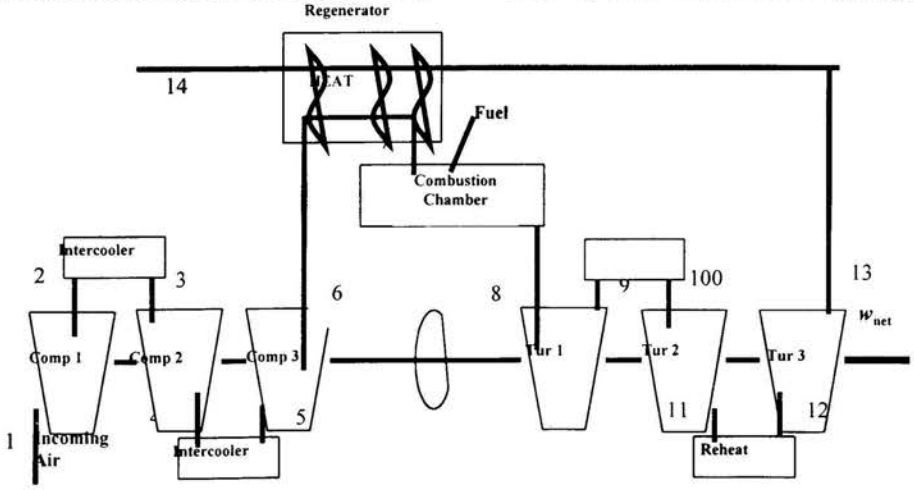

Figure 2. Modified Brayton Cycle with Multistage Compression/Expansion, Regeneration, and Reheat/Intercooling

shown in Figure 2. The analysis of this cycle allows the second category of efficiency improvement as listed above to be studied.

Employing regeneration to generate steam and, in turn, injecting the steam into the turbine (expander) can also modify the standard Brayton cycle. This cycle is labeled the "MBS cycle". This serves a dual purpose of capturing waste energy and cooling the fluid stream at the turbine inlet. This allows the third category of improvement as listed above to be examined. The hardware schematic for this improvement is shown in Figure 3.

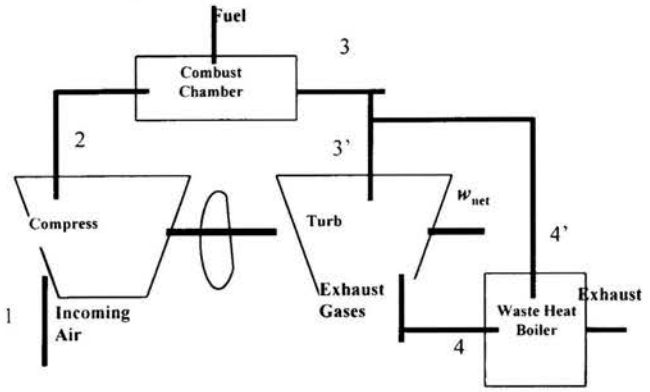

Figure 3. Schematic of a Brayton Open-Cycle with boiler

Air standard models of the three cycles described above were developed and use to parametrically examine the performance of the cycles. The modeling and analysis are not included in this paper since this information is well documented in many standard thermodynamics texts including a detailed presentation by the authors in reference [6]. Reference [6] includes the actual Fortran computer program listing used and its documentation. This paper concentrates on the results obtained and their significance for future gas turbine power plant development.

Results

Gas turbines can be applied to two broad areas of power generation: the stationary power plant and the jet engine. The jet engine does not allow significant variations from the Brayton Cycle because of weight limitations, reliability, cost, etc. Since this study is primarily concerned with changing/improving the Brayton cycle to enhance performance, this document primarily relates to stationary power plants.

Following the objective for this study, it is desired to see what categories of improvement portend the best potential for improving stationary power plant performance. To accomplish this objective the cycles as described above are modeled in a computer program. Results are obtained for each cycle's performance using "state-of-the-art" [7] operating conditions. These "state-of-art" conditions and resulting cycle performance are shown for the three cycles considered. It should be noted that the "state-of-the-art' conditions used represent the extreme of current practice. Hence, moving beyond these conditions would be technically difficult to achieve and would likely be extremely expensive. Experts in the field indicate that increasing Brayton cycle efficiency by one percent point from current "state of the art" would likely double the capital cost [7].

The parameters used in this table to indicate cycle performance are overall cycle efficiency and ratio of total power of compressor and turbine to net cycle power. These parameters were chosen to succinctly indicate performance. Net cycle efficiency is a direct indication of the fuel cost to operate the power plant. The ratio of total power of compressor and turbine to net cycle power is indicative of the cost of the power plant (a lower ratio indicates smaller compressors and turbines and, hence, less initial capital cost). For ease of reference, we will subsequently refer to this ratio as "size".

Table 1 State of the Art Gas Turbine Performance

Cycles	B	MB R	MBS
Compressor Efficiency, %	85	85	85
Turbine Efficiency, %	90	90	90
Regenerator Approach Temperature, F	n/a	400	n/a
Max. Pressure Drop as % of Compressor Exit Pressure	2	2	2
Maximum Cycle Temperature, R	3000	3000	3000
Compressor Pressure Ratio	10	10	10
Ratio of Compressor Plus Turbine Power to Net Power (Size)	2.47	1.79	2.02
Air Standard Cycle Efficiency, %	35.3	55.2	50.9

The results shown in Table 3.1 are consistent with theoretical expectations. The Brayton cycle yields the poorest performance due to the irreversibility present. The most significant irreversibility in the Brayton cycle is the transfer of heat through large temperature differentials in the simulated combustion process. An advancement that already has been employed to improve Brayton cycle efficiency is the use of regeneration. Regeneration improves efficiency in two significant ways: it captures waste energy for heating the gas leaving the compressor that would otherwise be discharged and it reduces the temperature differential through which heat is added in the simulated combustion process. However, other

means must be used to reduce the size of the power plant and to further improve the efficiency.

To decrease the size of the power plant from Brayton cycle requirements requires improvement in the compression and/or expansion processes. The MBR cycle presented in this paper incorporates these improvements. Ideally one desires isothermal compression and expansion into an otherwise conventional regenerated Brayton cycle. Unfortunately, there are significant practical limitations to employing isothermal compression and expansion. One possible means to approach ideal isothermal compression and expansion is to use multistage adiabatic compression with heat rejection coupled with adiabatic expansion with reheat. The MBR cycles described above incorporates three stages of compression and expansion with intercooling and reheat. This cycle yields more than a 50% increase in cycle efficiency as compared to the Brayton cycle and a comparable reduction in size. Clearly, these results indicate that the use of isothermal compression and expansion are the direction one should take to gain significant performance improvements in gas turbine power plants. In fact, if one could employ isothermal compression and expansion in an ideal way, the efficiency of the Ericsson cycle (the best possible efficiency) is achieved.

There has been great interest in combined cycles employing a gas turbine "topping" cycle and various forms of steam production/use generated from the waste energy leaving the turbine exhaust. In this work, one example of this form of power production is explored using the MBS cycle described above. In this cycle the generated steam is injected into the inlet of the expansion device (turbine). The results in Table 1 show that the MBS cycle is considerably more efficient than the Brayton cycle but less efficient than the MBR cycle.

The performance of all of the cycles studied can also be viewed on a parametric basis by using the computer program referenced above. For each of the three cycles studied the following figures show parametric results for the cycle efficiency as well as size versus several important parameters: compressor and turbine efficiency, regenerator approach temperature, maximum cycle temperature, and compressor pressure ratio. In each of the figures all parameters in this list except the one plotted on the abscissa are held constant at their base value. These base values are "state of the art" conditions used in the study as given in Table 1. In all calculations for the figures the pressure drop between the compressor and turbine is taken as 2% of the compressor outlet pressure.

Figure 4 shows that overall efficiency increases almost linearly with regenerator approach temperature for all cycles except the Brayton (the Brayton does not employ a regenerator). This result occurs because the amount of energy supplied externally decreases in proportion to the decrease in regenerator approach temperature. Figure 5 shows that the size of the power plant is independent of regenerator approach temperature. The amount of compression work required or expansion work produced is not affected by regeneration-only the required thermal energy input. Both of these figures show that for any regenerator approach temperature the MBR cycle is the most efficient and smallest in size.

Figure 6 gives a comparison of efficiency for the three cycles considered as the compressor pressure ratio increases. Increasing compressor pressure ratio is not desirable from the standpoint that compressor power and cost increase. Hence, a very desirable cycle trait is high efficiency at low compressor pressure ratios. For all of the cycles considered with the exception of the Brayton cycle, the cycle efficiency in Figure 6 is approximately independent of pressure ratio, which is very desirable. These use regeneration to reduce the amount of

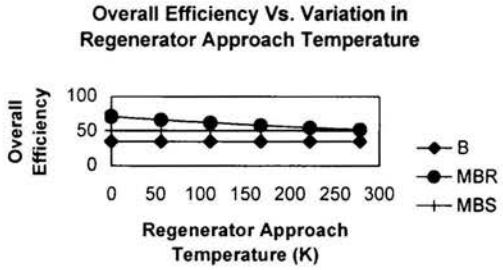

Figure 4. Overall Efficiency vs. Regenerator Approach Temperature

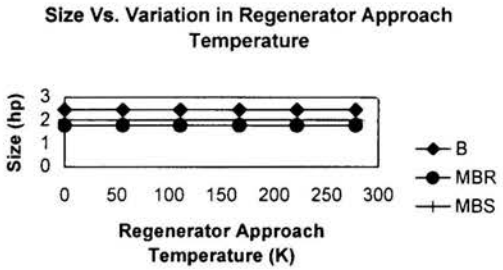

Figure 5. Size vs. Regenerator Approach Temperature

external heat that must be supplied. A low-pressure ratio maximizes the temperature difference between turbine exhaust and compressor outlet, and, hence, maximizes energy captured by regeneration. Therefore, cycle efficiency tends to be increased from a regeneration standpoint by decreasing pressure ratio. However, increasing pressure ratio increases net work and diminishes the effect of cycle component inefficiencies on overall cycle efficiency. The results of Figure 6 show that these two counterbalancing effects essentially cancel, yielding efficiency that is almost independent of pressure ratio. For the Brayton cycle the over riding factor is the decreased effect of cycle component inefficiencies with increasing pressure ratio.

Figure 7 shows how size is affected by pressure ratio. The results presented indicate negligible effect of pressure ratio on size for all cycles except the Brayton. For the Brayton cycle the size increases with pressure ratio. As pressure ratio goes up exit temperature leaving the compressor increases. Since there is a limit on the maximum temperature entering the expansion device (turbine), the amount of heat that can be added in a cycle is reduced. Hence, net work is reduced per cycle while, compressor work is increased to achieve the higher pressure. Therefore, the ratio of total compressor and turbine work to net work (size) is increased.

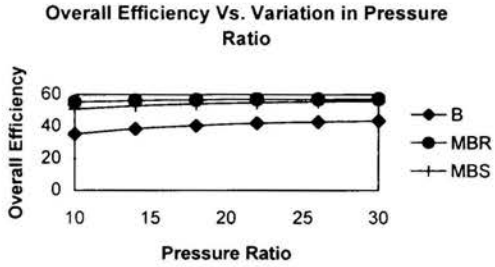

Figure 6. Overall Efficiency vs. Pressure Rat

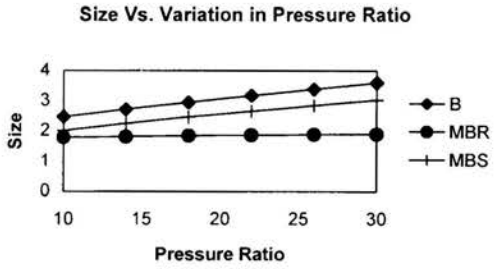

Figure 7. Size vs. Pressure Ratio

Figure 8 shows how the overall efficiency varies with turbine inlet temperature for the cycles considered. In all cases the efficiency increases with inlet temperature increase because heat transfer to the cycle occurs at a higher temperature decreasing irreversibility associated with heat transfer through a temperature difference. In all cases the potential increase is relatively small over temperature range indicated.

Figure 9 shows size versus inlet turbine temperature.

In all cases the size decreases with increasing turbine inlet temperature. Since the overall efficiency goes up with increasing inlet turbine temperature, the net work increases. The turbine inlet temperature does not affect compressor and turbine work. Therefore, the numerator in the size definition (turbine plus compressor work) is not changed but the denominator (net work) is increased thereby decreasing size.

While both efficiency and size are improved by increasing turbine inlet temperature, the effect of either change is small. Given the practical material problems posed by high temperature operation, raising turbine inlet temperature for any of these cycles is not attractive.

Figures 10 and 11 show how the overall cycle efficiency and power plant size, respectively, vary with the turbine efficiency. The results follow the expected trend- overall cycle efficiency increases and size decreases with increasing turbine efficiency for all cycles studied. Increasing turbine efficiency increases the amount of power out per unit mass while not increasing the compressor work per unit mass. Hence, more net power is obtained with less total horsepower. Hence, cycle efficiency increases and size decreases as the turbine efficiency increases.

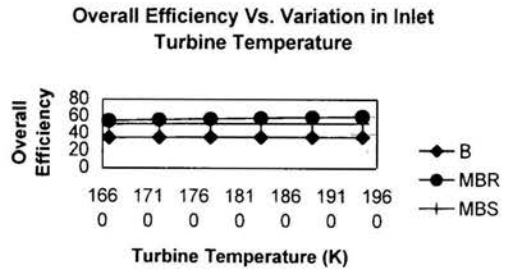

Figure 8. Overall Efficiency vs. Inlet TurbineTemperature

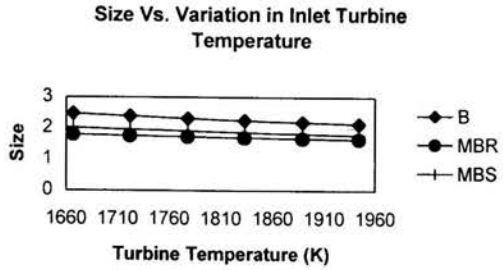

Figure 9. Size vs. Inlet Turbine Temperature

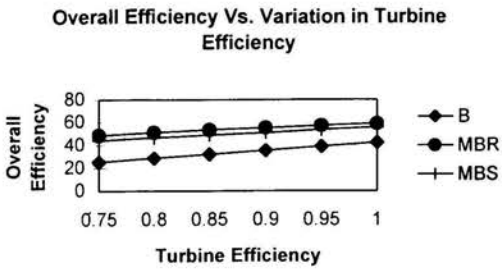

Figure 10. Overall Efficiency vs. Turbine Efficiency

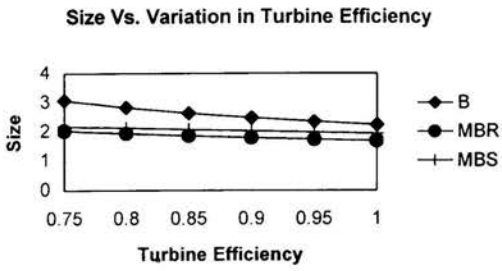

Figure 11. Size vs. Variation in Turbine Efficiency

CONCLUSIONS

Table 1 clearly shows that the use of regeneration and isothermal compression and expansion in the MBR cycle is far superior to the standard Brayton cycle. These data are calculated with current state-of-the-art conditions that will be difficult and expensive to improve. Figures 4 through 13 conclusively show for any cycle that improvements in these state-of-the-art conditions will at best only result in minor improvement in the performance of any of the cycles. Hence, this paper shows conclusively that future effort to improve the performance of stationary gas turbine power plants should concentrate on cycle characteristics (in particular regeneration and isothermal compression/expansion). Efforts to improve the Brayton cycle by use of higher cycle temperatures or improved efficiency of compressors and expanders are doomed to minimal improvement potential!

REFERENCES

[1] Harman, Richard T.C., Gas Turbine Engineering, John Wiley & Sons, New York, 1981.

[2] Bathie, William W., Fundamentals of Gas Turbines, John Wiley & Sons, New York, 1984.

[3] Sawyer, Tom R., The Modern Gas Turbine, Prentice-Hall, Inc., New York, 1947.

[4] Judge, Arthur W., Modern Gas Turbines, Jarrold & Son, LTD., Norwich, 1947.

[5] Cengal, Yunus A. & Boles, Michael A., Thermodynamics An Engineering Approach, McGraw-Hill, New York, 2000.

[6] Scott, Rodney, "An Analysis of the Direction for the Improvement of Gas Turbines", MS Thesis, Department of Mechanical Engineering, Auburn University, Auburn, AL, August 2001.

[7] Dyer, David F., Personal Communication, Auburn University, Auburn, Alabama, 2000.

HEFAT2002
1st International Conference on Heat Transfer, Fluid Mechanics and Thermodynamics
8-10 April 2002, Kruger National Park, South Africa
DM2

THERMODYNAMIC ANALYSIS OF STEAM INJECTED GAS TURBINE CYCLES

Michel De Paepe
Department of Flow, Heat and Combustion Mechanics
Ghent University
Sint-Pietersnieuwstraat 41
B 9000 Gent, Belgium
Email: Michel.Depaepe@rug.ac.be

ABSTRACT

In a STeam Injected Gas turbine (STIG) steam produced in a heat recovery steam generator, is injected into the combustion chamber. This results in a power augmentation and an efficiency gain. In this paper a detailed thermodynamic model of the steam injected gas turbine cycle is presented. This model includes turbine blade cooling and is validated on both existing simple cycle gas turbines and steam injected gas turbines. The importance of good modelling the turbine blade cooling is shown. With the model the (power output) efficiency of basic STIG-cycle as well as cycles with thermodynamic improvements as intercooling, heat recovery by heat exchanger and blade cooling using steam are studied. It is shown that steam-cooling is an interesting amelioration.

NOMENCLATURE

A heat transfer area (m^2)
c_p heat capacity (J/kgK)
f fuel to air ratio (kg/kg)
LHV Lower Heating Value (J/kg)
$\dot{m}$ mass flow rate (kg/s)
q heat per unit of mass (W/kg)
PR Pressure Ratio (-)
Q heat flux (W)
S flow area (section) (m^2)
T temperature (K)
TIT Turbine Inlet Temperature (^oC)
TOT Turbine Outlet Temperature (^oC)
u mid span rotor blade speed (m/s)
v flow velocity (m/s)
w work per unit air (J/kg)
W power (W)

Greek Symbols

α heat transfer coefficient (W/m^2K)
ε cooling effectiveness (-)
η efficiency (-)
κ cooling parameter (-)
Ψ work coefficient of a stage (-)
ρ density (kg/m^3)

Subscripts

b blade
c coolant
calc calculated
C Compressor
exp experimental - measured
g combustion gas
T Turbine

INTRODUCTION

Since the commercial introduction in the beginning of the 1980's, steam injected gas turbines have gained more importance on the power generation market. In a steam injected gas turbine the heat of exhaust gasses of the gas turbine is used to produce steam in a heat recovery steam generator. The steam is injected into the combustion chamber or between the high-pressure and low-pressure turbine (Figure 1). Steam injection allows improving the efficiency and specific power of a gas turbine.

The most common method to improve the efficiency of a simple cycle gas turbine in electric power applications consists of using the steam produced in the HRSG in a separate steam cycle with a steam turbine. This combined cycle of steam and

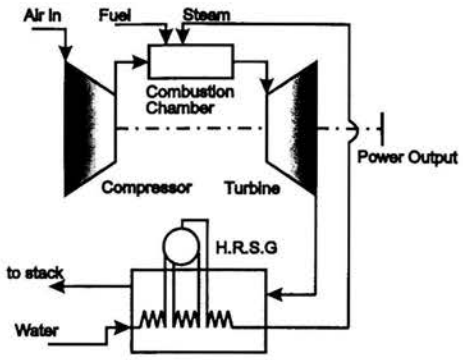

Figure 1. THE STEAM INJECTED GAS TURBINE CYCLE

gas necessitates the use of two turbines in contrast to the steam injected cycle.

Steam injected gas turbines are mostly used in co-generation applications. The regular way of operation is that steam is used for heating a process. If process steam is temporarily not required, it is injected into the gas turbine, increasing the electrical power output. A steam injected gas turbine becomes an extremely attractive system for co-generation if steam injection is possible for an extended period. The ratio of heat output to electrical power output is then completely flexible. Moreover, electrical power peak shaving is possible.

This article seeks to analyse the thermodynamic possibilities of steam injected gas turbines.

THERMODYNAMIC MODEL OF THE CYCLE

Cycle components

In Figure 1 the steam injected gas turbine cycle is represented by it's mayor components : the gas turbine and the heat recovery steam generator (HRSG). The gas turbine consists of a compressor, a combustion chamber and a turbine. The HRSG works with one pressure level and thus contains one economiser, evaporator and superheater. For every part of the cycle a calculation model was developed.

A heat balance describes each component of the HRSG. The temperatures of exhaust gas, water and steam are used as input, the steam mass flow rate is calculated. It is assumed that part of the heat released by the exhaust gasses is lost through the steam generator walls (defined by a steam generator efficiency η_{st}). The compressor is modelled by an adiabatic compression with a given polytropic efficiency ($\eta_{\infty,C}$). Given the temperatures of the air entering the combustion chamber and the exhaust gasses leaving the combustion chamber (TIT), the necessary fuel mass flow rate can be calculated. Methane (CH_4) is used as fuel. The turbine is modelled as a cooled expansion. The necessary equations are derived in the next paragraph.

Once the compression and expansion are calculated, the specific power and the thermal efficiency of the cycle can be

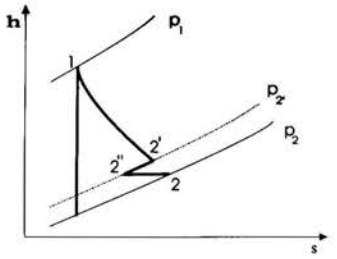

Figure 2. COOLED EXPANSION

calculated as :

$$\Delta w_{cycle} = \eta_{mech}\left(\Delta w_T - \Delta w_C\right) \tag{1}$$

$$\eta_{cycle} = \frac{\Delta w_{cycle}}{f\,\mathrm{LHV}} \tag{2}$$

Cooled expansion

The expansion process of a cooled stage is represented in a h-s diagram in Figure 2. Part 12′ is the distributed representation of the cooled expansion. Part 2′2" represents the temperature drop due to mixing of the mean gas flow and the coolant flow. The pressure drop $p_{2"} - p_2$ is the pressure loss due to mixing.

Expansion The infinitesimal efficiency (small stage efficiency - polytropic efficiency) for a turbine is defined by

$$\eta_{\infty,T} = \frac{-\delta w}{-\frac{1}{\rho}\mathrm{d}p} \tag{3}$$

The heat flux extracted from the mean flow and transferred to the coolant flow can be written for a full stage as

$$-\Delta Q = A_b \alpha \left(\bar{T}_g - T_b\right), \tag{4}$$

The power deliverd by the stage is expressed as :

$$-\Delta W = \dot{m}_g \Psi u^2. \tag{5}$$

The mass flow rate is $\dot{m}_g = \rho_g v_g S_g$. The ratio of cooling heat flux and power can be written as

$$\frac{-\Delta Q}{-\Delta W} = \left(\frac{A_b}{S_g}\right)\left(\frac{\alpha}{\rho_g v_g \bar{c}_{p,g}}\right)\left(\frac{1}{\Psi}\right)\frac{\bar{c}_{p,g}\left(\bar{T} - T_b\right)}{u^2}. \tag{6}$$

The surface ratio $\left(\frac{A_b}{S_g}\right) \approx 8$ (El-Masri, 1986). The heat transfer Stanton number $St = \frac{\alpha}{\rho_g v_g \bar{c}_{p,g}} \approx 0.005$ (El-Masri, 1986). We define

$$\kappa = \frac{A_b}{S_g} St \frac{1}{\Psi}. \tag{7}$$

With $\Psi \approx 1.2$, κ is around 0.033. Finally, for modern machines T_b can be assumed to be about 850 ^oC or 1123 K, and u is set to 275 m/s (El-Masri, 1986). By distributing the work and the

cooling heat rate over the expansion, we can assume that, on an infinitesimal basis, the following ratio holds,

$$\frac{-\delta q}{-\delta w} = \kappa c_{p,g} \frac{(T - T_b)}{u^2} \tag{8}$$

The expression is essentially the same as used by (El-Masri, 1986), though here no reference temperature is introduced in the constant κ. The coolant mass flow rate needed for a stage can be estimated from

$$-\Delta Q = \dot{m}_c c_{p,c} \varepsilon (T_b - T_c). \tag{9}$$

It is assumed that the maximum temperature increase of the coolant flow is from the coolant temperature at inlet T_c to the blade temperature T_b. For internal flow cooling the effectiveness ε can be around 0.5. For film cooling it can reach unity because the cooling flow is brought to the outside of the vanes and the blades, continuing the cooling till the blade temperature is reached.

Mixing of the coolant The final temperature $T_2 = T_{2''}$ can be obtained from the global energy balance

$$\dot{m}_g c_{p,g1} T_1 + \dot{m}_c c_{p,c} T_c = (\dot{m}_g + \dot{m}_c) c_{p,g2} T_2 - \dot{m}_g (-\Delta w) \tag{10}$$

The subscripts are added to the heat capacities to indicate the temperature dependence.

Assuming that the coolant flow does not impart momentum to the mean flow while mixing, the momentum reduction of the mean flow per unit time is $v\dot{m}_c$, where v is a mean flow velocity at mixing. The corresponding pressure loss is $-\mathrm{d}p$. So

$$-\frac{\mathrm{d}p}{p} = \frac{\dot{m}_c}{\dot{m}_g} \rho \frac{v^2}{p} = \frac{\dot{m}_c}{\dot{m}_{rg}} \gamma M^2. \tag{11}$$

Since mixing happens in the vicinity of the trailing edge of the vanes and the blades, this Mach number is assumed to be $M = 0.8$ (El-Masri, 1986).

Solution method To calculate the expansion through the turbine, the global pressure drop is subdivided into intervals of 1 bar. A pressure interval corresponding to $p_1 - p_2$ in Figure 2 is considered a stage. This fictitious stage has a smaller pressure drop than a stage in reality. In a first iteration the pressure difference is taken to be equal to $p_1 - p_2$. This pressure drop is subdivided into ten intervals. This is done to take into account the variation of the heat capacity with the temperature. For each subinterval the energy equation is written as

$$-\delta w = -c_{p,g} \mathrm{d}T = \eta_\infty \left(-\frac{R_g T \mathrm{d}p}{p} \right) \left(1 + \kappa c_{p,g} \frac{T - T_b}{u^2} \right) \tag{12}$$

Equation (12) is integrated as

$$T_{2'} = T_1 \frac{\left(1 - \frac{\kappa}{u^2} c_{p,g} T_b\right) \left(\frac{p_{2'}}{p_1}\right)^{\frac{R_g \eta_\infty}{c_{p,g}} \left(1 - \frac{\kappa}{u^2} c_{p,g} T_b\right)}}{\left(1 - \frac{\kappa}{u^2} c_{p,g} T_b\right) + \frac{\kappa c_{p,g} T_1}{u^2} \left(1 - \left(\frac{p_{2'}}{p_1}\right)^{\frac{R_g \eta_\infty}{c_{p,g}} \left(1 - \frac{\kappa}{u^2} c_{p,g} T_b\right)}\right)} \tag{13}$$

The work is obtained from Equation (12)

$$-\Delta w = \frac{u^2}{\kappa} \ln \left(\frac{1 + \kappa c_{p,g} \frac{(T_{2'} - T_b)}{u^2}}{1 + \kappa c_{p,g} \frac{(T_1 - T_b)}{u^2}} \right) \tag{14}$$

The heat transferred to the coolant flow is

$$-\Delta q = c_{p,g} (T_1 - T_{2'}) - (-\Delta w) \tag{15}$$

In the previous expressions $c_{p,g}$ is taken to be constant in the subinterval and equal to the value at T_1. In a first iteration the air flow rate entering the combustion chamber is set equal to 90 % of the air flow rate at the entrance of the compressor. With this flow rate the fuel flow rate necessary to obtain the prescribed TIT is calculated. The heat capacity and the gas constant for the first stage are determined using this preliminary gas composition. After each stage, coolant flow is added, changing the gas composition. New values of c_p and R are calculated. The results from the subintervals are added, giving the total transferred heat which determines by (9) the coolant mass flow rate necessary to cool the fictitious stage. The coolant flow is taken from the compressor at the pressure and temperature corresponding to p_1. The final temperature of the stage T_2 is obtained from (10). The pressure drop follows by (11). This pressure drop is taken into account in the next iteration of the calculation of the expansion path trough the turbine. The procedure given above is repeated for the following stages, until an entrance temperature is reached lower than T_b. From then on the calculations are continued without cooling, i.e. using forgoing expressions with $\kappa = 0$.

After finishing the calculations of the expansion, the air flow rate needed for cooling is subtracted from the compressor mass flow rate and a new fuel mass flow rate is determined. The calculation of the expansion path through the turbine is repeated until convergence is reached. After completing the calculation of the expansion, the work absorbed by the compressor is calculated taking the coolant flow extraction into account.

The results of the cycle calculation do not depend much on the choice of the pressure difference over a fictitious stage, provided that this difference is small enough. For $\Delta p = 1\,bar$, the influences on efficiency, specific power, coolant mass flow ratio and turbine outlet temperature are below 0.002, 1%, 0.001 and 1 K. In the same way the results do not depend much on the number of subintervals provided that this number is high enough. With ten subintervals the influence on the results is lower than the tolerances given above.

Component efficiencies

Table 1 shows the characteristic values used in the computation of the cycles. The efficiencies are typical for large axial gas turbines (Wilson, 1991). The pressure drop over the combustion chamber is taken from (Bolland et al., 1993). The pressure drops at inlet and in the stack are taken from (de Biasi, 1990). The temperature difference between superheated

polytropic compressor efficiency ($\eta_{\infty,C}$)	91 %
polytropic turbine efficiency ($\eta_{\infty,T}$)	88.5 %
combustion efficiency	99 %
steam generator efficiency (η_{steam})	96 %
mechanical efficiency (η_{mech})	98 %
pressure drop steam generator	0.0125 bar
pressure drop combustion chamber	4%
pressure drop inlet	0.01 bar
pressure drop stack	0.01 bar
atmospheric conditions	1.013 bar, 15 ^oC, φ=60%

Table 1. CHARACTERISTIC VALUES FOR THE SIMULATION

steam and turbine outlet is set to the 40 ^oC (Paren, 1992). The gas outlet temperature of the steam generator is calculated by taking the pinch point temperature difference at 10 ^oC with a steam pressure level of 3 bar above the gas pressure level in the combustion chamber.

VALIDATION OF THE MODEL

The model has been verified for four gas turbines in simple cycle : the GEC-ALSTHOM/GE MS 9001F (Brandt et al., 1991), the ABB GT13E2 (N.N., 1992), the Westinghouse 501F (N.N., 1995), and he GE LM 6000 (de Biasi, 1990) (Table 2).

	9001F	GT13E2	501F	LM6000
TIT (^oC)	1260	1100	1288	1245
PR	13.5	15	15	29.5
ε	0.55	0.55	0.7	1
η_{exp}(%)	34.8	35.7	36.0	41.5
η_{calc}(%)	34.76	35.24	36.04	41.31
TOT_{exp}(^oC)	583	525	584	452
TOT_{calc}(^oC)	584.3	522.4	583.7	450.5
w_{exp} (kJ/kg)	353.7	318.2	371.6	345.0
w_{calc}(kJ/kg)	352.2	316.2	373.2	349.0

Table 2. VALIDATION ON 4 GASTURBINES

The cooling parameters in the model have been adjusted to obtain the best possible correspondence for efficiency, TOT and specific power. The results for efficiency and TOT are significantly influenced by the compressor and turbine efficiencies. The values given in Table 2 were found to give the best results. The corresponding cooling effectiveness for the LM6000 is found to be 1. This is more or less arbitrary. Essentially the same result can be obtained with a lower value of κ and a lower value of ε, provided that the ratio $\frac{\kappa}{\varepsilon}$ is kept constant. For the GT13E2 T_b was set to 800 ^oC, as the GT13E2 is older.

For two different steam injected gas turbines enough data was obtained to be able to calculated the thermodynamic cycle, with and without steam injection : the Kawasaki MA-13-CC and the GE LM2500 (Table 3). The polytropic efficiencies of compressor and turbine were adjusted to obtain the best possible correspondence for efficiency, TOT and specific power, without steam injection. Then the steam injected cycle was calculated with these efficiencies, giving a good prediction of efficiency, TOT and specific power in both cases. The steam mass flow is not calculated, but taken out of the experimental data. The results are shown in Table 3.

	MA-13-CC		LM2500	
	Simple	Injected	Simple	Injected
TIT (^oC)	1010	1010	1230	1230
PR	7.7	8.9	18.4	21.6
$\frac{\dot{m}_{steam}}{\dot{m}_{air}}$	0	0.187	0	0.070
$\eta_{\infty,C}$	0.74	0.74	0.89	0.89
$\eta_{\infty,T}$	0.86	0.86	0.86	0.86
κ	-	-	0.033	0.033
ε	-	-	0.9	0.9
η_{exp} (%)	22.1	33.7	35.7	39.0
η_{calc}(%)	21.9	33.6	35.4	38.5
TOT_{exp} (^oC)	575	579	529	510
TOT_{calc} (^oC)	577	571	526	507
w_{exp} (kJ/kg)	180.1	344.8	325.4	390.5
w_{calc} (kJ/kg)	177.7	347.1	319.0	390.1

Table 3. STEAM INJECTED GAS TURBINES

IMPORTANCE OF THE COOLING MODEL

In Figure 3 the carpet-plot of efficiency as a function of specific power is shown for PR from 10 to 35 and variable TIT for the simple cycle gas turbine with and without cooling. For TIT=1100 ^oC the efficiency for the cooled turbine is about 0.5 % points lower than for the non-cooled cycle. The specific power is some 10 % lower.

For higher TIT this difference gets bigger. This is caused by the need for more coolant, reducing the work extracted in the turbine. For TIT=1400 ^oC the difference is 25 % for specific power. This efficiency difference is 2.5 % points for low PR and 3.5 % points for high PR. This clearly shows the effects of blade cooling and the necessity of modelling it.

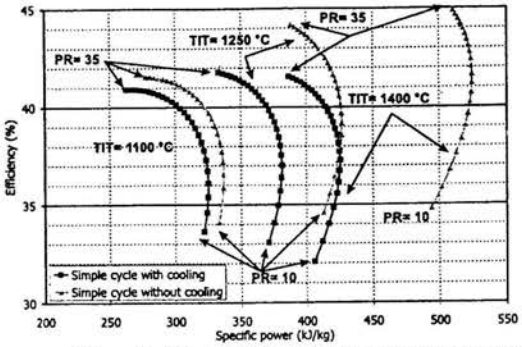

Figure 3. IMPORTANCE OF THE COOLING MODEL

COMPARISON BETWEEN SIMPLE, STEAM INJECTED, COMBINED AND INTERCOOLED REGENERATED CYCLE

In Figure 4 the results of the calculations for the simple cycle, the steam injected gas turbine cycle, combined cycle and intercooled regenerative cycle are put together. The cycle efficiency is displayed as a function of the specific power. Pressure ratio is varied from 10 to 35, TIT is set to 1100 ^oC, 1250 ^oC and 1400 ^oC. The cooling parameters are $\varepsilon = 1$, $\kappa = 0.0333$, $u = 275m/s$ and $T_b = 850^oC$, corresponding to a gas turbine with advanced film cooling.

For the combined cycle the steam cycle efficiency is set to 38 % corresponding with a three pressure level steam generator (Paren, 1992).

With the state of the art gas turbine technology the steam injected gas turbine cycle can reach a maximum efficiency of 49.5 %. The simple cycle can reach 41.5 %. Due to the extra mass flow in the turbine, specific power augments up to 750 kJ/kg, which is 60 % more than the simple cycle.

The combined cycle can reach an efficiency of 58.5 % with comparable assumptions as for the steam injected cycle. Specific power of a steam injected cycle can get higher. An intercooled regenerative cycle can reach an efficiency of 48.9 %. The specific power is smaller than for the steam injected cycle.

STEAM INJECTED GAS TURBINES WITH HEAT EXCHANGERS

In Figure 5 the carpet plot is shown for the STIG-cycle with added heat exchangers, for PR from 10 to 35 and TIT=1250 ^oC. For different TIT's the results are essentially the same.

Adding an intercooler to the steam injected gas turbine-cycle gives no amelioration of efficiency. By adding intercooling, the work of the compressor is reduced, but the temperature of the air is lowered, resulting in a higher fuel mass flow rate. The combination of all these effects results in no gain in efficiency of the steam injected cycle. These results are in accordance with the results found by Macchi et al. (1994). Specific

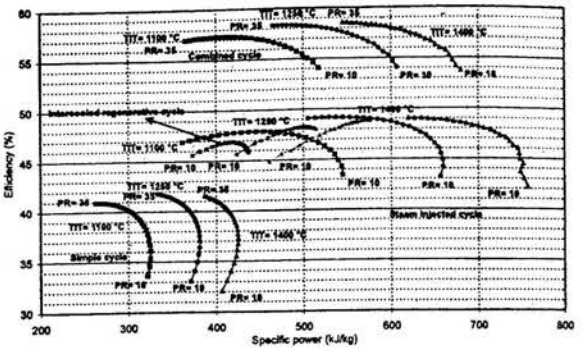

Figure 4. SIMPLE CYCLE, STIG, COMBINED CYCLE AND INTERCOOLED REGENERATIVE CYCLE

power is almost constant for the range of PR. There is a gain of about 10 % compared to the basic steam injected cycle for low PR and about 50 % for high PR.

By adding a heat exchanger between the gas turbine outlet and the steam generator inlet, a small efficiency gain can be made comparing to the steam injected cycle. In Figure 5 the results are presented for a regenerator effectiveness of 0.7 and pressure drops at the air side and gas side of 0.02 bar. The pressure drop in the intercooler is set to 0.025 bar. Lowering the effectiveness of the regenerator, thus making more heat available for the steam generator, lowers the efficiency. For TIT=1250 ^oC and PR=30 and effectiveness 0.7, 0.5, 0.25 and 0, the corresponding efficiencies are 49.7, 49.0, 48.3 and 47.8 %. This can be understood by considering that adding heat to the air leaving the compressor directly reduces the amount of fuel needed to obtain TIT, leaving the work output unaffected. Producing more steam gives a raise in work output, but also a raise in fuel consumption, thus resulting in a smaller efficiency gain. The specific power is in the same order as with the simple steam injected cycle, though it does not reduce with raising PR. Comparable results were obtained by (Bolland et al., 1993), though they propose the far more complex DRIASI-cycle (dual-regenerative intercooled aftercooled steam injected

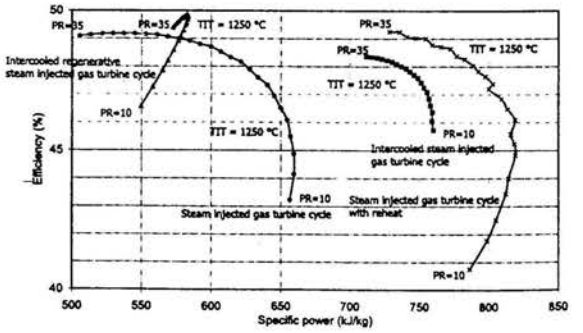

Figure 5. INTERCOOLED STIG, INTERCOOLED REGENERATIVE STIG AND STIG WITH REHEAT

cycle), which uses water injection.

Adding sequential combustion to a gas turbine, i.e. expanding the combustion gas in the first stage of the turbine and then reheat it to original TIT, has as a result that the TOT raises. The efficiency of a simple cycle decreases because of the extra fuel consumption. Specific power augments. In a steam injected cycle more steam is produced by implementing sequential combustion. This results in an increase in work output but a loss in efficiency. The loss in efficiency can be explained by the need for more coolant flow in the reheat cycle: the steam mass flow rate has risen and by adding reheat more stages have to be cooled. For low TIT these effects are less pronounced, resulting in a small efficiency gain.

It is practically not useful to add an intercooler or a regenerator to the steam injected cycle. Only a very small efficiency gain can be obtained at the expense of a large increase in system complexity. Adding reheat in a steam injected cycle is in general not beneficial where efficiency is the main concern.

STEAM COOLED STEAM INJECTED GAS TURBINE

Instead of using the compressor air as coolant fluid for the vanes and blades, it is possible for a steam injected cycle to use a part of the produced steam. By doing this the efficiency loss associated to the use of cooling air extracted from the compressor is avoided. A further beneficial effect is that the amount of steam to be injected in the combustion chamber is reduced.

In Figure 6 the steam cooled STIG is compared with the steam injected cycle. A steam cooled steam injected cycle gives a significant gain in efficiency and only a small change in specific power. For TIT=1250 ^oC an efficiency of 51 % can be obtained, for TIT=1400 ^oC even more than 52 % is possible. For the calculation of the cooling, the same cooling parameters have been used as mentioned before. The calculations showed that in all working points more steam is produced than needed for the cooling. This extra amount of steam is then injected into the combustion chamber. In the simulation all steam is produced at a pressure equal to combustion chamber pressure plus 3 bar. The efficiency gain obtained by steam cooling is not very high. The basic reason is that steam is now injected into the gas path at pressures lower than the combustion chamber pressure, resulting in a lower power production.

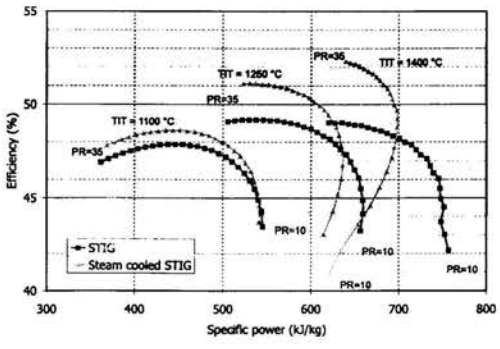

Figure 6. STEAM COOLED STIG

For low PR and high TIT the specific power diminishes significantly compared to the simple steam injected cycle. This is because in this case almost all the produced steam is used for cooling the turbine blades and vanes, resulting in a smaller work production of the steam. For higher PR this effect is reduced.

CONCLUSION

The previous study shows that a steam injected gas turbine can be very attractive for electric power applications and cogeneration. For the basic steam injected cycle configuration, the efficiency can be about 49 %. Specific power is raised with about 60 %. This confirms what is generally accepted to be the performance of the steam injected gas turbine.

Adding intercooling, regeneration or reheat to the simple steam injected cycle ameliorates the efficiency, but the gain is not worth the complication of the cycle.

Using steam as coolant fluid for the steam injected cycle is a relatively simple modification, which augments the efficiency to about 52 %. This is an attractive amelioration.

REFERENCES

Bolland, O. and Stadaas, J.F., Comparative Evaluation of Combined Cycles and Gas Turbine Systems with Water Injection and Recuperation, International Gas Turbine & Aeroengine Congress, Paper No. 93-GT-57,1993.

Brandt, D.E. and Colas, M., MS9001F A new advanced Technology 50 Hz Gas Turbine, GEC ALSTHOM Technical Review, 1991.

de Biasi, V., LM6000 dubbed the 40/40 machine due for full-load tests in late 1991, Gas Turbine World, 16–20, May-June, 1990.

El-Masri, M.A., On Thermodynamics of Gas Turbine Cycles : Part 2 - A Model for Expansion in Cooled Turbines, Journal for Engineering for Gas Turbines and Power, 108,151-159, January 1986.

Macchi E., Consonni S., Lozza G., Chiesa P., An assessment of the thermodynamic performance of mixed gas-system cycles: Part a: Intercooled and steam-injected cycles, Proceedings of ASME-IGTI TURBO, The Hague (Netherlands), ASME 94-GT-423, 1994.

Paren, J. and Parietti, C., Combined Cycle Plants Three-Pressure Reheat VEGA 109F, GEC ALSTHOM Technical Review, 1992.

Wilson, D.G., The Design of Gas Turbine Engines,IGTI home study course, IGTI, 1991.

N.N., GT13E An improved, high Efficiency and low-emission Gas Turbine, Asea Brown Bovery,ABB publication CH-KW 2069 92 E, 1992.

N.N., 501G Raising the Combustion Technology to the next Power, Westinghouse Electric Corporation Description of the WE 501 series, 1995.

HEFAT2002
1st International Conference on Heat Transfer, Fluid Mechanics, and Thermodynamics
8-10 April 2002, Kruger Park, South Africa
GZ1

GENERALISED CORRELATIONS FOR DETERMING HEAT TRANSFER IN TURBINE ROTOR–STATOR SYSTEMS

Z. Guzović*, B. Matijašević** and Ž. Tuković***
*Assistant Professor; ** Professor; *** Assistant
Faculty of Mechanical Engineering and Naval Architecture, University of Zagreb,
Lučićeva 5, HR-10000 Zagreb,
Croatia
E-mail: zvonimir.guzovic@fsb.hr; branimir.matijasevic@fsb.hr; zeljko.tukovic@fsb.hr

ABSTRACT

For the solving of different problems in designing of new and exploitation of the existing steam and gas turbines it is necessary to perform the calculation of heat transfer on disc surfaces (i.e. on rotor surfaces) and for this the values of convective heat transfer coefficients have to be known. The latter are most frequently determined on the basis of correlations obtained by means of experimental measurements, often without checking the possibility of their application in the individual case. In literature, there is a definite number of empirical correlations proposed by various researchers, which are mutually distinguished with regard to the range of change of the geometrical and gas-dynamics parameters and with regard to choosing physical properties. All this makes their application more difficult.

Therefore, in the paper, the systematisation of empirical correlations from literature is performed first, and after that the original generalised correlations are proposed obtained by means of statistical analysis of calculation results by systematised single correlations. The original generalised correlations proposed in the paper ensure accuracy of calculations which satisfy engineering applications.

INTRODUCTION

The first typical designing problem faced by the engineers involved in the design of steam turbines today, and especially for high temperature gas turbines, are temperature stresses, which are particularly high at transient working regimes, and the related useful life of turbine discs (of rotors). The flow of the working fluid of high temperature through the sealing clearance in the space between turbine discs and the corresponding stator elements can cause their overheating which causes shortening of their useful life [1]. The second problem is optimisation of air flow for cooling at cooled turbine discs [2]: excessive air reduces the isentropic efficiency while insufficient air can lead to catastrophic damages and fractures. The third problem is determination of power losses due to ventilation and friction of disc which causes the air flow for cooling [2]. For effective and reliable solution of previous problems it is necessary to determine the temperature field of discs (i.e. of rotors) for turbine working range, which requires the knowledge of local or average values of convective heat transfer coefficients, depending on the required accuracy of calculations.

The various systems exist by which the heat transfer on surfaces of steam and gas turbine rotors is modelled. First, it is the heat transfer on single disc which rotates in free space, i.e. free rotating disc (Fig.1a), and heat transfer on disc rotating close to stationary wall or between stationary walls, i.e. rotor-stator systems, which can be closed (Fig. 1b), open (Fig. 1c) and shrouded (Fig. 1d). The rotor-stator systems are distinguished with regard to the dimension of clearance between disc and stationary walls (large or small), presence or absence of the superposed flow in clearance, and in case of presence, how it is directed (from centre to periphery or vice versa). For all cases there is the heat transfer in laminar and turbulent regions, in dependence on the flow regime in the boundary layer on disc.

The simplest is the case of heat transfer on the free rotating disc for which there exists the exact solution of Navier-Stokes equations, while the cases of heat transfer on disc rotating between stationary walls are more complex [3].

Heat transfer by radial flow in the clearance between rotating discs and stationary diaphragms is most frequent in many designs of steam and gas turbines [3].

The shrouded system is obtained when the cylindrical shroud is added on the stator of the open system, e.g. the labyrinth seals in gas turbines which prevent inflow of cooling air in the space of working fluid (of hot gases), i.e. of working fluid in space around disc [3].

Along with the systems represented in Fig. 1 the cases of co-rotating discs and discs with rotating deflector are very frequent in gas turbines [3].

Heat transfer on disc surfaces is determined by Reynolds number, and at rotor-stator systems additionally by flow vortex which depends on the large number of geometrical and flow parameters (e.g. about the relative clearance between rotor and stator, conditions on neighbouring walls, fluid flow through clearance, initial vortex (pre-swirl), etc.) [3]. In real conditions, with

steam and gas turbines in case of rotating disc the Reynolds numbers are high and the flow is markedly turbulent [2].

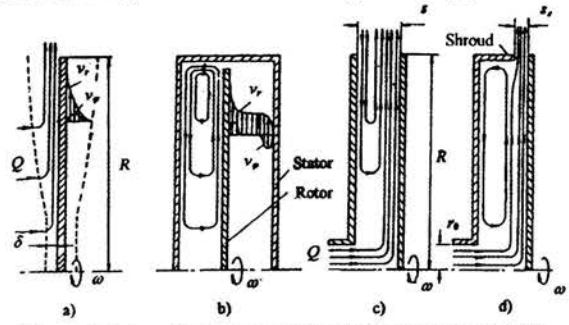

Figure 1: Schematic Representation of Free Rotating Disc (a), Closed Rotor-Stator System (b), Open Rotor-Stator System (c) and Shrouded Rotor-Stator System (d)

In general, the convective heat transfer coefficients can be determined on the basis of experimentally obtained dependencies (correlations), then by analytical methods and more recently by numerical methods as well [2, 3, 4].

Also, the tendency is still present that simple exponential equations (correlations) of type $\mathrm{Nu}_{av} = c\,\mathrm{Re}^{n}$ are used in the engineering practice for calculation of the average convective heat transfer coefficients [5]. Further text refers precisely to these.

NOMENCLATURE

e	base of natural logarithms
K_v	kinematic factor (-)
$\dot{m}$	mass flow (kg/s)
Nu	Nusselt number
Pr	Prandtl number
Q	volume rate of flow (m^3/s)
$\overline{Q}$	relative volume rate of flow [$\dot{m} / \rho\omega R^3$] (-)
R	outer radius of disc (m)
r	current radius of disc (m)
$\bar{r}$	relative radius (-)
Re	Reynolds number
s	clearance width (m)
$\bar{s}$	relative clearance (-)
T	temperature (K)
ΔT	temperature difference [T_d-T_f] (K)
v	velocity (m/s)

Greek Letters

β_φ	flow vortex (-)
δ	thickness of boundary layer (m)
ρ	density (kg/m^3)
ω	angular speed of disc (s^{-1})

Subscripts

av	average
c	shroud
d	disc
f	fluid
r	radial component
s	clearance
φ	rotational; tangential component
0	hub radius
1	starting radius
2	final radius

CHARACTERISTICS OF EXPERIMENTAL INVESTIGATIONS AND SINGLE CORRELATIONS FROM LITERATURE

In experimental investigations of heat transfer on lateral surfaces of the disc (of the rotor) the basic methodical difficulties appear in determining the heat flux which is transferred on the respective section of the disc radius [6, 7, 8, 9]. In the better case, when using the discs with lateral annular electrical or water surface heaters, it is possible to ensure measurement of heat amount which is transferred on the section no less than 15% of the radius. When using discs with internal electrical heaters or heat supply to disc over the cylindrical surface the limitation is usually the measurement of total amount of heat which participates in the heat transfer. The local values of heat transfer coefficients are sometimes determined by indirect method of heat conduction [10, 11].

Also considerable difficulties are caused by determining fluid temperature, which is used to calculate the heat transfer coefficient. In laboratory conditions it is ensured that the stator surface against disc is adiabatic, and the values of heat transfer coefficients are determined according to the difference of disc temperature and fluid temperature in the centre of the clearance on the given radius [7, 12, 13, 14]. In some investigations of heat transfer in rotor-stator systems with superposed flow, values of the heat transfer are determined according to the difference of disc temperature on the definite radius and fluid temperature at the clearance entrance [11]. In case of the indirect method of heat conduction for rotors of real turbines the heat transfer coefficient values are usually determined according to the difference of disc temperature and average fluid temperature in the clearance on the given radius [10]. The values of the latter are determined by calculation.

The reliability of the single used experimental method of the majority of investigators is checked by calculation of heat transfer on the free rotating disc for which there are theoretical solutions for laminar and turbulent boundary layer [4].

The experiments [6, 8, 9, 14, 15, 16, 17, 18] on the free rotating disc are performed by using electrical, water and discrete calorimeters. The experiment results agree well with the theoretical solution.

In all the experimental investigations of heat transfer on disc surfaces of open rotor-stator systems without superposed flow in clearance [7, 12, 13, 14], the obtained maximal values of the Reynolds numbers are lower than at modern stationary gas turbines (up to 10^7) and jet engines (up to $4*10^7$) [3]. The results of investigations indicate the presence of core with constant angle velocity and temperature in the centre of the clearance [7, 12]. Some of the correlations describe the heat transfer only in the central part of the disc [7, 12, 13]. Simultaneously, in the region of the disc hub and especially on its periphery the intensification of heat transfer has been observed, related to the phenomenon of three-dimensional flow in boundary layers. Data about the dependence of clearance width on heat transfer in open rotor-stator systems without superposed flow are contradictory [7, 12, 13, 14].

The air inflow (i.e. the existence of the superposed flow) in the clearance of opened rotor-stator systems results in considerable decrease of the critical Reynolds number. In investigations of heat transfer on disc surfaces, cooled by air flow directed to periphery of the disc, the values of heat transfer coefficients are determined both on laboratory experimental devices and by indirect method of heat conduction for rotors under conditions relatively close to the real ones [7, 10, 13, 19, 20, 21]. Essential dependence of heat transfer on the manner of air introduction into the clearance is noticeable: the pre-swirl of flow on the clearance entrance, presence of holes for air supply, etc., increase the heat transfer [7, 9, 13]. In some experiments [7, 9, 13] considerable decrease of heat transfer was observed with the increase of air flow through the clearance, while in case of others [10], the dependence of heat transfer coefficients on air flow has not been generally observed.

The presence of shroud in shrouded rotor-stator systems has two effects: on rotating disc it stipulates high shear stress due to viscous friction and it reduces amount of fluid which gets to the disc [2]. The first effect increases the Nusselt number while the second effect decreases the coefficient of the friction moment and with this the Nusselt number. Due to the second effect there exists the value of relative clearance up the shroud at which the Nusselt number obtains the minimal value. It will increase further with the decrease of relative clearance up the shroud. With lower values of the rotational Reynolds number the weaker influence of rotation on heat transfer is observed, which needn't be the case with real turbines. Investigations of heat transfer in shrouded rotor-stator systems are of the more recent date and are mostly investigated by numerical methods while the relatively few experiments serve only for determining of mutual influences of the geometrical and flow parameters and for the final confirmation of numerical results [2].

In all investigations of heat transfer on disc with rotating deflector the characteristic change of heat transfer coefficient along the radius by constant superposed air flow for cooling and rotational speed is observed [22, 23, 24]. The heat transfer shows considerable dependence on the design of element for introduction of air into the clearance. The values of heat transfer coefficients on the disc with rotating deflector depend slightly on the superposed air flow through clearance and they increase considerably when the radial velocity of flow exceeds 7 to 10 times the tangential velocity of disc. The dimension of the clearance between discs influences heat transfer after connecting the boundary layers. Further decrease of the clearance width leads to considerable decrease of heat transfer on disc surfaces, which is related to the increase of superposed flow vortex.

The basic qualitative difference between heat transfer on the stationary wall and the opposite rotating disc surface is stipulated by different absolute magnitudes of tangential components of velocity on the external and internal boundary of the boundary layer [3, 13, 14].

SYSTEMATISATION OF SINGLE CORRELATIONS

Everything that has been mentioned here complicates the practical usage of the collected experimental materials. Therefore, Guzović [5] systematises first the single correlations from the available literature into five groups:

1st group: correlations for calculating the average Nusselt numbers (of the average heat transfer coefficients) on the free rotating disc (Table 1);

2nd group: correlations for calculating the average Nusselt numbers (of the average heat transfer coefficients) in open rotor-stator system without superposed flow (Table 2);

3rd group: correlations for calculating the average Nusselt numbers (of the average heat transfer coefficients) in open rotor-stator system with superposed flow directed to periphery of the disc (Table 3);

4th group: correlations for calculating the average Nusselt numbers (of the average heat transfer coefficients) on the disc with rotating deflector i.e. on co-rotating discs (Table 4);

5th group: correlations for calculating the average Nusselt numbers (of the average heat transfer coefficients) on the stationary wall opposite the rotating disc (Table 5).

The tables also present the application scopes of the flow and geometrical characteristics for which the application is recommended.

The work [5] also describes in detail the single experiments.

Table 1: The Single Correlations for Calculating the Average Nusselt Numbers on the Free Rotating Disc

References	Correlations	Application ranges		Distribution of ΔT along radius
		$Re_\varphi * 10^{-5}$	r/R	
Cobb and Saunders [8]	$Nu_{av} = 0{,}015 Re_\varphi^{0.8}$	4-13	0,57-0,81	const.
Richardson and Saunders [15]	$Nu_{av} = 0{,}0138 Re_\varphi^{0.8}$	-	-	-
Kapinos [9]	$Nu_{av} = 0{,}027 Re_\varphi^{0.804}$	25-40	0,38-0,9	$\approx \bar{r}^3$
Nikitenko [14]	$Nu_{av} = 0{,}0194 Re_\varphi^{0.8}$	3,2-9	0,3-0,8	const.
Kapinos *et al.* [6]	$Nu_{av} = 0{,}0196 Re_\varphi^{0.8}$	3-10	0,3-0,85	const.
Gregory and Walker [16]	$Nu_{av} = 0{,}0145 Re_\varphi^{0.8}$	0,35-7	-	-
McComas and Hartnett [17]	$Nu_{av} = 0{,}0198 Pr\, Re_\varphi^{0.8}$	0,2-6	-	-
Owen *et al.* [18]	$Nu_{av} = 0{,}0171 Re_\varphi^{0.814}$	2-40	-	-

Table 2: The Single Correlations for Calculating the Average Nusselt Numbers in Open Rotor-Stator System without Superposed Flow

References	Correlations	Application ranges			Distribution of ΔT along Radius	β_φ
		$Re_\varphi * 10^{-5}$	s/R	r/R		
Mironov [12] and [13]	$Nu_{av} = 0{,}011\left(\frac{1}{\beta_\varphi} - 1\right)^{0,8} Re_\varphi^{0,8}\left(\frac{R}{r}\right)^{-m}\left(\frac{s}{R}\right)^{-0,2}$ *m*- from diagram	2-40	0,011-0,067	0,445-0,935	$\approx \bar{r}^{1,75}$	0,38–0,48
Nikitenko [14]	$Nu_{av} = 0{,}0217\, Re_\varphi^{0,8}$	3,5-10	0,02-0,07	0,3-0,8	Const.	0,44–0,5
Kuznecov [7]	$Nu_{av} = 0{,}024\left(1-\beta_\varphi\right)^{0,75} Re_\varphi^{0,8}$	0,9-12	0,011-0,027	0,57-0,81	$\approx \bar{r}^{0,2}$	

Table 3: The Sinle Correlations for Calculating the Average Nusselt Numbers in Open Rotor-Stator System with Superposed Flow Directed to Periphery of the Disc

References	Correlations	Application ranges			Distribution of ΔT along radius	β_φ
		$Re_\varphi * 10^{-5}$; (Kv_1)	s/R	r/R		
Caplin [19]	$Nu_{av} = 0{,}015^{0,8}\, Re_\varphi^{0,8} - \frac{0{,}636 * 10^5}{Re_\varphi^{0,5}}$	2,5-10	0,05-0,15	-	-	-
Caplin [19]	$Nu_{av} = \left(0{,}015\, Re_\varphi^{0,8} - \frac{0{,}636 * 10^5}{Re_\varphi^{0,5}}\right) * \left[\left(\frac{\overline{Q}}{2{,}5 * 10^{-2}}\right)^{0,2} + \left(\frac{\frac{s}{R}}{5 * 10^{-2}}\right)^{0,155} - 1\right]$	2,5-10	0,03-0,1	-	-	-
Kapinos [20] and [21]	$Nu_{av} = 0{,}0346\, Re_\varphi^{0,8}\, K_{v_1}^{-0,1}\left(\frac{R_1}{R_2}\right)^{0,3}\left(\frac{s}{R_2}\right)^{0,06}$	5-35 (0,6-7)	0,016-0,064	0,38-0,46	$\approx \bar{r}^{3}$	-
Mirnov [13]	$Nu_{av} = 0{,}011c\left(\frac{1}{\beta_\varphi} - \varphi\right)^{0,8} Re_\varphi^{0,8}\left(\frac{R_2}{r}\right)^{-m}\left(\frac{s}{R_2}\right)^{-0,2}$ *c*, φ - from diagrams	2-40 (6-260)	0,011-0,067	0,94-0,45	$\approx \bar{r}^{1,75}$	0,18-0,22
Kuznecov [7]	$Nu_{av} = 0{,}0235\left(1+c^2\right)^{\frac{3}{8}}\left(1-\beta_\varphi\right)^{0,75} Re_\varphi^{0,8}$	0,9-20 (2,5-210)	0,027-0,11	0,57-0,81	const.	-
Oprecht [10]	$Nu_{av} = 0{,}03\, Re_\varphi^{0,8}$	(10-100)	-	-	$\approx \bar{r}^{3}$	-
Kapinos [20]	$Nu_{av} = 0{,}035\, Re_\varphi^{0,7}\, Re_s^{0,1}\left(\frac{R_1}{R_2}\right)^{0,3}\left(\frac{2s}{R_2}\right)^{1,06}$	5-40	0,008-0,0375	-	-	-

Table 4: The Single Correlations for Calculating the Average Nusselt Numbers on the Disc with Rotating Deflector i.e. on Co-Rotating Discs

References	Correlations	Application ranges			Distribution of ΔT along radius	β_φ
		$Re_\varphi*10^{-5}$; (Kv_1)	s/R	r/R		
Buznik [22]	$Nu_{av} = 0{,}0339\,Re_\varphi^{0,8}\, e^{-0{,}148 K_v}$	0,1-2,5 (0,1-4,8)	-	0,94-0,34	$\bar{r}^{-0,6}$	0-0,65
Buznik *et al.* [23]	$Nu_{av} = 0{,}059\,Re_\varphi^{0,8}\, V \left(\frac{s}{R}\right)^{\frac{1}{3}}$ V- from diagram	0,6-10 (2-6)	0,015-0,06	0,86-0,33	≈ const.	0,2–6
Kapinos [24]	$Nu_{av} = 0{,}0235\,Re_\varphi^{0,8}\, V$	0,6-10 (2-6)	>0,06	0,86-0,33	≈ const.	0 – 0,2

Table 5: The Single Correlations for Calculating the Average Nusselt Numbers on the Stationary Wall Opposite the Rotating Disc

References	Correlations	Application ranges			Distribution of ΔT along radius	β_φ
		$Re_\varphi*10^{-5}$; (Kv_1)	s/R	r/R		
Shvec [3]	$Nu_{av} = 0{,}025\,Re_\varphi^{0,8}\,\beta_\varphi^{0,8}(n+2{,}6)^{0,2} * * \left(1 - 0{,}585\beta_\varphi^{0,9}\,Re_\varphi^{-0,1}\right)^{-1}$ n- from diagram	-	-	-	-	-
Mironov [13]	$Nu_{av} = 0{,}011\,Re_\varphi^{0,8}\left(\frac{r}{R_2}\right)^m\left(\frac{s}{R_2}\right)^{-0,2}$	2,0-40	0,011-0,067	0,45-0,94	$\approx \bar{r}^{1,75}$	0,38-0,48
Nikitenko [14]	$Nu_{av} = 0{,}0178\,Re_\varphi^{0,8}$	-	-	-	-	-
Mironov [13]	$Nu_{av} = 0{,}011 c\varphi^{0,8}\,Re_\varphi^{0,8}\left(\frac{r}{R_2}\right)^m\left(\frac{s}{R_2}\right)^{-0,2}$	2-40 (6-260)	0,011-0,067	0,94-0,45	$\approx \bar{r}^{1,75}$	0,18-0,22

STATISTICAL ANALYSIS AND ORIGINAL GENERALISED STATISTICAL CORRELATIONS

In order to simplify and accelerate the determining of average convective heat transfer coefficients in engineering application, Guzović [5] analyses statistically the groups of systematised correlations, i.e. the results of calculations of average Nusselt numbers, and the results are the original generalised statistical correlations of type $Nu_{av}=cRe^n$.

The statistical analysis is performed by means of a spreadsheet calculator on a computer (method based on the least square method and dragging of exponential "trendline"). The obtained original generalised statistical correlations which replace a particular group of the systematised single correlations from the literature are presented in Table 6. Table 6 also presents the ranges of flow and geometrical characteristics changes recommended during their usage.

Due to identical calculations of Nusselt numbers according to systematised correlations in single groups, equal values of geometrical and flow characteristics (e.g. relative radius, relative clearance, flow pre-swirl, flow vortex, kinematic factor, etc.) have been inserted as needed.

Also, Guzović [5] compares the calculation results obtained by the original generalised statistical correlations and by single correlations from literature.

CONCLUSION

In the course of the last several decades heat transfer on the surfaces of steam and gas turbines rotors has been continuously investigated experimentally and theoretically, and it has large significance in practice.

The original generalised statistical correlations obtained by generalising a larger number of single correlations available in literature give, as the comparisons show, the accuracy of calculation results which is acceptable for engineering applications. These correlations can be applied in heat transfer calculations on various types of rotor-stator systems. The application scope of the original generalised statistical correlations is considerably greater than of any single correlation, because generalised correlation covers the ranges of geometrical and flow characteristics of all the single correlations.

Table 6: The Original Generalized Statistical Correlations for Calculating the Average Nusselt Numbers in the Turbine Rotor-Stator Systems

Type of rotor-stator system	Correlations	Application ranges			β_φ
		$Re_\varphi * 10^{-5}$; (Kv_1)	s/R	r/R	
Free Rotating Disc	$Nu_{av} = 0{,}0088\,Re_\varphi^{0{,}8491}$	0,2-40	-	0,3-0,9	-
Open rotor-stator system without superposed flow	$Nu_{av} = 0{,}0066\,Re^{0{,}8817}$	0,9-40	0,011-0,07	0,3-0,935	0,38–0,5
Open rotor-stator system with superposed flow directed to periphery of the disc	$Nu_{av} = 0{,}5267\,Re_\varphi^{0{,}5515}$	0,9-40 (0,6-260)	0,008-0,15	0,38-0,94	0,18-0,22
Disc with rotating deflector i.e. co-rotating discs	$Nu_{av} = 0{,}1966\,Re_\varphi^{0{,}6821}$	0,1-10 (0,1-6)	0,015-0,06	0,33-0,94	0-6
Stationary wall opposite the rotating disc	$Nu_{av} = 0{,}0229\,Re_\varphi^{0{,}7445}$	2-40 (6-260)	0,011-0,067	0,45-0,94	0,18-0,48

REFERENCES

[1] Frolov, K.V., Izrailev, Yu.L., Makhutov, N.A., Morozov, E.M. and Parton, V.Z., 1991, "Thermal Stresses and Strength of Turbines: Calculation and Design", HPC, New York.

[2] Owen, J.M. and Rogers, R.H., 1989, "Flow and Heat Transfer in Rotating-Disc Systems", RSP Ltd., Taunton-England.

[3] Shvec, I.T. and Diban, E.P., 1974, "Vozdushnoe ohlazhdenie detaley gazovih turbin", Naukova dumka, Kiew.

[4] Dorfman, L.A., 1963, "Hydrodynamic Resistance and the Heat Loss of Rotating Solids", Oliver and Boyd, Edinburgh.

[5] Guzović, Z., 1998, "Applicability of Existing Correlations for Heat Transfer Determination at Steam and Gas Turbines", Ph.D. Thesis, Faculty of Mechanical Engineering and Naval Architecture, University of Zagreb, Zagreb, Croatia.

[6] Kapinos, V.M., Pustovalov, V.N. and Rudko, A.P., 1971, "Teploobmen pri techeni sredi od centra k periferii mezhdu dvumya vrashchayushchimisya diskami", Izv. AN SSSR Energetika i transport, No. 5, pp. 116-124.

[7] Kuznecov, L.A., 1964, "Teplootdacha diska vrashchayushchevosya v kozhuhe s radialnoy podachey ohlazhdayushchevo vozduha", in book "Teplovoe sostoyanie rotorov i cilindrov parovih i gazovih turbin", pp. 98-110, Mashinostroenie, Moscow-Leningrad.

[8] Cobb, E.C. and Sounders, O.A., 1956, "Heat Transfer from rotating disc", Proceedings of the Royal Society of London, Ser. A, Vol. 236, No. 1206, pp. 343-349.

[9] Kapinos, V.M., 1957, "Teploperedacha diskov gazovih turbin s vozdushnim ohlazhdeniem", in book "Trudi HPI", pp. 111-133, Mashinostroenie, Harkow.

[10] Oprecht., U., 1962, "Air Cooling of Small Gas Turbine Disc", Proc. of the ASME Heat Transfer Conference, New York.

[11] Kuznecov, A.L., Mironova, V.A and Korenevskiy, A.G., 1969, "Issledovanie temperaturnih poley diskov i korpusov gazovoj turbini GTK-10", Gazovaya promishlennost, No. 1, pp. 21-25.

[12] Mironov, B.P., 1959, "Teplovospriyatie ekranov, ustanovlennih po torcam vrashchayushchevosya goryachevo diska", Energomashinostroenie, No. 8, pp. 15-19.

[13] Mironov, B.P., 1960, "Issledovanie konvektivnovo teploobmena na ekranah ustanovlennih po torcam vrashchayushchevosya diska", Izv. AN SSSR, No. 3, pp. 129-137.

[14] Nikitenko, N.I., 1963, "Eksperimentalynoe issledovanie teploobmena diska i ekrana", IFZ, No. 6, pp. 3-9.

[15] Richardson, P.D. and Saunders O.A., 1963, "Studies of Flow and Heat Transfer Associated with a Rotating Disc", Journal of Mech. Engin. Sci.", No.5, pp. 336-342.

[16] Gregory, N. and Walker W.S., 1960, "Experiments on the Effect of Suction on the Flow due to a Rotating Disc", Journal Fluid Mech., Vol. 9, pp. 225-234.

[17] McComas, S.T. and Hartnett, J.P., 1970, "Temperature Profiles and Heat Transfer Associated with a Single Disc Rotating in Still Air", Proc. of 4th Conf., Paper No. FC7.7, Versailles.

[18] Owen, J.M., Haynes, C.M. and Bayley, F.J., 1974, "Heat Transfer from Air-cooled Rotating Disc", Proc. of Roy. Soc. Am., pp. 453-473.

[19] Caplin, M.I., 1975, "Teplootdacha i trenie vrashchayushchevosya diska pri nepodvizhnoy ogranichivayushchey stenke i rashodnom techenii", Energomashinostroenie, No. 10, pp. 16-18.

[20] Kapinos, V.M., 1965, "O toploobmene vrashchayushchevosya diska pri radialynom obduve", IFZ, No. 1, pp. 48-52.

[21] Kapinos, V.M., 1965, "Teploodacha diska vrashchayushchevosya v kozhuhe", Izv. vuz. Aviacionnaya tehnika, No. 2, pp. 76-86.

[22] Buznik, V.M., 1967, "Teploperedacha v sudovih energeticheskih ustanovkah", Sudostroenie, Leningrad.

[23] Buznik, V.M., Artemov, G.A. and Bandura, V.N., 1966, "Issledovanie teploodachi vrashchayushchevosya ekranirovannovo diska", in book "Sudostroenie i morskie sooruzheniya", pp. 3-10, Third Edition, HGU, Harkow.

[24] Kapinos, V.M., 1966, "Convective Heat Transfer in the Closed Cavity", Izv. vuz. Aviac. Techn., No.1, pp. 123-125.

HEFAT2002
1st International Conference on Heat Transfer, Fluid Mechanics, and Thermodynamics
8-10 April 2002, Kruger Park, South Africa
KJ2

EFFICIENCY IMPROVEMENT THROUGH INDEXING OF STATORS OF A TWO-STAGE TURBINE

J.E. Krysinski*, J.R. Blaszczak**, A. Smolny**
*Professor; **Assistant Professor
Institute of Turbomachinery, Technical University of Lodz, I - 10
ul. Wolczanska 219/223, 93-005 Lodz, POLAND, http://www.imp.p.lodz.pl
krysinski@ck-sg.p.lodz.pl, blaszczk@ck-sg.p.lodz.pl, asm1948@ck-sg.p.lodz.pl

ABSTRACT

The primary focus of the presented study is to determine the influence of the clocking effect on efficiency of a turbine. Experimental investigations of the detailed flow structures in a two-stage low-pressure turbine (TM-3) were conducted at the Institute of Turbomachinery (Instytut Maszyn Przeplywowych => IMP) of the Technical University of Lodz (=>TUL, Poland). TM-3 (situated at IMP laboratory) in order to perform these tests was modified in 1994/95. Modifications included special clocking mechanisms to allow the first stage vanes and the second stage vanes to be moved independently and in relation to the casing (more details can be found in [1]). Analysis of the experimental results included turbine performance as well as flow measurements throughout the flow field for different relative circumferential stator positions. Cyclic changes were observed for all measured parameters and the position of the maximum machine efficiency was found. The measurements were conducted for a strictly constant inlet/outlet pressure ratio and the rotational speed. In order to achieve high accuracy of the measurements a lot of detailed tests with a very high confidence level were performed. The averaged results showed an efficiency benefit from 0.1% to 0.5%.

INTRODUCTION

In order to improve performance and prediction methods for multistage turbomachines understanding of the unsteady flow is essential. Recently great attention has been paid to relative circumferential position of blade rows in consecutive stages. A growing number of experimental and numerical studies concerning clocking effect were carried out in recent years to investigate these flow phenomena both in turbines (e.g. [2], [3], [4], [5]) and compressors [6] (they are similar to those for turbines). It shows the interest in finding the new ways for improving the performance of the turbomachines.

This experimental work was carried out at IMP and was continuation of earlier studies since 1994 (e.g. [7][8]). The main objective of the test program was to experimentally investigate vane-clocking effect on the performance of the two-stage low-pressure turbine. Changing the clocking positions of the first and the second stator vanes was performed independently during the tests (without stopping the turbine and dismantling it) in the range of more than 2.5 relative pitches (based on stator vane geometry).

NOMECLATURE

b	cord of the vane [mm]
c	absolute velocity [m/s]
H	height of the vane (channel) [mm]
m	mass flow rate [kg/s]
M	shaft torque [Nm]
n	rotational speed [Hz] or part of nominal n
p	pressure [Pa]
P	shaft power [W]
Re	Reynolds number based on a chord
t	temperature [K]
T	pitch of the stator [mm]
Tu	turbulence level (rms)
x	circumferential position (along the pitch T)
y	radial position (along the height H)

Greek symbols

α	flow angle (absolute frame) [°]
η	efficiency

Subscripts

0	first stator inlet = turbine inlet
1	first stator exit = first rotor inlet
2	first rotor exit = second stator inlet
3	second stator exit = second rotor inlet
4	second rotor exit = turbine exit
m	midspan
t	total
nom	nominal

FACILITY

The series of tests were conducted on the two-stage low-pressure turbine with the eddy-current brake. The layout of the turbine test rig is presented in Fig. 1. A two-fan set provided a continuous airflow to the test rig. The inlet air parameters were as follows: total pressure p_{t0} = 15.5 ± 0.05 kPa, total temperature T_{t0} = 318 ± 3 K, mass flow rate m =3.50 ± 0.02 kg/s. The rotational speed was in the range 23 to 58 Hz. Variation of the rotational speed n at each working point was less then 0.02 Hz during the measurements.

The turbine geometry with some clocking positions is presented in Fig. 2. Both stages are identical. The number of the cylindrical vanes on the stators and the twisted blades on the rotors is 16 and 96, respectively. The clocking position x/T=0.00 determines the situation when the 2nd stator vane has the same circumferential coordinate as the vane of the 1st stator. The big stator vanes (compared by dimension to the twisted rotor blades) allowed performing detail studies of vane surface flow phenomena (the measurement and visualization techniques are presented in [9]). More detailed description of the test facility geometry and the flow measurements can be found in [1].

INSTRUMENTATION

The basic flow parameters (total and static pressure, total temperature, velocity vector) after the annular cascades were surveyed at the beginning (at each measuring plane) with pneumatic five-hole probes (with thermocouple mounted in the lower part of each probe [10]). The pneumatic signals were received by a 48-channel pressure system and recorded simultaneously with thermo-couple signals by the data acquisition-controlling system.

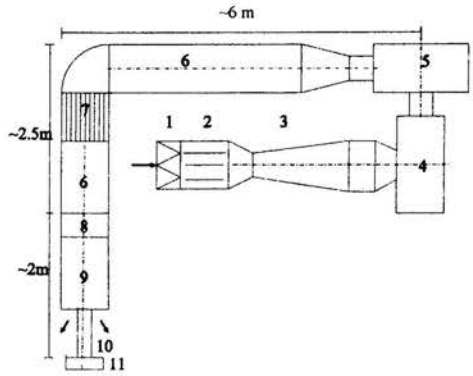

Figure 1: Layout of the TM-3 turbine (IMP TUL)
1.Air filter 2.Noise silencer 3.Venturi tube 4.Fan #1 5. Fan #2 6. Air-duct 7. Honeycomb straightener 8. Inlet ring 9. Turbine 10. Shaft 11. Brake

For unsteady 3D flow measurements three-sensor hot-wire probes were used. The sensors were 3 mm long, made of a 9 μm tungsten wire. The thermoanemometric probe was always aligned through on-line control with the mean flow direction, which was determined from the earlier five-hole pneumatic probe measurements.

The data from the hot-wire anemometers were simultaneously recorded by the digital multimeter (DC part of the signal) and the transient recorder (AC part of the signal) to obtain the maximum resolution. The data acquisition was triggered by a photocell located at the hub of the rotor.

Blade wakes were sampled in a one-time window with a digital resolution of 256 points at a sampling frequency of 250 kHz. After one rotor revolution, the next time-window was recorded, until 256 of these time-windows were stored.

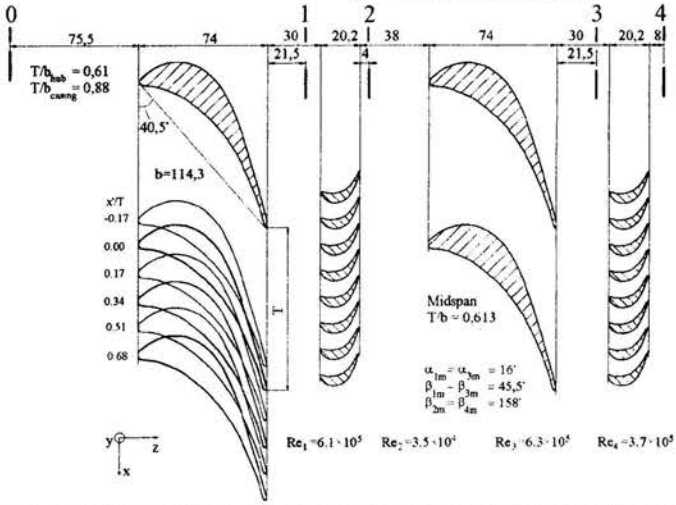

Figure 2: Turbine geometry with the measuring planes and some clocking positions presented

More detailed descriptions of the probe calibration method and the data reduction during measurement session (decomposition of the unsteady signal) is given in [11] and [12]. This part of work was done in cooperation with IST RWTH Aachen (Germany) and is similar to Gallus experiments [13].

The external characteristic measurement data (torque, rotational speed and power of the turbine) were obtained with the eddy-current brake controlling system.

EXPERIMENTAL RESULTS

For external characteristic measurements, experimental data have been obtained for 29 different clocking positions of the two stators.

It is worth noting that clocking effect influences the whole test rig, not only turbine. At earlier studies the changes of overall mass flow, inlet flow parameters etc. were observed due to the clocking effect (flow blocking effect). In this study the special precautions were taken to ensure the constancy (steadiness) of the overall characteristics of the test rig at each operating point, especially constant rotational speed and the difference between inlet total pressure and outlet static pressure (a special phase converter was used to control the first fan drive, Fig.1 => #4, to ensure the flow stability). The additional devices for controlling and eliminating outer disturbances and electromagnetic noise were also used. Aside from this, based on the earlier results, the number of measurements was significantly increased and more stringent statistical criteria were used during the measuring sessions.

Figures 3 and 4 show the torque and turbine efficiency (calculated with the mechanical method [2]) changes versus different rotational speed. They are presented relative to the value for the clocking position t/T=0 and nominal rotational speed $n=n_{nom}$ for different clocking position of the two stators. For such a presentation, due to the required scale, no differences can be observed. In this paper the presented values from the range of more then 2.5 T were averaged to the one-pitch range $<x/T=0;x/T=1>$.

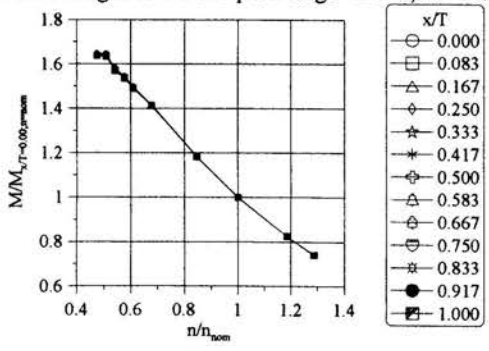

Figure 3: Relative torque versus different rotational speeds (see explanation in the text).

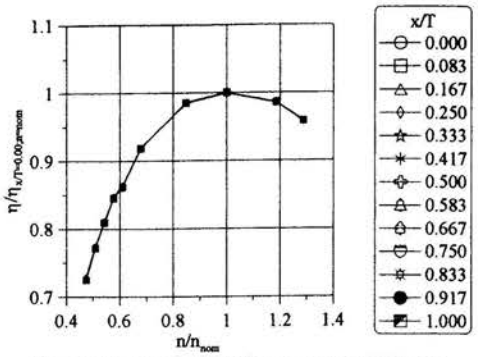

Figure 4: Relative efficiency versus different rotational speeds (see explanation in the text).

The differences are clearly detectable when they are related to clocking position x/T=0.00 individually for each rotational speed (Figures 5 and 6), especially for lower rotational speeds. For higher values of the rotational speed the differences are significantly smaller but still detectable.

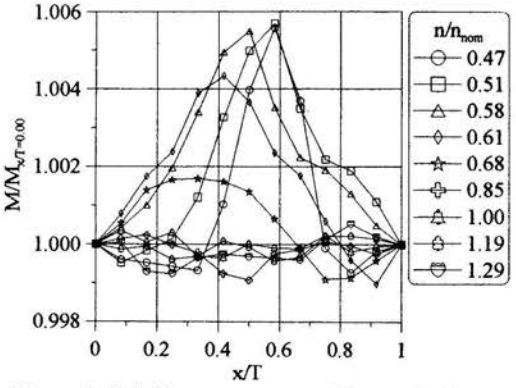

Figure 5: Relative torque versus different clocking positions (see explanation in the text).

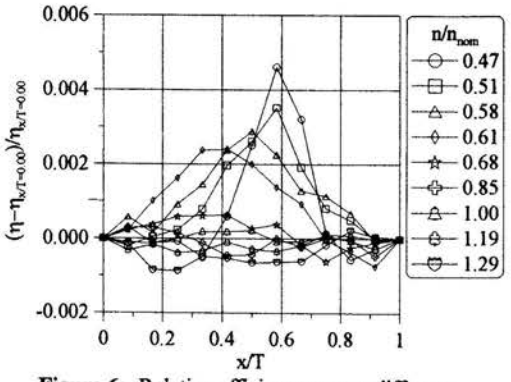

Figure 6: Relative efficiency versus different clocking positions (see explanation in the text).

The results presented in this paper are similar to those obtained by Huber et al. [2] but obtained in wider performance range.

During five-hole pneumatic probe measurements the measuring planes (see Fig.2) were traversed with the help of computer controlled stepper motors from the hub to the outer casing of the turbine for 39 radial and 29 (along one pitch) circumferential positions. The Fig. 7 presents, as the example, the flow angle after the second stator for six (every 1/6 of the pitch) different clocking positions along one pitch of the stator vanes. Fig. 8 (a and b) shows, as the continuation of the previous example, the comparison of the pitchwise-averaged flow angle downstream the annular vane cascades for the same six clocking positions (Fig. 2).

Subsequently the unsteady flow measurements for different rotational speeds were performed using 3D hot-wire probe for 13 (along one pitch) circumferential and 26 radial probe positions. It was found that with increasing rotational speed, the flow becomes more mixed and tranquillized, and the differences between stator clocking positions are becoming much less pronounced. Fig. 8 (c) presents, as the continuation of the example, some results of the pitch-wise averaged unsteady flow angle measurements downstream the rotors (clocking positions every 1/4 of the vane pitch in this case). The variation of the measured values influenced by the stator-to-stator clocking position is rather difficult to be detected due to the strong mixing phenomena but it could still be recognized [14].

Significant differences can be observed for the different clocking positions after the second stator and, of smaller magnitude, after the second rotor.

With the increase of the rotational speed it was also observed that the flow tends to calm down (lower level of Tu), especially in the central part of the flow channel (also due to bigger values of the velocity). The variation of the turbulence level Tu, influenced by the stator to stator clocking position was detectable and the differences were in the wider range for the clocking position $x/T = 0.5$ [8].

The results were consistent with those previously reported which had been, however, obtained utilizing different measuring method (three-sensor hot-wire probes versus pneumatic five-hole probes).

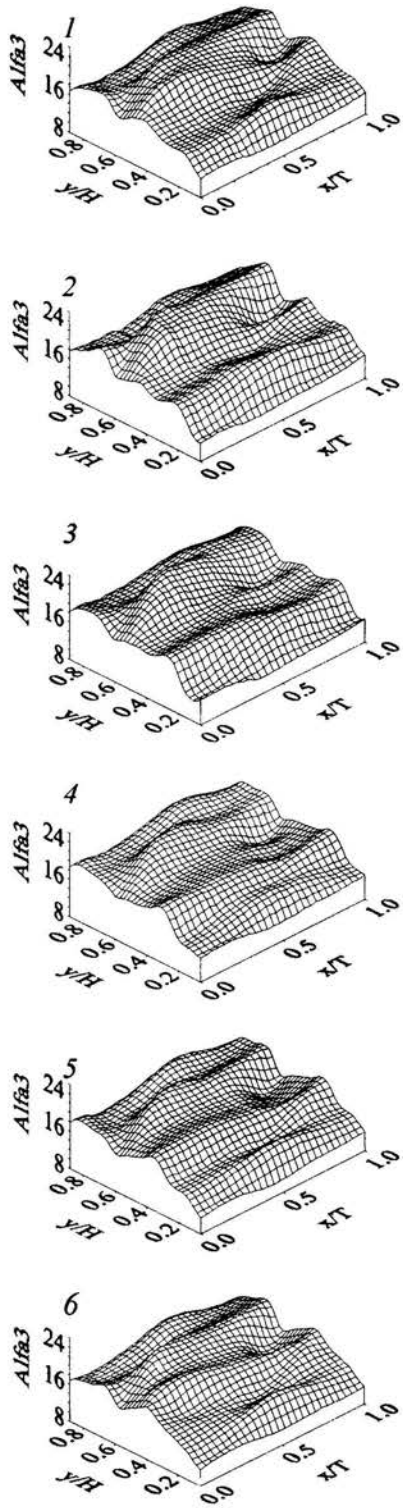

Figure 7: Flow angle after the second stator for six different clocking positions along one pitch of the stator vanes (every 1/6 of the pitch)

CONCLUSIONS

Experimental investigations aimed at detection of stator-to-stator interaction (by varying the circumferential relative position of consecutive vane rows) of a two-stage low-pressure turbine were performed.

The results of precise measurements of the power and torque output differed very slightly around the nominal operating point. Only for the off-design rotational speeds (high load conditions) the effect of the indexing is clearly detectable and the overall performance of the turbine is detectably influenced by the clocking position of the two stators.

It leads to the conclusion that, in some conditions, the measurement of the external characteristics (torque, power etc.) alone may provide insufficient evidence of the influence of the clocking position, especially close to the nominal operating point. For highly loaded machine, far from the nominal operating range in this case, the clocking effect is much more detectable.

The last figures (Fig.9 and 10) help to see overall tendency of the relative torque and efficiency changing.

The detailed distributions of the flow parameters demonstrated similarities downstream the first stage for different clocking positions but the exit flow was noticeably influenced though the strong flow mixing phenomena after the rotors (due to the big amount of blades comparing to the number of vanes). The number of the cylindrical vanes on the stators and the twisted blades on the rotors is 16 and 96, respectively, thus the ratio is far from 1:1. According to the recent numerical predictions made by the Arnone et al. [5] practically no clocking effect should be detected. In this case it was observed for each measured operating point, especially when carefully controlling the flow parameters. Presented in this paper flow angle changes (Fig.6) is a good example of this phenomenon.

The detailed studies of the 1st stator-passing wake showed that after leaving the first stator it immediately starts to rotate around the axial direction. Additionally it interacts with secondary flow vortices nearby the wall regions changing its shape and the flow phenomena are much more complicated then it was presented by other authors (e.g. Huber et al. [2]).

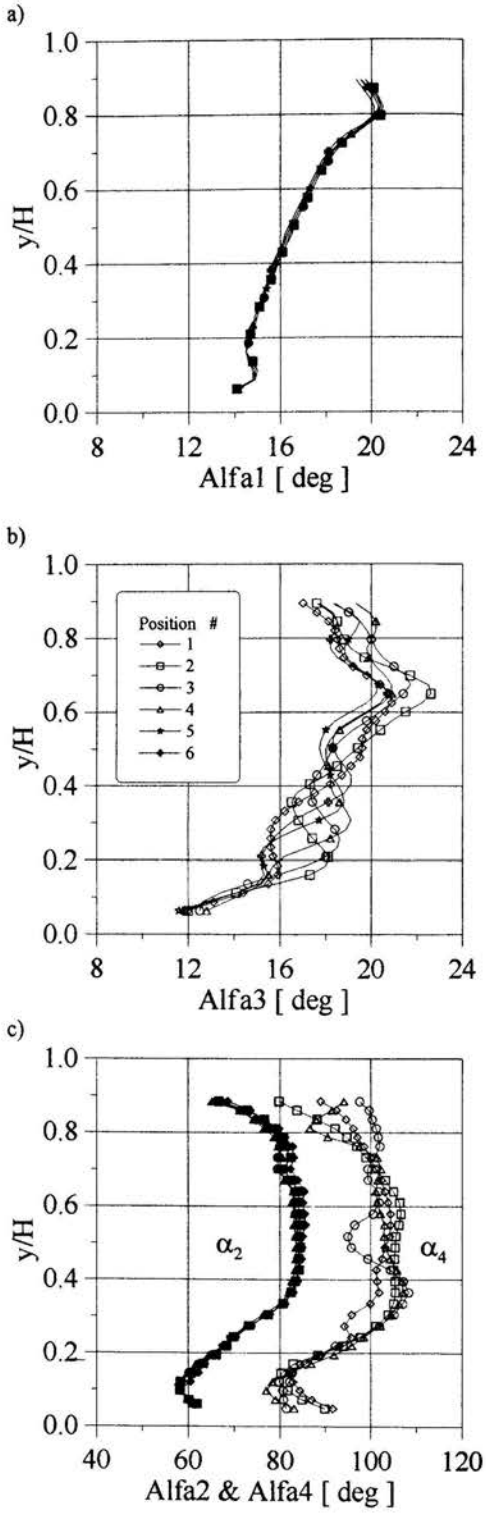

Figure 8: Pitchwise averaged flow angle for different clocking positions:
a) Downstream from the 1st stator [12],
b) Downstream from the 2nd stator [12],
c) Downstream from the 1st (on the left) and 2nd rotor (on the right) [7].

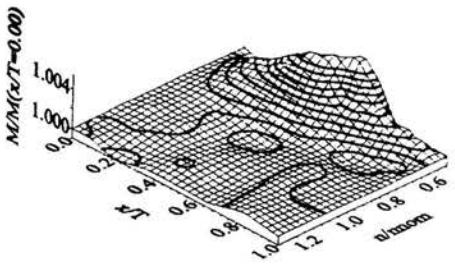

Figure 9: Relative torque change due to the clocking effect for different rotational speeds.

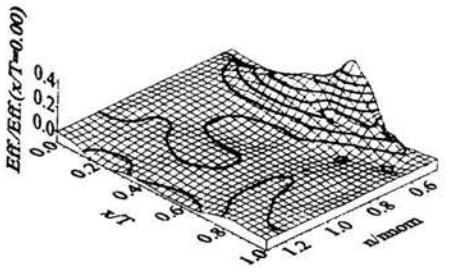

Figure 10: Relative efficiency change due to the clocking effect for different rotational speeds.

In this case the rotating first stator wake is divided into two parts (in ratio about 1:2) by the leading edge of the second stator. It indicates that axial gap plays also significant role in the clocking effect.

The results showed an efficiency variation from 0.1% to 0.5%, which may seem minute but considering the long working time of any turbomachine it could be a source of potential turbine performance benefits, especially outside the design conditions.

REFERENCES

[1] Krysinski J.E., Gallus H.E., Smolny A., Blaszczak J.R.: Axial Two-Stage Turbine Test Rig for Unsteady Flow Measurements, Int. Conf. SYMKOM'95, CMP-Turbomachinery 108, TUL, 1995

[2] Huber F.W. Johnson P.D., Sharma O.P., Staubach J.B. Gaddis S.W. Performance Improvement Through Indexing of Turbine Airfoils: Part 1 & 2. ASME J. of Turbomachinery, Vol. 118, 1996

[3] Dorney D.J., Craft R.R., Sondak D.L., Stang U.E., Twardochleb C.Z.: Computational Study of Clocking an Embedded Stage in a 4-Stage Industrial Turbine. ASME Paper 2001-GT-0509

[4] Gombert R., Hohn W.: Unsteady Aerodynamical Blade Row Interaction in a New Multistage Research Turbine Part 1&2. ASME Paper 2001-GT-0306/307

[5] Arnone A., Marconcini M., Pacciani R., Schipani C., Spano E.: Numerical Investigation of Airfoil Clocking in a Three-Stage Low Pressure Turbine. ASME Paper 2001-GT-0303.

[6] Savin W.E., Saren N.M.: Hydrodynamic Stator-Rotor-Stator Interaction in Axial-Flow Turbomachine. Izviestia Akademii Nauk, Fluid Mechanics #3, UDK 533. 6.011.34, 2000

[7] Krysinski J.E., Gallus H.E., Smolny A., Blaszczak J.R.: Stator Wake Clocking Effects on 3D Unsteady Flows In a Two-Stage Turbine. 3rd Euro Conference on Turbo-machinery, IMechE, London, 1999

[8] Krysinski J.E., Gallus H.E., Smolny A., Blaszczak J.R.: Stator Clocking Effect on Efficiency of a Two-Stage Low-Pressure Turbine. 4th Euro Conference on Turbo-machinery, IMechE, Florence, 2001

[9] Smolny A., Blaszczak J.R.: Boundary Layer and Loss Studies on Highly Loaded Turbine Cascade, AGARD, CP-571/4, 1996.

[10] Blaszczak J.R., Smolny A., Dalceggio A.: Pneumatic probes inside an unsteady flow field of the two-stage model turbine. KKM'98. TU Gdansk, 1998

[11] Smolny A., Blaszczak J.R., Pawlak R.: *3D* Flow Field Measurements In Multistage Turbomachinery Using a Computer Aided System, O&ESII Proc. of SPIE 3054-11, 1997

[12] Smolny A., Blaszczak J.R.: Experimental Investigations Of Unsteady Flow Fields in a Two-Stage Turbine, 2nd EuroConf. On Turbomachinery, Antwerp, 1997

[13] Walraevens R.E., Gallus H.E.. Three-Dimensional Structure of Unsteady Flow Down-stream the Rotor in a 1-1/2 Stage Turbine, Unsteady Aerodynamics and Aeroelasticity of Turbomachines, Elsevier Science B.V, 1995.

[14] Krysinski J., Blaszczak J.R., Smolny A., Gallus H.E.. 3D Unsteady Flow Experimental Investigations in a Two-Stage Low-Pressure Model Turbine. 9th International Symposium on Unsteady Aerodynamics, Aeroacoustics and Aeroelasticity of Turbomachines, Lyon 2000.

HEFAT2002
1st International Conference on Heat Transfer, Fluid Mechanics, and Thermodynamics
8-10 April 2002, Kruger Park, South Africa
SA1

QUASIADIABATIC METAL – CERAMIC ROTOR BLADES AND GUIDE VANES FOR GAS TURBINE APPLICATIONS

Soudarev A.V.*, Tikhoplav V.Yu.**,
Suryaninov A.A.***, Podgorets V.Ya.**, Grishaev V.V.**, Molchanov A.S.***
*Professor, **Ph.D, ***Engineer
Research-Engineering Center "Ceramic heat Engines", St.Petersburg, Russia
E-mail: Soudarev@tedvic.spb.ru

INTRODUCTION

Of late, an interest in the use of ceramic materials in the current gas turbomachinery to improve the economical and environmental values of the gas-turbine plants has been on a steady rise. The initial research and development works as well as the fresh findings of the commercial running of ceramic gas-turbine engines (GTE) both in the USA and Japan demonstrated that it would be more rational to keep a staged incorporation of the structural ceramic materials into the high-temperature gas-turbomachinery [1].

At the initial stages, it is particularly important to carry out researches and to embody combined metal-ceramic structures for the GTE high-temperature elements, including parts and components of gas turbine itself (guide vanes and rotor blades, protective lining for turbine discs and internal casing surfaces over the turbine wheel, etc); combustion chambers (liners, burners, igniters, etc); recuperative or regenerative air heaters (heat exchange matrix, manifold, casing lining, etc), hot media supply and discharge paths (volutes, inlet piping and exhaust diffusers lining, etc). To put the above into effect, the research-engineering center "Ceramic heat engines" (NIZ KTD) implemented as follows:

- produced the original aluminoboronnitride ceramic SUGRAV and its modification SUGRAV-M which are actually zero-shrinkage and easily adaptable to welding by the diffusive technique; furthermore, they have relatively high strength and corrosion resistance values at temperatures ranging from 1200°C to 1500°C [2,3];

- developed, manufactured and successfully tested the hybrid metal-ceramic structures of the high-temperature elements for GTE (turbine volute, hot gasducts, combustor liners, recuperative air heater, etc).

The hybrid structures are sectional. Their main components are:

- the high-temperature ceramic element in direct contact with the high-temperature working media flow (gas) meant to absorb the heat loads;

- the low-temperature cooled metal (or ceramic) strength element bearing the mechanical loads;

- the effective thermal insulation between the heat strength elements "cutting off" the heat flux supplied from gas to cooler.

The hybrid structures for GTE were produced on the basis of the quasiadiabaticity concept with the aim to provide a minimum (in theory, close to zero) heat flux from the thermal element heating gas to the cooler of the strength element. As a result, the relative air flow for cooling of the strength elements is reduced by nearly an order. At the same time, the concept of ceramic operating essentially on compression is put into effect in the hybrid structures, including the rotor elements (rotor blade shells, interblade inserts, lining for turbine disc surfaces, etc).

Since 1991 the activities have been in full swing at the NIZ KTD with the objective to produce a low-NOx high efficiency ceramic gas-turbine 2.5 MW KGTD-2.5 engine Its effective efficiency is within 42-45%. At present, the demonstrator of the engine is prepared for testing.

All the high-temperature parts and components of KGTD-2.5 and the demonstrator have been developed and manufactured on the basis of the aluminoboron-nitride ceramic SUGRAV-M with use of hybrid structures for the main elements and components meant to embody the quasiabaticity concept and the concept of

the aluminoboronnitride ceramic material operating essentially on compression.

DESIGN OF HYBRID GUIDE VANES AND ROTOR BLADES

The analysis of trends in the field of the development of the gas-turbine engines provides a basis for the conclusion that a reduction in the power losses caused by a high flow of the cycle air bled off from the compressor for an intensive cooling of the high-temperature gas turbine metal is one of the most effective techniques of upgrading the technical and economical characteristics of GTE [1,4,5,6,7,8].

As is well known, the open system of air cooling for high-temperature gas turbines is now the most widely applied to the current aviation, ship, drive and power GTEs. The reason for the above is that it is the most reliable and simple system. Though, this is right the open systems cause the greatest power losses due to cooling of the high-temperature gas turbine metal. E.g., the relative air flow for cooling the advanced aviation and ship GTEs may amount to 10-12% and higher.

Numerous experimental data show that with the supply of the cooling air into the flow passage of the turbine amounting to 1% of the total flow of the hot working media, the 0.4-0.6% reduction in turbine efficiency (depending on the air blowing-off spot, its direction and intensity) takes place. In turn, the 1% efficiency reduction for the turbine decreases the GTE cycle efficiency by 0.4-0.6% (depending on the gas temperature at the turbine wheel exhaust) [6]. Aiming to achieve a notable reduction in the cooling air flow in gas turbomachinery, a number of structures were developped, including the hybrid structures of the guide vanes and rotor blades for GTEs [5,8,9], though as a rule, these projects did not envisage a potent embodiment of the capability of the ceramic shells to operate at the compressive stresses. Implementation of the above and an appropriate increase in the reliability is achieved through manufacture of the hybrid rotor blades for the KGTD-2.5 engine.

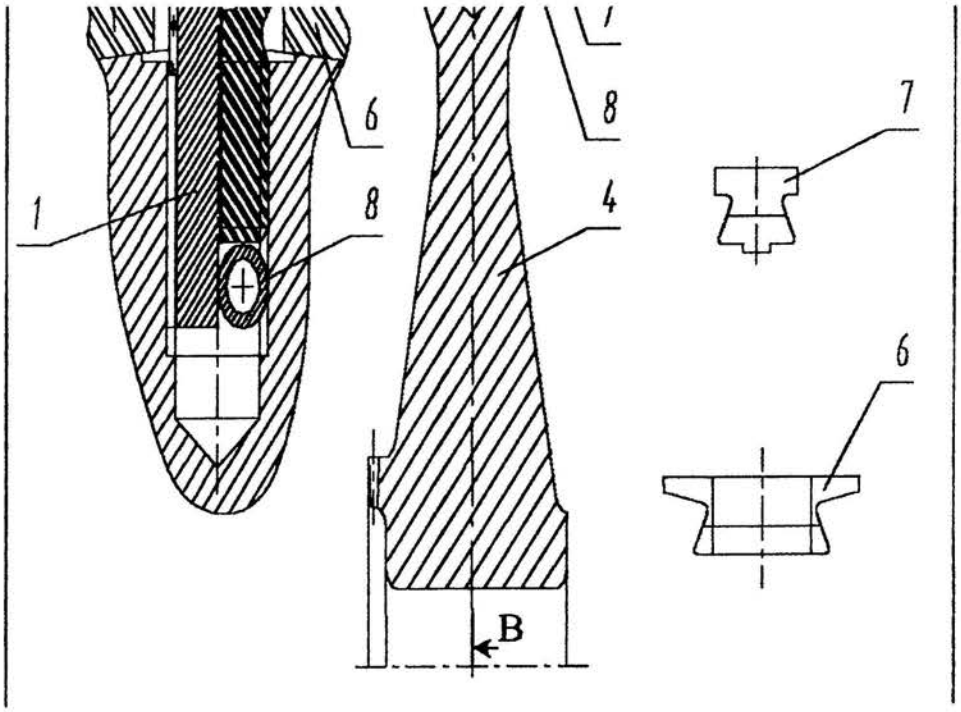

Fig.1. Engine KGTD-2.5. Turbine wheel for high-pressure turbine (HPT) with metal ceramic blades and ceramic thermal-insulating lining

1 – metal carrier core; 2 – metal peripheral platform; 3 – ceramic shell; 4 – turbine disc; 5 – ceramic block; 6, 7 – elements of ceramic lining for disc; 8 – lock; 9 – deflector for rotor blade.

As is evident from Fig.1, the turbine wheel of the high pressure turbine (HPT) for the KGTD-2.5 engine is the metal disc 4 with the hybrid rotor blades secured on the disc rim with use of the lock 8. The lock is a hollow sleeve through which the cold air delivery into the cooling channels of the carrier core of the blades is carried out. The disc rim between the blades is insulated from direct contact with the hot gases by the peripheral 7 and central 6 elements of ceramic lining and, also, by the ceramic block heads 5.

The hybrid rotor blade includes three structure elements, namely the external airfoil shell 3 made of a structural ceramic material and mounted loosely on the core of the thermal insulation layer as the screen-deflector 9 and the metal carrier core 1 with grooves for the cooling air, the peripheral platform on which the shell rests at rotation under the action of the centrifugal forces, and with the threaded tail to secure the turbine wheel in the disc. The high-temperature gas flows directly through the external airfoil shell 3 , i.e. the turbine working media and the cooling air protects the metal carrier core 1 against an overheating . The ceramic elements of the turbine wheel of the KGTD-2.5 engine are shown in Fig.2, while Fig.3 shows the snapshots of the turbine wheels as an assembly.

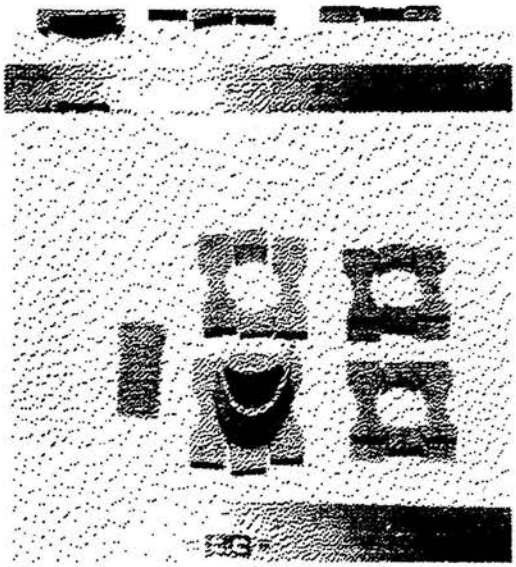

Fig.2. Engine KGTD-2.5. Ceramic elements of the turbine wheel for HPT

a) shell; b) block; c) elements of the central and peripheral lining turbine disc.

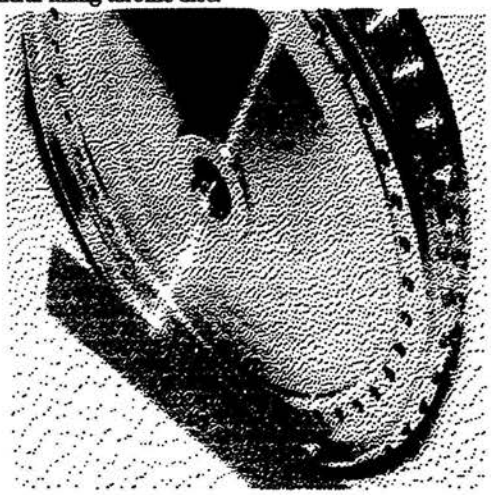

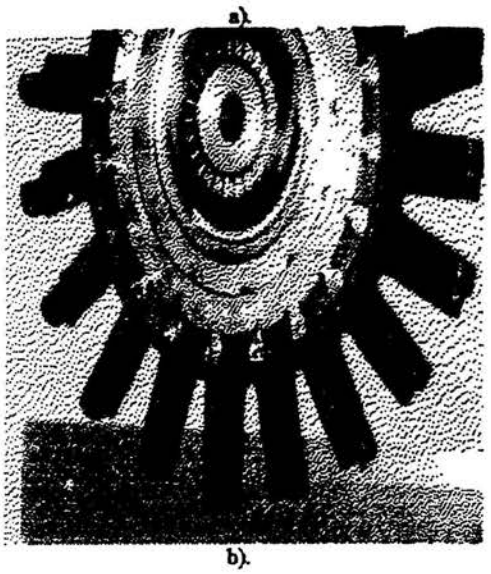

Fig. 3. Turbine wheel for axial turbine as an assembly

a) gas-turbine engine KGTD-2.5; b) GTE for Microturbo.

The ceramic shell is equipped at the same time, with the capability of free thermal expansion which reduces the heat stresses in it.

A similar concept is put into effect in the hybrid guide vanes design (Fig.4). Here, metal carrier elements are involved as well (cones, rings 3 and 7) the protective elements bearing the loads (shells 3, inserts 1 and 4) capable of expansion freely relative to the strength elements ensuring a required air-tightness of the cooling air channel (see section A-A, Fig.4).

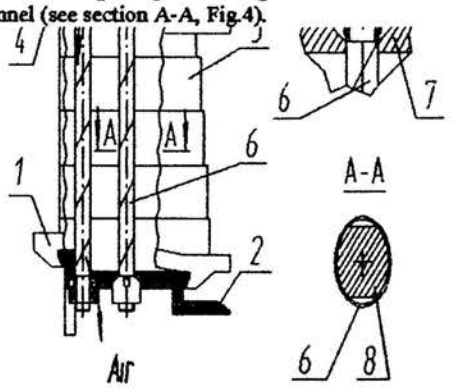

Fig.4. GTE for Microturbo. Hybrid guide vane

1 - root ceramic insert; 2 – root strength ring; 3 – ceramic shell; 4 – peripheral ceramic insert; 5 – ball nut; 6 – deflector; 7 – peripheral strength ring; 8 – metal carrier core.

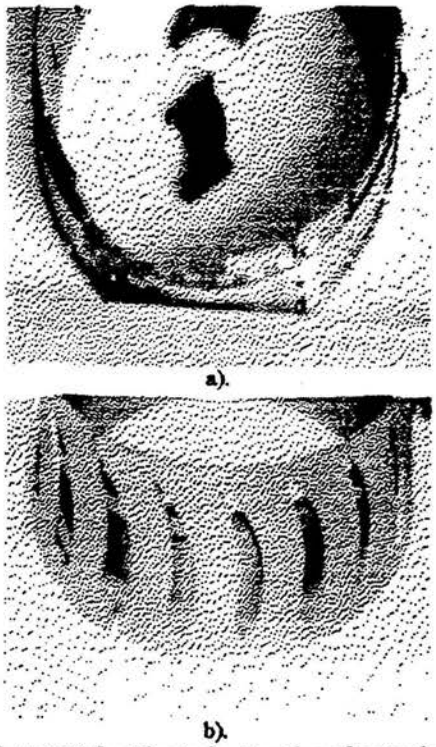

Fig.5. GTE for Microturbo. Location of protective ceramic inserts relative to strength metal spokes (a – peripheral, b – root) for guide vanes of hybrid structure.

Fig.5 shows location of the ceramic protective inserts of the guide vanes in relation to its strength rings, Fig.6 shows the hybrid metal-ceramic guide vanes as an assembly.

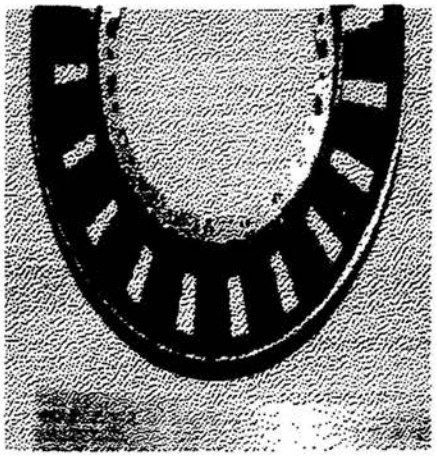

Fig.6. GTE for Microturbo. Hybrid metal-ceramic guide vanes as an assembly

TEST FINDINGS

Comprehensive tests (aerodynamic – Fig.7, spin – Fig.8, heat – Fig.9, thermocyclic – Fig. 10) verified the functionality of the hybrid structures of blading.

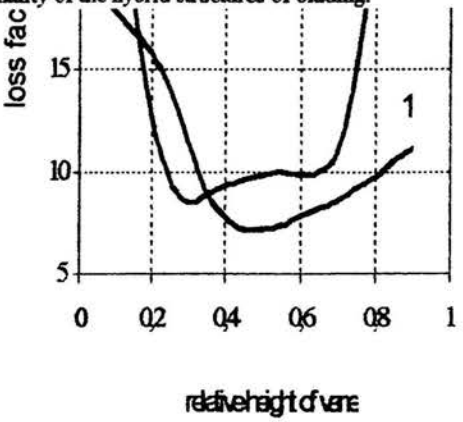

Fig.7. GTE for Microturbo. Results of hydrodynamic tests (identification of loss factors) of circular subscale cascades:

1 – guide vanes with staged twisting (see Fig.4), M=0.775, Re=380.000; 2 – rotor cylindrical blades M=0.76; Re=350.000 (M, Re are the Mach and Reynolds numbers).

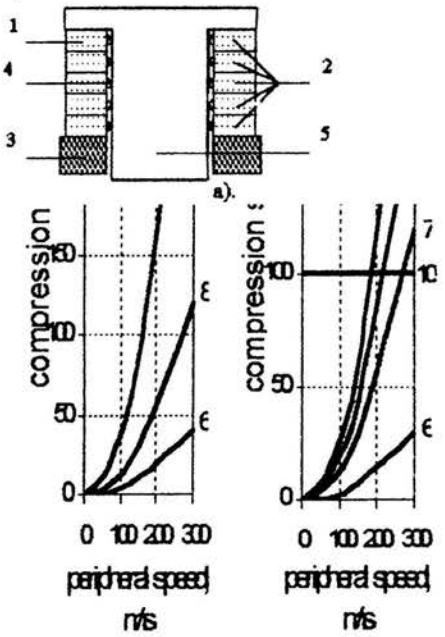

Fig.8. GTE for Microturbo. Results of spin tests of ceramic shells

a – test scheme; b – cylindrical subscale shells; c – full-scale airfoil shells; 1 – shell element; 2 – multi-element sectional shell; 3 – loading washer; 4 – deflector;

5 – carrier core with peripheral platform; 6 – shell element test conditions; 7 – sectional shell test conditions; 8 – test conditions for shell elements with loading washer; 9 – test conditions for sectional shell with loading washer; 10, 11 – level of operating stresses at the rated load for engines KGTE-2.5 and Microturbo, respectively.

First, it should be noted that

1. The cooling air flow in the heat tests (Fig.9) did not exceed

-1.2-1.5% for hybrid rotor blades (which is one order below that for the conventional designs) at the initial temperature of hot gases of 1350^{0}C and the maximum temperature of the carrier core of 660^{0}C for standard cooling systems, curve 1) or 850^{0}C (at malfunctions in the cooling system, e.g. when a portion of air does not flow along the cooling channels, curve 3). As for the hybrid guide vanes, the air flow for cooling of the carrier metal spoke (Fig.5) was altogether 0.5% with even the hot gas temperature being 1450^{0}C (it is shown in Fig.9), i.e. 0.03-0.15% of the flow required for the metal blades.

2. The hybrid structure of the blades is capable of sustaining high temperature gradients (100-200^{0}C/s) associated with the startup and shutdown of GTEs (Fig.10).

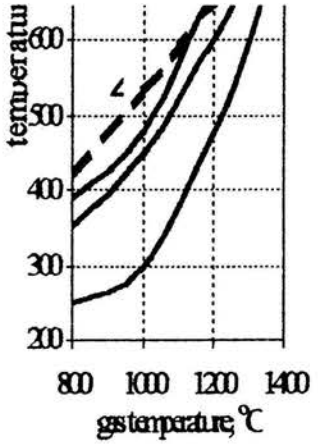

Fig.9. GTE for Microturbo. Results of heat tests of full-scale hybrid rotor blades and guide vanes

1 – temperature of metal core for rotor blade under platform (standard cooling); 2 – temperature of metal core for rotor blade under platform (non-standard cooling); 3 – temperature in blade rotor metal core platform; 4 – temperature in center of metal spoke for nozzle vane.

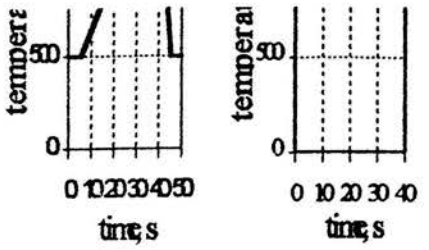

a). b).

Fig.10. GTE for Microturbo. Heat tests duties for hybrid turbine blades

a – rotor blades; b – guide vanes; temperature gradient and cycle number: 1-130 °C/c and 5; 2-190 °C/c and 5; 3- 110 °C/c and 5.

3. Operating under predominantly compressive load conditions, it is possible to produce low-stressed ceramic shells (Fig.8) for the hybrid blades ensuring high life values for the ceramic GTEs.

4. The research results of the aerodynamic losses in the tests of the circular cascades of the cylindrical blades and the blades with the staged twisting did not show a notable effect of the staged airfoil on the value of the hydrodynamic losses when testing the geometric characteristics of the airfoils.

Summing up the above, one can arrive at the conclusion that the level of adiabaticity, which implies a degree of keeping with the concept of "adiabatic (uncooled) turbine", is one of the most important determining properties of the turbine. A significant level of adiabaticity of the ceramic GTEs preconditions a significant increase in their maximum efficiency capability.

REFERENCIES

[1] Soudarev A.V. Prospect of production of environmentally friendly ceramic gas-turbine engines for stationary power. Energhetyka i transport, vol.38 M., RAN, 1992, pp.49-59.

[2] Soudarev A.V., Grishaev V.V., Podgorets V.Ya. Alumino – Boron – Nitride Ceramics microstructure, properties and manufacture techniques. Euromat 2000, Advances in Mechanical Behavior, Plasticity and Damage, 7-8 November, 2000, Tours, France, vol.1, pp.783-788.

[3] C.Duduay, C.Olagnon, G.Fantozzi. Etude du comportement thermomecanique de nitrides d'aluminium et de silicium, 1999, INSA, Lyon, France.

[4] Soudarev A.V., Podgorets V.Ya., Molchanov A.S., Souryaninov A.A., Soudarev B.V., Grishaev V.V. Metal-ceramic stationary gas-turbine engine of 2.5MW power. Turbiny i compressory, issue №2-97, St.Petersburg, NIKTIT, 1997, pp.5-13.

[5] Tikhoplav V.Yu., Principles of production of shell blades "Flox" for gas turbine, Energhetica (News of High Education Institutes and Power Mergers of C.I.S. countries), 1999, №1, pp.66-78.

[6] Tikhoplav V.Yu., Soudarev A.V. Shell turbine blades in high-temperature gas-turbine engines. Turbiny i compressory, issue №3, 4-97, St.Petersburg, NIKTIT, 1997, pp.26-31.

[7] Tikhoplav V.Yu. On concept of spontaneous cooling of blades "Flox" for high-temperature gas turbine. Turbiny i compressory, issue №6, 7 (2,3-98), St.Petersburg, NIKTIT, 1998, pp.17-22.

[8] Patent of USA №4396348, MKU FOID 11/02, 1983.

[9] Soudarev A.V., Tikhoplav V.Yu., Podgorets V.Ya., Grishaev V.V., Souryaninov A.A., Soudarev B.V. High Effeciency and Environmental Friendliness as Key Factors for Future Wide Use of Ceramic High – Temperature GTEs in Power Generation. IV Congreso Latinoamericano – Cenetacion y transporte de energia electrica, 7-10 November, 2000, Vina del Mar, Chile, section.

HEFAT 2002
1st International Conference on Heat Transfer, Fluid Mechanics, and Thermodynamics
8-10 April 2002, Kruger Park, South Africa
TT1

INTERRELATION BETWEEN IMPELLER BLADES INLET DIAMETER AND HYDRAULIC ENERGY JUMP IN TURBOMACHINERY

Takaharu Tanaka

Department of Mechanical Engineering
Kobe University
Rokko, Nada, Kobe 657-8501
Japan
Email: tanaka@mech.kobe-u.ac.jp

ABSTRACT

In the turbomachinery, which transfers mechanical energy to hydraulic energy, hydraulic energy jump is caused from the hydraulic energy at flow passage just before the entrance of leading edge of impeller inlet to that at leading edge of impeller inlet. It is caused only once and one kind in case of centrifugal turbomachinery, because impeller blade opens its entrance mouth radial inward and fluid particle enters to the impeller blade radial outward. However, in case of mixed and axial flow turbomachinery, impeller blade opens its entrance mouth across the axis of rotation and fluid particle enters to the leading edge parallel to the axis of rotation. Therefore, entrance radius varies between hub and tip. This indicates that grade of hydraulic energy jump varies by the entrance radius between hub and tip at the leading edge of impeller inlet. Hydraulic energy jump is the largest at the tip and the smallest at the hub.

1. INTRODUCTION

Turbomachinery is a machine, which transfers energy from mechanical to hydraulic energy and from hydraulic to mechanical energy. When impeller blade rotates together with fluid particle, if mechanical energy is supplied to the system, mechanical energy, which is supplied to the system from outside of the system, is transferred to hydraulic energy in the system. Therefore, fluid particle in the system increases its hydraulic energy along the flow passage in the system.

Let us image a conduit pipeline passing through the rotating flow passage in a turbomachinery. Fluid particle flows in the conduit pipeline from upstream non-rotating flow passage to downstream non-rotating flow passage passing through impeller blades rotating flow passage, and increases its hydraulic energy in order from the value at flow passage just before the entrance of leading edge of impeller inlet to the value at just after the discharge of trailing edge of impeller outlet. Examples for this kind energy transfer could be seen in pumps, fans, and blowers.

On the other hand, if fluid particle rotates together with impeller blade in a turbomachinery and hydraulic energy is transferred to mechanical energy in the system, fluid particle, which flows from upstream non-rotating flow passage to downstream non-rotating flow passage passing through impeller blades rotating flow passage, decreases its hydraulic energy in order from the value at flow passage just before the entrance of leading edge of impeller inlet to the value at just after the discharge of trailing edge of impeller outlet in the conduit pipeline. Hydraulic energy of a fluid particle passing through rotational flow passage is transferred to mechanical energy and demanded from the system through impelling blades rotating shaft. Examples for this kind energy transfer could be seen in water turbines.

Therefore, main subject to be discussed among engineers is a matter of course energy transfer, which is caused in the rotating flow passage of turbomachinery. Our most interested viewpoint is therefore on the subject how energy transfer is caused between impeller blade and a fluid particle in the rotating flow passage of turbomachinery. Then, mechanism of energy transfer, which is caused between hydraulic and mechanical energies, a fluid particles movement in the rotating flow passage, and its interrelation with energy transfer have to be discussed as the basic problem caused in rotating flow passage.

Hydraulic energy E, which is produced by a turbomachinery, can be explained simply as the product of mass flow rate ρ Q and head H. Hydraulic energy E itself changes in the conduit pipeline along the rotating flow passage. Partial hydraulic energies, such as pressure, velocity, and potential energies, construct hydraulic energy E in the conduit pipeline. However, special attention has to be made on hydraulic energy change. Our most interested viewpoint is on the change of hydraulic energy E, which varies itself in the conduit pipeline along the rotating flow passage of turbomachinery, but not on the partial hydraulic energy change, which is caused under the constant hydraulic energy E along the conduit pipeline.

By the way, H/ ρ Q indicates hydraulic energy of which unit mass of fluid particles has in the rotating flow passage of conduit pipeline. Conduit pipeline, in which fluid particles flow at mass flow rate ρ Q, could be equivalent to the conduit pipeline in which unit mass of fluid particles flows. Then, change of hydraulic energy E of mass flow rate ρ Q in the conduit pipeline along the rotating flow passage could be equivalent to the change of hydraulic energy H/ ρ Q in which unit mass of fluid particles flows in the conduit pipeline.

This result of discussion could be expanded as follow: Fluid flow in a conduit pipeline is equivalent to the fluid flow in a stream tube. Stream tube is lined along the streamline in the rotating flow passage of turbomachinery. Then, hydraulic energy H/ ρ Q of unit mass of fluid particles in the conduit pipeline is also equivalent to the hydraulic energy e of unit mass of fluid particles in the stream tube. Hence, it could be said that the change of hydraulic energy e along the streamline in the rotating flow passage could be the main subject to be solved and discussed among turbomachinery engineers.

In this point of view, basic mechanism of energy transfer from mechanical to hydraulic energy, which is caused on unit mass of fluid particles in the stream tube along the streamline in rotating flow passage of turbomachinery, hydraulic energy jump, which is caused from the hydraulic energy at flow passage just before the entrance of leading edge of impeller inlet to that at leading edge of impeller inlet, and their interrelation with overall efficiency are discussed in this paper.

NOMENCLATURE

$A \rightarrow B$ = fluid flow from above to below in figure
$B \rightarrow A$ = fluid flow from below to above in figure
E = hydraulic energy produced by a turbomachinery [N · m/s]
e = hydraulic energy of unit mass of fluid particles [N · m/s]
g = acceleration of gravity [m/s^2]
H = head [m], or hydraulic energy of a fluid particle [N · m/s]
HE = hydraulic energy [N · m/s]
ME = mechanical energy [N · m/s]
Q_A = flow rate at valve opening A [m^3/s]
U_P = peripheral velocity [m/s]
V_A = velocity of fluid particle at flow rate Q_A [m/s]
β =angle, blade chord makes with moving direction [°]
ρ = density of liquids [kg/m^3]

2. PRINCIPLE OF ENERGY TRANSFER IN ROTATING FLOW PASSAGE OF TURBOMACHINERYS

2.1 Non-Rotational motion

Fluid Flow in Perpendicular Blade Row

Blade chord of a blade row, shown in Fig.1 (a), is set perpendicular to moving direction and makes a right angle with the moving direction. If blade row moves left hand side parallel to the paper surface, blade chord forces fluid particle normal to moving direction. Therefore, a fluid particle, which is contained between impeller blades, moves left hand side together with impeller blades. However, neither the fluid flow from above to below ($A \rightarrow B=0$), nor from below to above ($B \rightarrow A=0$) is caused in the flow passage. That is, even if blade row moves toward the left hand side, right component of force, that is, perpendicular component of velocity across the moving direction is not caused on the fluid particle at all in the flow passage.

Fluid Flow in Inclined Blade Row

Blade chord of a blade row, shown in Fig.1 (b), makes angle β less than 90 degree with the moving direction. If blade row moves left hand side parallel to the paper surface, blade chord forces fluid particle above direction to flow at angle ($90 + \beta$) across the moving direction. Therefore right (perpendicular) component of velocity from below to above ($B \rightarrow A$) is caused on fluid particle across the impeller blades moving direction. However, if the blade chord makes angle β larger than 90 degree with the moving direction, blade chord forces fluid particle below direction to flow at angle ($90 + \beta$) across the moving direction. Therefore right (perpendicular) component of velocity from above to below ($A \rightarrow B$) is caused on the fluid particle across the impeller blades moving direction.

This indicates that even if blade row is installed in the flow passage, if blade chord is perpendicular and makes a right angle with the moving direction, right (perpendicular) component of velocity is not induced on the fluid particle at all. However, if impeller chord makes an angle with the moving direction, right (perpendicular) component of velocity is induced in the flow passage across the moving direction. And the fluid particle moves right (perpendicular) direction either from above to below or from below to above in the flow passage.

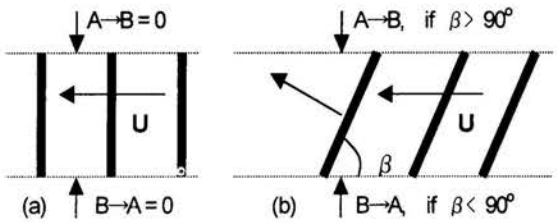

Fig.1 Movement of impeller blades and fluid flow.

2.2 Rotational motion

Rotational Motion of Perpendicular Blade Row

If the blade row, shown in Fig.1 (a), rotates counterclockwise around the axis of rotation at angular velocity ω, fluid particle, which is contained between impeller blades, rotates together with impeller blades toward left hand side around the axis of rotation. However, neither right (perpendicular) component of velocity from above to below ($A \rightarrow B$), nor from below to above ($B \rightarrow A$), is induced on the fluid particle in the flow passage.

Let us consider a material, which is rotating at a constant speed around the axis of rotation. What kind of forces is acting on it at that condition? As a string from the center of rotation pulls the material toward the axis of rotation, it could be said that rotational motion is held by the action of external centripetal force. In other words, material cannot continue its rotational motion without the action of external centripetal force. This indicates that if a material is rotating at a constant speed around the axis of rotation, material has a centrifugal force to move radial outward, because internal centrifugal and external centripetal forces are well balanced at that condition. In more direct explanation, rotational motion causes centrifugal force on material. This can be clear from that if a material is rotating around the axis of rotation, acceleration acts on it toward the axis of rotation. As the external acceleration acts on material toward the axis of rotation, it can rotate around the axis of rotation.

Application to Centrifugal Turbomachinery

In the rotating flow passage of centrifugal turbomachinery, fluid particle rotates together with impeller blade around the axis of rotation. This indicates that impeller blade, which is rotating at a constant speed, acts on fluid particle tangential force and rotates it around the axis of rotation at peripheral velocity U and causes centrifugal force on it. However, as fluid particle is not joined with a string, fluid particle moves radial outward by the action of centrifugal force. Fluid particle moves radial outward by the action of centrifugal force in the rotating flow passage. Therefore, radial outward flow from inner radius to outer radius is caused on the fluid particle in the rotating flow passage of centrifugal turbomachinery. See Fig.2 (a).

Fig.2 Illustration of fluid particle's radial movement.

Rotational Motion of Inclined Blade Row

If the blade row, shown in Fig.1 (b), rotates counterclockwise around the axis of rotation at constant angular velocity ω, fluid particle, which is contained between impeller blades, rotates together with impeller blade around the same axis of rotation. As the blade chord makes angle β less than 90 degree with the rotating direction, fluid particle, contained between impeller blades, moves not only from below (B) to above (A), but also from inner radius (I) to outer radius (O). Rotating impeller blade causes on the fluid particle, not only right (perpendicular) component of velocity, parallel to rotational axis from below (B) to above (A) across the moving direction, but also radial outward component of velocity in the rotating flow passage.

If the blade chord makes angle β larger than 90 degree with the moving direction, fluid particle, contained between impeller blades, moves, not only from above (A) to below (B), but also from inner radius (I) to outer radius (O). Fluid particle has not only right (perpendicular) component of velocity from above to below across the moving direction, but also radial outward component of velocity in the rotating flow passage. That is, fluid particle moves not only parallel to axis of rotation, but also radial outward from inner radius to outer radius.

Application to Axial and Mixed Flow Turbomachinery

In the rotating flow passage of an axial flow and a mixed flow turbomachinery, impeller chord makes angle β less than 90 degree with the moving direction. Rotating impeller blade acts on fluid particle not only axial force, but also centrifugal force. Centrifugal force causes on fluid particle radial outward movement. Therefore, fluid particle moves both axial and radial (outward) directions in the rotating flow passage.

In other point of view, turbomachinery is operated by the mechanical energy. Mechanical energy is supplied to the system from outside of the system. Impeller blade rotates together with fluid particle and energy transfer from mechanical to hydraulic energy is caused from impeller blade to fluid particle in the rotating flow passage. Therefore, fluid particles radial outward movement, which is caused by the action of centrifugal force in the rotating flow passage, results on fluid particle, not only rotational radius change from inner radius to outer radius, but also hydraulic energy change from lower energy to higher one. The larger the rotational radius becomes, the larger the hydraulic energy becomes. This indicates that when fluid particle moves radial outward in the rotating flow passage by the action of centrifugal force, energy transfer from mechanical to hydraulic energy is performed from impeller blade to fluid particle.

Whereas, a fluid particles axial movement means just the transportation of location from one position to the other in the rotating flow passage. Rotational radius is kept constant along the axis of rotation. This indicates that centrifugal force is kept constant. Therefore, hydraulic energy is kept constant. This means that axial movement is performed without the change of hydraulic energy in the rotating flow passage.

From above discussion, it could be said that head, which is produced by a turbomachinery, is equivalent to increasing of radius, centrifugal force, and hydraulic energy, and that the increasing of hydraulic energy is performed only when fluid particle moves radial outward in the rotating flow passage. Otherwise, fluid particle cannot increase its hydraulic energy.

3. BASIC THEORY (CENTRIFUGAL PUMP)

Let us consider energy change of a fluid particle in a stream tube along the streamline in the rotating flow passage of centrifugal turbomachinery. Fundamental energy change of a fluid particle in the stream tube could be explained as follow: If a fluid particle approaches to the leading edge of impeller inlet from upstream flow region, it may has some fundamental basic hydraulic energy e_0 till the flow passage just before the entrance

of leading edge of impeller inlet. If the fluid particle enters to the rotating flow passage, at the leading edge of impeller inlet, it rotates together with impeller blades around the axis of rotation at angular velocity ω and increases its hydraulic energy.

At non-rotational flow passage just before the entrance of leading edge of impeller inlet, fluid particle originally does not have hydraulic energy enough to rotate together with impeller blade. However, at leading edge of impeller inlet it rotates together with impeller blade around the axis of rotation. Why is this happened? This indicates that fluid particles rotational motion is caused by the hydraulic energy, which is transferred from mechanical to hydraulic energy through impeller blades rotational motion. That is, fluid particle, which is rotating together with impeller blade in the rotating flow passage, has hydraulic energy, which is transferred from mechanical to hydraulic energy by the impeller blades rotational motion. If e_1 expresses hydraulic energy, which is transferred from mechanical to hydraulic energy at radius r_1 through impeller blades rotational motion, it also expresses the hydraulic energy of which fluid particle has increased at radius r_1 at leading edge of impeller inlet. Fluid particle at radius r_1, therefore, has hydraulic energy $(e_0 + e_1)$ at leading edge of impeller inlet.

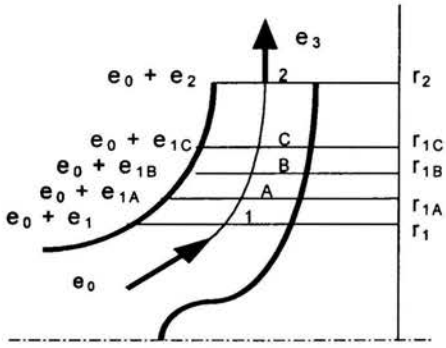

Fig. 3 Fluids flow in a stream tube in rotating flow passage of centrifugal turbomachinery and energy change of fluid particles.

Fluid particle at radius r_1 in the rotating flow passage proceeds forward, from leading edge of impeller inlet through radius r_{1A}, r_{1B}, r_{1C}, r_{1D}, r_{1E} ... toward downstream in the stream tube along the streamline by the action of centrifugal force, and discharges from radius r_2 at trailing edge of impeller outlet to non-rotating flow passage of turbomachinery, see Fig.3. A fluid particle, which has hydraulic energy $(e_0+ e_1)$ at radius r_1 at leading edge of impeller inlet, changes (increases) its rotational radius in order r_{1A}, r_{1B}, r_{1C}, ... and its hydraulic energy $(e_0+ e_{1A})$, $(e_0+ e_{1B})$, $(e_0+ e_{1C})$, ..., and reaches to radius r_2 and hydraulic energy $(e_0+ e_2)$ at trailing edge of impeller outlet, and discharges to downstream non-rotating flow passage by the action of centrifugal force.

At downstream non-rotating flow passage of impeller outlet, energy transfer is not caused. Fluid particle has hydraulic energy e_3 at downstream non-rotating flow passage of impeller outlet. If hydraulic energy losses, which are caused in the flow passage between the trailing edge of impeller outlet and the downstream non-rotating flow passage of impeller outlet, are negligibly small, hydraulic energy e_3 at the downstream non-rotating flow passage is equivalent to $(e_0+ e_2)$, see Figs.3 and 4.

Fluid particle increases its hydraulic energy during the flow in the streamline from upstream non-rotating flow passage to downstream non-rotating flow passage passing through impeller blades rotating flow passage. Therefore, difference of hydraulic energies of a fluid particle in the stream tube between hydraulic energy e_3 at downstream non-rotating flow passage just after the trailing edge of impeller outlet and hydraulic energy e_0 at upstream non-rotating flow passage just before the entrance of leading edge of impeller inlet expresses the grade of hydraulic energy, which is transferred by impeller blade during the flow in the rotating flow passage of stream tube. Hydraulic energy (e_3-e_0), produced by impeller blade A, is therefore given by e_2 as follow

$$e_3 - e_0 = (e_0 + e_2) - e_0 = e_2 \qquad (1).$$

See Figs 3 and 4.

In centrifugal turbomachinery, blade chord is perpendicular to moving (rotating) direction. It makes right angle with peripheral direction. If it rotates counterclockwise, blade chord forces fluid particle normal to peripheral direction. Therefore, perpendicular component of force, that is, axial component of velocity is not caused across the moving direction in the rotating flow passage. No fluid particle flows axial direction. All the fluid particles flow radial outward by the action of centrifugal force.

In case of centrifugal turbomachinery, therefore, impeller blade opens its entrance mouth radial inward. Entrance radius is constant to all the fluid particles at leading edge of impeller inlet. All the fluid particles enter to the rotating flow passage radial outward from inner radius and discharge radial outward from impeller outlet to non-rotating flow passage.

Therefore, hydraulic energy jump is caused only once and one kind from the hydraulic energy e_0 at non-rotating flow passage just before the entrance of leading edge of impeller inlet to the value $(e_0+ e_1)$ at rotating leading edge of impeller inlet.

Head to be Produced By Impeller Blade

Let us consider three impeller blades, named A, B, C. Their discharge radius r_{2A}, r_{2B}, r_{2C} are same at trailing edge of impeller outlet, that is, $r_{2A} = r_{2B} = r_{2C} \equiv r_2$, but entrance radius r_{1A}, r_{1B}, r_{1C} are different at leading edge of impeller inlet and they have the relation $r_{1A} < r_{1B} < r_{1C}$. Streamline of each impeller blade A, B, C lies from upstream non-rotating flow passage to downstream non-rotating flow passage passing through impeller blades rotating flow passage. Rotating flow passage therefore starts at entrance radius r_{1A}, r_{1B}, r_{1C} and ends at discharge radius r_2, see Fig.3. They are operated at same angular velocity ω. Hydraulic energy at leading edge of impeller inlet, therefore, differs by the entrance radius. Hydraulic energy is $(e_0+ e_{1A})$ at radius r_{1A} for impeller A, $(e_0+ e_{1B})$ at radius r_{1B} for impeller B, and $(e_0+ e_{1C})$ at radius r_{1C} for impeller C.

Impeller Blade A: Let us consider a fluid particles movement and its hydraulic energy change in the rotating flow passage of impeller blade A. A fluid particle, which has hydraulic energy e_0 at non-rotating flow passage just before the entrance of leading edge of impeller inlet, enters to the rotating flow passage at leading edge of impeller inlet. Rotational radius is r_{1A} and hydraulic energy is $(e_0+ e_{1A})$ at the leading edge of impeller inlet. Rotational radius changes (increases) from r_{1A} to r_{1B}, r_{1C}, r_{1D}, r_{1E}, ... and hydraulic energy changes from $(e_0+ e_{1A})$ to, $(e_0+ e_{1B})$, $(e_0+ e_{1C})$, $(e_0+ e_{1D})$, $(e_0+ e_{1E})$, ... along the streamline and reaches to radius r_2 and hydraulic energy $(e_0+ e_2)$ at the trailing edge of impeller outlet, and discharges to downstream non-rotating flow passage by the action of centrifugal force. Energy transfer is not caused at downstream non-rotating flow passage. Therefore, if hydraulic energy losses caused in the flow passage between trailing edge of impeller outlet and downstream non-rotating flow passage of impeller outlet are negligibly small, hydraulic energy e_3 obtained at downstream non-rotating flow passage of impeller outlet is equivalent to $(e_0+ e_2)$. Hydraulic energy (e_3-e_0), produced by impeller blade A is, therefore, given by equation (1). See Figs 3 and 4.

Impeller Blade B: Let us consider the case of impeller blade B. Its hydraulic energy is e_0 at upstream non-rotating flow passage of impeller inlet. If the fluid particle enters to the rotating flow passage, rotational radius is r_{1B} and hydraulic energy is $(e_0+ e_{1B})$ at leading edge of impeller inlet. Rotational radius increases from r_{1B} to r_{1C}, r_{1D}, r_{1E}, ... and hydraulic energy increases from $(e_0+ e_{1B})$ to $(e_0+ e_{1C})$, $(e_0+ e_{1D})$, $(e_0+ e_{1E})$, ... and reaches to radius r_2 and hydraulic energy $(e_0+ e_2)$ at trailing edge of impeller outlet, and discharges to downstream non-rotating flow passage by the action of centrifugal force.

At the downstream non-rotating flow passage, energy transfer is not caused. Therefore, if hydraulic energy losses, caused between trailing edge of impeller outlet and downstream non-rotating flow passage are negligibly small, hydraulic energy e_3 is equivalent to $(e_0+ e_2)$. Hydraulic energy (e_3-e_0), produced by impeller blade B, is also given by equation (1).

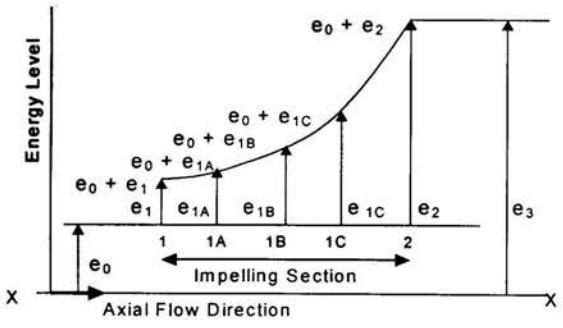

Fig. 4. Illustration of hydraulic energy transfer process increasing along flow passage between impeller inlet and outlet.

Impeller Blade C: Let us consider the case of impeller blade C. If the fluid particle at hydraulic energy e_0 at upstream non-rotating flow passage of impeller inlet enters to the rotating flow passage, its rotational radius is r_{1C} and hydraulic energy is $(e_0+ e_{1C})$ at leading edge of impeller inlet. Rotational radius increases from r_{1C} to r_{1D}, r_{1E}, ... and hydraulic energy increases from $(e_0+ e_{1C})$ to $(e_0+ e_{1D})$, $(e_0+ e_{1E})$, ..., and reaches to radius r_2 and hydraulic energy $(e_0+ e_2)$ at the trailing edge of impeller outlet, and discharges to downstream non-rotating flow passage.

Therefore, hydraulic energy e_3 is equivalent to $(e_0+ e_2)$ at downstream non-rotating flow passage. This indicates that hydraulic energy (e_3-e_0), produced by impeller blade C, is given by equation (1) again.

From above discussion it could be said that hydraulic energy transfer, which is performed during the flow from hydraulic energy e_0 at upstream non-rotating flow passage to hydraulic energy e_3 at downstream non-rotating flow passage passing through rotating flow passage, is merely depend on discharge radius r_2 at trailing edge of impeller outlet, but does not depend on inlet radius r_1 at all. If discharge radius r_2 is same among impeller blades A, B, and C, hydraulic energy e_3, obtained at downstream non-rotating flow passage, becomes same among them regardless their entrance radius r_{1A}, r_{1B}, r_{1C}.

However, hydraulic energy jump, which is caused from hydraulic energy e_0 at upstream non-rotating flow passage just before the entrance of leading edge of impeller inlet to hydraulic energy (e_0+e_1) at rotating flow passage at leading edge of impeller inlet, varies by the entrance radius r_1 at the leading edge of impeller inlet. If entrance radius r_1 differs among impeller blades, hydraulic energy jump varies. If impeller blade A, B, C, has different entrance radius r_{1A}, r_{1B}, r_{1C} and they have the relation $r_{1A} < r_{1B} < r_{1C}$, hydraulic energy jump is caused from hydraulic energy e_0 to hydraulic energy $(e_0+ e_{1A})$, $(e_0+ e_{1B})$, $(e_0+ e_{1C})$, and they has the relation $(e_0+ e_{1A}) < (e_0+ e_{1B}) < (e_0+ e_{1C})$.

4. BASIC THEORY (MIXED AND AXIAL FLOW PUMPS)

In an axial and a mixed flow turbomachinery, blade chord forms an incline angle with the moving direction. If blade row rotates counterclockwise around the axis of rotation, axial, tangential, and centrifugal forces are coursed on the fluid particle in the rotating flow passage. Fluid particle flows toward the direction of resultant force in the rotating flow passage. Our viewpoint is put on fluid particles axial and radial outward movements at this moment.

In an axial flow and a mixed flow turbomachinery, impeller blade opens its entrance mouth very wide between hub and tip across the axis of rotation at the leading edge of impeller inlet. Fluid particle at upstream non-rotating flow passage of impeller inlet flows axial direction in a conduit pipeline along the axis of rotation till the flow passage just before the entrance of impeller inlet. Therefore, fluid particle enters to the mouth parallel to the axis of rotation at the leading edge of impeller inlet. In other words, fluid particle enters to the rotating flow passage perpendicular to peripheral direction at right angle across the impeller blades rotational surface. See Figs 5 and 6.

This indicates that fluid particles entrance radius to the rotating flow passage varies between hub and tip at the leading edge of impeller inlet. Let us consider the mechanism of energy transfer caused in axial and mixed flow turbomachinery next.

4.1 When a Fluid Particle enters to the Rotating Flow Passage at Hub Radius

If a fluid particle, which flows at upstream non-rotating flow passage, has hydraulic energy e_0 at just before the leading edge of impeller inlet and enters to the rotating flow passage at hub radius r_{1HUB} of impeller inlet, fluid particle jumps its hydraulic energy from e_0 to $(e_0 + e_{1HUB})$ at the leading edge of impeller inlet. In the rotating flow passage fluid particle is forced to move under the action of resultant force. Resultant force tends radial outward. Therefore, fluid particle increases its rotational radius during the flow from leading edge of impeller inlet to trailing edge of impeller outlet by the action of centrifugal force.

In other words, fluid particle increases its hydraulic energy during the flow from $(e_0 + e_{1HUB})$ at leading edge of impeller inlet to $(e_0 + e_{2HUB})$ at trailing edge of impeller outlet. Fluid particle reaches to the maximum hydraulic energy at trailing edge of impeller outlet and discharges from rotating flow passage to downstream non-rotating flow passage. Therefore, discharge hub radius r_{2HUB} at trailing edge of impeller outlet is larger than inlet hub radius r_{1HUB} at leading edge of impeller inlet. Discharge hub radius r_{2HUB}, corresponds to r_{1HUB}, is regardless practical hub wall. Hydraulic energy $(e_0 + e_{2HUB})$ is larger than $(e_0 + e_{1HUB})$.

While, in an axial flow turbomachinery, geometrical hub radius at impeller outlet is same to that at impeller inlet, that is, $r_{1HUB,\,AX} = r_{2HUB,\,AX}$. However, in a mixed flow turbomachinery, hub radius at impeller outlet is larger than that at impeller inlet, that is, $r_{1HUB,\,MIX} < r_{2HUB,\,MIX}$. Energy transfer is strongly interrelated to impeller blades geometrical shape of the flow passage. Therefore, it could be said that geometrical shape, that is, hub radius is better situated for mixed flow turbomachinery than that of axial flow turbomachinery to accomplish the energy transfer in good efficiency. This indicates that hub radius has to be increased from inlet to outlet to improve the turbomachinery efficiency. Probably, the larger the gradient becomes the better the turbomachinery efficiency becomes. Result of discussion consists with experimental results. See Fig.7.

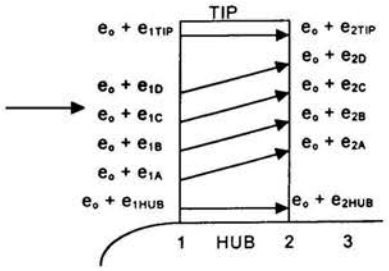

Fig.5 Illustration of fluid particle's hydraulic energy change along the streamline in rotating flow passage of an axial flow turbomachinery.

4.2 When a Fluid Particle enters to the Rotating Flow Passage at a radius between Hub and Tip

If a fluid particle, which has hydraulic energy e_0 at just upstream of leading edge of impeller inlet, enters to the rotating flow passage at radius r_{1X} between hub and tip of impeller inlet, it may jump its hydraulic energy from e_0 to $(e_0 + e_{1X})$ at leading edge of impeller inlet. If a fluid particle, named A, B, C, D, enters to the rotating flow passage at radius r_{1A}, r_{1B}, r_{1C}, r_{1D}, it may jump its hydraulic energy to $(e_0 + e_{1A})$, $(e_0 + e_{1B})$, $(e_0 + e_{1C})$, $(e_0 + e_{1D})$. If entrance radius has the relation $r_{1A} < r_{1B} < r_{1C} < r_{1D}$, hydraulic energy has the relation $(e_0 + e_{1A}) < (e_0 + e_{1B}) < (e_0 + e_{1C}) < (e_0 + e_{1D})$ at leading edge of impeller inlet.

Impeller blade tends fluid particles flow direction radial outward. Fluid particle moves radial outward under the action of centrifugal force. This makes both the fluid particles rotational radius and the hydraulic energy large. Fluid particle increases its hydraulic energy by increasing its rotational radius during the flow from radius r_1 at leading edge of impeller inlet to radius r_2 at trailing edge of impeller outlet, and reaches to the maximum value at the trailing edge of impeller outlet, and discharges to the downstream. Therefore, discharge radius r_2 at the trailing edge of impeller outlet becomes larger than inlet radius r_1 at the leading edge of impeller inlet. Rotational radius becomes $r_{1A} < r_{2A}$, $r_{1B} < r_{2B}$, $r_{1C} < r_{2C}$, $r_{1D} < r_{2D}$.

Therefore, if inlet radius has the relation $r_{1A} < r_{1B} < r_{1C} < r_{1D}$, discharge radius has the relation, not only $r_{2A} < r_{2B} < r_{2C} < r_{2D}$, but also $r_{1A} < r_{2A}$, $r_{1B} < r_{2B}$, $r_{1C} < r_{2C}$, $r_{1D} < r_{2D}$. This indicates that as hydraulic energy at impeller inlet has the relation $(e_0 + e_{1A}) < (e_0 + e_{1B}) < (e_0 + e_{1C}) < (e_0 + e_{1D})$, hydraulic energy at impeller outlet has the relation, not only $(e_0 + e_{2A}) < (e_0 + e_{2B}) < (e_0 + e_{2C}) < (e_0 + e_{2D})$, but also $(e_0 + e_{1A}) < (e_0 + e_{2A})$, $(e_0 + e_{1B}) < (e_0 + e_{2B})$, $(e_0 + e_{1C}) < (e_0 + e_{2C})$, $(e_0 + e_{1D}) < (e_0 + e_{2D})$.

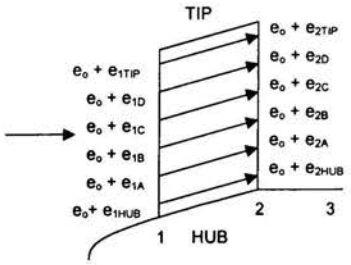

Fig.6 Illustration of fluid particle's hydraulic energy change along the streamline in rotating flow passage of a mixed flow turbomachinery.

4.3 When a Fluid Particle enters to the Rotating Flow Passage at Tip Radius

If a fluid particle, which has hydraulic energy e_0 at just upstream of leading edge of impeller inlet, enters to the rotating flow passage at tip radius r_{1TIP} of leading edge of impeller inlet, fluid particle jumps its hydraulic energy from e_0 to $(e_0 + e_{1TIP})$. As fluid particle moves under the action of resultant force in the

rotating flow passage, fluid particle tends its flow direction radial outward. Therefore, fluid particle increases its rotational radius from radius r_{1TIP} at leading edge of impeller inlet to radius r_{2TIP} at trailing edge of impeller outlet. In other words, fluid particle increases its hydraulic energy during the flow by increasing its rotational radius and reaches to the maximum value at trailing edge of impeller outlet, and discharges from rotating flow passage to downstream non-rotating flow passage. Therefore, discharge tip radius r_{2TIP} at trailing edge of impeller outlet is larger than inlet tip radius r_{1TIP} at leading edge of impeller inlet. And, hydraulic energy (e_0+ e_{2TIP}) at trailing edge of impeller outlet is larger than (e_0+ e_{1TIP}) at leading edge of impeller inlet.

While, in the practical operation of axial flow turbomachinery, tip radius at impeller outlet is geometrically same to that at impeller inlet, that is, $r_{1TIP,\,AX} = r_{2TIP,\,AX}$. But, in a mixed flow turbomachinery, tip radius at impeller outlet is larger than that at impeller inlet, that is, $r_{1TIP,\,MIX} < r_{2TIP,\,MIX}$. In the rotating flow passage of an axial flow turbomachinery, fluid particle, which flows at tip radius from leading edge of impeller inlet to trailing edge of impeller outlet along the casing wall, cannot increase its rotational radius radial outward. It flows along the casing wall and keeps its rotational radius constant during the flow. This indicates that fluid particle, which flows at tip radius along the casing wall, cannot increase its hydraulic energy at all during the flow from impeller inlet to outlet.

However, in case of mixed flow turbomachinery, as it has an incline angle on the casing wall, although its gradient from inlet to discharge is not large and not sufficient, fluid particle can increase its rotational radius radial outward during the flow from impeller inlet to outlet. This indicates that counterbalanced increasing can be expected on rotational radius and hydraulic energy better than axial flow turbomachinery.

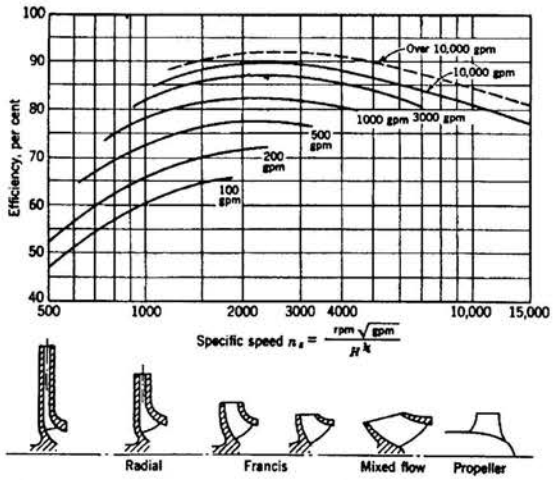

Fig.7 Pump efficiency versus specific speed and pump size (Worthington) from textbook by Stepanoff [1].

Therefore, it could be said that mixed flow turbomachinery is better situated than axial flow turbomachinery to accomplish energy transfer in good efficiency at casing wall. To improve the efficiency, impeller radius has to be increased at casing wall from impeller inlet to outlet as same as that at hub radius. Inclined angle from impeller inlet to outlet forms a gradient on blades shape. Impeller changes its geometrical shape from axial type to mixed type, and to centrifugal type with the increase in incline angle. From these observations, it could be said that the larger the gradient of inclined angle becomes at hub and casing wall, the better the turbomachinery efficiency becomes.

Result of these discussions consists with experimental results. See Fig.7. References [2-7] would be also useful to refer this conclusion. Very good agreement can be obtained from them. With the change of geometrical blade shape from axial type, to diagonal type, to mixed type, and to centrifugal type, pump efficiency is certainly improved. This indicates that pump efficiency can be improved with the fluid particle tends its flow direction radial outward in the flow passage.

5. HEAD PRODUCED BY TURBOMACHINERY

In turbomachinery technology, H [m] expresses head. From practical convenience of usage, it is very common to be used. However, H is the hydraulic energy [N·m/s] of unit mass of fluid particles. For example, performance characteristic curve shows H–Q relation. This H-Q curve expresses energy change of unit mass of fluid particles by the flow rate change at a constant rotational speed. Head H_A at flow rate Q_A at valve opening A expresses hydraulic energy of unit mass of fluid particles at that flow rate. Therefore, H is originally the mechanical energy, which is transferred to hydraulic energy and supplies to fluid particle through impeller blades rotational motion.

Mechanical energy is transferred to hydraulic energy. It is equivalent to hydraulic energy that fluid particle has increased by the rotational motion of impeller blades in the flow passage. During the flow, fluid particle increases its hydraulic energy from upstream non-rotational flow passage of impeller inlet to downstream non-rotating flow passage of impeller outlet, passing through impeller blades rotational flow passage in a stream tube which is lined along the stream line in the rotating flow passage of turbomachinery. Therefore, head H of a fluid particle to be increased can be measured as the difference of hydraulic energies at downstream and upstream non-rotating flow passages of impeller blades. In mathematical expression, this is given as follow:

$$H = H_3 - H_0 \qquad (2).$$

Where, H_3 is the hydraulic energy of unit mass of fluid particles at flow rate Q, measured at flow passage just after the energy supply has finished at trailing edge of impeller outlet in the streamline. H_0 is the hydraulic energy of unit mass of fluid particles, measured at flow passage just before the energy supply to fluid particle has started at leading edge of impeller inlet.

If hydraulic energy losses, which are caused in the flow passage between the trailing edge of impeller outlet and the downstream non-rotating flow passage of impeller outlet, are negligibly small, hydraulic energy H_3, which is measured at downstream non-rotating flow passage is equivalent to hydraulic energy (H_0+ H_2), which is measured at trailing edge of impeller outlet. Then, H_3 is given as follow:

$$H_3 = H_0 + H_2 \qquad (3).$$

Where H_2 is the hydraulic energy which impeller blade transfers mechanical energy to hydraulic energy and supplies to fluid particle as hydraulic energy at trailing edge of impeller outlet. Therefore, hydraulic energy H, transferred by impeller blade. can be explained as follow:

$$H = (H_0 + H_2) - H_0 = H_2 \qquad (4)$$

This indicates that head H, that is, hydraulic energy H, which is transferred from mechanical to hydraulic energy and supplied to the fluid particle as hydraulic energy in the streamline, is equivalent to hydraulic energy H_2, which impeller blade had finally supplied hydraulic energy to fluid particle at trailing edge of impeller outlet. In other words, H_2 is the maximum value which impeller blade can transfer mechanical energy to hydraulic energy in the rotating flow passage.

This indicates that head expresses the ability to push the fluid particle radial outward from trailing edge of impeller outlet and push the fluid particle up to the height H at impeller outlet. This is the reason why head is said equivalent to hydraulic energy which fluid particle has at trailing edge of impeller outlet.

Incorrect Determination of Head

In the textbook of Stepanoff [1], momentum theory, that is, principle of angular momentum is applied to the mass of fluid particles passing through rotating flow passage between impeller inlet and outlet sections. Change of moment of momentum is put equal to moment of all external forces applied to fluid particle contained between two impeller blades. From this theoretical application, head H* is determined as the function of hydraulic energy between impeller outlet and inlet sections. That is,

$$H^* = H_2 - H_1 \qquad (5)$$

In other expression,

$$H^* = \frac{U_2 C_{u2} - U_1 C_{u1}}{g} \qquad (6)$$

This result of application indicates that turbomachinery head H* is determined by the difference of hydraulic energies measured at trailing edge of impeller outlet and that at leading edge of impeller inlet, that is H_2 - H_1.

In this case, hydraulic energy H*, that is, (H_2 - H_1) expresses difference of hydraulic energies of unit mass of fluid particles at impeller outlet and inlet sections. Therefore, it expresses merely the hydraulic energy gradient, which is increased from impeller inlet to outlet. Hydraulic energy H* obtained in this application, therefore, expresses neither the hydraulic energy at impeller outlet, nor the turbomachinery head produced by impeller blades. Therefore, this application is not correct. This may be very clear at a glance from Fig.4.

6. CONCLUSIONS

In the turbomachinery, which transfers mechanical energy to hydraulic energy, hydraulic energy jump is caused from the hydraulic energy at flow passage just before the entrance of leading edge of impeller inlet to that at leading edge of impeller inlet. It is caused only once and one kind in case of centrifugal turbomachinery, because impeller blade opens its entrance mouth radial inward and fluid particle enters to the impeller blade radial outward.

However, in case of mixed and axial flow turbomachinery, impeller blade opens its entrance mouth across the axis of rotation and fluid particle enters to the leading edge parallel to the axis of rotation. Therefore, entrance radius varies between hub and tip. This indicates that grade of hydraulic energy jump varies by the entrance radius between hub and tip at the leading edge of impeller inlet. Hydraulic energy jump is the largest at the tip and the smallest at the hub.

REFERENCES

[1] Stepanoff, A.J., 1967, Centrifugal and Axial Flow Pumps, Theory, Design, and Application, 2nd edition, John Wiley & Sons, INC., pp.29-33 and p.76.

[2] Toyokura, T. etc., 1964, "Studies on the Improvement of High Specific Speed Pump Performance in the Domain of Low Flow Rates," J. of JSME, Vol.67, No.544, May, pp.682-691.

[3] Oshima, M., 1964, "A Study on the Improvement of Performance of Axial Flow Pump," Trans. of JSME, Part 2, Vol.30, No.210, February, pp.236-244.

[4] Hayami, K. and Tanaka, T., 1977, "A Study of a High Specific Speed Propeller Pump: Type of Propeller and Interrelation of Design Parameters," Journal of Fluids Engineering, Trans. ASME, pp.601-603.

[5] Tanaka, T., 1977, "An experimental Study of Diagonal Flow Propeller Pump: Design Performance with Various Types of Blading," ASME Paper No.77-WA/FE-9.

[6] Tanaka, T., 1997, "Mechanism of Downstream Backflows Occurrence and Its Interrelation with Pump Efficiency among Axial Flow Pumps," ASME Paper No.FEDSM97-3441.

[7] Tanaka, T., 2000, "Specific Speed and Efficiency of Turbomachinery," Proceedings of the 5th Biennial Conference on Engineering Systems Design & Analysis, ASME-ESDA 2000, pp.507-518.

HEFAT2002
1st International Conference on Heat Transfer, Fluid Mechanics, and Thermodynamics
8-10 April 2002, Kruger Park, South Africa
TS2

LOCAL HEAT TRANSFER IN NARROW CO-ROTATING DISKS WITH AXIAL THROUGH-FLOW

Shuye Teng* and Je-Chin Han**
*Researcher; **Marcus Easterling Chair Professor
Department of Mechanical Engineering
Texas A&M University
College Station, Texas 77845-3123
USA
Email: jchan@mengr.tamu.edu

ABSTRACT

Local heat transfer in a narrow rotating cavity with axial throughflow was experimentally investigated. The rotating cavity was bounded by two plane disks and a narrow cylindrical rim (shroud). The ratio of the rim span to the disk outer radius was 0.1 and the ratio of the disk inner radius to outer radius was 0.25. This study investigated the effects of axial coolant flow rate and rotation speed on the local heat transfer coefficient distributions inside the cavity. Tests were systematically performed for three axial flow Reynolds numbers (4000, 8000, and 16,000) and three rotational Reynolds numbers (0, 1.7×10^5, 3.4×10^5). Upstream and downstream disks had the same uniform temperature distribution. The results show that local heat transfer coefficients increase with increasing axial flow Reynolds number. Heat transfer coefficients are higher on the downstream disk surfaces than the upstream disk surfaces for low rotational Reynolds numbers. Heat transfer coefficients on the upstream disk surfaces increase with increasing rotational Reynolds number due to increased buoyancy effect. Comparison with previous study shows that a narrow rotating cavity leads to much lower heat transfer coefficients on the disk surfaces, especially at the entrance area.

INTRODUCTION

To achieve higher thermal efficiency and thrust modern aero-engines operate at a high compression ratios and high turbine entry gas temperatures. The compressor and turbine disks are cooled by air flowing through holes in the center of the disks. In order to estimate the thermal growth and fatigue life of turbine and compressor disks, gas turbine designers need to calculate the temperature distributions. The ability to predict disk cavity temperatures offers the cooling flow designer important benefits. An accurate knowledge of the distributions of the local heat transfer coefficient in rotating disks is particularly important to calculate temperature distributions for the compressor and turbine disks.

The rotating disk geometry in a real engine is complicated. The essential features of disks and cavities with net zero radial flow can be modeled as a rotating cylindrical cavity with axial throughflow as shown in Figure 1(a), i.e., a simplified representation of two co-rotating disks where cooling air passes axially through a central hole (or annulus if a central shaft is used). The axial throughflow of cooling air induces secondary flow inside the cavity between adjacent disks, and this flow can be greatly affected by the temperature difference between the disks and coolant under rotating conditions. The main parameters that affect the distributions of the cavity local heat transfer coefficient are coolant flow rate, disk temperature, rotation speed, and cavity configuration.

Farthing et al. [1, 2] studied the flow structure and local heat transfer in rotating cavities with axial throughflow of cooling air. Flow visualization and Laser-Doppler anemometry were used to study flow structure inside the isothermal and heated rotating cavities for ranges of axial-gap ratios, axial Reynolds numbers, rotational Reynolds numbers, and cavity temperature distributions. Also local heat transfer on the upstream and downstream disks were measured in two rotating cavity rigs in which cooling air passed axially through the center of the disks for a range of flows, rotational speeds, and temperature distributions. The distributions of local Nusselt numbers were similar for both the upstream and downstream disks for the case of a symmetrically heated cavity.

Long and Tucker [3] performed heat transfer measurements on the shroud (rim) of a rotating cavity with an axial throughflow of air. This study was an extension from Fathering et al. [1, 2], and focused on the shroud heat transfer coefficients with heated or unheated upstream and downstream

disks. The heat transfer coefficients were calculated based on the temperature of the air inside the cavity, instead of the temperature of the air at the inlet of the cavity as commonly used by Farthing et al. The results showed that the heat transfer from the shroud was only weakly affected by the disk surface temperature distribution and temperature level; heating the shroud did not appear to significantly affect the heat transfer from the upstream and downstream disks.

Kim et al. [4, 5, 6] investigated the effect of axial flow Reynolds number, rotational Reynolds number, and disk surface temperature on the local heat transfer coefficients from enclosed corotaing disks with axial throughflow. Tests were conducted for uniform wall heat flux, uniform wall temperatures, upstream and downstream disks with radially increasing temperature but lower than rim, upstream and downstream disks at uniform temperature but lower than rim upstream and downstream disks and rim at uniform temperature, upstream disk colder than downstream disk a rim, downstream disk colder than upstream disk and rim. The results showed that the local heat transfer coefficients initially decrease and then increase with increasing rotational Reynolds number. The uniform heat flux condition provided a slightly higher heat transfer coefficient than the uniform wall temperature condition.

This study is an extension from Kim et al. [4, 5, 6], and focuses on the effect of axial flow Reynolds number and rotational Reynolds number on the local heat transfer coefficients for enclosed corotating disks with a much smaller gap ratio than the previously studied one. The rotating cavity was comprised of two plane disks and a narrow cylindrical rim. The ratio of axial distance between disks to outer radius of disks (G = S/R) was kept at a constant value of 0.1 whereas the ratio of inner radius to outer radius of disks (R1/R) was maintained at a constant value of 0.25. Both the upstream and downstream disks were uniformly heated to the same temperature. Tests were systematically performed for three axial flow Reynolds numbers (4000, 8000, and 16,000) and three rotational Reynolds numbers (0, 1.7×10^5, 3.4×10^5).

NOMENCLATURE

A	Copper ring surface area
D	Disk bore diameter, =2×R1
G	Gap ratio, S/R
h	Local heat transfer coefficient, W/ ^{2}·C
k	Thermal conductivity of air
m	Coolant (air) flow rate, kg/s
q_{net}	Local net heat transfer rate
r	Radial coordinate
R	Outer radius of disk
R1	Inner radius of disk
Re_r	Rotational Reynolds number, $\Omega R^2/\upsilon$
Re_z	Axial Reynolds number, V_zD/υ
S	Axial distance between disks
T_{air}	Local cavity flow temperature
T_w	Local disk surface temperature
ΔT	Local temperature difference between disk surface and cavity flow, T_w-T_{air}
V_z	Axial flow velocity
Ω	Angular speed of rotating disk
υ	Kinematic viscosity of air

EXPERIMENTAL APPARATU

A detailed schematic of the rotating rig was presented by Kim et al. [4]. The hollow rotating shaft is driven by a 25-hp AC motor with a toothed belt drive pulley system by a frequency controlled motor with a maximum rotating speed of 3400 rpm. The rotation speed for this study varies up to 800 rpm. The rotating cavity is perpendicularly connected to the rotating shaft. Regulated compressor air is routed through an orifice meter to the entrance (upstream) of the hollow rotating shaft through a rotary seal. The cooling air, flows through the rotating cavity and is exhausted into the atmosphere at the exit (downstream) of the hollow rotating shaft. The slip ring assembly is attached to the exit portion of the hollow rotating shaft. This assembly is used to transfer outputs to the stationary data acquisition systems from heaters and thermocouples in the rotating cavity.

The rotating cavity consists of two plane disks and a cylindrical rim (shroud) as shown in Figure 1(a). The plane disk has a 5″ (12.55 cm) inner diameter (bore) and a 20″ (50.2 cm) outer diameter whereas the cylindrical rim has a 1″ (2.54 cm) width between the two disks (i.e., the S/R ratio is 0.1 and the R1/R ratio is 0.25, respectively). Note that stepped rotating tubes are used for this study in order to have a larger disk bore-to-outer diameter ratio, R1/R = 0.25. The disks and rim are composed of copper rings, supported by rigid Urethane foam and aluminum plate. Figure 1 (b) shows the dimensions of the upstream (or downstream) disk. The inner wall of each disk contains seven pieces of copper ring (width = 2.38 cm), and the inner wall of the rim contains one piece of copper ring (width = 1.27 cm). Note that the resistance heating wires are uniformly cemented between the backface grooves of the copper rings and the insulation foam to ensure good thermal contact. Each of the copper rings has its own resistance wires with an independently controlled variac transformer that provides a controllable surface temperature. A 1/16″ (0.158 cm) thick insulation material (model clay) is placed at every location between two copper rings to reduce heat conduction. There is no resistance heating wire thus no heat transfer measurement for the copper ring in the rim.

The slip ring system has 96 channels (points) for the heating and thermocouple wires. Fifty-six channels are used to transfer the output from 28 thermocouples attached to the 14 rings (i.e., each ring with two thermocouples) to a data logger. Another twelve channels are used to measure the coolant temperature inside the cavity through 6 thermocouples evenly distributed along the radial direction. These radially distributed thermocouples provide local coolant temperatures which help determine an accurate local heat transfer coefficient

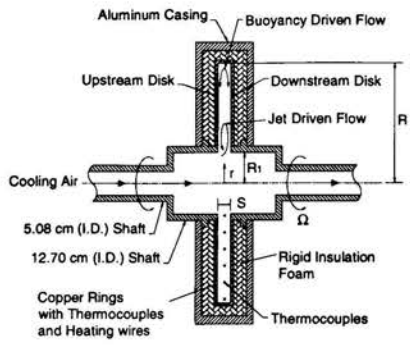

Figure 1(a): Sketch of narrow rotating cavit

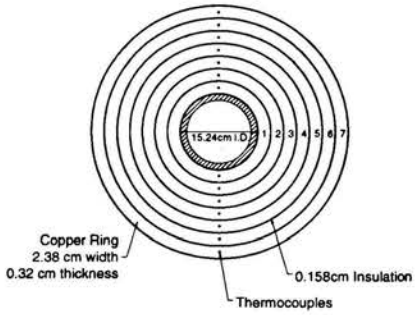

Figure 1(b): Sketch of disk dimensions for upstream or downstream disk

distribution inside the disk cavity. An additional 28 channels are used to control the power output to heating wires individually attached to the 14 rings (i.e., each ring with two channels through 14 variac transformer). The local wall temperature, coolant temperature, and heating power (calculated from voltage drop and current), can be measured using these slip ring assemblies and the associated meters. The velocity profile of the air at the inlet and outlet of the cavity were not measured.

DATA ANALYSIS

The local heat transfer coefficient (h, W/ ^{2}·°C) was calculated from the local net heat transfer rate (q_{net}) per copper ring surface area to the cooling air, the local wall temperature (T_w) on each copper ring, and the local air flow temperature (T_{air}) as:

$$h = q_{net} / [A(T_w - T_{air})]$$

The local net heat transfer rate was the electrical power generated from the heater minus the local heat loss from each copper ring. The electrical power generated from the heater was determined from the measured heater resistance and the voltage (current) on each ring of the cavity. Total heat loss from each copper ring was determined by heat loss tests for a no flow condition (with rotation but without coolant flow). These loss calibrations were performed by supplying several different power levels to each copper ring at steady state in order to determine the relation between the total heat loss from each copper ring surface and the corresponding surface temperature. The heat loss calibration was performed for the two different thermal conditions (uniform wall temperature of 48.9°C and 65.6°C) and three rotation speeds (0, 400, and 800 rpm). Note that the experimentally determined heat loss of this study includes: rotating convection loss to outside the test section, radiation loss to outside the test section, and radiation loss inside the cavity (among the copper rings or copper rims).

The local wall temperatures (around 65 °C~70°C) were obtained from the thermocouple output of each copper ring. The local cooling air temperatures inside the disk cavity were measured by several thermocouples as shown in Figure 1(a) (about 38.9°C~60°C). The uncertainty of the local heat transfer coefficient increases as ($_w$-T_{air}) and the net heat input decrease. The uncertainty also increases for low heat inputs such as low Reynolds numbers. Based on the method described by Kline and McClintock [7], the typical uncertaint in the heat transfer coefficient was estimated to be less than 8% for high Reynolds numbers (8,000 and 16,000). The maximum uncertainty, however, could be up to 20~25% for the lowest Reynolds numbers tested (4,000).

RESULTS AND DISCUSSION

Figures 2, 3 and 4 show the local heat transfer coefficient distributions for different flow rates at a given rotating speed. The rotating speeds (RPM) for the three figures are 0, 400, and 800, respectively, corresponding to the three rotational Reynolds number 0, 1.7×10^5, 3.4×10^5. Figures 5, 6 and 7 show the local heat transfer coefficient distributions at different rotating speeds for a given coolant flow rate. The coolant flow rates (m) for the three figures are 0.02 (0.009), 0.04 (0.018), and 0.08 (0.036) lbm/s (kg/s), respectively, corresponding to the three axial flow Reynolds number 4000, 8000, and 16,000.

Effect of axial flow rate

Figures 2, 3 and 4 show that, for both the upstream and downstream disks, (1) heat transfer coefficients are higher for higher flow rate regardless of the rotating speed; (2) heat transfer coefficient decreases as the r/R ratio increases; (3) heat transfer coefficient has the highest value at the cavity inlet (r/R = 0.35); (4) for the low axial flow Reynolds number Re_z = 4000, the heat transfer coefficient decreases very fast along the radial direction for all three types of rotating speeds. Heat transfer coefficients experience a sharp decrease on the innermost two copper rings. After that, the heat transfer coefficient has a low value of about 1.5 W/ ^{2}·°C for the rest five copper rings; (5) for the axial flow Reynolds number Re_z = 8000, the heat transfer coefficient decreases from r/R = 0.35 till

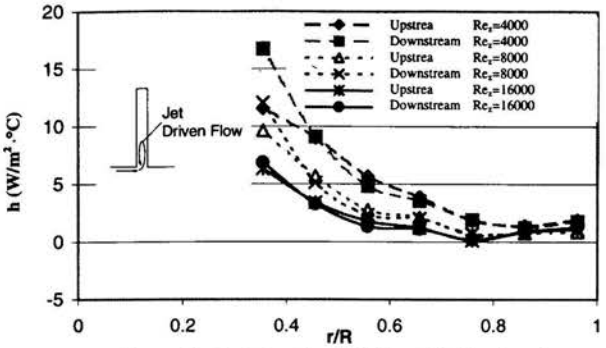

Figure 2: Heat transfer coefficient distributions for different flow rate at RPM = 0

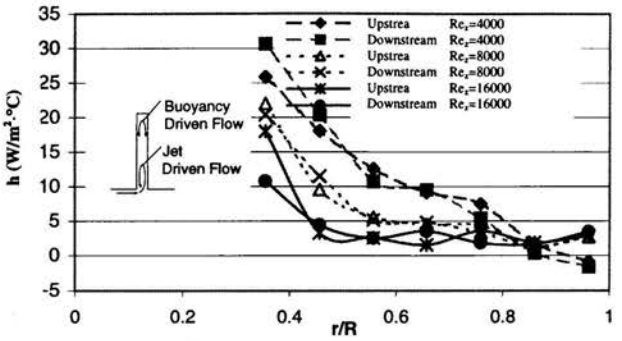

Figure 3: Heat transfer coefficient distributions for different flow rate at RPM = 400

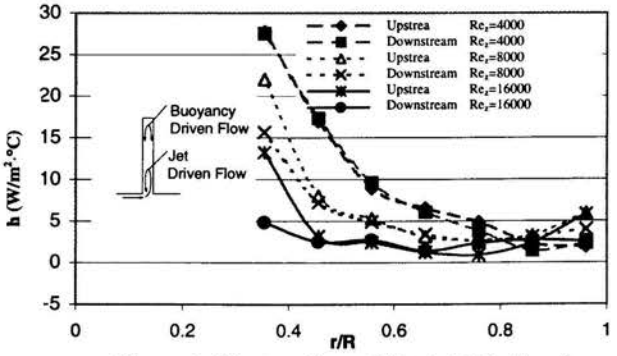

Figure 4: Heat transfer coefficient distributions for different flow rate at RPM = 800

r/R = 0.75 (the inner five copper rings) and has a low value of about 2W/m^2·°C for the rest two copper rings; (6) for the axial flow Reynolds number Re_z = 16000, the heat transfer coefficient decreases all the way along the radial direction from the innermost to the outmost copper ring.

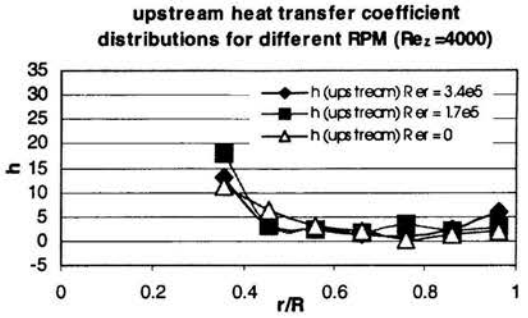

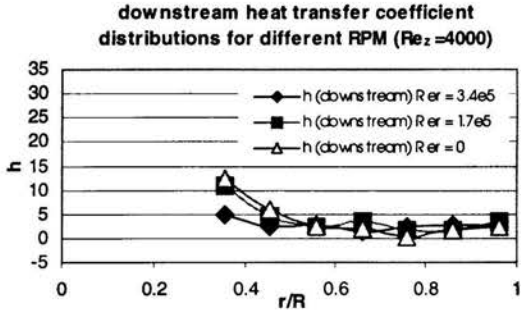

Figure 5: Heat transfer coefficient distributions for different rotating speed at Re_z = 4000

For the cases shown in Figure 2 (Re_r = 0), the heat transfer coefficient distributions in the cavity entrance area are very different for different axial flow rates. Higher axial Reynolds numbers (Re_z = 16000 and Re_z = 8000) result in higher heat transfer coefficients in the entrance area, i.e., the innermost copper ring (r/R = 0.35), on the downstream disk compared to the upstream disk. For Re_z = 16000, the heat transfer coefficient on the downstream innermost copper ring (r/R = 0.35) is 50% higher than that on the upstream innermost copper ring. Because of the cavity configuration, the cooling air hits the downstream disk inlet (the first copper ring) at a certain angle and moves into the cavity from the entrance of the downstream disk. The cooling air recirculates inside the cavit and hits the upstream disk (the second and third copper rings). Based on this jet driven cavity flow path, the heat transfer coefficient has a much higher value at the inlet of the downstream disk (the first copper ring) than that of the upstream disk. Due to cooling air recirculation, the heat transfer coefficients on the upstream copper rings (the second and third copper rings) are higher than that on the corresponding downstream copper rings. The heat transfer coefficients are almost the same on the upstream and downstream disk surfaces as the cooling air flows further into the cavity (the fourth copper ring and thereafter). The heat transfer coefficient distributions for cases Re_z = 8000 and Re_z =

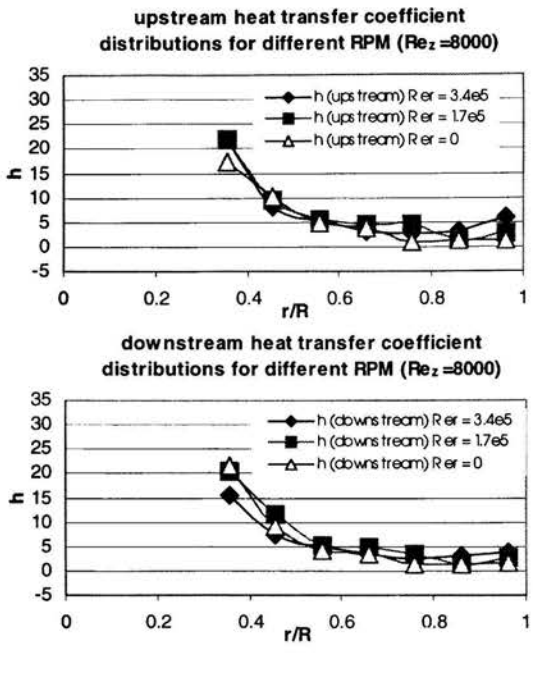

Figure 6: Heat transfer coefficient distributions for different rotating speed at $Re_z = 8000$

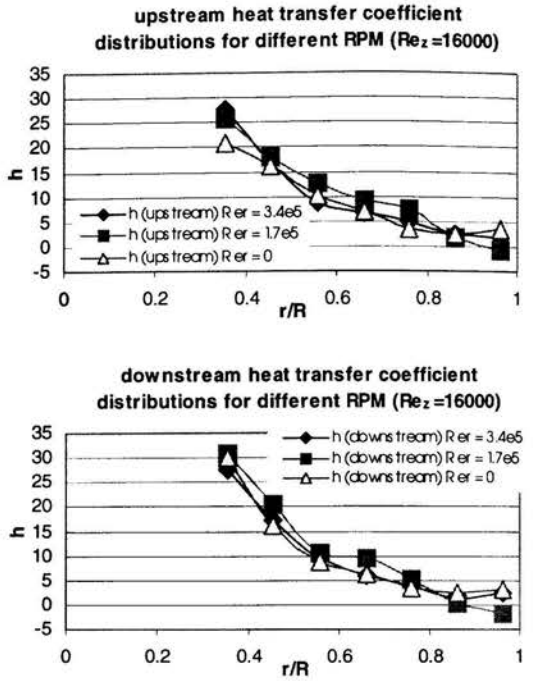

Figure 7: Heat transfer coefficient distributions for different rotating speed at $Re_z = 16000$

4000 show the same waving behavior along the radial direction, but the amplitude is less for $Re_z = 8000$ and much less for $Re_z = 4000$.

For the cases shown in Figure 4 ($Re_r = 3.4\times10^5$), the heat transfer coefficient distributions on the upstream a downstream disks are almost the same, except in the disk entrance area. However, unlike the cases of $Re_r = 0$, here lower flow rates (m = 0.018 kg/s and m = 0.009 kg/s) result in higher heat transfer coefficient in the entrance area (r/R = 0.35) of the upstream disk. This indicates that a rotating cavity tends to change the jet driven flow described in the above paragraph. This may be because that a rotating cavity tends to draw the recirculation flow at the entrance towards the upstream disk. The higher the rotating speed, the closer the recirculation flow is drawn towards the upstream disk, thus causing higher heat transfer coefficient on the upstream disk surface.

The effect of flow rate is kind of mixed for $Re_r = 1.7\times10^5$, as shown in Figure 3, with the higher flow rate (m = 0.036 kg/s) resulting in higher heat transfer coefficients in the entrance area of the downstream disk and the lower flow rate (m = 0.009 kg/s) resulting in higher heat transfer coefficients in the entrance area of the upstream disk.

In general, the higher the axial flow rate, the more coolant air hits the downstream disk with higher momentum, which causes higher heat transfer coefficient on the downstream disk. On the other hand, disk rotation tends to swirl the coolant air into the disk cavity. The higher the rotating speed, the higher the buoyancy driven flow on the disk surface. Thus heat transfer coefficients on the upstream disk surface increase due to the constructive (same direction) interaction between the buoyancy driven flow and the jet driven flow as shown in Figure 3 and 4, but heat transfer coefficients on the downstream surface decrease due to the destructive interaction (opposite direction) between this two flows. The heat transfer coefficient distributions on the upstream and downstream disks depend on the interplay of these two types of flow. The heat transfer coefficient is higher on the upstream disk inlet when the rotation induced upstream constructive buoyancy flow prevails over the axial driven downstream flow, such as the case of ($Re_z = 4000$ and $Re_r = 3.4\times10^5$). The heat transfer coefficient is higher on the downstream disk inlet when the axial driven downstream flow prevails over the rotation induced buoyancy flow, such as the case of $Re_z = 16000$ and $Re_r = 0$). The heat transfer coefficient is almost the same on both the upstream and downstream disk inlets when these two flows offset each other's effect, such as the cases of ($Re_z = 4000$ and $Re_r = 0$), ($Re_z = 8000$ and $Re_r = 1.7\times10^5$), and ($Re_z = 16000$ and $Re_r = 3.4\times10^5$).

As we also notice from Figures 3 and 4, as the rotating speed increases, the waving pattern of heat transfer coefficient distribution we have clearly seen in Figure 2 disappears. This

may be because the buoyancy driven flow induced by disk rotation inside the cavity has strongly interacted with the axial jet driven flow from the entrance, which causes a symmetric air recirculating flow along the disk cavity (see Figure 2~4).

Effect of rotating speed

As we can see from the Figures 5 to 7, for a given flow rate, the effect of different rotating speeds on local heat transfer coefficient distributions does not show an overall difference as strong as the flow rates do for a given rotating speed. The main difference in heat transfer coefficient distribution for different rotating speeds exists in the cavity entrance area. Heat transfer coefficient is higher at the entrance of the downstream disk for low rotation speed, i.e., RPM = 0. Heat transfer coefficient at the entrance of the upstream disk increases with increasing rotating speed. As previously discussed, this is because rotating cavity induces the constructive buoyancy flow at the entrance on the upstream disk and thus increases heat transfer coefficient on the upstream disk surface at the cavity inlet.

Kim et al. [4] have studied local heat transfer in enclosed co-rotating disks with wider cavity (S/R=0.4). Data comparison shows that, due to a bigger cavity width and thus a stronger jet driven flow into the disk cavity, the test section of Kim et al. [4] gives much higher local heat transfer coefficients on both the upstream and downstream disk surfaces for the same axial and rotational Reynolds numbers. In addition, heat transfer coefficients at the entrance area of the wider disk cavit (S/R=0.4) more sensitive to the change of rotational Reynolds numbers than that of the narrower disk cavity (S/R=0.1), while a smaller cavity width reduces the effect of rotational Reynolds number on disk surface heat transfer.

CONCLUSIONS

The effects of axial Reynolds number and rotational Reynolds number on local heat transfer in a narrow rotating cavity with axial throughflow were experimentally investigated. Upstream and downstream disks had the same uniform temperature distribution. The conclusions based on the experimental results are:

1. For both the upstream and downstream disks, heat transfer coefficients are higher for higher flow rate regardless of the rotating speed. Heat transfer coefficient decreases as the r/R ratio increases. Heat transfer coefficient has the highest value at the cavity inlet (r/R = 0.35).
2. For a narrow rotating disk as used in this study, the effect of different rotating speeds on local heat transfer coefficient distributions does not show an overall difference as strong as that of the flow rates.
3. Because of the cavity configuration, the cooling air hits the downstream disk inlet (the first copper ring) at a certain angle and moves into the cavity from the entrance of the downstream disk. Due to the small cavity width, the heat transfer coefficient might have a higher value at the inlet of the downstream disk (the first copper ring) than that of the upstream disk.
4. A rotating cavity affects the jet driven flow. This may be because that a rotating cavity induces the constructive buoyancy flow along the upstream disk. The higher the rotating speed, the higher the heat transfer coefficient on the upstream disk surface, indicating that the buoyancy flow is drawn closer towards the upstream disk.
5. Comparison of this study with Kim et al. [4] shows that: a bigger cavity width induces a stronger jet driven flow into the disk cavity, thus producing much higher local heat transfer coefficients in the entrance area of both the upstream and downstream disks; a smaller cavity width reduces the jet driven flow into the disk cavity, causing the heat transfer coefficients less responsive to the changes of axial or rotational Reynolds numbers.

ACKNOWLEDGEMENT

This project was sponsored by the Pratt & Whitney Company. Their support is greatly appreciated.

REFERENCES

[1] Farthing, P. R., Long, C. A., Owen, J. M., and Pincombe, J. R., 1992 "Rotating Cavity with Axial Throughflow o Cooling Air: Heat Transfer," ASME *Journal of Turbomachinery*, Vol. 114, pp. 229-236.

[2] Farthing, P. R., Long, C. A., Owen, J. M., and Pincombe, J. R., 1992 "Rotating Cavity with Axial Throughflow o Cooling Air: Flow Structure," ASME *Journal of Turbomachinery*, Vol. 114, pp. 237-246.

[3] Long, C. A. and Tucker, P. G., 1992, "Shroud Heat Transfer Measurements from a Rotating Cavity with an Axial Throughflow of Air," ASME Paper No. 92-GT-69.

[4] Kim, S. Y., Han, J. C., Morrison, G. L., and Elovic, E., 1993, "Local Heat Transfer in Enclosed Corotating Disks with Axial Throughflow," ASME *Journal of Heat Transfer*, Vol, 116, pp. 66-72.

[5] Kim, S. Y., Han, J. C., and Morrison, G. L., 199 3, "Influence of Surface Heating Condition on Local Heat Transfer in Enclosed Corotating Disks with Axial Throughflow," ASME paper 93-GT-258.

[6] Kim, S. Y. and Han, J. C., 1993, "Surface Heating Effect on Local Heat Tranfer in an Enclosed Co-rotating Disk with Axial Throughflow," presented at the 6 th International Symposium on Transport Phenomena in Thermal Engineering, Seoul, Korea, May 9-13.

[7] Kline, S. J. and McClintock, F. A., 1953, "Describing Uncertainties in Single-Sample Experiments," Mechanical Engineering, pp. 3-8.

HEFAT2002
1st International Conference on Heat Transfer, Fluid Mechanics, and Thermodynamics
8-10 April 2002, Kruger Park, South Africa
SM1

NUMERICAL INVESTIGATION OF SINGLE STAGE RADIAL CENTRIFUGAL TURBINE

M. Sekavčnik*, B. Drobnič** and M. Tuma***
*Assistant Professor; **Assistant; ***Professor
Faculty of Mechanical Engineering, University of Ljubljana,
Aškerčeva 6, SI-1000 Ljubljana,
SLOVENIA
E-mail: mihael.sekavcnik@fs.uni-lj.si

ABSTRACT

This paper presents the results of CFD calculations on a radial centrifugal turbine (RCT). A numerical model was created and boundary conditions were set according to an experimentally investigated RCT. A series of numerical experiments was performed with fluid volume flow and stator blade angle as varying parameters. The obtained integral energy characteristics of RCT are presented in a dimensionless form. In operating regimes without flow separation, the calculated results show good agreement with the experimental data. An example of transient calculation process is presented, which is used to calculate the timedependent excitation forces and their frequency characteristics.

Nomenclature

Symbol	Quantity	SI Unit
A	Area	m^2
b	Turbine rotor width	m
c_m	Meridional component of absolute velocity	m/s
D_2	Maximal diameter of rotor	m
f_1	First harmonic of interacting frequency	Hz
$\dot{m}$	Mass flow	kg/s
M	Torque applied to the turbine shaft	Nm
n_T	Rotor's rotational frequency	Hz
p	Static pressure	Pa
Δp_{tot}	Total pressure difference of fluid before and after the turbine	Pa
P	Turbine shaft power	W
P_{th}	Theoretically available fluid flow power	W
u_2	Rotor's circumferential velocity at D_2	m/s
$\dot{V}$	Volume flow	m^3/s
z_S	Number of stator blades	-
z_T	Number of rotor blades	-
x, y, z	Cartesian co-ordinates	-
φ	Flow number	-
η	Efficiency	-
θ	Stator blade angle	°
ψ	Pressure number	-
ω	Angular speed	rad^{-1}

The radial centrifugal turbine (RCT) can be described as an outflow turbine, and is commonly used as part of a hydrodynamic torque converter (HTC). The energy characteristics of an HTC containing RCT have been researched in detail by Browarzik *et al.* [1] and Schulz *et al.* [2]; however, they represent a combination of characteristics of its individual parts, namely the pump and turbine impeller, guide vane and torodial casing and the interactions between them.

Some experimental data on energy characteristics of an RCT were obtained by Sekavčnik *et al.* [3] and [4]. The influence of various geometrical parameters of stator and rotor cascades on energy characteristics has been systematically researched. Air was used for testing the RCT. Since the Mach number in the RCT at any tested operating regime did not exceed the value of Ma = 0.12, the fluid was assumed to be incompressible. The measured data were presented in the form of dimensionless shell diagrams, which indicate some interesting characteristics of RCT, e.g. favourable operating range and high efficiency. The experimental data were used in a Cordier Diagram to obtain a relevant comparison with other turbine types [4].

The present work focuses on numerical modelling of RCT. A series of numerical experiments was performed to verify the numerical model itself, and to determine the limits

of validity by comparing the calculated results with the measured ones. Furthermore, the stator-to-rotor flow interaction results in dynamic forces on the turbine's structure, which can be problematic, especially if resonance occurs. Thus, an attempt at transient calculation has been done to study the magnitude of dynamic forces on the rotor's blade caused by the fluid flow.

TURBINE DESIGN CONCEPT

The design of an RCT is characterised by simple geometry of the stator and rotor with parallel side walls, as shown in Fig. 1. The RCT consists of an inlet part where the fluid flow is redirected into a radial outflow direction, a stator, rotor and outlet diffuser.

The stator of the tested RCT consists of 30 guide blades. Its design allows adjustment of the guide blade angle (θ, see definition in Fig. 2). The turbine rotor has 40 blades. After transferring its energy onto the rotor, the fluid exits the RCT through the outlet diffuser. For simplicity's sake, neither the measured test turbine nor the numerical model contained the outlet diffuser.

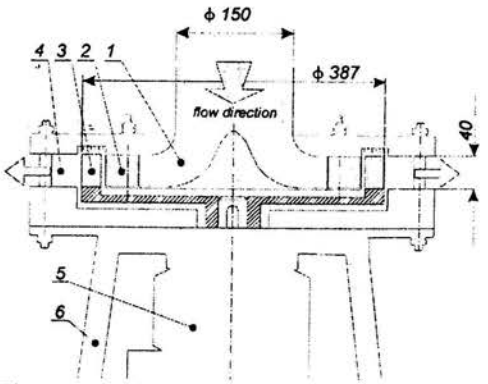

Figure 1: Radial centrifugal turbine: 1 - inlet part; 2 - stator; 3 - rotor; 4 - outlet diffuser; 5 - generator; 6 - frame

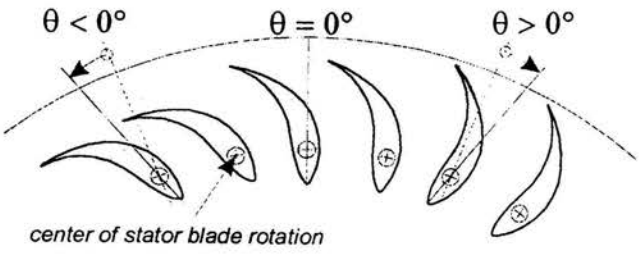

Figure 2: Definition of stator blade angle setting

NUMERICAL EXPERIMENT

Numerical simulation of flow conditions in the RCT was performed with the CFX-TASCflow CFD software package. The program calculates complex 3-D, turbulent, viscous fluid flow with a structured orthogonal grid created with an ICEM CFD Mesh editor.

The actual computational domain covered only 36° of the entire turbine, which included three stator blades and four rotor blades, as shown in Fig. 3.

The grid itself consisted of 24 blocks with about 400,000 nodes; this was expected to give satisfactory results, since calculations with larger grids were not possible due to hardware capability limitations. Fig. 4 shows a part of the grid used for the numerical experiment.

Calculation of energy characteristics

In order to enable comparison with measurement data, the boundary conditions for numerical simulations were set as close to actual conditions as possible. All walls in the turbine were considered to be hydraulically smooth, and the logarithmic law was used to determine the velocity profiles in the boundary layer. The turbulence was modelled with the standard k-ε turbulence model.

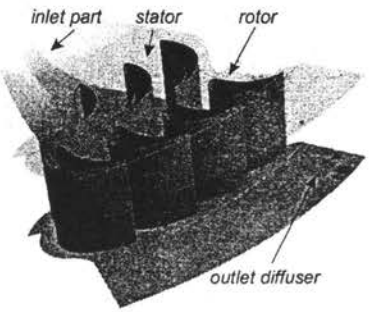

Figure 3: Computational domain of RCT

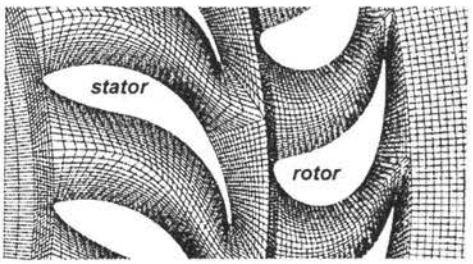

Figure 4: Discretisation grid

The inlet of the turbine was set as inflow (fluid is forced into the computational domain) with a specified, axially oriented mass flow of air (Table 1). The turbine outlet was set as outflow (fluid has to flow out of the computational domain) with a constant static pressure of 1 bar.

Interfaces between the stator and rotor, and also between the rotor and diffuser, were set as frozen rotor general grid interfaces. Here, the steady state solution is calculated where the velocity profile from one side of the interface is transferred unchanged to the other side of the interface according to the absolute frame.

To obtain the integral energy characteristics of RCT calculations had to be performed with various stator blade positions and various fluid mass flows. The changing stator blade position demanded the creation of several grids for the blocks enclosing the stator blades; however, the general topology of each stator grid was unchanged. Varying mass flow, on the other hand, only required a change in inflow boundary condition. Table 1 shows the combinations of stator blade position and air mass flow that were calculated.

stator blade position	mass flow. kg/s: 0.30	0.35	0.40	0.45	0.50	0.60	0.70	0.80	0.90	1.00
	volume flow. m^3/s: 0.26	0.30	0.34	0.39	0.43	0.52	0.60	0.69	0.77	0.86
+6		✓	✓	✓	✓	✓	✓	✓	✓	
+3		✓	✓	✓	✓	✓	✓	✓	✓	
0	✓	✓	✓	✓	✓	✓	✓	✓	✓	✓
-5		✓	✓	✓	✓	✓	✓	✓	✓	
-9	✓	✓	✓	✓	✓	✓	✓	✓	✓	
-13	✓	✓	✓	✓	✓	✓	✓	✓	✓	

Table 1: Calculated examples

Transient calculations

During the physical experiments with the actual turbine, special consideration was given to examination of dynamic behavior of aerodynamic forces on rotor blades as a consequence of stator-to-rotor interaction.

To simulate the same phenomena with numerical experiments, the boundary conditions had to be changed from stationary (time averaged) to transient (time dependent). Sliding interfaces were therefore not set as frozen rotor, which is used for steady state calculations only, but rather as a rotor/stator transient interface. In this way, a calculation is performed for every time step with appropriate relative position of stator and rotor. The latter is rotated in every time step for a certain angle depending on rotational speed and time step. With a time step of 2.7792E-05 s and rotational speed of 157 rad/s, the angle shift in every step was 0.25 degrees. This setup enabled calculation of time-dependent forces which apply to the rotor blade and represent the aerodynamic excitation of the rotor's structure.

RESULTS

The calculated energy characteristics of RCT were presented by means of dimensionless numbers in a shell diagram. The parameters presented in the diagrams are the flow number:

$$\varphi = \frac{c_m}{u_2} = \frac{\dot{V}}{\pi^2 n_T D_2^2 b} \qquad (1),$$

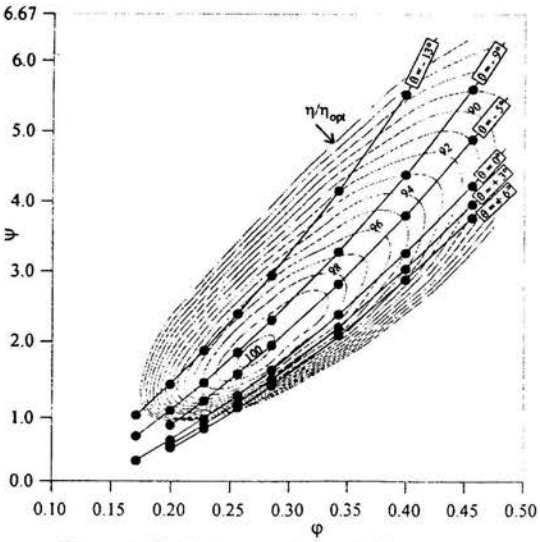

Figure 5: Shell diagram for RCT obtained by CFD

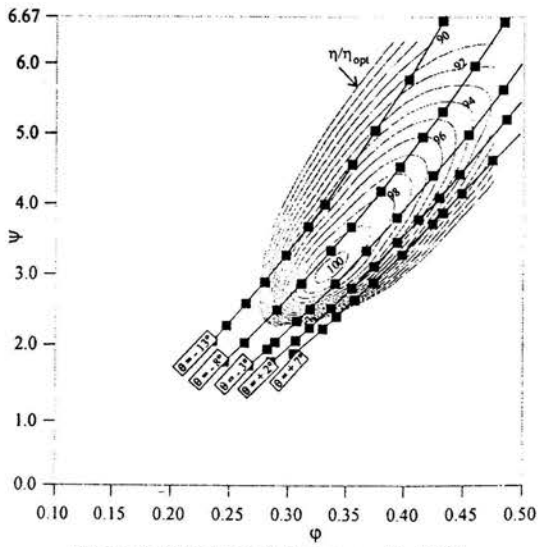

Figure 6: Measured shell diagram for RCT

the pressure number:

$$\psi = \frac{2\Delta p_{tot}}{\rho u_2^2} = \frac{2\Delta p_{tot}}{\rho \pi^2 D_2^2 n_T^2} \quad (2)$$

and turbine efficiency:

$$\eta = \frac{P}{P_{th}} = \frac{M\omega}{\dot{V}\Delta p_{tot}} \quad (3).$$

The torque which applies on the turbine impeller is defined by the integral:

$$M = z_T \int_A p\left(A_y x - A_x y\right) dA \quad (4).$$

Here the rotational axis coincides with co-ordinate z. The torque is calculated numerically during the post-processing of data obtained by CFD.

Calculated energy characteristics

Fig. 5 shows energy characteristics obtained by CFD calculations of 52 cases (see Table 1). A direct comparison with the measured data presented in Fig. 6 [4] is possible. The comparison shows a similar shape of the shell, which represents the efficiency distribution over the operating regime. Even though the stator blade angles used in numerical simulations do not always match the angle settings applied at the measurements, it can be clearly seen that the alignment of the φ–ψ lines in both cases is very similar.

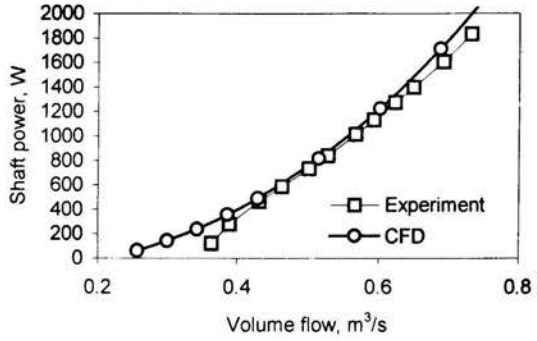

Figure 7: Measured and calculated shaft power in dependence on volume flow

The stator blade angle where the best efficiency point occurs can be estimated by interpolation from shell diagrams and is for both cases $\theta_{opt} = -7°$. The shapes of the shells in both cases (Figs. 5 and 6) clearly show that the best efficiency corresponds to the same stator blade setting θ at any flow number (which is a dimensionless representation of flow rate). In other words, after the optimal stator (regarding hydraulic losses vs. spacing to chord ratio) for a particular RCT is found, there is no need to equip the RCT with the stator blade angle setting mechanism. The blades can be fixed in the housing, which is very favourable for manufacturing and maintenance of the stator.

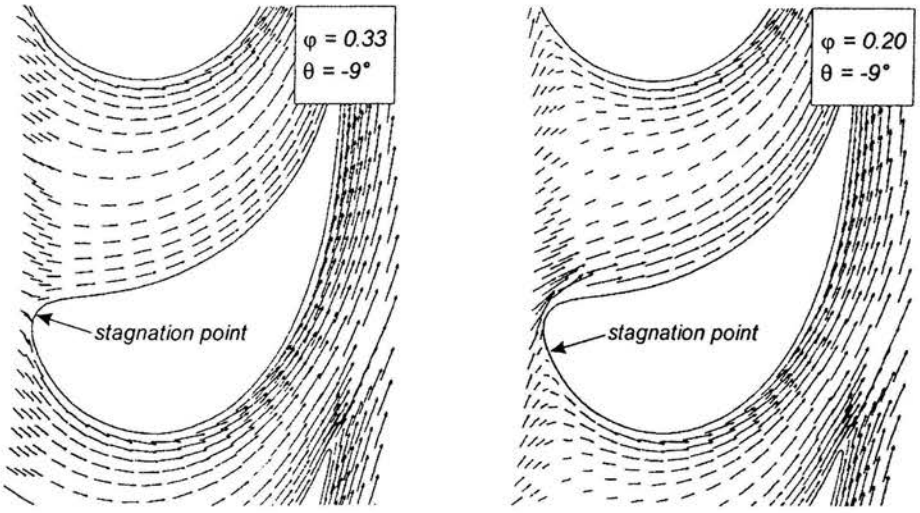

Figure 8: Calculated relative velocity fields inside the rotor of RCT at two characteristic operating regimes

However, some deviations in the best efficiency point and part load regime are evident. The best efficiency point obtained by present CFD calculations occurs at a lower flow number φ_{opt} and pressure number ψ_{opt}, compared to the measured values. At this point it must be mentioned that in the numerical model volumetric losses that occur in reality were not taken into account, but they are assumed not to be responsible for the deviations mentioned above.

The reasons for these deviations were researched using a detailed study of calculated results. In Fig. 7 shaft power is shown in dependence on the volume flow for modelled and measured stator blade angle near θ_{opt}. The diagram shows that the calculated shaft power is over-predicted at low volume flows, which according to the definition in Eq. (3) leads to higher efficiencies.

The velocity field inside the rotor was observed to explain this disagreement between measured and calculated results. In Fig. 8 the velocity fields in relative frame for two characteristic operating regimes are presented. On the left-hand side the velocity field corresponds to the measured best efficiency point. As expected, the angle of flow attack at this operating point coincides with the rotor's profile. With reduction of the volume flow (i.e. flow number φ), a change in the angle of flow attack occurs which causes the stagnation point to move along the suction side of the rotor's profile (Fig. 8, right-hand side). Since the flow near the front side of the turbine's profile is subjected to high adverse pressure gradients flow separation may be suspected. It is shown in [5] that flow separation using the k-ε turbulent model is poorly predicted. However, the measured shell diagram (Fig. 8) shows that at low flow numbers flow separation inside the rotor obviously occurs, which is indicated by rapid efficiency drop. Here the k-ε turbulent model fails, so the turbulence should be handled with different models.

The measured efficiency of the RCT at the operating point is 81% [3]. This is lower than the calculated value of over 90%. As stated in [5], there are still many limitations in CFD which make the absolute validation of particular quantities inaccurate. However, present analyses show that the numerical model used reaches good agreement with the experiment at regimes where the flow is regular, without intensive separation.

Transient calculations

Transient calculations were performed with the RCT grid at operating conditions which approached the calculated best efficiency point, Fig. 5: $\theta = -5°$; $\varphi = 0.28$ and $\psi = 1.94$.

Since the spiral casing at the outlet of the diffuser was excluded, the outlet conditions may be assumed to be constant. When observing the stator-to-rotor transient interaction it is therefore enough to define the computational domain which covers only 36°, using the symmetry conditions at the boundaries. This convenience was used to avoid the additional enlargement that computational memory and time demand.

A time increment was chosen which enables the observation of expected dynamic forces on the rotor's blade. The sampling frequency was 36,000 Hz, which is more than an order of magnitude larger than the first harmonic of the rotor's blade when passing the stator, namely:

$$f_1 = n_T \cdot z_S = 750\,\text{Hz} \qquad (5).$$

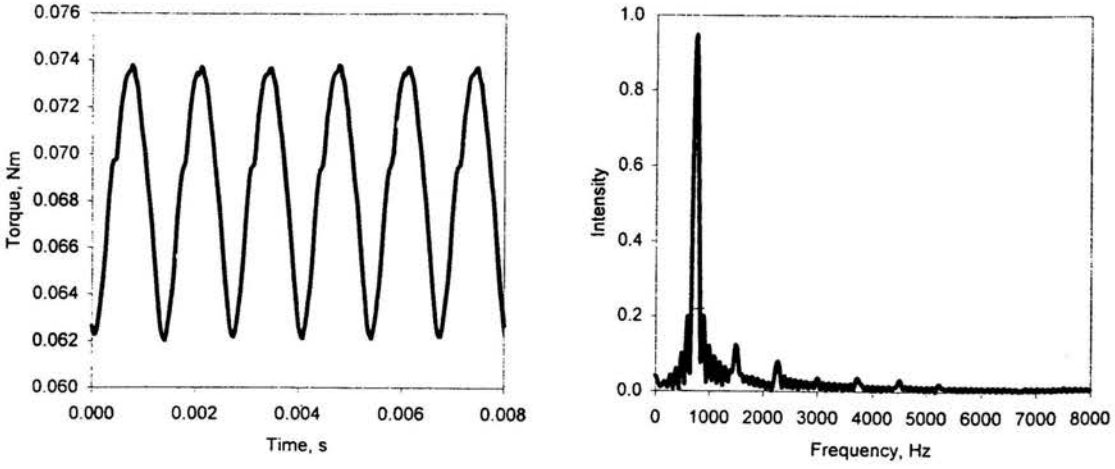

Figure 9: Calculated dynamic signal torque on one blade as a consequence of stator-to-rotor interaction (left) and its frequency spectrum (left)

The dynamic phenomena were evaluated as a time-dependent reacting torque which the fluid flow affects on one blade. It can be derived from Eq. (4), whereas the pressure on the blade's surface must be regarded as a time-dependent integrand. In Fig. (9), left-hand side, the stator-to-rotor interaction is presented as a dynamic behaviour of torque. From the presented signal in the time domain, the initial period (48 out of total of 360 values) was excluded from the analyses due to the transient phenomena caused as a consequence of inconsistent initial condition. After that period the signal shows periodicity, which is analysed using the digital Fourier transformation. The frequency decomposition of the time-domain torque signal shows the largest content of the first harmonic of 750 Hz, which agrees with our expectations (Fig. 9, right-hand side). Furthermore, the higher super-harmonics were also detected in the signal's frequency domain. They indicate the existence of information on adjacent blades in the flow field, which would otherwise be lost when using the steady-state model during the averaging process.

Irrespective of the relatively low amplitude of the dynamic torque the stator-to-rotor interaction causes the dynamic excitation with its frequencies (the first harmonic and higher ones) which can become problematic if one of its frequencies coincides with the resonance of the rotor's structure. The calculated time-dependent pressure distributions over the rotor's blades can be used as a boundary condition in further FEM structure analyses to study the modal dynamic of the rotor's structure, as shown in [6].

CONCLUSION AND OUTLOOK

The numerical model was created according to the experimentally investigated radial centrifugal turbine (RCT). A series of steady-state numerical experiments was performed with fluid volume flow and stator blade angle as varying parameters. The obtained integral energy characteristics of RCT are presented in a dimensionless form.

Comparison of measured and calculated characteristics shows good agreement in the range where flow separation is not developed. The general shape of both the measured and calculated shell diagrams shows the same basic characteristics of RCT. The alignment of the $\varphi-\psi$ lines for both cases is very similar. The best efficiency corresponds to the same stator blade setting at any flow number, which is very convenient with regard to construction.

As a consequence of using a standard k-ε turbulence model, flow separation in part-load regimes is underestimated, which moves the calculated best efficiency point toward smaller values of flow and pressure numbers. The next approach to predicting the flow at part load regimes should be focused on the choice of a better turbulent model, such as the k-ω SST (Shear-Stress-Transport) model.

The transient calculations were performed to study the stator-to-rotor interaction. The dynamic phenomena were evaluated as time-dependent reacting torque which the fluid flow affects on one rotor's blade. The frequency content of the calculated time-domain torque signal was analysed using digital Fourier transformation. In addition to the first harmonics of the stator-to-rotor interaction, higher super-harmonics were also detected, which indicate the availability of information on adjacent blades in the flow field.

The calculated time-dependent pressure distributions over the rotor's blades can be used as a boundary condition in further FEM structure analyses to study the modal dynamic of the rotor's structure.

REFERENCES

[1] Browarzik, V., Grahl, K.G., 1992 "Non-Steady Flow Measurements Inside a Hydrodynamic Torque Converter Using Hot-Film Anemometry," ASME Paper 92-GT-161.

[2] Schulz, H., Greim, R., Volgmann, W., 1994, "Calculation of Three-Dimensional viscous flow in Hydrodynamic Torque Converters, ASME Paper 94-GT.

[3] Sekavčnik, M., Tuma, M., Florjančič, D., 1998, "Characteristics of One Stage Radial Centrifugal Turbine," ASME Paper, 98-GT-494.

[4] Sekavčnik, M., Tuma, M., Florjančič, D., 1999, "Meßtechnische Untersuchungen einer einstufigen Radial-Turbine.

[5] Casey, M., Wintergerste, T., 2000, "Best Practice Guidelines, ERCOFTAC, Edition of special interest group on "Quality and Trust in Industrial CFD"

[6] Filsinger, D., Sekavčnik, M., Kreuz-Ihli, T., Schulz, A., Wittig, S., 1999, "Finite Element Analyses of the Vibration Characteristics of a Turbocharger Impeller," Proceedings of first international Conference on Advances in Structural Engineering and Mechanics, Seoul, Korea.

HEFAT2002
1st International Conference on Heat Transfer, Fluid Mechanics, and thermodynamics
8-10 April 2002, Kruger Park, South Africa
CM3

CONVECTIVE FLOWS IN DIRECTIONAL SOLIDIFICATION UNDER INCLINED ROTATION

Min Hsing Chang [1] and Falin Chen [2]
[1] Department of Mechanical Engineering,
Yung-Ta college of Technology, Pingtung, Taiwan 909, ROC
[2] Institute of Applied Mechanics, National Taiwan University,
Taipei, Taiwan 106, ROC
falin@iam.ntu.edu.tw

ABSTRACT

As the unidirectional-solidifying melt rotates respect to an inclined axis, a shear flow is induced to move parallel to the melt/solid interface while changes its direction along the axis perpendicular to the interface, like an Ekman spiral flow. This induced flow will in turn alter the morphology of the solidifying melt/solid interface and eventually influence the quality of the final casting. In the present paper we investigate this induced flow in the system rotates in a general way while physical conditions vary: different rotating conditions, different thermal and solutal gradients, and the non-Boussinesq effect due to variable viscosity of the melt. Results show that, in brief, the induced flow is driven by the gravity due to inclination while modified by rotation. As each of the following parameters is higher: the effective Taylor number (T_e), the thermal Rayleigh number (R_t), the solutal Rayleigh number (R_c), or the Lewis number (L_e), the induced flow is of larger velocity. The variable-viscosity effect is more complex, depending on the value of other physical parameters.

1. INTRODUCTION

The directional solidification is one of the major industrial techniques by which semiconductor materials such as silicon and gallium-arsenic are manufactured. During the solidification process, the latent heat releases from the melt/solid interface due to phase change and is conducted away into the solid and the melt, forming a thermal boundary layer above the interface. In the meantime, a compositional boundary layer forms above the interface because the solidifying binary solution rejects or incorporates the solute at the interface, enhancing the solutal diffusion in the vicinity of the melt/solid interface. After the thermal and compositional boundary layers form, the morphological instability may occur and disturb the interface into non-planar shape [1]. On the other hand, another kind of instability, or the convective instability, can also occur if the rejected solute is lighter or the incorporated solute is heavier than the solvent, rendering the density distribution in the compositional boundary layer hydro-statically unstable and eventually leading to the onset of double-diffusive convection above the interface [2]. This convective instability may couple with the morphological instability and result in an undesired change of the quality of final casting. An effective scheme to control these two instability modes has accordingly become an important issue discussed in the research of directional solidification.

The influence of the imposed shear flow on these two instability modes was first investigated by Delves [3,4] who imposed quadratic and Blasius boundary-layer flows and by Coriell et al. [5] who imposed a plane Couette flow onto the melt/solid interface. Later, MacFadden et al. [6] imposed a plane stagnation flow vertically onto the melt/solid interface and Forth and Wheeler [7,8] imposed an asymptotic suction boundary-layer flow above the interface. Chung and Chen [9] showed that as the imposed shear flow (a Blasius type boundary-layer flow) becomes strong enough, a transverse mode (roll-axis perpendicular to the imposed flow) of very unstable characteristics is induced. Instead of imposing the shear flow artificially as did by the above-mentioned studies, Sample and Hellawell [10] proposed to rotate the casting mode with respect to an axis inclined to the gravity so that a shear flow can be induced naturally due to inclination. Although no vigorous evidence was provided, they nevertheless conjectured that the shear flow might inhibit greatly the instability of the melt solidifying from below. Their conjecture was later investigated analytically by Chung and Chen [11], in which they showed that a strong helical shear flow was induced and the shear flow generally enhanced the stability of the system.

In the present paper, we consider the directional solidification of binary alloy under inclined rotation, in which a shear flow is possibly induced by inclination and modified by rotation as well as the viscosity variation. We

present the mathematical model of the flow induced by the inclined rotation in section 2. The equations are solved by an analytical approach and the solutions are shown in section 3. Based on this solution, the features of the induced flow are discussed in section 4. The changes of the induced flow under different physical situations including variable viscosity are discussed in section 5. Finally, concluding remarks are given in section 6.

2. PROBLEM FORMUATION

Consider the system as shown in figure 1, a dilute binary solution of temperature T_∞ and concentration C_∞ is solidifying upwards, in which a solid layer is formed below the semi-infinite bulk melt. The melt/solid interface described by $z = h(x, y, t)$ is assumed to be initially planar and advances into the fluid with a constant speed V. The cooling tank rotates in a general way including precession and spin that the angular velocity can be expressed by

$$\begin{aligned}\dot{\Phi} = &(\dot{\phi}_p \sin\phi_n \sin\phi_s)\mathbf{e}_x + \\ &(\dot{\phi}_p \sin\phi_n \cos\phi_s)\mathbf{e}_y + \\ &(\dot{\phi}_p \cos\phi_n + \dot{\phi}_s)\mathbf{e}_z\end{aligned} \tag{2.1}$$

where ϕ_p, ϕ_n and ϕ_s are the angles of precession, nutation and spin, respectively and $\dot{\phi}_p$ and $\dot{\phi}_s$ are the angular velocities of precession and spin, respectively (see Fig. 1). Besides, $\mathbf{e}_x$, $\mathbf{e}_y$ and $\mathbf{e}_z$ are the unit vectors of Cartesian coordinate, which sits on the melt/solid interface as denoted by the *x*-*y*-*z* frame in Fig. 1.

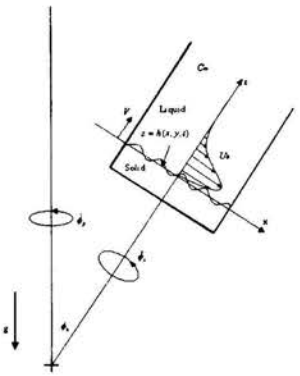

Fig. 1 The schematic description of the system considered. The solid layer is solidifying with a constant velocity V upwards. An induced flow moves parallelly along the melt/solid interface. The casting mode rotates, including spinning and precession, with respect to an inclined axis.

In such a coordinate system, the governing equations in the fluid region $h < z < \infty$ are

$$\nabla \cdot \mathbf{u} = 0, \tag{2.2a}$$

$$\left(\frac{\partial}{\partial t} - V\frac{\partial}{\partial z} + \mathbf{u}\cdot\nabla\right)\mathbf{u} + 2\dot{\Phi}\times\mathbf{u} = -\frac{\nabla P}{\rho_0} + \left(\frac{\rho}{\rho_0} - 1\right)\mathbf{g} + \frac{1}{\rho_0}\nabla\cdot(\mu\mathbf{D}) \tag{2.2b}$$

$$\left(\frac{\partial}{\partial t} - V\frac{\partial}{\partial z} + \mathbf{u}\cdot\nabla\right)C = D_f\nabla^2 C, \tag{2.2c}$$

$$\left(\frac{\partial}{\partial t} - V\frac{\partial}{\partial z} + \mathbf{u}\cdot\nabla\right)T = k_f\nabla^2 T. \tag{2.2d}$$

In above equations, $\mathbf{u}$ represents the velocity vector (u, v, w) measured with respect to the cooling tank, P is the pressure, and ρ_0 is the reference density. The density of the fluid is assumed to be constant except in the gravity term that $\rho = \rho_0[1 - \alpha(T - T_m) - \beta C]$, where α and β are the thermal and solute expansion coefficients, respectively, and T_m represents the freezing temperature of the pure solvent. The vector of gravitational acceleration

$$\begin{aligned}\mathbf{g} = -g(&\sin\phi_n \sin\phi_s \mathbf{e}_x \\ &+ \sin\phi_n \cos\phi_s \mathbf{e}_y + \cos\phi_n \mathbf{e}_z)\end{aligned}$$

depends on both the nutation and spin angles, where g is the gravitational constant. $\mathbf{D} = \nabla\mathbf{u} + \nabla\mathbf{u}^{\mathbf{T}}$ is the deviatoric strain tensor and the superscript "**T**" denotes the transverse of the tensor, C is the concentration, D_f is the solute diffusivity, T is the temperature and k_f is the thermal diffusivity. The viscosity of the fluid μ is considered as an exponential function of temperature

$$\mu = \mu_0 \exp[-c(T - T_m)], \tag{2.3}$$

where $c > 0$ is an arbitrary constant, indicating that the viscosity of the fluid decreases with increasing temperature, and $\mu_0 = \nu_0\rho_0$ is the reference dynamic viscosity, ν_0 is the reference kinematic viscosity. The exponential model is applied because of its wider use for hydrogen-bonded liquids than the other models [14], which suits the aqueous ammonium chloride solution considered in the present paper well.

In the solid region $z < h$, we neglect the diffusion of solute concentration and consider the diffusion of heat only. Then the heat equation is

$$\left(\frac{\partial}{\partial t} - V\frac{\partial}{\partial z}\right)T = k_s\nabla^2 T, \tag{2.4}$$

where k_s is the thermal diffusivity of the solid phase. The boundary conditions at infinite far field are assumed to be that the fluid experiences a rigid-body rotation with the tank and both the concentration and temperature of the fluid remain unchanged during solidification process. Furthermore, it is assumed that the height of the tank is large enough that the influence on the induced flow due to the possible deformation of the free surface can be neglected. Accordingly, at the infinite far field $z \to \infty$ we have

$$\mathbf{u} \to 0,\ C \to C_\infty,\ T \to T_\infty \tag{2.5}$$

At the melt/solid interface $z = h(x, y, t)$, the boundary conditions are

$$\mathbf{u} \times \mathbf{n} = 0, \tag{2.6a}$$

$$\mathbf{u} \cdot \mathbf{n} = 0, \tag{2.6b}$$

$$C^+(1-k)(V + \frac{\partial h}{\partial t})\mathbf{e}_z \cdot \mathbf{n} = -D_f \frac{\partial C^+}{\partial n}, \tag{2.6c}$$

$$T^+ = mC^+ + T_m(1 - \Gamma\xi), \tag{2.6d}$$

$$T^+ = T^-, \tag{2.6e}$$

$$L(V + \frac{\partial h}{\partial t})\mathbf{e}_z \cdot \mathbf{n} = \kappa_s \frac{\partial T^-}{\partial n} - \kappa_f \frac{\partial T^+}{\partial n}, \tag{2.6f}$$

where $\mathbf{n}$ is the unit vector normal to the interface directing toward the fluid. The subscripts "+" and "−" account for the quantities right above and below the interface, respectively. Equation (2.6a) is the no-slip condition. Equation (2.6b) expresses the conservation of mass at the interface by neglecting the difference of the densities between the solid and liquid phases. Equation (2.6c) accounts for the conservation of the solute across the interface, where $k = C^-/C^+$ is the segregation or partition coefficient. Equation (2.6d) is the thermal-dynamical equilibrium condition that describes the dependence of the freezing temperature of a binary alloy upon its composition. The capillary effect (the Gibbs-Thompson effect) is included in the last term and the liquidus slope m is assumed to be a constant. Γ is the capillary length and ξ is the curvature of the interface that is assumed to be negative for a concave projection into the fluid. Equation (2.6e) expresses the continuity of the temperature across the interface and Eq. (2.6f) accounts for the energy balance at the interface, where κ_s and κ_f are the thermal conductivity of the solid and fluid, respectively, L is the latent heat per unit volume of solid.

3. ANALYTICAL SOLUTION

The induced flow during solidification before the melt/solid interface losing the planar shape is induced by the inclination of cooling tank while is modified by rotation. To investigate this induced flow analytically, it is assumed that the melt/solid interface remains planar during solidification, namely,

$$h_b = 0. \tag{3.1}$$

It is assumed also that the horizontal dimension of the cooling tank is much larger than the characteristic length of the solute scale H. Consequently, it can be seen from the scale analysis of the continuity equation that the velocity along the height of the tank is much weaker than that along the x-y plane when small-scaled convection is absent from the system, and the differential derivatives in the x-y planes are negligible in comparison with that along the height of tank as the horizontal size of tank is sufficiently large. As a result, the temperature and concentration are not affected by the presence of the flow induced by inclination and then should be similar to those of previous studies [6, 8, 15], which are shown in the following for convenience for subsequent discussion.

In the melt $z > 0$, the concentration and temperature distributions are represented by a concentration boundary layer and a thermal boundary layer, respectively, i.e.,

$$C_b = 1 - G_c e^{-z}, \tag{3.2}$$

$$T_b = T_\infty - L_e G_l e^{-\frac{z}{L_e}}, \tag{3.3}$$

where the local concentration gradient and temperature gradient are

$$G_c = \frac{k-1}{k}, \tag{3.4}$$

$$G_l = \frac{T_\infty - M/k}{L_e}. \tag{3.5}$$

In the solid layer $z < 0$, the concentration keeps constant and the temperature decreases exponentially,

$$C_b = 1, \tag{3.6}$$

$$T_b = T_\infty + \mathbf{L} - (\mathbf{L} + L_e G_l) e^{-\frac{z}{L_s}}. \tag{3.7}$$

Regarding the induced flow, it is shown from scale analysis that the z-component of the induced velocity can be assumed to be zero, i.e.

$$w_b = 0. \tag{3.8}$$

By applying Eqs. (2.8b-d) and boundary condition Eq. (2.13), we obtain the pressure distribution in the melt as

$$P_b = \overline{P}_b(z,t) + (R_c + R_t T_\infty)\,[x S_\alpha S_3(t) + y S_\alpha C_3(t) + z C_\alpha] \tag{3.9}$$

The reduced pressure $\overline{P}_b(z,t)$ can be obtained by substituting equation (3.9) into (2.8d) and yields

$$\frac{\partial \overline{P}_b}{\partial z} = \left[(-1)^{n_y} T_{ay}^{\frac{1}{2}} S_\alpha C_3(t)\right] u_b - \left[(-1)^{n_y} T_{ay}^{\frac{1}{2}} S_\alpha S_3(t)\right] v_b + \left[R_c(C_b - 1) + R_t(T_b - T_\infty)\right] C_\alpha \tag{3.10}$$

Note that the pressure gradient in z-direction balances the z-component of the fluid weight, leading the melt far above the solidifying front to be quiescent and makes the whole melt motionless in the z-direction. Namely, in the far field from the interface, the pressure gradient can be seen as the buoyancy due to the density variation in the z-direction. On the other hand, however, due to the fact that the density changes greatly within both of

concentration and thermal boundary layers, the pressure gradient in both x- and y-directions cannot balance the weight of the fluid along corresponding directions and causes a flow along the interface, which is then modified by the Coriolis force due to the rotation. The x- and y-components u_b and v_b of the induced flow can be solved by substituting Eqs. (3.8) and (3.10) into Eqs. (2.8b,c), yielding

$$\mu\frac{d^2\hat{U}_b}{dz^2}+(\mu'+S_c^{-1})\frac{d\hat{U}_b}{dz}-iT_e\hat{U}_b = [R_c(C_b-1)+R_t(T_b-T_\infty)]S_n \qquad (3.11)$$

where $U_b \equiv u_b + iv_b = \hat{U}_b e^{i\phi_g}$,

$$\phi_g = -(\Omega t+\pi/2),\quad \mu' = d\mu/dz$$

and T_e is defined as

$$T_e = (-1)^{n_p} T_{ap}{}^{\frac{1}{2}} C_n + \frac{(-1)^{n_s}}{2} T_{as}{}^{\frac{1}{2}}. \qquad (3.12)$$

The associated boundary conditions are

$$\hat{U}_b = 0 \text{ , at } z=0 \text{ and } z\to\infty. \qquad (3.13)$$

Since the gravity component on the x-y plane can be expressed by $g_x + ig_y = S_n g e^{i\phi_g}$, where ϕ_g indicates the orientation of the gravity component on the x-y plane. Equations (3.11) and (3.13) can be solved by asymptotically expanding the dependent variables with respect to , where $= 1/L_e$

4. THE INDUCED FLOW

From Eq.(3.18) one can see that, whether the viscosity is constant or variable, the direction of the induced flow varies with time periodically with a frequency equal to the spin angular velocity Ω. The induced velocity varies with the height of the tank and can be separated into three components of different length scales. The first component is of the length scale of the solute boundary layer, varying vertically with the exponential function e^{-z} and will be called the solutal-layer flow. The second component is of the length scale of the thermal boundary layer, varying with e^{-z/L_e} and will be called the thermal-layer flow. The third component varies its magnitude with e^{-z/d_E} and changes its direction with a period $2\pi/f$, being apparently a kind of spiral Ekman flow and will accordingly be called the Ekman-layer flow.

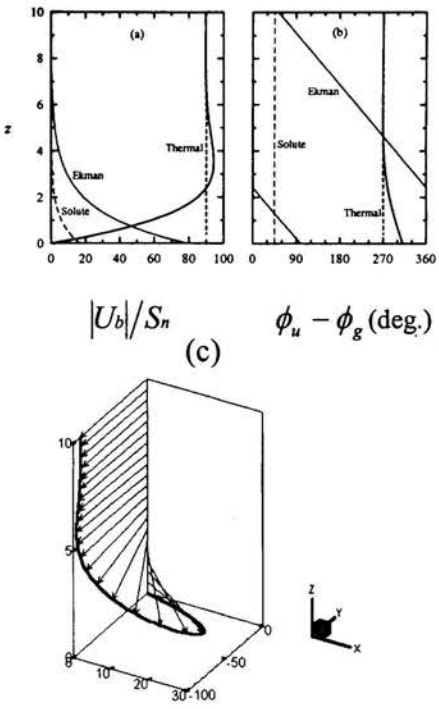

Fig. 2 An example of the induced flow. (a) The velocity amplitudes along the z-axis of the three components: the solutal layer flow, the thermal layer flow, and the Ekman layer flow. (b) The phase angle variations of the three flow components; the phase of Ekman layer flow changes periodically with height. (c) The three-dimensional velocity profile of the induced flow, showing that the spiral structure is mainly confined to a shallow layer above the melt/mush interface.

To more clearly illustrate the variation of these three components, we show in Fig. 2 the variations of both the velocity magnitude and the direction along with the tank height for the case $T_e = 1$, $R_c = 10$, $R_t = 250$, $L_e = 3600$, $S_c = 81$, which corresponds to the aqueous ammonium chloride solution of constant viscosity (i.e. $\gamma = 0$) under small angular velocity rotation (such as $1rpm$) with an inclined angle about 10 degree. It is seen from Fig. 2(a) that both the solutal-layer flow and the Ekman-layer flow are of the maximum velocity at the melt/solid interface and decay exponentially with height, while the thermal layer flow is essentially of constant velocity along the height and is of largest velocity compared to the other two components. By combining these three components, the induced flow vanishes at the interface, satisfying the boundary condition, while increases its velocity exponentially with height within the region where both the solutal-layer flow and Ekman-layer flow decay upwards. After reached the maximum, the

induced flow velocity reduces a bit and remains to be that of thermal-layer flow up to the far field. In other words, the induced flow is dominated by the thermal-layer flow in a large region of the melt, while both the solutal-layer flow and the Ekman-layer flow contribute to the induced flow by reducing the thermal-layer flow exponentially to zero when across the shallow region above the interface.

On the other hand, the three component-flows are of different directions, which can be seen from Fig. 2(b) where ϕ_u is the phase angle of U_b. The solutal-layer flow and the thermal-layer flow are of constant directions, differing from the direction of gravity by 45 and 90 degree, respectively, while the direction of Ekman-layer flow changes periodically with height, forming the main body of spiral structure. To illustrate the spiral structure, we show the velocity vector in Fig. 2(c) that the induced flow in the far field stays in the *y-z* plane, while near the interface the flow has a component in *x*-direction. This component has its maximum on the interface and decays rapidly with height. Note that the direction of thermal-layer flow on the interface is virtually opposite to that of Ekman-layer flow, the combination of these two component-flows therefore becomes a flow of small velocity, which is then vanished due to the solutal-layer flow, leading to the non-slip condition on the interface. At $z \approx 3.2$, on the other hand, the Ekman-layer flow and the thermal-layer flow are of the same direction, resulting in the largest amplitude of the induced flow velocity. A small contribution is made by the solutal-layer flow, which modified a little the position of maximum velocity.

The coefficients of the induced flow velocity of Eq. (3.18) contain the parameter S_n, indicating that the induced flow is a result of the imbalance between gravity and pressure gradient along *x-y* plane when the angle between these two forces is larger than zero. On the other hand, one may infer that as the system is rotating with respect to the vertical axis, i.e. the gravity and the pressure gradient are in the same direction, there will have no induced flow no matter the fluid viscosity is constant or variable. Because of the inclined rotation, the fluid is driven by the resultant force of gravity and pressure gradient to move parallel along the *x-y* plane. When the rotation includes spin, the induced flow varies periodically with a frequency Ω, the spin angular velocity, because both the gravity and pressure gradient change their directions with Ω. While this case cannot be applied to the case of precession, since the phase angle difference between the induced flow and the gravity is independent of time, implying that the induced flow due to precession shall be a steady flow. This physical explanation can also apply to the occurrence of the three component-flows: Both the thermal-layer flow and the solutal-layer flow are the results of system inclination while the Ekman-layer flow is mainly resulted from system rotation. In brief, one may conclude that the induced flow is driven by system inclination and is modified by the system rotation.

5. CONCLUSION

We have investigated analytically the flow in the directional-solidifying melt under inclined rotation including spin and precession. Results show that the flow is driven by the gravity component along the melt/solid interface and is modified by the rotation including spin and precession through the interaction between the Coriolis force and the density gradient. The induced flow moves parallel to the interface while changes the direction along the direction perpendicular to the interface, forming a spiral structure like an Ekman flow. Neither of the temperature nor the concentration distribution is influenced by the formation of induced flow. The induced flow consists of three components: the solutal layer flow, the thermal layer flow, and the Ekman layer flow; the third component dominates the induced flow by changing the flow direction periodically along vertical axis.

ACKNOWLEDGEMENTS

The financial support to this research by National Science Council through NSC 89-2212-E-002-124 is gratefully acknowledged.

REFERENCES

[1] J. W. Rutter and B. A. Chalmers, Can J. Phys. 31 (1953) 15.

[2] S. R. Coriell, M. R. Cordes, W. J. Boettinger and R. F. Sekerka, J. Cryst. Growth 49 (1980) 13.

[3] R. T. Delves, J. Crystal Growth 3 (1968) 562.

[4] R. T. Delves, J. Crystal Growth 8 (1971) 13.

[5] S. R. Coriell, G. B. McFadden, R. F. Boisvert and R. F. Sekerka, J. Cryst. Growth 69 (1984) 15.

[6] G. B. McFadden, S. R. Coriell and J. I. D. Alexander, Comm.Pure Appl. Maths. 41 (1988) 683.

[7] S. A. Forth and A. A. Wheeler, J. Fluid Mech. 202 (1989) 339.

[8] S. A. Forth and A. A. Wheeler, J. Fluid Mech. 236 (1992) 61.

[9] C. A. Chung and F. Chen, J. Fluid Mech. 436 (2001) 85.

[10] A. K. Sample and A. Hellawell, Metall. Trans. A15 (1984) 2163.

[11] C. A. Chung and F. Chen, J. Fluid Mech. 412 (2000) 93.

HEFAT2002
1st International Conference on Heat Transfer, Fluid Mechanics, and Thermodynamics
8-10 April 2002, Kruger Park, South Africa
HE1

A STUDY ON THE IMPACT AND SOLIDIFICATION OF THE LIQUID METAL DROPLET IN THE THERMAL SPRAY DEPOSITION ONTO THE SUBSTRATE WITH SURFACE DEFECTS

Eung-Ji Ha* and Woo-Seung Kim**
*M. Eng. Student; **Professor
Department of Mechanical Engineering,
Hanyang University,
1271 Sa 1-dong Ansan, Kyunggi-do, 425-791,
Korea,
E-mail: wskim@hanyang.ac.kr

ABSTRACT

In this study, numerical investigation has been performed on the impingement, spreading and solidification of a coating material droplet impacting onto a solid substrate in the thermal spray process. The numerical model is validated through the comparison of the present numerical result with experimental data for the flat substrate without surface defects. An analysis of deposition formation on the non-polished substrate with surface defects is performed. The parametric study is also conducted with various surface defect sizes and shapes to examine the effect of surface defects on the impact and solidification of the liquid droplet on the substrate.

INTRODUCTION

Thermal spray deposition processes are an efficient means of manufacturing materials that require significantly fewer manufacturing steps than conventional processes. This processes begin with coating materials in powder form being injected into a gas jet passing through a high temperature environment, where they are heated up, melted and accelerated towards a substrate where a thin deposited layer is formed after impingement, spreading and solidification. Due to the complex physical changes occurring in a very short time, it has been very difficult to develop a good understanding of the thermal spray deposition processes and the related physical phenomena [1,2]. The complexities include the dynamics of a rapidly moving free surface, the importance of both convective and diffusive energy transfer, and the existence of a moving liquid-solid phase-change boundary. In last decades, a few experimental studies have examined impact and solidification of the thermal spray deposition and several numerical models have been developed to simulate it for largely the mono molten droplet on a substrate [3,4]. Recently, Pasandideh-Fard *et al.* [5] and Aziz *et al.* [6] experimentally examined the impact and solidification of molten tin droplets on a flat stainless steel plate. They photographed droplet impact and measured splat diameter from these photographs. They also measured substrate temperature variation under the impacting droplet. Pasandideh-Fard *et al.* [5], Tong and Holt [7] developed numerical models based on fixed grid method to simultaneously predict fluid flow inside the spreading liquid droplet and heat transfer between the droplet and substrate. However, none of experiment and numerical analysis of droplet impact and solidification have been performed on the substrate with non-polished surface. In real situation, non-polished substrate has small defects of which shapes are convex or concave. These defects prohibit spreading of droplet and degrade the quality of the spray deposition. The objective of the present work is to provide an insight into deposition formation during droplet spreading and solidification on the substrate that has small surface defects.

NOMENCLATURE

a	coefficient of matrix
c	specific heat (J/kgK)
C	porosity of the material
D_0	diameter of liquid metal droplet (mm)
D_{max}	maximum splat diameter (mm)
F	volume fraction of fluid
$\mathbf{F}_b$	body force
$\mathbf{F}_{sv}$	continuous surface force
g	volume fraction of liquid phase
ΔH	latent heat of fusion (J/kg)
k	thermal conductivity (W/mK)
$\hat{n}$	unit vector normal to the free surface
$\hat{n}_w$	unit vector normal to the wall
p	pressure
R_c	thermal contact resistance (m^2K/W)
Re	Reynolds number based on the drop diameter
S	Darcy source term for momentum equation
t	time

$\hat{t}_w$ unit vector tangent to the wall
T temperature (°C)
$\mathbf{V}$ velocity (m/s)

Greek Letters
κ curvature of free surface
θ contact angle (°)
ρ density (kg/m^3)
σ surface tension (N/m)
τ viscous stress tensor
ξ spread factor (D/D_0)
Θ volume fraction of obstacle

subscripts
p node point
nb neighboring nodes to p

superscripts
m iteration level
n old time value

NUMERICAL MODEL DESCRIPTION

In order to accurately predict the formation of a splat on the substrate, it is necessary to solve the full Navier-Stokes equations and track both the deforming liquid metal droplet and the moving solid/liquid phase boundary. The fixed-grid model considered in this work couples a two-dimensional axisymmetric incompressible Navier-Stokes equation solver for fluid flow with free surfaces [8] and solidification algorithm proposed by Swaminathan and Voller [9].

Fluid Flow

For incompressible fluids in presence of solid phase, the continuity and momentum equations are given by

$$\nabla\cdot(\Theta\mathbf{V}) = 0 \tag{1}$$

and

$$\Theta\frac{\partial \mathbf{V}}{\partial t} + \nabla\cdot(\Theta\mathbf{V}\mathbf{V}) = -\frac{\Theta}{\rho}\nabla p + \frac{\Theta}{\rho}\nabla\cdot\tau + \Theta\mathbf{F}_b + \Theta\mathbf{S} \tag{2}$$

A unit value of Θ corresponds to a cell full of fluid, whereas a zero value of Θ indicates that the cell contains all solid substrate. $\mathbf{S}$ is the source term to model the velocity reduction in the solidified region. Eqs. (1) and (2) can be combined into a single Poisson equation for the pressure given below

$$\nabla\cdot\left[\frac{\Theta}{\rho^n}\nabla p^{n+1}\right] = \frac{\nabla\cdot(\Theta\tilde{\mathbf{V}})}{\delta t} \tag{3}$$

and it can be solved using an ICCG(incomplete Cholesky conjugate gradient) solution technique.

In the above equation, tilde velocity $\tilde{\mathbf{V}}$ is obtained by using the previous quantities as

$$\Theta\frac{\mathbf{V}-\mathbf{V}^n}{\delta t} = -\nabla\cdot(\Theta\mathbf{V}\mathbf{V})^n + \frac{\Theta}{\rho}\nabla\cdot\tau^n + \Theta\mathbf{F}_b^n \tag{4}$$

The tracking of free surface is given by a volume-of-fluid (VOF) transport equations:

$$\frac{\partial}{\partial t}(\Theta F) + \nabla\cdot(\Theta F\mathbf{V}) = 0 \tag{5}$$

where F is the VOF function defined as the volume fraction of fluid whose value is unity in the fluid and zero in void. More details concerning VOF method are given in Ref. [8]

A continuum surface force (CSF) method [10] is used to model surface tension. The CSF method interprets surface tension effects as a continuous body force effects. The volume force used in the modeling of surface tension effects in the CSF method is given by

$$\mathbf{F}_b = \mathbf{F}_{sv} = \sigma\kappa\nabla F \tag{6}$$

At points that fluids contact with wall or solidified obstacle, wall adhesion forces are calculated in the same manner as volume forces except that a wall adhesion boundary condition is applied to the unit vector normal to the free surface:

$$\hat{n} = \hat{n}_w\cos\theta + \hat{t}_w\sin\theta \tag{7}$$

where θ is the contact angle between fluid and the wall, $\hat{n}_w$ is the unit vector normal to the wall, and $\hat{t}_w$ is tangent to the wall. In our calculation, contact angle is assumed to be 90° for simplicity.

Solidification

The solidification process is described by source-based energy equation given by

$$\frac{\partial}{\partial t}(\rho cT) + \nabla\cdot(\rho c\mathbf{V}T) = \nabla\cdot(k\nabla T) - \rho\Delta H\frac{\partial g}{\partial t} \tag{8}$$

where g is the liquid volume fraction of metal droplet. When g takes a value between 0 and 1, a cell becomes phase boundary cell which has both a liquid and a solid phase. Eq. (8), subject to appropriate boundary and initial conditions, can be integrated fully implicitly as

$$a_P T_P^{m+1} = a_P^n T_P^n + \sum_{nb} a_{nb} T_{nb}^{m+1} + \rho\Delta H(g_P^n - g_P^{m+1}) \tag{9}$$

where superscript $m+1$ represents the current iteration level. Above system of equations is nonlinear since the liquid fraction depends on the temperature. Following the Ref. [9], a truncated Taylor series expansion for g^{m+1} gives

$$g^{m+1} = g^m + \frac{dg}{dT}[T^{m+1} - T^m] \tag{10}$$

Substitution of Eq. (10) into Eq. (9) yields a liner source term in the temperature and results in the iterative equation as follows:

$$\left[a_P + \rho\Delta H \frac{dg}{dT}\right] T_P^{n+1} = a_P^n T_P^n + \rho\Delta H \frac{dg}{dT} T_P^n + \sum_{nb} a_{nb} T_{nb}^{n+1} + \rho\Delta H (g_P^n - g_P^n) \quad (11)$$

To implement surface adhesion boundary, the shape of solidified droplet is reconstructed by the gradient of function g.

The source term is used to modify the momentum equation for the mush region and it takes the following form

$$\mathbf{S} = -\frac{C(1-g)^2}{g^3 + \varepsilon}\mathbf{V} \quad (12)$$

where C represents the porosity of the material and ε is small constant.

RESULTS AND DISCUSSION

To validate that our numerical model can reasonably simulate the droplet impacting and solidification, numerical results are compared with experimental data of Pasandideh-Fard *et al.* [5] and Aziz *et al.* [6] The material properties and other information pertaining to the simulation are given in Table 1. Thermal properties of liquid and solid tin are assumed constant and equal to each other. The constant thermal contact resistance between the droplet and substrate is estimated by comparing the experimental substrate temperature variation and maximum diameter of splat with numerical values of the present work. Calculated value of spread factor, i.e., $\xi = D/D_0$ during the impact of droplets on flat surface with initial temperature of 25°C for Re = 1.3×10^4 and Re = 2.1×10^4, respectively, is shown in Fig.1 (a) and (b). The constant thermal contact resistances used for the numerical calculation are $R_c = 5\times10^{-6}$ m^{2}K/W, $R_c = 1\times10^{-6}$ m^{2}K/W and $R_c = 5\times10^{-7}$ m^{2}K/W. The thermal contact resistance of $R_c = 5\times10^{-6}$ m^{2}K/W among others yields the better agreement between the predicted and measured values of spread factor as shown in both Fig. 1 (a) and (b). The temporal variation of substrate surface temperature at the center is shown in Fig. 2 for Re = 1.3×10^4. It is indicated that there is a good agreement between the experimental and present numerical results for $R_c = 1\times10^{-6}$ m^{2}K/W. These results show that one cannot accurately estimate both the spread factor and the surface temperature of the substrate by using a single thermal contact resistance. In the present work, the constant value of $R_c = 5\times10^{-6}$ m^{2}K/W is used for all the calculations since this value yields more accurate predictions on the spread factor and the variation of the splat shape. The splashing and solidification sequence of a liquid tin droplet on the flat stainless steel substrate are shown in Fig. 3 for Re = 1.3×10^4. In this figure, the dark shaded area represents the solidified metal droplet. Results indicate that the shape of the droplet before the solidification of the edge of the splat (t < 3ms) is very similar to the experimental result [5].

Table 1: Material properties and initial conditions of molten tin droplet and stainless steel substrate.

Liquid Tin	
Density (kg/m^3)	7000
Kinematic viscosity (m^2/s)	2.64×10^{-7}
Surface tension coefficient (N/m)	0.544
Thermal diffusivity (m^2/s)	1.714×10^{-5}
Thermal conductivity (W/mK)	30
Latent heat of fusion (J/kg)	6.07×10^4
Melting temperature (°C)	232
Impact velocity (m/s)	1.6[5] or 2.0[6]
Droplet diameter (mm)	2.1[5] or 2.7[6]
Initial temperature (°C)	240
Stainless Steel	
Thermal diffusivity (m^2/s)	3.95×10^{-6}
Thermal conductivity (W/mK)	14.9
Initial temperature (°C)	25

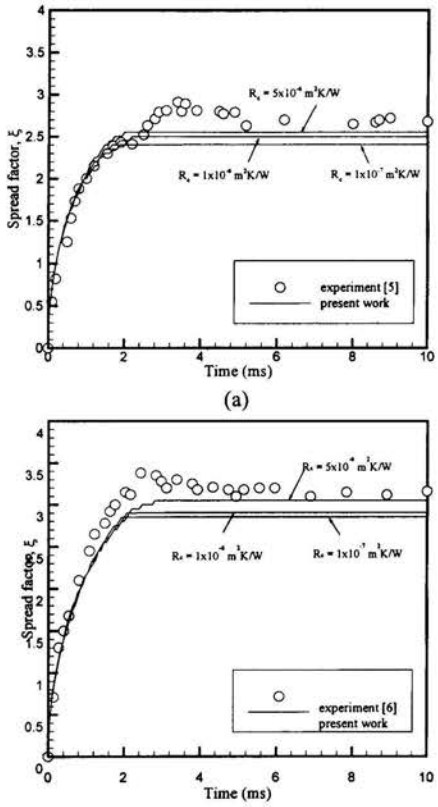

Figure 1: Variation of spread factor during impact of tin droplets on a flat stainless steel surface at (a) Re = 1.3×10^4, (b) Re = 2.1×10^4.

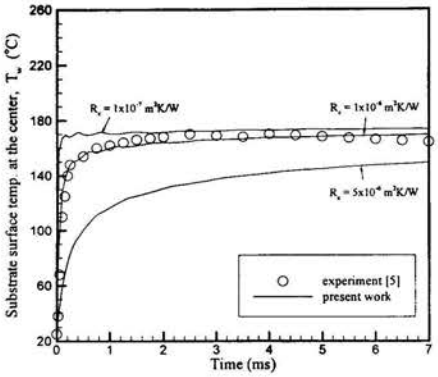

Figure 2: Evolution of substrate surface temperature during the impact of a molten tin droplet on a flat stainless steel at Re = 1.3×10^4.

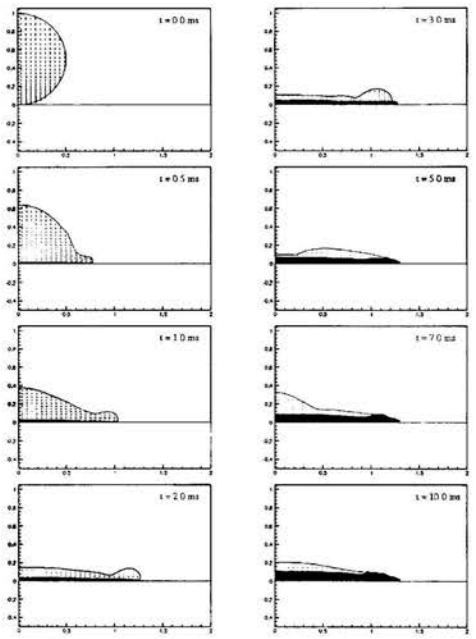

Figure 3: Splashing and solidification sequence of a liquid tin droplet on the flat stainless steel substrate at Re = 1.3×10^4.

However, numerical prediction of the solidified region is preceded by experimental result [5] after the edge of the splat is solidified (t > 3ms). It seems that disagreement between the numerical prediction and experimental data is attributed to the fact that the two-dimensional axisymmetric model could not properly predict Rayleigh-Taylor instability as shown in the experiment. However, this model reasonably simulates the process of droplet impacting, solidifying, and recoiling on the flat substrate.

An analysis of deposition formation on the non-polished substrate with surface defects is performed based on the result for flat substrate. As shown in Fig. 4, the shape of the defects is modeled with axisymmetric simple triangular or rectangular geometry. Figures 5 (a) and (b) show the maximum spread factor for droplet impacting on the substrate that has only one defect at various positions for Re = 1.3×10^4 and Re = 2.1×10^4, respectively. The spread factor at zero defect position in Fig. 5 indicates the one without surface defect. The width of the defects in Fig. 5 is the $0.05D_0$. The depth for concave defect and height for convex defect have the same dimension as width. Maximum spread factor with concave defect did not change greatly with the shape of the defect. It is also found that there is little effect of the position of defect on the spread factor when the defect is located near the impacting point. Spread factor for the case with concave surface defect is reduced by a small amount when the radius of defect is greater than about 0.75 D_0 and 1.0 D_0 for Re = 1.3×10^4 and Re = 2.1×10^4, respectively. However, the spread factor is reduced drastically with the increase of the distance between the impacting point and defect position when the shape of surface is convex. In this case, it is shown that the spread factor varies with the defect shape even though the position of the defect is the same. In general, the spread factor increases with Re number, but it is observed that the opposite case in which the spread factor for the small value of Reynolds number is large occurs when the defect position is located at 0.75 D_0 in the case of the convex surface defect. This result shows that the concave defect only acts as a decelerator which reduces the spreading velocity of the liquid tin droplet. However, the convex defect acts as an obstacle since the droplet collides with the convex defect and then the direction and magnitude of its velocity are largely altered. Thus, it is very difficult to predict general tend of the spread factor in the case with convex surface defect. The droplet could not spread outside the defect and spread factor is limited by only the distance between the impacting point and the position of the defect if the position of defect is over the certain critical value, irrespective of the shape of the defect.

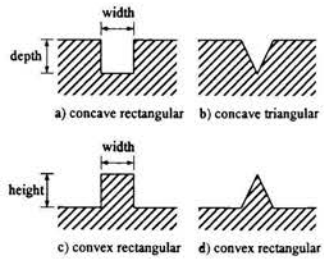

Figure 4: Geometries of the various surface defects.

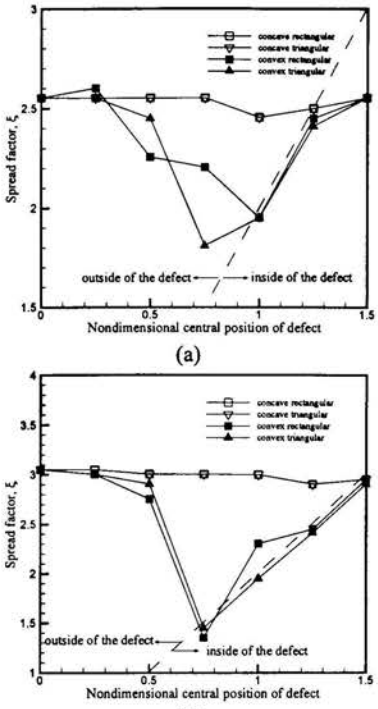

Figure 5: Maximum spread factor for a tin droplet impacting on the stainless steel substrate having one defect with width of 0.05 D_0 at (a) Re = 1.3×10^4, (b) Re = 2.1×10^4.

Figure 6 shows the shape of the splat for four different defect geometries in the case of the same defect position and width at 10ms for Re = 1.3×10^4. It is shown that an air remains in the cavity since the solidified layer is formed before the liquid tin fills up the cavity with the concave defects. Figure 6 (c) indicates the shape of the splat in the case with rectangular convex defect. It is shown that there exists pores behind the defect and the thickness of solidified layer at 10 ms is not uniform, not like the other cases. Figure 7 shows the maximum spread factor in the case with the defect width of 0.1 D_0. The spread factor is decreased compared to that of 0.05 D_0. However, the spread factor is almost identical to that of the case with the defect width of 0.05 D_0, if the defect is very close to the impaction point. In order to investigate the relation of spread factor with the number of concave surface defects, numerical study for the surface defects with periodic constant pitch has been performed. The pitch of defect is defined as the distance between the two defect's centers and the defects are located periodically along the radial direction. Figure 8 shows the maximum spread factor for various pitches. Liquid drop flows over more concave surface defects during the spreading as the pitch decreases and each defect causes the velocity of the

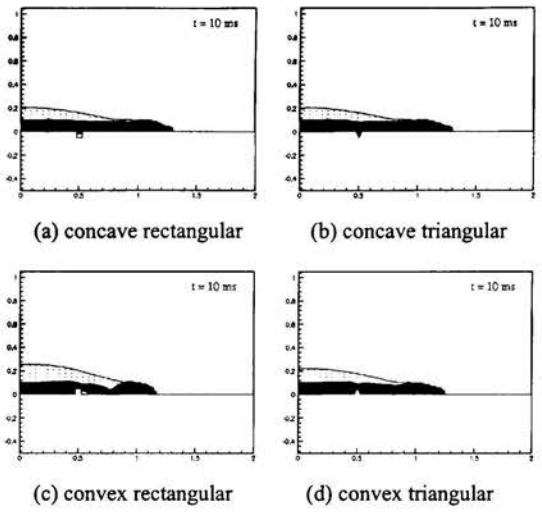

Figure 6: Shape of the splat for various surface defects with width of 0.05 D_0 at Re = 1.3×10^4.

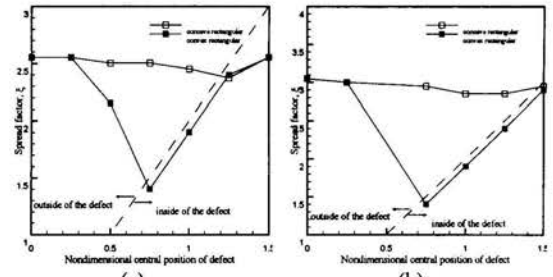

Figure 7: Maximum spread factor for a tin droplet impacting on the stainless steel substrate having one defect with width of 0.1 D_0 at (a) Re = 1.3×10^4, (b) Re = 2.1×10^4.

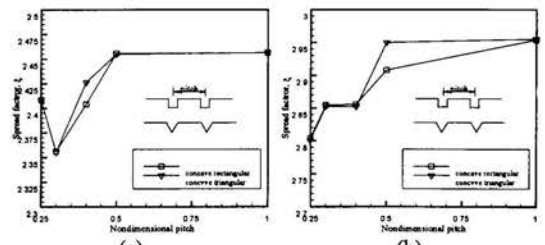

Figure 8: Maximum spread factor for a tin droplet impacting on the stainless steel substrate with various defect pitch at (a) Re = 1.3×10^4, (b) Re = 2.1×10^4.

HEFAT2002
1st International Conference on Heat Transfer, Fluid Mechanics, and Thermodynamics
8-10 April 2002, Kruger Park, South Africa
KY1

AN OBSERVATION OF THE GROWTH OF A PORE TRAPPED IN SOLID DURING SOLIDIFICATION

P. S. Wei and Y. K. Kuo
Professor and Graduate Student
Department of Mechanical and Electro-Mechanical Engineering
National Sun Yat-Sen University
Kaohsiung, Taiwan 80424
Republic of China
E-mail: pswei@mail.nsysu.edu.tw

ABSTRACT

Unsteady growth of pores in solid behind the interface advancing in the upward direction is experimentally investigated. The working medium is distilled water which is poured into a heat-treated glass tube with the lowest temperature of -18 C at the bottom and the surrounding temperature at the top. Observing from a zoom microstereoscope shows the nucleation and growth of the bubbles on the interface and the subsequent formation of the pores in solid. The wall of the pore can be corrugated, melted and solidified, or remain the same shape depending on the pore filled or partially filled with gases or water. The shape of the pore is strongly affected by solidification rate. In earlier stage of solidification, rapid freezing enhances mass transfer and gas pressure in the pore. The growth of cap radius is attributed to the decreasing rate of gas pressure overriding that of hydrostatic pressure on the cap. An oscillating interface fluctuates mass transfer and gas pressure. As the decreasing rate of gas pressure becomes the same order of that of hydrostatic pressure in later time, the wall of the pore readily corrugates.

INTRODUCTION

In metals processings such as casting, welding, and crystal growth the workpieces usually accompany with porosities, whose distributions, sizes and volume fractions determine the extent of any degradation in mechanical properties [1,2,3]. Porosity is the term to describe gas pockets or voids in a workpiece. Hydrogen, oxygen, and nitrogen are usually soluble to any significant extent in a molten pool, and their solubilities in the solidified metal are significantly less than in liquid metal. Therefore, bubbles are readily nucleated by the solidification front where the dissolved gases accumulated [4,5,6]. A bubble after nucleation behaves in different ways: (i) it can float away, collect (or lose) gas and grow (or collapse) in the process and escape to the surroundings, (ii) it can move and grow on the interface, (iii) it can be trapped by the interface and become an elongated blowhole, (iv) it can be rapidly overgrown by the interface and entrapped as an isolated round pore. Bubbles or pores can be reduced by (1) chemical combination to remove dissolved gases, (2) treatment of the liquid in vacuum, (3) pumping an inert gas to liquid, and (4) generating ultrasonic vibrations in liquid [5]. Generally speaking, the pore in solid can be reduced by any method which can decrease the amount of the dissolved gases in liquid.

In order to facilitate an observation, the freezing of water has been effectively used to interpret that of liquid metals [7]. Observing the pores during freezing, Chalmers [8] interpreted that air rejected by the solidification front accumulates in water near the interface until concentration is high enough for bubbles to nucleate. The bubble grows because air diffuses into it. If the interface continues to move forward, the bubble cannot grow laterally but forward to form a cylindrical pore, known as an ice worm. The ice worm that frequently looks like a string of pearls was proposed to be due to the fluctuations of the freezing rate caused by intermittent operation of the compressor of the refrigerator. When freezing is slow, bubbles are bigger. During fast growth the bubble decreases in cross section and the formation of ice worms is suppressed. The ice contains a large number of very small, round pores. In very slow freezing neither bubbles nor ice worms appear since the rejected air is diffused away from the interface. Ice grown in flowing water is usually free of bubbles and ice worms, because a continuous removal of water prevents the build-up of a high concentration of dissolved air.

Observing the freezing of water between horizontal glass slides, Carte [9] found that the density of the separated bubbles was related to the solidification rate by a power of -1.7. A critical supersaturation for bubbles to nucleate was about 30. Wilcox and Kuo [10] reviewed nucleations of bubbles in freezing multicomponent gas solutions and showed that the tendency to form gas bubbles increases with increasing growth rate and decreasing stirring and height of liquid over solid. Vasconcellos and Beech [11] studied the effects of CO_2 dissolved in water on the formation of blowholes. From the observed radii gas pressure and solute concentration in the blowhole were evaluated by satisfying momentum balance and physico-chemical equilibrium. A blowhole exists when the concentration of solute at the interface proceeds that in equilibrium with gas pressure. The growth of blowholes can be explained in terms of a steady-state solute profile.

Geguzin and Dzyuba [12] observed the bubbles captured by the solidification front. The bubbles were found to arise chiefly in the region of coarse distortions of the solidification front at which a local increase in gas concentration exists. From photographic observations the measured density and mean size of pores were found to increase and decrease with increasing solidification speed, respectively. Geguzin and Dzuba [13] evaluated air concentration near the advancing interface by proposing a test bubble method. Gas inclusions in solid were also found to be periodic. It showed that a bubble is not captured, captured as an elongated inclusion, and isolated pore as the solidification front is, respectively, less, equal, and greater than the rate of displacement of the top surface of the growing bubble. Lipp et al. [14] also applied the test bubble method to study the bubble growth ahead of the solidification front and analyzed momentum and energy

transport in a quasi-steady state and physico-chemical equilibrium on a bubble.

Tagavi et al. [15] observed void formation in gassed and degassed cyclohexane and 1,4-Butanediol solidified from above and below. Blowholes appear for gassed liquids irrespective of the direction of solidification. The freezing process starts with liquid shrinkage and decreasing pressure. In upward solidification, the shrinkage is spread as several voids. Freezing from below causes the void to appear at the top under gravity and at the center under microgravity. The dissolved gases have a tendency to distribute the shrinkage as small worms.

Wei et al. [16] observed the pores trapped in solid during solidification, and provided a theoretical model to interpret the formation of the pores. The axisymmetric shape of a pore resulting from a bubble trapped by a solidification front is experimentally and theoretically investigated. Accounting for momentum, energy, mass, and species transport and physico-chemical equilibrium at the moving cap surface of the pore and introducing a time-dependent mass transfer coefficient derived from a scale analysis, the results find the effects of dimensionless parameters governing mass transfer coefficient, the maximum and decaying rate of displacement of the solidification front, Henry's constant, concentration in bulk liquid, surface tension, and cap angle on the shape of the pore. Comparisons between the computed and measured variations in the pore length and cap radius with time are also presented.

In this work, nucleated bubbles trapped by the advancing interface between water and ice are experimentally observed. A simple model to interpret the growth of a bubble trapped in solid is presented. A better understanding of the processes, growth, and shapes of a bubble trapped in solid as a pore during freezing therefore is provided.

NOMENCLATURE

Bo	Bond number = $\rho g h_{i0}^2/\sigma_{fv}$
C_w	gas concentration on liquid side at cap surface
C_∞	solute concentration in liquid far from bubble
C_∞^*	dimensionless concentration in bulk liquid $= RTC_\infty/\rho g h_{i0}$
h	dimensional length, $h^* = h/h_{i0}$
h_{eff}^*	quantity governing steady component of mass transfer coefficient = $\sqrt{h_{i0}/h_g}$
h_g	effective length of pore
h_D	mass transfer coefficient
K^*	dimensionless Henry's constant, $K^* = K/RT$
n	number of mole, kg-mole
p^*	dimensionless pressure = $p/\rho g h_{i0}$
p_a	atmospheric pressure
r_i	dimensional pore radius, $r_i^* = r_i/h_{i0}$, as illustrated in Fig. 2
S	cap area
s_i	displacement of solidification front after nucleation,, $s_i^* = s_i/h_{i0}$, as illustrated in Fig.2
t	dimensional time, $t^* = tD/h_{i0}^2$
z	dimensional coordinate, $z^* = z/h_{i0}$, as illustrated in Fig. 2
ϕ	cap angle, as illustrated in Fig.2

Superscript

*	dimensionless quantities

Subscript

i	liquid-gas or liquid-solid interface
0	initial

OBSERVATION

The main components of the experimental setup are the test liquid, glass tube, constant-temperature bath, and zoom microstereoscope, as illustrated in Fig. 1. A heat-treated glass tube was selected to reduce radial heat transfer to the surroundings. The outer and inner diameters and height are 0.0401, 0.0353 and 0.315 m, respectively. The working medium in the glass tube is distilled water in a height of 0.0975 m. The top of the tube is covered by a copper plate to avoid contaminations from the surroundings and maintain a nearly constant atmospheric temperature. The temperature at the bottom can be as low as -25 $\pm$ 0.3 °C maintained by the constant-temperature bath, where the circulating coolant is 40% volumetric fraction of glycol dissolved

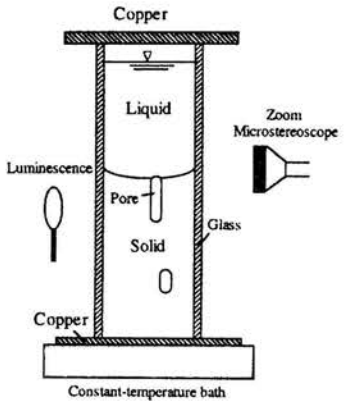

Fig. 1: Schematic sketch of experimental setup.

in water. The lowest temperature is changed by varying the amount of glycol. The pipes in the constant-temperature bath are insulated by wool to avoid condensation and freezing of the vapor in the surroundings. Wool is also placed between the compressor and stirring motor to reduce vibration. To reach a long focal distance and clear image a zoom microstereoscope equipped with a camera is used. The magnification is between 6-60. Four light sources are utilized for luminescence. They are cold so that temperature in water and ice is not disturbed.

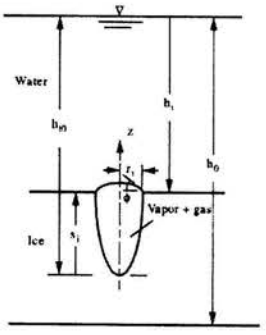

Fig. 2: Physical model and coordinate

The pore growth simultaneously accounting for unsteady mass, energy, and species transport, momentum balance and physico-chemical equilibrium on the pore has been proposed by Wei et al. [16]. As illustrated in Fig. 2, a force balance applied at the cap surface of the pore in solid yields

$$p_g + p_v = p_a + \rho g(h_{i0} - s_i) + \frac{2\sigma_{\ell v}\sin\phi}{r_i} \qquad (1)$$

where the displacement of the solidification front measured from the location where the pore occurs is s_i , which is also equal to the length of the pore. Terms on the left-hand-side of Eq. (1) represent gas pressure in the pore and vapor pressure of pure water, terms on the right side are atmospheric pressure on the top free surface of liquid, hydrostatic pressure, and pressure due to surface tension, respectively. The partial pressure of the gas can be determined from Henry's law $p_g = KC_w$, where the proportionality constant K is the Henry's constant. Vapor pressure of the solvent p_v evaluated from Clausius-Clapeyron equation at the ice point can be ignored. Introducing a mass transfer coefficient h_D , the amount of the gas in the pore can be evaluated

$$\frac{dn_g}{dt} = h_D S(C_w - C_\infty) \qquad (2)$$

The equation of state is needed

$$p_g V = n_g RT \qquad (3)$$

The Stefan boundary condition is also required

$$\rho L_{s\ell}\frac{ds_i}{dt} = k_s\frac{dT_s}{dz} - k_\ell\frac{dT_\ell}{dz} \qquad (4)$$

where the term on the left-hand side represents latent heat due to solidification. The initial condition is $s_i = 0$ at $t = 0$. In view of Lewis number for solid and liquid much greater than unity, temperature profiles in solute-rich regions near the solidification front can be assumed to be linear. Integrating Eq. (4) over time therefore leads to

$$s_i^* = A(1 - e^{-Bt^*}) \qquad (5)$$

where dimensionless parameters A and B govern the maximum displacement of the solidification front and exponential decay of displacement, respectively. Combining Eqs. (2)-(4) with Henry's law gives [16]

$$p_g^* = K^* C_\infty^* \left(1 - \frac{K^*}{h_{eff}^*}\sqrt{\frac{ds_i^*}{dt^*}}\right)^{-1} \qquad (6)$$

which indicates that gas pressure in the pore increases with solidification rate. A dimensionless form of Eq. (1) yields

$$r_i^* = \frac{2\sin\phi}{Bo\,(p_g^* - p_a^* + p_{sat}^* - 1 + s_i^*)} \qquad (7)$$

It showed that in an earlier stage cap radius increases with time, even though solidification rate fluctuates. This is because the decreasing rate of the total gas pressure overrides that of hydrostatic pressure. In view of a rapid decrease in gas pressure, the decreasing rate of gas pressure becomes the same order of that of hydrostatic pressure in the later stage of solidification. This readily results in an oscillation of cap radius and the formation of a wormhole.

Fig. 3: A photograph of bubbles nucleated at the advancing interface

RESULTS AND DISCUSSION

In this study, water is freezed from the bottom of the glass tube. As solidification proceeds, concentrations of the dissolved gases accumulate near the interface between the water and ice. Supersaturation of dissolved gases gives rise to heterogeneous nucleation of bubbles on the rough solid-liquid interface, as shown in Fig. 3. The size of the biggest bubble is approximately 10^{-4} m. It can be seen that many bubbles are strongly nucleating on the left-hand side of the solidification front. A lot of tiny bubbles, which come from evolution of gases from rupture of the nucleated bubbles on the solidification front, float in the upper region of the water. This reveals that the nucleated bubbles are filled with dissolved gases. A more detailed observation and interpretation is interesting and currently undertaking.

With a magnification of 6, Fig. 4(a) shows that a bubble grows after nucleation. In Fig. 4(b), it shows that at a later time of 36 min the growth of the biggest bubble is similar to the way mentioned previously [16]. Referring to Eqs. (6) and (7), in earlier stage of solidification, rapid freezing enhances mass transfer and gas pressure in the pore. The growth of cap radius is attributed to the decreasing rate of gas pressure overriding that of hydrostatic pressure on the cap. For an oscillating interface, as the decreasing rate of gas pressure becomes the same order of that of hydrostatic pressure in later time, the wall of the pore readily corrugates. It can be seen that several small bubbles also nucleate on the right-hand side. In Fig. 4(c) at a time of 140 min other small bubbles nucleate on the left. The right bubble becomes slim and disappeared. Fig. 4(d) shows that bubbles grow with the wall corrugated.

A development of long pores in ice is shown in Fig. 5(a). It can be seen that pores exhibit a bulged region near the

solidification front. As time proceeds, pores are necked near the interface, as shown in Fig. 5(b). The bulged region moves downward. This can be interpreted as a result from an existence of liquid in the pore. Since water has higher temperature than ice a downward flow melts ice and expands the pore. The shape of a pore in solid therefore can be changed. Long pores therefore are separated into two parts.

(a)

(b)

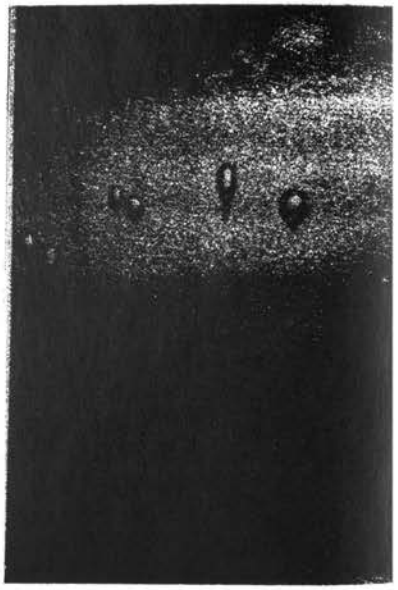

(c)

(d)

Fig. 4: Photographs with magnification of 6 to describe number of bubbles trapped by the solidification front, (a) 18, (b) 36, (c) 140, (d) 180 min.

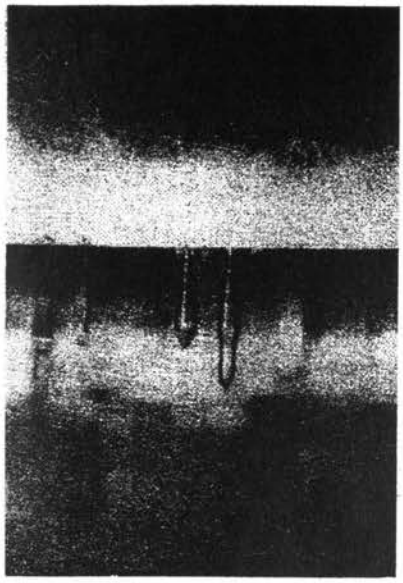

(a)

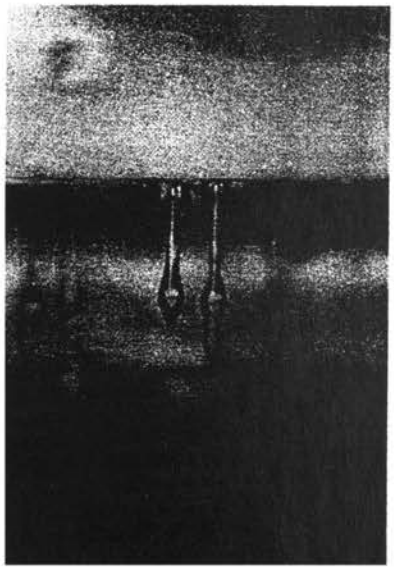

(b)

Fig. 5: Photograph showing development of long pores in ice.

CONCLUSIONS

The conclusions drawn are the following:

1 The bubbles nucleated on the solidification front between water and ice are trapped as pores in solid are observed. The pores may be filled or partially filled with water or gases, as deduced from the variation in the shape of the pore in solid.

2 Cap radius of a pore increases with time in earlier stage of solidification. As time becomes large cap radius readily oscillates. Hence, rings of streak on the wall of the pore appear.

3 The corrugation for the wall of a pore is due to either oscillation of cap radius or the existence of water which freezes after melting the wall.

4 A long pore in solid is observed to be deformed, expanded, necked, cut off, and solidified. This is because the pore partially filled with liquid which melts or freezes alternatively during solidification. A more detailed study is interesting and currently undertaking.

5 In earlier stage of solidification, rapid freezing enhances mass transfer and gas pressure in the pore. The growth of cap radius is attributed to the decreasing rate of gas pressure overriding that of hydrostatic pressure on the cap. For an oscillating interface, as the decreasing rate of gas pressure becomes the same order of that of hydrostatic pressure in later time, the wall of the pore readily corrugates.

REFERENCES

[1] Flemings, M. C., 1974, Solidification Processing, McGraw-Hill, New York, pp.203-213.

[2] Ramirez, J. E., Han, B., and Liu, S., 1994,"Effect of Welding Variables and Solidification Substructure on Weld Metal Porosity," Metallurgical and Materials Transactions A, Vol.25A, pp.2285-2294.

[3] Wei, P. S., 1999, "Pore Formation in Metals Processing-Research Trends," Trends in Heat, Mass & Momentum Transfer, Vol. 5, pp. 101-125.

[4] Bianchi, M. A., and Viskanta, R., 1997,"Gas Segregation during Solidification Processes," International Journal of Heat and Mass Transfer, Vol.40, pp.2035-2043.

[5] Fast, J. D., 1965, Interaction of Metals and Gases, translated from Dutch by M. E. Mulder-Woolcock, Academic Press, New York, pp.112-120.

[6] Grigorenko, G. M., 1970, "Formation of Pores in Welds, Avt. Svarka, No. 10, pp. 12-17.

[7] Jackson, K. A., and Hunt, J. D., 1965,"Transparent Compounds That Freeze Like Metals," Acta Metallurgica, Vol.13, pp.1212-1215.

[8] Chalmers, B., 1959, "How Water Freezes," Scientific American, Vol.200, pp.114-122.

[9] Carte, A. E., 1961, "Air Bubbles in Ice," Proceedings Physical Society London, Vol. 77, pp. 757-768.

[10] Wilcox, W. R., and Kuo, V. H. S., 1973,"Gas Bubble Nucleation during Crystallization," Journal of Crystal Growth, Vol.19, pp. 221-228.

[11] Vasconcellos, K. F., and Beech, J., 1975,"The Development of Blowholes in the Ice/Water/Carbon Dioxide System," Journal of Crystal Growth, Vol.28, pp.85-92.

[12] Geguzin, Ya. E., and Dzyuba, A. S., 1977,"Gas Evolution and the Formation and Capture of Gas Bubbles at the Crystallization Front When Growing Crystals from the Melt," Soviet Physics, Crystallography, Vol.22, pp.197-199 (from Kristallografiya, 1977, Vol. 22, pp.348-353).

[13] Geguzin, Ya. E., and Dzuba, A. S., 1981,"Crystallization of a Gas-Saturated Melt," Journal of Crystal Growth, Vol.52, pp.337-344.

[14] Lipp, G., KÖ rber, Ch., Englich, S., Hartmann, U., and Rau, G., 1987,"Investigation of the Behavior of Dissolved Gases during Freezing," Cryobiology, Vol.24, pp.489-503.

[15] Tagavi, K., Chow, L. C., and Solaiappan, O., 1990,"Void Formation in Unidirectional Solidification," Experimental Heat Transfer, Vol.3, pp.239-255.

[16] Wei, P.S. , Kuo, Y. K., Chiu, S. H., and Ho, C. Y., 2000,"Shape of a Pore Trapped in Solid during Solidification, " International J. Heat and Mass Transfer, Vol. 43, pp. 263-280.

HEFAT2002
1st International Conference on Heat Transfer, Fluid Mechanics, and Thermodynamics
8-10 April 2002, Kruger Park, South Africa
MC3

Heat Transfer Characterization of the Solidification Process Resulting from a Spray Forming Process

Calvin Mackie* and Xiaoling Sheng **
*Assistant Professor, **Ph.D. Candidate
Dept. of Mechanical Engineering
Tulane University
New Orleans, LA 70118
Email: Calvin.Mackie@Tulane.edu

Carsie A. Hall, III
Assistant Professor
Dept. of Mechanical Engineering
University of New Orleans
New Orleans, LA 70148

Jorge E. González, Ph.D.
Associate Professor & Chair
Dept. of Mechanical Engineering
University of Puerto Rico-Mayagüez
Mayagüez, PR 00681-9045

ABSTRACT

Spray forming is achieved by atomizing a liquid metal sheet with an inert gas to form molten droplets, which are then subsequently deposited on a moving cold substrate. During spray deposition processes, the developing pre-form loses thermal energy through a combination of heat transfer processes. To investigate such issues, a heat transfer model was developed to simulate the layer growth. This investigation involves the simultaneous consideration of heat transfer on the substrate, in the growing solid, and in the mushy and/or melt region. The model considered a heat transfer source at the boundary to model the deposition and substrate/coating thermal contact. The deposition rate is assumed to be continuous rather than discrete. Thus, the heat transfer process describing the growth of a layer that results from gas-atomizing a liquid metal on a cold substrate is mathematically formulated assuming a continuous flow assumption. The influence of the system's controlling parameters such as substrate temperature and velocity, deposition rate, and radiation are identified. The effect of the controlling parameters on the final deposit are presented.

NOMENCLATURE

a	coefficient
b	coefficient
Bi	$h_c\Delta z/k_l$ grid Biot number
c	coefficient
Cp	specific heat, kJ/kg-K
d_p	particle diameter prior to impact, m
f	coefficient
Fo	$= \alpha\Delta t/\Delta z^2$ grid Fourier number
h	thickness of the single particle after impact, m
hc	convection heat transfer coefficient, W/m^2-K
h_{ls}	latent heat of solidification, J/kg
h(t)	total thickness of the deposited material, m
m"	spray mass density, kg/m^2-s
k	thermal conductivity, W/m-K
s(t)	thickness of the solid layer, m
t	time, s
Δt	time-step, s
t_t	total time in spraying zone, s
T_m	melting temperature, °C
T_p	temperature of impinging particles, °C
T_∞	environmental temperature, °C
V	velocity of the substrate, m/s
x	co-ordinate
X	the total length in the spray zone, m
z	co-ordinate
Δz	space-step
δ_s	thickness of the solid in the solid/liquid interface grid, m
m	spray mass density, kg/m^2-s
δ_l	thickness of the liquid in the solid/liquid interface grid, m
ε	emissity
σ	Stefan-Boltzmann constant, 5.67e-8 $W/m^2\cdot K^4$
ρ	density, kg/m^3
α	$k/\rho c_p$ thermal diffusivity, m^2/s
ξ	parameter describing the spread of the liquid particles impacting the substrate

Subscripts

s	solid
l	liquid
i	spatial grid node number

int interface

Superscript

n time grid node number

INTRODUCTION

There is a need for more efficient and inexpensive metal production processes which are less energy intensive and less damaging to the environment. The need is causing the metals industry to consider new flexible manufacturing processes. One such process is the spray forming or spray casting technique to manufacture near net-shape parts such as aluminum alloys plate/sheet pre-forms. Spray forming is achieved by atomizing a liquid metal sheet with an inert gas to form molten droplets which are then subsequently deposited on a moving cold substrate. A coherent and fully dense preform is produced as the trajectory of droplets is altered by a moving substrate as shown in Fig. 1. The continuous movement of the substrate relative to the atomizer makes it possible to produce a geometrical variety of components such as tubes, billets and strips or sheets. The ability to control the atomization and the solidification process governs the production of near net-shape parts with this technique.

Although spray formed material is metallurgically superior to other continuous cast materials there are impediments that threaten the use of this technology as a commercial process [1]. The disadvantages include substrate and shrinkage porosity, deposition overspray, bounce-off of impacting droplets and yield/rejection due to insufficient metallurgical quality. Technical issues for the process may be examined focusing on the three stages of the process, namely (a) the atomization parameters, (b) in-flight thermohydraulic phenomena, and (c) the final preform solidification process including substrate/particle interaction. Inadequate control in any of these stages may result in enhancing such disadvantages [2]. Porosity is inherent and present in all spray deposited materials regardless of the process conditions or the atomized material [3]. Extensive model experiments and numerical simulations have been applied to ascertain the underlying physics of the process [2, 4].

The cross sectional profile of preforms produced by spray forming onto a flat substrate usually approximate a Guassian distribution profile. For strip or sheet preform production, a flat preform profile is desired and as such, the development is intimately linked to fluid flow and heat transfer characteristics of the spray forming process. Heat transfer studies of the spray forming process have been primarily concerned with determining the heat flow within the developing solidifying layer to develop the cooling rate [5-7]. However such models have failed to incorporate the continuous dynamic fluid flow that occurs during the spray deposition process that intimately affects the developing microstructure. Fluid flow as it relates to spray forming has been relegated to the study of the impact and spreading of single drops [3, 4, 8]. The single drop theory is only applicable for a short period at the beginning of the process. Subsequent particles actually impinge a mushy or fully liquid surface and are affected by the dynamics of being part of a sheet of liquid [9,10].

The Stefan classical problem has been used to model the heat transfer aspect of numerous phase-change heat transfer problems. However, such models fail to incorporate the fluid

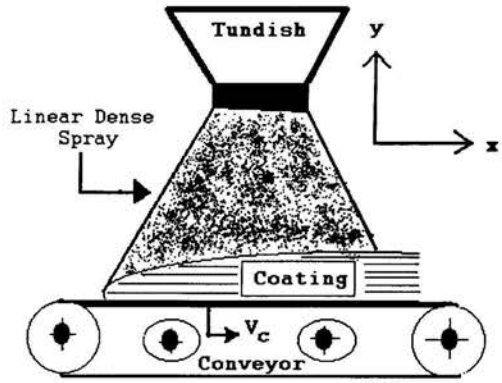

Fig. 1 General Spray Deposition (Forming) Model

flow dynamics and development of the solidifying layer is intimately affected by the fluid motion in the adjacent layer [11, 12]. The Stefan model for phase change is insufficient to model dynamic solidification as posed by the spray forming process since it fail to incorporate the movement of the substrate in the system [13]. As in static or directional solidification, fluid motion adjacent to the solidifying surface affects the developing microstructure [11, 12] as well as preform shape, which is also intimately linked with the heat flow. The final deposit thickness is affected by the rate of solidification, the mass source at the top of the surface within the spray cone and the thermal conditions of the immediate surroundings. Thus, in order to fully simulate or predict an industrial process the model must address the subsequent heat transfer and fluid flow effects after the initial deposition at the leading edge. Understanding such effects will provide a greater insight to the development of the surface profile and defects. The study developed a simplified model to predict final thickness in the deposited layer and ascertained the impact of system parameters on the layer thickness.

PROBLEM STATEMENT

As previously stated, although extensive research has been reported on the deposition and deformation of liquid droplets, fundamental uncertainties still exist concerning the continuous growth of a layer from the spray forming process. During the spray deposition process the developing preform loses thermal energy through a combination of three processes: conduction to the constant low temperature substrate,

convection to the surroundings, and radiation to the environment. This investigation involves the simultaneous consideration of heat transfer on the substrate, in the growing solid and in the liquid phase or mushy region. The developed

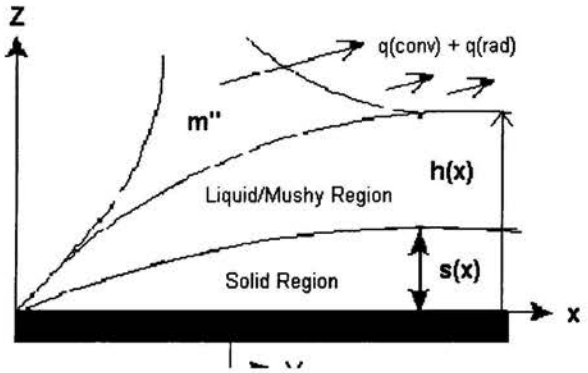

Fig. 2 *Qualitative Spray Deposition (Forming) Model*

heat transfer model considers a heat transfer source at the boundary to model the deposition and substrate/coating thermal contact. The deposition rate is assumed to be continuous rather than discrete. The single drop theory is applicable at the beginning of the deposition process, but thereafter droplets or sheets of droplets are impinging on a mushy or liquid surface. The sheet of atomized droplets is therefore considered to be a continuous flow of molten metal. Also, the model considers undercooling and assumes no slip at the molten boundary. Thus, the heat transfer process describing the growth of a layer that results from gas atomizing a liquid metal on a cold substrate was mathematically formulated. Initially the solid layer begins to grow with with thickness s(x) then a liquid/mushy layer of thickness h(x) develops on top as the thickness of the solid grows as shown in Fig. 2. The heat transfer model was developed mathematically under the following equations:

Solid phase equation for the region $0 \le z \le s(x)$ is,

$$(\rho C_p)_S V \frac{\partial T_S}{\partial x} = k_S \frac{\partial^2 T_S}{\partial z^2}. \quad (1)$$

Liquid phase for $s(x) \le z \le h(x)$ requires,

$$(\rho C_p)_l V \frac{\partial T_l}{\partial x} = k_l \frac{\partial^2 T_l}{\partial z^2} \quad (2)$$

Substrate heat transfer equation for $-\infty \le z \le 0$ is,

$$(\rho C_p)_{su} V \frac{\partial T_{su}}{\partial x} = k_{su} \frac{\partial^2 T_{su}}{\partial z^2} \quad (3)$$

The upper surface or interface conditions consist of the interface velocity,

$$V_{int} = k_f (T_m - T_{nti}) \quad (4)$$

where k_f is the linaer kinetics relation used to correlate the interface velocity (V_{int}) with the derivation of the interface. The source or an accumulation term which give rise to the total system thickness,

$$h(x) = \frac{1}{\rho_l V} \int_0^x m''(x)\, dx \quad (5)$$

with boundary condition between the air and the liquid layer,

$$-k_l \frac{\partial T_l}{\partial z}|_{z=h(x)} = h_c (T_l - T_\infty) - \dot{m}(x) C_p T_p + \varepsilon\sigma (T_l^4 - T_\infty^4) \quad (6)$$

and between the deposited material and the liquid region,

$$V_i \rho_s h_{ls} = k_s \frac{\partial T_s}{\partial z} - k_l \frac{\partial T_l}{\partial z}|_{z=s(x)} \quad (7)$$

where m"(x) is the rate of mass flux term of the particles at the boundary. The difference, T_M - T_i, defines the amount of undercooling. If undercooling exists and T_i is below T_M, the equation will result in a rate of latent heat release in excess of that which can be conducted away at the interface as denoted in the thermal energy heat balance equation. In this limit, the propagation of the solidification front is said to be controlled by the freezing kinetics. The rapid propagation of the freezing interface will cause its heating and subsequent retardation. As the freezing interface temperature approaches equilibrium freezing temperature, the solidification becomes heat transfer limited [14].

SOLUTION METHODOLOGY

The governing equations were solved using an implicit finite difference approach with the initial layer thickness assumed to correspond to the classical Madjeski's splat solution for a molten metal droplet [15]. The equations governing the interface speed was discretized and solved iteratively while grid independence was also addressed. Results have been generated to show accuracy of methodology, as well as to demonstrate the influence of such variables as the conveyor speed, mass flow entrainment and substrate temperature.

Implicit finite-difference approach was used to solve the governing equations. We used 500 time steps, and the longest time step Δt had the order of 10^{-5} s. For the simple implicit finite-difference approximation, the computation has the error of the same order as Δt, thus the method obtained results sufficiently close to the exact solution for the classical Stefan problem for zero substrate velocity.

The moving substrate has velocity V as it enters the spray zone at time t = 0, then the x-coordinate has a relation with time t as $x = V \cdot t$. It was assumed that the length covered by the spray zone in x-direction is X, so the total time $t_t = X/V$. When $t \le t_t$, there were incoming liquid droplets impinging upon the substrate as a heat source, and when $t \ge t_t$, no liquid droplets were adding to the substrate. We focused on when $t \le t_t$, i.e. the substrate in the spraying zone, and assumed that all the deposited material was moving with the substrate at V and rewrote the governing equations as as a function of t and z such that s=s(t) and h=h(t).

The first droplet impinging upon the substrate was simulated using Madjeski's formula, so initial thickness of the deposited materials was determined by the diameters of the impinging particle and the coefficient ξ,, $h = 2d_p / 3\xi^2$. The

initial thickness of the solid layer was estimated using the Stefan solution. Then the spatial-step, Δz, was chosen according to the initial solid layer thickness and the entire domain was overlaid with a one-dimensional uniform grid. For internal nodes for both solid and liquid, the discretization equation is:

$$\left(T_i^{n+1} - T_i^n\right)/\Delta t = \alpha\left(T_{i+1}^{n+1} - 2T_i^{n+1} + T_{i-1}^{n+1}\right)/\Delta z^2 \quad (8)$$

where Δt and Δz are time- and space-steps, n denotes time-steps separated by Δt and i denotes spatial grid nodes separated by Δz. α is the thermal diffusivity for the deposited materials, α_s is for the solid and α_l is for the liquid. The discretization equation was rewritten as

$$\left(2 + \frac{1}{Fo}\right)T_i^{n+1} - T_{i-1}^{n+1} - T_{i+1}^{n+1} = \frac{T_i^n}{Fo} \quad (9)$$

where the grid Fourier number $Fo = \alpha\Delta t / \Delta z^2$. The location of the interface was calculated separately according to the former time-step, and the node i was the grid node including the solid/liquid interface. The discretization equation for the solid/liquid interface is:

$$\left(\frac{\Delta z/2 + \delta}{\alpha_l \Delta t} + \frac{1}{\Delta z} + \frac{1}{\delta}\right)T_i^{n+1} - \frac{1}{\Delta z}T_{i-1}^{n+1} = \frac{T_m}{\delta} + \left(\frac{\Delta z/2 + \delta}{\alpha_l \Delta t}\right) \quad (10)$$

where T_m is the melting temperature and

$$\delta_l = \Delta z/2 - \left(s_{(t)} - \Delta z \cdot i\right)$$
$$\delta_s = \Delta z/2 + \left(s_{(t)} - \Delta z \cdot i\right) \quad (11)$$

For the upper surface of the deposition materials, the discretization equation is:

$$-2T_{i+1}^{n+1} + \left(2 - Bi - \dot{m}c_p\Delta z/k_l\right)T_i^{n+1} = -BiT_\infty - \dot{m}c_pT_p\frac{\Delta z}{k_l} + \varepsilon\sigma\left(T_p^4 - T_\infty^4\right)\frac{\Delta z}{k_l} \quad (12)$$

So the discretization equation were rewritten for the whole domain as

$$a_i T_{i-1}^{n+1} + b_i T_i^{n+1} + c_i T_{i+1}^{n+1} = f_i\left(T_i^n\right). \quad (13)$$

The linear algebraic equations were solved to get the temperature profile, then the processed continued to solve for the solid/liquid interface location:

$$s^{n+1} = s^n + c_1\left(T_m - T_{si}^n\right) + c_2\left(T_m - T_{li}^n\right) \quad (14)$$

where

$$c_1 = \frac{\Delta t \cdot k_s}{\rho_s h_{ls} \delta_s}$$
$$c_2 = \frac{\Delta t \cdot k_l}{\rho_s h_{ls} \delta_l} \quad (15)$$

RESULTS AND DISCUSSION

The dynamic process of spray forming of a solid thin coat formed on a moving substrate is simulated. A one-dimensional heat transfer model has been obtained and numerical methods applied to solve the governing equations. The results presented agree with trends for solid thickness, deposition and substrate rate for the results presented in literature [2, 16, 17].

Result show accuracy of methodology, as well as demonstrate the influence of such variables as the conveyor speed, mass flow entrainment and substrate temperature. Convergence was verified by comparing the analytic Stefan solution to the numerical finite difference approach; identical solutions were obtained. Results indicate that the mushy zone or the overlaying liquid layer grows faster than the developing solid layer as depicted in Fig. 2 and verified numerically in Figs. 3-5; thus, the impinging droplets strike a liquid or mushy layer. The substrate velocity affects the thickness as expected: increasing speed decreases the thickness of the layer.

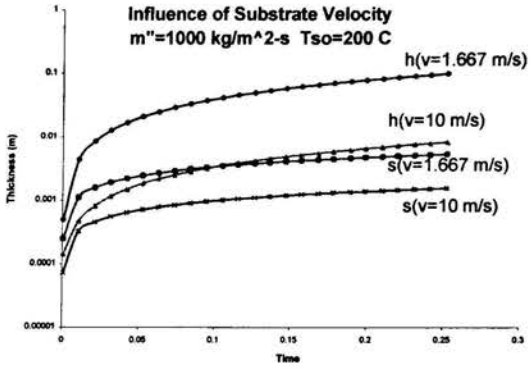

Fig. 3 *Influence of the substrate velocity on deposit growth.*

Figures 3-7 show the effect of the process controlling parameters: Substrate velocity, substrate temperate, deposition rate and radiation on the growing solid thickness, s(t). A typical set of solid and liquid thickness curves are shown in Fig. 3 for a fixed deposition rate and substrate temperature. The substrate velocity as expected influence the thickness of the solidified layer. The slower velocity achieves the greater solid thickness and the slower velocity has the greater departure

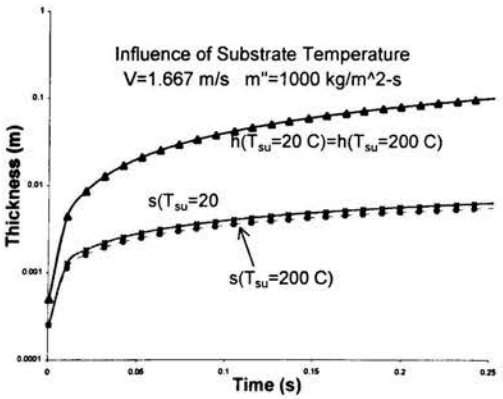

Fig. 4 *Influence of Substrate Temperature on Deposit v=1.667 m/s and m"=1000 kg/m^2-s..*

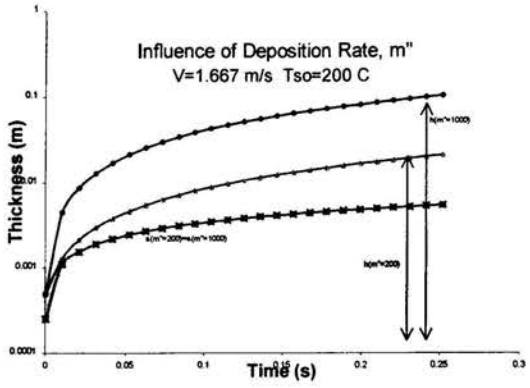

Fig. 5 *Influence of Deposition Rate for v=1.667 m/s and T_{su}=200 °C.*

between the solid and liquid layer thickness. Figure 4 displays the influence of the substrate temperatures, 20 °C and 200 °C. The substrate temperature has no impact on the height of the liquid layer; however, the lower substrate temperature produces a thicker solidified region. The rate of propagation is greater for the lower substrate temperature due to the greater rate of heat transfer at the substrate due to the larger temperature difference. The 200 °C substrate temperature is closer to the liquid deposition temperature thus constraining the rate of conductive heat transfer through the substrate. Comparing Figs 3 & 4, one can see that the substrate velocity and temperature must be optimized simultaneously to produce a desired substrate quality.

The deposition process can have a critical impact on the quality of deposited material [Xu, Gupta, 1999]. All aspects of the deposition portion of the process are integral to producing a high quality product. Liquid fraction within the impinging droplets may also affect the microstructure development via grain size or defects. In this model, a continuous process of liquid droplets was assumed. Fig. 5 demonstrates the influence of the deposition rate on the solid growth. The solidified layer thickness is independent of the deposition rate as the solid grows accordingly. The thickness of the liquid layer is the direct result of the deposition rate. The trends of Fig.5 indicate that there may exist a critical value of the deposition rate where no liquid layer would form. Furthermore, these results present an upper and lower limit on the possible solid thickness that may result from the deposition process. Once the substrate has departed the spray cone as shown in Fig. 1, no additional mass is added to the liquid layer except via spreading. Spreading is very important but should be minimal when compared the overall thickness of the developing solid.

There is a correlation between the deposition rate and the upper surface temperature. The rise in temperature is higher for the higher deposition rate. A large deposition rate means that the impinging liquid carries high thermal enthalpy per unit

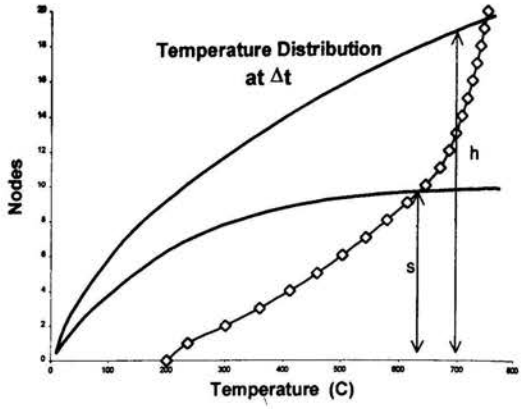

Fig. 6 *Temperature distribution throughout the system after a finite time period.*

time and the time for the preceding deposit to cool is small, thus a rapid rise in temperature. As the deposition rate decreases, the time to cool for the proceeding deposit increases thus the slower rise to the surface temperature. Figure 6 shows the rise of the temperature distribution through the solid and the liquid layer. The rise in temperature is greater in the liquid layer as the heat transfer rate decreases with increasing solid thickness. This heat transfer rate can be compared with the amount of enthalpy added to the liquid layer with the rate of deposition. The faster the deposition, the greater the influence on the solid thickness and thus rise to the upper surface temperature demonstrated in Fig. 6.

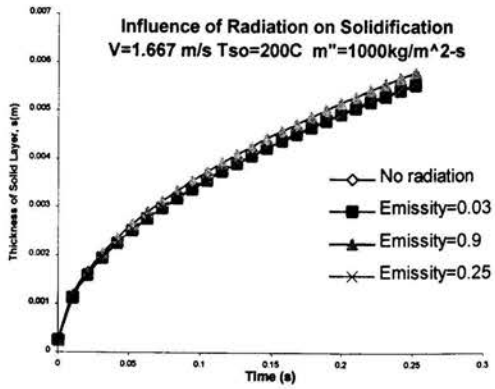

Fig. 7 *Effect of radiation on deposit development for v=1.667 m/s, T_{su}=200 °C, and m"=1000 kg/m^2-s.*

The influence of radiation on the thickening material is determined by the magnitude of the emittance or emissivitiy of the material. The radiation effect proves negligible unless near black body radiation (emissitivty =0.9) is assumed as

shown in Fig 7. Due to the low emittance of materials like Aluminum, the radiation at the surface can be neglected when compared to the effect and influence of the convection at the surface during deposition. Our results confirm that that convection at the surface is the dominant heat removal mode at the surface.

CONCLUSIONS

The heat transfer model developed identified relative trends through parametric investigations of controlling parameters. The substrate velocity and temperature, radiation, and deposition rate were considered. It was shown that the all of the parameter except radiation must be considered to produce optimum results. The solid thickness growth may be restricted by a critical value of the deposition rate. Depending on magnitude, the deposition rate increases or decreases enthalpy at the interface thus affecting the heat transfer within the liquid layer. The rate at which the upper surface temperature is obtained may affect microstructure development. This rate is influence by all of the investigated parameters. While the radiation displayed no influence, further analysis should be perform to quantify the relative magnitude versus the other possible heat transfer modes. The factors and trends documented in this one-dimensional study provide the foundation for a more robust model.

REFERENCES

[1] P. Mahner, P.S. Grant, B. Cantor, and Ketgerman,"Manufacture of spray formed aluminum-based alloys and composites," First International Conference on Spray Forming, U.K., 1990.

[2] P.S. Grant, " Spray Forming", Progress in Materials Science, Vol. 39, pp. 497-545, 1995

[3] J. P. Delplanque, E. J. Lavernia and R.H. Rangel, "Multidirectional Solidification model for the Description of Micropore Formation in Spray Deposition Processes, Numerical Heat Transfer, Part A, Vol. 30, pp. 1-18, 1996.

[4] G. Trapaga, E. F. Matthys, J.J. Valencia and J. Szekely, "Fluid Flow, Heat Tansfer, and Solidification of Metal Droplets Impinging on Substrates: Comparison of Numerical and Experimental Results", Metall. Trans B. Vol. 23B, pp. 701-718, 1992.

[5] A. G. Leatham. "Spray Forming Technology", Journal of Applied Manufacturing Systems, v.8 no.2 p65-68, 1996

[6] J. L. Estrada and J. Duszczyk, "Characteristics of Rapidly Solidified Al-Si-X Preforms Produced by the Osprey Process", J. Mat. Sci, 25, p. 1381 (1990)

[7] X. Liang and E. J. Lavernia, Met. Mat. Trans. A 25A, p. 2341 (1994)

[8] P.S. Grant, P.P. Maher and B. Cantor, "Heat Flow in Spray-Formed AL-4 Cu", Mat. Sci. Engng A179/A180, 72 (1994)

[9] H. Lui, R.H. Rangel and E.J. lavernia, Acta Metall., 42 (1994) 3277.

[10] R. Vetter, L.Z. Zhuang, I. Majewska-Glabus, and J.Duszczyk, " Microstructure of the Osprey Processed Cr-containing Ni/3Al-X intermetallic in conjuction with solidification model at the deposition" , Scripta Metall. Et mater., 24 (1990) 2089.

[11] C. Mackie, "Convective Instability of a Solidification Interface in a Porous Media", Ph.D. Dissertation, Georgia Tech, 1996

[12] Glicksman, M.E., Coriell, S.R. and McFadden, G.B., "Interaction of Flows with the Crystal-Melt Interface", *Ann. Rev. Fluid Mech.*, Vol.18, pp.307-35, 1986.

[13] X. Bian and R.H. Rangel, "The Viscous Stagnation-Flow Solidification Problem", Int. J. Heat and Mass Transfer, vol. 39 No. 17, pp. 3581-3594, (1996)

[14] Kang, B., Zhoa, Z., and Poulikakos, D. " Solidification od Metal Droplets Impacting Sequentially on a Solid Surface", ASME J. Heat Transfer, Vol. 16, 436-445, 1994.

[15] J. Madejski, "Solidification of Droplets on a Cold Surface", Int. J. Heat Mass Transfer, Vol. 19, pp. 1009-1013, 1976

[16] Xu, Q., Gupta, V., and Lavernia, E. J., "On the Mechanism of Mushy Layer Formation during Droplet-Based Processing.", Metall. Trans B. Vol. 30B, 527538, 1999.

[17] M. Epstein, "The Growth and Decay of a Frozen Layer in Forced flow", Int. J. Heat Mass Transfer, Vol 19. pp. 1281-1288. 1976

HEFAT2002
1st International Conference on Heat Transfer, Fluid Mechanics, and Thermodynamics
8-10 April 2002, Kruger National Park, South Africa
MM3

NUMERICAL STUDY OF HEAT AND MASS TRANSFER DURING DIRECTIONAL SOLIDIFICATION USING THE AHP METHOD

M. Marchenko, I. Frjazinov,
Institute of Mathematical Modelling RAS,
4A Miusskaya St., Moscow, 125047, Russia

V. Golyshev,
CTR "Thermo", 1 Institutskaya St.,
Alexandrov, 601650, Russia

V. Timchenko, E. Leonardi and G. de Vahl Davis*
School of Mechanical & Manufacturing Engineering,
The University of New South Wales,
Sydney, Australia 2052

R. Abbaschian
The University of Florida,
Materials Science & Engineering,
Gainesville, Florida 32611, USA

ABSTRACT

A two-dimensional transient model of crystal growth using the AHP method (Axial Heat flux close to the Phase interface) [1] is presented. A numerical study was made of effect of the temperature boundary conditions and pulling velocity of the crucible on heat and mass transfer processes, during a particular experiment on the growth of germanium doped with antimony. The geometric data, boundary conditions and initial conditions measured during the experiment were used in the computations.

Concentration levels of antimony obtained from the experiment and computations have been compared and discussed.

INTRODUCTION

The AHP method is a technique for directional solidification which has, in addition to other heaters, a heater submerged in the melting zone [1-2]. To grow crystals, a seed and polycrystalline is placed at the bottom of the crucible; this is then melted using both the sidewall heaters and the submerged heater, as shown in Figure 1. The crucible is then moved with speed V relative to the stationary heater, causing melt with a dopant concentration c_2 to flow from zone $W2$ above the heater through the gap between the heater and the crucible into zone $W1$ below, where melt with dopant concentration c_1 is formed. When the crucible moves, the melt in the zone $W1$ cools and solidifies. During the experiment, the temperature is measured using thermocouples located at points $T1$ to $T8$. Temperature measurements are used to control the crystal growth process. The temperature regime is chosen depending on the requirements set in the experiment. For example, the achievement of a certain height h of the melt in zone $W1$, a particular solid/liquid interface velocity V, a specified shape of the interface and/or a predefined concentration distribution in the axial direction and across the grown crystal sample.

In previous work on the modelling of heat and mass transfer during crystal growth using the AHP method [3-5], steady conditions were investigated *i.e.*, the pulling velocity of the crucible and the temperature boundary conditions were constant with time. Experimentally measured temperatures were used for boundary conditions in the computations. The possible reasons for discrepancies between numerical and experimental results were investigated. First, it was found that in some cases small variations in the temperature in the crucible walls (even within the range of measurement accuracy) can strongly affect solutal distribution [5]. Obtaining accurate temperature measurements is a very complicated and costly procedure. During each experiment it is necessary to use a large number of thermocouples to increase the accuracy of the data. And since the error estimates of the data always exceed the claimed accuracy of the thermocouples, there will always be some uncertainty about the temperature values used as boundary conditions in the calculations. Second, initial values of the concentrations c_1 and c_2 which also determine the composition of the grown crystal are not defined exactly [6-8].

* Corresponding Author (g.devahldavis@unsw.edu.au)

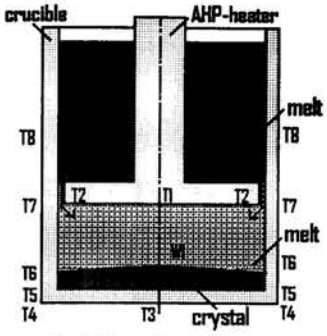

Fig.1 Experimental set up.

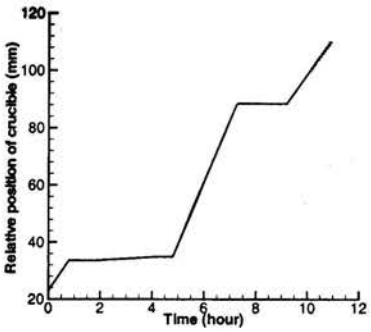

Fig.2 Relative position of the AHP heater.

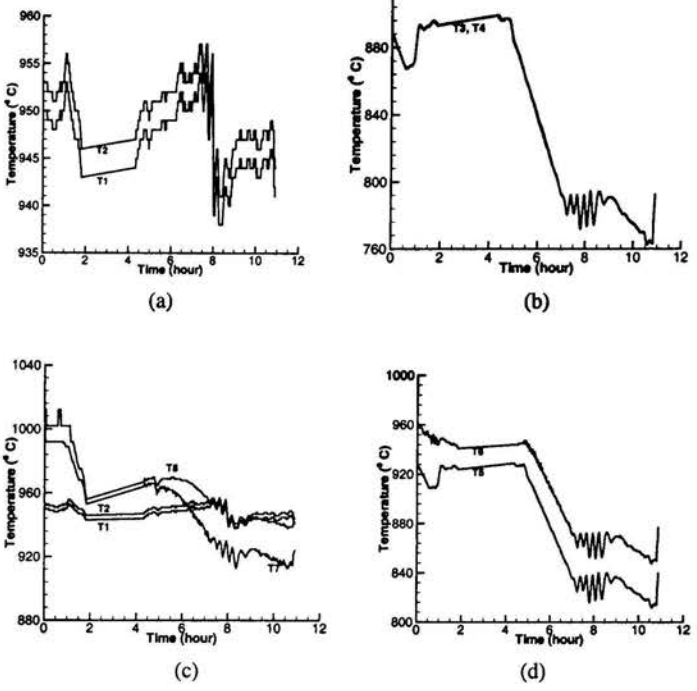

Fig.3 Time history of experimental temperatures. Thermocouples (a) *T1* and *T2*, (b) *T3* and *T4*, (c) *T7* and *T8*, (d) *T5* and *T6*

In this paper we describe a numerical study of the crystal growth process during a particular *unsteady* AHP experiment on germanium doped with antimony. The transition in the shape of the interface, the movement of the melt, the distribution of solute and the composition of the grown crystal are discussed and compared with experiment.

The numerical modelling included the imposition of realistic, time dependent (oscillatory) temperature boundary conditions and unsteady movements of the crucible, both of which were measured during the experiment.

DESCRIPTION OF THE EXPERIMENT

The crystal was grown in a graphite crucible of 46 mm inside diameter. The outer casing of the AHP heater is also made from graphite. Thermocouples were buried in the graphite walls at 2 mm from the melt and solidified crystal. The gap δ between the AHP heater and crucible was 0.5 mm. The distance between thermocouples *T1* and *T2*, and between *T3* and *T4* was 20mm. Thermocouples *T1* and *T3* were situated at the axis of the crucible. Thermocouples *T5* to *T8* were on the sidewall of the crucible. *T5* was 5mm from the bottom of crystal, with 20mm between *T5* and *T6*, 40mm between *T6* and *T7*, and 20mm between *T7* and *T8*. The thermocouples *T3* to *T8* move with the crucible. The thermocouples *T1* and *T2* are firmly held in the casing of the AHP heater and are stationary.

For the particular experiment considered, the relative position of the heater is shown in Fig. 2 and the transient thermocouple readings (*T1* to *T8*) are shown in Fig. 3(a)-(d).

The experiment can be sub-divided into 5 stages (see Fig. 2, 3):

Stage 1: The crucible is moved with a speed of 3.3mm/h. During the first 0.8h, the temperatures initially decrease and then start to increase;

Stage 2: The crucible is stationary. From $0.8h < t < 1.83h$, the temperatures at points 1 and 2 first increased by 50K, and then decreased by 100K. There is a slight increase in all temperatures from $1.83h < t < 4.17h$;

Stage 3: The crucible is moved with a speed of 22mm/h. For $4.17h < t < 6h$, there is an increase in temperature at points 1 and 2; at the same time they exhibit oscillatory behaviour. *T1* eventually reaches 954°C. For the next hour, the temperatures at points 1 and 2 increase sharply;

Stage 4: The crucible is again stationary. For 7h < t < 8h, the temperatures at points 1 and 2 oscillate strongly and then decrease by 8h to the melting temperature. For the next half hour the temperature oscillates about this value;

Stage 5: The crucible is moved with a speed of 12.5mm/h. For the final 2.5 hours (8.5h < t < 11h) the oscillations of temperatures at points 1 and 2 continue.

The distribution of the concentration in the grown crystal was then determined from measurements of electrical resistance using a four-point probe technique. These measurements were independently performed by both Russian and US investigators [9].

MATHEMATICAL MODEL

The unsteady AHP crystal growth experiment was modelled using an axi-symmetrical cylindrical *(r, z)* coordinate system with the origin located at the bottom of the crucible (see Fig. 4). The movement of the incompressible viscous liquid in the melting zone was found by solving the Navier-Stokes equations with the Boussinesq approximation. The equations were written in a vorticity-Stokes stream function formulation. In the melt zone, both heat and solute transport were considered.

The solution of the transient solidification problem included explicit tracking of the solid/liquid interface at each time step. The Stefan condition as well as continuity of temperature at the interface was applied, whilst a mass balance was used for the concentration.

The equations were non-dimensionalized using the following scaling factors: R_c, the crystal radius for length; $t_o = R_c / u_o$ for time; $u_o = \nu\sqrt{Gr} / R_c$ for the velocity and $\theta = (T - T_o)/\Delta T$ for temperature, where ν is the viscosity, $\Delta T = T_{max} - T_o$ (which for the experiments modelled is typically *5K*), T_{max} is the maximum temperature in the melt and T_o is the melting temperature of Ge.

The non-dimensional parameters Grashof (*Gr*), Prandtl (*Pr*), Schmidt (*Sc*), Stefan (*St*) and Peclet (*Pe*) numbers are defined as:

$$Gr = \beta_T g R_c^3 \Delta T / \nu^2, \quad Pr = \nu / \chi_L, \quad Sc = \nu / D_L,$$
$$St = \gamma \rho_s / (\rho_L c_{pL} \Delta T), \quad Pe = Pr\sqrt{Gr}, \quad Pe_d = Sc\sqrt{Gr}$$

where β_T is the coefficient of volumetric expansion, g is the gravitational acceleration, χ_L is the thermal diffusivity of the melt, and D is the diffusion coefficient.

Thermal conductivity λ, specific heat c_p, density ρ are non-dimensionalized by their value in the melt λ_L, c_{pL}, ρ_L,

$$\bar{\lambda} = \lambda / \lambda_L, \quad \bar{c_p} = c_p / c_{pL}, \quad \bar{\rho} = \rho / \rho_L.$$

In the melting zone *W1*, the Navier-Stokes equations for an incompressible viscous liquid in which the Boussinesq approximation is applied, may be written in vorticity-stream function form as:

$$\frac{\partial \omega}{\partial t} + D(\psi)\omega = \frac{1}{Re}\frac{1}{r}\left[\frac{\partial}{\partial r}\left(\frac{1}{r}\frac{\partial r^2 \omega}{\partial r}\right) + \frac{\partial}{\partial z}\left(\frac{1}{r}\frac{\partial r^2 \omega}{\partial z}\right)\right] + \frac{Gr}{Re^2}\frac{1}{r}\frac{\partial T}{\partial r}$$

and

$$\frac{1}{r}\left[\frac{\partial}{\partial r}\left(\frac{1}{r}\frac{\partial \psi}{\partial r}\right) + \frac{\partial}{\partial z}\left(\frac{1}{r}\frac{\partial \psi}{\partial z}\right)\right] + \omega = 0$$

in which the stream function and vorticity are defined as

$$u = \frac{1}{r}\frac{\partial \psi}{\partial z}, \quad w = -\frac{1}{r}\frac{\partial \psi}{\partial r}, \text{ and } \omega = \frac{\zeta}{r} = \frac{1}{r}\left(\frac{\partial w}{\partial r} - \frac{\partial u}{\partial z}\right)$$

The equations for heat and mass transfer are solved in the melting zone W1

$$\frac{\partial T}{\partial t} + D(\psi)T = \frac{1}{Pe}\nabla^2 T \quad , \quad \frac{\partial c}{\partial t} + D(\psi)c = \frac{1}{Pe_d}\nabla^2 c$$

In the above equations, the operator for the advective terms ($\phi = \omega, T, c$) is defined as

$$D(\psi)\phi = \frac{1}{r}\frac{\partial}{\partial r}\left(\frac{\partial \psi}{\partial z}\phi\right) - \frac{1}{r}\frac{\partial}{\partial z}\left(\frac{\partial \psi}{\partial r}\phi\right).$$

The equation for heat conduction is considered within the area occupied by the crystal and crucible walls:

$$\bar{c}_p \bar{\rho}\frac{\partial T}{\partial t} = \frac{1}{Pe}\nabla \cdot \left(\bar{\lambda}\nabla T\right)$$

Time dependent experimentally measured temperatures were imposed at the external boundary of the crucible, at the AHP heater and gap δ between the AHP heater and crucible wall. These transient values were recorded at the thermocouple locations; the temperature between these locations was determined using interpolation techniques.

The discontinuity of the properties λ, c_p and ρ and continuity of the heat flow are imposed at the crystal-crucible and melt-crucible boundaries:

$$[T] = 0, \quad \left[\frac{\bar{\lambda}}{Pe}\frac{\partial T}{\partial n}\right] = 0.$$

Here and below, [ ] denotes the change of the function inside the brackets across the interface.

A symmetry condition is imposed at the axis for both temperature and velocity.

The normal component of the velocity of the melt-solid interface, V_{n_z}, is determined at each time step from the Stefan condition

$$T = T_0, \quad \left[\frac{\bar{\lambda}}{Pe}\frac{\partial T}{\partial n_z}\right] + St\, V_{n_z} = 0,$$

where T_0 is the temperature at which phase change occurs.

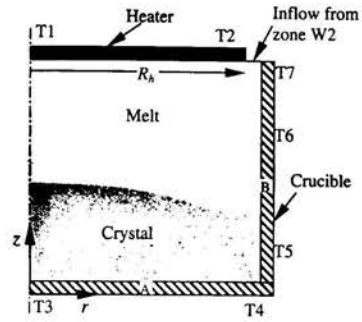

Fig.4 Computational domain.

In the experiment the AHP heater was stationary and the crucible moved; however since we define the co-ordinate system relative to the crucible, in the calculations the AHP heater is moving up with pulling speed $V > 0$ [10]. The vertical component of velocity at the inflow region (see Fig. 4) is determined from a mass balance, *viz*:

$$V_\delta = -V\frac{R_h^2}{1-R_h^2}$$

where R_h is the radius of the AHP heater. The imposed stream function conditions on the top melt boundary therefore become

$$\psi = -V\frac{r^2}{2} \quad \text{for } 0<r<R_h, \quad \frac{1}{r}\frac{\partial\psi}{\partial n}=0 \quad \text{for } 0<r<1,$$

$$\psi = -V\frac{R_h^2}{2}+\frac{r^2-R_h^2}{2}\frac{VR_h^2}{1-R_h^2} \quad \text{at } R_h<r<1$$

On the phase change boundary and on the side surface of the melt:

$$\psi = 0, \quad \frac{1}{r}\frac{\partial\psi}{\partial n}=0.$$

A symmetry condition for the concentration is imposed along the axis and a zero concentration flux set on the crucible wall and heater. The condition of the balance for the concentration flux and dependence of concentration in the solid and the liquid phases is determined by an equilibrium condition at the interface

$$\frac{1}{Pe}\frac{\partial c}{\partial n_z}+V_{n_z}c=V_{n_z}c_s \quad , \quad c_s=k_0c$$

in which k_0 is the partition coefficient.

A mass balance condition is used at the inflow region:

$$\frac{1}{Pe_d}\frac{\partial c}{\partial z}+(V-V_\delta)c=(V-V_\delta)c_2$$

where c_2 is the concentration in zone *W2*. It is assumed that above the AHP heater, in *W2* (see Fig. 1), the melt is well mixed, and the concentration in this zone is time independent. The initial temperature distribution is set to $T(z) = T_{ini}$ for the whole calculation domain. The initial melt velocity was set to zero. Since a dilute alloy was considered, the melting temperature was taken as constant and equal to melting temperature of Ge, 937 °C.

NUMERICAL METHOD

The solution was obtained using a finite-difference method with preliminary mapping of the melt and crystal areas into rectangular computational blocks. A non-uniform mesh clustered near the boundaries of the liquid zone was used for all the blocks. A conservative monotonic unconditionally stable difference scheme based on extended stencils with monotonizing scheme regularizers of the third order was used for approximating the equations and boundary conditions [11].

The stream function, vorticity, temperature and concentration were determined for each time step. Then, the phase front velocity and position were calculated. To solve the systems of algebraic equations, a direct Gaussian method was used. The code is a modified version of the KARMA1 program [10].

COMPUTATIONAL SOLUTION

Temperature conditions on the upper surface of the computational domain (including the graphite wall of the heater, the melt in the gap and the upper surface of the crucible) were imposed in the following way. The temperature in the graphite wall of the heater was set as a parabolic function based on the values *T1* and *T2* and the symmetry condition at the axis (see Fig. 4). The temperature at the boundary between the melt and the crucible was found from the equality of the heat fluxes. Based on this temperature and temperature on the side boundary of the heater, the temperature in the gap between the heater and the crucible was defined by linear interpolation. Temperatures on the upper surface of the crucible were also found using linear interpolation.

At the bottom of the crucible, but excluding the corner point, the temperature was set as a parabolic function based on the values of *T3*, *T4* and the condition of symmetry at the axis. In the corner point between the bottom and side wall of the crucible, temperature was extrapolated from *T5* and *T6*. On the wall of the crucible, temperature was calculated by linear interpolation using *T5*, *T6*, *T7*, and *T8*. As can be seen from Fig. 3a-3d, the duration of the experiment considered in the calculations was 11 hours. Initial values for concentration were chosen from the experiment but there was indeterminacy in setting these values because of the lack of data on all the history of the technological process (melting and holding). Some estimates give a concentration under the AHP heater of $c_1 = 6.67\times10^{19}$ At/cm^3 and a concentration above the heater of

c_2 = 3.2×10^{19} At/cm^3. In the solidified crystal, the initial concentration was taken to be c_s = 9.0×10^{17} At/cm^3. All the computations were performed using an 800 MHz PC over 4 hours with a non-uniform mesh of 16×37 and a time step of 0.24 sec. A finer mesh was tested with little change in the solutions.

RESULTS AND DISCUSSION

Here we consider the dynamics of the crystal growth according to boundary conditions imposed during the various stages discussed above. In the numerical modelling, the solidification process was started from 492 min. into the experiment; thus the initial stage was omitted.

Numbers 1-21 on the figures presented in this section correspond to times from 0.5h to 10.5h in steps of 0.5h.

At the first stage the height of the melting zone increases and solidification occurs (Fig. 5a-b). The concentration at the interface increases slightly towards the wall of the crucible (curve 1 on Fig. 7), the concentration in the liquid is well mixed due to convection (the radial component of velocity has value of 0.3 – 0.4cm/s, Fig. 9a). During solidification a rejection of solute occurs in the boundary layer in front of the interface (curve 1 Fig. 8). There is one convective cell in the melt (Fig. 10a); the interface shape is concave into the melt (curve 1 Fig. 6).

During the second stage at 0.8h < t < 1.83h the temperature at the bottom of AHP-heater initially increases and then decreases. Therefore at t = 1h a melting process takes place (curve 2 in Fig. 6-8), but by t = 1.5h solidification occurs (Fig.5a, curve 3 Fig. 6-8). The interface positions at 0.5h and 1.5h (curves 1 and 3) are practically the same. During melting, the concentration at the interface decreases due to diffusion (curve 2, Fig. 7), but then increases during solidification (curve 3, Fig. 7). The flow pattern in the melt remains the same, but the radial component of velocity decreases by the factor of 2. Curves 4-8 on Fig. 6-8 represent the period of time 1.83h < t < 4.17h when temperatures slightly increase. Due to the increase of temperature, melting takes place and the interface moves down (curves 4-8, Fig. 6). Concentration in the melt is well mixed with only a small variation near the interface (curves 5-8, Fig. 8).

During the stage 3, averaged along the radius, the height of the melting zone increases from 18mm to 21mm, then decreases to 17mm (Fig. 5b). Curves 9-12 on Fig. 6-8 correspond to time interval 4.17h < t < 6h. The shape of the phase change front is fairly flat with a small upwards curvature near the walls (Fig. 6). During this time solidification takes place. By t = 6h, the temperature at the point 7 (at the wall) strongly decreases. Therefore the flow along the bottom of the AHP heater slows down due to a decrease in the temperature gradient (compare Fig. 9b and 9c). A small convective cell created near the crucible wall and interface increased and replaced the initial cell under the heater by occupying the entire region in front of the interface (Fig. 9c). Creation of two cells is shown on Fig. 10b. Solute is

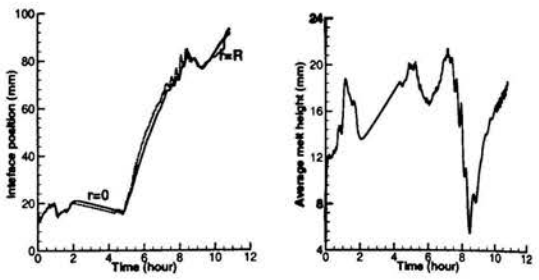

(a) (b)

Fig 5. Time history of the interface position at the axis and the wall (a), of the average along the radius melting height (b)

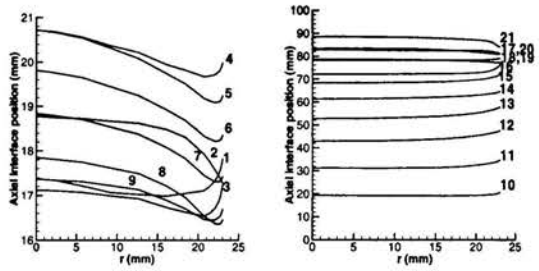

Fig 6. The interface shape and position evolution

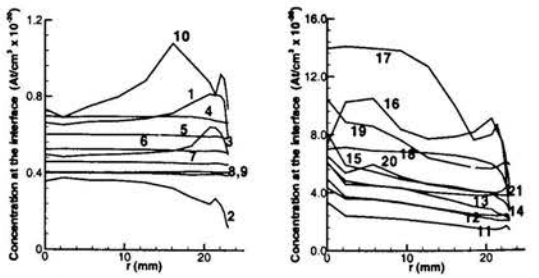

Fig 7. Concentration at the interface from 0.5h to 10.5h

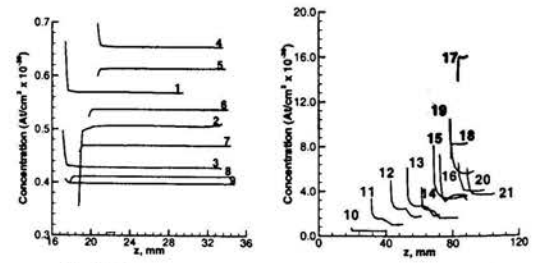

Fig 8. Concentration at the axis from 0.5h to 10.5h

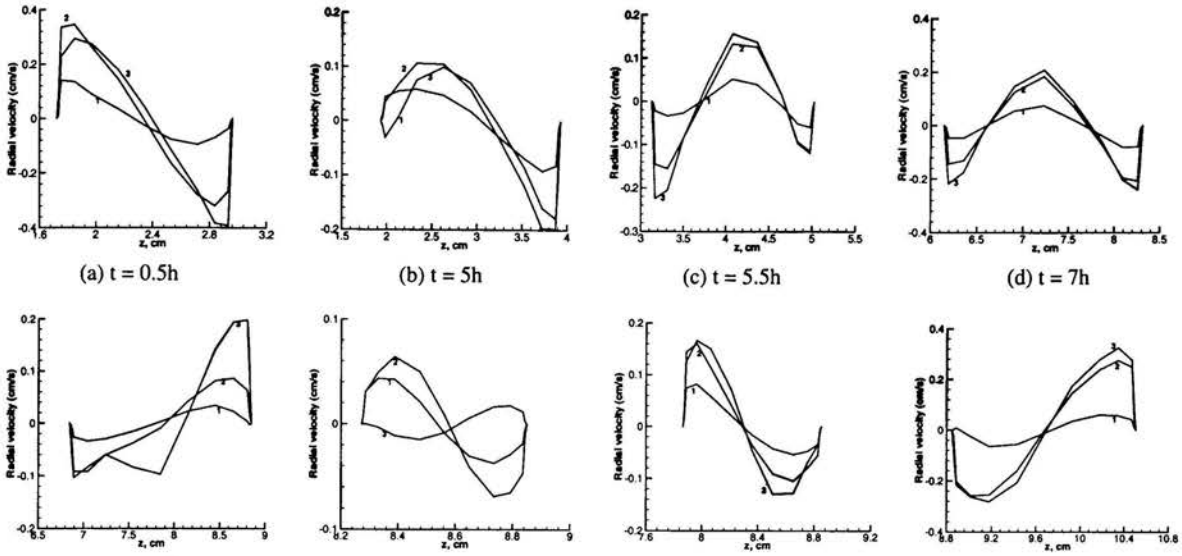

(a) t = 0.5h (b) t = 5h (c) t = 5.5h (d) t = 7h

(e) t = 7.5h (f) t = 8.5h (g) t = 9h (h) t = 10.5h

Fig. 9. Radial components of velocity along the melting height at the different radial locations (1 - $r = 0.25R$, 2 - $0.55R$, 3 - $0.8R$.) at the different moments of time

moving from the side to the axis, (Fig. 9c, 10c), together with melt coming through the gap. Concentration at the interface has a maximum value on the axis, well mixed (Fig. 7). Due to solidification, concentration sharply decreases in the boundary layer and then instead of approaching a constant value far away from the interface (as happens in the presence of one convective cell) exhibits a change in slope in the area when two convective cells meet each other (curves 11, 12, Fig. 8). The maximum absolute radial component of velocity increased to 0.2cm/s (Fig. 9). For the next hour temperatures at the points 1 and 2 started to increase, with some oscillations, and therefore the interface velocity decreased (curves 13-14 on Fig. 8) despite the translation of the crucible with the same speed. Streamlines on Fig. 10d (also Fig. 9d) show that two convective cells still exist. The melting zone height increases up to 22 mm.

At stage 4, from 7 to 8 hours, the temperature at the bottom of the heater has a very large amplitude oscillation (up to 3^0C) but decreases almost to the value of the melting temperature (938^0C) at the point 1. Therefore a non-monotonic (because of oscillations) decrease of the melting zone height to 10mm can be seen (Fig. 5b). All oscillations of temperature are repeated in the oscillations of the radially averaged interface velocity. During this time transitions in the flow pattern can be seen (Fig. 9e), and as result, the flow pattern changes from one convective cell with flow moving along the interface from the wall towards the axis (Fig. 10e and curve 15 on Fig. 8) to two cells (curve 16 on Fig. 8 or Fig. 7). For the next half hour, the melting zone decreases further in height to 4.5 mm (Fig. 5b) due to a strong temperature decrease (with oscillations) at the points 1 and 2 (Fig. 3a). The flow consists of two adjacent cells (Fig. 10f, 9f). The concentration distribution at the axis exhibits a strong maximum at the axis (curve 17, Fig. 7-8).

The remaining period of the experiment is combined into one last time interval. The temperatures at points 1 and 2 (as can be seen from Fig. 3a) sharply increase in the beginning with oscillations following. On Fig. 6, curves 17, 18, 19, 20, showing the position and shape of the phase change front, remain unchanged. Concentration at the axis has a different behaviour in the longitudinal direction. It can increase with distance from the interface as happens during melting because solute with a low concentration ($k_0 = 0.003$) enters the melting zone (curve 18 on Fig. 8). Alternatively, it may sharply decrease within a thin boundary layer next to the interface during solidification (curves 19-21 on Fig. 8). Because of the crucible translation, solidification occurs (Fig. 5a). Flow in the melting zone consists of one cell with flow moving along the interface from the axis to the wall (Fig. 9g). Towards the end of this time interval the temperature at the wall *T8* becomes less than *T1* and *T2* causing the direction of flow to reverse (Fig. 9h).

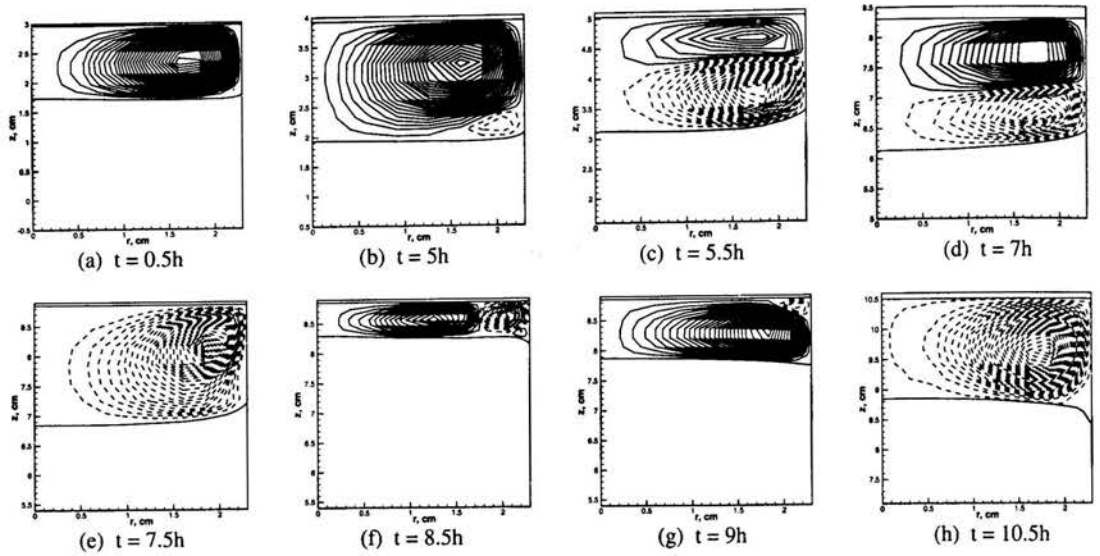

Fig. 10. Stream functions and interface shape at the different times (dashed lines indicate negative value).

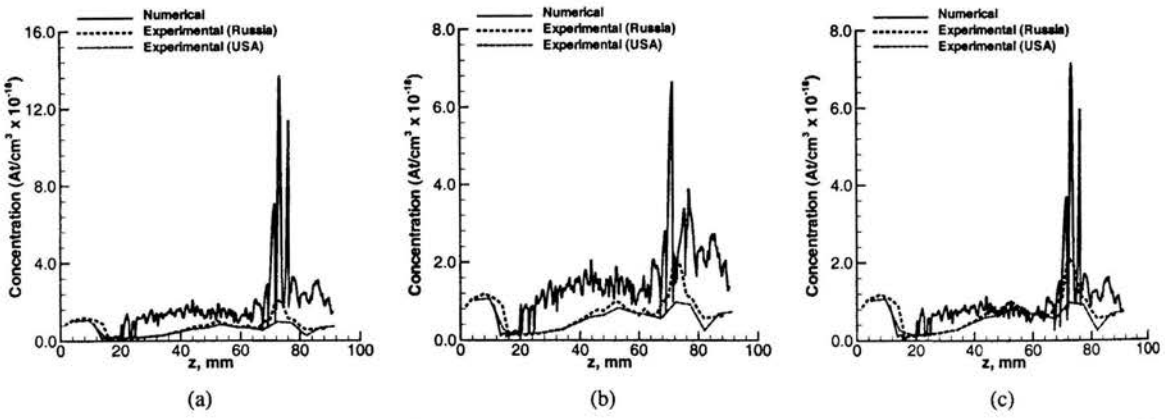

Fig 11. Sb concentration distribution along the grown crystal axis: (a)original temperature boundary conditions and the original value of concentration above the baffle $c_2 = 3.2\times10^{19}$, (b) modified temperature boundary conditions (the value $T2 = T1+5^0C$ instead of $T2 = T1+3^0C$ in original formulation), (c) original temperature boundary conditions and the modified value of concentration above the baffle $c_2 = 1.6\times10^{19}$.

Fig. 11 shows a comparison of numerical results with measured values of longitudinal Sb concentration distribution along the grown crystal axis. The numerical distribution of concentration (solid line) exhibits the same character of behaviour as the experimental one, but there is a large discrepancy in the values. Experimental data obtained from Russia and USA also give different values in the region of the sharp increase of concentration, but this difference is much less than the difference between the computational and experimental results. In a similar fashion to works ([3-6]), the sharp increase in the concentration at the axis occurs in the case of small values of the height h in the melting zone $W1$ To increase the height of zone $W1$, the temperature at the bottom of the AHP heater at point 2 was increased. Instead of using $T2 = T1+3$, which was the experimental value, $T2 = T1+5$ was used. In this case a smaller value of concentration in the region of the sharp increasing was obtained (see Fig. 11b) and the numerical results became closer to experimental. However, the discrepancy still remained.

In [7] it was shown that the longitudinal concentration distribution is strongly affected by the initial values of concentration in zones *W1* and *W2*. Considering the fact that initial values of concentration are not very well defined, computations were performed with a modified initial value of concentration in *W2*, namely 1.6×10^{19}, or half the previous value. Results for the longitudinal concentration distribution at the axis are shown on Fig. 11c. As can be seen, in this case there is a greatly improved agreement between experimental and numerical results.

CONCLUSIONS

Computational predictions for the dopant concentration at the crystal axis showed good qualitative agreement with values measured from the grown crystal. Analysis of the reasons for the discrepancy between experimental and numerical results showed the importance of using, in the modelling, correct values for initial concentrations in the different zones of the melt. Numerical studies showed the complexity of the heat and mass transfer processes occurring during transitions between different regimes of crystal growth. The investigation shows the necessity for detailed planning of the experiment because initial and boundary conditions strongly influence all the dynamics of the heat and mass transfer processes during solidification.

ACKNOWLEDGMENTS

The authors acknowledge with thanks the financial support of the Australian Research Council. This work is supported by INTAS-ESA grant 99-01814 and by NASA under the grant 450975812.

REFERENCES

1. Golyshev V.D., Gonik M.A., Patent of RF # 180085415 (1990).
2. Golyshev V.D. and Gonik M.A., A temperature field investigation in the case of crystal growth from the melt with a plane interface on exact determined thermal conditions, Crystal Properties and Preparation 36-38, 623-630, 1991.
3. Fryazinov, I.V., Golyshev, V.D., Gonik, M.A., Marchenko, M.P., Tsvetovsky, V.B., Influence of temperature gradient on Ga distribution in Ge for AHP method, Proceedings of VNIISIMS, v XV, p. 56-63, 1998.
4. Golyshev, V.D. , Gonik, M.A. , Marchenko, M.P. , Fryazinov, I.V.,Tsvetovsky, V.B., Character of thermal conditions in Ge crystal growth by AHP method, Proceedings of IV Inter. Confer. "Crystal: growth, properties, real structure, application", Alexandrov, VNIISIMS, v. 1, p. 218 - 233, 1999.
5. Golyshev, V.D., Gonik, M.A., Tsvetovsky, V.B., M.P. Marchenko, M.P., Frjazinov, I.V. 'Investigation of features of lateral dopant distribution in Ge single crystals grown by AHP method', CHT'01 Advances in Computational Heat Transfer II, G. de Vahl Davis and E. Leonardi (eds), Begell House Inc., New York, pp. 1137-1144, 2001
6. V.D.Golyshev, M.A.Gonik, V.B.Tsvetovsky, I.V. Frjazinov, M.P. Marchenko, Computational and experimental investigation of heat and mass transfer features in growth of Ge by the AHP method, Proceedings of the 3rd Int. Conference on Single Crystal Growth, Strengthen Problems, and Heat and Mass Transfer, 21-24 Sept.1999, Obninsk (Russia), 2000, p.125-134.
7. S.V. Bykova, I.V. Frjazinov, V.D. Golyshev, M.A. Gonik, M.P. Marchenko, V.B. Tsvetovsky, Modelling of heat and mass transfer in growth of Ge crystals by AHP method, J. Crystal Growth (submitted May 2001).
8. I.V Frjasinov., V. D Golyshev., M.P. Marchenko, Influence of the boundary temperature conditions on the shape of the phase interface, on melt flow and dopant distribution in single crystals grown by the AHP method. Proceeding of the 4th Int. Conference on single crystal growth and heat & mass transfer, Obninsk, Russia, 24-28 September, 2001 (to be published)
9. E. Balikci, A. Deal, R. Abbaschian, M. Gonik, V. Golyshev, Growth of antimony doped germanium single crystals by axial heat processing technique, Proceedings of 2nd Pan Pacific Basin Workshop on Microgravity Sciences, 2001 (paper CG-1151).
10. Friazinov, I.V. and Marchenko, M.P, Program complex KARMA1 for solution of transient problem of crystal growth in ampoules, J. Comput. Math. and Math. Phys., Vol. 37, No. 8, pp. 988-998, 1997.
11. Friazinov, I.V., Mazhorova, O.S., Marchenko, M.P., Monotonic corrective terms and coupled algorithm for Navier-Stokes equations of an incompressible flow, Math. Modelling (Russian), Vol. 6, No. 12, pp. 97-116, 1994.

HEFAT2002
1st International Conference on Heat Transfer, Fluid Mechanics, and Thermodynamics
8-10 April 2002, Kruger Park, South Africa
WP2

DISTINCT PROPERTY EFFECTS ON HEAT TRANSFER OF A LIQUID LAYER RAPIDLY SOLIDIFIED ON A SUBSTRATE

P. S. Wei and F. B. Yeh
Professor and Graduate Student
Department of Mechanical and Electro-Mechanical Engineering
National Sun Yat-Sen University
Kaohsiung, Taiwan 80424
Republic of China
E-mail: pswei@mail.nsysu.edu.tw

ABSTRACT

The heat transfer of a splat rapidly solidified on a cold substrate is self-consistently and quantitatively investigated. In this work, the solidification front in the splat is governed by nonequilibrium kinetics while the melting front in the substrate undergoes equilibrium phase change. By solving one-dimensional unsteady heat conduction equations and accounting for distinct properties between phases and splat and substrate, the results show that the time-dependent Biot number representing heat transfer can be divided into five regimes: liquid splat-solid substrate, liquid splat-liquid substrate, nucleation of splat, solid splat-solid substrate, and solid splat-liquid substrate. Biot number during liquid splat cooling increases and nucleation time decreases with increasing contact Biot number, solid conductivity of the substrate, and decreasing specific heat ratio. Decreases in melting temperature and liquid conductivity of the substrate further decrease Biot number after the substrate becomes molten.

NOMENCLAURE

Bi	$hs/k_{1\ell}$
C_{pr}	c_{p1}/c_{p2}
d	substrate thickness, m
K	$k/k_{1\ell}$
s	splat thickness, m
Ste	$c_{p2}T_\infty (C_{pr}\theta_{10}-1)/\Delta H_1\theta_{10}$
Ste_1	$c_{p1}T_{10}/\Delta H_1$
u_i	dimensionless solidification velocity

Greek letters

γ	kinetics coefficient, m/s-K
Γ	dimensionless kinetics coefficient = $\rho_1 s c_{p1} T_\infty \gamma / k_{1\ell}$
δ	dimensionless solid or liquid thickness
ξ	dimensionless coordinate = x/s
ΔH	latent heat, J/kg
θ	dimensionless temperature = T/T_∞
λ_2	$(\theta_2-1)/(C_{pr}\theta_{10}-1)$
τ	dimensionless time $\equiv k_{1\ell}\,Ste\,t/[\rho_1 c_{p1} s^2(1+Ste)]$

Subscript

b	bottom
i	solid-liquid interface
m, N	melting and nucleation
0	initial
1,2	splat and substrate

INTRODUCTION

Rapid solidification takes place in splat cooling, plasma or powder spray deposition, single and twin-roller melt-spinning, strip and slab casting, melt-extraction, etc. Extensive reviews have been presented by Anantharaman and Suryanarayana [1], Jones [2], Zaat [3], and Cahn [4]. In all these processes, the molten metal is brought in contact with a cold substrate, and heat is transferred from the melt into the substrate. Advantages of rapid solidification are that the workpiece surface can improve resistances to abrasion, wear, corrosion, or oxidation. Rapid solidification differs from slow equilibrium solidification [5,6] in that the temperature at the solid-liquid interface is allowed to vary and the growth rate is determined by supercooling between the melting and interface temperatures [7,8]. Rapid freezing takes place as the interface temperature is decreased to the nucleation temperature. Hence, a sudden increase in solidification rate results in recalescence, provided that the latent heat evolution is much greater than the dissipation of heat [9]. The contact heat transfer coefficient between the liquid splat and substrate should reflect a strong variation of temperature and phase change near the substrate at an initial stage. In view of the complexity of the process for rapid solidification, a study of contact heat transfer coefficient affected by significant heat transfer, distinct properties in different phases, and kinetic effect becomes the objective of this work.

A numerical heat transfer analysis combining a realistic kinetic effect of nucleation and rapid growth of the interface appears to be started from Levi and Mehrabian [9] in treating a supercooled atomized droplet. They provided a dimensionless enthalpy-temperature diagram to describe solidification following isothermal, isenthalpic, and recalescence paths. Clyne [10] proposed a parameter involving the kinetics coefficient and contact heat transfer coefficient to interpret the occurrence of recalescence. Significant recalescence was induced near the splat-substrate surface in an early stage by increasing supercooling, thermal diffusivity, heat transfer coefficient, initial temperature of the molten layer, and

the splat is much smaller than radius of curvature or the time scale for rapid solidification is shorter than 0.15 s [17]. Convection in molten regions of the splat and substrate is ignored, since Peclet number is less than unity for freezing a liquid splat in a typical thickness of 10^{-5} m and maximum velocity of 1 m/s near the solidification front. Physical and thermal properties are averaged within temperature ranges considered in the phases, splat, and substrate, but are allowed to be distinct. The splat freezes rapidly at a solidification velocity governed by a kinetic condition

$$\tilde{u}_{1i} = \begin{cases} \gamma(T_{1m} - T_{1i}) & \text{for} \quad t \geq t_N \\ 0 & \text{for} \quad t < t_N \end{cases} \tag{1}$$

while the substrate experiences possible melting with the equilibrium temperature at the melting front. Rapid freezing proceeds only after time is greater than the time for nucleation. With the above assumptions, the heat conduction equation reduces to

$$\rho_j \frac{\partial H_j}{\partial t} = \frac{\partial}{\partial x}\left(k_j \frac{\partial T_j}{\partial x}\right) \tag{2}$$

where the subscript j =1, 2 stand for the splat and substrate, respectively. Internal energy H_j including sensible and latent heats $H_j = c_{pj} T_j + f_j \Delta H_j$ The heat conducted through the splat and substrate is removed at the top and bottom surfaces by convection, respectively. Stefan boundary conditions are satisfied at the solid-liquid interfaces. Conservation of heat flux at the contact surface between the splat and substrate is

$$k_1 \frac{\partial T_1}{\partial x} = k_2 \frac{\partial T_2}{\partial x} \tag{3}$$

Distinct temperatures resulting from imperfect contact of contact surfaces between the splat and substrate are governed by

$$-k_2 \frac{\partial T_2}{\partial x} = h_{12}(T_2 - T_1) \tag{4}$$

where h_{12} is an empirical contact heat transfer coefficient. Provided that the contact heat transfer coefficient is large, discontinuity of temperatures across the contact surface vanishes. For convenience, thermal analysis of the substrate can be avoided if a heat transfer coefficient h_{1b} is introduced and satisfied by

$$k_1 \frac{\partial T_1}{\partial x} = h_{1b}(T_1 - T_\infty) \tag{5}$$

This work is to predict heat transfer coefficient h_{1b} affected by different parameters.

Numerical method. The numerical scheme accounting for distinct properties across an interface provided by Lee and Tzong [21] has been generalized to include nonequilibrium rapid solidification in the splat and equilibrium melting in the substrate. A discretized heat conduction Eq. (2) yields

$$a_{1W} T_{1\,j-1} + a_{1P} T_{1\,j} + a_{1E} T_{1\,j+1} = a_{1R} \tag{6}$$

A discretized heat conduction equation of the substrate can be similarly obtained. Stefan boundary condition of the splat is used to determine the enthalpy at the solid-liquid interface in interval $[\xi_j, \xi_{j+1}]$. Interface velocity is obtained from the kinetic Eq. (1). Thickness of the frozen region is then calculated from

$$\delta_1 = \delta_1^0 + u_{1i}\Delta\tau \tag{7}$$

The location of the melting front in the substrate is determined by using Stefan boundary condition

$$\delta_2 = \xi_j + \frac{K_{2s}(\lambda_{2i} - \lambda_{2j})\Delta\xi_j}{K_{2s}(\lambda_{2i} - \lambda_{2j}) + K_{2l}(\lambda_{2j+1} - \lambda_{2i})} \tag{8}$$

where truncation error would always be less than the grid size $\Delta\xi_j$. Eq. (8) is a good approximation as long as the grid size is sufficiently small. The solution procedure was as follows:

1 Specify initial and working conditions, and physical and thermal properties of the splat and substrate.

2 Solve energy Eqs. of the splat and substrate together with boundary conditions.

3 Calculate the location of the melting front in the substrate from Eq. (8),

4 Check convergence of enthalpy and total energy balance of the substrate and splat to relative errors less than 10^{-7}, and 10^{-3}, respectively. Otherwise, go to step 2.

6 Calculate Biot number, Go to step 2 for the next time if time is less than nucleation time. Otherwise, after calculating interface temperature interface velocity from the kinetic Eq. (1), and thickness of the solidified splat from Eq. (7), go to step 2 for the next time.

A successive relaxation method with a relaxation factor 0.3 was used. The grid system is in uniform spaces in the splat and substrate, respectively. The predicted regions of the solidified splat and molten substrate by using different grid systems, 31x121, 101x501, and 201x1001 in the splat and substrate were examined. The grid system 101 x501 is quite good to obtain solutions independent of the variation in meshes. The predicted velocity and temperature at the solid-liquid interface agree with those obtained from Wang and Matthys [22], as shown in Fig. 2.

RESULTS AND DISCUSSION

In this study, the values of these parameters were chosen from the data provided by Wang and Matthys [22] and presented in Table 1. The effects of the contact Biot number at the splat-substrate interface on the growths of solidification and melting fronts in the splat and substrate in an earlier stage are, respectively, shown in Fig. 3. The positive and negative values of the ordinate represent locations of the solid-liquid interfaces in the splat and substrate, respectively. Referring to Eq. (5) it can be seen that the higher the contact heat transfer coefficient (or contact Biot number) is, the more perfect the contact surface is. In view of high cooling rates, an increase in contact Biot number reduces times for phase changes and increases thicknesses of the solidified splat and melted substrate. The difference in the onset times for freezing the splat and melting the substrate reduces with increasing contact Biot number. Since Biot number changes from 5 to 0.8 dimensionless time for freezing delays approximately from 0.004 to 0.1. The effects of contact Biot number on rapid solidification therefore are significant.

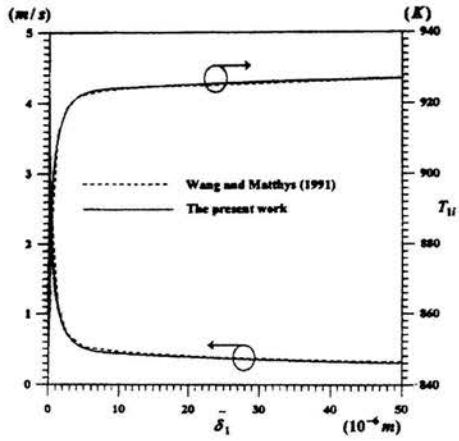

Fig. 2: A comparision between the predicted dimensional interface velocities and temperatures from Wang and Matthys [22] and this work.

The use of contact Biot number or contact heat transfer coefficient to evaluate cooling rate requires a determination of the top surface temperature of the substrate [11, 18]. An often-used Biot number is Bi_{1b} , which is based on the difference in temperatures at the bottom surface of the splat and surroundings. In this work, it is called the Biot number. The effects of contact Biot number on unsteady Biot number are presented in Fig. 4. It can be seen that the maximum of Biot number is identical to contact Biot number. This is because the temperature at the top surface of the substrate is the initial or surrounding temperature as the splat contacts the substrate. Biot number and its decreasing rate reduce with increasing time and decreasing contact Biot number. Biot number exhibits a slight jump at nucleation time (see Fig. 3).

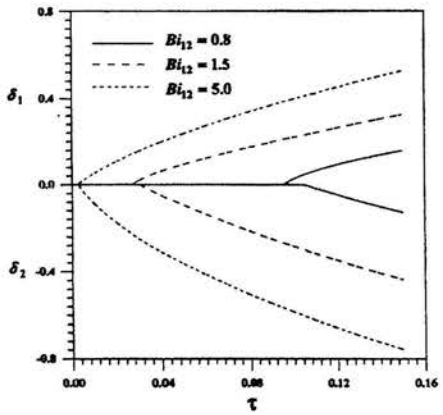

Fig. 3: Dimensionless thicknesses of the solidified splat and melted substrate versus time for different contact Biot numbers.

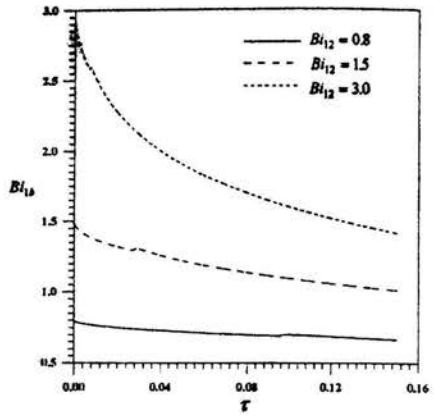

Fig. 4: Unsteady variations of Biot number for different contact Biot numbers.

The effects of dimensionless solid conductivity of the substrate on the variations of Biot number with time are presented in Fig. 5. In view of greater heat transfer dissipated to the surroundings through the substrate, an increase in dimensionless solid conductivity of the substrate increases Biot number.

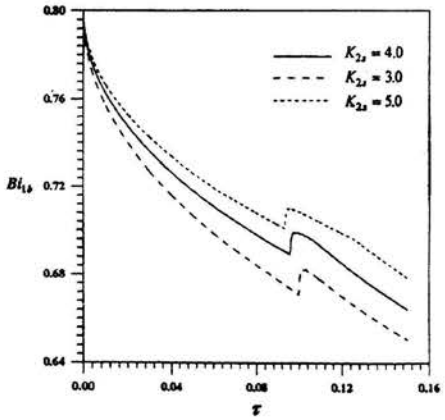

Fig. 5: Unsteady variations of Biot number for different dimensionless solid conductivities of the substrate.

Nucleation time and the extent of the jump decrease with increasing solid conductivity of the substrate.

The unsteady variations of Biot number for different dimensionless liquid conductivities of the substrate are presented in Fig. 6. Evidently, as long as the substrate remains solid, liquid conductivity of the substrate has no effect on Biot number. Interestingly, Biot number splits into three curves at a dimensionless time of around 0.105. This is because the substrate becomes molten. A low liquid conductivity of the substrate reduces Biot number, because heat transfer to the surroundings through the substrate decreases.

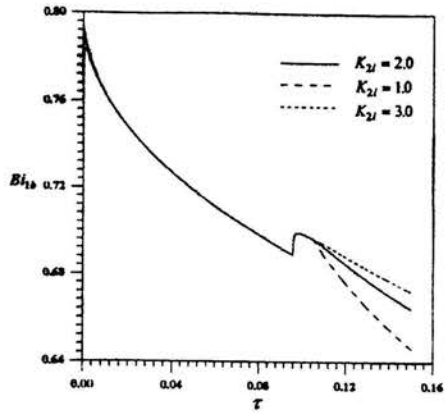

Fig. 6: Unsteady variations of Biot number for different dimensionless liquid conductivities of the substrate.

Fig. 7 shows that when the substrate remains solid, Biot number is independent of equilibrium melting temperature of the substrate. Interestingly, Biot number for a dimensionless equilibrium melting temperature of 1.2 deviates from that of 1.25 and 1.3 at a dimensionless time of 0.04. This is because the substrate starts to become molten.

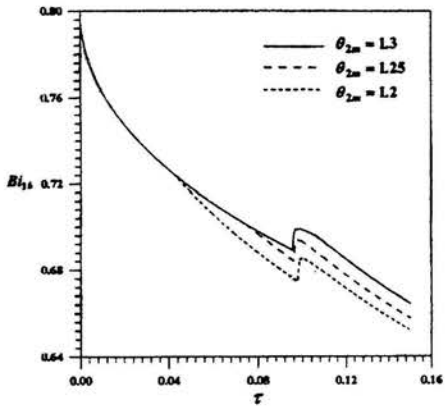

Fig. 7: Unsteady variations of Biot number for different dimensionless equilibrium melting temperatures of the substrate.

Since thermal conductivity of liquid is less than that of solid, the decrease of cooling rate reduces Biot number. Being subject to a molten substrate, freezing of the splat occurs at a dimensionless time of around 0.1. Similar result can be seen for dimensionless equilibrium melting temperature of 1.25. The time for melting the substrate, however, increases to around 0.07. The nucleation time and the extent of the jump for Biot number slightly increase by decreasing equilibrium melting temperature.

Fig. 8 shows that an increase in the splat-to-substrate specific heat ratio decreases Biot number. This is because a high specific heat implies that changing a unit temperature requires a greater energy. Hence, a high specific heat ratio indicates that the temperature gradient and the resulted heat conduction in the splat at the contact surface between the splat and substrate are low. The nucleation time is also delayed by increasing the specific heat ratio. The height of the jump slightly increases with the specific heat ratio. Interestingly, the slope of Biot number versus time exhibits a slight discontinuity at a dimensionless time around 0.12 for a specific heat ratio of 2.5. The reason for this is that the substrate becomes molten. As discussed previously, Biot number at the bottom surface of the splat decreases. Similar results can be found for the substrate-to-splat density ratio. Since energy required to increase a unit temperature is less for a low density, an increase in the substrate-to-splat density ratio enhances heat transfer to the substrate. This results in an increase of Biot number at the bottom surface of the splat, and decreases of nucleation time and height of the jump.

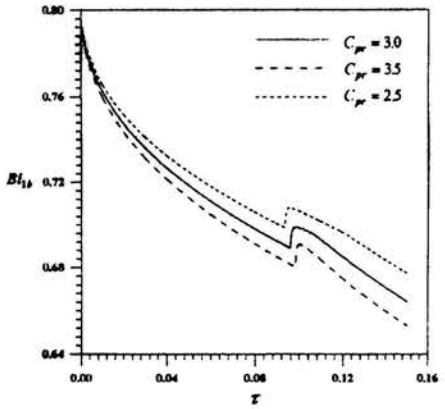

Fig. 8: Unsteady variations of Biot number for different splat-to-substrate specific heat ratios.

This work also found that increasing dimensionless equilibrium melting temperature, solid conductivity of the splat, and decreasing latent heat ratio slightly increase Biot number.

CONCLUSIONS

The conclusions drawn are the following:

1. The effects of Biot number representing heat transfer on rapid solidification of the splat are significant. The Biot number is based on the temperature difference between the bottom surface of the splat and the surroundings. The Biot number is determined by simultaneously satisfying energy equations in the splat and substrate. As a result, energy equation in the splat with a boundary condition evaluated from this Biot number at the bottom surface of the splat can be solely solved to obtain the correct results in the splat without solving energy equation in the substrate.
2. The Biot number cannot be considered a constant during rapid freezing. Time-dependent Biot number can be divided into five regimes:
   (a) Biot number decreases with increasing time for a liquid splat in an early stage.
   (b) Biot number is further lowered if the substrate becomes molten
   (c) Biot number jumps for the splat on nucleating.
   (d) Biot number gradually decreases in the course of rapid solidification.
   (e) Biot number further decreases if the substrate is melted.
3. Increases in solid conductivity of the substrate, and a decrease in specific heat ratio increase Biot number before nucleation takes place.
4. Nucleation is delayed by decreasing solid conductivity of the substrate, and increasing specific heat ratio of the splat.

5. Biot number during rapid solidification increases with increasing melting temperatures and solid conductivities of the splat and substrate, and decreasing specific heat ratio.

6. Decreases in melting temperature and liquid conductivity of the substrate further decrease Biot number after the substrate becomes molten.

REFERENCES

[1] Anantharaman, T. R., and Suryanarayana, C., 1971, "Review: A Decade of Quenching from the Melt," J. Materials Science, Vol. 6, pp. 1111-1135.

[2] Jones, H., 1982, Rapid Solidification of Metals and Alloys, The Institution of Metallurgists, London, Monograph No. 8.

[3] Zaat, J. H., 1983, "A Quarter of a Century of Plasma Spraying," Annual Review of Materials Science, Vol 13, pp. 9-42.

[4] Cahn, R. W, 1983, "Chapter 28 Alloys Rapidly Quenched from the Melt," in Physical Metallurgy, Part 2, Cahn, R. W., and Haasen, P., (editors), 3rd ed., Elsevier Science Publ., pp. 1779-1852.

[5] Frederick, D., and Greif, R., 1985, "A Method for the Solution of Heat Transfer Problems with a Change of Phase,"ASME J. Heat Transfer, Vol.107, pp.520-526.

[6] Viskanta, R., 1988, "Heat Transfer during Melting and Solidification of Metals," The 50th Anniversary Issue, ASME J. Heat Transfer, Vol. 110, pp. 1205- 1219.

[7] Turnbull, D, 1949, Thermodynamics in Physical Metallurgy, American Society for Metals, Cleveland, pp.283-306.

[8] Kurz, W. and Fisher, D. J., 1989, Fundamentals of Solidification, Trans. Tech. Publ., Aedermannsdorf, Switzerland, pp. 220-225.

[9] Levi, C. G., and Mehrabian, R., 1982, "Heat Flow during Rapid Solidification of Undercooled Metal Droplets," Metallurgical Transactions, Vol.13A, pp.221-234.

[10] Clyne, T. W., 1984,"Numerical Treatment of Rapid Solidification," Metallurgical Transactions, Vol. 15B, pp.369-381.

[11] Wang, G.-X., and Matthys, E. F., 1996, "Experimental Investigation of Interfacial Thermal Conductance for Molten Metal Solidification on a Substrate," ASME J. Heat Transfer, Vol. 118, pp. 157-163.

[12] Scott, M. G., 1974, "The Effect of a Glass Substrate on Cooling Rate in Splat-Quenching," J. Materials Science, Vol. 9, pp. 1372-1374.

[13] Kuijpers, T. W. and Zaat, J. H., 1974, " Influence of Oxygen and Cooling Rate on the Microstructure and Microhardness of Plasma-Sprayed Molybdenum, " Metals Technology, Vol. 1, pp. 142-150.

[14] Carslaw, H. C. and Jaeger, J. C., 1959, Conduction of Heat in Solids, 2nd ed., Clarendon Press., Oxford, pp. 87-89.

[15] Steffens, H.-D., Wielage, B., and Drozak, J., 1991, "Interface Phenomena and Bonding Mechanism of Thermally-Sprayed Metal and Ceramic Composites," Surface and Coatings Technology, Vol. 45, pp. 299-308.

[16] Amon, C. H., Merz, R., Prinz, F. B., and Schmaltz, K. S., 1994, "Thermal Modelling and Experimental Testing of MD* Spray Shape Deposition Processes, " In Heat Transfer 1994, ed. G. F Hewitt, Proceedings of Tenth International Heat Transfer Conference, IChemE Publishing, Brighton, UK, Vol. 7, pp. 321-326, .

[17] Amon, C. H., Schmaltz, K S., Merz, R., and Prinz, F. B., 1996, "Numerical and Experimental Investigation of Interface Bonding via Substrate Remelting of an Impinging Molten Metal Droplet," ASME J. Heat Transfer,Vol.118, pp.164-172.

[18] Wang, S.-P, Wang, G.-X., and Matthys, E. F., 1998, "Melting and Resolidification of a Substrate in Contact with a Molten Metal: Operational Maps," Int. J. Heat Mass Transfer, Vol. 41, pp. 1177-1188.

[19] Wei, P. S., and Yeh, F. B., 2000, "Heat Transfer Coefficient in Rapid Solidification of a Liquid Layer on a Substrate," ASME J. Heat Transfer, Vol. 122, pp. 792-800.

[20] Wei, P. S., Yeh, F. B., and Chiu, S. H., 2000, "Rapid Solidification of a Thin Liquid Layer on a Substrate Subject to Melting Affected by Distinct Properties." (submitted to Int'l. J. Heat Mass Transfer).

[21] Lee, S. L., and Tzong, R. Y., 1991, "An Enthalpy Formulation for Phase Change Problems with a Large Thermal Diffusivity Jump across the Interface," Int. J. Heat Mass Transfer, Vol. 34, pp. 1491-1502.

[22] Wang, G.-X., and Matthys, E. F., 1991, "Modelling of Heat Transfer and Solidification during Splat Cooling: Effect of Splat Thickness and Splat/Substrate Thermal Contact," Int. J. Rapid Solidification, Vol. 6, pp. 141-174.

Table 1 Typical values of independent dimensionless parameters

$Bi_{1\infty}$, $Bi_{2\infty}$, Bi_{12}	0.01, 0.01, 0.8
C_{pr}	**3.0**
K_{1s} , K_{2s}	**2.0**
K_{2s}	**4.0**
Ste_1	**3.6**
Γ	**20**
θ_{10}	**3.6**
θ_{1N}	**3.0**
θ_{1m}	**3.5**
θ_{2m}	**1.3**

HEFAT2002
1st International Conference on Heat Transfer, Fluid Dynamics and Thermodynamics
8-10 April 2002, Kruger National Park, South Africa
ZP1

ON MODELS FOR THE NUMERICAL SIMULATION OF CRYSTAL GROWTH

P. Zhao and J. C. Heinrich

Department of Aerospace and Mechanical Engineering
The University of Arizona
Tucson AZ 85721-0119

ABSTRACT

It is well known that the results of numerical solutions to solidification problems in the sharp interface limit depend critically on the initial conditions. In fact, slightly different initial conditions can yield very different solutions. This fact is related to the influence of the initial conditions on the interface velocity, which in turn determines the thickness of the thermal boundary layer adjacent to the interface. It is shown that, for high enough rates of solidification, solutions obtained using discrete, fixed-mesh finite difference or finite element methods are apparently mesh dependent. Ways to resolve this problem are examined and numerical experiments are reported.

INTRODUCTION

Driven by the technological importance of solidification processes in the manufacturing of advanced materials for the aerospace and semiconductors industries, as well as in other areas of engineering and science, several numerical methods have been developed to model the change-of-phase process, including the accurate calculation of the interface position and shape (McCartney and Hunt, 1984; Sullivan et al., 1987; Sethian and Strain, 1992; Brattkus and Meiron, 1992; Wheeler et al., 1993; Juric and Tryggvason, 1996; Palle and Dantzig, 1996; Udaykumar et al., 1999; Zhao and Heinrich, 2001). In this work, emphasis is on numerical methods that calculate directly the position of the interface using finite differences or finite elements.

Sullivan et al. (1987) and Sullivan and Lynch (1988) developed a finite element model based on an adaptive mesh of linear triangular elements. They used different computational strategies depending on whether the problem involved stable or unstable solidification and concluded that the contribution of curvature to the interface motion must be treated implicitly in time and within the iteration required at each time step. They applied the model to solidification of a perturbed planar interface using thermal properties of succinonitrile and of water. They provided the first finite element algorithm to solve the full transient two-dimensional heat equation and demonstrated the bifurcation of dendrite tips.

Palle and Dantzig (1996) developed an adaptive finite element method for the solidification of binary alloys based on bilinear elements on a fixed grid that is locally refined in the proximity of the interface and used linear triangles to handle the mesh transitions. The refinement is controlled by the local error using an error estimator. They used an enthalpy formulation for the energy equation, from which the interface position is recovered as the freezing isotherm. The solute conservation equation is reformulated in terms of the chemical activities in order to obtain two equations of the same form. They applied the method to stable solidification in a square region with the temperature of the lower left corner reduced below the solidus and assuming insulated boundaries, using properties of Fe – 0.05 wt% C.

Juric and Tryggvason (1996) developed a fixed-mesh finite difference method that uses an indicator function similar to that in phase-field (Wheeler et al., 1993) or level-set methods (Sethian and Strain, 1992) but where the interface is tracked explicitly using a set of marker points. They applied it successfully to the modeling of solidification of equiaxial dendrites in an undercooled liquid in two dimensions. Another fixed-mesh finite difference method that tracks the interface directly using markers was developed by Udaykumar et al. (1999). They reproduced many of the calculations given by Juric and Tryggvason (1996) and showed what appears to be an improvement in accuracy. However, both of these methods are only first order in the approximation of the interface position. A finite element method based on a fixed grid of bilinear elements that tracks the interface using markers was developed by Zhao and Heinrich (2001) and it was shown that the method is second-order accurate in the approximation of the interface. Calculation for the cases reported by Juric and Tryggvason (1996) and Udaykumar et al. (1999) showed that the methods

do not always yield the same solution and in some cases great differences were observed in the simulation time required for the dendrites to grow, i.e., the different models are calculating very different solidification velocities. These discrepancies are addressed and explained in this work. The effect of the initial conditions on the solidification velocity is examined, as is the effect of the solidification velocity on the final solution when the latter is obtained in a fixed discrete mesh.

MATHEMATICAL MODEL

We address the solidification of a pure substance, assuming that conduction is the only mechanism of heat transport. The energy equation is given by

$$\eta \frac{\partial T_S}{\partial t} = \Lambda \nabla^2 T_S \quad \text{in the solid phase} \tag{1a}$$

$$\frac{\partial T_L}{\partial t} = \nabla^2 T_L \qquad \text{in the liquid phase} \tag{1b}$$

The conditions at the solid-liquid interface are

$$T_S = T_L \tag{2a}$$

$$\Lambda \frac{\partial T_S}{\partial n} - \frac{\partial T_L}{\partial n} = (1-\gamma T_I)V \tag{2b}$$

In this work, the subscripts S and L denote the solid and liquid phase, respectively. The equations are made non-dimensional using a reference length H, the reference time $\tau = H^2/\alpha_L$, and the non-dimensional temperature $T = c_{PL}(T^* - T_m^*)/L$, where $(^*)$ indicates a dimensional quantity. The parameters in equations (1) and (2) are $\alpha_L = \kappa_L/\rho_L c_{PL}$, $\eta = \rho_S c_{PS}/\rho_L c_{PL}$, $\Lambda = \kappa_S/\kappa_L$, $St = c_{PL}(T_\infty^* - T_m^*)/L$, and $\gamma = (c_{PS} - c_{PL})/c_{PL}$. In the above, ρ denotes density, c_P is specific heat, κ is thermal conductivity, T_m is the melting temperature, T_∞ is the far-field temperature, L is the latent heat, $V = (d\vec{S}_I/dt)\cdot\hat{n}$ is the non-dimensional local interface velocity, $\vec{S}_I$ is the interface, and T_I is the local non-dimensional interface temperature. T_I is given by the Gibbs-Thompson equation (Alexiades and Solomon, 1993)

$$T_I - \gamma T_I^2 + \sigma\kappa + \mu^{-1}V = 0 \tag{3}$$

where κ is the local interface curvature, σ is the surface tension, and μ is the kinetic mobility, given by $\sigma = c_{PL}T_{m0}\sigma^*/HL^2$ and $\mu^{-1} = c_{PL}\alpha_L/HL\mu^*$. The last two quantities may vary locally to account for anisotropic effects. In equation (2b), the normal derivative is defined as

$$\frac{\partial T}{\partial n} = \hat{n}\cdot\nabla T \tag{4}$$

where $\hat{n}$ denotes the unit vector normal to the interface and pointing toward the liquid phase.

The finite element model utilized to solve equations (1)-(3) has been described in full detail by Zhao and Heinrich (2001a) and will not be repeated here.

INITIAL CONDITIONS

In problems of unstable solidification into an undercooled liquid, it must be assumed that a solidified seed already exists that will grow into the liquid. This poses a difficulty in defining the initial temperature field, which is unknown. Sullivan et al. (1987) utilized the solution to a one-dimensional convection diffusion equation with an assumed convective velocity in their calculations of unstable solidification from a perturbed plane front. In this case, a planar steady-state solution exists for any positive convective velocity as long as the undercooling at infinity is equal to one (Langer, 1980). For more complicated initial shapes, it becomes significantly more difficult to find a "good" initial condition. Therefore, in most simulations of equiaxial growth, the initial temperature field is assumed to be a step function with values T_m in the solid and T_∞ in the liquid. Juric and Tryggvason (1996) argue that this affects only the first time step in the calculation, the results of which can be considered the proper initial conditions for the remainder of the calculation. However, this is not entirely realistic because the temperature discontinuity at the interface implies an infinite initial interface velocity and, therefore, the interface velocity calculated for the first time step will depend on the mesh and the time-step size. Furthermore, the interface velocity will continue to be determined by the mesh size as long as the heat diffusion layer next to the interface remains smaller than the mesh size, and the interface shape will be altered.

To illustrate this, consider results of calculations performed for a square region with sides 4 units long. The initial seed is specified by $x = x_c + R\cos(\theta)$ and $y = y_c + R\sin(\theta)$, where (x_c, y_c) is the center of the region and $R = 0.1 + 0.02\cos(4\theta)$, a case with four-fold symmetry. The initial temperature of the seed is T_m, and the initial temperature of the liquid is set to $T_\infty < T_m$. The undercooling, $T_\infty - T_m$, is chosen so that $St = -0.8$. The surface tension and kinetic mobility are chosen to have six-fold anisotropy and are chosen as $\sigma(\theta) = \mu(\theta) = 0.001\left[1.0 + 0.4[8/3\ \sin^4(3\theta) - 1.0]\right]$. The heat capacity and thermal conductivity are the same in both phases, i.e., $\eta = \Lambda = 1$.

The boundaries of the domain are adiabatic. This problem was also solved by Juric and Tryggvason (1996) and Udaykumar et al. (1999). Figure 1 shows the results obtained in two simulations: (a) in a mesh of 400 by 400 elements and (b) in an 800-by-800 mesh. The calculations were carried out until the top branch reached $y = 3.85$, which was attained at $t = 0.045$ in case (a) and at $t = 0.035$ in case (b). The same problem was solved by Juric and Tryggvason (their Figure 15) on an 800-by-800 mesh and by Udaykumar et al. (their Figure 24b) on a 500-by-500 mesh until the top branch reached approximately $y = 3.75$. In the first reference, it was reached at $t = 0.021$ and, in the second, at $t = 0.6$. Furthermore, all four simulations yielded a different morphology. Clearly, the solutions are algorithm and mesh dependent and span an enormous range of average solidification velocities.

The cause of these discrepancies will be explained in the context of the algorithm of Zhao and Heinrich (2001). Similar arguments can be applied to the methods used by Juric and Tryggvason (1996) and Udaykumar et al. (1999). Figure 2a shows a one-dimensional sketch of a temperature field on an element that contains the interface, together with the linear interpolant to the temperature. The kink in the temperature field due to the latent heat makes the linear interpolant inaccurate over the element. For this reason, values of the temperature obtained at the adjacent elements, or $h \geq \Delta x$, are desired in order to estimate the temperature gradients at the interface. In practice, $h = \Delta x$ suffices, but smaller values can greatly decrease the accuracy. Therefore the evaluation of the gradients must take place on the length scale of the mesh. If the solidification velocity is of the same order or larger than the diffusion velocity in the liquid, $1/\Delta x$, the thermal boundary layer ahead of the solidification front, which scales with $2\alpha_L/V$, becomes very thin and a very fine grid is required to capture the temperature gradients, as is the case in the example above. Figure 3 illustrates this, where the temperature gradients G_1, G_2, and G_3, evaluated using $h = \Delta x, \Delta x/2$, and $\Delta x/4$, respectively, are very different.

Solutions obtained with them will exhibit mesh dependence. Moreover, the detrimental effect is maximized if the initial conditions exhibit a discontinuity at the interface. This is a disadvantage of fixed-mesh methods, where the meshes must be very fine to model problems with large solidification velocity. The situation can be improved with the use of adaptive meshes, finely refined close to the interface, where small values of h can be used. This possibility is currently being explored.

Fortunately, however, this difficulty does not affect a large number of cases nor, in particular, our main problem of interest—the directional solidification of binary alloys in a stable temperature gradient. In this case, the numerical challenges arise from the solute conservation equation that contributes to the destabilizing mechanism through the formation of an extremely thin solute boundary layer in the interdendritic liquid, which must be properly resolved.

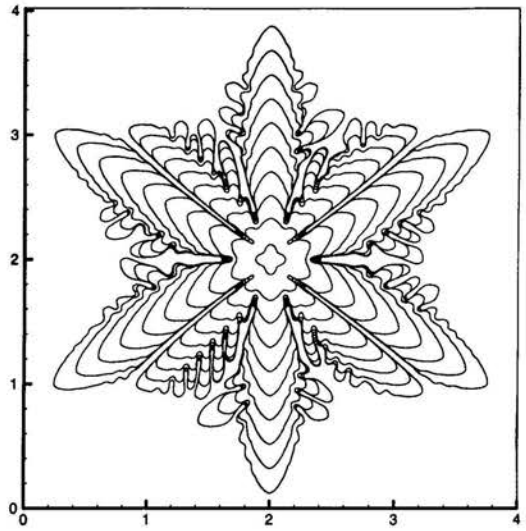

(a) Solution in a 400-by-400 Element Grid

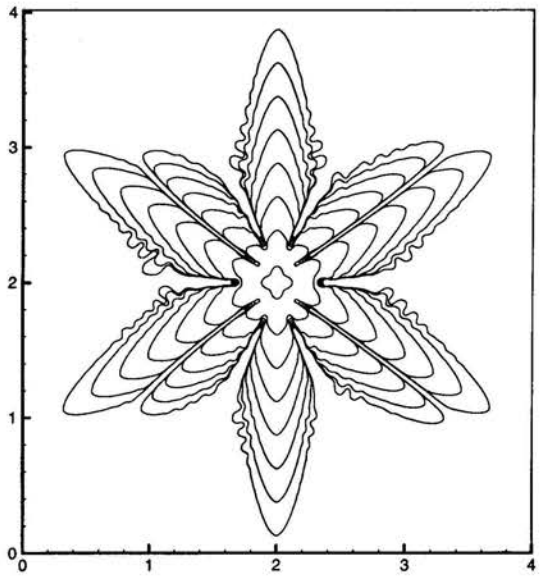

(b) Solution in an 800-by-800 Grid

Figure 1. Dendritic growth with four-fold symmetry and six-fold anisotropy.

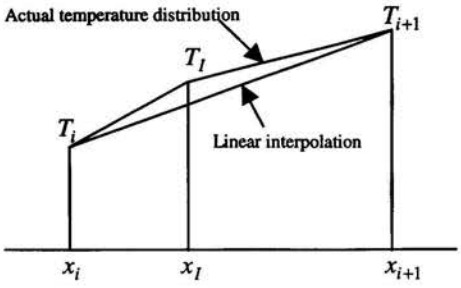

(a) Temperature Profile and Linear Interpolant

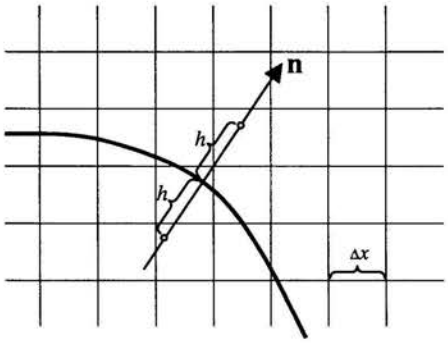

(b) Numerical Estimation of Temperature Gradients

Figure 2. Interface temperature and gradients.

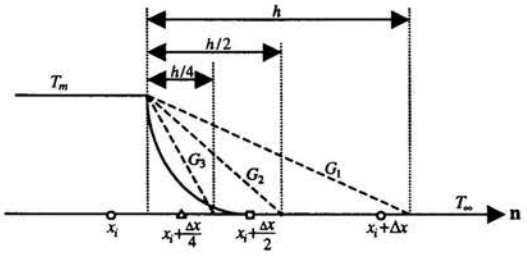

Figure 3. Temperature boundary layer at the interface and numerical evaluation of the gradients.

DIRECTIONALLY SOLIDIFIED BINARY ALLOYS

For simplicity, we ignore solute diffusion in the solid phase. The solute transport equation in the liquid is

$$\frac{\partial C_L}{\partial t} = \frac{1}{Le}\nabla^2 C_L \qquad (5)$$

and satisfies the interface condition

$$-\frac{1}{Le}\nabla C_L \cdot \hat{n} = (1-k)(C_L - 1)V \qquad (6)$$

where k is the equilibrium partition ratio and the non-dimensional concentration $C_L = C_L^*/C_0^*$, where C_0^* is the initial concentration in the melt. The Gibbs-Thompson equation (3) must be modified to

$$T_I - T_m - \gamma(T_I - T_m)^2 + (1+\beta C_I)\sigma\kappa + \mu^{-1}V = 0 \qquad (7)$$

The interface concentration C_I and temperature T_m are related by the liquidus line in the phase diagram, which we assume is a straight line

$$T_m = \lambda C_I \qquad (8)$$

where $Le = \alpha_L/D_L$, $\beta = mC_0^*/T_{m0}^*$, and $\lambda = mc_{PL}C_0^*/L$. D_L is the solute diffusivity; m is the slope of the liquidus line, and T_{m0}^* is the melting temperature of the pure solvent.

Consider one-dimensional solidification of the hypoeutectic alloy Pb-2.2wt%Sb in the domain $0 \le x \le 20$ mm under a stable temperature gradient of 100 K/cm, where the initial temperature at $x = 0$ is the liquidus temperature of the alloy, $T_{m0}^* = 585.47$ K, and a cooling rate is applied at time $t > 0$. The right end, $x = 20$ mm, is kept at the initial temperature gradient. The material properties used in the simulation are $\rho_S = \rho_L = 10{,}190$ kg/m^3, $c_{PS} = 141$ J/kgK, $c_{PL} = 151$ J/kgK, $\kappa_S = 20$ J/msK, $\kappa_L = 15$ J/msK, $m = -6.83$ K/wt%, and $L = 28{,}770$ J/kg. Results of simulations for two cooling rates, 0.03 K/s and 0.1 K/s, using a uniform mesh of 200 elements for the temperature and an adaptive mesh of 400 elements for the solute concentration are shown in Figure 4. The interface position and velocity as a function of time are shown in Figures 4a and 4b, respectively. Figure 4c shows the concentration profiles at various times. The boundary layer that scales with D_L/V and requires the adaptive mesh refinement to be resolved is evident. The accuracy of the one-dimensional model has been assessed for the case of a pure substance for which analytical solutions are available (Zhao and Heinrich 2001b), in this case very accurate solutions can be obtained. For binary alloys analytical solutions do not exist. Nevertheless, theoretical estimates for the steady-state solidification velocity and solute concentration profile in the liquid phase are available, and were used to determine the degree of refinement needed at the interface for the adaptive mesh. In our example we observe from Figure 4b,c that for a cooling rate of 0.1*K/s* a steady state is reached when the front is near $x = 12$ mm, after this point the solute concentration in Figure 4c is within 2% of the estimated steady-state approximation.

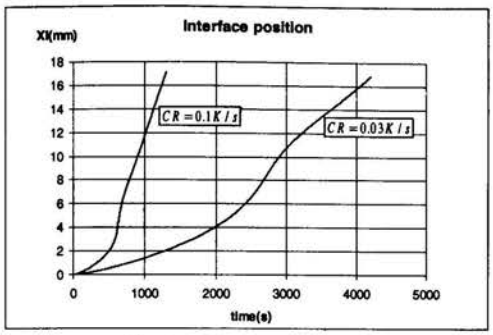

(a) Interface Position

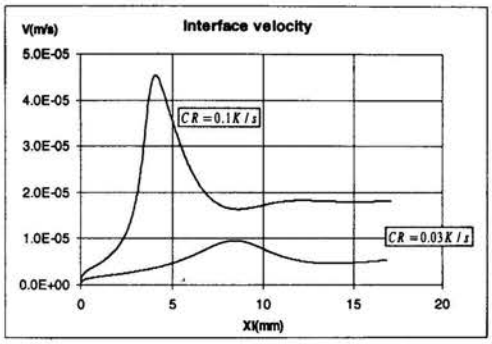

(b) Interface Velocity

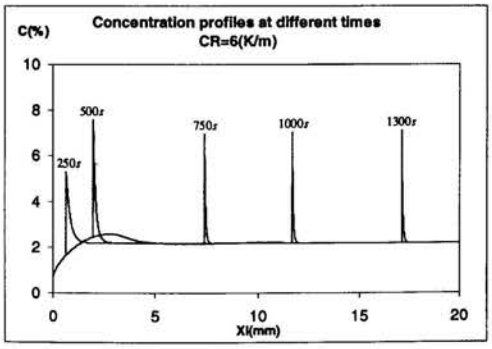

(c) Solute Concentration

Figure 4. One-dimensional solidification of Ph-2.2wt%Sb at cooling rates of 0.1 K/s and 0.03 K/s.

In two dimensions, the mesh adaptation is more complex and is still under development. Linear triangular elements are used, starting with a basic coarse mesh that is refined several levels according to the distance to the interface. An example of such a mesh is shown in Figure 5. The mesh depicted contains 40328 nodes and 75351 elements, which is representative of

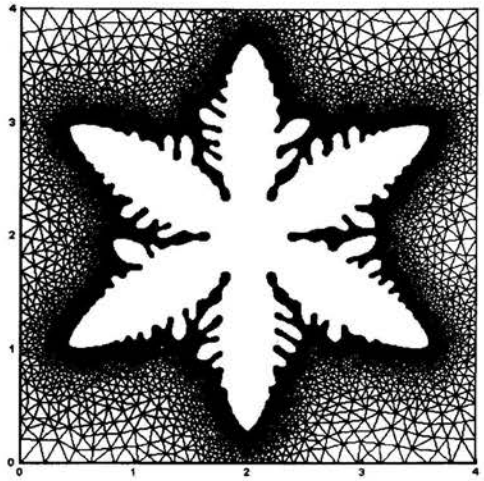

Figure 5. Adaptive meshes required in two-dimensional simulations of solidification of binary alloy.

what is expected to be required in these problems. The mesh must be generated at every time step and the data interpolated from the old to the new mesh. Efficient ways to achieve this are being developed, and the goal sought is to be able to perform a time step in a mesh of 160000 elements for the temperature field and 100000 elements for the solute concentration field in one to two seconds of CPU, depending on the hardware.

FURTHER EXTENSIONS

Two important further developments of the model are the introduction of convection and the extension to three dimensions. In the two-dimensional case, convection will utilize the mesh for the temperature field with the elements intersected by the mesh described by a combination of linear triangles and isoparametric quadrilaterals. This is made possible by the fact that only two types of intersections are possible in this model (Zhao and Heinrich, 2001a). In elements split into two quadrilaterals by the interface, the contribution of the one lying in the liquid phase is readily calculated using an isoparametric transformation. For those intersected into one triangle and one pentagon, the contribution of a triangle is calculated by standard methods. If the pentagon lies in the liquid, it is split into a triangle and a quadrilateral, and their contributions are calculated as before.

The extension to three dimensions does not offer significant difficulties, other than those related to the description and motion of the interface. Powerful mesh generators are available that are capable of discretizing the interface with linear triangular interpolants whose nodes determine the markers. As the surfaces evolve, a criterion similar to that used in two dimensions is used to re-mesh and re-define the marker points as necessary.

CONCLUSIONS

Numerical simulations of dendritic solidification of a binary alloy pose a formidable computational problem. The simplest case of two-dimensional solidification into an undercooled liquid creates scaling difficulties that can require extremely fine meshes to achieve converged answers. A finite element model that tracks the interface directly and is second-order accurate has been shown to be an extremely useful tool to understand the difficulties associated with this kind of modeling due to its simplicity and its ability to follow the physical variables directly. Its extension to the simulation of the solidification of binary alloys has been established and further developments to include convection and extend it to three dimensions have been outlined.

ACKNOWLEDGMENTS

This research was supported by the National Aeronautics and Space Administration under Grant NCC8-96.

REFERENCES

Alexiades, V. and Solomon, A. D., 1993, *Mathematical Modeling of Melting and Freezing Processes*, Hemisphere Publishing Co., Washington, D.C.

Brattkus, K. and Meiron, D. I., 1992, "Numerical Simulation of Unsteady Crystal Growth," *SIAM Journal of Applied Mathematics*, Vol. 52, pp. 1303-1320.

Juric, D. and Tryggvason, G., 1996, "A Front-Tracking Method for Dendritic Solidification," *Journal of Computational Physics*, Vol. 123, pp. 127-148.

Langer, J. S., 1980, "Instabilities and Pattern Formation in Crystal Growth," *Reviews of Modern Physics*, Vol. 52, pp. 1-28.

McCartney, D. G. and Hunt, J. D., 1984, "A Numerical Finite Difference Model of Steady-State Cellular and Dendritic Growth," *Metallurgical Transactions A*, Vol. 15A, pp. 983-994.

Palle, N. and Dantzig, J. A., 1996, "An Adaptive Mesh Refinement Scheme for Solidification Problems," *Metallurgical and Materials Transactions A*, Vol. 27A, pp. 707-717.

Sethian, J. A. and Strain, J., 1992, "Crystal Growth and Dendritic Solidification," *Journal of Computational Physics*, Vol. 98, pp. 231-253.

Sullivan, J. M., Jr. and Lynch, D. R., 1988, "Non-Linear Simulation of Dendritic Solidification of an Undercooled Melt," *International Journal for Numerical Methods in Engineering*, Vol. 25, pp. 415-444.

Sullivan, J.M., Jr., Lynch, D. R., and O'Neill, K., 1987, "Finite Element Simulations of Planar Instabilities During Solidification of an Undercooled Melt," *Journal of Computational Physics*, Vol. 69, pp. 81-111.

Udaykumar, H. S., Mittal, R., and Shyy, W., 1999, "Computation of Solid-Liquid Phase Fronts in the Sharp Interface Limit on Fixed Grids," *Journal of Computational Physics*, Vol. 153, pp. 535-574.

Wheeler, A. A., Murray, B. T., and Schaefer, R. J., 1993, "Computation of Dendrites Using a Phase Field Model," *Physica D*, Vol. 66, pp. 243-262.

Zhao, P. and Heinrich, J. C., 2001a, "Front-Tracking Finite Element Method for Dendritic Solidification," *Journal of Computational Physics* (submitted).

Zhao, P. and Heinrich, J. C., 2001b, "Approximation to the Interface Velocity in Phase Change Front-Tracking," *Communications in Numerical Methods in Engineering* (to appear).

HEFAT2002
1st International Conference on Heat Transfer, Fluid Dynamics and Thermodynamics
8 – 10 April 2002, Kruger National Park, South Africa
AF2

LAMINAR NATURAL CONVECTION INSIDE A TRIANGULAR CAVITY WITH A UNIFORM HEAT FLUX ON ONE WALL.

F.R.Q. Aquino
Basic Department
Faculty of Chemical Engineering of Lorena
Lorena - São Paulo State - Brazil
Email: felipe@debas.faenquil.br

M. A. Zanardi
Energy Department
São Paulo State University - UNESP
Guaratinguetá - SP
Brazil
Email: mzardi@feg.unesp.br

ABSTRACT

In the present work we consider the natural laminar convection for an enclosure of right triangular shape filled with air, with a constant heat flux imposed on their inclined face, with vertical face and bottom cold. Two dimensional equations of mass, momentum and energy conservation, with the Boussínesq approximation are solved. The solution of the differential equation set is performed by using a finite volume method. The discretization scheme chosen was the Patankar's Power-Law Scheme and the SIMPLE algorithm is adopted to get a pressure correction equation. The resultant algebraic equations are solved by a line-by-line procedure that is a combination of a direct method (TDMA) and an iterative Gauss-Siedel method. Governing parameters used were: $10^3 \le Gr \le 10^8$, Pr=0.72 and $0.2 \le H/L \le 2.0$. The isotherms and streamlines are presented and a Nusselt number correlation in terms of Grashof number and ratio aspect is proposed. The influence of the Grashof number and the enclosure aspect ratio is discussed.

INTRODUCTION

Natural convection is important in many engineering applications. Over the past years, many studies in rectangular, trapezoidal and cylindrical geometries have been carried out due to the interest they have from the view point of application. For such geometries, a large number of both experimental and theoretical studies, covering wide ranges of Grashof number and aspect ratios can be found in the literature.

More recently triangular geometry have received attention. This is the suitable geometry to deal with heat transfer in attic areas of domestic buildings, and in some solar energy and electronic cooling systems.

One of the first numerical simulation of convection in an enclosure of triangular cross section is due to Gershumi et al (1974). Akinset and Coleman (1979, 1982) studied the problem of a prismatic cavity of the right triangular cross-section with the bottom cooled and the vertical wall adiabatic. Kushawara (1982) solved a similar problem using finite element method.

Experiments on the natural convection of air within triangular enclosures were first reported by Flack et al (1979) and his collaborators. Some authors reported theoretical results with a large combination of boundary conditions. Del Campo et al (1988) presented several different combinations of heated, cooled and adiabatic wall conditions. They found strong gradients of temperature near to the walls; and stratification of the fluid in the center of the cavity. When it is hot from bottom, the flow acquires a turbulent form for great values of Gr.

The unsteady natural convection in an enclosure with the cross section in the form of isosceles triangle was considered by Poulikakos and Bejan (1983a, 1983b) assuming all the walls isothermal. Other cases, changing the boundary conditions were presented by Karyakin et al. (1985, 1985a, 1985b, 1988). They considered adiabatic and constant temperature walls.

The use of heat flux condition at the enclosures surfaces is important in the study of heat transfer in attic spaces. However, the use of such conditions is not widely available in the literature.

In the present work we consider the natural laminar convection for a enclosure with the form of a triangle with a right angle, with a constant heat flux imposed on one of their faces. Two dimensional equations of mass, momentum and energy conservation, with the Boussinesq approximation are solved using a finite difference method. The numerical

procedure adopted is based on SIMPLE algorithm. The isotherms and streamlines are presented for different aspect ratios and Grashof numbers and a normalized Nusselt number correlation in terms of the Grashof number and ratio aspect is proposed.

NOMENCLATURE

a	coeficients of equation (12) and (13)
A	aspect ratio, H/L
g	acceleration due to gravity, m/s^2
Gr	Grashof number, $g\beta L^4 q / \nu^2 k$
h	convection heat transfer coefficient, $W/m^2.K$
H	cavity height, m
k	thermal conductivity, W/m.K
l	dimensionless length
p	dimensionless pressure
Pr	Prandtl number, ν/α
q	heat flux, W/m^2
t	dimensionless time
T	temperature, K
u, v	dimensionless velocity in x and y direction

Greek Symbols

α	thermal diffusivity, m^2/s
β	thermal expansion coefficient, 1/K
θ	dimensionless temperature, $(T-T_c)/(Lq/k)$
μ	dynamic viscosity, kg/m.s
ρ	density, kg/m^3
Γ	general diffusion coefficient
ν	kinematic viscosity, m^2/s

Superscripts

′	dimension quantities

Subscripts

c	cold wall
l	local

MATHEMATICAL MODELING

The considered geometry is show in Figure 1. The gravity vector is normal to the base of the angle.

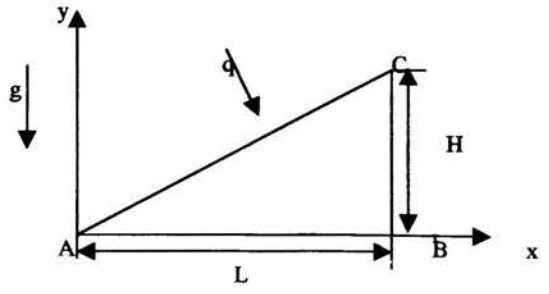

Figure 1 - Problem geometric

In order to formulate the fluid convection in the cavity it was considered the following assumptions:

- the flow is two dimension, incompressible and laminar;
- the temperature gradients are moderate for which the Boussinesq approximation is valid;
- viscous dissipation and the work done by compression forces are negligible.

The basic equations for the unsteady-state natural convection can be written in the dimensionless form as:

$$\frac{\partial u}{\partial x}+\frac{\partial v}{\partial y}=0 \tag{1}$$

$$\frac{\partial u}{\partial t}+u\frac{\partial u}{\partial x}+v\frac{\partial u}{\partial y}=-\frac{\partial p}{\partial x}+Pr\left(\frac{\partial^2 u}{\partial x^2}+\frac{\partial^2 u}{\partial y^2}\right) \tag{2}$$

$$\frac{\partial v}{\partial t}+u\frac{\partial v}{\partial x}+v\frac{\partial v}{\partial y}=Pr^2\,Gr\theta-\frac{\partial p}{\partial y}+Pr\left(\frac{\partial^2 v}{\partial x^2}+\frac{\partial^2 v}{\partial y^2}\right) \tag{3}$$

$$\frac{\partial \theta}{\partial t}+u\frac{\partial \theta}{\partial x}+v\frac{\partial \theta}{\partial y}=\frac{\partial^2 \theta}{\partial x^2}+\frac{\partial^2 \theta}{\partial y^2} \tag{4}$$

For the construction of dimensionless quantities the following non-dimensionless variables are defined:

$$x=\frac{x'}{L} \qquad y=\frac{y'}{L} \qquad u=\frac{u'L}{\alpha} \qquad v=\frac{v'L}{\alpha}$$

$$p=\frac{p'+\rho_0 g y'}{\rho_0(\alpha/L)^2} \qquad \theta=\frac{T-T_c}{Lq/k} \qquad t=\frac{\alpha}{L^2}t' \tag{5}$$

The boundary conditions for the velocity vector components in impermeable solid surfaces were the no-slip and no-flow conditions. The vertical wall and the base are assumed to be isothermal (cold), and the other receives a constant heat flux (q).

$$\begin{aligned} &u=v=0,\ \partial\theta/\partial n=-1 \text{ for } 0\le x\le 1; && y=Hx/L\\ &u=v=0,\ \theta=0 \text{ for } x=1; && 0\le y<1\\ &u=v=0,\ \theta=0 \text{ for } 0<x<1, && y=0 \end{aligned} \tag{6}$$

As it is only possible to determinate the pressure differences, from equation (2) and (3), it will be assumed that p=0 at the point with the coordinates x=y=0.

The local Nusselt number is calculated using

$$Nu_{loc}=\frac{hL}{k}=\frac{1}{\theta} \tag{7}$$

and the average Nusselt number can be obtained by integrating the local Nusselt number along the wall

$$\overline{Nu} = \frac{1}{l}\int_0^l Nu_{loc}\,dl \qquad (8)$$

The normalized Nusselt number is defined as

$$Nu = \frac{\overline{Nu}\,|_{Gr}}{\overline{Nu}\,|_{Gr=0}} \qquad (9)$$

where $\overline{Nu}\,|_{Gr=0}$ is for pure conduction for the same conditions. We prefer to use this way in order to facilitate the heat transfer correlation determination.

The normalized Nusselt number along the wall is calculated as the ratio of local Nu and Nu on the center point of the wall, for Gr=0.

NUMERICAL PROCEDURE

In order to perform the discretization of the governing equations, the power law scheme introduced by Patankar (1980) is adopted.

All the govern equations can be written in the following form

$$\frac{\partial}{\partial t}(\rho\phi) + \frac{\partial J_x}{\partial x} + \frac{\partial J_y}{\partial y} = S \qquad (10)$$

with $J_x = \rho u\phi - \Gamma\frac{\partial\phi}{\partial x}$ and $J_y = \rho v\phi - \Gamma\frac{\partial\phi}{\partial y}$

As in all control volume methods, the discretized equations are obtained by the integration of the equation over control volumes surrounding each grid point. The result of the integration is:

$$J_x^e A_e + J_y^n A_n = J_x^w A_w + J_y^s A_s + \bar{S}\,V \qquad (11)$$

where A's are the areas of the faces of the control volume, V is its volume and $\bar{S}$ is the average value of the term S over the control volume.

Evaluating the terms of the integrated equation, using the Power Law Scheme, a set of algebraic equations is obtained with the general form

$$a_P\phi_P = a_E\phi_E + a_W\phi_W + a_N\phi_N + a_S\phi_S + b \qquad (12)$$

The solution of the momentum equations requires a procedure to calculate the pressure fields. Since there is no specific equation for the pressure, the SIMPLE algorithm developed by Patankar and Spalding (1972), with use the mass conservation equation to obtain an equation in terms of the pressure in the grid points, is considered. To solve the set of algebraic equations an interactive line-by-line process is used. This process is a convenient combination of a direct method TDMA for one dimensional situation and the Gauss Siedel method. The construction of the discretized equations was done considering a fully implicit method.

As show by Patankar (1980), to avoid non realistic solutions, independents grids for the variables u, v and p are required. The use of the staggered grids was adopted here. This process facilitate the application of the boundary conditions. Other advantage is that the u and v velocity components coincide with the faces of control volume for pressure and temperature. On the other hands, it imposes the necessity of using interpolation schemes for the u and v grids.

Its very difficulty to guarantee the convergence of a non linear system of equation. To achieve the convergence, under-relaxation factors are applied in the solution procedure to avoid large corrections in one step of iteration, with may cause the divergence of the process.

The convergence must be verified in each iteration following a predetermined criterion. In this work we selected the criterion which considers the average error for each control volume, as

$$\frac{\|r_p\|^\kappa}{n_p} \le \varepsilon \qquad (13)$$

where

$$\|r_p\|^\kappa = \left[\sum\left(a_E\phi_E + a_W\phi_W + a_N\phi_N + a_S\phi_S + b - a_P\phi_P\right)^2\right]^{1/2}$$

is the Euclidian norm of the iteration κ, and n_p is the number of grid points. The convergence parameter ε could be different for each variable depending on the order of magnitude of the variable in study. Here we set the convergence parameters as 10^{-5} to all variables.

In order to obtain grid independent results, grids with 1189, 2377 and 4753 uniform volumes were tested. The differences between the 2377 and 4753 internal volume grids were minimal.

RESULTS AND DISCUSSION

Simulations of natural convection were performed in the range of Grashof numbers $10^3 \le Gr \le 10^8$ and the values of geometrical parameters H/L: $0.20 \le H/L \le 2.0$, for Pr=0.72.

Figure 2 shows the isotherms and streamlines for the steady state considering different Grashof numbers. When $Gr \approx 10^3$, the isotherms in the central part of the enclosure take on almost a position indicating that conduction is the main process occurring. The recirculation eye stays at the center of the cavity. With the increase of the Grashof number, convection process is much more intense and the flow becomes stratified.

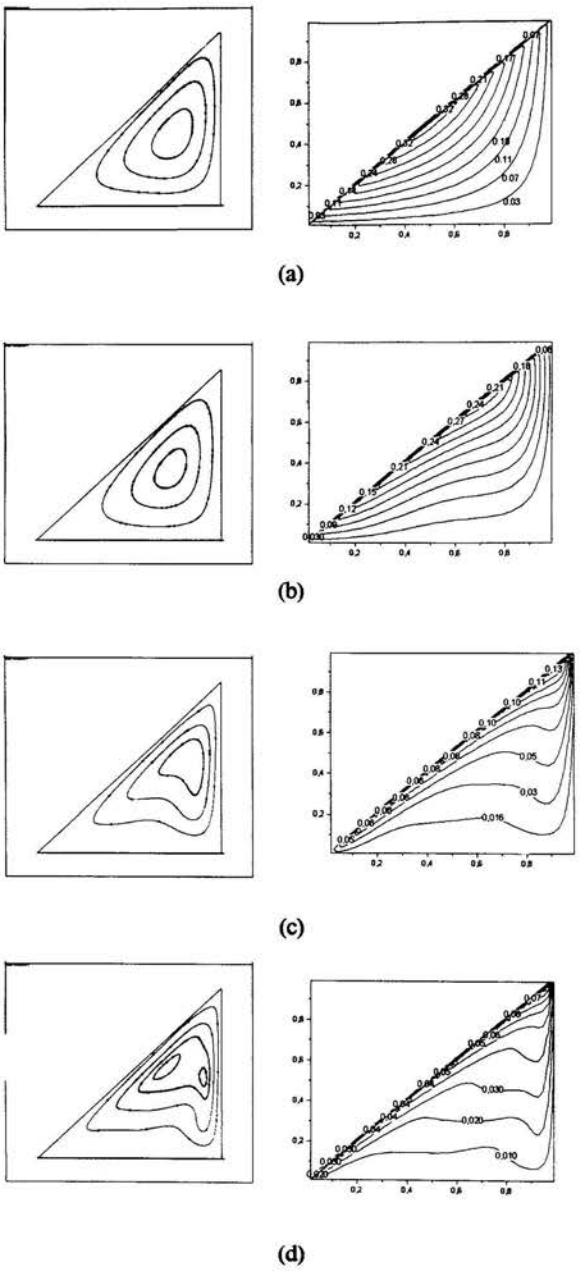

Figure 2 : Isotherm and streamlines for the steady state flow with H/L=0.5 - (a) Gr=10^3, (b) Gr= 10^5, (c) Gr= 10^7, (d) Gr= 10^8

Figure 3 shows the influence of the Grashof number over the dimensionless temperature along the wall with constant heat flux for H/L=0.5.

For Grashof number less than 10^4, we can notice that maximum of temperature is obtained approximately near the center of the hot wall of the cavity; when Grashof number increase, the maximum value of the temperature tends to move to the apex of the enclosure because the effect of the convection.

The effect of the geometrical parameters H/L variation on the main characteristics of convection of the enclosure was investigated.

Figure 4 shows the local normalized Nusselt number along the hot wall of the cavity. For Gr < 10^5 there is small variation for these values; but when Gr>10^5, Nu increase sharply for less values of the aspect ratio.

Figure 5 represents the normalized Nusselt variation as a function of the Grashof number, for different values of the geometric parameter H/L. The Nusselt number increases with increasing Grashof number for values higher than 10^5.

Figure 6 presents the dependence of the average normalized Nusselt number of the hot wall on the geometrical parameters H/L for some Grashof number. From Figure, it can be noted that for low Grashof numbers the intensity of convective process in this enclosure increases monotonically with the growth of the parameters H/L. For higher values of Grashof numbers, Nu increases with the aspects ratio up to a certain maximum value. This occurs because, for large aspect ratios, the angle of the top of the enclosure is very sharp and it causes an stagnation of the fluid reducing the convective heat transfer.

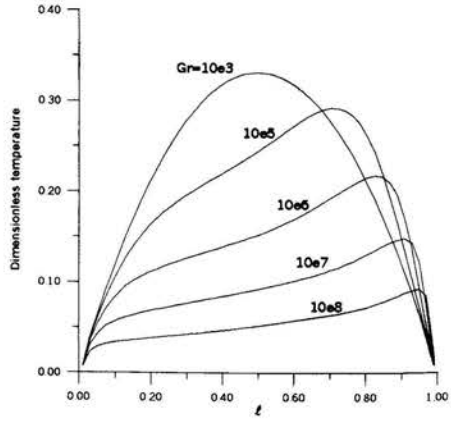

Figure 3: Influence of Gr in the dimensionless temperature along the hot wall in the enclosure with H/L=0.5

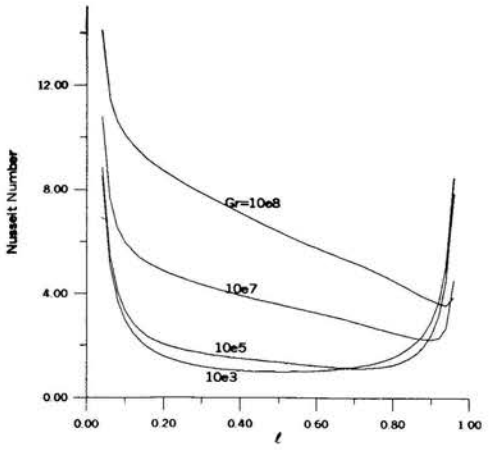

Figure 4: Average normalized Nusselt number in the hot wall of the enclosure as a functions of H/L for some values of Gr.

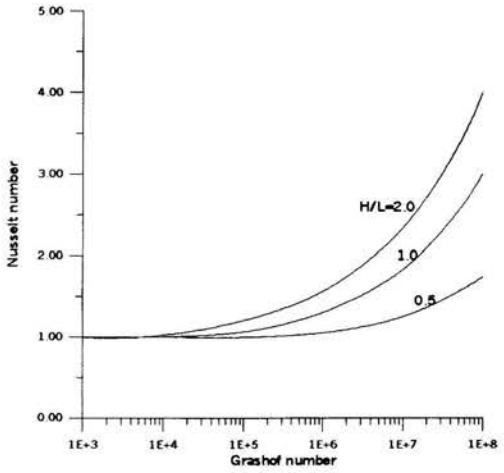

Figure 5: Average normalized Nusselt number in the hot wall as a function of the Grashof number for some values of H/L

HEAT TRANSFER CORRELATION

From the numerical analysis for natural convection in a triangular cavity with a right angle, submitted to heat flux in one wall, a formula is obtained which correlates the average normalized Nusselt number on the surface with Gr and H/L. Using non linear fittings, it was possible to get a expression for $0.3 \leq H/L \leq 2.0$:

$$Nu = 1.0323\left[1 + 0{,}008194Gr^{0{,}3169}\ln\left(0.245\sqrt{H/L}\log Gr\right)\right]$$

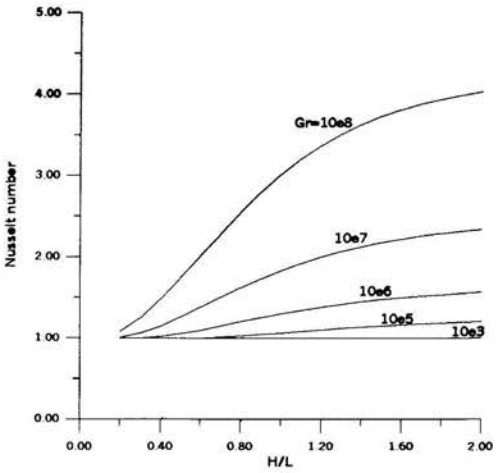

Figure 6: Average Nusselt number as a function of H/L for various values of Gr.

This expression fits the numerical results with a sum of square error equal to 0.92.

Figure 7 represents the comparison between the numerical results and the expression (14) for Nu.

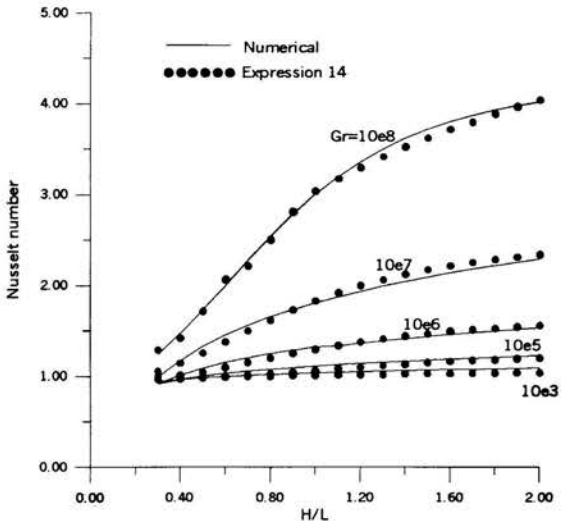

Figure7: Comparison between expression 14 and numerical results.

CONCLUSIONS

Natural convection in an triangular enclosure with a right angle, receiving a constant heat flux in the inclined wall has been studied. Two dimensional non-stationary equations of conservation mass, momentum and energy, with the Boussinesq approximation have been solved using the method of Patankar's control volume in the variables velocity-pressure-temperature.

Governing parameters used were: $10^3 \leq Gr \leq 10^8$; $0.20 \leq H/L \leq 2.0$; $Pr=0.72$.

When Grashof number is more than 10^6, the isotherms tends to horizontal position, which corresponds to the conditions of fluid stratification; and gradient regions, which resemble dynamic and thermal boundary layers, are formed on the walls.

Heat transfer showed to be noted a monotonically increasing function of the Grashof number and of the geometric parameter H/L.

A correlation for the normalized Nusselt number as a function of the Grashof number and geometric parameters is presented.

ACKNOWLEDGMENTS

The authors wish to thank the CNPq for the financial support during this study.

REFERENCES

AKINSETE, V. A.; COLEMAN, T. A. Heat transfer by steady laminar free convection within triangular enclosures. *Numerical Methods in Thermal Problems*, p. 259-268,1979

AKINSETE, V. A., COLEMAN, T. A. Heat transfer by steady laminar free convection in triangular enclosures. *Int. J. Heat Mass Transfer*, v. 25, p. 991-998, 1982.

CAMPO, E. M; SEM, M.; RAMOS, E. Analysis of natural convection in a triangular enclosure. *Numerical Heat Transfer*, v. 13, p. 353-372, 1988.

CHORIN, A. J. Numerical solution of Navier-Stokes equations. *Math. Comput.*, v.22, p. 745-762,1968.

FLACK, R.D.; KONOPNICKI, T.T.; ROOKE, J. H. The measurement of natural convective heat transfer in triangular enclosures. *J. Heat Transfer*, v. 101, p. 648-654, 1979.

GERSHUNI, G. Z.; ZHUKHOVITSKIY, E. M.; SHVARTZBLAT, D. L. Overcritical convective motions in asymmetric region. *Hydrodynamics*, n. 7, p. 89-95, Perm. 1974.

KARYAKIN, Y. E., SOKOVISHIN, Y.A. Unsteady-state natural convection in a triangular enclosure with isothermal walls. Izv. *AN SSSR, Ser. Fiz. Energ. Nauk*, v. 4, p. 104-110, 1985a.

KARYAKIN, Y. E., SOKOVISHIN, Y.A. Unsteady-state natural convection in an enclosure of triangular cross-section. Izv. *AN SSSR, Mekh. Zhidk, Gaza*, v. 5, p.169-173, 1985b.

KARYAKIN, Y. E.; MARITYNENKO, O. Z.; SOKOVISHIN, Y.A. Numerical simulation of unsteady-state natural convection in triangular enclosures. *Heat Transfer - Sov. Res.*, v. 17, n.3, p. 1-33, 1985.

KARYAKIN, Y. E.; SOKOVISHIN, Y.A. Transient natural convection in triangular enclosures. *Int. Journal Heat Transfer*, v. 31, n.9, p. 1759-1766, 1988.

KUSHAWAHA, H. S. Finite element computation of natural convection in enclosures. *Bhabha Atomic Research Centre*. BARC-1148, 1982.

PATANKAR, S. V. *Numerical heat transfer and fluid flow*. Washington: Hemisphere Pub. Corporation, 1980, 197 p.

PATANKAR, S. V.; SPALDING, D. B. A Calcultation procedure for heat, mass and momentum transfer in the three dimensional parabolic flows. *Int. J. Heat and Mass Tranfer*, v. 15, p. 1787, 1972.

POULIKAKOS, D.; BEJAN, A. Natural convection experiments in a triangular enclosure. *J. Heat Transfer* , v. 105, p. 652-655, 1983.

POULIKAKOS, D.; BEJAN, A. The fluid dynamics of an attic space. *J. Fluid Mech.* v. 131, p. 251-269, june, 1983.

HEFAT2002
1st International Conference on Heat Transfer, Fluid Mechanics, and Thermodynamics
8-10 April 2002, Kruger Park, South Africa
BA2

AN EXPERIMENTAL INVESTIGATION OF MELTING IN THE PRESENCE OF NATURAL CONVECTION

A. Bose, D.A. Scott, and B.R. Baliga
Department of Mechanical Engineering
McGill University
817 Sherbrooke Street West
Montreal, Quebec H3A 2K6, Canada

ABSTRACT

An experimental investigation of melting in the presence of natural convection is presented in this paper. The investigation was limited to a relatively simple and essentially two-dimensional melting problem. The test section consisted of a long outer tube of square cross-section with an equally long inner tube of rectangular cross-section located inside it. The space between these two tubes was filled with 95% pure lauric acid, which served as the phase-change material (PCM) in this work. This PCM has a melting temperature that lies between 43 °C - 44 °C. In each experiment, initially, the entire test-section and the PCM were heated to 42 ± 1°C, and then the outer tube temperature was maintained at this value throughout. At the start of an experimental run, the inner tube temperature was raised to a uniform value, T_w, and then maintained constant throughout the run. Four different cases were considered: T_w = 50 °C, 55 °C, 60 °C, and 65 °C. The results presented here include detailed temperature measurements, photographic records of the evolution of the solid-liquid interface, and the variation of melt fraction with time.

INTRODUCTION

Numerous engineering systems and processes involve solid-liquid phase change with heat conduction in the solid and buoyancy-driven natural convection in the liquid. Examples of this phenomenon are encountered in latent-heat thermal energy storage and control systems, equipment used in the production of silicon crystals for the electronics industry, food processing plants, and facilities that produce and process metals [Goldstein and Ramsey, 1979; Ostrach, 1983; Viskanta, 1985; Yao and Prusa, 1989; Feldman et al., 1989; Prescott and Incropera, 1996]. This phenomenon is also encountered in the formation and melting of ice in ponds and lakes [Lock, 1990; Fukusako and Yamada, 1993; Xu and Oosthuizen, 1994]. The aim in this work is *not* the study of any particular engineering system or environmental process. Rather, the goal here is to experimentally investigate a relatively simple problem, and obtain reliable data that could be used as checks in the validation and performance evaluation of numerical methods for computer simulations of melting in the presence of buoyancy-driven natural convection in the liquid phase.

In the published literature, there are many numerical and experimental investigations of solid-liquid phase change in the presence of buoyancy-driven natural convection. Extensive reviews of such investigations are available in the works of Viskanta (1985), Yao and Prusa (1989), and Prescott and Incropera (1996). Details of some of the numerical methods used in these investigations can be found, for example, in the works of Usmani et al. (1992), Oosthuizen (1993), Swaminathan and Voller (1997), Bertrand et al. (1999), Mbaye and Bilgen (2001), and Scanlon and Stickland (2001). Many of the available experimental studies were aimed at elucidating the fundamental physics of melting and freezing in the presence of natural convection. The PCMs used in these studies include naphthalene, pure metals and metallic alloys, salts, pure and saline water, paraffins, and fatty acids. The associated techniques include deployment of arrays of thermocouples embedded inside the PCM and along the boundaries, dye and particle injection, direct photographic observations, ultrasound maps of the interface, shadowgraphy, and holographic interferometry. Details of these experimental techniques can be found, for example, in the works of Goldstein and Ramsey (1979), Viskanta (1985), Yao and Prusa (1989), Spatz and Poulikakos (1991), Prescott and Incropera (1996), Wang et al. (1999), and Scanlon and Stickland (2001).

The work reported in this paper complements and extends the repertoire of the aforementioned fundamental experimental investigations. The test section consisted of a long outer tube of square cross-section with an equally long inner tube of rectangular cross-section located inside it, as shown Fig. 1. The space between these two tubes was filled with 95% pure lauric acid, which served as the phase change material (PCM). Some of the properties of this substance and the motivation for using it as the PCM are given later in the paper. In each experiment, initially, the entire test cell and the PCM were heated to a uniform temperature, T_i, just below the melting temperature,

T_m, of the PCM. Then, the outer tube temperature was maintained at $T_w = T_i$ throughout the experiment. At the start of an experimental run, the inner tube temperature was raised to T_w ($> T_m$) and then maintained constant throughout the run. As a result, the solid PCM melted, and this melting process was influenced by buoyancy-driven natural convection in the liquid phase. The results presented here include detailed temperature measurements, photographic records of the time evolution of the solid-liquid interface, and the variation of melt fraction with time.

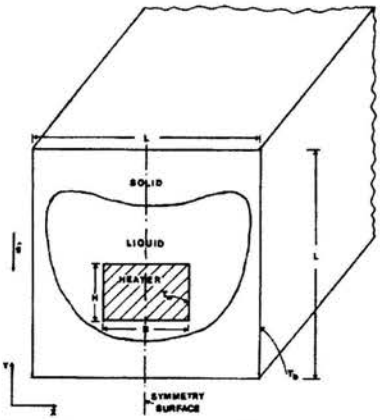

Figure 1: Schematic representation of the test section.

NOMENCLATURE

c_p	Specific heat at constant pressure [J/kg-°C]
g	Acceleration due to gravity [m/s^2]
k	Thermal conductivity [W/m-°C]
PCM	Acronym for phase change material
t	Time [s]
T	Temperature [°C]
λ	Latent heat of fusion [J/kg]
μ	Dynamic viscosity [kg/m-s]
ρ	Mass density
$\mathcal{F}$	Melt fraction [see Eq. (1)]
$\mathcal{F}_{vol}$	Volume melt fraction [see Eq. (2)]
Subscripts	
b	Pertaining to the outer tube of the test section
i	Initial condition
ℓ	Pertaining to the liquid phase
m	Pertaining to the melting temperature of the PCM
s	Pertaining to the solid phase
w	Pertaining to the inner tube of the test section

EXPERIMENTAL SETUP

Sectional views of the test cell, along with its dimensions, are given in Fig. 2.

The discussion in this and the next two paragraphs is tied to Fig. 2 and the number-keys therein. The outer tube of the test cell (9) was made of aluminum: 15.775" long, 4"x4" square outer cross-section, and a wall thickness of 3/16". The inner

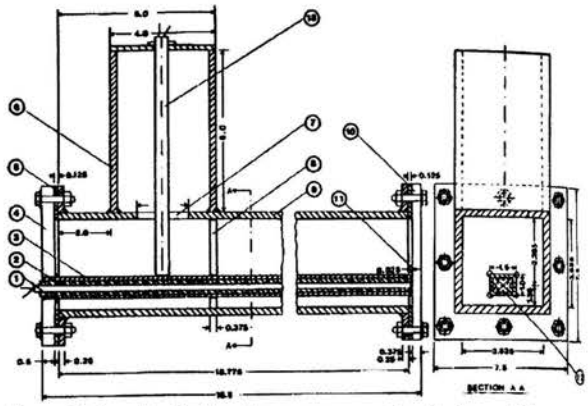

Figure 2: Longitudinal and transverse sectional views of the test cell. All dimensions are in inches (1" = 0.0254 m).

tube (3), was also made of aluminum: rectangular outer cross-section of 1.5"x1", and a wall thickness of 0.095". The vertical symmetry planes of these tubes were coincident, and their axes were parallel but offset: the axis of the inner tube was located 0.4525" below that of the outer tube. A welded aluminum plate was used to seal off the front-end of the inner tube; its back-end was left open to allow the insertion of heaters and cooling tubes. Aluminum flanges were welded to the front- and rear-ends of the outer tube. The front-end of the outer tube was closed off by a 3/8" thick Plexiglas plate (10), which was attached to the front-flange by eight 0.25" bolts and nuts, with a buna-rubber gasket (5) in between. The rear end of the outer tube was closed off by a solid aluminum plate (4), 0.5" thick, that was attached to the rear-flange by eight 0.25" bolts and nuts, with a buna-rubber gasket (5) in between. The inner tube was supported as a cantilever beam from this back-plate. A 6" long aluminum tube (6), made of the same stock as the outer tube, was welded on the top surface of the outer tube, and a 2" diameter hole (7) was used to connect these two tubes. The 6" long tube (6) served as an expansion chamber for the PCM during the melting process, and it was used as a reservoir of molten PCM to feed the test cell during the filling and freezing operations. An auxiliary electrical cartridge heater (13) was inserted into the expansion chamber. It was powered up at a relatively low level to ensure that an unbroken column of molten PCM connected the test cell and the expansion chamber during the melting experiments, and also during the filling and freezing operations. A Plexiglas separator-plate (8) was inserted in the aluminum outer tube (9) so as to isolate the auxiliary heater and the expansion chamber from the main test section. A gap of 0.025" was provided between the front-end of the inner tube (3) and the inner surface of the Plexiglas plate (10) to accommodate any possible differential expansion between the inner and outer tubes. The outer aluminum tube (9) of the test cell was wrapped with an electrical tape heater. The entire test cell, except the front Plexiglas plate (10), was the wrapped with a double layer of 0.5" thick fiberglass insulation.

Two 0.5" diameter 18" long electrical cartridge heaters (1) were connected in series and used as the main heat source for the melting experiments. The space between the cartridge heaters and the inner aluminum tube was filled by nine 2" long aluminum blocks, machined to slide smoothly in the inner tube: two 0.5" diameter holes were drilled in each of these blocks to allow the insertion and removal of the cartridge heaters; and longitudinal rectangular grooves were machined on the top, bottom, and vertical surfaces of these blocks to accommodate a total of 22 thermocouples.

The overall experimental setup is shown schematically below in Fig. 3.

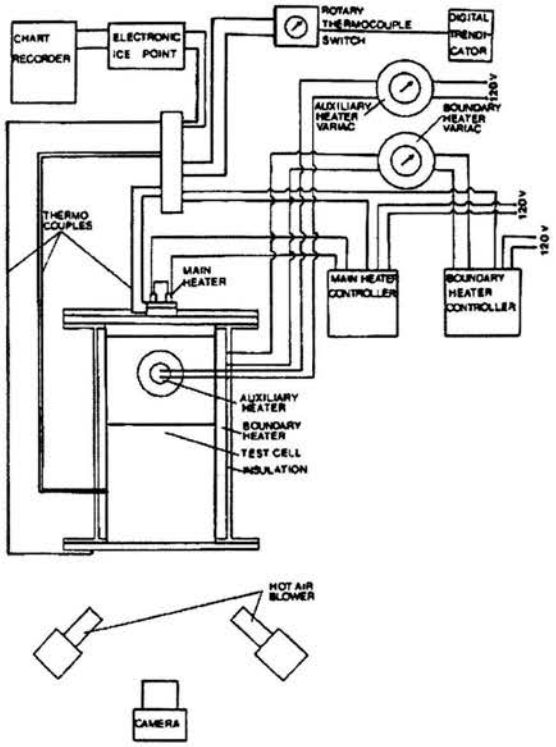

Figure 3: Schematic of the overall experimental setup.

The power supplies to the boundary and main heaters were controlled with proportional temperature controllers to provide various constant-temperature boundary conditions in the range 42 °C to 65 °C, with an accuracy of ± 1°C. Two hot air blowers were used as heat guns to maintain the front Plexiglas plate close to $(T_w + T_b)/2$, the mean of the temperatures of the inner and outer tubes. This caused the PCM adjacent to the Plexiglas to melt faster than that in the interior of the test cell. As a result, it was possible to make visual observations and photographic records of the essentially two-dimensional melting process in the interior of the test cell, as illustrated schematically in Fig.4.

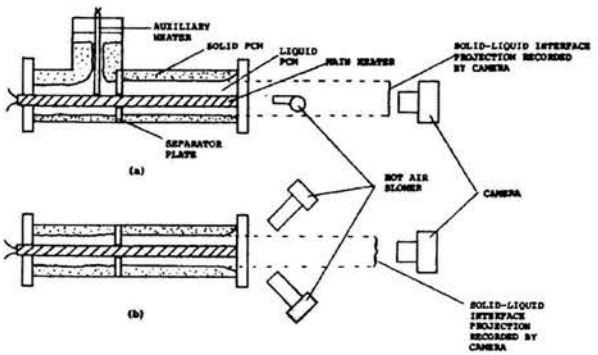

Figure 4: Longitudinal sectional drawings of the test cell and the photographic setup: (a) side view, and (b) top view.

All temperature measurements were done using calibrated 30-guage type E thermocouples and related instrumentation shown in Fig. 3, with an accuracy of better than ± 0.5 °C. An electronic digital clock, with a black liquid crystal display against a white background, was used to keep track of time during the experiments. Photographs of the solid-liquid interface were taken with a single-lens reflex camera fitted with an 80-200 mm zoom lens. Lighting was supplied by two 500 W photoflood lamps, and a fine-grain black-and-white print film (50 ASA) was used for the photographs. A single-pen plotter driven by a personal computer was adapted to serve as a digital planimeter. It was used to determine area fractions of the molten PCM (liquid) region in photographic records of the time evolution of the solid-liquid interface. Data from many initial runs showed that this overall experimental setup was able to produce results with maximum uncertainty, or scatter, of less than ± 5% of their mean values.

THE PCM AND ITS THERMOPHYSICAL PROPERTIES

Lauric acid of 95% purity was used as the PCM in this investigation. The main reasons for choosing this material were the following: it is nontoxic; it is not corrosive to aluminum, steel, buna-rubber, and Plexiglas; it is chemically and physically stable; it has a sharply defined melting temperature; the solid phase is essentially opaque and the liquid phase is highly transparent to visible light, facilitating visual observations and photographic recordings of the solid-liquid interface; its thermophysical properties are quite well documented; it is readily available; and it is not expensive.

The melting point of pure lauric acid is listed as 43.85 ± 0.15 °C [Washburn, 1930]. The 95% pure lauric acid was obtained from the Aldrich Chemical Company, which lists its melting temperature as 43 °C - 44 °C. The latent heat of fusion, λ, of lauric acid is listed as 183 ± 2 kJ/kg [Garner and Randall, 1924]. Other relevant thermophysical properties of this substance, taken from Dunstan (1915), Garner and Randall (1924), Garner and Ryder (1925), Jamieson et al. (1975), and Feldman et al. (1989) are given in Table 1.

Table 1: Thermophysical properties of lauric acid

Property and Units	Phase	Temperature [°C]	Value of the property
ρ [kg/m^3]	Solid	35.0	1009.9
		40.0	1005.5
	Liquid	50.0	869.0
		70.0	854.4
		90.0	838.6
c_p [J/kg-°C]	Solid	- 30.0 to 40.0	2155.0
	Liquid	40.0 to 100.0	2394.0
k [W/m-°C]	Liquid	50.0	0.1468
		72.5	0.1110
μ [kg/m-s]	Liquid	50.0	0.00730
		60.0	0.00561
		70.0	0.00443
		80.0	0.00362
		90.0	0.00299

The density of the liquid phase varies essentially linearly with temperature in the range 50 °C to 90 °C (thus, just three pairs of data points in this temperature range are adequate). The values of c_p presented in Table 1, for both the solid and the liquid phases, are average values in the corresponding temperature ranges. The authors were unable to find reliable information on the variation of c_p with temperature for lauric acid (solid and liquid phases). However, based on property data available for other fatty acids, it is expected that in the range of temperatures reported in Table 1, the c_p values would vary by no more than ±10% about the corresponding average values.

RESULTS AND DISCUSSIONS

Cases Studied

Four cases, denoted as Cases 1 – 4, were investigated.

Table 2: Steady-state temperatures in the cases studied

Case	T_i [°C]	T_b [°C]	T_w [°C]
1	42.0	42.0	50.0
2	42.0	42.0	55.0
3	42.0	42.0	60.0
4	42.0	42.0	65.0

Time Variation of Outer- and Inner-Tube Temperatures

The outer tube temperature was 42 °C at the start of each experiment, and it was maintained at that value throughout. However, once the power supply to the main electrical cartridge heaters was turned on, because of the finite heat capacity of the inner tube/heaters assembly, its outer surface took a finite amount of time to reach its set value.

The time variations of the inner tube temperature, T_w, for Cases 1 to 4, are presented in Fig. 5.

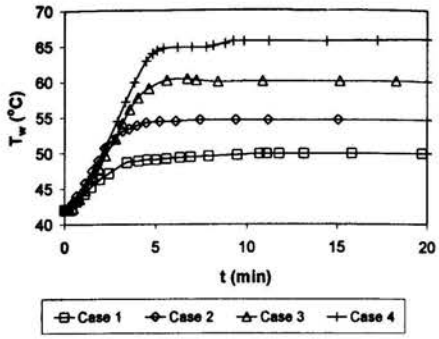

Figure 5: Time variation of the inner tube temperature, T_w.

Time Evolution of the Solid-Liquid Interface

Photographs of the solid-liquid interface at twelve different times following the start of the experiment pertaining to Case 4 are presented sequentially in Figs. 6(a) to 6(l).

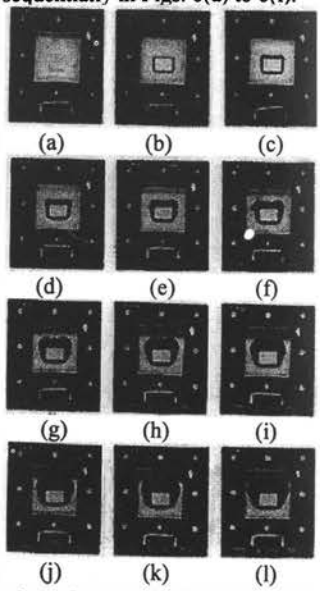

Figure 6: Interface photographs for Case 4: (a) t = 0 min.; (b) t = 5 min.; (c) t = 10 min.; (d) 15 min.; (e) t = 20 min.; (f) t = 25 min.; (g) t = 30 min.; (h) t = 35 min.; (i) t = 40 min.; (j) t = 45 min.; (k) t = 50 min.; and (l) t = 55 min.

The photograph in Fig. 6(a) corresponds to the start of the experiment (t = 0 min.): the white region is the solid lauric acid at a temperature of 42 ± 1°C; and the black border that frames the solid PCM is the buna-rubber gasket that is used as a seal between the front Plexiglas plate and the connecting-flange on the outer tube. The second photograph, Fig. 6(b), corresponds to t = 5 min.: the solid-liquid interface is essentially concentric with the inner tube, indicating that conduction has been the

dominant mode of heat transfer in the PCM until this stage of the melting process.

The first indication of the influence of buoyancy-driven natural convection on the melting process is evident in Fig. 6(c), which corresponds to t = 10 min.: the hot liquid PCM adjacent to the vertical sides of the inner tube rises up and impinges on the solid-liquid interface adjacent to its top corners, producing the highest melting rates in these regions; the thickness of the melt region adjacent to the top surface of the inner tube is larger than that adjacent to its bottom surface; and three-dimensional Bénard convection in the melt layer on the top of the inner tube causes the corresponding solid-liquid interface to display several little ripples. However, the amplitudes of these ripples in the vertical plane were small compared to the thickness of the melt layer, and, but for these ripples, the solid-liquid interface all around the inner tube was remarkably two-dimensional. Another feature worthy of note in this and in all the other photographs in Fig. 6 is the excellent symmetry of the melt pattern about the vertical, geometrical, symmetry surface of the test cell, attesting to the care taken in its design and construction, and also in its preparation for each melting experiment. The photograph in Fig. 6(d) corresponds to t = 15 min. and reveals features that are qualitatively similar to those in the previous one. At t = 20 min., as seen in Fig. 6(e), melting is still most advanced in regions adjacent to the top corners of the inner tube, reflecting the continued strong influence of natural convection flows along its hot vertical surfaces, but the top portion of the solid-liquid interface is less rippled at this stage, indicating a transition from multi-cellular Bénard convection to, perhaps, a dual-cell pattern, with one cell on each side of the vertical symmetry surface. The photographs in Figs. 6(f) to 6(h), corresponding to t = 25 min., 30 min., and 35 min., show features that are qualitatively similar to those in Fig. 6(e): the melting in all these photographs is still most advanced in regions adjacent to the top corners of the inner tube, giving rise to a cat's-ears look to the melt patterns.

The photographs in Figs. 6(i) to 6(l) correspond to t = 40 min., 45 min., 50 min., and 55 min., respectively. The melting is now fastest along the top-central portion of the interface. A possible conclusion from this observation is that for $t \geq 40$ min., the convection cells on the top of the inner tube and adjacent to its sides coalesce into two main counter-rotating cells, one on each side of the vertical symmetry surface.

Finally, one of the most interesting features revealed by the photographs in Fig. 6 is that during the natural convection-controlled phase of the melting process, the bottom part of the solid-liquid interface progresses so slowly that it appears stagnant. The thermal stratification in the melt layer below the inner tube is stable (light liquid above, heavier liquid below), so Bénard convection is not expected to occur there. Nevertheless, even with pure conduction heat transfer across the melt layer, the bottom portion of the interface should have progressed relatively slowly, but surely, downward. A possible explanation is the following: the relatively cold liquid adjacent to the solid-liquid interface flows *into* this melt region, *along the interface*, and then *returns along the lower surface of the inner tube*; consequently, the rate of heat transfer is higher from the bottom surface of the inner tube to the adjacent liquid PCM, but it is lower to the bottom portion of the solid-liquid interface, than that which would occur with only pure heat conduction across the lower melt layer. Preliminary computer simulations have confirmed this explanation.

Photographic records of the time evolution of the solid-liquid interface were also obtained for Cases 1, 2, and 3. Qualitatively, Cases 1 – 4 yielded similar results. The information contained in these photographic records was consolidated into interface evolution plots. These plots for Cases 1 to 4 are presented in Figs. 7(a) to 7(d), respectively.

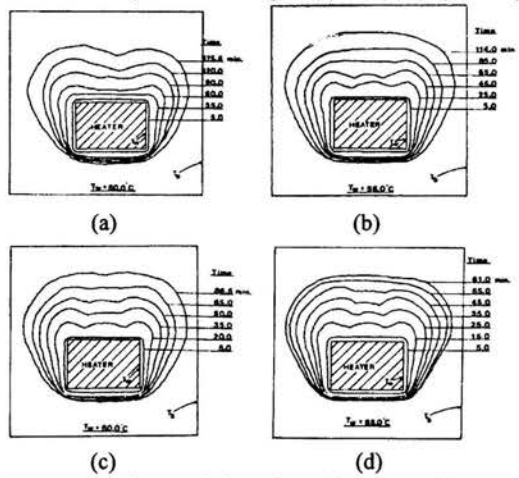

Figure 7: Interface evolution plots: (a) Case 1; (b) Case 2; (c) Case 3; and (d) Case 4.

Time Variation of Melt Fraction

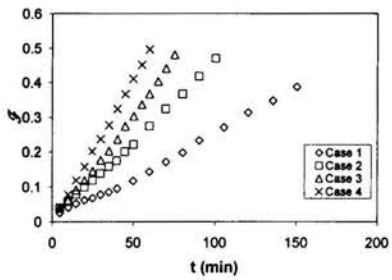

Figure 8: Variation of mass melt fraction, $\mathcal{F}$, with time.

Photographs of the solid-liquid interface, such as those shown in Fig. 6, contain information about the variation of the melt fraction with time. Assuming that the solid-liquid interface is essentially two-dimensional inside the test cell, the melt fraction is given by the following equation:

$$\mathcal{F} = \text{Area}_{\ell} / \text{Area}_{s,\, t=0} \qquad (1)$$

where $Area_\ell$ is the area of molten PCM (liquid phase), and $Area_{s,\,t=0}$ is the initial area of the solid PCM.

The variation of $\mathcal{F}$ with time, for Cases 1 to 4, is presented in Fig. 8. Consider the curve for Case 1 (T_w = 50 °C). The melt fraction increases continuously with time, as expected. However, the rate of melting ($d\mathcal{F}/dt$) starts off at a high value, then decreases for the first 20 – 25 min., then increases again until about t = 40 min., and finally remains essentially constant during 40 min. < t < 150 min. This behavior reflects the transition from conduction-controlled melting to natural convection-controlled melting, as discussed in the previous subsection. The curves for Cases 2 – 4 also exhibit this behavior, but not as clearly as the curve for Case 1: with the higher values of T_w, natural convection manifests itself earlier, when the melting rate is relatively high; thus, the transition from conduction- to natural convection-controlled melting is not as evident as that in Case 1. As is to be expected, the curves in Fig. 8 show that as T_w increases from 50 °C to 65 °C, from Cases 1 – 4, the melting rates also increase.

The density of the liquid phase of the PCM is less than that of its solid phase. Thus, during the melting process, the excess volume of the liquid that did not fit in the test cell flowed into the expansion chamber. The *volume* melt fraction can be obtained from the *mass* melt fraction, $\mathcal{F}$, as follows:

$$\mathcal{F}_{vol} = \mathcal{V}_\ell \,/\, \mathcal{V}_{s,\,t=0} = \mathcal{F}\,(\rho_s / \rho_\ell) \qquad (2)$$

where $\mathcal{V}_\ell$ is the volume of the molten (liquid) PCM, and $\mathcal{V}_{s,\,t=0}$ is the volume of the solid PCM at the start of the experiment.

ACKNOWLEDGMENTS

The authors gratefully acknowledge financial support of this work by the Natural Sciences and Engineering Research Council (NSERC) of Canada. Dr. S. K. Bhat provided help in the preparation of some of the figures in this paper.

REFERENCES

Bertrand, O., Binet, B., Combeau, H., Couturier, S., Delannoy, Y., Gobin, D., Lacroix, M., Le Quere, P., Medale, M., Mencinger, J., Sadat, H., and Vieira, G. (1999), "Melting driven by natural Convection", *Int. J. Thermal Science*, Vol.38, pp. 5-26.

Dunstan, A.E. (1915), "The relation between viscosity and chemical constitution, Part IX: The viscosity and fluidity of aliphatic acids", *J. Chem. Soc.*, Lond., Vol. 107, pp. 667-672.

Feldman, D., Shapiro, M.M., Banu, D., and Fuks, C.J. (1989), "Fatty acids and their mixtures as phase-change material for thermal energy storage", *Solar Energy Materials*, Vol. 18, pp. 201-216.

Fukusako, S. and Yamada, M. (1993), "Recent advances in research on water-freezing and ice-melting problems", *Expt. Thermal and Fluid Science*, Vol. 6, pp. 90-105.

Garner, W.E. and Randall, F.C. (1924), "Alteration in the heats of crystallization of the normal monobasic fatty acids: Part I, *J. Chem. Soc.*, Lond., Vol. 125, pp. 881-896.

Garner, W.E. and Ryder, E.A. (1925), "The alteration in molecular volume of the normal monobasic fatty acids, *J. Chem. Soc.*, Lond., Vol. 127, pp. 720-730.

Goldstein, R.J. and Ramsey, J.W. (1979), "Heat transfer to a melting solid with application to thermal energy storage systems", in *Studies in Heat Transfer, A Festschrift for E.R.G. Eckert*, J.P. Hartnett et al., Eds., pp. 199-208, McGraw-Hill, Washington D.C.

Jamieson, D.T., Irving, J.B., and Tudhope, J.S. (1975), "Liquid thermal conductivities: A data survey to 1973", *Natl. Eng. Lab. Report*, Her Majesty's Stationery Office, Edinburgh.

Lock, G.S.H. (1990), *The Growth and Decay of Ice*, Cambridge University Press, Cambridge, U.K.

Mbaye, M. and Bilgen, E. (2001), "Phase change process by natural convection-diffusion in rectangular enclosures", *Heat and Mass Transfer*, Vol. 37, pp. 35-42.

Oosthuizen, P.H. (1993), "A numerical study of the steady state freezing of water in a rectangular enclosure", in *Numerical Methods in Thermal Problems*, R.W. Lewis Ed., Pineridge Press, Vol. VIII, Part I, pp. 92-103.

Ostrach, S. (1983), "Fluid mechanics in crystal growth", *ASME J. Fluids Engineering*, Vol. 105, pp. 5-20.

Prescott, P.J. and Incropera, F.P. (1996), "Convection heat and mass transfer in alloy solidification", in *Advances in Heat Transfer*, Academic Press, Vol. 28, pp. 231-338.

Scanlon, T.J. and Stickland, M.T. (2001), "An Experimental and Numerical Investigation of Natural Convection Melting", *Int. Comm. Heat Mass Trans.*, Vol. 28, pp. 181-190.

Spatz, T.L. and Poulikakos, D. (1991), Holographic interferometry experiments on the growth of ice from a horizontal pipe", *Int. J. Heat Mass Trans.*, Vol. 34, pp. 1847-1859.

Swaminathan, C.R. and Voller, V.R. (1997), "Towards a general numerical method for analysis of solidification systems", *Int. J. Heat Mass Trans.*, Vol. 40, 2859-2868.

Usmani, A.S., Lewis, R.W., and Seetharamu, K.N. (1992), "Finite element modelling of natural-convection-controlled change of phase", *Int. J. for Num. Meth. Fluids*, Vol. 14, pp. 1019-1036.

Viskanta, R. (1985), "Natural convection in melting and solidification", in *Natural Convection: Fundamentals and Applications*, S. Kakac et al., Eds., Hemisphere, Washington D.C., pp. 845-877.

Wang, Y., Amiri, A., and Vafai, K. (1999), "An experimental investigation of the melting process in a rectangular enclosure", *Int. J. Heat Mass Trans.*, Vol. 42, 3659-3672.

Yao, L.S. and Prusa, J. (1989), "Melting and freezing", in *Advances in Heat Transfer*, Academic Press, Vol. 19, pp. 1-95.

Xu, Z. and Oosthuizen, P.H. (1994), "An experimental study of ice formation around a horizontal cylinder in a square enclosure", Proc. 10th Int. Heat Transfer Conference, Vol. 4, pp. 175-180.

HEFAT2002
1st International Conference on Heat Transfer, Fluid Mechanic, and Thermodynamics
8-10 April 2002, Kruger Park, South Africa
BT2

EXPERIMENTAL AND NUMERICAL INVESTIGATION OF FREE CONVECTION IN OPEN ENDED HORIZONTAL RECTANGULAR CHANNEL HEATED FROM THE TOP

T. Bunnag*, R. Sarachitti**, J. Khedari**, J. Hirunlabh** and L.Elegant***
Building Scientific Research Center
* Dhurikijpundit University
110/1-4 Prachachune Laksi Bangkok 10210
Tel: (662) 9547300-29 Ext. 586, Fax: (662) 9547356
E-mail: Tbunnag@hotmail.com
** King Mongkut's University of Technology Thonburi
Bangmod, Thungkru, Bangkok 10140, THAILAND
Tel: (662) 4708695-9 Ext. 125, Fax: (662) 4708623
*** Laboratoire de Thermodynamique Expérimentale, U. de Nice Sophia-Antipolis,
06100 Parc Valrose, FRANCE

ABSTRACT

This paper reports on experimental and numerical investigation of free convection in open-ended horizontal rectangular channel heated from the top with a uniform heat flux. Apart from convection coefficient the objective is to understand the flow patterns with respect to designing passive solar buildings. The experimental setup was made by using two parallel horizontal plates of 1 m wide, and 1.5 m long. The distance between the upper and lower plates could be adjusted up to 19 cm. Data analysis was made under steady stage conditions to develop Nusselt number correlationship. Both experimental results and numerical simulation indicated that air circulation occurs in a "C" loop mode and flow field depended strongly on the intensity of heat flux supplied to the lop plate.

INTRODUCTION

The study of natural air flow inside a horizontal rectangular channel with open ends and upper heated plate is beneficial for the designing performance of natural air ventilation in buildings. In fact such configuration could be an integral part of ceiling design. Our team, the Building Scientific Research Center (BSRC) is interested in using free convection to reduce heat accumulation and energy consumption in buildings [1-7]. First, a simple roof design was developed for decreasing heat accumulation inside European style houses by using double layer technique called the Roof Solar Collector, (RSC) [1]. Subsequently we have continuously conducted investigation on the Roof Solar Collector [2-4,8], Trombe wall [5], Modified Trombe wall [6].

In this paper our interest is to study the free convection in a flat roof or ceiling enclosure composed of two plates; the top one being heated while the lower is unheated. A recent study [8] conducted for such configuration showed that the fluid flows inside the system could show very complex patterns due to an interaction between heated plate and the other surfaces. Experimental investigation on uniform heated upward facing horizontal covered by a parallel insulated surface was reported in [9]

NOMENCLATURE

A_p = Surface area of heated plate, m^2

g = acceleration of gravity, m/s^2

Gr = Grashof Number ($g\beta Q_s S^4/\nu^2 k$)

h_c = Convective heat transfer coefficient, $W/m^2\,°C$

k = Thermal conductivity of air, W/mK

L = Length of plate, m

p, p_o = pressure and atmospheric pressure, N/m^2

Q_s = Constant heat flux supply, W

Ra = Rayleigh Number ($Gr.P_r$)

S = High of air gap, m

S/L = Aspect ratio of the channel

T = Absolute temperature, K

T_{bm} = Mean bulk temperature, °C

$\overline{T}_i$ = air inlet temperature of the channel, °C

T_o = ambient air temperature of the channel, °C

T_s = heated plate temperature, °C

u = horizontal velocity component, m/s

v = vertical velocity component, m/s

Greek symbols

β = Volumatric coefficient of thermal expansion of air ($=1/T_o$), 1/K

μ = Dynamic Viscosity of air, kg/m.s

ρ = Air density, kg/m^3

ν = Kinematic viscosity of air, m^2/s

α = Thermal diffusivity of air, m^2/s

EXPERIMENTAL EQUIPMENT AND DATA CORRELATION

A schematic view of the experimental set-up is shown in figure 1. Its dimensions are as follows: 1 m wide, 1.5 m long with an adjustable air gap up to 0.19 m. The heated plate was made by using a CPAC board 12 mm thick while the unheated plate was made by gypsum board 10 mm thick. Both sides of the experimental set-up were protected by using glass wool insulator installed inside a plywood cover box (see figure 1 A).

Extensive description of the experimental set up was reported in [10]. Thermocouples were installed at 5 sections (Fig.1 B) at different distances from the left channel side opening: 10, 43.5, 75, 107.5 and 140 cm. The heat flux and the electrical power on the upper plate were measured by using heat flux, Voltage and Amp sensors respectively. The sensors accuracy was ±0.1% approximately.

The air velocity was measured at 4 centered points located at 15, 55, 95 and 135 cm from the left side channel opening. The hot wire anemometer velocity range was: 0-2 m/s. The resolution of velocity reading was 0.01 m/s with an accuracy of 0-1 V output at ± 1%.

The heat transfer coefficient inside the channel (h_c) could be found from:

$$h_c = Q_s / (A_p(T_s - T_{bm})) \quad (1)$$

The mean bulk temperature could be found as follows:

$$T_{bm} = \left(\frac{\overline{T}_i + \overline{T}_{out}}{2}\right) = \frac{1}{L}\int_0^L T_{bm}(X)dX \quad (2)$$

The integral of eq. (2) could be determined using appropriate numerical integration method, for more details, see ref [11]. On the other hand, convective heat transfer coefficient (h_c) could be calculated using Nusselt number as follows:

$$Nu = (h_c S)/k \quad (3)$$

In this study, data analysis was made to develop a correlation between Nu and Rayleigh number Ra using the following form:

$$Nu = CRa^n \quad (4)$$

The values of C and n could be determined using experimental plots between log Nu and log Ra for the different power supply and air gap space conditions considered with an appropriate regression method.

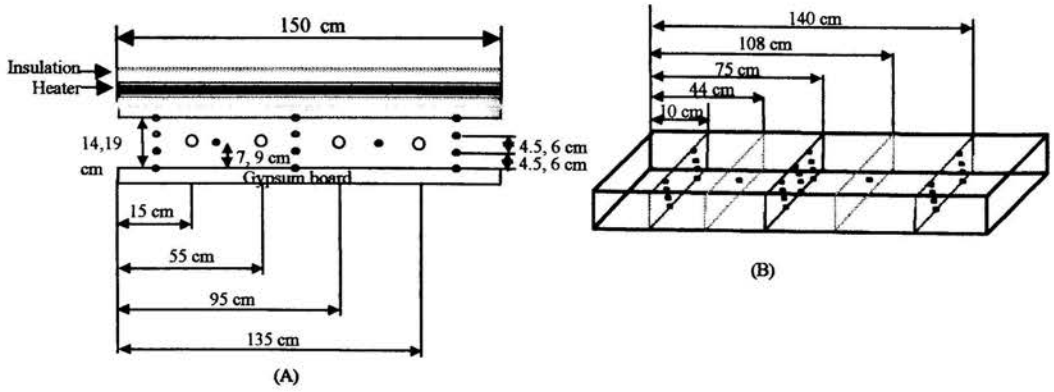

Figure 1. schematic view of the experimental set-up and thermocouple setting

SIMULATION OF NATURAL AIR FLOW

A computer code was developed to simulate the natural flow in the channel. The flow was assumed to be two-dimensional, steady and laminar. The temperature gradient in the flow field gaves rise to density gradient, which acted as a driving force for natural convection. Boussinesq's approximation was used to simplify the buoyancy term. The system was governed by the following set of conservation equations of mass, momentum, and thermal energy:

$$\frac{\partial u}{\partial x}+\frac{\partial v}{\partial y}=0 \tag{5}$$

$$u\frac{\partial u}{\partial x}+v\frac{\partial u}{\partial y}=-\frac{1}{\rho}\frac{\partial(p-p_o)}{\partial x}+\nu\nabla^2 u \tag{6}$$

$$u\frac{\partial v}{\partial x}+v\frac{\partial v}{\partial y}=-\frac{1}{\rho}\frac{\partial(p-p_o)}{\partial y}+\nu\nabla^2 v+g\beta(T-T_o) \tag{7}$$

$$u\frac{\partial T}{\partial x}+v\frac{\partial T}{\partial y}=\alpha\nabla^2 T \tag{8}$$

From the experimental study, with a uniform constant heat flux, it was found that apart from the openings the gradual increase of temperature of the top and bottom plates were not so important. Therefore, in the model, we assume uniform temperature at both plates for simplicity and zero velocity components. At the openings, zero gradients of flow variables except temperature are used. For the temperatures of fluid coming from ambient region into the channel, they are set equal to ambient while the temperatures of fluid going out they have satisfy the upwind condition. By assuming convection to be predominant, then, the zero gradients are used [12]. These are done by checking the sign of velocity component in the x direction. If u is positive at the left opening, at that point, fluid is coming inside. On the other hand, if u is negative, the fluid is going outside. A similar manner is used for the right opening.

The computational domain was divided into non-overlapping rectangular control volumes as suggested by Patankar [13] to avoid wavy pressure and velocity fields. All scalar quantities namely pressure, temperature, density, etc. were located at the center of the control volumes, while the velocity components were located at the volume faces. The solution technique for solving the governing equations was based upon the Marker and Cell (MAC) algorithm [14,15] with an upwind differencing scheme for convection terms.

RESULT AND DISCUSSION

In this paper three power supply (500, 700 and 900 W) and two channel aspect ratio (0.093 and 0.127) were considered. The corresponding heat flux supplied to the channel was 262, 408 and 574 W/m^2. We only varied the air gap (14 and 19 cm) while the channel length remained constant. The data analysis was performed when study state conditions were reached. Actually, the system took 3.5-4.5 hours to reach it.

Temperature distribution

Average temperature distributions inside the channel are shown in figure 2 at three positions near the channel openings and at the channel center. Although some disparities exist between the right and the left sides of the channel, Fig. 2 indicates that experimental temperature profiles are quite symmetric around the vertical centeral axis of the channel. It could also be observed that the variation of the temperature difference between heated and unheated plates for all power supply varied similarly. Obviously, the maximum difference occurred at the channel ends whereas the minimum at the center of channel. The temperature of the unheated plate increased slightly from the ends to the middle. The heated plate temperature was practically uniform when heat flux increased.

Even though plate temperatures are considered uniform, the simulation results (Fig. 3) indicate that the temperature distribution was in the same trend as the experimental study. The temperature of air inside the channel of all cases was highest at the middle of the channel. In addition heat loss and effect of the uncontrolled ambient air are also important affecting parameters.

When air gap increased (Fig. 2 right side), the temperature of the heated plate and the air channel decreased significantly due to the increase of the volume of air and associated air circulation inside the channel. Simulated temperature profiles clearly indicate that the air circulation occurred at both ends, the air flows parallel to the unheated heated a distance that depends on the buoyancy force. Next it moves outward and turns towards the exists. For low heat flux (i.e. low upper Plate temperature), a special zone is observed near the top corner. That merits further investigation.

Air Velocity profiles

First, we should remind that air velocity in the experimental study was measured at only four points which is certainly not enough to make exact analysis. But when considering the experimental study with the numerical simulation, subjective conclusions could be presented. When small heat flux is supplied to the channel, figs 4 and 5 show that the air velocity is too low inside the channel while near the ends higher air velocity is observed. When heat flux is increased the air velocity of the "C" loop was more stronger and air flows deeper to the middle of the channel. The vector velocity profiles indicate that the air circulation is in a "C" loop mode as shown in figure 5. When low heat flux is supplied i.e, lower temperature of the top plate and 14 cm air gap, the vector velocity profile (fig.5) is low and air is quite "still". Significant velocity flows are observed at both ends of the channel near the center.

With the highest heat flux supply and 14 cm air gap, the "C" loop air circulation inside the channel became important at the center of the channel. Such observations are very close to those reported in [8] for a short channel giving us good satisfaction. The increase of air gap space affected air velocity inside the

channel. Also the higher was the air gap, the smaller the air velocity.

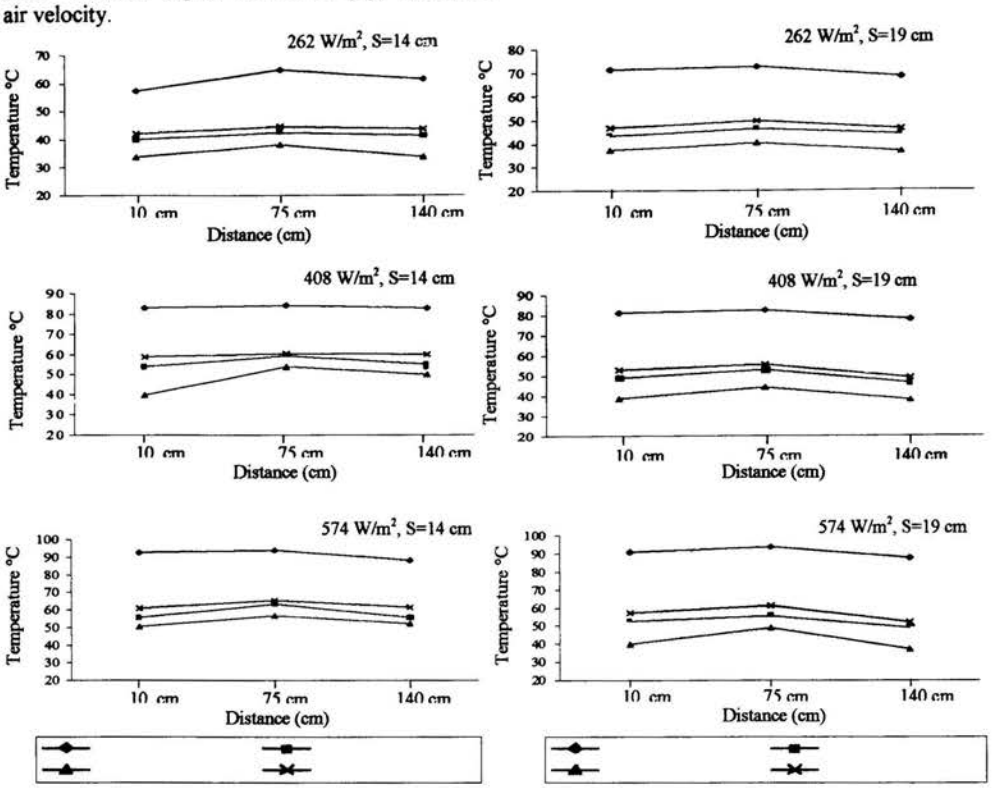

Figure 2. Temperature profiles along the channel at difference positions for difference power supply at 14 cm (left side) and 19 cm (right side)

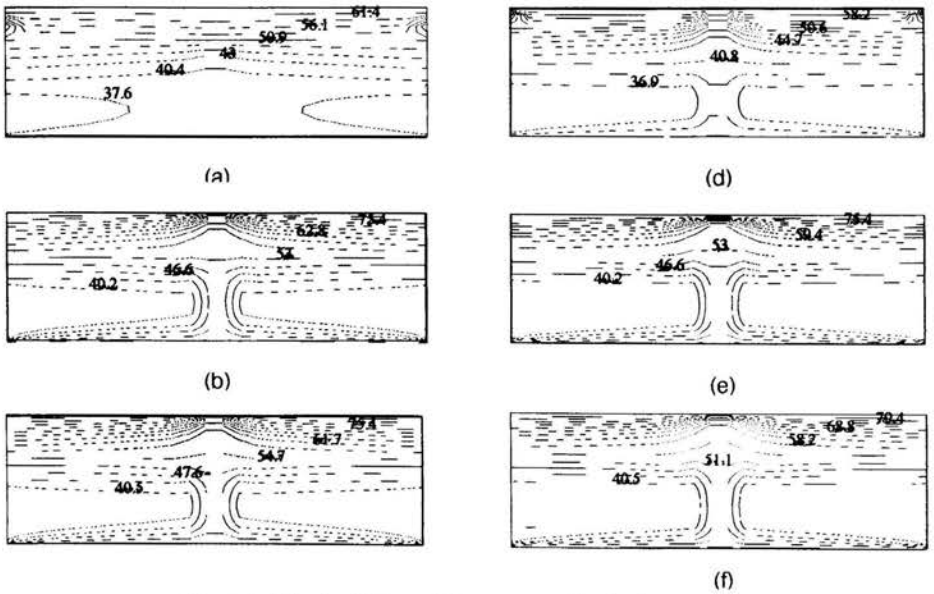

Figure 3. The simulations of temperature distribution.
(a-c) gap = 14 cm, T_{upper} = 64, 85 and 90°C, T_{lower} = 40, 54 and 55°C
(d-f) gap = 19 cm, T_{upper} = 64, 85 and 90°C, T_{lower} = 40, 54 and 55°C

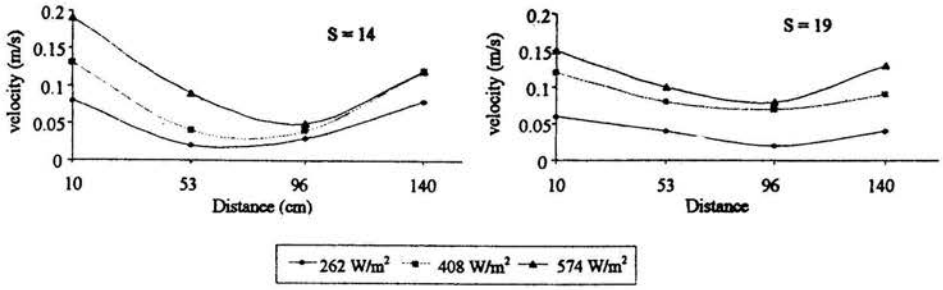

Figure 4. Shows Air velocity inside channel of all experimental study at 14 cm (Left side) and 19 cm (Right side).

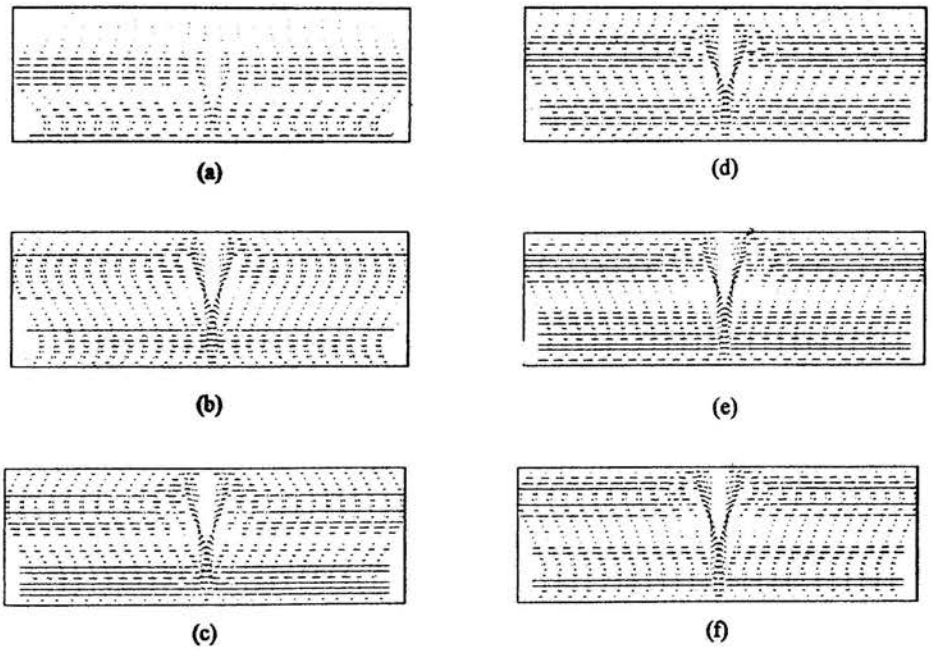

Figure 5. Velocity vector field of natural flow in a horizontal channel.
(a-c) gap = 14 cm, T_{upper} = 64, 85 and 90°C, T_{lower} = 40, 54 and 55°C
(d-f) gap = 19 cm, T_{upper} = 64, 85 and 90°C, T_{lower} = 40, 54 and 55°C

CONCLUSION

Experimental and numerical simulation on free convection in open ended horizontal rectangular channel heated from the top with uniform heat flux indicated that air circulation occurred in a "C" loop mode. It depended closely on both air gap and heat flux supplied. The higher is the air gap the smaller the velocity. Increasing the heat flux supply accelerated the "C" loop air circulation inside the channel with a deep flow penetration.

ACKNOWLEDGEMENTS

The authors would like to thank the National Energy Policy Office (NEPO) of Thailand and the Thailand Research Fund (TRF) for providing financial support to this research work.

REFERENCES

1. Khedari J., Hirunlabh J., Bunnag T., 1997, "Experimental study of Roof Solar Collector towards the Natural Ventilation of New Houses", Energy & Buildings 26, PP 159-164.

2. Khedari J., et al , 2000, "Field measurement of Performance of Roof Solar Collector", Energy & Buildings, 31, PP.171-178.
3. Hirunlabh J. et al., 2000, "New Configuration of Roof Solar collector for maximizing Natural Ventilation", Building & Environment , Vol 4., PP.1-9.
4. Hirunlabh J.,et al, 1997, "An improved design of passive roof solar collector", Proceeding of the First Arab Mechanics Congress CAM 97, Vol 1, June 1-3, Damascus (Syria), PP. 469-474 .
5. Khedari J., et al., 1997, "Natural Ventilation of Houses by Trombe Wall under the climatic conditions in Thailand ", The Int. J. of Ambient Energy , Volume 20, No.2, PP.85-94.
6. Khedari J, et al., 1997, "The Modified Trombe Wall: A simple ventilation meams and an efficient insulating material", International Journal of Ambient Energy Vol. 19, No 2, PP 104-110.
7. Boonsri. B., Khedari J., Hirunlabh J., 2000, " Ventilation impact of a solar chimney on indoor temperature fluctuation and air change in a school building", Energy & Buildings, 32, PP 89-93.
8. Manca O. et al., 2000, " Experimental Analysis of Thermal Instability in Natural Convection Between Horizontal Parallel Plates Uniformly Heated", Journal of Heat Transfer, 22, PP 50-57.
9. Sparrow, E. M., and Carlson,C. K., 1986, " Local and Average Natural convection Nusselt Numbers for Uniformly Heated, Shrouded or Unshrouded Horizontal Plate", Int. J. Heat Mass Transfer, 28, PP 369-379.
10. Bunnag T., et al., 2001, "Experimental Investigation of Free Convection in Open Ended Horizontal Rectangular Channel Heated from the Top", Proceeding of the ASEAN Science & Technology Week Conference, International Conference Center, Brunei. (in press)
11. Bunnag T., 2001, "A study of free convection in inclined open ended rectangular channel heated from the top", Ph.D. Thesis, King Mongkut's University of Technology Thonburi.
12. Chan, Y.L. and C.L. Tien, 1985, "A Numerical Study of Two-Dimensional Laminar Natural Convection in Shallow Open Cavities", Int, J. Heat Mass Transfer, Vol. 28, No. 3, pp. 603-612.
13. Patankar, S.V., 1980, Numerical Heat Transfer and Fluid Flow, Hemisphere Publishing Corporation.
14. Harlow, F.H. and J.E. Welch, 1965, "Numerical Calculation of Time-Dependent Viscous Incompressible Flow of Fluid with Free Surface", Phys. Fluids, Vol. 8, pp. 2182-2189.
15. Nakamura, S., 1977, Computational Methods in Engineering and Science with Applications to Fluid Dynamics and Nuclear System, John Wiley & Sons.

HEFAT 2002
1st International Conference on Heat Transfer,
Fluid Mechanics, and Thermodynamics
8-10 April 2002, Kruger Park, South Africa
EA1

FREE CONVECTION FROM A HORIZONTAL CYLINDER IN A NON-LABORATORY ENVIRONMENT

A. F. Emery and L. van Belle
Dept. Mechanical Engineering
University of Washington, Seattle, WA 98195
emery@u.washington.edu

Keywords: Free Convection, Empirical Correlations, Parameter Estimation

ABSTRACT

Free convection from a horizontal cylinder was measured for both steady and transient heating under non-laboratory conditions. The measured temperatures were used to infer the constants C and n in the correlation $Nu = CRa^n$ and the surface emissivity. An analysis of the experiment revealed that the exponent could be estimated with precision, but not if the emissivity were also to be estimated. Transient measurements showed that the temperature history during cooling, but not during heating, could be reasonably well predicted using steady state empirical correlations. The results reaffirm the observation that published empirical correlations should be used only as a guide and that care must be taken in determining the consequences of inexactness in any system parameters used in the design of a thermal system.

Introduction

Almost every thermal design involves the estimation of convective heat tranfer. The designer typically does this by using correlations of the form $Nu = C\ Re^n Pr^m$ which are available in textbooks and standard references [1,2]. These correlations are usually based upon data reported by several investigators who have conducted laboratory experiments. Because of the scatter of the data, such correlations are often stated as having an accuracy of $\pm$P% where P is often in the order of 20. In designing for a general or industrial application, such correlations should be regarded only as a guide since the conditions in practice rarely match those that existed in the experiments. In addition, these correlations are almost always restricted to steady state.

We are interested in examining a realistic problem and determining how satisfactory such correlations are in estimating transient and steady state temperatures. We have chosen the problem of the transient heating and cooling of a horizontal cylinder under free convection heat transfer. The temperature history will be a function of the convective and radiative heat transfer. Using the standard correlation, $Nu = C\ Ra^n$, the temperature history will be a function of C, n, and the emissivity ϵ. The experimental protocol will be designed to estimate these three parameters. If only steady state measurements are made a substantial number of tests will be needed to give an accurate estimate. On the other hand, if the transient convective flow approximates that of steady state, then we should be able to obtain reasonably accurate values.

The Experiment

The experiment consisted of measuring the temperature history of a hollow copper cylinder, 33.5 mm OD, 9.33 mm ID and 33.6 cm long. Twelve thermocouples were staked slightly below the surface and an electrical heater inserted into the center. The cylinder was suspended in room air and surrounded by a wire mesh, located 30 cm horizontally away from the cylinder, to dampen any air flow perturbations. Local air temperature was measured 6 cm horizontally from the cylinder axis. The cylinder surface was covered with a very thin dense layer of dense soot so that it radiated as a black surface. The entire apparatus was in a screen enclosed area of a large laboratory whose windows were closed and whose ventilation was turned off. While the ambient air

was not quiescent, the environment reflected what is likely to be found in practice. The heater power and temperatures were measured with a data acquisition system at 30 second intervals. A statistical analysis of the measurements gave the uncertainties and autocorrelation coefficients shown in Table 1.

Table 1

Measurement	σ	ρ
Heater Power	0.05W	0
Cylinder Temperatures	0.02C	0.1
Ambient Air Temperatures	0.05C	0.2

Both the heater power and the cylinder temperatures were found to be uncorrelated, in both cross and auto correlation. As expected, the room air was slightly autocorrelated, but the amount (as indicated by the auto correlation coefficient at a lag of 1) was not so great that it seriously affected the statistical analysis of the experiment.

The test protocol consisted of three transient histories:
Step Heating

Power in the amount P_1 was applied and the cylinder allowed to heat until the equilibrium temperature, T_1 was reached. After equilibrium, the power was increased to P_2. A typical heating profile is shown on Figure 1.

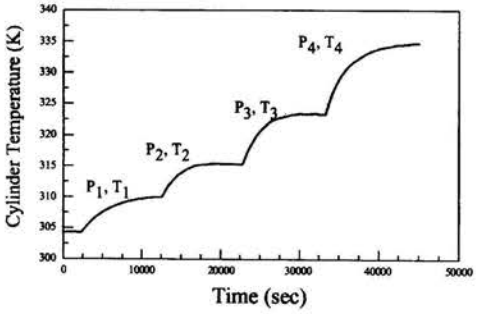

Figure 1: Typical Transient Heating History

Power off Cooling

After the cylinder had reached its maximum temperature, T_n, the power was turned off and the cylinder allowed to cool to T_{n-1}, at which point the power in the amount of P_{n-1} was applied and the cylinder allowed to come to steady state. This process was continued until the cylinder cooled to ambient temperature. This procedure produced a fast cooling history.

Power On Cooling

After the cylinder had reached its maximum temperature, T_n, the power was reduced to P_{n-1} and the cylinder allowed to stabilize at a equilibrium temperature of T_{n-1}. This process was continued until the cylinder cooled to ambient temperature. This procedure produced a relatively slow cooling history.

Sensitivity and Variance Estimation

The purpose of the experiment is not only to estimate the parameters, but also to quantify the precision of the estimates by estimating the standard deviation of the parameters. To achieve reasonable precision requires that the experimental protocol be defined to achieve minimum standard deviations.

Let the measured temperature, T_i at time t_i be represented by

$$T_i = F(t_i, C, n, \epsilon) + s \tag{1}$$

where $F(t, C, n, \epsilon)$ is the model of the system and s represents noise whose covariance matrix is denoted by $\Sigma[s]$. The expected parameter values, $\overline{C}, \overline{n}, \overline{\epsilon}$ are those values that minimize the least squares objective function L

$$L = \sum_{i=1}^{N} \left(T_i - F(t_i, C, n, \epsilon)\right)^2 \tag{2}$$

While the variances (standard deviations squared) of the parameters are proportional to the curvature of the objective surface $L(C, n, \epsilon)$, for any statistical distribution of noise [3], the need for experimental data to determine L and the difficulty in determining the curvature makes this approach to optimizing the experiment design unworkable.

Instead let us follow the following procedure. Expand the model temperature $F(t_i, C, n, \epsilon)$ in a Taylor series about the expected values of the parameters,

$$T_i = F(t_i, \overline{C}, \overline{n}, \overline{\epsilon}) + \frac{\partial F}{\partial C}|_{\overline{C}}(C - \overline{C}) + \frac{\partial F}{\partial n}|_{\overline{n}}(n - \overline{n}) + \frac{\partial F}{\partial \epsilon}|_{\overline{\epsilon}}(\epsilon - \overline{\epsilon}) \tag{3}$$

then finding $\overline{C}, \overline{n}, \overline{\epsilon}$ by minimizing L is equivalent to solving the system of equations

$$\theta = (A^T \Sigma^{-1} A)^{-1} A^T \Sigma^{-1} (\{T_i - F(t_i, \overline{C}, \overline{n}, \overline{\epsilon}\}) \tag{4}$$

where θ is the vector of expected values

$$\theta = \begin{pmatrix} C \\ n \\ \epsilon \end{pmatrix} \tag{5}$$

and A is the matrix of sensitivities given by

$$\begin{pmatrix} A_{11}, A_{12}, A_{13} \\ \vdots \\ A_{N1}, A_{N2}, A_{N3} \end{pmatrix} = \begin{pmatrix} \frac{\partial F(t_1)}{\partial C}, \frac{\partial F(t_1)}{\partial n}, \frac{\partial F(t_1)}{\partial \epsilon} \\ \vdots \\ \frac{\partial F(t_N)}{\partial C}, \frac{\partial F(t_N)}{\partial n}, \frac{\partial F(t_N)}{\partial \epsilon} \end{pmatrix} \quad (6)$$

and $(\{T_i - F(t_i, \overline{C}, \overline{n}, \overline{\epsilon}\})$ is a vector of measured temperatures. Because F is a non-linear function of C, n and ϵ, the equations must be solved iteratively and care must be taken to ensure that the initial estimates of the parameters are such that the one term Taylor series suffices [4].

The standard deviations are given by $\sigma[C] = \sqrt{\Theta_{11}}$, $\sigma[n] = \sqrt{\Theta_{22}}$, $\sigma[\epsilon] = \sqrt{\Theta_{33}}$, where

$$\Theta = (A^T \Sigma^{-1} A)^{-1} \quad (7)$$

For example if Eq. 1 is being used to fit a constant, A is a Nx1 matrix of ones and $\sigma[T]$ equals $\sigma[s]/\sqrt{N}$; the usual result for the standard deviation of an average. For problems in which F is a function, it is necessary to determine the sensitivities to form A and the standard deviations of the parameters are functions of these sensitivities. Figure 2 shows the sensitivity of the temperature to the three parameters, C, n, and ϵ when the cylinder is cooling.

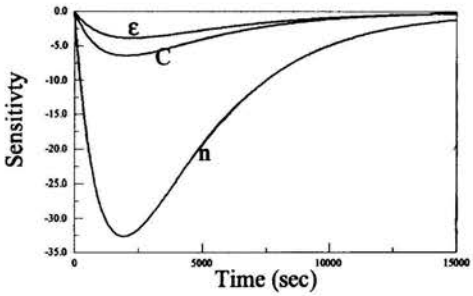

Figure 2: Sensitivity of the Temperature to the Parameters C, n, ϵ for cooling from 350K to 300K

The sensitivities for heating differ only in that they do not have a maximum, instead they asymptotically approach maximum values at steady state. The sensitivity to n is much greater than to C and ϵ at all times for both heating and cooling. These sensitivities suggest that, if the correlation $Nu = C\ Ra^n$ reflects the convective heat transfer, the exponent, n, should be estimated with reasonable accuracy.

Evaluation of Θ requires a knowledge of $\Sigma[s]$, the covariance of the noise. If the noise is random and uncorrelated, $\Sigma[s]$ is simply $\sigma^2[s]$ times the identity matrix. Emery [4] has shown that autocorrelated noise has a substantial effect on the estimated precision. If the sensitivities are approximately constant, the effect of autocorrelation can be approximated by multiplying the standard deviation of the correlated noise by $\sqrt{(1+\rho)/(1-\rho)}$ where ρ is the correlation coefficient. In this experiment the noise can be expressed as the sum of the measurement noise, s_m, the random perturbations of the ambient air, s_{T_a}, and the heater power, s_Q,

$$s = s_m + \frac{\partial T}{\partial T_a}\Delta T_a + \frac{\partial T}{\partial Q}\Delta Q \quad (8)$$

Using the usual equation for propagation of variances [5] then gives

$$\Sigma[s] = \Sigma[s_m] + \{\frac{\partial T}{\partial T_a}\}\Sigma[T_a]\{\frac{\partial T}{\partial T_a}\}^T + \{\frac{\partial T}{\partial Q}\}\Sigma[Q]\{\frac{\partial T}{\partial Q}\}^T \quad (9)$$

The values of Σ were found by statistically analyzing the different quantities and the correlation coefficients are listed in Table 1. Although the sensitivities are not constant, assuming that they are equal to the maximum value for all times, the approximation given above for an effective noise standard deviation will give some idea of the maximal effect of the correlation. The result is an effective uncorrelated noise standard deviation of $\sigma[s]$ of 0.09C.

Figure 3 depicts the normalized standard deviations when each parameter is sought independently, i.e., the other parameters are assumed known. It is clear that this experiment is not appropriate for determining neither C nor ϵ using early time data.

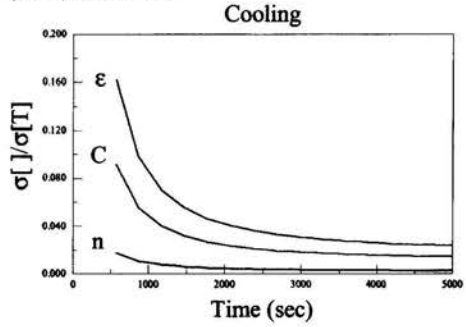

Figure 3 Normalized Standard Deviations of the Parameters when estimated individually

Figure 4 displays the corresponding normalized standard deviations of the parameters when a) the emissivity is assumed known, the solid lines, and b) when it is to be estimated, the dashed lines. Particularly noticeable are the high values at early times and the tendency to increase at long times. At early times the sensitivities are very small and their ratios are quite constant with respect to time. The result is a nearly singular $A^T \Sigma A$ and thus large components of Θ. As time, and thus the number of measurements

increases, the sensitivities increase and the standard deviations reduce, just as they do in evaluating average values. When cooling, the cylinder is within approximately 10% of the ambient temperature at 3000 seconds and the standard deviations shown at this time are the minimum that can be achieved for cooling. For heating, information continues to be accumulated, but while the sensitivities remain high at long times, the matrix becomes more singular and eventually the standard deviation increase. This simply reflects the fact that at steady state it is not possible to separate the radiative and convective heat transfer.

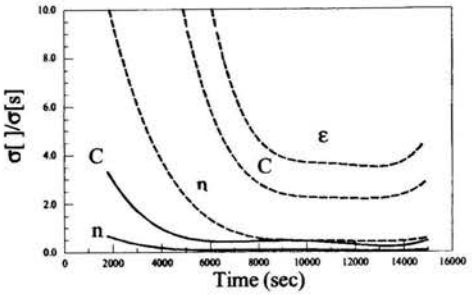

Figure 4: Normalized Standard Deviation of the parameters when simultaneously estimated
dashed line = estimating C, n and ϵ
solid line = estimating only C and n

When the emissivity is to be estimated, *none* of the parameters can be estimated with any acceptable precision. On the other hand, when the emissivity is known, then the precision of n is acceptable, giving achievable normalized values of $\sigma[n]/\sigma[s] = 0.1$. The figure indicates that data taken at early and late times contributes very little to the reduction in the standard deviations and attention should be focussed on the intermediate times when the sensitivities are large and varying.

Experimental Results

The first efforts to estimate the parameters were based upon minimizing L using NPSOL [6] and Matlab [7] and specifically written Fortran code. The range of results is shown in Table 2a. The difficulty is in the nature of the objective surface. As illustrated in Figure 5a it is very flat and upon close examination is found to have many small irregularities leading the optimizing programs to get stuck in local minima. Because of the inability of the optimizers to find the global minima, we resorted to searching over a very fine grid in three dimensions, working with two dimensions at a time. Even here, the flatness caused difficulties. Of course the obvious conclusion is that the experiment is not well suited to determining all three parameters, particularly C and ϵ simultaneously as indicated by Figure 4. It was for this reason that the cylinder was then coated with soot, whose emissivity is approximately 0.95 [8].

Table 2a
Range of Parameters found from minimizing L

	n	C	ϵ
Steady state	0.162	2.29	0.0
	0.412	0.06	1.0
Cooling	0.126	3.98	0.0
	0.227	0.28	1.0
Heating	0.092	4.32	0.3
	0.132	1.10	1.0

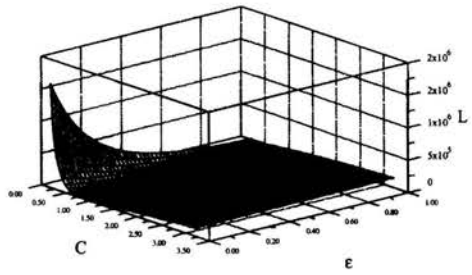

Figure 5a: Objective Function, $L(C, n, \epsilon)$ for a specified n=0.25

We then specified the value of ϵ and tried to estimate only C and n. The situation was no better as indicated by the values of Table 2b and the surface shown in Figure 5b where it is seen that the surface is equally flat.

Table 2b
Range of Parameters found from minimizing L with a specified $\epsilon = 0.95$

	n	C
Steady state	0.412	0.06
	0.233	0.42
Cooling	0.100	2.31
	0.294	0.18
Heating	0.091	2.06
	0.116	1.47

We then tried to solve Eq. 4 simultaneously for C and n, but found that convergence was difficult to attain. The minimum lies in a trough whose floor is very flat and locally irregular. Figure 5c depicts the locus of the trough floor and the diamond pattern in the figure reflects the irregularities. It should be noted that any pair of n, C in the trough fit the measured temperatures with almost equal sufficiency, leading to an arbitrariness in choosing n. Because boundary

layer theory leads to a value of n= *0.25*, it is the practice to fit data to this exponent.

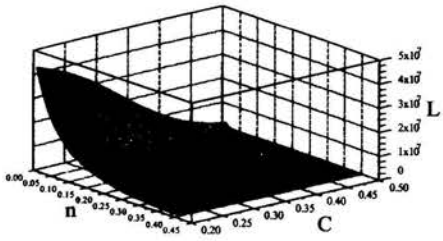

Figure 5b: Objective Function, $L(C, n)$ for a specified ϵ=0.95

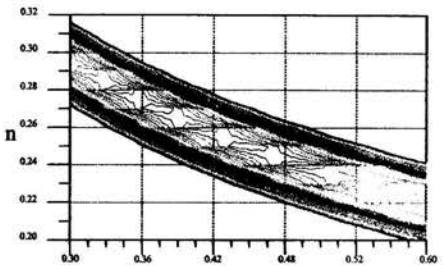

Figure 5c: Locus of the Minimum of the Objective Function, $L(C, n)$ for a specified ϵ=0.95

Steady State Results

The solution was to specify $\epsilon = 0.95$ and to compute the convective heat transfer coefficient during the steady state heating periods by solving the discretized energy equation in finite difference form. A sequence of values of h, usually of the order of 100 values, was averaged. Figure 6 shows the computed Nusselt numbers compared to two least squares fits. Fitting all of the data gives the correlation

$$Nu = 0.53\ Ra^{0.232}$$

with (6a)

$$\sigma[n] = 0.01 \quad \text{and} \quad \sigma[C] = 0.06$$

The standard deviations are in line with the estimation shown on Figure 4 with n being more precisely estimated than is C.

At the 95% confidence limits, n varies from 0.21 to 0.26 suggesting that it is not unreasonable to fit by requiring n=0.25 as developed from the laminar boundary layer solutions. Doing this we obtain

$$Nu = 0.44\ Ra^{0.25} \tag{6b}$$

with σ [C]=0.004

with a much tighter tolerance on C. A comparison of the two fits shown on the figure suggests that the data can be reasonably expressed in terms of the usual correlations

$$Nu = 0.48 Ra^{0.25} \tag{7a}$$

$$Nu = \left(0.6 + \frac{0.387 Ra^{1/6}}{[1 + (0.559/Pr)^{9/16}]^{8/27}}\right)^2 \tag{7b}$$

as suggested in References [1] and [2].

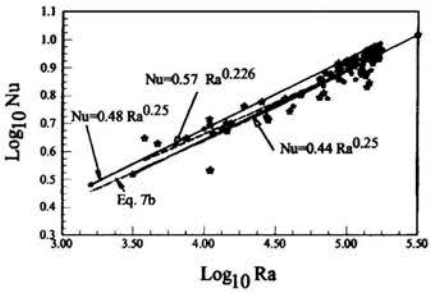

Figure 6: Nu vs Ra for Steady State, $\epsilon = 0.95$

Transient Results

Part of the problem with estimating the parameters from the objective surface, aside from the local irregularities, is that the heat transfer behaved differently in the cooling and heating transient phases. When the heater was first turned on or when the power was suddenly increased, there was a momentary large increase in the heat transfer coefficient and then a gradual diminution to the values associated with the steady state Rayleigh number. During the majority of the heating period, the convective heat transfer coefficient remained substantially higher than that computed from the correlation using the instantaneous Rayleigh number.

When the power was reduced, there was an corresponding sudden decrease in the heat transfer coefficient. But then during the remainder of the cooling transient, the convective heat transfer coefficient decreased according to the 1/4 power law. Finally, as steady state was approached h approached the value given by the correlation. These effects are illustrated in Figure 7. The instantaneous changes are due to the sudden changes in the buoyancy force near the surface. For heating, this resulted in a velocity which increased at a rate faster than that predicted from the steady

state relationship between velocity and surface temperature. While there is a corresponding change when the heater power is reduced, the flow appears to behave in a quasi-steady fashion.

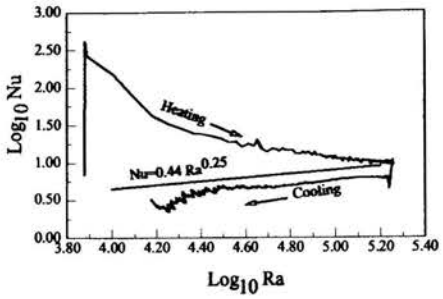

Figure 7: Transient History of Nu vs Ra

Conclusions

This example experiment demonstrates the importance of optimal experimental design. In this case, we were able to determine in advance that it was not an appropriate experiment to estimate the surface emissivity, and we have demonstrated this fact. However, given a known emissivity, the experiment is quite satisfactory for estimating the exponent, n, and the coefficient, C, provided that the analysis is done at those times specified from an analysis of the variance matrix, Eq. 7.

These results which were obtained in real, not laboratory, situations are slightly lower than those from published correlations. We attribute some of the differenes to the stochastic nature of the ambient conditions (temperature variations and drafts) and to uncertainties in the radiant losses. It should be noted, that other correlations have been recommended, and the bases for the different recommendations are rarely provided in the standard sources. For example, Reference 2 notes that McAdams recommends C=0.53, which is 10% higher than that given in References 1 and 2 and 25% higher than that recommended by Churchill and Chu [1].

Finally we note that one rarely has sufficient information for real problems. Although natural convection flow responds reasonably rapidly to changes in the driving force, the use of steady state correlations is likely to give rise to substantial errors in predicting temperature histories during transient heating or cooling. It is intuitively obvious that transient and steady state convection are different, but what choice does the designer have? We can only conclude that designers must use empirical information only as guides and must fully analyze the consequences of any variability of design data on the functioning of the system being designed.

REFERENCES

1 Incropera, F. and DeWitt, D., 1996, *Introduction to Heat Transfer*, J. Wiley and Sons, Publ., New York, NY

2 Kakac, S., Shah, R. K. and Aung, W., 1987, *Handbook of Single- Phase Convective Heat Transfer*, J. Wiley and Sons, Publ., New York, NY

3 Sorenson H. W., 1980, *Parameter Estimation: Principles and Problems*, Marcel Dekker, Inc., N. Y., NY

4 Emery 2001, "The Relationship Between Information, Sampling Rates, and Parameter Estimation Models," Paper NHTC01-12433 *Proc. ASME National Heat Transfer Conference*, Anaheim, CA.

5 Stark, H. and Woods, J. W., 1994, *Probability, Random Processes and Estimation Theory for Engineers*, Prentice Hall, N. Y., NY

6 Gill, P. E. et al., 1986, "User's Guide for NPSOL - A Fortran Package for Nonlinear Programming," Department of Operations Research, Stanford University, Palo Alto, Calif.

7 MatLab, The MathWorks, Inc., Natick, MA

8 Modest, M., 1993, *Radiative Heat Transfer*, McGraw-Hill Publ. New York, NY

NOMENCLATURE

	Roman
A	Matrix of sensitivity coefficients
C	Constant in empirical correlation
h	Convective heat transfer coefficient
F	Predicted temperature
L	Objective function
n	exponent in empirical correlation
N	Number of readings
Nu	Nusselt number
P	Power of heater
Pr	Prandtl number
Ra	Rayleigh number
t	Time
s	noise
T	Temperature
	Greek and Mathematical Symbols
ϵ	Emissivity
ρ	Correlation coefficient
$\sigma[x]$	Standard deviation of x
$\Sigma[x]$	Covariance matrix of x
θ	Parameter vector
Θ	Variance matrix
$\overline{x}$	Expected value of x
$\{x\}$, $\mathbf{x}$	Vector
$\{x\}^T$, $\mathbf{x}^T$	Transpose of vector

HEFAT2002
1st International Conference on Heat Transfer, Fluid Dynamics and Thermodynamics
8 – 10 April 2002, Kruger National Park, South Africa
FM1

FREE CONVECTION FROST FORMATION ON A COLD PLATE IN A VERTICAL CHANNEL

Marco FOSSA and Giovanni TANDA

Dipartimento di Termoenergetica e Condizionamento Ambientale (DITEC)
Università degli Studi di Genova
via all'Opera Pia 15a, I-16145 Genova, ITALY
E-mail: mfossa@ditec.unige.it, tanda@ditec.unige.it

ABSTRACT

Processes involving heat transfer from a humid air stream to a vertical plate with simultaneous deposition of frost are of great importance in a variety of refrigeration equipment. In this work, frost growth on a vertical plate in free convection has been experimentally investigated. The plate, cooled by the internal circulation of glycol, was placed in a vertical channel open at the top and bottom in order to permit the natural circulation of ambient air. The cold plate temperatures were varied in the -13 to -4°C range, while the relative humidity and temperature of the ambient air were taken in the 31-85% and 26-28°C ranges respectively. Frost thickness, surface temperature,and deposited mass as well as heat flux to the cold plate were recorded as functions of time and experimental data were used to identify parameters affecting the frost growth.

INTRODUCTION

Frost formation processes are of great importance in numerous industrial applications including refrigeration, air-conditioning, cryogenics, and process industries. In most cases, frost formation is undesirable because it contributes to the increase in heat transfer resistance and pressure drop. Frost formation is a complicated transient phenomenon in which a variety of heat and mass transfer mechanisms are simultaneously present. Typical frost formation periods have been described by Hayashi et al. [1]: an initial 1-D crystal growth is followed by a frost layer growth period while a so-called frost layer full-growth period characterises long time processes, in which frost surface can reach melting temperature. Each growth mode is characterised by special values of frost density, which in turn affects the other frost parameters (thickness, apparent thermal conductivity). Furthermore, as observed in several studies [2-5], the features of the heat transfer rate (through the wall-to-air temperature difference) and of the mass transfer rate (which also depends on air moisture content) affect frost structure and control the length of the growth periods. Owing to the complexity of the phenomenon, the development of reliable frost formation models as well as of correlations to evaluate frost properties is a demanding task; experimental data are required to check both the assumptions made in the theoretical analyses and the predicted results.

As clearly reported in a few review papers [6-8], frost formation during the forced convection of humid air has been extensively studied, while, on the other hand, only a limited number of investigations deal with mass-heat transfer during natural convection on a surface at subfreezing temperatures. This aspect was tackled by Kennedy and Goodman ([9], study of frost formation on a vertical surface), Tajima et al. ([10], flat surface with different orientations), Cremers and Mehra ([3], outer side of vertical cylinders), Tokura et al. ([4], vertical surface). To the authors' knowledge, no data are available for natural convection in channels, despite the practical significance of this phenomenon in such devices as evaporative heat exchangers for cryogenic liquid gasification.

The present paper reports the results of an experimental investigation of frost formation on a vertical plate inside a rectangular channel where ambient air is flowing by natural convection. Experiments, conducted for a variety of air relative humidity and wall temperature conditions, were aimed at identifying the main parameters affecting frost thickness, surface temperature and deposited mass as well as the heat flux transferred from the humid air flow to the cold plate across the frost layer.

THE EXPERIMENTS

The apparatus and instrumentation

A schematic view of the experimental apparatus is shown in Figure 1. The entire apparatus and the instrumentation were placed in a large laboratory where relative humidity could be regulated over the 30-90 percent range at 27 ±1°C. The channel, made of Plexiglas and rectangular in shape, had a section of 20 mm x 360 mm and was 2.4m long: it was open at the top and bottom in order to permit natural circulation of ambient air. The test section, located at 1.3m from the channel top section and at 1.0m from the bottom section, consisted of a 95 mm long, 282 mm wide, cold plate and three Plexiglas walls forming a channel as deep and as wide as the entrance and exit channels. The plate was made of copper and cooled by an internally circulating glycol solution coming from a thermostatic bath. The plate was framed inside a Plexiglas wall and separated from it by 10 mm-thick polystyrene strips to minimise the thermal conduction at the plate boundaries and thus prevent dew and frost formation on surfaces other than the test surface.

The surface temperature of the copper plate was measured by five pre-calibrated thermocouples, fitted inside small holes drilled into the wall material positioned as close as possible to the exposed surface. Two of them were able to move inside the frost layer driven by micrometers. The relative humidity of the convective air flow was measured by capacitance hygrometers, carefully calibrated in the 10-95 percent range and positioned at the inlet and outlet of the test section. Numerous fine-gauge thermocouples were employed to evaluate the temperature of the air flow at the test section inlet and outlet. Additional thermocouples were located in the Plexiglas wall opposite to the cold plate (to allow the evaluation of the thermal radiation exchange) and in the material surrounding the cold plate (to allow the checking of thermal conduction to the plate from the surrounding). An infrared thermocouple was used to measure the average frost layer surface temperature with an estimated uncertainty of 0.4°C. The heat flux entering the cold plate was measured by three pre-calibrated heat flux sensors flush-mounted on the test surface at different positions (A, B, C) as shown in Fig.1.

The thickness of the frost layer was continuously monitored at the three locations A, B, C corresponding to the positions of the heat flux sensors. The employed sensors were mounted on micrometers to allow careful checking of their position when they were moved from the Plexiglas wall facing the cold plate towards the frost surface.

Two alternative types of sensors were used: impedance sensors and nylon sensors. The impedance probes were made by eliminating the junction in a shielded thermocouple in order to obtain a pair of closely spaced electrodes (at a distance of about 0.3 mm). A DC low voltage, applied to the thermocouple

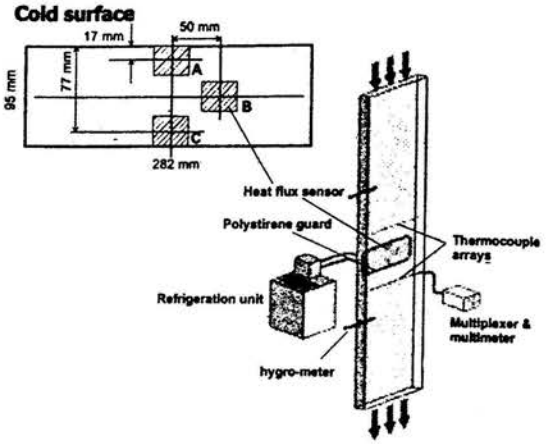

Figure 1: Schematic layout of the vertical channel and cold plate.

wires, gave rise to light current circulation when the probe tip was in contact with the frost layer. This kind of measurement was particularly suitable in the presence of a rather compact frost layer, while, in the presence of a fragile frost layer structure, a nylon tip probe was employed to prevent frost melting, and the contact with the frost surface was visually observed. The estimated uncertainty of the frost layer thickness was 0.1 mm, regardless of the type of probe employed.

The heat transfer coefficient h at the frost-to-air interface is given by

$$h = -k(\partial T/\partial n)_f/(T_f - T_a) \qquad (1)$$

where k is the thermal conductivity of air evaluated at the frost surface temperature, $(T_f - T_a)$ is the frost surface to ambient air temperature difference and $(\partial T/\partial n)_f$ is the thermal gradient of air, in the direction normal to the plate, evaluated at the frost/air interface and obtained by the schlieren technique, as described by Tanda [11]. A typical schlieren image is reported in Fig.2: the thin dark line in the optical field is the shadow of a strip filter placed on the focal plane of the schlieren head. Moving the strip filter on the focal plane of the schlieren head allows the light angular deflections (i.e. the thermal gradients of air) to be detected The heat transfer coefficient h, spanwise averaged along the long side of the plate, was

Figure 2: A typical schlieren image of the test section. The thin dark line between the cold plate (on the left) and the shrouding adiabatic wall (right) represents the loci of points at equal thermal gradient.

evaluated, at regular time intervals, at different spots along the vertical co-ordinate x. The uncertainty (at 95 percent confidence level) in the h measured values was in the 8-20 percent range.

Finally, additional runs were performed at reduced time intervals to measure the frost mass deposited on the test plate; at the end of each test the frost was scraped off the plate and weighed by a precision balance.

The operating procedure

Each experiment was conducted with constant values of ambient air temperature and relative humidity and for a given value of the cold plate surface temperature. Namely, the temperature of the ambient air was set at 26-28°C, with relative humidity varying in the 31 to 85 percent range. The surface temperature of the cold plate was varied in the -13 to -4°C range, with variations in time and along the surface confined within ±0.3 °C.

Before test plate cooling, the surface was covered with a thin polyethylene film so that water vapour could not condense on the test plate before the starting of the test. After the prescribed temperature of the plate was reached, the test was started by taking off the film. The standard duration of each test was 7.5 hours; the monitored quantities (air, plate and frost temperatures, heat fluxes entering the cold plate, frost thickness, and local heat transfer coefficients) were measured at regular time intervals (typically 45 min) after the test inception. When the test was completed, additional measurements of frost thickness were made by using the two shielded, 0.5mm-dia thermocouples travelling through the cold plate and connected to a micrometer. These were also used to check frost temperature as measured by the infra-red thermometer.

RESULTS AND DISCUSSION

As previously described, the input parameters of the study were ambient air temperature and relative humidity, and the surface temperature of the cold plate. The natural convective airflow was driven inside the channel by the air-to-frost surface temperature difference. Owing to the long development section of the channel, the airflow at the test section inlet was expected to be fully developed and within the laminar regime (typically the Reynolds number based on the hydraulic diameter of the channel ranged from 250 to 500).

First, attention is focused on the measured thickness of the frost layer. As found in previous works [3, 4, 12, 13], the thickness of the growing frost layer is generally only slightly affected by location. Therefore, results shown in Fig.3 are based on mean frost thickness (estimated as the average of the three independent measurements performed at the three different spots A, B, C) as a function of time, at two different values of the relative humidity (31 and 70 percent) and three values of the cold plate temperature (in the range from -13 to -4°C). Different symbols refer to the experimental results, while lines refer to the predictions obtained by the theoretical model. Generally speaking, largest frost thickness values are achieved at the highest relative humidities and largest air-to-plate temperature differences. However, when relative humidity is higher than about 50 percent, it only slightly affects the frost layer thickness, as emerges from the inspection of Fig.4, where frost thickness versus time is reported for different humidity values at a given wall-to-air temperature difference.

In Figure 5 frost thickness is reported against the frost growth parameter introduced by Schneider [12] and given by the product of time τ and the frost surface-to-wall temperature difference (T_f-T_w). Measured data are in good agreement with the following relationship:

$$S = 0.20\,[\tau\,(T_f - T_w)]^{0.40} \qquad (2)$$

where S is expressed in mm and τ in min. Eq.(2) was obtained by Cremers and Mehra [3] for free-convection frost formation on vertical cylinders, including data in the 65-94 percent humidity range, with values of the frost growth parameter higher than 1000. Seemingly, the correlation also applies to lower humidities (up to 31%). When the frost growth parameter is lower than 1000, a large spread of data occurs and the frost growth law probably depends also on the relative humidity. It is worth noting that in these conditions frost growth is not uniform and the uncertainty in the average thickness measurement (here given by the arithmetic mean of only three independent local measurements) can be very high.

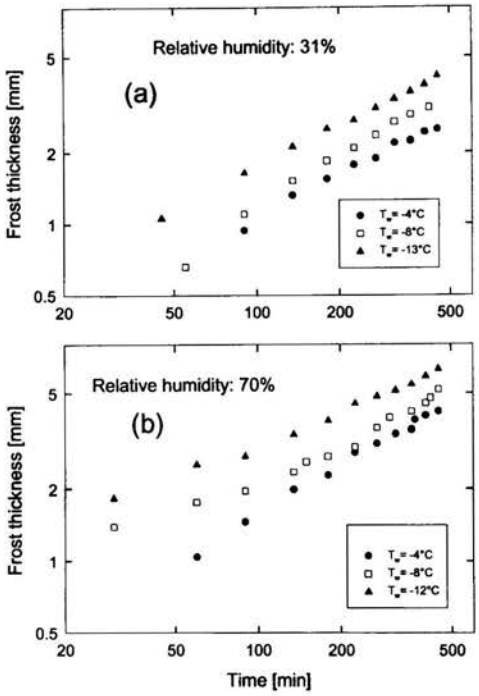

Figure 3: Average thickness of the frost layer versus time. Relative humidity: (a) 31 percent, (b) 70 percent.

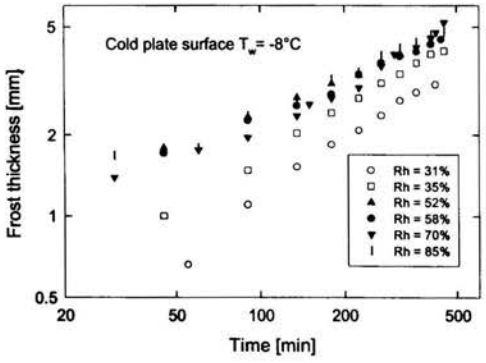

Figure 4: Average thickness of the frost layer for T_w=-8°C and different values of relative humidity Rh.

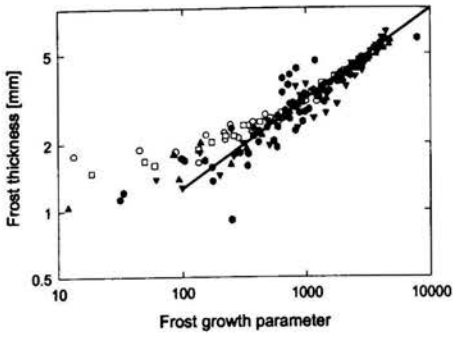

Figure 5: Average frost thickness versus the frost growth parameter defined by Schneider [12]. Symbols: experiments (open Rh<50%, closed Rh<50%), line: correlation by Cremers-Mehra [3].

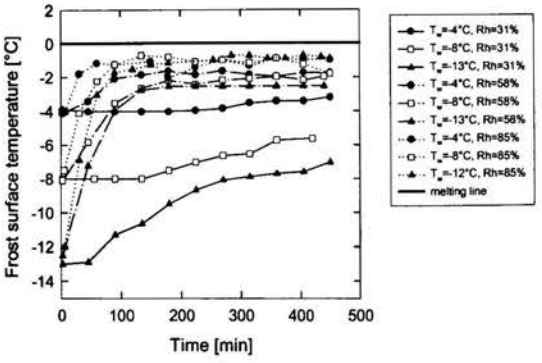

Figure 6: Surface temperature of frost versus time at different values of relative humidity Rh and cold plate temperature T_w.

Figure 6 shows the measured values of the mean frost surface temperature versus time, for three different values of relative humidity (in the 31-85 percent range) and three values of the cold plate temperature (in the -13 to -4°C range). It is apparent from the figure that, when humidity is relatively high, frost surface temperature approaches a value close to the triple-point value in a rather short time (one or two hours). Conversely, for the lowest value of relative humidity, frost surface temperature and thickness increase very slowly with time; moreover, visual observation revealed irregular frost growth over the cooled plate (as typically occurs in the "one-dimensional growth period").

The dimensionless local heat transfer coefficient (Nu_x= hx/k, x being the downward vertical co-ordinate and k the air thermal conductivity), measured by means of the schlieren technique, is reported in Fig.7 against the local Grashof number ($Gr_x=\beta g(T_a-T_f)x^3/\nu^2$, g being the gravitational acceleration and β and ν the coefficient of thermal expansion and the kinematic viscosity of air, respectively). Experimental results, obtained at different vertical spots with and without frost, are denoted by symbols. They are in satisfactory agreement with the theoretical results obtained by Ostrach [14] for a vertical isothermal plate with air as the convective fluid. It is inferred that the presence of either the wall facing the cold plate or the long development and exit sections does not significantly affect the heat transfer behaviour of the vertical plate for the range of air-to-wall temperature differences and for the values of the geometric parameters (channel height and depth, cold plate height) considered.

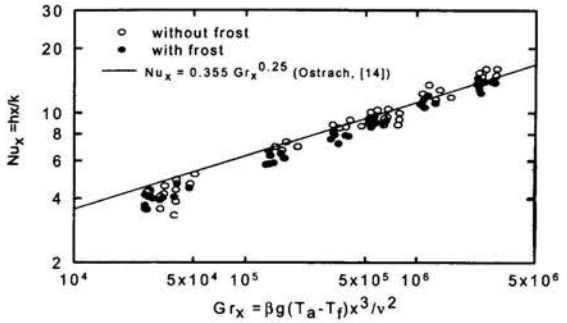

Figure 7: Local Nusselt number versus Grashof number. Symbols: experimental values, line: correlation by Ostrach [14] for a vertical, unbounded, isothermal plate.

The measured mass of frost (per unit of surface area) deposited onto the cold surface is plotted in Figure 8 for different values of the cold wall temperature and air relative humidity. As shown in the figure, the total mass of frost deposited increases linearly with time and is markedly affected by relative humidity. Conversely, the cold plate temperature exerts only minor influence on the frost mass, especially for medium-high values of air humidity.

Attention is now focused on the heat flux at the cold plate/frost interface. Data reported in Figure 9 (a-c) refer to measurements at the plate midheight (corresponding to the heat flux sensor at location B). In general, the local heat flux to the cold plate during frost formation is markedly reduced for the lowest values of the cold wall temperature; conversely, slight heat transfer reductions only (or even heat transfer enhancements) were observed for T_w= -4°C. This can be ascribed to the fact that at the highest plate temperature the frost layer is very thin (causing only slight additional thermal resistance) and not regular in surface (thus increasing the effective heat transfer area on the air side). The total heat flux was found to be higher at the highest relative humidities (at the same cold plate temperature), owing to the increased rate of latent heat transfer, driven by the higher air-to-frost vapour concentration difference. Moreover, as found for frost surface temperature and frost mass, the role played by the cold plate temperature is strongly reduced as relative humidity is increased. In particular, at Rh=70%, heat flux distributions reach a common value after a short transient. Alternate frost densification and thickening are responsible for the oscillations shown by heat flux distributions far from the frost growth inception.

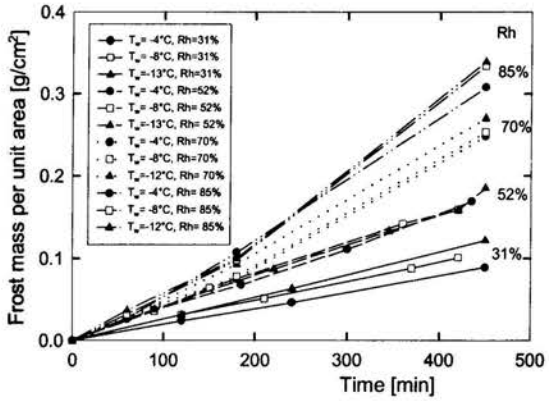

Figure 8: Mass of deposited frost (per unit surface area) versus time for different values of relative humidity Rh and cold plate temperature T_w.

CONCLUSIONS

Heat and mass transfer during the formation of a frost layer on a cold surface (placed inside a long vertical channel) was experimentally investigated. Experiments were conducted by varying the temperature of the cold plate between -13 and -4°C and relative humidity of ambient air from 31 to 85 percent. Frost layer thickness was found to vary with a parameter given by the product of time and frost surface-to-air temperature difference, in agreement with previous literature works. Relative humidity was found to markedly affect the deposited mass, the surface temperature and the thickness of frost in the range from 31 to about 50 percent. For higher values, the effect of relative humidity on frost thickness is strongly reduced and the frost surface temperature after a short transient attains a value close to melting temperature. The heat flux transferred to the cold plate, measured at the plate midheight, turned out to decrease with time owing to frost growth especially at the lowest cold plate temperatures (-13/-12°C). Slight reductions - or even enhancement - in heat flux occurred at the highest cold plate temperature (-4°C).

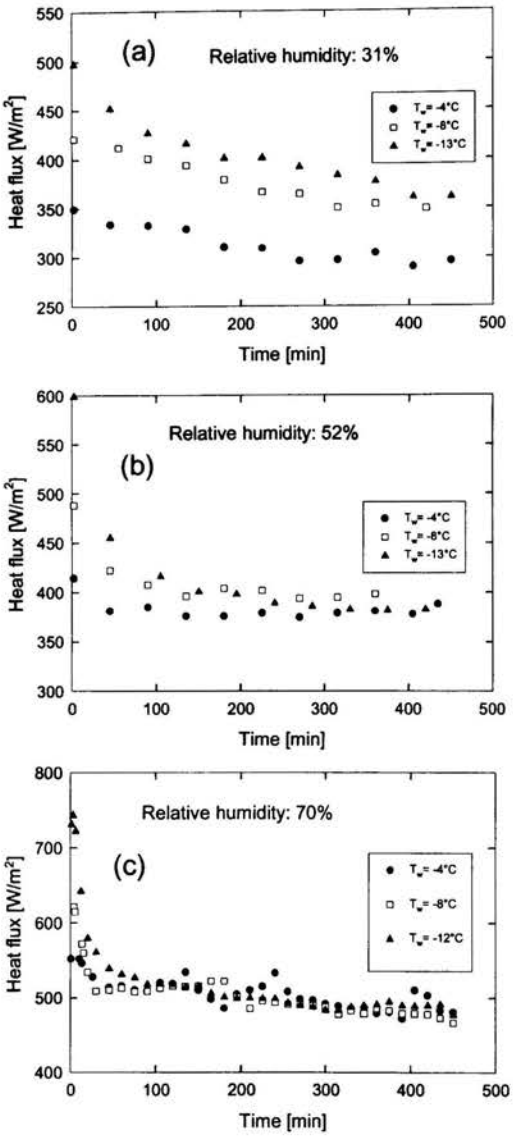

Figure 9: Heat flux transferred to the cold plate at midheight versus time. Relative humidity: (a) 31 percent, (b) 52 percent, (c) 70 percent.

REFERENCES

[1] Hayashi Y., Aoki A., Adachi S., and Hori K., 1977, "Study of frost properties correlating with frost formation types", ASME J. Of Heat Transfer, Vol. 99, pp.239-245.

[2] Jones B.W., and Parker J.D., 1975., "Frost formation with varying environmental parameters", ASME Journal of Heat Transfer, Vol.97, pp.255-259.

[3] Cremers C.J., and Mehra V.K., 1982, "Frost formation on vertical cylinders in free convection", ASME Journal of Heat Transfer Vol.104,pp.3-7.

[4] Tokura I., Saito H., and Kishinami K., 1983, "Study on properties and growth rate of frost layers on cold surfaces", ASME Journal of Heat Transfer, Vol.105, pp. 895-901.

[5] O'Neal D.L., and Tree D.R., 1984, "Measurement of frost growth and density in a parallel plate geometry", ASHRAE Trans., Vol.90, pp.278-290.

[6] O'Neal D.L, and Tree D.R., 1985, "A review of frost formation in simple geometries", ASHRAE Trans., Vol.91, pp.267-281.

[7] Padki M.M., Sherif S.A., and Nelson R.M., 1989, "A simple method for modeling the frost formation phenomenon in different geometries", ASHRAE Trans., Vol.95, pp.1127-1137.

[8] Mishra S., Gidwani A., Ohadi M.M., and Dessiatoun S.V., 1997, "An overview of basic models of frost formation phenomenon and recent progress on the use of an electric field in suppressing or promoting frost", AIChE Symp. Series Heat Transfer, Vol.93, pp.197-210.

[9] Kennedy L.A., and Goodman J., 1974, "Free convection heat and mass transfer under conditions of frost deposition", Int. Journal of Heat and Mass Transfer, Vol.17, pp.477-484.

[10] Tajima O., Naito E., Nakashima K., and Yamamoto H., 1974., "Frost formation on air coolers, part 3: natural convection for a cooled vertical plate", Heat Transfer Jap. Research, Vol.3, pp.55-66.

[11] Tanda, G., 1993, "Natural convection heat transfer from a staggered vertical plate array", ASME Journal of Heat Transfer, Vol. 115, pp. 938-945.

[12] Schneider, H.W., 1978, "Equation of the growth rate of frost forming on cooled surfaces", Int.Journal of Heat Mass Transfer, Vol. 21,pp.1019-1024.

[13] Tanda G., and Fossa M., 2001, "An experimental study of the frost formation on a cold surface in free convective flow", 5th World Conf. on Exp. Heat Tr., Fluid Mech. and Thermodyn., 24-28 September, Thessaloniki, Greece.

[14] Ostrach S., 1952, "An analysis of laminar free-convection flow and heat transfer about a flat plate parallel to the direction of the generating body force", NACA TN 2635.

HEFAT2002
1st International Conference on Heat Transfer, Fluid Dynamics, and Thermodynamics
8-10 April, 2002, Kruger National Park, South Africa,
OP1

NATURAL CONVECTION IN A SQUARE ENCLOSURE WITH A PARTIALLY HEATED WALL SECTION COVERED BY A BLIND-LIKE ATTACHMENT WITH HEAT GENERATION IN THE ATTACHMENT

Patrick H. Oosthuizen
HEAT TRANSFER LABORATORY
Department of Mechanical Engineering
Queen's University, Kingston, Ontario, Canada K7L 3N6, email: oosthuiz@me.queensu.ca

ABSTRACT

The natural convective heat transfer rate across a square enclosure with one vertical wall partially heated to a uniform high temperature and with the opposite vertical wall cooled to a lower uniform temperature has been numerically investigated. The remaining wall sections are adiabatic. The heated wall section is covered at the top and in the front by thin straight walls that offer no resistance to heat transfer. There is a uniform rate of heat generation in the portion of the covering wall that is parallel to the heated wall section. The flow in the enclosure has been assumed to be laminar and two-dimensional. Fluid properties have been assumed constant except for the density change with temperature that gives rise to the buoyancy forces, this being treated by means of the Boussinesq type approximation. The governing equations have been written in dimensionless form, the size of the enclosure being used as the characteristic length scale and the overall temperature difference being used as the characteristic temperature. The dimensionless equations have been solved using a finite-element method. The solution has the Rayleigh number, the Prandtl number, the dimensionless distance of the barrier from the hot vertical surface, the dimensionless rate of heat generation in the barrier and the dimensionless size of the heated wall section as parameters. Because of the possible applications that motivated the study, results have only been obtained for a Prandtl number of 0.7. The effect of the other dimensionless variables on the heat transfer rate across the enclosure has then been numerically determined.

NOMENCLATURE

H'_B height of heated side wall section
H_B H'_B/W'
k thermal conductivity
Nu_c Nusselt number for cold surface based on W' and on $T'_H - T'_C$
Nu_h Nusselt number for hot surface based on H' and on $T'_H - T'_C$
Nu_{hmin} minimum hot surface Nusselt number
Pr Prandtl number
Q'_B heat transfer rate per unit length in blind
Q_B dimensionless heat transfer rate per unit length in blind
$\overline{q'}_c$ mean heat transfer rate per unit area from cold surface
$\overline{q'}_h$ mean heat transfer rate per unit area from hot surface
Ra Rayleigh number based on W' and on $T'_H - T'_C$
T' temperature
T dimensionless temperature
T'_c temperature of cold vertical surface
T'_h temperature of hot vertical surface
u' velocity component in x' direction
u dimensionless velocity component in x direction
v' velocity component in y' direction
v dimensionless velocity component in y direction
W' width and height of enclosure
w'_B gap between heated section and vertical covering
w_B w'_B/W'
x' horizontal coordinate
x dimensionless horizontal coordinate
y' vertical coordinate
y dimensionless vertical coordinate
α thermal diffusivity
ν kinematic viscosity
ψ' stream function
ψ dimensionless stream function

ω' vorticity
ω dimensionless vorticity

INTRODUCTION

The natural convective heat transfer rate across a square enclosure with one vertical wall partially heated to a uniform high temperature and with the opposite vertical wall cooled to a lower uniform temperature has been numerically investigated. The remaining wall sections are adiabatic. The heated wall section is covered at the top and in the front by thin straight walls that offer no resistance to heat transfer. There is a uniform rate of heat generation in the portion of the covering wall that is parallel to the heated wall section. The flow situation considered is therefore as shown schematically in Fig. 1. The covering over the heated section is indicated by bgh in this figure and there is a uniform rate of heat generation in gh.

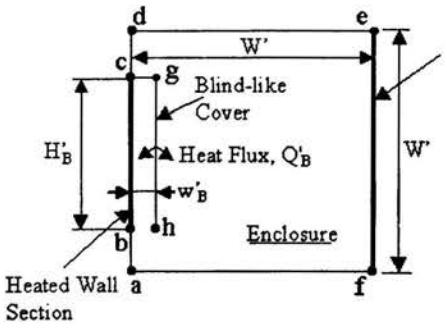

FIGURE 1: FLOW SITUATION CONSIDERED.

The present work was undertaken as part of a wider study of the effect of window coverings on the heat transfer rate from windows, particularly for the case where the window is hotter than the room air, i.e. where air-conditioning is being used, the situation here considered being an approximate model of a window covered by a plane blind. In such situations there is often effectively heat generation in the blind as a result of the absorbtion of solar energy. The situation considered in the present study does not, of course, directly model the real situation. The results obtained here will however give an indication of the effect of window-to-blind gap and of the effect of solar radiation on the heat transfer rate from a window and thus act as a guide to studies of heat transfer from actual windows.

As already mentioned, the present work was undertaken as part of a wider study of the effect of window coverings on the heat transfer rate from windows, see for example Machin et al. (1998), Phillips et al. (1998), Machin et al. (1997), and Rheault and Bilgen (1990), particularly for the case where the window is hotter than the room air, i.e. where air-conditioning is being used. These studies and that described by Ye et al. (1999) have concentrated on venetian blinds. The situation considered in the present study is an initial step in the development of a simplified model of the effect of a plane solar-irradiated blind on the heat transfer from a window. The effect of the distance of a partial partition in an enclosure from the heated wall has been considered by Oosthuizen (1999a) and Ghosh et al. (1992) and these results have some similarity to those obtained here. More general studies of natural convection in enclosures with various forms of partition are described by Kirkpatrick et al. (1987), Zimmerman and Acharya (1987), Shaw et al. (1987), Chao et al. (1989), Olson et al. (1990), Kelkar-Kanchan and Patankar(1990), Karayiannis et al. (1992), and Hanjalic et al. (1996). A study of the situation being considered here but without the heat generation on the covering wall is described by Oosthuizen (1999a). The present study, as is the case in most of the previous studies mentioned above, considers only the convective heat transfer. In window heat transfer situations the radiant heat transfer can be very important and can interact with the convective flow, e.g. see Jayaram et al. (1997).

GOVERNING EQUATIONS AND SOLUTION PROCEDURE

The flow has been assumed to be laminar and two-dimensional. Fluid properties have been assumed constant except for the density change with temperature that gives rise to the buoyancy forces, this being treated by means of the Boussinesq type approximation. The solution has been obtained in terms of the stream function, ψ', and vorticity, ω', defined, as usual, by:

$$u' = \frac{\partial \psi'}{\partial y'} \quad , \quad v' = \frac{\partial \psi'}{\partial x'} \quad , \quad \omega' = \frac{\partial v'}{\partial x'} - \frac{\partial u'}{\partial y'} \qquad (1)$$

where x' is the coordinate in the horizontal direction and y' is the coordinate in the vertical direction. The prime ($'$) denotes a dimensional quantity.

The following dimensionless variables have then been defined:

$$\psi = \psi'/\alpha \ , \ \omega = \omega' W'^2/\alpha \ , \ x = x'/W' \ ,$$

$$y = y'/W' \ , \ T = (T' - T'_C)/(T'_H - T'_C) \qquad (2)$$

where T' is the temperature, $T_H{}'$ is the temperature of the hot wall, AB, and $T_C{}'$ is the temperature of the cold wall, gh.

In terms of these dimensionless variables, the governing equations are:

$$\frac{\partial^2\psi}{\partial x^2} + \frac{\partial^2\psi}{\partial y^2} = -\omega \tag{3}$$

$$\frac{\partial\psi}{\partial y}\frac{\partial\omega}{\partial x} - \frac{\partial\psi}{\partial x}\frac{\partial\omega}{\partial y} - Pr\left(\frac{\partial^2\omega}{\partial x^2} + \frac{\partial^2\omega}{\partial y^2}\right) = Ra\frac{\partial T}{\partial x} \tag{4}$$

$$\frac{\partial\psi}{\partial y}\frac{\partial T}{\partial x} - \frac{\partial\psi}{\partial x}\frac{\partial T}{\partial y} - \left(\frac{\partial^2 T}{\partial x^2} + \frac{\partial^2 T}{\partial y^2}\right) = 0 \tag{5}$$

Here Ra is the Rayleigh number based on, W', i.e.:

$$Ra = \frac{\beta g(T'_H - T'_C)W'^3}{\nu\alpha} \tag{6}$$

Considering the surfaces indicated in Fig.1, the boundary conditions on the solution are, basically, that the dimensionless stream function is constant on abcdefa and on bgh, that the dimensionless temperature has a value of 1 on bc and a value of 0 on ef, that the gradient of dimensionless temperature normal to ab, cd, de and fa is zero and that the gradient of dimensionless temperature normal to cg is equal on the two sides at any point on the barrier. and that the difference between the dimensionless heat flux on the two sides of gh is equal to Q_B which is defined by:

$$Q_B = \frac{Q'_B W'}{k(T'_H - T'_C)} \tag{7}$$

The dimensionless equations have been solved using a finite-element method. The solution for the temperature distribution allows the local heat transfer rate distributions over the hot and cold surfaces to be determined. The local heat transfer rate distribution can then be integrated to give the mean heat transfer rates for these surfaces. The mean heat transfer rate has been expressed in terms of a mean Nusselt number, Nu, based on the height of the surface considered , i.e., H'_h for the hot surface and W' for the cold surface, and on the overall temperature difference $T_H{}' - T_C{}'$, i.e. the following are defined:

$$Nu_h = \frac{\overline{q'}_h H'_h}{k(T'_H - T'_C)} \tag{8}$$

$$Nu_c = \frac{\overline{q'}_c W'}{k(T'_H - T'_C)} \tag{9}$$

If there is no heat generation in the covering surface, i.e., if Q_b is zero, $Nu_h = Nu_c$. When there is heat generation in the covering surface:

$$Nu_c - Nu_h = Q_B \tag{10}$$

RESULTS

The solution has the following parameters:

the Rayleigh number, Ra
the Prandtl number, Pr
the dimensionless distance of the barrier (blind) from the hot vertical surface, w_B
the dimensionless rate of heat generation in the barrier (blind), Q_B
the dimensionless size of the heated wall section, H_B

Because of the possible applications that motivated the study, results have only been obtained for a Prandtl number of 0.7. The effect of the other dimensionless variables, i.e. Ra, Q_B, w_B and H_B on Nu, on the solution has then been numerically determined. The effects of Q_B and w_B on Nu have in particular been studied.

Figure 2 shows a typical variations of Nu with w_B for fixed values of Ra and H_B for various values of Q_B. It will be seen that in all cases for small values of w_B, the Nusselt number decreases as w_B is increased. This is because for small values of w_B there is no significant convective motion in the fluid layer between the wall and the cover and the heat transfer from the heated wall section to the cover is essentially by conduction. Therefore as w_B increases in this range of w_B values the heat transfer resistance associated with the fluid layer between the wall increases leading to the observed reduction in the heat transfer rate. However, as w_B is further increased, a point is eventually reached at which w_B is large enough for convective motion to develop in the space between the heated wall section and the cover and as a result the Nusselt number passes through a minimum and then increases somewhat with further increase in B. The changes in flow pattern are illustrated by the typical streamline and isotherm patterns shown in Figs.3 and 4.

It will also be seen from Fig. 2 that the presence of heat generation in the covering surface decreases the temperature difference between the heat surface and the covering surface leading to a decrease in Nu_h with increasing Q_b for a particular value of w_B. However, because:

$$Nu_c = Nu_h + Q_B \tag{11}$$

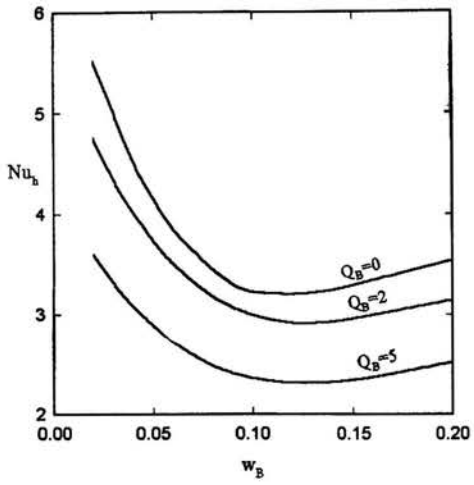

FIGURE 2: VARIATION OF Nu_h WITH w_B FOR $Ra = 10^6$ AND $H = 0.5$ FOR VARIOUS VALUES OF Q_B.

Nu_c increases with increasing Q_B. The effect of Q_B on the minimum value of Nu_h for the conditions considered in Fig. 2 is shown in Fig. 5. For large values of Q_B the blind temperature will exceed the hot wall temperature and the heat transfer rate at the hot surface can become negative, i.e., there can be a heat flow into the hot wall. This is illustrated by the results given in Fig. 6 which shows the variation of Nu_h with Q_B for fixed values of w_B, Ra and H_B.

The results given in Fig. 2 were for $Ra = 10^6$ and $H_B = 0.5$. The effect of changes in these parameters on the variation of Nu_h with w_B are illustrated by comparing the results shown in Figs. 7 and 8 with those given previously.

CONCLUSIONS

The results indicate that there is a specific value of the dimensionless side enclosure width, w_B, that for particular values of Ra gives a minimum heat transfer rate. The minimum arises as the result of the development of convective motion between the covering and the heated surface as w_B increases. The effect of Ra on the value of w_B that gives a minimum Nu and on the minimum value of N_u has been determined.

ACKNOWLEDGMENT

This work was supported by the Natural Sciences and Engineering Research Council of Canada.

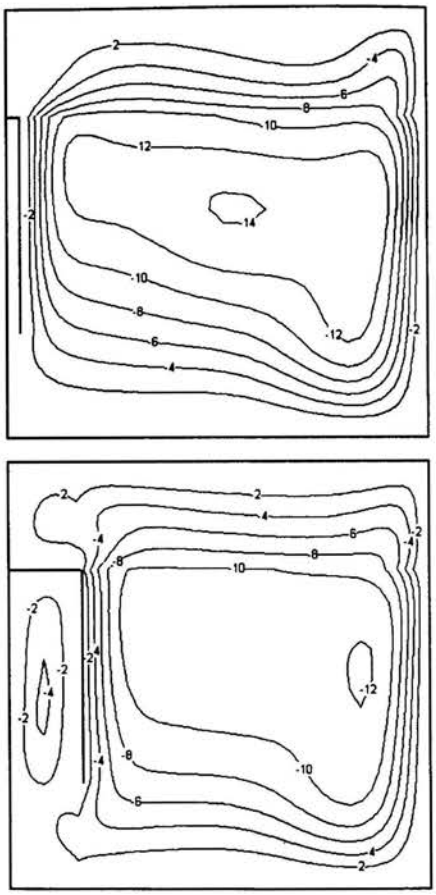

FIGURE 3: STREAMLINE PATTERNS FOR $Ra = 10^6$, $H_B = 0.5$ AND $Q_b = 5$ FOR w_B EQUAL TO 0.04 (TOP) and 0.18 (BOTTOM).

REFERENCES

Chao, P.K.-B., Lior, N., Churchill, S.W. and Ozoe, H., 1989, "Effect of partitions on natural convection in enclosures", *Proceedings of the ASME National Heat Transfer Conference*, HTD-107, Heat Transfer in Convective Flows. ed. R.K. Shah, ASME, pp. 315-322.

Ghosh, P.K., Sarkar A. and Sastri, V.M.K., 1992, "Natural convection heat transfer in an enclosure with a partition-a finite-element analysis", *Numerical Heat Transfer Int J Comput Methodol* Part A: Appl. Vol. 21, No. 2, pp. 231-248.

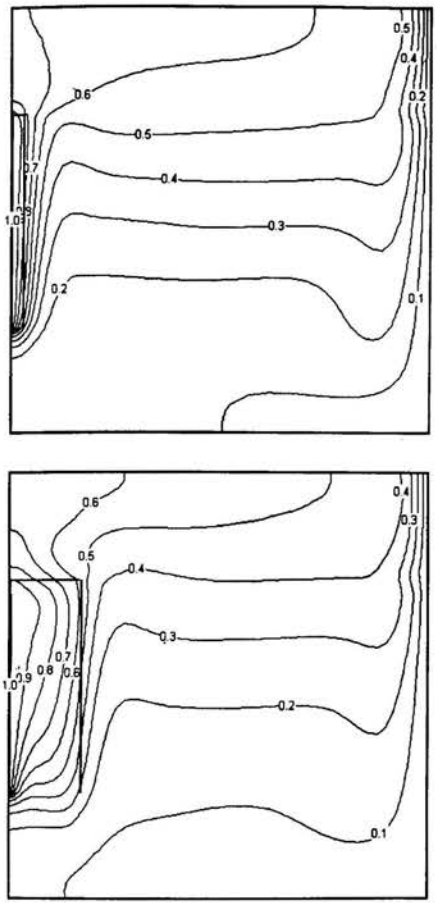

FIGURE 4: ISOTHERM PATTERNS FOR $Ra = 10^6$, $H_B = 0.5$ AND $Q_b = 5$ FOR w_B EQUAL TO 0.04 (TOP) and 0.18 (BOTTOM).

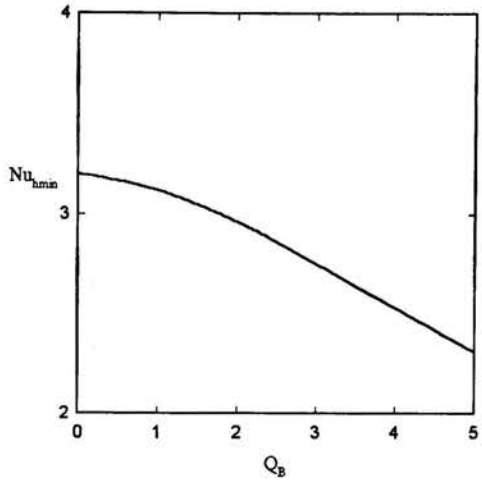

FIGURE 5: VARIATION OF MINIMUM VALUE OF Nu_h WITH Q_B FOR $Ra = 10^6$ AND $H_B = 0.5$.

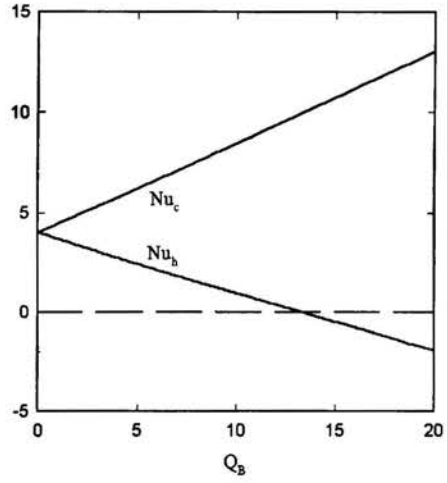

FIGURE 6: VARIATION OF Nu_h WITH Q_B FOR w_B =0.12, $Ra = 10^6$ AND $H_B = 0.5$.

Hanjalic, K., Kenjeres, S. and Durst, F., 1996, "Natural convection in partitioned two-dimensional enclosures at higher Rayleigh numbers", *International Journal of Heat and Mass Transfer*, Vol. 39, No. 7, pp. 1407-1427.

Jayaram, K. Sri, Balaji, C. and Venkateshan, S.P., 1997, "Interaction of surface radiation and free convection in an enclosure with a vertical partition", *Journal of Heat Transfer*, Vol. 119, pp. 641-645.

Karayiannis, T.G., Ciofalo, M. and Barbaro, G., 1992, "On natural convection in a single and two zone rectangular enclosure", *International Journal of Heat and Mass Transfer*, Vol. 35, No. 7, pp. 1645-1657.

Kelkar-Kanchan, M. and Patankar Suhas V., 1990, "Numerical prediction of natural convection in square partitioned enclosures", *Numerical Heat Transfer Int J Comput Methodol* Part A: Appl. Vol. 17, No. 3, pp. 269-285.

Kirkpatrick, A.T, White M.D. and Winn, C.B., 1987, "Numerical study of high Rayleigh number natural convection

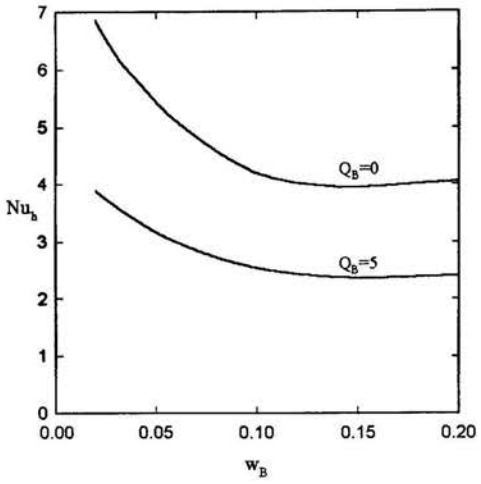

FIGURE 7: VARIATION OF Nu_h WITH w_B FOR $Ra = 10^6$ AND $H_B = 0.75$ FOR TWO VALUES OF Q_B.

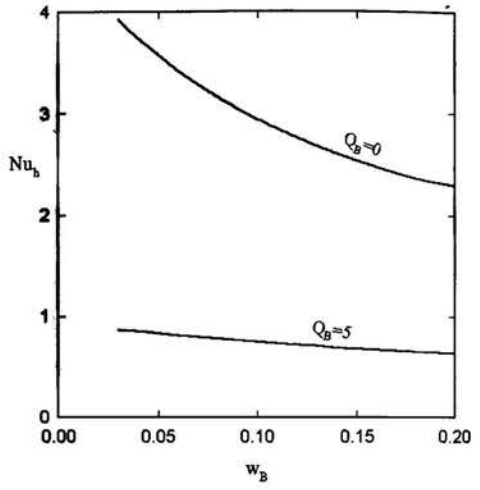

FIGURE 8: VARIATION OF Nu_h WITH w_B FOR $Ra = 10^5$ AND $H_B = 0.75$ FOR TWO VALUES OF Q_B.

flows in partitioned enclosures", *Proceedings of the 1987 ASME-JSME Thermal Engineering Joint Conference*. eds. P.J. Marto and I. Tanasawa, ASME, pp. 327-334.

Machin, A.D., Naylor, D., Harrison, S.J. and Oosthuizen, P.H., 1998, "Experimental study of free convection at an indoor glazing surface with a venetian blind", *International Journal of HVAC&R Research*, Vol. 4, No. 2, pp. 153-166.

Machin, A.D., Naylor, D. and Oosthuizen, P.H., 1997. "An interferometric study of the effect of louvers on free convection from a vertical surface", *Proc. Conf. Experimental Heat Transfer, Fluid Dynamics and Thermodynamics*, pp. 2175-2182.

Olson, D.A., Glicksman, L.R. and Ferm, H.M., 1990, "Steady-state natural convection in empty and partitioned enclosures at high Rayleigh numbers", *Journal of Heat Transfer*, Vol. 112, pp. 640-647.

Oosthuizen, P.H., 1999, "A numerical study of heat transfer across a square enclosure containing a partial dividing wall", *Proceedings of the Sixth UK National Conference on Heat Transfer*, IMechE Conference Transactions 1999-7, pp. 95-100.

Phillips, J., Naylor, D., Harrison, S.J. and Oosthuizen, P.H., 1998, "Free convection from a window glazing with a venetian blind: Numerical Model Development", *Proc. CSME Forum*, Vol. 1, Ryerson Polytechnic Univ., Toronto, pp. 88-95.

Rheault, S. and Bilgen, E., 1990, "Heat Transfer Analysis in an Automated venetian blind window system", *Journal of Solar Energy Engineering*, Vol. 11, pp.89-95.

Shaw, Heiu Jou, Chen Cha' o Kuang and Cleaver, J.W., 1987, "Cubic spline numerical solution for two-dimensional natural convection in a partially divided enclosure". *Numerical Heat Transfer*, Vol. 12, No. 4, pp. 439-455.

Ye, P., Harrison, S.J., Oosthuizen, P.H. and Naylor, D., 1999, "Convective heat transfer from a window with a venetian blind: detailed modeling". *ASHRAE Transactions*, Vol. 105, No. 2.

Zimmerman, E. and Acharya, S., 1987, "Free convection heat transfer in a partially divided vertical enclosure with conducting end walls ", *International Journal of Heat and Mass Transfer*, Vol. 30, No. 2, pp. 319-331.

HEFAT2002
1st International Conference on Heat Transfer, Fluid Dynamics, and Thermodynamics
8-10 April, 2002, Kruger National Park, South Africa,
OP2

NATURAL CONVECTIVE FLOW IN A SQUARE ENCLOSURE WITH A PARTIALLY HEATED WALL AND WHICH IS PARTLY FILLED WITH A HIGH CONDUCTIVITY POROUS LAYER

Patrick H. Oosthuizen
HEAT TRANSFER LABORATORY
Department of Mechanical Engineering
Queen's University, Kingston, Ontario, Canada K7L 3N6, email: oosthuiz@me.queensu.ca

ABSTRACT

In order to assess, in a very basic way, the possibility of using high conductivity porous inserts to enhance heat transfer rates in natural convective flows, a numerical study of natural convective heat transfer across a square enclosure with part of one vertical wall heated to a uniform high temperature and with the opposite vertical wall cooled to a uniform lower temperature and with the remaining wall sections adiabatic has been undertaken. There is a rectangular porous layer adjacent to the vertical wall containing the hot surface, this layer, in general, filling part of the enclosure and with the remainder of the enclosure being filled with pure fluid. The porous layer is assumed to be saturated with this fluid. The flow has been assumed to be laminar and two-dimensional. Fluid properties have been assumed constant except for the density change with temperature that gives rise to the buoyancy forces, this being treated by means of the Boussinesq type approximation. The flow in the porous layer has been treated using the Darcy model. The governing equations have been written in terms of dimensionless variables and the resultant dimensionless equations have been solved using a well-tested finite-difference method. Solutions have been obtained for a Prandtl number of 0.7. The results show that the presence of the porous layer leads to an enhancement of the heat transfer rate in some situations.

NOMENCLATURE

c specific heat
Da Darcy number
H'_h Height of heated surface
H_h Dimensionless height of heated surface
K permeability of porous medium
k thermal conductivity
k_R conductivity ratio
Nu Nusselt number based on W'
Nu_{max} maximum Nusselt number
Pr Prandtl number
$\overline{q_w}$ cold wall mean heat transfer rate
Ra Rayleigh number based on W'
T' temperature
T'_C temperature of cold vertical surface
T'_H temperature of hot vertical surface
T dimensionless temperature
u' velocity component in x' direction
v' velocity component in y' direction
W' width and height of enclosure
w'_p width of porous layer
w_p dimensionless width of porous layer
x' horizontal coordinate
x dimensionless horizontal coordinate
y' vertical coordinate
y dimensionless vertical coordinate
α thermal diffusivity
ν kinematic viscosity
ρ density
ψ' stream function
ψ dimensionless stream function
ω' vorticity
ω dimensionless vorticity

Subscripts

f fluid

p porous layer

INTRODUCTION

The use of porous inserts with a relatively high thermal conductivity to enhance the heat transfer rate from surfaces when there is a forced convective flow has been quite extensively discussed, e.g. see Bhattacharya and Mahajan (2000). When the heat transfer is by natural convection, such porous inserts are often rejected because the high pressure loss associated with the porous insert can lead to a decrease in the flow rate over the surface with the result that there is little enhancement of the heat transfer rate. However, if the thermal conductivity of the porous insert is high and the flow resistance of the insert relatively low this may not be true, i.e., there may be an enhancement of the heat transfer in natural convective flow. In order to assess this possibility in a very basic way, a numerical study of natural convective heat transfer across a square enclosure with part of one vertical wall heated to a uniform high temperature and with the opposite vertical wall cooled to a uniform lower temperature and with the remaining wall sections adiabatic has been undertaken. The heated wall section is centrally placed on the vertical wall. There is a rectangular porous layer adjacent to the hot vertical wall, this layer, in general, filling part of the enclosure and with the remainder of the enclosure being filled with pure fluid. The flow situation being considered is thus as shown in Fig. 1. The porous layer is assumed to be saturated with this fluid.

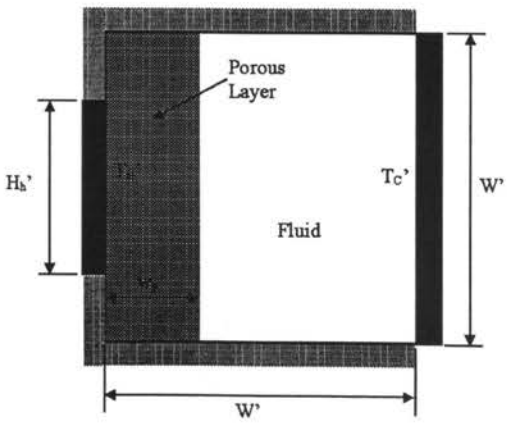

FIGURE 1: FLOW SITUATION CONSIDERED.

There have been a number of previous studies of natural convective heat transfer across enclosures partly filled with a porous layer or with multiple porous layers, e.g, see Poulikakos and Bejan (1983) Beckerman et al. (1986), Naylor and Oosthuizen (1994, 1995, 1996a, 1996b) Oosthuizen (1987, 1995) Oosthuizen and Paul (1987, 1993, 1996a, 1996b) Song and Viskanta (1991) and Tong and Subramaniam (1986). Most of these studies have however been considered situations that arise in the application of insulating materials and do not give results that indicate the effectiveness of porous layers in enhancing heat transfer rates. Preliminary results for the situation here being considered but with the vertical wall fully heated are described by Oosthuizen (2001)

GOVERNING EQUATIONS AND SOLUTION PROCEDURE

The flow has been assumed to be laminar and two-dimensional. Fluid properties have been assumed constant except for the density change with temperature that gives rise to the buoyancy forces, this being treated by means of the Boussinesq type approximation. The porous layer is assumed to be saturated. The solution has been obtained in terms of the stream function, ψ', and vorticity, ω', these being defined as usual by:

$$u' = \frac{\partial \psi'}{\partial y'} \ , \ v' = -\frac{\partial \psi'}{\partial x'} \ , \ \omega' = \frac{\partial v'}{\partial x'} - \frac{\partial u'}{\partial y'}$$

The following dimensionless variables have then been defined:

$$\psi = \psi'/\alpha_f \ , \ \omega = \omega' W'^2/\alpha_f \ , \ x = x'/W' \ ,$$

$$y = y'/W' \ , \ T = (T' - T'_C)/(T'_H - T'_C) \qquad (1)$$

where x' is the coordinate in the horizontal direction, y' is the coordinate in the vertical direction, T' is the temperature, T_H' is the temperature of the hot wall section and T_C' is the temperature of the cold wall. The prime ($'$) denotes a dimensional quantity.

In terms of these dimensionless variables, the governing equations in the fluid region are:

$$\frac{\partial^2 \psi}{\partial x^2} + \frac{\partial^2 \psi}{\partial y^2} = -\omega \qquad (2)$$

$$\frac{1}{Pr}\left(\frac{\partial \psi}{\partial y}\frac{\partial \omega}{\partial x} - \frac{\partial \psi}{\partial x}\frac{\partial \omega}{\partial y}\right) - \left(\frac{\partial^2 \omega}{\partial x^2} + \frac{\partial^2 \omega}{\partial y^2}\right) = Ra\frac{\partial T}{\partial x} \qquad (3)$$

$$\left(\frac{\partial\psi}{\partial y}\frac{\partial T}{\partial x}-\frac{\partial\psi}{\partial x}\frac{\partial T}{\partial y}\right)-\left(\frac{\partial^2 T}{\partial x^2}+\frac{\partial^2 T}{\partial y^2}\right)=0 \qquad (4)$$

Here Ra is the Rayleigh number based on, W', i.e.:

$$Ra=\frac{\beta g(T'_H-T'_C)W'^3}{\nu_f\alpha_f} \qquad (5)$$

and Pr is the fluid Prandtl number ν_f/α_f.

The flow in the porous layer has been treated using the Darcy model except that the viscous shear stress has been retained in the governing equations, i.e., the Brinkman extension of the Darcy model has been used. The governing equations in the porous layer are therefore assumed to be:

$$\frac{\partial^2\psi}{\partial x^2}+\frac{\partial^2\psi}{\partial y^2}=-\omega \qquad (6)$$

$$\left(\frac{\nu_p}{\nu_f}\right)\left[\left(\frac{\partial^2\omega}{\partial x^2}+\frac{\partial^2\omega}{\partial y^2}\right)-\frac{\omega}{Da}\right]=Ra\frac{\partial T}{\partial x} \qquad (7)$$

$$\left(\frac{\partial\psi}{\partial y}\frac{\partial T}{\partial x}-\frac{\partial\psi}{\partial x}\frac{\partial T}{\partial y}\right)-\left(\frac{k_p}{k_f}\right)\left(\frac{\partial^2 T}{\partial x^2}+\frac{\partial^2 T}{\partial y^2}\right)=0 \qquad (8)$$

Here k_p is the effective thermal conductivity of the saturated porous medium and Da is the Darcy number K/W'^2.

The boundary conditions on the solution are that:(i)On all walls: $\psi=0$, $\partial\psi/\partial n=0$; (ii) At $x=0$ on hot wall section: $T=1$; (iii) At $x=1$: $T=0$; (iv) On remaining wall sections: $\partial T/\partial n=0$ where n is measured normal to wall section being considered. Across the interface between the liquid and the porous layers the velocity components, the pressure, the shear stress, the temperature and the heat flux are assumed to be continuous.

The dimensionless equations have been solved using a well-tested finite-difference method. The solutions for the porous and fluid layers were obtained simultaneously using the matching conditions across the interface between the porous and fluid layers, nodal points being selected to lie on this interface. Extensive grid independence and convergence-criteria independence testing was undertaken and this indicates that the results given here are grid and convergence-criteria independent to better than one per cent.

The solution for the temperature distribution allows the local heat transfer rate distributions over the hot and cold surfaces to be determined. The local heat transfer rate distribution can then be integrated to give the mean heat transfer rates for these surfaces. The mean heat transfer rate has been expressed in terms of a mean Nusselt number, Nu, based on W', the overall temperature difference $T_H'-T_C'$ and the thermal conductivity of the fluid, i.e.,:

$$Nu=\frac{\overline{q_w}W'}{k_f(T_H'-T_C')} \qquad (9)$$

Here $\overline{q_w}$ is the mean heat transfer rate for the cold wall and k_f is the thermal conductivity of the fluid.

RESULTS

The solution has the Rayleigh number, Ra, the Darcy number, Da, the Prandtl number, Pr, the dimensionless thickness of the porous layer, w_p, the dimensionless height of the heated surface, H_h, the conductivity ration, $k_R=k_p/k_f$, and the viscosity ratio, ν_p/ν_f as parameters. Results have been obtained here assuming that $\nu_p/\nu_f=1$ and $Pr=0.7$. This leaves Ra, Da and k_p/k_f as parameters. Results are presented here for Ra values between 10^5 and 10^6, Da values between 10^{-3} and 10^{-5}, and k_R values between 1 and 10. In fact, both Da and k_R are dependent on the porosity of the porous medium. Relatively conservative values of k_R have been used here because only the potential for the use of porous layers to enhance natural convective heat transfer rates is being investigated.

Figure 2 shows the variation of Nu with w_p for various values of H_h for a Rayleigh number of 10^6, a Darcy numbers of 10^{-3} and $k_R=10$ while Figs 3 and 4 show the variations of Nu with w_p for two values of k_R for a Rayleigh number of 10^6, a Darcy numbers of 10^{-3} and for H_h values of 0.5 and 1 respectively. With $H_h=1$, the hot wall is fully heated, It will be seen that for the two value of k_R considered, the Nusselt number tends to increase with increasing w_p at the lower values of w_p and then to pass through a maximum and decrease with further increase in w_p until w_p is close to 1 when the Nusselt number again increases towards its porous enclosure value (the value at $w_p=1$). The Nusselt number thus tends to have a maximum for values of w_p between roughly 0.1 and 0.4, this maximum value however being lower than the porous enclosure value. This maximum for relatively small values of w_p is of importance in heat transfer enhancement because it is often not feasible to consider filling the entire enclosure with a porous medium. The maximum at relatively low values of w_p arises basically because while the presence of the porous layer decreases the temperature gradient at the wall, for small porous layer thicknesses the effect of this on the heat transfer rate is more than compensated for by the higher thermal conductivity of the material near the wall and the addition of the

into account the influences of individual draw-offs (user behaviour), temperature setting and climatic conditions.

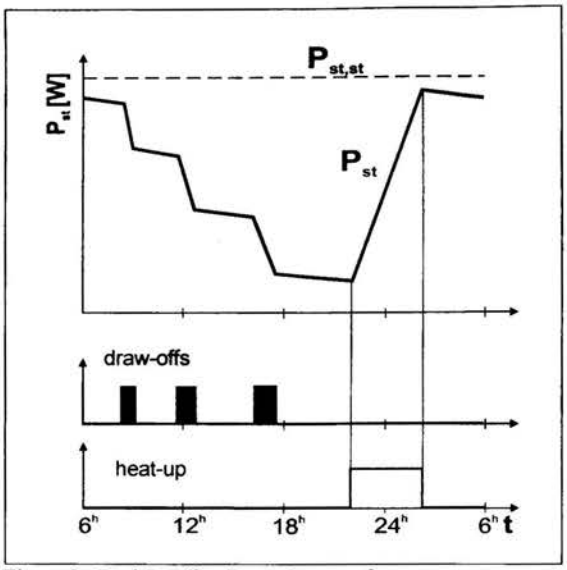

Figure 5: Real Standing Power Losses of a Low Tariff Storage Heater (power on 22...6h)

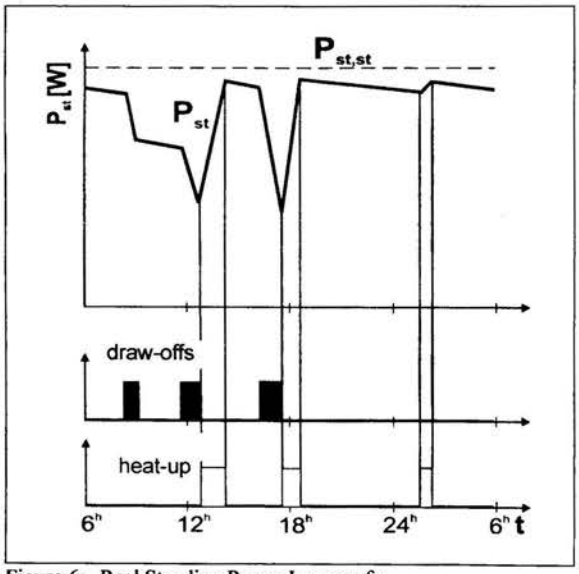

Figure 6: Real Standing Power Losses of a High Tariff Storage Heater (power on 0...24h)

Figure 5 shows the time schedule of draw-offs and its influence on the losses for a low tariff LT storage heater. For storage tanks applying the low tariff the input power is switched off during day time. They are usually switched on by ripple control signals for a period of only 4 to 8 hours per day between 10 p.m and 6 a.m. Therefore, the power losses decrease during draw-offs and increase only in the heat up period during the night.

Figure 6 shows the same time schedule in case of a high tariff (HT) storage heater. Input power is permanently available, thus, the storage tank can be reheated immediately depending on the position of the thermo sensor. As can be seen, power losses of HT heaters are higher than those of the LT storage heaters.

$$L_{st} = \int_0^{24} P_{st}\, dt = f_{real} \cdot L_{st,st} \qquad (3)$$

L_{st} real standing losses [kWh/d]
$L_{st,st}$ standard standing losses [kWh/d]
P_{st} real standing losses [W]
f_{real} real influence factor

The real standing losses L_{st} of the storage tank differ from the above described standard standing losses due to the following reasons:

- other ambient temperature than $T_{amb} = 20$ °C
- other hot water temperature than $T_h = 65$ °C
- real tapping patterns (time schedule of draw-offs)
- heat-up time schedule of the storage tank depending on the tariff system *(high tariff or low tariff)*

Real losses are the basis for the real energy consumption and only these real figures can be used for further economical considerations or an estimation of the real CO_2-emissions. The problem, however, is that the above mentioned real conditions can vary in an extremely wide range due to different usage and environmental conditions. On the contrary, the standard standing losses $L_{st,st}$ are determined by measurement under exactly defined conditions for one stationary heat flow.

To close the missing link between standards and reality, a dynamic simulation model is applied in the following for the calculation of the real losses in dependency of the various tapping patterns, the heat-up time schedules and all other influence factors.

This dynamic model called WATERSIM [1] simulates the dynamic procedure of tapping patterns and re-heating conditions. It provides a detailed calculation of the momentary heat losses P_{st} of the storage tank. For this purpose, it uses a two layer model dividing the tank volume into a upper hot volume and a lower colder volume. Integrating the heat transmission over the hot surface only, the dynamic model allows an correct determination of the real influence factor. The momentary losses are proportional to the remaining hot and warm surface areas of the tank.

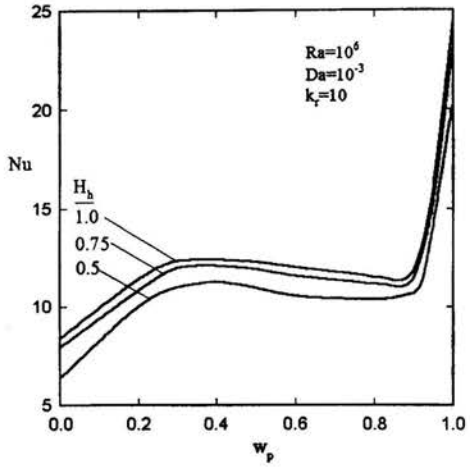

FIGURE 2: VARIATION OF NUSSELT NUMBER WITH DIMENSIONLESS POROUS LAYER THICKNESS FOR VARIOUS HEATED SECTION HEIGHTS FOR $Ra = 10^6$, $k_R = 10$ AND $Da = 10^{-3}$.

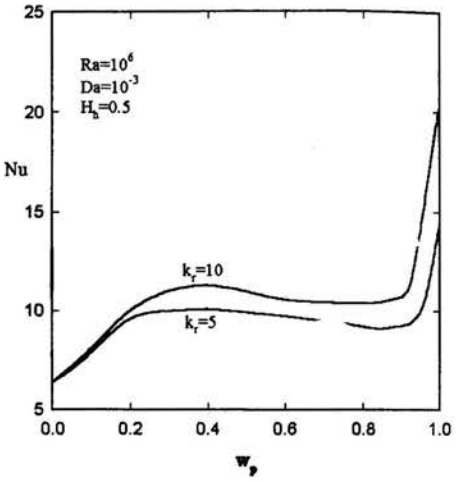

FIGURE 3: VARIATION OF NUSSELT NUMBER WITH DIMENSIONLESS POROUS LAYER THICKNESS FOR TWO VALUES OF k_R for $Ra = 10^6$, $H_h = 0.5$ AND $Da = 10^{-3}$.

porous layer therefore produces a higher heat transfer rate. This is illustrated by the streamline and isotherm patterns shown in Figs. 5 and 6 respectively.

The effect of the Darcy number on the heat transfer rate is illustrated by the results given in Fig. 7. The magnitude of the increase in the heat transfer rate at low values of the porous layer thickness increases with increasing values of Da because the higher the value of Da, i.e., the lower the porosity, the smaller is the alteration of the flow caused by the porous layer near the heated wall and the less the reduction in the temperature gradient at the heated wall.

The results presented above were all for $Ra = 10^6$. To illustrate the effect of Ra, some typical results for $Ra = 10^5$ for k_R of 10 are shown in Fig. 8.

CONCLUSIONS

The use of relatively thin porous layers can produce an enhancement of natural convective heat transfer rates in the situation here considered.

ACKNOWLEDGMENT

This work was supported by the Natural Sciences and Engineering Research Council of Canada.

REFERENCES

Bhattacharya A. & Mahajan R.L., 2000, "Finned metal foam heat sinks for electronics cooling in forcrd convection", Proceedings 2000 National Heat Transfer Conference, Pittsburgh, ASME, Paper NHTC2000-12256.

Beckerman C., Ramadhyani S., & Viskanta R., 1986, "Natural convection flow and heat transfer between a fluid layer and a porous layer inside a rectangular enclosure", Proceedings of AIAA/ASME Fourth Thermophysics and Heat Transfer Conference, Boston, ASME HTD-Vol. 56, pp 1-12.

Naylor D. & Oosthuizen P.H., 1994, "Free convection in an enclosure partly filled with a porous medium and partially heated from below", Proceedings of 10th Int Heat Trans Conference, Brighton, Vol. 5, pp 351-356.

Naylor D. & Oosthuizen P.H., 1995, "Free convection in a horizontal enclosure partly filled with a porous medium", J Thermophysics Heat Transfer 9(no 4):797-800.

Naylor D. & Oosthuizen P.H., 1996a, "Natural convective heat transfer in an enclosure partly filled with a non-porous insulation", Int J Num Meth Heat Fluid Flow 6(no 5):37-48.

Naylor D. & Oosthuizen P.H., 1996b, "A numerical study of the optimum thermal insulation of air spaces", Proceedings of CSME Forum, Hamilton, pp 183-190.

Oosthuizen P.H., 1987, "Natural convection in an inclined partitioned square cavity half-filled with a porous medium", Presented at the ASME National Heat Transfer Conference, Pittsburgh, Paper no ASME 87-HT-15.

Oosthuizen P.H., 1995, "Natural convection in an inclined square enclosure partly filled with a porous medium and

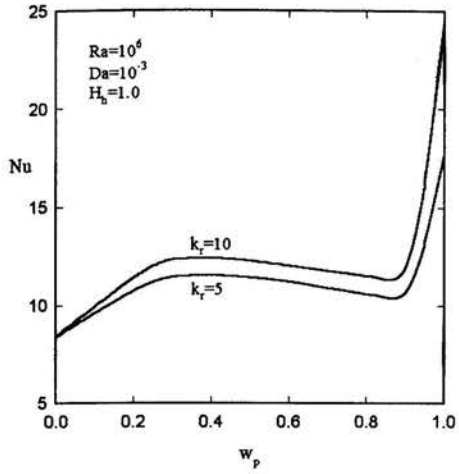

FIGURE 4: VARIATION OF NUSSELT NUMBER WITH DIMENSIONLESS POROUS LAYER THICKNESS FOR TWO VALUES OF k_R for Ra= 10^6, H_h = 1 AND Da = 10^{-3}.

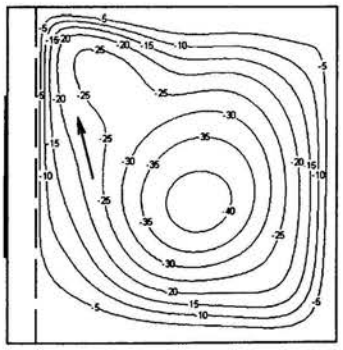

FIGURE 5a STREAMLINE DISTRIBUTION FOR A DIMENSIONLESS POROUS LAYER THICKNESS OF w_p of 0.1, FOR A CONDUCTIVITY RATIO OF 5 FOR $Ra = 10^6$, $H_h = 0.5$, AND FOR $Da = 10^{-3}$.

with a partially heated wall. "Proceedings of ASME Energy Sources Technology Conference and Exhibition, Houston, ASME HTD-302, pp 29-42.

Oosthuizen P.H., 2001, "Free Convective Flow in a Square Enclosure Partly Filled With a High Conductivity Porous Layer", Paper NHTC2001-20171, Proc. 2001 ASME National Heat Transfer Conference, Anaheim, June 10-12, 2001.

Oosthuizen P.H. and Paul J.T., 1987, "Natural convective flow in a square cavity partly filled with a porous medium", Proceedings ASME/JSME Thermal Engineering Joint Conference, Honolulu, 1987, Vol 2, pp 407-412.

Oosthuizen P.H. and Paul J.T., 1993, "Natural convection in a rectangular enclosure with a partially heated wall and partly filled with a porous medium"Proceedings 8th Int Conf on Numerical Methods in Thermal Problems, Swansea, Vol. VIII, Part 1, pp 467-478.

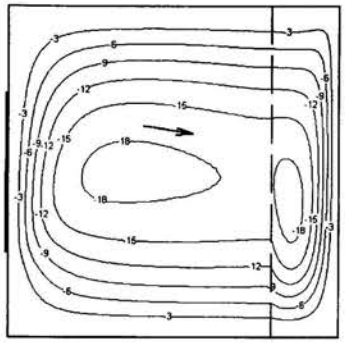

FIGURE 5b STREAMLINE DISTRIBUTION FOR A DIMENSIONLESS POROUS LAYER THICKNESS OF w_p of 0.7 FOR A CONDUCTIVITY RATIO OF 5 FOR $Ra = 10^6$, $H_h = 0.5$, AND FOR $Da = 10^{-3}$.

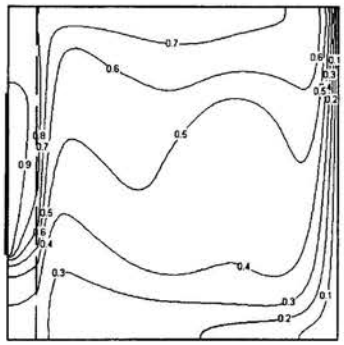

FIGURE 6a ISOTHERM DISTRIBUTION FOR A DIMENSIONLESS POROUS LAYER THICKNESS OF w_p of 0.1, FOR A CONDUCTIVITY RATIO OF 5 FOR $Ra = 10^6$, $H_h = 0.5$, AND FOR $Da = 10^{-3}$.

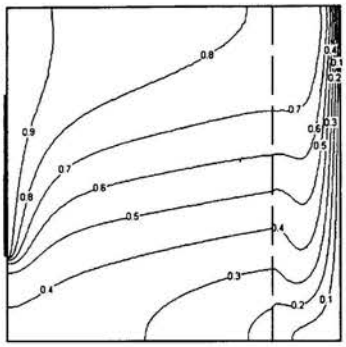

FIGURE 6b ISOTHERM DISTRIBUTION FOR A DIMENSIONLESS POROUS LAYER THICKNESS OF w_p of 0.7, FOR A CONDUCTIVITY RATIO OF 5 FOR $Ra = 10^6$, $H_h = 0.5$, AND FOR $Da = 10^{-3}$

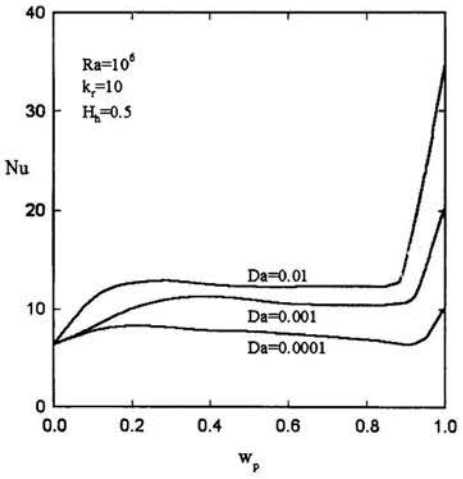

FIGURE 7: VARIATION OF NUSSELT NUMBER WITH DIMENSIONLESS POROUS LAYER THICKNESS FOR VARIOUS VALUES OF Da for Ra= 10^6, H_h = 0.5 AND k_R = 10.

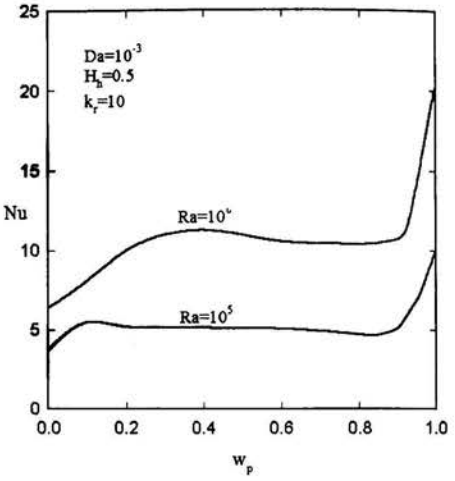

FIGURE 8: VARIATION OF NUSSELT NUMBER WITH DIMENSIONLESS POROUS LAYER THICKNESS FOR TWO VALUES OF Ra for k_R= 10, H_h = 0.5 AND Da = 10^{-3}

Oosthuizen P.H. and Paul J.T., 1996a, "Natural convection in a square enclosure partly filled with two layers of porous material", Proceedings Fourth International Conference on Advanced Computational Methods in Heat Transfer, Udine, pp 63-72.

Oosthuizen P.H. and Paul J.T., 1996b, "Natural convection in a square enclosure partly filled with a centrally positioned porous layer and with a partially heated wall", Proceedings 2nd Thermal-Sciences and 14th UIT National Heat Transfer Conference, Rome, Vol. 2, pp 851-856.

Poulikakos D. & Bejan A., 1983, "Natural Convection in a Vertically and Horizontally Layered Porous Media Heated From the Side", Int. J. Heat and Mass Transfer, Vol. 26, pp 1805-1813.

Song M & Viskanta R., 1991, "Natural convection flow and heat transfer between a fluid layer and an anisotropic porous layer within a rectangular enclosure", Proceedings ASME Winter Annual Meeting, Atlanta, ASME HTD-177, pp 1-12.

Tong T.W. & Subramaniam E., 1986, "Natural Convection in Rectangular Enclosures Partially Filled With a Porous Medium", Int. J. Heat and Fluid Flow, Vol. 7, pp 3-10.

HEFAT2002
1st International Conference on Heat Transfer, Fluid Mechanics, and Thermodynamics
8-10 April 2002, Kruger Park, South Africa
BM1

Critical Buckling Temperature in Composite Plates

Stuart Wylie, Graduate Student
Masoud Bagheri, Research Associate
Suresh Chandra, Research Professor
NASA-CAR, College of Engineering
North Carolina Agricultural and Technical State University
1601 East Market Street, Greensboro, NC 27411
Email: Chandra@ncat.edu

ABSTRACT

Temperature distribution and thermal buckling analyses were performed on square composite plates with central cutouts exposed to a uniform temperature increase. The cutouts were square holes. Analysis shows buckling temperatures generally increase with hole size. The results show that introducing appropriately sized holes in a composite plate can actually increase its thermal buckling strength and at the same time reduce the weight of the panel.

INTRODUCTION

Buckling may adversely affect structural performance and lead to significant performance penalties [1]. For example, if the Space Shuttle Orbiter were exposed to excessive buckling of the aluminum skin, debonding of the tiles used in the thermal protection system (TPS) could occur. This can lead to a failure of the TPS, which could have catastrophic results [2]. In hypersonic flights, aerodynamic heating can cause non-uniform temperature distributions, induce thermal stresses and cause thermal buckling. Critical compressive stresses can build up in panels due to non-uniform temperature distributions [3]. Uniform temperature distributions under clamped edge conditions and coefficient of thermal expansion (CTE) mismatches in composite materials can also induce thermal stresses that can cause buckling. Definition of edge constraints is another significant problem when modeling the aforementioned buckling. While modeling tends to be done with either fixed or free boundaries, the actual restraint often lies somewhere between a simply supported panel and a clamped panel, thus creating difficulty in the proper modeling for a finite element analysis [4].

Material properties are affected by temperature and generally increase the probability of buckling [5] as temperature increases. With temperature dependent properties, it then becomes necessary to perform material property iterations to determine the most accurate critical buckling temperature in an analysis.

Thermal stresses found in simply supported composite plates are due to temperature gradients found within the material and/or CTE mismatches between the fiber and the matrix [6] or tangential and longitudinal differences in CTE between lamina in a cross-ply laminate. Clamped edge composite plates will buckle due to these conditions as well as to uniform temperature increases.

DESCRIPTION OF THE PROBLEM

The geometry of the perforated plates to be studied is shown in Figure 1. All plates are assumed to be perfectly flat initially. The basic configuration is a plate with a central square cutout. Analysis was done on plates having a length l, width w, total laminate thickness t, individual lamina thickness t', and square central cutout of side length c. An aspect ratio (l/w) of 1.0, 1.5, and 2.0 was used for each cutout size and fiber orientation. A range of cutout sizes was considered from c/w = 0.00 (no hole case) to c/w = 0.70 in 0.05 increments. The plates used in this analysis have width w = 20 inches, laminate thickness t = 0.064 inches and lamina thickness t' = 0.008 inches. Table 1 summarizes the physical dimensions used in each case.

Two fiber orientation schemes were used in the analysis. All fiber orientation angles are measured counterclockwise positive from the positive x-axis. Models 1 and 2 consist of $[90/0/0/90]_2$ and $[45/-45/-45/45]_2$ laminations respectively. The composite plates were assumed to consist of eight perfectly bonded layers with no debonding of the matrix and fibers in any of the lamina layers. The square hole geometry was chosen because it has been shown to exhibit higher critical thermal buckling temperatures than plates with a circular hole geometry [7]. This geometry adheres to the

models used by Ko [8] for comparison with mechanical buckling load data.

The plate material used is a standard titanium matrix composite (TMC) with two different fiber orientation schemes. The material properties used are for a silicon carbide silicon fiber reinforced titanium alloy matrix (SCS-6/Ti-15-3) [9]. Material properties for the TMC used are shown in Table 2.

Mechanical constraints were applied to each plate. For the purposes of this work, it was assumed that all four outer edges of each plate were clamped. The plate was considered to be in the x-y plane and the z-rotation was restricted. Each plate was then subjected to a uniform increase in temperature (ΔT) across the entire plate.

FINITE ELEMENT ANALYSIS

A finite element analysis was performed using STARS (STructural Analysis and RoutineS), developed at NASA Dryden Research Center [10]. The models shown in Figure 1 were modeled in STARS as a quarter plate making use of the symmetry about the x and y axes.

Due to changes in the value of the material properties as a function of temperature, the critical buckling temperature ΔT_{cr} would have to be solved for iteratively. If ΔT_{cr} was not within an acceptable temperature range of the material properties, the iteration process would be repeated until the value of the calculated ΔT_{cr} falls within an acceptable range [7].

Validation of the numerical results uses the modified Timoshenko solution. This method is based on a simply supported plate with fixed edges (no in-plane translational motion). Using the modified Timoshenko solution for the no hole case, it can be seen in Table 3 that the percent error is quite small.

EFFECT OF HOLE SIZE

Figures 2a-2c show ΔT_{cr} (change in critical buckling temperature above the reference temperature of 70°F) as a function of *c/w* (cutout size) for both the TMC fiber orientations under each plate aspect ratio.

The symmetric and antisymmetric buckling temperatures each exhibit similar shapes for both fiber orientations. It was observed that the antisymmetric buckling modes appeared at a lower temperature than the symmetric mode for a given range of moderately large cutout sizes for most of the plate cases studied. As cutout sizes increase, the critical buckling temperature increases for both materials. This increase in buckling temperature with the increase in cutout size does not seem to be intuitive, however in this case, anomalous behavior is observed as was the case with the work of Ko [8]. Conventional wisdom says that as the plate loses more material, it becomes weaker. Therefore, a larger hole should decrease the buckling temperature. However, increases in the buckling temperature are observed for larger hole sizes. This effect could be explained as follows. As the hole size increases, most of the thermal load is carried by the narrow side strips of material along the edges of the plate. While the clamped edge boundary condition increases the buckling strength, the stress concentration can reduce the buckling strength. Square holes tend to produce fairly uniform stress fields, thus allowing the clamped edge effect to dominate. This in turn, increases the buckling temperature for larger hole sizes [7,8]. As the hole size increases, the bending moments along the centerline of the plate decrease. This requires a larger force, i.e., larger temperature difference to produce the same effect.

EFFECT OF FIBER ORIENTATION

Figures 2a-2c show essentially the same buckling temperature pattern for both fiber orientations in all three plates aspect ratios. Fiber orientation can affect the critical buckling temperature, however, the effect appears to be minimal as the critical buckling temperatures only varied by a few degrees at most. The maximum difference due to fiber orientation is less than 5.85 percent. These results lead to the conclusion that while fiber orientation has been shown to have an effect on mechanical buckling [8], it has no appreciable effect on the critical buckling temperature under the given conditions.

EFFECT OF ASPECT RATIO

Plate aspect ratio can be seen to be a key factor in the critical buckling temperature of plates. Figures 2a-2c show that as the aspect ratio decreases, the critical buckling temperature increases. This holds true for all fiber orientations and cutout sizes.

Figure 3 shows the mode 1 symmetric buckling curves for all three aspect ratio plates. Here it can be seen that square plates (aspect ratio = 1.0) have the highest critical buckling temperatures of the three aspect ratios studied. This advantage is most pronounced for the larger cutout sizes.

CONCLUSIONS

The effects of cutout size, plate aspect ratio and composite fiber orientation on the buckling temperature of various plates have been observed to verify the following conclusions.

- Increasing the cutout size initially results in a slightly lower critical buckling temperature, but as the cutout size increases, the critical buckling temperature increases significantly.
- Plates with an aspect ratio of 1.0 provide higher critical buckling temperatures than plates with higher aspect ratios.
- The cutout size can cause antisymmetric buckling modes to appear in a range of moderately large cutout sizes. As the cutout size increases, the symmetric and antisymmetric modes tend to converge.
- The increase in buckling temperature with the increase in cutout size does not seem to be intuitive, however, this anomalous behavior allows for weight reduction and improved thermal buckling performance.
- The critical buckling temperature is not affected significantly by fiber orientation for the two orientations used.

- By applying the methods used in this analysis, aircraft structural members can be optimized for weight, strength, and thermal buckling tolerance.
- Removing material from the center of flat plates can result in weight savings and at the same time increase the thermal buckling temperature of the plate. Both of these benefit the aerospace industry in the area of hypersonic flight and point out the possible implications TMCs have for the future.

Table 1. Composite Plate Physical Dimensions

w, in.	*t, in.*	*t', in.*	*l/w*	*c/w*
20	0.064	0.008	1.0	0.00~0.70
20	0.064	0.008	1.5	0.00~0.70
20	0.064	0.008	2.0	0.00~0.70

Table 2. TMC Material Properties

E_L, 10^6 lb/in^2	E_T, 10^6 lb/in^2	G_{LT}, 10^6 lb/in^2	ν_{LT}	$\alpha_L=\alpha_T$, 10^{-5} (in/in·°F)	ρ, 10^{-3} (lbm/in^3)
27.72	18.09	8.15	0.3	0.1	0.3753

Table 3. Validation of ΔT_{cr} Numerical Results

Aspect Ratio	Numerical Result	Analytical Result	Percent Error
1.0	12.985328	12.957019	0.218
1.5	9.599750	9.357847	2.585
2.0	8.459723	8.098137	4.465

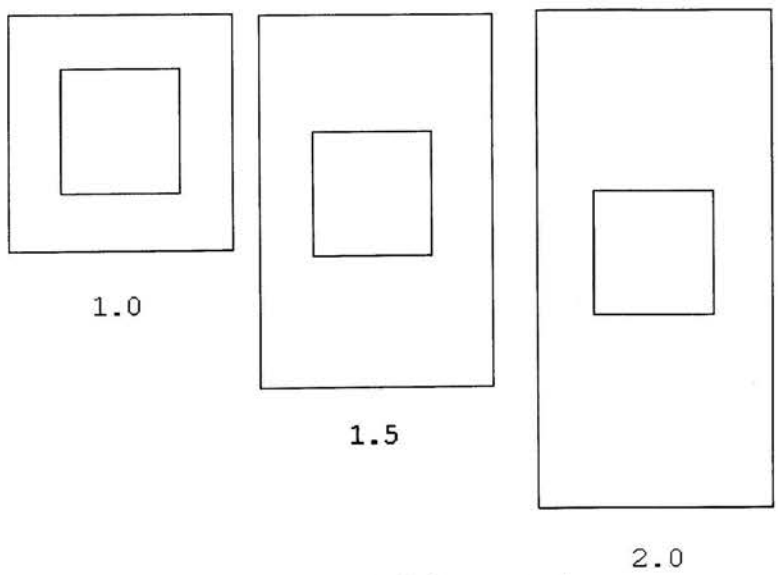

Figure 1: Plate model with three aspect ratios

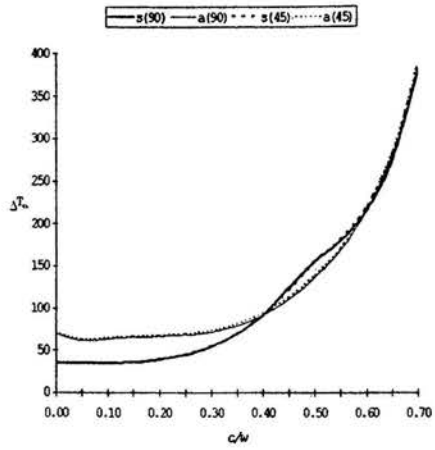

Figure 2a: Symmetrical (s) and Antisymmetrical (a) ΔT_{cr} vs. Cutout size (l/w = 1.0)

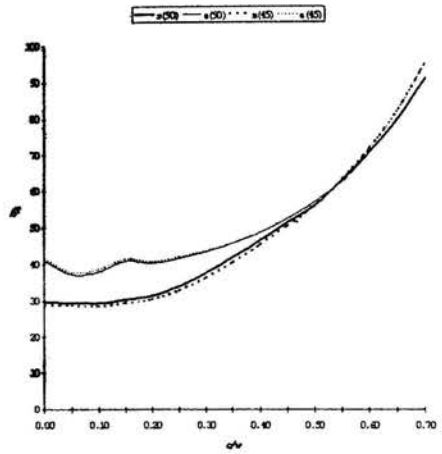

Figure 2b: Symmetrical (s) and Antisymmetrical (a) ΔT_{cr} vs. Cutout size (l/w = 1.5)

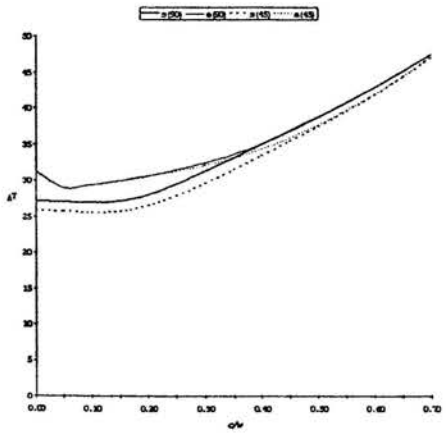

Figure 2c: Symmetrical (s) and Antisymmetrical (a) ΔT_{cr} vs. Cutout size (l/w = 2.0)

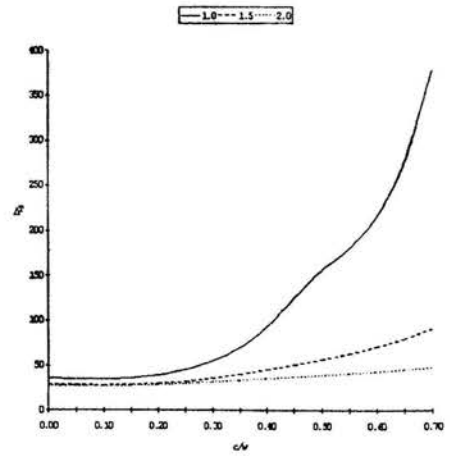

Figure 3: Mode 1 symmetrical buckling ΔT_{cr} vs. Cutout size (l/w = 1.0, 1.5, 2.0)

REFERENCES

1. Gossard, M., Seide, P., Roberts, W., *Thermal Buckling in Plates*, NACA TN 2771, August 1952
2. Ko, W.L., Quinn, R.D., Gong, L., *Effect of Internal Convection and Internal Radiation on the Structural Temperatures of Space Shuttle Orbiter*, NASA-TM-100414, October 1988
3. Ko, W.L., *Thermostructural Behavior of a Hypersonic Aircraft Sandwich Panel Subjected to Heating on One Side*, NASA TM 4769, April 1997
4. Jenkins, J.M., *The Effect of Thermal Stresses on the Integrity of Three Built-up Aircraft Structures*, NASA TM 81352, November 1980
5. Dryden, H., Duberg, J., *"Aeroelastic Effects of Aerodynamic Heating"*, Proceedings of the Fifth AGARD General Assembly, June 1955
6. Taya, M., Arsenault, R.J., *Metal Matrix Composites Thermomechanical Behavior*, Pergamon Press Inc., Elmsford NY 1989
7. Ko, W.L., *Mechanical and Thermal Buckling Behavior of Rectangular Plates With Different Central Cutouts*, NASA TM 1998-206542, March 1998
8. Ko, W.L., *Anomalous Buckling Characteristics of Laminated Metal-Matrix Composite Plates with Central Square Holes*, NASA/TP-1998-206559, July 1998
9. Ko, W.L., Jackson, R., *Combined-Load Buckling Behavior of Metal-Matrix Composite Sandwich Panels Under Different Thermal Environments*, NASA TM 4321, September 1991
10. Gupta, K.K., *STARS – An Integrated, Multidisciplinary, Finite Element, Structural, Fluids, Aeroelastic, and Aeroservoelastic Analysis Computer Program, NASA TM 4795, May 1997*

HEFAT2002
1st International Conference on Heat Transfer, Fluid Mechanics, and Thermodynamics
8-10 April 2002, Kruger Park, South Africa
CB1

INVESTIGATION OF TURBULENT FLOW IN PHARMACEUTICAL PIPE TEE-JUNCTIONS

Mr Brian G. Corcoran, Dr. Harry Esmonde and Prof M.S.J.Hashmi

Mechanical and Manufacturing Engineering
Dublin City University, Glasnevin
Dublin 9
Rep of Ireland

ABSTRACT

The problem of piping system dead-legs are frequently encountered in high purity water systems throughout the pharmaceutical and semi-conductor industries. The installation of a pipe tee in sterile process pipework often creates a stagnant dead-leg zone which can result in the formation of bio-film and compromise the entire system. Considerable basic research is required to address the lack of understanding of this problem and to assist during design, manufacture, installation and operation of these critical systems. This research involves the application of CFD (computational fluid dynamics) techniques to study of turbulent flow and also dead-leg flow in pharmaceutical pipe tee-junctions.

A numerical model has been developed to study turbulent flow in a 50mm diameter 90° pharmaceutical tee-junction during divided flow conditions and also under dead-leg flow conditions. Numerical predictions were compared with previously presented experimental results based on Laser Doppler Velocimetry (*Sierra-Espinosa et al, 1997*) where static pressure distributions were used as exit boundary conditions. The Reynolds-Stress Model was used to analyse the complex flow patterns. A back flow region was found in the branch of the divided flow configuration. Regions of low turbulence were identified within the dead-leg branch. The wall region, which is critical to bio-film formation in the pharmaceutical industry, was also found to be a region of low velocity under dead-leg conditions and of low shear stress providing conditions conducive to bio-film formation. Measurements in both the branch and straight through legs indicate that the flow is highly complex and the most consistent results are found using the RSM model.

INTRODUCTION

Stainless steel pipe tees are employed extensively and play an important role in power plants, chemical plants, dairy and in particular the semi-conductor and pharmaceutical industries. High quality process tubing and fittings were developed to meet the needs of the highly regulated pharmaceutical and biotechnology industry. Increased quality demands have recently been accompanied by rigorous validation procedures in these areas. These tubes and fittings (including tee-junctions) create the processing environment of many of these processes the inner surface of which are in contact with the process fluid. These surfaces must be smooth, corrosion free and without dead-legs which can entrap harmful bacteria.

The formal definition of a pipe dead-leg, as given by the Food and Drug Administration in GMP (LVP) Sect 212.49 CFR21 1972, requires that;

'Pipelines for the transmission of purified water for manufacturing or final rinse should not have an unused portion greater in length of 6 diameters (the 6d rule) of the unused portion of pipe measured from the axis of the pipe in use' (see Fig. 1)

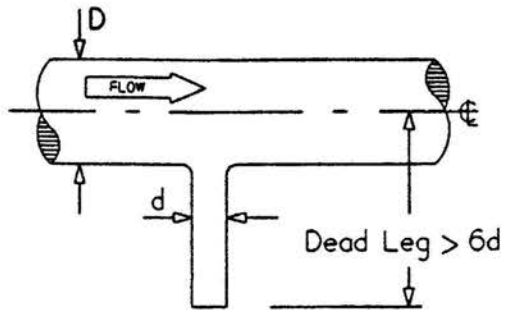

Figure 1. Classic dead-leg configuration

Dead legs are a misunderstood problem in high purity water systems and much confusion exists within industry related to this topic. The FDA suggest the above 6d rule, however industrial experts are designing systems with dead legs limited to 3d or less. Some systems and fittings claim to have zero dead legs. The result of this confusion is an escalation in design and manufacture cost within an already highly expensive industry.

Manufactured from 316L stainless steel these fitting have low carbon content (<0.035%) which eliminates carbide precipitation during welding. Class AA fittings are generally specified for use in high purity applications including Water for Injection (WFI) systems and have an internal finish of 0.5μm to 0.25μm Ra. This is achieved following mechanical and/or electro-polishing. The problem of piping system dead-legs is frequently encountered in high purity water systems throughout the pharmaceutical and semi-conductor industries. The installation of a pipe tee in sterile process pipework often creates a stagnant dead-leg zone. The current literature contains few detailed reports related to dead-legs caused by the installation of pipe tee-junctions in these high purity water systems. Problems arise due to the following

1) Dividing flow through the pipe tee (50/50)
2) Full flow through the tee branch
3) Full flow across the top of the tee

Problems 1 and 3 will be addressed in this publication while results related to problem 2 were considered to be outside the scope of this paper.

Ito and Imai (1973), Miller (1978) and Hager (1984) provide detailed reports of loss coefficients associated with flow through 90° tee-junctions. These relate to dividing flow through both right angled and short radius corner tees between the inlet and straight through legs of the tee and the branch. Pollard (1981) investigated flow in a symmetrical uniformly dividing tee-junction with equal area exit legs and a wedge shaped inlet duct. He found that due to symmetry in the flow minimum time and computer resources were necessary during modelling. Kired et al (1975) identified a closed region of reversed flow in dividing tees with rounded corners. Karino et al (1979) noted that the use of a sharp edged tee increased the vorticity within the branch of the tee.

Bates et al (1995) used Laser Doppler Anemomerty (LDA) measurements to study flow in a 90° tee-junction. The branch to inlet flow rate ratio of this study was unity. Highest velocities were found adjacent to the down stream wall of the branch and details were provided on the size and strength of the branch recirculation zone. Numerical comparisons made between the k-e, RNG and RSM turbulent models in FLUENT V4.2 found that the most consistent results were achieved using the RSM model. Recent work by Sierra-Espinosa et al (1997) studied dividing flow of water at high Reynolds Number in a 50mm diameter equal tee-junction. Numerical predictions were compared with experimental results based on LDA measurements. Static pressure distributions were used as exit boundary conditions and separation and recirculation regions presented. Again the RSM model was found to be the most consistent model in analysing tee-junction flow.

To date the authors have found little published data related to the problem of piping system dead-legs. This configuration arises when the branch exit of the tee is closed off often by use of an isolating valve. Research data presented in this report will investigate the problem of divided flow through an equal branch tee and then study the effects induced by closing the branch valve fully (ie a classical dead-leg configuration).

NOMENCLATURE

d	Diameter of the tee Junction
Q1/Q3	Ratio of branch exit to inlet flow rate
r	Radius of curvature of tee
u	mean axial velocity
u_x	bulk velocity at inlet of the tee
Re	Reynolds number
X	Streamwise co-ordinate in x-direction
Y	Streamwise co-ordinate in y-direction

COMPUTATIONAL MODELLING

The computational model used in this report was developed within the latest version of FLUENT CFD software (version 5.5). Construction, preprocessing and meshing of the model was carried out using FLUENT'S current preprocessing package GAMBIT 1.3. The model was developed using recently published data by Sierra-Espinosa et al (1997). This research offered detailed analysis of divided flow within a 50mm pipe tee. A Section of the grid developed to represent the 90° tee is presented in Figure 2. Careful consideration was given to decomposition of the grid to reduce numerical diffusion and to accurately model the geometry used in this investigation. The mesh quality was evaluated within Gambit and found to be well within current guidelines for Aspect Ratio, EquiAngle Skew etc (Figure 3). This ensured that profiles verified experimentally by the use of Laser Doppler Anamometry and by individual pressure measurement by Sierra-Espinosa were valid as boundary conditions within the current model (Figure 4).

The boundary conditions at the inlet of the pipe junction were set up with velocity profiles from the LDA measurements at x/D= -2 (ie 100mm upstream of the branch). Measured static pressure distributions were entered as individual pressure boundary conditions in the straight through leg and the branch exit. The tee junction internal diameter was 50mm and the branch radius 12.5mm. Flow conditions included a Reynolds number of $1.26*10^5$ based on an inlet velocity of 2.56m/s. The ratio of branch to inlet flow rate for divided flow was set to 0.5 with dead-leg flow flow conditions resulting in a straight through to inlet flow rate ratio of 1. Fluent's default values were used for all empirical constants and the pipe radius declared as the characteristic length. The convergence criteria was set for each residual to $1x10^{-4}$

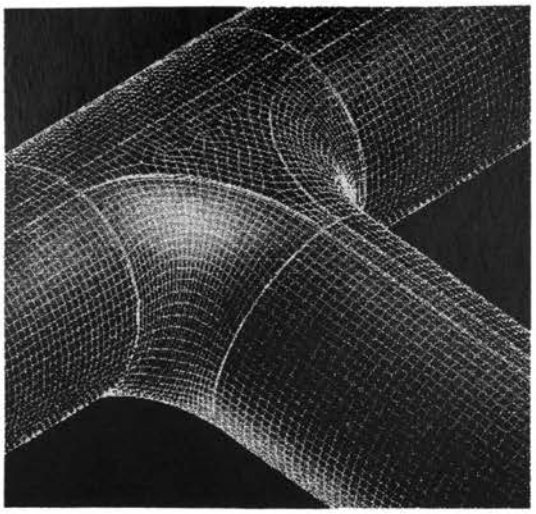

Figure 2: Computational grid developed in Gambit

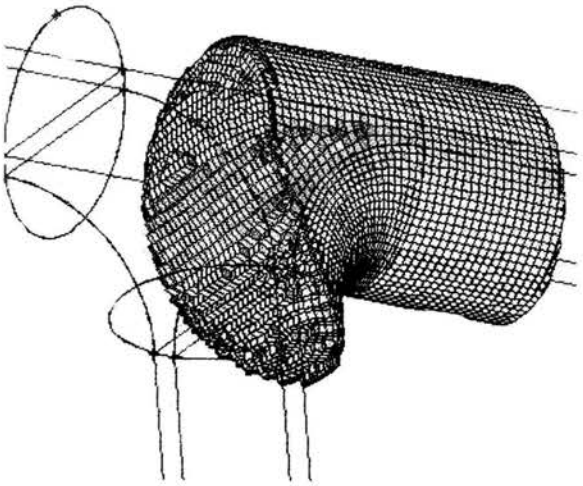

Figure 3: Mesh Quality Analysis within Gambit

Numerical predictions were conducted within the FLUENT V5.5 CFD package. This package accommodates a range of turbulence models. These include the standard k-ε model, the Renormalisation k-ε model, the Realisable k-ε model and the Reynolds Stress Model. Following numerous trials and using experimental results of Bates and Sierra-Espinosa (1997) the Reynolds Stress Model was found to accurately predict the flow field. All the k-ε models had difficulty predicting flow profiles particularly in regions of high swirl, deficiencies which have been well documented by previous researchers (Martin and Bates, 1992). The co-ordinate system of the tee was set up with respect to the centre of the tee junction (denoted as 0,0,0) and all distances have been measured in positive and negative directions from this point (Figure 5).

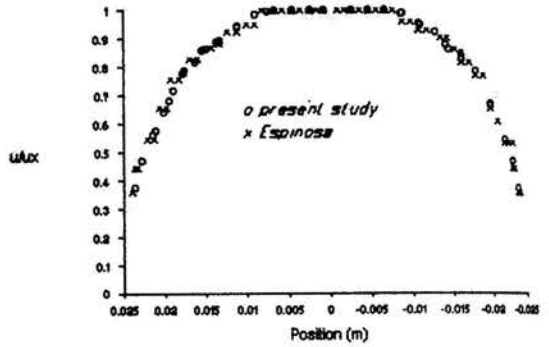

Figure 4: Inlet velocity profile

BRANCH ANTICIPATION AND VELOCITY PROFILES

Analysis of the velocity profiles as the fluid approaches the tee branch (Figure 6) indicate that the flow anticipates the branch during divided flow. The fluid was found to accelerate towards the branch in the region between y/D = -0.2 to +0.4. When dead-leg flow conditions were induced, by preventing flow through the branch, the inlet velocity profile retained its initial profile with a slight anticipation within the branch wall region. A gradual acceleration along the wall of the branch was noted indicating a slight penetration of the flow from the main pipe into the branch.

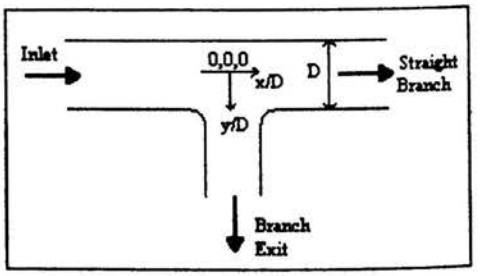

Figure 5: Tee-junction co-ordinate system

Figures 7 and 8 present velocity contours for divided and dead-leg flows respectively along the centreline of the tee. Figures 11 and 12 illustrate velocity contours within the branch of the tee. Analysis of the divided flow contours indicate that the inlet velocity profile is maintained along the length of the inlet section

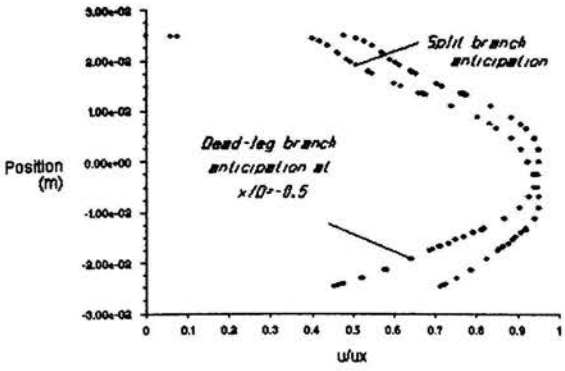

Figure 6: Branch anticipation for divided and dead-leg flow

of the tee apart from some branch anticipation acceleration as the fluid approaches the upstream radius of the branch. A separation region emanating from the upstream branch wall can be identified, as the highly strained fluid flows into the branch. A stagnation point was also found on the downstream branch wall at x/D = 0.5 along with a region of low flow in the straight through branch. By preventing flow through the branch leg a flow induced cavity was created in the dead leg. Fluid from the main straight through pipe enters the branch to a depth of the radius of curvature of the branch inlet. The stagnation point moves further into the branch for this configuration again to a depth of the radius of curvature.

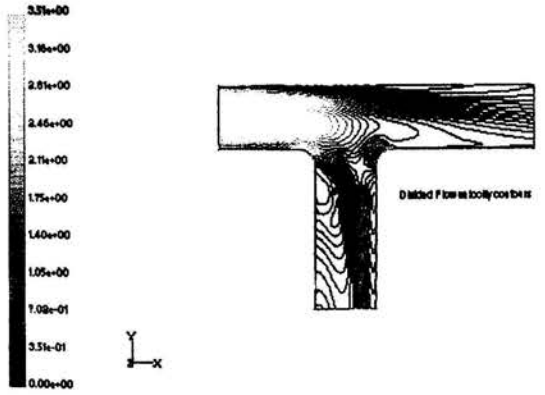

Figure 7: Divided flow velocity contours

The fluid separates around the stagnation point. Fluid above the stagnation point re-enters the main pipe flow. Fluid below the stagnation point impacts the downstream wall of the branch dead-leg and flows down the wall into the cavity. Some of the fluid was found to bounce off the wall and contribute to a region

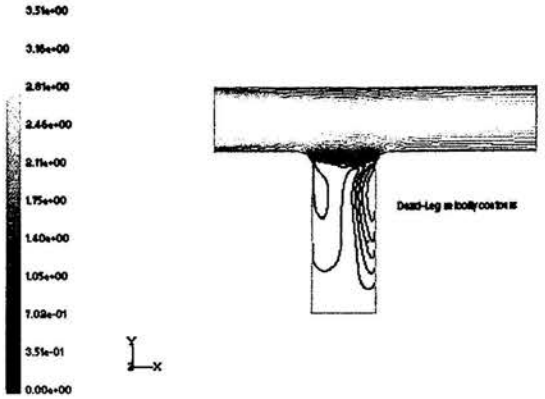

Figure 8: Dead-leg velocity contours

of high swirl adjacent to and below the stagnation point (Figure 13). Typical fluid flow within the dead-leg included flow down the branch wall, across the branch exit and up the upstream branch wall. This pattern induced a slow rotating cavity within the dead-leg. Maximum velocities of 0.58m/s were noted along the downstream wall of the branch while upstream wall velocities peaked at 0.23m/s.

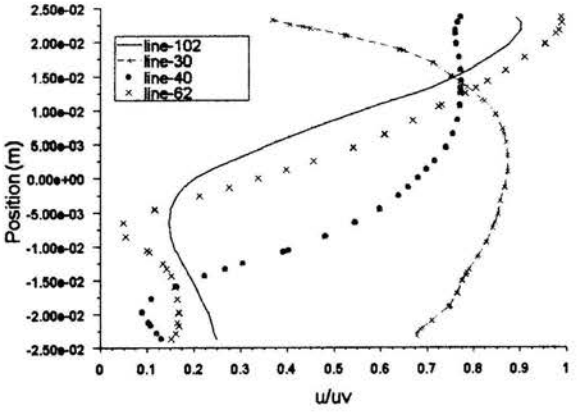

Figure 9: Divided flow branch velocities at 30, 40, 62 and 102mm into the branch

The mean axial velocity profiles across the branch centerline plane from y/D = 0.6 to y/D = 2.04 are shown in Figures 9 and 10 for divided flow and dead-leg flow respectively . For divided flow it is evident that the flow separates at the entrance to the branch creating a reverse flow region. Outside this region the flow was found to accelerate to a maximum of 3.3m/s and then decelerate to zero on the downstream wall of the branch. Analysis of velocity profiles within the branch indicate that

high velocities are maintained on the downstream side of the branch. The separated flow region was found to almost reach the centreline of the pipe. Reattachment of the flow was found to occurs at y/D = 1.6. Following the introduction of a dead-leg configuration the separated flow region was eliminated at the entrance to the branch. Fluid from the main pipe was found to enter the branch only slightly giving rise to a ripple effect. This ripple effect was noted across the top of the branch as fluid was prevented from entering the branch by fluid already within the dead-leg. This ripple effect coupled with fluid separation around the stagnation point induced a region of swirl or a small vortex between the centreline of the dead-leg and the branch downstream wall. Maximum velocities on the downstream side of this region were 0.23m/s and on the upstream side 0.117m/s.

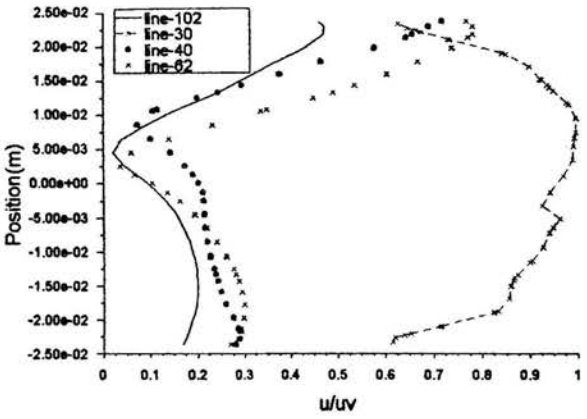

Figure 10: Dead-leg branch velocities at 30, 40, 62 and 102mm into the branch

The higher values on the downstream side may be attributed to reflection form the branch wall. Velocities at the base of the dead leg were found to be 0.0003m/s indicating little, if any, movement.

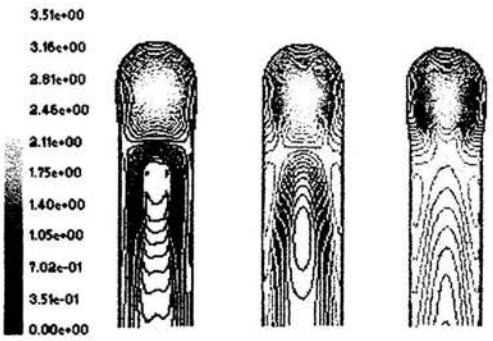

Figure 11: Divided flow branch velocity profiles at -10, 0 and +10mm across the branch

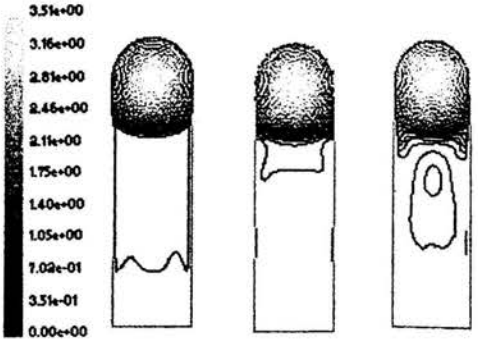

Figure 12: Dead-leg branch velocity profiles at -10, 0 and +10mm across the branch

Apart from the vortex region mentioned above, movement within the dead-leg was divided approximately along the centreline of the branch. Fluid on the downstream side of the dead-leg flowed down into the dead-leg with a reversal of patterns occuring on the upstream side. Higher velocities were clearly noted on the down stream side of the dead-leg.

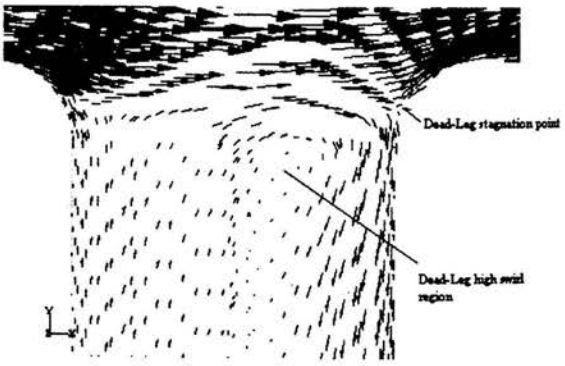

Figure 13: Dead-leg high swirl region and separation point

WALL SHEAR STRESS

Figure 14 presents data related to upstream and downstream wall shear stress for divided and dead-leg flows. Analysis of the data indicated that maximum values of wall shear stress are achieved on the down stream wall of the branch during divided flow. A maximum value of 35Pa is achieved 25 mm into the branch decreasing to 25Pa as the fluid flows further into the tee junction. On the upstream wall lower levels of 1 to 2Pa were noted with the shear stress reaching zero at the reattachment point of y/D = 1.6.

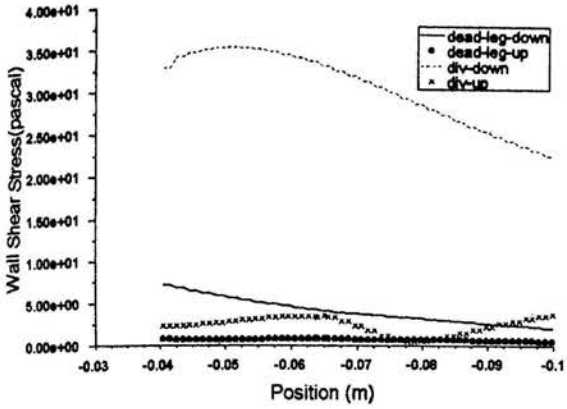

Figure 14. Upstream and downstream wall shear stress for divided and dead-leg flow.

In contrast to these values the dead-leg configuration resulted in extremely low levels of shear stress within the entire cavity. Again maximum levels were noted on the downstream wall of the branch peaking at 7.5Pa close to the stagnation point previously noted. However the wall shear continually decreased with increasing penetration into the dead-leg. Wall shear stress on the upstream wall of the dead-leg was found to be virtually non-existent over the entire length of the branch.

FLOW VISUALISATION STUDIES

Using a flow plate developed to analyse patterns within a dead-legs, flow visualisation studies were carried out to examine activity within the branch dead-leg (Figure 15). The rig consists of a flat plate on top of which sits a perspex viewing screen separated only by an O-ring seal thus generating a small gap of 2mm. A dead-leg configuration was set up within the rig using two thin sheets of aluminum. A series of holes drilled within the dead-leg area of the flow plate allowed dye to be injected from beneath the rig. Water entered the rig at the inflow and flowed across the plate at high velocity to the outflow. No fluid was allowed to flow out of the dead-leg branch.

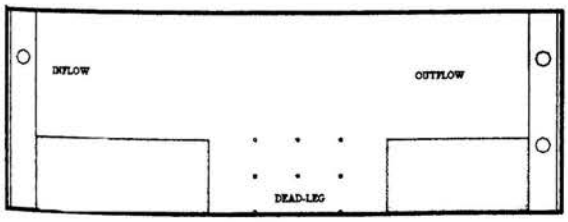

Figure 15: Flow visualisation plate

Initial studies investigated the degree of depreciation (penetration) of the bulk fluid into the branch of the dead-leg. (Photo 1).

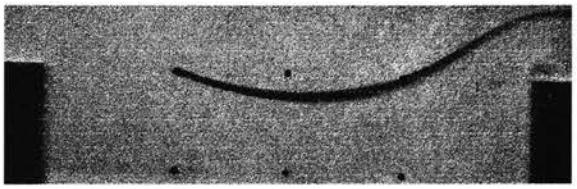

Photo 1: Dead-leg depreciation

It is clear that the fluid flowing across the top of the branch only 'dips' slightly into the dead-leg. This concurs with data generated during CFD modeling of this configuration. Fluid entering the dead-leg is quickly re-entrained into the fast flowing outflow fluid. Further visualisation studies investigated the near wall region by moving the inflow aluminium sheet closer to the dye injection points while maintaining the main pipe to branch diameter ratio at unity (Photo 2).

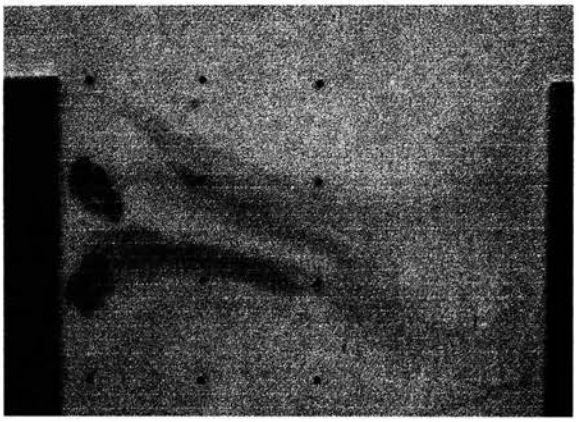

Photo 2: Near wall flow investigation

Following injection of the dye along the upstream wall of the branch, the dye was found to coagulate with little dispersion occuring. This clearly indicated an area of little activity. Some dye was eventually drawn, over a long time period (1 to 2 minutes), towards the centre of the branch and continued gradually drifting down into the dead-leg. These slow moving currents dragged the dye across and towards the downstream wall of the branch. These findings again corrobate the CFD results of a slow moving cavity within the dead-leg.

Further into the branch towards the bottom of the dead-leg less movement was found. Dye injected at this point simply remained stagnant indicating a region of very low velocity. After three to four minutes the dye began to creep up slowly along the upstream wall of the branch (Photo 3). This lack of motion does not concur with the industrial and FDA accepted policy that turbulent flow in the main pipe will flush the dead-leg branch and prevent stagnant regions.

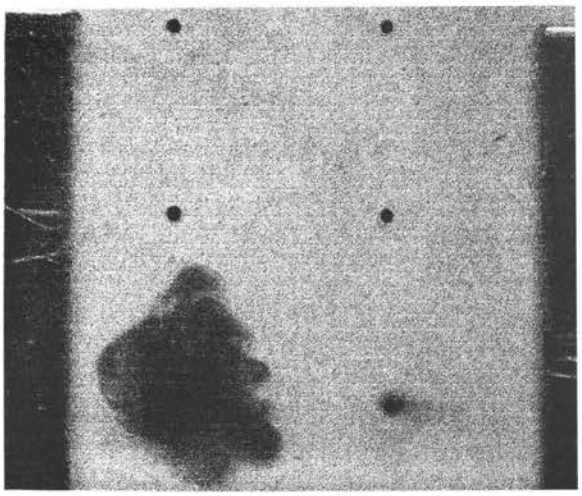

Photo 3: Stagnant region at base of dead-leg

CONCLUSION

Purified water systems often use pipe tee fittings to divert flow from a main distribution pipe into a reaction vessel. Initially fluid is allowed to flow into these vessels through an isolating valve. The closing of this valve following filling often creates a dead-leg zone within the branch of the pipe tee. FDA regulations have limited this dead-leg drop to six pipe diameters in the hope that turbulent activity within the distribution pipework will flush this dead-leg and prevent stagnation (Bukay, 1987). The results of this investigation indicated that this is not the case. This research carried out on a 3D dead-leg clearly shows a lack of activity within the branch. Very little exchange of fluid occurs between the branch and the main distribution pipework. Wall shear stresses were found to be low and conducive to bio-film build up. Velocities within the dead leg were so low that contaminants entering the dead-leg could easily proliferate in regions of low flow rate along the upstream wall and the base of the branch. A particularly worrying area is the region of separation noted during divided flow in the branch. This section of the upstream wall remains undisturbed during both divided and dead-leg flow conditions. Even during 'cleaning in place', a process employed to scour and clean the walls of pipework, this area would not be exposed to high velocity scouring (Nobel, 1994). Flow visualisation studies also confirm the lack of activity within the branch.

REFERENCES

Bates, C. Zonuzi, F. Faram, M. and O'Doherty, T., 'Experimental and Numerical comparison of flow in a 90° tee junction', *Separated and Complex flows, ASME Summer meeting*, Vol 217, pp 43-50, 1995.

Bukay, M. 'Dead-legs: a widespread threat to DI water systems', *Ultrapure Water*, pp 66-70, April, 1987.

Food and Drug Administration Good Manufacturing Practice, Section 212.49. Code of Fedral Regulations 21, 1972.

Hager, W.H., 'An approximate treatment of flow in Branches and Bends', *Proc Instrn Mech Engrs*, Vol. 198C, No4, pp. 63-69. 1984.

Ito, H. and Imai, K., 'Energy Losses at 90°pipe junctions' *Proc ASCE J Hydraul Div*, Vol. 99 HY9, pp1353-1368, 1973.

Karino, T., Kwong, H and Goldsmith, H.L., Particle flow behavour in Models of Branching Vessels in 90° T-junctions. *Biorehology*. Vol.16. No. 3, pp 231. 1979.

Kired, D. K., Chung, C.J. and Crowe, C.T., 'Measurement of flow in Tee-junctions by LDV technique', *Trans ASME, J Appl Mech*, Vol. 97. pp. 498-499. 1975.

Martin, S.R and Bates, C.J., 'Small-probe-volume laser Doppler Anemometry measurement of turbulent flow near the wall of a rib-roughened channel', *J. Flow Meas. Instrum.*, Vol 13, No.2 1992.

Miller, D.S., 'Internal Flow Systems', BHRA publications, Cranfield, Bedford, England. 1978.

Nobel, P. 'Transport considerations for microbiological control in piping', *J of Pharm Sci and Tech*, Vol. 48, No. 2, pp 76-85, 1994.

Pollard, A., 'Computer modelling of flow in tee-junctions', *PCH Physico Chemical Hydrodynamics*, Vol. 2, pp. 203-227, 1981.

Sierra-Espinosa, F., Bates, C and O'Doherty, T., 'Reverse and fully developed flow in an equally divided 90° pipe junction.' *ASME Summer Meeting* June 22-26, 1997.

HEFAT2002
1st International Conference on Heat Transfer, Fluid Mechanics, and Thermodynamics
8-10 April 2002, Kruger Park, South Africa
CM1

POLAR SUB-SUPERFICIAL HABITATION MODULES: NUMERICAL MODELLING OF HEAT TRANSFER

Helder Cavaca
Mechanical Engineering Department
Instituto Superior Técnico
Technical University of Lisbon

Miguel Caldas
Mechanical Engineering Department
Instituto Superior Técnico
Technical University of Lisbon

Viriato Semião
Mechanical Engineering Department
Instituto Superior Técnico
Technical University of Lisbon

ABSTRACT

This work presents a numerical model based on the finite volume approach to predict the ice temperature distribution around buried habitation modules in cold regions such as the Antarctic continent. The model allows for the prediction of the potential melting of the ice surrounding the module, which stems from the heat load generated inside it to ensure the specified comfort conditions. Analytical equations for the atmospheric temperature variation, and for the ice temperature distribution without the influence of the habitation module, based on monthly averaged experimental data, are obtained and used in the present work to specify the boundary and initial condition required for the numerical solution of the governing energy equation. The value of the convection heat transfer coefficient between the atmosphere and the soil was calculated using the atmospheric and thermal boundary layer theories. The specify conditions of the place under study yielded a value of $38.6 W/m^2K$ for this parameter in spite of the fact that a value of $25 W/m^2K$ can be found in building technology handbooks. The model is applied to an ice volume surrounding a cylindrical habitation module, having 2m of radius and 2m height, with the walls composed of two layers: a 4cm thick layer of insulation (polyurethane) and a layer of structural reinforcement (glass fiber) with 1cm. The results show that for the conditions simulated herein, that is, for the heat load required to ensure a comfort temperature of 15°C inside the module, the ice temperature is kept everywhere far below its melting point throughout the year and, therefore, the module's sinking will not occur.

INTRODUCTION

During the last decades several countries have marked their presence in the Antarctic continent in order both to establish a strategic position and to develop scientific research in areas like meteorology, glaciology and geology, among others. As a consequence, numerous permanent habitation and laboratory stations exist in this continent. Countries with permanent research stations (as of 1999) in Antarctica are: Argentina, Australia, Brazil, Chile, China, France, Germany, India, Italy, Japan, New Zealand, Poland, Russia, South Africa, South Korea, Ukraine, United Kingdom, United States and Uruguay.

In the present work, sub-superficial habitation modules (SSHM) are studied as they avoid snow accumulation problems that require regular and expensive snow removal operations. In fact, in the interior of the Antarctic continent the precipitation is hardly any. The main reason for the snow accumulation is the existence of buildings or other obstacles at a level higher than the ice surface, that act as barriers for the snow dragged from the coast by the wind. Although the snow accumulation is clearly minimised with this constructive method, there is a considerable increase of the heat transfer area between the module and the ice, which may lead to ice melting around and beneath the module, causing its sinking. This event will depend simultaneously on the heat load required to maintain comfort conditions inside, on the construction materials used and on the exterior atmospheric conditions. Clearly, this problem has to be analysed prior to the modules' construction.

The potential melting of the ice surrounding the SSHM is dependent on a considerable number of parameters. Indeed, atmospheric air temperature, wind velocity, construction materials, inside comfort temperature, ice thermal inertia, SSHM geometry and convection heat transfer coefficient are all variables that exert a determinant influence on the ice temperature value close to the SSHM. Notice that radiation was not considered in the present study. In fact, incident radiation flux can be as high as $900 W/m^2$ in Antarctica and its penetration into snow and ice is considerable. However, snow and ice surface present very high albedo (≈ 0.8) and emissivity (≥ 0.95). This will result in a negative radiation heat balance and, therefore, neglecting radiation makes the present study conservative. In [1] data referring to Mizuho Station (70°S) for a typical summer day can be observed. It shows that the largest energy gain due to radiation occurs at about noon and that it's value ($\approx 80 W/m^2$) is only about 10% of the incoming solar radiation. It further shows that that although the day length is 21h the total daily net radiation balance is negative, confirming what was said above.

The place under study is know as Patriot Hills and is located at approximately 80°S, 80°W. In the last few years, this region has been used both as a research site for the *Instituto Antarctico Chileno* and as a tourist resort by the travel agency *Adventure Network International*. The particularity of this region, that makes of it one excellent alternatives to maintain human activities in this continent, is the existence of a blue ice field. This field possesses the appropriate characteristics to be used as a runway for large transport aeroplanes, such as the C-130 Hercules, without the need to resort to special landing devices such as skis [2]. The meteorological data for this place was obtained mainly from the Antarctic Network of Automated Meteorological Stations (AWS).

The study was performed for a cylindrical module (r=2m, x=2m), with the walls composed of two layers: a 4cm thick layer of insulation (polyurethane) and a 1cm thick layer of structural reinforcement (glass fibre). The interior comfort temperature was set to 15°C. Notice that, as the very simple geometry indicates, this is a preliminary study. Therefore, there are some important details, such as the access to the module, the dept of the module's roof and the snow removal at the entrance, that have not been addressed at this stage.

NOMENCLATURE

C_f	Friction coefficient
h	Convection heat transfer coefficient [W/m^{2}K]
k	Thermal conductivity [W/mK]
Nu_δ	Nusselt number based on δ
Pr	Prandtl number
q	Convection heat flux [W/m^2]
Re_δ	Reynolds number based on δ
t	Time [month]
T	Ice temperature [°C]
T_z	Air temperature at a height of z metres [°C]
T_z^*	Dimensionless air temperature at a height of z metres
T_∞	Air temperature outside the atm. boundary layer [°C]
$T_{surface}$	Ice temperature at the surface [°C]
u_τ	Friction velocity [m/s]
U_z	Wind velocity at a height of z metres [m/s]
U_z^*	Dimensionless wind velocity at a height of z metres
U_∞	Wind velocity outside the atm. boundary layer [m/s]
x	Depth [m]
z	Height [m]
z_0	Reference height [m]
δ	Atmospheric boundary layer thickness [m]
δ_t	Thermal boundary layer thickness [m]
κ	Von-Karman constant
ν	Kinematic viscosity [m^2/s]

Meteorological conditions for Patriot Hills were calculated from a linear interpolation of the data from the Byrd (USA), Siple (USA) and General Belgrano II (Argentina) AWS stations [3]. These stations were selected in order to form a mesh with Patriot Hills inside of it, and a local rectangular coordinate system was constructed to make the interpolation easier – Fig.1. The values obtained from interpolation for the temperature and wind velocity at Patriot Hills compare well against isolated *in situ* measurements supplied by *Adventure Network International* [4].

The data obtained by the above-described linear interpolation, referring to experimental monthly averages over the last 25 years [3], was fitted to simple expressions using the least squares method, yielding a constant value for the wind velocity (U_3=5.8m/s) throughout the year and an harmonic variation for the air temperature represented by Eq.(1). Subscript 3 means that all measurements were taken at a height of 3m.

$$T_3(t) = -22.37 + 8.83\cos(0.524\,t) + 3.92\sin(0.524\,t) \qquad (1)$$

In Eq.(1) t is the time of the year in months, t=1 representing January, t=2 February and successively up to t=13 representing January again.

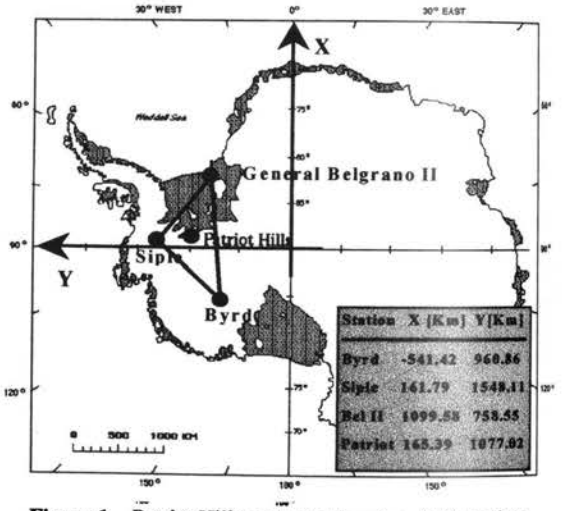

Figure 1 – Patriot Hills and neighbouring AWS stations location in the Antarctic continent.

As for the heat transfer coefficient, it can be obtained from the Nusselt number based on the atmospheric boundary layer thickness, $Nu_\delta = h\delta/k$. This latter parameter can be calculated if the friction coefficient, C_f, Prandtl number, Pr, and the Reynolds number based on δ, $Re_\delta = U_\infty \delta/\nu$ are known, as expressed in Eq.(2) – see, *e.g.*, [5].

$$Nu_\delta = \left(C_f/2\right) \mathrm{Re}_\delta \, \mathrm{Pr}^{1/3} \qquad (2)$$

The friction coefficient is obtained from:

$$U_\infty/u_\tau = \left(2/C_f\right)^{1/2} \qquad (3)$$

To obtain both the values of the wind velocity at the exterior of the atmospheric boundary layer, U_∞, and of the

friction velocity, u_τ, recourse can be made of Eq.(4). This equation has often been used in the atmospheric boundary layer theory as a possible wind velocity profile – see, *e.g.*, [6] or [7] - and runs:

$$U_z/u_\tau = (1/\kappa)\ln(z/z_0) \quad (4)$$

In the previous equation U_z is the wind velocity at a height of z meters and z_0 is a reference height. The value of the Von-Karman constant, κ=0.4, was used following [8] and the value of z_0=0.03m was obtained from [9]. With the pair of known values (z=3m, U_3=5.8m/s) the friction velocity may be calculated as $u_\tau=\kappa U_3/\ln(3/z_0)$. With this u_τ value, and assuming that the boundary layer thickness has the value of δ=275m - see, *e.g.*, [9] - the wind velocity outside the atmospheric boundary layer is given by $U_\infty=(u_\tau/\kappa)\ln(\delta/z_0)$.

Performing the calculations indicated above the value of h=38.6W/m^{2}K is obtained. This value is about 50% higher than the h values commonly used values for building calculations: around 25W/m^{2}K. Different factors may contribute to that discrepancy. Two of the most important are the low air temperature at Patriot Hills, much lower than at most of inhabited locations in the earth, which increases the value of h in about 25%, and the smoothness of the ice surface – the value of z_o is 0.03m in opposition to a value rounding 25m for the surface roughness in cities - which causes the velocity profile of the atmospheric boundary layer to exhibit a deeper gradient at the air/ice interface, fact that also contributes to the increase of h.

The value of h had to be corrected to account for the effects of the thermal boundary layer as a consequence to the fact that the known values of the wind velocity and temperature refer to a height of 3m, deep inside the boundary layer. Defining a dimensionless air temperature by $T^*_z=(T_z-T_{surface})/(T_\infty-T_{surface})$ it is easy to demonstrate that the convection heat flux can be calculated through Eq.(5) instead of the usual formula $q=h(T_{surface}-T_\infty)$.

$$q = \left(h/T^*_3\right)\left(T_{surface} - T_3\right) \quad (5)$$

To calculate T^*_3 based on the available wind velocity data an analogy between the thermal and aerodynamic boundary layers was used: defining a dimensionless wind velocity by $U^*_z=U_z/U_\infty$ and assuming that $T^*=U^*f(Pr)$ [10] it is possible to demonstrate that when $\delta_t=\delta$ (the case of turbulent flows [10]) we have $T^*_z=U^*_z$. Therefore, since of $T_3^*=U_3^*=0.505$ the value h/T^*_3=76.4W/m^{2}K is obtained.

To obtain analytically the formulation of the ice temperature distribution (without the SSHM), which constitutes the problem's initial condition, the ice was considered a semi-infinite solid with a transient surface convection boundary condition. This is a one-dimensional heat transfer problem very similar to that described by [11], and that can be solved in a like manner. Using the above value for h/T^*_3, Eq.(1) to represent the annual variation of T_3 and standard thermophysical properties of ice at –22ºC, the following expression results for the variation of the ice temperature with time and depth:

$$T(x,t) = -22.37 + e^{-0.296x}\left[8.73\cos(0.524\,t - 0.296\,x) + \right. \\ \left. + 3.96\,sen(0.524\,t - 0.296\,x)\right] \quad (6)$$

The cylindrical shape of the SSHM determines the problem's geometric character: cylindrical coordinates with axial symmetry. The SSHM and a large cylindrical volume of ice surrounding it constitute the problem's physical domain. The module's dimensions are r=2m and x=2m, as said before, and those of the ice surrounding it were set to R=100m and X=100m. These values were chosen in order not to allow the heat flux from the SSHM to influence the values of the temperature at the domain boundaries, which, ideally, would be set at infinity.

All the surfaces of the SSHM - walls, roof and floor - have a thickness of 5cm being composed by a 4cm layer of polyurethane for insulation and a 1cm layer of glass fibre for structural reinforcement [12]. This combination of materials exhibits a thermal conductivity of 0.03W/mK [13]. This value along with interior convection thermal resistance [14] yielded the following values for the overall heat transfer coefficients: walls – 0.57W/m^{2}K; roof – 0.55W/m^{2}K; floor – 0.56W/m^{2}K. As said before, the interior comfort temperature the SSHM was set to 15ºC [12].

The two-dimensional, cylindrical coordinates, transient heat equation that governs the present problem was solved numerically using the control volume formulation [15] and the pure implicit method for the ice volume surrounding the SSHM. Convection heat transfer boundary conditions were set at the interface with the atmosphere and in the contact surfaces with the SSHM's walls and floor. All other boundaries were made adiabatic. A non-uniform grid of 68×68 nodes, respectively in the axial and radial directions, was generated to obtain the solution of the governing energy equation. This grid, which is partially sketched in Fig.2, was chosen after a grid independence study. In fact, other grids comprising 51×51, 85×85 and 102×102 nodes, respectively in the axial and radial directions, were also tested and the results showed that the 68×68 nodes grid was refined enough.

The results obtained from this analysis in what concerns the temperature distribution in the ice surrounding the SSHM were calculated for all the months of the year. Among the entire set of results those referring to January, March and July are presented in this work, as they are the months representative of the different seasons and heat flux phenomena.

The month of January is the one that establishes the pattern of the summer season. In this month the atmospheric air temperature attains its maximum value (–12.8ºC at a height

of 3m) and the ice temperature at a depth of 15m is –22.4°C. This temperature difference originates a heat flux from the atmosphere to the ice: not surprisingly, in the summer the ice is being heated up by the atmosphere.

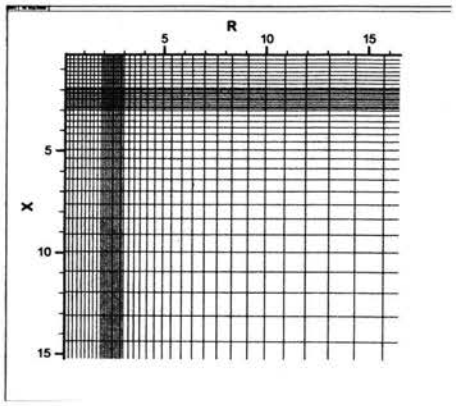

Figure 2 – The grid in the SSHM vicinity.

Fig.3 displays the ice temperature distribution around the SSHM for the month of January. In this figure it is possible to observe the influence of the SSHM on the initial ice temperature field. Indeed, it is clear that the non-parallel isothermals arrangement is a consequence of the heat flux from the SSHM. On the other hand, away from the SSHM, the temperature decreases with the ice depth up to 5m, as it can be observed at a radial distance of 20m away from the SSHM. This parallel distribution of the isothermals represents the temperature distribution of the ice in the absence of the SSHM.

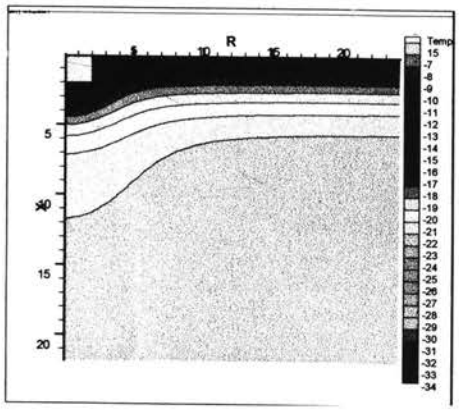

Figure 3 – Ice temperature around the SSHM in January.

The heat load from the SSHM acts as a heat source to the ice mass surrounding the buried module, and if its value is intense enough it may lead to the ice melting and to the consequent module sinking. However, in January, the intensity of such heat flux is not sufficient to melt the surrounding ice, as its maximum registered temperature is –8.5°C. The effect of the heat flux from the module is felt until a depth of approximately 12m. In the radial direction the effect of the heat flux from the SSHM is less pronounced. Due to the counter-influence of the heat flux from the atmosphere to the ice, the direction of the heat flux originated in the SSHM penetrates obliquely into the ice mass.

The month of March is presented herein as it is during this month that the ice temperature reaches its maximum value, -7.9°C, for the studied conditions. Fig.4 depicts the ice temperature distribution for the above-mentioned month. As it can be observed from this figure, and relatively to January, in March the influence of the heat flux from the SSHM in the radial direction is more pronounced as the hotter isothermals exhibit a deeper penetration into the ice mass in that direction. The location of the ice highest temperature value is the symmetry axis close to the floor of the SSHM (see Fig.5), as this is the most distant point from the surface in contact with the SSHM and, therefore, it is the less affected by the atmospheric conditions. Considering that the warmer month in terms of atmospheric temperature is January, this should be the month for which the ice temperature was highest. However, this maximum value occurs later on, in March, due to the thermal inertia of the ice that appears to delay two months the ice response to the atmospheric temperature changes.

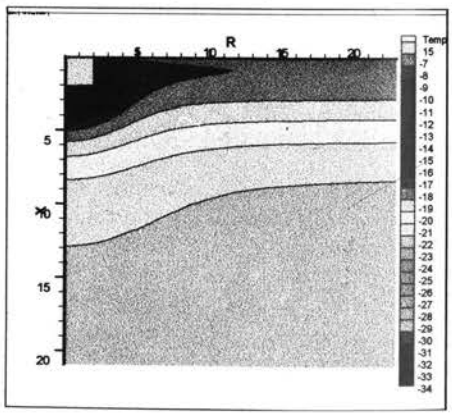

Figure 4 – Ice temperature around the SSHM in March.

July is chosen as the typical month to establish the winter pattern of the ice temperature distribution, the atmospheric temperature being at its minimum value (-32°C at 3m height). As for this month the air is at a lower temperature than the ice, the latter is being cooled down, in opposition to what happens in January. Heat is, therefore, being transferred from the ice to the atmosphere. As a consequence the ice temperature exhibits the distribution depicted in Fig.6.

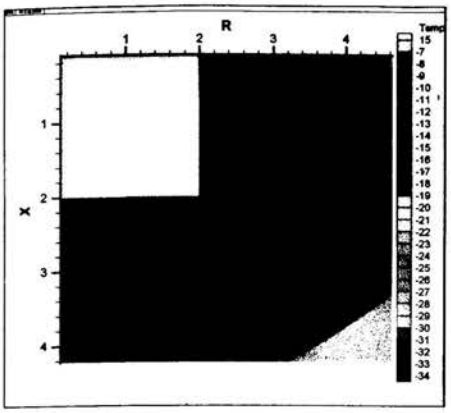

Figure 5 – Ice temperature around the SSHM in March: Magnification of the SSHM vicinity.

As observed for the summer situation, the isothermals away from the SSHM (R=20m) are parallel to the ice surface. This pattern represents, as mentioned earlier, the temperature distribution of the ice when the habitation module is absent. As far as the penetration of the heat flux from the SSHM into the surrounding ice is concerned, this month represents the most critical situation of the three cases presented. In fact, the heat flux from the habitation module changes the isothermal lines below it up to a depth of 15m. However, the maximum ice temperature is around –11°C wich makes this situation fairly safe.

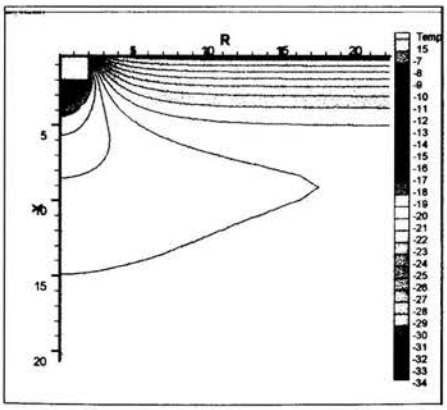

Figure 6 – Ice temperature around the SSHM in July.

In order to quantify better the problem under study and to test the robustness of the numerical tool described herein, two additional parametric studies were performed. The first envisages the analysis of the effect of the SSHM walls' thermal resistance, *l*/*k* (*l* being the wall thickness and *k* it's thermal conductivity), on the ice temperature distribution. The second parametric study intends to quantify the effect of the comfort temperature inside the SSHM on the ice's temperature distribution.

The parameter *l*/*k*, that is a measure of the module walls thermal resistance, is very influent as it determines the ice's annual maximum temperature at the SSHM surroundings. Therefore, its is the subject of a parametric study performed in order to determine the minimum value of *l*/*k* that induces the maximum annual ice temperature close to the melting point. The month of March was used to set exterior atmospheric conditions and a comfort temperature of 15°C was used.

Figure 7 shows the results obtained. As expected, the maximum temperature of the ice in the surroundings of the SSHM is inversely proportional to the thermal resistance *l*/*k* and exhibits a limit value (approximately 0.6m^{2}K/W) below which the ice starts to melt. As it can be observed from Fig.7, the thermal resistance value used in this work (1.67m^{2}K/W) is rather conservative and leads to a safe value of –7.9°C for the maximum annual ice temperature.

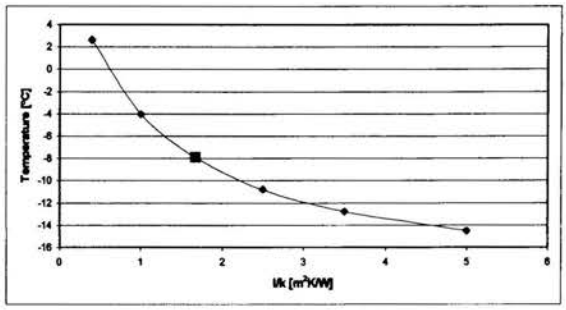

Figure 7 – Maximum annual ice temperature as a function of the walls thermal resistance.
■ - Standard conditions. ♦ - Parametric study values.

The maximum annual value of the ice temperature at the surroundings of the SSHM is also dependent on the comfort temperature, established as 15°C in the present work. In order to evaluate its effect on the ice temperature, keeping the walls thermal resistance at the reference value of 1.67m^{2}K/W, the model was applied to several interior conditions while considering the most unfavorable weather conditions for the ice melting: March. The results are shown in Tab.1. As it can be observed, the comfort temperature inside the SSHM can go up to 21 °C without melting the surrounding ice.

With the reference value for the walls' thermal resistance (1.67m^{2}K/W), the total heat flux from the SSHM varies from 700W to 1000W along the year. The highest value occurs during the winter, in July, while the lowest value is attained during the summer, in January. As far as the required heating power is concerned, and considering that 25% of the air inside

the module is hourly renewed, the total heat power required to keep the inner temperature at the reference comfort value (15°C) varies from 825W to 1200W.

Comfort temperature inside the SSHM (°C)	Maximum annual ice temperature (°C)
13	-8.56
15	-7.88
17	-7.20
19	-6.52
21	-5.84

Table 1 – Effect of the comfort temperature inside the SSHM on the maximum annual ice temperature.

Concluding:

Ice melting in the surroundings of sub-superficial habitation modules (SSHM) in cold regions, such as those in the Antarctic continent, is a possibility that requires a study prior to the modules' construction. This possible ice melting stems from the heat load generation inside habitation modules required to maintain the comfort temperature.

A numerical tool to predict the ice temperature distribution, based on the finite volume approach, was presented in this work. This model was applied to the ice volume surrounding a cylindrical SSHM (r=2m, x=2m) in Patriot Hills, Antarctica, with 5cm thick walls possessing a thermal resistance of $1.67 m^2K/W$, and with a comfort temperature of 15°C.

An analytical equation for the annual variation of the atmospheric air temperature, characterized by a monthly frequency, was obtained from linear interpolation of data gathered in three selected neighboring AWS stations. The analytical equation for the ice temperature distribution in the absence of the SSHM was derived and used as initial condition. The convection heat transfer value $h=38.6 W/m^2K$ for the ice/atmosphere interface was calculated.

The results have shown that, for the above conditions, the maximum ice temperature reached (-7.9°C) was far below the ice melting point.

A parametric study for the walls thermal resistance, l/k, yielded the minimum value of $0.6 m^2K/W$ required in order to avoid the melting of the ice surrounding the cylindrical SSHM. This value is considerably below the reference value used in this work ($1.67 m^2K/W$), for which the comfort temperature can go up to 21°C without the risk of ice melting.

ACKNOWLEDGMENTS

The authors would like to thank Dr. Luísa Caldas from MIT for setting the current research in motion and to acknowledge the technical support provided by both Architect Paul Taylor from *Universidad Técnica Federico Santa Maria*, Chile, and *Adventure Network International* travel agency.

REFERENCES

[1] Oke, T.R., 1987, Boundary Layer Climates, Routledge, London (ISBN: 0-415-04319-0).

[2] Swithinbank, C., 1987, *Ice Runways in the Heritage Range Antarctica*, a report prepared for Adventure Network International, Inc. and Fuerza Aérea de Chile, Unpublished.

[3] WEADAC/3700, Database with compilation of the British Meteorological Office and Japan Meteorological Agency data. Also available in ftp://ice.ssec.wisc.edu and http://bsweb.nec-bas.ac.uk/public/icd/metlog.

[4] Adventure Network International, 1999, private communication (web-page: www.adventure-network.com).

[5] Bejan, A., 1984, *Convection Heat Transfer*, John Wiley & Sons, New York (ISBN: 0-471-89612-8).

[6] Fernholz, H.H., 1976, External Flows - Topics in applied physics, Vol.12, Turbulence, Bradshaw, P., Springer-Verlag, Berlin (ISBN: 0-387-07705-7).

[7] Davenport, A.G., 1965, The Relationship of Wind Structure to Wind Loading, *Wind Effect on Buildings and Structures*, Vol.I, Proceedings of the conference held at the National Physical Laboratory, Teddington, Middlesex, on 26th, 27th and 28th June, 1963, pp.53-83.

[8] Garratt, J.R., 1994, *The Atmospheric Boundary Layer*, Cambridge University Press, Cambridge (ISBN: 0-521-46745-4).

[9] Gould, P.L. and Abu-Sitta, S.H., 1980, *Dynamic Response of Structures to Wind and Earthquake Loading*, Pentech Press, London (ISBN: 0-7273-0403-8).

[10] Incropera, F.P. and DeWitt, D.P., 1996, *Fundamentals of Heat and Mass Transfer*, John Wiley & Sons, New York (ISBN: 0-471-30460-3).

[11] Carslaw, H.S. and Jaeger, J.C., 1959, *Conduction of Heat in Solids*, Claredon Press, Oxford Science Publications, Oxford (ISBN: 0-19-853368-3).

[12] Taylor, P., 1999, private communication.

[13] Toulokian, Y.S., Powell, R.W., Ho, C.Y. and Klemens, P.G., 1970, Thermophysical Properties of Matter – Vol.2 – Thermal Conductivity, Non-Metallic Solids. IFI/Plenum, New York-Washington (SBN: 306-67020-8).

[14] Santos, C.A. and Paiva, J.A., 1990, *Coeficientes de Transmissão Térmica de Elementos da Envolvente dos Edificios* (in Portuguese), Laboratório Nacional de Engenharia Civil, Lisboa (ISBN: 972-49-1374-0).

[15] Patankar, S.V., 1980, *Numerical Heat Transfer and Fluid Flow*, Hemisphere Publications, Washington (ISBN: 0-07-048740-5).

HEFAT2002
First International Conference on Heat Transfer, Fluid Mechanics, and Thermodynamics
8-10 April 2002, Kruger Park, South Africa
EH1

Evaporation Rates from Fresh and Saline Water in Moving Air

Hisham T. El-Dessouky*, Hisham M. Ettouney,
Imad M. Alatiqi, and Maha A. Al-Shamari+
Department of Chemical Engineering, College of Engineering and Petroleum,
Kuwait University, P.O.Box 5969 -Kuwait,
+ Kuwait Institute for Scientific Research - Kuwait
Email: eldessouky@kuc01.kuniv.edu.kw

Abstract

Three methods are used for measuring the evaporation rate. These methods include change in the water height, water weight, and air humidity. Two evaporation modes are considered; the first is for water at ambient temperature into hot air and the second for heated water into air at ambient temperature. The air and water temperatures are varied over a range of 25-60 °C. As for the air velocity it is varied over a range of 2-4 m/s. Also, the water salinity is changed from 26 ppm for fresh water up to 69,000 ppm for rejected brine in desalination processes. The measured data is correlated as a function of the evaporation mode, the pressure difference of the water vapor at the water surface and in the air bulk, and the air velocity. Measured rates compares favorably against a number of literature correlations. Results show decrease in the evaporation rate upon the increase of the water salinity because of the reduction in the water vapor pressure at the water surface.

Introduction

Water evaporation in air occurs in nature and industrial processes such as: drying, air conditioning, air fogging in gas turbines, thermal desalination, production of concentrates, and film cooling. In all systems, it is necessary to have good predictive models for the evaporation rate as a function of various system parameters. Examples of such variables are: temperatures and flow rates of the air or water streams, system geometry, presence of dissolved or suspended material in the water, biological activity, and deviation from saturation conditions.

Figure 1 shows psychometric charts for two modes of water evaporation. The first is for hot air flow past water at ambient temperature (line A-C), and the second is for air at ambient temperature flowing past heated water (line A-B).

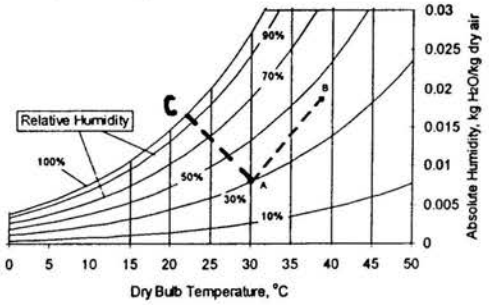

Since the early 1990's, water evaporation is investigated in several configurations that include: water evaporation in air and superheated steam, evaporation from flat pans, wetted-wall columns, and water droplets. The following is a summary for the main findings in these studies (1):

- Measurements of the water evaporation rates are very sensitive to various effects within the system, which includes the following: heat loss to surroundings, contamination of the water surface, and error in measurement of water surface temperature.
- Compiling available literature correlations show wide deviations among a large number of these correlations. However, a number of the older and newer correlations provide compatible results.
- Investigators reported an inversion temperature of 250 °C, below which the water evaporation rate is highest in dry air, followed by humid air, and then superheated steam. The opposite trend is found above the inversion temperature.
- Presence of thin oil films on the water surface reduces the evaporation rates.
- Presence of dissolved salts in the evaporating water reduces the water evaporation by as much as 20%.

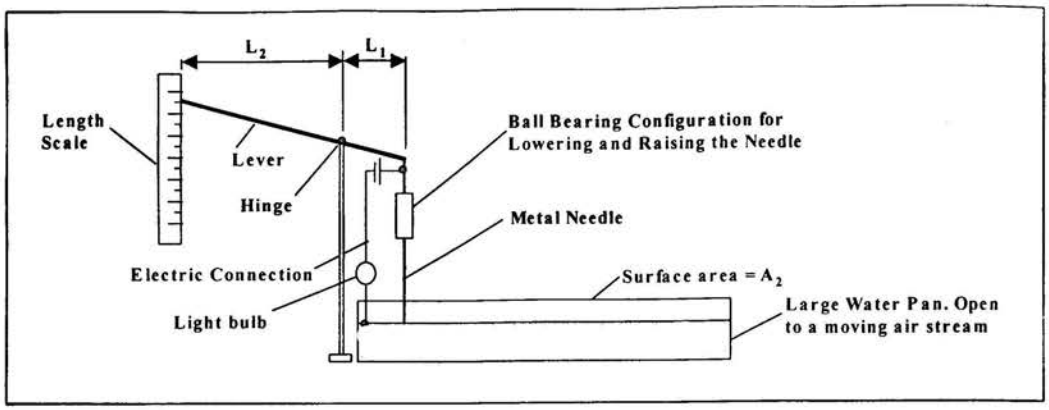

Fig. 2a. Schematic of the water level measurement method.

This paper focuses on measuring the effect of water salinity on the evaporation rate of water in moving air. The experiments are performed for two evaporation modes; the first is for water evaporation from heated water in air at ambient temperature and the second is for water at ambient temperature into heated air.

Water Evaporation Rate

Three methods are used for measuring the water evaporation rate, which include change in the air humidity, water weight, and water level. The results for various measuring methods are only accepted if the deviations among the different measuring techniques are below 5%.

Calculations of the change in the water absolute humidity require measurement of the dry and wet bulb temperatures for the inlet and outlet air. The two temperatures are used to calculate the absolute humidity at the inlet and outlet conditions, Therefore the water evaporation flux is defined by

$$R = M_d (W_o - W_i)/A \qquad (1)$$

Evaluation of the evaporation rate by Eq. (1) involve the following calculations:

1. Determine the saturation pressure at the wet bulb temperature, P_w
2. Calculate the water vapor pressure at the dry bulb temperature (3 &4)
3. Calculate the air humidity at the inlet and outlet points (3 &4)
4. Calculate the air specific volume (3 &4)
5. Calculate the air density
6. Calculate the mass flow rate of moist air
7. Calculate the mass flow rate of dry air

Measuring the change in the water level is shown in Fig. 2a. As is shown the measuring system includes an electric circuit, a sharp end needle, a lever arm, and a length scale. Since, variations in the height of the water level in the water pan are very small, then, the length of the lever arm is adjusted to reduce the measuring error. Therefore, the ratio of L_1 and L_2 is adjusted at a value of 50. For a ratio of 50, lowering the needle a distance of 0.02 mm would correspond to 1 mm on the length scale. The following equation is used to calculate the evaporation rate from the water level measurements

$$R = \frac{\rho \, \Delta h \, (A_1 + A_2)}{A_2 \, \Delta t} \qquad (2)$$

where h is the water level, A_1 is the surface area of the small pan, A_2 is surface area of the large pan, ρ is the water density, and Δt is the time interval.

The weight change measuring system is shown in Fig. 2b. The system constitutes, the water

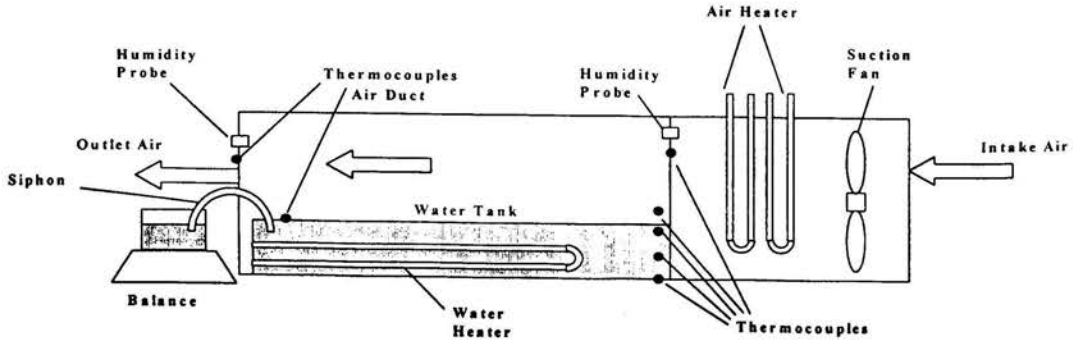

pan used for evaporation, a small water pan with covered surface or zero evaporation, a weighing balance, and a connection between the two pans. The mass of the small and large pans is given by

$$m_1 = \rho A_1 h \quad (3)$$

$$m_2 = \rho A_2 h \quad (4)$$

where

m_1 and m_2 are water mass in the small and large pans.

$$m_1/m_2 = A_1/A_2 \quad (5)$$

Since the cross section area for both pans

Equations (11) and (12) are combined to yield the following relation

$$R = \frac{(\Delta m_1)(A_1 + A_2)}{A_1 A_2 \, \Delta t} \quad (6)$$

Experimental Apparatus

The experimental system for water evaporation in air is shown in Fig. 2a. The system specifications include the following:

- The air duct and water holding tank are made of Plexiglas and reinforced with aluminum frame.
- The water tank dimensions are 0.575x0.195x0.1 m in length, width, and depth.
- The air duct dimensions are 1.583x0.2x0.3 m in length, height, and width.
- The air fan is axial flow type with a power rating of 0.9 kW.
- The air heaters have power rating of 1 kW.
- The water heaters have power rating of 1 kW.

The system instrumentation include the following:

- An anometer is used to measure the air velocity with an accuracy of 0.1 m/s.
- Ten thermocouple probes are used to measure the temperature at various points within the system. The accuracy of the thermocouples is ±0.01 °C.
- Two humidity probes are used to measure the relative humidity of the intake ambient air and the outlet air. The accuracy of the humidity probes is rated at 0.1%.
- The weight balance has a measuring accuracy of 0.01 gm.
- Conductivity meter for measuring the water salinity with an accuracy of ± 0.01 µS/m

Temperature and relative humidity measurements are stored in a data logger. Data logging is made at intervals of 10 minutes. The logger allows for automatic calibration of the thermocouples and relative humidity probes.

Experimental Procedure

System operation and measurements are conducted according to the following procedure:

- Prior to system operation and calibration of instruments, all power and thermocouple wiring are visually inspected as well as fitting of the fan, the air duct, and the water pan.
- Water sample is prepared, which include deionized tap water, seawater, rejected brine water from the desalination plant, and their mixtures.
- All instrumentations are calibrated, which include the thermocouples, velocity probe, relative humidity probes, level meter, conductivity meter, and weight balance.
- The water pan is filled with water to a specified level and the beaker placed on the balance is also filled with the same water to have a constant density.
- Operation starts with switching the air fan and adjusting to the desired velocity. Also, the air or water heaters are switched on to the desired power rate.
- Automatic data logging commences for various system temperatures, humidity, and weight or level.
- Each power setting experiment is conducted for period of 3 hours with measurements at 10 minutes interval.

Error Analysis

Error analysis in calculating the evaporation rates is performed using the Kline-McClintock Procedure. The following is the estimated errors in calculating the evaporation rates, which depends on the method for measuring the amount of water evaporated:

- Change in inlet/outlet absolute humidity of the air stream:
  The measured errors in the temperature, air velocity, time, surface area of the water pan, and air relative humidity are 1.5%, 0.5%, 0.1%, 0.1%, and 1%, respectively. These errors give an error of 1.3% in the calculated evaporation rate.
- Change in water mass:
  The measured errors in the water mass, time, and surface area are 0.5%, 0.1%, and 0.1%, respectively. These errors give an error of 0.47% in the calculated evaporation rate.
- Change in the water level:
  The measured errors in the water level, time, and surface area are 3%, 0.1%, and 0.1%, respectively. These errors give an error of 2.75% in the calculated evaporation rate.

Results and Discussion

The experimental parameters include the following:

- Air velocity of 2, 3, and 4 m/s.
- Air temperatures of 20, 30, 40, and 50 °C.
- Water temperatures of 25, 30, 40, 50, and 60 °C.
- Water salinity of 26, 34,000, 56000, 69000 ppm.

The measured evaporation rate for the mode of heated water as a function of the water salinity and air velocity is shown in Fig. 3. As is shown, the evaporation rate increases upon increasing the air velocity and decreasing the water salinity. Increasing the air velocity results in increase of mixing, turbulence, and reduction in the boundary layer resistance. All these effects enhance the water evaporation rate. Increasing the water salinity increases the boiling point elevation, which reduces the temperature of the evaporated water and its vapor pressure.

Results for water evaporation into a hot air stream are shown in Fig. 4. As is shown, the evaporation rates can increase by as much as 100% upon the increase in the air velocity at the same vapor pressure difference. The salinity effect in these experiments is very evident.

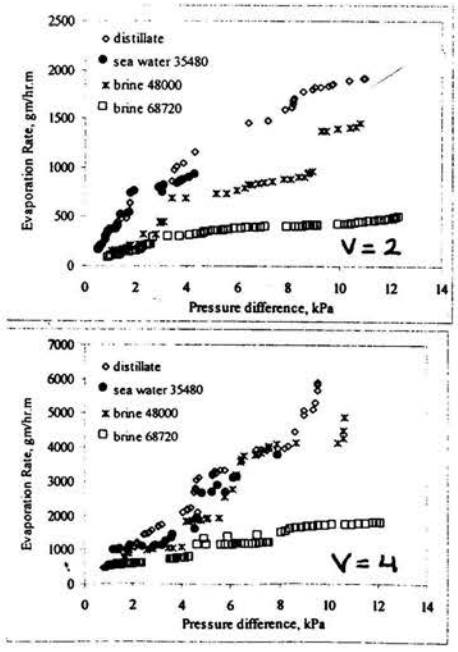

Fig.3 Evaporation Rate of Hot Water in Air

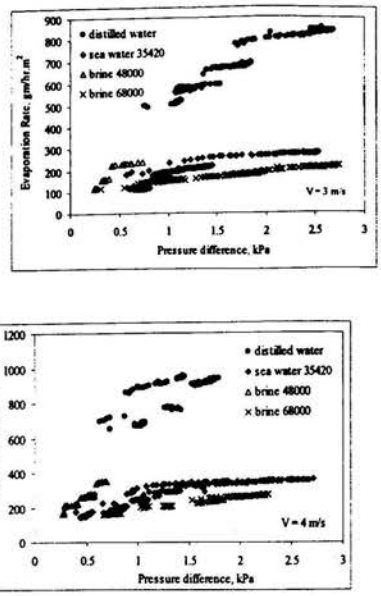

Fig.4 Evaporation Rate of Water in Hot Air

Fitting Correlations

The dimensional correlation for the case of water evaporation from hot water into unheated ambient air is given by:

$$R=169\ V^{(1.5)}\ X^{(-0.1)}\ \Delta P^{(0.654)} \qquad (7)$$

The correlation predictions versus the measured evaporation rate is shown in Fig. 5a.

The dimensional correlation for the case of water evaporation from unheated water into heated air is given by:

$$R=(294.5)V^{(1.058)}X^{(-0.16)}\Delta P^{(0.376)} \qquad (8)$$

The correlation predictions against the measured evaporation rate is shown in Fig. 5b.

The dimensionless correlation for the above correlation's include three dimensionless groups, which include Reynolds number, $Re = \rho VD/\mu$, the dimensionless evaporation rate, $\overline{R} = R/(\rho V)$, and the dimensionless difference of the water vapor pressure, $\overline{\Delta P} = \Delta P/(\rho V^2)$. The dimensionless correlation for the case of water evaporation from hot water into unheated ambient air is given by:

$$\overline{R} = 1.1\times10^{-7}\ \overline{\Delta P}^{\ 1.78} X^{-0.103} Re^{0.65} \qquad (9)$$

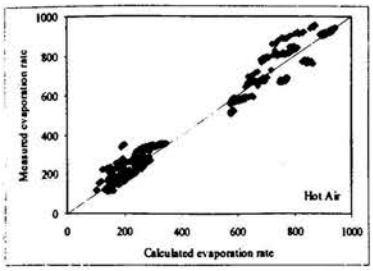

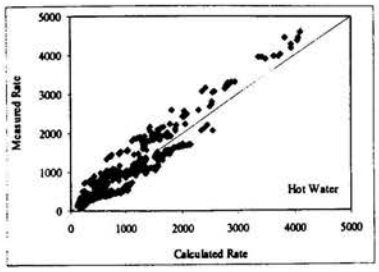

Fig.5 Measured and Calculated Dimensional Evaporation

Display of the correlation predictions versus the measured evaporation rate is shown in Fig. 6a.

The dimensionless correlation for the case of water evaporation from hot water into unheated ambient air is given by:

$$\overline{R} = 0.011\,\Delta\overline{P}^{\,0.81} X^{-0.16} Re^{0.38} \qquad (10)$$

Display of the correlation predictions against the measured evaporation rate is shown in Fig. 6b.

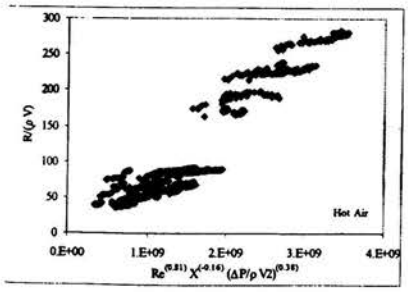

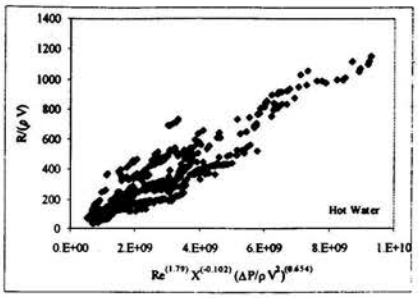

Fig.6. Measured & Calculated Dimensionless Evaporation Rates

Comparison Against Literature Correlations

The literature includes a number of empirical correlations for water evaporation. All correlations are developed for distilled water and for the case of water evaporation from hot water pool into a moving air stream at ambient conditions. The most common correlations are summarized below:

Pauken (5)

$$J = a\,(P_w - P_a)^b \qquad (11)$$

$$a = 74 + 97.97\,V + 24.91\,V^2$$

$$b = 1.22 - 0.19\,V + 0.038\,V^2$$

The above data is valid over a temperature range of 25-50 °C and air velocity of 0.33-1.45 m/s.

Carrier (6)

$$J\ 3370\ (95 + 83.7\,V)\,(P_w - P_a)/\lambda \qquad (12)$$

The above data is valid for air velocity of 0-7 m/s.

- Hinchley and Himus (7)

$$J = (232.5 + 101\,V)\,(P_w - P_a) \qquad (13)$$

The above data is valid for air velocity of 0.95-5.8 m/s.

- Rowher (8)

$$J = (125 + 75.5\,V)(P_w - P_a) \qquad (14)$$

The above data is valid for air velocity of 0-0.67 m/s.

Comparison for the predictions of the above correlations is shown in Fig. 7 against the correlation for the distilled water developed in the previous section. The figures correspond to air velocities of 2, and 4 m/s, respectively. As is shown, the measured

evaporation rates are well within the predictions of the correlations by Hinchley and Himus (5) and by Rowher (6). The highest evaporation rates are obtained for the

correlation by Pauken (3) followed by the relation of Carrier (4).

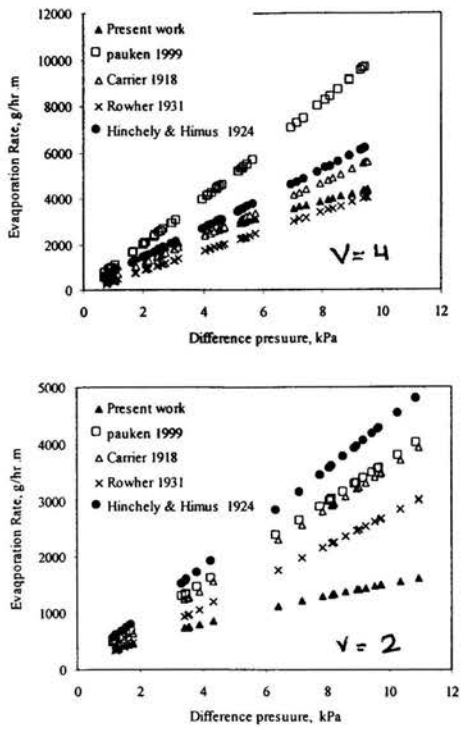

Fig.7 Comparison of Evaporation Rates against Literature for Fresh Water

Conclusions

Experimental measurements are performed to determine the evaporation rate of water in air. Two evaporation modes are considered. These include evaporation from hot water in moving air at ambient temperature or evaporation from water at ambient temperature in a stream of hot air. The experiments are performed as a function of the water salinity, which includes fresh water with a salinity of 26 ppm and brine with a salinity of 69,000 ppm. The experiments are performed over a temperature range of 25 – 60 °C and air velocity of 2-4 m/s.

Results show increase in the evaporation rate upon the increase in the temperature, air velocity, and reduction in water salinity. Also, evaporation rates for the hot water mode is much higher than evaporation for the hot air mode. Measured data are correlated in dimensional and dimensionless for both modes of evaporation. The developed correlations are compared against literature correlation. The comparison is only limited to the case of evaporation from hot water and low salinity water. Results show good agreement with literature correlations.

The data and results presented here are of importance to the desalination industry and other applications that may include environmental considerations, food drying, indoor air conditions, and evaporative cooling. The experimental system can be further exploited to examine effects of chemical additives on the evaporation. This can be of great value for flashing and evaporation desalination processes.

Acknowledgement

The authors would like to acknowledge financial support of the Kuwait University research administration, Project # ELC012.

REFERENCES

(1) El-Dessouky, H.T., Ettouney,H.M., Al-Atiqi, I.M., and Al-Shamari, M.A., Evaporation Rate from Fresh and Saline Water in Moving Air, Ind. Eng. Chem Res., In print.

(2) Jones, F. Evaporation of Water; Lewis Publishers, Michigan, 1992

(3) Olivierie, J.; Singh, T.; Lovodocky, S. Psychometrics: Theory and Practice, American Society of Heating Refrigeration and Air-Conditioning Engineers, Georgia, 1996.

(4) El-Dessouky H., and Ettouney,H , Fundamentals of Salt Water Desalination, Elsevier, 2002.

(5) Pauken, M.T. An Experimental Investigation of Combined Turbulent Free and Forced Evaporation. Experimental Thermal and Fluid Science. 1999, *18*, 334.

(6) Carrier, W.H. The Temperature of Evaporation. ASHRAE Trans. 1918, *24*, 25.

(7) Hinchley, J.W.; Himus, G.W. Evaporation in Currents of Air. J. Soc. Chem. Indust. 1942, *7*, 57.

(8) Rowher, C. Evaporation from Free Water Surface. US Department of Agriculture in cooperation with Colorado Agricultural Experiment Station. Technical Bulletin no. 271, 1931.

HEFAT2002
1st International Conference on Heat Transfer, Fluid Mechanics, and Thermodynamics
8-10 April 2002, Kruger Park, South Africa
FJ2

HEAT AND MOISTURE TRANSFER THROUGH FIBROUS INSULATION WITH PHASE CHANGE AND MOBILE CONDENSATES

J. Fan* and X. Wen**
*Associate Professor; **Research Associate
Institute of Textiles and Clothing
Hong Kong Polytechnic University
Hung Hom, Kowloon, Hong Kong
E-mail:tcfanjt@inet.polyu.edu.hk

ABSTRACT

This paper reports on a transient model of coupled heat and moisture transfer through fibrous insulation, which for the first time takes into account of evaporation and mobile condensates. The model successfully explained the experimental observations of Farnworth, and the numerical results of the model were found to be in good agreement with the experimental results of a drying test.

INTRODUCTION

Condensation in fibrous insulation is a serious problem in clothing and many other applications such as building insulation and refrigerated space envelopes, as it can result in drastic reduction in thermal insulation of the system.

Despite of the vast published work on heat and moisture transfer in fibrous insulation, little has been done on the coupled heat and moisture transfer with phase change until 1980s. Ogniewicz and Tien [1] are the first workers who have contributed the subject through theoretical modeling and numerical analysis, assuming heat is transported by conduction and convection and the condensate is in pendular state. The analysis was limited to a quasi steady-state, viz. the temperature and vapor concentration remain unchanged with time before the condensates become mobile. Motakef and El-Masri [2] first considered the quasi steady-state corresponding to mobile condensate, and presented an approximate solution by neglecting the condensation during the initial transient period and effects of condensate motion on the temperature distribution. This theoretical model was later extended by Shapiro and Motakef [3] to analyze the unsteady heat and moisture transport processes through the calculation of quasi-steady fields in time-varying domains and compared the analytical results with experimental ones under some very limited circumstances. This analysis was only appropriate when the time scale for the motion of the dry-wet boundary in porous media is much larger than the thermal diffusion time scale, which may however not be the case with frosting and small moisture accumulation [4].

Farnworth [5] presented the first dynamic model of coupled heat and moisture transfer with sorption and condensation. This model was rather simplified and only appropriate for multi-layered clothing as it was assumed that the temperature and moisture content in each clothing layer were uniform. Vafai and Sarkar [6] first modeled the transient heat and moisture transfer with condensation rigorously. For the first time, the interface between the dry and wet zones was found directly from the solution of the transient governing equations. In this work, the effects of boundary conditions, the Peclet and Lewis number on the condensation process is numerically analyzed. Later Vafai and Tien [7] extended the analysis to two-dimensional heat and mass transport accounting for phase change in a porous matrix. Tao, et al [4] first analyzed the frosting effect in an insulation slab by applying Vafai and Sarker's model to the case with temperature below the triple point of water. They [8] have also for the first time considered the hygroscopic effects of insulation materials in the modeling. Murata [9] first considered the falling of condensate under gravity and built the phenomena into his steady-state model. The effect of condensates on the effective thermal conductivity and radiative heat transfer were for the first time considered in Fan et al's transient model [10] on condensation in porous media.

Although considerable work has been carried out in the past on heat and moisture transfer with phase change, the transient solution to the problem with mobile condensates has not been found. The present work is to extend the previous transient model [10] to take into account of the movement and evaporation of condensates.

NOMENCLATURE

C_a water vapor concentration in the inter-fiber void space ($kg\ m^{-3}$)

C_a^* saturated water vapor concentration in the interfiber void space ($kg\ m^{-3}$)

C_f water vapor concentration in a fiber over its radius at a position of the fibbrous batting at a certain time ($kg\ m^{-3}$)

C_v effective volumetric heat capacity of the fibrous batting ($kJ\ m^{-3}\ K^{-1}$)

C_{v0} volumetric heat capacity of the dry fibrous batting ($kJ\ m^{-3}\ K^{-1}$)

C_w volumetric heat capacity of water ($kJ\ m^{-3}\ K^{-1}$)

D_a diffusion coefficient of water vapor in the air ($m^2\ s^{-1}$)

D_l disperse coefficient of free water in the fibrous batting ($m^2\ s^{-1}$)

E the evaporation coefficient, dimensionless

$e_{\square}$ surface emissitivity of the lining fabrics (1: inner lining; 2: outer lining)

F total thermal radiation incident on a point (W) (i.e. R: travel to the right, L: travel to the left)

H_c convective mass transfer coefficient ($m\ s^{-1}$)

H_T convective thermal transfer coefficient ($kJ\ m^{-2}\ K^{-1}$)

k_e effective thermal conductivity of the fibrous batting ($kJ\ m^{-1}\ K^{-1}$)

k_f thermal conductivity of fiber ($kJ\ m^{-1}\ K^{-1}$)

k_a thermal conductivity of air filling in the fabric batting ($kJ\ m^{-1}\ K^{-1}$)

k_w thermal conductivity of water in the fabric batting ($kJ\ m^{-1}\ K^{-1}$)

L thickness of the fabric batting (m)

M the molecular weight of the evaporating substance, 18.0152 (g/mol) for water

p pressure of water vapor in the inter-fiber void ($mmHg$)

p_{sat} saturation vapor pressure of water at absolute temperature T_s ($mmHg$)

P_{sat} the saturated vapour pressure at the temperature T_v($mmHg$)

p_v vapor pressure in vapor region at T_s ($mmHg$)

r radius of fibers (m)

R the universal gas constant, 8.314471×10^7 ($joules\ K^{-1}\ mol^{-1}$)

$R_{t\square}$ resistance of direct heat transfer ($s\ m^{-1}$)(i.e. 0:inner fabric, 1:outer fabric)

$R_{w\square}$ resistance of water vapor transfer ($s\ m^{-1}$)(i.e. 0:inner fabric, 1:outer fabric)

$RH_{\square}$ relative humidity (%)(i.e. 0: surface next to human body, 1:surranding air)

$T_{b\square}$ temperature of the boundaries (K) (i.e. 0: surface next to human body, 1:surranding air)

$C_{a\square}$ moisture concentration at the boundaries (K) (i.e. 0: surface next to human body, 1:surranding air)

T_s temperature at the interface (K)

T_v temperature in vapor region (K)

t real time from change in conditions (s)

w resistance to water vapor resistance (i.e. 0:inner fabric, 1: outer fabric)

W_f water content of the fibers in the fabric, $W_f = C_f/\rho$

W water content of the fibrous batting

W_c Critical level of water content above which the liquid water becomes mobile

W_i Initial water content.

x distance (m)

ε porosity of the fabric

λ latent heat of (de)sorption or condensation of water vapor b7y the fibers ($kJ\ kg^{-1}$)

ρ density of the fibers ($kg\ m^{-3}$)

τ effective tortuosity of the fabric

β radiative sorption constant

σ Boltzmann constant

Γ the rate of (de)sorption, condensation, freezing and/or evaporation ($kg\ s^{-1}\ m^{-3}$)

MATHEMATICAL MODEL

We consider a physical system (i.e. a clothing assembly) consisting of a thin inner fabric layer close to human body, a thick porous fibrous batting and a thin outer fabric next to the cold environment as shown in Figure 1. The following assumptions are made:

(1). The porous fibrous batting is isotropic.

(2). Volume changes of the fibers due to changing moisture and water content are neglected.

(3). Local thermal equilibrium exists among all phases and as a consequence, only sublimation or ablimation is considered in the frozen region.

(4). Convective heat transfer in the fibrous batting is negligible. This is justified based on the past experimental work on dry heat transfer in fibrous insulation [11].

(5). The moisture content at the fiber surface is in sorptive equilibrium with that of the surrounding air.

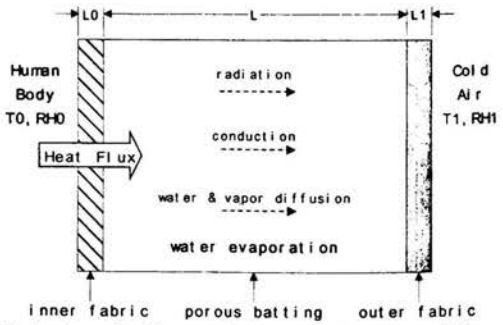

Fig.1 schematic diagram of the porous fabric assemblies

Consider the heat and moisture transfer within the porous batting, based on the conservation of heat energy and applying the two-flux model of radiative heat transfer [10,11], at position x and time t, we have

$$C_v(x,t)\frac{\partial T}{\partial t}=\frac{\partial}{\partial x}(k_e(x,t)\frac{\partial T}{\partial x})+(\frac{\partial F_L}{\partial x}-\frac{\partial F_R}{\partial x})+\lambda(x,t)\Gamma(x,t) \quad (1)$$

where, $\frac{\partial F_L}{\partial x}=\beta F_L-\beta\sigma T^4(x,t)$

$$\frac{\partial F_R}{\partial x}=-\beta F_R+\beta\sigma T^4(x,t)$$

According to mass conservation, moisture transfer in the inter-fiber void is governed by the following equation:

$$\varepsilon\frac{\partial C_a}{\partial t}=\frac{D_a\varepsilon}{\tau}\frac{\partial^2 C_a}{\partial x^2}-\Gamma(x,t) \quad \textbf{(2)}$$

The diffusion of free water in the porous batting is governed by:

$$\rho(1-\varepsilon)\frac{\partial(W-W_f)}{\partial t}=\rho(1-\varepsilon)D_l\frac{\partial^2(W-W_f)}{\partial x^2}+\Gamma(x,t) \quad (3)$$

where, $W_f(x,t)=C_f(x,t)/\rho$, which is the water absorbed within the fibre; W is the total water content including that absorbed by the fibres and on the fibre surface,

$$W(x,t)=\frac{1}{\rho}\int_0^t\Gamma(x,t)dt\,; \quad \textbf{(4)}$$

W-W_f is the water content on the fibre surface and is defined as the free water content. D_l is defined phenomenologically, and is dependent on water content, temperature and properties of the fiber batting. D_l=0 when the condensate is immobile, which is the case when the water content is less than a critical value W_c, or when the free water is frozen. Equation (3) only applies when $W > W_f$.

When the relative humidity is less than 100%, viz. there is no condensation, $\Gamma(x,t)$ is the rate of absorption or desorption, which may be determined according to the Fick's law of diffusion with a diffusion coefficient D_f dependent on the temperature and water content in fibers [10], viz.

$$\frac{\partial C_f'}{\partial t}=\frac{1}{r}\frac{\partial}{\partial r}(D_f\frac{\partial C_f'}{\partial r}) \quad \textbf{(5)}$$

where, r is the radius, C_f' is the volumetric moisture concentration in the fiber. The boundary condition for equation (5) can be determined by assuming that the moisture concentration at the fiber surface $C_f'(x,R_f,t)$ (R_f is the radius of the fiber) is instantaneously in equilibrium with the surrounding air. Consequently, $C_f(x,R_f,t)$ is a known function of the relative humidity of the surrounding air *RH(x,t)*, i.e.,

$$C_f'(x,R_f,t)=f(RH(x,t)) \quad \textbf{(6).}$$

The function, f, is a known empirical functional relationship, which can be found in textile textbooks in data or graphical form. With C_f, the water content absorbed by the fibers W_f may be integrated by

$$W_f(x,t)=\{2/(\rho R_f^2)\}\int_0^{R_f}C_f\,rdr \quad (7),$$

where, ρ is fiber density. After determining the fiber water content, the absorption rate $\Gamma(x,t)$ in the non-condensation region can then be calculated by:

$$\Gamma(x,t)=\Gamma_s(x,t)=\rho(1-\varepsilon)\frac{\partial W_f(x,t)}{\partial t} \quad (8)$$

When the relative humidity reaches 100%, condensation takes place in addition to absorption. The water condensation rate $\Gamma_c(x,t)$ can be uniquely determined by the mass balance equation, i.e.

$$\Gamma_c(x,t)=(\frac{D_a}{\tau}\frac{\partial^2 C_a^*(x,t)}{\partial x^2}-\frac{\partial C_a^*(x,t)}{\partial t})\varepsilon \quad (9)$$

where, $C_a^*(x,t)=216.5\times P_{sat}\times10^{-6}/T(x,t)$

When liquid water diffuses to the region where the relative humidity is below 100%, evaporation takes place. Many models had been proposed to determine water evaporation [12]. The model applied in the present study is expressed as follows:

$$\Gamma_e=E\sqrt{M/2\pi R}(P_{sat}/\sqrt{T_s}-P_v/\sqrt{T_v}) \quad (10).$$

Base on the definition of relative humidity, we have:

$RH=P_v/P_{sat}'$, therefore

$$P_v=RH\cdot P_{sat}' \quad (11).$$

According to our third assumption, T_v=T_s, therefore

$$P_{sat}'=P_{sat} \quad (12),$$

Substitute P_v in Equation (10) with Equation (11), and then substitute P_{sat}' with P_{sat}, we get:

$$\Gamma_e = E\sqrt{M/2\pi R}(1-RH)P_{sat}\Big/\sqrt{T_s} \qquad (13)$$

The effective thermal conductivity in Equation (1) is calculated by

$$k_e = \varepsilon k_a + (1-\varepsilon)(k_f + wk_w) \qquad (14)$$

and the effective volumetric heat capacity of the fibrous batting is calculated by

$$C_v = C_{v0} + WC_w \qquad (15)$$

The boundary conditions to main differential equations (1) and (2) are the same as those reported previously [10]. Consider the conductive heat transfer at the interface between the inner thin fabric and the fibrous batting and that between the outer thin fabric and the fibrous batting, we have

$$\begin{cases} k_e(x,t)\dfrac{dT^{n+1}(x)}{dx}\Big|_{x=0} = \dfrac{T_0^{n+1} - T_{b0}}{R_0} \\ k_e(x,t)\dfrac{dT^{n+1}(x)}{dx}\Big|_{x=L} = \dfrac{T_{b1} - T_N{}^{n+1}}{R_1 + 1/H_T} \end{cases} \qquad (16).$$

Consider the moisture diffusion at the interface between the inner thin fabric and the fibrous batting and that between the outer thin fabric and the fibrous batting, we have

$$\begin{cases} D_a\varepsilon\dfrac{\partial C_a^{n+1}}{\partial x}\Big|_{x=0} = \dfrac{C_{a0}^{n+1} - C_{ab0}}{w_0} \\ D_a\varepsilon\dfrac{\partial C_a^{n+1}}{\partial x}\Big|_{x=L} = \dfrac{C_{ab1} - C_{a1}^{n+1}}{w_1 + 1/H_c} \end{cases} \qquad (17)$$

Consider the radiative heat transfer at the interface between the inner thin fabric and the fibrous batting and that between the outer thin fabric and the fibrous batting, we have

$$\begin{cases} (1-e_1)F_L(0,t) + e_1\sigma T^4(0,t) = F_R(0,t) \\ (1-e_2)F_R(L,t) + e_2\sigma T^4(L,t) = F_L(0,t) \end{cases} \qquad (18)$$

NUMERICAL COMPUTATION

The differential equations in the above section were solved by the Implicit Finite Difference Method, with assumed initial conditions simulating different practical circumstances. The computational procedure was such that, at each time step and each position, the computed vapor concentration $C_a(x,t)$ was compared with the saturation vapor concentration $C_a^*(T(x,t))$ at the corresponding temperature. If the calculated vapor concentration was greater than, or equal to, the saturation one, $C_a(x,t)$ was then set to $C_a^*(T(x,t))$. The condensed water content was then calculated by equation (9). At each time step and position, the free water content is checked, if $W > W_f$, Equation (13) was used to calculate the rate of evaporation and Equation (3) was used to calculate the free water diffusion. The liquid water diffussivity D_l will initially be set to be zero as there is no liquid movement at the start. At each time step and position, the calculated water content W was also compared with the critical water content W_c. If W was greater than W_c and the temperature was greater than 0°C, D_l will be set to $D_l(W)$. With the new water content, the effective thermal conductivity $k(x, t)$ was updated at each position and time step.

ANALYSIS AND VERIFICATION OF THE MODEL

Farnworth [5] reported qualitatively based on his experimental observation that, heat flux through wet fibrous batting was 3 to 5 times as much as that through dry batting. This dramatic increase in heat flux must be caused, he believed, by the extra heat transport due to the evaporation and diffusion of water vapor, since the increase in conductive heat transport due to the increased water content could only explain for an increase of 10% or 20%.

Table I: Parameters used in the Calculation

ρ	λ			ε	τ
	Dry region	Wet region	Freezing region		
910.0	2522.0	2260.0	2593.0	0.87	1.2
D_a	D_f	D_l	C_{v0}	C_{w0}	E
2.5×10^{-5}	1.3×10^{-13}	9.0×10^{-4}	1715.0	4200.0	7.0×10^{3}
R_{w0}	R_{wl}	R_{l0}	R_{l0}	RH_0	RH_1
0.1	0.1	0.3	0.3	96%	90%
k_a	k_f	k_w	β	σ	W_c
0.025	0.1	0.57	8	5.672×10^{-12}	5
E_1	e_2	T_{b0}	T_{bl}	R	L
0.9	0.9	306 (33 °C)	253 (-20°C)	1.03×10^{-5}	0.04

Note: the fibrous batting was assumed to be made of polypropylene

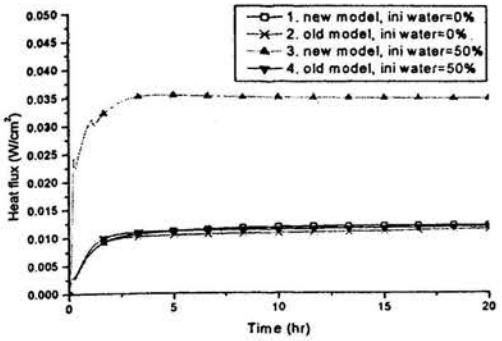

Fig. 2 Predicted heat flux for an initially dry and wet batting

The new model proposed in this paper and the old model reported previously [10] were both applied to calculate the heat flux through an initially dry and an initially wet batting to see whether the inclusion of evaporation and liquid water movement in the new model can better explain the experimental observation by Farnworth [5]. The parameters used in this calculation are listed in Table I. The results are plotted in Figure 2. As can be seen, when the fibrous batting is initially dry, the heat flux predicted by the new model and that by the old model are very similar, indicating that evaporation and movement of liquid water considered in the new model have only small effect on the insulation property of the batting. However, when the initial water content is 50%, simulating a initially wet batting, the heat flux predicted by the new model is about 3 time of that by the old model, which indicates that evaporation and movement of liquid water in the batting are very important mechanism accounting for the dramatic increase in heat flux. The calculated results are in agreement with Farnworth's observation.

To better understand the mechanism of the phenomena, change of water content distribution with time predicted by the new model was plotted in Figure 3 for the initially dry batting and in Figure 4 for the initially wet batting, respectively. As can be seen, when the batting is initially dry the accumulation of condensed water is slow even under the cold condition of -20°C. The condensed water may diffuse to areas having lower water content and re-evaporate, resulting a rather flat water content distribution as shown in Figure 3. However, the situation is very different for an initially wet batting. In this case, the water content in the inner region (i.e. close to the warm human body) reduces very quickly due to evaporation and the released moisture is diffused towards outer (or cold) region, where it is re-condensed. The condensed, but unfrozen (liquid) water in the outer region may move back to the inner warm region by liquid water diffusion and get re-evaporated in the inner region. The evaporation, moisture diffusion, condensation and liquid water movement create a cyclic effect, which greatly increases the heat flux through the system.

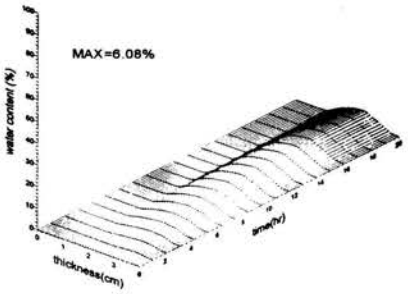

Fig. 3 change of water content distribution with time in batting.

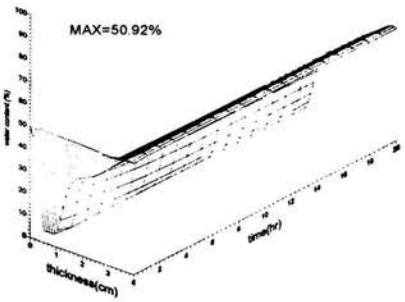

Fig. 4 change of water content distribution with time in batting.

The model was also used to fit the experimental results of a drying test carried out by Farnworth [5]. In this test, a 13mm thick polyester batting of 1.3% fiber volume (230g/m²), having an initial water content of 150%, was contained in a polyester mesh within a cylindrical holder (There was a 5 mm hole drilled through the holder to permit the exchange of water or moisture). The assembly was prepared and placed on a hot plate controlled at 35°C in an atmosphere of 22°C and 30% RH. In the theoretical calculation, some parameters listed in Table I were adjusted to reflect the experimental condition. The value of adjusted parameters are listed in Table II.

Table II. Value of the Adjusted Parameters

ρ	ε	L	Initial water
1361.0	0.987	0.013	150%
T_{b0}	T_{bl}	RH_1	
307 (35 °C)	255 (-22°C)	30%	

Figure 5 compares the calculated results using our model with the experimental ones. The theoretically predicted results matches well with the experimental ones in trend. The generally

lower heat loss may be due to the fact that additional heat energy was required in the experiment to dry off the water on the holder and absorbed by the polyester mesh.

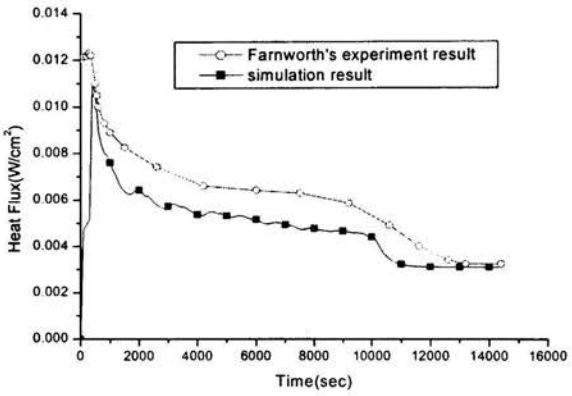

Figure 5. Heat flux comparison between experiment result and simulated result

CONCLUSIONS

Water evaporation and movement in porous media are important phenomena, which can greatly affect the coupled heat and moisture transfer. In our work, this phenomena has been modeled incorporating radiative heat transfer, evaporation and mobile condensates. Based on the comparison between the theoretical and experimental results, the proposed model is believed to be appropriate for porous fibrous insulation. The model may be further extended to other porous media.

ACKNOWLEDGEMENTS

The authors would like to thank the Research Grant Committee of the Hong Kong University Grant Council for funding the project (RGC Ref: PolyU 5142/00E).

REFERENCES

[1]. Ogniewicz, Y. and Tien, C. L., Analysis of condensation in porous insulation, J. Heat Mass Transfer, 1981;24: 421-429.

[2]. Motakef, S., El-Masri, M. A., Simultaneous heat and mass transfer with phase change in a porous slab, J Heat Mass Transfer, 1986;29(10):1503-1512.

[3]. Shapiro, A. P. and Motakef, S., Unsteady heat and mass transfer with phase change in porous slab: analytical solutions and experimental results, J. Heat Mass Transfer, 1990;33(1): 163-173.

[4]. Tao, Y. X., Besant, R. W., and Rezkallah, Unsteady Heat and Mass Transfer with Phase Changes in an Insulation Slab: Frosting Effects, Int. J. Heat Mass Transfer, Vol. 34, No. 7, pp. 1593-1603, 1991.

[5]. Farnworth, B. A Numerical Model of the Combined Diffusion of Heat and Water Vapor Through Clothing, Tex. Res. J., Vol. 56, No. 11, pp.653-665, (1986).

[6]. Vafai, K. and Sarkar, S., Condensation Effects in a Fibrous Insulation Slab, J. Heat Transfer, Vol. 108, No. 8, pp.667-675, 1986.

[7]. Vafai, K. and Tien, H. C., A Numerical Investigation of Phase Change Effects in Porous Materials, Int. J. Heat Mass Transfer, Vol. 32, No. 7, pp.1261-1277, 1989.

[8]. Tao, Y. X., Besant, R. W., and Rezkallah, The Transient Thermal Response of a Glass-fiber Insulation Slab with Hygroscopic Effects, Int. J. Heat Mass Transfer, Vol. 35, No. 5, pp. 1155-1167, 1992.

[9]. Murata, K., Heat and mass transfer with condensation in a fibrous insulation slab bounded on one side by a cold surface, Int. J. Heat Mass Transfer, 1995;38(17): 3253-3262.

[10]. Fan, J., Luo, Z. and Y. Li, Heat and Moisture Transfer with Sorption and Condensation in Porous Clothing Assemblies and Numerical Simulation, Int. J. Heat Mass Transfer, 43(2000) 2989-3000.

[11]. Farnworth, B., Mechanics of heat flow through clothing insulation, Tex. Res. J., 1983,717-725

[12]. Jones, Frank E., Evaporation of Water – with emphasis on application and measurements, Lewis Publishers, Michigan, USA, 1992, 25-43

HEFAT2002
1st International Conference on Heat Transfer, Fluid Mechanics and Themodynamics
8-10 April 2002, Kruger Park, South Africa
GJ2

APPROPRIATE SCALING METHODS FOR STUDYING BLOOD FLOW THROUGH A DISTAL ANASTOMOSIS

J.D. Gray, I. Owen and M.P.Escudier
Department of Engineering, Mechanical Engineering
University of Liverpool,
Liverpool, L69 3GH.
United Kingdom

ABSTRACT

The flow through a distal anastomosis has been studied experimentally with the aid of a Particle Image Velocimetry system. Trends of axial wall shear stress with Reynolds number were produced for two blood analogues: a non-Newtonian power-law fluid, and a Newtonian fluid. By using two separate scaling methods for the two fluids it has been possible to investigate the effect of assuming that blood can be modeled with a Newtonian liquid without the rheological effects and Reynolds number effects becoming confused. It has further been possible to investigate two common methods of comparing Newtonian flows with non-Newtonian flows and assess their respective ability to predict the wall shear stress trends of a power-law fluid (such as blood).

It is found that the Newtonian assumption can lead to errors well in excess of 100% in the prediction of peak wall shear stress, although general flow parameters such as stagnation points are largely unaffected. It is concluded that in any scaling procedure where a non-Newtonian fluid is being modeled, it is preferable to include some measure of the non-Newtonian nature of that fluid.

INTRODUCTION

Scaling methods for Newtonian fluid flow are well established and are in widespread use throughout engineering research and practice. However, the majority of synthetic fluids are non-Newtonian and the methods of scaling are far more complex. Many natural liquids e.g. blood, synovial fluid and sputum are also non-Newtonian. One reason for the scaling complexity is that it is difficult to separate the effects of Reynolds number from the viscous (or rheological) effects in any comparison between the flow of fluids of a different rheological character. In the case of blood flow through an artery, for example, the flow of blood *in vivo* is usually modeled using a Newtonian liquid *in vitro*. Various methods for calculating 'equivalent' flow rates for blood flow are currently employed in the literature, but there is uncertainty as to which method is most appropriate. For this reason, a suitable approach to scaling applied to experiments in which both non-Newtonian and Newtonian blood 'analogues' are employed is needed.

The specific case under consideration in this study is the flow in an arterial bypass graft (a distal anastomosis). Ideally, any model used to study this (or any other) type of flow will be dynamically similar to the in vivo case, i.e. all the relevant forces will be in the same ratio for both model and life scale and therefore all the flow phenomena at life scale will be reproduced in the model. Since blood is a non-Newtonian fluid, this would clearly involve including at least one parameter to describe the non-Newtonian nature of the fluid. However, in an effort to simplify what is a complex collection of conditions, many authors [e.g. 1, 2, 3] have chosen to neglect the non-Newtonian character of blood. This has generated considerable debate as to how big an effect this has on the flow conditions being studied.

Unfortunately, despite many years of research there is still considerable confusion in the literature about the comparison between non-Newtonian and Newtonian blood analogues. Some authors [e.g. 4] report no differences in the essential flow characteristics, with errors limited to 50% in the prediction of secondary flows. The majority of authors conclude that there are differences, but due to the myriad of different flow conditions in the body, cannot come to a consensus about the magnetude of these differences, or the conditions under which they appear.

For example, Ballyk *et al* [5] report in a study of a distal anastomosis that the rheological effects are important in steady flow conditions, but largely disappear under pulsatile conditions, while Rodkiewicz *et al* [6] conclude that for a straight artery, the non-Newtonian effects only appear in pulsatile flows. Chakravarty and Mandal [7] also find seemingly contradictory results, reporting that a Newtonian fluid can model blood flow satisfactorily in the parent aorta of the aortic arch, but 'drastic change' is seen further downstream in the daughter artery.

Much of the confusion arises from the fact that most authors do not give due attention to the scaling procedures that arise from a process of dimensional analysis. The approach taken in much of the

literature is to assume the non-Newtonian fluid (blood) can be satisfactorily represented by a Newtonian fluid if the viscosity is chosen correctly. Doing this makes it possible to then study the two fluids (of different rheological character) at apparently similar Reynolds numbers. In general there are two schools of thought as to how best to generate a representative viscosity for blood. Since blood has a high shear Newtonian plateau, many [e.g. 8] use this value as a representative viscosity (in the order of 3.5mPa.s). Others [e.g. 9] prefer to take into account more of the low shear behavior of blood and choose to use a higher 'characteristic' viscosity. Either way, since the Reynolds number depends fundamentally upon a measure of the viscosity, any such assumption will lead to changes in Reynolds number effects, rendering this method of comparison somewhat clouded. This paper aims to avoid this problem by dealing with two separately defined Reynolds numbers; the Metzner-Reed Reynolds number for describing the non-Newtonian conditions, and the standard Newtonian Reynolds number for describing the Newtonian conditions.

DIMENSIONAL ANALYSIS AND SCALING

In this study it is assumed that blood rheology can be described by a power law relationship (equation 1) with n = 0.63 and κ = 0.015Pa.s^n, and that blood density, ρ = 1060kg.m^{-3}. It is further assumed that the blood flows at a steady rate with mean velocity U, through rigid-walled arteries of diameter D = 6mm (typical of femoral artery).

$$\eta = \kappa \dot{\gamma}^{(n-1)} \qquad (1)$$

It can be shown using standard dimensional analysis that the conditions described above can be entirely characterised by two non-dimensional groups. The first is the well-established Metzner-Reed Reynolds (Re_{MR}) number, and the second is the non-dimensional power law index, n (equation 2).

$$\frac{\rho D^n U^{(n-2)}}{\kappa}, \quad n \qquad (2)$$

Since the power law is a simple relationship, the scaling procedure is straightforward, with only one extra dimensionless group compared with the Newtonian case. If more detailed rheological models are used, it should be borne in mind that one more dimensionless group has to be incorporated for each extra parameter employed, making practical experimentation very difficult. It should also be noted, perhaps more importantly, that it is impossible to achieve dynamic similarity between a non-Newtonian and a Newtonian flow, and any attempt to compare the two can only be for practical purposes. For this reason the procedure adopted in this study will avoid a direct comparison between the Newtonian and power-law fluids, and deal with the two types of fluid separately. In particular, trends in axial wall shear stress with the Metzner-Reed Reynolds number will be studied using a power-law fluid and then similar trends will be produced with a Newtonian fluid but will be characterised by the standard Newtonian Reynolds number. Thus no assumption as to how best to relate the power-law to a Newtonian viscosity will be necessary and, by comparing the two sets of trends, conclusions can be made about which of the Newtonian trends best represents any given power-law trend.

Experimental Methods and Procedure

The experimental apparatus is shown schematically in figure 1. The test section (shown in inset) consists of a 45° end to side junction (representative of an end to side anastomosis graft) made from borosilicate glass tube of internal diameter 38.5mm. Typical fillet radii were 5mm and 10mm for the heel and toe respectively. An entry length of 47 pipe diameters is formed by 1m of 38.5mm glass tubing, together with the flowmeter section. Flow is provided by means of two gear pumps, whose speeds are controlled via a computer. (The two pumps enable the rig to produce a pulsatile flow, although only steady flows are reported in this paper.) The flow rate was measured using a combination of the Electro Magnetic flowmeter (Fischer & Porter DS4111A) and a PC30AT data collection card. Two flow control valves were positioned downstream of each branch of the testing section to allow the flow to be split in any proximal: distal ratio. Each of the three ratios used in the study (100% distal, 75%

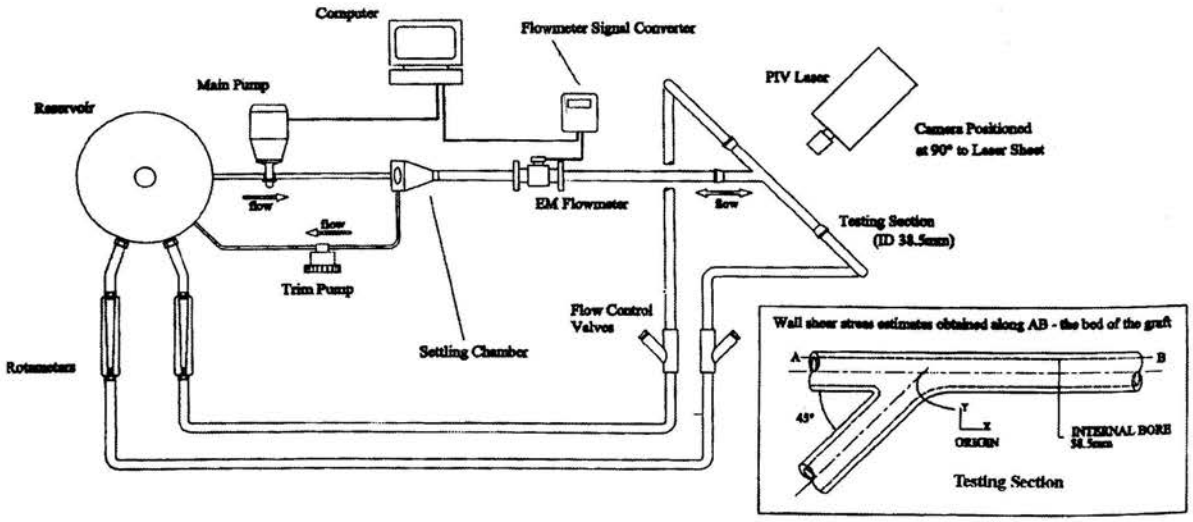

Figure 1 Schematic Diagram of Testing Apparatus

distal, and 50% distal) were measured by the rotameters (Fischer & Porter 10A3500) located at the end of each return branch.

As has already been stated, the test was conducted in two separate parts: power-law trends and Newtonian trends. The power-law fluid employed was an aqueous solution of 0.07%wt Xanthan Gum (a high molecular weight polymer). Its rheological characteristics (see equation 1) were measured using a TA *AR1000N* cone and plate rheometer (n = 0.63, K = 35.6mPa.s), and its density was found to be 1002kg/m^3. An aqueous solution of 60%wt glycerine (viscosity = 11.0mPa.s, r = 1152kg/m^3) was used as the Newtonian fluid. Since the experimental rig was larger (approx. 6 times) than a life-scale artery, some scaling calculations were necessary to obtain 'rig-scale' flow rates that were equivalent to the flow rates *in vivo*. For the power-law fluid the Metzner-Reed scaling procedure outlined by equation 2 was employed, while for the Newtonian case a suitable range was found to be 130 – 1200. The in vivo flow rates are typical of conditions in the femoral artery. Table 1 summarises these values.

Table 1 Metzner-Reed Reynolds Numbers calculated from *in vivo* parameters

Flow rate *in vivo* (ml/min)	Mean velocity (mm/s) (*in vivo* diameter = 6mm)	Metzner -Reed *Re*	Flow rate in rig (l/min) (from MR scaling)
120	70.1	76	4.16
270	159.2	232	9.39
415	244.6	420	14.49
563	331.9	640	19.70

Fluorescent seeding particles were added to the testing fluid to enable a Particle Image Velocimetry (PIV) system to be used to record the velocity distribution in the center plane of the graft. This raw information was then represented by a velocity vector map, an example of which is shown in figure 2. Each vector on the map represents an average of 100 readings.

In order to investigate dynamic similarity, it was necessary to use a parameter that showed a clear trend with Reynolds number. It was found that axial wall shear stress information along the bed of the graft, extracted from the velocity vector maps could be used for this purpose. These trends provided a clearer, more exact means of comparison than could be afforded by the vector maps alone, or by a comparison in the shape of velocity profiles. Wall shear stress is also of central importance to the study of arterial disease. Estimates of axial wall shear stress were found using the following equations:

$$\tau_w = \eta\dot{\gamma} = \kappa\dot{\gamma}^n \qquad \text{(from equation 1)}$$

so that:

$$\tau_w = \kappa\left(\frac{u}{\delta}\right)^n \qquad (3)$$

(where u is the velocity a distance δ from the wall)

Thus the wall shear stress distributions along the bed of the graft (A-B in fig. 1) were determined using the local velocities nearest to the wall, the distance of these velocities from the wall, and the rheological characteristics of the fluid. In order to eliminate errors in the measurement of δ due to refraction, a calibration target was used to find a relationship between the pipe radius recorded by the PIV system and the actual radius. (The measurements were taken typically 1mm from the wall.)

Discussion of Results

The first test performed was a check to demonstrate that the Metzner-Reed scaling procedure worked experimentally. A second, thicker power law fluid (0.05%wt Xanthan gum, 50%wt Glycerine, aqueous) was used to obtain results that could be compared to the Xanthan gum results. The power law index (n) of this fluid was the same as the 0.07%wt Xanthan gum solution, but the value of κ was increased (81.0 mPa.s). This enabled results to be obtained at the same Re_{MR} but at different flow rates and the results can be seen in figure 3. The values of axial wall shear stress along the bed of the graft are plotted non-dimensionally by dividing by ½ρU^2, and similarly the axial distance along the bed is plotted without dimensions, the origin being at the intersection of the centerlines of the two pipes.

The results show good agreement and therefore demonstrate that the Metzner-Reed procedure does work in practice, and can be used to accurately model a power law flow. These results also increase the confidence in the rig and instrumentation, since the trends are not only repeatable, but can be reproduced with fluids of different viscosities (with the same n value) flowing at different flow rates.

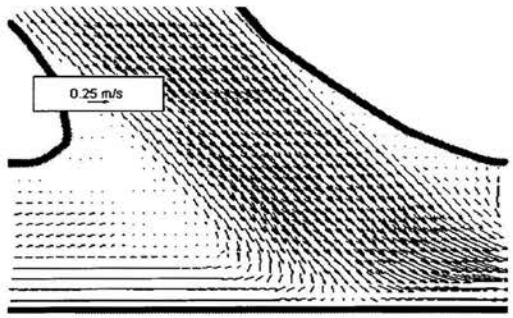

Figure 2 Velocity vector map for 0.07% Xanthan Gum, 75% distal split. Example of PIV output.

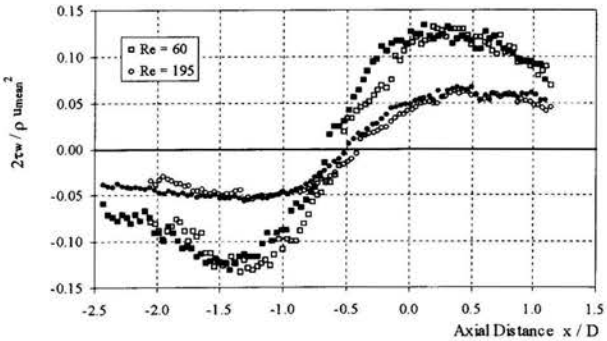

Figure 3 Wall shear stress predictions obtained using two fluids: Xanthan Gum (closed symbols) and Xanthan/Glycerine (open symbols)

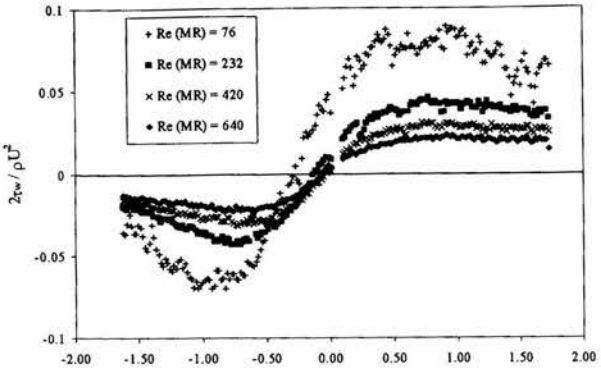

Figure 4 0.07% Xanthan Gum
50% Distal Flow

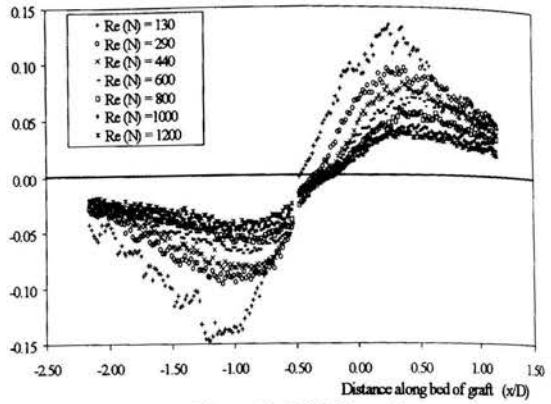

Figure 5 60% Glycerine
50% Distal Flow

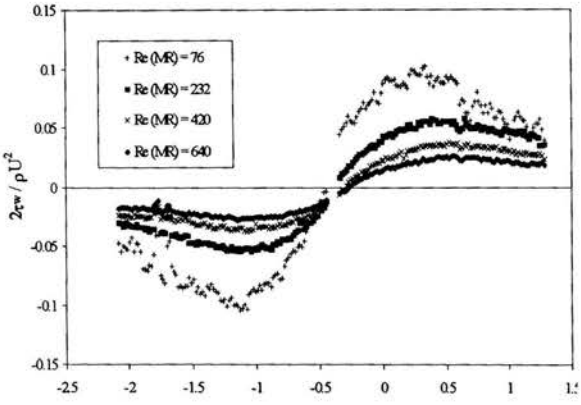

Figure 6 0.07% Xanthan Gum
75% Distal Flow

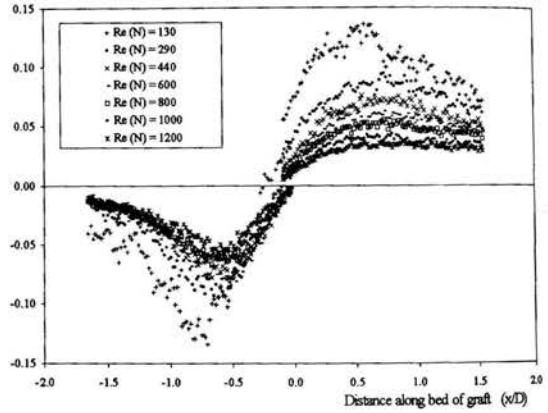

Figure 7 60% Glycerine
75% Distal Flow

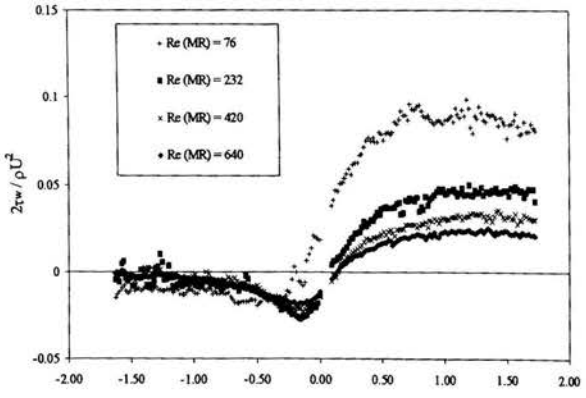

Figure 8 0.07% Xanthan Gum
100% Distal Flow

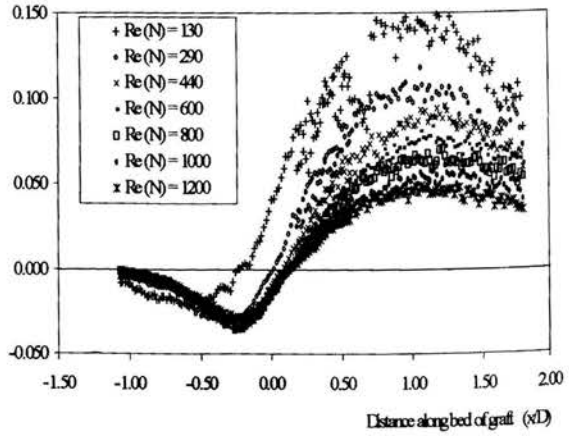

Figure 9 60% Glycerine
100% Distal Flow

Figures 4-9 show the results obtained for the 0.07%wt Xanthan gum solution and Newtonian fluid, at the three different flow splits. The graphs are presented in a similar way to figure 3. Upon initial inspection it is clear that there are similarities in the two sets of trends. Perhaps one of the most noteworthy points of similarity is that the stagnation points are in the same region for both types of fluid at each flow split. Another similarity is the general shape of the curves, although the peaks tend to be more clearly defined for the Newtonian fluid.

To obtain a more thorough understanding of the extent to which the trends match up, it is necessary to consider the two main assumptions made about blood rheology that were outlined in the Introduction of this paper. Table 2 shows the four main *in vivo* flow rates that were given in table 1. Alongside them is a list of the Newtonian Reynolds numbers that would be calculated if blood were assumed to have a Newtonian viscosity of 3.5mPa.s [8] and 7.8mPa.s [9]. It is now possible to compare the results obtained with a non-Newtonian fluid with those obtained for the Newtonian one, and see what effect the above assumptions have.

Table 2 Newtonian Reynolds numbers calculated from original flow rates, but assuming different blood viscosities (see above)

		Newtonian *Re* if:	
Flow rate *in vivo* (mm/s)	Metzner-Reed Re_{MR}	μ=3.5mPa.s [8]	μ=7.8mPa.s [9]
70.1	76	127	57
159.2	232	286	129
244.6	420	440	198
331.9	640	597	268

For example, consider the 50% distal flow split trends. To ascertain which Newtonian Reynolds number should be used to model, say, the second power-law trend (Re_{MR}=232), it is a simple matter of looking at the set of Newtonian trends and deciding which is closest to the Re_{MR}=232 trend. From table 2 it can be seen that the first assumption (blood viscosity = 3.5mPa.s) would suggest a Reynolds number of 286. By glancing across to the Newtonian graph, it can be seen that this would give an over-prediction of peak axial wall shear stress of approximately 50%. If the viscosity were assumed to be 7.8mPa.s, the suggested Reynolds number would be 129. This time a glance across to the Newtonian graph demonstrates that this would generate a peak stress value of double the true value. According to the graph the best Newtonian Reynolds number to predict the wall shear stress would be 800. It can be shown that this would be the equivalent of assuming a blood viscosity of only 1.25mPa.s, i.e. below the second Newtonian plateau level.

Unfortunately this does not present an end to the problem. If a similar analysis is performed with the second trend in the 100% distal split group the result is quite different. It would appear that the 'best' Reynolds number for this case would be 1200 (equivalent to a blood viscosity of 0.84mPa.s). Thus markedly different assumptions are needed to even accommodate a change in the flow split.

There is one more point that needs to be made to highlight the dangers of assuming that blood behaves as a Newtonian fluid. In the analysis performed so far, the aim has been to find a Newtonian trend that is numerically similar to a given power-law trend for one flow parameter (the wall shear stress). However even when a numerical match is found, there is no guarantee that the Reynolds number suggested will produce flow conditions able to predict any other flow characteristic. When studying flow through an anastomosis model, it is possible to observe three distinct flow regimes. In the first, at very low Reynolds numbers, the flow is simply two-dimensional with very little secondary flow. As the Reynolds number is increased, three-dimensional flow develops, and the classical helical flow patterns can be seen. If the Reynolds number is increased further, the beginnings of unsteady flow can be observed. It would therefore be entirely possible to find conditions that predicted one parameter (e.g. wall shear stress) well, but was actually in a completely different flow regime, totally uncharacteristic of the *in vivo* conditions.

Conclusion

A comparison has been made between the axial wall shear stress along the bed of a distal anastomosis predicted by a Metzner-Reed scaling method and a Newtonian scaling method. By using two separate scaling methods, it was possible to draw conclusions about the results without Reynolds effects confusing the issue.

It was found that by using the most popular Newtonian assumption (i.e. blood viscosity = 3.5mPa.s), errors well in excess of 100% were generated in the prediction of the wall shear stress values. Furthermore, if a higher value for blood viscosity is assumed these errors will increase, not decrease. It was also found that there is no single value of Newtonian viscosity that can be assumed to give a close numerical match with the non-Newtonian flow for every case. In light of this, and due to excellent agreement obtained when the Metzner-Reed scaling procedure was used, it must be concluded that in experiments in which the numerical values of wall shear stress are not irrelevant, the Metzner-Reed Reynolds scaling procedure is highly preferable.

References

1 Perktold, K., Hofer, M., Rappitsch, G., Loew, M., Kuban, B.D., Friedman, M.H., 1998. Validated computation of physiologic flow in a realistic coronary artery branch. Journal of Biomechanics 31, 217-228.

2 Ojha, M., Cobbold, R.S.C., Johnston, K.W., 1994. Influence of angle on wall shear stress distribution for an end-to-side anastomosis. Journal of Vascular Surgery 19, 1067-1073.

3 Hughes, P.E., How, T.V., 1996. Effects of geometry and flow division on flow structures in models of the distal end-to-side anastomosis. Journal of Biomechanics 29, 855-872.

4 Perktold, K., Resch, M., Florian, H., 1991. Pulsatile non-Newtonian flow characteristics in a three-dimensional human carotid bifurcation model. Journal of Biomechanical Engineering 133, 464-475.

5 Ballyk, P.D., Steinman, D.A., Ethier, C.R., 1994. Simulation of non-Newtonian blood flow in an end-to-side anastomosis. Biorheology 31, 565-586.

6 Rodkiewicz, C.M., Prawal Sinha, Kennedy, J.S., 1990. On the application of a constitutive equation for whole human blood. Journal of Biomechanical Engineering 112, 198-206.

7 Chakravarty, S., Mandal, P.K., 1997. An analysis of pulsatile flow in a model aortic bifurcation. Int. J. Engng. Sci. 35, 409-422.

8 Cho, Y.I., Kensey, K.R., Effects of the non-Newtonian viscosity of blood on flows in a diseased arterial vessel. Part 1: Steady flows. Biorheology 28, 241-262.

9 Gijsen, F.J.H., Allanic, E., van de Vosse, F.N., Janseen, J.D., 1999. The influence of the non-Newtonian properities of blood on the flow in large arteries: unsteady flow in a 90° curved tube. Jornal of Biomechanics 32, 705-713.

HEFAT 2002
1st International Conference on Heat Transfer, Fluid Mechanics, and Thermodynamics
8-10 April 2002, Kruger Park, South Africa
HM1

ELECTRIC STORAGE WATER HEATERS – TECHNICAL AND ECONOMICAL EFFICIENCY

Manfred Hoelblinger*, Manfred Sakulin**
*Assistant Professor; **Associate Professor
Department for Electrical Power Systems, TU Graz - Austria
Inffeldgasse 18, A-8010 Graz
Austria, Europe
e-mail: hoelblinger@ifea.tu-graz.ac.at; sakulin@ifea.tu-graz.ac.at

ABSTRACT

Besides space heating warm water supply is the second largest energy consumer in the domestic sector, covering around 10 to 20% of the residential energy consumption.

In a first step, the paper shows the present situation concerning the standard standing losses of electric storage water heaters. For that purpose, a simulation model was developed calculating the standard standing losses as a function of the geometrical dimensions of the tank and the used insulation performance. The simulation model also allows to determine the optimal insulation thickness to reach minimum life cycle cost for given electricity and insulation prices.

Standard standing losses are characteristic energy figures which only allow to compare the performance of similar appliances. For further analyses like estimation of energy savings or CO_2 emissions the knowledge of the real standing losses is of importance. Therefore, another simulation model (WATERSIM) calculating the real energy demand was developed. With this simulation model the real energy demand for each tapping profile can be determined.

Both models - for standard standing and real standing losses - form the basis for an economical analysis to find out the optimal insulation thickness for electric storage heaters and the resulting CO_2 emission saving potential.

INTRODUCTION

About 30 % (42,5 million) of the 142 million households in the European Union are using electric water heating systems, mostly electric storage water heaters (ESWH) – see figure 1.

Storage water heaters allow to provide a larger amount of hot water with only a small heating power. However, due to unavoidable heat transmission those hot storage tanks cause remarkable standing losses.

The goal of this paper is to perform a technical and economical analysis to figure out the design characteristics of efficient appliances and to calculate the resulting energy and cost saving potentials for electric storage water heaters, - by means of an exact technical simulation model on the one hand, and a dynamic cost analysis on the other.

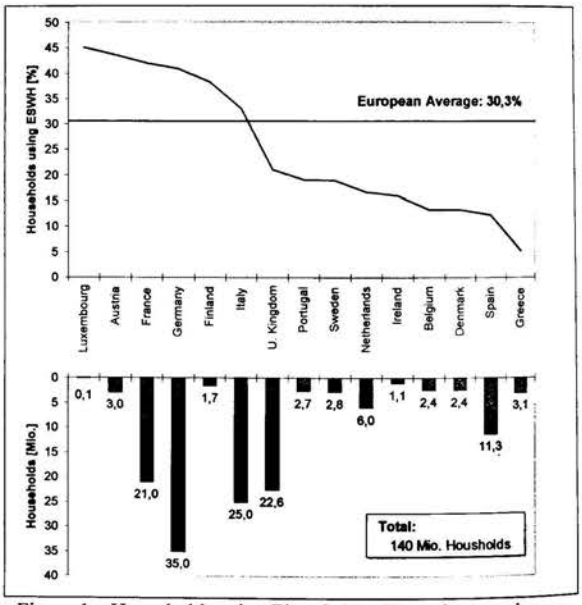

Figure 1: Households using Electric Hot Water Systems in European Countries 1995

STANDARD STANDING LOSSES

Standard standing losses $L_{st,st}$ are the characteristic figure which allows energy classification and makes storage heaters of the same capacity comparable, but they do not describe real life conditions. The situation of the electric storage heaters concerning standard standing losses is shown in the data base

supplied by CECED (the organisation of the European manufactures) - see figure 2, which is covering about 80 % of the European market.
As can be seen, the situation of the European ESWHs shows an extremely large spread of standard standing losses for heaters of the same capacity. For nearly all capacities a ratio in the standing losses up to four between the most inefficient and the best models was found on the market.

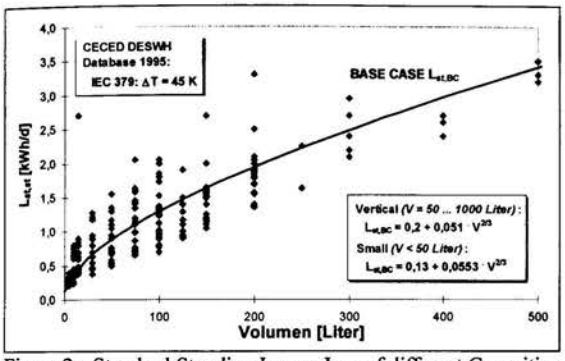

Figure 2: Standard Standing Losses $L_{st,st}$ of different Capacities of Hot Water Storage Tanks - CECED Database 1995

A Base Case $L_{st,BC}$ is defined as the average of the existing models in the CECED data base and is expressed by an approximation formula as a function of the capacity of the storage tank.

Vertical Capacities (50 ... 1000 litres):

$$L_{st,BC} = 0,2 + 0,051 \ V^{2/3} \ [kWh/d] \quad (1)$$

Small Capacities (< 50 litres):

$$L_{st,BC} = 0,13 + 0,0553 \ V^{2/3} \ [kWh/d] \quad (2)$$

• Testing conditions:

Standard standing losses $L_{st,st}$ have to be measured under standardised conditions according IEC 379/HD 500 with:

- ambient temperature $T_{amb} = 20$ °C
- and hot water temperature $T_h = 65$ °C

without any draw-off during the test (> 48 hours).

• Technical influences:

A simulation model for the calculation of the standard standing losses has to consider the physical behaviour of the heat transfer losses of the storage tank as a function of all energy relevant conditions. At a given temperature difference ΔT between hot water and ambient air, the standing losses of the full hot tank depend on the quality of heat insulation, i.e. the insulation thickness on side and top, the thermal conductivity of the insulation material, the effect of heat bridges (water outlets, thermo-sensors, anodes, circulation lines, mounting constructions, etc.) and the geometrical dimensions of the tank (i.e. mainly the ratio height to radius H/R).

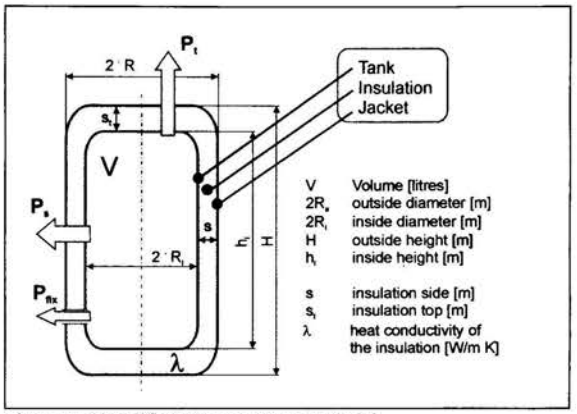

Figure 3: Simplified Storage Heater Model

• Sensitivity analysis:

A sensitivity analysis for the standard standing losses identifies and quantifies the main influence factors on the heat transfer and the resulting heat losses. The sensitivity analysis shows that the main influence on the standard standing losses follows from the ratio s/λ. All other design parameters are of minor influence and can not explain the big range for $L_{st,st}$ of the market models in the CECED data base – see figure 2. Assuming that the same insulation foam is used for nearly all models the most important influence factor is the insulation thickness.

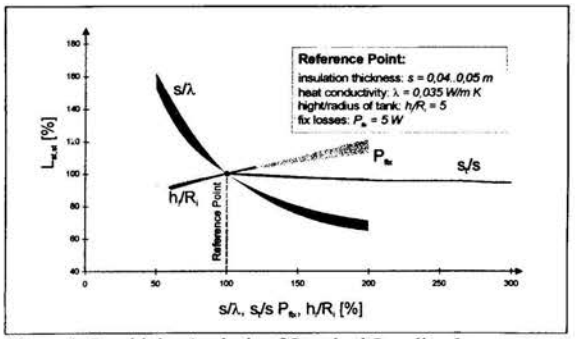

Figure 4: Sensitivity Analysis of Standard Standing Losses

REAL STANDING LOSSES

Standard testing conditions neglect all usage conditions, they only describe the stationary standing condition and quantify the resulting losses of a 24hour hot standing period after a 48 hour warm-up. Real life conditions, in contrary, take

The lower layer is heated up as soon as the power supply of the heating element is activated and as long as the thermo-sensor, which is situated above the heating element, gets "less than the set temperature". Heating procedure is assumed to take place only in the lower layer as long as its temperature is less than in the upper part, afterwards the total volume is heated up till the set temperature is reached.

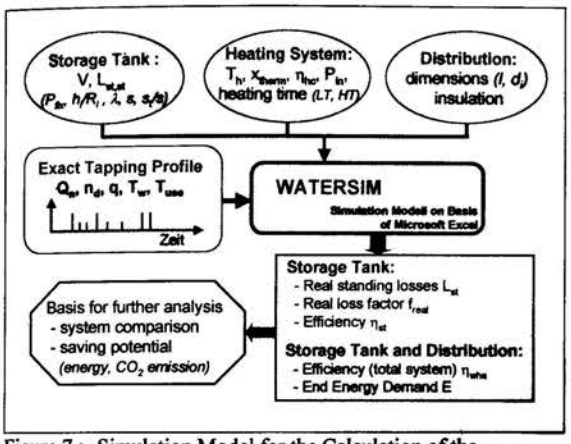

Figure 7 : Simulation Model for the Calculation of the Real Losses – WATERSIM

With this simulation model the real energy demand of low and high tariff storage heaters for each tapping profile is possible. It needs the input of the parameters for the storage tank, the heating system, the distribution system and the desired tapping profile.

In a next step, by introduction of some simplifications and by concentration on the most relevant influence factors, an easy to use approximation formula for the calculation of the real standard losses was developed on the basis of the exact calculation. With this tool it is now possible to estimate the real standing losses of electric storage water heaters in a simple way from the measured standard standing losses. The detailed simulation model and the simple approximation formulas were examined by measurements under standardised and under real conditions and showed sufficiently high accuracy [1].

The time schedule of draw-offs is determined by people's living habits which usually lead to a concentration of draw-offs in the morning and evening time in the bath-room, and a distributed demand, sometimes concentrated to noon in the kitchen. Therefore, as a simplification for some of the following energy analysis it is useful to define a 3-point tapping pattern by concentrating the draw-offs to only three time points expressed by the parameter v_8 and v_{19}.

As an approximation function for the real influence factor f_{real} the following formulas for the selected capacities can be derived:

200 litres low tariff:

$$f_{real} = 0{,}92 - 0{,}03 \cdot Q_{st} + 0{,}014 \cdot (v_{19} - v_8) \cdot Q_{st} \quad (4)$$

150 litres low tariff:

$$f_{real} = 0{,}92 - 0{,}038 \cdot Q_{st} + 0{,}018 \cdot (v_{19} - v_8) \cdot Q_{st} \quad (5)$$

50 ... 100 litres high tariff:

$$f_{real} = 0{,}88 \quad (6)$$

Q_{st} daily hot water output of the storage tank [kWh/d]
v_8 morning demand between 6 and 10 a.m. in percentage of the daily energy demand Q_{st}
v_{19} evening demand after 4 p.m. in percentage of the daily energy demand Q_{st}

ECONOMICAL ANALYSIS

For an economical analysis, besides the technical parameters and the real conditions, expressed by the real influence factor f_{real} (exact simulation or approximation formula), all economical parameters must be introduced.

Technical parameters:

- Volume V [litres]
- Ratio between height and radius h_i/R_i [-]
- Fix losses P_{fix} [W]
- Thermal conductivity of the insulation λ [W/m K]
- Ambient temperature T_{amb} [°C]
- Hot water temperature T_h [°C]
- Real standing losses $L_{st} = f_{real} \cdot L_{st,st}$ [kWh/d]

Economical parameters

- the energy price (electricity) p_{el} [€/kWh]
- the insulation price p_{ins} [€/litres]
- the life cycle LC [years]
- the real interest rate i_r [%]
  (discount rate minus inflation rate)

Life cycle cost LCC is the sum of the purchase price and the discounted operating cost of an appliance. For the investigation of energy saving measures the life cycle cost analysis, however, only comprises the (additional) cost of insulation or performance improvement on the one hand, and the resulting savings in the operating cost on the other. Therefore, only the cost for the insulation and the cost for the real standing losses of the storage tank have to be considered. By means of the economical analysis, for example, the optimal insulation thickness, i.e. the one with the minimal life cycle cost, can be calculated. Furthermore, other ways to express economical cost effectiveness, like payback period, internal rate of return etc, can be introduced.

$$LCC = PP + PWF \cdot OC(s) \quad (7)$$

LCC	Life Cycle Cost [€]
PP	Purchase Price for the Insulation [€]
OC	Operating Cost for the Storage Losses [€/year]
PWF	Present Worth Factor

$$PWF(LC, i_r) = \frac{(1+i_r)^{LC} - 1}{(1+i_r)^{LC} \cdot i_r} \quad (8)$$

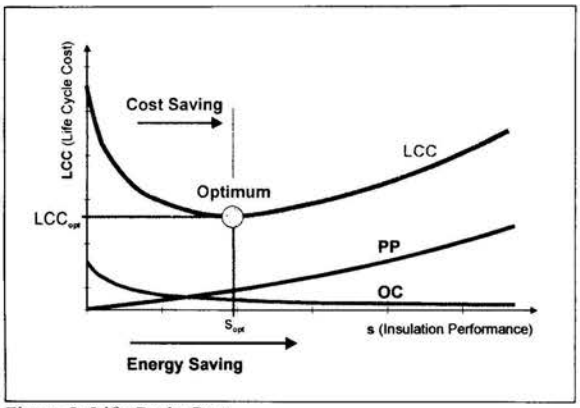

Figure 8: Life Cycle Cost

The economic optimum with the lowest life cycle cost is reached at the optimum s_{opt}. This optimum insulation thickness is independent from the initial status. On the contrary, the payback period depends on the initial status. Improving from a worse situation leads to a shorter amortization than improving from a rather good status.

The pay back period represents the duration of time it takes, to pay back the additional investments as a result of lower operating cost. The pay back period can be used as a quick and clear indicator if the cost effectiveness of an improvement is given. Cost effectiveness is reached, if the pay back period is shorter than the life cycle of the appliance.

Therefore the developed simulation model – see figure 9 - for an economical analysis is a good tool for calculating the saving potentials and a helpful basis for introducing a labelling scheme.

Figure 10 shows the optimal insulation thickness for different storage capacities. Compared with the Base Case Models and Poor Models there are considerable differences which lead to remarkable energy saving potentials.

The economical analysis showed very low payback periods from 0,5 to 5 years, depending on the tank size and the initial insulation state before improving.

This could be realized in two ways. As a first step, a minimum efficiency requirement should be introduced - legally or voluntary - e.g. corresponding approximately to the existing Base Case.

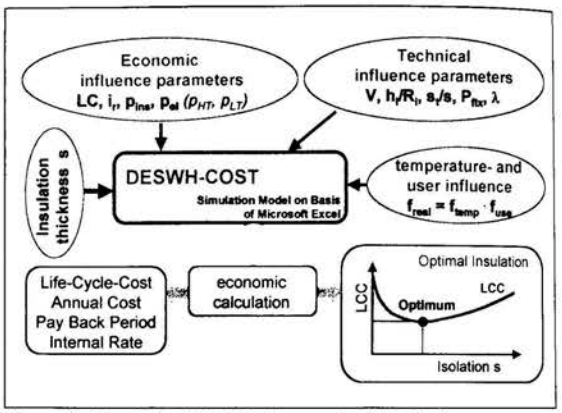

Figure 9: Simulation Model – Economical Analysis

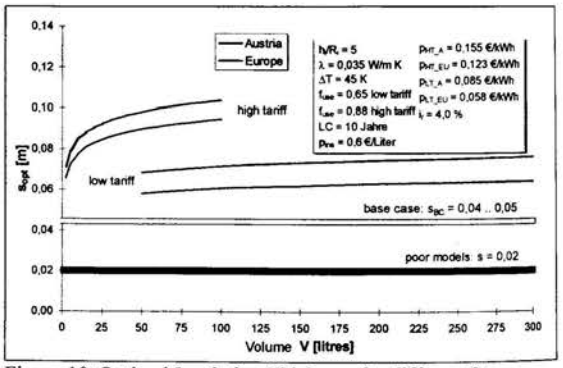

Figure 10: Optimal Insulation Thickness for different Storage Capacities (High Tariff and Low Tariff)

The second step - to reach the best existing model and the various national economical optima - could be properly done on the basis of labelling. A labelling scheme (see also other household appliances e.g. washing machine) visualises the energy efficiency of a product by means of quality symbols which have to cover the whole range of quality from the (future) best model on the market to the most inefficient models on the market or to a (negotiated) minimum requirement threshold.

ENERGY SAVING AND CO_2 EMISSION REDUCTION POTENTIALS

In the following, based on the distribution of the market model stock - see figure 2 - and applying average usage conditions, the energy saving potential and the CO_2 reduction potential due to the improvement of the insulation performance from Poor Model or from the Base Case up to the optimum have been investigated.

For the calculation of the CO_2 saving potentials – see figure 11 it is assumed that electricity is produced with the Austrian mix of hydro thermal power plants.

Austrian mix of hydro thermal power generation:
CO_2 = 0,25 kg/kWh

Austrian mix of (only) thermal power generation:
CO_2 = 0,82 kg/kWh

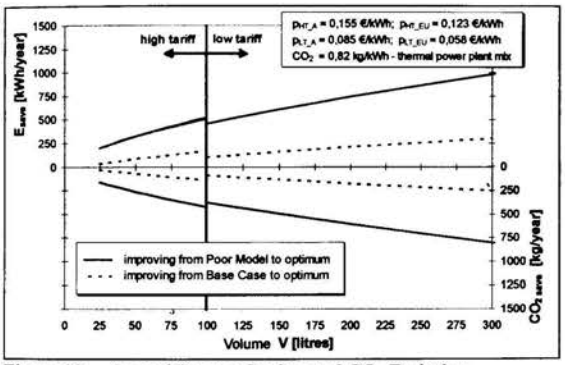

Figure 11: Annual Energy Saving and CO_2 Emission Reduction Potential for different Storage Capacities

CONCLUSION

Market data of electric storage heaters show a large range of standard standing losses for each storage capacity. Therefore, underlined by the economical analysis, there are high cost and energy saving potentials on the market with already existing technology – see figure 11.

For the technical and economical analysis for electric storage heaters several simulation models

- determination of the standard standing losses
- determination of the real standard losses
- economical analysis

were developed.

As an overall result, for electric storage water heaters a very high energy and cost saving potential was found which could be realised in a very short pay back period, and which, in consequence, also represents a high CO_2 reduction potential.

The profitable situation (pay back periods down to 0,5 years), seems to be a rather seldom result of energy saving studies. Taking into account that warm water is the second largest domestic energy consumer after room heating it seems to be of highest priority that this very cost effective and energy efficient saving potential will be realized as soon as possible.

Similar technical and economical analyses were performed [1] for electric hot water direct heaters and, including a comparison of different energy sources, also for non electric warm water supply systems.

REFERENCES

[1] Hoelblinger, M.: "Energieeffizienz in der Warmwasserbereitung – Modellbildung und technisch/ökonomische Optimierung", Doctoral Thesis, Technical University Graz, Austria, May 2001.

[2] Recknagel H.; Sprenger E.; Schramek E.: "Taschenbuch für Heizung und Klimatechnik", München: Oldenbourg Verlag, 1995.

[3] Hoelblinger, M.: "Modellierung elektrischer Warmwasserbereitungsanlagen - Technische und wirtschaftliche Analyse von Warmwasserspeichern", Master Thesis, Technical University Graz, Austria, February 1997.

[4] EU -Research Project Save - Analysis of Energy Efficiency of Domestic Electric Storage Water Heaters DESWH - Phase 3: "Technical and Economical Analysis of Energy Efficiency Improvements", Technical University Graz, Austria, 1998.

AUTHORS

Dr. Manfred Hoelblinger is Assistant Professors at the Department for Electrical Power Systems at the Technical University in Graz, Austria. His main research interests are energy efficiency, new technologies and market liberalization.

Dr. Manfred Sakulin is Professor and Senior Researcher at the Department for Electrical Power Systems at the Technical University in Graz, Austria. His main research interests are power systems, energy efficiency, power quality, new technologies and market liberalization.

Department for Electrical Power Systems, TU Graz
Inffeldgasse 18; A-8010 Graz, Austria
Email: hoelblinger@ifea.tu-graz.ac.at
Email: sakulin@ifea.tu-graz.ac.at

HEFAT2002
1st International Conference on Heat Transfer, Fluid Mechanics, and Thermodynamics
8-10 April 2002, Kruger Park, South Africa
QY1

ARE VISCOELASTICITY, HIGH APPARENT EXTENSIONAL TO SHEAR VISCOSITY RATIO AND THREADLIKE MICELLE NETWORKS VITAL FOR SURFACTANT DRAG REDUCTION?

Yunying Qi
Chemical Engineering Department
The Ohio State University

Jacques L. Zakin
Chemical Engineering Department
The Ohio State University

ABSTRACT

Certain surfactants which form large network microstructures in solution are effective drag reducers. Due to their "self-repairability" after mechanical degradation, they are very promising for use in recirculating water flow applications like district heating or cooling systems.

Viscoelasticity (in the forms of non-zero first normal stress difference, quick recoil and stress overshoot), high extensional viscosity and threadlike micellar microstructures are three characteristics found in many drag reducing surfactant solutions. It has been frequently postulated that they are vital to surfactant drag reduction. However, drag reducing surfactant solutions with low viscoelasticity have been found by Lu (1997a & b) and Lin (2000). Thus, it does not appear that viscoelastic behavior (Criterion 1) is vital for a surfactant solution to be drag reducing. Large (100 or more) apparent extensional viscosity to shear viscosity ratios are commonly observed in drag reducing surfactant solutions. However, one drag reducing surfactant solution was found by Lin (2000) with low apparent extensional viscosity to shear viscosity ratio in the shear/extensional rate range of 20 to 1000 s^{-1}. However, the extensional viscosity of that system began to increase at higher extensional rates so that Criterion 2 may be valid. Finally, cryo-TEM images of some drag reducing surfactant micelle microstructures were observed which lacked threadlike structures. However, Zheng et al. (2000) showed that vesicle microstructures in the quiescent state can change to threadlike micelles under shear, supporting the third criterion.

INTRODUCTION

Drag reduction, first reported more than 50 years ago, is a turbulent flow phenomenon in which friction energy losses can be significantly reduced with the addition of small amounts of drag reducing additives such as polymers or surfactants (Zakin et al., 1998).

The first major commercial application of drag reduction was injection of a high molecular weight polymer into the Alaskan pipeline in 1979 allowing throughput increases up to 25% without increasing pumping capacity. Polymer additives are now used extensively in oil pipelines all over the world. Polymer additives have a major deficiency, however, as they are susceptible to irreversible mechanical degradation in high shear regions such as passing through a pump. Thus, fresh polymer must be injected downstream of each pump feeding a "bottleneck" section of a pipeline. So they are useful only for "once through" applications.

Another potentially important application of drag reducing solutions is district heating and cooling systems where hot or chilled water is circulated through a district to heat or cool buildings. Pumping energy in these systems are costly with water circulating day and night. There is, therefore, considerable interest in reducing the pumping energy of the systems by adding drag reducing additives into the circulating water. For these circulating systems, polymer additives are not suitable because of their irreversible mechanical degradation properties.

Certain surfactants such as cetyltrimethylammonium bromide and cetyltrimethlammonium chloride with appropriate counterions, form large network microstructures at very low concentrations (a few ppm to 4000ppm), and are very effective in reducing friction factors in turbulent flow. These surfactant solutions also degrade under shear, but their microstructures are thermodynamically stable and self-assemble quickly after degradation enabling them to be used in recirculation flows like district heating or cooling systems.

Despite the low concentrations required for effective drag reduction, most drag reducing surfactant solutions exhibit strong non-Newtonian fluid properties. However, the non-Newtonian fluid properties of drag reducing solutions and how they interact with the turbulent flow are not well-understood. Possible drag reduction mechanisms such as damping of small turbulent eddies by the elastic properties of the solutions, high extensional viscosity providing resistance to vortex stretching

and turbulent eddy growth, etc. have been proposed but are difficult to verify experimentally.

For practical applications, however, it is important to be able to predict the drag reducing ability of solutions from small-scale laboratory tests such as rheological experiments or from their microstructures. Since viscoelasticity, high extensional viscosity and threadlike micellar microstructures are three properties commonly found in many drag reducing surfactant solutions, it has been frequently postulated that they are necessary for surfactant drag reduction. In this paper, these three proposed criteria for surfactant drag reduction are examined to see if they are valid criteria.

VISCOELASTICITY

Most drag reducing surfactant solutions exhibit viscoelastic properties in the form of non-zero first normal stress difference (N_1), quick recoil and stress overshoot. Many researchers (for example, Savins, 1967; Ohlendorf etc., 1986; Bewersdorff and Ohlendorf, 1988; Rose et al., 1989; Gyr and Bewersdorff, 1995) who studied drag reducing surfactant systems, have stated that viscoelastic properties of the surfactant solutions are responsible for the drag reduction behavior. It was also suggested that elastic properties of the solutions help to damp small turbulent eddies and to store and recover otherwise dissipated turbulent energy. However, drag reducing surfactant solutions with low viscoelasticity and solutions with strong viscoelasticity but no drag reduction have been found recently.

Lu (1997a & b) described a dilute drag reducing surfactant solution Arquad S-50 (soya-trimethylammonium chloride)/NaSal (sodium salicylate) (5mM/12.5mM) with excellent drag reduction ability up to 70% drag reduction from 20°C to 80°C as shown in Figure 1. These turbulent drag reduction experiments were conducted in a recirculation system with a 1.22 m long, 6mm inner diameter stainless steel tube test section. Surprisingly, first normal stress differences of the solution, which were measured in a Rheometric Scientific Inc. RMS-800 rheometer with a cone-and plate fixture (50 mm in diamter and 0.04 radians cone angle), were found to be close to zero up to a shear rate of about 1000 s^{-1} (Figure 2). In addition, no recoil was observed after adding a swirling motion to the solution and there was no stress overshoot in a step rate shearing experiment on the solution. However, this solution exhibits high apparent extensional/shear viscosity ratios indicating that there is also no correlation between viscoelasticity and extensional/shear viscosity ratio.

Another drag reducing solution with water-like properties was found by Lin et al. (2000) using the same experimental equipment. The effective drag reduction temperature range of Arquad 16-50 (cetyltrimethylammonium chloride)/3,4-Cl-Benzoate (5mM/10mM) solution is 20-80°C. This solution also showed no N1, no recoil after swirl and no stress overshoot.

Conversely, Myska et al. (1996) found a system which has large first normal stress differences at 20°C but no drag reduction at the same temperature. The solution they studied is Arquad 18-50 (octadecyltrimethylammonium chloride)/sodium salicylate (NaSal) (1.6mM/4.0mM) and the first normal stress differences were measured in a Haake Rheometer Rotovisco RV 20 and CV20 N with a cone-plate fixture (0.035 radian angle). They also observed that, for this solution, the values of the first normal stress difference decreased with temperature while drag reduction effectiveness, observed at higher temperatures, increased with temperature. This again indicates that viscoelasticity does not correlate directly with drag reduction.

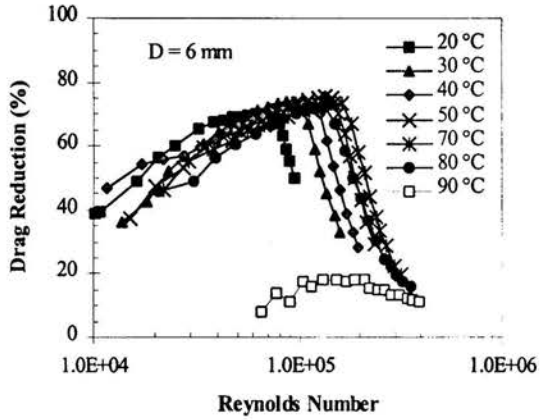

Figure 1. Drag reduction of Arquad S-50/NaSal (5mM /12.5mM) system (Lu, 1997a)

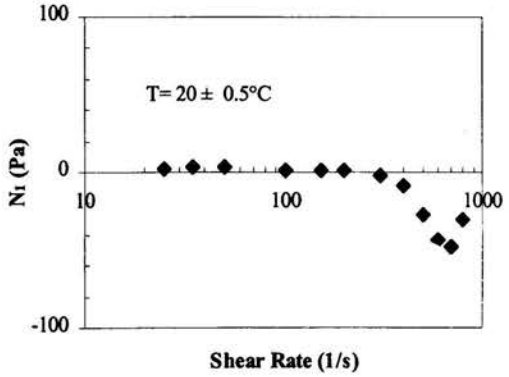

Figure 2. First normal stress difference of Arquad S-50 /NaSal (5mM/12.5mM) system (Lu , 1997a)

From the above three examples, it can be seen that there is no necessary close relationship between viscoelasticity and drag reduction. Therefore, it does not appear that viscoelastic behavior is vital for a surfactant solution to be drag reducing.

EXTENSIONAL/SHEAR VISCOSITY RATIOS

There are only limited studies on extensional viscosities of drag reducing surfactant solutions due to difficulties in measuring extensional viscosities of low shear viscosity liquid solutions. The extensional viscosity measured in opposed nozzles instruments RFX (Rheometric Scientific Inc.) is not the "true" extensional viscosity of the liquids. It includes contributions from dynamic pressure, shear on the nozzles and liquid inertia. Therefore, RFX can be used as an indexer rather than using the measured apparent extensional viscosities quantitatively (Macosko, 1994).

Although Gyr and Bewersdorff (1995) stated that extensional viscosity is of minor importance to surfactant drag reduction, relatively high apparent extensional viscosity to shear viscosity ratios (100 or more) are commonly seen in drag reducing surfactant solutions. It is said that high extensional viscosity of drag-reducing surfactant solution results in additional resistance to vortex stretching and turbulent eddy growth and leads to energy reduction or drag reduction (Zakin et al., 1998). However, using RFX to measure the apparent extensional viscosities of the solutions, Lin (2000) recently found two drag reducing solutions with low extensional viscosity/shear viscosity ratios in the extensional (shear) rate range tested.

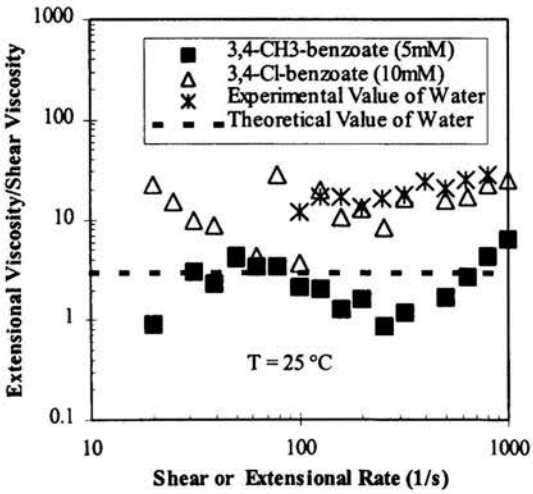

Figure 3. Extensional viscosity/shear viscosity ratio of a). Arquad 16/50 (5mM)/3,4-Cl-Benzoate (10mM); b). Arquad 16/50 (5mM)/3,4-CH_3-Benzoate (5mM) solutions (Lin, 2000)

The two solutions are Arquad 16-50/3,4-CH_3-Benzoate (5mM/5mM) and Arquad 16-50/3,4-Cl-Benzoate (5mM/10mM). As mentioned earlier, the Arquad 16-50/3,4-Cl-Benzoate (5mM/10mM) solution is a non-viscoelastic drag reducing solution. In addition to that, as shown in Figure 3, the extensional viscosity/shear viscosity ratio of the solution was also found to be unusually low (around 10) for this drag reducing solution over the apparent extensional and shear rates tested from 20 s^{-1} to 1000 s^{-1}. The uniaxial extensional viscosity/shear viscosity ratio should be around 3 for Newtonian fluids (Trouton ratio). Experimental values obtained with water in the same opposing nozzles instrument were around 10. From Figure 3, the extensional viscosity/shear viscosity ratio of Arquad 16-50/3,4-Cl-Benzoate (5mM/10mM) solution is close to the experimental value for water.

Good drag reduction ability has been observed with another surfactant solution Arquad 16-50/3,4-CH_3-Benzoate (5mM/5mM) in the temperature range of 5 to 40°C. The extensional viscosity/shear viscosity ratio, as shown in Figure 3, is however between 1 and 10, comparable or even lower than that of water measured in the same instrument.

From the above two drag reducing solutions with low apparent extensional viscosity/shear viscosity ratios in the shear/extensional rate tested, it can be concluded that low extensional viscosity/shear viscosity ratio does not lead to no drag reduction of surfactant solutions. However, as can be seen in Figure 3, apparent extensional viscosity/shear viscosity ratios are rising at high extensional rates (above 1000 s^{-1}). Thus, high extensional viscosity/shear viscosity ratios may be a valid criterion for drag reducing surfactant solutions. Stresses would, of course, have to be below critical wall stresses at which surfactant microstructures are degraded.

THREADLIKE MICELLE NETWORK

In turbulent flow, microstructures of surfactant solutions are deformed, stretched and aligned in the direction of the flow. For solutions full of threadlike micelles, this alignment in the direction of the flow can cause different resistances to the development and movement of turbulent vortices in different directions, low resistances in the flow direction and high resistances in the radial direction. The high resistances in the radial direction can suppress the frequency and amplitude of the flow fluctuations in the cross flow direction resulting in drag reduction. Therefore, the presence of threadlike micelle networks, which are similar to the long entangled polymer chains in drag reducing polymer solutions, is usually regarded as another vital criterion for drag reducing surfactant solutions.

Microstructures of surfactant solutions can be observed by cryo-TEM techniques. In the cryo-TEM technique, a drop of the surfactant sample is placed on an electron micrograph grid mounted in a controlled environment chamber. The drop is blotted to form a very thin film which subjects the sample to high shear. The grid and sample are then rapidly plunged into liquid ethane. The cooling is so rapid that no crystallization of water which might disturb the surfactant microstructure can occur. The water vitrifies and allows the subsequent low temperature TEM images to reveal the surfactant microstructure present in the original controlled environment chamber.

As expected, threadlike micelle networks are commonly seen in drag reducing surfactant solutions. However, Zheng et al. (2000) showed that a commercial CTAC(cetyltrimethyl ammoniumchloride)/3-methyl salicylate (5mM/5mM) drag reducing (20°C to 80°C), viscoelastic system surprisingly showed a vesicle microstructure in cryo-TEM images.

To analyze the effect of shear on surfactant microstructures, Zheng et al. (2000) chilled one blotted sample very quickly (within 0.5 second of the high shear caused by the blotting) and he observed a network structure. When the chilling was delayed 15, 30 and 90 seconds after blotting, the microstructure was transformed to a more and more vesicle-like structure depending on the time allowed for relaxation after blotting (see Figure 4). Thus, for certain systems like 3-methyl salicylate, the microstructure in the quiescent state is vesicles, but under shear, network structures which can be drag reducing are formed.

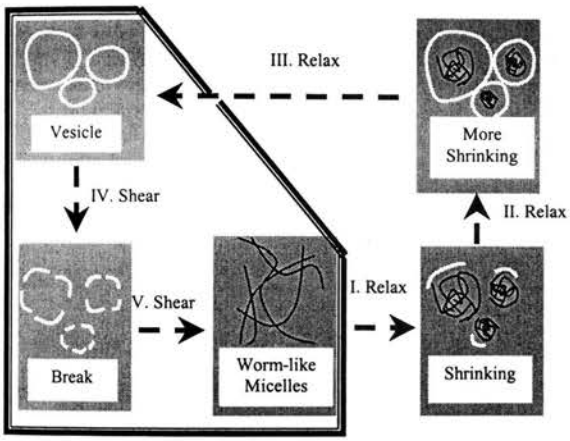

Figure 4: Structure Transition due to Shear & Relaxation

The results of Zheng et al. (2000) showing that threadlike micelles are present in drag reducing solutions even when their microstructures are vesicles in the quiescent state, supports the criterion that threadlike micelle networks are required for surfactant solutions to be drag reducing.

CONCLUSIONS

1). Nonviscoelastic drag reducing solutions Arquad S-50/NaSal (5mM/12.5mM) and Arquad 16-50/3,4-Cl-Benzoate (5mM/10mM) indicate that viscoelastic behavior, though common, is not vital for surfactant solutions to be drag reducing. The opposite trends of drag reduction and viscoelasticity with temperature observed in Arquad 18-50 /NaSal (1.6mM/4.0mM) solution supports this conclusion.

2). Two drag reducing solutions, Arquad 16-5/3,4-Cl-benzoate (5mM/10mM) and Arquad 16-50/3,4-CH_3-benzoate (5mM/5mM), with low extensional/shear viscosity ratios in the tested range were observed. However, the extensional/shear viscosity ratio began to increase at extensional/shear rates above 1000 s^{-1}. Therefore, high extensional viscosity/shear viscosity ratios may be required for surfactant solutions to be drag reducing but experiments at very high extensional/shear rates are needed to confirm this.

3). Threadlike micelles are commonly observed in drag reducing surfactant solutions. The finding that the drag reducing surfactant solution (cetyltrimethylammonium chloride–3-methyl salicylate) which has a vesicle structure in the quiescent state is transformed into a network of threads under shear supports the conclusion that thread-like microstructures are associated with surfactant drag reduction.

REFERENCES

1. Bewersdorff H. W. and D. Ohlendorf, "The Behaviour of Drag-Reducing Cationic Surfactant Solutions", *Colloid & Polymer Science*, **266**, 941-953 (1988)
2. Gyr A. and H. W. Bewersdorff, "Drag Reduction of Turbulent Flows by Additives", Kluwer Academic Publishers, Dordrescht, The Netherlands (1995)
3. Lin Z., "The Effect of Chemical Structures of Cationic Surfactants or Counterions on Solution Drag Reduction Effectiveness, Rheology and Micellar Microstructures", PhD Thesis, The Ohio State University (2000)
4. Lu B., "Characterization of Drag Reducing Surfactant Systems by Rheology and Flow Birefringence Measurements", PhD Thesis, The Ohio State University (1997a)
5. Lu B., X. Li, J. L. Zakin, Y. Talmon, "A Non-Viscoelastic Drag Reducing Cationic Surfactant System ", Journal of Non-Newtonian Fluid Mechanics, **71**, 59-72 (1997b)
6. Macosko C. W., "Rheology: Principles, Measuremetns, and Applications", 1st edition, VCH Publishers, Inc. (1994)
7. Myska, J., J.L. Zakin and Z. Chara, "Viscoelasticity of a Surfactant and it's Drag-Reducing Ability", *Appl. Sci. Res.*, **55**(4), 297-310 (1996)
8. Ohlendorf D. and W. Interthal, "Drag Reduction in Aqueous Solution of Hexadecyltrimethylammonium Salicylate", *Surfactants in Solution*, Vol. **6**, Edited by K. L. Mittal and P. Bothorel, 1589-1597 (1986)
9. Rose G. D. and K. L. Foster, "Drag Reduction and Rheological Properties of Cationic Viscoelastic Surfactant Formulations", *Journal of Non-Newtonain Fluid Mechanics*, **31**, 59-85 (1989)
10. Savins J. G., "A Stress-Controlled Drag-Reduction Phenomenon", *Rheologica Acta*, Band 6, Heft 4, 323-330 (1967)
11. Zakin, J. L., Lu, Bin, Bewersdorff, H. W., "Surfactant Drag Reduction", *Rev. Chem. Eng.*, **14**, 253-320 (1998)
12. Zheng, Y., Z. Lin, J. L. Zakin, Y. Talmon, H. T. Davis and L. E. Scriven, "Cryo-TEM Imaging the Flow-Induced Transition from Vesicles to Threadlike Micelles", *J. Phys. Chem. B*, **104**, 5263 (2000)

HEFAT2002
1ST International Conference on Heat Transfer, Fluid Mechanics, and Thermodynamics
8 – 10 April 2002, Kruger National Park, South Africa
VV3

SIMILARITY FOR THE VORTEX ELECTRO-DISCHARGED PLASMOTRON

Vyacheslav T. Volov

Samara Scientific Center of the Russian Academy of Science, Department of transport problems,
Studencheski per. 3a, 443001, Samara, Russia, phone/fax (+7 846 2) 42 40 43, e-mail: sgi@samtel.ru

ABSTRACT

This report presents results theoretical and experimental investigation of a new type of the heat-mass exchanger with the strong rotated supersonic flows for gas lasers and plasmatrons.

It has been shown that heat transfer inside supersonic vortex flow can be related to convection-diffusion type and electrical power coupling in discharge can reach the level of 300 W/cm^2. It is more than two order higher than in ordinary gas discharge. The relations of similarity and scaling laws for vortex electro-discharged laser has been proposed.

The idea of using strongly rotated supersonic flows as a basis of the vortex electro-discharged lasers (VEL) and plasmotrons consist in the fact that near the axis of the vortex tube there is region with low pressure and temperature. The vortex tubes have strongly rotated flows as their basis. The investigation of the self-vacuumed vortex tube (SVVT) (Merculov, 1969) is special interest because inside the SVVT the coefficient of turbulent kinematic viscosity and diffusion are 10^4 times higher than in the corresponding laminar flows. Combining those facts, the purpose of this research was to design of new type of heat-mass transfer for the laser the vortex electro-discharge systems, portable, water-cooled free source for biological, agricultural and forestial processing.

Keywords: Vortex tube, strongly rotated flows, radial diffuser, electrical coupling, turbulent diffusion.

THE PURPOSE OF INVESTIGATION

The idea of using strongly rotated supersonic flows as a basis of the vortex electro-discharged lasers (VEL) and plasmotrons consist in the fact that near the axis of the vortex tube there is region with low pressure and temperature. The vortex tubes have strongly rotated flows as their basis. The investigation of the self-vacuumed vortex tube (SVVT) (Merkulov, 1969) is special interest because inside the SVVT the coefficient of turbulent kinematic viscosity and diffusion are 10^4 times higher than in the corresponding laminar flows. Combining those facts, the purpose of this research was to design of new type of heat-mass transfer for the laser the vortex electro-discharge systems, portable, water-cooled free source for biological, agricultural and forestial processing.

THEORETICAL INVESTIGATION AND BACKGROUND

As shown Volov (1992), heat transfer from the discharge area can be realized by heat conductivity to the cooling wall of the discharge tube, or by way of changing a heated mass of gas to new a new portion of gas (the convectional method).

The investigated the vortex decaying discharge inside the self-vacuumed vortex tube (SVVT) can not be referred to ether the first or the second type of cooling, because inside the SVVT there are superior values of the turbulent diffusion $D_T \sim D_L \cdot 10^4$ and the average output velocity in the potential flow area can reach $v = 50 \div 100$m/sec .

Near the axis of the vortex tube there are only several percent of the gas mixture mass which is at the moment in the tube, because the output area is the potential flow area.

That is why heat transfer from the axis area to the periphery potential flow area in realized by turbulent diffusion, and heat transfer from the periphery of the vortex area is realized by convection.

Therefore the discussed new type of vortex decaying discharge can be referred to convectional-diffusional type of cooling.

For the determining of the vortex discharge heating we should know the share of the total gas output taking place in the periphery because of turbulent diffusion can be on the axis for the period of renewal by the new gas portion. It can be described by the following equation

$$\frac{dq}{qz} = -\beta q \qquad (1)$$

where q - is the share of the total gas output, which can not be on the vortex tube axis, β - is some dimensionless multiplayer.

This equation has shown that increasing of the vortex tube length leads to decreasing this share q .

The solution of this equation is the following formula

$$q = q_0 \exp\{-\beta(z - z_0)\} \qquad (2)$$

That is why the following equation has presented the related output share of the gas mixture which had been played near the vortex tube axis:

$$\eta_{ex} = \frac{q_0 - q}{q_0} = 1 - \exp\left(-C\frac{\overline{L}_{Bk}^2 \widetilde{B}}{R_{Bk}\overline{R}_p \widetilde{v}_z}\right) \qquad (3)$$

where $q = q_0$ when $z = z_0$, $C \sim 1$ - is an experimental constant, $\overline{L}_{VK} = L_{VT}/d_{VT}$ - is the related vortex tube length, d_{VT}, R_{VT} - are the vortex tube diameter and radius, $\widetilde{D}$ - is the average discharge area turbulent diffusion coefficient, $\overline{R}_d = R_d/R_{VT}$ - is the related discharge radius, $\widetilde{v}_z$ - is the average output velocity of the potential flow. For the typical regimes and geometrical sizes of the SVVT the heat exchange coefficient approximately equals $\eta_{ex} \sim 1$, at the same time the first cooling method (diffusion cooling) has the heat exchange coefficient volume $\eta_{ex}^{I} << 1$ and the second cooling way (conventional cooling) has the heat exchange coefficient volume $\eta_{ex}^{II} >> 1$

Thus the heat-mass transfer inside the strong rotated supersonic flows can relate to special type of the heat transfer – the convection - diffusion method of cooling. The average discharge heating can be determined in the following way:

$$\Delta\widetilde{t}_n = \frac{W^{\Sigma}}{C_p G_1 \eta_{ex}} \qquad (4)$$

where W^{Σ} - is the total electrical power coupling into the vortex discharge, C_p - is the heat volume under constant pressure, G_1 - is the gas mixture output through the vortex tube. The average temperature of the discharge area equals

$$\widetilde{T}_d = \widetilde{T}_d^{s} + \Delta t_h \qquad (5)$$

where $\widetilde{T}_d^{s}$ - is the average gas mixture temperature of the discharge area without discharge.

Some theoretical research has been dedicated to the VEL and plasmatron (Volov 1992, 1986, 1988; Shmelev et al., 1980). In the author's investigations (1992, 1986, 1988, 1986) the semi-empirical theory of the VEL and the vortex plasmotron has been suggested. This theory includes the mathematical model of the SVVT (Volov, 1983), the mathematical calculations for the electronic diffusion at the vortex decaying discharge, kinetic equation of the radiation in non-uniform turbulent flows with comparative analysis between the VEL and known types of the gas electro-discharged systems. The theoretical analysis has shown that electrical power density distribution is non-uniform inside the vortex discharge (Fig. 1).

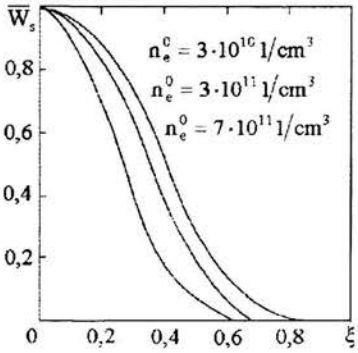

Fig. 1 Illustration of the electron power density coupling distribution as a function of the demationless radius

In the case of a weak electrical power coupling into the vortex discharge adiabatic radial distribution of gas temperature (cold model) is always assumed. Under the considerable electrical power coupling into the vortex discharge we should take into account non-adiabatic gas temperature distribution (hot model)by using the following dimensionless formula

$$\theta = 1 - \zeta \int_0^{\xi} \frac{\int_0^{\xi} \overline{w}_S \rho d\rho}{\xi \overline{\lambda}_T(\xi)} d\xi, \qquad (6)$$

where dimensionless constant ζ can be written as:

$$\zeta = \frac{1 - \theta_{ad}(\xi_{dis})}{\int_0^{\xi_{dis}} \frac{\int_0^{\xi} \overline{w}_s \rho d\rho}{\xi \overline{\lambda}_T(\xi)} d\xi},$$

where $\theta = T/T_{ax}$ - is the related gas temperature, $\overline{\lambda}_T = \lambda_T/\lambda_{ax}$ - is the coefficient of turbulent heat conductivity, $w_s = w_s/w_{sax}$ - is the dimensionless radial electrical

power coupling, T_{ax}, λ_{ax}, w_{ax} - are the volumes of the gas temperature, coefficient of turbulent heat conductivity, dimensionless electrical power density coupling near the axis of discharge accordingly, $\theta_{ad} = T_{ad}(\xi_{dis})/T_{ad}$, T_{ad} - is the adiabatic volume of gas temperature under condition $\xi = \xi_{dis}$.

As shown in Fig.2 the gas temperature distribution is similar to the electrical power density curve. Under the considerable electrical power coupling inside the vortex decaying discharge we can receive overheating near the discharge axis. Hence circular regime of radiation takes place inside the vortex discharge.

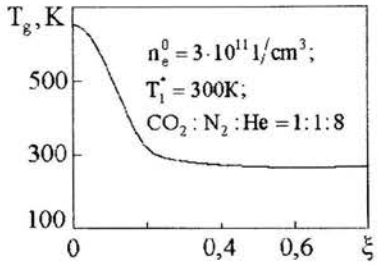

Fig.2 The radial gas temperature distribution

The adiabatic coefficient distribution inside vortex decaying discharge has shown in Fig. 3.

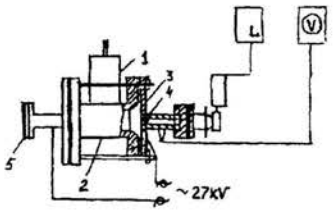

Fig. 3. The radial adiabatic the VEL

To reduce the number of trial experiment for the making the required VEL, we have suggested the similar relation and scaling laws. The proposed relations of similarity and scaling laws of the VEL include the relations of gas discharge similarity (Konuhov, 1970), the relations of the similarity theory for heat-mass transfer, and the vortex tube properties. Those relations are shown in the Table I. From the calculating results comparison we can see satisfactory agreement for the similar relations used (see Table II) W_{sp} - is the electrical power coupling for the unit length of the vortex discharge and discharge and deterioration of the one under invalidity of those relation[5] (Table III, W_{sp}).

Thus the similarity relations and scaling laws allow us to design the vortex electro-discharged laser with certain parameters without additional expensive experiments.

Table I.

(b-dimensionless discharge parameters)

N Physical Volume	Law of Transformation
1. Radius of tube	$R_m = R_n \cdot b$
2. Gas density	$N_m = N_n / b$
3. Current of Discharge	$I_m = I_n \cdot b$
4. Concentration of electrons	$N_e^m = N_e^n / b$
5. Voltage of the longitudinal electric field	$E_m = E_n / b$
6. Temperature of electrons	$T_e^m = T_e^n$
7. The electrical power on unit tube length	$W_{sp}^m = W_{sp}^n$
8. The electrical power on unit tube length	$W_{sp}^m = W_s^n / b^2$
9. Average temperature of the gas in discharge	$T_m = T_n$
10. The relative settlements of power levels	$(N_n/N)_m = (N_n/N)_n$
11. Frequency of the electronic and molecular hits	$Z_m = Z_n / b$
12. Radius of the SVVT	$R_{vt}^m = R_{vt}^n \cdot b$
13. The dimensionless square of tangential nozzle entry	$F_c^m = F_c^n$
14. Diameter of the diffuser	$D_{dif}^m = D_{dif}^n \cdot b$
15. Radius of the diffuser	$R_{dif}^m = R_{dif}^n \cdot b$
16. Split of the diffuser	$\Delta m_{dif}^m = \Delta n_{dif}^n$
17. The whole gas pressure on SVVT entry	$P_m = P_n / b$
18. Available degree of the gas expansion	$\pi_m^* = \pi_n^*$
19. The gas temperature at the SVVT entry	$T_g^m = T_g^n$
20. Degree of gas expansion into swirl	$\pi_m = \pi_n$

Table II.

Numerical modeling of the vortex discharge.

n_e^0	U	P	π	π^*	W_{sp}	R_{dis}	E_{error}
cm^{-3}	V/cm	Pa			W/cm^3		%
$3x10^{11}$	2490	$5x10^5$	5	30	580	0.76	
$2.3x10^{11}$	1992	$4x10^5$	5	30	554	0.69	4.4
$1.9x10^{11}$	1660	$3.3x10^5$	5	30	690	0.691	13.3

Table III.

Numerical modeling of the vortex discharge.

n_e^0	U	P	π	π^*	W_{sp}	R_{dis}	E_{error}
cm^{-3}	V/cm	Pa	-	—	W/cm^3	—	%
$3x10^{11}$	2490	$5x10^5$	4	20	200	0.5	190
$2.3x10^{11}$	2138	$4x10^5$	5	30	1468	0.73	152
$1.9x10^{11}$	2483	$3.3x10^5$	5	30	1150	0.61	106

EXPERIMENTAL METHOD OF THE VORTEX ELECTRODISCHARGED LASER INVESTIGATION

Figure 4 shows a principle scheme of the VEL.

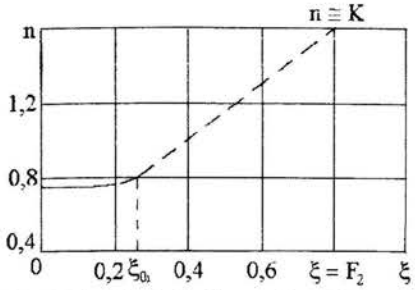

Fig. 4. The Principal scheme of coefficient distribution

The vortex consist of the tangential inlet (1), the vortex tube (2), radial diffuser (3), circular electrons (4), Mirrors (5) and gas mixture supply systems (6). The VEL works the following way: the gas mixture (CO_2: N_2:He) is injected through the inlet (1), where velocity of flow is increasing. Then flow of gas mixture goes to the vortex tube (2), where the latter is intensively rotating. In the vortex tube the energy separation is realized: near the axis of the tube we have low pressure and temperature. On the periphery of the tube we have considerably higher pressure and temperature. At the moment of the minimum pressure voltage is applied to the circular electrodes (4). The decaying discharge was realized in the SVVT. Optical feedback is provided with mirrors (5). In our experiment resonators length was 0, 13 m, and diameter of the SVVT was d=0, 05 m. Table IV shows a comparison between experimental data and corresponding theoretical calculations one can see that an experimental electrical power coupling into discharge can reach the level of 300 W/cm^3 without contraction. As shown (see Table IV) theory predicts the experiment with satisfactory accuracy. The optimization of the VEL is the next step of our research.

Table VI.
Comparison of calculated and experimental parameters of the decaying discharge of VEL

$\overline{R}_{dis}$	p^{ex}, T_{orr}	p^{th}, T_{orr}	U, KV	I, A	W_{ε}^{ex}, W/cm^3	W_{ε}^{th}, W/cm^3	E_{error}, %
0.21	10	10.3	3.36	1.275	241	205	4.2
0.31	20	21.8	4.5	0.28	63	55.78	11.4
0.357	80	81.6	11.2	0.05	28	20.8	25.7

APPLICATIONS OF VORTEX LASER AND PLASMOTRON

Even without optimization of this type of laser, the VEL can find a variety of application for agricultural, biological productions plants. It is due compactness, higher efficiency and absence of cooling system. Besides, the VEL can work by using the surrounding air. In this case the VEL will be working under non-optimal mixture ratio (CO_2:N_2:He). In addition, the efficiency of the VEL will be increased due to the absence of gas mixture system and the system of cooling. The vortex plasmatron and the VEL can be used for plasma-chemical investigations, medical applications, technological processing.

SUMMARY

At has been shown that electrical power coupling into discharge can reach level of 300 W/cm^3, i.e. it is more than two orders of magnitude higher than in ordinary gas discharge. The similarity relations and scaling laws for the vortex discharge have been proposed. The vortex electrodischarge systems are related to convection-diffusion type of cooling.

ACKNOWLEDGEMENTS

I wish to thank prof. A.D. Margolin, V.M. Shmelev, Dr. H. D. Lamashapov for helpful discussions.

REFERENCES

1. A.P. Merculov, 1969, Vortex Effect and its Application in Technic, Mech. buld. puble., Moscow.
2. V.T. Volov and V.A. Shahov, 1992, Termodynamics and Heat-Mass-Transfer of Strongly Rotated Flows. Kharkov Aviation Univ., Int. Aviat. Ass. Publ., Kharkov, Ukraine.
3. V.M. Shmelev, A.D. Margolin and A. Mischenko, 1980, On a Theory of the Vortex Electrical Discharge. JETP, 4, Vol. 50.
4. V.T. Volov, 1986, Theory of the Vortex Electro-Discharged CO_2 Laser, VINITY, Moscow.
5. V.T. Volov and H.D. Lamashapov, 1988, Eelectron Diffusion into Decaying Discharge of the Strongly Rotated Compressible Turbulent Flow, JETP, 4, Vol. 58,.
6. V.T. Volov, 1986, Vortex Decaying Discharge Theory, VINITY, Moscow.
7. V.T. Volov, 1983, Calculation Method the Vortex Diffuser Apparatuses, JIP, 1, Vol. 4.
8. V.K. Konuhov, Similar Gas Discharges for the CO_2 Laser, JETP, 8, v.12, 1970.

HEFAT2002
1st International Conference on Heat Transfer, Fluid Mechanics, and Thermodynamics
8-10 April 2002, Kruger Park, South Africa
YH1

STUDIES ON THE CO-PRECIPITATION OF CALCIUM OXALATE AND AMORPHOUS SILICA

H. Yu*, [α], R. Sheikholeslami**, [β] and W.O.S. Doherty***, [χ]
*Postgraduate Student; **Senior Lecturer; ***Principal Scientist
[α, β] School of Chemical Engineering and Industrial Chemistry
University of New South Wales, Sydney, NSW 2052, Australia
h.yu@student.unsw.edu.au, r.sheikholeslami@eng.unsw.edu.au
[χ] Sugar Research Institute, Mackay, Queensland 4740, Australia
b.doherty@sri.org.au

ABSTRACT

Amorphous silica (SiO_2) and calcium oxalate monohydrate (COM) deposit on the surfaces of calandria tubes and foul sugar mill evaporators. No study on the composite fouling of these components has ever been carried out. This work investigates the mechanisms and behavior of COM precipitation and SiO_2 polymerization in binary systems. Batch tests conducted at various pH values (6-8) and temperatures (60-80°C) show that the presence of SiO_2 decreased the precipitation rate of COM and invariably increased COM solubility. The presence of COM in SiO_2 precipitation, on the other hand, accelerated the polymerization of SiO_2 and lowered the level of initial silica supersaturation required for polymerization. The effect of COM on the solubility of SiO_2 was comparatively small.

INTRODUCTION

One of the main problems found in many sugar mill evaporators is the deposition of amorphous silica and calcium oxalate monohydrate on the surfaces of calandria tubes. These deposits reduce the heat transfer co-efficient of the evaporator station and are intractable rendering current cleaning methods either costly or ineffective [1].

Calcium oxalate (CaOx) is present in evaporator scales in two hydrate forms, viz., calcium oxalate monohydrate (COM) and calcium oxalate dihydrate (COD) with COM being the thermodynamically stable form [2]. CaOx is sparingly soluble in water and the solubilities of both CaOx and SiO_2 in sugar solutions decrease with increasing sucrose concentration and decreasing temperature [1, 3, 4]. Consequently, their deposition occurs in the later effects of the evaporator units [2, 5].

There is no information in the literature on the mechanisms of composite fouling of amorphous silica and calcium oxalate. The objective of this work was to investigate the interactions between COM and SiO_2 and how these interactions would influence the thermodynamics and kinetics of CaOx (as COM) and SiO_2 precipitation in binary systems. This paper presents the results of the preliminary investigations on the precipitation kinetics and thermodynamics of COM and SiO_2 in both single and binary systems in aqueous solutions.

EXPERIMENTAL

Materials

Stock solutions of calcium chloride, sodium oxalate and silica were prepared by dissolving known amounts of AR grade calcium chloride, sodium oxalate and sodium metasilicate in CO_2 free distilled water, respectively. All other reagents used were also AR grade.

Methods

Batch experiments were carried out at initial pH 6.0, 7.0 and 8.0 and at temperatures of 60°C, 70°C and 80°C. The initial concentrations for COM (all concentrations of CaOx will be represented in COM hereafter) were between 20ppm and 200 ppm and between 50ppm and 600 ppm for SiO_2. The initial molar ratio of calcium and oxalate ions for all the runs was kept constant at 1.

Spontaneous precipitation of calcium oxalate monohydrate from supersaturated solutions was conducted by mixing calcium chloride and sodium oxalate solutions. The initial pH values of the individual and mixed solutions were adjusted to desired values using dilute HCl or NaOH. All COM and SiO_2 solutions were then transferred to capped plastic tubes and placed in the water bath until equilibria were reached.

For COM precipitation kinetics tests, samples were withdrawn from the plastic vessel in the water bath at predetermined intervals and immediately filtered through 0.22 μm syringe end membrane filters (Millipore Corporation). To prevent further reaction after the filtration, samples were

immediately treated with concentrated HCl to pH <1.5. The solutions were analysed for calcium and oxalate contents using ICP-AES (Inductively Coupled Plasma Atomic Emission Spectrometer; Varian Vista AX) and UV-visible spectrophotometer (Varian Cary 1E), respectively.

Similar sample preparation procedures were followed for the batch tests of amorphous silica polymerization except that the filtration step was omitted because it was difficult, if not impossible, to differentiate between dissolved and colloidal silica with 0.22 μm membrane filter. Alternatively, we utilized different analytical methods to characterize SiO_2 in solution based on its reactivity [6]. Silica molybdate colorimetric method was used to selectively determine soluble silica species ('reactive' silica) because of its capability to form rapidly the silica molybdate complexes under acidic conditions. ICP was used for the measurement of 'total' SiO_2 content, a collective term including all reactive and non-reactive (colloidal) forms of SiO_2, as small SiO_2 colloidal particles can be destroyed in the plasma and quantified together with soluble species. Thus the difference in the concentration of SiO_2 measured by these two methods can be interpreted as the evidence for the appearance of colloidal SiO_2 particles in solution.

Following the determination of thermodynamics and kinetics of COM precipitation and SiO_2 polymerization in single systems, comparative COM/SiO_2 binary tests were carried out by mixing neutralised sodium metasilicate solutions with freshly prepared supersaturated solutions of calcium oxalate using identical experimental conditions to the corresponding single systems.

RESULTS & DISCUSSION

Single Systems

COM Precipitation

The rate equation generally used to describe the kinetics of COM precipitation can be expressed as [7]:

$$\frac{d(C)}{dt} = k\sigma^n \qquad (1)$$

where C is the molar concentration of COM, k is the rate constant, σ is the relative supersaturation and n is the order of reaction. The relative supersaturation, σ, may be defined as [7]:

$$\sigma = [(q_t^{1/2} - q_e^{1/2})/q_e^{1/2}] \qquad (2)$$

where q_t and q_e are the ionic products ((mol/L)^2) of Ca^{2+} and Ox^{2-} at time t and at equilibrium, respectively. After combining Eqn 2 with Eqn 1 and applying boundary conditions, t = 0 to t = t and $q_t = q_0$ to $q_t = q_t$, the integrated form of Eqn. 1 becomes:

$$q_t = \frac{q_0 - q_e}{\left[1 + [(q_0 - q_e)/q_e]^{n-1} \frac{1-n}{q_e} kt\right]^{1/n-1}} + q_e \qquad (3)$$

Equation (3) can be used to calculate the kinetic parameters of COM precipitation at constant pH and temperature.

Under the current experimental conditions, the spontaneous precipitation of calcium oxalate from a supersaturated solution was rapid and the equilibrium was reached within several hours of reaction (data not shown). However, for the thermodynamic tests, all samples were allowed to equilibrate for at least 24 h, prior to analysis to ensure complete COM precipitation.

The observed solubility of calcium oxalate in dilute aqueous solutions, is expressed in terms of concentration solubility product, K_{csp} ((mol/L)^2) is given as:

$$K_{csp} = [Ca^{2+}][Ox^{2-}] \qquad (4)$$

where $[Ca^{2+}]$ and $[Ox^{2-}]$ are the concentrations of calcium and oxalate ions (mol/l) at equilibrium, respectively. The solubility concentration of calcium oxalate, $C^*=[Ca^{2+}]=[Ox^{2-}]$ (mol/L). Therefore Eqn. 1 can be written as:

$$C^* = \sqrt{K_{csp}} \qquad (5)$$

Table 1 summarizes the average solubility product values and solubility concentrations of COM calculated using Eqns. 4 and 5 for different pH and temperatures, showing good agreement with data published in the literature. As shown in Table 1, the solubility concentration increased with the increasing temperature but there were only minor changes in the solubility concentrations with pH within the range tested. The differences between C* values obtained in the present study and those in the literature may be due to the differences in the experimental conditions used.

Table 1. The average solubility concentrations, C* (x10^5(mol/L)) and K_{csp} (x10^{-9}(mol/L)^2) values for COM in comparison with literature values [8]

	Temperature (°C)					
	60		70		80	
	K_{csp}	C*	K_{csp}	C*	K_{csp}	C*
pH 6	9.3	9.6	11.0	10.5	17.0	13.0
pH 7	9.2	9.6	11.6	10.8	17.0	13.0
pH 8	8.7	9.3	11.5	10.7	16.4	12.8
Average	9.1	9.5	11.4	10.7	16.8	12.9
Literature data	--	8.8	--	10.1	--	11.5
% Diff.	--	7.4	--	5.6	--	10.9

Silica Polymerization

Table 2 shows the effect of initial silica concentration and pH on the kinetics of silica polymerization at 60°C. An increase in the rate of polymerization could be observed when the initial pH increased from 6.0 to 8.0. At pH 8.0, the polymerization rate was also found to increase with increasing initial silica concentration between 350 and 500ppm. These effects are consistent with results obtained in the previous studies [9, 10].

Amorphous silica has been shown to be able to deposit onto surfaces in two different modes, depending on the level of initial concentration. One mode is the direct or molecular deposition onto solid surfaces; the second mode is homogeneous formation and growth of a colloid in the bulk or boundary layer and its subsequent deposition on the surface. The latter process usually requires a supersaturation factor of about 2.5 or higher to take place [6, 11].

Table 3 illustrates the effect of initial supersaturated concentration of SiO_2 on the type of silica deposited at 60°C. At high supersaturation (initial $[SiO_2]$>400ppm) the total silica concentrations became higher than the reactive silica concentrations indicating the presence of non-reactive (e.g., colloidal) forms of silica in the solution, some of which eventually deposited leading to a decrease in the total SiO_2 concentrations. The deposition of dissolved silica directly onto

Table 2. Estimated equilibration times and induction periods for silica polymerization at different initial silica concentration and pH levels at 60°C

	Equilibration time (hr)	Induction periods (hr)
pH 6.0, $[SiO_2]$=400ppm	336	168
pH 7.0, $[SiO_2]$=400ppm	264	4.0
pH 8.0, $[SiO_2]$=350ppm	290	120
pH 8.0, $[SiO_2]$=400ppm	100	0.5
pH 8.0, $[SiO_2]$=450ppm	100	1.0
pH 8.0, $[SiO_2]$=500ppm	100	0.5

Table 3. Silica polymerization at different initial silica concentrations at initial pH 8.0 and 60°C

Initial $[SiO_2]$ (ppm)	Reactive $[SiO_2]$ at equilibrium (ppm)	Total $[SiO_2]$ at equilibrium (ppm)
350	227	243
400	222	225
450	222	351
500	225	408

tube surface was the only reaction found at low supersaturation levels. The formation of colloidal SiO_2 and eventual deposition was able to occur from an initial supersaturation ratio of 2.0 (initial SiO_2 concentration: 450ppm) instead of 2.5, probably because our experiments were conducted at higher temperature, which resulted in high reaction rate [9].

As shown in Fig 1, the solubility of amorphous silica is little dependent on pH in the range of 6-8 (diff. <6%) and increased with increasing temperature (from ~225ppm at 60°C to ~295ppm at 80°C), agreeing well with results obtained in the literature [9, 12].

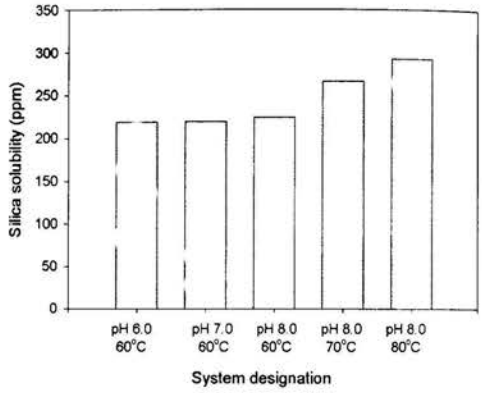

Figure 1: Silica solubility at different pH and temperatures

Binary Systems

Kinetics

Table 4 presents the calculated kinetic parameters (Eqn. 3) for COM precipitation in the presence and absence of SiO_2. The results show the kinetics of COM precipitation was affected by the presence of amorphous silica, as indicated by lower rate constants and higher n values. The extent of rate reduction increased with increasing initial SiO_2 concentration.

As illustrated in Fig 2, the rate of silica polymerization at a low initial supersaturation level at 60°C was enhanced by the presence of COM in comparison to that of the corresponding single system. As reflected by the differences between total and reactive silica concentrations, colloidal particles of SiO_2 were found to occur in all binary mixtures (Fig 2) in contrast to direct deposition of dissolved silica in SiO_2 single systems.

Table 4 Kinetic parameters for COM precipitation in binary systems with different initial SiO_2 conc. at initial COM conc. 150ppm, at pH 8.0 and 60°C

Initial SiO_2 conc. (ppm)	log(k)	N	%Equilibrium reached in 4h
0	0.5	3.4	97
150	0.06	3.6	90
200	-1.1	3.8	90
300	-2.1	4.5	92
400	-2.8	5.6	86

Thermodynamics

The precipitation thermodynamics of a compound is usually studied in a 2D plane, where the initial concentration of a compound is plotted against its final equilibrium (solubility)

concentration. However, when more than one precipitating species is present in the solution, the evaluation, interpretation and representation of precipitation equilibria become more complicated. In the case of binary systems, the evaluation of precipitation thermodynamics leads to a series of three-dimensional (3D) equilibrium (solubility) surfaces.

The 3D solubility surfaces in this study were obtained by plotting the initial concentrations of COM and SiO_2 on the x and y co-ordinates, respectively, against the solubility concentration of either one of them on the z co-ordinate. Computer software Matlab (version 6.0) was adopted for this purpose to connect random data points using an interpolating mesh.

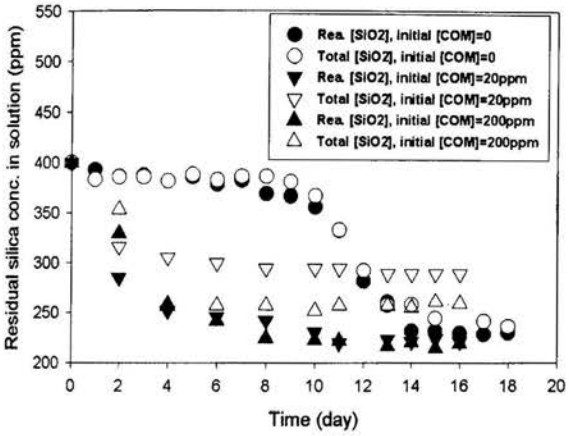

Figure 2: The effect of COM on the kinetics of SiO_2 polymerization at initial SiO_2 conc. 400ppm, initial pH 6.0 and 60°C

Figs. 3 and 4 show the 3D solubility surfaces of COM and SiO_2, respectively. The solubilities of COM were increased with increasing SiO_2 concentrations in the binary systems when compared with those obtained for COM single systems (upward surface curvature along y co-ordinate), indicating potential interferences of SiO_2 species on COM precipitation (see next section). However, the solubilities of SiO_2 in binary systems were found to be virtually unchanged compared to the situation where SiO_2 was present alone (plane B levelled off after an initial rise along x co-ordinate).

To obtain two-dimensional solubility curves for SiO_2 at constant initial concentrations of COM, the 3-D solubility surface can be "cut" by the constant COM concentration planes representing various initial COM values.

This surface-cutting exercise (data not shown) indicated that colloidal silica was formed at a lower initial supersaturation level in the binary systems than that in the respective single systems, i.e., at initial SiO_2 concentration of ~250ppm in binary systems as against ≥~400ppm in single systems. These results are similar to those obtained in the kinetics runs (Fig. 2).

Mechanisms

A number of mechanisms may be proposed to explain the results obtained for the binary COM/SiO_2 mixtures. Iler [13] demonstrated that SiO_2 was able to form a variety of soluble or insoluble silicates in the presence of non-alkali metals such as

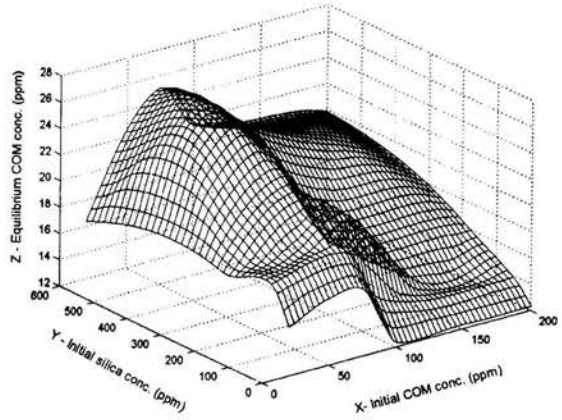

Figure 3: Interpolated solubility surface for COM in binary systems at initial pH 7.0 and at 60°C

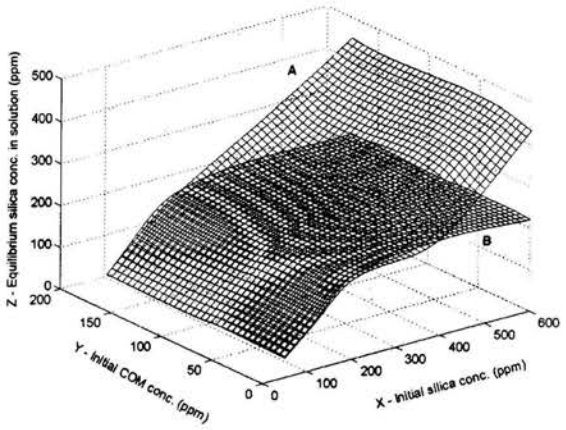

Figure 4: Interpolated solubility surfaces for SiO_2 in binary systems, initial pH 7.0 and at 60°C, (A) Total SiO_2 conc. (B) Reactive SiO_2 conc.

calcium and magnesium (pH ≥8.5). In another study, Iler [14] examined the coagulation of colloidal silica by calcium ions. The author proposed that calcium ions act as bridging units between negatively charged SiO_2 particles.

It is likely, therefore, that the above-mentioned mechanisms are applicable to the interactions between COM and SiO_2 observed in this work. The reduced precipitation rate and increased solubility for COM may be the result of the formation

of COM-SiO_2 species through complexation and bridging etc., thereby maintaining high COM concentration in solution. Previous work [15] on COM crystallization also showed that many agents could inhibit COM crystal growth by binding selectively to the COM crystal faces. Hence, the decreased precipitation rates for COM might possibly be attributed to the blocking of active growing sites of COM by the adsorption of SiO_2 ions or COM-SiO_2 species.

Furthermore, the formed COM/SiO_2 complexes may act as additional nucleation sites for SiO_2 polymerization, leading to high SiO_2 polymerization rates in the binary systems.

Because the total SiO_2 concentration dropped in the binary systems, it is also postulated that some soluble or colloidal SiO_2 may be co-precipitated with COM by specific adsorption onto COM crystal faces, or as a consequence of coagulation of colloidal COM-SiO_2 complexes. Further work on crystal characterization is underway to verify these assumptions.

CONCLUSION

Batch experiments have been conducted to evaluate the co-precipitation of amorphous silica and COM in pure solutions. This work has shown that the presence of SiO_2 hindered the rates of COM precipitation and increased the observed solubilities of COM, the extent of which increased with increasing initial SiO_2 concentration. The presence of COM in SiO_2 precipitation, however, was found to enhance the SiO_2 deposition, but had little effect on the solubility of SiO_2. COM-SiO_2 complex formation and specific adsorption may be used to explain the co-precipitation of COM and SiO_2.

Foulant characterization studies, batch tests of COM/SiO_2 co-precipitation in sugar solutions and dynamic tests based on a circulating heat exchange unit are underway to further establish composite fouling mechanisms of amorphous silica and calcium oxalate monohydrate under conditions similar to those in the sugar mill evaporator.

ACKNOWLEDGMENTS

The authors gratefully acknowledge the assistance of Mr. P. Doidge of Varian Australia with ICP analysis. This work is supported by an ARC-SPIRT research scheme in collaboration with Sugar Research Institute and the funding is gratefully acknowledged.

REFERENCES

[1] Doherty, W. O. S., 2000, "Chemical Cleaning of Sugar Mill Evaporator," Proc. Aust. Soc. Sugar Cane Technol., vol. 22, pp. 341-346.

[2] Walthew, D. C., Turner, L.M., 1995, "Analysis of Scale from Some South African Sugar Mills," presented at Proceeding of South African Sugar Technologist Association.

[3] Walford, S. N., Walthew, D.C., 1996, "Preliminary Model for Oxalate Formation in Evaporator Scale," Proceeding of South African Sugar Technologist Association, vol. 70, pp. 231-235.

[4] Walthew, D. C., *et al.*, 1998, "Some Factors Affecting the Concentration of Silica in Cane Juice Evaporators," Proceeding of South African Sugar Technologist Association, vol. 72, pp. 223-227.

[5] Crees, O. L., Cuff, C., Doherty, W.O.S., Senogles, E., 1992, "Examination of Evaporator Scales for the Far Northern Regions of the Sugar Industry," Proc. Aust. Soc. Sugar Cane Technol., pp. 238-245.

[6] Sheikholeslami, R., Tan, S., 1999, "Effects of Water Quality on Silica Fouling of Desalination Plants," Desalination, vol. 126, pp. 267-280.

[7] Nancollas, G. H., *et al.*, 1991, "Physical Chemical Studies of Calcium Oxalate Crystallization," Am. J. Kid. Des., vol. 17, pp. 392-395.

[8] Stephen, O. B. E., *et al.*, 1963."Solubilities of Inorganic and Organic Compounds," vol. 1: Pergamon Press.

[9] Rothbaum, H. P., Rohde, A.G., 1979, "Kinetics of Silica Polymerization and Deposition from Dilute Solutions between 5 and 180°C," Journal of Colloid & Interface Science, vol. 71, pp. 533-559.

[10] Sheikholeslami, R., *et al.*, 2001, "Pretreatment and the Effect of Cations and Anions on Prevention of Silica Fouling," Desalination, vol. 139, pp. 83-96.

[11] Chan, S. H., 1988, "Fouling of Geothermal Energy Systems," in Fouling Sci. & Tech., L. F. Melo, Ed.: Kluwer Academic Publisher,, pp. 649-667.

[12] Chan, S. H., 1989, "A Review on Solubility and Polymerization of Silica," Geothermics, vol. 18, pp. 49-56.

[13] Iler, R. K., 1979, "The Chemistry of Silica - Solubility, Polymerization, Colloid and Surface Properties, and Biochemistry," John Wiley & Sons, Inc.

[14] Iler, R. K., 1975, "Coagulation of Colloidal Silica by Calcium Ions, Mechanism, and Effect of Particle Size," Journal of Colloid & Interface Science, vol. 53, pp. 476-488.

[15] Ryall R., *et al.*, "Urolithiasis 2," in Inter. Symposium on Urolithiasis. New York: Plenum Press, 1994

HEFAT2002
1st International Conference on Heat Transfer, Fluid Mechanics, and Thermodynamics
8-10 April 2002, Kruger Park, South Africa
KY4

EFFECTS OF HEAT LOSS AND FINITE PULSE-TIME ON THE MEASUREMENT OF THERMAL DIFFUSIVITY OF MOLTEN SLAG USING DOUBLE HOT THERMOCOUPLE TECHNIQUE

Yoshiaki Kashiwaya* and Kuniyoshi Ishii**
*Associate Professor. , **Professor
Division of Materials Science and Eng.,
Graduate School of Eng., Hokkaido Univ.
Sapporo 060-8628, Hokkaido
JAPAN
E-mail:yoshiaki@eng.hokudai.ac.jp

ABSTRACT

The molten slags that are used not only in the continuous caster but also in many metal industries play an important role and affect the quality of products. The authors initially developed the double hot thermocouple technique (DHTT) for *in situ* observation of mold slag crystallization.

In this study, the DHTT was further developed to allow the measurement of the overall thermal diffusivity of molten slag applying the principle of the laser flash method. The affecting factors (finite pulse time, shape of pulse and heat loss from sample surface) on the measurement of thermal diffusivity using DHTT were discussed theoretically using both the analytical and the numerical methods. New relationship between the thermal diffusivity α and the time at half-maximum temperature $t_{0.5}$ was obtained as follows:

$$\alpha\ (\times 10^4 m^2/s) = 0.000707\left(t_{0.5}/t_p\right)^{-1.8946}$$

The thermal diffusivity obtained from the experimental half-maximum time $t_{0.5}/t_p$ (t_p is the time of peak on the heat pulse) was in good agreement with the one from the literatures.

INTRODUCTION

The physicochemical and the thermal properties of molten slag have large influences on the quality of products not only in the continuous caster but also in the every high temperature process using a slag-metal reaction. The former properties such as the viscosity and melting-solidifying behavior have been widely investigated. Although the thermal conductivity (or diffusivity) was also measured by many researchers, the interests might mainly be fucused on the inherent value such as a phonon conduction to eliminate the effect of radiation and the effect of other phenomena (convection, crystallization and bubble formation). Scientifically it would be important, however, practically, the overall heat transfer that includes the complicated phenomena such as the bubble formation and the crystallization will be more important and useful. Under such situation, the direct observation during measurement of the thermal diffusivity can be a key technique to understand the obtained results adequately. The authors initially have developed the double hot thermocouple technique (DHTT) for *in situ* observation of mold slag crystallization [1,2]. These studies have indicated that the overall heat transfer rate in the actual process must be very complicated due to the interaction of crystallization of slag with the primary mechanisms of heat transfer: radiation, conduction and convection. DHTT has a superior feature on the rapid heating and cooling of melted sample during observation, whereas the extremely high sensitivity on the temperature change makes it unamenable. The measurement of thermal diffusivity using DHTT should be overcome the following problems belonging to two categories:

(i) contents of effective thermal diffusivity (effects of phonon conduction, radiation conductivity, electron conductivity and effect of convection)
(ii) influences of experimental setup on the measured value.

In the present study, we focused on the problem in the second category (ii). The problem in the first one (i) will be discussed in the following paper.

The final purpose of present project is to clarify the effective thermal diffusivity during the bubble formation and crystallization. In this study, the DHTT was further developed and the measurements of thermal diffusivity using the standard sample (B_2O_3) were carried out. The affecting factors (finite pulse-time effect(shape of pulse) and heat loss from sample

surface) on the measurement using DHTT were elucidated and new relationship between the thermal diffusivity α and the time at half-maximum temperature $t_{0.5}$ was obtained, which was the modified relationship of Parker's method [3,4].

EXPERIMENTAL

The details of experimental apparatus have been shown in previous study[1,2]. Figure 1 illustrates the principle of the thermal diffusivity measurement and the comparison of the alignment of heat source and detector between DHTT and laser flash method. The laser flash method is excellent method and can predict a relatively suitable value of thermal diffusivity using Parker's Method [4] (Eq.(3)). However, it will need a special alignment for the measurement of liquid and/or transparent material. Furthermore, a direct observation during measurement is almost impossible. On the other hand, the DHTT can observe the molten sample *in situ*. As shown in previous study,[1,2] the solidification of mold slag is complicate phenomena including the bubble formation/breaking and the crystallization. It would be very important to know the sample image during measurement. The thermal diffusivity obtained from DHTT, however, is not yet established and it is not reported what kinds of factors affected on the measurement until now.

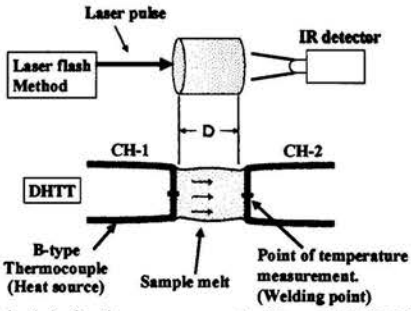

Fig.1 Principle for the measurement of thermal diffusivity by DHTT and the laser flash method.

For the preliminary approach to the application of DHTT on the measurement of thermal diffusivity, the affecting factors on the measurement were elucidated both from the theoretical and experimental method. In the case of laser flash method, an instantaneous laser pulse was used as a heat source and the temperature increase at rear surface was measured by an infrared pyrometer (IR detector). In the case of DHTT, the temperature of one side thermocouple (CH-1, in Fig.1) increased in a pulse shape and the other side of thermocouple (CH-2) was used as a detector. The typical temperature profiles both of CH-1 and CH-2 are shown in Fig.2. The time $t_{0.5}$ at the half-maximum temperature ($1/2\ \Delta T_{max}$) was defined as shown in Fig.2 and used for the calculation of thermal diffusivity according to the laser flash method (the details will be shown in below). The large differences between the laser flash method and DHTT are as follows:

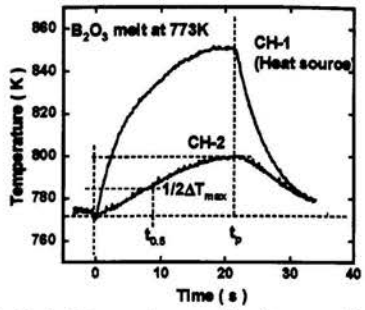

Fig.2 Typical temperature profiles for measuring the thermal diffusivity

(1) Heat source is the order of several seconds (millisecond order in laser flash method).
(2) Shape of pulse is not square. This factor might be decisive in both the methods, however, the extent of delay on the pulse (finite pulse-time) is significant on the DHTT.
(3) Heat loss owing to the radiation and the conduction to the thermocouple (CH-2) for detection is significant for the DHTT.

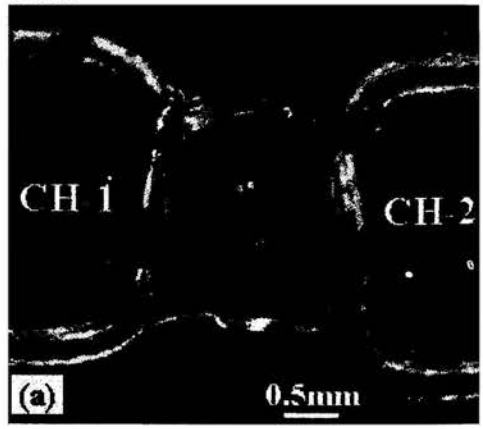

Fig.3 Sample melts on the double hot thermocouple. (B_2O_3)

In the present paper, these difficulties will be overcome for using the DHTT on the measurement of thermal diffusivity, because it can provide us with the other benefits such as the measurement of transparent slag melt and the direct observation. Figure 3 shows the examples of the observations during measurements. Figure 3(a) shows the clear and transparent B_2O_3 melt, in which many reflections could be seen because it was working as a lens. In this experiment, the bubbles were eliminated and the clean melt was used.

RESULTS AND DISCUSSIONS

The one dimensional heat transfer under an insulating condition with an instantaneous heat source was given by Carslaw and Jaeger. [3]

$$T(x,t)=\frac{1}{D}\int_0^D T(x,0)dx+\frac{2}{D}\sum_{n=1}^{\infty}\exp\left(\frac{-n^2\pi^2\alpha t}{D^2}\right)\times\cos\frac{n\pi x}{D}\int_0^D T(x,0)\cos\frac{n\pi x}{D}dx \quad (1)$$

where $T(x,0)$ is the initial temperature distribution, $T(x,t)$ is the temperature distribution at any later time t and α is the thermal diffusivity. D means the thickness of sample. The temperature history V at the rear surface (x=D) can be expressed by Eq.(2).

$$V=\frac{T(D,t)}{T_M}=1+2\sum_{n=1}^{\infty}(-1)^n\times\exp\left(\frac{-n^2\pi^2}{D^2}\alpha t\right) \quad (2)$$

where T_M is the maximum temperature at the rear surface ($T_M=Q/\rho C_p D$, Q is the radiant energy of pulse, ρ is the density of sample and Cp is the heat capacity). From Eq.(2), Parker, et al [4] gave the simplest equation expressed by Eq.(3). The time $t_{0.5}$ can be defined by that at V = 0.5, which means the half-maximum temperature. Then, the thermal diffusivity α can be calculated by Eq.(3).

$$\alpha=0.1388\frac{D^2}{t_{0.5}} \quad (3)$$

Eq.(3) is very useful equation to obtain the thermal diffusivity. Many commercial devices for measuring the thermal diffusivity have been developed on the basis of Eq.(3).

Since the Eq.(3) was very convenient one to obtain the thermal diffusivity, the meaning of Eq.(3) was analyzed. Then, the analogical and fundamental equation was derived as follows:

$$\alpha=\vartheta_1\cdot t_{0.5}^{-\vartheta_2} \quad (4)$$

where ϑ_1 and ϑ_2 are the parameters determined by the sample thickness D, the heat loss and finite pulse time (pulse shape). In the case of instantaneous pulse and insulated condition ($\vartheta_1=0.1388D^2$ and $\vartheta_2=1$), Eq.(4) is equal to Eq.(3) (Parker' equation). In the present study, the parameters, ϑ_1 and ϑ_2 were obtained for getting the adequate thermal diffusivity using DHTT.

EFFECT OF HEAT LOSS

In the DHTT, the heat loss from the sample surface is relatively large and the conduction to the thermocouple for the detection (CH-2) is considerably large comparing to the radiation loss. Watt [8] has shown the theoretical approach for the radiation loss from the sample surface based on the equation by Carslaw et al [3]. Heckman [9] has studied the finite pulse-time effect and the heat loss using Green's function based on the result of Watt. For the triangular heat pulse (Fig.4), Heckman has presented the relationship shown as Eq.(5).

$$V=\frac{T(D,t)}{T_\infty}=2\sum_{n=1}^{\infty}Y_n(0)Y_n(D)\left[M_n(t)+N_n\exp(\frac{-\beta_n^2 t}{t_c})\right] \quad (5)$$

where

$$Y_n(x)=\frac{2^{1/2}\left(\beta_n^2+L_2^2\right)^2\left[\beta_n\cos(\beta_n x/D)+L_1\sin(\beta_n x/D)\right]}{\left[\left(\beta_n^2+L_1^2\right)\left(\beta_n^2+L_2^2+L_2\right)+L_1\left(\beta_n^2+L_2^2\right)\right]^{1/2}} \quad (6)$$

and the $\beta_n(n=1,2,3....)$ are the positive roots of the following equation.

$$\left(\beta_n^2-L_1L_2\right)\tan\beta_n=\beta_n\left(L_1+L_2\right) \quad (7)$$

where L_1 and L_2 mean the heat loss by radiation at the front and rear surface, respectively [8].

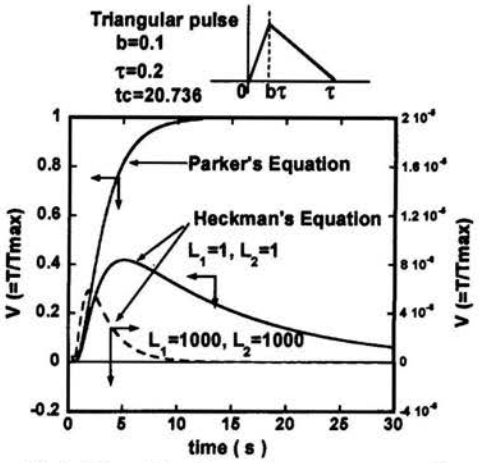

Fig.4 Effect of heat loss on the temperature profile.

In Figure 4, the calculation results using Heckman's equation (Eq.(5)) under two conditions (L_1=L_2=1 and L_1=L_2=1000) are shown in comparison with Parker's equation (Eq.(2)). It was found that the existence of heat loss made the temperature profile lower and the local maximum point appeared on the temperature profile. Furthermore, the maximum point decreased with the increasing heat loss, intensely. It should be noted that the temperature profile never decrease in an insulated condition (Parker's equation, Eq.(2)) and the actual one must decreased more or less, because some extent of heat loss always exist.

These temperature profiles from Heckman's equation were compared in Figure 5 with experimental data of B_2O_3 melt using DHTT at 773K (the curves were normalized with T_{max} (the maximum temperature) and t_{max} (the time at T_{max})). Even if the fairly large heat loss was assumed in the Heckman's equation (L_1=L_2=1000, broken line), the calculated temperature profile could not represent the experimental data, especially, the decreasing curve beyond the t_{max} did not represent the observation.

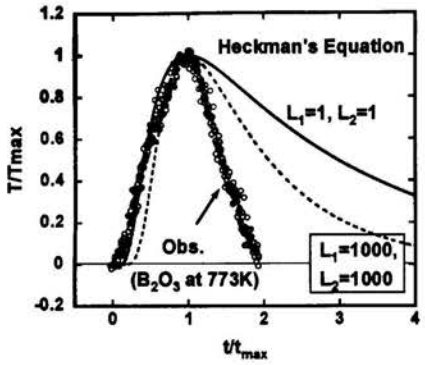

Fig.5 Comparison of temperature profile between the observation and the calculation by Heckman's equation.

NUMERICAL METHOD FOR DHTT MEASUREMENT

From above results, it was found that the analytical method was difficult to express the experimental results owing to the complex pulse shape and the heat loss in the present study. Then, the numerical analysis was carried out based on the following fundamental equation

$$\rho Cp\frac{\partial T}{\partial t}=\kappa\frac{\partial^2 T}{\partial x} \qquad (8)$$

where ρ is the density, Cp is the heat capacity and κ is the thermal conductivity. The finite difference method with the forward differences was adopted for numerical analysis and the equation could be rewritten as follows[3]:

$$T_n^{i+1}=T_n^i+\alpha\frac{\Delta t}{\Delta x^2}\left(T_{n+1}^i-2T_n^i+T_{n-1}^i\right) \qquad (9)$$

where 'n' means the position corresponding to the space-derivative and 'i' means the time corresponding to the time-derivative. The numerical calculation using Eq.(9) was carried out with $\Delta t=4\times10^{-6}$ (s) and $\Delta x=0.001$ (cm). The boundary condition at the front surface (heat source) was changed according to the experimental heat pulse.

$$T_0^i=f(t) \qquad (10)$$

and the initial condition was

$$T_n^0=0 \qquad (11)$$

Using Eq.(9), the temperature variation at the rear surface T_D^i (D means the position of rear surface) was calculated and compared with the analytical method (Eq.(2)), when the maximum temperature was kept at the rear surface for simulating the thermally insulated condition (without heat loss) and the instantaneous heat pulse was defined as $T_0^i=1$ in Eq.(10). The calculated results between the numerical method (Eq.(9)) and the analytical method (Eq.(2)) were compared and it was confirmed that the present numerical method was in excellent agreement with the analytical method.

Using experimental heat pulse (Fig.6(a); the curve of pulse was divided into two region at the maximum point t_p ($0\le t\le t_p$ and $t>t_p$) and the two curves were expressed by the three dimensional polynomial), the numerical calculations were carried out and the temperature variations with different thermal diffusivities ($\alpha=0.001\times10^{-4}\sim0.005\times10^{-4}$ m^2/s) were compared with the observation in Fig.6(b). It was found that the calculation result using the thermal diffusivity, $\alpha=0.003\times10^{-4}$ m^2/s was in good agreement with the observation. In this case, the heat pulse and the response curve were normalized by the t_p that was the time at the maximum temperature in the heat pulse.

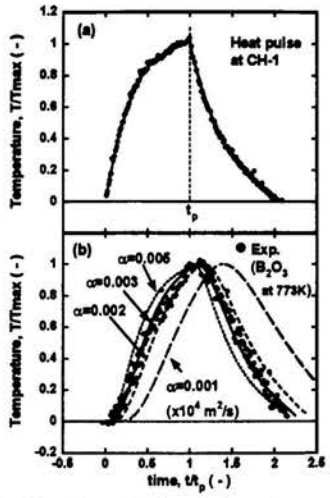

Fig.6 Results of numerical analysis and comparison with the observation.

From these results, it could be concluded that not only the shape of pulse but also the heat loss affected the measurement of thermal diffusivity significantly in the DHTT measurement. The numerical method was useful to analyze the experimental heat response curve, because the shape of heat pulse was not geometric one and the heat loss from sample surface to both the ambient and the thermocouple was large. However, it is not practical method for getting a thermal diffusivity to use the numerical method owing to the necessity of huge work.

The Eq.(4) will be convenient to obtain the thermal diffusivity. The parameters (ϑ_1 and ϑ_2) were determined as shown in the following section.

PARAMETERS FITTING (ϑ_1 AND ϑ_2)

Using two kind of heat pulses, the numerical method was carried out as mention above. The obtained results are shown in Fig.7. The values of the parameter ϑ_1 in both conditions were one order of magnitude smaller than that obtained using Heckman's equation[13]. The result was caused by the difference

of the amount of heat loss. The numerical method could simulate the situation that the large heat loss occurred in the DHTT. The relationship between α and $t_{0.5}$ obtained can be expressed as follows in the case of experimental heat pulse:

$$\alpha\,(\times 10^4 m^2/s) = 0.000707\left(t_{0.5}/t_p\right)^{-1.8946} \qquad (12)$$

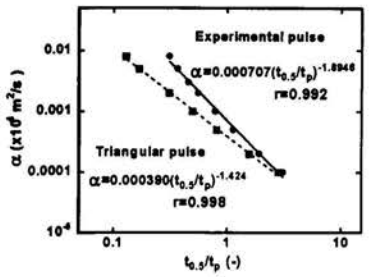

Fig.7 Relationship between the thermal diffusivity α and the time at half-maximum temperature $t_{0.5}$ by the numerical method.

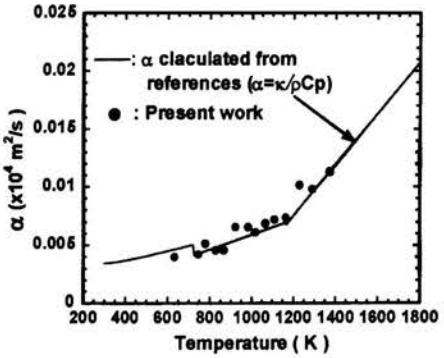

Fig.8 Comparison of thermal diffusivity between the observation and the literatures.

In the present experiment, $t_{0.5}/t_p$ was measured at the desired temperatures from 630K to 1373K using reagent grade B_2O_3 and also the thermal diffusivity α of B_2O_3 was calculated from the literature value [13] Figure 8 shows the temperature dependence of thermal diffusivities obtained in the present study (using the observed $t_{0.5}/t_p$ and Eq.(12)) and the references value[13] The excellent agreement was obtained and the relationship between α and $t_{0.5}$ expressed by Eq.(12) was quite useful one to determine the thermal diffusivity using the DHTT.

However, another factor might govern the value obtained in high temperature range. That is a effect of radiation in a transparent sample[10,11,12] Moreover, this effect must dominant in both the data from the present study and the reference data [13], which was obtained by the steady-state method for thermal conductivity measurement, because both the thermal diffusivities increased with increasing temperature (normally, the thermal conductivity of glasses decreased in high temperature range[12]

CONCLUSION

New method to measure the thermal diffusivity using double hot thermocouple technique (DHTT) was developed. The factors affecting on the thermal diffusivity measurement were elucidated. The finite pulse-time effect and the heat loss were quite different from that of laser pulse method and it was found that the analytical method could not used for the DHTT. Then, numerical method was applied to analyze the heat conduction on the DHTT.

The results obtained are as follows:

(1) The heat loss in DHTT was quite high and the analytical method presented by Heckman could not apply.

(2) In addition , since the shape and duration of pulse in the heat source was entirely different from the laser flash method, the numerical method was useful to simulated the heat transfer on the DHTT.

(3) The new relationship between the thermal diffusivity α and the time at the half-maximum temperature t_{05} was obtained using the numerical method, which was in excellent agreement with the observation.

$$\alpha\,(\times 10^4 m^2/s) = 0.000707\left(t_{0.5}/t_p\right)^{-1.8946}$$

REFERENCES

1) Y. Kashiwaya, C.E. Cicutti, A.W. Cramb and K. Ishii: ISIJ International 38(1998), p.348.
2) Y.Kashiwaya, C.E. Cicutti and A.W. Cramb: ISIJ International 38(1998), p.357.
3) H.S. Carslaw and J. C. Jaeger, Conduction of Heat Transfer in Solids (Oxford University Press, New york, New York, 1959), 2nd ed., p.101.
4) W.J.Parker, R.J. Jenkins, C.P. Butler and G.L. Abbott: J. App. Phys. 32(1961), p.1679-1684
5) K.B.Larson and K. Koyama: J. Appl. Phys., 38(1967), p.465-474.
6) R.E.Taylor and J.A.Cape, Appl. Phys. Lett., 5(1964), p.212-214.
7) J.A.Cape and G.W.Lehman: J. Appl. Phys., 34(1963), p.1909-1913.
8) D.A.Watt: Brit. J. Appl. Phys.,17(1966), p231-240.
9) R.C. Heckman: J. Appl. Phys. 44(1973), p.1455-1460.
10) R.Gardon: J. Am. Ceram. Soc., 44(1961), p.305-312
11) W.D.Kingery: J. Am. Ceram. Soc., 44(1961), p.302-304
12) K.Nagata, M.Susa and K.Goto: Tetsu-to-Hagane, 69(1983), p.1417-1424
13) Y.Kashiwaya and K.Ishii: ISIJ International, 42(2002), in press.

HEFAT2002
1st International Conference on Heat Transfer, Fluid Mechanics, and Thermodynamics
8-10 April 2002, Kruger Park, South Africa
AA3

Numerical Investigation of Human Thermal Response to Extreme Environmental Conditions: Part I, Nude Body

A. F. Alfahaid
Mechanical Technology Department
Riyadh College of Technology
P.O. Box 91471
Riyadh 11633, Saudi Arabia
E-mail: alfahaid@rct.edu.sa

ABSTRACT

The present study pertains to the numerical investigation of human thermal response to extreme environmental conditions with the help of a human thermal stress model. The human thermal model based on finite element method is implemented. This model utilized as a "Computational Environmental Chamber" to conduct simulations for examining human thermal responses under different environmental conditions. It is well established that thermal discomfort causes degradation of human performance. This leads to drain of attentional resources and vigilance capabilities of decision makers (e.g. pilots, aircrew). Thus, extreme environmental conditions can cause significant changes in human thermal stress responses. The purpose of this study is to investigate the human core and skin temperatures behavior under different humidity ratios and extreme air temperature. The study is expected to provide deeper understanding of the combined effect of relative humidity and air temperature on human thermal responses.

INTRODUCTION

Considerable fundamental research has been conducted in response to the increased interest in the development of computer models to study the human thermal behavior. The human body continuously exchanges heat with its environment to maintain the inner body temperature within a certain range. Heat is not generated uniformly throughout the body, nor it dissipated uniformly [1]. Consequently, human body must exchange heat with the environment in a controlled manner to keep the human body temperature in certain range. The system responsible for maintaining the inner or core temperature at a normal level is thermoregulatory system, which enhances or inhibits heat production and heat loss.

Mathematical models have been used by several investigators in the past fifty years to study the human thermoregulation [2]. From early forties to late sixties, human thermoregulation was studied primarily using analog computers. Some of the well-known thermal models developed during this period were those of Pennes [3], Mach and Hatch [4], Wyndam and Attkins [5,6], and Smith [7]. With the advent of digital computers, from seventies onward, new and more sophisticated models have been developed. Description of some of these models can be found, for instance, in studies by Gagge [8], and Stolwijk [9].

Presently, there is a strong need to develop a model that can study the human-environment interface more accurately. Smith [10] developed a comprehensive three-dimensional thermal model for the nude body. Finite element method used for the numerical solution provides more realistic model for the human body in this model. Jones et al. [11] developed a new unsteady-state thermal model for the whole clothing system.

This is the first stage of the study in which the aim is to develop code validation and to apply this code to study the human thermal response to extreme environmental conditions for nude body. Subsequently, other applications for modeling clothed human body will be implemented.

NOMECLATURE

A	area (cm^2)
Cp	specific heat or heat capacity (J/g-°C)
D_{AB}	mass diffusivity of water in dry air (cm^2/hr)

h	surface heat transfer coefficient (J/hr-°C-cm^2)
h_{fg}	latent heat of vaporization (J/g)
K	thermal conductivity (J/hr-°C-cm)
M	metabolic rate of entire body (J/hr)
mresp	moisture transfer rate between the air in the respiratory tracts and the surrounding tissue (cm^2/hr)
q_m	internal heat generation by metabolic reactions per unit volume of tissue (J/hr- cm^3)
P	pressure or vapor pressure (KPa, mm Hg)
r_o	blood vessel radius (m)
RH	humidity ratio
RQ	respiration quotient
T	temperature (°C)
T_a	air temperature (°C)
t	time (hr)
V_b	volumetric blood flow rate (cm^3/hr)
V_{o2}	volumetric oxygen consumption rate (cm^3/hr)
w	humidity ratio (g H_2O/g dry air)
w_b	volumetric blood flow rate in capillary bed (cm^3/hr)
Z	coordinate or length along axial direction of 1-D elements

Greek Symbols

α	fraction of the total body mass in the skin node
μ	viscosity (g/hr-cm)
ρ	density (g/ cm^3)

GENERAL FORMULATION

The human thermal model shown in Fig. 1 is investigated. It has three important interactive systems [2], namely:

1. Passive System: This has the body tissues, internal organs, circulatory, and respiratory systems.
2. Control System: Which represents thermal control functions of the body.
3. Clothing Systems: In which the thermal functions of the clothing is taking into account.

The development of the thermal model for the clothed human includes governing energy equations of these three systems. The human thermoregulatory responses are obtained by solving these systems of energy equations. Auxiliary equations, such as the blood pressure governing equation of the macro circulatory system, the humidity ratio equation of the respiratory system, mass transfer equation of the clothing system, etc., form the complete system of governing equations.

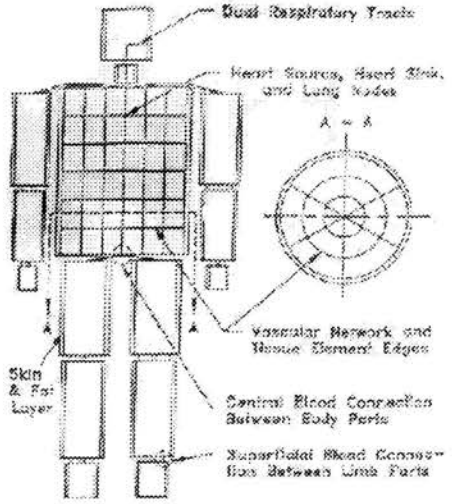

Figure 1 Human thermal model [7]

The governing equations for the three systems can be classified as follows [12]:

(1) Blood pressure governing equation
(2) Humidity ratio governing equation
(3) Thermal energy governing equation
  (i) Tissue energy governing equation
  (ii) Blood energy governing equation
  (iii) Air energy governing equation
(4) Control system governing equation
  (i) Vasomotor response equation
  (ii) Sudomotor response equation
  (iii) Metabolic response equation
  (iv) Cardiac response equation
(5) Clothing system governing equation

(1) Blood pressure governing equation

To determine the blood pressure distribution, Navier-Stokes equations were applied to blood flow in the macro circulatory system.

The basic assumptions include: blood is a Newtonian fluid flowing in the axial direction, 1-D, incompressible, steady, constant viscosity, laminar, fully developed, and axisymmetric flow. Navier-Stokes equations, with the above assumptions, in cylindrical coordinates simplify to [12]:

$$V_{bl} = \frac{-r_o^2}{8\mu}\frac{dP}{dz} \quad (1)$$

or

$$\frac{-r_o^2}{8\mu}\frac{d^2P}{dz^2} = 0 \quad (2)$$

where z is the coordinate along the axial direction of the blood vessel, V_{bl} is the mean blood velocity in the blood vessels, and P is blood pressure. Equation (2) may be expressed in terms of average volumetric blood flow rate, V_b, as

$$V_b = \frac{-\pi r_o^4}{8\mu}\frac{dP}{dz} \quad (3)$$

(2) Humidity ratio governing equation

The quantity of water vapor in a mixture relative to the amount of dry air represents the humidity ratio. Inside the respiratory tract, latent heat loss due to respiration is a function of the humidity ratio. The respiratory tract walls experience a cooling effect due to heat and mass transfer between the inhaled air and the surrounding tissues.

For any given respiratory tract element, a mass balance equation may be expressed in terms of the humidity ratio W_{air} [12], as:

$$D_{AB}\frac{d^2W_{air}}{dz^2} - v_a\frac{dW_{air}}{dz} + \frac{m_{res}}{A_{res}} = 0 \quad (4)$$

where A_{res} is the cross-sectional area of the windpipe, v_a is the air velocity (constant).

The magnitude of the air velocity can be calculated from the volumetric oxygen consumption rate, V_{o_2} [12], as:

$$V_{o2} = \frac{M}{21.21(0.23RQ + 0.77)} \quad (5)$$

$$v_a = 4.762\frac{V_{o_2}}{\pi r_o^2} \quad (6)$$

where RQ is the ratio of volumetric flow rate of exhaled carbon dioxide to that of inhaled oxygen.

(3) Thermal energy governing equations

Three thermal energy differential equations governing the thermal response in the passive system. These equations are tissue, blood, and air energy equations.

(i) Tissue energy governing equation

The energy balance equation for a tissue element, is given by [12]:

$$\rho C\frac{\partial T}{\partial t} = \nabla.K\nabla T + q_b + q_m + q_a + q_v + \alpha q_{res} \quad (7)$$

The left-hand side of Eq. (7) is the rate of accumulation of thermal energy per unit volume due to changing temperature of the tissue. It equals the sum of six different terms on the right-hand side which are summarized as follows [12]:

1) $\nabla.K\nabla T$ = net rate of heat conduction into unit volume.
2) $q_b = \rho_b w_b C_{Pb}(T_a - T_v)$ rate of heat transfer into unit volume due to capillary blood perfusion.
3) q_m = rate of heat generation by metabolic reaction.
4) $q_a = 2\pi r_a h_a(T_a - T)$ = rate at which heat is transferred from the blood the in large arterial vessels to tissue.
5) $q_v = 2\pi r_v(T_v - T)$ = rate at which heat is transferred from the blood in large venous vessels to the tissue.
6) $q_{res} = 2\pi r_{res}h_{res}(T_{res} - T) + 2\pi r_{res}h_{res}\rho_{da}h_{fg}(W_{air} - W_{sat})$ = rate at which heat is transferred from the respiratory system to the tissue. Where $\alpha = 1$ at the head, neck, and torso and $\alpha = 0$ for other body parts.

(ii) Blood energy governing equation

The energy balance equation for a blood vessel element, is expressed as [12]:

$$\rho_b C_{p,b}\frac{\partial T_b}{\partial t} = K_b\frac{d^2T_b}{dz^2} - \rho_b C_{p,b}v_{bl}\frac{dT_b}{dz} + \frac{q_{bd}}{A_b} \quad (8)$$

A_b refers to the cross-sectional area of the large blood vessels.

(iii) Air energy governing equations

The energy balance equation for a respiratory tract element, is given by [12]:

$$\rho_{res}C_{p,res}\frac{\partial T_{res}}{\partial t} = K_{res}\frac{d^2T_{res}}{dz^2} - \rho_{res}C_{p,res}v_{res}\frac{dT_{res}}{dz} + \frac{q_{res}}{A_{res}} \quad (9)$$

(4) Control system governing equations

Due to the lack of understanding of the thermal control function of the human body, development of any

thermoregulation model is limited. It is known that thermo receptors sense local temperature changes and transmit these thermal signals to the hypothalamus [4]. However, at this time it is not understood how the hypothalamus integrates these incoming signals [12]. Whatever the form and relative significance of thermal signals utilized by the hypothalamus, the thermoregulatory responses are known: vasodilatation and sweating to enhance heat loss, vasoconstriction to inhibit heat loss, and shivering to increase metabolic heat production. The governing equations for this system have been discussed in detail in Ref. [12], and therefore, will not be repeated here.

(5) Clothing System Governing Equations

The clothing system to be investigated is developed by Jones et al. [11]. Because of its moisture adsorbing or desorbing mechanisms, clothing system plays a very important role in affecting the thermal responses. Only nude human cases will be considered in this study, and therefore, governing equations for clothing system will not be needed here.

INITIAL CONDITIONS

The thermo-neutral conditions are used as initial conditions for the human body. Temperature distribution of the whole human body is needed for the initial thermo-neutral, instead of just the core and skin temperatures because of the finite elements used in the body. The model is simulated for a nude sedentary human body, in order to obtain initial condition, starting with an approximate initial thermo-neutral temperature distribution. The relative humidity (RH) and air temperature used in the simulation are 32% and 28 °C respectively. The obtained temperatures are used as the initial condition for all other simulations.

RESULTS AND DISCUSSION

A transient model for the nude human thermal system has been developed to simulate the thermal responses to various conditions [10]. The validation of any computer code involves the comparison of the code result with one or two of the independent sources such as experimental data and exact solution. This model has been validated by comparing model skin and core temperatures with experimental data of Hardy [13].

Figure 2 shows the core temperature comparison of the experimental data and the computer model. In this experiment, a quietly sit nude human exposed to 23.3 °C air temperature with 40% relative humidity for 60 minutes. Then the subject walked quickly to another chamber that has 43.5 °C air temperature with 38% relative humidity for another 60 minutes. Figure 3 shows skin temperature comparison of the experimental data and the computer model for the same above case of two-hour period time.

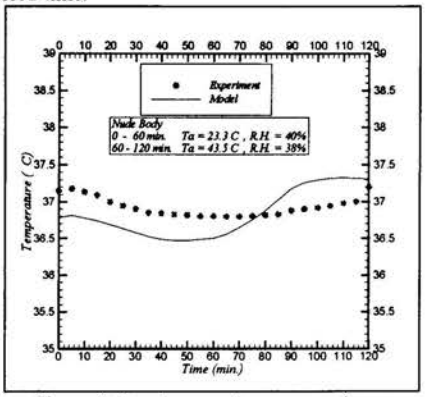

Figure 2 Core temperature comparisons

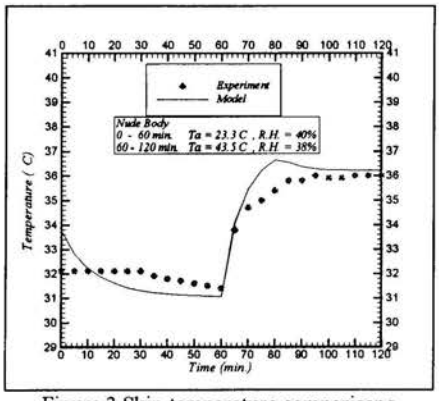

Figure 3 Skin temperature comparisons

Computer simulations were conducted for a variety of environmental conditions. The environmental temperatures are 0 °C and 43.33 °C, humidity ratios are 10%, 50% and 90%, and the activity level was maintained at 1.0 MET (metabolic activity). The radiant temperature of the environment is approximated to be the same as the environmental air temperature. The radiation heat transfer coefficient is 1.7 J/hr-cm^2-°C and the convection heat transfer coefficient is taken as 1.12 J/hr-cm^2-°C [1].

Figures 4-6 show the influence of air temperature on core temperature with metabolic rate of 1.0 MET (21 J/hr-cm^2) which corresponds to resting condition for 10%, 50%, and 90% relative humidity respectively. It is

clear that the effect of the relative humidity is insignificant at low air temperature (0 °C). However, relative humidity effect is noticeable at high air temperature (43.33 °C).

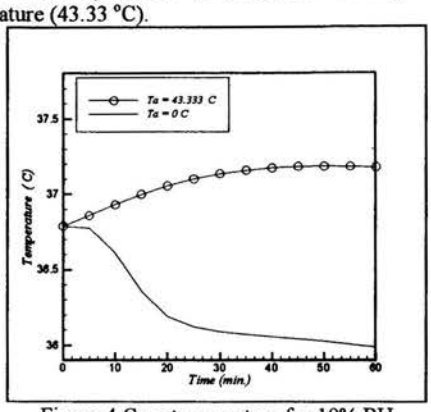

Figure 4 Core temperature for 10% RH

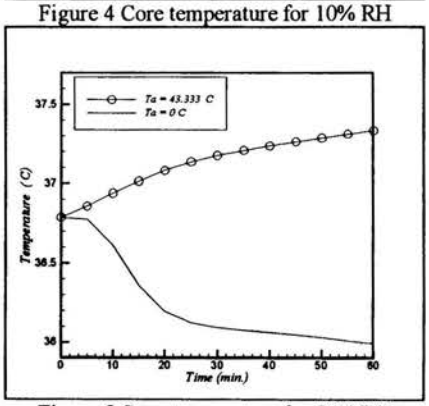

Figure 5 Core temperature for 50% RH

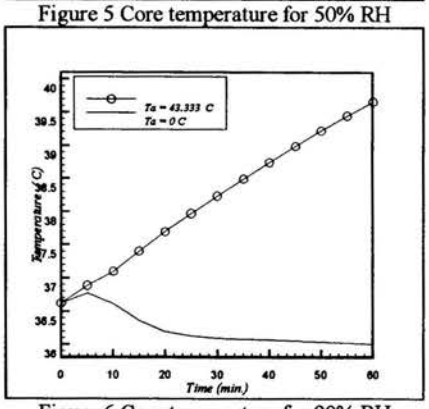

Figure 6 Core temperature for 90% RH

Figures 7-9 show the influence of air temperature on skin temperature with metabolic rate of 1.0 MET for 10%, 50%, and 90% relative humidity respectively. The air temperature of 43.33 °C causes the skin temperature to remain high.

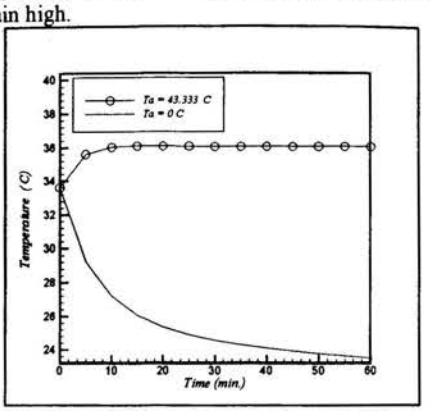

Figure 7 Skin temperature for 10% RH

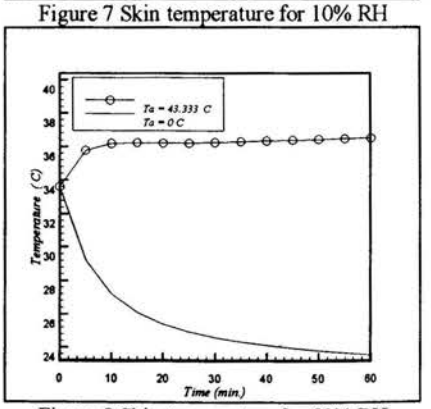

Figure 8 Skin temperature for 50% RH

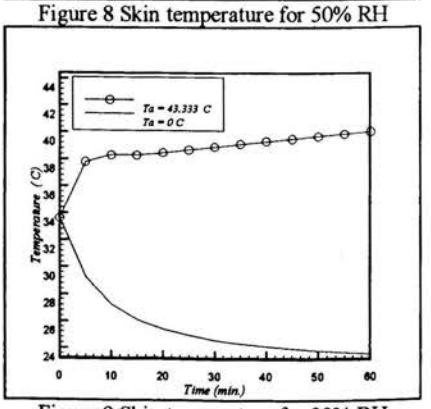

Figure 9 Skin temperature for 90% RH

CONCLUSIONS

An attempt has been made to characterize human thermal response under extreme thermal environment for nude human body. In this study, air temperatures of 0 °C and 43.333 °C have been used along with 10%, 50 % and 90% relative humidity to simulate extreme thermal environment. In general, the effect of relative humidity is insignificant compared to the effect of air temperature. At high air temperature, the effect of the relative humidity is important.

The ultimate goal is to characterize human thermal responses under extreme thermal environment for nude as well as clothed human.

REFERENCES

1. ASHRAE 1993, "ASHRAE Handbook of fundamentals," Chapter 8, Atlanta, American Society of Heating, Refrigerating, and Air Conditioning Engineers Inc.

2. Alfahaid, A.F., Chaturvedi, S. K. and Tiwari, S. N. "Evaluation of Aerospace Environmental Control System Using an Objective Thermal Stress Index (OTSI)," AIAA Paper No. 99-3502; 37th Aerospace Sciences Meeting & Exhibit, Norfolk, VA, July 12-15, 1999.

3. Pennes, H. H., "Analysis of Tissue and Arterial Blood Temperatures in the Resting Human Foream," Jornal of Applied Physiology, Vol. 1, No. 2, pp.93-122, 1948.

4. Machle, W., and Hatch, F. F., "Heat: Man's Exchanges and Physiological Responses," Physiological Review,Vol. 27, pp. 200-227, 1947 .

5. Wyndam, C. H., and Atkins, A. R., "An Approach to the Solution of the Human Biothermal Problem with the Aid of an Analogue Computer," Proceedings of the 3rd International Conference on Medical Electronics, London, England, pp. 32-38, 1960.

6. Wyndam, C. H., and Atkins, A. R., " A Physiology Scheme and Mathematical Model of Temperature Regulation in Man," Pflugers Archives, Vol. 303,pp. 14-30, 1969.

7. Smith, P. E., " Analog Simulation of the Physiological Responses of Men Working in Hot Environments," Proceedings of 2nd Symposium for Biomedical Engineering, San Diego, CA, 1962.

8. Gagge, A. P., " A Two-Node Model of Human Temperature Regulation in FORTRAN," Bioastronautics Data Book, 2nd ed.,ed: J. F. Parker and V. R. West, Washington D.C., pp. 142-148, 1973.

9. Stolwijk, J. A. J., " A Mathematical Model of Physiological Temperature Regulation in Man," NASA Technical Report No. NASA CR-1855, 1971.

10. Smith, C. E., " A Transient Three-Dimensional Model of the Human Thermal System," Ph.D. Thesis, Kansas State University, Manhattan, Kansas, 1991.

11. Jones, B. W., Ogawa, Y., and McCullough, E. A., " Transients in Clothing System," Submitted to Textile Research Jounal, 1993.

12. Boregowda, S. C., " Thermodynamic Modeling and Analysis of Human Stress Responses," Ph.D. Thesis, Old Dominion University, Norfolk, Virginia, 1998.

13. Hardy, J. D., and Stolwijk, J. A. J., "Partitional Calorimetric Studies of Man During Exposures to Thermal Transients," Journal of Applied Physiology, Vol. 31, No. 6, April 1966, pp. 1799-1806.

HEFAT2002
1st International Conference on Heat Transfer, Fluid Mechanics, and Thermodynamics
8-10 April 2002, Kruger Park, South Africa
CK1

SADDLE POINTS IN THE OPTIMIZATION OF THERMOFLUID SYSTEMS

K.J. Craig
Professor
Multidisciplinary Design Optimization Group (MDOG),
Department of Mechanical and Aeronautical
Engineering, University of Pretoria, Pretoria 0002
South Africa
ken.craig@eng.up.ac.za

ABSTRACT

This paper describes the use of saddle points in the design of thermofluid systems. With saddle points are meant points in the design space where in a mathematical optimization process, the objective function is maximized with respect to one set of design variables, while it is minimized with respect to other design variables simultaneously. For saddle points to exist, the maximization variables have to be separable from the minimization variables, otherwise a transformation is necessary. The philosophy behind the saddle-point optimization approach is described first and applied to a simple analytical saddle-point function. Thereafter, the process is illustrated through the design optimization of two thermofluid systems. Both thermofluid studies employ the coupling of Computational Fluid Dynamics (CFD) with a version of the DYNAMIC-Q optimization algorithm of Snyman, modified to locate saddle points instead of minima. The studies illustrate how parameters over which the engineer has little control, can be treated as maximization design variables in a worst-case sense, thereby providing thermofluid designs which will perform at least as well as the saddle-point performance.

INTRODUCTION

The general plant optimization process can be depicted as in Figure 1. Shown are the successive steps that are typically followed when a new plant or any machinery is first designed using mathematical modeling techniques, then built, commissioned, and optimized during operation and upgrades. Also shown in Figure 1 is the influence of environmental, or random, variables. These variables represent those over which the engineer has no control. The influence of these variables is usually countered using feedback or even optimal control techniques, but the ability of the plant to reject this influence using optimal control may be limited due to the fixed nature of the plant already in operation. In this paper, it is shown that it would be advantageous to consider these variables in a worst-case scenario framework during the mathematical modeling pnase using so-called saddle points. In this plant design optimisation stage, the main advantage is that the plant is not yet built, implying that changes are cheaper to implement. Examples of these environmental variables are environmental temperature, plant operating parameters that are not measured or controlled, unknown disturbances, manufacturing uncertainties, etc. The influence of these variables would typically be rejected using an optimal control strategy when operating a plant provided the variables are measurable or can be constructed from measurements, but when the plant is designed, and major decisions as to plant lay-out and geometrical parameters are still being made, their effect could be minimized in the optimal design process or synthesis described in this paper. Another field where worst-case design can be applied, is that of design optimization where dimensions or material properties are uncertain due to some manufacturing process. The variation due to manufacturing can then be investigated using the worst-case concepts described here.

To the best of the author's knowledge, no systematic algorithm exists that is specifically tailored to search for saddle points instead of the usual minima. As the optimization method used in this study is gradient-based and uses gradients only, i.e. no explicit function information, it is relatively straightforward to modify it to search for saddle points instead of minima. It should be mentioned that because the method is gradient-based, it is not generally applicable to discrete or integer programming problems, unless dynamic rounding can be used. This modification has been implemented by other authors using the core solver of the algorithm presented here[1,2]. In the first instance, it was used during the optimization of chemical molecular structures, while in the second study it was used in the optimal synthesis of planar mechanisms. In the latter case, the eigenvalues of the Hessian matrix (second-order derivatives of the objective function with respect to the design variables) was used to transform the problem by rotating the variable axes, and switching the sign of the gradients corresponding to the negative eigenvalues, such that a saddle point could be found.

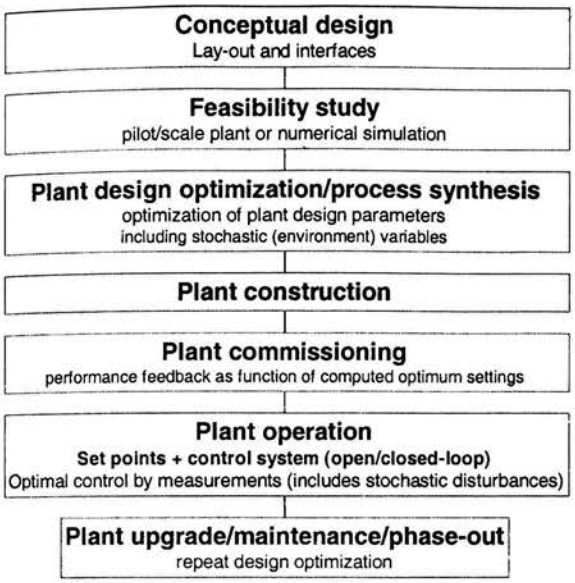

Figure 1 – General plant optimization process

To test how the optimization algorithm operates when the function that contains the saddle point is not separable, i.e. there exist a cross influence between the design variables, the methodology is first applied to a simple analytical function with varying degrees of rotation. The degree of rotation is determined where the cross influence of the variables lead to sufficient inaccuracy in the objective function gradients that the saddle point cannot be found.

Two engineering tests are presented in the paper. The first, that of urban air pollution minimization, was the first implementation of saddle points performed by the author[3]. In this study, the geometrical plant variables considered are those of the lay-out and configuration of an idealized urban design, as represented by street width and building height. The environmental (random) variables considered are the wind direction and speed.

The second case study presented extends the concept to the continuous casting field. The plant to be designed is that of the tundish of a continuous caster. The tundish acts as both a reservoir and a flow control device during the casting of liquid steel. The geometrical variables chosen for this study are related to the configuration and position of the so-called furniture in the tundish. The environmental (or saddle-point) variable is the steel inlet temperature to the tundish. This variable is chosen as it is not measured directly in the plant and typically has some unknown variation that could have a large impact on the flow patterns due to the density-driven buoyancy in the tundish.

The next section will define the saddle-point optimization problem and its solution methodology. This includes a description of the DYNAMIC-Q algorithm and how it is modified to accommodate saddle points. To illustrate the effect that separability has on the success of the optimization, the process is first applied to a simple analytical saddle-point function. This is followed by two thermofluid case studies, each with its own formulation, theoretical modeling, and results section. Conclusions made from the results conclude the paper.

METHODOLOGY

The saddle-point problem to be solved is as follows. Determine $(\boldsymbol{x}^*, \boldsymbol{y}^*)$ such that

$$f(\boldsymbol{x}, \boldsymbol{y}^*) \geq f(\boldsymbol{x}^*, \boldsymbol{y}^*) \geq f(\boldsymbol{x}^*, \boldsymbol{y}) \qquad (1)$$

subject to

$x_j^{\min} \leq x_j \leq x_j^{\max}$ and $y_j^{\min} \leq y_j \leq y_j^{\max}$

Assume that the solution lies at the saddle point $(\boldsymbol{x}^*, \boldsymbol{y}^*)$, and that f is convex with respect to $\boldsymbol{x}$, and concave with respect to $\boldsymbol{y}$. If these two sets of variables are separable (i.e.,

$$f(\boldsymbol{x},\boldsymbol{y}) = f_1(\boldsymbol{x}) + f_2(\boldsymbol{y}), \qquad (2)$$

so that they do not have a significant cross-influence on each other), then this problem becomes tractable. In order to solve this problem, a modification is made to an existing minimization algorithm, DYNAMIC-Q.

For pure minimization problems, the DYNAMIC-Q method of Snyman et al[4,5] involves the application of a dynamic leap-frog trajectory method for unconstrained optimization[6,7], adapted to handle constrained problems through appropriate penalty function formulations[8]. The penalty function used is defined by

$$p(\boldsymbol{x}) = f(\boldsymbol{x}) + \sum_{i=1}^{m} \alpha_i g_i^2(\boldsymbol{x}) \qquad (3)$$

where $\alpha_i = \begin{cases} 0 & \text{if} \quad g_i(\boldsymbol{x}) \leq 0 \\ \rho_i & \text{if} \quad g_i(\boldsymbol{x}) > 0 \end{cases}$

For simplicity the penalty parameters, $\rho_i, i = 1,2,\ldots,m$ take on some positive value, $\rho_i = \mu$. The unconstrained minimum of $p(\boldsymbol{x})$ tends to the constrained minimum of problem (1) as μ tends to infinity. The choice of μ has received a lot of attention. In the application of the dynamic trajectory method (LFOPC[8]) used here, the penalty parameter μ is introduced at a certain specified value, here $\mu = 10^2$, during a so-called Phase 0, and then increased to $\mu = 10^4$ for Phase 1, when during Phase 2 the intersection of active constraints is found. The dynamic

trajectory method is applied to approximate subproblems as follows.

Successive approximate quadratic subproblems, P[k] : $k = 1,2,...,$ are formed at successive design points $\boldsymbol{x}^{(k)}$. For simplicity, only the approximation of the objective function is described here, but the inequality constraints are approximated in a similar fashion. The approximation $\tilde{f}(\boldsymbol{x})$ to $f(\boldsymbol{x})$ is given by

$$\tilde{f}(\boldsymbol{x}) = f(\boldsymbol{x}^{(k)}) + \nabla^T f(\boldsymbol{x}^{(k)})(\boldsymbol{x} - \boldsymbol{x}^{(k)}) + \frac{1}{2}(\boldsymbol{x} - \boldsymbol{x}^{(k)})^T A^{(k)} (\boldsymbol{x} - \boldsymbol{x}^{(k)}) \quad (4)$$

where ∇f denotes the gradient vector. The approximate Hessian matrix is given by

$$A^{(k)} = diag(a^k, a^k, ..., a^k) = a^k I \quad (5)$$

The initial value $a^{(1)}$ or curvature is taken as 0.0 for the first subproblem, i.e. a linear approximation is formed initially. Thereafter the curvatures $a^{(k)}$ are calculated using the expression:

$$a^{(k)} = \frac{2\left\{f(\boldsymbol{x}^{(k-1)}) - f(\boldsymbol{x}^{(k)}) - \nabla^T f(\boldsymbol{x}^{(k)}) \Delta \boldsymbol{x}^{(k-1)}\right\}}{\left\|\Delta \boldsymbol{x}^{(k-1)}\right\|^2} \quad (6)$$

with $\Delta \boldsymbol{x}^{(k-1)} = (\boldsymbol{x}^{(k-1)} - \boldsymbol{x}^{(k)})$

As a further aid in controlling convergence, a spherical intermediate move limit is imposed on the design variables during the minimization of the subproblem. This constraint is described by

$$\left\|\boldsymbol{x}^{(k)} - \boldsymbol{x}^{(k-1)}\right\|^2 - \delta^2 \le 0 \quad (7)$$

where δ is an appropriately chosen move limit.

The gradient vector of the objective function at a specific design point $\boldsymbol{x}$, with respect to each of the design variables x_i, is approximated by the first-order forward differencing scheme

$$\frac{\partial f(\boldsymbol{x})}{\partial x_i} \approx \frac{f(\boldsymbol{x} + \Delta \boldsymbol{x}_i) - f(\boldsymbol{x})}{\Delta x_i} \quad (8)$$

where $\Delta \boldsymbol{x}_i = [0,0,\ldots,\Delta x_i,\ldots,0]^T$, Δx_i is a suitable step size and $f(\boldsymbol{x})$ represents the objective function.

The DYNAMIC-Q minimization algorithm has been applied with success to a number of minimization problems in fluid flow and heat transfer[9-11].

To illustrate the implementation of DYNAMIC-Q in the determination of saddle points, consider the unconstrained problem:

$$\underset{w.r.t.x}{\text{minimize}} \left\{\underset{w.r.t.y}{\text{maximum}} f(\boldsymbol{x}, \boldsymbol{y})\right\}, \ \boldsymbol{x} \in R^p, \boldsymbol{y} \in R^q \quad (9)$$

If the values of $f(\boldsymbol{x},\boldsymbol{y})$ and the associated gradient vectors are known at two successive design points $(\boldsymbol{x}^{(k-1)}, \boldsymbol{y}^{(k-1)})$ and $(\boldsymbol{x}^{(k)}\boldsymbol{y}^{(k)})$, then the spherical quadratic approximation to the objective function (Equation 4) is modified to become

$$\tilde{f}(\boldsymbol{x},\boldsymbol{y}) = f(\boldsymbol{x}^{(k)}, \boldsymbol{y}^{(k)}) + \nabla_x^T f^k (\boldsymbol{x} - \boldsymbol{x}^{(k)}) + \nabla_y^T f^k (\boldsymbol{y} - \boldsymbol{y}^{(k)}) + \frac{1}{2} a^{(k)} \left\|\boldsymbol{x} - \boldsymbol{x}^{(k)}\right\|^2 - \frac{1}{2} a^{(k)} \left\|\boldsymbol{y} - \boldsymbol{y}^{(k)}\right\|^2 \quad (10)$$

with $a^{(k)}$ (previously Equation 6) given by

$$a^{(k)} = \frac{2\left\{f^{k-1} - f^k - \nabla_x^T f^k \Delta \boldsymbol{x}^{(k-1)} - \nabla_y^T f^k \Delta \boldsymbol{y}^{(k-1)}\right\}}{\left\{\left\|\Delta \boldsymbol{x}^{(k-1)}\right\|^2 - \left\|\Delta \boldsymbol{y}^{(k-1)}\right\|^2\right\}} \quad (11)$$

where $f^k = f(\boldsymbol{x}^{(k)}, \boldsymbol{y}^{(k)})$ and $\Delta \boldsymbol{y}^{(k-1)} = (\boldsymbol{y}^{(k-1)} - \boldsymbol{y}^{(k)})$

For application in DYNAMIC-Q, the saddle point of a fictitious function $fic(\boldsymbol{x}, \boldsymbol{y})$ is found if the gradients in the dynamic trajectory algorithm are chosen as follows:

$$\nabla_x fic := \nabla_x f^k + a^{(k)} (\boldsymbol{x} - \boldsymbol{x}^{(k)}) \quad (12)$$

and

$$\nabla_y fic := -\nabla_y f^k + a^{(k)} (\boldsymbol{y} - \boldsymbol{y}^{(k)}) \quad (13)$$

By switching the sign of the actual gradient with respect to y of $\tilde{f}$ in Equation 10, as shown in the latter expression (13), the algorithm, since it uses only gradient information, effectively minimizes a 'fictitious' convex function $fic(\boldsymbol{x}, \boldsymbol{y})$, the minimum of which $((\boldsymbol{x}^{(k+1)}, \boldsymbol{y}^{(k+1)}))$ corresponds to the saddle point of $\tilde{f}(\boldsymbol{x}, \boldsymbol{y})$.

The computed function and gradient values at the point $(x^{(k+1)}, y^{(k+1)})$ may now be used to construct the next approximation $\tilde{f}(x, y)$ to $f(x,y)$, as given by Equation 10 but for $(x^{(k+1)}, y^{(k+1)})$, and the approximation procedure is continued until convergence is obtained to (x^*, y^*). It is further assumed that this procedure, as applied to the objective function above, is also valid in the presence of constraints with, of course, no such adjustment (Equations 12 and 13) applied to the gradients of the constraint functions.

CASE 1: INVESTIGATION INTO SEPARABILITY OF ANALYTICAL SADDLE POINT

Consider the simplest analytical function of a saddlepoint in two variables, namely

$$f(x) = x_1^2 - x_2^2 \tag{14}$$

To investigate the effect of separability on this function, the variable axes are rotated by an angle θ. Equation 14 then becomes

$$f(x) = (x_1 \cos\theta + x_2 \sin\theta)^2 - (-x_1 \sin\theta + x_2 \cos\theta)^2 = y_1^2 - y_2^2 \tag{15}$$

When solving for the saddlepoint of Equation 15 using the procedure outlined above, the gradients are obtained with respect to x_1 and x_2, and not with respect to the rotated variables (y_1 and y_2). This means that as θ is increased, these gradients will become less accurate in their indication of which direction to proceed towards the saddlepoint. Therefore, by increasing θ, one can illustrate the effect of trying to locate a saddlepoint of an objective function where there is a cross-influence between the variables, i.e. they are not purely separable.

Shown in Figure 1 is the optimization history from a starting location of $x = (-10; -5)$ for no rotation and a spherical move limit on the design with a radius of 1. The function in Equation 11 is also plotted to show the location of the saddlepoint. As expected, for no rotation ($\theta = 0°$), the solution history shows that the solution path proceeds directly to the saddlepoint (0;0) independent of the move limit. But as the rotation is increased, i.e. separability breaks down, the optimization algorithm still proceeds rapidly towards the location of the saddlepoint, but it takes longer to converge absolutely to this point. An example of this is shown in Figure 2, where the rotation is 15°, as can be seen by the contours on the base of the plot. The solution path proceeds towards the saddlepoint in an arc because of the inaccurate gradient information.

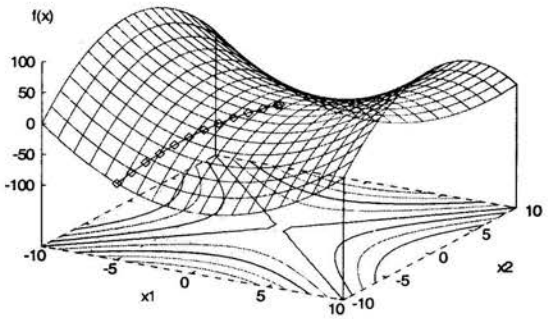

Figure 1 - Convergence history of analytical saddlepoint optimization – No rotation ($\theta = 0°$)

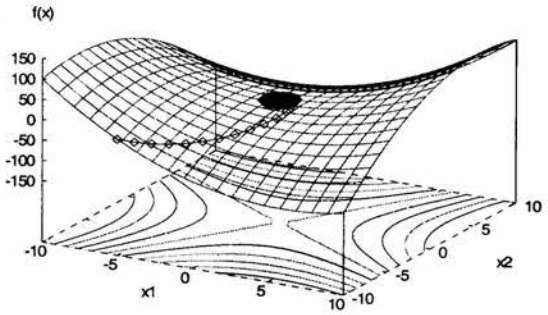

Figure 2 - Convergence history of analytical saddlepoint optimization – With rotation ($\theta = 15°$)

Apart from the rotation angle, θ, the move limit was also varied. Although not shown here, the convergence process was sensitive to the move limit used in the optimization. In general, the smaller the move limit, the more direct the solution path towards the saddlepoint, but the longer the solution takes to reach the region of the saddlepoint. Once in the region of the saddlepoint, the move limit prevents the solution from wandering too far way from this point due to inaccurate gradient information. Nevertheless, the fact that the algorithm quickly proceeds to the region of the saddlepoint, is the property that is valuable in the use of this procedure for worst-case design in engineering applications. This is because in such applications, a design in the region of the optimum or saddlepoint is usually a sufficient result given the inherent inaccuracy of the modeling method.

Now that it has been shown that the optimization algorithm can find the saddle point of a function with some cross influence of the design variables, it is next applied to some thermofluid engineering case studies.

CASE 2: OPTIMIZATION OF URBAN GEOMETRY TO MINIMIZE THE EFFECT OF AUTOMOTIVE POLLUTION

Problem definition and formulation

Refer to Ref. 3 for a detailed motivation and background to this problem. In short, the idealized urban automotive air pollution optimization problem shown in Figure 4 is solved. Shown is a 3x3 array of buildings with two streets in each of the two main directions. The buildings are square-shaped when viewed from above, and the streets are assumed to have a constant width with uniform spacing. The geometrical design variables considered are street width and building height. The size of the urban section considered is 500m by 500m, while an up- and downwind fetch of 5km and 300m high is modeled.

The two urban geometry design variables are shown in Figure 4. $x_1 = w$ is the street width and $x_2 = h$ is the building height, i.e. $\boldsymbol{x} = (x_1,x_2)$. The upper and lower limits on w are 5 and 14m, and for h, 6 and 30m. Due to the symmetric lay-out of the geometry, the range of wind directions that needs to be considered is only one quarter of all wind directions, i.e. from 0° to 45° in Figure 4. The atmosphere is considered as neutrally stable in this study. The wind profile is assumed to be steady and to follow a power law distribution. In general, pollutant episodes with transient wind conditions can be considered if instantaneous pollutant levels are required. The current type of analysis is more suited for averaged or accumulative pollutant scenarios. The wind direction, α and wind speed V are variables that affect the pollutant level and are allowed to vary continuously between the limits: 0 – 45° for α and 2 to 5m.s-1 for V. The aim is to find values of the variables $y_1 = \alpha$ and $y_2 = V$, i.e., $\boldsymbol{y} = (y_1,y_2)$, that would produce the worst-case scenario as far as carbon monoxide (CO) pollutant concentration level is considered, and then minimizing this level by varying the geometrical variables, $\boldsymbol{x}$. The objective function, $f(x,y)$ (refer to Equation 1), is the CO level obtained from a Computational Fluid Dynamics (CFD) simulation given a specific geometry (defined by x) at a 2-m level in the streets for the specified wind speed and direction (defined by y). Refer to Ref.3 for a detailed description of the CFD modelling performed. The numerical grid contained approximately 300 000 cells, and the commercial CFD code, STAR-CD [12], solving for the Reynolds-average Navier-Stokes equations with turbulent closure provided by the k-ε turbulence model, was employed in the solution of, first, the steady-state wind field, and then the dispersion and convection of the pollutant, CO.

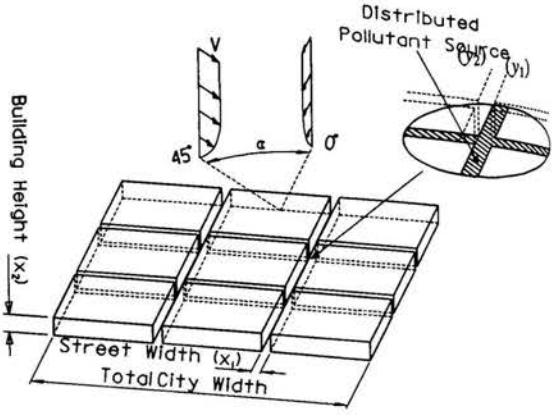

Figure 4 – Graphical representation of automotive urban air pollution problem

Results

The histories of the objective function as well as that of the design variables for Case 1 are given in Figure 5. The first design has the lowest CO pollution value, but it does not represent a worst-case scenario as far as wind speed and direction are concerned. The saddle point (where the objective function is minimized with respect to the geometrical variables, and maximized with respect to the meteorological (wind) variables), is essentially found in 6 iterations.

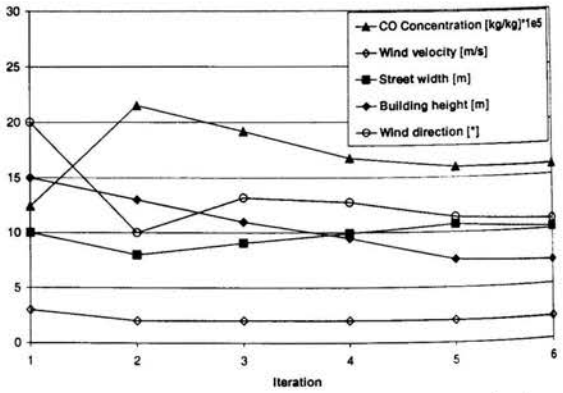

Figure 5 – History of CO concentration, wind speed and direction, and street width and building height.
CO source: 15g/km/lane (Initial design: α = 20°; sV = 3.000m.s^{-1}, w = 10m, h = 15m)

CASE 3: MINIMIZATION OF TUNDISH DEAD VOLUME BY VARYING BAFFLE CONFIGURATION AND POSITION FOR RANDOM TEMPERATURE VARIATION

Problem definition and formulation

A diagrammatic view of the continuous casting process is given in Figure 6. The figure shows the position of the tundish relative to the other components of the caster. The molten steel is poured from the ladle into the tundish. The steel flows through the tundish and exits the tundish through the submerged entry nozzle (SEN) into the mold. The purpose of the tundish is to remove impurities and as well as to act as a reservoir during a ladle change.

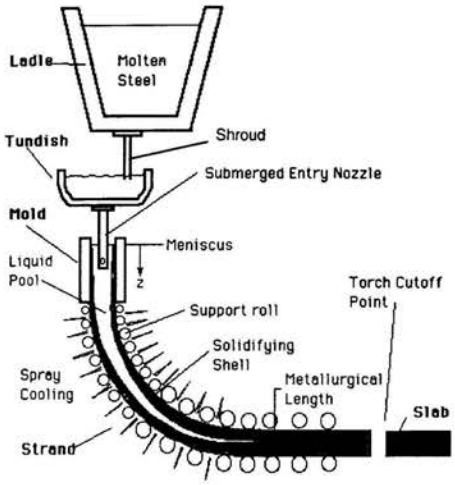

Figure 6 – Diagram of the continuous casting process [13]

Time is normalized by the theoretical average mean residence time ($\bar{t} = V/Q$ = tundish volume/flow rate through tundish) for easy comparison. For the tundish under consideration this time was calculated to be, $\bar{t} = 38.78\,\text{sec}$. The tundish geometry considered is shown in Figure 7. This geometry corresponds to the single-strand stainless steel continuous caster in operation at the Middelburg plant of Columbus Stainless. Only a two-dimensional center-line section of the tundish is considered here. Related work by the authors [14-16] considered three-dimensional effects. The flow rate is controlled by the position of a stopper in the outlet (not shown). When injecting a tracer element at the shroud (inlet), this tracer is detected at the SEN (outlet) after a certain amount of time. The concentration at the outlet increases to a maximum where after it decreases. This time history of the tracer concentration as measured at the outlet is called the residence time distribution (RTD). The rate of decay is of interest since it correlates with the ratio of plug flow versus mixed flow in the tundish.

The amount of tracer left in the tundish after $2\bar{t}$ (twice the mean residence time) is defined in this study as the dead volume, and is minimized in the optimization problem, i.e. it is the objective function, f = dead volume = (1 - concentration at $t = 2\bar{t}$), in Equation (1). The geometrical variables ($\boldsymbol{x} = (x_1, x_2)$) are shown in Figure 7, together with the environmental or saddle-point variable ($\boldsymbol{y} = (y_1)$). The objective function is minimized with respect to the former, while it is maximized with respect to the latter. The location of the baffle shown is the starting design, i.e. $x_1 = 0$.

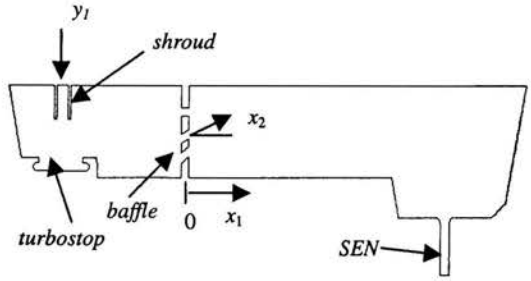

Figure 7 – Side view of tundish showing baffle position and configuration

The evaluation of the objective function is done through a CFD simulation with the commercial CFD code, Fluent[17] and its pre-processor, Gambit[18]. The realizable k-ε turbulence model is used, while the influence of temperature is modeled through a Boussinesq approximation. A new 2-D mesh is obtained in each iteration for the tundish based on the geometry prescribed by the optimizer. The environmental variable is posed as part of the boundary condition specification in Fluent. The mesh is solution-adapted using y^+ and velocity gradients. A steady-state solution is first obtained, where after only the convection and dispersion due to a step input of a tracer scalar are solved for in a transient simulation. The result is a concentration history at the tundish outlet (SEN), of which a sample is shown in Figure 8.

Results

The optimization history for first a case excluding the saddle-point variable and then a case including it, are shown in Figures 9 and 10, respectively. For the two-variable minimization problem in Figure 9, the inlet temperature is taken at a constant value of 1850K, while the temperature of the surroundings is held at 310K. Note how the optimizer pushes the baffle towards the inlet, while a maximum baffle angle of around 20° appears to be the optimum. The variable ranges allowed were x_1 = (-500mm, 1000mm) and x_2 = (0°, 50°). Note that the dead volume decreases by about 1% from over 11% to just over 10%.

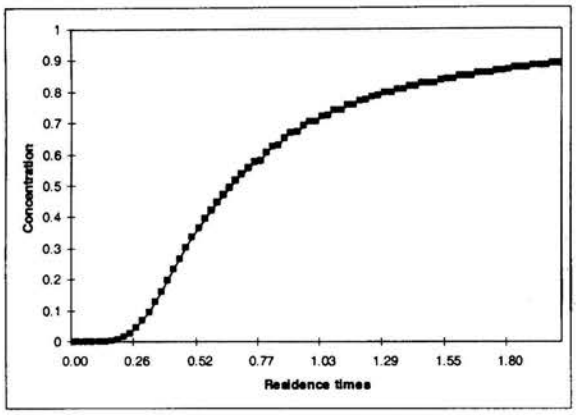

Figure 8 – Outlet concentration of scalar due to step input

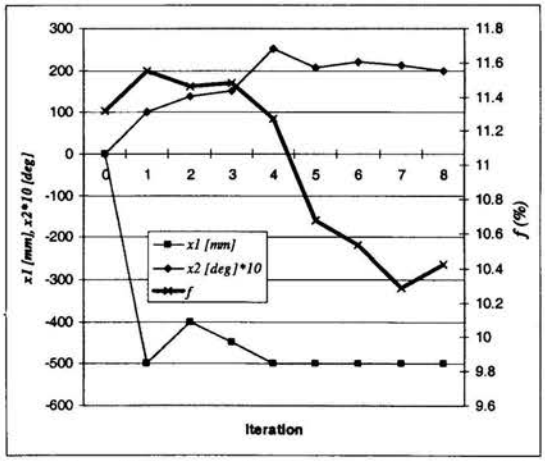

Figure 9 – History of dead volume (f), relative baffle position (x_1) and maximum baffle hole angle (x_2)

When the saddle-point variable (inlet temperature) is included, the optimum geometrical design tends towards $x_1 = -500$mm and $x_2 = 50°$ (minimum and maximum bounds, respectively), while the inlet temperature tends towards an average value of 1775K.

The higher baffle angle can be explained by the fact that the lower inlet temperature has reduced the buoyancy of the steel in the tundish. Previous research has shown that one of the main contributors to dead volume is the region in the corner above the outlet, and this region is only reached if a 'jet' is directed towards it. In the current design, the direction of this jet is determined both by the baffle position and the baffle hole angles, and this combination is influenced by the temperature patterns in the tundish.

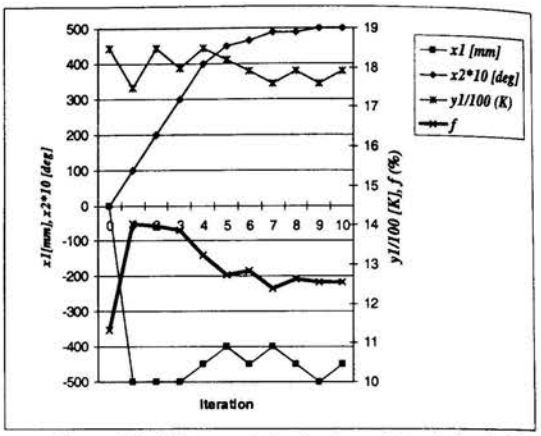

Figure 10 – History of dead volume (f), relative baffle position (x_1), maximum baffle hole angle (x_2), and inlet temperature (y_1)

With the addition of the saddle-point variable, the dead volume minimization shown in Figure 9 now becomes irrelevant, as a fixed inlet temperature of 1850K was used there. The aim is now to find the best design for a worst-case inlet temperature scenario. The difference in dead volume percentages for similar geometrical designs (x_1, x_2) between the two cases is due to the fact that the reduction in inlet temperature brought about by the simultaneous maximization (worst-case) process, changes the flow field to such an extent that the dead volume is increased to the value of 12.5% as shown in Figure 10. The temperature of the surroundings is held at 293K in the Figure 10 results. The oscillatory nature of the baffle distance and the inlet temperature history is indicative of numerical noise that exists in the design space of this problem.

CONCLUSIONS

The following conclusions can be made from this study:

1. Worst-case design can be performed using an optimization algorithm modified to search for saddlepoints instead of minima when the minimization and maximization variables are separable.
2. Using an analytical function, it was shown that the algorithm used can find saddlepoints even when there exists a cross influence between the minimization and maximization variables.
3. Finally, the saddlepoint approach was illustrated using two diverse case studies from the thermofluids field.

ACKNOWLEDGMENTS

The author would like to acknowledge the contribution of colleagues Danie de Kock and Jan Snyman, and students KW

Makgata and Gideon de Wet in the solution of the case studies and formulation of the problems.

REFERENCES

1. Smith, C.M., How to find a saddle point, *Int. J Quantum Chemistry*, Vol. 37, p.773, 1990.
2. Minnaar, RJ. Optimal dimensional synthesis of planar mechanisms. MEng thesis, Department of Mechanical Engineering, University of Pretoria, Pretoria, South Africa, April 1999.
3. Craig KJ, De Kock DJ, Snyman, JA. Minimizing the effect of automotive pollution in urban geometry using mathematical optimization. *Atmospheric Environment* 2001; **35**(3):579-587.
4. Snyman JA, Roux WJ, Stander N. A dynamic penalty function method for the solution of structural optimization problems. *Applied Mathematical Modeling* 1994; **18**:453-460.
5. Snyman JA, Hay AM. The DYNAMIC-Q optimization method: An alternative to SQP? *Proceedings of the International Workshop on Multidisciplinary Design Optimization.* Pretoria, South Africa, 2000. Also submitted to *Computers and Mathematics with Applications* 2001.
6. Snyman JA. A new and dynamic method for unconstrained optimization. *Applied Mathematical Modeling* 1982; **6**:449-462.
7. Snyman JA. An improved version of the original leap-frog algorithm for unconstrained optimization. *Applied Mathematical Modeling* 1983; **7**:216-218.
8. Snyman JA. The LFOPC leap-frog algorithm for constrained optimization. *Computers and Mathematics with Applications* 2000; **40**:1085-1096.
9. De Kock DJ, Craig KJ, Snyman JA. Using mathematical optimization in the CFD analysis of a continuous quenching process. *International Journal for Numerical Methods in Engineering* 2000; **47**(5):985-999.
10. Craig KJ, De Kock DJ, Snyman JA. Using CFD and Mathematical Optimization to Investigate Air Pollution due to Stacks. *International Journal for Numerical Methods in Engineering* 1999; **44**:551-565.
11. Craig KJ, De Kock DJ, Gauché P. Minimization of heat sink mass using CFD and mathematical optimization. *ASME Journal of Electronic Packaging* 1999; **121**(3):143-147.
12. STAR-CD. Version 3.05 manuals. Computational Dynamics Ltd.. London, United Kingdom, 1998.
13. Thomas BG. Introduction to continuous casting, *Continuous Casting Consortium*, URL: http://bgtibm1.me.uiuc.edu, 1999.
14. De Kock DJ, Craig KJ, Venter PJ. Optimization of tundish configuration for a single-strand stainless steel continuous caster. *Proceedings of SACAM2000, International Conference on Applied Mechanics*, Durban, South Africa, January 11-13, 2000.
15. Craig, KJ, De Kock DJ, Snyman JA. Continuous casting optimization using CFD and DYNAMIC-Q, ICTAM2000, Chicago, USA, August 27 – September 1, 2000.
16. De Kock, DJ, Craig KJ. Optimal tundish design using CFD with inclusion modeling. *Proceedings of the International Workshop on Multidisciplinary Design Optimization*, Pretoria, South Africa, 8-10 August 2000.
17. FLUENT. Version 5.3. Fluent Inc., Lebanon, NH, USA, 2000.
18. GAMBIT. Version 1.2. Fluent Inc., Lebanon, NH, USA, 2000.

HEFAT2002
1st International Conference on Heat Transfer, Fluid Mechanics, and Thermodynamics
8-10 April 2002, Kruger Park, South Africa
LC3

AN EXPERIMENTAL STUDY OF A CEILING-TYPE FREE CONVECTED THERMOELECTRIC AIR CONDITIONER

C. Lertsatitthanakorn*, J. Hirunlabh*, J. Khedari*, and M. Daguenet**
* Building Scientific Research Center,
King Mongkut's University of Technology Thonburi, Bangmod, Thungkru,
Bangkok 10140, THAILAND.
E-mail: freeconvect@hotmail.com
** Laboratoire de Thermodynamique et Energetique,
Universite de Perpignan, Perpignan 66860, FRANCE

ABSTRACT

This paper describes experimental performance of a ceiling type free convected thermoelectric (TE) air conditioner. A lab-scale free convected TE Air Conditioner (TEAC) was designed and built. Two types of heat exchangers were considered: free convected inclined rectangular fin heat exchanger at the cold side and force convected skive fin heat exchanger at the hot side of TE modules. Seven TE modules (Tianjin Lantian model TEC1-12708) were used. The TEAC was fixed along the long side of a rectangular test chamber volume of 0.024 m^3. The whole set-up was slightly inclined (5°) from the horizontal plane to collect the condensed water at the fins of the cold fin heat exchanger. Various operating conditions were considered to assess the cooling performance of the TEAC. It was found that the cooling performance of the system depended on three factors: the electrical supply, the ambient air temperature and flow rate of air circulated through the skive fin heat exchanger. The suitable conditions are 3 amps electric and 0.027 $kg.s^{-1}$ and the corresponding cooling capacity is 169 W with an average chamber temperature of 16°C. Thus, the design concept used here can be used for limited cooling load.

INTRODUCTION

Today, thermoelectric (TE) cooling technique is receiving increased attention for air conditioning systems. In recent years the feasibility of large-scale TE air conditioning systems have been investigated. For example, a TE air conditioner was used on railway coach [1]. The railway coach has operated the TE system for over 20,000 hours without a TE failure. TE cooling has also been considered for naval application [2], military vehicle [3] and parked aircraft [4]. Apart from the research work above mentioned, most TE air conditioner is done by considering forced convection mode at the hot and cold side heat exchangers. A first study of free convected TE air conditioner [5] was investigated considering vertical configuration (wall-type). It was found that the wall-type TEAC was not appropriate to cooling a room as the COP was relatively low and higher temperature difference was deserved at different levels of the chamber. Therefore, in this paper a slightly inclined (ceiling-type) configuration is investigated in order to improve the cooling performance of free convected TEAC. A free convected rectangular fin heat exchanger was used at the cold side and force convected skive fin heat exchanger was used at the hot side of TE modules. The effect of various operating parameters namely the current supply, the ambient air temperature and flow rate through the skive fin heat exchanger is examined.

SYSTEM DESCRIPTION AND EXPERIMENTAL METHODOLOGY

First, a lab-scale free convected TE air conditioner was designed using a computer model [6] developed earlier. The principal components of the air conditioner are shown schematically in Fig. 1a. The volume of the chamber is about 0.024 m^3 as shown in Fig. 1b. The walls were insulated using Aeroflex insulator. The skive fin heat exchanger used on the hot side is made of aluminum. The fins are 2.5 cm high, spaced at 10 fins per inch. The base dimensions of commercial units are 8.9 cm long and 8.9 cm wide. Therefore, four skive fin heat exchangers were used on the hot side. They were installed in an air duct as shown in Fig. 2. The rectangular fin heat exchanger used on the cold side is also made of aluminum. The fins are 0.2 cm thick, 34 cm long in the vertical direction and have a height of 3.9 cm from the base and a fin space of 0.6 cm. It was installed in the test chamber. The system (including the chamber) was inclined at 5° from the horizontal plane. A high

performance DC blower with two rotors was used to reject the heat from the hot side of TE. Seven TE modules (Tianjin Lantian model TEC1-12708, 127 couples) were used. Several series connections of TE modules were made to accommodate the 4 amps supply current.

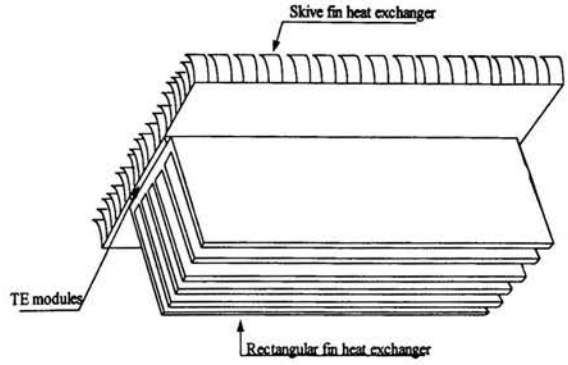

(a)

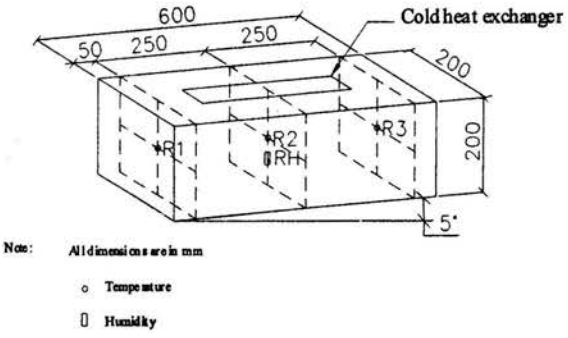

(b)

Figure 1: Schematic view of the free convected TEAC and position of the temperature and humidity measurement in the chamber

The instrumentation in the test setup included temperature, humidity and flow sensors. Temperature sensors were T-type (accuracy ±0.1°C) thermocouples connected to a datalogger. Testo humidity sensor (accuracy ±3%RH) was used to record the relative humidity of the air chamber. Hot wire anemometer (accuracy of 0-1 V ±1%) was used for airflow measurement. The distribution of the sensors is shown in Fig. 1b and 3. Two DC power supply, which can provide variable voltage were used to power the TE modules and drive the blower respectively. A data acquisition system was used to collect the data at regular intervals every 5 minutes.

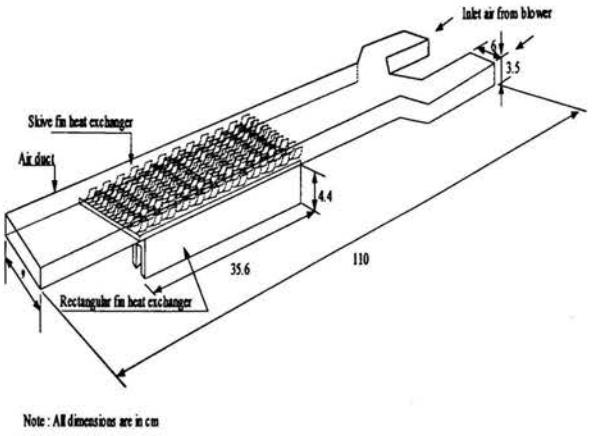

Figure 2: Air duct design and dimensions

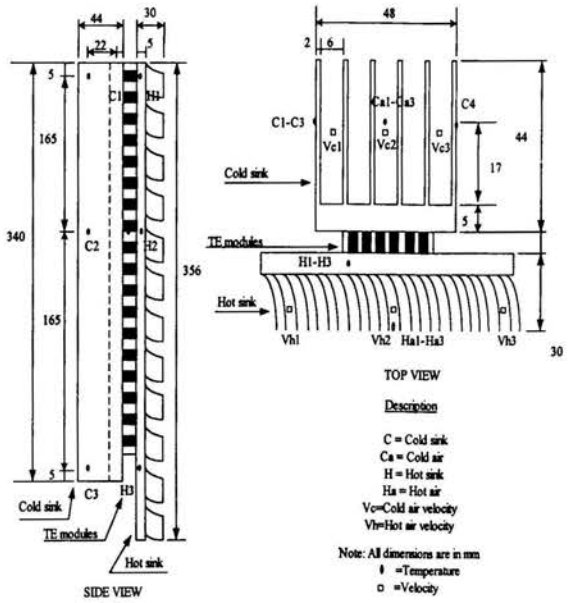

Figure 3: Position of temperature measurement at cold and hot heat exchangers

RESULTS

Fig. 4 shows an example of temperature profiles of hot and cold heat exchangers at 3 amps current supply. The minimum cold heat exchanger temperature was about 5 °C. The temperature of hot heat exchanger increased as the long side of heat exchanger increases. The maximum temperature was 45 °C at the exit of heat exchanger. Fig. 5 shows the air temperature profiles near the hot and cold fins. The temperature of air near the cold fins decreased from 31 to 7.8 °C while at the hot fins, it increased from 31 to 45 °C.

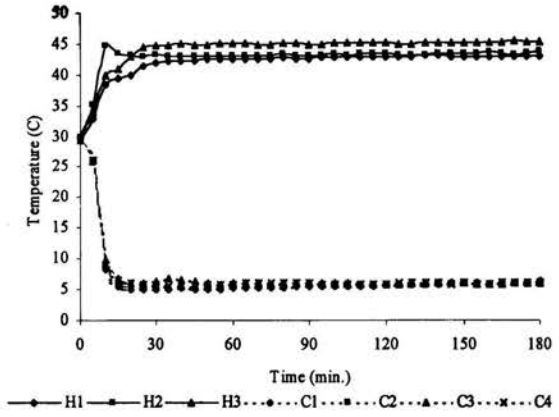

Figure 4: Temperature profile of hot and cold heat exchangers at different positions (3 amps, airflow rate 0.027 kg.s^{-1}, Slope: 5 °, Vol: 0.024 m^3, Tamb: 31°C)

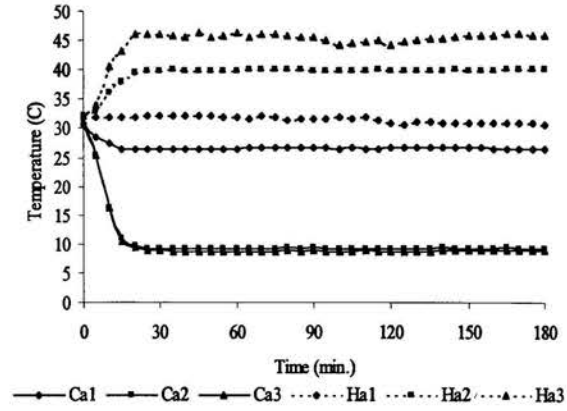

Figure 5: Air temperature profile close to the hot and cold fins at different positions (3 amps,airflow rate 0.027 kg.s^{-1}, Slope: 5 °, Vol: 0.024 m^3, Tamb: 31°C)

Fig. 6 shows the effect of varying the electrical current on the cold and hot fluid temperatures. Tests were conducted at four different currents: 1, 2, 3 and 4 amps. When electric current increases, the cold air temperature decreases from 17 to 8°C. At 4 amps, the cold air temperature re-increased and was higher than at 3 amps. This is due to the Joule heating effect, which prevail over the Seebeck cooling i.e. too large temperature difference is applied to TE modules. The hot air temperature increases steadily as electric current increases. At 4 amps, the air temperature leaving the skive fin heat exchanger is about 47°C. Fig. 7 shows that the cooling capacity increases as electric current increases and vary between 74 to 216 W. However, the COP decreases significantly as electric current increases.

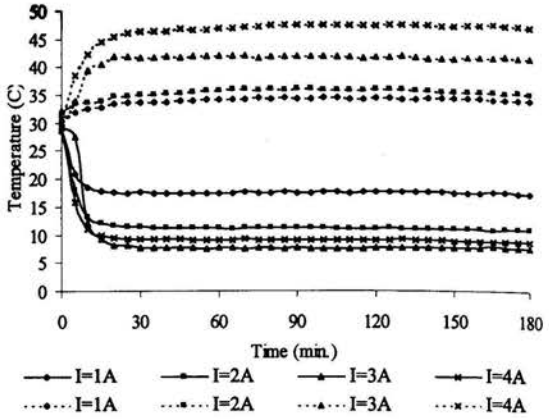

Figure 6: Hot and cold air temperatures versus time for different supply electric current (airflow rate 0.027 kg.s^{-1}, Slope: 5 °, Vol: 0.024 m^3, Tamb: 31°C)

Figure 8 shows the effect of varying the supply current on the water condensation and chamber air temperature. The water condensation increased from 3.2 to 7.5 g as electric current increases. Meanwhile, the chamber air temperature decreases as electric current increases expect at 4 amps. Thus under design conditions used here a 3 amps electric current is recommended. Fig. 9 shows the effect of ambient air temperature on the hot and cold TEAC air temperatures. Tests were conducted at two different ambient conditions: 25 and 30 °C. Obviously when the ambient temperature decreases, more heat could be released at the TE hot side leading therefore to better cooling performance. Consequently the cold air temperature decreases from 7.5 to 2.7 °C and the cooling capacity and COP increased to 190.9 W and 1.22 respectively (Table 1). Therefore, ambient temperature is a determining factor and a special care must be paid when designing such TEAC.

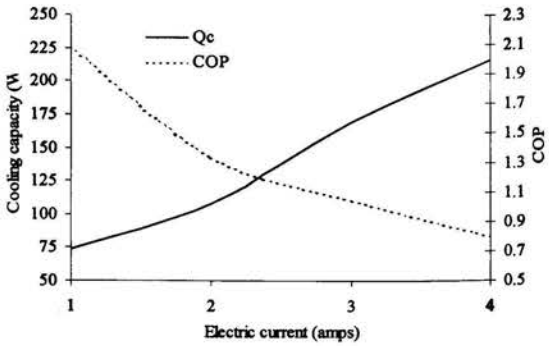

Figure 7: Effect of electric current supply on cooling capacity and COP (airflow rate 0.027 kg.s^{-1}, Slope: 5 °, Vol: 0.024 m^3, Tamb: 31°C)

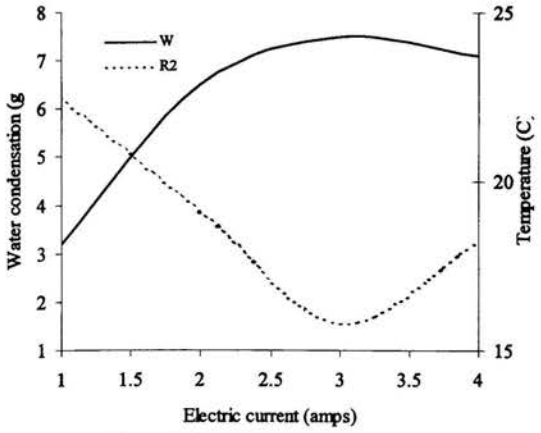

Figure 8: Effect of electric current on water condensation and chamber air temperature (airflow rate 0.027 kg.s^{-1}, Slope: 5 °, Vol: 0.024 m^3, Tamb: 31°C)

The effect of ambient airflow rate circulating through the skive fin heat exchanger at the hot side of TE modules is shown in Fig. 10. Tests were conducted at two different airflow rates (0.009 and 0.027 kg.s^{-1}). It can be seen that the cold air temperature decreased when the airflow rate increases as more heat can be rejected to the ambient. Thus, when airflow rate increases from 0.009 to 0.027 kg.s^{-1}, the cooling capacity and COP increased from 10.71 W to 169 W and 0.074 to 1.05 respectively as shown in Table 2. Consequently, a high airflow rate (0.027 kg.s^{-1}) is recommended which should be considered depending on the efficiency of heat exchanger used.

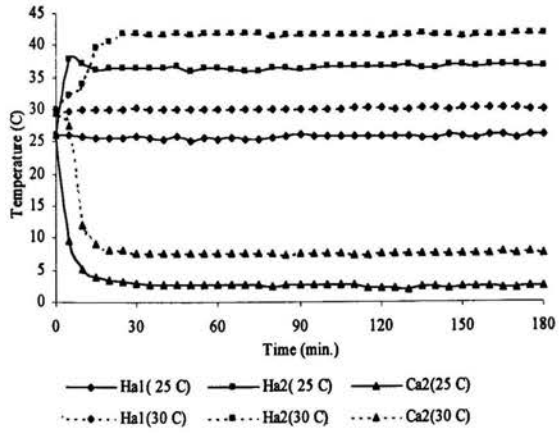

Figure 9 : Hot and cold air temperatures versus time for different ambient air temperature (3 amps, airflow rate 0.027 kg.s^{-1}, Slope: 5 °, Vol: 0.024 m^3)

Table 1 Comparison between the cooling capacity and COP for different ambient air temperatures (3 amps, airflow rate 0.027 kg.s^{-1}, Slope: 5 °, Vol: 0.024 m^3)

Air temperature (°C)	Cooling capacity (W)	COP
25	190.9	1.22
30	169	1.05

Table 2 Comparison between cooling capacity and COP for different ambient airflow rates (3 amps, Slope: 5 °, Vol: 0.024 m^3, Tamb: 31°C)

Air flow rate (kg.s^{-1})	Cooling capacity (W)	COP
0.009	10.7	0.07
0.027	169.3	1.05

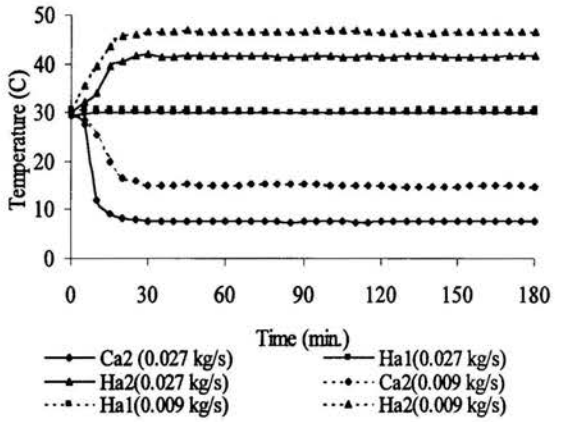

Figure 10: Hot and cold air temperatures versus time for different ambient airflow rate (3 amps Slope: 5 °, Vol: 0.024 m^3, Tamb: 31°C)

CONCLUSION

The cooling performance of a lab-scale free convected TEAC was investigated experimentally. Test results showed that the unit can cool the air in the chamber (0.024 m^3) from 30.5 to 16°C. The corresponding cooling capacity is 169 W with a COP of 1.05. Therefore, this concept is found to be appropriate for limited cooling capacity such as small refrigerator or special boxes. Further investigation implies large-scale testing of TEAC in cooling and dehumidifying.

ACKNOWLEDGEMENTS

The authors would like to acknowledge the financial support of the Thailand Research Fund (TRF) on this research work.

REFERENCES

1. Stockholm, J.G. and Pujol-Soulet L., 1982, "Prototype Thermoelectric Air Conditioning of a Passenger Railway Coach," 4th International Conference on Thermoelectric Energy Conversion, 10-12 March, Arlington, USA, pp. 136-141.
2. Stockholm, J.G. and Schlicklin P.M., 1988, "Thermoelectric Cooling Naval Applications," 7th International Conference on Thermoelectric Energy Conversion, 16-18 March, Arlington, USA, pp. 235-238.
3. Heenan, P. and Mathiprakasam B., 1992, "Development of Two-Men TE Microclimate Conditioner for Use in Army Ground-Vehicles," 11st International Conference on Thermoelectric Energy Conversion, , October, Arlington, USA, pp. 181-184.
4. Gwilliam, S., "Feasibility and Prototype Developments of a Thermoelectric Cooler for Parked Aircraft," 10th International Conference on Thermoelectric Energy Conversion, 10-12 September, Cardiff, UK, pp. 218-221.
5. Lertsatitthanakorn, C., Hirunlabh J., Khedari J. and Scherrer H., 2001, "Cooling Performance of Free Convected Thermoelectric Air Conditioner," 20th International Conference on Thermoelectrics, 8-11 June, Beijing, China.
6. Lertsatitthanakorn, C., 2001, "3-D Numerical Modeling of Laminar Free Convection in Fin Heat Exchanger: Application to the Design of Thermoelectric Air Conditioner," Ph.D. Dissertation, King Mongkut's University of Technology Thonburi, Bangkok, Thailand.

HEFAT2002
1st International Conference on Heat Transfer, Fluid Mechanics, and Thermodynamics
8-10 April 2002, Kruger Park, South Africa
SM2

THERMODYNAMIC ANALYSIS OF A VAPOUR COMPRESSION REFRIGERATION SYSTEM

M. Sasso*, S. Sibilio*, L. Vanoli**
*DETEC, Università degli Studi di Napoli Federico II, P.le Tecchio 80, 80125 Napoli, Italia
Ph.: +39 0817682304 - Fax: +39 0812390364 - email: sassom@unina.it
**DiMSAT, Università degli Studi di Cassino, Via Di Biasio 43, 03043 Cassino (FR), Italia

ABSTRACT

Many methods can be used to perform a thermodynamic analysis of a thermal systems. The most established thermodynamic approaches, Exergetic Analysis, EA [1], and Entropy Generation Minimisation method, EGM [2], usually identify the components that are responsible of thermodynamic losses trying to minimise local and/or global irreversibility and, considering also economic principles, the Thermoeconomics analysis allows to evaluate and minimise the total costs associated with the energy systems. The above mentioned methods compare the performance of an actual energy conversion systems with a reference model: the well-known full reversible equipment, Carnot Machines. The aim of this paper is to find thermodynamic model more useful than the Carnot model: in fact, linking thermodynamic balances, energy and entropy, and basic heat transfer, irreversible thermodynamic model is able to predict efficiency upper boundary more realistic than common limit of reversibility for all the plant.

Therefore the results provided by a model of a vapour compression refrigeration, that takes into account the irreversibility allocated in the heat exchangers due to finite temperature differences between the heat reservoirs and the working fluids, have been compared with those of a refrigerator simulation program, based on manufacturing data. To this aim three water-cooled water-chillers have been analysed in different operation conditions and with different working fluids, R-134a and R-22.

INTRODUCTION

Particular attention must be paid to improve energy savings of refrigerators and heat pumps due to their increasing influence in global energy consumption. The traditional methods of process analysis, EA and EGM, are based on the evaluation of the thermodynamic losses of an actual vapor compression system when it departs from fully reversible processes.

Unfortunately an accurate evaluation of the degree of thermodynamic perfection of all the devices of an energy plant requires complex simulation of the components and of the working fluids.

It is possible to introduce simplified thermodynamics models that take into account only the irreversibility in heat exchangers due to heat fluxes under finite temperature differences, in this way two aims can be achieved:

- to introduce upper boundary of the performance index more realistic than the common limit of reversibility;
- to predict a first approximation of the actual performance. Obviously these simplified models are not able to realise an accurate prediction of thermal plant performance that takes into account all the irreversibility sources and consequently cannot compete with a simulation allowing an in-depth investigation.

For this reason a simulation program for vapor compression refrigerators able to predict the performance of the components one by one and assembled in a whole plant has been used. The thermodynamic analysis has been carried out on two different water-cooled liquid-chillers using two different working fluids, R-134a and R-22. The results obtained have been compared to those provided by an irreversible model of a refrigerator and to the reversible one. These examples prove how the use of simple thermodynamic methodology in refrigeration could contribute to address a correct design of new equipment, in a sector characterised by emerging technologies and by new working fluids.

NOMENCLATURE

a_i	with i=1,9 coefficients in Eq. (1)
b_i	with i=1,9 coefficients in Eq. (2)
C	Thermal conductance (kW/K)
c_i	with i=1,4 coefficients in Eq. (3)
COP	Coefficient Of Performance
d_i	with i=1,4 coefficients in Eq. (4)
m	mass flow rate (kg/s)
Q	thermal flow rate (kW)
S	entropy rate (kW/K)
T	temperature (°C or K)
$\overline{T}$	thermodynamic mean temperature of the working fluid (°C or K)
W	work transfer rate (kW)

Greek symbols

η_{II}	second law efficiency
η_{HT}	normalized COP referred to irreversible thermodynamic model
η_{HT^*}	normalized COP referred to simplified irreversible thermodynamic model

τ	external temperature ratio	$\frac{T_H}{T_L}$
τ_c	refrigerator temperature ratio	$\frac{\overline{T}_H}{\overline{T}_L}$

Subscripts

gen	generated
H	referred to high thermal reservoir
HT	referred to irreversible thermodynamic model
HT*	referred to simplified irreversible thermodynamic model
i	inlet
L	referred to low thermal reservoir
MC	Carnot Machine
o	outlet
w	water

Superscripts

co	condenser
ev	evaporator

THE SIMULATION ALGORYTHM

The components making up a plant never work in isolation but are combined into a system so that their behavior is interdependent; therefore to simulate steady state performances of an assembled refrigerating plant it is necessary to determinate its "balance point" [3]. To this aim the procedure performs the simultaneous solution of an algebraic equations set representing the functional relationship between appropriate independent variables and the performances of the components one by one. Assuming polynomial relationships, the related coefficients are determined, with an accuracy within the range 1-3%, by an equation-fitting procedure based on data supplied in manufacturer's catalogues, [4, 5, 6], usually as curves or tables.

The procedure will be resumed in the following, a more detailed description can be found in [5].

Compressor

For the convenience of users, the refrigerating effect of compressors, Q^{ev}, is usually tabulated or given in graphical form, and is shown as the net cooling capacity based on the evaporating, T^{ev}, and condensing, T^{co}, temperatures. Such published data will include power input, W, as a function of T^{ev} and T^{co}.

The compressor performance can be represented immediately by the following relantionships, [3, 5]:

$$Q^{ev} = a_1 + a_2T^{ev} + a_3(T^{ev})^2 + a_4T^{co} + a_5(T^{co})^2 + a_6T^{ev}(T^{co}) + a_7(T^{ev})^2(T^{co}) + a_8T^{ev}(T^{co})^2 + a_9(T^{ev})^2(T^{co})^2 \quad (1)$$

$$W = b_1 + b_2T^{ev} + b_3(T^{ev})^2 + b_4T^{co} + b_5(T^{co})^2 + b_6T^{ev}(T^{co}) + b_7(T^{ev})^2T^{co} + b_8T^{ev}(T^{co})^2 + b_9(T^{ev})^2(T^{co})^2 \quad (2)$$

Evaporator

For this equipment, and generally for the heat exchangers, the availability of rating data at different operating conditions is really scanty. The lack of information is due to the diffusion of packaged units incorporating the heat exchangers. Furthermore often these devices are designed "ad hoc" and manufactured in-house.

For an evaporator used to chill water, the refrigerating capacity can be expressed as a function of evaporating temperature, inlet water temperature, $T^{ev}_{w,i}$, and mass flow rate, m^{ev}_w:

$$Q^{ev} = c_1 + c_2(T^{ev}_{w,i} - T^{ev}) + c_3\, m^{ev}_w + c_4\,(T^{ev}_{w,i} - T^{ev})m^{ev}_w \quad (3)$$

Condenser

The rating curves or tables of manufacturer's catalogues show the heat rejected at a water cooled condenser as a function of water mass flow rate, m^{co}_w, and of the difference between condensing temperature and water inlet condenser temperature, $T^{co}_{w,i}$.

The polynomial relationship adopted is:

$$Q^{co} = d_1 + d_2(T^{co} - T^{co}_{w,i}) + d_3\, m^{co}_w + d_4\,(T^{co} - T^{co}_{w,i})m^{co}_w \quad (4)$$

Performance of complete system

In a simplified analysis of the refrigeration plant the system consists of the three above listed components.

In this way it has tacitly been assumed the valve is able to regulate the flow of refrigerant that matches the required refrigerating capacity. The simulation program assumes the valve outlet enthalpy is equal to the inlet one.

The program determines the actual operating conditions, by solving the system of Eqs. (1) to (4) and the energy balance referred to the whole plant, for a given set of external variables.

By means the iterative solution technique of the "successive substitutions", the software is able to calculate the evaporating and condensing temperatures starting by a set of trial values.

By interacting with the code, EASY [7], which supplies the thermodynamic properties of twenty refrigerants, the simulation alghorytm is able to perform the energetic and exergetic analysis of the assembled system as well as of each equipment.

The program has been tested with different types of refrigerators: the results of the software are in good agreement with the ones provided by the manufacturers of assembled plant. For example, referring to a commercially available water cooled liquid chiller (Q^{ev}=116 kW, COP=4.60), the software performs with a percentage deviation of about ±0.50 % for the cooling capacity and about ±5.0 % for the COP.

IRREVERSIBLE THERMODYNAMIC MODEL

Performance of energy conversion systems is based on a comparison of the system under study with the ideal system: using EA and EGM techniques the Carnot Machine, ($S_{gen} = 0$), is assumed as ideal system, and simple performance relations are obtained for the efficiency. To approximate the real working condition of the plant, different irreversibility causes have to be considered: in a simplified approach the irreversibility, allocated in the heat exchangers, due to finite temperature differences between the heat reservoirs and the working fluids can be considered. In fact, heat transfer theory allows to evaluate the heat flow rate in a heat exchanger as a function of the thermal resistance and, obviously, temperature difference between the working fluids.

In this case the reference thermodynamic model, HT, is shown in Fig. 1. The refrigeration system interacts with two different heat reservoirs at temperature $T_H > T_L$: if the working fluid of the equipment does not interact with thermal reservoires but with secondary fluid streams, T_H and T_L are the thermodynamic mean temperatures (ratio of enthalpy variation to entropy variation) between inlet and outlet of the secondary fluids. An actual refrigerator departs significantly from the ideal reversible Carnot Machine, MC: one of the most important departures is related to heat transfer between refrigerants at temperature $\overline{T}$ (thermodynamic mean temperature), and the surrounding heat reservoires at different temperatures.

The actual thermal flow rate through the wall of an heat exchanger is a function of finite temperature difference and thermal resistance, 1/C: the coefficients C_H and C_L in Fig. 1 are respectively the thermal conductance of condenser and evaporator. They represent the product of the heat transfer area times the overall heat-transfer coefficient based on that area. Therefore, considering steady state conditions, the heat flow rates in the heat exchangers are:

$$Q_H = C_H(\overline{T}_H - T_H) \tag{5}$$

$$Q_L = C_L(T_L - \overline{T}_L) \tag{6}$$

The first law of thermodynamic applied to the refrigerator provides the equation:

$$W = Q_H - Q_L \tag{7}$$

If the equipment is endoreversible, the second law of thermodynamics is:

$$\frac{Q_L}{\overline{T}_L} = \frac{Q_H}{\overline{T}_H} \tag{8}$$

defining τ_c as follows:

$$\tau_c = \frac{\overline{T}_H}{\overline{T}_L} \tag{9}$$

it is possible to demonstrate that from Eqs. (5, 6, 7, 8, 9) the refrigerating capacity and the power input can be obtained:

$$Q_L = C_L T_L - \frac{\tau_c \frac{C_L}{C_H} T_L + T_H}{\tau_c(\frac{C_L}{C_H} + 1)} \tag{10}$$

$$W = C_L T_L - \frac{\tau_c \frac{C_L}{C_H} T_L + T_H}{\tau_c(\frac{C_L}{C_H} + 1)} (\tau_c - 1) \tag{11}$$

Finally the Coefficient of Performance of the refrigerators is:

$$COP_{HT} = \frac{1}{\tau_c - 1} \tag{12}$$

It can be noted that the performance of the irreversible thermodynamic model are function only of the ratio between the mean working fluid temperatures, τ_c. Furthermore, COP_{HT} formula is very similar to the well known COP of the reversed refrigerating Carnot machine, $COP_{MC} = (\tau - 1)^{-1}$ with $\tau = \frac{T_H}{T_L}$, that is referred to the temperatures of the external reservoires rather than the working fluid ones.

It is important to observe that the energy flow rates are function of:

T_H, T_L, C_H, C_L, τ_c.

In particular τ_c depends on the condensing and evaporating temperature of the refrigerants: these temperatures, and pressures, are not independent variables, but as previously demonstrate, vary with the external conditions (mass flow rates and temperature levels of the fluids interacting with the refrigeration machine). So to evaluate the performance of the irreversible model (Eqs. (10, 11, 12)) many information must be assigned.

Therefore, a further simplification can be introduced: it is assumed $C_H = C_L$ and conductance calculated by empirical equations (usually adopted by heat exchanger manufactures for different models and size) as a function of the refrigerating capacity. Fixing the refrigeration capacity, T_H and T_L by Eq. (10) τ_c can be calculated and then W by Eq. (11). Finally the COP of this simplified irreversible approach, COP_{HT*}, can be evaluated by Eq. (12).

WATER COOLED LIQUID CHILLER SIMULATION

The analysis has been performed on three plants consist of water-cooled water-chiller. Chosen the plant components, the actual operating conditions are fixed by the value of the following variables [5]:

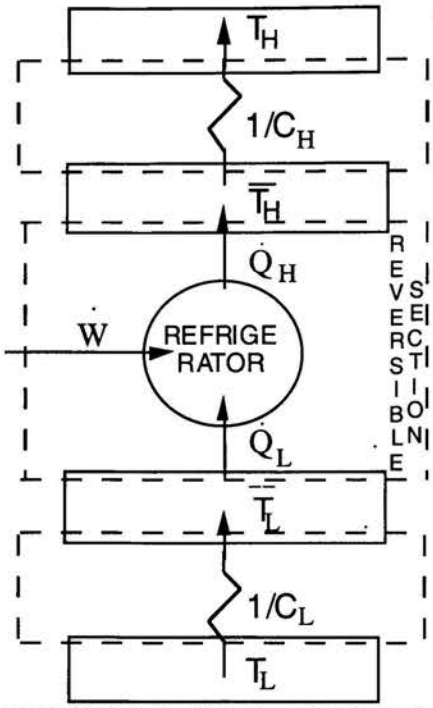

Figure 1: Model of refrigerator with thermal resistances.

- working fluid;
- water flow rate at the evaporator, m^{ev}_w;
- water flow rate at the condenser, m^{co}_w;
- water temperature at the evaporator inlet, $T^{ev}_{w,i}$;
- water temperature at the condenser inlet, $T^{co}_{w,i}$.

Two different working fluids have been considered, R-134a and R-22, and for each of them a suitable compressor has been considered too.

The main characteristics of the cases analised are reported in Tab. 1:

- the working fluids and the vapour compression components are reported (all the compressors are cooled by the refrigerant);
- the input variables such as load temperature, water cooling temperature and mass flow rates, are showed too.

The schemes #1 and #2 are able to chill the same mass flow rate of water using different refrigerants, while the case #3 is related to a small size plant.

In order to analyse the sensitivity of the plant operating parameters to external factors, in the cases #1 and # 2 the evaporator inlet water temperature has been assumed to vary. In the case #3 the analysis has been detailed by varying the condenser inlet water temperature.

The results provided by the simulation have been compared to those available using the previously described irreversible thermodynamic model. The independent (T_H, T_L, C_H, C_L, τ_c) of the Eqs. (10, 11, 12) are calculated using the results of the plant simulation. Moreover, a further comparison, at fixed Q^{ev}, has been accomplished with the simplified irreversible approach.

Table 1: Main characteristics of the plants.

	Case #1	*Case #2*	*Case #3*
Compressor type	Accessible-hermetic	Accessible-hermetic	Hermetic
Evaporator type	Shell and tube dry expansion	Shell and tube dry expansion	Shell and tube dry expansion
Condenser type	Shell and tube	Shell and tube	Coaxial counter flow
Working fluid	R-134a	R-22	R-22
m^{ev}_w *(kg/s)*	5.2	5.2	0.70
m^{co}_w *(kg/s)*	6.5	6.5	0.50
$T^{ev}_{w,i}$ *(° C)*	6 - 18	6 - 18	12
$T^{co}_{w,i}$ *(° C)*	30	30	25 - 15

In order to evaluate how different thermodynamic models can predict the performance of the plants the COP has been normalized to a reference COP.

In a second law approach the COP upper boundary is the common limit of reversibility for all the plant devices, COP_{MC}, and the second law efficiency is:

$$\eta_{II} = COP/COP_{MC} \qquad (13)$$

If the reference thermodynamic model takes into account only the irreversibility, allocated in the heat exchangers, due to finite temperature differences between the heat reservoirs and the working fluids, the corresponding COP can be evaluated by (12) and consequently a normalized COP can be calculated as follows:

$$\eta_{HT} = COP/COP_{HT} \qquad (14)$$

In this case $\overline{T}_H$ and $\overline{T}_L$, and consequently their ratio τ_c, can be evaluated by means of the thermodynamic properties of R-134a and R-22 at the inlet and outlet of the heat exchangers.

Finally as previously described a further simplification can be done to evaluate the upper bound of COP, COP_{HT^*}. In this case the COP can be normalized as follows:

$$\eta_{HT^*} = COP/COP_{HT^*} \qquad (15)$$

Results

Varying one of the characteristics of external load the operation conditions of the plant vary. In order to understand the refrigerator performance behavior it is interesting to analyse the trend of temperatures levels of water and refrigerant.

In Fig. 2 for the case # 1 the mean temperatures of the water and of the R-134a are showed as a function of the water temperature at evaporator inlet. Increasing $T^{ev}_{w,i}$ the temperatures of the fluids interacting in the evaporator are very

influenced while the mean temperatures at the high level show a constant behaviour. The increase of T^{ev} at constant T^{co}, causes the increase of the refrigerating capacity from 90 to 130 kW, (Eq. (1)) and a small increase of the power input, in the range of 27.1 - 31.2 kW, (Eq. (2)). As a consequence the COP increases from 3.35 to 4.16. A further consequence of the variation of the condensing and evaporating temperature, the pressure ratio decreases, from 3.64 to 2.80.

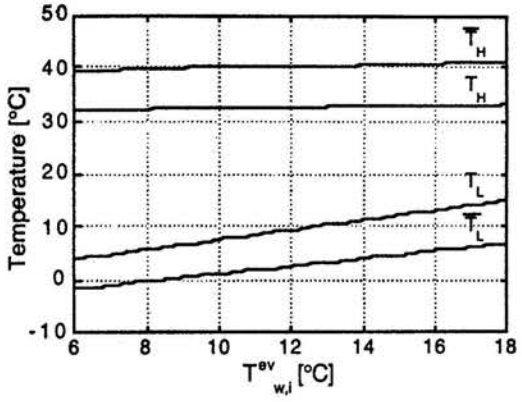

Figure 2: Thermodynamic mean temperatures of the secondary fluids and of the R-134a in the case #1.

The figures of merit, COP_{MC} and COP_{HT} are only functions of the temperatures showed in Fig. 2: COP_{MC} ranges from 9.80 to 16.5 while COP_{HT} increases from 6.59 to 8.18.

In Fig. 3 a sensitivity analysis has been performed in order to evaluate the influence of the variation of Q^{ev} on the second law efficiency and on the two normalized COPs (Eqs. (13, 14, 15)). The results of the comparison shows:

- the reference model influenced by irreversible heat transfer gives results closer to actual performance than the full reversible one;
- η_{HT} is lightly influenced by external variation while the second law efficiency η_{II} strongly decreases with refrigerating capacity ($T^{ev}_{w,i}$) from 34.2 to 25.9%.

At least also using the simplified model it is possible to obtain accurate information on the plant performance.

The results obtained in the case #2 using a different working fluid, R-22, are in agreement with the case #1. The COP ranges between 3.76 and 4.80 and, as shown in Fig. 4:

- η_{HT} assumes a constant value of about 57%;
- η_{II} decreases with refrigerating capacity from 38.2 to 29.7%.

In the last case, #3, a small size plant utilizing R-22 has been analyzed. Decreasing $T^{co}_{w,i}$ the temperatures of the fluids interacting in the condenser are very influenced while the mean temperatures at the low level show a constant behaviour. The decrease of T^{co} at constant T^{ev}, causes the increase of the refrigerating capacity from 16 to 18 kW and COP increases from 3.07 to 3.87.

COP_{MC} ranges from 13.7 to 25.5 while COP_{HT} increases from 6.41 to 7.91. In Fig. 5 the results of the comparison has been reported:

- the reference irreversible thermodynamic model, also in the simplified version, gives results closer to the simulation than the Carnot one;
- η_{HT} is lightly influenced by external variation while the second law efficiency η_{II} strongly decreases with refrigerating capacity ($T^{co}_{w,i}$) from 22.5 to 15.2%.

CONCLUSIONS

Water-cooled water-chillers, operating with different components and working fluids, have been studied by means a simulation procedure based on manufacturing data.

The results of the energetic sensitivity analysis on external variables have been compared to the ones obtained by two reference thermodynamics models: the Carnot inverse machine and an endoreversible refrigerator. In the first case the second law efficiency is in a large range of variation, 15-34%, with a mean value of about 27%; in the second case the ratio between plant COP and its endoreversible limit is within the range 48-57%, with a mean value of about 52%. Furthermore, a simplified irreversible approach has been considered too.

It is important to observe that the irreversible thermodynamic system considered, in which only the irreversibility due to heat transfer under finite temperature differences have been considered, is in agreement with the so-called Finite Time Thermodynamics approaches, FTT: recently many examples of FTT applications appear in literature [8, 9, 10], involving a large amount of criticisms basically focused on the impossibility to separate the different irreversibility contributes, on the consideration that the FTT approach is fundamentally nothing other than the well established EGM method, and finally on the accuracy of the results provided by its models, [11, 12, 13]. This paper tries to demonstrate that some of the above mentioned criticisms derive by an inappropriate use of FTT approach and of its results: in fact FTT theory, linking thermodynamic balances, energy and entropy, and basic heat transfer equations is not able to realise an accurate prediction of thermal plant performance that takes into account of all the irreversibility and that can compete with a simulation allowing an in-depth investigation. A FTT approach can supply a more realistic upper limit of the performance figures of merit, that seems to be not very influenced by variation of external operation conditions.

REFERENCES

[1] Kotas, T.J., 1995 "The exergy method of thermal plant analysis" Kriger Publishing Company, Malabar, Florida

[2] Bejan A., 1996 "Entropy Generation Minimization", CRC Press.

[3] Stoecker, W.F. and Jones J.W., 1982, "Refrigeration and air conditioning". Mc Graw-Hill, New York.

[4] Trott, A.R., 1981, "The compilation and interpretation of catalogue data with a simple mathematical models", Proceeding of Institute of Refrigeration

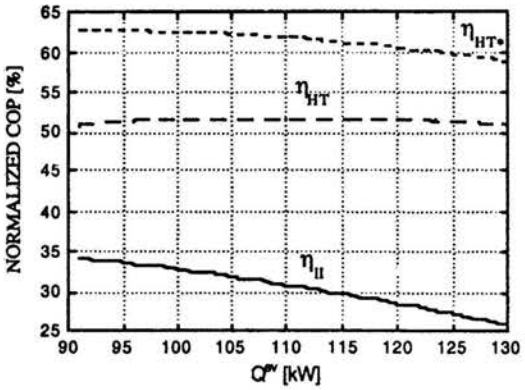

Figure 3: Normalized COPs and second law efficiency in the case #1.

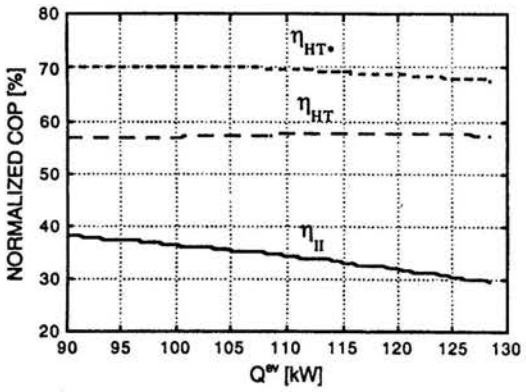

Figure 4: Normalized COPs and second law efficiency in the case #2.

[5] Aprea, C., de Rossi, F., Mastrullo, R., and Sasso, M., 1992, "A code for predicting refrigerating vapor compression plants performances", Proceedings 2th International Congress Energy, Environment and Technological Innovation, 12-16 October, Rome, Italy, Vol. 3, pp. 183-188.

[6] Grosu, L., Benelmir, R. and Feidt, M., 1998" Technico-economic simulation and optimization of a compression refrigerating machine", Proceedings ECOS 98, Nancy, France, pp. 323-329.

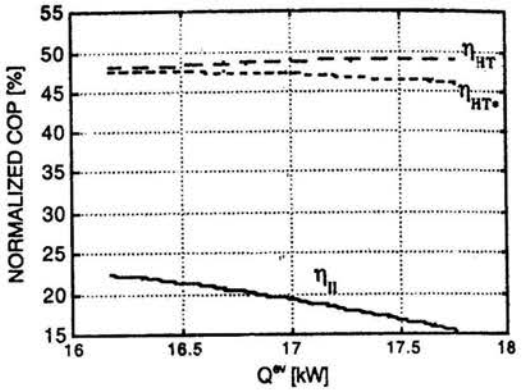

Figure 5: Normalized COPs and second law efficiency in the case #3.

[7] de Rossi, F., Mastrullo, R., Mazzei, P. and Sasso, M., 1998, "EASY: Exergetic Analysis of vapour compression SYstems", LIGUORI Editore, Napoli, ISBN 88-207-2805-2.

[8] Bejan A., 1996 "Maximum power from fluid flow", Int. J. Heat Mass Transfer, Vol. 39, No 6, pp 1175-1181.

[9] C Wu, C., Chen, L. and Chen, J., 1999 "Recent Advanced in Finite-Time Thermodynamics", Nova Science Publisher, Inc., Commack, New York.

[10] Sieniutycz, S. and Salamon, P., 1990, "Finite-Time Thermodynamics and Thermoeconomics", Advanced in Thermodynamics, Vol. 4, Taylor & Francis.

[11] Chua H.T., NG, K.C. and Gordon J.M., 1996 "Experimental study of the fundamental properties of reciprocating chillers and their relation to thermodynamic modelling and chiller design", Int. J. Heat Mass Transfer, Vol. 39, No 11, pp 2195-2204.

[12] Moran M.J., 1998, "A critique of finite-time thermodynamics", Proceedings of ECOS'98, Nancy, France Vol. 2, pp. 1147-1149.

[13] Gyftopoulos E.P., 1997 "Fundamentals of analyses of processes", Energy Conversion Mgmt, Vol. 38, No 15-17, pp 1525-1533.

HEFAT2002
1st International Conference on Heat Transfer, Fluid Mechanics, and Thermodynamics
8 – 10 April 2002, Kruger Park, South Africa
SR1

EFFICIENT EQUIPMENT WITH SPECIAL HEAT EXCHANGER FOR THERMAL TREATMENT OF POLLUTED AIR – EXPERIMENTS, COMPUTATIONS, APPLICATIONS

Roman Stulir*, Petr Stehlik**
* PhD Student, ** Professor
Institute of Process and Environmental Engineering,
Technical University of Brno,
Technicka 2, Brno, 616 69
Czech Republic
E-mail: Stulir@kchz.fme.vutbr.cz
Stehlik@kchz.fme.vutbr.cz

Jaroslav Oral
Industrial Specialist – Director of Company
EVECO Brno Ltd.
Rybkova 1, Brno, 602 00
Czech Republic
E-mail: eveco@netbrno.cz

ABSTRACT

A quite new and unique system for the thermal treatment of gas wastes (incineration of volatile organic compounds contained in polluted air) has been developed. This comprises a process placed into one compact equipment consisting of a combustion chamber (incinerator) combined with heat exchanger (polluted air preheater). It can be used in various branches of industry.

The equipment is characterized by a cylindrical combustion chamber which is placed inside a heat exchanger – polluted air preheater. This cylindrical preheater consists of several concentric stainless sheets. Both flue gas from the combustion chamber and polluted air (which is heated by flue gas) flow in the spaces between each couple of cylindrical sheets. Narrow distance strips which are helically placed between the sheets form helical rectangular ducts. Thus we can reach counter-current flow of process fluids.

It was necessary to develop a mathematical model for the calculation and/or simulation of the equipment. This model consists of submodels of heat exchanger, combustion chamber and annular space in between them. Based on results of measurements on an industrial scale experimental facility new correlations for the thermal and hydraulic calculations of the heat exchanger were developed. Some industrial applications are briefly mentioned.

INTRODUCTION

Air polluted by organic compounds or carbon monoxide is a consequence of industrial production. However, it can be encountered in the municipal sector, too. The thermal processing can be considered due to its simplicity and reliability as the most effective way of the polluted air treatment. Heat of exhaust flue gas can be utilized for preheating the air in a recuperator.

Units in common use consist of two main independent pieces of equipment (Fig.1a) – combustion chamber (incinerator) and a sizeable heat exchanger (polluted air preheater). A unit like this where two pieces of equipment are connected with piping also involves thermal expansion systems, bulky refractory lining and a thick insulation. Therefore it occupies a large space. A quite new and original solution [1, 2] is based on integration of the two main pieces of equipment into one compact unit and thus it eliminates the above problems (Fig. 1b).

The fully integrated unit has several advantages. Since the combustion chamber equipped with a burner is installed inside a recuperative cylindrical heat exchanger the equipment is very compact, and heat losses from the combustion chamber are effectively utilized to share in preheating the polluted air. Therefore the equipment has lower weight and increased thermal efficiency comparing with a conventional arrangement.

Due to a wide scope of applications a systematic research and development of this equipment has been performed as follows:

- idea and basic conception of this incineration unit (a compact equipment consisting of the combustion chamber and heat exchanger) taking into consideration industrial demands
- using simulation [3] for setting basic process parameters
- developing a computer program for thermal and hydraulic calculation of this equipment
- design of a research facility in an industrial scale
- experimental research and measurements
- verification of mathematical models and CFD (Computational Fluid Dynamics) simulation
- evaluation of results, discussion and recommendation for industrial applications

A mathematical model for thermal and hydraulic calculations of the equipment (after being validated) provides the researcher with a useful tool for evaluation of basic parameters.

Some examples of applications in various branches of industry include: treatment of polluted air from paint shops, chemical cleaning systems, degreasing processes, printing machines, gas wastes from various chemical processes, for the thermal treatment of off-gases originating in refineries, in production of plastics, pharmaceutical industry, food industry, laboratories etc.

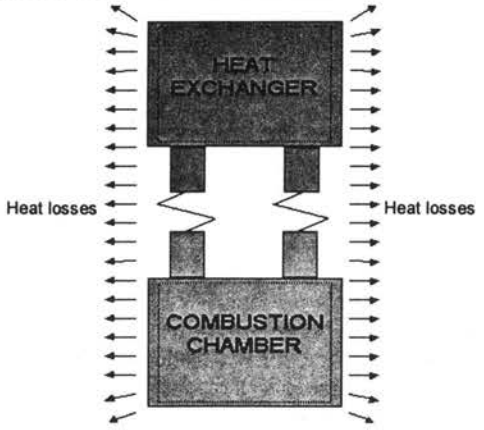

a) Two independent pieces of equipment

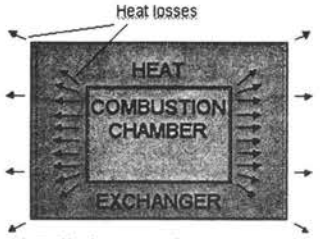

b) Fully integrated compact unit

Figure 1: Comparison of conventional and new arrangement of unit for thermal treatment of gas wastes

NOMENCLATURE

A	heat transfer area (m^2)
B	width of the heat exchanger duct (m)
D	diameter (m)
D_c	central diameter (m)
d_h	hydraulic diameter (m)
f	friction factor (-)
g	symbol for gas zone (-)
H	height (m)
h	heat transfer coefficient (W/m^2K)
h_d	lead of helix (=height of the heat exchanger duct) (m)
k	overall heat transfer coefficient (W/m^2K)
m	exponent in equation for Nusselt number (-)
n	symbol for number of items in relation to geometry (-)
Nu	Nusselt number (-)
p	pressure (Pa)
Δp	pressure drop (Pa)
Pr	Prandtl number (-)
Q	heat duty (W)
Q_c	heat flux through the combustion chamber wall (W)
Re	Reynolds number (-)
s_1, s_2, s_3	symbols for surface zones (-)
T	temperature (°C)

Subscripts

a	air
crit	critical
d	ducts
fg	flue gas
i	inner
o	outer

Greek symbols

ϕ	angle of lead of helix (°)

EXPERIMENTAL FACILITY, MEASUREMENTS AND DATA ACQUISITION

Equipment

An industrial scale experimental facility is shown in Fig. 2. It can be briefly described using a three-dimensional schematic drawing showing a cut through the equipment (see Fig. 2).

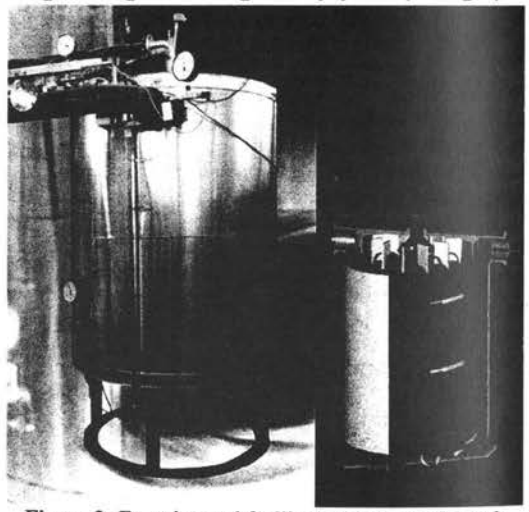

Figure 2: Experimental facility in full industrial scale

Air polluted by organic compounds and CO enters the unit at its upper part. As obvious from Fig. 2 the area of the exchanger consists of several concentric stainless cylindrical sheets surrounding the combustion chamber. There are helical coiled fins around each of the cylinders' outer surface. In addition to a supporting effect they form rectangular ducts for process fluids flows between each couple of cylinders. The heat exchanger is designed in such a way so that a counter-current flow of the polluted air and flue gas would be achieved. A simplified scheme of the heat exchanger and fluids flows is shown in Fig. 3.

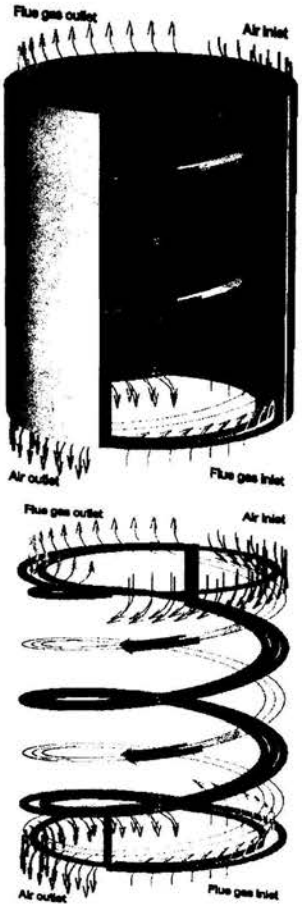

Figure 3: Heat exchanger and fluid flow

The combustion chamber is placed inside the heat exchanger, and therefore an annular duct separates these two pieces of equipment. Polluted air preheated in the heat exchanger flows through this annular duct and enters the combustion chamber at the top where a burner is installed.

A swirling generator rectifies the fluid flow of air into the combustion chamber and ensures relatively good flow distribution. In some cases an auto-thermal process can occur, depending on type and concentration of pollutants. Then the burner takes only a stabilizing function. Flue gas leaves the combustion chamber at the bottom and enters the cylindrical heat exchanger where it is cooled by polluted air.

Basic parameters

Basic process parameters of the experimental equipment were evaluated with the aid of software for simulation of processes for the thermal treatment of wastes [3]. Input data for simulation (given parameters characterising the equipment capacity and process conditions) and results of simulation are summarised in Table 1. These parameters were considered for the design of the research experimental facility. However, flowrate of polluted air can range within the interval 150 to 1200 m_N^3/h and temperature of flue gas at the combustion chamber outlet ranges from 600 to 1000°C. (*Note*: The flowrate in cubic meters per hour (m_N^3/h) refers to reference conditions, i.e. T = 0 °C and p = 101.3 kPa.)

Table 1: Basic process parameters

input data	inlet	outlet
polluted air flowrate, m_N^3/h	600	-
inlet temperature of polluted air, °C	20	-
temperature of polluted air preheating, °C	-	635
temperature of flue gas at combustion chamber outlet, °C	-	750
excess air, -	1.05	-
main results		
atural gas flowrate necessary, m_N^3/h		3.7
lue gas flowrate, m_N^3/h		637
emperature of flue gas at the equipment outlet, °C		190

Process data were used as basic input parameters for the equipment design. Some constraints were determined as follows: maximum allowable pressure drop in the equipment Δp_{max} = 3 kPa, maximum outer diameter D_{max} and maximum height H_{max} measured from the foundation up to the burner flange should not exceed 1400 and 2000 mm, respectively. Further, basic dimensions of the combustion chamber (inner diameter D_{ki} = 600 mm, outer diameter D_{ko} = 840 mm and minimum height H_{min} = 1000 mm) were determined with respect to the required time of residence of the polluted air.

Unfortunately, no relations exist for this type of heat exchanger. Therefore, a tentative mathematical model with an approximate description of transfer phenomena was necessary to be created and applied for the design of the experimental equipment (as described below). Basic geometrical parameters obtained from thermal and hydraulic calculations can be found in Table 2.

Table 2: Geometrical and other selected parameters of heat exchanger

HEAT EXCHANGER		
Parameter	Polluted air	Flue gas
heat transfer coefficient, $W/m^2.K$	48	54
pressure drop, Pa	1303	1443
heat exchanger area, m^2	39.2	
outer diameter, mm	1222	
inner diameter, mm	995	
height of cylindrical sheets, mm	1250	
number of cylinders, -	9	
heat exchanger duty, kW	139	
COMBUSTION CHAMBER AND ANNULAR DUCT		
burner duty, kW		40.7
temperature at the combustion chamber inlet, °C		647
average temperature in the combustion chamber, °C		811

Layout of facility

The experimental research facility provides a possibility for testing a wide range of operational regimes, which can be met in industry. Since the unit was built as that in full industrial scale it can serve as a reference base for testing various conditions of operation.

The research facility is equipped with action controllers that afford a possibility to change process parameters while all measured data are processed by a computer in-line system in real time. Due to this process control system it is possible to verify the unit functionality in a wide range of regimes of operation, to acquire and evaluate all the important data and to make suggestions for further improvement of the unit. The layout of the research facility together with measured points within the equipment is obvious from Figure 4. This figure shows the screen of the computer monitor.

Experimental research was aimed at the following achievements:

- measurements for verifying the functionality of the equipment
- systematic data acquisition for validating the mathematical model of the equipment
- experiments based on changing regime of operation and investigating an optimum regime of combustion in case of the thermal treatment of various pollutants considering:
  a) conventional way of combustion
  b) catalytic treatment

Measured parameters

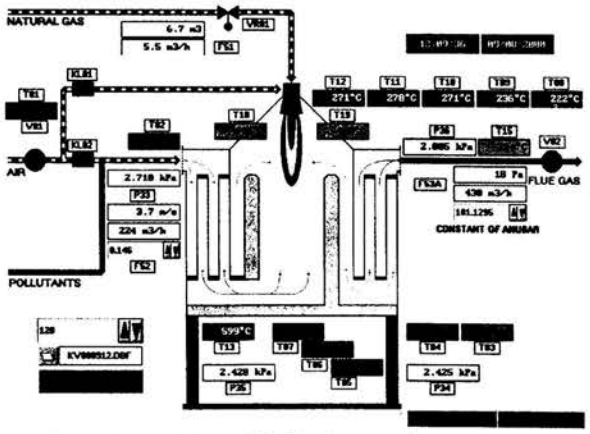

Figure 4: Experimental facility layout with real-time data monitoring and operation

Level of process control is solved in such a way to enable both fully automatic operation and changing parameters by an operator in the frame of systematic measurements. The main aim of measurements is to obtain data necessary for validating the mathematical model, therefore flowrates of both process fluids as well as temperatures and pressures in various points of equipment are measured.

Layout of the facility and measured parameters as shown on the monitor screen of the computer-aided measurement and control system are obvious from Fig. 4. E.g. symbols F51, F52, F53 indicate flowrates of fuel (natural gas), air and flue gas, respectively. Measurement of pressures represents a double system based on both local and remote manometers. Installation of four manometers guarantees evaluation of both polluted air and flue gas sides pressure drops. A total of thirteen shell-type thermoelectric thermometers are installed inside the unit. NiCr and NiAl conductors of these thermocouples are placed in stainless capillary tubes with diameters of 3 mm, which can be shaped according to need to locate it at optimum measurement points. Each of the process fluids occupies five rectangular ducts formed by the cylindrical stainless sheets and helically coiled fins. Therefore both air (T03 to T07) and flue gas (T08 to T012) temperature sensors are installed at the duct outlets. Temperatures at the heat exchanger inlets are measured by thermocouples T02 at the air side and T13, T14 at the flue gas side, however, the value of T14 (and/or exactly TIC14) is used as that for the burner control system. The temperature of air at the combustion chamber inlet is measured by the thermometers T18 and T19. Based on the difference of measured temperatures T03 to T07 and T18, T19 a quantitative evaluation of heat losses from the combustion chamber is possible. Polluted air in the annular duct between the combustion chamber and the heat exchanger is heated by these heat losses. This fact represents one of principle advantages of the new equipment as mentioned above. Thermometer T15 measures temperature of flue gas at the equipment outlet.

The combustion chamber is equipped with a burner having heat duty of 160 kW with a control system consisting basically of PID (Proportional + Integral + Derivative) controller with a control flap. This system can be considered from the process control point of view as an autonomous system maintaining the given temperature of flue gas at the outlet in cases of a change in flowrate of treated polluted air.

Data acquisition

A systematic data acquisition has been carried out especially with a view to validate and/or modify equations for calculation. These equations based on combustion, heat and mass transfer and equipment geometry form the core of the mathematical model.

Distribution of measured points is obvious from the layout in Figure 4. A wide range of flexibility in operation was considered, therefore regimes with flowrates (150 to 1200 m_N^3/h) and temperatures of flue gas (600 to 800 °C) occuring in industrial practice were considered. Experimentation started with a minimum flowrate of polluted air and increasing the flowrate by 100 m_N^3/hr while temperatures of flue gas 600, 700 and 800 °C were set up for each flowrate.

MATHEMATICAL MODEL

From the point of view of the equipment character it was necessary to consider a related structure of the mathematical model. This model has been developed with the aim to provide a designer or an operator with a tool for evaluation of all the parameters important for a successful design and/or operation. A relatively simple model is a core of a computer program, which is used for this purpose.

Structure of the model

A structure of the complete mathematical model is obvious from Fig. 5. The model consists of submodels of the heat exchanger and combustion chamber connected through a submodel of the annular space which represents an interface between them. Selected parameters put together the submodels in such a way that an output parameter from one submodel is at the same time an input parameter of consequential submodel. The structure shown in Fig. 5 indicates an iterative character of calculations.

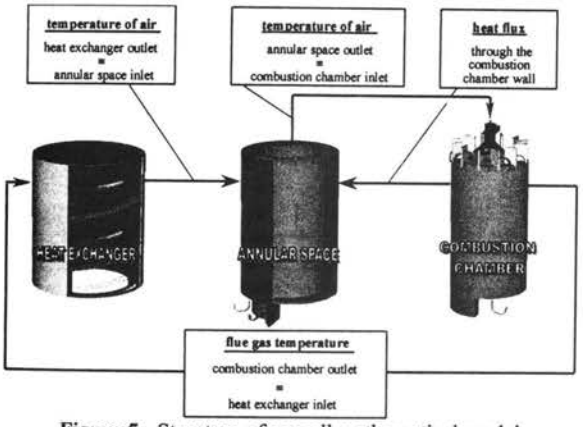

Figure 5: Structure of overall mathematical model

Heat exchanger

As it can be understood from the foregoing description the conception of the equipment is of primary importance. Therefore a non-conventional design including the heat exchanger was necessary.

Equations for the thermal and hydraulic calculation and relations describing geometry of the heat exchanger form a core of the exchanger mathematical model. General equations for heat balance and heat transfer are used as in case of any heat exchanger. However, a specific design has to be taken into consideration. It means we need to have relations for the evaluation of heat transfer coefficient h and friction factor f at our disposal. Unfortunately, no relations exist for this type of heat exchanger. Therefore, a tentative mathematical model with an approximate description of transfer phenomena was necessary to be created to be able to make a design of the experimental equipment (as already mentioned above). We selected equations based on a geometrical and hydraulic similarity from reputable literature like e.g. [4 to 6]. Experience from the research of shell-and-tube heat exchangers was utilized where equations used for the calculation of segmentally baffled heat exchangers were used as a basis for those derived for a new type of heat exchangers with helical baffles [7, 8].

Many equations for fluid flow in various types of ducts exist. Equations for systems with a high degree of similarity were taken into account, tested and analyzed in details and the results were compared and evaluated [9]. Finally, relations for the calculation of helically coiled tubes were selected. This geometrical arrangement appeared to be very close to that of the heat exchanger in question. Therefore all the calculation is related to a central channel with diameter D_c (see Fig. 6) and a rectangular (non circular) cross section of the channel can be considered as the only difference. Hydraulic diameter for rectangular cross section provided $h_d >> B$ is as follows: $d_h = 2B$ [5]. However, in case of laminar flow we cannot obtain exact results with the aid of this substitution and only data from experiments provide us with a possibility to derive correct relations. Nevertheless, for the purpose of designing research experimental facility the relations for helically coiled tubes were helpful and satisfying.

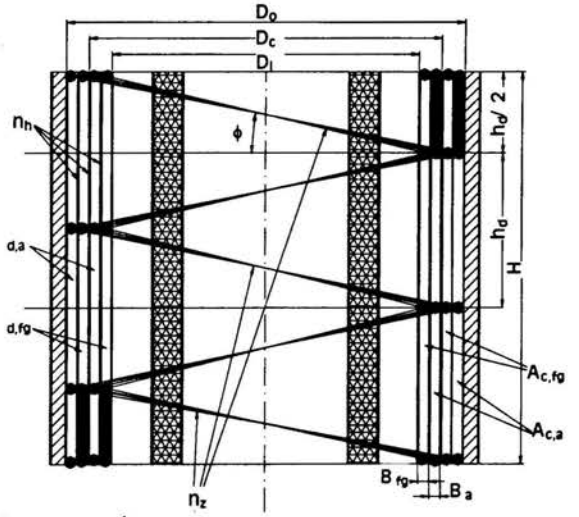

A_c.....cross section area
n_d.....number of ducts
n_h.....number of cylinders with heat exchange areas
n_z.....number of turns

Figure 6: Heat exchanger

A review of newly derived correlations (using results of experiments) for calculation of heat transfer is given below.

Based on evaluation of experimental results and taking into account convenient shapes of correlations [9] the following relation for Nusselt number is obtained:

$$Nu = \left(3.66 + 0.08\left[1 + 0.8\left(\frac{d_h}{D}\right)^{0.9}\right]\cdot Re^{m}\cdot Pr^{1/3}\right)\cdot\left(1 - 121\cdot Re^{-0.739}\right) \quad (1)$$

where $$m = 0.5 + 0.2903\left(\frac{d_h}{D}\right)^{0.194} \quad (2)$$

and $$D = D_c\left[1 + \left(\frac{h_d}{\pi\cdot D_c}\right)^2\right] \quad (3)$$

All the characteristic dimensions are obvious from Fig. 6.

When Reynolds number increases ($Re > Re_{crit}$) we use a correlation which revises expression derived for straight ducts so that the curvature of the rectangular channel would be involved. The resulting relation based on regression is as follows:

$$Nu = \left(1 + 1.77\frac{2d_h}{D}\right)\cdot 0.0184\cdot Re^{0.792}\cdot Pr^{1/3} \quad (4)$$

The critical value of Reynolds number which determines a boundary between laminar flow (Eq. (1)) and turbulent flow (Eq. (4)) is evaluated as follows:

$$Re_{crit} = a\left[1 + b\left(\frac{d_h}{D}\right)^{c}\right] \quad (5)$$

where a = 2300, b = 8.6 and c = 0.45 [5].

Since there is an acceptable continuity in Nusselt number (between laminar and turbulent region (see Fig. 7)) a transition region need not be considered and evaluation of Re_{crit} using the above relation can be used [9].

A similar approach is applied for evaluation of friction factors. The following correlations have been derived for laminar and turbulent flows, respectively:

$$f = \frac{64}{Re^{1.393}}\left[1 + 0.128\cdot Re\cdot\sqrt{\frac{d_h}{D}}\right] \quad (6)$$

$$f = \frac{0.3164}{Re^{0.296}}\left[1 + 0.095\cdot\sqrt{\frac{d_h}{D}}\cdot Re^{0.425}\right] \quad (7)$$

Like in the case of Nusselt number we can consider continuity in calculations of friction factor (see Fig. 8).

Data necessary for creating and further improving equations (1) to (7) were obtained from measurements at the research experimental facility and processed using professional statistic software packages *ADSTAT* [10] and *STATGRAPHICS* [11] for evaluation of regression parameters, dispersion variance analysis, and determining intervals of reliability and residue analysis. Data processing for regression like this is as follows:

- From the measured data heat duties both at the air side (Q_a) and flue gas side (Q_{fg}) are calculated. If the relation: $\left|\frac{(Q_a - Q_{fg})}{Q}\right| \le 0.05$ where $Q = (Q_a + Q_{fg})/2$ is valid then it can be stated that the measured data are acceptable and convenient for further processing.
- Overall heat transfer coefficient k is evaluated from the heat transfer equation based on the exchanger heat duty Q, and known heat transfer area A.
- Heat transfer coefficients h_a and h_{fg} for air side and flue gas side, respectively, are based on the known overall h.t.c. k and consequently the related values of Nusselt number are evaluated. Thus a $Nu - Re$ relation is obtained which is convenient for the regression analysis mentioned above.
- Pressure drops of both process streams are also determined based on measured data and then we can evaluate values of friction factors f. As in the above case a $Re - \Delta p$ relation is obtained which is necessary for finding unknown regression parameters.

A special computer program for processing measured data has been created. All the necessary data are extracted directly from the database of measured values. In Fig. 7 heat transfer results in the form "Nusselt number vs. Reynolds number" are plotted. Experimental work covers a wide range of flowrates common in real industrial applications with different operational regimes to ensure the equipment flexibility. The graphical representations show us also a comparison with a geometrically closest system with helically coiled tubes. A similar graphical representation can be obtained for friction factors as shown in Fig.8.

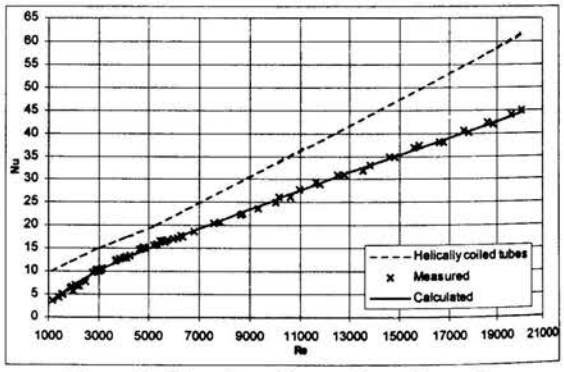

Figure 7: Nusselt number vs. Reynolds number

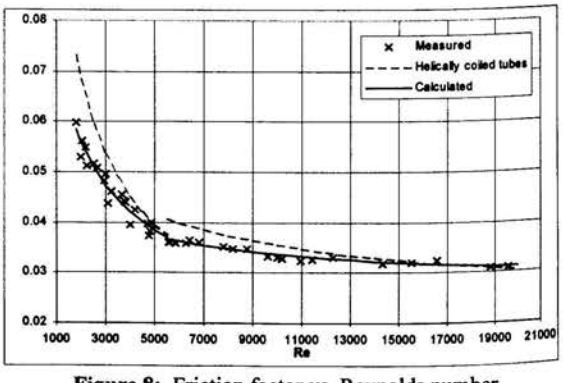

Figure 8: Friction factor vs. Reynolds number

Combustion chamber

The zone method was applied for creating the submodel of the combustion chamber based on the fact that it was from the point of complexity consistent with the model of heat exchanger. It is convenient for solving a problem like this one where radiation prevails.

From the radiation point of view the combustion chamber is considered as a cylinder with diameter D_{ki} and height H (see Fig. 9). The combustion chamber is substituted by a simple one gas zone (g) with dimensions of the above cylinder. This simplification is quite appropriate for modeling. While surface zones s_1, s_2 represent bases of the cylinder, the surface zone s_3 represents the inner cylindrical wall of the combustion chamber. After completing the calculation (consisting of evaluating direct, total and oriented exchange areas, emissivity of gas, and solving heat balance [12, 13]) we obtain values of an average and/or effective temperature of flue gas in the combustion chamber, surface temperatures, and heat flux Q_c from the combustion chamber through the cylindrical wall into the annular space between the combustion chamber and the heat exchanger as main results.

For example provided the average temperature of flue gas in the combustion chamber was T_g = 650 °C heat flux Q_c ranged from 100 to 4000 W for flowrates of polluted air within the interval 120 to 1150 m_N^3/h.

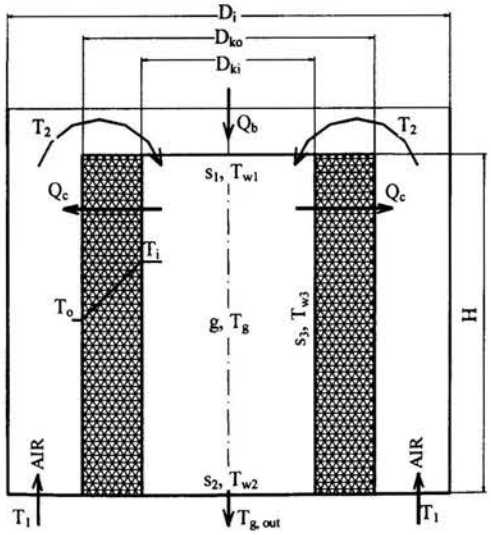

Figure 9: Combustion chamber

Annular space between combustion chamber and heat exchanger

The annular space can be considered from the computational point of view as an interface between the combustion chamber and the heat exchanger (see Fig. 10). Consider that polluted air leaving the heat exchanger (with the temperature T_1) is heated in the annular space by the heat flux (and/or heat losses) Q_c from the combustion chamber up to the temperature T_2. Heat exchange between flue gas in the inner duct of the heat exchanger and air in the annular space can be neglected. These channels are separated by a refractory wall and taking into account all the other simplifications this assumption can be considered as an appropriate one.

From the above description it is obvious that the complete model (consisting of submodels of the combustion chamber, heat exchanger and the annular channel in between them) is in fact that for a simulation mode with given input process parameters, geometry and estimated other parameters necessary for running the computer program. If this model is used for a design mode the related software is conceived in such a way that repeating runs for a certain range of geometrical parameters provide us with required results.

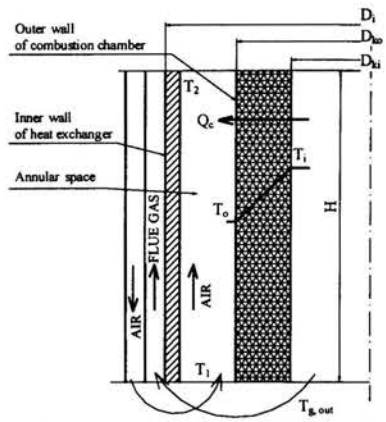

Figure 10: Annular space between combustion chamber and heat exchanger

Using CFD (Computational Fluid Dynamics) and experimental validation

CFD analysis shows us parts of the system or phenomena happening within the system that would not otherwise be visible through any other means. CFD gives possibility of visualizing and enhancing the understanding of our designs.

The commercial software system FLUENT [14] was used for simulation based on three-dimensional CFD modelling. A detailed description of this approach including experimental validation can be found elsewhere [15]. Based on a current evaluation of simulation results, some conclusions and suggestions for improving the equipment can be made (e.g. improving the burner arrangement, considering a different inclination of blades of the swirl generator or considering an alternative with two swirl generators, increasing inclination angle of the heat exchanger hellical channels) [15]. (*Note*: Improvement of the swirl generator has been realized.)

PRACTICAL INDUSTRIAL ALTERNATIVE ARRANGEMENTS AND APPLICATIONS

Requirements coming from the industrial practice influence the further development of the equipment and give rise to various alternatives of units based on this new equipment.

It is possible to specify several eligible options of arrangement. According to equipment type one can consider a conventional one (e.g. basic alternative of research facility as described above) and that for catalytic treatment. Taking into account fluids transport and compactness, i.e. room for installation and conditions of operation it is possible to make a design of a compact arrangement, over-pressure or under-pressure one. It consists in a convenient assembly of air and flue gas fans or in installing only one of them. One can also speak about waste to energy alternative, especially in case of excessive concentration of combustibles when energy of flue gas can be utilized e.g. for heating water or steam generation. Some industrial cases (e.g. thermal treatment of air polluted by methyl-ethyl-keton or off-gases from natural gas production) are described in [16].

CONCLUSION

A complex approach in research and development of new equipment for the thermal treatment of polluted air, where heat transfer and fluid flow play a predominant role, is shown. A mathematical model of this equipment, consisting of submodels of heat exchanger for preheating the polluted air, combustion chamber and annular space in between them, is described. New correlations for thermal and hydraulic calculations of the heat exchangers have been developed based on experimental validating the model.

REFERENCES

[1] Stulir, R., Stehlik, P., Oral, J. and Fabikovic, V., 2001, "Fully Integrated Unit for Thermal Treatment of Gas Wastes," Applied Thermal Engineering, Vol. 21, No. 12–13.

[2] Oral, J. and Stehlik, P., 1999, "Equipment for Combustion of Wastes – Incinerator," Patent No. PV1999 – 3651 (Czech Republic).

[3] Stehlik, P., Puchyr, R. and Oral, J., 2000, "Simulation of Processes for Thermal Treatment of Wastes," Waste Management, Vol. 20, pp. 435-442.

[4] Hewit, G. F., (ed.), 1998, "Heat Exchanger Design Handbook," Begell House, New York

[5] Verein Deutscher Ingenieure, 1987, "Waermeatlas," VDI - Verlag GmbH, Düsseldorf .

[6] Hewit, G. F., Shires, G. L. and Bott, T. R., 1994, "Process Heat Transfer," CRC Press, Florida.

[7] Kral, D., Stehlik, P., van der Ploeg, H. J. and Master, B. I., 1996, "Helical Baffles in Shell-and-Tube Heat Exchangers, Part I: Experimental Verification," Heat Transfer Engineering, Vol. 17, pp. 93-101.

[8] Stehlik, P., Nemcansky, J., Kral, D. and Swanson, L. W., 1994, "Comparison of Correction Factors for Shell-and-Tube Heat Exchangers with Segmental or Helical Baffles", Heat Transfer Engineering, Vol. 15, pp. 55-65.

[9] Stulir, R., 2001, "Design of Heat Exchanger for a Specific Purpose," PhD. Thesis, Technical University of Brno, Czech Republic.

[10] "Adstat 2.0 – User's Guide", 1992, Trilobyte Inc., Pardubice, Czech Republic.

[11] "Statgraphics 7.0 - User's Manual", 1993, Manugistics Inc., Rockville, USA.

[12] Hottel, H. C. and Sarofim, A. F., 1967, "Radiative Transfer," McGraw-Hill, New York.

[13] Fabikovic, V., 1998, "Modelling of Specific Equipment for Thermal Treatment of Wastes," MSc. Thesis, Technical University of Brno, Czech Republic.

[14] "User's Guide for FLUENT 5", Vol. 1-4, 1998, Fluent Inc., Lebanon, NH, USA.

[15] Fabikovic, V., Stehlik, P., Strasak, P., Kolar, P., Stulir, R. and Oral, J., May 2001, "Simulation of Compact Equipment for Thermal Treatment of Wastes Using *CFD* and Experimental Validitation," 2nd International Symposium on Advances in Computational Heat Transfer CHT'01, Palm Cove, Queensland, Australia.

[16] Stulir, R., Oral, J., Bebar, L., Stehlik, P. and Trunda, P., July 2001, "Integrated Unit for Thermal Processing of Polluted Gases - Alternative Arrangement," 3rd International Symposium on Incineration and Flue Gas Treatment Technologies, Brussels, Belgium.

HEFAT 2002
1ST International Conference on Heat Transfer, and Thermodinamics
8-10 April 2002, Krugher Park, South Africa
TP2

OPTIMIZATION OF THE EQUIPING AND OPERATION OF THE THERMAL PROCES SUBSTATIONS IN THE DISTRICT HEATING SYSTEMS

Petre TERZI
President of SPERIN-
Promotions Society for Renewable, Inexhaustible and New Energies
Energetic Faculty POLITEHNICA Univ. Bucharest – Romania.
Head of Investigations Group for Efficient Management of Energy
Bucharest District Heating Company
Str. Anastasiu Constantin nr.4 Ap.4
75253 Bucuresti sector 5 ROMANIA
E-mail: terzi_p@yahoo.com

ABSTRACT

The article presents an assessment algo-ritm of the investement and operation expences, to be used in the analysis of the equipping variants or in determining the operating mode of the thermal process substations, in the district heating for residential buildings. It is designed to be used by designers, as well as by the operating personnel in the district heating units.

The rehabilitation works, for the refurbishment with modern heat exchangers, should be carried out to provide for a maximum thermal efficiency. The algorithm submitted adopts as its main optimisation criterion the minimisation of the cost per transferred thermal energy unit, in order to prepare hot water for heating and tap water for domestic use.

INTRODUCTION

The expenses for the modernisation of the thermal process substations in the residential buildings are one of cost of the thermal transferred energy unit, -CTTEU – supplied by the thermal power distributors, to the tenants' associations, is made up.

The technical solution as to the thermal process substation refurbishing within the modernisation action, brings about, in this turn, changes in the annual amortisation expenses - AAE - in the expenses for the second heat carrier pumping, - SHCP - as well as in maintenance and repair expenses - MARE.

Tubular heat exchangers, were applied as early as 1962, that is when type were thermal process substation in district heating were built in Romania. They proved to be thermally low efficiency, of low warranty bulky and extremely difficult to remote, with a view to their cleaning and repairing. Consequently, the heat exchangers used to get clogged up quite during operation, which caused high hydraulic load loses, and therefore transferred power consumption, in order to pump up the secondary heat carrier.

With a view to improving this situation, modern plate ex-changers are resorted to at present, to eliminate the above shortcomings, yet they are found out to cost more than the tubular ones. In order to point out the share of the above mentioned expenses in the prices of the energy distributed through the thermal process substations, an assessment algorithm is submitted in what follows, which should allow for the economic operation for thermal process substations, to be determined.

The same algorithm allows as well selecting out of the exchangers types provided by various suppliers, so that the most economical refurbishing solution may be chosen, as offers are very numerous and diversified at present.

It is considered that help can be given thus to the decisions makers in the operation line, and to the designers drawing up the technical documentation's for the thermal process substations modernisation.

NOMENCLATURE

Ve- equipment prise value;
Snec – is the heat transfer surface necessary to the heat exchangers a modernised thermal process substation is to be refurbished with $[m^2]$;
CFISTU – the cost of the transfer surface unit installing expressed in $[ROL/m^2]$

N – Is the amortisation duration [years];
D – The bank interest with which the credit for the modernisation expenses could be been (expressed as a decimal number).
N - The term for paying back the credit used for the financing of a thermal process substation modernisation [years].
PAEP – the electric pump – absorbed power [kW];
EPP – electrical power price [ROL/kWh];
YOTP – yearly operation time period [hours/year]
T4 – exit temperature on secondary circuit [^{0}K];
T3 – inlet temperature on secondary circuit [^{0}K];
EYT – yearly transferred energy [kJ/year] can be determined by means of the following: EYT = ρGs. Cs (t4-t3). YOTP / 10^3 [ROL/kJ] .
Qp – is the thermal power yielded by the hot water in the primary circuit [kW]
Qs – The thermal power taken over from the primary circuit by the secondary circuit [kW]
Qt – the thermal power transferred by the heat exchanger surface [kW];
Gp and Gs – circulating flows on the primary, and the secondary circuits, respectively [m^3/.s];
Cp and Cs – specific heats of the heat carrier on the primary and the secondary circuits, respectively [J / kg.K];
φ - Dirt coefficient of the heat exchanger surfaces;
s – Heat exchange surface [m^2];
k – Overall heat exchange coefficient of the heat exchanger [W /m^2.K];
DTML – average logarithmic temperature difference [K];
Cp and Cs – specific heats of the primary heat carrier, and the secondary heat carrier, respectively [J/Kg .K];
ρ - Primary and secondary heat carrier density [Kg/m^2];
g – Acceleration of gravity [m/s^3].
Hs – Discharge head on the secondary circuit, resulting out of the relation:
Hs = (P3-P4)/ (ρg) [m] – see fig.1, where pressures P3 and P4 [Pa]; correspond to the notations on figure 1
η_p - Pump efficiency;
Q and r are dimensionless indexes
p - Exchanger design factor [$J.s^{(p+q-1)}/m^{3(p+q)-2}$.K] in rel.(6)
q and r exponents in rel. (6)
Msc – stand for the hydraulic resistance module of the heat exchangers;
Mcd - – stand for the hydraulic resistance module of the distribution network;
Mic - stand for the hydraulic resistance module of the installations inside the buildings.
PAE – is the electric pumps – absorbed power [kW];
EPP – electric power price [ROL/kWh];
YOTP – annual operation period [hours];

PREZENTATION OF THE ALGORITHM FOR ASSESSING THE THERMAL ENERGY UNIT COST – CTTEU

The leading equipment in a thermal process substation is the heat exchanger, as it holds the biggest share in the annual amortisation expenses, and also an important share in the expenditures for circulating the heat carrier for heating or domestic hot water, as a result of hydraulic load losses introduced into the secondary circuit. As the heat exchanger main feature, in from the point of view of construction and operation is the transfer surface, the cost for installing the transfer surface unit, as expressed in ROL/sq.m and referred to as CFITSU , has been adopted as an appraisal indicator of the investment expenses determining the annual amortisation expenses – AAE. For this indicator to be more relevant for a thermal process substation, it shall be determined by considering both the price of the heat exchangers, and that of its related equipment, such as the circulating pumps, fittings, filters, sludge separators, expansion tanks, etc.

The value of the equipment replaced in a modernised thermal process substation is determined with the following relation:

$$Ve = Snec \cdot CFISTU \quad [ROL]$$

In order to evaluate the annual amortisation costs expressed in ROL /sq.m (referred to as AAE), the following relation will be used:

$$AAE = Ve \{1/N+d(1+d)^n]/[(1+d)n-1]\}, [ROL/year] \quad (1)$$

Relation (1) takes into account the proportional amortisation rule over a determined period, and it allows the bank interest to be ignored, when the modernisation is financed out of public or government funds, bearing no interest. (When d=0)

Another component part of the costs of the supplied, transferred thermal energy unit-CTTEU, as already shown above, are the expenses for circulating the secondary heat carrier (for heating or for domestic hot water) by means of the circulating pumps, in the case of the heating circuit, and of the pressure raising pumps, in the case of domestic hot water (refereed to as SHCP), expressed in [ROL /kJ].

In order to evaluate the expenses for pumping the secondary heat carrier (referred to as SHCP), the following relation was adopted:

$$SHCP = (PAEP \cdot EPP \cdot YOTP)/EYT \quad [ROL/kJ] \quad (2)$$

Summing up the amortization costs AAE, related to the Energy transferred, over the annual operation period, with the costs for the secondary heat carrier pumping SHCP and with the annual ones for maintenance, repairs and operation,

referred to as CIRE, can be get with below the relation, (who represent the evaluation relation for the modernization participation share in the cost of the thermal energy unit supplied to the consumers)

$$CTTEU = AAE / EYT + SHCP + CIRE \quad [ROL/kJ] \quad (4)$$

In order to determine the analytical calculation formulas for the component factors in relation (4), the energy balance relation shall be considered, using the notation in figure 1.

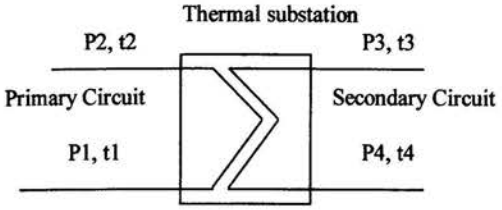

Figure 1: Heat transfer process in a substation

The energy balance relation in a substation is following:

$$Qp = \rho Gp.\ Cp\ (t1-t2)/\ 10^3;$$

$$Qs = \rho Gs.\ Cs\ (t3-t4)/\ 10^3; \quad (5)$$

$$Qt = \varphi.ks.\ DTML;$$

ASSESSMENT OF ANNUAL AMORTIZATION COSTS.

In order to get a correlation between the heat exchange on the two transfer surfaces in contact with the primary and the secondary heat carrier [1], the following relation shall be adopted for the overall heat exchange coefficient:

$$k = \varphi.\rho \cdot (Gs)^r \cdot (Gp)^q \quad [W/m^3.K] \quad (6)$$

If it considering a null heat losses in substation, out of relation (5) their results:

$$Gp = Gs\ [\ Cs\ .\ (t4-t3)] \quad [m^3/s]; \quad (7)$$

This allows us to write the relation which points out the dependence of the heat exchange overall coefficient upon the flows on the secondary and the primary circuits, as follows:

$$k = \rho\ .\ Gs^{(q+r)}.\ [\ Cs^r\ .\ (t4-t3)^r\ ]\ /\ [\ Cp^r (t1-t2)^r\ ]\ ; \quad [W/m^2.K] \quad (8)$$

Considering that, in keeping with the regulations in force, the thermal energy distributor for the urban consumers may control only the secondary circuit thermal and hydraulic condition, the secondary circuit flow Gs has been adopted as reference flow in relation (7).
Out of relation (5) and (8) their results the following relation for the annual amortization costs:

$$AAE = \{1/N + [d\ (1+d)^n] / [d\ (1+d)^n.\ 1]\}.\ \{[0{,}278.\ Cp^r.\ (t1-t2)^r.\ CFISTU]/\ [\varphi\rho.\ Gs^{(q+r)}.\ (t4-t3)^r.\ DTML.\ YOTP]\};\ [ROL/kJ] \quad (9)$$

As one can notice, the specific annual amortization costs, [ROL / kWh], depend on the thermal operation of the thermal substation, as well as on the hydraulic operation on the secondary circuit, which are actually at the operating personnel's disposal.

ASSESSMENT OF THE SECONDARY HEAT CARRIER-CIRCULATING COSTS.

The electric power absorbed by de electric pumps in order to circulate the heating heat carrier on the secondary circuit, according to the discharge head and the flow circulated results out of the following relation:

$$PAE = (\rho.\ Gs.\ Hs0\ /\ (102.\eta\rho); \quad [kW] \quad (10)$$

(were: 102 is a conversion factor be twin HP and kW)

The actually required discharge head depends on the hydraulic resistance of the heat exchangers, the distribution network, and the inside installations; thus, the actual discharge head can be assessed by means of the following relation:

$$Hs = Msc.\ Gs^b + (Mcd + Mic).Gs^2 \quad [mWH] \quad (11)$$

In this case, relation (2) for the assessment of the secondary heat carrier circulating electric pumps drive power can be written as follows:

$$PAE = [\rho.\ Gs\ (Msc.Gs^b + (Mcd+Mic).Gs^2\ ]/\ (102.\eta_{\rho}) \quad [kW] \quad (12)$$

In order to assess the expenses for secondary heat carrier pumping – SHCP – the following relation will be used:

$$SHCP = 2.78*PAE*EPP*YOTP/10^4.\ YET \quad (13)$$

By analyzing relations (9) and (13) can be find out that the flow circulated on the secondary circuit (Gs) is a main parameter common both to the determining term assessing the specific annual amortization costs (AAE), and to the costs for the secondary heat carrier pumping (SHCP).

Thus, for a modernized thermal process substation, there can be determined the optimum hydraulic condition able to allow for thermal energy supplying at minimum distribution costs. This condition is reached by minimizing of cost of the thermal transferred energy unit CTTEU

[ROL/kJ] as per relation (4), which represents the share of the modernization cost to the thermal energy unit cost to be supplied to the end users.

Analytically, this condition is reached by zerowing of the first derivative, of relation (9) as to the flow circulated by the circulating pumps Gs, and therefore also of that of the thermal load corresponding to a certain temperature difference between the flow and the return of the secondary circuit for heating or for domestic use hot water, as expressed by the following relation:

$$\delta (CTTEU) / \delta (Gs) = 0 \ ) \quad [ROL/kJ] \qquad (14)$$

Figure 2 shows as an example, an assessment of the economic effect of the modernization of a thermal station where the heating exchangers should be replaced; two heat exchangers types shall be considered to this effect.

The algorithm means for the refurbishing of the thermal substations in the district heating system is found to be efficient, in that the computing programs elaborated allows on one hand, for the total cost variation per thermal energy unit to be pointed out according to the thermal load, and, on the other hand, for the cost elements variation to be shown, which provides extremely useful information to the operation personnel.

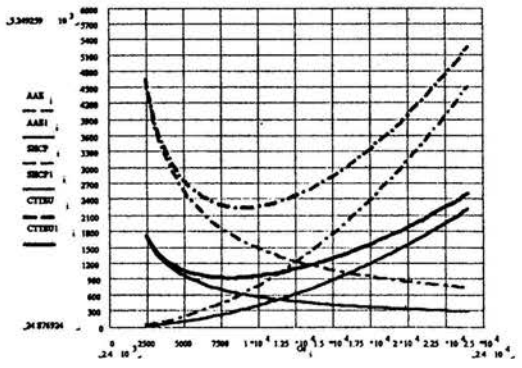

For old heat exchangers - dado curves for
new heat exchangers - solid curves

Legend:
AAE – annual payment as revenue ROL/kJ;
SHCP – pumping costs ROL/kJ;
CTTEU – total costs for unity of transferred energy ROL/kJ.

Figure 2: An assessment at the economic effect at the modernization at a thermal station

In case a maximum acceptable cost is imposed as far as the modernization costs are concerned, so that it should not required for any change in the thermal energy distribution price, there result the optimum operation ranges.

Mention should be made that in the example given in figure 2, the maintenance and operation expenses have not been considered, out of lack of data; however, as these expenses do not vary according to the thermal load, including these expenses as well in the calculation shall not influence the optimum operation range.

The calculation program elaborated based on the algorithm shown referred only to the case of modernization as financed from budget sources, as, considering the population's present incomes, the price charged for the heat supplied is granted from the local bodies budget.

The calculation program elaborated can also bring a solution to modernization supporting by financing credits obtained from the banks, when the bank interest must be covered by the economic effect.

In this case, a modernization share able to cover the bank interest should be included into the thermal energy sales tariff. A quite interesting aspect is that when the modernization economic effect can cover the bank interest to excess; then, what is left is a benefit obtained as a result of modernization.

The program can also analyze the effect of the modernization per sections of a thermal process substation a condition of separating the expenses related to domestic hot water preparing from those for preparing the heating heat carrier.

In case a maximum allowable cost is imposed for the modernization costs, there can be determined o solution for the refurbishing of a thermal process substation, so that it should not call for any change in the thermal energy-supplying tariff.

It should be specified that, in the analysis made, no maintenance and operation expenses have been included (CIRE =0) out of lack of data; however, as these expenses do not differ according to the thermal load, the optimum operation range shall not be influenced. Yet by knowing them, the contribution of these expenses to the operation costs shall be pointed out as well.

CONCLUSIONS

The application on particular cases, as shown in figure 2, points out the utility of the proposed method, for assessing both the thermal condition effect on the cost of the thermal energy supplied, and the refurbishing solution for the modernization of a thermal process substation for district heating networks.

REFERENCES

[1] Krischer,L Uber der Kriteriale Gleichungen der Warmeubertragers. *VDI-Zeitschrift nr.45, Band 56, 1912, p.1823-1827.*

[2] Terzi P: *Energetically and economical aspects about the optimization of the HVEAC units.* Energy today – International Conference TECHNICAL UNIVERSITY Cluj – Napoca Romania. Mai 1993. PAPERS OF CONFERENCE, p.234 – 237.

[3] Terzi P: *Regarding about the efficiency of the LIQUID – GAS heat exchangers.* Papers of 8th IFOAM International Congress 30 Aug 1990, Budapest – Hungary, p. 186-189.

[4] Terzi P: *Optimizarea echiparii si functionarii punctelor de transformare termica din sistemele urbane de alimentare centrlizata cu caldura.* Rev. ENERGETICA. Anul 44 nr. 6, seria A noembrie-decembrie 1996, p. 278-284.

[5] Trip: *Aspecte privind optimizarea modernizarii punctelor termice.* Sesiunea stiintifica-50 Ani de invatamant energetic in Universitatea POLITEHNICA Bucuresti, 2000, vol II, Ingineria mediului si termoenergetica, p. 469-475.

[6] Terzi P: *Optiminization of the equipping and the thermal process in the district heating systems substations.* Papers of Euroheat and Power Congress. Gdynia-Poland, 6-7 June 2001.

[7] Terzi P: Evaluarea eficientei functionale pentru compo-nentele retelelor hidraulice. Prima conferinta a hidroenergeti-cienior din Romania, Bucuresti 26-27 mai 2000.

HEFAT2002
1st International Conference on Heat Transfer, Fluid Mechanics, and Thermodynamics
8-10 April 2002, Kruger Park, South Africa
WS3

ANALYSIS OF FINNED HEAT EXCHANGER WORKING IN ADSORPTION REFRIGERATION SYSTEN USING ZEOLITE AND METHANOL

S. Waszkiewicz, H. Saidani-Scott, M. Tierney
Mechanical Engineering Department,
University of Bristol,
Queens Building, University Walk, Bristol BS8 1TR, UK

ABSTRACT

A new refrigeration system using specially designed finned plate heat exchanger and working with zeolite and methanol is presented. The integration of heat transfer and adsorption via a finned surface coated with zeolite CBV 901 and the use of connected, twin active bed system to enable heat recuperation, are novel features. The thermophysical properties of zeolite and methanol were first studied with the intention of designing a high performance heat exchanger (generator) for adsorption refrigeration system, where the major problem is connected with poor conductivity at the interface between heat exchanger and zeolite. The adsorbent must be heated (desorption phase) and than cooled (adsorption phase) back to ambient temperature in order to complete a thermodynamic cycle. The system, as the cycle, should be small. This requires high rates of heat transfer in and out of the adsorbent. Therefore, the surface of the heat exchanger is finned in order to increase the heat transfer area (which is coated with 2-mm layer of specially prepared zeolite paste). The following characteristics were estimated from initial calculation: heating temperature 120 ^{0}C, outside tube temperature 119.6 ^{0}C, middle fin temperature 117 ^{0}C and coated layer of zeolite paste temperature 115.3 ^{0}C.

The mathematical mode developed to calculate the effects of operating conditions and Coefficient of Performance (COP) has been presented at HPC'2001 in Paris*. It is based on Dubinin-Astakhov equation and thermodynamic analyses. The results obtained shows that for single bed the COP is 0.535 and 0.935 for a twin bed.

INTRODUCTION

The research development on adsorption cycles for heat pump/refrigeration increased noticeably in the last few years. Additional costs associated with the efficiency of using conventional refrigeration unit, as well as the greenhouse gasses emanating from the refrigerants used, have taken their toll on both the wealth of society and ozone layer. Therefore, conventional refrigerants have to be replaced with new substances, which are non-toxic, efficient, and flexible. The successful design of an adsorption refrigeration system could potentially solve the problem of ozone depleting chemicals and provide a cheaper alternative to recent systems in the form of higher overall energy conversion efficiencies. This will in turn lower primary fuel costs through less demand. Additionally, current methods of refrigeration are not portable and require a ready source of electricity. Consequently, the adsorption systems are considered interesting but more efforts are needed for their development.

The main disadvantage of the gas-solid systems proposed is related to the high weight and volume of the solid adsorber, which make the system not compact, expensive, thus not well suitable for domestic applications. [1-3]

Other limitations originating from the inefficient nature of heat and mass transfer inside the adsorber may lead to significant reductions in the performance of the adsorption system. The two types of resistance to heat transfer that can be observed originate from the lack of good physical contact at the metal-adsorbent interface and from the generally low thermal conductivity values of the adsorbent bed. [4] On the other hand, resistances to mass transfer depend on the magnitude of the diffusion coefficient value of the adsorbate in the adsorbent as well as thickness of the adsorbent bed. It is difficult to achieve an optimum compromise between the high porosity necessary for fast vapour diffusion and the high density required for good thermal conductivity. [5]

Therefore, research has focused on improvement of the heat and mass transfer inside the adsorber bed, in order to increase COP of these systems. Additionally, new adsorbent-adsorbate pairs have been studied to improve energy efficiency. New designs of heat exchangers, use of additives to get better heat transfer and different bed constructions have been proposed. [6], [7]

In this work a review of a design of a finned plate heat exchanger as part of a novel twin-bed adsorption system that, in principle, would halve the heat demand for a given refrigeration effect is given. The characteristics of this system are:

(a) by using twin bed, heat rejected from the first bed can be recuperated and used to regenerate the second;
(b) to mitigate mass and heat transfer limitations , the adsorbent is coated onto a compact heat exchanger, as opposed to being in a packed bed;
(c) a new type of zeolite, CBV 901, requires a lower regeneration temperature than normally expected.

* Heat Powdered Cycles Conference, 5-7 September 2001, Paris, 'Analysis of adsorption refrigeration system using zeolite and methanol', S. Waszkiewicz, H. Saidani-Scott, M. Tierney

NOMENCLATURE

Nu- Nusselt number [-]
Re- Reynolds number [-]
Pr- Prandtl number [-]
d- diameter [m]
u- velocity [m/s]
ρ- density [kg/m^3]
μ- dynamic viscosity [Ns/m^2]
c_p- specific heat capacity [kJ/kgK]
V- volume [m^3]
δ- thickness [m]
λ- thermal conductivity [W/mK]
h- heat transfer coefficient [W/m^{2}K]
l_{typ}- typical length [m]
A- area of body [m^2]
C- circumference of the cut body area [m]
n- number [-]

Subscripts

f- fin
p- pipe
z- zeolite

TWIN-BED SYSTEM

A system, which consists of an evaporator, two beds and condenser, is schematically presented in Figure 1. It is envisaged as working continuously; one bed is cooled (and adsorbing), the other one is heated (and desorbing). Periodically, opening valve V1 allows the two-beds to achieve equilibrium. This not only reduces the adsorbate inventory in the lower bed, but also facilitates the recuperation of the heat and a higher COP.

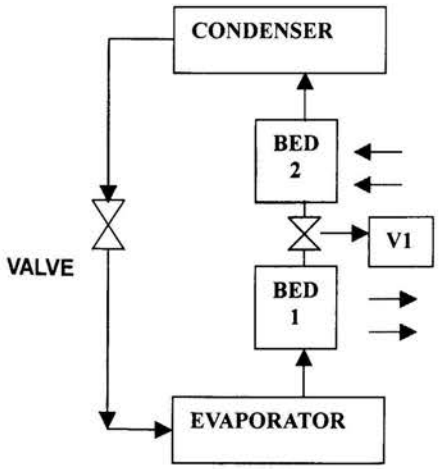

Figure 1: Twin bed system

ADSORBENT-ADSORBATE PAIR

There are several limitations to the use of conventional granular forms of adsorbent. Firstly, heat transfer through packed beds is slow, limiting the refrigeration effect. Secondly, most conventional adsorbents require a regeneration temperature in the range of 200°C to 250°C, restricting the coefficient of performance. Issues related to the choice of adsorbate include flammability, toxicity, stability and gas dynamics.

It has been proposed that monoliths, prepared by binding powder to a substrate, would result in effective heat and mass transfer [3], [8]. However, it has been difficult to prepare sufficiently resilient layers with thickness in excess of 2mm.

The specific volume of the adsorbate also limits performance, either because of choking or frictional resistance. Generally, water is not useful for high heat loads. Alternatively, ammonia is toxic and corrodes copper and brass fittings. Most alcohols are environmentally friendly but are dehydrated and catalytically decomposed during desorption at 150 °C to 200 °C. Zeolite CBV 901 and methanol were selected as a pair by Tchernev [9], because this new type of zeolite needs only 100 °C to be fully regenerated. This temperature does not cause methanol to decompose. The adsorption properties of selected pair were studied in order to establish its performance. Specially designed vacuum chamber was used. Samples of zeolite were placed inside (under vacuum) and small amounts of methanol were added in time intervals. The chamber was kept in a thermally controlled bath. (See figure 2) Pressure changes were recorded.

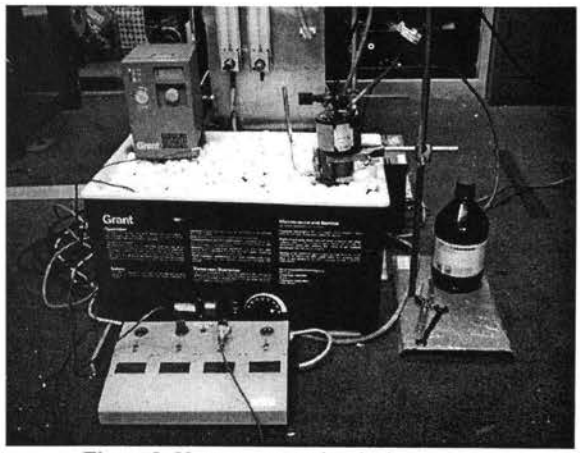

Figure 2: Vacuum system in a bath

Experiments were done for different temperatures. Results can be seen on figure 3. It can be seen from the experiments, as expected, that high adsorption, around 25%, can be observed at low temperatures of zeolite. The amount of methanol adsorbed is decreasing when system temperature is increasing.

Figure 3: Isotherms of zeolite CBV 901 and methanol

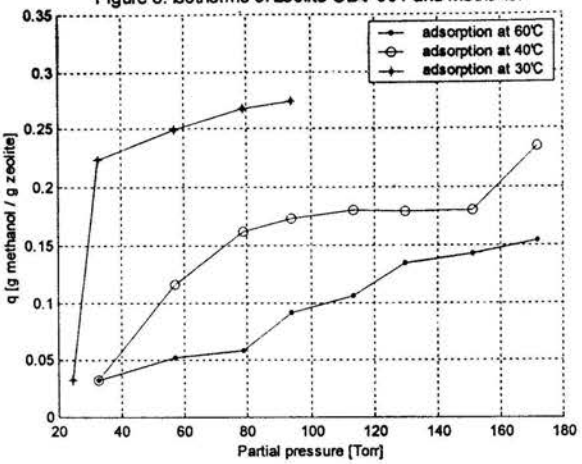

In twin-bed system model, the minimum temperature of adsorbent 35 ^{0}C (16.5% adsorption) and the maximum 100 ^{0}C (2% refrigerant concentration within zeolite) were taken into consideration.

GENERATOR DESIGN

The most important aspect when designing the generator is to maximize the heat transfer within the bed. This is because rapid heating and cooling is necessary for an efficient cycle, which in turn means that good heat transfer is essential. Unfortunately, adsorbents, like zeolite, are very poor thermal conductors. Therefore, a finned heat exchanger, which is the best known system for increasing effective heat transfer, has been chosen. If the fin-tube heat exchanger is used to better heat transfer, the adsorbent will have to be packed on and between the fins. Coating the fins with an adsorbent paste could be a suitable way of performing this task. The surface area of the fins is a factor that should be taken into serious consideration when designing a heat exchanger for this purpose. A larger fin surface area would not only lead to better conduction, but probably a better adsorption due to more mass of adsorbent.

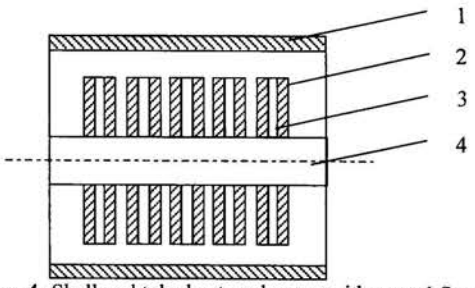

Figure 4: Shell and tube heat exchanger with coated fins; 1- shell, 2- zeolite coating, 3- fin, 4- inner tube.

It was decided that the best heat exchanger for the generator in the adsorption cycle is a shell and tube type with fins on it. (See figure 4)

The heat exchanger consists of a single tube with circular plates fitted on it. All plates are coated with zeolite paste. First, the fluid that will circulate through the tube of the heat exchanger needs to be heated and cooled rapidly. Hence, it requires having good thermal conduction and specific heat capacity. Therefore a turbulent flow is the best and it was decided to use mineral oil Transcal N. Also, aluminium was votes as the most suitable material for heat exchanger because it does not react with methanol. The methanol vapour is designed to pass through the shell of the heat exchanger.

HEAT TRANSFER

The heat exchanger (generator) was designed as a part of refrigeration system. The type of the heat exchanger was chosen in relation to the good heat transfer to the zeolite. The effective U-value of a shell and tube heat exchanger with coated fins was calculated as a function of the tube diameter, the diameter of the fins and thickness of the layer. (Figure 4)

Initially, zeolite volume per plate coated on both sides, was calculated from:

$$V_z = 2 \cdot \frac{\pi}{4} \cdot (d_f{}^2 - n_p \cdot d_p{}^2) \cdot \delta_z \qquad (1)$$

Zeolite mass per plate:

$$m_z = \rho_z \cdot V_z \qquad (2)$$

After that the number of fins situated on a pipe were obtained from:

$$n_f = \frac{m_{z,needed}}{m_z} \qquad (3)$$

It was found that 50 fins of 60-mm diameter and 2 mm thickness were needed. They were placed on ½" tube.

Then, the heat transfer coefficients were calculated. The assumptions were:

1. a fully developed flow
2. physical properties apply to the mean oil temperature
3. pipe wall is highly conductive
4. steady flow
5. temperature is constant across pipe diameter.

Hence, if the speed of the oil is 1m/s, the heat transfer coefficient can be calculated using the Dittus Boelter equation for Nusselt number:

$$Nu = 0.0023 \cdot \mathrm{Re}^{0.8} \cdot \mathrm{Pr}^{n} \qquad (4)$$

where n=0.4 for heating and 0.3 for cooling.

The Reynolds and Prandtl numbers were calculated from the following equations:

$$\mathrm{Re} = \frac{u \cdot \rho \cdot d_p}{\mu} \qquad (5)$$

$$\mathrm{Pr} = \frac{c_p \cdot \mu}{\lambda} \qquad (6)$$

Heat transfer coefficient is connected with Nusselt number:

$$Nu = \frac{h \cdot d_p}{\lambda} \qquad (7)$$

Now, by substituting equations (5), (6), and (7) in equation (4), the heat transfer coefficient of oil can be calculated for heating and cooling at different temperatures. The necessary data were inputted into an Excel spreadsheet and the variations of the heat transfer coefficient with pipe diameter and oil temperature were generated. These predictions calculated for oil velocity of 0.5 m/s is graphically represented in figures 5 and 6 given below.

Figure 5: Variation of heat transfer coefficient with pipe diameter and oil temperature FOR ADSORPTION

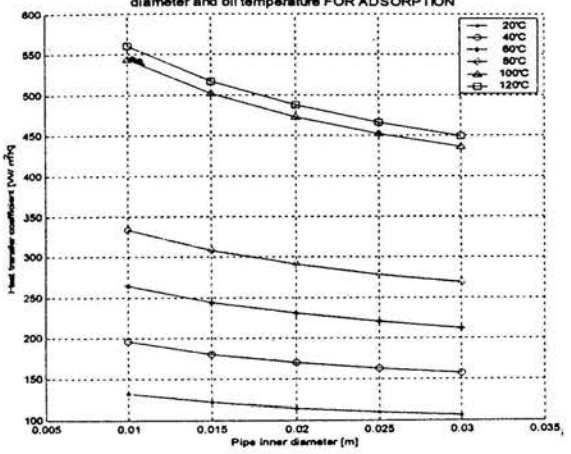

Figure 6: Variation of heat transfer coefficient with pipe diameter and oil temperature FOR REGENERATION

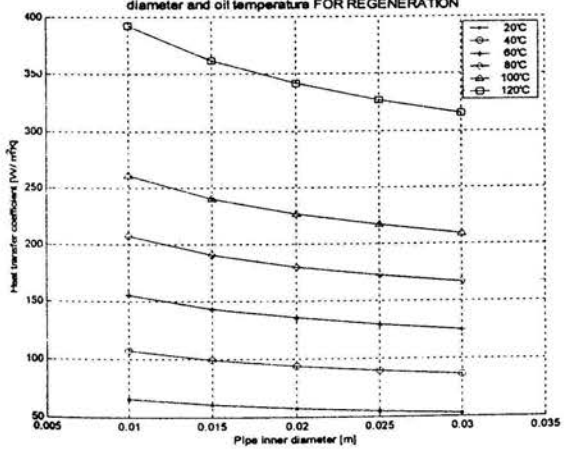

As can be expected and seen in a figure 5 and 6, the heat transfer coefficient is high for higher oil temperature and decreases with pipe diameter. In addition, the heat transfer coefficient for regeneration process (figure 6) is lower than the one for adsorption (figure 5).

Some comparisons can be made after calculating h in various environments plotted on figures 7, 8 and 9.

Figure 7: Variation of heat transfer coefficient with oil temperature for pipe diameter 0.01 m

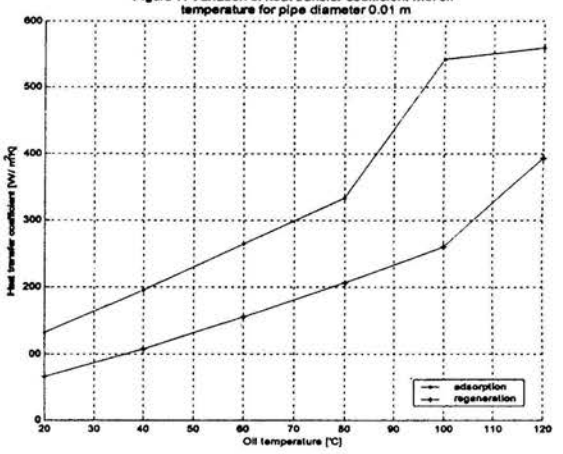

In figure 7, the h has been plotted for a fixed diameter of 0.01m. A noticeable difference appears after 80^0C. The heat transfer coefficient is stabilizing from 100^0C for adsorption, so the higher value of h is not possible to obtain with rising the oil temperature. It can be done in regeneration process.

Figure 8: Variation of heat transfer coefficient with pipe diameter and velocity FOR ADSORPTION at temperature 100°C

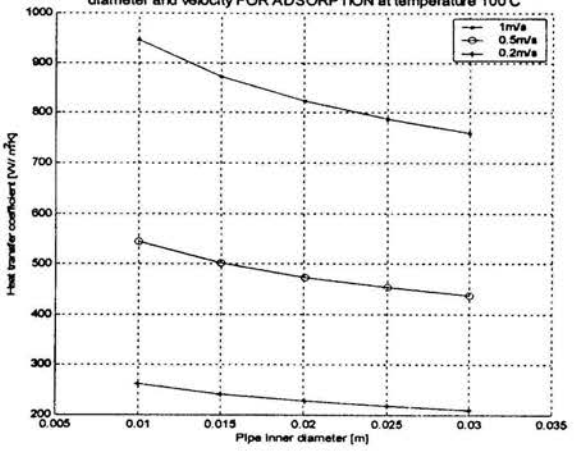

Both shapes of curves from figures 8 and 9 are similar. It can be observed that heat transfer coefficient is decreasing with lower

velocity values and it is higher for adsorption for the same velocity than regeneration.

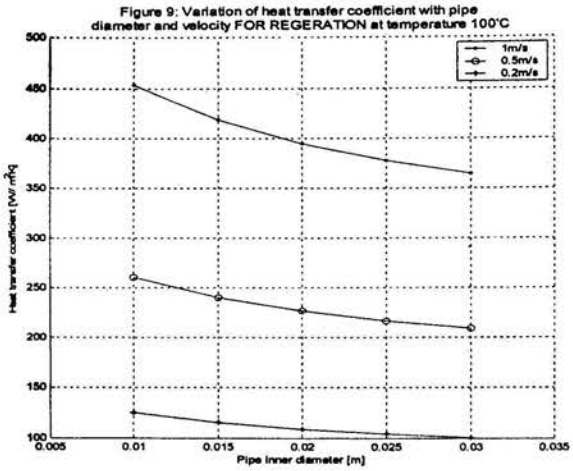

The following calculations were made with an oil temperature 120 ^{0}C, the pipe diameter of 12mm, velocity 0.5 m/s and the zeolite temperature 100 ^{0}C.

It was assumed that the methanol vapour is the temperature of 7.5 ^{0}C and under vacuum. Heat transfer coefficient from methanol to aluminium fins can be obtained using the same Dittus Boelter method described earlier. However, when calculating the Reynolds number, instead of diameter d, a typical length l_{typ} used as defined by:

$$l_{typ} = \frac{A}{C} \qquad (8)$$

The predictions of heat transfer coefficient are shown in figure 10.

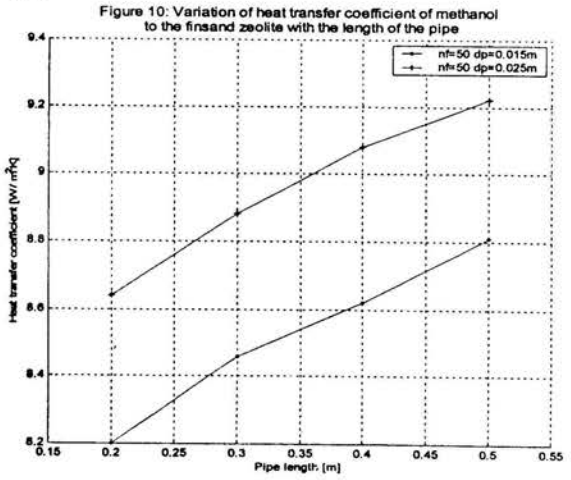

The figure shows a variation of the heat transfer coefficient with the length and outer diameter of the pipe. The outer diameter has been estimated when the pipe wall is 3mm thick. Again, the results show a predicted shape and variation.

All heat transfer coefficients for various parts of heat exchanger were calculated, using the data and equation above. The values are given in table 1.

	OIL-TUBE	METHANOL -FINS	METHANOL -ZEOLITE
Heat transfer coefficient [W/m^{2}K]	355.31	9.11	9.02

Table 1: Heat transfer coefficients

The temperature distributions from inside the tube to the outer surface also calculated and given in table 2.

	TUBE	FINS	ZEOLITE
Temperature [^{0}C]	119.6	117	115.3

Table 2: Temperature distribution

Then the temperature distribution in the part of plate coated with zeolite (figure 11) was modeled using Femlab. [10]

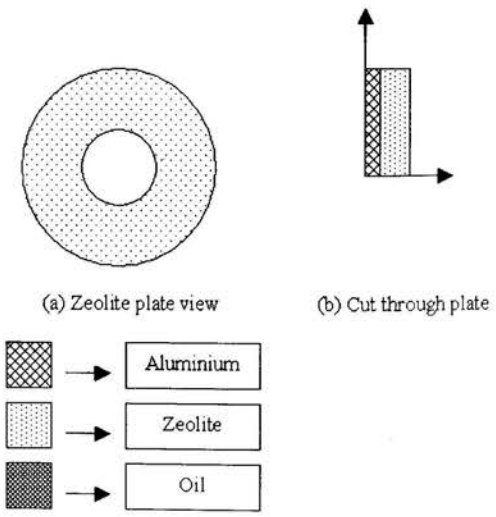

Figure 11: Fin coated with zeolite scheme

Temperature distribution was obtained for different values of heat transfer coefficient. (See figure 12 and 13)

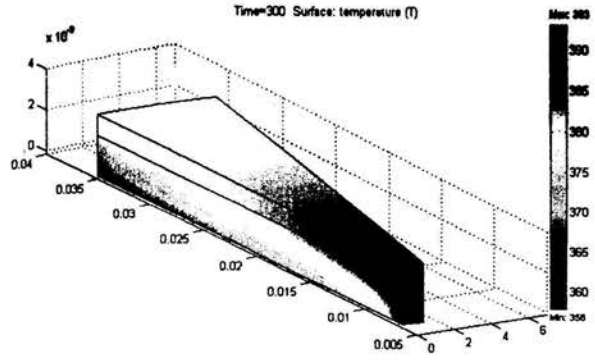

Figure 12: Heat transfer from oil to aluminium fin (top layer) and zeolite coating (bottom layer), h=100 W/m^{2}K

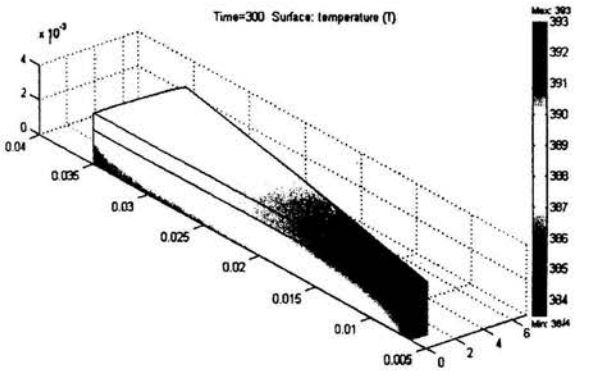

Figure 13: Heat transfer from oil to zeolite, h=50 W/m^{2}K

It can be seen that lower temperatures in zeolite will be connected with higher heat transfer coefficient.

CONCLUSION

This project, which has been looking at a novel adsorption pair, mainly zeolite and methanol, has shown very promising results. The simulations done using real data gave a first insight into the temperature distribution as well as heat transfer coefficients variation in the heat exchanger.

The values are attainable and can be achieved experimentally hopefully give a decent COP. Experimental work to confirm the good results obtained by the model will be done in the near future.

REFERENCES

[1] D. J. Miles, S. V. Shelton, 'Design and testing of a solid sorption heat pump system', Applied Thermal Engineering, vol. 16, no 5, pp. 389-394, 1996

[2] E. C. Boelman, B. Saha and T. Kashiwagi, 'Experimental investigation of a silica gel-water adsorption refrigeration cycle-The influence of operating conditions on cooling output and COP', ASHRAE Transactions, vol. 101, part 2, pp. 358-366, 1995

[3] G. Restuccia, G. Cacciola, 'Performance of adsorption systems for ambient heating and air-conditioning', International Journal of Refrigeration, vol. 22, pp. 18-26, 1999

[4] G. Cacciola, G. Restuccia, 'Progress on adsorption heat pumps', Heat Recovery Systems & CHP, vol. 14, no 4, pp. 409-420, 1994

[5] M. Tatlier, A. Erdem-Senatalar, 'Effects of metal mass on the performance of adsorption heat pumps utilizing zeolite 4A coatings synthesized on heat exchanger tubes', International Journal of Refrigeration, vol. 23, pp. 260-268, 200

[6] M. Picon- Nunez, G.T. Polley, E. Torres-Reyes, A. Gallegos-Munoz, 'Surface selection and design of plate-fin heat exchangers', Applied Thermal Engineering 19, pp. 917-931, 1999

[7] R.Z. Wang, J.Y. Wu, Y. Teng, W. Shi 'Experiment on a continuous heat regenerative adsorption refrigerator using spiral plate heat exchanger as adsorbers', Institute of Refrigeration and Cryogenics, Shanghai Jiao Tong University, Applied Thermal Engineering Vol. 18, no 1-2, pp. 13-23, 1998

[8] G. Restuccia, A. Freni, G. Cacciola, 'Adsorption beds of zeolite on aluminium sheets', ISHPC, Proceedings of the International Sorption Heat Pump Conference, Munich, Germany, pp. 343-347, 1999

[9] D. Tchernev, 'A waste heat driven automotive air conditioning system', ISHPC'99, Munich, 24-26 March, pp. 65-70, 1999

[10] http://www.femlab.com/

HEFAT2002
1st International Conference on Heat Transfer, fluid Mechanics, and Thermodynamics
8-10 April 2002, Kruger Park, South Africa
AS1

ANALYSES OF LOSS OF FLOW ACCIDENTS IN THE XADS DEMONSTRATION FACILITY

S. Aliotta °, F. Castiglia °, M. Giardina °, R. Vaghetto °

° Dipartimento di Ingegneria Nucleare – Università degli Studi di Palermo
Viale delle Scienze – 90128 PALERMO, Italy

A. Alemberti *, L. Barucca *

* Ansaldo Nucleare – Division of Ansaldo Energia S.p.A.
Corso Perrone, 25, 16161 Genova, Italy

ABSTRACT

When a new nuclear system such as the ADS (Accelerator Driven System) [1] is proposed, design basis accidents (DBAs) analyses are very important because they may influence the ongoing design.

In the present paper, a demonstration facility of the above system, named XADS (Experimental Accelerator Driven System) [2], is analysed during total and partial loss of flow accidents (LOFAs). A LOFA event with loss of offsite power is also presented.

For these analyses, the plant behaviour is analysed by RELAP5/MOD3.2.2β code, modified to take into account the fluids used in the plant as well as to allow proper simulation of its peculiar features [3].

INTRODUCTION

The final disposal of radioactive wastes resulting from the industrial nuclear energy production represents a problem not yet fully solved in terms of environmental and social acceptability.

In the last years, in some countries (Europe, US and Japan) different strategies have been studied for the incineration or transmutation of long lived fission products in subcritical nuclear reactors, supported by an external source of spallation neutrons. Such neutrons are foreseen to be produced in suitable accelerator driven systems (ADS).

Among the alternatives presented to the international attention, the Energy Amplifier (EA) plant [1] has been recently proposed.

A preliminary design for a demonstration facility of such a plant, called XADS [2], has been the object of several basic R&D activities involving ENEA (the italian national research body energy), INFN (the italian national research institute for nuclear physics) and Ansaldo industry.

Such a demonstration plant, is a low power system (about 80 MWt) cooled by Pb-Bi eutectic liquid.

In the primary system, the coolant natural circulation is enhanced by injecting inert gas into the bulk of the coolant flowing through suitable vertical pipes (risers) located at the core outlet. The density difference between the two-phase mixture in the risers and the liquid flowing down through the heat exchangers located in the downcomer, promotes the coolant circulation.

In the framework of the research activities of CIRTEN (Consorzio Interuniversitario per la Ricerca Tecnologica e Nucleare) and in a collaboration with Ansaldo Nucleare, our research group is carrying out an extensive research activity on XADS plant safety analyses, which includes different thermal hydraulic transients following several hypothesized initiating accidental events. These analyses are performed by using RELAP5/MOD3.2.2β code, suitably modified to take into account the Pb-Bi eutectic and the diathermic oil employed in the above mentioned plant, as well as, to allow proper simulation of its peculiar features [3].

The present paper presents and discusses the results obtained in the analyses of loss of flow accidents (LOFAs), due to partial or total gas injection failure. In the last case, the transient will be analysed with or without offsite power availability.

XADS PLANT DESCRIPTION AND RELAP5/MOD3.2.2β NODALIZATION

The XADS primary system configuration is presented in Fig. 1. The core, placed in the lower part of the vessel, is shaped like an annulus coaxial with a vacuum pipe carrying the protons coming from the accelerator (proton beam).

The protons interact with Pb-Bi eutectic that, at core level, acts also as target for spallation reactions. The spallation neutrons allow the subcritical core to sustain the neutron chain reaction. The power generated in the core, together with the one deposited in the target (about 3 MW_t), is removed by the eutectic circulating through the whole primary system.

The above described scheme, with the core in the lower part of the vessel and the intermediate heat exchangers (IHXs) in the upper part of the downcomer, allows in principle the coolant natural circulation without pumping systems, limited only by the available height of the vessel. In the XADS plant, in order to reduce the vessel height the coolant natural circulation is enhanced by injecting inert gas

(argon) into suitable vertical pipes (risers), 22 of which, placed at the core outlet, are fed by a single gas compressor (two more risers, collecting the eutectic coming from the above core volume, are supplied by a separate gas feeding). The increased density difference between the two phase coolant flowing through the risers and the single phase one through the downcomer, allows primary coolant flowrates greater than that achievable by single phase natural circulation alone. Moreover, the coolant flowrates can be controlled by the amount of injected gas.

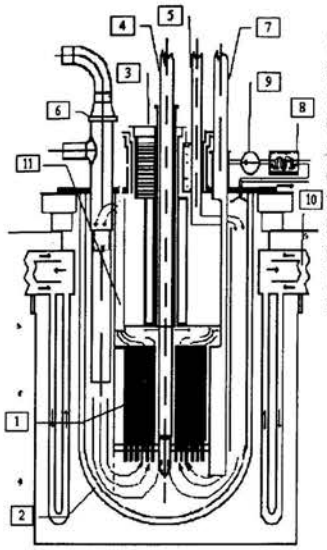

Figure 1: XADS primary system

In normal conditions the coolant in the primary system works between 573 K (inlet core) and 673 K (outlet core) temperatures. If, following an accident, the coolant core outlet temperature reaches 693 K (core outlet high temperature set point), the proton beam trip occurs reducing the generated power to decay value, with a delay of 2.5 s.

In case of complete loss of the secondary system (loss of heat sink) the decay heat is removed by a passive Reactor Vessel Air Cooling System (RVACS).

The secondary system consists of two closed loop circuits, filled by subcooled diathermic oil (working in forced circulation between 551 K and 591 K), each one removing power from primary coolant in two IHXs, and releasing it to the environment by a series of three air coolers (ACs), equipped by regulating fans and louvers.

In case of pumps failure, pumps by-pass lines allow the oil natural circulation through lower friction losses paths.

In Fig. 2 the primary system nodalization of the plant, used for the RELAP5/MOD3.2.2β analyses, is reported.

A quite detailed nodalization was used, where all the components were schematised by cylindrical volumes (single volumes as well as pipes), connected to each other by junctions; heat releasing or absorbing structures; control system components. The secondary system nodalization includes the above mentioned components and also pumps and valves (Fig. 3). To be conservative, for all analyses no credit is given to reactivity feedback which could mitigate both the plant heat up and cool down.

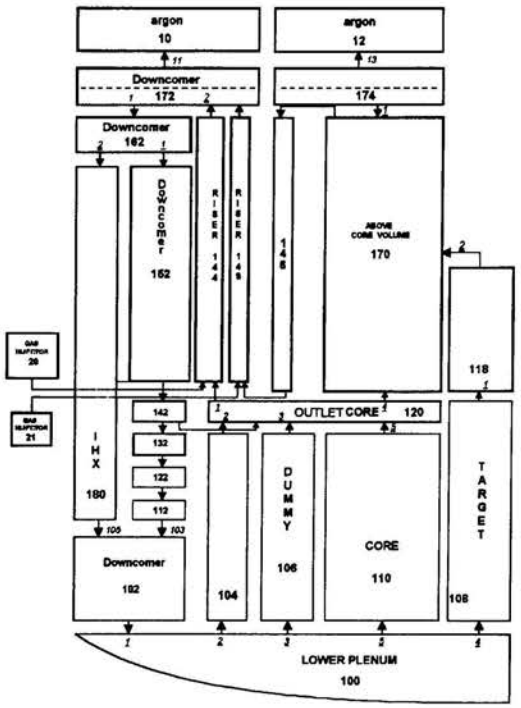

Figure 2: XADS primary system nodalization

LOSS OF FLOW ACCIDENTS DESCRIPTION AND RELAP5/MOD3.2.2β SIMULATION

In this section some postulated accidental events that result in reactor coolant flow rate decrease or loss (partial or total LOFAs) are analysed. These events, classified as design basis accidents (DBAs) category 2 [4], can originate from total or partial loss of gas injection due to injection system malfunctions or gas compressor trip. In particular, the following accidental events will be discussed:

- Gas injection malfunction leading to halve the total gas injection mass flow rate with respect to the nominal value;
- Gas compressor trip, both with or without offsite power availability.

In the last case the loss of offsite power is assumed to take place after the proton beam trip, to conservatively worsen the accidental sequence. In fact, under these circumstances, the heat removal from the primary system by the oil secondary coolant, as well as, from the secondary system by the ambient air in the ACs relies only on natural circulation.

Besides, the external environmental temperature is assumed at the maximum design safety value of 315 K in order to conservatively reduce the plant heat sink capability.

In all the simulations a steady state calculation of 100 s with plant at nominal conditions is performed before the accident begins. At t = 100 s argon flow rate reduction or loss within 2 s takes place.

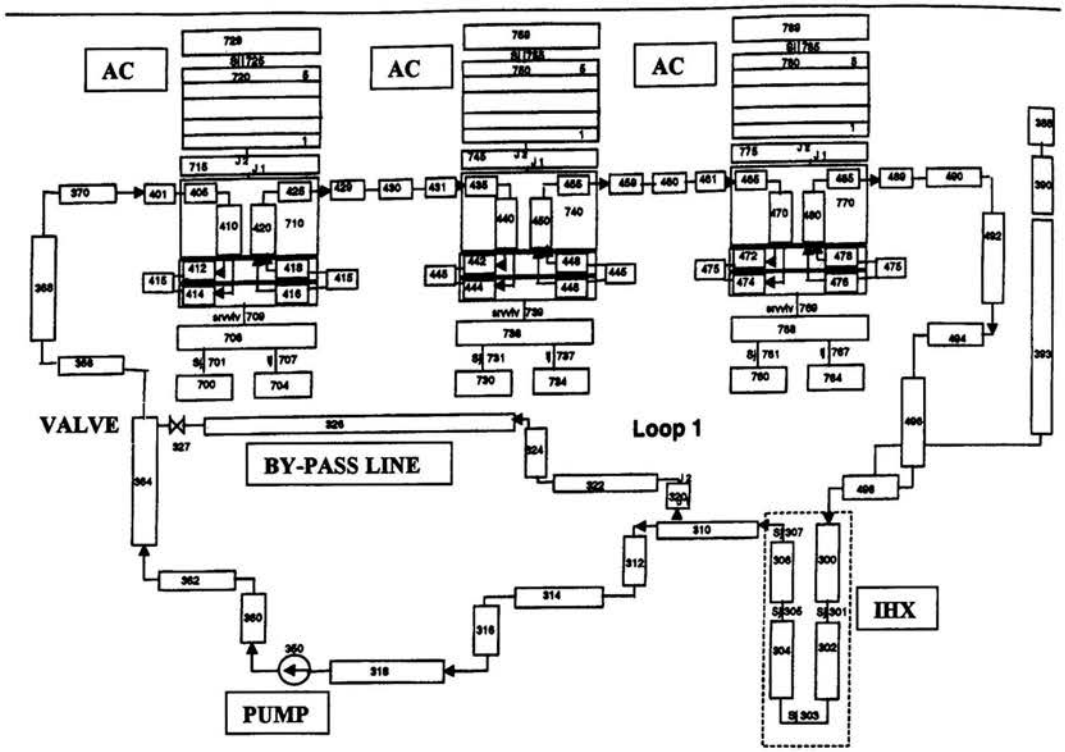

Figure 3: XADS secondary system nodalization

Gas mass flow rate reduction to 50% of nominal value

For the accidental transient analysed in this section, the hypothesized initial event originates from a gas injection system malfunction leading the argon injection in the 22 risers to be halved with respect to the nominal value. Two different alternatives have been tested according to whether all the 22 risers are fed by a single air compressor or they are subdivided in two groups, each one supplied by a separate gas feeding. This in order to investigate which between these two design solutions minimizes the impact of the accident. Consequently the two following nodalizations have been employed:

- in the first one, all the risers are schematised by a single vertical pipe component, interested by the total gas mass flowrate. When the accident occurs, the gas flowrate is halved.
- in the second, all the risers are schematised by means of two different pipes, each one supplied by 50% gas mass flowrate injection. When the accident occurs, in one of them the gas injection is lost.

First nodalization

Following the accident, the primary coolant flowrate through the core is reduced by about 10% (Fig. 4), reaching the value of about 4780 kg/s (from the initial 5350 kg/s). Early in the transient, the core inlet and outlet temperatures exhibit a slight increase. As the first one keeps below the maximum core outlet temperature set point (Fig. 5), the proton beam trip doesn't occur and new steady conditions are achieved (Fig. 6). In such a figure the little difference between the generated and removed power has to be attributed to the RVACS heat removal.

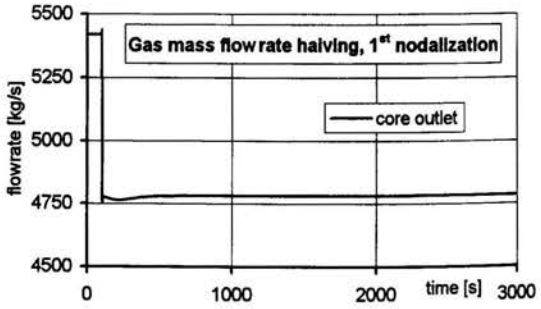

Figure 4: Primary coolant mass flowrate at core outlet

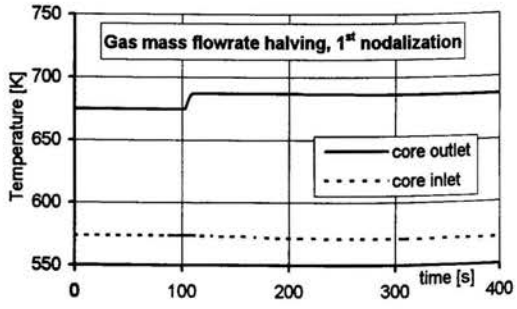

Figure 5: Primary coolant temperature at core inlet and outlet

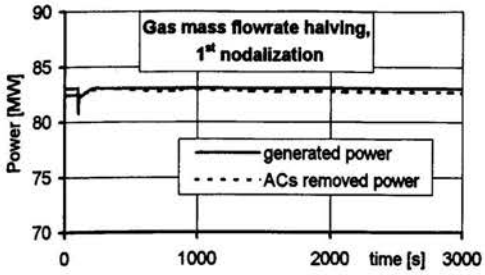

Figure 6: Generated and removed power

Second nodalization

In this case, after the accident initiation, the primary coolant mass flowrate through the core quickly undergoes a reduction (by about 40%), higher than the previous one, reaching the value of about 3210 kg/s (Fig. 7). This is due to the recirculation effects involving the two riser pipes (Fig. 8). In fact, the mass flowrate through the affected risers rapidly decreases and, after about 10 s, it reverses. Subsequently, it keeps negative values, exhibiting an oscillating course: damped at first, persisting with negligible amplitude during the remaining part of the transient.

As a consequence of the less core mass flowrate, its outlet temperature suddenly increases (see Fig. 9) and, when the core outlet high temperature set point is reached, the proton beam shutdown occurs (with a delay of 2.5 s). This causes the core outlet temperatures to drop as the generated power turns to decay one. During the subsequent part of the transient, the primary and secondary coolant temperatures gradually go down, the removed power being quite higher than the produced one (Fig. 10).

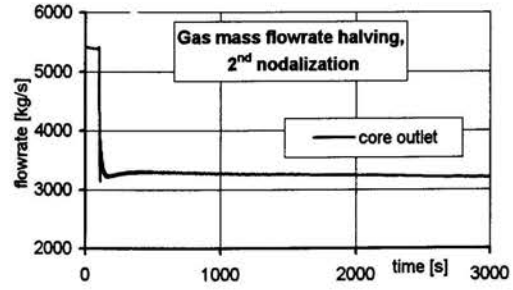

Figure 7: Primary coolant mass flowrate at core outlet

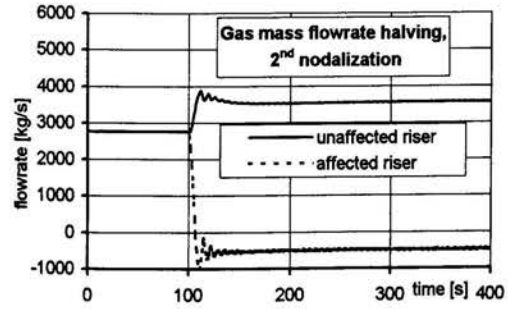

Figure 8. Flowrate recirculation between affected and unaffected riser

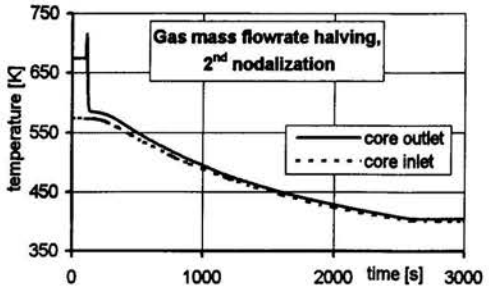

Figure 9 : Primary coolant temperature at core inlet and outlet

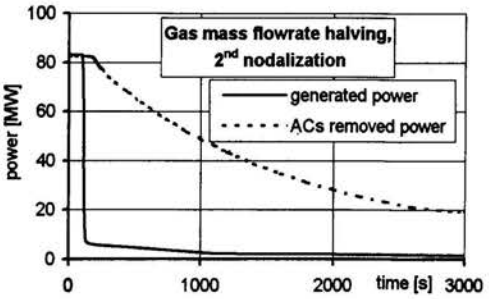

Figure 10 : Generated and removed power

Gas compressor trip

The initiating event consists in a total argon injection failure, with the plant at nominal power and flows conditions.

As already said, the two cases of availability and loss of offsite power are considered. Obviously, in both cases until the proton beam trip occurs the transients exhibit exactly the same behaviour. Indeed, the initiating event leads to a sudden core coolant mass flow rate reduction of about 85% (Figs. 11 and 18) due to the transition to natural circulation as well as to the recirculation established between the downcomer and the IHXs components (Figs. 12 and 21). As a consequence, the eutectic coolant heats up and, when the core outlet temperature reaches the high temperature set point, the proton beam trip occurs.

After the proton beam trip, the generated power turns to the decay one and the transient proceeds according to the two different scenarios described in the following.

Offsite power availability

As one can see from Fig. 12, the recirculation flow involving downcomer and IHXs components persists during the whole transient. About half of the flow rate coming from the IHXs is directed to the core, while the remaining one is reversed through the downcomer.

In Fig. 13 both the total generated thermal power (core and target) and that removed by the ACs are reported.

As one sees, after the proton beam trip takes place, the heat sink heat removal capability is greater than the decay power, thus causing the primary and secondary coolants to cool down (Figs.14 and 15).

The fuel and clad temperatures in the hot pin, after a very slight increase (maximum reached values 1169 K and 787

K, respectively) decrease, first quickly due to the generated power reduction, subsequently lie down on low values (Fig. 16) according to the primary coolant temperature behaviour.

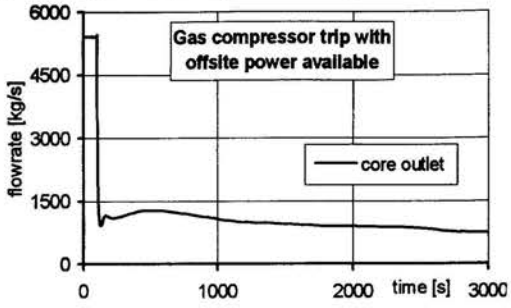

Figure 11 : Primary coolant mass flowrate at core outlet

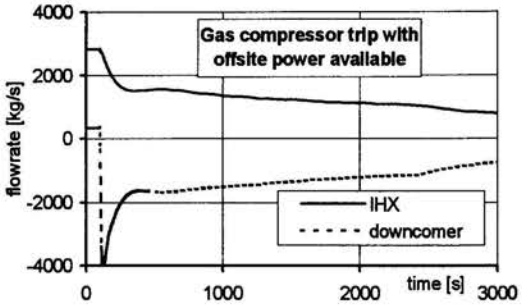

Figure 12 : Recirculation mass flowrate between two IHXs and downcomer

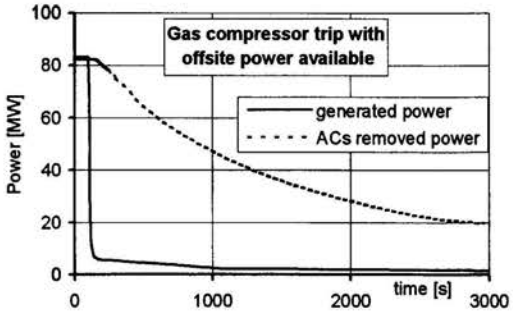

Figure 13: Generated and removed power

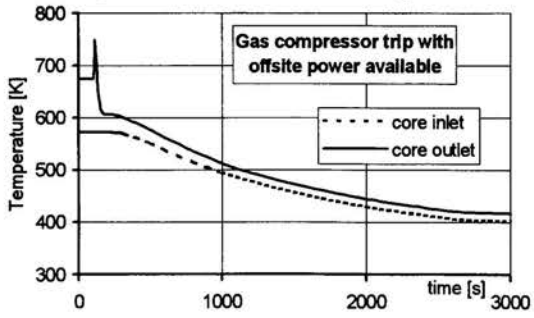

Figure 14: Primary coolant temperature at core inlet and outlet

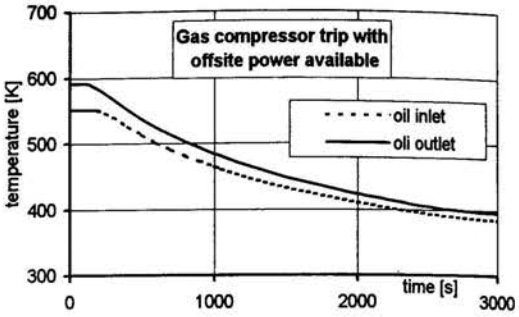

Figure 15: Oil coolant temperature at IHX inlet and outlet

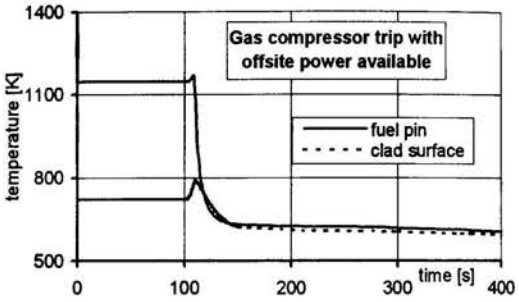

Figure 16: Hot rod fuel and the cladding temperatures

Loss of offsite power

As above said, in this scenario, after the reactor shutdown, the loss of offsite power is supposed to suddenly occur. Subsequently the following events take place in succession: the pump in each secondary loop trips, the secondary loops by-pass lines open, the fans in all ACs stop. Moreover, two out of three louvers in each loop close.

As it can be deduced from Fig. 17, the heat sink efficiency becomes very poor (Fig. 13), as both the secondary coolant oil and ambient air circulations switch to natural mode. This causes a primary coolant natural circulation reduction, with respect to the case with off-site power availability (Fig. 18). Also the primary coolant temperature experiences a milder cool down (Fig. 19). A different time history is predicted for the secondary coolant temperature. The decreased heat removal capability of the ACs causes the inlet oil temperature to increase during the first 1000s of the transient. After that time a secondary side oil cool down starts (Fig 20).

Finally, we note that the recirculation between the IHXs and downcomer considerably attenuates (Fig. 21).

CONCLUSIONS

In this paper with reference to the XADS system, a demonstration facility of a Pb-Bi eutectic cooled ADS, some postulated accidental events that result in reactor coolant flow rate decrease or loss (partial or total LOFAs) have been analysed. These events, classified as design basis accidents (DBAs) category 2, can originate from total or partial loss of gas injection due to injection system malfunction or gas compressor trip.

In particular, the following accidental events have been discussed: gas injection malfunction leading to the halving

of the gas mass flow rate and gas compressor trip.

For the first case, two different nodalizations of the risers have been employed showing that the first noding, which simulates the present design solution,

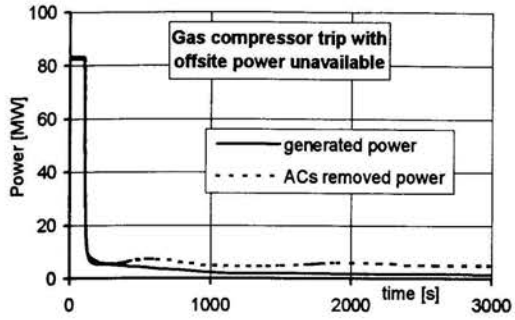

Figure 17 : Generated and removed power

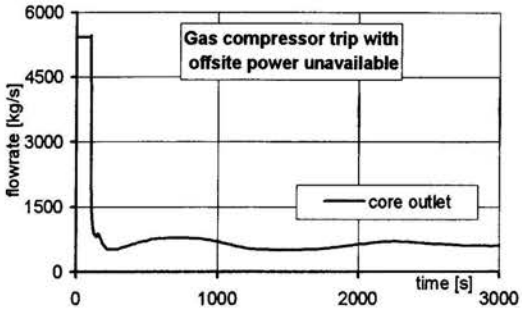

Figure 18: Primary coolant mass flowrate at core outlet

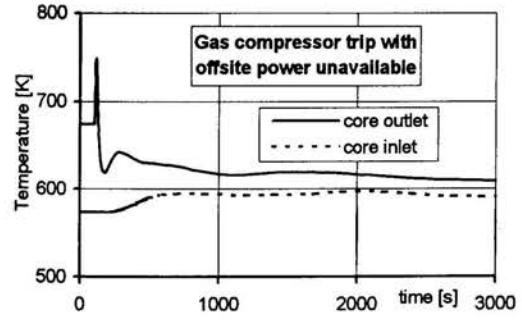

Figure 19 : Primary coolant temperature at core inlet and outlet

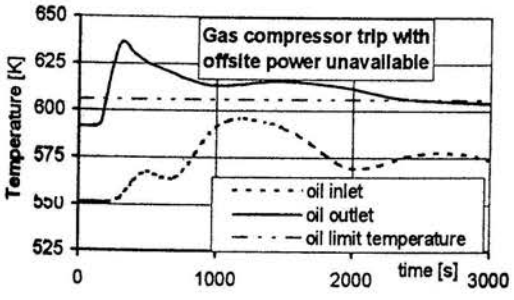

Figure 20: Oil coolant temperature at IHX inlet and outlet

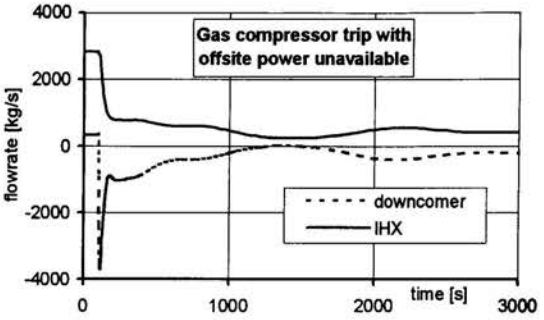

Figure 21: Recirculation mass flowrate between two IHXs and downcomer

minimises the impact of the accident on the plant response. For the second case the analysis has been performed assuming both availability and loss of offsite power, after the proton beam trip. The analyses of the transients show that the secondary coolant system, also when the heat sink capability is strongly reduced, is able to remove the decay thermal power. Indeed, in all cases the fuel maximum and cladding hot rod temperatures reach values well below the limits established for Category 2 events.

For the case of gas compressor trip with loss of offsite power, high values of IHXs outlet secondary coolant temperature (exceeding 610 K) are predicted for about 1800 s, which in any case does not represent a violation of the maximum allowable time at temperature criterion for the category to which the accident belongs (Fig. 20, [4]).

REFERENCES

1. F. Carminati, R. Klapisch, J.P. Revol, Ch. Roche, J.A. Rubio and C. Rubbia, An Energy Amplifier for cleaner and inexhaustible nuclear energy production driver by a particle beam accelerator, European Organization for Nuclear Research, CERN/AI/93-47 (ET), Geneva, 1 Novembre 1993.
2. Energy Amplifier Demonstration Facility Reference Configuration, Ansaldo Nucleare summary report EA B0.00 1 200 Rev.0 January 1999;
3. A. Alemberti, Relap5 Code Modifications for ADS Demonstration Facility Simulation, Ansaldo Nucleare technical report no. ADS 1TRIX 0243, march 2000.
4. L. Barucca, Identification and categorization of Design Basis Accidents and Acceptance criteria, Ansaldo Nucleare technical report no. ADS 1TRIX0249, march 2001.

Work supported by Università di Palermo and Ministero dell'Università e della Ricerca Scientifica e Tecnologica (MURST): cofin. 1999.

HEFAT2002
1st International Conference on Heat Transfer, Fluid Mechanics, and Thermodynamics
8-10 April 2002, Kruger Park, South Africa
AS2

EXPERIMENTAL INVESTIGATION OF HEAT TRANSFER COEFFICIENT IN FLUIDIZED BEDS WITH IMMERSED HEATING SURFACE

S. Abu-Ein
Department of Mechanical Engineering
Amman College for Engineering Technology, Al-Balqa' Applied University
P.O. Box 15008, Marka, Amman, Jordan

ABSTRACT

This paper proposes an empirical formula that could calculate the heat transfer coefficient between the fluidized bed and the immersed surface inside it. To verify the empirical equation, a series of experiments were conducted in a cylindrical reactor of 142mm ID and a height of 1m, at ambient conditions. The bed was heated by means of a cylindrical heater made of copper with a diameter of 28.5mm and a length of 60mm and a constant power of 7W. Experiments were performed at a gas velocity ranging from 0.03 – 1.6m/s, and for five different solid particles sizes. The predicted results were compared with the experimental data, as well as with models and experimental data of other investigations.

INTRODUCTION

Since their first large-scale application in the chemical processing in the early 1920s, gas-fluidized beds have been developed into one of the main types of commercial reactors used to carry-out gas-solid reaction. These reactors offer a number of potential advantages compared to packed beds. These included the isothermal conditions in the reaction zone, low-pressure drop when small particles are used, ease of solids transportation and the possibility of operation at increased gas velocities and even countercurrent operation (Holger, 1984; Perkle et al, 1988).

As a consequence to the complete combustion reactions in these reactors, emissions of harm gases to the environmental are expected to be at their lowest level. In addition, the thermal efficiency of these reactors is usually high compared with typical columnar reactors (Al-Busoul, 1999; Gunn et al, 1996; Ouyang et al, 1996). For these reasons gas-solid fluidized bed reactors is extensively used in different sectors of industry including combustion and gasification of coal and oil shale, drying and cooling of granules, cooling of granules surfaces and granulation in fertilizer technology.

One of the most important parameters in the design of gas-solid fluidized bed reactors when used, as a combuster is its heat transfer characteristics. A limited number of publications concerning modeling of the heat transfer processes was published in 1984.inside the fluidized bed are found in the literatures. These limited studies include the boundary layer model, the double layer model and the packets model (Davidson et al, 1986). Subsequently, the more comprehensive model of Martin.

In the previous models the researchers have used different analytical methods to illustrate the mechanism of heat transfer inside the bed. These analytical methods have lead to different empirical equations such as that of Botterils (1975), Kunii and Levenspiel (1991). It is evident for these models that many differences are found between them because they were based on different assumptions. In addition, those models contain many parameters of limited practical use.

The behavior of heat transfer between the bed and the immersed surface is usually considered as a tedious task, because it depends on different parameters, such as the fluid and the solid particles properties, the heater and reactor shape and dimensions in addition to the operation conditions. For these reasons, this mechanism could be understood more easily if it is analyzed based on experimental work.

There is a limited number of studies used the experimental approach to explain the mechanism of heat transfer process in gas-solid systems (Al-Busoul, 2000; Howard, 1989; Kharchenko et al, 1964). The results of these studies were simple and could not be extended to different conditions, but they reflect the individual experimental fact very well.

In this study, the experimental approach is followed to explain the heat transfer mechanism. It is expected that the resulted experimental equations would cover a wider range of operational conditions, because many different parameters are included in this study.

NOMENCLATURE

A	area of heat transfer, (m^2)
Ar	Archimedes number ($d_p^3 \rho_g g (\rho_p - \rho_g)/ \mu_g^2$)
D	bed diameter, (m)
d_p	particle diameter, (m)
H_o	static bed height, (m)
H	fluidized bed height, (m)
h	heat transfer coefficient, ($W/m^2 k$)
k_g	thermal conductivity of gas, (W/m k)
Nu	Nusselt number, ($h d_p/ k_g$)

Q	heat transfer rate, (W)
Re	Reynolds number ($U \rho_g d_p/\mu_g$)
T_b	bed temperature, (k)
T_s	temperature of heat transfer surface, (k)
U	gas velocity, (m/s)
U_{mf}	minimum fluidizing velocity, (m/s)
$1-\varepsilon$	concentration of particles in fluidized bed
$1-\varepsilon_o$	concentration of particles in static bed
ρ_g	density of gas, (kg/m^3)
ρ_p	density of solid particles, (kg/m^3)
ρ_u	apparent density of solid particles, (kg/m^3)
μ_g	viscosity of gas, (kg/m s)

EXPERIMENTAL APPARATUS AND PROCEDURE

A schematic diagram of the experimental Apparatus is shown in Fig. 1.
The unit includes the main column of 142 mm I.D., and 1m height. The column was made of an acrylic to assist visual observations of the flow pattern. The distributor plate was of straight hole orifice type, located at the bottom of the main column, to ensure a uniform distribution of the fluidized gas. The air needed for fluidization was supplied by a blower, regulated by a valve, and measured by a digital flowmeter. A manometer was used to measure the pressure drop a cross the fluidized bed.

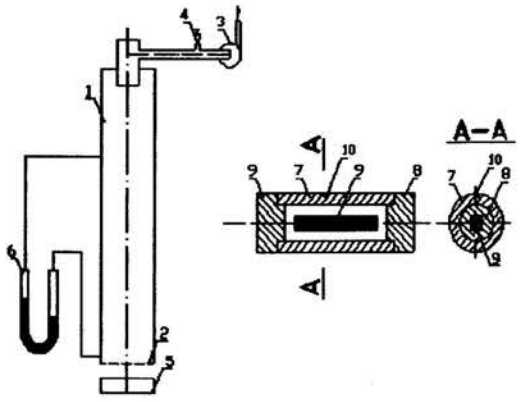

Fig. 1. A Schematic diagram of the experimental unit: 1- Reactor, 2- Distributor, 3- Blower, 4- Valve, 5- Digital flow meter, 6- Manometer, 7- Cylindrical copper heater, 8- Teflon, 9- Electrical resistance, 10- Thermocouple.

To determine the convective heat transfer coefficient, an electrical heater was used. It was made of a 28.5 mm diameter cylindrical copper heater with a length 60 mm. The cylinder house imbedded the electrical resistance, and the ends of the cylinder were covered with Teflon support to reduce axial heat losses which is estimated to be less than 1%. The heater was mounted horizontally with its center axis 120 mm above the distributor. The power input to the heater was controlled by a variac, and measured with a multimeter. A thermocouple placed on the surface of the heater was used to measure the surface temperature (T_s), and another thermocouple installed at 50 mm from the distributor plate, at the same axial plane of the previous thermocouple, was used to measure the bed temperature (T_b).

Experiments were performed at a constant input power to the heater (Q = 7 W), at atmospheric pressure, and at low temperature to exclude the effect of radiation heat transfer. The air velocity was varied from 0.03 – 1.6 m/s, and five different solid particle sizes were used, as shown in Table 1.

Table 1. Properties of Solid Particles

Substance	d_p μm	ρ_p kg/m^3	ρ_u kg/m^3	U_{mf} m/s	$1-\varepsilon_o$ -
Oil Shale A	102	1500	975	0.033	0.65
Oil Shale B	195	1500	930	0.090	0.62
Oil Shale C	856	1500	840	0.1652	0.56
Sand D	400	2600	1516	0.129	0.583
Sand E	743	2600	1482	0.162	0.570

The concentration of solids in the fluidized bed ($1-\varepsilon$), was calculated using the following equation [4]:

$$H_i(1-\varepsilon) = H_o(1-\varepsilon_o) \quad (1)$$

Where, $1-\varepsilon_o = \rho_u/\rho_p$ (2)

The minimum fluidizing velocity for a given bed of the solid particles was determined using Kunii equation and measuring the axial pressure drop as a function of the fluidizing velocity. The minimum fluidizing velocity was established by the intersection of the linear plots describing the constant and decreasing pressure drop with decreasing fluidizing velocity.

The convective heat transfer (h) was determined using the following equation:

$$h = \frac{Q}{A(T_s - T_b)} \quad (3)$$

RESULTS AND DISCUSSION

Fig. 2 shows the experimental values of the heat transfer coefficient (h_{exp}) as a function of gas velocity (U), for five different of solid particles. It is evident in Fig. 2, that a sharp rise in h_{exp} was occured as U increased, until a maximum value was reached at a velocity 2 to 5 times the minimum fluidizing velocity (U_{mf}). The maximum value was attained at smaller values of U/U_{mf} for larger particles. This behavior occured because as U increases, the particle movement increases, and this behavior enhances the mixing between the particles. And hence, causes h_{exp} to increase. The maximum h_{exp} obtained in any one of the whole series of such experimental runs exhibit a non-monotonic variation with particle size (d_p). In addition, it could be seen in Fig. 2 that, for higher gas velocities a fall in h_{exp} occurred which persisted with further increase in U. This is because, as U increases to a value greater than five times U_{mf}, the fluidized

bed expanded to a very large extent, and the solid particles swept faster past the test section, resulting in reduced h_{exp}.

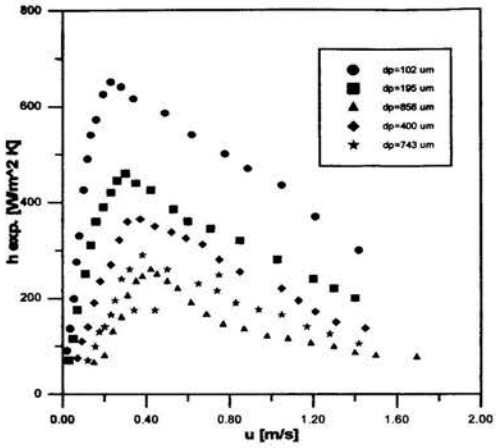

Fig. 2 Heat transfer coefficient as a function of gas velocity for various diameter of solid particles.

Based on the experimental results shown in Fig. 2 and applying both of the least square technique, and Gauss – Jordan Elimination method the following correlation was obtained:

$$N_u = 2.51\ R_e^{0.72}\ A_r^{-0.82}\ (1-\varepsilon)^{0.50} \qquad (4)$$

A comparison between the results predicted from the equ. (4) for d_p = 400 μm particle sizes, and the experimental results (Al-Busoul, 2000; Wnmder, 1979) are shown in Fig. 3.

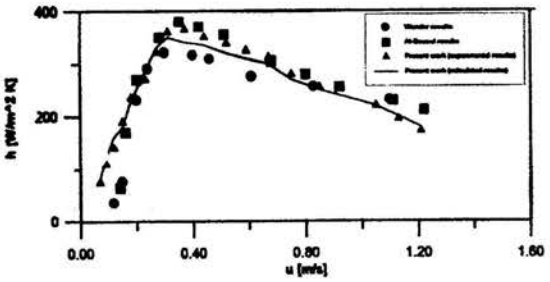

Fig. 3 Comparison of predicted model with experimental data.

Fig. 3 demonstrates a very reasonable agreement between the predicted and the experimental data. This agreement extended over a wide range of fluidizing conditions.

The effect of particle size on heat transfer coefficient estimated from the proposed empirical equ. (4), was compared with different models found in the literature, evaluated under the same operating conditions, are shown in Fig. 4.

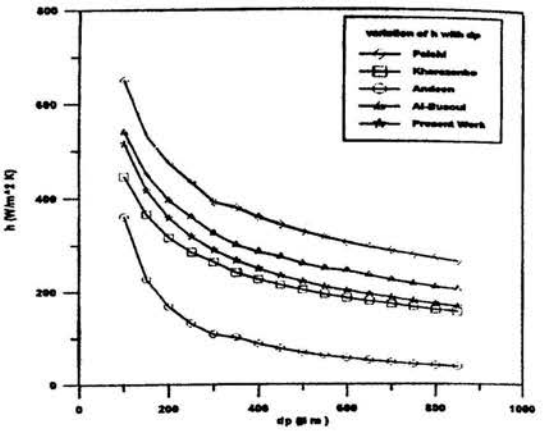

Fig. 4 Comparison of predicted model with experimental data and models of other investigators at a gas velocity of 0.7m/s.

It is clear in Fig. 4, that the heat transfer coefficient (h) for all runs decreases as the particle size increase. This is because, as the particle size increases, the spontaneous surface area of the solid particles in contact with the heater decreases, resulting in a decrease in heat transfer coefficient. It is clear from Fig. 4, that the proposed equ. (4) shows a closer behavior to Al-Busoul and Kharchenko models and a reasonable agreement between the proposed equ. and another models can be seen.

Comparison of the values of heat transfer coefficient, predicted by equ. (4), with the experimental values of present work is shown in Fig. 5.

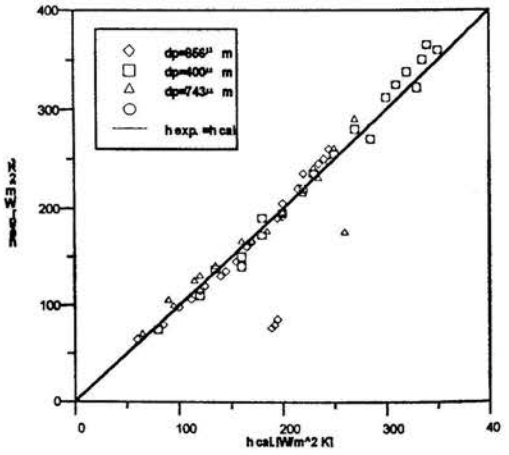

Fig. 5 Comparison of heat transfer coefficient predicted by the model with the experimental results of the present work.

The values computed from the equ. (4) corresponds to the operating conditions prevailing in each case. A very satisfactory agreement is clear, since the values are seen to cluster around the line of perfect agreement, and the deviation did not exceed beyond ± 16%. This indicates that,

the proposed equ. is capable of predicting, a satisfactory values of heat transfer coefficient obtained in the present experiments, at all operating conditions.

CONCLUSIONS

1) Based on this experimental study and calculations from different correlations the The proposed empirical equation successfully predicts the heat transfer following conclusions might be drawn:
coefficient obtained experimentally under all operating conditions studied.
2) The results indicate that the heat transfer coefficient is directly proportional to the gas velocity up to a value of two to five times the minimum fluidization velocity. (two for large particles and five for small particles). For higher gas velocities a fall in heat transfer coefficient occurred which persisted with further increase in gas velocity.
3) The heat transfer coefficient is inversely proportional to the solid particle diameter in the range 102 – 856 μm.

REFERENCES

Al-Busoul, M, "Local Heat Transfer Coefficient in a Fluidized Bed," Dirrasat Eng. Sciences, **26**, (1), 147 (1999).

Al-Busoul, M, and M. Abu-Zaid, "Prediction of Heat Transfer Coefficient Between Immersed Surfaces and Fluidized Beds," Int. Comm. Heat Mass Transfer, **27**, (4), 549 (2000).

Botteril, J. S. M., Fluidized Bed Heat Transfer, Academic Press, London, (1975).

Davidson, J. F., Clift, R. and Harrison, D., Fluidization, Academic Press, London, (1986).

Gunn, D. J., and N., Hilal, "Heat Transfer Vertical Inserts in Gas Fluidized Beds,"
Int. J. Heat Mass Transfer, **39**, (16), 3357 (1996).

Holger, M., "Heat Transfer Between Gas Fluidized Beds of Solids Particles and the Surfaces of Immersed Exchanger Elements," Part I, Chem. Eng. Process, **18**, 157 (1984).

Howard, J. R., "Fluidized Bed Technology, Principles and Application," Adam Hidger, Bristol and New York, (1989).

Kharchenko, N. V., and Makhorin K. E., "The Rate of Heat Transfer Between a Fluidized Bed and Immersed Body at Heighten, " Int. Chem. Eng., **4**, (4), 654 (1964).

Kunii, D., and Levenspiel, O., "Fluidaization Engineering," (2^{nd} ed), Butterwoth-Heinemann, Stoncham, (1991).

Martin, H., "Heat Transfer Between Gas Fluidized Beds of Solid Particles and Surfaces of Immersed Heat Exchanger Elements," Chemical Engineering and Processing, **18**, 157 (1984).

Ouyang, S., Li, X., Davies, G. and Potter, O., E., "Heat Transfer Between a Vertical Tube Bundle and Fine Particles in a CFB Downcomer with and without Circulation of Solid," Chem. Eng. and Proc., **35**, (1), 21 (1996).

Perkle, J., C., Ruziska, L., J., and Shulik, "Circulating Magnetically Stabilized Bed Reactors," Chem. Eng. Commun., **67**, 89 (1988).

Wunder, R., and Mersmann, A., Chem. Eng. Tech., **51**, (1979).

HEFAT2002
1st International Conference on Heast Transfer, Fluid Mechanics, and Thermodynamics
8-10 April 2002, Kruger Park, SgouthAfrica
AZ1b

THE EFFECT OF MAGNETIC FIELD ON WALL-TO-BED HEAT TRANSFER COEFFICIENT IN MAGNETO-AIR FLUIDIZED BEDS

Z. Al-Qodah* and M. Al-Busoul[+]

* Assistant Professor, Department of Chemical Engineering
[+] Assistant Professor, Department of Mechanical Engineering
Amman College for Engineering, Technology Al-Balqa' Applied University,
Jordan, Ammanan, Marka, 11134, P.O. Box 340558

ABSTRACT

The effect of a transverse magnetic field on the wall-to-bed heat transfer coefficient in a gas-solid fluidized bed was investigated. The effect of the magnetic field intensity and gas superficial velocities on the wall to bed heat transfer coefficient was studied using several sizes of magnetic particles. A correlation between Reynolds number, magnetic field intensity, and Nuselt number was obtained. The results obtained indicates that magnetically stabilized beds show a better heat transfer characteristics than packed beds. On the other hand, magnetically stabilized have lower thermal efficiency that that of fluidized beds.

INTRODUCTION

The earliest contribution on the effect of magnetic field on fluidized beds was reported by Filippov [1] who described some hydrodynamic behavior of a liquid fluidized bed utilizing a magnetic field. After that the hydrodynamics of magnetically stabilized fluidized beds (MSFBs) as well as some of their applications, have been extensively studied. These communications have recently been reviewed by Liu et al., [2].

It is evident from the published studies that magnetic stabilization of fluidized beds of magnetically susceptible particles, could be considered as one of the technologies developed to modify the behavior of fluidized beds [3]. It has been shown both experimentally and by modeling that magnetic stabilization of fluidized bed results in an improved fluid-solid contactor that combines the most desirable characteristics of both fluidized and packed beds. The primary advantage of magnetically stabilized beds (MSFBs) is the combination of low-pressure drops of fluidized beds with the bubble-free operation at high gas flow rates of packed bed [3-8].

However, the suppression of the solid phase mixing movements is considered as one of the major consequences of the application of magnetic field on a fluidized beds. This consequence becomes very significant if this approach is applied to fluidized beds where exothermic reactions are taking place. In the case of exothermic reactions, temperature control throughout the bed may represent a primary requirement. In magntically stabilized beds, whers heat transfer rate is relatively low compared with fluidized beds, this control could not be attained [9, 10]. The suppression of the solid phase mixing movements could be considered as drawback of magnetic stabilization process. Nevertheless, only a few studies have paid attention to thermal behavior of these systems [11-12]. Lucchesi *et al.* [11] found in tests of bed-to-wall heat transfer, that the MSFBs performance agreed well with literature values for packed beds of the same superficial velocity. Neff and Rubinsky [12] studied the effect of magnetic stabilization on wall-to-bed heat transfer coefficient and found that each flow regime of the magnetized bed is characterized by a different heat transfer rate.

Arnaldos *et al.*, [13] studied the influence of different operating variables on the heat transfer coefficient and on the radial and axial temperature profiles inside the magnetized bed. They proposed a model to calculate the effective thermal conductivity of the bed from experimental data. Arnaldos *et al.* [13] studied the effect of magnetic field stabilization on the temperature distribution for beds with an immersed heating surface under different operating conditions, and proposed a model to calculate the effective thermal conductivity of the bed from experimental data. Recently, Qian and Saxena [14] reported that the heat transfer rates in all flow regimes of the magnetized bed are similar.

In previous studies [15, 16] the effect of a transverse magnetic field on the effect of a transverse magnetic field on the hydro-thermal behavior of fluidized beds with an immersed uniformed surface has been studied. The effect of the magnetic field intensity combined with the effect of gas velocity and particle properties on the thermal behavior of gas fluidized beds was investigated. As an extension, intent of this study is to characterize the effect of a transverse magnetic field and some hydrodynamic parameters on the wall-to-bed heat transfer coefficient in a gas-solid fluidized bed.

EXPERIMENTAL

EXPERIMENTAL SETUP AND MATERIALS:

A schematic diagram of the experimental setup is shown in Figure 1.

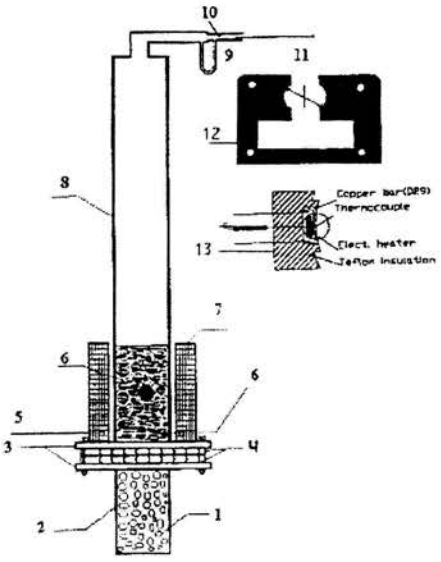

Figure 1: Schematic of the experimental setup: 1. Gas entrance, 2. Polyethylene particles, 3. Flanges, 4. Supporting grid, 5. Heater, 6. Magnetic particles, 7. Magnetic system, 8. Column, 9. Manometer, 10. Orifice, 11. Gas suction, 12. Details of the magnetic sheets, 13- Details of the heater.

The column is constructed from Plexiglas to facilitate visual observations. The column height is 0.9m with 0.07m I.D. At the base of the column, a stainless steel non-magnetic grid of 0.33-mm whole diameter is used to support the solid phase. Below the supporting grid, the gas enters from a calming section filled with polyethylene particles of 1.5-mm dia. This section serves to distribute the gas phase uniformly in the bed. The gas phase is withdrawn from the top of the column using a suction fan. In this way, the gas enters the bed uniformly and at the ambient temperature.

The magnetic system is made of a cast steel core and 1500 copper coils made of a copper wire of 0.9mm diameter. Glass wool was used as an insulator between the layers of coils. The core consists of 180 painted cast steel sheets with 0.9mm thickness. The cast steel sheets were formed as shown in Figure (1-12) in order to house the riser. The net height and weight of the magnetic system are 0.2m and 40kg, respectively. The DC current can be varied from 0 to 5 ampere and the corresponding magnetic field intensity changes from zero to 200 m T. Magnetic particles are prepared in the same manner as described earlier [17]. Some of their characteristics are shown in Table 1. The magnetic particles consist of a ferromagnetic core of magnetite (Fe_3O_4) covered by a stable layer of activated carbon or zeolite by using epoxy resin as an adhesive. These particles are normally fluidized in the absence of the magnetic field.

The heating system (Figure 1-13) consists of a circular plate with a surface area of 6.6×10^{-2} m^2, mounted vertically on the internal wall of the column at 0.06m above the supporting grid and connected by a DC power supply. A copper constantan thermocouple with a digital readout was joined with the heating probe to give the temperature difference between the heater and the inlet gas directly.

PROCEDURE

The effect of radiation heat transfer in this study is neglected. Temperature is measured with a copper constantan thermocouple that gives the difference between the heater and the inlet gas temperature. Gas flow rate was measured using an orifice meter (Armfield, England) located on the line between the suction fan and the top of the column. The magnetic field intensity is measured using Hall probe (Leybolo-Heraeus, Germany).

Heat transfer coefficient is calculated from the following equation:

$$q = h \times A \times \Delta T \qquad (1)$$

Where $q = V^2 / R$

$A = 6.605 \times 10^{-4}$ m^2

ΔT = thermocouple readout.

In this study, experiments were conducted in in two modes of operation:

1. "Magnetizing first" mode of operation, which means that the magnetic field is set at the desired value and applied to a static bed. After that the gas velocity is started. In this mode of operation and before starting to carry out each experiment the bed is fluidized in the absence of the magnetic field for 3 minutes, and followed by slow decrease of the gas flow down to the formation of the initial packed bed.

2. "Magnetizing last " which means that the the bed is fluidized then the magnetic field intensity was varied.

RESULTS AND DISCUSSION

To understand the wall-to-bed heat transfer characteristics in magnetically stabilized beds it is necessary to combine the thermal behavior with the hydrodynamic behavior governed these systems as a result of the presense of a magnetic field. Both the magnetic field intensity and gas superficial velocity have major effects in this behavior.

In magnetically stabilized beds, it is usually noticed that as the superficial gas velocity increases, while maintaining a constant magnetic field intensity, the bed structures shows three distinguished flow regimes: The initial packed bed, the stable expanded bed, and the fluidized bed. The fluidized bed regime starts with the bubbling phase passing through a slugging phase and ends with a homogeneous fluidization of strings of particles. This order of flow regime agrees with that of Penchev and Hristov [18].

It could be noticed that in magnetically stabilized beds, the stabilized bed regime represents an additional regime to the packed bed and the fluidized bed regimes that are usually found in conventional fluidized beds. This stabilized regime is bounded between two transitional velocities. Beyond the first transitional velocity, which demarcates the stabilized bed regime from the packed bed regime, and called the expansion velosity U_e, the pressure drop starts to attain a constant value as the gas velocity

increases and while the bed expands with restricted and fixed particles. At the second transitional velocity, the stabilized bed breaks down and unrestricted movement of the bed particles starts. As a result, the definition of U_{mf} in magnetically stabilized beds represents a matter of argument between the researchers who are concerned in this technology. The properties of the bed regimes under the effect of a magnetic field are described earlier (16).

Bed expansion behavior or bed void fraction, ε, is considered as an important parameter affecting the heat transfer rate in fluidized beds. Beyond the the bed expansion velocity U_e, and as the gas velocity U_g increases, both the bed porosity and the gas turbulence inside the it usually increases. As a result the convection heat transfer coefficient h is expected to increase.

In a previous study [16] it was found that an initial small expansion occurs in the packed bed directly after the application of the magnetic field and before starting the gas flow. This initial expansion increases from 0 to 8% of the initial porosity as the magnetic field intensity increases from 0 to 40m T. This expansion is attributed to the fact that as the bed height is shorter than that of the magnetic system, the field lines tend to stretch up the magnetic particles to cover the whole height of the magnetic system. In the stabilized regime i.e. $U_e<U_g< U_{mf}$, ε rapidly increases as the Reynolds number increases. For example, at B equal 20mT, ε increases from 0.435 to 0.51 as Re increases from 0 to 48. Bed porosity at the onset of fluidization increases from 0.42 to 0.71 as the magnetic field intensity increases from 0 to 40 mT. In the fluidized regime, the bed porosity increases as Re increases in the same manner as in conventional fluidized beds.

Variations of Nusselt number with magnetic field intensity

Figure 2 shows the effect of Reynolds number on Nuselt number for various magnetic field intensities in a bed of ACM3 particles. It is evident that Nuselt number increases as Reynolds number increases but in different rates depending on the magnetic field intensity. For example at 0 magnetic field intensity, Nu directly increases from 2 to 11 as Re increases from 15 to 40. The behavior of the bed changes with Re similar to what happened in conventional fluidized bed. The turbulance of the gas phase and that of the solid phase increases continuously with increasing Re and this increases the heat transfer coefficient and hense Nu. As Re increases beyound 40 the bed should contain large gas bubbles and this reduses the rate of heat transfer and Nu starts to decraese. At a magnetic field of 20 m T where the bed is magnetized no increase in Nu is noticed until Re reaches a value of 23 because very little bed expansion occurs in this regime. As Re increases beyond 23, Nu increases in a similar rate of the unmagnetized bed but with a lower value. This behavior is reffered to the increase in the convective heat transfer rate in the porous stabilized bed. This behavior is attributed to the lower degree of turbulance in the solid phaes as a result of string formation. The solid particles tend to agglomerate in radial chains under the effect of the magnetic field. The movement of the se strings is limitted compared with the unmagnetized particles. As the magnetic field intensity changes to 40 m T, bed expansion is delayed until Re exceeds 45. In this case the onset of fluidization is postponded due to the high magnitizability of the bed. At Re 0of 45 fluidization of large string occur and sudden increase of the Nu is noticed. On the othe hand, at a magnetic field intensity of 50 m T the bed is said to be frozen. No fluidization takes place regardless of the value of the gas velocity. The bed behaves as a packed bed. In this case the slow increase in Nu is attributed to the turbulance in the gas phase only.

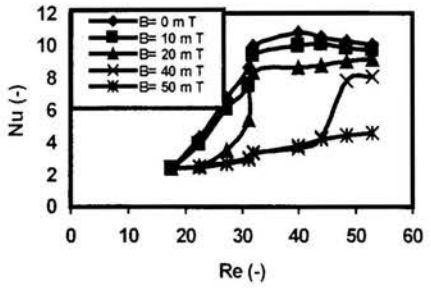

Figure 2: The effect of Reynolds number on Nuselt number at various magnetic field intensities.

Figure 3 shows the variation of Nuselt number with the magnetic field intensity at five different Reynolds numbers of 22.5, 27.5, 32.1, 44 and 52.9 in a bed of ACM3 particles. For a particular Reynolds number, Nuselt number decreases drastically at the onset of stabilization and continues to decrease until the value of B reaches that of the minimum stabilization intensity, B_{fi}. At that point Nu reaches its minimum value. It can be seen that the minimum value of Nu decreases from 5.2 to 3.1 as Re decreases from 52.9 to 22.5. This behavior could be attributed to the fact that the porosity and hence the gas holdup in the frozen bed increases as the gas velocity increases.

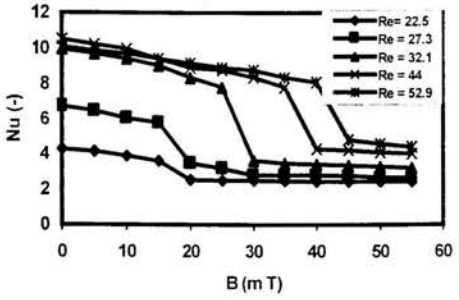

Figure 3: Variation of Nuselt number with magnetic field intensity at various Reynolds numbers.

In the fluidized bed regime (particulate to strings fluidized bed), and as the magnetic field intensity increases, the heat transfer coefficient and hence Nu number slightly decreases owing to the particles agglomeration and the reduction of the intensity of particles mixing. This decrease continues at the same rate while passing in the stabilized regime. However, the range of the magnetic field intensity that correspond to the constant rate decrease depends on the value of Re. Higher values of Re cause a wider range of B. In the stabilized regime two processes of opposite effect on heat transfer rate take place: suppression in the solids

movement and reduction in the bubbles size. The effect of solids movement suppression on lowering the heat transfer coefficient is greater than the effect of reduction of the bubble size. As a consequence, a net decrease in the heat transfer rate is noticed.

At the onset of the frozen bed regime where the whole bed behaves as a porous stationary mass, the heat transfer coefficient considerably drops to a certain level depending on the gas velocity. Then it keeps constant as the magnetic field intensity increases.

When comparing these results with those of Neff and Rubinsky [12], who applied an axial magnetic field to a fluidized bed, one finds that h in the present study has higher values. This difference is attributed to the bed porosity, which, in this study increases as the magnetic field intensity increases, while in the former case the opposite behavior takes place. In addition, the rate of change in the heat transfer coefficient while passing from the fluidized to the frozen bed regimes is lower than that in reference No. [12], because in the present case the difference in the gas holdup between the different regimes is relatively low.

Based on the experimental data, The following empirical equation, which represents the relation between the Nuselt number and Reynolds number was obtained:

$$Nu = 1.04\ Re^{0.5}\ (B/Bs)^{-0.1} \qquad (1)$$

The range of parameters in this equation covers Re from 22.5 to 52.9 and B from 5 to 58 m T.

Effect of Gas Superfecial Velocity

The effect of gas superfecial velocity on the heat transfer cpefficient for different particle size is shown in Figs 4, 5, and 6. The applied magnetic fields were 5, 20, and 40 m T in the experiments of of Fig. 4, Fig. 5 and Fig. 6 respectively. It is evident in these figures that the values of h are always higher than those for the smaller particles. The smaller particles have larger surface area for heat transfer. For example at a magnetic field intensity of 5 m T the maximum value of h for a 0.52mm particles was 495 W/m^2K whereas that of 1.1mm particles was 290 W/m^2K. These maxima change at a magnetic field intensity of 40 m T to 350 and 130 W/m^2K, respectively. These differences could attributed to the fact that at a certain value of magnetic field intensity and certain gas velocity, particles of different sizes are found in different flow regimes. For example at a magnetic field intensity of 40mT and a gas velocity of 1.2 m/s, the particles of 0.52mm diameter are completely fluidized and those of 1.1mm diiameter are still packed.

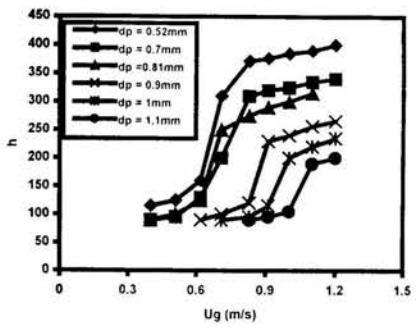

Figure 4: Effect of particles diameter on the heat transfer coefficient at a mgnetic field intensity of 5 mT.

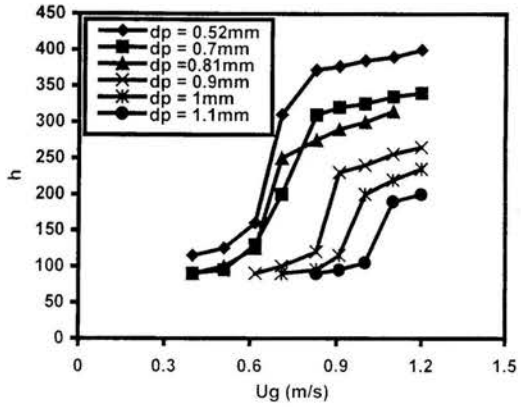

Figure 5: Effect of particles diameter on the heat transfer coefficient at a mgnetic field intensity of 20 mT.

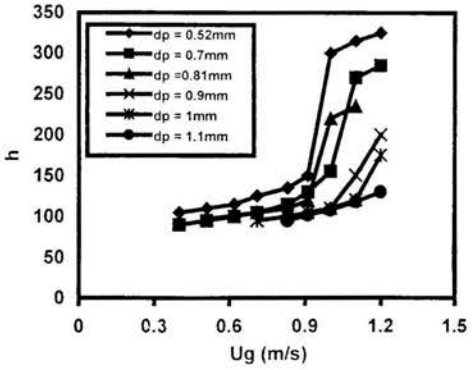

Figure 6: Effect of particles diameter on the heat transfer coefficient at a mgnetic field intensity of 40 mT.

CONCLUSION

The hydrodynamic and thermal behavior of a gas-solid fluidized magnetic stabilized bed under the effect of a transverse magnetic field is investigated. Heat transfer coefficients for a flat vertical heater of a circular cross sectional area and the resulted heat transfer coefficients in the bed were measured in two different modes of operation, magnetizing first and magnetizing last modes.

At constant magnetic field intensity, as the Re number increases Nu number increases for all particle sizes. In addition the bed passes from a packed through a stabilized and finally to a fluidized state. On the other hand, at constant gas superficial velocity, as the magnetic field intensity, increases, Nu number decreases and the bed height slightly increases. In addition the bed passes from a fluidized to a stabilized and finally to a frozen bed regime.

The carried out experiments shows that magnetically stabilized beds may suffer from temperature gradients across the bed especially if they are used to carry out highly exothermic processes. However, these reactors seem to be good candidates to house processes of low heat loads such as bioprocesses.

Table 2:Characteristics of the magnetic particles used.

Type	ρ_b (kg/m^3)	ρ_s (kg/m^3)	d_p (mm)	U_{mfo} (m/s)	B_s (m T	Porosity ε_o (-)
Ac1	1360	2305	0.52	0.39	590	0.41
Ac2	1600	2760	0.7	0.46	590	0.42
Ac3	1750	3020	0.9	0.574	590	0.42
Ac4	1905	3230	1.0	0.690	590	0.41
Osa	1428	2420	0.81	0.512	590	0.41
Z	2100	3500	1.1	0.803	590	0.40

NOMENCLATURE

A surface area of the heater [m^2]
B magnetic field intensity [mT]
B_{fi} minimum stabilization intensity [m T]
B_{msi} magnetic intensity above which a frozen bed exists [mT]
d_p Particle diameter [m]
H_b bed height [m]
H_{bo} initial bed height [m]
M_s saturation magnetic intensity [mT]
U_e minimum expansion velocity [m/s]
U_g gas superficial velocity [m/s]
U_{mf} minimum fluidization velocity [m/s]
U_{mfo} minimum fluidization velocity in the absence of magnetic field [m/s]
U_t transitional velocity [m/s]

Greek letters

ε_o initial bed porosity [-]
ε_s solid holdup [-]
ε_{so} initial solid holdup [-]

REFERENCES:

1. Filippov, M.V; "The Effect of a Magnetic Field on a Ferromagnetic Particle Suspension Bed," Prik. Magnet Latv. SSR, 12, 215 (1960).
2. Liu, Y.A., Hamby R.K., and R.D. Colberg; "Fundamental and Practical Developments of Magneto Fluidized Beds: a Review," Powder Technol., 64, 3 (1991).
3. Pirkle, J.C., P.A. Ruziska and L.J. Shulk, "Circulating Magnetically Stabilized Bed Reactors," Chem. Eng. Comm., 67, 89 (1988).
4. Geuzens, P. And D. Phoenes, "Magnetically Stabilized Fluidization, Part I: Gas and Solid Flow," Chem. Eng. Comm. , 67, 217 (1988).
5. Syutkin, V., and M.K. Bologa, Effect of Magnetic Field in Heat Transfer in Fluidized Bed, Electron Obrab. Mater., 67, 61-67 (1976).
6. Rosensweig, R.E.; Fluidization: Hydrodynamic Stabilization with a Magnetic Field, Science, 204, 57 (1979).
7. Rosensweig, R.E., Magnetic Stabilization of the State of Uniform Fluidization. Ind. Eng. Chem. Fund., 18, 260-265(1979).
8. Al-Qodah, Z., "Performance of a Three-phase Fluidized bed with Immobilized Cells in the Presence of a Transverse Magnetic Field." Ph. D. Thesis, Sofia University of Chemical Technology, Sofia, Bulgaria (1991).
9. Levenspiel, O., and K. Kamholtz, "Enhancing the Characteristics of Magnetically Stabilized Beds," U.S. Part 4 272 893 (1981).
10. Syutkin, V., and M.K. Bologa, Effect of Magnetic Field in Heat Transfer in Fluidized Bed, Electron Obrab. Mater., 67, 61-67 (1976).
11. Lucchesi, P.J., W.H. Hatch, F.X. Mayer, and R.P. Rosensweig, "Magnetically Stabilized Beds: New Gas-solids Contacting Technology," Proc. 10th World Petroleum Congress, Bucharest, Heyden, Philadelphia, PA, 4, 419 (1979).
12. Neff, J.J., and B. Rubinsky, "The Effect of a Magnetic Field on the Heat Transfer Characteristics of an Air-fluidized Bed of Ferromagnetic Particles." Int. J. Heat and Mass Transfer, 26, 1885 (1983).
13. Arnaldos, J., M. Lazaro, and J. Casal, "The Effect of Magnetic Stabilization on the Thermal Behavior of Fluidized Beds," Chem. Eng. Sci., 42, 1501 (1987).
14. Qian, R.Z., and S.C. Saxena, "Heat Transfer from an Immersed Surface in a Magneto Fluidized Bed," Int. Comm. Heat and Mass Transfer, 20(6), 859 (1993).
15. Z. Al-Qodah, M. Al-Hassan, M. Al-Busoul, Hydrodynamic and Heat Transfer Characteristics of an Air Fluidized Bed Utilizing a Transverse Magnetic Field. J. Chin. Chem. Engrs. Vol. 31, No. 2(211-218) 2000.
16. Z. Al-Qodah and M. Al-Busoul, The effect of Magnetic Field on Local Heat Transfer Coefficient in Fluidized Beds with Immersed Surface, J. Heat Transfer, Vol.123(1), (157-161) 2001.
17. Al-Qoda, Z, V. Evanova, E. Dobreva, I. Penchev, J. Hristov and R. Petrov, "Non-porous Magnetic Support for Cell Immobilization," J. Fer. Bioeng. 71 (2), 114 (1991).
18. Penchev, I., and J.Y. Hristov, "Fluidization of Beds of Ferromognetic Particle in a Transverse Magnetic Field." Powder Technology, 62, 1 (1990).

HEFAT2002
1st International Conference on Heat Transfer, Fluid Mechanics, and Thermodynamics
8-10 April 2002, Kruger Park, South Africa
DC1

THE PEBBLE-BED REACTOR: EFFECT OF WALL CHANNELLING ON THE FLOW IN THE CORE

C.G. du Toit**
**Professor
School for Mechanical and Materials Engineering
Potchefstroom University for CHE
Private Bag X6001, Potchefstroom 2520,
South Africa
E-mail: mgicgdt@puknet.puk.ac.za

ABSTRACT

The purpose of this study was to determine the occurrence and the scale of wall channelling in the core of the proposed pebble-bed nuclear reactor. This was done using a finite element approach to solve the one-dimensional momentum equation for the radial distribution of the axial velocity. The results first of all showed that, to obtain useful data, the use of an adequate grid was essential. It was secondly found that due to the non-uniform velocity distribution the coefficients of pebble-bed Ergun equation had to be adjusted to obtain the correct mass flow of rate for the specified axial pressure gradient. Lastly it was concluded that wall channeling does occur in the core and that it can not be neglected. The effect, therefore, that it might have on associated phenomena, such as heat transfer, must be investigated.

INTRODUCTION

The core of the pebble-bed reactor consists of a central cylindrical collection of spherical graphite balls surrounded by an annular collection of spherical fuel balls. The graphite and fuel balls will be added regularly at the top of the reactor and removed at the bottom of the reactor. The flow rate of the balls will translate into an average ball velocity of approximately 4.5 [mm/h]. The pebble-bed reactor can therefore, as a first approximation, be considered as a fixed or a packed bed reactor.

The design of a packed bed is based upon mechanisms of heat and mass transfer, and the flow and pressure drop of the fluid through the bed of solids. The mechanisms in turn are all sensitive to the porosity of the packed bed. Therefore, knowledge of the porosity distribution within a packed bed is important to any rigorous analysis of the transport phenomena in the bed [1]. In a packed bed reactor the porosity varies sharply near the wall, since the geometry of the packing is interrupted there. For flow through a porous medium the permeability increases with the porosity. As a result the velocity profile inside a packed bed is severely distorted near the wall, reaching a maximum in the near-wall region. This phenomenon is known as flow or wall channelling. Wall channelling has a significant impact on heat and mass transfer in packed beds used in chemical reactors [2].

It is therefore important that in the design and analysis of the pebble-bed reactor, the occurrence of wall channeling should be investigated and that the scale of the effect it has on all the associated phenomena in the reactor should also be determined. The variation in the porosity of the core near the wall of the reactor has been recognized. In part 3 of the document on the core design of gas-cooled high temperature reactors [3], the authors discuss the pressure loss due to friction in the pebble bed. They state that in a thin layer near the wall the porosity of the pebble bed is much larger than it is in the core zone of the bed. Due to the strong coupling between the porosity and the pressure loss or gradient, the flow velocity in the wall layer is higher than the velocity in the core zone. From the results of experiments carried out by a number of researchers to determine the reactor diameter to particle diameter ratios versus Reynolds numbers for which it could be said with certainty that no wall influence could be detected anymore, the authors of the document [3] assumed that the influence of the wall channelling could be neglected. The effect that it has on the flow and temperature distribution was therefore not taken into account by Verfondern [4].

As part of an investigation into the movement of the spheres through a pebble bed, Bedenig [5] also determined the porosity of the bed. By slowly filling a model of a pebble bed with water he could determine the variation of the porosity of the bed as a function of the height from the bottom of the reactor. The results show that the porosity near the bottom is large and rapidly diminishes away from the bed until it attains an average or bulk value approximately five sphere diameters away from the bottom. This is confirmed by the investigation of Goodling *et al.* [1] who studied the radial distribution of the porosity in cylindrical beds packed with spheres. They observed that the radial porosity distribution exhibited an exponential variation combined with a damped oscillation. A mathematical expression for the oscillatory variation was fitted by Cohen and Metzner [6].

Vortmeyer and Schuster [7] evaluated the steady-state flow profiles in rectangular and circular packed beds. They solved the Brinkman equation by an equivalent variational method. They extended the validity of the Brinkman equation to higher flow rates by incorporating a slightly modified form of the Ergun pressure loss relation [8]. They also approximated the radial variation of the porosity with a smooth exponential expression. The quite large deviations between the calculated and the measured velocity profiles were attributed to the problems to obtain reliable experimental data. However, the observed trends were similar. They also did some calculations with an oscillatory porosity variation in accordance with the results obtained by Goodling *et al.* [1]. They assumed the Ergun relation for pressure loss to be locally valid according to the drastic variation in porosity. The validity of this assumption is, however, debatable if the origin of the Ergun relation is considered. White and Tien [2] performed a similar analysis using Green's functions to solve the equation for the radial variation of the axial momentum equation.

Kuipers [9] solved the transient continuity and momentum equations for packed beds in two-dimensional Cartesian and axi-symmetric coordinates by discretizing the equations using finite differences and employing an approximate factorisation implicit algorithm. The porosity distribution was modelled using the smooth exponential expression derived by Vortmeyer and Schuster [7], whilst the flow resistance was modelled using the Ergun pressure loss relation [8].

The purpose of this paper is to investigate the occurrence and the scale of wall channelling in the core of the proposed pebble-bed nuclear reactor using a finite element approach to solve the one-dimensional momentum equation for the radial distribution of the axial velocity. The flow will be assumed to be isothermal and fully developed.

NOMENCLATURE

A_1, A_2	coefficients in equation for friction coefficient
C	constant in equation for porosity distribution
D_R	diameter of reactor (m)
E	number of elements
e	element counter
F^e	element force vector
f_i^e	coefficient of element force vector
d_p	diameter of sphere (m)
g_z	gravitational acceleration in axial direction (m/s^2)
i, j	local counters
J	global counter
K^e	element coefficient matrix
k_{ij}^e	coefficient of element coefficient matrix
N	number of global nodal points
n	local number of nodal points
p	pressure (Pa)
Q_L^e, Q_R^e	element flux vectors
q_{Li}^e, q_{Ri}^e	coefficients of element flux vectors
r	radial coordinate (m)
V_0	superficial velocity (m/s)
W_J	nodal value of global axial velocity (m/s)
w	axial velocity component (m/s)
w_j^e	nodal value of local axial velocity (m/s)
w_N	approximate solution for velocity (m/s)
z	axial coordinate (m)

Greek Letters

β	friction coefficient
ε	porosity
ε_0	bulk porosity
Φ	global interpolation function
ψ^e	local interpolation function
ρ_f	density of fluid (kg/m^3)
μ_f	dynamic viscosity of fluid (N-s/m^2)
υ_f	kinematic viscosity of fluid (m^2/s)
τ_w	wall shear stress (N/m^2)

NUMERICAL APPROACH

Governing Equations

Momentum Equation

The steady-state equation for the conservation of momentum in the axial direction for one-dimensional axi-symmetric fully developed flow in a packed bed is given as

$$0 = -\frac{\partial p}{\partial z} - \beta \varepsilon \rho_f w + \frac{1}{r}\frac{\partial}{\partial r}\left[r \varepsilon \mu_f \frac{\partial w}{\partial r} \right] + \varepsilon \rho_f g_z \qquad (1)$$

Radial Porosity Distribution

The radial distribution or profile of the bed porosity ε is given as [7],[9]

$$\varepsilon = \varepsilon_0 \left[1 + C \exp\left(1 - \left[D_R - 2r \right] / d_p \right) \right] \qquad (2)$$

where C is a constant which has to be adjusted according to ε_0 [7] such that $\varepsilon = \varepsilon_0$ at $r = 0$ and $\varepsilon = 1$ at $r = D_R/2$.

Friction Coefficient

The Ergun friction coefficient β for the pebble-bed is given as [3]

$$\beta = \frac{A_1 \upsilon_f}{d_p^2} \cdot \frac{(1-\varepsilon_0)^2}{\varepsilon_0^3} + \frac{A_2 |V_0|}{d_p} \cdot \frac{(1-\varepsilon_0)^{1.1}}{\varepsilon_0^3} \cdot \left(\frac{\mu_f}{\rho_f |V_0| d_p} \right)^{0.1} \qquad (3)$$

The coefficients A_1 and A_2 in Eq. (3) will be discussed later. The superficial velocity is defined as [9]

$$|V_0| = \varepsilon\sqrt{w^2} \qquad (4)$$

Boundary Conditions

To obtain the radial velocity distribution, the momentum equation must be solved subject to the prescribed axial pressure gradient $\partial p/\partial z$ and the boundary conditions

$$w(r = D_R/2) = 0 \qquad (5)$$

at the wall of the reactor and

$$\tau_w(r = 0) = -\mu_f \, \partial w/\partial n = 0 \qquad (6)$$

at the centerline of the reactor.

Galerkin Finite Element Formulation

Let w_N now be the (finite element) approximation to the radial distribution of the axial velocity with

$$w_N(r) = \sum_{J=1}^{N} W_J \Phi_J(r) = \sum_{e=1}^{E}\left[\sum_{j=1}^{n} w_j^e \psi_j^e(r)\right] \qquad (7)$$

Substituting the approximate solution Eq. (7) along with the appropriate weighting function into the weak formulation of Eq. (1) and applying the Galerkin finite element method [10] then leads to the system of equations in matrix form

$$\left[\sum_{e=1}^{E}\left[K^e\right]\right]\{W\} = \left\{\sum_{e=1}^{E}\{F^e\}\right\} + \left\{\sum_{e=1}^{E}\{Q_L^e\}\right\} + \left\{\sum_{e=1}^{E}\{Q_R^e\}\right\} \qquad (8)$$

with the coefficients of the element matrices and the element vectors given as

$$\left.\begin{aligned} k_{ij}^e &= \int_{\Omega_e}\left\{r\varepsilon\mu_f \frac{\partial\psi_i}{\partial r}\frac{\partial\psi_j}{\partial r} + r\beta\varepsilon\rho_f\psi_i\psi_j\right\}dr \\ f_i^e &= \int_{\Omega_e}\psi_i\left\{r\left(-\frac{\partial p}{\partial z}\right) + r\varepsilon\rho_f g_z\right\}dr \\ q_{Li}^e &= \psi_i^e(0)\left[r\varepsilon\overline{\tau}_w\right]_0 \\ q_{Ri}^e &= \psi_i^e(r_o)\left[r\varepsilon\overline{\tau}_w\right]_{r_o} \end{aligned}\right\} \text{ for } i,j = 1,..,n$$

After discretizing the domain into a suitable collection of non-overlapping elements and selecting the appropriate interpolation functions, the integrals over each element can be evaluated and the global equations can be assembled. After the application of the boundary conditions, the set of linear algebraic equations can be solved using any suitable direct or iterative linear equation solver to obtain the values of the velocities at the nodal points. Due to the presence of the velocity in the friction coefficient β (Eq. (3)) the differential equation is non-linear and therefore has to be solved iteratively.

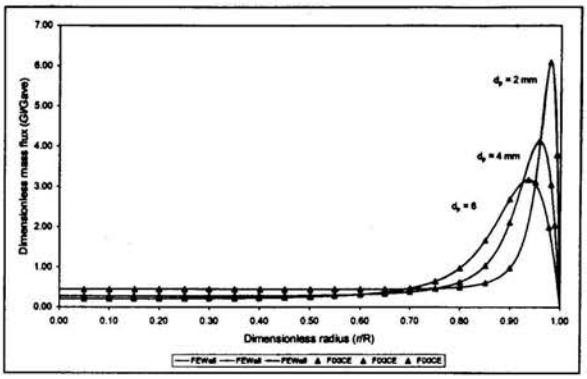

Figure 1: Dimensionless mass flux rate as function dimensionless radius for benchmark cases.

RESULTS

Four sets of results emanating from the study will be discussed. First of all the validity of the finite element code is tested by benchmarking it against the finite difference code of Kuipers [9]. Secondly the applicability of the equation for the pebble-bed friction coefficient is considered. Then in the third place the effect of the fineness of the computational grid is discussed. Lastly the occurrence of wall channeling and its magnitude is dealt with.

Benchmarking

The validity of the one-dimensional axi-symmetric finite element code, FEWall, to calculate the radial distribution of the flow through the core of the pebble bed reactor, was checked by comparing its results for selected test cases with those produced by the two-dimensional axi-symmetric code, FIXICE, by Kuipers [6]. FIXICE calculates the flow distribution in fixed bed reactors.

As test cases the examples given by Vortmeyer *et al.* [7] were selected, except for the fact that cylindrical instead of square reactors were considered. In the case of FEWall the domain was discretized into 512 uniform linear elements, whilst in the case of FIXICE the computational domain consisted of 513 uniformly spaced nodal points. In the case of FEWall the pressure gradient is the driving force and must therefore be specified, whilst in the case of FIXICE the driving force is the inlet mass flow rate (inlet velocity) that must be specified. Figure 1 shows the comparison of the results produced by the

two codes for the dimensionless mass flux as a function of the dimensionless radius. From the good agreement between the results it can be concluded that the results produced by FEWall are valid.

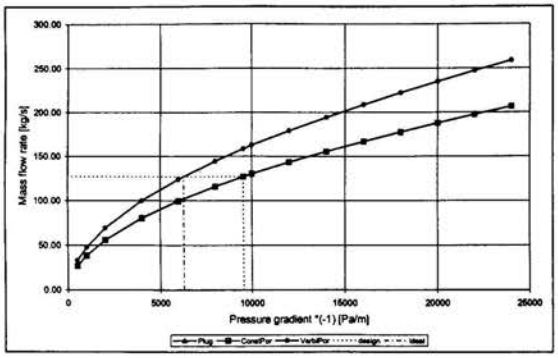

Figure 2: Mass flow rate as function of pressure gradient for constant porosity and variable porosity flows.

Adjustment of Equation for Friction Coefficient

The correlation for the friction coefficient β (which accounts for the pressure gradient or drop due to the presence of the spheres) is based on experimental results in which the pressure drop was measured as a function of the mass flow rate (see e.g. [11]) or vice versa. It was furthermore assumed that the porosity and therefore also the flow velocity were uniform. In [3] it was recommended that the values of the coefficients in Eq. (3) be taken as

$$A_1 = 160 \quad \text{and} \quad A_2 = 3 \tag{9}$$

Figure 2 shows the mass flow rate as a function of the pressure gradient for the pebble-bed core based on the assumption of a uniform porosity using the coefficients in Eq. (9). For any calculation based on a variable porosity to be accurate, it should give the same mass flow rate for a given pressure drop or vice versa as the calculation based on the assumption of a uniform porosity. The mass flow rate as a function of the pressure gradient for the pebble-bed core based on the assumption of a variable porosity using the coefficients in Eq. (9) is also shown on Figure 2. There is a significant discrepancy between the two curves. This is due to the presence of wall channelling resulting in an overshoot near the wall similar to those that can be seen in Figure 1. In order to obtain the same mass flow rate for a given pressures gradient, the correlation for the friction coefficient will have to be adjusted. As a first approximation the constants in the equation for the pebble-bed friction coefficient were both multiplied by the same factor. By trial and error suitable values for the coefficients were found to be:

$$A_1 = 244.3547 \quad \text{and} \quad A_2 = 4.581651 \tag{10}$$

The average difference between the adjusted friction coefficient and the one based on a constant porosity is 0.13% with the maximum being 1.34% for the smallest pressure gradient. Although the effect of the presence of the wall on the friction coefficient has been recognised, see e.g. Cohen and Metzner [6] and Sodré and Parise [11], the analyses were still based on measurements of the overall pressure drop and the associated mass flow rate. A more fundamental understanding is needed of what happens inside the packed bed. The correlation for the friction coefficient, therefore, needs to be investigated in much greater detail using for instance the Lattice Boltzmann method [12].

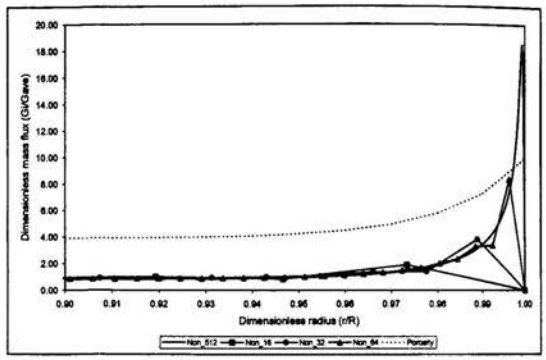

Figure 3: Dimensionless mass flux as function of dimensionless radius for various grids.

Grid Dependence of Solution

A grid dependence study was also performed to determine the minimum number of elements required to obtain a grid independent solution. This was done for both linear and quadratic elements. The values given in Eq. (9) were used for the constants in the equation for the friction coefficient. The investigation was performed using grids consisting of 16, 32, 64, 128, 256, 512 and 1024 uniformly and non-uniformly distributed quadratic elements. The ratio between the lengths of successive elements was taken to be 0.99 with the smallest element against the wall. It was concluded that a grid independent solution could be obtained for 512 non-uniformly spaced quadratic elements. The investigation also highlighted a few other interesting facts.

Figure 3 shows the dimensionless mass flux as a function of the dimensionless radius for grids consisting of 16, 32, 64 and 512 non-uniformly distributed elements. It can be seen that up to 64 elements the mass flux exhibits an oscillatory behaviour near the wall. In the case of the uniformly distributed elements the oscillatory behaviour could, however slight, still be observed on the grid consisting of 256 elements. It can be seen that the magnitude of the overshoot is also considerably less for the coarser grids. Also shown in Figure 3 is the variation of the porosity multiplied by a factor of 10. The overshoot near the wall is clearly linked to the increase in the porosity.

Table 1 summarises the values of the mass flow rate, dimensionless mass flux at the centreline of the reactor and the maximum dimensionless mass flux near the wall for the various grids. The effect of the number and distribution of the elements can be seen. In all the cases the same pressure gradient was specified. The mass flow rate and the maximum mass flux increase asymptotically whilst the mass flux at the centreline decreases asymptotically as the number of elements is increased. The solution for the uniform grid of 1024 elements can not be considered as fully converged, whilst the non-uniform grid of 256 elements can be considered as almost converged.

	16	32	64	128	256	512	1024
	UNIFORM						
$\dot{m}$	132.86	139.78	146.05	151.17	155.02	157.49	158.38
G_i	0.956	0.909	0.870	0.840	0.819	0.806	0.802
G_{max}	1.680	2.923	5.092	8.310	12.691	17.197	17.379
	NON-UNIFROM						
$\dot{m}$	134.41	142.89	151.24	157.83	158.47	158.47	158.47
G_i	0.945	0.889	0.840	0.805	0.801	0.801	0.801
G_{max}	1.884	3.835	8.373	17.827	18.539	18.541	18.541

Table 1: Mass flow rate, dimensionless mass flux at centerline and maximum dimensionless mass flux for various grids consisting of uniform and non-uniform quadratic elements.

A grid dependence study was also performed in the case the benchmark calculations. A set of calculations was also performed where the mass flow rate was kept constant and the corresponding pressure gradients were evaluated. The trends were the same as for the abovementioned cases with the pressure gradient decreasing asymptotically, as the number of elements was increases. From the investigation it could be concluded that the use of an adequate grid is absolutely essential. If the grid is not adequate, apart from the fact the details of the flow near the wall will not be correct, it may also lead to an incorrect mass flow rate and or pressure gradient. If circumstances do not permit the use of an adequate grid, but the overall effect of the packed bed is important, it would be better to specify a uniform porosity.

Bypass Flow

The distribution of the dimensionless mass flux as a function of the dimensionless radius for the design mass flow rate and associated pressure gradient for the pebble-bed core is shown in Figure 4. Only the last 10% of the radius is shown. Also shown on the figure, as a dashed line, is the average dimensionless mass flux.

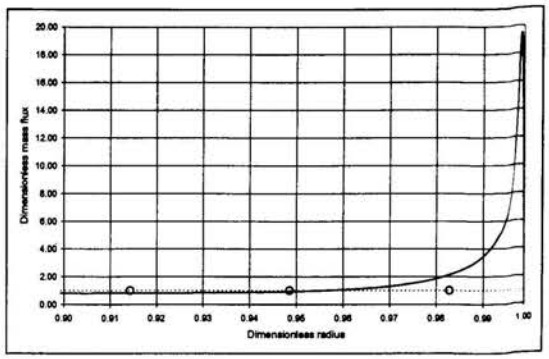

Figure 4: Dimensionless mass flux as function of dimensionless radius for design mass flow rate.

Over approximately the first 80% of the radius of the core the mass flux is only 80% of the average (or plug flow) value. The mass flux then gradually increases until it shoots up near the wall to reach a value of 19.5 times the average dimensionless mass flux. Integrating the mass flux distribution from the centerline of the core to determine the cumulative mass flux distribution revealed that: 51.5% of the mass flow passes through the last 20% of the radius; 35% through the last 10% of the radius; 27.3% through the last 5% of the radius; and 20% through the last 2% of the radius. The mass flux exceeds the average mass flux at 0.956 of the dimensionless radius. If the area under the curve from the point where the dimensionless mass flux exceeds 1.0 is calculated, the quantity obtained is defined as the bypass flow according to Vortmeyer *et al.* [7]. It is also known as wall channeling according to Kuipers [9]. In the current case the bypass flow was found to be 26.2%. It should be remembered that apart from the fact that the largest velocities occur near the wall, this also coincides with the larger radial positions and therefore the larger annular area. If the mass flux distribution had been uniform, only 8.61% of the mass flow would have passed through the last 4.4% of the radius. The percentage bypass flow as a function of the Reynolds number based on the sphere diameter and average superficial velocity is shown in Figure 5. As the Reynolds number decreases the percentage bypass flow slowly decreases as well until it increases sharply. This is in accordance with what had been found by Vortmeyer *et al.* [7]. It can therefore be concluded that in the case of the pebble-bed reactor wall channeling can not be neglected and that it needs to be investigated in more depth.

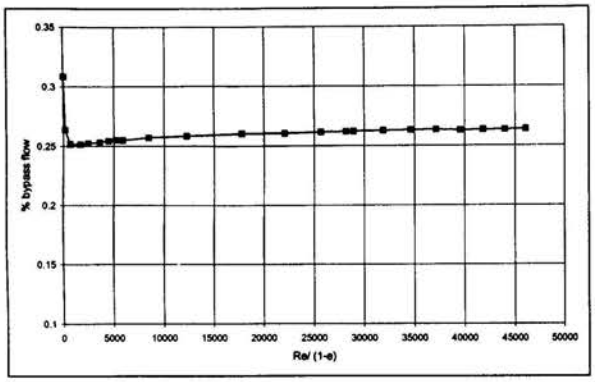

Figure 5: Percentage bypass flow as function of Reynolds number.

CONCLUSION

A one-dimensional axi-symmetric finite element model was developed to study the occurrence and scale of wall channeling in the core of the proposed pebble-bed nuclear reactor. The analysis was performed under the assumption that the flow could be considered as isothermal and fully developed.

The study first of all revealed that the pebble-bed Ergun equation for the friction coefficient had to be adjusted to obtain the correct mass flow rate for the prescribed pressure gradient. This is due to the fact that the original correlation had been derived under the assumption of a uniform velocity distribution through the core.

The study secondly showed that the use of an adequate grid is absolutely essential to obtain accurate results. The use of an inadequate grid may not only give incorrect detail of the flow near the wall, but may also lead to an incorrect estimate of the mass flow rate and or pressure gradient.

Lastly it was concluded that in the case of the pebble-bed wall channeling could not be neglected and that it needs to be investigated in greater depth. The effect, therefore, that it might have on associated phenomena must also be determined.

In order to ensure the validity of the analysis the following also needs to be addressed. The porosity distribution in the core must be characterized accurately due to the impact that it has on the flow distribution. Secondly the correlation for the friction coefficient needs to be investigated in much greater detail, using for instance the Lattice Boltzmann method, to determine a more consistent formulation for two- and three-dimensional models. Lastly, in order to validate the results, suitable experiments must be devised to measure the velocity distribution in a packed bed.

ACKNOWLEDGMENTS

This work was carried out in association with M-Tech Industrial on contract for PBMR (Pty) Ltd.

REFERENCES

[1] Goodling, J.S., Vachon, R.I., Stelpflug, W.S. and Ying, S.J., 1983, "Radial porosity distribution in cylindrical beds packed with spheres," Powder Technology, Vol. 35, pp. 23-29.

[2] White, S.M. and Tien, C.L., 1987, "Analysis of flow channeling near the wall in packed beds," Wärme- und Stoffübertragung, Vol. 21, pp. 291-296.

[3] Kerntechnische Ausschuss, 1980, KTA 3102.3: "Auslegung der Reaktorkerne von gasgekühlten Hochtemperaturreaktoren, Teil 3: Reibungsdruckverlust in Kugelhaufen."

[4] Verfondern, K., 1983, "Numerische Untersuchung der 3-dimensionalen stationären Temperatur- und Strömungsverteilung im Core eines Kugelhaufen-Hochtemperaturreaktors," Jül – 1826, Institut für Reaktorentwickelung, Kernforschungsanlage Jülich GmbH.

[5] Bedenig, D., 1966 "Experimentelle Untersuchungen zum Strömungsverhalten eines Kugelhaufens im Hinblick auf den Brennelementkreislauf im Core eines Kugelhaufenreaktors," Institut für Reaktorentwickelung, Kernforschungsanlage Jülich GmbH.

[6] Cohen, Y. and Metzner, A.B., 1981, "Wall effects in laminar flow of fluids through packed beds," AIChE Journal, Vol. 27, pp. 705-714.

[7] Vortmeyer, D. and Schuster, J., 1983, "Evaluation of steady flow profiles in rectangular and circular packed beds by a variational method," Chemical Engineering Science, Vol. 38, pp. 1691-1699.

[8] Bird, R.B., Stewart, W.E. and Lightfoot, E.N., 1960, "Transport phenomena," John Wiley & Sons, New York.

[9] Kuipers, J.A.M., 2000, "Modelling of fluid flow in fixed bed reactors", Short course on Computational fluid dynamics for multiphase flows, Potchefstroom, South Africa.

[10] Du Toit, C.G., 2000, "The student's companion to the finite element method," Classnotes, Potchefstroom University for CHE, Potchefstroom, South Africa.

[11] Sodré, J.R., and Parise, J.A.R., 1998, "Fluid flow pressure drop through an annular bed of spheres with wall effects," Experimental Thermal and Fluid Science, Vol. 17, pp. 265-275.

[12] Inamuro, T., Yoshino, M. and Ogino, F., 1999, "Lattice Boltzmann simulation of flows in a three-dimensional porous structure," Int. J. Num. Meth. Fluids, Vol. 29, pp. 737-748.

HEFAT2002
1st International Conference on Heat Transfer, Fluid Mechanics, and Thermodynamics
8-10 April 2002, Kruger Park, South Africa
GG1

DYNAMIC MODELLING OF HEAT, MASS AND MOMENTUM TRANSFER IN THE PEBBLE BED MODULAR REACTOR

G.P. Greyvenstein**, J.P. van Ravenswaay and P.G. Rousseau**
**Professor
Faculty of Engineering
Potchefstroom University for CHE
Private Bag X6001, Potchefstroom 2520,
South Africa
E-mail: dingpg@puknet.puk.ac.za

ABSTRACT

In this paper the development of a system simulation model that can predict the dynamic behaviour of the Pebble Bed Modular Reactor (PBMR) will be described. The model predicts the transient mass, momentum and energy transfer in all components in a coupled manner. Very important is that the nuclear reactor and heat exchangers are not treated as lumped systems but as 2-D distributed systems. This allows one to take full account of the thermal inertia of the system. Another feature of the model is that it can deal with conduction heat transfer through solid structures.

The paper will focus on the overall modelling approach and the simultaneous solution of the mass, momentum and energy equations.

A few cases emanating from a benchmark study are presented in this paper. This includes the sudden closure of a valve in a pipeline, transient heat transfer through a reservoir wall and transient heat transfer in the recuperator.

INTRODUCTION

The Pebble Bed Modular Reactor (PBMR) is a new type of high temperature gas nuclear reactor currently being developed by the company PBMR (Pty.) Ltd. in South Africa. The heat released in the nuclear reactor is converted to work in a recuperative Brayton Cycle.

When designing a plant such as the PBMR one must not only be able to predict the steady-state performance of the system as a whole (including all the heat transfer equipment) but also the dynamic behaviour of the system. This is necessary for the design of the operating procedures and control system.

Systems simulations of complete systems such a power plants present unique challenges in dealing with issues such as speed, stability, accuracy, flexibility and the interfacing of different types of components such as turbines, compressors, valves and heat exchangers.

With simulating complete systems the major objective is not to model the processes in each component in great detail but to accurately predict the performance of the system as a whole. However, with the modelling of sub-systems one must avoid over simplifications that may negatively impact the accuracy of the overall system simulation.

In this paper the development of a system simulation model, which can predict both the steady state and the dynamic behaviour of the PBMR, is discussed. The model predicts the transient mass, momentum and energy transfer in all components in a coupled manner. Very important is that the nuclear reactor and heat exchangers are not treated as lumped systems but as distributed systems. This allows one to take full account of the thermal inertia of the system. Another feature of the model is that it can deal with conduction heat transfer through solid structures.

NOMENCLATURE

d	mass source
E	energy transfer to node or element i.e. heat transfer to element minus shaft work
f	$f(\rho, Q)$, frictional pressure drop as function of ρ and Q
g	gravitational acceleration
h	enthalpy
m	mass
$\dot{m}$	mass flow rate
p	pressure
Q	volumetric flow rate
r	continuity error
s	value which indicates whether the positive flow direction of an element is directed toward a node or away from the node with $s=1$ towards the node and $s=-1$ away from the node
t	time
T	temperature
V	volume
x	length
z	elevation

Greek Letters

α	time integration weighing factor
ρ	density
Δ	increment

Subscripts

amb	ambient condition
i	node

j branch

Superscript

o previous time level

NETWORK APPROACH TO MODELLING OF THERMAL-FLUID SYSTEMS

The approach that will be followed is a general network approach where components such as compressors and heat exchangers are represented by one-dimensional elements. Elements, denoted by circles, can be connected at their end points to form any arbitrary network as shown in Figure 1. The end points of elements are called nodes and are denoted by squares.

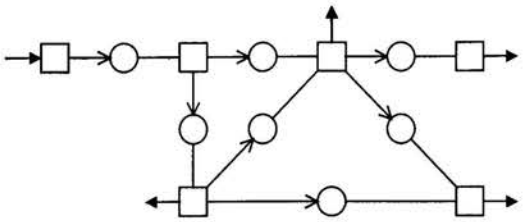

Figure 1: Arbitrary network created by connecting elements at common nodes.

An important feature of the model is that elements such as pipes, heat exchangers and the reactor, although depicted on the systems level as single elements or pairs of elements, can be discretized into sub-networks. Networks can therefore be embedded within networks thereby enabling the model to treat complex elements as distributed systems rather than lumped systems.

Consider for instance the recuperator depicted on the systems level as two associated elements as shown in Figure 2.

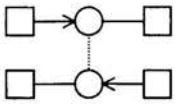

Figure 2: Recuperator depicted as a pair of associated elements on the systems level.

Internally the recuperator is discretized as shown in Figure 3.

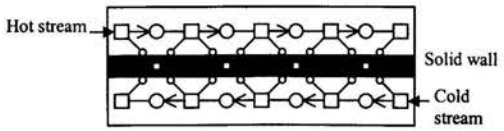

Figure 3: Discretization of the recuperator.

In Figure 3 the smaller circles denote convective heat transfer links while the smaller squares denote temperatures nodes in the metal separating the hot and cold streams.

The network approach allows for the discretization of more complex components such as shell and tube heat exchangers. Figure 4 shows the discretization of part of a shell and tube heat exchanger. As in the previous figure larger circles and squares denote flow elements and nodes respectively while smaller circles and squares denote convective heat transfer links and metal temperatures respectively.

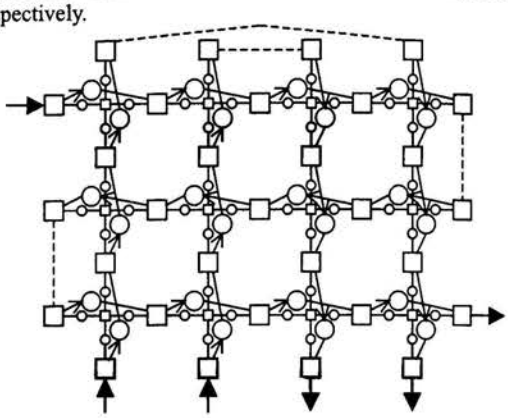

Figure 4: Discretization of a shell-and-tube heat exchanger.

Figure 5 shows the discretization scheme for the pebble bed reactor. Again the larger circles and squares denote flow paths while the smaller open circles denote convective heat transfer links to the surface of the fuel pebbles (denoted by the smaller open squares). The solid circles and squares denote conductive heat paths inside the pebbles while the semi-solid circles denote radiation and convective heat transfer in the packed pebble bed.

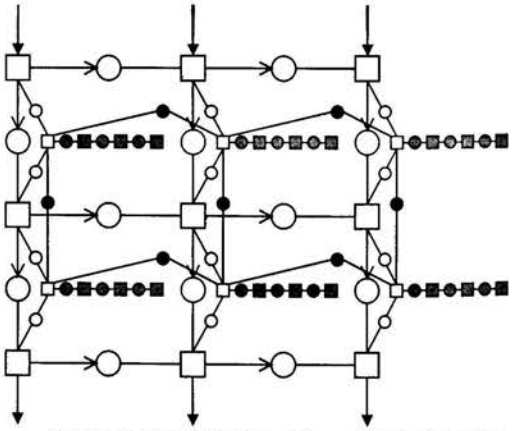

Figure 5: Discretization of the pebble bed reactor.

The model can also handle 2-D conductive heat transfer structures connected to flow elements. The discretization of these elements is beyond the scope of this paper.

NUMERICAL APPROACH

The numerical method, which can be described as an implicit pressure correction method (IPCM), has been described elsewhere by the author with reference to single pipe lines [1]. Following is a brief explanation of the method with

reference to unstructured meshes as encountered in generalised networks.

Governing Equations

The equations governing the solution of mass flows, pressures and temperatures are the continuity, momentum and energy equations.

Consider a general node i with J branches as shown in Figure 6.

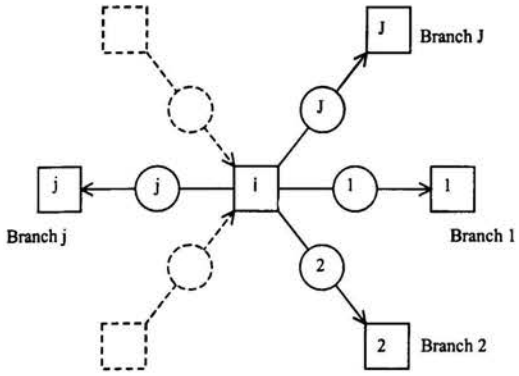

Figure 6: General node with neighbouring nodes connected through branch elements.

The continuity equation for node i can be expressed as.

$$\forall_i \frac{\partial \rho_i}{\partial t} = \sum_{j=1}^{J} \rho_j Q_j s_j + d_i \qquad (1)$$

where s_j is the 'sign' of element j with $s_j = 1$ if the positive flow direction of element j is from node j to node i and $s_j = -1$ if the positive flow direction is from node i to node j

The momentum equation for element j can be written in the following form:

$$f(\rho_j, Q_j) + \frac{\rho_j \Delta x}{A} \frac{\partial Q_j}{\partial t} + s_j (p_i - p_j) = 0 \qquad (2)$$

The energy conservation equation for node i is given by:

$$\frac{\partial (m_i h_i)}{\partial t} - \forall_i \frac{\partial p_i}{\partial t} = \sum_{in,j} \left[s_j \dot{m}_j (h_j + g z_j) + \dot{E}_j \right] + d_i^+ (h_{amb} + g z_i) + (h_i + g z_i) \left(\sum_{out,j} s_j \dot{m}_j - d_i^- \right) + \dot{E}_i \qquad (3)$$

Solution algorithm

When solving the set of equations (1) to (3) one can either use an explicit method, such as the two-step Lax-Wendroff method or the Method of Characteristics, or an implicit method. The advantages of explicit methods are that they are generally simpler to program and faster than implicit methods per time step. The stability of explicit methods is, however, governed by the Δx-Δt relationship, which implies that Δt will be determined by the shortest length increment in the system. This usually results in very small time steps, which makes explicit methods very slow when calculating slow transients or steady-state flows where many time steps are required to cover the time period under interest. Since most transient simulations require the steady-state solution as the initial condition, the speed advantage of explicit methods per time step is cancelled by the fact that many time steps are required to calculate the steady-state condition.

The main advantage of implicit methods is that they are formally unconditionally stable, which means that the restrictive Δx-Δt relationship that applies to explicit methods, does not apply to implicit methods. Although accuracy may be lost when using large time steps, most of the transients that need to be analysed in control studies can be classified as slow transients. For slow transients one can usually use time steps much larger than that predicted by the Δx-Δt relationship without loss of accuracy. It was therefore decided to follow an implicit approach.

The method used to solve the flow and pressure fields can be classified as a simultaneous node pressure correction method. Following is a brief description of the method. Integration of (1) over a time step Δt yields

$$\forall_i \left(\frac{\rho_i - \rho_i^o}{\Delta t} \right) = \alpha \left(\sum_{j=1}^{J} \rho_j Q_j s_j + d_i \right) + (1-\alpha) \left(\sum_{j=1}^{J} \rho_j Q_j s_j + d_i \right)^o \qquad (4)$$

where terms with the superscript o are evaluated at the previous time level and terms without a superscript are evaluated at the new time level. α is a weighing factor between the new and old time levels. When $\alpha = 1$ the scheme becomes fully implicit and when $\alpha = 0$ the scheme becomes explicit. When $\alpha = 0.5$ the scheme is equivalent to the Crank-Nicholson time integration scheme, which is second order accurate in time.

The continuity error at node i can therefore be expressed as:

$$r_i = \alpha \left(\sum_{j=1}^{J} \rho_j Q_j s_j + d_i \right) + (1-\alpha) \left(\sum_{j=1}^{J} \rho_j Q_j s_j + d_i \right)^o - \forall_i \left(\frac{\rho_i - \rho_i^o}{\Delta t} \right) \qquad (5)$$

Integration of (2) over a time step Δt yields:

$$\alpha \left[f(\rho_j, Q_j) + s_j (p_i - p_j) \right] + (1-\alpha) \left[f(\rho_j, Q_j) + s_j (p_i - p_j) \right]^o + \frac{\rho_j \Delta x}{A} \left(\frac{Q_j - Q_j^o}{\Delta t} \right) = 0 \qquad (6)$$

where $f = f(\rho, Q)$ such as the Darcy-Weisbach equation which expresses the frictional pressure drop in terms of density and volumetric flow rate.

Since the flow field is related to the pressure field through (6) we can write that

$$r_i = r_i(p_i,..., p_n) \tag{7}$$

for all nodes in the network.

According to the Newton-Raphson method when there are n equations to be satisfied $[r_1(p_1,...,p_n) = 0,...,r_n(p_1,...,p_n) = 0]$ and n unknowns $(p_1,...,p_n)$ to be solved for, the set of improvements $(\Delta x_1,...,\Delta x_n)$ is the solution of the set of simultaneous linear equations:

$$r_i + \sum_{k=1}^{n} \frac{\partial r_i}{\partial p_k} \Delta p_k = 0 \qquad i = 1,2...n \tag{8}$$

Substitution of (5) into (8) and assuming constant densities we get:

$$r_i + \alpha \left(\sum_{j=1}^{J} s_j \rho_j \frac{\partial Q_j}{\partial p_i} - \frac{\forall_i}{\Delta t} \frac{\partial \rho_i}{\partial p_i} \right) \Delta p_i + \alpha \sum_{j=1}^{J} s_j \rho_j \frac{\partial Q_j}{\partial p_j} \Delta p_j = 0 \qquad i = 1,2...,n \tag{9}$$

Using (6) to evaluate the $\partial Q/\partial p$ terms in (9) we get

$$\frac{\partial Q_j}{\partial p_i} = -\frac{s_j}{\frac{\partial f_j}{\partial Q_j} + \frac{\rho_j \Delta x_j}{\alpha A_j \Delta t}} \tag{10}$$

and

$$\frac{\partial Q_j}{\partial p_j} = \frac{s_j}{\frac{\partial f_j}{\partial Q_j} + \frac{\rho_j \Delta x_j}{\alpha A_j \Delta t}} \tag{11}$$

The term $\partial\rho/\partial p$ in (9) can be evaluated with an equation of state Substitution of (10) and (11) into (9) leads to an equation, which can be solved for the pressure corrections. The pressure corrections are now applied to the pressures at the previous time level to give an updated pressure field at the new time level. Following the updating of pressures, the flow field is corrected using (6). The process is repeated until the flow and pressure field are sufficiently converged at the new time level. Next the temperature field is solved (as will be discussed later) after which the process of alternately solving the flow/pressure fields and temperature fields is repeated until convergence. This gives the solution of flows, pressures and temperatures at the new time level. The time is now progressed to the new level and the whole process repeated. Although the algorithm seems laborious, convergence is quite fast and robust.

Equation (3) can be written in the following form:

$$\frac{\partial (m_i h_i)}{\partial t} - \forall_i \frac{\partial p_i}{\partial t} = B_i \tag{12}$$

which when integrated over a time step gives

$$\frac{m_i h_i - m_i^o h_i^o}{\Delta t} - \forall_i \frac{p_i - p_i^o}{\Delta t} = \alpha B_i + (1-\alpha) B_i^o \tag{13}$$

Written in the proper form Eq. (13) gives an equation, which can be solved for the enthalpy field. Using thermodynamic relationships the enthalpy values can be converted to temperatures.

RESULTS

A few examples emanating from a benchmark study will be presented in this section.

Pressure waves in a pipe due to the sudden closure of a valve

The first example is the simulation of pressure pulses due to the sudden closure of a valve at the downstream end of a 20 m, 0.5 m diameter pipe. The fluid is helium. The simulation starts with the steady-state solution in which the inlet pressure is 700 kPa, the inlet temperature is 283 K and the outlet pressure is 680kPa. This gives an outlet Mach number of 0.21 prior to the closing of the valve. A constant friction factor of 0.02 was used while the pipe was divided into 20 increments.

Figure 7 shows the pressure variation at the downstream end of the pipe for the case of adiabatic flow. The results of the following cases are presented: the present method with a time integration factor $\alpha = 1$, the present method with $\alpha = 0.6$, and the two-step Lax-Wendroff method [2], which is a second order explicit method. A time step of 0.0009 was used, which is approximately 90 percent of that prescribed by the Courant condition [2].

The two-step Lax-Wendroff (LW) method and present method with $\alpha = 0.6$ compare very well. The present method with $\alpha = 1$ exhibits a larger dampening of the pressure wave. This is due to the numerical approximation error of the time derivative term. This error cannot be reduced by refining the grid spacing, as α has no effect on the accuracy of the spatial derivative term. An obvious method to reduce the numerical approximation error is to decrease the time step. This will, however, slow down execution time. A better approach is therefore to decrease the value of α.

With $\alpha = 1$ the present method is only first order accurate in time while it is second order accurate when $\alpha = 0.5$. The method, however, becomes unstable for α-values close to 0.5 and it was found that a α-value of 0.6 offers a good compromise between accuracy and stability.

The execution times of the two methods for a 2 second simulation period on a 386 PC were as follows: two-step Lax-Wendroff method, 0.8 s; and the present method, 24 s. This implies that the present method is approximately 30 times slower than the two-step Lax-Wendroff method. It should, however, be kept in mind that the present example represents a fast transient case where the time step had to be made approximately the same as that of the two-step Lax-Wendroff method to achieve the same level of accuracy. However, in the case of slow transients the time step of the implicit method can be made much larger than that of the two-step Lax-Wendroff without significant loss of accuracy, which makes the implicit method faster than the explicit method in the case of slow transients.

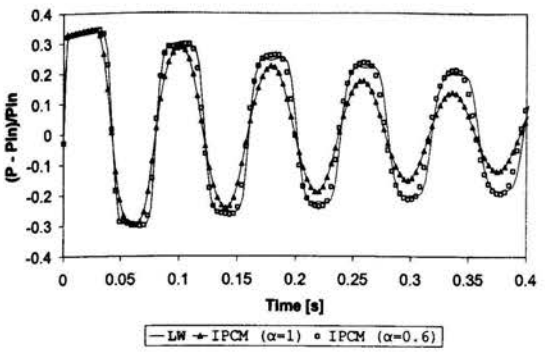

Figure 7: Variation of pressure at the end of a 20 m long, 0.5 m diameter pipe due to the sudden closure of a valve at the downstream end of the pipe for the case of adiabatic flow.

Heat transfer through a reservoir wall due to varying ambient conditions

In this example a cylindrical reservoir of 10 m^3, with water flowing through at a constant rate of 5kg/s at 323.15 K is considered. The reservoir wall consists of three layers with characteristics as shown in Table 1. The outside of the reservoir is exposed to air at 373.15 K.

Starting at steady-state conditions the outside convection temperature is varied with a step function from 273.15 K to 373.15 K for 100-second intervals.

Figure 8 shows the temperatures variation with time for the outside, middle and inside of the reservoir respectively. The IPCM results are compared with an analytical solution (BM). As can be seen the results correlate well.

Layer	Thickness [m]	λ [W/ m^2k]	ρc_p [Kj/ m^3K]	Outside Area [m^2]
1	0.02	20.0	2000	10.1
2	0.03	30	1500	10.25
3	0.04	40	3000	10.45

Table 1: Layer properties

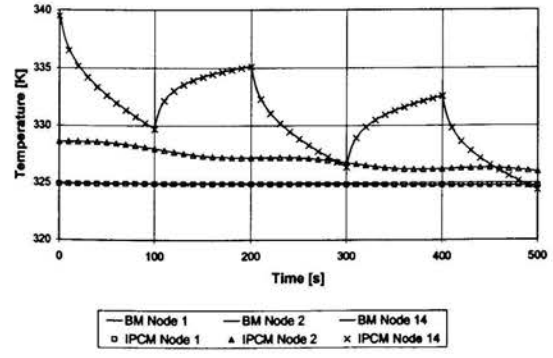

Figure 8: Temperature transient in a reservoir wall due to varying ambient conditions.

Temperature transient in a recuperator

In this example a recuperator with a total heat transfer area of 300 m^2 and a thermal capacitance of 9 kJ/K is considered. The hydraulic diameter and cross flow area of both conduits are 0.5 m and 0.1963 m^2 respectively. Both the hot and cold fluids are helium at an inlet pressure of 700 kPa and an outlet pressure of 670 kPa. Initially the total inlet temperature of both streams is the 300 °C. Starting at steady-state conditions the total inlet temperature of the hot stream is stepped to 500 °C at time t=0 s.

Figure 9 shows the outlet temperatures with time of the hot and cold streams for a counter flow arrangement. The results of the IPCM are compared to that of the two-step Lax-Wendroff (LW) method.

The LW method shows a fluctuation in the hot outlet temperature shortly after the beginning of the transient. After about 0.03 s the curve becomes smooth with a very good agreement between the IPCM and the LW method.

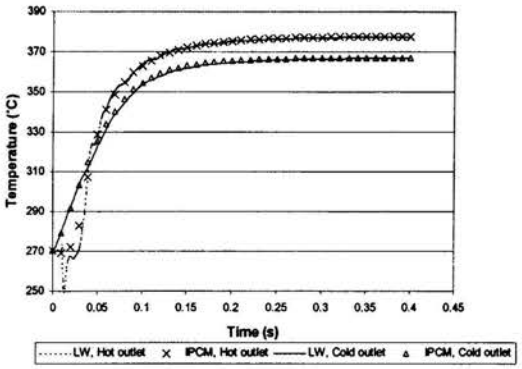

Figure 9: Recuperator exit temperatures due to a temperature step at the inlet of the hot stream for the case of counter flow.

Figure 10 shows the outlet temperatures with time of the hot and cold streams for a parallel flow arrangement. Again the agreement between the IPCM and the LW method is very good apart from the temperature fluctuation of the LW method at the start of the transient.

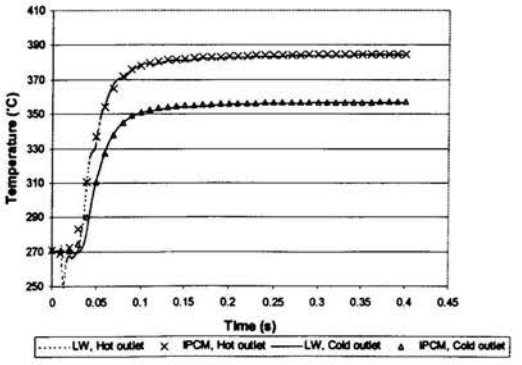

Figure 10: Recuperator exit temperatures due to a temperature step at the inlet of the hot stream for the case of parallel flow.

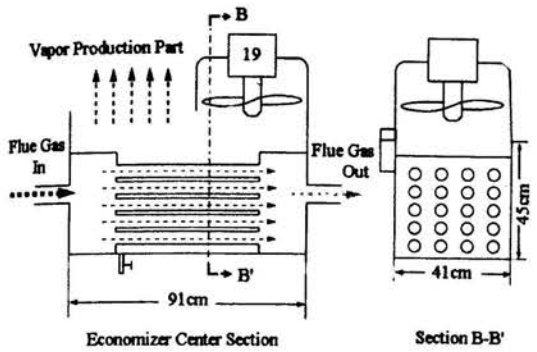

Fig. 4 Economizer Sections

If O_2 is supplied as airflow, N_2 should be accounted for the reaction equation.

$$n_A \cdot C_{18}H_{38}(l) + n_B(air) + n_C(air) = n_A \cdot 79/21 \cdot 55/2 \cdot N_2(g) + n_A \cdot 19H_2O(g) + n_A \cdot 18CO_2(g) + (n_B - 100/21 \cdot 55/2 \cdot n_A + n_C)(air) \quad (2)$$

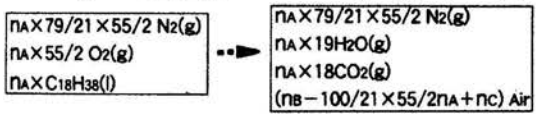

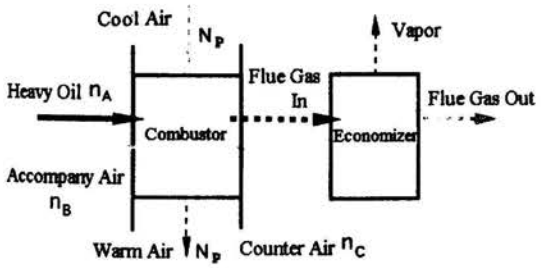

Fig. 5 Material Balance Block Diagram

3.2 Heat Balance Equations

Heat balance equation should be given to evaluate the system, according to the heat balance block, as shown in Fig. 6. If the heavy oil enthalpy, H_A, the accompany air flow enthalpy, H_B, the counter air flow enthalpy, H_C, the flue gas enthalpy, H_D, the heat amount transferred to warm air, Q_P, the heat recovery of the economizer, Q_q, are respectively defined, the energy balance become as follows.

$$H_A + H_B + H_C = H_D + Q_p + Q_q \quad (3)$$

This is total heat balance equation and used to discuss the results of experiment. If substituting $H_i = H_A + H_B + H_C$, $H_o = H_D$ and $Q = Q_p + Q_q$, we can get simpler familiar equation such as;

$$-(H_o - H_i) = Q \quad (4)$$

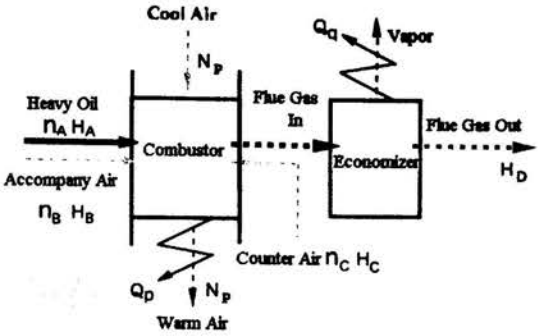

Fig. 6 Heat Balance Block Diagram

3.3 Definition of Performance for the Heating System

The heat recovery Q_p of the warm air heated by the heat transfer surface of the periphery of combustor should be presented for supply fuel oil consume, W_A, or the theoretical heat formation, ΔH, to evaluate the heating system as follows.

Performance Factor of Heating System η

$$\eta = Q_p / W_A \quad (5)$$

Heat Efficiency α

$$\alpha = Q_p / \Delta H \quad (6)$$

Taking account of heat recovery Q_q from economizer, these should be modified;

$$\eta' = (Q_p + Q_q) / W_A \quad (7)$$

$$\alpha' = (Q_p + Q_q) / \Delta H \quad (8)$$

Combustion Efficiency β

As the combustion efficiency is taken account for total heat release ΔH, it should be expressed for including flue gas energy Q_D.

$$\beta = (Q_p + Q_q + Q_D) / \Delta H \quad (9)$$

4. Results and Discussion

4.1 Properties and Flow Rate

(1) Heavy Oil A

We name this supplied heavy oil "A". The formula of fuel oil is assumed $C_{18}H_{38}$ as stated previous section. The calculated heat formations are respectively presented as;

Upper heat formation $\Delta H_{C,H}$ =-11697 (kJ/mole)
Lower heat formation $\Delta H_{C,L}$ =-10861(kJ/mole)
Standard heat formation $\Delta H_{f,C_{18}H_{38}(l)}$ =-816.2(kJ/mole)

Heavy Oil Supply n_A

This is calculated as;

$$n_A = 8.7(l/h) = 8.7 \cdot 0.776 = 6.7512(kg/h)$$
$$= 1.8753 \cdot 10^{-3}(kg/s) = W_A$$
$$= 7.369 \cdot 10^{-3}(mole/s) \quad (10)$$

Enthalpy of Heavy Oil H_A

This is given in general as follows.

$$H_A = n_A(\Delta H_{f,C_{18}H_{38}} + \int_{298}^{t_A} Cp_A \, dt) \quad (11)$$

From the estimation formula given by Pachaiyappan [4], Cp_A is calculated as;

$Cp_A = 0.873 \cdot 254.5^{-0.113}$ (cal/g·℃)

$= 479.52$ (J/mole·℃) (12)

Enthalpy is calculated as;

$$H_A = 7.369 \cdot 10^{-3} \{(-1675.14) + \int_{25}^{7} 479.52 \cdot 10^{-3}\, dt\}$$

$$= 7.369 \cdot 10^{-3} \{(-1675.14) + (-8.631)\}$$

$$= -12.410 \text{ (kJ/s)} \quad (13)$$

(2) Flue Gas

The measured components are respectively O_2; 13.3%, CO_2; 5.6%, CO; 212ppm, NOx: 6ppm. Insoluble components are mainly guessed N_2 (g) and H_2O(g). However, Hydro-carbon might be contained.

Outflow of Flue Gas n_D

This is calculated with substituting the data of measurement from the state equation.

$$n_D = P_D V_D / RT_D$$

$$= (101.3 \cdot 10^3 \cdot 106.03 \cdot 10^{-3}) / (8.314 \cdot 372)$$

$$= 3.473 \text{ (mole/s)} \quad (14)$$

Here, flue pipe diameter; d_D=10cm=0.1m, section area; $a = \pi/4 \cdot 0.1^2 = 7.854 \cdot 10^{-3}$($m^3$), temperature; T_D=372K, velocity; u_f=13.5m/s, flowrate of volume; $V_D = u_f \cdot a = 106.03 \cdot 10^{-3}$($m^3$/s), P_D=1(atm)=101.3(kPa), R=8.314(N·m/mole·K).

The flow rates of compositions in flue gas are respectively calculated as follows.

O_2 : 3.473(mole/s) ·13.3/100=0.461909(mole/s)

CO_2: 3.473(mole/s)·5.6/100=0.194488(mole/s)

CO_2: 3.473(mole/s) ·212/10^6=0.00073628(mole/s)

NO_x: 3.473(mole/s) ·6/10^6=0.00002084(mole/s)

Enthalpy of Flue Gas H_D

If we define χ as molecular fraction, the enthalpy is presented as;

$$H_D = n_D \{(\chi_{N2} \cdot C_{pN2} + \chi_{O2} \cdot C_p O_2 + \chi_{CO2} \cdot C_{pCO2} + \chi_{H2O} \cdot C_{pH2O} + \chi_{res} \cdot C_{pRes}) \cdot (t_D - 25) \cdot 10^{-3} + (\chi_{CO2} \cdot \Delta H_{f,CO2} + \chi_{H2O(g)} \cdot \Delta H_{f,H2O} + \chi_{res} \cdot \Delta H_{f,res})\} \quad (15)$$

This calculation is impossible because residuals are uncertain.

Heat Taken Away by Flue Gas Q_D

If atmosphere temperature 7℃ is referred, this is given as;

$$Q_D = n_D\, Cp_D (t_D - 7) \cdot 10^{-3} \quad (16)$$

(3) Warm Air N_p

Probe of hotwire anemometer was set to measure the velocity downstream of the duct inlet. From the state equation $P_p V_p = N_p R T_p$,

$$N_p = (101.\ 10^3 \cdot 2.8665) / \{8.314 \cdot (17+273)\}$$

$$= 120.4 \text{(mole/s)} \quad (17)$$

Here, duct diameter; d_p=53(cm)=0.53(m), section area; $a_p = \pi/4 \cdot 0.53^2 = 0.2205$($m^2$), velocity; u_p=6.5(m/s), warm air temperature;17℃, P_p=1(atm)=101.3(kPa), R=8.314(Nm/mole·K).
flow rate of volume; $V_p = 2 \cdot 0.2205 \cdot 6.5 = 2.8665$($m^3$/s)
(duct outlet is separated to both sides).

Warm air Recovery Heat Q_p

This is given in general as follows.

$$Q_p = \int_{t_{in}}^{t_{out}} N_p \cdot Cp_{air}\, dt \quad (18)$$

Here, cool air temperature t_{in}=7℃,
warm air temperature t_{out}=17℃.

$$Cp_{air} = 28.94 + 0.4147 \cdot 10^{-2} t + 0.3191 \cdot 10^{-5} t^2 - 1.965 \cdot 10^{-9} t^3 \quad (19)$$

By substituting these values,

$$Q_p = 120.4 \cdot 28.99 \cdot (17-7)$$

$$= 34909 \text{(J/s)} = 34.909 \text{ (kJ/s)} \quad (20)$$

(4) Accompany Air Flow

Accompany Air n_B

This is calculated from the state equation as;

$$n_B = (101.3 \cdot 10^3 \cdot 0.02574) / \{8.314 \cdot (7+273)\}$$

$$= 1.120 \text{ (mole/s)} \quad (21)$$

Here, P_B=1 (atm)=101.3(kPa), R=8.314(Nm/mole·K),
accompany air temperature at inlet; t_C=7℃,
flow velocity;u_B= 2.2m/s, inlet vent section area;

$$a_B = (16/100)^2 - (11.3/100 \cdot 12.3/100)$$

$$= 0.01170 \text{ (}m^2\text{)}$$

flow rate of volume; V_B=2.2x0.0117=0.02574 (m^3/s)

If composition of air are assumed O_2 and N_2 and the other species are neglected,

O_2: 1.120·21/100=0.23522 (mole/s)

N_2: 1.120·79/100=0.88487 (mole/s)

Enthalpy of Accompany Air n_B

This is given in general as follows.

$$H_B = \int_{25}^{t_B} n_B \cdot Cp_{air}\, dt \quad (22)$$

By substituting n_B =1.120[mole/s] and t_B =7℃,

$$H_B = 1.12 \int_{25}^{7} 29.006 dt$$

$$= -584.76 \text{ (J/s)}$$

$$= -0.5848 \text{ (kJ/s)} \quad (23)$$

(5) Counter Air Flow

If N_2 fraction is the residual except the measured components,O_2, CO_2, CO and NOx for simplicity, it is calculated to 81.0782%.

As the total flue gas flow rate is 3.478 (mole/s), the each airflow rates are calculated as;

N_2(in n_D)=0.811·3.473=2.817 (mole/s)

N_2(in n_B)=0.811·3.473=0.885 (mole/s)

N_2(in n_C)=2.817-0.8849=1.9317 (mole/s)

If air composition is assumed to N_2 and O_2 (fraction is 79:21) and the other species are neglected, the counter airflow rate is calculated as;

n_C=100/79·1.9317 (mole/s)

$= 2.447$ (mole/s) **(24)**

Table 1 Experimental Data

Time	Place	Items	Symbols	Value
16:30	Greenhouse	Temp.	t	7℃
16:30	Duct	Dia.	d	53cm
16:30	Duct	Temp.		
		Inlet	t_{in}	7℃
		Outlet	t_{out}	17℃
16:30	Accompany Air	Flow Rate	v_B	2.2m/s
	Inlet	Temp.	t_B	7℃
15:00	Counter Air Inlet	Temp.	t_C	7℃
17:00	Flue Gas Exhaust	Pipe Dia.	d_D	10cm
		Composition	O_2	13.3%
			CO_2	5.6%
			CO	212ppm
			NO_x	6ppm
		Flow rate	v_D	13.5m/s
		Temp.	t_D	99℃
16:45	Economizer	Water Temp.		
16:50		Start	t_{w1}	41℃
		Final.	t_{w2}	42℃
		Weight	W	115.7kg
16:30	Heavy Oil Tank	Temp.	t_A	7℃
16:50	Combustor	Max. Temp.	t_{max}	860℃

(Measured on 18th in January, 2000)

Counter Air Flow Enthalpy H_C

This is given in general and calculated as;

$$H_C=n_C\int_{25}^{t_c} Cp_{air}\,dt$$

$$=0.5963\int_{25}^{7} 29.006dt$$

$$=-311.3\ (J/s)$$

$$=-0.331\ (kJ/s) \quad (25)$$

(6) Economizer

Economizer Recovery Heat Q_q

$$Q_q=\{W\cdot Cp_w\cdot(T_{w2}-T_{w1})+w\cdot\gamma_w\}/(\theta_2-\theta_1) \quad (26)$$

By substituting the experimental data,

$$Q_q=\{117.5\cdot1\cdot(42-41)+0.04095\cdot573\}/\{(50-45)\cdot60\}$$

$$=176.25+23.46)/(5\cdot60)$$

$$=1966\ (kJ/s) \quad (27)$$

4.2 System Evaluation

Input Enthalpy H_i

$$H_i=H_A+H_B+H_C$$

$$=-12.41\ (kJ/s)-0.5848\ (kJ/s)-0.3113\ (kJ/s)$$

$$=-13.306\ (kJ/s) \quad (28)$$

Output Enthalpy H_o

As this must equal to flue gas enthalpy, H_2 equals to H_D. Propriety of the experimental results should be discussed by below equation.

$$H_i=H_o+Q \quad \text{where, } Q=Q_p+Q_q \quad (29)$$

However, it is hard to calculate in this measurement because the data are not sufficient for the accuracy and requirements.

Performance factor and heat efficiency are respectively calculated from the equations (6), (7), (8) and (9) as follows.

$$\eta=Q_p/W_A=34.909(kJ/s)/1.8753\cdot10^{-3}(mole/s)$$

$$=18615(kJ/kg)$$

$$\approx4450(kcal/kg) \quad (30)$$

$$\alpha=Q_p/\Delta H_{CL}=34.909(kJ/s)/(7.369\cdot10^{-3}\cdot10861(kJ/mole))$$

$$=0.436$$

$$\approx44\% \quad (31)$$

$$\eta'=Q/W_A=36.875kJ/s)/1.8753\cdot10^{-3}(mole/s)$$

$$=19664(kJ/kg)$$

$$\approx4700(kcal/kg) \quad (32)$$

$$\alpha'=Q/\Delta H_{CL}=36.875kJ/s)/(7.369\cdot10^{-3}\cdot10861(kJ/mole))$$

$$=0.461$$

$$\approx46\% \quad (33)$$

4.3 Comparison of Fuel Consume

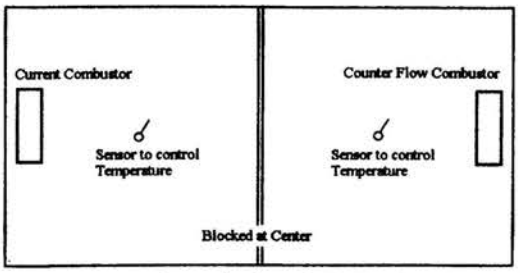

The experimental setup is shown in Fig.7, where the control temperature is set to 14℃.

Fig.7 Experiment Setup for Fuel Consume Comparison

Table 2 Comparison of Fuel Consume

	Start of Measurements (AM0:00)	Final of Measurements (AM 8:00)	Fuel Consume	Fuel Save
Current Combustor	210620.5 (l)	210644.6 (l)	24.1(l)	18.3%
Counter Flow Combustor	206725.5 (l)	206745.2 (l)	19.7 (l)	

The comparison of the fuel consume of the newly developed combustor with the current fuel-air conical supply one for running 8 hours is shown in Table.2. It was demonstrated experimentally that the developed combustor attained to save 18% of fuel running cost.

4.4 Prediction Work

This is executed about excess air 30% for 2[l/s] of methane flow rate with package of Fluent ver.5. 5. Fuel nozzle diameter is 50mm and counter airflow nozzle 100mm as shown in Fig.8. The distance between fuel nozzle and counter air nozzle is set to 800mm according to the combustor real dimension.

The periphery wall of combustor, which is heat transfer surface for warm air supply, is assumed to be constant of 293℃. Fuel inlet velocity is firstly defined to 1m/s for simplicity. Turbulence and reaction models are respectively employed eddy-dissipation and k-ε models. The accompany air inlet velocity is 0.38m/s from calculation (10% of total air flow rate). Counter airflow inlet velocity is –2.85m/s (minus denotes the opposite direction).

This prediction results show that the high temperature combusting flow go through along the periphery inner wall to the exhaust with the high axial velocity for the newly developed combustor, compared with the current one without the counter air flow as shown in Figs.9 and 10. Therefore, it seems that the heat transfer to the cool air is increased. In addition to that, it is also expected that the combustion efficiency becomes much better since the counter airflow enhances the mixing the fuel with the air. It appears that these facts mainly caused high performance of this newly developed heating system.

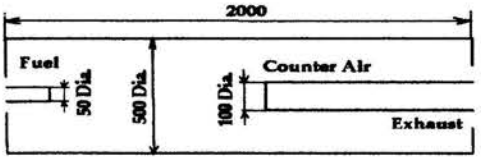

Fig.8 Combustor Dimension for Prediction

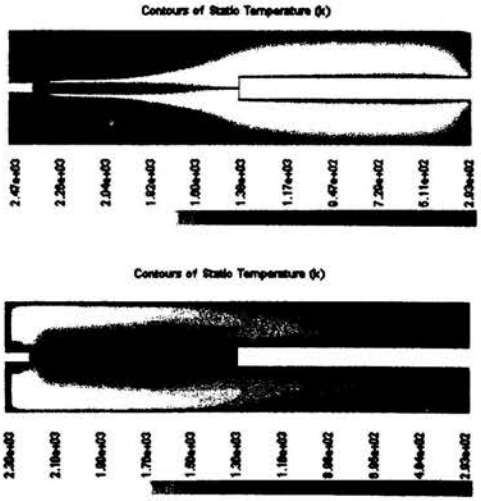

Fig 9 Comparison of Temperature Distribution of Current Combustor (Upper) with Counter Air Flow One (Below)

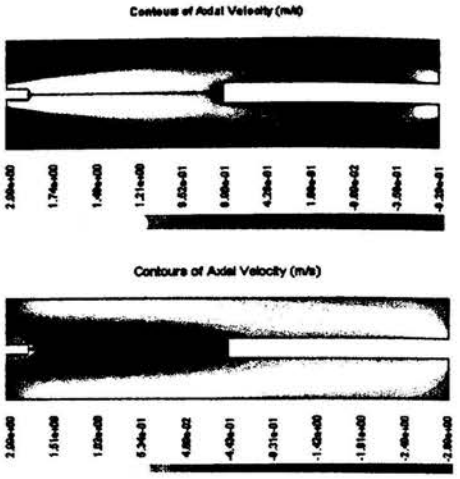

Fig.10 Comparison of Axial Velocity Distribution of Current Combustor (Upper) with Counter Air Flow One (Below)

5. Conclusion

Newly developed high performance combustor was tested. Heat balance equation was formed and calculated specifically by substituting the experimental data. The performance factor and the heat efficiency were also calculated and the system was evaluated. As every data required to calculation was not measured, several estimates and assumption were taken.

The experimental measurement was time-dependent to some extent but it seems to be enough to compare the performance of this developed combustor with the current one. The measurements and the results investigated in this research give the design method of the counter air flow combustor for heating system of greenhouse, of which the performance is further higher than the current one (18% fuel oil save attained in Field work). It seems to be possible to adapt this combustion technology to another application and save fuel oil consume as well as this figure.

Acknowledgements

We would like to acknowlege Mr. M. Niu and Mr. V. Paranisamy in Fluent Asia Pacific Co., Ltd for useful suggestions and Mr. K. Oikawa and H. Miura, students in Dept. of Chemical Engineering in Ichinoseki National College of Technology, for helping with this project.

References

[1] Madanahalli , A.V., Gollahalli S. R., 1993 "Effects of Nozzle Orientation on the Structure and Emission of Spray Flames", J. of Energy Resource Technology, Vol.115, pp.183-189.

[2] Kim, Y.-H., Kim, H.-J., 1998, "Multidimensional Effects on Structure and Extinction Process of Counter flow Non premixed Hydrogen-Air Flames, Combustion Science Technology, Vol.137, No.137, pp.51-80.

[3] Chiba, Y., Oikawa, K., Miura, H., 2000, "Evaluation of Countercurrent Flow Combustion by Air, Research Report of Ichinoseki National College of Technology, No.35, pp.79-85.

[4] Himmelblau, D. M., 1982, Basic Principles and Calculations in Chemical Engineering, Prentice-Hall, Inc., Englewood Cliffs, New Jersey, p.333.

HEFAT2002
1st International Conference on Heat Transfer, Fluid Mechanics, and Thermodynamics
8-10 April 2002, Kruger Park, South Africa
ZB1

ACTIVE CONTROL OF COMBUSTION INSTABILITIES USING FUEL INJECTION RATE MODULATION*

E. Lubarsky, Y. Neumeier, and B.T. Zinn
Schools of Aerospace and Mechanical Engineering
Georgia Institute of Technology
Atlanta, GA 30332-0150

ABSTRACT

This paper describes the development and performance of an active control system (ACS) that was developed at Georgia Tech to damp detrimental combustion instabilities in different combustors. The ACS consists of a pressure transducer, an observer, a controller and a fuel injector actuator (FIA). The pressure transducer continuously measures the combustor pressure. The measured pressure is analyzed by the observer that determines the amplitudes, frequencies and phases of the most unstable combustor modes in real time. These data are used by the controller to determine the control signal for the FIA whose task is to modulate the injection rate of all or a fraction of the injected fuel with the proper gain and phase. The goal of the fuel injection rate modulations is to produce combustion process heat release oscillations within the combustor that damp the unstable oscillations. The FIA is forced by a magnetostrictive actuator that changes its length in response to changes in a magnetic field generated by a current flowing through a coil wound around the actuator. The controller determines the time dependence of the actuator's current. The paper presents results obtained in two different combustors under two different modes of the control. The first study actively damped instabilities in a gas rocket using a controller that employed measured open loop combustor response data. It was able to significantly damped large amplitude instabilities within 30-40 milliseconds! The second study investigated the manner in which an adaptive ACS damped instabilities in a liquid fueled combustor. The adaptive controller required about 1-2 seconds to damp the instability. It apparently damped the Instability by modulating the fuel injection rate with a phase delay that modified the spatial dependence of the phase between the reaction rate and pressure oscillations along the combustion zone in a manner that reduced the overall driving of the instability by the combustion process.

INTRODUCTION

This paper describes the performance of an active control system (ACS) that has been developed under AFOSR and DOE support at Georgia Tech to control detrimental combustion instabilities in propulsion systems, e.g., rocket motors[1], and power generating, low NO_x, gas turbines[2]. These instabilities occur when energy supplied by the combustion process excites large amplitude oscillations of one or more natural acoustic modes of the combustor. The developed ACS is based upon Rayleigh's criterion, which states that an oscillatory heat addition process locally drives or damps pressure oscillations when the *magnitude* of the phase difference between the heat addition and pressure oscillations is smaller or larger than 90 degrees, respectively[3]. This criterion indicates that an active control system that excites combustion process heat addition oscillations within an unstable combustor that are 180 degrees out of phase with respect to the unstable pressure oscillations would damp the instability. The successful development of such an ACS is briefly described in this paper. The reader is referred to Refs. 4 and 5 for descriptions of additional studies of active control of combustion instabilities at other institutions.

* This research was supported by AFOSR (Dr. M. Birkan, contract monitor), AGTSR (Dr. Richard Wenglarz, contract monitor) and Siemens/Westinghouse (Drs. Gulati and Hoffman, contract monitors).

THE DEVELOPED ACS

Figure 1 describes the developed ACS. It consists of a pressure transducer that measures the combustor pressure and sends it to an observer that determines the frequencies, amplitudes and phases of one or more unstable combustor modes in practically real time. The observer's output is sent to the controller where the needed control signal is generated using data measured in open loop control tests[6] or adaptively[8]. The generated control signal is sent to a fuel injector actuator (FIA) that modulates the injection rate of all or a fraction of the injected fuel at the frequency of the most unstable mode and a phase that generates combustion process heat release oscillations within the combustor that are 180 degrees out of phase with respect to the unstable pressure oscillations.

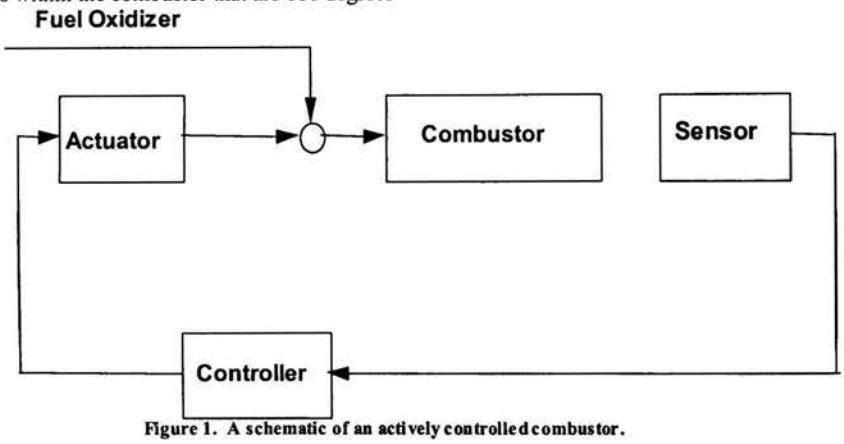

Figure 1. A schematic of an actively controlled combustor.

One of the important accomplishments of this program was the development of an observer[6,9,10] that analyzes the measured pressure to determine the characteristics of a predetermined number of unstable combustor modes in practically real time, which could not be done with FFT. The observer analysis assumes that the measured pressure $P_m(t)$ can be expressed in the following Fourier-like series:

$$P_m(t) = \sum_{n=1}^{N} [a_n(t)\sin(\omega_n(t)t) + b_n(t)\cos(\omega_n(t)t)] \quad (1)$$

whose as yet unknown coefficients, i.e., $a_n(t)$ and $b_n(t)$, and frequencies $\omega_n(t)$, are expressed as functions of time because their values change as they are determined in an iterative process. This iterative solution procedure starts by assuming a value for the unknown frequency $\omega_n(t)$ and substituting it into the integrands and limits (which depend upon the as yet unknown period of the oscillations) of "classical" Fourier series integrals that determine the unknown coefficients $a_n(t)$ and $b_n(t)$. The resulting integrals are then solved for the unknown coefficients $a_n(t)$ and $b_n(t)$. The calculated values of $a_n(t)$ and $b_n(t)$ and assumed $\omega_n(t)$ are then substituted into another relationship (not given here) that determines an improved value of the unknown frequency $\omega_n(t)$. The latter is then substituted back into the integrals for the coefficients $a_n(t)$ and $b_n(t)$ and the calculation procedure is repeated until the calculated values of $a_n(t)$ and $b_n(t)$ and $\omega_n(t)$ converge to final values, which are then used to determine the unstable mode's amplitude, frequency and phase. This procedure determines the characteristics of the mode with the largest amplitude first. Once this mode has been identified, it is subtracted from the measured signal $P_m(t)$, see Eq. 1, and the above described analysis is applied to the resulting signal to determine the amplitude, phase and frequency of the largest amplitude mode in the "remaining" signal. This procedure can be repeated for a desired number of modes, e.g., five modes[6,9,10].

Another significant contribution of this program was the development of a unique fuel injector actuator. It uses a magneto-strictive actuator (i.e., Terfrnol D) that changes its length in response to changes in the intensity of an imposed magnetic field. As the length of the actuator varies, it changes the cross sectional area through which the "control" fuel stream is supplied to the combustor, thus providing means for modulating the fuel's injection rate in a controlled manner. Special attention was given to the design of the various flow passages within the injector to minimize the injector's response time and, thus, provide capabilities for high frequency fuel flow rate modulation. To date, FIAs that can handle gaseous[6,9] and liquid[11] fuels over wide range of fuel

flow rates have been developed. Both actuators include a secondary controller that prevents variation of their mean flow rate due to a mean actuator drift caused by heating and hysteresis, and the liquid fuel actuator possesses capabilities for exciting high frequency oscillations that atomize the liquid stream. To date, these FIAs have been operated over a 0-1,000 Hz frequency range. One of the reviewers of this paper has informed us that a FIA with a higher upper frequency limit is described in Ref. 12. Such FIAs provide means for damping combustion instabilities over a wide frequency range.

ACS PERFORMANCE

At the outset of this program, open loop tests were conducted to investigate whether the ACS can excite heat release oscillations within the combustor over a wide frequency rang[7], and determine the frequency dependence of the response of the combustion process to fuel injection rate modulations. These tests were conducted in two different combustors using different experimental techniques, and both yielded practically identical combustion process open loop response data. These data described the frequency dependence of the gain and phase of the excited combustion process heat release oscillations and was subsequently used by the controller to determine the control signal for the actuator. Typical results, obtained in a 600Hz open loop response test are presented in Fig. 2. It shows that the fuel injection rate modulation produced 600Hz spikes in the spectra of the pressure and CH radicals emissions oscillations, which are proportional to the reaction rate and, thus, heat release oscillations. These spikes indicate that the developed ACS can excite reaction rate oscillations within the combustor at the frequency of the fuel injection rate modulations. Figure 2 shows that the pressure spectrum contains several spikes at the frequencies of the natural acoustic modes of the combustor that are much larger than the driven 600 Hz spike, and that the magnitudes of the CH oscillations at the natural acoustic modes frequencies are practically within the noise level. This result shows that small amplitude reaction rate (i.e., CH) oscillations can excite large amplitude pressure oscillations at the natural acoustic modes of the system and that a non-resonant (i.e., 600 Hz), large amplitude, reaction rate oscillation can only excite moderate pressure oscillations. These data also indicate that an "accidental" small amplitude reaction rate oscillation at a frequency of one of the natural acoustic modes of the combustor can readily excite combustion instability.

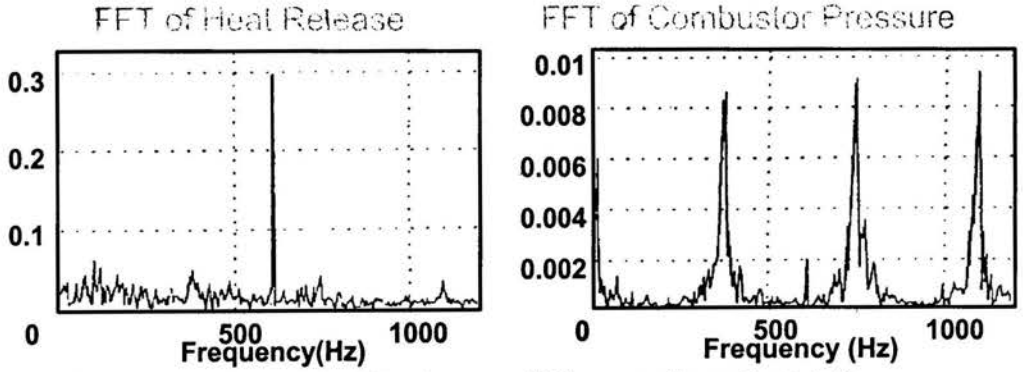

Figure 2. Spectra of CH radiation (left) and pressure oscillations measured in open loop test with 600 Hz fuel injection rate modulations.

At the outset of this program, the developed ACS used the measured open loop frequency response data, similar to that shown in Fig. 2, to determine the gain and phase of the control signal for the actuator during closed loop active control of combustion instabilities in a gas rocket[6,8]. Figure 3 describes the performance of this ACS. Specifically, it shows the time dependence of the pressure in the unstable gas rocket before and after activation of the ACS at .1 seconds. In this case, the ACS damped a large amplitude, 15 psi (peak to peak), instability within twelve cycles or .03-.04 seconds without any apriori information about the characteristics of the instability. Subsequent FFT analysis[6] of the measured data showed that the ACS damped the amplitude of the dominant, 380Hz mode, by more than 26 dB and that five harmonics of the fundamental were also significantly attenuated.

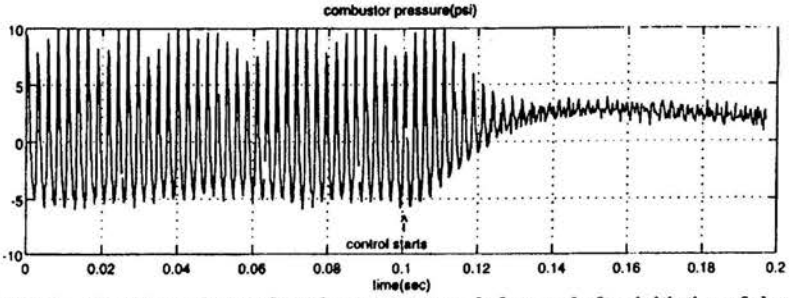

Figure 3. Time dependence of combustor pressure before and after initiation of close loop control at 0.1 seconds.

The above-described mode of active control requires, however, measured (or calculated) open loop response data that is difficult to obtain in many practical situations because of lack of expertise of the operators of the system. Consequently, an alternate, *adaptive*, close loop control approach that does not require measured response data was developed[8]. It determines the control signal "on the fly" by changing the gain and phase of the control signal in a "specified", proprietary, manner, and uses the observer to determine the combustor response to the "latest" control signal in real time. This procedure is continued until the control signal's gain and phase converge to their optimal values.

The manner in which the adaptive ACS damps the instability was studied in a liquid fueled, 500 mm. long, quartz combustor that was open at its downstream end, see Fig. 4. The combustor burned air and n-heptane (C_7H_{16}), and was retrofitted with the adaptive ACS. A Terfenol D magnetostrictive actuator was connected to a pintle-type injector (2) whose oscillatory motion modulated the liquid fuel injection rate in a controlled manner. The time dependence of the actuator's length and, thus, the pintle's position, was controlled by the magnitude and phase of a current that was sent to a coil wound around the actuator. As the control current changed, the coil's magnetic field also changed, thus changing the length of the magnetostrictive rod (1). As the actuator's length changed, it pushed the pintle (2) against a pressure force exerted by the liquid fuel supplied into the volume (3) between the pintle's conical termination and the injector's casing. The resulting force imbalance set the pintle in motion. As the pintle moved backwards, the annular clearance (4) between the two cones opened and allowed fuel to flow through the plenum (5) into the wedge shape nozzle (6). The pressure difference across the nozzle (6) changed as the width of the annular cross sectional area (4) changed. This pressure difference forced the liquid to move through the nozzle and produce a spray in the combustor (7). In the reported tests, thirty three percent of the airflow rate was tangentially injected (8) into the space where the liquid spray formed, and the remaining air (9) entered the combustor through an annular space around the conical flame holder.

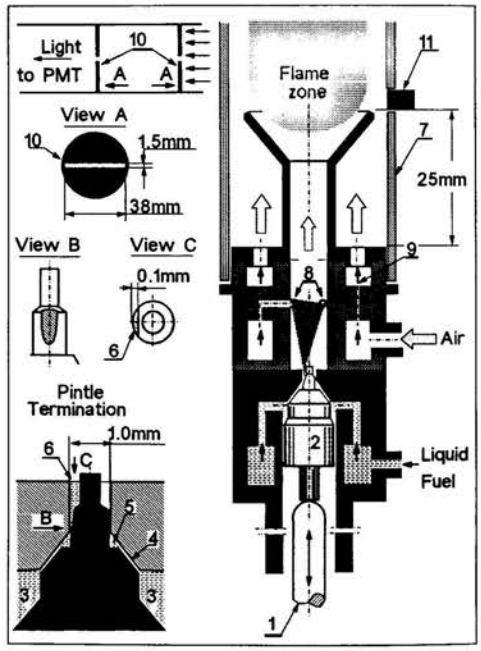

Figure 4. A schematic of the adaptively controlled, liquid fueled combustor and related components. 1-actuator; 2-pintle; 3-fuel plenum; 4-annular passage; 5-plenum; 6-nozzle; 7-quartz combustor; 8-tangential air inlets; 9-secondary, axial, air supply; 10-radiation viewing aperture; 11-pressure sensor.

In this study, the time dependence of the combustion process heat released at various axial locations along the flame was determined from measurements of the spatial dependence of CH radicals (λ=431.5nm) chemiluminescence. This was measured using a setup consisting of a photomultiplier (PMT), a narrow band pass interference filter centered at wavelength λ=430±5nm and an appropriate system of lenses and apertures. This system limited the PMT's instantaneous line of sight to a 3mm thick cross-section of the reaction zone. The PMT setup was

mounted on the remotely controlled support system and slowly moved along the combustor as it measured the spatial dependence of the CH radicals chemiluminescence. Simultaneously, the combustor pressure oscillations were measured using a piezo-electric pressure sensor. The phase of the oscillatory CH chemiluminescence was determined in reference to the measured pressure. The PMT and pressure signals and a signal indicative of the PMT position were acquired and sampled by a computerized data acquisition system.

This setup was used to study the manner in which the adaptive ACS damps instabilities. It was done by comparing the axial dependence of the amplitude, phase and local driving/damping of the heat release oscillations along the combustor with and without active control. Typical results are shown in Fig. 5. They present data measured at global, average, combustor equivalence ratios ϕ of 0.45 and 1.0 when the combustor exhibited large amplitude instabilities. Figure 5-a shows that while the ACS

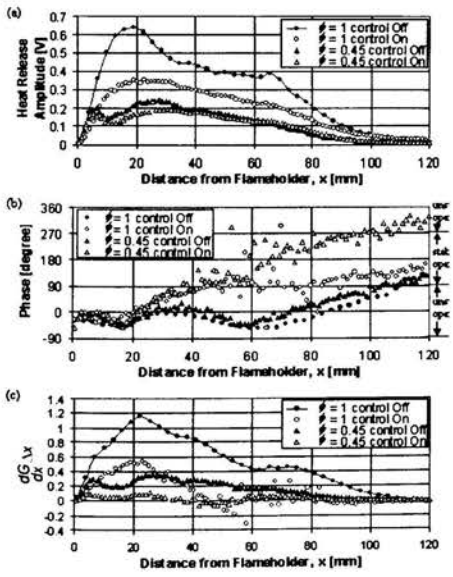

Figure 5. Spatial dependence of the amplitude (top) of heat release, phase (middle) and driving of the instability in a liquid fueled combustor at f=0.45 and f=1.

significantly reduced the amplitude of the heat release oscillations all along the combustor when ϕ=0.45, it had little effect on the CH amplitude distribution at ϕ=1. Figure 5-b shows that the ACS modified the "nearly flat" phase distributions at both values of ϕ, which were repeatedly observed when instabilities occurred in this combustor, to "continuously varying" phase distributions similar to those exhibited under conditions in which the amplitude of the instabilities were low. For example, at ϕ=1, the "controlled" phase varied between approximately –50 and 0 degrees along the first 20 mm. of the combustion zone, and then gradually increases from 0 to approximately 100 degrees in the reaction zone between 20 and 60 mm., and it remained at a nearly constant value of 100 degrees along the remainder of the combustion zone. In this connection it should be noted that the driving by the combustion process is nearly zero when the phase is 90 degrees and the combustion process damps the instability when the phase is 100 degrees. Finally, Fig. 5-c compares the spatial dependence of $dG(x)/dx$, which is the x derivative of the gain G(x) of the combustion process and describes its local driving/damping; i.e., driving occurs when $dG(x)/dx$ is positive and vice versa. Figure 5-c shows that the adaptive controller significantly reduced the magnitude of $dG(x)/dx$ all along the combustion zone when ϕ=0.45 and along part of the combustion region when ϕ=1. Figure 5-c also shows that when the controller is "on" the combustion process damped the instability in some regions of the combustion zone where $dG(x)/dx$ is negative. A comparison of the results in Figs. 5-b and 5-c shows that the spatial dependence of $dG(x)/dx$ depends the phase variations shown in Figure 5-b. These results show that active modulation of the fuel spray injection rate damped the instability by essentially modifying the spatial dependence of the phase between the heat addition and pressure oscillations.

SUMMARY AND CONCLUSIONS

This paper describes the successful development and performance of a novel ACS that uses fuel injection rate modulations and various control approaches to damp combustion instabilities. It shows that this ACS can significantly damp instabilities by changing the phase between the heat release and pressure oscillations. It is noteworthy that the effectiveness of this ACS has been recently demonstrated on a Siemens/Westinghouse high pressure, low NO_x combustor rig[13]. Comparison of the performance of the two investigated modes of control shows that the one that uses previously measured open loop response data attained larger attenuation of the unstable oscillations in a shorter period of time, suggesting that the performance of the adaptive ACS could be further improved.

REFERENCES

[1] Harjee, D. and Reardon, F. (Eds.), "Liquid Propellant Rocket Combustion Instability", NASA SP 194, 1972.

[2] Langton, L. S., "Good Times with a Double Edge", Mechanical Engineering Power, June 2001.

[3] Zinn, B. T., and Neumeier, Y. "An Overview of Active Control of Combustion Instabilities," AIAA 97-0461. AIAA 35th Aerospace Sciences Meeting and Exhibit, Reno, NV, Jan., 1997.

[4] McManus, R. K., Poinsot, T. and Candel, S. M., "A Review of Active Control of Combustion Instabilities," Progress in Energy and Combustion Sciences, Vol. 19, pp. 1-29, 1993.

[5] Candel, S. M., "Combustion Instabilities Coupled by Pressure Waves and Their Active Control," 24th Symposium (International) on Combustion, Sydney, Australia, July 1992.

[6] Neumeier, Y. and Zinn, B. T., "Experimental Demonstration of Active Control of Combustion Instabilities Using Real-time Modes Observation and Secondary Fuel Injection," Proc. 26th Int. Symp. on Combustion, The Combustion Institute, Naples, Italy, July 29 - Aug. 2, 1996.

[7] Neumeier, Y., Nabi, A. and Zinn, B. T. "Investigation of the Open Loop Performance of an Active Control System Utilizing a Fuel Injector Actuator," AIAA 96-2757, 32nd AIAA/ASME/ SAE/ASEE Propulsion Conf. 1996.

[8] Johnson, C. E., Neumeier, Y. and Zinn, B. T. "Online Identification Approach for Adaptive Control of Combustion Instabilities," AIAA Paper No. 99-2125, 35th AIAA/ASME/SAE/ASEE Joint Propulsion Conf. 1999.

[9] Neumeier, Y. and Zinn, B. T. "Active Control of Combustion Instabilities using Real Time Identification of Unstable Combustor Modes," AIAA Paper No. 95-0604, January 9-12, 1995.

[10] Neumeier, Y., Markopoulos, N. and Zinn, B. T., "A Procedure for Real-Time Mode Decomposition, Observation, and Prediction for Active Control of Combustion Instabilities," Proc. IEEE Conference on Control Applications, Hartford, CT, Oct. 5-7, 1997

[11] Heising, R., Lubarsky, E., Neumeier, Y., Neumaier, M. and Zinn, B. T. "Experimental Characterization of an Oscillating Liquid Fuel Spray Combustion for Suppression of Combustion Instabilities," AIAA Paper No. 2000-1024. *38th Aerospace Sci. Meeting* Reno, NV, Jan. 10-13, 2000.

[12] Anderson, T. J., Proscia, W., and Cohen, J. "Modulation of a liquid-fuel jet in an Unsteady Cross-Flow," presented in *ASME Turbo Expo '01*, New Orleans, LA, June 4-7, 2001, paper #2001-GT-0048.

[13] Neumeier, Y., and Zinn, B.T., "Experimental Demonstration of Active Control of Combustion Instabilities Using Real Time Modes Observation and Secondary Fuel Injections," 26th International Symposium on Combustion, Naples, Italy, July, 1996.

HEFAT2002
1st International Conference on Heat Transfer, Fluid Mechanics, and Thermodynamics
8-10 April 2002, Kruger Park, South Africa
FP1

QUASISIMILARITY BEHAVIOUR OF HELICAL FLOW BETWEEN CONCENTRIC CYLINDERS FOR POWER-LAW FLUIDS

P.Filip and J.David
Institute of Hydrodynamics, Acad.Sci.Czech Rep.,
Pod Patankou 5, 166 12 Prague 6, Czech Republic
E-mail: filip@ih.cas.cz, david@ih.cas.cz

ABSTRACT

Steady laminar isothermal helical flow of incompressible power-law fluids through a concentric annulus is analysed for the case of the stationary outer cylinder and the inner one rotating under a constant torque. Pressure force is imposed in the axial direction. Using dimensionless analysis a quasisimilarity solution is derived for a sufficiently broad region of entry (rheological, geometrical and dynamical) parameters. In this region it is possible to determine the relation between flow rate and pressure gradient eliminating any numerical calculations.

INTRODUCTION

Flow of non-Newtonian fluids through an annulus is often encountered in various industrial processes such as e.g. transportation of drilling fluids in petroleum industry and extrusion of polymers (in a mandrel region).

In the annular flow one of the most difficult complications consists in the inhomogeneous distribution of shear stresses in the annular region. The analysis of helical annular flow originated by a combination of the torsional drag and pressure forces (Couette-Poiseuille flow) is further complicated by the fact that no superposition principle takes place; in other words, this flow field is not possible to obtain as a mere superposition of corresponding Couette and Poiseuille flow fields. This is a direct consequence of the dependence of fluid viscosity on velocity field invariants.

a) non-helical case

First theoretical contribution dealing with flow of a power-law fluid through a concentric annulus with steady cylinders (of radii κR and R) is a paper by Fredrickson and Bird [1]. They derived a relation between flow rate and axial pressure gradient by means of infinite series for the cases when a reciprocal value of flow behaviour index n is a natural number. In their derivation a parameter λ (λR is a location of maximum velocity) plays a crucial role. For its determination it is necessary to solve an integral equation. Due to this fact and to the form of the derived solution (infinite series) the role of the individual entry parameters is not sufficiently elucidated.

Substantial improvement was presented by Hanks and Larsen [2] who derived an analytical relation between flow rate and pressure gradient for an arbitrary value of flow behaviour index n. Nevertheless, their relation still requires knowledge of a parameter λ - thus demanding the numerical solution of the integral equation introduced in Fredrickson and Bird [1]. The same result was derived by Prasanth and Shenoy [3].

Non-helical flow was also analysed by Bird et al. [4] using a variational method. They minimised the corresponding functional using supposed one-parametrical distribution of velocity. They finally obtained a relation that eliminated a parameter λ but in fact they derived the relation identical to that in McKelvey [5] for flow of a power-law fluid between two parallel plates (in other words, they implicitly supposed $\lambda=(1+\kappa)/2$). Inaccuracy of their result to the numerical solution is in full correspondence with Fig.8 in Worth [6]. Worth discussed the difference between the solution in a concentric annulus with that between parallel plates. This difference does not exceed 2% for $\kappa \geq 0.5$ and $n \geq 0.25$. Another possible approach is given in David and Filip [7].

The given problem is also possible to treat from the viewpoint of the similarity behaviour. It was shown (David and Filip [8]) that a solution exhibits various features of similarity behaviour – not in an exact form but only approximately (it implies the term 'quasisimilarity'). Nevertheless, even this 'weak' similarity enables to derive a 'universal' solution which is possible to rewrite to a concrete form for given entry parameters by means of derived transformations. This fully eliminates the role of the parameter λ, on the other side, quasisimilarity is not valid in the whole range of entry parameters κ,n. However, based on this quasisimilarity behaviour, the approximate relations (David and Filip [9]) were derived for the whole range of entry parameters. The

Load rejection in the PBMR

In this example a load rejection case of the PBMR plant is considered. Figure 11 shows the network representation of the PBMR plant. Initially the plant operates at maximum power and at time t=0.9 s the generator power is reduces by 50 percent. The generator speed is controlled by a PID controller that adjusts the bypass flow by opening and closing a control valve.

Figure 12 shows the variation in turbine temperatures while Figure 13 shows the variation in compressor temperatures during the transient.

The example demonstrates the capability of the model to predict transient flows in complex thermal-fluid systems.

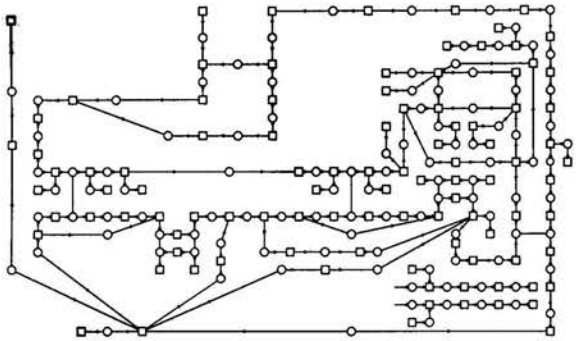

Figure 11: Network presentation of PBMR.

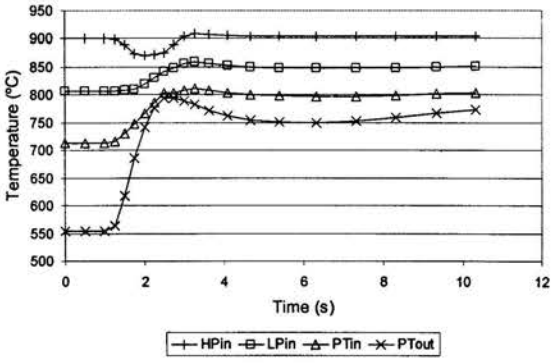

Figure 12: Turbine temperatures.

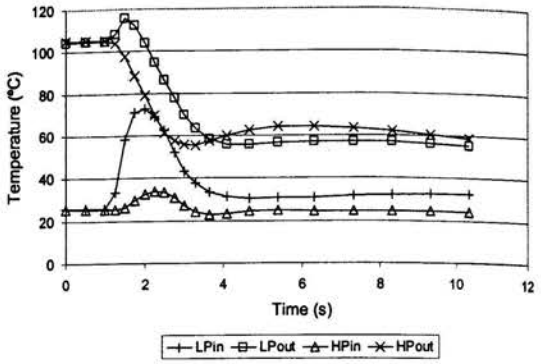

Figure 13: Compressor temperatures.

CONCLUSION

An implicit finite difference method for the prediction of transient flows in general thermal-fluid networks has been presented in this paper. Although only a few gas flow cases have been presented, the method is suitable for both liquid and gas flows, for both isothermal and non-isothermal flows and for both fast and slow transients. Although the method is slower than explicit methods when applied to fast transients, it is faster than explicit methods in the case of slow transients.

The main advantages of the present method are its average speed over a range of problems including both fast and slow transients, its accuracy and its stability. The method is also very flexible and it has been extended to deal with a large variety of non-pipe components such as compressors, turbines, orifices, pumps and heat exchangers.

ACKNOWLEDGMENTS

This work was carried out in association with M-Tech Industrial on contract for PBMR (Pty.) Ltd.

REFERENCES

[1] Greyvenstein, G.P., 2001, "An implicit method for the analysis of transient flows in pipe networks", accepted for publication in the International Journal of Numerical Methods in Engineering.

[2] Anderson, D. A., Tannehill, J. C. and Pletcher, R. H., 1984, Computational Fluid Mechanics and Heat Transfer, Hemisphere Publishing Corporation, New York.

HEFAT2002
1st International Conference on Heat Transfer, Fluid Mechanics, and Thermodynamics
8-10 April 2002, Kruger Park, South Africa
HS2

AN INTEGRAL EFFECTS TEST OF LOSS OF RESIDUAL HEAT REMOVAL DURING MID-LOOP OPERATION

Sang Jun HA, Hyung Suk OH and Sang Doug Park

Nuclear Power Laboratory, Korea Electric Power Research Institute
103-16 Munji-dong Yusong-gu, Taejon 305-380, Korea

ABSTRACT

Loss of residual heat removal (RHR) during a mid-loop operation after plant shutdown has occurred in several nuclear power plants and some of the events resulted in the boil of the reactor coolant. Now it is recognized as an accident situation whose relevant physical phenomena require improved understanding. An integral effect test facility was established to simulate the thermal hydraulics of Korea Nuclear Standard Power Plant under abnormal conditions during shutdown operations and several experiments were conducted at the facility. The major results from these experiments are presented in this paper, which addresses the thermal-hydraulic phenomena in case of manways opened at various locations in the reactor coolant system. Also the effects of nozzle dam failure and steam generator to remove decay heat in reflux condenser mode on core heat-up time were investigated.

1. INTRODUCTION

The safety of pressurized water reactors (PWRs) has been subject of extended investigations in nuclear engineering and related thermal hydraulics. Whereas in the earlier years of nuclear power generation research was mainly focused on the accidents occurring during power operation, nowadays the investigations are extended to the accidents occurring during shutdown operation.

The RHR system is used to remove the core decay heat during reactor shutdown operation of a PWR. The system can be operated at the reduced reactor coolant system (RCS) inventory condition, for inspection or maintenance of certain components such as steam generator (SG) U-tubes and reactor coolant pumps. This specific operation mode is called mid-loop operation. Loss of RHR system capability during such a mid-loop operation has occurred in several plants as a result of loss of AC power or air binding of the RHR pump [1-5]. It is well known that, if a loss of RHR occurs and the alternative heat removal capability is insufficient to remove the core decay heat, heating up of coolant may lead to coolant boil-off, fuel rod heat up and even core damage. As the loss of RHR event has been occurring repeatedly, US NRC requested all licensees to respond to GL 88-17[6] regarding the improvement in the equipment for the mid-loop operation and the comprehensive analysis for systems behavior during loss of RHR.

An experimental investigation of the thermal hydraulic responses associated with PWR loss of RHR capability during mid-loop operations has been conducted at several integral systems test facilities such as PKL-III [7], ROSA-IV/LSTF [8], BETHSY[9] and IIST[10]. Each facility was establish to simulate the thermal hydraulics of specific power plant type under abnormal conditions during mid-loop operation. PKL-III is a full-height volumetrically scaled down (1/145) 1300 MWe KWU-type PWR. ROSA-IV/LSTF is a full-height volumetrically scaled down (1/48) two-loop model of a Westinghouse-type four-loop 3423 MWt PWR. BETHSY is a full-pressure full-height volumetrically scaled down (1/100) model of a three-loop 900 MWe Framatome PWR. And IIST is a reduced height (1/4) and volumetrically scaled down (1/400) three-loop Westinghouse-type Maanshan PWR.

In addition, the transient thermal hydraulic phenomena for loss of RHR during mid-loop operations have been analyzed using best-estimate transient analysis codes, such as RETRAN, RELAP5/MOD3, etc. [11-13]. Recently, International Standard Problem 38 was performed to establish the status of best estimate codes for mid-loop operation conditions, to compare different computer models and to increase the common understanding of mid-loop operation conditions [14]. However, partly due to the inherent code limitations and partly due to the lack of complete experimental data for checking, some important controlling phenomena, such as PZR venting effect, depression of core liquid level and redistribution of the liquid inventory, cannot be predicted easily using these codes. Therefore it is necessary to provide data against which the performances of codes may be assessed.

With the considerations mentioned above, series of six experiments were conducted at the Korea Electric Power Research Institute (KEPRI) Integral Effect Test (KIET) facility to identify the controlling mechanisms for loss of RHR during mid-loop operation and to investigate the time required to heat-up the simulated fuel rod according to plant configurations and

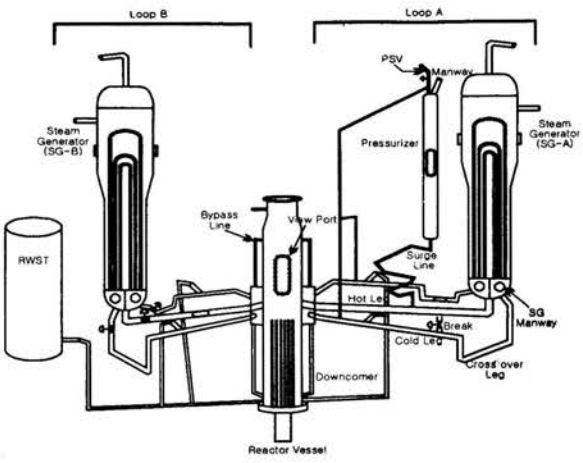

Fig. 1. Schematic view of KIET.

system openings. The heat-up time of the fuel rod is the maximum time available for the appropriate operator action to be started.

2. KIET FACILITY

KIET is a reduced height (1/5) and volumetrically scaled down (1/2055) integral effect test facility established to simulate the thermal hydraulics phenomena of a 2x4 loop 1000 MWe Korea Standard Nuclear Power Plant (KSNP) under abnormal conditions during mid-loop operation. The facility is well suited for a loss of RHR accident test as it represents the primary circuit of a typical KSNP design. The most parts of the facility have been constructed according to an integral response scaling method [15]. This facility consists of a reactor pressure vessel, two hot legs, four cold legs and two steam generators as shown in Fig. 1. The downcomer, which links the four cold legs to the lower plenum, is made up of external tubes and an annulus. Core power has been limited to 0.66% nominal power, 45 kW for 11 heater rods which make up the core. The data acquisition system of KIET involves over 70 instruments located on the primary and secondary sides, used to measure the temperature, pressure, flow rate, liquid level and differential pressure. Four view ports are specially designed for flow visualization within the pressure vessel, hot leg, crossover leg and PZR.

3. EXPERIMENTAL CONDITIONS

Among the diversity of possible real situations, tests PMO, SGOMO, SGIMO, HLDF, CLDF and PMOSG2 were performed to investigate the thermal hydraulic phenomena with loss of RHR during mid-loop operations. The initial conditions for the six experiments are summarized in Table 1. The initial values of the major parameters are common to these experiments as follows. Pressure and temperature in both the primary and secondary systems are equal to atmospheric pressure and close to room temperature, respectively. To simulate mid-loop operation condition, liquid level in the primary loop is set approximately at the centerline of the hot legs. Tests PMO, SGOMO and SGIMO investigate those where the PZR manway, and PZR and SG outlet plenum manways, PZR and SG inlet plenum manways are open respectively. Boil-away and liquid entrainment through manways are the physical phenomena which mainly determine the RCS behavior. Tests HLDF and CLDF deal with situations where the RCS openings are limited to the removal of one PZR Safety Valve (PSV) and nozzle dams are installed in loop B. Nozzle dams are simulated by quick opening valves. The valves installed at hot leg and crossover legs connected to SG-B are closed initially and then opened quickly when the pressures of core upper plenum or crossover leg reach to nozzle dam design pressure, 0.24MPa. Test PMOSG2 investigates the availability to remove decay heat in reflux condenser mode when the SGs are available with a full secondary side mass inventory and the presence of air above the initial primary level as it is expected that air redistribution in the RCS influences primary-to-secondary heat transfer.

4. EXPERIMENTAL RESULTS AND DISCUSSION

4.1. SCENARIO

As the KIET facility does not include a RHR system, the transients are initiated in the following way: the manways (or vents) specified at test cases are initially opened with a zero core power value and liquid level at mid-loop. At t = 0 s core

Table 1. Initial Experimental Conditions

Condition	experiment					
	PMO	PMOSG2	SGIMO	SGOMO	HLDF	CLDF
Primary side pressure	Atmospheric					
Liquid level	Middle of hot legs					
Core power	29.5 kW					
SG secondary side Pressure	Atmospheric					
Liquid level	Unavailable	Normal	Unavailable			
Fluid temp.		290.8 K				
Openings	PZR manway	PZR manway	PZR manway & SG-B inlet manway	PZR manway & SG-A outlet manway	1 PSV	1 PSV
Nozzle dam	Not installed				Dams at Loop B	

power is rapidly raised to the required value. No operator actions are taken after a loss of RHR and the tests come to end when the simulated fuel surface temperature reaches 423K.

4.2. TESTS PMO AND PMOSG2 RESULTS

Figures 2-4 are the primary parameters measured in test PMO. Following the initiation of the experiment, the RCS pressure is kept at atmospheric pressure before core boiling (Fig. 2). Core decay heat causes a rise in core coolant temperature (Fig. 3). After core boiling, the RCS pressures increase steadily from 530 s to the end of experiment due to core boiling and a pressure difference between core upper plenum and the cold leg builds up. The generated steam flows rapidly into all RCS internal space above the liquid level. In about 110 s, the temperatures of the upper and lower part of the hot leg increase and reach to saturation temperature at 800 s. Fluid temperatures measured in both PZR and SG inlet plenum immediately increase at 600 s and 750 s respectively. This suggests that the steam and liquid mixture in the hot legs are conveyed into these regions due to steam generated in the core. The liquid come in PZR is subcooled initially and reaches to saturation temperature at 1300 s. The temperature decreases of the cold leg and downcomer at about 930 s and 1350 s, respectively, occur due to inflow of cold liquid in the crossover leg according to the pressure difference between core upper plenum and cold leg. Also the pressure difference allows a steam flow to the cold leg to take place via the upper head to downcomer bypass. The steam heats continuously the liquid in the downcomer and cold leg. Thus, the temperatures of liquid in the cold leg and downcomer increase when the inflow of cold liquid in the crossover leg to cold leg is reduced. The temperature of crossover leg remains subcooled throughout the experiment.

The PZR level increases steeply from 600 s to a maximum of 1.5 m at about 1130 s (Fig. 2). At this time, it seems that the mixture level reaches to the top of the PZR judging by the temperature and pressure variations of the top of the PZR (not shown here). When the PZR level is high, the steam/water mixture flow from hot leg to surge line decreases for a while and then increases steadily to the end of the experiment. Through the view port located at the PZR, it is observed that the void fraction in the PZR is increased as the experiment proceeds. At about 1200 s a loss of coolant starts through PZR manaway opening (Fig. 4).

Figure 4 shows the collapsed liquid levels in the reactor vessel and the downcomer. The liquid level in the reactor vessel decreases monotonically because the steam/water mixture starts to flow into the PZR and SGs after 600 s and discharge through the PZR manway. The level difference between the reactor vessel and the downcomer exists after core boiling and has a maximum value, 0.14m, at about 1800 s, when the loop pressure difference is maximized. At about 4000 s the liquid levels decrease rapidly as the steam/water mixture level decreases below the bottom of the hot leg. At the end of experiment mass balances show that of the initial 123 kg of coolant, 45 kg of coolant is discharged through the PZR manway and 34 kg, 12 kg and 32kg are remained in the reactor vessel and downcomer, the PZR and crossover legs respectively. The time required to heat up the simulated fuel rod is about 4736 s and the RCS pressure rises to 0.19 MPa.

In test PMOSG2, the trends of primary parameters are similar to those of test PMO (Figs. 5 and 6). According to the heat transfer to the SG secondary side, the RCS pressure and the discharge rate of the coolant through the PZR manway are lower than those of test PMO. Thus, the core heat up time in test PMOSG2 delayed by 2168 s as compared to test PMO. Figure 6 shows the temperature variations of the SGs primary and secondary sides. An average temperature increase of the

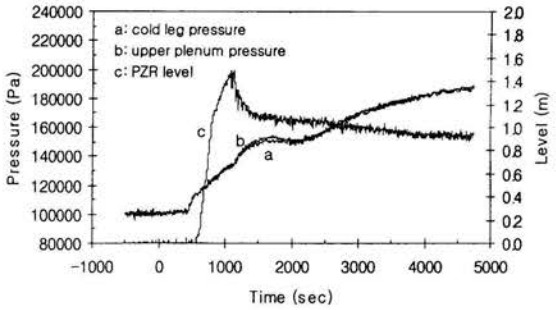

Fig. 2. RCS pressures and level in test PMO.

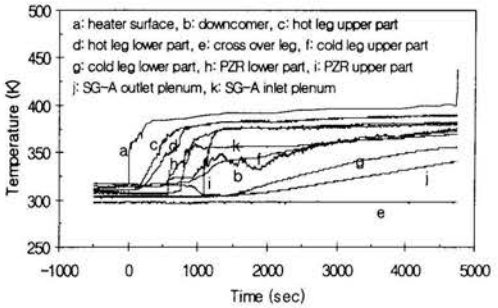

Fig. 3. RCS temperature variations in test PMO.

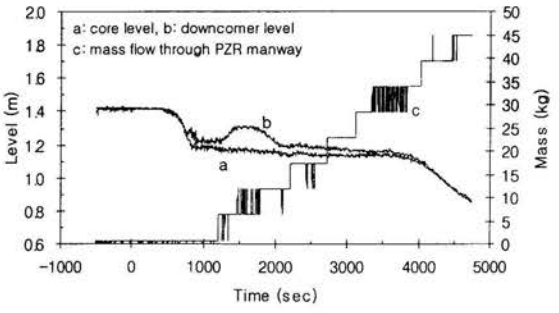

Fig. 4. Collapsed levels and integrated mass flow in test PMO.

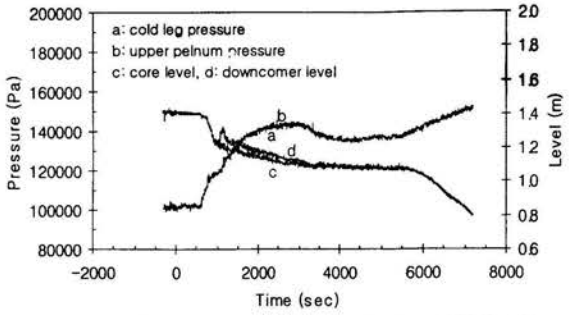

Fig. 5. RCS pressure and levels in test PMOSG2.

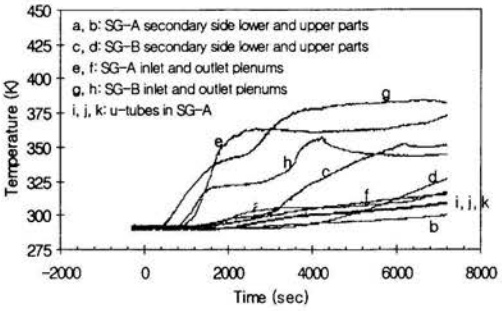

Fig. 6. Temperature variations at the SG in test PMOSG2.

secondary side of the SGs is 36 K. The temperature behaviors, which are instrumented at the top of three different height u-tubes, are almost the same. The most of heat transfer to the SG secondary side is accomplished at the lower region of the SG-B u-tubes.

4.3. TESTS SGOMO AND SGIMO RESULTS

Typical measured results of tests SGOMO and SGIMO are given in Figs. 7-12. The initial and boundary conditions of these two experiments are the same, except the location of the manways opened. When there exist openings at cold leg side or the hot leg side as well as the PZR manway, the RCS pressure and the pressurization rate are reduced significantly and a loss of primary mass inventory occurs rapidly. In case of test SGOMO, there is a slight pressure difference between core upper plenum and the cold leg after 800 s and this result in the level difference between core and downcomer (Fig. 9). However, in the case of test SGIMO, since the near path for steam and liquid to atmosphere exists, the pressure and level differences are negligible (Figs. 10 and 12). A large amount of steam/water mixture has been released at the early period (700-1100s) through the SG manway and this results in early heat-up of the simulated fuel rod. The times required to heat up the simulated fuel rod in tests SGOMO and SGIMO are about 4736 s and 2760 s, respectively.

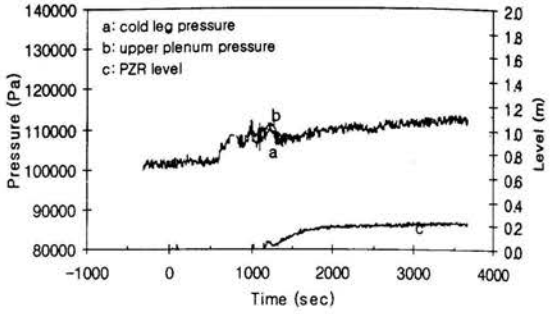

Fig. 7. RCS pressures and level in test SGOMO.

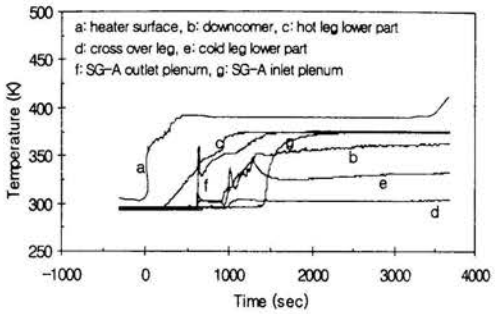

Fig. 8. RCS temperature variations in test SGOMO.

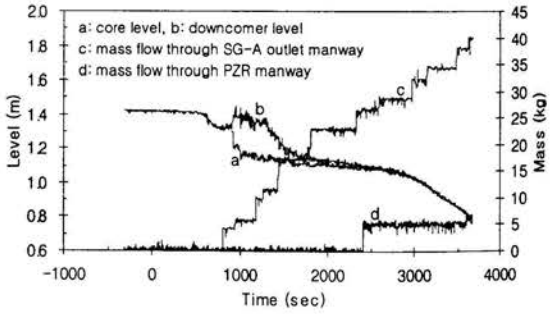

Fig. 9. Collapsed levels and integrated mass flow in test SGOMO.

4.4. TESTS HLDF AND CLDF RESULTS

Figures 13-18 are the primary parameters measured in tests HLDF and CLDF. The initial and boundary conditions of these two experiments are the same, except that test PMO involves PZR manway opening and HLDF and CLDF involve PZR safety valve removal. The PZR vent size effect on the mid-loop operations with loss of RHR can be seen by comparing the results of test PMO with tests HLDF and CLDF. Following the initiation of the experiments, the fluid behaviors are similar to those of test PMO except rapid RCS pressure increase because the vent size is smaller than that of test PMO. Also the pressure

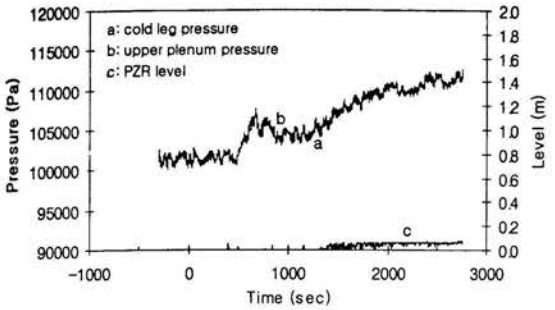

Fig. 10. RCS pressures in test SGIMO.

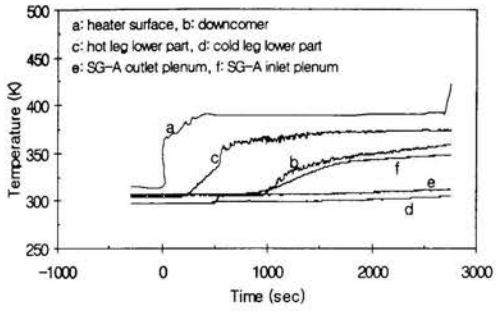

Fig. 11. RCS temperature variations in test SGIMO.

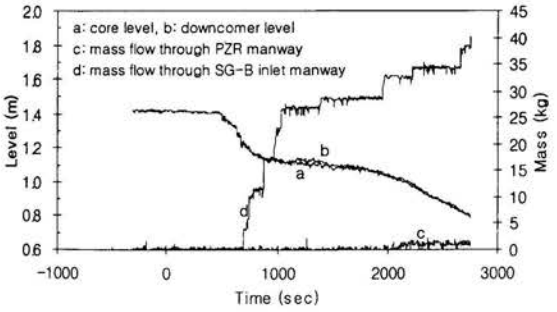

Fig. 12. Collapsed levels and integrated mass flow in test SGIMO.

difference is larger than that of test PMO and this results in larger collapsed level difference as shown in Figs. 15 and 18. The RCS pressures in tests HLDF and CLDF increase rapidly to 0.24MPa, the nozzle dam design pressure after 2160 s. After the nozzle dam failure, a major loss of primary mass inventory from the failed dam and SG manway to the atmosphere occurs due to the pressure difference between RCS and atmosphere. After that, the liquid held in the PZR flows down to the hot leg and core and liquid level in core increases. In test CLDF, the loop seal clearing (LSC) took place in both loop A and B. The LSC is visualized from the view port located at the horizontal section of the crossover leg and the fluid temperature in the loop seal reaches its saturated value (Fig. 17). In loop B, core steam/water mixture flows along cold leg and crossover leg into the SG-B outlet plenum. However, in loop A, liquid in the crossover leg moves into downcomer and core due to the pressure difference between core upper plenum and cold leg. Also, liquid held in the PZR drops to the hot leg and core. Therefore, the core liquid level recovers significantly. In test HLDF, the level variation of the crossover leg after nozzle dam failure is not significant. And a large amount of coolant is released through SG inlet manway after nozzle dam failure (Fig. 15) and this results in early heat up of the simulated fuel rod. The times required to heat up the simulated fuel rod in tests HLDF and CLDF are about 3076 s and 4348 s respectively.

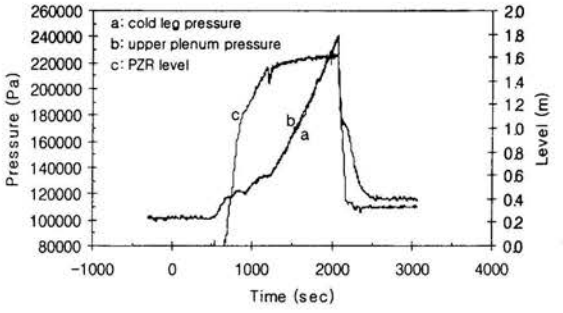

Fig. 13. RCS pressures and level in test HLDF.

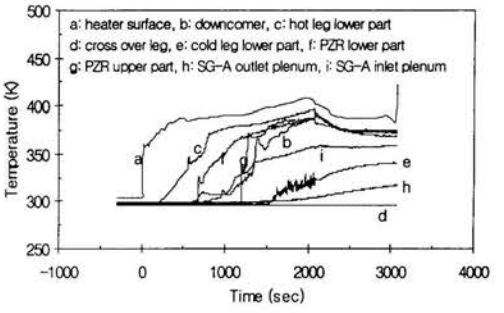

Fig. 14. RCS temperature variations in test HLDF.

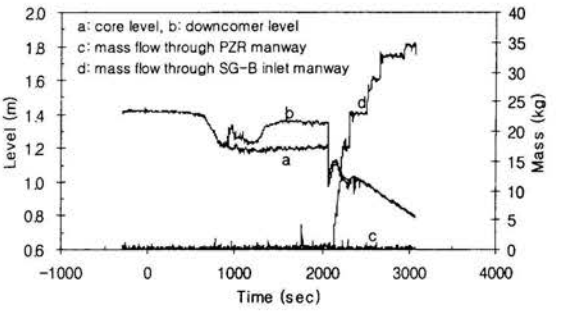

Fig. 15. Collapsed levels and integrated mass flow in test HLDF.

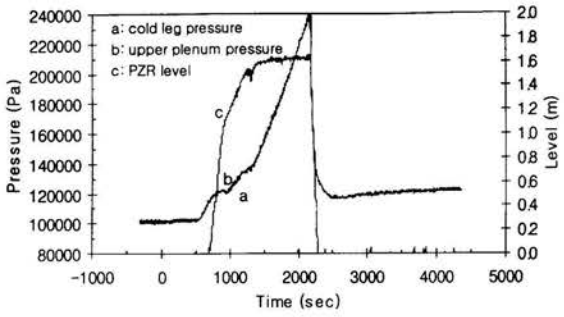

Fig. 16. RCS pressures and level in test CLDF.

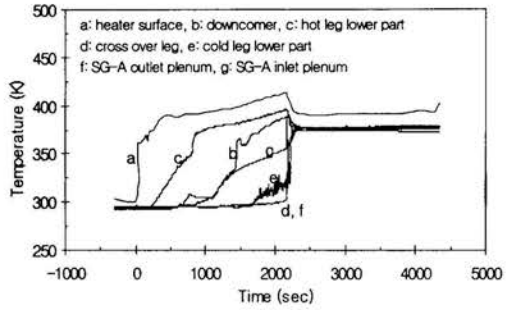

Fig. 17. RCS temperature variations in test CLDF.

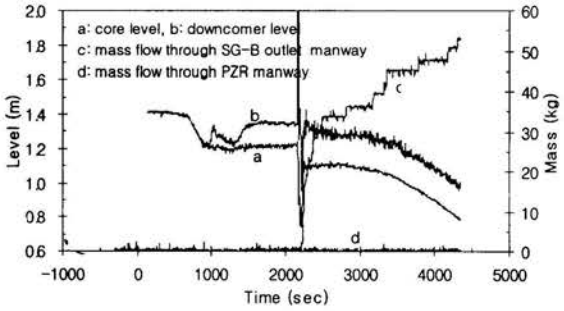

Fig. 18. Collapsed levels and integrated mass flow in test CLDF.

5. CONCLUSIONS

Series of six experiments were conducted at the KIET facility to investigate the thermal hydraulic phenomena with loss of RHR during mid-loop operations. The times required to heat up the simulated fuel rod are 4736 s in test PMO, 7188 s in test PMOSG2, 3627 s in test SGOMO, 2760 s in test SGIMO, 3076 s in test HLDF and 4328 s in test CLDF. This implies that the time required to heat up the simulated fuel rod is significantly dependent on the loss of mass inventory due to venting, as well as liquid holdup in the PZR. When there exists a large opening near the hot leg, the early core heat-up occurs. Also, as results of the failure of temporary closures, the time required to heat up the simulated fuel rod is reduced significantly. Test PMOSG2 shows that the availability of steam generators as a heat sink is very beneficial in limiting RCS heat-up and pressurization once the RHR system fails even though the PZR manway opens. Experimental data obtained from these tests are provided for the assessment of thermal hydraulic codes for the analysis of RCS behavior during PWR mid-loop operation.

REFERENCES

1. U.S. NRC, "Loss of residual heat removal system - Diablo Caynon unit 2, Apr. 10, 1987 ", NUREG-1269, 1987.

2. U.S. NRC, "Loss of vital AC power and the residual heat removal system during mid-loop operations at Vogtle unit 1 on march 20, 1990", NUREG-1410, 1990.

3. N. Watanabe and M. Hirano, "Analysis of operating experience involving loss of decay heat removal during reactor shutdown in pressurized water reactors", Journal of Nuclear Science and Technology, 29(12), 1212-1223, 1992.

4. U.S. NRC, "Shutdown and low-power operation at commercial nuclear power plants in the United States", NUREG-1449, 1993.

5. U.S. NRC, "Operational data analysis of shutdown and low power licensee event reports", AEOD/S93-05, 1993.

6. U.S. NRC, Generic Letter No. 88-17, "Loss of decay heat ", Oct. 1988.

7. R.M. Mandl, K.J. Umminger and J.V.D. Logt, "Failure of PWR-RHRs under shutdown Conditions: experimental Results from PKL test Facility", 18th Water Reactor Safety Information Meeting, Rockville, 433-448, 1990.

8. H. Nakamura, Y. Anoda and Y. Kukita, "Loss of residual heat removal(RHR) during PWR mid-loop operation: experiments in ROSA-IV/LSTF", International Topical Meeting on Safety of Thermal Reactors of The ANS Nuclear Reactor Safety Division, July 21-25, Portland, 497-503, 1991.

9. D. Dumont, G. Lavialle, B. Noel and R. Deruaz, "Loss of residual heat removal during mid-loop operation: BETHSY Experiments", Nuclear Engineering and Design, vol. 149, 365-374, 1994.

10. C.H. Lee, T.J. Liu, Y.S. Way and D.Y. Hsia, "Investigation of mid-loop operation with loss of RHR at INER Integral System Test (IIST) facility", Nuclear Engineering and Design, vol. 163, 349-358, 1996.

11. N. Fujita and D.A. Rice, "Core boiling during mid-loop operation", Nuclear Technology, 93, 33-46, 1991.

12. Y.A. Hassan and L.L. Raja, "Simulation of loss of RHR during mid-loop operation and the role of steam generators in decay heat removal using the RELAP5/MOD3 code", Nuclear Technology, 103, 310-319, 1993.

13. K.W. Seul, Y.S. Bang and H.J. Kim, "Plant behavior following a loss-of-residual-heat- removal event under a shutdown condition", Nuclear Technology, 126, 265-278, 1998.

14. OECD, "ISP-38 on BETHSY test 6.9c", NEA/CSNI/R(97)38, vol 1-2, 1998.

15. H.T. Kim and H.C. NO, "An integral response scaling method for reduced-height test facilities and its validation using RELAP5 for the loss of RHR during the mid-loop operation", Nuclear Technology, 136(2), 2001.

HEFAT2002
1st International Conference on Heat Transfer, Fluid Mechanics, and Thermodynamics
8-10 April 2002, Kruger Park, South Africa
JI1

SIMULATION OF SNUF TEST FACILITY LARGE BREAK LOSS-OF-COOLANT ACCIDENT USING MARS

Ik Jeong*, Soon Jun Hong*, Jin Wook Jang*, Goon Cherl Park**, Un Chul Lee**, Kune Y. Suh**
*Graduate Student, **Professor
Department of Nuclear Engineering, Seoul National University
San 56-1 Sillim-Dong, Kwanak-Gu, Seoul, 151-742, Korea
E-mail: kysuh@snu.ac.kr

ABSTRACT

The MARS code is a best-estimate nuclear power reactor analysis tool comprising a three-dimensional reactor vessel module and a number of one-dimensional component modules. To evaluate the applicability of this code, simulation was performed for a large-break loss-of-coolant accident (LOCA) in the SNUF test facility. The simulation result shows good agreement with the measured data in the test. It is found that the MARS code is a predictive tool with a great potential for the analysis of LOCA.

INTRODUCTION

A multi-dimensional realistic thermal-hydraulic system analysis code, MARS, is being developed at the Korea Atomic Energy Research Institute (KAERI). MARS performs realistic analysis of two-phase thermal hydraulics of pressurized water reactors (PWRs) especially during a large-break loss-of-coolant accident (LBLOCA) where the multi-dimensional phenomena dominate the transient [1]. The result of the international 2D/3D program apparently showed the necessity of multi-dimensional analysis of nuclear reactor thermal hydraulics [2]. The state-of-the-art system analysis codes at present have multi-dimensional modules allowing for more realistic simulation of the fluid dynamics in the reactor coolant system.

MARS was initially developed from COBRA-TF, a three-dimensional reactor vessel analysis code, and RELAP5/MOD3.2, a one-dimensional reactor system analysis code. Jeong et al. [3] assessed COBRA/RELAP, the former version of MARS, using data from the LOFT L2-3 LBLOCA experiment.

The COBRA-TF thermohydrodynamic model is a three-dimensional, two-fluid, three-field representation of the two-phase flow. Three fields represent vapor, continuous liquid and entrained liquid droplets, respectively [4].

SNUF AND TEST DESCRIPTIONS

Facility Description

The Seoul National University Facility (SNUF) is a scaled integral experimental test facility of the YGN Units 3&4, one of the ABB-CE type PWRs in Korea. Its length scale ratio is 1/6.4, area scale ratio $(1/13.4)^2$, and resultantly, the volume scale ratio 1/1144. Figure 1 shows the configuration of SNUF, and Figure 2 shows the schematic diagram. Its design and scaling were based on Ishii's three level scaling [5,6]. The important geometric design parameters are presented in Table 1 [7].

The SNUF has appropriate components of the primary system and the secondary system for the mass and energy release experiment. The facility consists of a reactor vessel, two steam generators (SGs), an intact loop with one cold leg and one hot leg, a broken loop with one hot leg and two cold legs, two discharge tanks, and the safety injection (SI) system. The reactor vessel contains 60 kW electrical heaters to simulate the scaled 2.2% of core decay power. The SG is equipped in each loop, and each SG contains four U-tubes with the height of 1725 mm, six U-tubes with the height of 1643 mm and six U-tubes with the height of 1562 mm. The inner and outer diameters of the U tubes are 19 mm and 21 mm, respectively. The secondary system is composed of the SG shell, the steam line and the feedwater line.

In the intact loop two cold legs are scaled into a lumped single cold leg to maintain a similar volume. In the hot leg a viewport is installed to observe the behavior of fluid.

The broken hot leg is designed to simulate double ended guillotine break, and thus comprises two broken sections, i.e. one on the reactor side and the other on the SG side. The broken sections are simulated using ball valves, and an isolation valve is installed between the two broken sections. Since the isolation valve is instantaneously closed at the beginning of the experiment, the mass releases from each broken section can be measured independently. Two viewports are installed in the hot leg for direct visualization of the flow behavior. A viewport is also installed in the cold leg suction part for the sake of visualization in the early stage of the emergency core cooling system (ECCS) injection.

Discharge tanks connected to each broken section simulate the containment. Hence the discharge tanks were sized to accommodate for the expected amount of discharge flow. The capacity of the reactor vessel side discharge tank was determined to be about 150 liter with the diameter of 600 mm and the height of 700 mm, while that of the SG side discharge tank was 30 liter with the diameter of 300 mm and the height of 700 mm. The two discharge tanks were connected to each

other with 1/2 inch pipes in order to equilibrate the pressure. Each discharge tank contains a cooling system to condense the steam immediately, and then the discharge amount can be measured by a level meter.

The safety injection system is composed of a storage tank, a SI pump and a flow controller. The storage tank is equipped with electrical pre-heaters of 20 kW in order to control the temperature of the SI water. The SI line is connected to the cold leg.

Experimental Conditions and Procedures

The SNUF experiment simulated the post-blowdown transient of the hot leg LBLOCA. Thus, the initial condition is the end-of-blowdown (EOB), which was carefully established in the experiment. The result of the RELAP5 analysis for YGN Units 3&4 was used as the reference initial condition [8]. In the experiment, the EOB was assumed to be about 15 sec elapsed from the initiation of accident. The RELAP5 analysis at this time indicated that the primary system was depressurized close to the containment pressure, and that the core was fully voided. Resultantly, the collapsed liquid level of the reactor fell to a minimum value.

The experiment was conducted in the following procedure: pressure drop test, normal operation, drain-down, and post-blowdown. The result of the pressure drop test was to check on the flow characteristics of the experimental loop, whose results were reflected in the determination of the loss coefficients.

In the normal operation, the primary system and the secondary system were maintained nearly saturated at 0.8 MPa and 0.5 MPa, respectively. The core power was 60 kW. From this condition, the primary water was drained until the water remained only in the lower plenum. This procedure is the drain-down phase. In the drain-down phase, the coolant in the cold leg suction part did not flash up, but rather remained as either saturated or subcooled. Thus, in the experiments the coolant was manually drained. The temperature of the secondary system was higher than that of the primary system. The secondary system could play a role of heat source if the injected SI water passed through the U tubes. From this drain-down process, the initial condition of the experiment was obtained and compared against the EOB condition of YGN Units 3&4 in Table 2 [9].

At the commencement of the experiment, the SI pump was operated, each discharge valve was opened to simulate the break, and the isolation valve was closed simultaneously. The main power was turned on for preheating 30～40 sec prior to the start of the experiment. The SI temperature was maintained at 60℃, which was a little higher than that of the actual plant in order to compensate for the lack of the heat capacity of the reactor coolant system (RCS) metal. The SI flow rate was maintained constant at 2.2 lit/sec. The core power was set equal to 60 kW.

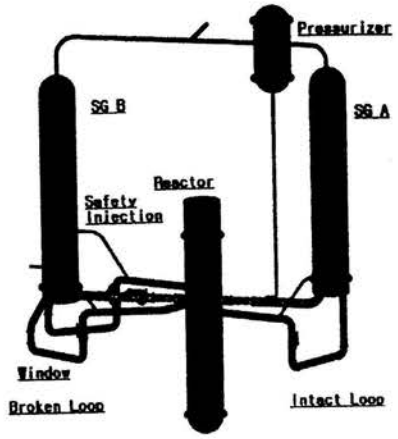

Figure 1: Overview of SNUF

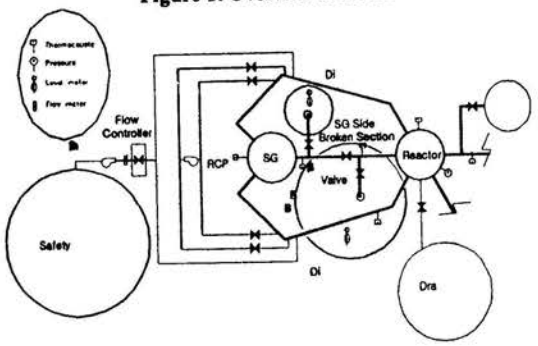

Figure 2: Schematic Diagram of SNUF

Table 1. Design Parameters for SNUF

	SNUF	YGN3&4
Vessel height (mm)	1975	12.7×10^3
Flow area (mm^2)	74748	13.3×10^6
Hot leg flow length (mm)	683	4.83×10^3
Flow area (mm^2)	4990	0.89×10^6
Suction leg flow length (mm)	1172	7.52×10^3
Flow area (mm^2)	2579	0.46×10^6
Discharge leg flow length (mm)	916	5.88×10^3
Flow area (mm^2)	2579	0.46×10^6
Fuel hydraulic diameter (mm)	14	3
Fuel conduction depth (mm)	2.5	2.4

Table 2. Initial Condition in the Prototype

	SNUF	YGN3&4
Core pressure (MPa)	0.35	0.5
Core coolant condition	Saturated	Saturated
Mean power (kW)	60	60×10^3
Core exit void fraction (%)	100	100
Liquid rise velocity (m/sec)	0.0111	0.276

CODE INPUT PREPARATION

In the analysis of the SNUF experiment, the calculation procedure traced that of the experiment, i.e. initialization of the test loop reflecting the measured pressure drop through the vessel and the SGs, calculation of the normal operation, calculation of the drain-down (blowdown) phase and finally calculation of the post-blowdown (reflood) phase.

The MARS input for SNUF consists of a three-dimensional reactor vessel input and a one-dimensional primary system component input. The SNUF vessel including the lower plenum, the heating section and the upper plenum is nodalized as shown in Figures 3 and 4. The channels of the vessel are illustrated on the left side, the gaps connecting the channel are on the right side and the vertical meshes of the vessel are at the center of Figure 3. The heating rods are marked in square symbol in the active core region. The vertical mesh of the nodalization including the vertical elevation is shown in Figure 4.

The cells are laid in the vertical direction and consist of channels, which are connected crosswise. The gaps connect the channels where the cross flow exists. The vessel is composed of the lower plenum, the active core, the upper core and the upper plenum in the axial direction. In each region the downcomer consists of eight channels. The central flow area consists of nine channels. The heating rods are located in the central flow area. The hot legs are connected to the lowest inner mesh of the upper core, and the cold legs are connected to the lowest downcomer mesh of the upper core.

The primary loops connected to the vessel are composed of two independent pipings. The loop for simulating the broken hot leg consists of two cold legs and one hot leg. The intact loop has one lumped cold leg and one hot leg. The two independent secondary loops comprise a feedwater pump. A steam dump facility in each loop lies adjacent to SGs of each primary loop. The nodalization of the primary and secondary loops is shown in Figure 5.

The drain-down phase was simulated using the motor operated valves connected to the bottom of the vessel and the lowest part of the cold leg. The main circulation pump and the feed water pumps were stopped. The steam dump facility was isolated.

The EOB was selected at the time when the level of the coolant in the vessel and the pressure of the primary system were maintained at a sufficiently minimum stable value. Then the SI water was injected into each cold leg. The mass release rate from the broken hot leg to the atmosphere after that time was the main concern of this simulation.

RESULTS OF SIMULATIONS

Normal Operation

For the exact simulation of the test facility, the measured local pressure drop was reflected in determining the loss coefficients of the vessel and the SGs. A steady state was obtained from the calculation of the normal operation. The results are presented in Table 3 in comparison with the experimental condition. The primary system pressure was 0.8 MPa, and nearly saturated. The secondary system pressure was 0.5 MPa.

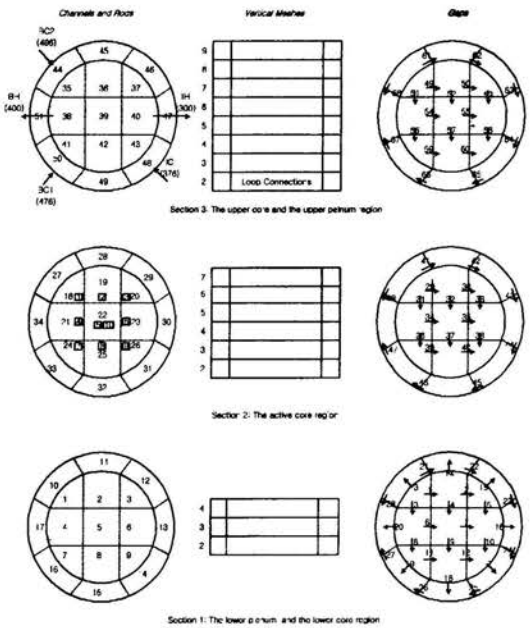

Figure 3: Vessel Nodalization of SNUF in the Crosswise Direction

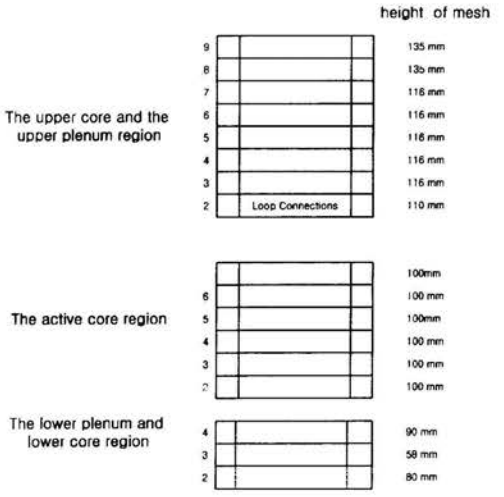

Figure 4: Vertical Meshes of Vessel

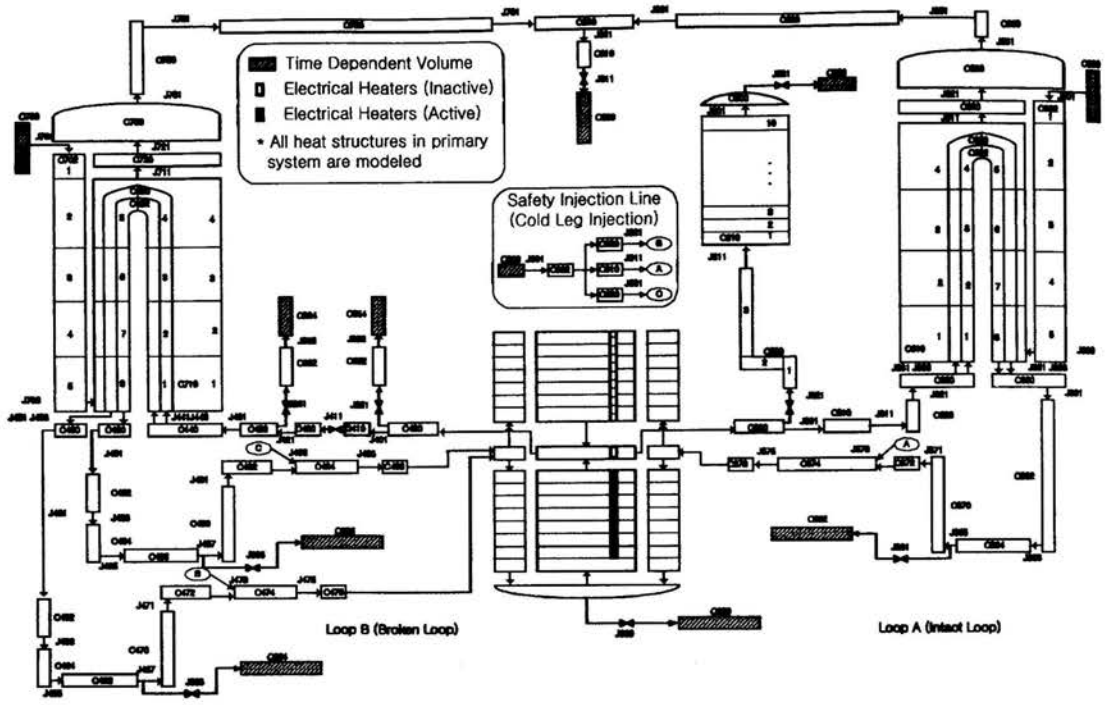

Figure 5: Nodalization of SNUF

Drain-down and the EOB Condition

In the beginning of the SNUF experiment, all the coolant in the primary system was drained except in the reactor lower plenum, and the primary system pressure was 0.35 MPa. To obtain these conditions, the drain-down valves were opened and the primary system coolant was drained from the lower plenum and the bottom of each cold leg. The drain was stopped when the liquid levels in the vessel and each cold leg fell below 65 mm and 20 mm, respectively.

The EOB conditions obtained from this calculation are shown in Table 4, which are consistent with the initial condition of the experiment.

SI Injection of Post-blowdown

For the simulation of the post-blowdown, the drain-down components were removed. The SI line and the breaks at the hot leg were added. The SI water was branched to each cold leg, the flow rate was set constant at 2.2 kg/sec, the temperature was 60℃. The break was modeled as a double-ended one. The coolant was released from the two broken sections. The important conditions are listed in Table 4, compared with the experimental conditions.

Results

Figure 6 compares the pressure at the reactor vessel upper head between the calculation and the experiment. In the experiment, the pressure behavior can be classified into three distinguished steps. In the first step the primary system pressure decreases rapidly. In the second step the pressure increases slightly. In the last step the pressure decreases slowly toward a steady state. The first step extends from 0 to 40 sec, the second step from 40 to 80 sec, and the third step from 80 sec to the end of the test.

The first step is characterized by rapid decrease of the pressure due to steam release. For this step, the calculation shows good agreement with the experiment. The second step is characterized by slight increase of pressure due to steam generation in the core. The predicted pressure rise is higher than that from the experiment due to the two-phase pressure drop in the break junction. In the third step, no more transient is expected in the experiment. The calculation reveals intermittent increase and decrease of the pressure, which may be attributed to the unstable direct contact condensation of steam and subcooled water in the reactor upper plenum.

The integrated break flow through the reactor vessel side broken section and the SG side broken section are presented in Figure 7. It is demonstrated that there is only steam release during the first step of the pressure behavior. However, it seems that the steam release in the experiment was not sufficiently measured since the release was measured by condensing the steam.

The calculation result demonstrated that a little amount of steam is released before 10 sec when the pressure decreases rapidly. However, after 15 sec, little steam is released, and no

increase in the discharged mass is observed. After 60 sec, the experiment shows a stable release, whereas the calculation result shows the direct contact condensation in the reactor vessel upper plenum. Figure 8 shows that the void fraction in the core fluctuates widely.

The temperature measured in the experiment is a local, time averaged value, while the calculated temperature is a volume averaged and time averaged value. Figure 9 compares the experimental and calculated temperatures near the measured point. In the figure, the temperatures of MARS represent the liquid. The calculated temperatures are higher than the measure values on account of the condensation of steam in the experiment. The void fraction in the lower plenum is low initially, but then increases and decreases in order. Thus, the predicted temperatures are higher than the experiment values. Figure 9 shows such oscillation of the void fraction.

The liquid fractions in the downcomer and the inner vessel are illustrated using a two-dimensional contour map. Figures 10 and 11 show that the SI water injected from the cold leg fill the downcomer in the earlier phase of the experiment. They also illustrate that water from the downcomer is transported to the core and evaporated in the heated section in the later phase.

Table 3. Normal Operation Condition

Parameters	SNUF	MARS
Pressure of reactor top head (MPa)	0.8	0.829
Temperature of coolant	Saturated	Saturated
Core power (kW)	60	60
Pressure of secondary system	0.5	0.5

Table 4. EOB Conditions of Experiment and Simulation

Parameters	SNUF	MARS
Pressure of reactor top head (MPa)	0.35	0.36
Pressure of secondary system (MPa)	0.5	0.499
Temperature of lower plenum (℃)	142	140
Temperature of U tube entrance (℃)	139	139
Temperature of feedwater (℃)	154	153
Core power (kW)	60	60
Total SI flow rate (kg/sec)	2.2	2.2
Temperature of SI (℃)	60	60

SUMMARY AND CONCLUSION

Overall the system pressure was adequately predicted. It was shown, however, that the calculated pressure decreased somewhat earlier than in the experiment, and that the predicted pressure in the second step was a little higher than the measured value due to the two-phase pressure drop in break junction.

The discharged mass through the reactor side broken section showed agreement in tendency with the test results. The time when the main release began because of two-phase release was predicted to be earlier than in the experiment.

The discharged mass through the SG side broken section showed a similar trend with the experiment. In the second step, a small mass release was also calculated because the pressure in the second step was predicted to be higher than in the experiment.

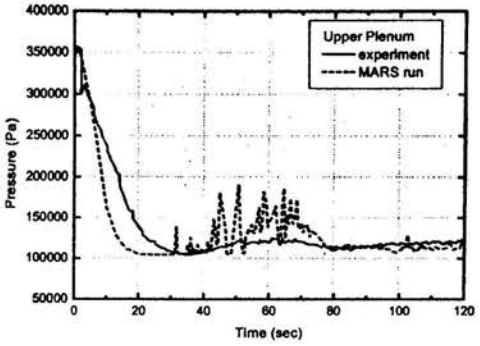

Figure 6: Comparison of Upper Plenum Pressure

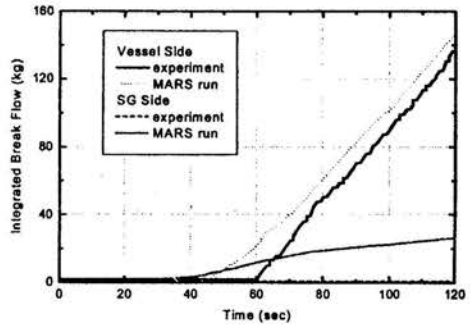

Figure 7: Comparison of Discharged Mass

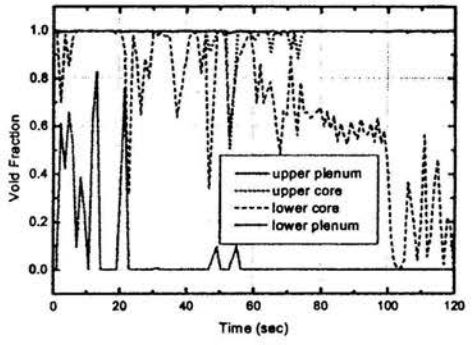

Figure 8: Calculated Void Fraction in Vessel

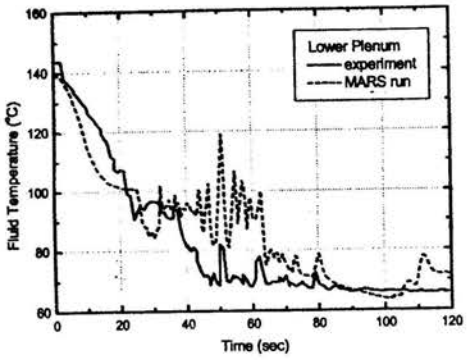

Figure 9: Comparison of Lower Plenum Temperature

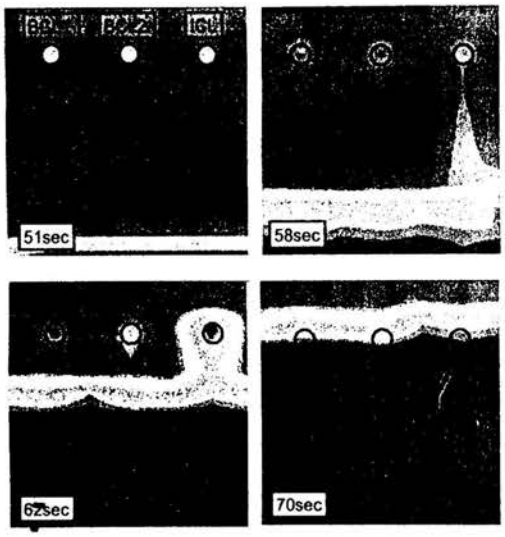

Figure 10: Calculated Downcomer Liquid Fraction

The temperature in the reactor vessel lower plenum was computed slightly higher than in the experiment. However, the temperature near the lower plenum generally concurred with the measured value.

The MARS analysis for the SNUF experiment showed that the code could properly predict the important features of the hot leg LBLOCA during post-blowdown. The releases from reactor side broken section and SG side broken section were also reasonably predicted. MARS is thus concluded to be a promising predictive tool for LOCA analysis of PWRs.

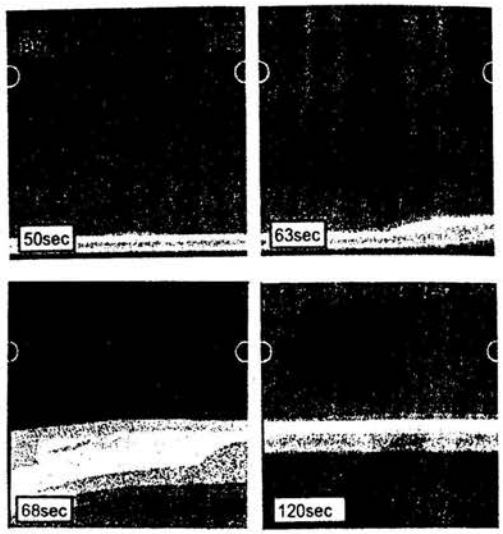

Figure 11: Calculated Reactor Core Liquid Fraction

REFERENCES

[1] Lee W. J. et al., 1998, "Development of a Multi-Dimensional Realistic Thermal-Hydraulic System Analysis Code, MARS 1.3 and Its Verification," KAERI/TR-1108/98, Taejon, Korea.

[2] Damerell, P. S. and Simons, J. W., 1993, NUREG/IA-0126, GRS-100, MPR-1345, USA.

[3] Jeong, J. J., Sim, S. K. Ban, C. H. and Park, C. E. , 1997, "Assessment of the COBRA/RELAP5 Code Using the LOFT L2-3 Large-Break Loss-of-Coolant Experiment, Annals of Nuclear Energy, Vol. 24, No. 14, pp. 1171-1182.

[4] Thurgood, M. J. et al., 1983, NUREG/CR-3046, U.S. Nuclear Regulatory Commission, Washington, DC, USA.

[5] Hong, S. J., Kim J. H. and Park, G. C., 2000, "An Experimental Study on the Mass and Energy Release for a Hot Leg Break LBLOCA during Post Blowdown," J. of the Korean Nuclear Society, Vol. 32, pp. 108-127.

[6] Ishii, M. et al., 1996, "Scientific Design of Purdue University Multi-Dimensional Integral Test Assembly (PUMA) for GE SBWR," NUREG/CR-6309, West Lafayette, IN, USA.

[7] Final Safety Analysis Report for YGN3&4, Korea Electric Power Corporation, Chap. 6.

[8] Kwon, Y. M., Park, C. E. and Song, J. H., 1998, "Comparative Mass and Energy Releases and Containment Analysis for a Large-Break Loss-of-Coolant-Accident Using RELAP5/CONTEMPT4 and Design Computer Codes," Nuclear Technology, Vol. 122, pp. 295-305.

[9] Song, J. H. et al., 1996, "An Analysis Methodology for Hot Leg Break Mass and Energy Release," KAERI/TR-746/96, Taejon, Korea

HEFAT2002
1st International Conference on Heat Transfer, Fluid Mechanics, and Thermodynamics
8-10 April 2002, Kurger Park, South Arfrica
KY3

Experimental Study on Two-Phase Mixture Depletion During a Loss-of-Coolant Accident

Y. S. Kim*, B. U. Bae*, T. W. Kim*, S. J. Hong**, K. Y. Suh***, G. C. Park***, U. C. Lee***

* Graduate Student, ** Post-doctor, ***Professor
Department of Nuclear Engineering, Seoul National University
San 56-1 Sillim-Dong, Kwanak-Gu, Seoul, 151-742, Korea
E-mail: kysuh@snu.ac.kr

ABSTRACT

Severe accidents have so far been studied rather separately from the design-basis accidents (DBAs) in the conventional nuclear reactor safety analysis. Such a discontinued approach cannot predict the initial state of severe accidents precisely. This study is intended to experimentally investigate the depletion rate of the two-phase mixture level in the core after the reflood phase in a large-break loss-of-coolant accident (LBLOCA). The integral test facility, named as SNUF (Seoul National University Facility), was scaled down to 1/6.4 in length and 1/178 in area of the APR1400 (Advanced Power Reactor 1400MWe) through the three-level scaling method. The initial test condition is the plant state at two hours from the accident initiation when the safety injection (SI) is assumed to cease. The measured parameters are the two-phase mixture level in the core and the collapsed liquid level in the downcomer according to the steam generator temperature conditions. The test result shows that the core mixture level decreased faster in the former half than in the latter half of the test duration. Also, the MAAP4 code is shown to estimate the core mixture level higher than the measured data due to the incapability of the code to account for the increased break flow resulting from the sweepout and entrainment by the superheated steam.

INTRODUCTION

In the conventional nuclear reactor safety analysis, a severe accident involving fuel melting has been studied rather separately from the design-basis accidents (DBAs). The DBA analysis is terminated after all the fuel rods are quenched after hitting the peak clad temperature (PCT). On the other hand, the severe accident analysis focuses on the core degradation, melting and relocation when the safety injection (SI) fails, for instance. The thermal hydraulics and fuel degradation during transition from the DBA to the severe accident still defy fully comprehensive understanding. The core mixture level is calculated in MAAP4 [1], which is devoted to the severe accident analysis, considering only the steam generation by the fuel below the core mixture level as shown in Fig. 1. It is thus believed that the mixture level in the core may potentially be overestimated in MAAP4 during the transient dealt with in this study against the conservatism required for the analysis.

This study is geared to experimentally investigating the thermal hydraulics during the transition from the SI failure after reflood to the core uncovery for the large-break loss-of-coolant accident (LBLOCA) in the cold leg. This study is part of the effort to examine the transition process from the DBA to the severe fuel damage and relocation accident whose results are slated to be incorporated into a unified code to continually deal with the accidents from the initial stage to core melt. Experiments were conducted in an integral test loop, SNUF (Seoul National University Facility), which was scaled down to 1/6.4 in length and 1/178 in area of the APR1400 (Advanced Power Reactor 1400MWe) [2] through the three-level scaling method.

The measured parameters are the two-phase mixture level in the core, which is a major parameter in the severe accident analysis during the core uncovery, and the collapsed water level in the downcomer according to the steam generator temperature conditions. The results are compared with those estimated by the MAAP4 code.

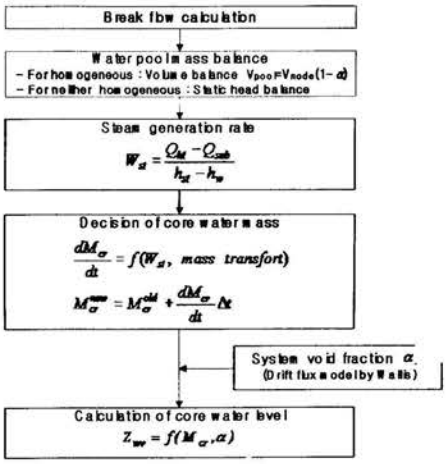

Figure 1: Core mixture level calculation algorithm in MAAP4

NOMENCLATURE

A	flow area or flow area ratio
a	component flow area [mm^2]
c_p	specific heat [kJ/K-kg]
d	hydraulic diameter [mm]
E	energy [kJ]
f	friction factor
g	gravitational constant [9.8m/sec^2]
i	specific enthalpy [kJ/kg]
K	loss coefficient
l	component length [m]
N	dimensionless number

p	pressure [MPa]
$\dot{q}$	heat generation rate [kW]
T^*	Time ratio number
u	velocity [m/sec]
V_{gj}	drift velocity [m/sec]
w	work [kJ]
x	quality

Greek Letters

α	void fraction
Δ	difference
δ	conduction depth [m]
μ	viscosity [N sec/m^2]
ρ	density [kg/m^3]
τ	time constant
ξ	wetted perimeter [mm]

Subscripts

0	reference
e	exit
f	liquid or fluid
g	gas or vapor
m	model
p	prototype
R	ratio
sub	subcooling

EXPERIMENTAL METHOD

Accident Scenario

According to the probabilistic safety assessment (PSA) results of the APR1400 [2], the core damage frequency (CDF) of the LBLOCA ranks the fifth among the considered accidents due to the low probability of the initiating event. However, the LBLOCA in cold leg is selected as the reference scenario because of its high CDF compared to the low initial occurrence probability as shown in Table 1. The initial test condition, as shown in Table 2, represents the plant condition when the SI is ceased at two hours after the accident initiation.

Table 1: PSA results for APR1400

Initial Event	Initiating Event Frequency (a)	Core Damage Frequency (b)	CDF/IEF (b/a)
Station Blackout	1.24E-05	1.21E-06	9.76E-02
Large LOCA	6.97E-05	6.91E-07	9.91E-03
Medium LOCA	1.40E-04	6.10E-07	4.36E-03
Small LOCA	3.00E-03	1.36E-06	4.53E-04
Steam Generator Tube Rupture	4.50E-03	7.05E-07	1.57E-04
Loss of Main Feedwater	1.70E-01	1.25E-06	7.35E-06

Table 2: Initial conditions in APR1400 and SNUF

Parameters	APR1400[3]	SNUF
Upper Plenum Pressure	< 0.2 MPa	0.1 MPa
Core Temperature	< 115℃	~ 95℃
Core Exit Void Fraction	100%	100%
Core Level	< Btm of cold leg	Btm of cold leg
Core Power	42.09MW	90kW
Steam Generator Temperature	-	120℃/172℃

The SI failure is assumed to take place when the operator switches the SI flow path to the hot leg and vessel synchronous injection mode to avoid the loss of coolable geometry by the boron precipitation in the core.

Scaling of Test Facility

The three-level scaling methods were adopted to design the SNUF [4,5,6]. The method involves the top-down and bottom-up approaches to account for the global, boundary flow and local phenomena scaling. In the global scaling, the important dimensionless numbers for the kinematic, dynamic and energetic similarities [5] are as follows.

Phase change number:

$$N_{sub} \equiv \left[\frac{4\bar{q}_0''\delta l_0}{du_0\rho_f i_{fg}}\right]\left[\frac{\Delta\rho}{\rho_g}\right] \tag{1}$$

Subcooling Number:

$$N_{sub} \equiv \left[\frac{i_{sub}}{i_{fg}}\right]\left[\frac{\Delta\rho}{\rho_g}\right] \tag{2}$$

Froude number:

$$(N_{Fr})_R \equiv \left[\frac{u_0^2}{gl_0\alpha_0}\right]_R\left[\frac{\rho_f}{\Delta\rho}\right]_R \tag{3}$$

Drift-flux number:

$$N_{di} \equiv \left[\frac{V_{gj}}{u_0}\right]_i \tag{4}$$

Time ratio number:

$$T_i^* \equiv \left[\frac{l_0/u_0}{\delta^2/\alpha_s}\right]_i \tag{5}$$

Thermal inertia ratio:

$$N_{thi} \equiv \left[\frac{\rho_s c_{ps}\delta}{\rho_s c_{pf} d}\right]_i \tag{6}$$

Friction number

$$N_{fi} \equiv \left[\frac{fl}{d}\right]_i\left[\frac{1+x(\Delta\rho/\rho_g)}{(1+x(\Delta\mu/\mu_g)^{0.25}}\right]\left[\frac{a_0}{a_i}\right]^2 \tag{7}$$

Orifice number:

$$N_{oi} \equiv K_i[1+x^{3/2}(\Delta\rho/\rho_g)]\left[\frac{a_0}{a_i}\right]^2 \tag{8}$$

In addition to the above physical similarity groups, the geometric similarity groups are given as

$$\begin{aligned} &\text{Axial length scaling} : L_i \equiv l_i/l_0 \\ &\text{Flow area scaling} : A_i \equiv a_i/a_0 \end{aligned} \tag{9}$$

The geometric scaling criterion requires the following relations to be satisfied for all the components of system

$$L_{iR} = (l_i / l_0)_R = 1$$
$$A_{iR} = (a_i / a_0)_R = 1 \qquad (10)$$

Based on the requirements of Eq. (10), the SNUF was scaled down to 1/6.4 in length and 1/178 in area of the APR1400 as shown in Figs. 2 and 3. Table 3 shows the detailed dimensions of both the APR1400 and the SNUF.

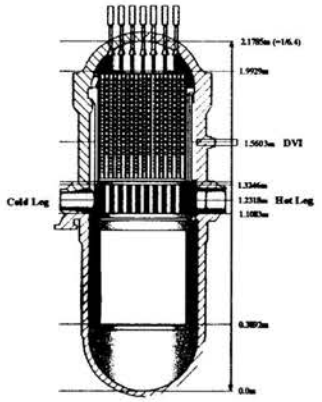

Figure 2: Cross-sectional front view of reactor vessel

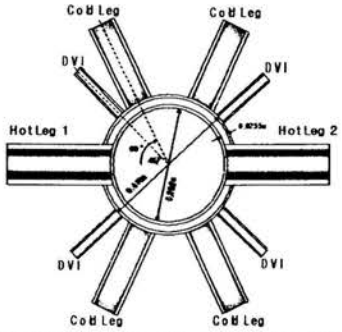

Figure 3: Cross-sectional top view of reactor vessel

Table 3: Design values for APR1400 and SNUF

Parameter		Unit	APR1400	SNUF
Vessel	Height	mm	13,942.2	2,178.0
	Area	mm^2	1.33×107	74,748.0
Hot leg	Length	mm	4,298.0	672.0
	Area	mm^2	0.89×106	4,999.0
Cold leg	Length	mm	7,608.0	1,189.0
	Area	mm^2	0.46×106	2,579.0
Break area		mm^2	0.46×106	1,018.7
Fuel hydraulic diameter		mm	3.0	24.8
Fuel conduction depth		mm	2.4	3.1
Heater power		kW	4.2×104	96.0

The hydraulic diameter and the conduction depth in the fuel, given in Table 3, are defined as follows.

$$d_i \equiv 4a_i / \xi_i \qquad (11)$$
$$\delta_i \equiv a_{si} / \xi_i \qquad (12)$$
$$d_i \equiv 4(a_i / a_{si})\delta_i \qquad (13)$$

According to the TRAC results [3] for the LBLOCA of the APR1400, the plant state at two hours from accident initiation is below 0.2MPa of pressure and the coolant is subcooled by more than 5℃. Since the test facility can be maintained in the similar thermal hydraulic condition with the prototype, the fluid properties are almost the same. This experiment is intended to measure the core mixture level. The similarity of the parameters affecting the core level has to be absolutely preserved. The most important nondimensional parameter is the Froude number [7].

$$(N_{Fr})_R \equiv \left[\frac{u_0^2}{g l_0 \alpha_0}\right]_R \left[\frac{\rho_f}{\Delta\rho}\right]_R = \frac{(u_0^2)_R}{(l_0)_R} = 1 \qquad (14)$$

$$u_{0R} = l_{0R}^{1/2} \qquad (15)$$

$$\tau_R = \frac{(l_0)_R}{(u_0)_R} = (l_0)_R^{1/2} \qquad (16)$$

Since the length ratio is 1/6.4, time ratio of the test facility is 0.395 from Eq. (16), the transient proceeds 2.5 times faster in the test facility than in the prototype.

The similarity in the drift flux number requires the following void relation to be satisfied

$$(\alpha_e)_R \left[\frac{\Delta\rho}{\rho_f}\right]_R = 1 \quad \text{or} \quad (\alpha_e)_R \cong 1 \qquad (17)$$

Since the core exit void fractions are the same as 1.0 in both prototype and test facility, the requirement of Eq. (17) is satisfied.

The orifice number is composed of the loss coefficient, the properties of fluid and the geometrical ratio. The ratio of the loss coefficient can be set equal to 1.0 when the area ratio among the system components is kept constant. Since nearly the identical temperature and pressure are maintained in both the prototype and the model, the properties are essentially the same. Thus, the similarity of the orifice number is conserved.

Since the subcooling number consists of the fluid properties, similarity is achieved by maintaining the similar temperature and pressure between the prototype and the model.

The thermal inertia number is defined as the ratio of the heat capacity of working fluid and the structure. Since the temperature of the structure is close to that of the fluid at two hours from the accident initiation, the heat addition to the fluid from the structure is neglected in the experiment.

The test condition corresponds to the plant state at two hours from the LBLOCA initiation. The decay heat of the prototype is 42.09MWth pursuant to the decay heat model of the ANS-1979 [8]. The required total heater power of the test facility was determined as follows.

Thermal power:

$$(q_0)_R = \frac{(q_0)_m}{(q_0)_P} = a_{0R} \times \sqrt{l_{0R}} \quad (18)$$

$$(q_0)_m = (q_0)_P \times q_{0R}$$
$$= 93.47(kW)$$

Number of heaters:

$$(V_{heater})_m = (V_{fuel})_P \times a_{0R} \times l_{0R}$$
$$= \frac{\pi}{4} \times D_m^2 \times L_m \times N \quad (19)$$
$$= 1.406 \times 10^{-2}$$
$$N = 25$$

Although the heater power of 93.47kW was calculated by the similarity relation of Eq. (18), the heater power was designed to 96kW to consider the operation margin and the sensitivity study in the future. The similarity of the flow area was conserved by installing twenty-four (24) heaters of diameter of 20mm and 1 rod-type mixture level transmitter of diameter of 23mm in the core.

In the second-level scaling of the boundary flow and inventory scaling, the important parameter is the break flow that must satisfy the following relations:

$$(a_{break})_R = (l_{0R})^{1/2} (a_0)_R = 0.395 \times (a_0)_R \quad (20)$$

The required break area was kept by installing an orifice at the break location.

In the energy inventory scaling, the following relation must be considered

$$\frac{dE}{dt} = q - w + \sum m_{in} i_{in} - \sum m_{out} i_{out} \quad (21)$$

It can be seen from Eq. (21) that only the total heat without considering the heat addition mechanism is treated. When the heat addition from structure except fuel needs to consider, it can be compensated with the increase of heater power as much as that. As previously described, the heat addition from structure is not significant in this experiment.

The third-level scaling is the local phenomena scaling. The major phenomena are the sweepout in the downcomer and the entrainment in the core, which governs the coolant level in the core and the downcomer. These phenomena can be preserved by conserving the flow regime of the prototype. The related parameters are the void fraction, the gas temperature and the Froude number, which governs the gravitational force and the behavior on the free surface. The similarity of the void fraction has already been ascertained in Eq. (17), The gas temperature ratio has been satisfied due to the similar pressure and temperature conditions between the prototype and the model. The similarity of the Froude number has also been checked in Eq. (14).

The major design parameters of the SNUF determined from the above similarity requirement are compared with those for the APR1400 in Table 3.

Description of Test Facility

The design parameters of the test facility based on the scaling study are shown in Figs. 2, 3 and Table 3. The test facility simulates the APR1400, which consists of one hot leg and two cold legs in each loop as shown in Fig. 4. The major components are the reactor vessel, the steam generator, the pressurizer and the piping. The reactor vessel contains 24 heaters to simulate the decay heat of the prototype core. The steam generator is equipped in each loop and each contains sixteen (16) U-tubes. The secondary system consists of the steam generator shell, the steam line and the feedwater line.

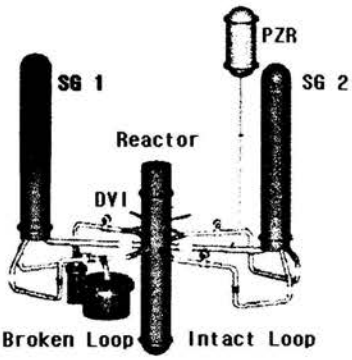

Figure 4: Bird's eye view of the SNUF

The SI system consists of a storage tank, a pump and a flow control valve. The piping is connected to the upper reactor vessel as illustrated as DVI (direct vessel injection) in Figs. 2 and 3.

The broken cold leg was designed to simulate the double-ended guillotine break between the reactor coolant pump and the reactor vessel. The cold leg break is simulated with two broken section valves and one separation valve. The two discharge tanks connected to the broken section simulate the containment and simultaneously measure the break flow using the level gauge equipped in the tank.

Instrumentation

The principal measured parameters are the two-phase mixture level in the core and the collapsed water level in the downcomer by the float type level transmitter equipped with the reed switches in the tube and the DP (differential pressure) transmitter by Rosemount Co. The absolute pressure was measured at the reactor vessel upper plenum with DPI 260 model by Druck Co. The orifice meter equipped in each loop measured the steam flow rate entering the downcomer from each intact cold leg. The differential pressure between the reactor upper plenum and the downcomer was measured with the DP transmitter of Rosemount Co. The temperatures were measured by T-type thermocouples in the reactor upper plenum, downcomer, each cold leg, each hot leg, and each steam generator primary exit. The steam generator reverse heat flux can be computed using the steam generator (SG) temperature data and the steam flow rates in the intact cold legs.

Test Procedure

The structures of the primary system are pre-heated to about 100℃ to minimize the heat loss during the test duration.

The temperature of the secondary system is maintained according to the required test condition. The primary liquid is drained through the drain valve installed underneath the bottom of the reactor vessel until the liquid level falls below the bottom of the cold leg. The drain valve equipped in each suction leg drains the remaining coolant in the pipe. At the start of the test, all the discharge valves are opened and the separation valve is closed simultaneously to simulate the break and the heater power is turned on.

EXPERIMENTAL RESULTS

The liquid level was maintained close to the bottom of the cold leg and the liquid temperature was maintained about 90℃ in the atmosphere to simulate the plant state when the SI failure occurs at two hours from the LBLOCA initiation. On turning on the heater power at about 100sec, the liquid in the core was boiled up to the saturated condition and the swelled-up mixture began to spill over into both the hot legs at about 120sec as shown in Figs. 5 and 6.

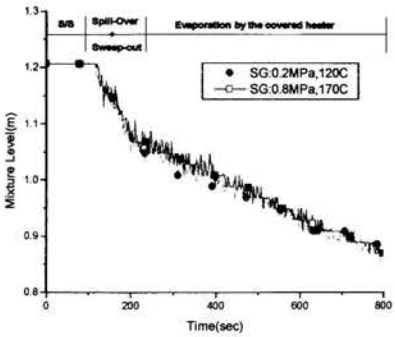

Figure 5: Core two-phase mixture level

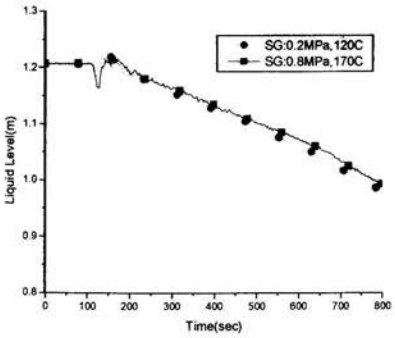

Figure 6: Downcomer collapsed water level

This spillover reduced the static head in the core so that the liquid in the downcomer surged into the core by the static head difference to lower the level in the downcomer as shown in Fig. 6. The spillover liquid in the hot legs was gradually heated up by the reverse heat transfer from the steam generator. The upper plenum pressure was gradually increased in proportion to the steam generation as shown in Fig. 7. The pressure buildup in the upper plenum gave rise to the out-surge of the liquid from the core into the downcomer. This restored the downcomer level up to the bottom of the cold leg and eventually generated the spillover into the broken cold leg at about 150sec as shown in Fig. 6. During the cold leg spillover, the downcomer water level was maintained nearly constant but the core level was decreased almost as much as the spillover from 150 to 180sec as shown in Figs. 5 and 6. At about 180sec, the cold leg spillover was terminated when the downcomer water level was lowered below the bottom of the cold leg as shown in Fig. 6.

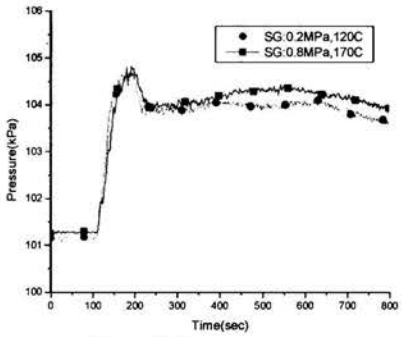

Figure 7: System pressure

On the other hand, the differential pressure between the upper plenum and the downcomer and the steam flow rate were increased due to the buildup of the upper plenum pressure as shown in Figs. 8 and 9. The core two-phase mixture level was decreased faster from 180sec after the termination of the cold leg spillover to about 250sec than during the latter half of the test as shown in Figs. 5 and 10.

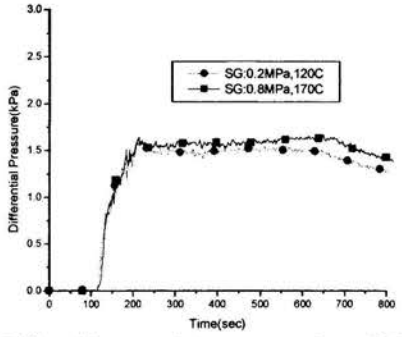

Figure 8: Differential pressure between upper plenum & downcomer

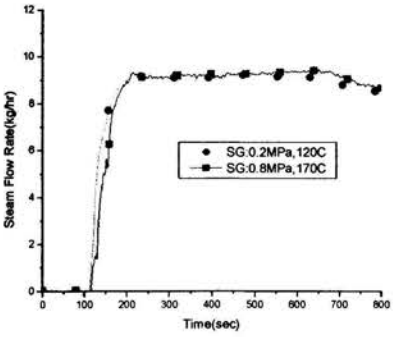

Figure 9: Steam flow rate in loop 1

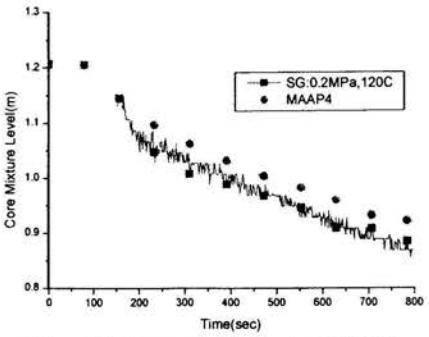

Figure 10: Measured core level vs. MAAP4

The downcomer water level was gradually decreased while the steam flow rate through the intact cold leg remained nearly constant as shown in Figs. 6 and 9. The thermal hydraulic behavior may be explained in terms of sweepout of water in the downcomer. While the steam entering the downcomer from the intact cold leg was gushing through above the surface of water in the downcomer, the steam dragged the liquid into the broken cold leg to reduce the coolant inventory in the reactor vessel whereby accelerating the decrease rate of core two-phase mixture level. The core mixture level in Fig. 10 indicates that the sweepout contributed to decreasing the core mixture level faster than the results predicted by MAAP4 considering only the steam generation by heaters submerged underneath the core mixture level as illustrated in Fig. 1. When the downcomer water level came down below the critical height for sweepout, the sweepout was terminated such that the core and downcomer coolant levels almost linearly decreased from 250sec on as demonstrated in Figs. 5 and 6.

During the rest of the test the core mixture level decreased slightly faster than was calculated by MAAP4 as shown in Fig. 10. The difference is attributed to entrainment on the surface of two-phase mixture in the core. The primary steam temperatures increased by the SG reverse heat transfer while passing through the U-tubes as shown in Fig. 11. However, the steam at the inlet of the cold leg was cooled down to almost 100℃ due to heat loss to the piping and subsequent condensation. It was thus observed that the SG reverse heat transfer did not significantly affect the core mixture level.

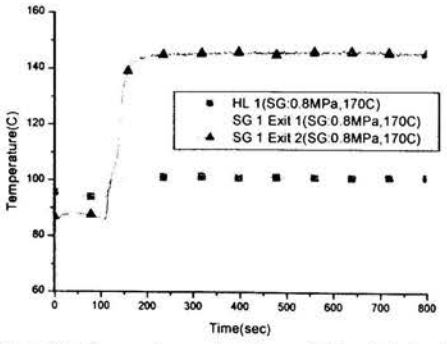

Figure 11: Temperatures at hot leg and SG exit in the broken loop

CONCLUSION

Experiments were performed to determine the two-phase coolant level in the core during the uncovery initiated by a LBLOCA. Test results demonstrate that the core mixture level decreased rather rapidly in the early period of core uncovery and slowly in the latter part of the transient. The differential thermal hydraulic behavior resulted from the sweepout by the steam and water interaction in the downcomer as well as the entrainment of droplets in the core on top of evaporation in the core. As the steam flow rate increased with the core power and the SG reverse heat flux, the coolant level in the core decreased faster. MAAP4 estimated the core level higher than the measured value because the code did not account for the various thermal hydraulic phenomena such as sweepout and entrainment. When the downcomer coolant level fell below the critical void height for the occurrence of sweepout, the core mixture level decreased linearly pursuant mostly to evaporation in the core.

On the basis of these test results it is recommended that the core water level computation in MAAP4 be improved to consider the multi-dimensional thermal hydraulic phenomena such as sweepout and entrainment.

REFERENCES

[1] "MAAP4 User's Guide," Electric Power Research Institute, Palo Alto, CA, USA, 1994.

[2] "Standard Safety Analysis Report for the Korean Next Generation Reactor," Korea Electric Power Corporation, Seoul, Korea, 1999.

[3] "Verification for Conservatism of EM Code Using TRAC (Draft)," Korea Electrical Power Research Institute, Daejon, Korea, 2000.

[4] Hong, S.J. and Park, G.C., "Study on Post-Blowdown of Hot-Leg Large Break Loss-of-Coolant-Accident in the View of Mass and Energy Release Analysis," Nuclear Engineering and Design, 2001.

[5] Ishii, M. and Kataoka, I., 1984, "Scaling Laws for Thermal Hydraulic System under Single Phase and Two Phase Natural Circulation," Nuclear Engineering and Design,

[6] Yun B.J. et al., 2000, "Development of Scaling Law for the Direct ECC Bypass During LBLOCA Reflood Phase with Direct Vessel Injection System," Proceedings of the Korean Nuclear Society.

[7] Tong, L.S., 1965, "Boiling Heat Transfer and Two Phase Flow," Wiley and Sons, Inc., New York, NY, USA.

[8] "RETRAN-3D - A Program for Transient Thermal Hydraulic Analysis of Complex Fluid Flow Systems," NP-7450, Electric Power Research Institute, 1996.

HEFAT2002
1st International Conference on Heat Transfer, Fluid Mechanics, and Thermodynamics
8-10 April 2002, Kruger Park, South Africa
LD2

ANALYSIS OF LOSS-OF-COOLANT ACCIDENT BEHAVIOR OF ADVANCED POWER REACTOR USING MAAP4.03 AND RELAP5/MOD3.2.2

Doo Yong Lee*, Chang Hwan Park*, Ik Jeong*, Un Chul Lee**, Kune Y. Suh**, Goon Cherl Park**
*Graduate Student, **Professor
Department of Nuclear Engineering, Seoul National University
San 56-1 Sillim-Dong, Kwanak-Gu, Seoul, 151-742, Korea
E-mail: kysuh@snu.ac.kr

ABSTRACT

Analysis was performed for a large-break loss-of-coolant accident (LOCA) of the APR1400 (Advanced Power Reactor 1400MWe) with the RELAP5/MOD3.2.2 and MAAP4.03 codes. The two codes predicted different behavior even with the same initiating conditions. The MAAP4.03 code predicted considerably higher break flow and emergency core cooling (ECC) flow rates during the initial stage of the transient than the RELAP5/ MOD3.2.2 code, which causes the LOCA sequences to deviate from one another. Hence, the break flow model in MAAP4.03 was modified by implementing the two-phase homogeneous critical flow model with a correction term. The ECC flow model in MAAP4.03 was also improved by changing the hardwired friction factor based on the sensitivity study. Results of the MAAP calculation with these modified models were compared with those of the RELAP5/MOD3.2.2 computation.

INTRODUCTION

The break flow model and the emergency core cooling (ECC) model play a major role in determining the sequence of events during a loss-of-coolant accident (LOCA) in the nuclear power plant. Thus, accurate calculations of the break flow and the ECC flow are prerequisite to evaluating the optimized emergency core cooling system (ECCS) for an advanced reactor.

This work is concerned with evaluation of the severe accident analysis code MAAP4.03 [1] for the case of a LOCA in the pressure boundary of the primary system. Normally the initial phase of a severe accident in MAAP4.03 is calculated roughly as a precursor condition for the severe accident leading to the core uncovery, heatup, melting and relocation. So far the design-basis LOCA and the severe core melting LOCA have been analyzed using two dedicated codes for each purpose. For instance the thermal hydraulic computer codes like RELAP5/MOD3.2.2 [2] performed the calculation for the design-basis LOCA until the core uncovery. On the other hand the severe accident computer codes including MAAP4.03 accounted for LOCA involving severe core damage.

It is proposed to predict the design-basis accident (DBA) and the beyond DBA to severe accident on a continual, consistent, coherent basis utilizing one single code rather than separate, dedicated codes for each phase of the one accident. Preliminary results for a large-break LOCA analysis for the APR1400 (Advanced Power Reactor 1400MWe) between MAAP4.03 and RELAP5/MOD3.2.2 indicate that there exists a considerable difference in thermal hydraulic behavior predicted by the two codes. One of the most salient is the calculated result for the break flow rate. The ECC behavior also differs considerably between the two codes. Thus a sensitivity study is performed for the parameters related to the differences between the two codes with the improvement made to the MAAP4.03 break flow and the ECC flow models. In particular the Henry-Fauske [3] two-phase critical flow model in RELAP5/MOD3.2.2 was transplanted in MAAP4.03 along with an auxiliary function to prevent overestimation of the break flow rate in the high-pressure region.

Results of the simulation of the APR1400 LOCA using the modified break flow and ECC flow models in MAAP4.03 show that the break flow rate for the modified model concurs with that calculated by RELAP5/ MOD3.2.2 in the earlier phase. But it turns out that the overall APR1400 LOCA behavior is only slightly influenced by the modified break flow and ECC flow models. Since there is no momentum equation in MAAP4.03 for the primary system, pressures for each of the fourteen nodes of the primary system are not individually computed. Therefore, for more realistic simulation of the initial stage of the LOCA using MAAP4.03, more detailed and mechanistic thermal hydraulic calculations are required for the primary system.

NOMENCLATURE

A	area of the opening (m^2)
A_{pipe}	cross-sectional area of one accumulator pipe (m^2)
C	constant
C_d	discharge coefficient
CF	correction factor (Pa)
f	friction factor
f_{CD}	opening discharge coefficient
G^2	critical mass flux ([kg/m^{2}sec]^2)
L/D	length to diameter ratio of the safety injection tank

(SIT)

P_1, P_2 pressure in the upstream and downstream compartment, respectively (Pa)

P_a pressure in the SIT (Pa)

P_{ps} pressure in the primary system (Pa)

P_{sat} saturation pressure (Pa)

r pressure ratio

ω mass flow rate (kg/sec)

ω_g, ω_w mass flow rate for the gas-steam mixture and water, respectively (kg/sec)

Greek Letters

α void fraction of the mixture

γ ratio of the specific heats of steam

η_{crit} critical pressure ratio

ρ density (kg/m^3)

v_g, v_l specific volumes of gas steam mixture and water, respectively in the upstream compartment (m^3/kg)

$v_{w,a}$ specific volume of water in the SIT (m^3/kg)

χ quality

IMPROVEMENT OF THE BREAK FLOW MODEL

Break Flow Model In Maap4.03

The current MAAP4.03 code calculates the mass flow rate of the subcooled water or a two-phase mixture through an opening between two compartments using a simplified version of the Henry-Fauske two-phase critical flow model. The functional basis of the simplified version of the Henry-Fauske two-phase critical flow model is as follows.

The density ρ of the two-phase mixture is defined by

$$\rho = \frac{\alpha}{v_g} + \frac{1-\alpha}{v_l} \tag{1}$$

The quality χ of the two-phase mixture is given by $\chi = \frac{\alpha}{v_g \rho}$. Flow is calculated as a function of a pressure ratio, r, which is either the actual pressure ratio P_1 / P_2 for the unchoked flow or the critical pressure ratio η_{crit} for the choked flow as expressed by

$$r = \max(\eta_{crit}, P_2 / P_1) \tag{2}$$

In addition η_{crit} is taken to be the minimum of the saturation pressure ratio P_{sat} / P_1 and the critical pressure ratio η for the critical flow of the two-phase mixture as

$$\eta_{crit} = \min(\eta, P_{sat} / P_1) \tag{3}$$

A simplified fit to the Henry-Fauske model is used to calculate η as

$$\eta = \begin{cases} 0.83 - \dfrac{0.15}{0.22}\chi & \chi \le 0.2 \\ 0.69 - \dfrac{[0.69 - (\frac{2}{1+\gamma})^{\frac{\gamma}{\gamma-1}}]}{0.8}(\chi - 0.2) & \chi > 0.2 \end{cases} \tag{4}$$

For water flow with $\alpha < 0.001$, the mass flow rate ω is given by

$$\omega = A f_{CD} \left[\frac{2P_1(1-r)}{v_l} \right]^{1/2} \tag{5}$$

For a two-phase flow with $\alpha \ge 0.001$, the mass flow rate ω is expressed as

$$\omega = A f_{CD} \left\{ \frac{2P_1 \rho \left[\frac{1-\alpha}{\alpha}(1-r) + \frac{\gamma}{\gamma-1}(1 - r^{\frac{\gamma-1}{\gamma}}) \right]}{\alpha \left[\frac{1-\alpha}{\alpha} + \frac{1}{r^{1/\gamma}} \right]^2} \right\}^{1/2} \tag{6}$$

The mass flow rates ω_g, ω_w for respectively the gas-steam mixture and water through the opening are then calculated by

$$\begin{aligned} \omega_g &= \omega\chi \\ \omega_w &= \omega(1-\chi) \end{aligned} \tag{7}$$

Modification of the Break Flow Model

The break flow model for the two-phase mixture in MAAP4.03 is modified by using the Henry-Fauske two-phase critical flow model as implemented in RELAP5/MOD3.2.2.

The critical mass flux G^2 used to modify the model is given by

$$\begin{aligned} G^2 &= 2\rho_t^2 \left[\frac{P_0}{\rho_0} - \frac{P_t}{\rho_t} \right] \\ \rho_t &= 1/[(1-\chi_0)v_{l,0} + \chi_0 v_{g,t}] \\ \rho_t' &= 1/\left[(1-\chi_0)v_{l,0} + \frac{\gamma}{\gamma-1}\chi_0 v_{g,t} \right] \\ \rho_0' &= 1/\left[(1-\chi_0)v_{l,0} + \frac{\gamma}{\gamma-1}\chi_0 v_{g,0} \right] \end{aligned} \tag{8}$$

In Equation (8) subscripts 0 and t signify the stagnation and throat values, respectively. Since there are no throat values in MAAP4.03, the donor compartment values are used instead. The critical pressure ratio η of MAAP4.03 is used to

calculate P_t / P_0 of the modified model.

Since the following relations hold as

$$\chi_0 = \frac{\alpha_0 v_{l,0}}{(1-\alpha_0)v_{g,0} + \alpha_0 v_{l,0}} \quad , \quad v_{g,t} = v_{g,0}\left(\frac{P_t}{P_0}\right)^{-\frac{1}{\gamma}} \tag{9}$$

Equation (8) can be rearranged as

$$G^2 = 2\rho_t^2 P_0\left[\frac{1}{\rho_0} - \frac{\eta}{\rho_t}\right]$$

$$\rho_t = \frac{(1-\alpha_0)v_{g,0} + \alpha_0 v_{l,0}}{v_{g,0}v_{l,0}[1-\alpha_0 + \alpha_0(\eta)^{-1/\gamma}]} \tag{10}$$

$$\rho_t' = \frac{(1-\alpha_0)v_{g,0} + \alpha_0 v_{l,0}}{v_{g,0}v_{l,0}[1-\alpha_0 + \frac{\alpha_0\gamma}{\gamma-1}(\eta)^{-1/\gamma}]}$$

$$\rho_t' = \frac{(1-\alpha_0)v_{g,0} + \alpha_0 v_{l,0}}{v_{g,0}v_{l,0}[1-\alpha_0 + \frac{\alpha_0\gamma}{\gamma-1}]}$$

To correlate the values of the donor compartment and the earlier phase of the break flow rate, a new discharge coefficient is considered as follows

$$f_{CD}' = f_{CD} \times \left|1 - \frac{(P_0/P)^2}{C}\right| \tag{11}$$

where constant C can be found by sensitivity study to get a relative break flow rate. This treatment is intended to correct for the over-estimated break flow rate dominantly resulting from large pressure difference.

As a result, the break flow rate is given by

$$\omega = A f_{CD}' \rho_t \left[2P_0\left(\frac{1}{\rho_0} - \frac{\eta}{\rho_t}\right)\right]^{1/2} \tag{12}$$

EVALUATION OF THE ECC FLOW MODEL

MAAP4.03 represents the flow from one safety injection tank (SIT) into the primary system by the equation

$$\omega = C_d A_{pipe}\sqrt{\frac{2(P_a - P_{ps})}{v_{w,a}}} \tag{13}$$

$$C_d = \frac{1}{\sqrt{1 + fL/D}}$$

In Equation (13), L/D is the input value and the friction factor f is a hardwired value. From the analysis of the APR1400, using the hardwired friction factor of 0.02, the ECC flow rate calculated by MAAP4.03 is higher than that computed by RELAP5/MOD3.2.2. Therefore changing the friction factor from 0.02 to 0.1 through sensitivity study, the ECC flow rates are compared between two codes.

SIMULATION OF APR1400 LOCA

Primary System Nodalization

The APR1400 is a 4000MWt pressurized water reactor with an advanced design feature of the direct vessel injection (DVI) as the safety injection system. Both the RELAP5/MOD3.2.2 and MAAP4.03 input decks were prepared for analysis of the double-ended large-break LOCA for the APR1400. The primary system nodalizations for MAAP4.03 and RELAP5 are shown in Figures 1 and 2, respectively. The nodalization for MAAP4.03 is hardwired in the code. As illustrated in Figure 1, the loop is divided into one broken loop and the unbroken loop. A total of fourteen nodes are allotted for the primary system. But in RELAP5 as shown in Figure 2, the nodalization is at the users' disposal. In this respect the nodalization in RELAP5 provides with more user flexibility.

Accident Sequence Description

The accident sequences as predicted by the two codes are summarized in Table 1.

RESULTS

As shown, rather differing LOCA sequences are predicted by the two codes. The primary system pressure as calculated by MAAP4.03 and the upper plenum pressure as computed by RELAP5/MOD3.2.2 are compared in Figure 3. The break flow and the ECC flow rates are compared in Figures 4 and 5, respectively. MAAP4.03 predicted significantly higher break flow and ECC flow rates than those determined by RELAP5/MOD3.2.2 in the earlier phase of the transient. MAAP4.03 results with the modified Henry-Fauske break flow model along with the modified ECC flow rate are also comparatively shown in Figures 4 and 5. From 15 to 60sec, the break flow rates of the two codes differ from each other. However, the difference is relatively minor considering various computational factors arising from basically different numerical schemes adopted in the two codes. The modified MAAP4.03 predicts similar break flow and ECC flow rates with those given by RELAP5/MOD3.2.2. The primary system pressure is changed to some degree as the result of the break flow and ECC flow rate change. As shown in Figure 4, the break flow rate is calculated more accurately by combination of the modified break flow and ECC flow models than by the modified break flow model only.

Overall, it is believed that modification of the break flow model alone ought to be complemented by the surrounding primary system and the ECCS model improvements to extend the calculational capability of MAAP4.03 so as to more rigorously account for the global behavior of the primary system in the early phase of the LOCA.

CONCLUSION

Results of the simulation of the APR1400 LOCA using the modified break flow model in MAAP4.03 show that the break flow rate for the modified model concurs with that of RELAP5/MOD3.2.2 in the earlier phase.

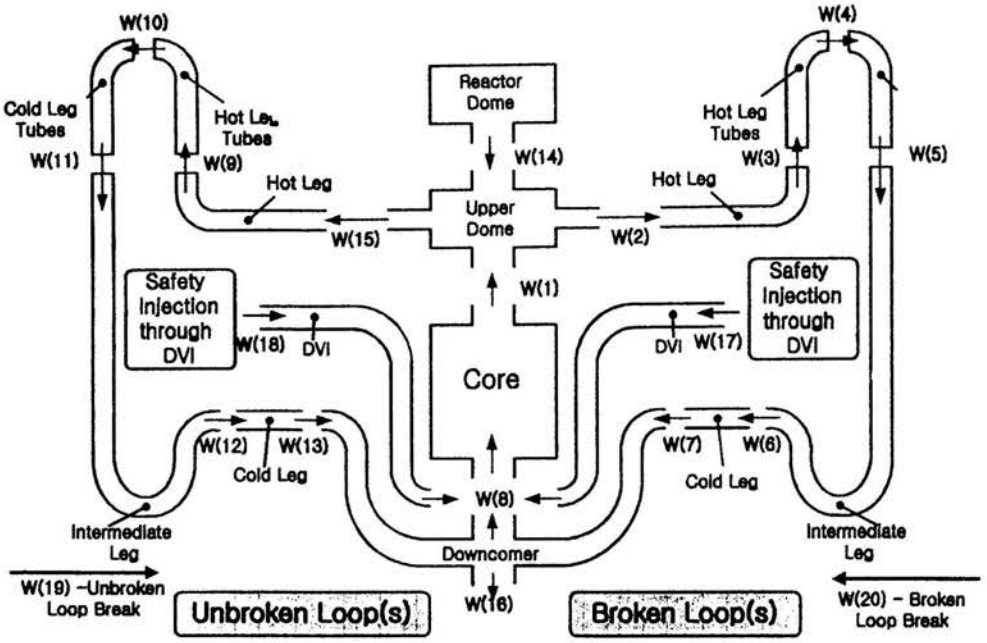

Figure 1: Primary System Nodalization and Flows in MAAP4.03

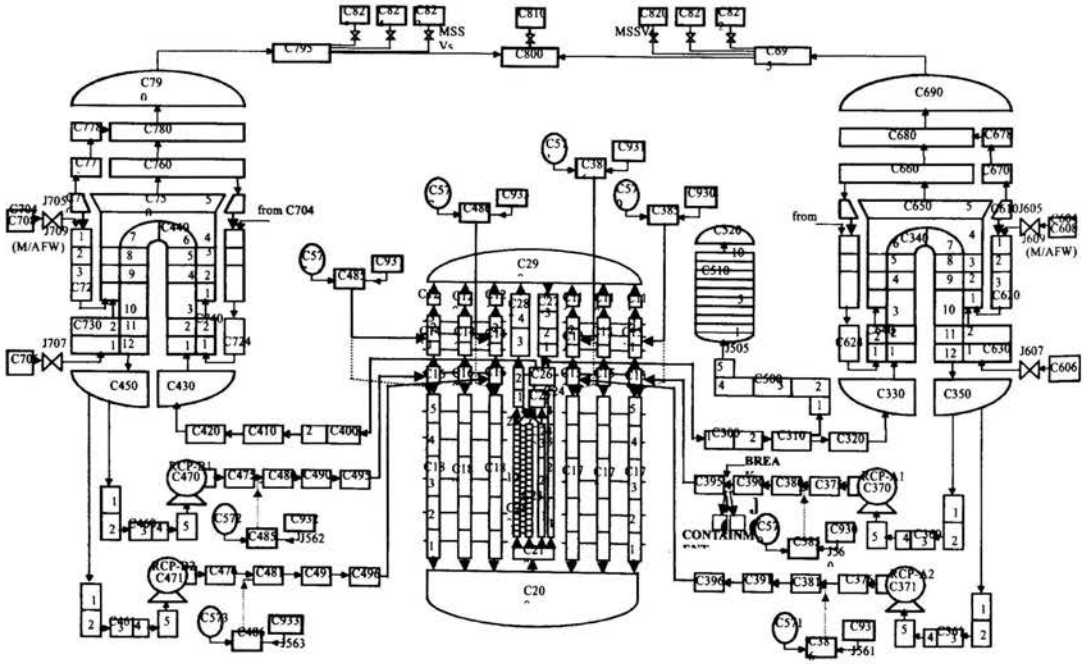

Figure 2: Primary System Nodalization in RELAP5/MOD3.2.2

Table 1. Accident Sequence

Time (sec)	Event in RELAP5	Event in MAAP4.03
0.0	Break opens & MCP off	Break opens
0.14	MSIV closed & turbine stop valve closes	
0.36		HPSI on & reactor scram MSIV closed
4.28		MCP off
9.24		Pressurizer empty
10.4	Primary pressure falls below secondary pressure Blowdown PCT occurs	
11.2		SITs actuated
15.0	Pressurizer pressure reaches low pressure setpoint	
16.0	SITs actuated	
25.0	Containment pressure reaches maximum	
30.0	Downcomer pressure equal to containment pressure	
37.0	Reflood starts	
41.0	Reflood PCT occurs	
55.0	Downcomer mixture level reaches cold leg nozzle	
56.8		SIT water depleted
79.0	HPSI starts	

The break flow rate from the modified model is reduced to about half the original value during the earlier phase (0~10sec). When the modified ECC flow model is combined with the modified break flow model, the break flow and ECC flow rates are calculated more accurately than those calculated by the modified break flow model only. But it turns out that the overall APR1400 LOCA behavior is only slightly influenced by the modified break flow and ECC flow models. The reason for this may be that calculation of the coolant properties like the pressure, void fraction, specific volume of the donor compartment (i.e., the primary system) must also be simultaneously modified in the MAAP4.03 primary system models together with localized modification of the break flow and ECC flow models. Since there is no momentum equation in MAAP4.03 for the primary system thermal hydraulic modeling, the pressures for each of the fourteen nodes of the primary system are not individually calculated. Rather, MAAP4.03 considers only one average pressure for the whole primary system. In the absence of the momentum equation in MAAP4.03 the water mass flow rate is calculated by the mass balance of the six water pool nodes including parts of the fourteen primary system nodes. On the other hand, the gas flow rate is computed by the quasi-steady momentum balance for the fourteen primary system nodes considering only the hydrostatic pressure of each node. Therefore, for more realistic simulation of the initial stage of the LOCA using MAAP4.03, more detailed calculations are required of the primary system. One possible way of improving the MAAP4.03 primary system may be that all fourteen primary system nodes are applied to the water flow rate calculation in the primary system so that the quasi-steady momentum balance is used to calculate the water mass flow as well as the gas flow. The hydrostatic pressure effects on the water flow rate calculation will be considered in the proposed method.

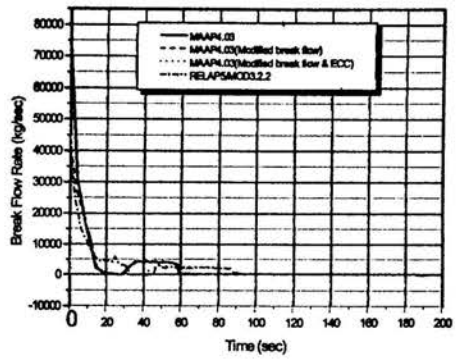

Figure 3: Primary System Pressure

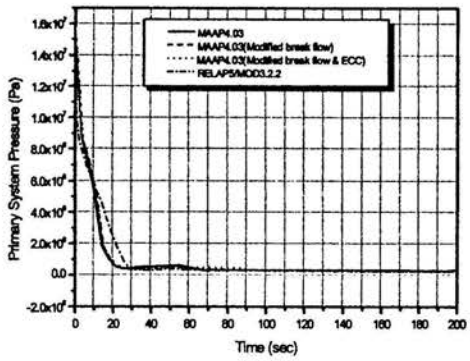

Figure 4: Break Flow Rate

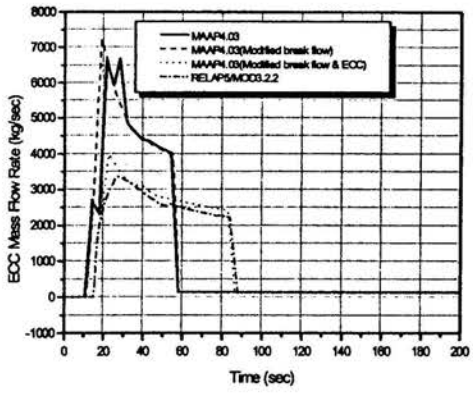

Figure 5: ECC Mass Flow Rate

REFERENCES

[1] MAAP4 Computer Code Manual, May 1994, Electric Power Research Institute, Palo Alto, CA, USA.

[2] RELAP5/MOD3.2.2 Gamma Code Manual, June 1999, Volume IV: Models and Correlations, formally NUREG/CR-5535, EGG-2596, Scientech, Inc. Rockville, MD, USA.

[3] Henry, R. E. and Fauske, H. K., May 1971, "The Two-Phase Critical Flow of One Component Mixtures in Nozzles, Orifices, and Short Tubes," Journal of Heat Transfer, p. 179.

[4] Bae, K. H., Chung, Y. J., Chung, B. D. and Sim, S. K., October 2000, "Evaluation of the KNGR Direct Vessel Safety Injection System for a Large Break LOCA Using MARS1.4," Proc of the 4th JSME-KSME Thermal Engineering Conference, Kobe, Japan.

HEFAT2002
1st International Conference on Heat Transfer, Fluid Mechanics, and Thermodynamics
8-10 April 2002, Kruger Park, South Africa
NV1

THERMODYNAMIC ANALYSIS OF POWER PLANT BASED ON EXERGY FLOW GRAPH

V. Nikulshin[1], C. Wu[2], V. Nikulshina[3]
[1] Odessa State Politech. Univ., 65044, Odessa, Ave. Shevchenko 1;e-mail: vnikul@paco.odessa.ua
[2] U.S. Naval Academy, Annapolis, MD 21402-5000; e-mail: wu@gwmail.usna.edu
[3] Odessa State Academy of Refrigeration, 65100, Odessa, Dvorjankaja Str. 1/3

ABSTRACT
In the design and operation of energy intensive systems the need to improve its efficiency is very clear. The main way to address this problem is through thermodynamic analysis. This paper describes the general approach for calculation the exergy efficiency of complex energy intensive systems with arbitrary structure. A novel general equation of systems exergy efficiency is provided. An example of the analysis method, as applied to a nuclear power plant, is given.

INTRODUCTION
The processes taking place in thermal-power and other complex energy intensive systems are characterised by mutual transformation of quantitatively different power resources. The thermodynamic analysis of such systems requires combined application of both laws of thermodynamics and demands the exergy approach [1].
In contrast to the methods of thermodynamic investigation, the new exergetic method takes into account not only quantity but also quality of energy flows. The quality of energy is a more important objective rather than the quantity. The first important feature of the exergetic methods is their universality. It is possible to estimate the fluxes and balances of all kinds of energy for every element of the system using a common criterion of efficiency. Therefore, the exergetic methods are meaningful in analysis and calculations. The second important feature of the exergetic methods is their direct ties with the technical-economical characteristics of system. The economical investigations based on exergy cover a wide area of problems, from systems optimisation to prices of installations. This approach is known as thermo-economic analysis. The use of exergy permits an easy way to choose the objective criterion for the estimation and optimisation of systems. As result, exergy and its functions in systems analysis provide a very good guide to practical engineers.
Despite its usefulness, the exergetic approach was not fully realised for a long time. One reason for this situation is its underestimation abilities, which is available in exergetics functions for mathematics modelling synthesis and the optimisation of flow sheets. Another reason is its mathematical difficulty in thermodynamic analysis. As a result, the increasing of complexity of optimisations problems requires more effective and powerful mathematics methods. Many papers with different applications [2-6] have been published in this area within the last few years. The scope of these papers and our investigations [7-12] showed that one of the most effective mathematical methods is the "method of graphs" theory [13].
The approach by the graphs theory is very effective in systems investigations, because the binary connection between the elements of any multitude can be conveniently displayed by graphs.
The usefulness of the graphs models can also be demonstrated by its flexibility in wide varieties of applications. Consequently, the most effective way to solve the problems of thermodynamic analysis and the optimisation of the flow sheets is to combine the methods of exergetics analysis with mathematical methods of graphs theory.
The unit exergy-graphs method developed by the authors [7] as exergy-topological is herewith described.
The exergy topological method is based on the combination of exergy flow graph, exergy losses graph and thermo-economic graphs. In this article, the exergy flow graph is used.
The models described in References [10,11] can be employed to find degrees of thermodynamic perfection and exergy losses for separate elements as well as for the whole system. However, these methods do not take into account the technological aim of the system activities. Such an aspect can be taken into account with the help of exergy efficiency of the system. A simple and effective example of the difference between the degree of thermodynamic perfection of an element and its exergy efficiency can be given by a pipeline. In the best case, the exergy losses in it can be very small (approximately zero), and the degree of thermodynamic perfection will be near 100%. This element has no useful efficiency from the thermodynamic point of view, so its efficiency will be equal to zero in all cases.

GENERAL EQUATION FOR EXERGY EFFICIENCY OF COMPLEX SYSTEMS
The equation which joins the exergy efficiency of separate elements and the exergy efficiency of the system as a whole was developed in Reference [7] as:

$$\eta_{ex}^{\Sigma}=\frac{E_{\Sigma}^{u}}{E_{\Sigma}^{a}}=\sum_{i=1}^{m_1}\eta_{ex}^{i}\beta_i+\sum_{i=1}^{m_2}(\eta_{ex}^{i}-1)\beta_i \quad (1)$$

where

$\eta_{ex}^{i}=\frac{E_i^u}{E_i^a}$ - exergy efficiency of *i*th-element

$\beta_i=\frac{E_i^a}{E_{\Sigma}^a}$ - influence coefficient of *i*th-element

E_i^u, E_i^a - *i*th-element exergy used and available

$E_{\Sigma}^u, E_{\Sigma}^a$ - whole system exergy used and available

m_1 - the number of head elements of the system

m_2 - the number of other (not head) elements of the system.

$m = m_1 + m_2$ - the total number of elements of the system.

Elements which use energy resources from external sources belong to head elements. Notice that on one hand, the calculation of the values of inlet-E_i^{in} and outlet-E_i^{out} exergies is independent on the type of the element. On the other hand, the calculation of E_i^u and E_i^a is closely associated with the concrete type of exergy conversion in that element. In the analysis of different thermal power systems, six types (groups) of elements [8] are allotted and the used and available exergies of the allotted elements are calculated by the same formulas [8]. In other energy-intensive systems such as chemical-technological ones, the number of types of elements may be increased if it is necessary.

The model EEF (see below) works with the exergy flow graph [10]. As it was shown in [10], the exergy flow graph of a system with arbitrary structure is a graph $E=(A, \Gamma)=(A, U)$ whose nodes multitude $A=\{a_1, a_2, ...,a_i, ...,a_m\}$ corresponds to the system elements and arcs multitude $U=\{a_i, a_l\}$; $i \neq l$; $i = 1, 2, ..., m$; $l = 1,2, ..., m$; to the distribution of exergy flows in system, while Γ represents a multivalued display of multitude A into itself.

The numbering of graph nodes (elements) is arbitrary. For the effective calculation of E_i^u and E_i^a for elements of the sixth type (multiflows recuperative heat exchanger [8]), items should be numbered in a special order: the number for the flow at the exit of the element should be a unit larger than that of the flow at the inlet to the element. The numbering of exergy flows for other types of elements is also arbitrary.

The method and algorithm for the calculation of exergy efficiency work with a matrix of incidence [13].

The elements of the matrix can have one of three meanings: 0, 1, -1; where 0 means that *j*th-flow and *i*th-element are not tied; 1 means that *j*th-flow enters *i*th-element; and -1 means that *j*th-flow leaves *i*th-element, respectively.

OUTLINE OF A MODEL EEF

A model EEF for the determination of exergy efficiency for a system of arbitrary structure consists from four main blocks.

In the first block, exergy flow graph E = (A, U) and its matrix of incidence are built corresponding to the system under consideration using the rules described in [10].

In the second block, the procedure for recognizing the types of flows on arcs on graph E = (A, U) and for calculation of their exergies are made.

For example, the exergy flows of five types: exergy of mass-flow, exergy of heat-flow, exergy of work, exergy of fuel, and nuclear bound exergy are considered in a thermal power system. The calculation method for these five types is given in [1].

In the third block, the procedure for computing different types of elements and for the calculation of used and available exergies of elements by formulas given in [8] is realized.

In the fourth block, exergy efficiency of the *i*th-element $\eta_{ex}^{i}=E_i^u/E_i^a$, coefficient of influence $\beta_i=E_i^a/E_{\Sigma}^a$ and exergy efficiency of the whole system are calculated by formula (1).

EXAMPLE: DETERMINATION OF EXERGY EFFICIENCY FOR A NUCLEAR POWER PLANT

The model EEF described above is applied to the exergy efficiency calculation of a nuclear power plant (Fig. 1). The exergy flow graph for this flow sheet is given in Fig. 2, and matrix of incidence is given in Fig. 3.

The parameters of the flows are calculated in [7] and shown in Table 1 (parameters of environment were taken: $P_0 = 0.1$ MPa, $T_0 = 273.15$ K).

Applying the model EEF, the calculation results of the exergetic characteristics of a power plant are given in Table 2.

From Table 2, it is observed that the largest exergy losses are in the nuclear reactor I because of the large irreversibility of the process converting exergy of radiation to the exergy of the steam. The large irreversibility explains the low exergy efficiency of the nuclear reactor ($\eta_{I} = 0.680$).

Exergy losses in the boiler II are due to the transfer of heat flow from the high temperature level (flows 1,2) to the lower temperature level (flows 17,18).

The exergy efficiency of the heat exchangers are in a wide range - from $\eta_{IX} = 0.397$ (for low pressure heater IX) to $\eta_{XIV} = 0.943$ (for high pressure heater XIV). The exergy losses in heat exchangers are caused by high irreversibility of heat exchange with large temperature difference between "hot" and "cold" fluid flows. The larger the temperature difference, the larger the exergy loss, resulting in a lower exergy efficiency. Another factor in the exergy efficiency of the heat exchangers is the total temperature level of "hot" and "cold" flows. The bigger is this level, the larger the exergy efficiency and the smaller the exergy losses.

Table 1. Parameters of flows in flowsheet of nuclear power plant in Fig.1

Number of flow	Temperature T, K	Pressure P, MPa	Specific enthalpy h, kJ/kg	Specific entropy s, kJ/(kg·K)	Mass flow rate $\dot{m}$, kg/s	Specific exergy e, kJ/kg	Exergy flow rate $\dot{E}$, MW
1	2	3	4	5	6	7	8
1	817.2	10.0	1189.6	2.9736	3738	378.0	1412
2	798.2	9.80	1095.6	2.7977	3738	332.0	1240
3	-	0.90	2628.8	6.2997	8.428	909.0	7.661
4	777.2	2.85	2801.8	6.2032	178.3	1108	197.6
5	-	0.201	2436.0	6.4399	139.4	677.9	94.50
6	-	0.181	2679.9	7.1071	77.30	739.6	57.18
7	573.8	0.004	2250.0	7.4681	67.09	211.2	14.7
8	573.8	0.004	116.90	0.4027	67.09	6.963	0.4476
9	574.0	1.20	117.40	0.4056	67.09	6.671	0.4671
10	613.5	1.00	282.80	0.9126	67.09	33.52	2.249
11	612.2	1.00	279.60	0.9116	150.3	30.73	4.619
12	632.2	0.80	360.90	1.1448	150.3	48.36	7.269
13	667.8	0.60	510.30	1.5432	150.3	89.01	13.38
14	684.4	0.35	581.40	1.7194	178.3	112.0	19.97
15	684.8	4.00	585.50	1.7205	178.3	115.8	20.65
16	713.0	3.80	707.00	2.0058	178.3	159.4	28.42
17	742.2	3.60	830.90	2.2798	178.3	208.5	37.18
18	780.2	3.05	2801.9	6.1832	178.3	1114	198.6
19	-	0.465	2548.2	6.4135	8.428	797.3	6.719
20	-	0.843	2628.8	6.3000	8.428	908.9	7.660
21	-	1.50	2703.7	6.2600	11.20	994.7	11.14
22	740.8	1.50	828.50	2.2782	11.20	206.7	2.310
23	715.2	0.84	714.90	2.0311	19.63	160.4	3.100
24	-	0.50	2548.2	6.3501	8.420	814.6	6.865
25	-	0.27	2472.8	6.4132	10.89	722.0	7.862
26	-	0.088	2578.2	7.1454	4.270	527.5	2.679
27	-	0.038	2474.5	7.2278	5.973	501.3	2.994
28	-	0.035	2474.5	7.2281	5.973	501.2	2.993
29	-	0.081	2578.1	7.1454	4.270	627.5	2.678
30	-	0.241	2472.8	6.4135	10.89	721.9	7.861
31	662.7	0.240	488.90	1.4892	10.89	82.35	0.897
32	636.4	0.080	376.90	1.1925	77.26	51.35	3.967
33	612.5	0.034	278.80	0.9121	83.23	29.79	2.480
34	-	1.60	2703.7	6.2556	11.20	995.9	11.15
35	-	0.20	504.70	1.5301	62.10	86.98	5.401
36	612.5	1.00	277.00	0.9047	83.23	29.82	2.487
37	-	-	-	-	-	-	0.100
38	-	-	-	-	-	-	0.812
39	-	-	-	-	-	-	0.100
40	-	-	-	-	-	-	47.32
41	-	-	-	-	-	-	24.41
42	566.2	0.30	84.100	0.2962	3415	3.230	11.03
43	576.2	0.30	126.00	0.4384	3415	6.860	23.43
44	-	-	-	-	-	-	253.0
45	-	-	-	-	-	-	70.00

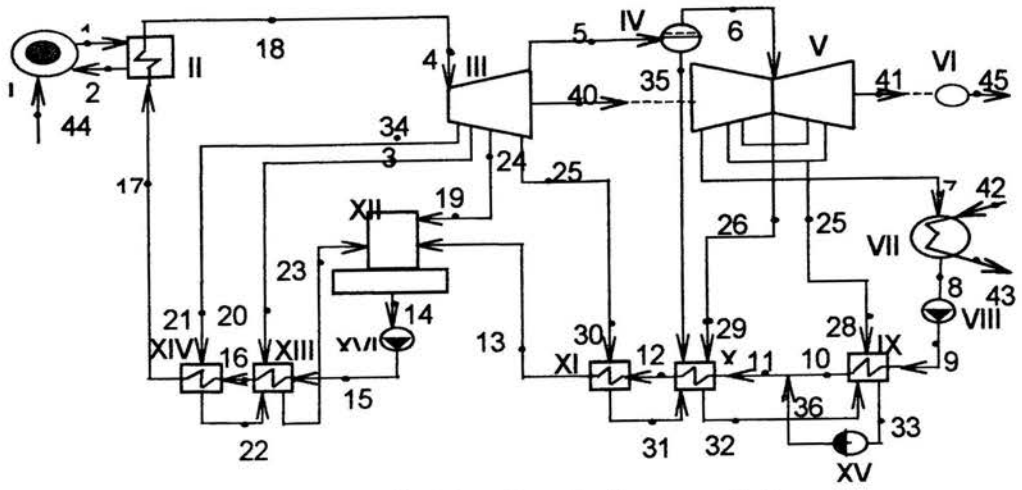

Fig.1. Flowsheet of nuclear power plant

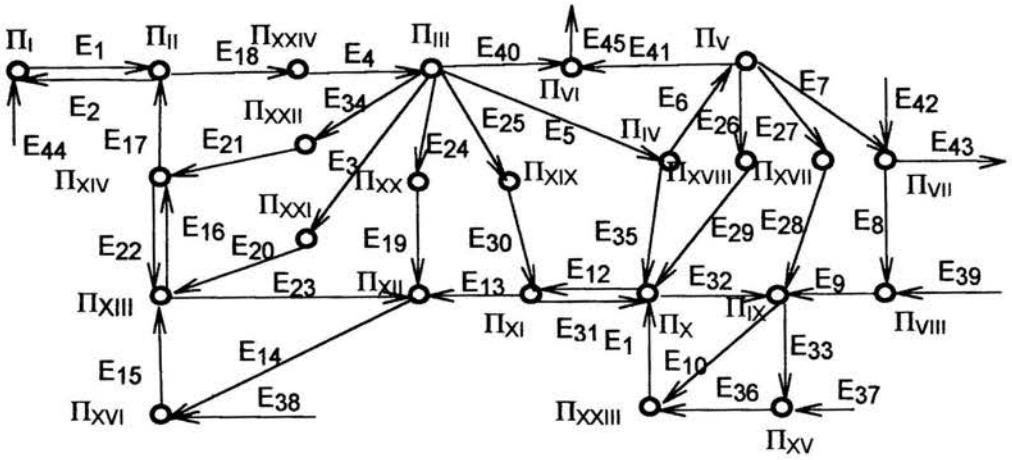

Fig. 2. Exergy flow graph corresponding to the flowsheet in Fig.1

	1	2	3	4	5	6	7	8	9	10	11	...	40	41	42	43	44	45
I	-1	1															1	
II	1	-1																
III			-1	1	-1								-1					
IV					1	-1												
V						1	-1							-1				
VI													1	1				-1
VII							1	-1							1	-1		
VIII																		
IX									1	-1								
X											1							
...																		
XX																		
XXI			1															
XXII																		
XXIII										1	-1							
XXIV				-1														

Fig. 3. Matrix of incidence of the exergy flow graph shown in Fig. 2.

Table 2. Thermodynamic characteristics of nuclear power plant in Fig.1

N	Name of Element	Number of corresponding node of graph	Used exergy flows rates E_i^u, MW	Available exergy flows rates E_i^a, MW	Coefficient of influence, β_i	Rates of exergy losses, Π_i, MW	Exergy efficiency, η_i
1	2	3	4	5	6	7	8
1	Reactor	I	172	253	1.0	81	0.680
2	Steam generator	II	161	172	0.677	11	0.938
3	Turbine of high pressure	III	47.3	69.5	0.274	22.2	0.680
4	Separator	IV	0	31.9	0.126	31.9	0
5	Turbine of low pressure	V	24.4	37.3	0.147	12.9	0.654
6	Generator	VI	70.0	71.7	0.282	1.70	0.975
7	Condenser	VII	12.4	13.7	0.0539	1.31	0.905
8	Condenser pump	VIII	0.0195	0.10	$7.6 \cdot 10^{-5}$	0.0805	0.195
9	Low pressure heater	IX	1.78	4.48	0.0176	2.70	0.397
10	Low pressure heater	X	2.65	5.00	0.0197	2.35	0.529
11	Low pressure heater	XI	6.11	6.96	0.0274	0.85	0.878
12	Deaerator	XII	0	3.23	0.0127	3.23	0
13	High pressure heater	XIII	7.77	8.83	0.0347	1.06	0.879
14	High pressure heater	XIV	8.76	9.23	0.0363	0.47	0.943
15	Pump of low pressure heaters	XV	0.007	0.10	0.000394	0.093	0.07
16	Feed pump	XVI	0.68	0.81	0.0032	0.13	0.837
17	Pipe line between turbine of low pressure and heater of low pressure IX	XVII	0	0.001	$3.94 \cdot 10^{-6}$	0.001	0
18	Pipe line between turbine of low pressure and heater of low pressure X	XVIII	0	0.001	$3.94 \cdot 10^{-6}$	0.001	0
19	Pipe line between turbine of low pressure and heater of low pressure XI	XIX	0	0.001	$3.94 \cdot 10^{-6}$	0.001	0
20	Pipe line between turbine of low pressure and deaerator	XX	0	0.146	$5.75 \cdot 10^{-4}$	0.146	0
21	Pipe line between turbine of high pressure and heater of high pressure XIII	XXI	0	0.001	$3.94 \cdot 10^{-6}$	0.001	0
22	Pipe line between turbine of high pressure and heater of high pressure XIV	XXII	0	0.001	$3.94 \cdot 10^{-6}$	0.01	0
23	Mixture of flows	XXIII	0	0.117	$4.61 \cdot 10^{-4}$	0.117	0
24	Pipe line between steam generator and turbine	XXIV	0	1.0	$3.94 \cdot 10^{-3}$	1.0	0

Exergy losses in the turbines and pumps are the result of the dissipation of the expansion and compression processes in real installations. . Exergy losses in the generator are the result of mechanical (friction) and electrical dissipations. Exergy efficiency of these devices also depends on the quality of its construction

Exergy losses in other elements of the system (pipe lines and mixture) are caused by dissipation of the flow.

All these elements have zero exergy efficiency ($\eta = 0$).

The dominant influential elements in the system are the nuclear reactor, the boiler, and the turbines, because these devices transform the main exergy flows in the flow sheet for the system as a whole.

Exergy losses:

$$\Pi_{\Sigma} = \sum_{i=1}^{24} \Pi_i = 171.6\,MW$$

Exergy efficiency:

$$\eta_{ex}^{\Sigma} = \frac{E_{\Sigma}^{u}}{E_{\Sigma}^{a}} = \frac{82.4}{253} = 0.326$$

The exergy efficiency η^{Σ}_{ex} is less than that of the majority of elements of the system (excluding that which have zero efficiency). There are a few elements having less exergy efficiency than the system as a whole is characterized (for example condensate pump $\eta_{VIII} = 0.195$). These elements have very small coefficient of influence ($\beta_{VIII}=0.000076$) and little impact on the exergy efficiency of the whole system.

CONCLUSION

A novel calculation method for the exergy efficiency of complex systems is described in this paper. This method is based on the general equation for systems of arbitrary structure and on special properties of exergy-topological models. It can be constructed for every energy- intensive system. The method is applicable, regardless of the technological aim and structure of the system. It can be applied for the investigation of various energy intensive systems in different branches of industry. The illustrative example given above demonstrates the application of the proposed method for thermodynamic analysis of nuclear power plant.

REFERENCES

1. Bejan, A, Tsatsaronis, G., Moran, M., *Thermal Design and Optimization*, John Wiley & Sons Inc., New York 1996.
2. Cornelissen, R.L., van Nimwegen, P.A., Hirs, G.G., " Exergetic life cycle analysis", *Proceedings of ECOS'2000*, Twente, Netherlands, 1131-1143, 2000.
3. Finnveden, G., Ostlund, P., "Exergies of natural resources in the life Cycle assessment and other applications", *Energy*, 22(9), pp.923-932, 1997.
4. Falsetta, M, Sciubba, E, "Exergy-Based Analysis of the start up Transient of combined Cycle plant", *Proceedings of ECOS'98*, Nancy, France, pp. 775-787, 1998.
5. Sciubba, E., "A nested black-box exergetic method for the analysis of complex Systems", *Proceedings Advances in Energy Studies*, Venere, Italy, pp. 62-69, 1998.
6. Oh, S.D., Pang, H.S., Yong , K.H., "Exergy Analysis of a Gas Turbine cogeneration Systems", *Journal of Gas Turbine sand Power*, 118(4), pp. 253-260, 1996.
7. Andreev, L., Nikulshin, V, *Thermodynamic Analysis of Power-Technological Systems on Computer*, The Center of Higher Education and Methods of Ukraine, 1992.
8. Nikulshin, V., Andreev, L., "Exergy Efficiency of Complex Systems", *Proceedings of International Conference of Ocean Technology and Energy, OTEC/DOWA'99*, Imari, Japan, pp. 162-161, 1999.
9. Nikulshin, V., Wu, C., " Method of thermodynamic analyzes and optimization of energy intensive systems on exergy flow graphs", *Proceedings of IASTED International Conference on Power and Energy Systems* ,Las Vegas, Nevada, USA, pp. 489-491. 1999.
10. Nikulshin, V., Wu, C., " Thermodynamic analysis of energy intensive systems on exergy topological models", *Proceedings of 12-Th. International Simposium on transport phenomena, ISTP-12*, Istanbul, Turkey, pp.341-349, 2000.
11. Wu, C., Nikulshin, V., " Method of thermoeconomical optimization of energy intensive systems with linear structure on graphs", *International Journal of Energy Research*, 24, pp.615-623, 2000.
12. Nikulshin, V, Klemes, J., "Method of developing ecology safe technologies based on exergy flow graph", *Proceedings of 13-Th. International Congress of Chem. Engineering " CHISA-98"*, Praha, Vol.6, pp.79-80, 1998.
13. Harary F., *Graph Theory*, Narosa Publishing House, New Deli, 1995.

HEFAT2002:
1st International Conference on Heat Transfer, Fluid Mechanics and Thermodynamics
8-10 April 2002, Kruger Park, South Africa
OJ1

THE PERFORMANCE OF HIGH–PRESSURE STEAM BOILERS AS A FUNCTION OF COAL COMPOSITION

Andrej Senegačnik*
* University of Ljubljana
Faculty of Mechanical Engineering
1000 Ljubljana, Slovenia
Email: andrej.senegacnik@fs.uni-lj.si

Janez Oman*
Boris Dejanovič**
** Power Plant Šoštanj
C.L.Ribarja 18
3325 Šoštanj, Slovenia

ABSTRACT

This article deals with the influence of lignite and other low-rank coals on the heat transfer and the conversions taking place in large coal-fired steam boilers. The lower heating value of the investigated coal ranged from 9 to 10 MJ/kg with 20 % ash and about 38 % moisture. Our analysis of the energy conversions is mainly concerned with the heat loss due to the exhaust flue gas. Changes in the composition of coal are reflected in the quality of the processes expressed as the efficiency of the boiler and the unit and in the quantity of power needed for the operation of the power-plant. On the basis of measurements on power plant units our attention was focused on the influence of moisture, hydrogen, ash and sulphur changes in the coal. The heat loss and the other performances of the boiler due to the exhaust flue gas are determined in relation to the efficiency of the steam boiler and the power-plant unit.

INTRODUCTION

Changes in the composition of coal are not only reflected in changes to the boiler's specific consumption but also in the quality of the processes taking place in the power-plant unit. So, while striving to produce power at the lowest possible cost, the quality i.e. the composition of the coal becomes an important parameter. The composition of coal can be described with a simple analysis of five characteristics: total moisture, air-dried moisture, volatile matter, ash and fixed carbon, or a more sophisticated analysis that involves the determining the elemental composition of the organic fraction in addition to the ash and moisture content of the coal. The basic data to provide a coal-quality specification are heating value, moisture, ash and sulphur content. A review of lignite specifications and the influence of lignite composition on the combustion process in the boiler and the related effects on overall power-plant performance was presented in Refs. [2-4]. The effects in the boiler can be described as immediate and indirect. For instance, the immediate effects of ash content and ash composition are a lower heating value and consequently a larger mass flow of coal, as well as fouling, slagging, abrasion, erosion and corrosion; while the indirect influences are reflected in the amount of power consumption required for coal grinding, gas cleaning, transportation of the coal and ash and also in heat losses from the boiler and in the overall efficiency of the unit. The influence of moisture in the coal is also complex. The origin of the water-steam in the flue gas, which has an important influence on the value of the flue-gas loss, is twofold. The first is the mass fraction of water in the coal that is related to the inherent and surface moisture, and the second is that originates from the combustion of the hydrogen in the coal. The surface moisture of the coal is converted to vapour during milling and forms part of the coal-air mixture in the feed system [4]. The vapour then enters the furnace, where it can cause a delay in coal ignition, a increase in the flame length and a change in the optical properties of the flame. This effect is important for coals with higher moisture contents. The inherent moisture has a direct influence on coal ignition while the release of the volatiles from the coal particles cannot start prior to the evaporation of the moisture. To prevent any delay in volatilisation for coals with a high inherent moisture content the mill's air inlet temperature should be increased.

In this paper theoretical examinations are compared with the results of measurements on two units at the Šoštanj power plant, Slovenia. The treated coal was lignite, dug from the nearby Velenje coal mine, with lower heating values ranging

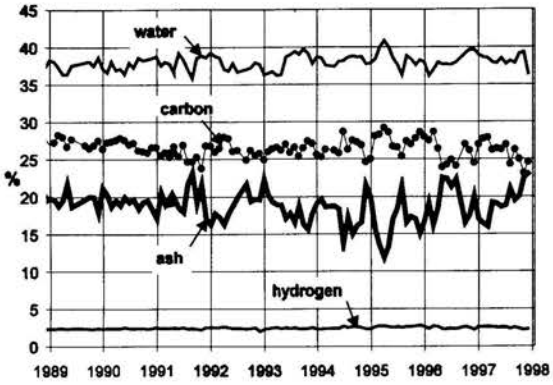

Figure 1: THE LIGNITE COMPOSITION, LIGNIT MINE VELENJE–PESJE, SLOVENIA.

from 9 and 10 MJ/kg, and ash contents of about 20 % and moisture contents of about 38 %. The power plant has five units, the examined units were unit 4 with 275 MWe and unit 5 with 345 MWe, both with a pulverised coal firing system.

NOMENCLATURE

H	heating value (kJ/kg)
h	mass fraction of hydrogen in the fuel (kg/kg)
l	heat loss (%)
m	mass fraction (kg/kg)
P	electric power
t	temperature (°C)
$\dot{Q}$	heat flow (W)
w	mass fraction of moisture (water) in the fuel (kg_{water}/kg_{fuel})

Greek Letters

γ_a	mass portion of ash in the fuel (kg_{ash}/kg_{fuel})
λ	excess air quotient (-)

Subscripts

A,min	stoichiometric amount of dry air
f	free
F	fuel
fgd	flue-gas desulphurisation
g	generator terminals
G	flue gas
Go	flue gas at temperature of the environment
i	inferior, lower
oth	other

THE FUEL SPECIFICATIONS

The fuel used in the examined power plant is yellow-brown lignite with a wooden structure, extracted from the nearby Velenje mine. The lignite composition, guaranteed by the coal supplier, had the following properties: lower heating value 9200 kJ/kg, total moisture 38 %, ash content 20 % and ultimate analysis: S, 1.4 %; C, 27.1 %; H_2, 2.1 %; O_2, 11.0 %; and N_2, 0.4 %. The water, ash, carbon and hydrogen content of the coal used in the Šoštanj power plant in the period 1989-98 is presented in Fig.1.

The variations in the composition and the lower heating

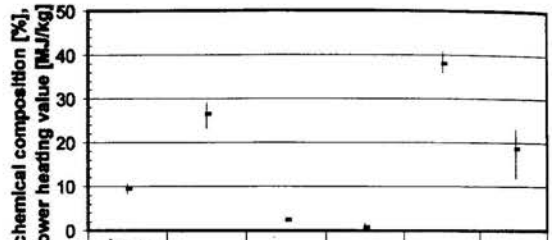

	lower heating value	carbon [%]	hydrogen [%]	sulphur [%]	moisture [%]	ash [%]
max	10.58	29.2	2.8	1.7	40.8	23.16
min.	8.26	23.11	2	0.4	35.85	11.8
- average	9.45	26.45	2.44	0.76	37.98	18.66

Figure 2: THE VARIATION OF LIGNITE COMPOSITION.

value of the lignite are presented in Fig.2. The extremes and the average values for each parameter are also indicated.

BOILER EFFICIENCY AND LOSSES

Direct losses

The first-law thermal efficiency of the boiler is calculated on the basis of the heat losses that occur during boiler operation at a constant load [1]. The individual loss is defined as the ratio of the unutilised or lost heat flow $\dot{Q}_x$ and the heat flow supplied to the boiler by means of fuel $\dot{Q}_F$. Our earlier study [2] suggested that the boiler efficiency is affected predominantly by the heat loss due to the exhaust flue gas l_G which is the highest and gives us an order of magnitude value for the boiler efficiency. The empiric equation [2] for calculating the loss due to the exhaust wet flue-gas yields:

$$l_G = \frac{\dot{Q}_G}{\dot{Q}_F} = \frac{(m_{A,\min}\lambda + 1 - \gamma_a + m_w)(t_G - t_{Go})}{H_i}.100[\%] \quad (1)$$

The advantage of this equation is that all the parameters that influence the loss value are clearly evident. It is obvious that the influential parameters in the equation that depend on the composition of the coal are: lower heating value, stoichiometric amount of dry air, mass fraction of ash in the coal and the fraction of moisture in the flue gas. The parameters that are not directly dependent on the composition of the coal are: the temperature of the exhaust flue gas and the excess air quotient. Ash is the residue remaining after complete combustion of the coal, and the excess air quotient is defined as the ratio of actually used combustion air and the theoretical amount of air needed for burning a mass unit of the fuel. The water-steam m_w in the flue gas, equation (1), has two sources, the mass fraction of total moisture in the coal and the mass fraction of hydrogen in the coal:

$$m_w = w + 9h. \qquad (2)$$

It should be pointed out that for lignite the factors that depend on the composition of the coal have a weak influence on

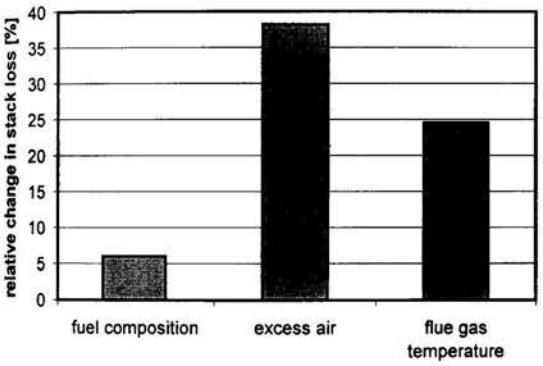

Figure 3: FLUCTUATIONS OF THE STACK LOSS.

the value of the heat lost by the exhaust flue gas. Fig. 3 shows the ranges of possible fluctuations of the stack loss for three cases: changes to the lignite composition, excess air and the exhaust flue-gas temperature. Among them the influence of the lignite composition on the stack loss is the weakest, a change in the temperature and change to the actually used mass flow of combustion air have a much stronger influence.

The impact of the different components of the lignite on stack losses is very varied. For instance, while an increase in the carbon or hydrogen content decreases the losses, an increase in the moisture in the causes losses to increase, Fig.4. The level of losses due to the heat associated with water vapour in the flue gas is, for lignite, up to 20 %. Although there are only a few per cents of hydrogen in the lignite, its influence on heat loss is significant. For instance, with 5 % hydrogen and 50 % moisture in the coal the portion of water vapour in the flue gases which results from the combustion of hydrogen is bigger than the

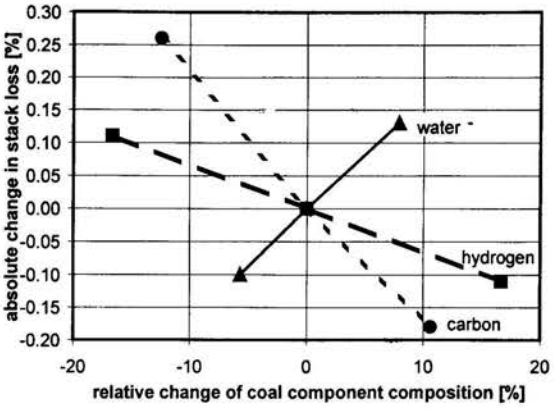

Figure 4: FLUCTUATIONS OF STACK LOSS DUE TO CHANGES OF LIGNITE COMPOSITION.

portion that results from coal moisture. Calculations show [2] that over 60 % of the heat loss due to exhaust flue gas is connected with the amount of nitrogen and carbon dioxide that originates from the theoretically required quantity of combustion air. Rationalisation by decreasing the mass of the flue gas and consequently the stack loss is thus only possible on less than 40 % of the mass flow of flue gas leaving the boiler. This part belongs to the excess air and water vapour. The operating conditions for power plants in connection with the actual excess air are frequently very different in comparison with theoretically desired values or values recommended by the boiler manufacturer. While the quantity of excess air has the most important influence on the value of the stack loss the actually used excess air needs to be frequently supervised by independent measurement. As an illustration, Fig. 5 represents the actual state of operation on unit 5 at Šoštanj power plant. The consequence of the catch state is an increase in the stack loss due to an increase in the amount of excess air, as presented in Fig.3.

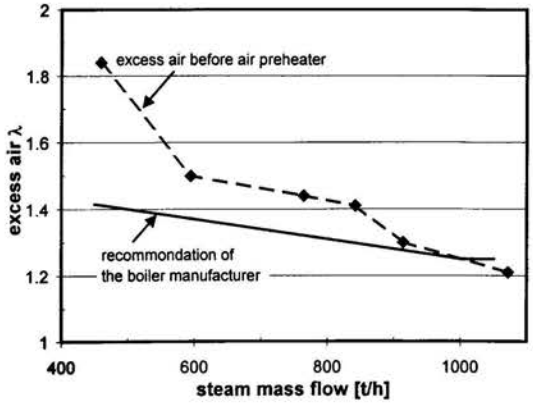

Figure 5: ACTUALLY USED EXCESS AIR.

Indirect losses

The composition of the coal has a strong effect on the electrical power needed for the operation of the boiler auxiliaries and the combustion byproducts, processing and handling. The power used for these power consumers can be considered as an indirect loss that increases the specific power consumption of the unit and reduces the free electrical power. In coal-fired power plants there are two important power consumers that are the most dependent on coal composition: the coal pulverising equipment P_{pe} and the device for flue-gas desulphurisation P_{fgd}. The useful electrical power of the unit is thus the power at the generator terminals P_g reduced by the power consumption of the unit P_{oc}:

$$P_f = P_g - P_{oc} \quad \text{and} \quad P_{oc} = P_{pe} + P_{fgd} + P_{oth}. \qquad (3)$$

Here, P_{oth} stands for the power consumption of all the other consumers in the unit.

The results of the measurements on unit 4 show that the power needed for lignite grinding represents 12 % to 14 % of the unit's own power consumption and could increase by as much as 1 MW if the portion of ash in the lignite increases by 4 %. For unit 4 each 1% change in the amount of ash alters the energy yield of the unit by 0.1 %.

The power needed for the flue-gas desulphurisation depends mostly on the type and the system of the device. Unit 4 has a wet flue-gas desulphurisation (FGD) system which is placed on the cold part of flue-gas tract after the electrostatic precipitator. The measurements on this unit showed that the power consumption of the FGD device with 95 % efficiency is between 2 % and 3 % of the produced electrical power. For the same load on the unit the difference in power consumption is caused by the different quantities of sulphur that have to be removed from the flue gases. The reason for the increase in the sulphur mass flow through the FGD device is the increasing sulphur content in the lignite or the increasing lignite mass flow for an unchanged content of sulphur. The mass flow of the fuel will increase if the heating value of coal decreases – more ash or moisture and less combustible matter in the lignite. The results of the measurements of power consumption of the FGD system on unit 4 performed in the years 1995 and 1999 are presented in Fig. 6 and Fig. 7. It is evident that although the sulphur content of the lignite and the specific power consumption of the FGD system remained almost equal, the power consumption of the FGD system in 1999 was greater. The reason is the increased mass flow of the sulphur through the flue-gas system as a result of the lower heating value of the lignite.

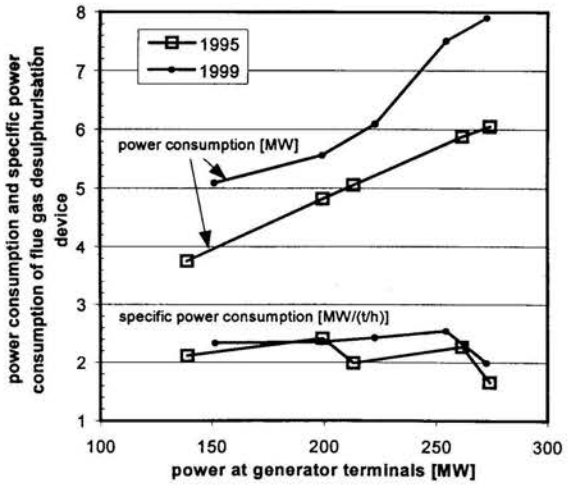

Figure 6: POWER CONSUMPTION OF FLUE GAS DESULPHURIZATION DEVICE.

Disguised losses

There are some disguised effects on the efficiency of the steam boiler and the power-plant performances caused by a variation in the lignite composition.

The increase in the overall coal moisture enlarges the flue-gas volume flow, which leads to a reduction in the flame temperature in the furnace. Consequently, the heat flow carried by radiation into the evaporator becomes smaller. On the other hand, the moisture in the lignite that enters the furnace can cause a delay in lignite ignition, an increase in the flame length and a change to the optical properties of the flame. Because of the selective emisivity of water molecules an increase in the partial pressure of the water molecules in flame increases the emission coefficient of the flame. The overall effect of

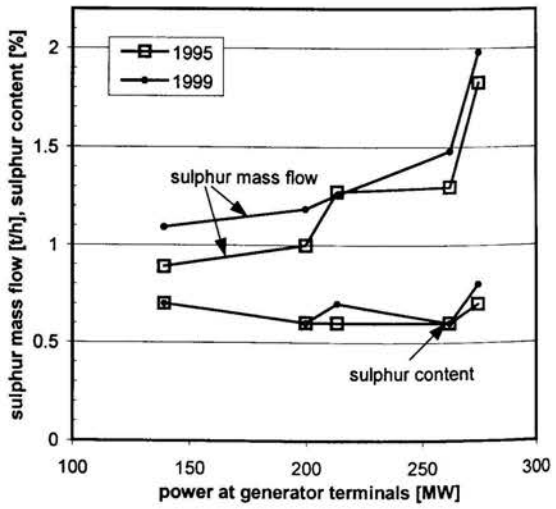

Figure 7: SULPHUR MASS FLOW.

increasing the flame volume and emisivity and decreasing its temperature is usually a smaller radiative heat flux to the evaporator in the furnace. As a consequence, the heat flux that remains for convective heat transfer in the convective part of the boiler is greater. This effect causes the higher temperatures of the flue gases leaving the furnace as well as the higher temperatures in the cold part of the boiler. The consequence is an increasing heat loss due to exhausted flue gases [3]. The situation is clear in Fig. 8, where a part of results of the comparative measurements in 1995 and 1997 is presented. During both measurements the operation mode and the

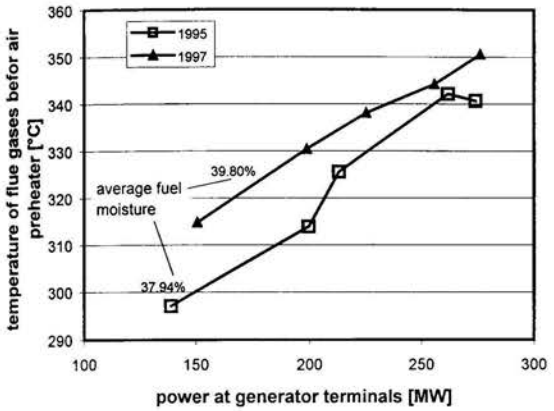

Figure 8: TEMPERATURE OF THE FLUE GASES BEFOR AIR PREHEATER.

parameters of the unit were the same, only the composition of the coal (in particular the moisture) was different. For lignite with a higher moisture content the radiative heat transfer in the furnace was reduced, the temperatures of the flue gas at the entrance of the convective part of the boiler increased and they remained higher until they reached the air preheater at the cold end of the boiler.

CONCLUSIONS

This article deals with the influence of lignite and low-rank coal compositions on the conversions and heat transfer taking place in large coal-fired steam boilers. The changes in the composition of the coal are reflected not only in changes to the boiler efficiency and the overall quality of the processes in the power-plant unit, but also in the emission requirements the boiler must meet. Accordingly, while striving to produce power at the lowest cost possible, the composition of coal, which reflected as coal quality, becomes an important parameter.

The basis of the analyses presented in this paper is the first-law thermal efficiency of the boiler. The efficiency is expressed as heat losses, mainly with the value of the heat flux of flue gas lost up the stack. The losses in the steam boiler that are affected by coal composition can be classified as: direct, indirect and secondary or disguised losses. To determine these losses the principal data of coal composition needed are: heating value, moisture, ash, sulphur, carbon and hydrogen content. Among the direct losses the loss of heat due to exhaust flue gas, also called stack loss, is the biggest. We showed that the changes in coal composition can cause relatively small changes in the stack loss. Much more influential parameters are the quantity of excess air and the temperature of the exhausted flue gas.

The indirect losses are all the electrical power needed for the operation of auxiliary installations at the power plant. Here, the power required for coal grinding and the power for the desulphurisation system are the most important.

The results pointed out the weak influence of ash content on heat transfer in the boiler. More significant is its influence on the unit's power consumption and the handling costs. More important effects on boiler efficiency include the alteration of the moisture content of the lignite. The water vapour in the flue gases resulting from the total moisture and hydrogen content in the lignite causes heat losses with the exhausted flue-gas flow and indirect losses in the form of an increase in the power consumption for grinding and transportation of the lignite with higher moisture contents. The changes to the moisture content of the lignite also influence the conditions of the radiative heat transfer in the furnace and consequently the convective heat transfer. The result of these changes is a variation in both the exhaust flue-gas temperature and the boiler efficiency.

Sulphur, in any form, is not welcome in coal, primarily because of the huge costs of desulphurisation. The measurements show that for a unit of about 300 MWe power the consumption of the desulphurisation device is between 2 % and 3 % of the produced electric power. This share depends on the mass flow of sulphur in the treated flue gas.

The fact is that the influence of the lignite composition on the performances of the steam boilers is reflected more through the consumption of electric power than through the heat losses That means, even the changes of lignite composition cause small changes of the boiler efficiency the changes of power plant efficiency can be significant.

REFERENCES

[1] Deutsche Norm, DIN 1942, Februar 1994, Abnahme-versuchen an Dampferzeugern, VDI-Dampferzeugerregeln.

[2] Oman, J., Senegačnik A., Dejanovič B., 2001, "Influence of lignite composition on thermal power plant performance, Part 1: Theoretical survey," Pergamon, Energy Conversion and Management, Vol.42, pp. 251-263.

[3] Oman, J., Senegačnik A., Dejanovič B., 2001, "Influence of lignite composition on thermal power plant performance, Part 2: Results of test," Pergamon, Energy Conversion and Management, Vol.42, pp. 265-277.

[4] Skorpuska, N.M.1993, "Coal specifications-impact on power station performance," IEACR/52, IEA Coal Research, London.

HEFAT2002
1st International Conference on Heat Transfer, Fluid Mechanics and Thermodynamics
8-10 April 2002, Kruger Park, South Africa
PG1

FEATURES OF HEAT EXCHANGE IN FURNACES OF POWER BOILERS

G. Polupan, G. Jarquin Lopez
National Polytechnic Institute, SEPI-ESIMEZ, Av. IPN, s/n, UPALM, 07738, Mexico D.F.
polupan@maya.esimez.ipn.mx
A. Mikhlevskiy
National Technical University of Ukraine, Pr. Peremogy, 37, Kyiv, Ukraine, 252056.

ABSTRACT

The interest to examination of heat exchange peculiarities in furnaces of power boilers was connected with appearing on an outside surface of furnace screen tubes the cross cracks during their operation. These cracks are the result of instability of a temperature regime of water wall tubes. The instability of a temperature regime leads to sharp temperature stresses and the development of thermo fatigue processes in tube metal.

The processes connected with the formation of interior tube deposition and it influence on tube metal temperature and work stability of boiler have been considered also.

INTRODUCTION

The reasons of emergency damages of water wall tubes.

Generally the damages of water wall tubes are the result of unfavorable combination of following processes:

1. The high temperature of frontal surface of water wall tubes.
2. The essential changes of a level of heat flow density in the time.
3. The incrustation and deposition formation inside of water wall tubes.

These physicochemical processes taking place in furnace water walls of powerful boiler and can accelerate considerably the wearing of water wall heating surfaces.

The damages of water wall tubes can be classified as:

- **Friable or brittle damages, without deformation**. This damage is characterized by the presence on frontal surface of water wall tubes of cross cracks penetrating into a body of a tube on the depth 1 mm and more. These cracks are stimulated by thermal fatigue.
- **Corrosion defeat of tubes**. This damage accompanied by the decrease of wall's thickness on a frontal surface of tube and its subsequent longitudinal break takes place.
- **Longitudinal break of tubes** is caused by metal overheating due to increasing internal deposition layer thickness, or due to blocking by deposition of tube cross section area. All damages mentioned above can be referred as damages due to poor conformity of the heating surface design to conditions of its operation.

NOMENCLATURE

A_{lf} – low frequency amplitude of incident heat flow density, W/m^2;
A_{abs} - amplitude of absorbable heat flow density, W/m^2;
G_q (f) - function of a spectral density of heat flow, (kW/m2)/Hz;
$q_{abs}(\tau)$ - specific absorbable heat flow in moment τ, W/m^2;
q_{abs} - specific absorbable heat flow on tube internal surface, W/m^2;
q_{lf} - specific absorbable heat flow at low frequency, W/m^2;
$q_{abs\ lfn}$ - specific absorbable heat flow at low frequency noise, W/m^2;
q_{inc} - specific incident heat flow, W/m^2;
t_m , t_{out} - temperature of tube outside surface, oC;
T_{lf} - period of low frequency oscillations of heat flow, oC;
S - thickness of depositions, mm;
Δt - difference of temperature, °C;
λ - thermal conductivity of the depositions, W/m · K;
$\rho\omega$ - mass velocity of a working medium in a tube, kg/m^2s;
ψ - coefficient of thermal efficiency of water walls;
η_h . thermal maldistribution;
SCP- supercritical pressure;
Cr-Mo-V - chromium-molybdenum-vanadium.

EXRERIMENTAL METHOD

Incident heat flow measurements were carried out by heat-radiation pyrometer. Thermoelectric couples were used for the measurement of tube metal temperature. The thermoelectric couples were installed in special drilling in tube body. The construction allowed measuring of metal temperature at outside and interior tube surfaces nearly the place of heat flow application.

The properties and amount of interior depositions were explored in tube samples in chemical lab of thermal electrical station. Tube samples were taken out from furnace screens after 6 thousand operation hours.

RESULTS

Operation conditions of power boiler water wall tubes.

1. Local heat exchange in boiler furnaces.

The maximum heat emission in power boiler with chamber furnaces and single-level of burner place arrangement is a little bit higher than burner level. For two- and third-level arrangement of burners the maximum heat emission corresponds to top burner level. The average value of incident heat flow density on water walls equals q_{inc} = 700-750 kW/m^2 for mineral coal boilers and q_{inc} = 950-1000 kW/m^2 for gas-oil boilers. The local values of incident heat flow density can excess the average one in 1,4 times (η_{lh} = 1,4) and are located in a central part of furnace lateral water walls as well in burner regions at front and back walls (fig.1).

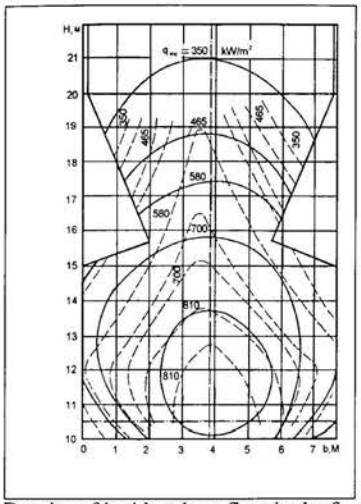

Fig.1 Density of incident heat flow in the furnace of 300 MW steam generator at combustion of mineral coal.

2. Temperature regimes of water walls in boiler furnaces during long-term operation.

Despite of high levels of local perceived heat flows the temperature regime of wall tubes on initial stage of operation does not cause the fears for powerful boiler both subcritical, and supercritical pressures. For example, the average temperatures of tube outside surface t_{out} did not excess 470 ... 500 °C for mineral coal in boilers of supercritical pressure (SCP) and 490 ... 500 °C for gas-oil in SCP boilers. The low doped alloy Cr-Mo-V pearlitic steel is applied for production of water wall tubes for SCP boilers. This steel can work at temperature strength up to the temperature equals of 585 °C.

However, during boiler operation the temperature of tube metal growths and has reached of 80 ... 100 °C for every 4 ... 6 thousand operation hours. The greatest value was received in gas-oil boilers. The furnace water walls are subjected to effect of high local heat loads. So, in SCP boiler PK-41 (300 MW) the value of local incident heat flows in a furnace at average operation loading was q_{inc} = 520-580 kW/m^2. The growth rate of wall tube temperature has reached 12...18 °C per month due to up-building internal depositions.

Wall tube metal temperature growth was monitored in boilers using mineral coal also. At the first 1000 hours the temperature growth did not excess 4...8 °C. In future it reached 18...24 °C for every 1000 hours. The extrapolation of the relation t_{out} = f (τ) demonstrates, that the level of the temperature of 600 °C can be reached after 7,5-8 thousand of operation hours (fig. 2).

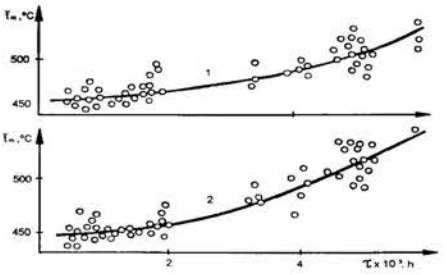

Fig.2. Wall metal temperature changes during operation of the 300 MW generator, using: 1- mineral coal, 2- boiler oil.

4. Internal tube depositions in the boiler.

A main reason of tube metal temperature growth in SCP boilers is the formation on its internal surfaces of depositions from corrosion products (fig.3).

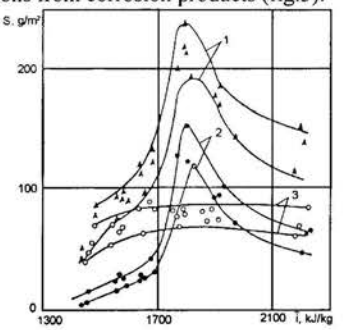

Fig.3. Quantity of water wall tube depositions in 300MW generator in dependence on enthalpy of medium. 1- total depositions; 2 - deposition in porous layer; 3 - deposition in internal layer.

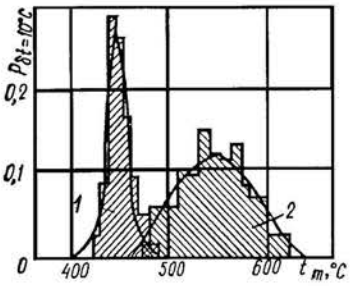

Fig.4.Deviation of tube temperature on different operation states. 1 - the initial period of operation with clean tubes; 2 - after 6000 operation hours.

The deposition includes two layers and consists on iron oxides lactase - up to 90%, oxides of copper, aluminum and zinc, and minor quantities of hardness salts also. The friable layer (porosity 30-60%) is easily cleaned with mechanical cleaning and is partially cleaned with water wash-downs. This layer has low heat conduction (1,5...0,3 W/m · °K) in temperature range 350... 450°C and makes the basis of deposition thermal resistance. Internal layer, contacting with tube metal, has porosity 10...30% and low thickness. It is homogeneous on internal perimeter of a tube. The heat conduction of this layer is approximately three times higher, than mentioned before layer. Therefore internal layer practically does not influent on growth of tube temperatures.

The friable layer is formed predominantly as result of a deposition in tubes of corrosion products introduced in the boiler by feed-water. The deposition layer with maximum thickness is formed in most heat-stressed segments of furnace water wall tubs. Thus, on a frontal surface of tube the quantity of depositions is in 2...5 times more than on back surface.

The definite contribution in the formation of the depositions creates the process of steam-water corrosion of wall tubes

$$3 \cdot Fe + 4 \cdot H_2O \rightarrow Fe_3O_4 + 4 \cdot H_2$$

The products of steam-water corrosion not only form a hard layer, but also partially can pass in a friable layer, increasing thermal resistance of depositions. At internal tube surface temperature growth, as result of the formation of friable deposition layer, the intensity of steam-water corrosion exponentially increases. This process results into acceleration of deposit formation.

The difference of the temperature in a deposition layer can be estimated by formula:

$$\Delta t = 108 \cdot 10^{-6} \cdot S^{1,3} \cdot q_{abs}{}^{1,25} / \lambda \, (\rho\omega)^{0,2},$$

Experimentally it was discovered, that a kind of combustion fuel (solid, liquid or gas) does not render noticeable influence on regularity of iron oxide deposition formation in furnace water walls of SCP boilers, as well as on their structure and thermal properties.

It is necessary to note, that the formation of internal depositions in furnace water walls of boiler results not only to growth of an absolute level of metal temperature, but also to destabilizing of tube temperature regimes in conditions of instability of heat release in furnace. So, in initial stage of operation (the tubes of wall were subject to pre-launch cleaning and they were practically cleaned) 95 % confidence interval of a temperature variation of SCP boiler wall tubes with average loading did not excess 60 °C. At the end of experiment during 6000 hours it was reached 120 °C (fig. 4). An average value of metal temperature on frontal surface is 546 °C. Due to considerable deviations of temperature from average, a definite part of time the tube metal worked at 600 °C and more. Such high instability of a tube temperature regime limits the long-term strength operation of metal. It leads to more low level of tube resource, than it would be at stable heat loading of furnace water walls.

Thus, the reliable temperature regime of furnace water walls includes the decrease of formation intensity of internal iron-oxide deposition and it's well-timed deleting, as well as the increase of stability of thermal regime of furnace water walls.

5. Instability of heat release in combustion chamber and thermal regimes of furnace water walls.

During the powerful boiler activity the longitude cracks of water wall tubes are caused by the appearance of cross cracks on external and internal tube surfaces.

The investigation has shown one of the main reasons of cross crack formation is high instability of heat and temperature regimes of the tubes. Instability of heat and temperature regimes enhances the development of the thermal fatigue processes and also the intensification of creeping phenomena and corrosion.

The researches, carried out in National Technical University of Ukraine, on the boilers with power 200, 300 and 800 MW, have allowed to establish that the main contribution in instability of heat release in a furnace is introduced by two harmonically varied components of heat flow. There are low frequency and high frequency oscillations of heat flow and also aperiodic component - low frequency noise (fig.5).

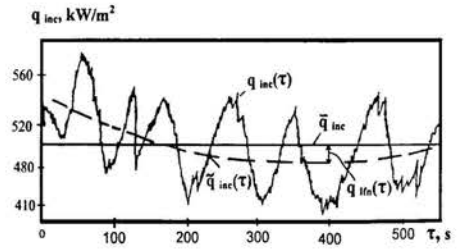

Fig.5. Fluctuation of the heat release in combustion chamber of 300 MW steam generator.

The low frequency oscillations of heat flow are characterized by the frequency band 0,006 ... 0,016 Hz. The local maximum of spectral density function $G_q(f)$ is placed in frequencies ranges 0,010 ... 0,011 Hz, that corresponds to oscillation period of $T_{lf} = 90$ ... 100 s. It has been established, that ***the low frequency oscillations*** q_{lf} are due to the fluctuation of fuel consumption, generated by the boiler regulator of the heat loading mainly. Switching-off the regulator and transition to manual control result to full disappearance of low frequency oscillations. But at the same time the essential increase of power of low frequency noise q_{lfn} was received. In outcome the general dispersion of heat release process did not decrease, but even increase.

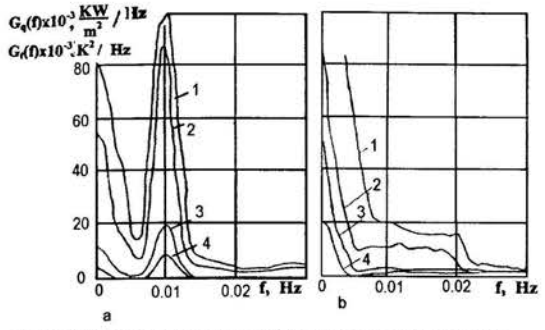

Fig.6. The power spectrum of incident heat flow in the furnace of 300MW steam generator (1,2,3 - $G_q(f)$), 4 - $G_f(f)$, in the low frequency range. Regulator of thermal loading is switch on (a) or switch off (b).

The presence of a strong correlation between the value of low frequency oscillations of heat flow density q_{lf} and the temperature of water wall tube metal are established. Thus, the temperature on frontal tube surface changes only. The back tube surface has the temperature close to temperature of working medium. In result the temperature stresses are formed, which stimulate the thermal metal fatigue and formation of cross-section micro cracks on frontal tube surface.

The high frequency oscillations of heat flow are characterized by the frequency band 0,5 ... 4,0 Hz with a local maximum at frequency 0,7 Hz (oscillation period equal to 1,3 s). At combustion of different kinds of fuels (solid, liquid and gas) the oscillation frequency q_{inc} is practically identical. The distinctions are only in amplitude of high frequency oscillations. The greatest amplitude q_{inc} was received at combustion of solid fuel. The lowest amplitude was at gas combustion. It has been discovered that the high frequency oscillations of the heat flow q_{inc} practically did not influent on temperature regimes of wall tubes. The absence of high frequency component in a power spectrum t_m testifies this conclusion. Therefore, high frequency oscillations can be eliminated from the consideration at the reliability prediction of boiler radiation heating surfaces.

The low frequency noise q_{lfn} occupies in a power spectrum the frequency band 0...0,005 Hz. It is created by the different kind of aperiodic processes and resulting into the change of tube thermal regime. These processes are: changes of fuel characteristics, reallocating of air and fuel in burners, changes in the scheme of burner actuation, changes of boiler loading etc. The low frequency noise in the spectrum of heat released in furnace q_{lfn} can be interpreted as a difference between the current pseudo-steady value of density of dropping heat flow q_{inc} and its mathematics expectation q_{inc} (fig. 5). From physical sense a low frequency noise is the accidental variable, distributed under the normal law with zero mathematics expectation.

The thermal regime of boiler wall tubes at operation reliability estimation can be described by following way:

$$q_{abs}(\tau) = \psi \cdot (q_{lf} + q_{lfn} + A_{lf} \cdot \sin(2\pi / T_{lf}) \cdot \tau),$$

Such model allows presenting a thermal condition of water wall tubes as set of temperature regimes with duration equal to period of low frequency oscillations. These regimes are distinguished from each other by level of the low frequency noise $q_{abs.lfn}$ and by the value of amplitude A_{abs} of density of absorbed heat flow.

The low frequency instability of the thermal absorption of wall tubes causes the instability of metal temperature on frontal tube surface. The absolute value of density of absorbed heat flow q_{abs} is determined by the thermal efficiency of water walls ψ. The lower thermal efficiency (higher foiling of external tube surface) indicates the thermal and temperature regimes of tube metal are less sensitive to instability of heat release in combustion chamber. At local thermal efficiency of the tubes ψ = 0,5...0,6 (characteristic for uncontaminated tubes) and standard deviation of relative heat load from average S = 0,175 (characterized of furnaces at the combustion of mineral coals) the number of temperature variation cycles on external tube surface for 1000 operation hours is equal 4000...5000 with amplitude 10...20 °C (oscillation period 1...2 minutes).

During the process of tube internal deposition building the oscillation amplitude of tube metal temperature increases at the same values ψ and S (fig. 2). Thus definite period the tube metal works at temperature superior of maximum allowed one for low doped alloy Cr-Mo-V pearlitic steel, T=585 °C. At the same time the average temperature of metal on frontal tube surface was lower than 540 °C.

CONCLUSION

Thus, the instability of heat release in boiler combustion chamber causes the decrease of lifetime of tube metal. This is due to the fatigue process in metal during temperature cycling variations and because of the building of internal depositions on frontal tube surface as result of the work part time at the temperature superior of the granted one.

REFERENCES

1. Mikhlevskiy A., Polupan G. Boiler installation of Power Stations. NTUU, Kyiv, Ukraine, 1998, 44 p.
2. Polupan G. State of art on steam generators for Power Stations. Proceeding of 2nd International Congress in Heat Engineering, Mexico, 1999.
3. Mikhlevskiy A., Polupan G., Pysmennyy Ye., Jarquin-Lopez G. Inestabilidad del calor liberado en el hogar. To be published in Proc. of Congress CIDIM, Venezuela, 2001.

HEFAT2002
1st International Conference on Heat Transfer, Fluid Mechanics, and Thermodynamics
8-10 April 2002, Kruger Park, South Africa
PJ1

THE ASSESSMENT OF CRITICAL HEAT FLUX FOR LOADING DUPIC FUEL IN HEAVY WATER REACTOR

J.-W. Park, C.J. Jeong and M.S. Yang
Korea Atomic Energy Research Institute
P.O. Box 105, Yusong
Taejon, 305-600, Korea
E-mail:jwpark@kaeri.re.kr

ABSTRACT

The CHF characteristics of DUPIC (Direct Use of spent PWR Fuel in CANDU Reactor) fuel has been assessed for its feasibility for loading in heavy water reactor. The minimum critical heat flux ratios of the DUPIC and standard fuel bundle strings have been obtained under the same operating condition of the reactor. Based upon the result of simulations, there is no much difference in CHFR values of the two fuels regardless of differences in the power distribution and the fuel geometry. This study shows that different types of fuel can be reasonably assessed by using subchannel analysis which has proper lateral flow model.

INTRODUCTION

The limiting critical heat flux characteristics of DUPIC (Direct Use of spent PWR fuel in CANDU) fuel has been presented.

The DUPIC fuel cycle has received renewed interest as a PWR to CANDU fuel recycling option[1]. The benefit of a DUPIC fuel cycle is not only the use of spent PWR fuel for electricity generation in CANDU, but also the significant reduction of spent fuel produced owing to the increased burnup in CANDU. The DUPIC fuel can be directly manufactured from the spent PWR fuel by the remote fabrication technique which can be proliferation-resistant and safeguardable. Moreover, in the light of recent developmental initiatives of novel nuclear reactor concepts in the nuclear R & D regime, the possibility of DUPIC fuel utilization can be significantly increased.

Compared to the standard CANDU fuel bundle which has 37 fuel rods, the DUPIC fuel bundle adopts an advanced CANDU bundle geometry, which has 8 large and 35 small fuel rods supposedly yielding enhanced fuel performance and thermal margins. The 43-element natural uranium fuel bundle recently underwent design basis safety analysis, successfully loaded and being burnt in the CANDU reactor. This advanced fuel bundle can be used as a high burnup fuel in CANDU with a greater thermal-hydraulics margin compared to the standard design.

Among many different technical issues in developing DUPIC fuel bundle, the critical channel power (CCP) prediction is one of most important tasks in determining the reactor operation margin since the CHF prediction uncertainty is known to be the highest when compared to the others such as, the simulation and the calibration errors in nuclear power plants.

The CCP prediction technique requires experimentally validated CHF correlation which can be consistently used in the single channel analysis. Unfortunately, however, it is impossible to run the experiment for all of the flow and thermal boundary conditions since the CHF experiment is quite expensive. Therefore, a finite amount of the experimental data needs to be interpolated (or, sometimes, extrapolated) when applied to a specified flow condition in the single channel analysis[2]. This type of design analysis methodology requires independent set of experimental data for new type of fuel (e.g., 43-element fuel) of which the geometry and the radial power distribution is quite different from the conventional fuel bundle. A correlation for 43-element fuel bundle was recently generated and the validity of this correlation for wider range of thermophysical condition is of interest.

Therefore, the subchannel analysis can be used for simulating the effect of multi-dimensional flow phenomena which occur in various fuel bundle geometries[3]. Through the lateral flow model, the radial geometry of the fuel bundle can be efficiently taken into account. Nevertheless, the subchannel analysis has not been adopted as the fuel design analysis for the heavy water reactor yet. One of important reasons for this can be that the subchannel analysis may not be able to provide significant improvement in predicting accuracy of CHF in 37-element bundle strings which could substitute the existing design practice of the single channel analysis. It is obvious, however, that the effect of the radial flow distribution within a fuel bundle cannot be mechanistically taken account by the single channel analysis. The radial geometry and power changes of the DUPIC fuel bundle over the standard fuel bundle can be

best-estimated by the subchannel analysis with proper embedded models.

In this study, the combined effect of the axial power distribution and the radial bundle geometry changes in the 43-element DUPIC fuel have been studied. The effect of the power distribution and the geometry on the CHF has been quantified and discussed.

MODELS FOR TRANSVERSE INTERCHANGE

The transverse interchange phenomenon between subchannels can be decomposed into three components in models being used in subchannel codes:

$$w_{i-j} = (w_{i-j})_{CF} + (w_{i-j})_{MIX} + (w_{i-j})_{VD} \quad (1)$$

where

$(w_{i-j})_{CF}$: flow diversion due to imposed transverse pressure gradients,

$(w_{i-j})_{MIX}$: turbulent (eddy diffusivity) mixing,

$(w_{i-j})_{VD}$: "void drift" due to tendency to approach equilibrium conditions.

The so-called void diffusion includes the second and the third terms in Eq.(1). The second effect can be modeled by the classical Reynolds stress term. Unfortunately, however, it is known that the turbulent mixing alone fail to produce the required results since infinite turbulent mixing implies that subchannel void fractions must be the same for a finite value of crossflow while the observed void distribution is a nonuniform equilibrium distribution. Therefore, it was hypothesized that net two-phase turbulent mixing is proportional to the nonequilibrium void fraction gradient. This hypothesis implies that there is a strong trend toward the equilibrium distribution and that when this state is achieved, the net exchange due to mixing ceases. It should be noted that the equilibrium void distribution in a horizontal channel may be different from that in a vertical channel. The net buoyancy effect (i.e., the gravity effect) was claimed[3] to be taken into account by using the drift flux model.

The crossflow is directed flow caused by pressure gradients between the subchannels. In CANDU reactors, the gravity influences the crossflow since the direction of gravity is perpendicular to the channel flow while the phasic slip is close to unity in the major flow direction. When the phasic slip in the major flow direction is close to unity, the behavior of two-phase flow was found to be quite different from that of the large slip flow. For example, the bubble-to-slug regime transition was found to be more gradual and speeds of the thermal-hydraulic information propagation (i.e., characteristics) become smaller[4]. Under this flow condition, the two-phase transverse momentum exchange (i.e., the void drift model) must be very important since the void and enthalpy distributions in the fuel bundle can be strongly influenced by the void drift model. Since, in general, the exit flow quality in CANDU fuel channels are often greater than zero, the void drift model should be validated further under such a flow condition. Since in two-phase flow, not only the energy and the momentum exchange but also the mass exchange occur between subchannels, the equal volume exchange concept is normally applied. It should be noted that the effect of the transverse exchange on the void distribution in the fuel bundle can be larger as the channel flow rate decreases. The transverse exchange model that controls thermophysical property exchanges, may affect the location of CHF in the fuel bundle significantly in the fuel channel of CANDU reactors.

The ASSERT subchannel code was developed to address the computation of flow and phase distribution within subchannels of CANDU fuel bundles. Unlike conventional subchannel codes such as COBRA[5], which are designed primarily to model in vertical fuel bundles and use a homogeneous mixture model of two-phase flow, a drift-flux model[6][7] is used which permits the phase to have unequal velocities. Also, the gravity terms that may make it possible to analyze separation tendencies which could occur in horizontal flow. During developmental stage of the code, computational results were validated against the real scale 37-element bundle experimental data[8].

The thermal-hydraulic modeling equations used in the code were derived from the two-fluid formulation[9]. Like COBRA-IV computer code, the ASSERT Code is based upon subchannels which are divided axially into a number of control volumes. The closure relationships for the governing equations include the equation of state, relative velocity relationship, fluid friction, wall heat transfer and the thermal mixing to primary variables, phasic flow velocities, densities, enthalpies and pressure.

The numerical solution scheme can be subdivided into two parts: The first part solves the energy and the state equations using block iterative method to calculate the mixture and phasic enthalpies for all subchannels using the current estimates of flow. Once the inner iteration for energy equation solution converges, the second part calculates the flows and pressure gradients at that axial position by direct matrix solution of the crossflow equations. With this information, axial flows and pressures can be calculated. Both parts are repeated once to ensure a higher level of convergence of both energy and flow solutions prior to moving to the next axial position. The channel is successively swept from the inlet to the exit. This outer iteration continues until convergence is achieved, or until an iteration limit is reached. Successful completion could yield a steady-state solution, or one time-step of a transient solution. The solution scheme works with either a flow boundary condition or a pressure boundary condition.

The CHF prediction can be performed subsequent to flow distribution calculation by using one of the CHF correlations such as BAW-2, W-3, Whalley's or AECL's CHF Table. In this study, AECL's CHF look-up table option[2] was used for all simulations.

MODELS FOR THE DUPIC FUEL BUNDLE

The radial power distribution of the DUPIC fuel bundle has been obtained from the DUPIC reference fuel design which is based upon the neutronic properties of a CANDU core loaded with the DUPIC fuel. The resulting ring power ratios, as shown in Fig. 1, have been used in this study. As can be seen, the DUPIC fuel bundle has less uniform than the standard fuel bundle. This power distribution is that of the fresh fuel bundle which was found to be the most serious (i.e., the least uniform) through the burnup history of the DUPIC fuel bundle.

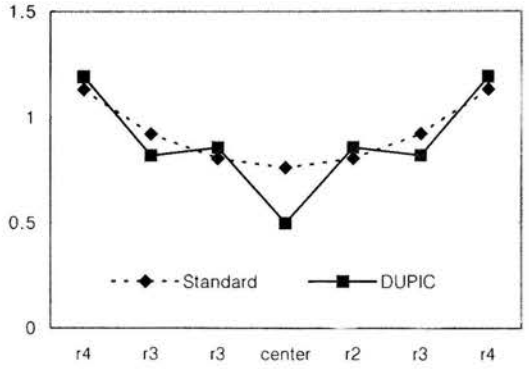

Figure 1. Ring Power Ratios

Since the proposed refueling scheme of DUPIC fuel is two bundle shift instead of eight bundle shift used for standard fuel, the axial power distribution of the DUPIC fuel loaded core has inlet peak as shown in Fig. 2. It should also be noted that there is an exit power peak which is caused by the effect high reactivity of the fresh fuel loaded in the neighboring fuel channels. It was, however, found that this type of off-cosine shape of axial power profile does not degrade the CHF margin when compared with the standard fuel loaded fuel channel.

The channel power to channel flow ratio has been frequently used as the parameter to regulate the burden of energy removal from each fuel channel. As can be seen in Figs. 3 and 4, the channel power and flow are properly balanced in both of the fuel types. The calculated power to flow ratios suggest that no much difference between two fuel types is expected for most of the fuel channels in the reactor core.

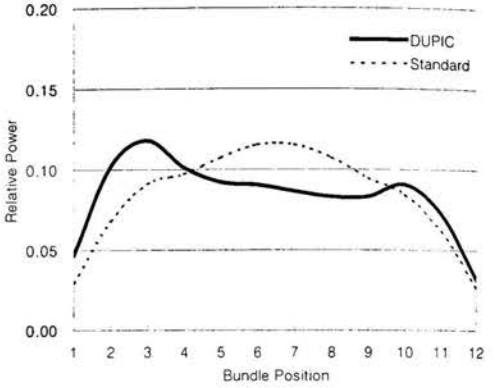

Figure 2. Axial Power Distribution of DUPIC and Standard Fuel for Channel L11 at 100% F.P. Normal Operating Condition

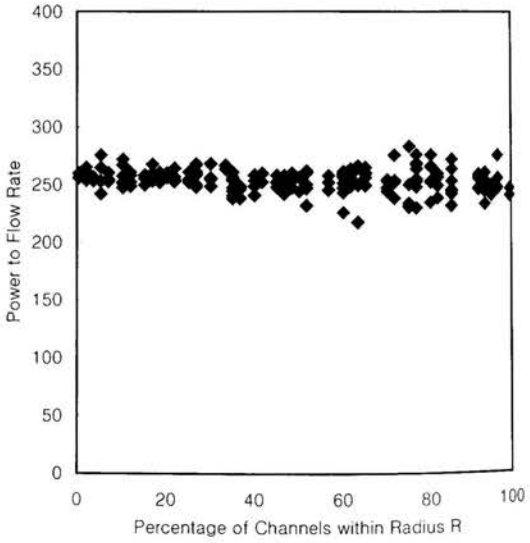

Figure 3. Power to Flow Ratio of Standard (NU) Fuel

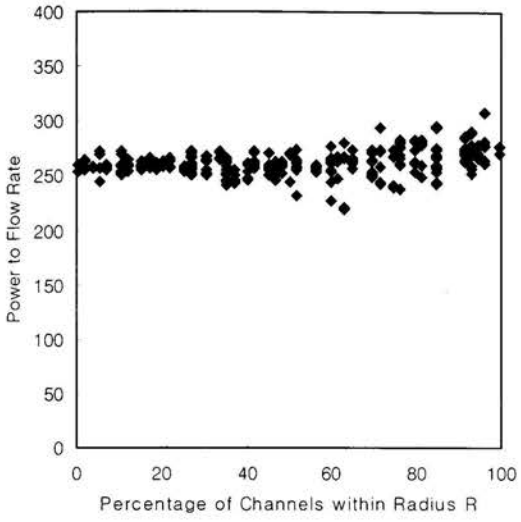

Figure 4. Power to Flow Ratio of DUPIC Fuel

Half bundle subchannel models for the DUPIC and the standard CANDU fuel bundles have been constructed. Since gravity is perpendicular to the direction of channel flow in CANDU reactors, at least half of the bundle should be modeled for the subchannel analysis. The model for the DUPIC fuel bundle includes 23 powered elements and 35 subchannels. It should be noted that a slight difference is expected between different rotations of fuel bundles in the fuel channel since the half symmetry can not be maintained for all angular positions of the fuel bundle.

Table 1. Fuel Parameters and Operating Conditions

Description	Standard	DUPIC
Flow Area [m^2]	.00176	.00180
Heated Perimeter [m]	.7603	.8018
Wetted Perimeter [m]	.9236	.9641
Avg. Mass Velocity [Mg/m^2-s]	5.00	4.89
Avg. Heat Flux [MW/m^2]	1.100	1.043
System Pressure [MPa]	10.0	
Inlet Temperature [Degree C]	260.0	
Inlet Enthalpy [KJ/KG]	1095	

The operating conditions and thermal-hydraulic parameters of the fuel bundles used in the subchannel analysis are shown in Table 1, in which the power level was intentionally chosen to be higher than the normal operating value to study the behavior of the transverse interchange model in two-phase flow regime.

For the purpose of valid comparison between two fuel types, the channel average mass flux and the average heat flux of the DUPIC fuel have been adjusted. By doing this, for specified values of channel average mass and heat fluxes, the difference in the flow area between two fuel types may yield the equivalent channel energy balance for the coolant. The axial power distribution has been assumed identically to be the cosine shape for both fuel bundle strings to isolate the effect of radial geometry difference. The effect of the skewed axial power distribution has not been considered in this work.

To calculate the CHF ratio accurately, we may need accurate estimation of the thermal-hydraulic parameters in subchannels around the fuel element. It should be noted that the CHF correlation or the look-up table have their own uncertainty. Therefore, the CHF ratio presented in this study has uncertainties from two different sources, that is, one from the subchannel model and the other from the CHF correlation.

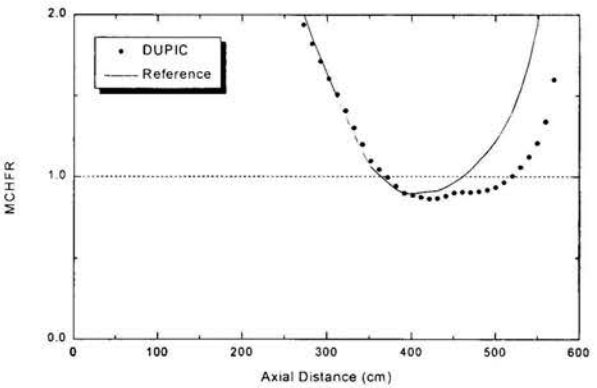

Figure 5. Minimum CHFR of Standard and DUPIC Fuel Bundle Strings

RESULTS AND DISCUSSION

In Figure 5, the minimum CHF ratios (MCHFR) among the fuel elements at a certain axial location are plotted against the axial distance from the inlet of the coolant channel. It can be seen that the MCHFR is less than 1.0 over wider axial region for the DUPIC fuel bundle. We may therefore find that the flow near the CHF condition in the DUPIC fuel bundle is quite different from that of the standard fuel bundle. The difference in the flow condition could cause, specially near the CHF condition, a dramatic change in the heat transfer coefficient. It should be further investigated how much the location of CHF in the fuel bundle string is sensitive on different CHF correlations

It is found that the mixture enthalpies in the upper subchannels are consistently higher than those in the lower

subchannels neighboring the central fuel element. Since the fuel element powers are symmetric around the central fuel element, we may find that the ASSERT-IV Code can take into account the gravity effect properly. This fact was confirmed from the subchannel-wise density distribution. It is clear that this type of non-uniform enthalpy distribution is impossible for the flow through a fuel assembly of LWRs where the fuel assemblies are vertically loaded. Under the thermal conditions used in this simulation, the bundle average quality and the void fraction at the exit of the fuel channel were found to be 0.23 and 0.77, respectively, which means the fuel element is mainly cooled by the vapor convection. The mixture enthalpy peak has been found to be in the central region of the standard fuel bundle. However, this may not be necessarily true near the location where the CHF occurs. In contrast, for the DUPIC fuel bundle, the mixture enthalpy peak is in the upper peripheral region of the fuel bundle at the fuel channel exit. It is not clear at this moment why this different tendency in the radial enthalpy distribution between two fuel bundles occurs at the high void fraction regime[10] (i.e., at the exit of the fuel channel). It is interesting to note that the mixture enthalpies of subchannels around the center fuel element of DUPIC fuel bundle are much less uniform than those in the standard fuel bundle.

The radial void distributions at the exit of the fuel channel are shown in Figures 6 and 7. From these figures, the tendency of void migration toward the upper region of the fuel bundle is clear and the void fraction in the central region is highest for the standard fuel bundle, while the void fraction is highest in the upper region of the DUPIC fuel bundle. For these simulations, the CHF locally occurs before the exit of the fuel channel, where some fuel elements in Ring 4 hit the CHF condition already. Therefore, the void distribution at the exit of the fuel channel may not be directly related with that near the CHF location in the fuel bundle. From this view, the CHF should be predicted by local parameter based correlations to obtain more accurate values. As shown in Figures 8 and 9, the radial CHF locations in the DUPIC fuel bundle is similar to those in the standard fuel bundle.

SUMMARY AND CONCLUSION

The thermal behavior of the DUPIC fuel bundle in a CANDU reactor has been assessed. The mixture enthalpy and the density distributions around the central region of the fuel bundle show clear net buoyancy effects, which are pronounced in the DUPIC fuel bundle. The locations of fuel elements where the CHF occurs are similar in the standard and the DUPIC fuel bundles. It is found that the wall temperature of the central fuel element of the DUPIC fuel bundle is significantly lower than that of the standard fuel bundle in the subcooled region.

This result seems to reflect the intention of the 43-element fuel design in which diameter of the fuel elements in the central region is larger than the others. It should be noted that validity of this analysis strongly depends on the transverse interchange model and the related parameters so that further effort should be devoted for validating transverse interchange model.

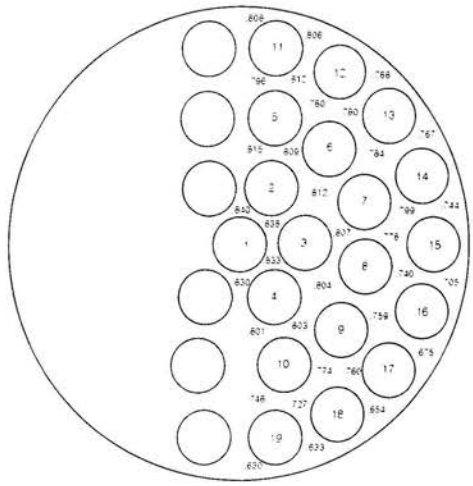

Figure 6. Channel Exit Void Distribution of Standard Fuel Bundle

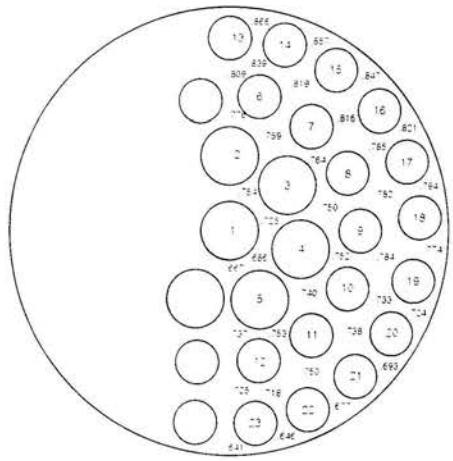

Figure 7. Channel Exit Void Distribution of DUPIC Fuel Bundle

The conclusions of this study can be summarized as follows:

- The DUPIC fuel bundle has very similar CHF characteristics with the standard fuel bundle, that is, the location of CHF occurrence and MCHFR.
- The change in fuel geometry of DUPIC fuel bundle may pronounce the net gravity effect, which is expected to be more severe for reduced values of channel flow rates.

- The fuel geometry and/or the power distribution changes may result major change in the fuel element wall temperature change in the subcooled region.

Further study should be performed in the fllowing areas for better assessment of CHF phenomenon of the DUPIC fuel bundles:

- Experimental validation of void migration near CHF condition in horizontal flows
- Three dimensional modeling of the flow field under CHF condition with increased number of spatial nodes
- Sensitivity study of equilibrium void distribution model horizontal flow channel

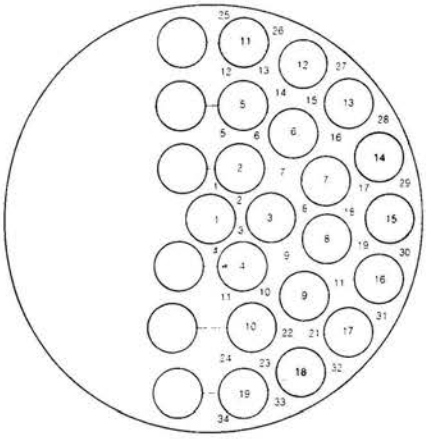

Figure 8. Location of CHF in the DUPIC Fuel Bundle

It is hoped that this study would be useful for developing constructive numerical analysis tool for assessing thermal behaviors of fuel bundles in nuclear reactors

NOMENCLATURE

A_H	heated area
h_{wall}	heat transfer coefficient at the wall of fuel element
q	fuel element power
T_C	coolant temperature
w_{i-j}	transverse flow between subchannels per unit area

REFERENCES

[1] Choi, H., Ko, W. and Yang, M.S., 2001, Economic Analysis on Direct Use of spent PWR Fuel in CANDU Reactor, *Nuclear Technology*, **134**.

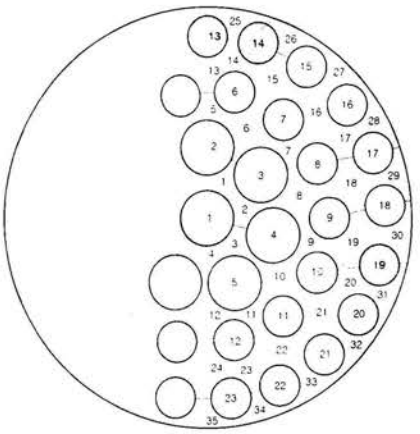

Figure 9. Location of CHF in the DUPIC Fuel Bundle

[2] Leung, L.K.H. and Groeneveld, D.C. (1990) Revision of the AECL-UO Look-Up Table for Critical Heat Flux (CHF) in Tubes, COG-90-69, CANDU Owner's Group, Canada.

[3] Carver, M.B, Kiteley, J.C., Zhou, R.Q.N. and Junop, S.V. and Rowe, D.S. (1995) Validation of the ASSERT Subchannel Code: Prediction of Critical Heat Flux in Standard and Nonstandard CANDU Bundle Geometries, *Nuclear Technology*, **112**.

[4] Park, J-W., Drew, D.A. and Lahey, R.T., Jr. (1994) The Measurement of Void Waves in Bubbly Two-Phase Flows, *Nuclear Eng. & Dsn.*, **149**, 37.

[5] Rowe, D.S. (1973) COBRA-IIIC: A Digital Computer Program for Steady-State and Transient Thermal-Hydraulic Analysis of Rod Bundle Nuclear Fuel Elements, BNWL-1965, Battelle Northwest Pacific Laboratory.

[6] Zuber, N. and Findlay, J.A. (1965) Average Volumetric Concentration in Two-Phase Flow System, *Trans. ASME*, **87**, Series C, 453.

[7] Ishii, M. (1977) One-Dimensional Drift-Flux Model and Constitutive Equations for Relative Motion Between Phases in Various Two-Phase Flow Regimes, ANL-77-47, Argonne National Laboratory.

[8] Kiteley, J.C., Carver, M.B., Waddington, G.M., Zhou, R.Q.N. and Liner, Y. (1994) ASSERT Development and Validation Recent Progress, Proc. of the 1994 Nuclear Simulation Symposium, 127, October, Pembroke, Ontario.

[9] Judd, R.A., Tahir, A., Carver, M.B., Kiteley, J.C., Rowe, D.S., Stewart, D.G. and Thibeault, P.R. (1984) ASSERT-4 User's Manual, AECL-8573, Atomic Energy Canada Limited, Canada.

[10] Lahey, R.T., Jr. and Moody, F.J., 1993, The Thermal-Hydraulics of a Boiling Water Reactor, 2nd Edition, ANS Monograph

HEFAT2002
1st International Conference on Heat Transfer, Fluid Mechanics, and Thermodynamics
8-10 April 2002, Kruger Park, South Africa
RP1

ONE-DIMENSIONAL REACTOR MODEL FOR THE INTEGRATED SIMULATION OF THE PBMR POWER PLANT

P.G. Rousseau* and G.P. Greyvenstein**
*Professor and Director, School of Mechanical and Materials Engineering,
**Professor and Dean, Faculty of Engineering,
Potchefstroom University for CHE
Private Bag X6001, Potchefstroom 2520, South Africa
E-mail: mgipgr@puknet.puk.ac.za

ABSTRACT

The Pebble Bed Modular Reactor (PBMR) power plant is currently being developed by PBMR (Pty) Ltd in South Africa together with ESKOM and other industrial partners. This high temperature gas cooled reactor (HTGR) plant is based on a three-shaft Brayton cycle with helium gas as coolant. The complexity associated with the thermal-hydraulic design of the cycle calls for the use of a variety of analysis techniques and simulation tools. One of the most prominent of these is the Flownet thermal-hydraulic network simulation software. Flownet allows detailed steady-state and transient thermal-hydraulic simulations of all components in the plant fully integrated with core neutronics and controller algorithms. This paper describes the theory and integration of the neutronics and thermal-hydraulic models for the reactor core and presents sample calculations to illustrate the results obtained.

INTRODUCTION

The pebble bed reactor core is made up of fuel spheres and pure graphite spheres. Each fuel sphere consists of an inner fuel region with a 50 mm outer diameter made up of coated UO_2 particles set inside a graphite matrix. The fuel region is covered by a fuel-free graphite protective layer with an outer diameter of 60 mm.

A schematic three-dimensional representation of the geometry of the reactor core is shown in Figure 1. The inner core region contains pure graphite spheres while the outer active core region is filled with fuel spheres. Helium gas enters the top of the reactor core at approximately 500 °C. The gas is heated primarily through the active core region where heat is generated inside the fuel spheres. Upon leaving the core at the bottom the hot gas is mixed with gas from the pure graphite region to obtain a fully mixed exit temperature of approximately 900 °C.

Integration of core neutronics and power conversion unit (PCU) thermal-hydraulics has been done successfully before for HTGR systems. One example of this is the coupling of Panther, Thermix-Direkt and Relap 5 by Verkerk [1] for the simulation of the pebble bed reactor for the Dutch INCOGEN and ACACIA [2] studies. Panther was used to solve the neutron diffusion equation in Cartesian coordinates, Thermix-Direkt took care of the core thermal-hydraulics and Relap 5 of the PCU thermal-hydraulics. This allowed the integrated simulation of thermal-hydraulics and 3-D neutronics of a pebble bed HTGR together with its PCU. Note however, that the PBMR system differs from the Dutch systems in the sense that it is based on a multi-passage fuelling scheme as opposed to a bit-by-bit fuelling scheme.

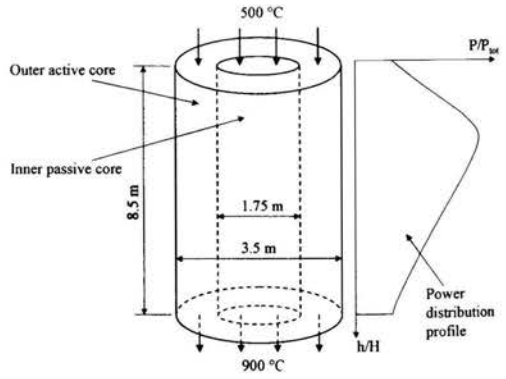

Figure 1: Schematic three-dimensional representation of the pebble bed reactor core.

Since most transient reactor phenomena are at least two-dimensional in nature, it is clear that the development of an accurate one-dimensional model for detailed reactor design and optimisation is not a realistic goal. However, the main aim of Flownet is to simulate the integrated system performance, focussing on the detail of the PCU, while still ensuring acceptable calculation times. Therefore, a fully integrated, simplified reactor model was called for that could supply sufficiently accurate values of pressure drop and heat transfer across the reactor. The calculation of the heat generated within the fuel spheres is therefore based on a point kinetics neutronics and decay heat generation model that requires as input the temperatures within the fuel spheres inside the reactor. Point

kinetics refers to the approach whereby the global reactor behaviour is simulated dynamically as a single point having certain weighted average properties that may be assumed to be constants over time. This simplification is valid when the reactor is sufficiently small so that it is well-coupled and the space and time variables are essentially separable. This means that the spatial neutron flux shape changes negligibly during a transient even though the amplitude may be strongly time-dependent. Although these assumptions exclude the use of such a heat generation model for detailed reactor design calculations, it is quite sufficient for the integrated simulation of the overall power plant behaviour.

It is important to note that the point kinetics model by definition at any time step provides as output a single value of power generation for the reactor as a whole. This total power generation is equal to the total internal heat generation in all of the fuel spheres contained in the reactor. In order to apply this in the heat conduction model for each representative fuel sphere in each layer, the total heat generation is first distributed among the layers according to the prescribed normalised power distribution profile that was shown schematically in Figure 1. This is consistent with the underlying assumptions of the point kinetics model. The normalised power distribution profile is typically obtained from stand-alone calculations with more detailed three-dimensional reactor simulation models for the specific reactor geometry and fuel characteristics.

The model is further based on a one-dimensional approach for the thermal-hydraulics, consistent with the overall approach followed in the Flownet software. The one-dimensional approach implies that the reactor core is divided into a number of layers along its height, each with two separated flow elements representing the pure graphite inner leg and an active outer leg respectively. Consistent with the one-dimensional approach it is assumed that all spheres contained in a single core section have exactly the same temperature distribution and internal heat generation per unit volume. Each reactor section is therefore characterized by a single representative sphere. Fluid flow in the radial direction is assumed to be negligible. However, the combined effect of radial and axial contact conduction and radiant heat transfer between the surfaces of spheres in the different reactor sections are taken into account via an effective thermal conductivity.

The temperature distribution within each representative sphere is calculated in detail based on a transient heat conduction model taking into account the thermal storage, the internal heat generation, conduction between material layers at different radii as well as the convective heat transfer to the coolant gas flowing over the sphere. This results in a representative sphere surface temperature which when applied to the total sphere surface area contained in the core section, can be used to calculate the heat transfer rate to the gas passing through that section. The one-dimensional reactor model therefore consists of the three sub-models shown in Figure 2. These are:

- The transient point kinetics neutronics and decay heat generation model. It requires as input the temperatures within the fuel spheres and provides as output the total internal heat generation within all the fuel spheres contained in the reactor core.
- The detailed transient internal heat conduction for each representative sphere in each core section. It requires as input the heat generation density within the fuel as well as the temperature of the gas surrounding the spheres. It provides as output the temperature distribution within the spheres as well as the heat transfer through convection between the surfaces of the spheres and the surrounding coolant.
- The fully transient fluid flow model that determines the temperature and pressure variations in the gas contained in each core section. It requires as input the surface heat transfer rate and provides as output the coolant temperatures and pressures.

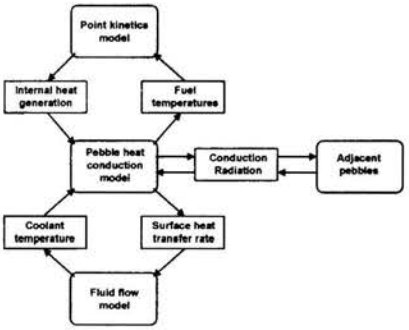

Figure 2: Schematic illustration of the interaction between the three models.

The approach outlined above allows for fully transient simulations of temperature distributions along the height of the reactor as well as the calculation of the radial temperature distribution within each representative sphere in each of the core sections.

The purpose of this paper is to describe the theory and integration of the neutronics and thermal-hydraulic models for the reactor core and to present sample calculations to illustrate the results obtained.

NOMENCLATURE

A	cross-sectional area of flow element (m^2)
C_i	normalized precursor atom density for group i
c_p	specific heat capacity of fluid (J/kg K)
D	hydraulic diameter of fluid element (m)
f	Darcy-Weisbach friction factor
g	gravitational acceleration (m/s^2)
J	normalized Iodine concentration

L	length of flow element (m)
m_i, m_e	inlet and outlet mass flow rates (kg/s)
Nu	Nusselt number
p	static pressure (Pa)
p_{oi}, p_{oe}	inlet and outlet total pressures (Pa)
P_n	normalized reactor power
Pr	Prandtl number
Q	heat addition to flow element (W)
Q_{ex}	reactivity addition due to external sources (nile)
Re	Reynolds number
T	static temperature (°C)
T_{oi}, T_{oe}	inlet and outlet total temperatures (°C)
V	fluid velocity (m/s)
$\forall$	volume of flow element (m^3)
X	normalized Xenon concentration
z_i, z_e	inlet and outlet elevations (m)

Greek Letters

α	weighting factor for implicit time-wise integration
β_i	delayed neutron fraction for group i
Δt	size of time step (s)
ε	void fraction
Λ	average neutron lifetime (s)
Γ	feedback coefficients
λ_i	decay constant for delayed neutron group i (s^{-1})
λ_J	decay constant for Iodine (s^{-1})
λ_X	decay constant for Xenon (s^{-1})
ρ	reactivity (nile)
$\bar{\rho}$	average fluid density (kg/m^3)
$\sigma_X \varphi_0$	absorption cross section times average equilibrium neutron flux (s^{-1})
$\sum K$	sum of the loss coefficients for flow element

POINT KINETICS AND DECAY HEAT MODEL

The model consists of twelve coupled differential equations that must be solved simultaneously though time-wise integration. A good explanation of the fundamentals can be found in Glasstone and Sesonske [3]. The first seven equations are collectively known as the point kinetics equations and describe the prompt and delayed neutron balance due to precursor atoms. There are numerous fission products that can lead to delayed neutron emission. However, the net effect of all precursors can be adequately represented by six effective groups of precursors.

Decay heat generation is the result of unstable fission fragments produced during fission that undergo a series of beta decays liberating additional energy. Decay heat is a complex function of the time and power history of the fuel elements. However, the simulation will make use of a rough approximation by means of three exponentially decaying functions which is only valid for approximately three days after shut-down.

It is also essential to track the concentration of Xenon in the reactor since it effectively acts as a neutron poison. Since Xenon is mostly produced during the decay of Iodine, the Iodine concentration in the reactor must also be tracked. The rate of Iodine production is proportional to the reactor power level.

The rate of change of Xenon concentration equals the rate of Xenon production minus the rate of Xenon loss. The absorption of neutrons depends on the reactor power level, the Xenon concentration and the absorption cross-section. We will neglect the direct production of Xenon by fission and any time dependence of cross-sections.

Governing Equations

Implicit integration of the governing differential equations for the point kinetics, decay heat and Iodine and Xenon decay leads to the following set of simultaneous equations:

Point Kinetics

$$\left(\frac{\Lambda}{\Delta t}-\alpha\left(\rho-\beta\right)\right)P_n-\alpha\sum_{i=1}^{6}\lambda_i C_i = \frac{\Lambda}{\Delta t}P_n^o+\alpha Q_{ex}+\left(1-\alpha\right)\begin{pmatrix}\left(\rho^o-\beta\right)P_n^o \\ +\sum_{i=1}^{6}\lambda_i C_i^o+Q_{ex}^o\end{pmatrix} \quad (1)$$

and

$$-\alpha\beta_i P_n+\left(\frac{1}{\Delta t}+\alpha\lambda_i\right)C_i = \frac{1}{\Delta t}C_i^o+\left(1-\alpha\right)\left(\beta_i P_n^o-\lambda_i C_i^o\right) \text{ for } i=1 \text{ to } 6. \quad (2)$$

Decay Heat

$$-\alpha\beta_k P_n+\left(\frac{1}{\Delta t}+\alpha\lambda_k\right)P_k = \frac{1}{\Delta t}P_k^o+\left(1-\alpha\right)\left(\beta_k P_n^o-\lambda_k P_k^o\right) \text{ for } k=1 \text{ to } 3. \quad (3)$$

Iodine and Xenon Decay

$$-\alpha\lambda_J P_n+\left(\frac{1}{\Delta t}+\alpha\lambda_J\right)J=\frac{1}{\Delta t}J^o+\left(1-\alpha\right)\lambda_J\left(P_n^o-J^o\right) \quad (4)$$

and

$$\alpha\sigma_X\varphi_0 X P_n-\alpha\left(\lambda_X+\sigma_X\varphi_0\right)J+\left(\frac{1}{\Delta t}+\alpha\lambda_X\right)X = \frac{1}{\Delta t}X^o+\left(1-\alpha\right)\begin{pmatrix}\left(\lambda_X+\sigma_X\varphi_0\right)J^o \\ -\left(\lambda_X+\sigma_X\varphi_0 P_n^o\right)X^o\end{pmatrix}. \quad (5)$$

In these equations Δt represents the size of the discrete integration time step and α a weighting factor. The superscript o refers to the values at the previous time step.

Total Heat Generation

The total heat generation in the core P_{tot} can be calculated from

$$P_{tot} = P_{nom}\frac{(P_n + P_{decay})}{(1+\sum_{k=1}^{3}\beta_{kk})} \quad (6)$$

with

$$P_{decay} = \sum_{k=1}^{3}\lambda_{kk}P_k \quad (7)$$

and P_{nom} the design nominal power output of the reactor.

Reactivity feedback equations

The total reactivity can be calculated from

$$\rho = \rho_f + \rho_m + \rho_X + \rho_{ex}. \quad (8)$$

The first three terms on the right-hand side are dependent on the fuel and moderator temperatures. The value of ρ_{ex} is determined by the insertion depth of the control rods. The relations used for the PBMR reactor were derived by Scherer et.al. [4] and are as follows:

$$\rho_f = \Gamma_{f1}(T_f - T_{f0}) + \Gamma_{f2}\ln\left(\frac{T_f}{T_{f0}}\right) - \Gamma_{f3}\left(\frac{1}{T_f} - \frac{1}{T_{f0}}\right), \quad (9)$$

$$\rho_m = \Gamma_{m1}(T_m - T_{m0}) + \Gamma_{m2}(T_m - T_{m0})^2 + \Gamma_{m3}(T_m - T_{m0})^3 \quad (10)$$

and

$$\rho_X = (\Gamma_{X1} + \Gamma_{X2}(T_m - T_{m0}))(X - 1). \quad (11)$$

The reference moderator (T_{m0}) and fuel (T_{f0}) temperatures are determined by the detail design of the fuel and the reactor.

SPHERE HEAT CONDUCTION MODEL

The sphere heat conduction model is based on a finite difference solution of the transient one-dimensional spherical heat conduction equation [5]. Each sphere is divided into a number of discrete 'onion ring' shaped control volumes each represented by a single node. Half control volumes represent the inner- and outermost layers. Implicit integration of the governing differential equation for each node leads to a set of equations that must be solved simultaneously for each node in the representative sphere.

The node on the surface of the sphere represents the surface temperature of all the spheres in that section of the reactor that is exposed to the coolant. From the viewpoint of the coolant the spheres will therefore have the same effect as a constant surface temperature heat exchanger with a total area equal to the sum of the surface areas of all the spheres in that layer. The convection heat transfer can therefore be simulated quite easily with the aid of the effectiveness-NTU method[6].

For the calculation of the surface heat transfer coefficient the correlation put forward by Kugeler & Schulten [7] is employed which states that the Nusselt number is given by

$$Nu = 1.27\frac{\mathrm{Pr}^{0.33}}{\varepsilon^{1.18}}\mathrm{Re}^{0.36} + 0.033\frac{\mathrm{Pr}^{0.5}}{\varepsilon^{1.07}}\mathrm{Re}^{0.86} \quad (12)$$

Re is the Reynolds number and Pr the Prandtl number which are based on the pebble outer diameter. The void fraction ε is taken as 0.39. The correlation is valid for core outer diameter to pebble diameter ratios greater or equal to 20, core height to pebble diameter ratios greater or equal to four, $100 \le \mathrm{Re} \le 10^5$ and $0.36 \le \varepsilon \le 0.42$.

FLUID FLOW MODEL

The fluid flow model is based on the differential equations for the conservation mass, momentum and energy for compressible gasses [8].

Governing Equations

Implicit integration of the governing differential equations for a flow element leads to Equations (13) through (15) which are solved simultaneously for all the nodes and elements in the complete reactor network with the aid of the so-called 'Pressure Correction Implicit Method' (PCIM) that is described elsewhere by Greyvenstein [8].

Conservation of Mass

$$\bar{\rho} - \bar{\rho}^o = \frac{\Delta t}{V}\left(\begin{array}{l}\alpha\left(\sum m_i - \sum m_e\right)\\ +(1-\alpha)\left(\sum m_i^o - \sum m_e^o\right)\end{array}\right). \quad (13)$$

Conservation of Momentum

$$\begin{aligned}&\bar{\rho}\bar{V} - \bar{\rho}^o\bar{V}^o\\ &= -\frac{\Delta t}{L}\left(\begin{array}{l}\alpha\left(\begin{array}{l}\frac{\bar{p}}{\bar{p}_o}\left(p_{oe} - p_{oi}\right) + \bar{\rho}g\left(z_e - z_i\right)\\ +\left(T_{oe} - T_{oi}\right)\frac{1}{\bar{T}_o}\frac{\bar{m}^2}{2\bar{\rho}A^2}\\ +\left(\frac{fL}{D} + \sum K\right)\frac{|\bar{m}|\bar{m}}{2\bar{\rho}A^2}\end{array}\right)\\ +(1-\alpha)\left(\begin{array}{l}\frac{\bar{p}^o}{\bar{p}_o^o}\left(p_{oe}^o - p_{oi}^o\right) + \bar{\rho}^o g\left(z_e - z_i\right)\\ +\left(T_{oe}^o - T_{oi}^o\right)\frac{1}{\bar{T}_o^o}\frac{\left(\bar{m}^o\right)^2}{2\bar{\rho}^o A^2}\\ +\left(\frac{f^o L}{D} + \sum K^o\right)\frac{|\bar{m}^o|\bar{m}^o}{2\bar{\rho}^o A^2}\end{array}\right)\end{array}\right).\end{aligned} \quad (14)$$

Conservation of Energy

$$\begin{aligned}&\left(\bar{\rho}c_p\bar{T}_o - \bar{p}\right) - \left(\bar{\rho}^o c_p\bar{T}_o^o - \bar{p}^o\right)\\ &= -\frac{\Delta t}{V}\left(\begin{array}{l}\alpha\left(\begin{array}{l}\left(\sum m_e c_p T_{oe} - \sum m_i c_p T_{oi}\right)\\ +\sum m_e g z_e - \sum m_i g z_i - Q\end{array}\right)\\ +(1-\alpha)\left(\begin{array}{l}\left(\sum m_e^o c_p T_{oe}^o - \sum m_i^o c_p T_{oi}^o\right)\\ +\sum m_e^o g z_e - \sum m_i^o g z_i - Q^o\end{array}\right)\end{array}\right).\end{aligned} \quad (15)$$

Friction Factor

For the pebble bed the friction factor (f) is calculated with the aid of the correlation also put forward by Kugeler & Schulten [7] namely

$$f = \psi \frac{1-\varepsilon}{\varepsilon^3} \tag{16}$$

with

$$\psi = \frac{320}{\left(\frac{\mathrm{Re}}{1-\varepsilon}\right)} + \frac{6}{\left(\frac{\mathrm{Re}}{1-\varepsilon}\right)^{0.1}}. \tag{17}$$

The correlation is valid for core outer diameter to pebble diameter ratios greater or equal to 20, core height to pebble diameter ratios greater or equal to four, $1 \le \mathrm{Re}/(1-\varepsilon) \le 10^5$ and $0.36 \le \varepsilon \le 0.42$.

RESULTS

Grid- and time-step independence

The evaluation of grid dependence was done by comparing steady-state solutions based on simulations employing different numbers of layers in the reactor as well as different numbers of material layers in each of the representative pebbles. For all of these cases the resultant gas outlet conditions are exactly the same since it is independent of the grid size. However, different values of pebble temperatures and reactivity resulted.

An analysis of the results showed that 10 layers in each pebble is sufficient. Furthermore, for 20 layers or more along the length of the reactor the average pebble temperature is within 0.3 % of that obtained with 500 layers or more. The external reactivity is within 3.8 % of that obtained with 500 layers or more. From this it can be concluded that 20 layers along the length of the reactor is sufficient.

In order to investigate the time step size dependence, a reactivity transient was investigated. The transient entails a ramp release of 500 mNile at a rate of 10 mNile per second for different simulation time step sizes varying between 5 seconds and 0.005 seconds.

A detailed analysis of the results show that for a time step of 0.5 seconds or smaller, the maximum error is less than 1 % when compared to the results obtained with a 0.005 second time step. For a time step of 0.1 second or smaller the maximum error is less than 0.2 %.

Similar results were obtained for the average pebble temperatures. Therefore, based on both the neutronic power and temperature results, it can be concluded that an acceptable degree of time step independence is obtained for any time step size smaller than 0.5 seconds.

Sample calculation 1: Reactivity transient

The first sample calculation entails a ramp release of 500 mNile [0.5 %] at a rate of 10 mNile [0.01 %] per second over a time span of 50 seconds. Figure 3 shows the results obtained for the reactor power output, coolant outlet temperature and average pebble temperature.

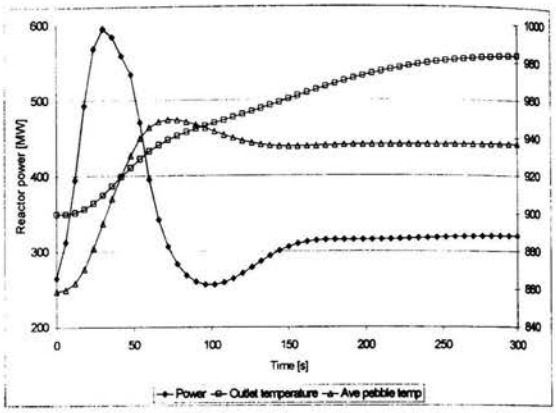

Figure 3: Results of reactivity transient simulation.

The figure shows that the reactivity release results in an increase in power followed by a sharp increase in the pebble temperature. This in turn results in a decrease in power output due to the negative temperature gradient characteristics of the fuel. After 300 seconds the gas outlet temperature is still rising in response to the continuing power and pebble temperature rise which is less noticeable on the graph.

Sample calculation 2: Mass flow transient

The second sample calculation entails a ramp reduction in mass flow rate to 50 % of the initial value over a time span of 300 seconds. Figure 4 shows that the decrease in coolant flow initially results in an increase in the pebble temperature which in turn results in a decrease in the power output. Following this, the pebble temperature starts to decrease again. However, despite the decrease in pebble temperature, the power continues to drop. This is due to an increase in the Xenon concentration with Xenon acting as a neutron poison.

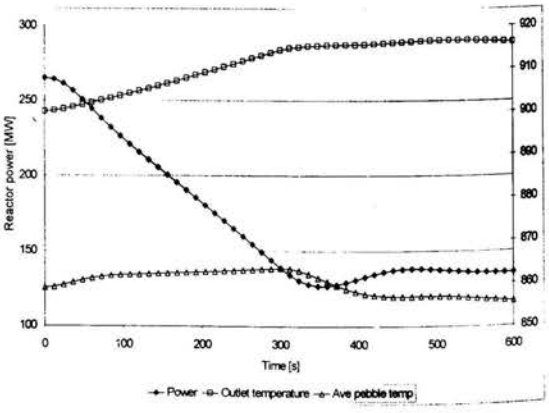

Figure 4: Results of mass flow transient simulation.

Sample calculation 3: Gas inlet temperature transient

The third sample calculation entails a ramp increase of the inlet gas temperature to 100 °C higher than the initial value over a time span of 600 seconds. Figure 5 shows the same phenomena as in Sample 2.

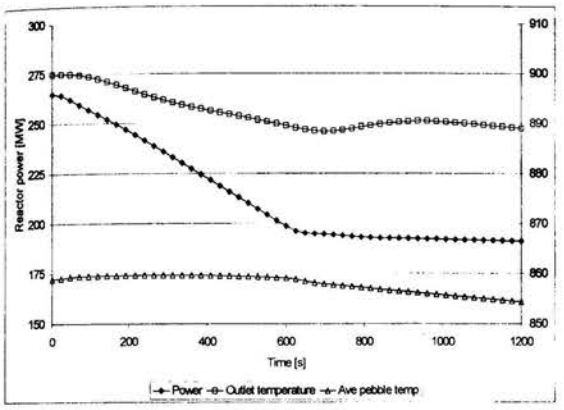

Figure 5: Results of gas inlet temperature transient.

Sample calculation 4: Simultaneous inlet temperature, pressure and mass flow transient

This sample entails a simultaneous ramp increase in the inlet gas temperature to 100 °C higher than the initial value, a ramp reduction in the inlet pressure by 45 bar and a ramp reduction in mass flow rate to 40 % of the initial value over a time span of 600 seconds.

Figure 6 shows the same phenomena as in Samples 2 and 3, including the Xenon effect.

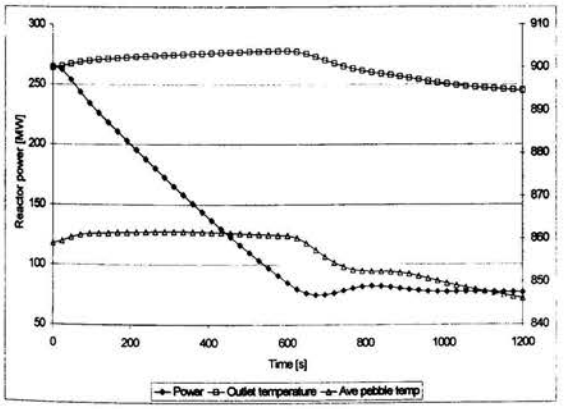

Figure 6: Results of simultaneous temperature, pressure and mass flow transient.

CONCLUSIONS

This paper described the integrated one-dimensional simulation model for the pebble bed nuclear reactor contained in Flownet. The simulation consists of three distinct models namely the point kinetics and decay heat generation model, the sphere heat conduction model and the fluid flow model. These three models are solved simultaneously at each time step to obtain the integrated transient response of the reactor.

Results obtained with the new model showed that grid independence is obtained with at least 10 layers in each representative fuel sphere and 20 layers along the height of the reactor. An adequate degree of time step independence is obtained for time step sizes smaller than 0.5 seconds.

Sample calculations have shown that the correct qualitative results are obtained. However, detailed comparative studies must still be undertaken with more comprehensive software models such as TINTE in order to properly quantify the accuracy of the results obtained with the new model.

ACKNOWLEDGMENTS

This work was carried out in association with M-Tech Industrial (Pty) Ltd. and funded by PBMR (Pty) Ltd.

REFERENCES

[1] Verkerk, E.C., 1998, "Coupling thermal hydraulics with neutronics for pebble-bed high temperature reactor calculations," IAEA Technical Committee Meeting on Safety Related Design and Economic Aspects of High Temperature Gas Cooled Reactors, Beijing, China, 2-4 November.

[2] Haverkate, B.R.W., Van Heek, A.I. & Kikstra, J.F., 1998, "An HTR cogeneration system for industrial applications," IAEA Technical Committee Meeting on Safety Related Design and Economic Aspects of High Temperature Gas Cooled Reactors, Beijing, China, 2-4 November.

[3] Glasstone, S. & Sesonske, A., 1981, "Nuclear reactor engineering," 3rd Ed., Van Nostrand Reinhold company, New York.

[4] Scherer, W., Rütten, H-J. and Haas, K.-A., 1997, "Feasibility study on PBMR-SA, Contributions to the simulation of the main Helium loop," German Working Group, April-September.

[5] Anderson, D.A., Tannehill, J.C. and Pletcher, R.H., 1984, "Computational fluid mechanics and heat transfer," McGraw-Hill, New York.

[6] Stoecker, W.F., 1989, "Design of thermal systems," McGraw-Hill, New York.

[7] Kugeler, K. and Schulten, R., 1989, "Hochtemperaturreaktortechnik," Springer-Verlag.

[8] Greyvenstein, G.P., 2001, "Pressure correction implicit method," International. Journal of Numerical Methods in Engineering, Accepted for publication.

HEFAT2002
1st International Conference on Heat Transfer, Fluid Mechanics, and Thermodynamics
8-10 April 2002, Kruger Park, South Africa
SD1

INVESTIGATION OF THE SULPHUR TRIOXIDE FORMATION AND REDUCTION IN THE HEAVY-OIL FIRED FURNACE

D.R. Schneider* and Z. Bogdan**
*Research Assistant; **Professor
Power Engineering Department
Faculty of Mechanical Engineering and Naval Architecture,
University of Zagreb,
I. Lucica 5, 10000 Zagreb,
Croatia
E-mail: Daniel.Schneider@fsb.hr, Zeljko.Bogdan@fsb.hr

ABSTRACT

In this paper formation of sulphur trioxide in the furnace of the steam generator was investigated. The mathematical model that could realistically describe SO_3 generation and reduction was developed. The model was applied on a real steam generator combustion chamber. Different combustion parameters were varied: the combustion air excess ratio, the magnitude of the swirl of combustion air, the fuel droplet size, and the fuel injection spray angle. The greatest influence on SO_3 reduction exhibited the air excess ratio. The problem of this particular case lied in fact that the air excess ratio could not be notably decreased due to incomplete combustion (increase of CO and H_2 appearance of the soot and unburned hydrocarbons above legal emission limits) that it would cause. It was shown that by applying the other measures (increasing magnitude of the swirl of combustion air, increasing fuel spray angle and finer spraying i.e. smaller fuel droplet size) simultaneously with the excess air ratio reduction this problem could be alleviated.

INTRODUCTION

Economic reasons impose use of heavy-oil fuel of lower quality, rich in sulphur, in combustors of steam generator furnaces. Combustion of such a fuel has, as a consequence, an increased SO_X emission. In combustion process, certain amount of SO_2 is transformed into SO_3. Sulphur trioxide reacts, at lower temperature, with water vapour forming sulphuric acid, which, on one hand impacts eco-systems and human health through acid aggregates, so called "acid rain" and, on the other hand, it causes low-temperature corrosion of the steam-generator sections [1,2].

In the past, number of authors examined formation of SO_3 [3-8]. Two main mechanisms were recognized: the homogenous SO_3 formation reactions in the gas phase and the heterogeneous catalytic reactions on the heat exchanger surfaces and ash particles. This paper focuses attention on formation and reduction of SO_3 in the furnace, where the homogenous gas-phase reactions are dominant. Many authors suggested variety of different SO_3 formation reaction sets [3-6]. The SO_3 reactions that showed the greatest importance at conditions (temperature and pressure) prevailing in the steam-generator furnaces were chosen.

The second part of the paper deals with the possible means for SO_3 reduction. There are several ways to fight low-temperature corrosion: combustion of low-sulphur fuels, use of fuel additives, implementation of acid-resistant materials for steam generator "cold-end" surfaces, regular maintenance of the steam-generator and control of the combustion process [1,2]. In this paper the last technique was investigated.

NOMENCLATURE

d	fuel droplet diameter (μm)
f	mixture fraction
k	reaction rate constant ($(cm^3/mol)^n \cdot s^{-1}$)
	$n = 1$ for bimolecular reactions
	2 for third body reactions
K_C	equilibrium constant ($(mol/m^3)^{\Delta m}$)
	Δm is sum difference of stoichiometric coefficients
M	molar mass (kg/kmol)
R	universal gas constant, R=1.987e-3 (kcal/mol·K)
S	swirl number
S_i	source term of species i ($kg/m^3 \cdot s$)
t	time (s)
T	flue gas temperature (K)
u	velocity (m/s)
x	spatial coordinate (m)
Y_i	mass fraction of species i (kg/kg)
$[i]$	concentration of species ($kmol/m^3$)

Greek Letters

σ	Schmidt-Prandtl number
λ	air excess ratio
ρ	density (kg/m^3)
Γ	diffusion coefficient (Pa·s)
μ	dynamic viscosity (Pa·s)
ϕ	fuel spray angle (°)

Subscripts

b	backward reaction
eff	effective
eq	equilibrium
f	forward reaction
F	fuel stream inlets
O	oxidiser stream inlets

MATHEMATICAL MODEL

Possible means for the SO_3 reduction during combustion process were investigated using mathematical modelling. The 3D mathematical model comprises coupled gas flow and liquid spray physics. It simulates combustion of the non-premixed turbulent flame by solving conservation equations for mass, momentum, energy and mixture fractions [9]. The turbulent flow is modelled by using the k-ε model with non-equilibrium wall functions. The radiation heat transfer is treated by the discrete ordinates radiation model. Formation of the pollutants, NO_X and soot, is also included into the model. The liquid fuel spray was simulated as a discrete second phase in a Lagrangian frame of reference (so called "particle in cell" model).

The combustion model is based on the probability density function (PDF) formulation [10]. The empirically prescribed PDF model was used (β-function) and value of the mixture fraction f was chosen as a conserved scalar

$$f = \frac{Y_i - Y_{iO}}{Y_{iF} - Y_{iO}} \qquad (1)$$

where Y_i represents elemental mass fraction of element i. Subscript O denotes value at the oxidiser stream inlet and subscript F denotes value at the fuel stream inlet. The PDF combustion model involves solution of the transport equations for the mixture fraction and its variance. Interaction of turbulence and chemistry was included in the model by the mixture fraction variance.

The reaction system was described by the equilibrium chemistry formulation [11], which implicates that the chemistry is fast enough to preserve chemical equilibrium at the molecular level. That assumption is valid for main reactions and species in the combustion process but it fails in the case of slow kinetics, like the SO_3 formation. For this reason, an additional model, which describes the sulphur trioxide generation and destruction more realistically, was developed. According to many authors [4-7] the predominant reaction of SO_3 formation is

$$SO_2 + O + M \leftrightarrow SO_3 + M \qquad (2)$$

The rate constant for this reaction [12,13] is given by

$$k_{2f} = 9.2 \cdot 10^{10} \exp\left(\frac{-1200.38}{RT}\right) \qquad (3)$$

and recommended values for the third body reactants [M]: of N_2 /1.3/, SO_2 /10.0/ and H_2O /10.0/. Reaction (2) is opposed by reaction (4), which acts to revert SO_3 back to SO_2

$$SO_3 + O \leftrightarrow SO_2 + O_2 \qquad (4)$$

and its reaction rate constant is

$$k_{4f} = 2 \cdot 10^{12} \exp\left(\frac{-10064.95}{RT}\right). \qquad (5)$$

Rates for the reverse reactions are obtained from the equilibrium constants for each reaction

$$k_{2b} = \frac{k_{2f}}{K_{C2}} \qquad (6)$$

$$k_{4b} = \frac{k_{4f}}{K_{C4}} \qquad (7)$$

The assumption made in this model is that sulphur trioxide could be examined independently of the complete reaction set, whereby all other molecular species are maintained at constant concentrations. This assumption is correct for low percentage conversion of SO_2 to SO_3 (lower than 10%) [6] as it is the case for typical combustion processes in furnaces.

The model was implemented as a User Defined Function routine in Fluent™ code [9]. The transport equation for SO_3 is written in the following form

$$\frac{\partial}{\partial x_j}\left(\rho u_j Y_{SO_3}\right) = \frac{\partial}{\partial x_j}\left(\Gamma_{SO_3} \frac{\partial Y_{SO_3}}{\partial x_j}\right) + S_{SO_3} \qquad (8)$$

where Γ_{SO_3} is diffusion coefficient of SO_3

$$\Gamma_{SO_3} = \frac{\mu_{eff}}{\sigma} \qquad (9)$$

and Schmidt-Prandtl number $\sigma = 0.7$.

The source term S_{SO_3} in equation (8) is defined as

$$S_{SO_3} = \frac{\partial}{\partial t}\left(\rho Y_{SO_3}\right) \qquad (10)$$

Relation between SO_3 mass fraction Y_{SO_3} and concentration $[SO_3]$ is given by

$$Y_{SO_3} = \frac{M_{SO_3}}{\rho}[SO_3] \qquad (11)$$

Finally, one gets

$$S_{SO_3} = M_{SO_3} \frac{\partial}{\partial t}[SO_3] \qquad (12)$$

where M_{SO_3} is molar mass of SO_3.

The rate of SO_3 change for the reactions (2) and (4) is

$$\frac{d[SO_3]}{dt} = k_{2f}[SO_2][O][M] + k_{4b}[SO_2][O_2] - \\ -k_{2b}[SO_3][M] - k_{4f}[SO_3][O] \qquad (13)$$

This expression, with the above assumption of reaction independency, is only temperature dependent.

RESULTS

Previously described model was applied to simulate the SO_3 formation in the furnace of a real steam generator of the 210 MW oil-fired Power Plant Sisak. PP Sisak, which burns heavy-oil fuel with 2-3% sulphur and exhibits flue gas temperatures of 135-140 °C at the exit of the regenerative Ljungström air-heater, reported occurrence of the severe low-temperature corrosion of the generator "cold-end" surfaces. There are two oil burners (Fig. 1) on each side-wall of the chamber. The burner consists of the axial/radial inflow type swirl generating register and the steam atomiser (Y-nozzle). The airflow is divided into three streams: unswirled primary stream and then secondary and tertiary streams, which are swirled.

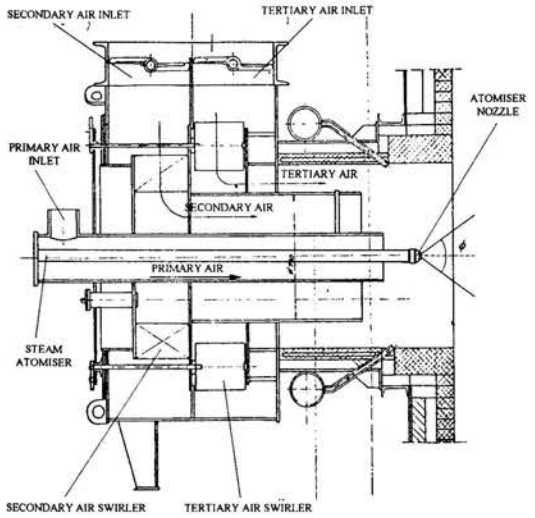

Fig. 1 Schematic of the burner

Influences of different combustion parameters were analysed: combustion air excess ratio, magnitude of the swirl of combustion air, fuel droplet size, and fuel injection spray angle.

Combustion air excess ratio

It is well known that the sulphur trioxide concentration could be decreased by the improvement of the combustion process, primarily by lowering the air excess ratio (Fig 2). The fact that sulphur trioxide depends on the combustion mode and the surplus of air, implies that SO_3 primarily arises in flame and that is in much lesser extent a consequence of the catalytic effect.

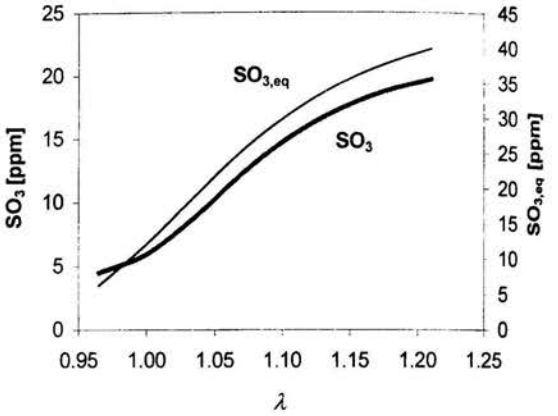

Fig. 2 SO_3 versus air excess ratio

By decreasing the air excess ratio λ from 1.210 to 0.965, the SO_3 production was also reduced. That could be explained by lower amount of oxygen that was at disposal for reactions (2) and (4). The upper curve $SO_{3,eq}$ (thinner line) on Fig. 2 represents values of equilibrium SO_3 mole fractions (in ppm's by volume) at the exit of the furnace . The lower curve SO_3 comprises non-equilibrium SO_3 mole fractions (this value too, as all other parameters presented in results section, relates to the exit cross-section of the furnace). Equilibrium SO_3 values were obtained by the equilibrium chemistry model while non-equilibrium values by the model presented in previous section (Eq's 2-13). At this point it is worth to note that non-equilibrium values are lower than equilibrium ones, which is also indicated by some authors [3,6].

On the other hand, the lack of oxygen led to incomplete combustion that resulted in higher CO and H_2 concentrations (Fig. 3).

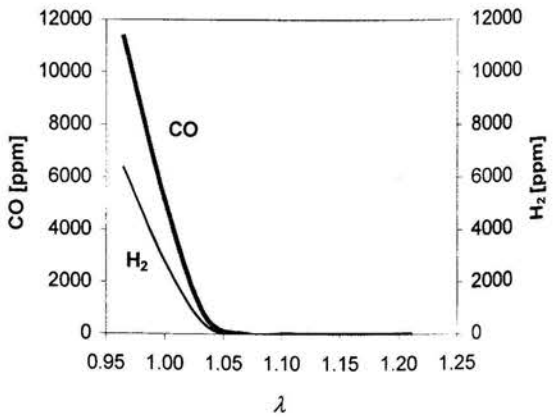

Fig. 3 CO and H_2 mole fractions

Fig. 4 shows predicted NO concentrations and flue gas temperatures at the exit of the furnace. Given values of NO should not be taken as absolute values, only trend of NO mole fraction should be considered.

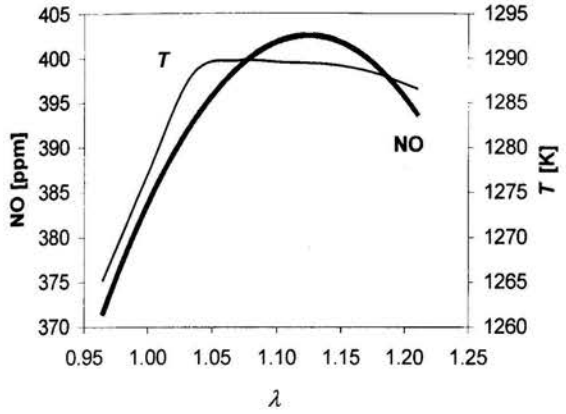

Fig. 4 NO mole fraction and temperature versus air excess ratio

The maximum value of temperature at cca. λ=1.05 corresponds to complete combustion. Values of soot concentrations are not presented in these graphs because all soot was completely burned in the furnace and did not appear at the chamber exit (except in two cases of incomplete combustion when excess air ratio was 0.965 and 1.000).

Swirl number

It was expected that an increase of the magnitude of the swirl number of the combustion air stream would decrease the SO_3 production due to better combustion.

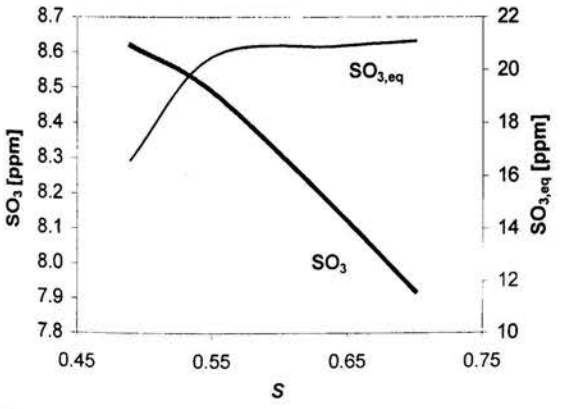

Fig. 5 SO_3 mole fraction versus swirl number S (swirl number is calculated at the exit of the burner, Fig. 1)

Results of equilibrium SO_3 production at the furnace exit showed no such a tendency (Fig. 5). It was observed that only region where the equilibrium presumption is valid is at high temperatures (flame zone near burner exit) where the relaxation time is very short (fast kinetics) but at (relatively) lower temperatures (e.g. below 1500°C) the relaxation time becomes longer and assumption of fast chemistry is not anymore correct. That justifies implementation of the (previously described) non-equilibrium model whose results are in accordance with predicted behaviour of SO_3 concentration (thicker line).

Negative slopes of CO and H_2 (Fig. 6) confirm improvement of the combustion process with an increase of the swirl number.

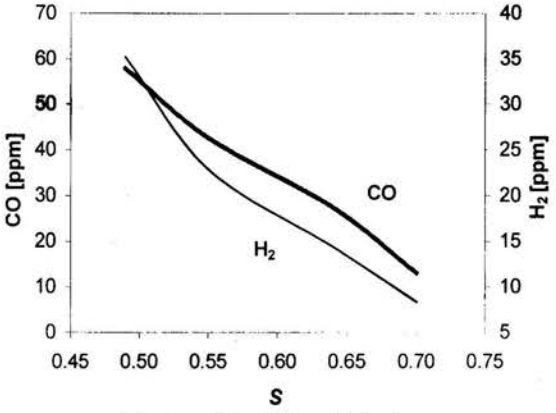

Fig. 6 CO and H_2 mole fractions

Higher swirl number causes better (and faster) mixing of fuel and combustion air that shortens the flame length. Shorter flame means higher temperatures in the flame zone and lower flue gas temperature at the exit of the furnace (Fig. 7).

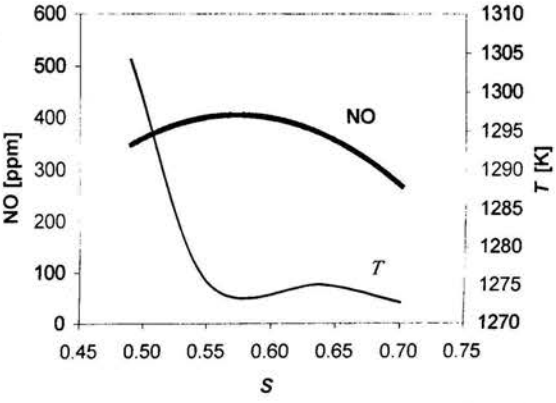

Fig. 7 NO mole fraction and temperature versus swirl number

Fuel droplet size

Diminution of fuel droplet size is usually achieved by raising fuel atomising steam pressure. By finer fuel spray, better combustion would be expected, what is indicated by the results plotted on Fig's 8, 9, and 10. In this case, fuel droplet initial diameter is varied in the range 50-160 μm. Smaller fuel droplets resulted in shorter combustion times, shorter flame length and caused higher combustion temperatures and lower flue gas exit temperatures.

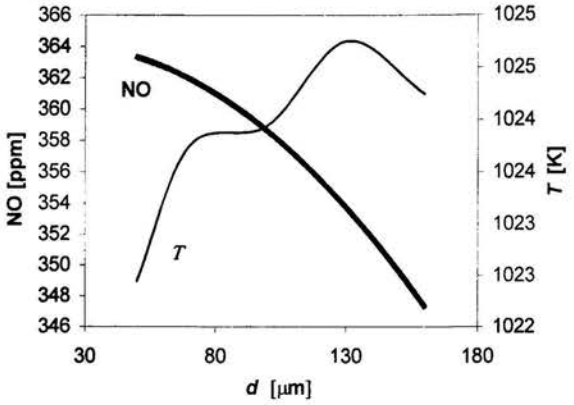

Fig. 8 NO mole fraction and temperature versus fuel droplet diameter

Unoxidised CO and H_2 were also lowered by decreased fuel droplet diameter (Fig. 9).

Higher combustion temperature leads to acceleration of kinetics of the process and consequently to shorter time that is available for reaction of sulphur trioxide formation (Eq. 2). That can be observed in Fig. 10 where (non-equilibrium) SO_3 mole fractions descend with decrease of fuel droplet size. Results of SO_3 equilibrium model are also shown, with pronounced unrealistic behaviour.

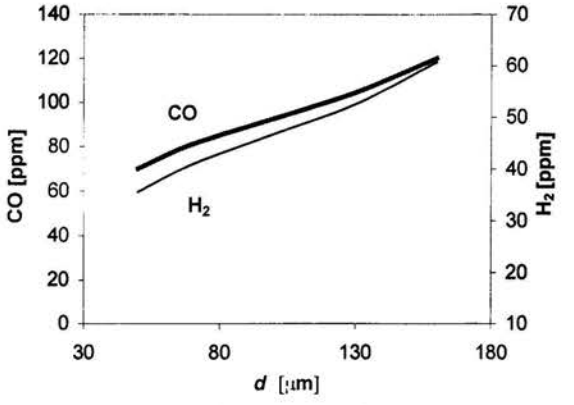

Fig. 9 CO and H_2 mole fractions

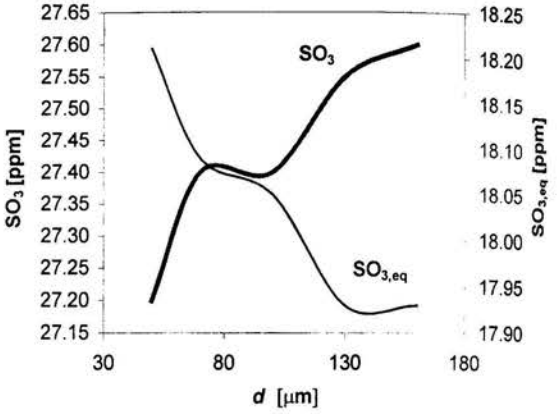

Fig. 10 SO_3 mole fraction versus fuel droplet diameter

Fuel spray angle

An increase of the fuel spray angle of steam atomiser Y-nozzle led to shorter flame length and, in global, to better combustion. For lower SO_3 production with increasing fuel spray angle (Fig. 11), again, higher combustion temperature (consequently lower flue gas temperature at exit, Fig. 12) was meritorious. Once more equilibrium chemistry assumption for the SO_3 production resulted in unphysical trends.

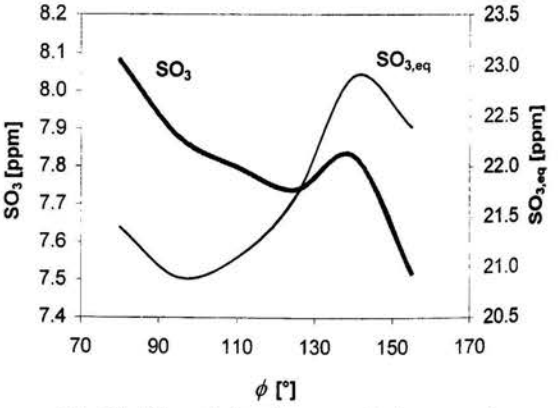

Fig. 11 SO_3 mole fraction versus fuel spray angle

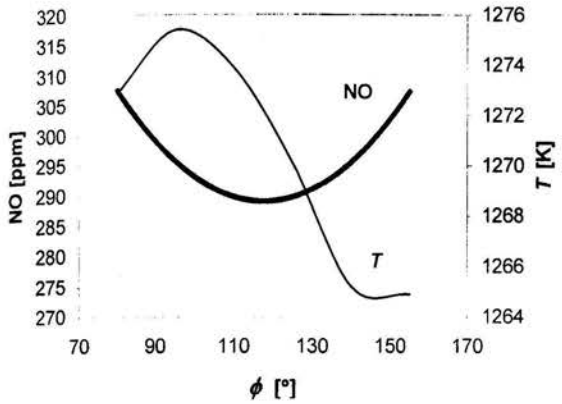

Fig. 12 NO mole fraction and temperature versus fuel spray angle

The curves of CO and H_2 mole fractions decrease with widening of the spray angle confirming the former observation of better combustion (Fig. 13).

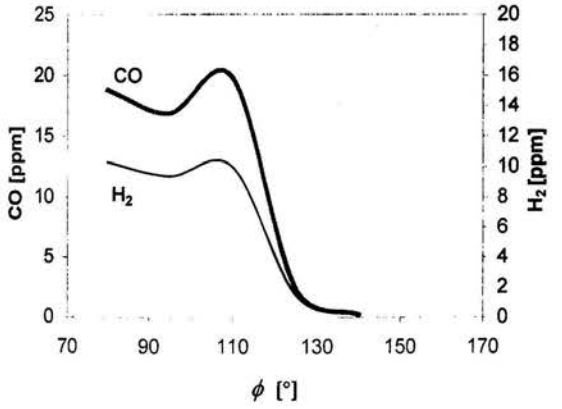

Fig. 13 CO and H_2 mole fractions

CONCLUSION

In order to investigate formation and reduction of sulphur trioxide in the furnace of the steam-generator, the non-equilibrium SO_3 model was developed. It was shown that is possible to realistically simulate SO_3 production and that such a model could be used in analysis of SO_3 reduction.

Different combustion parameters were varied: the combustion air excess ratio, the magnitude of the swirl of combustion air, the fuel droplet size, and the fuel injection spray angle. Decrease of the air excess ratio exhibited the greatest influence on SO_3 reduction. Still, results of simulation have shown that in the particular case the air excess ratio could not be notably decreased (<1.05) due to incomplete combustion (increase of CO, H_2, appearance of the soot and unburned hydrocarbons above legal emission limits).

Increase of magnitude of the swirl of combustion air, the fuel spray angle and finer spraying (smaller fuel droplet size) would decrease production of SO_3 in lesser extent than the air excess ratio, but they would improve combustion and reduce CO, H_2 and soot formation. The right strategy would be in combination of all these techniques.

REFERENCES

[1] Niepenberg, H.P., *Industrie-Ölfeuerungen*, Deutche Babcock & Wilcox, Oberhausen (1968)

[2] Niepenberg, H.P., Reidick, H., *Die Niedertemperaturkorrosion als Funktion der Schweröl verbrennung*, Das Ölfeuerjahrbuch, Deutche Babcock & Wilcox, Oberhausen (1962)

[3] Hedley, A.B., Factors affecting the formation of sulphur trioxide in flame gases, *Journal of the Institute of Fuel*, **40**, 142-151 (1967)

[4] Merryman, E.L., Levy, A., Sulfur trioxide flame chemistry-H_2S and COS flames, *13th Simposium (International) on Combustion*, The Combustion Institute, 427 (1971)

[5] Cullis, C.F., Mulcahy, M.F.R., The kinetics of combustion of gaseous sulphur compounds, *Combustion and Flame*, **18**, 225-292 (1972)

[6] Hunter, S.C., Formation of SO_3 in gas turbines, *Journal of Engineering for Power*, **104**, 44-51 (1982)

[7] Harris, B.W., Conversion of sulfur dioxide to sulfur trioxide in gas turbine exhaust, *Journal of Engineering for Gas Turbine and Power*, **112**, 585-589 (1990)

[8] de Blas, L.J.M., Pollutant formation and interaction in the combustion of heavy liquid fuels, PhD thesis, University College London, London (1998)

[9] *FLUENT 5 User's Guide* (1998), Fluent Incorporated, Lebanon, NH

[10] Kuo, K.K., *Principles of Combustion*, John Wiley & sons, New York (1986)

[11] Warnatz, J., *Combustion*, Springer-Verlag, Berlin (1996)

[12] Stull, D.R., Prophet, H., *JANAF Thermochemical Tables*, Office of Standard and Reference Data, NBS, Washington, D.C. (1971)

[13] Garvin, D., *Chemical Kinetics Data Survey IV*, NBSIR-203, National Bureau of Standards (1973)

HEFAT2002
1st International Conference on Heat Transfer, Fluid Mechanics and Thermodynamics
8-10 April 2002, Kruger Park, South Africa
SZ2

A DETAILED THREE-DIMENSIONAL THREE-FLUID NUMERICAL INVESTIGATION OF TWO-PHASE FLOW IN COMPLEX GEOMETRY BASED ON THE POROUS MEDIA CONCEPT: CRITICAL HEAT FLUX PREDICTIONS

Zoran V. Stosic[1] and Vladimir D. Stevanovic*[1]

Framatome ANP GmbH, Bunsenstr. 43, D-91058 Erlangen, Germany, Zoran.Stosic@Framatome-ANP.de

ABSTRACT

A new model for the three-dimensional numerical simulation and analyses of the thermal-hydraulic processes and the Critical Heat Flux (CHF) prediction for the advanced nuclear fuel rod bundles of the complex geometry is presented. It is based on the porous medium concept, three-fluid model of the coolant two-phase flow, proposed correlations for the interfacial drag momentum transfer and on mechanistic models for dry-out occurrence in churn and annular flow patterns. The nuclear fuel rod bundle thermal-hydraulics is analysed under the CHF conditions. Predicted CHFs are in good agreement with the measured data. Presented three-fluid modelling approach is an improvement of the recently developed multidimensional two-fluid porous medium model [1, 2]. Also, its ability to predict the spatial three-dimensional mass flux vectors of liquid and steam phases within the rod bundle is an advantage in comparison with the presently used methods for the nuclear fuel rods bundle thermal-hydraulics built into one-dimensional subchannel analysis computer codes.

INTRODUCTION

Thermal-hydraulic and neutron kinetic optimisation of nuclear fuel elements is being performed in order to increase the thermal margin and energy exploitation economy. Modern design of nuclear fuel rod bundles for Boiling Water Reactors (BWRs) is characterised with increased number of rods, part-length fuel rods and a water channel positioned along the bundle. Such design causes significant spatial differences of volumetric heat flux, steam void fraction distribution, mass flux rate and other thermal-hydraulic parameters important for efficient cooling of nuclear fuel rods during normal steady-state and transient conditions.

Classical subchannel analysis computer codes have deficiencies in predicting the two-phase coolant cross flows between neighbouring channels. Some of these codes allow subchannel coupling, but these calculation algorithm could be quite artificial in regard to the real liquid and steam cross-flows, especially for the rod bundle of the modern design with high spatial non-uniformity of geometric and thermal-hydraulic parameters. Also, present algorithms for steam-liquid exchange between neighbouring subchannels are not applicable in regions of one-phase subcooled liquid or steam flows. This shortcoming could cause higher uncertainties in CHF predictions [3]. Application of the three-dimensional Computational Fluid Dynamics (CFD) numerical methods, where the flow field is determined with the actual free passages between the fuel rods, requires great number of control volumes in order to simulate the whole rod bundle flow field, and consequently, substantial computer time. Practical benefits from these modelling improvements are not expected to equal increase in computer calculation time cost and modelling complexity. Therefore, the need for the prediction of spatial thermal-hydraulic steady-state and transient phenomena within the advanced nuclear fuel bundles, such as two-phase coolant cross flows between neighbouring channels, spatial void distributions, spatial dry-out propagation etc., as well as the requirement for the efficient computer tool which does not require substantial computational time and memory have led to the development of the multidimensional porous medium two-phase flow model. The previous work was based on the two-fluid modelling approach [1], and it was successfully applied to the prediction of advanced nuclear fuel rod bundle thermal-hydraulics under CHF conditions for different axial and radial power distributions, coolant flow rates and inlet

*Temporarily at Framatome ANP GmbH, P.O.Box 3220, D-91050 Erlangen, Germany
A.T.H.A. - Advanced Thermal Hydraulics with Applications. e-Mail: ATHA@Stosic.de , URL: http://www.Stosic.de

subcoolings [2]. In order to provide necessary closure laws for stated modelling approach, as well as to get more insight into the local two-phase phenomena within the bundle, several separate effects test were performed, such as regarding the hydraulic resistance to two-phase flow across rod bundle [4], or the influence of spacer geometry and position on coolant turbulent flow structure and relaxation lengths [5, 6, 7]. Obtained results of the CHF predictions with two-fluid approach [8] have shown the need for the consideration of the liquid film formation and depletion on the rod wall for the higher mass fluxes and steam voids with annular flow pattern formation, in order to improve the accuracy of the mechanistic dry-out model in the high void region. The criterion of the critical void fraction for the dry-out occurrence, introduced into the two-fluid modelling approach, is based on the pre-assumption of the minimum possible liquid film thickness and liquid phase split between the entrained droplets and liquid film flows. Its results showed strong dependence of the discrepancy between calculated and measured CHF values on the steam superficial velocity. This indicates the need for the inclusion of the droplets entrainment and deposition influence on the liquid film depletion and corresponding dry-out occurrence. Hence, the modelling approach is improved by the inclusion of the third fluid stream, which models liquid film flow along the rods' wall.

In presented numerical modelling approach, the fuel rod bundle is observed as a porous medium with a two-phase flow through it. The positions and dimensions of the fuel rods and spacers determine the porosity and flow resistance within the bundle. Evaluation of the coolant flow structure within the bundle requires the application of the multi-fluid modelling approach [9]. One-phase multidimensional coolant flow is modelled for the heating of subcooled coolant up to the saturated conditions. Two-fluid model is applied to the bubbly and churn-turbulent or slug flow, while three-fluid model is used for annular flow pattern. Three-fluid modelling approach is based on the mass, momentum and energy balance equations for three fluid streams: liquid film on the rod's wall, steam flow and droplets entrained in the steam stream. Closure laws for the prediction of interfacial transfer processes are stated with the special emphasis on the prediction of the steam-water interface drag force, through the interface drag coefficient, and droplets entrainment and deposition rates. The model implies non-equilibrium thermal and flow conditions. Mechanistic models of liquid film dry-out are applied for the CHF prediction. The criterion for the CHF occurrence in the churn two-phase flow pattern is the rod dry-out with the local steam void fraction value of 0.98. In annular flow pattern, a part of the water is carried by the steam flow in the form of entrained droplets, while the rest is flowing in the form of film on the rods' walls. Water film evaporation and droplets entrainment reduces the film flow rate. The criterion for the dry-out occurrence is the complete depletion of the liquid film, which is the result of the three-fluid model solution. The transition from churn to annular flow pattern is prescribed for local steam superficial velocity of 15 m/s [1, 2]. The steam and droplets governing equations are discretized in three-dimensional Cartesian co-ordinates, while the liquid film balance equations are solved along the rods' direction. The model is numerically solved with the control volume SIMPLE type method. Scalar control volumes (CVs) are centred to the fuel rods, while momentum CVs are staggered. Convective terms are approximated with up-wind finite differences. Fully implicit time integration is applied. Pressure correction method (proposed within the SIMPLE method) for the pressure field calculation is revised due to the presence of two phases. Difference equations are solved iteratively by the Alternating Direction Implicit (ADI) numerical method.

In this paper results of 3D numerical simulation and analyses of thermal-hydraulics in a complex geometry of nuclear reactor fuel assembly are presented for different axial and radial power shapes. Chopped cosine, top peak and bottom peak axial power generation profiles are applied. Numerical prediction of water and steam mass flux rates and steam void fraction distribution give a complete 3D thermal-hydraulic picture of steam-water flow within the bundle, including two-phase mixture cross-flows between neighbouring subchannels.

NOMENCLATURE

- A area (m^2)
- F force per unit volume (N/m^3)
- g gravity (m/s^2)
- h enthalpy (J/kg)
- $h^{"}$ enthalpy of saturated vapour (kJ/kg)
- j superficial velocity
- $\vec{k}$ unit vector in z-direction
- P tube/rod pitch
- p pressure (Pa)
- $\dot{q}'''$ volumetric heat flux (W/m^3)
- S perimeter (m)
- t time (s)
- u velocity (m/s)
- W entrainment/deposition rates (kg/m^2s)

Greek letters:

- α volume fraction
- Γ phase transition rate
- ρ density

Subscripts:

- e entrainment
- d deposition
- w wall
- 1 water
- 2 steam
- 3 liquid film
- 4 rods.

MODELLING APPROACH

Three-dimensional coolant liquid and vapour two-phase flow within the nuclear fuel rod bundle is modelled by the "three-fluid" model. Fluid flow conservation equations are written for both phases and three fluid streams. Mass, momentum and energy transfer at the vapour-liquid interfaces, as well as rod bundle hydraulic resistance to two-phase flow, heat transfer from hot rod walls and boiling within tube bundles are modelled by "closure laws". This approach implies non-equilibrium thermal and flow conditions.

Modelling Assumptions and Features

a) The porous medium concept is used in the simulation of two-phase flow within tube bundles. The space of the numerical control volume can be occupied by one, two or three fluid streams as well as by rods. The flow volume reduction due to the presence of rods in a space occupied by a bundle is taken into account. Therefore, the conservation of the vapour and liquid flow parameters is performed only for the fractions of the numerical control volume occupied by corresponding fluid stream.

b) Rod bundle flow resistance is assumed to be continuously distributed in the space occupied by these elements.

c) Flow governing equations are written in the non-viscous form, while the turbulent viscosity effects are taken into account indirectly through friction coefficients for the tube bundles flow resistance and two-phase interfacial drag forces.

d) The two-phase flow is observed as semi-compressible, that is the acoustic flow effects are neglected, while the influence of the pressure change on the vapour and liquid thermo-physical properties is taken into account.

e) The surface tension is neglected, as it is not important for bulk two-phase flow phenomena. Hence, pressure is the same for both phases and all fluid streams within the numerical control volume.

f) Multi-fluid modelling approach is applied as described in [9]. Heating entrance section of the rod bundle, up to the incipience of boiling, is model only by the one-fluid, one-phase mass, momentum and energy conservation equations. Subsequent bubbly, churn or slug flow patterns are modelled by the two-fluid model consisting of the conservation equations for the liquid and vapour phase. The annular flow pattern is reached when the void fraction is higher than 0.3 and the vapour superficial velocity exceeds the prescribed value of 15 m/s, and it is modelled by the three-fluid model written for liquid film on the rod's wall, entrained liquid droplets and vapour core. One-fluid and two-fluid models are derived from the three-fluid model by simple elimination of corresponding conservation equations and interfacial transfer terms from the three-fluid model equations.

g) Water phase flow in the form of liquid films on the rods' walls is one-dimensional, because it is directed along the vertically positioned rods in z-direction. Water droplets flow is three-dimensional. In prediction of liquid film surface interfacial shear stress and entrainment and deposition rates with appropriate closure laws, involved are phases' scalar parameters, liquid film velocity and vapour and droplets vertical (z-direction) component of velocity. At present no reliable laws are developed for the prediction of the influence of horizontal vapour and droplets velocity components on the entrainment, deposition and liquid film surface interfacial friction. On the other hand, these influences are believed to be small due to the predominant vertical direction of the two-phase flow especially in the high void and high velocity region of annular flow with entrained droplets.

Governing Equations

Liquid continuous phase or droplets mass conservation (the last term on the r.h.s. is included in case of droplets flow)

$$\frac{\partial(\alpha_1\rho_1)}{\partial t}+\nabla\cdot(\alpha_1\rho_1 u_1)=-\Gamma_{12}+\Gamma_{21}-S/A(W_d-W_c) \quad (1)$$

Vapour mass conservation

$$\frac{\partial(\alpha_2\rho_2)}{\partial t}+\nabla\cdot(\alpha_2\rho_2 u_2)=\Gamma_{12}-\Gamma_{21}+\Gamma_{32}-\Gamma_{23} \quad (2)$$

Liquid film mass conservation

$$\frac{\partial(\alpha_3\rho_3)}{\partial t}+\frac{\partial(\alpha_3\rho_{31}u_3)}{\partial z}=-\Gamma_{32}+\Gamma_{23}+S/A(W_d-W_c) \quad (3)$$

Liquid continuous phase or droplets momentum conservation (the last term on the r.h.s. is included in case of droplets flow)

$$\frac{\partial(\alpha_1\rho_1 u_1)}{\partial t}+\nabla\cdot(\alpha_1\rho_1 u_1 u_1)=-\alpha_1\nabla p+\alpha_1\rho_1 g-\dot{F}_{L2}+\dot{F}_{VM}+\dot{F}_{21}-\dot{F}_{41}-\Gamma_{12}u_1+\Gamma_{21}u_2-\frac{S}{A}(W_d u_{1Z}\bar{k}-W_c u_3) \quad (4)$$

Vapour momentum conservation

$$\frac{\partial(\alpha_2\rho_2 u_2)}{\partial t}+\nabla\cdot(\alpha_2\rho_2 u_2 u_2)=-\alpha_2\nabla p+\alpha_2\rho_2\vec{g}+\vec{F}_{L2}-\vec{F}_{VM}-\vec{F}_{21}-\vec{F}_{23}-\vec{F}_{42}+\Gamma_{12}u_1-\Gamma_{21}u_2+\Gamma_{32}u_3-\Gamma_{23}u_2 \quad (5)$$

Liquid film momentum conservation

$$\frac{\partial(\alpha_3\rho_3 u_3)}{\partial t}+\nabla\cdot(\alpha_3\rho_3 u_3 u_3)=-\alpha_3\nabla p+\alpha_3\rho_3 g-\dot{F}_{23}-\dot{F}_{43}-\Gamma_{32}u_3+\Gamma_{23}u_2+\frac{S}{A}(W_d u_{1,Z}\vec{k}-W_e u_3) \quad (6)$$

Liqud continuous phase or droplets energy conservation (the last term on the r.h.s. is included in case of droplets flow)

$$\frac{\partial(\alpha_1\rho_1 h_1)}{\partial t}+\nabla\cdot(\alpha_1\rho_1 h_1 u_1)=-(\Gamma_{12}-\Gamma_{21})h^{"}+\dot{q}^{"}_{41}-\frac{S}{A}(W_d h_1-W_e h_3) \quad (7)$$

Vapour energy conservation

$$\frac{\partial(\alpha_2\rho_2 h_2)}{\partial t}+\nabla\cdot(\alpha_2\rho_2 h_2 u_2)=(\Gamma_{32}-\Gamma_{23})h^{"}+(\Gamma_{12}-\Gamma_{21})h^{"} \quad (8)$$

Liquid film energy conservation

$$\frac{\partial(\alpha_3\rho_3 h_3)}{\partial t}+\nabla\cdot(\alpha_3\rho_3 h_3 u_3)=-(\Gamma_{32}-\Gamma_{23})h^{"}+\dot{q}^{"}_{43}+\frac{S}{A}(W_d h_1-W_e h_3) \quad (9)$$

The source terms for mass, momentum and thermal energy conservation are written on the r.h.s. of Eqs. (1) – (9). The intensity of phase transition, which is the mass of evaporation or condensation per unit volume and time, is denoted with Γ. The interfacial drag forces per unit volume are denoted with $\vec{F}_{21}$ for vapour and continuous liquid or droplets drag, and $\vec{F}_{23}$ for vapour and liquid film drag. Wall-vapour friction force is $\vec{F}_{42}$, wall-continuous liquid or droplets $\vec{F}_{41}$, and wall-liquid film $\vec{F}_{43}$. Terms $\vec{F}_{L2}$ and $\vec{F}_{VM}$ represent lift force and virtual mass force, respectively. The term $\dot{q}_{4k}$ represents volumetric heat rate from rods to corresponding fluid phase per unit volume.

Closure Laws

The necessary closure laws for the calculation of these terms are presented in [1, 10]. The deposition rate is calculated with the correlation for the deposition coefficient in steam-water two-phase flow from [11]. Entrainment rate is predicted with correlation from [12]. The volume balance is added to the above equations

Volume fraction balance

$$\alpha_1+\alpha_2+\alpha_3+\alpha_1=1\ . \quad (10)$$

Dry-out Criteria

The dry-out criteria for churn-turbulent two-phase flow, which is assumed to prevail for voids higher than 0.3 and steam superficial velocities lower than 15 m/s [1, 2], is the condition under which the steam void fraction reaches the value of 0.98 [8].

For annular flow, it is adopted that the dry-out occurs when the complete liquid film depletion happens. The complete film disappearance is triggered at the minimum possible film thickness, which is determined by the complex effects of annular flow conditions, such as droplets entrainment and deposition, hydrodynamic stability of liquid film surface waves, bubble nucleation and bursting on the wall surface etc. For adiabatic water-air atmospheric flow within experimental rod bundle, the minimum liquid film thickness was predicted to be 100 microns [14]. The films on the heated walls should be of the smaller minimum thickness. In [15] experimentally and theoretically predicted results on minimum film thickness under saturated pool boiling conditions are reported to be in the range from 2 to 10 microns. Numerical results on stable minimum film thickness, but not close to the dry-out conditions, are reported to be as low as 35 microns [16]. These previous results show that the minimum possible film thickness, prior to the dry-out triggering are in the range of 10 microns. Therefore, in this paper, the minimum possible film thickness at the onset of dry-out is assumed to be equal or less than 10 microns. The same range of values was successfully applied and verified in the one-dimensional multi-fluid predictions of CHFs for boiling tubes [9].

NUMERICAL SOLUTION

A finite volume method is applied for the solution of governing partial differential equations. The discretization of these partial differential equations is carried out by their integration over rectangular control volumes of variable size in the 3D Cartesian coordinate system. The conservation

equations for liquid and steam mass and enthalpy are integrated over the scalar control volumes, while the liquid and vapour momentum conservation equations are integrated over the staggered control volumes. The convective terms at the control volume boundaries are determined with the upwind numerical scheme. Fully implicit time integration is applied. Numerical schemes have been developed for the calculation of the void fractions and pressure fields. Liquid and steam mass conservation equations are discretized with the finite differences. The pressure field is calculated according to the modified SIMPLE numerical method [13], taking into account the presence of two phases - liquid and vapour. The resulting set of discretized equations is solved iteratively by the Alternating Direction Implicit (ADI) method. For the calculation of a steady-state condition, the transient calculation procedure is performed with constant boundary conditions.

RESULTS AND DISCUSSIONS

Results of 3D numerical simulation and analyses of thermal-hydraulics in a complex geometry of ATRIUM™-10 fuel assembly (Fig. 1) are presented for different axial and radial power shapes (Figs. 2 and 3). Chopped cosine, top peak and bottom peak axial power generation shapes are applied (Fig. 3). Numerical prediction of water and steam mass flux rates and steam void fraction distribution give a complete 3D thermal-hydraulic picture of steam-water flow within the bundle, including two-phase mixture cross-flows between neighbouring subchannels. The rod dry-out conditions are predicted for more than 100 cases.

Typical results of steam void fraction predictions within the rod bundle at the condition of Critical Power (CP) are presented in Fig. 4-a. The influence of spacers is clearly seen. Void fractions are higher in front of the spacers, while at the spacers and downstream the void fraction decreases. According to the temperature measurements, the rod numbered 87 first experienced the dry-out. Numerical simulations also show that the dry-out occurs at the same rod No. 87, Fig. 4-b. Zooming the attention at the rod 87 it could be seen that the dry patch formation is initiated on the side towards the rod No. 77, as presented in Fig. 5.

The obtained results are compared with experimental data measured at an electrically heated test rod bundle. For the annular flow regime the results of previous two-fluid model approach [8] are compared with experimental data in Fig. 6. Symbols in Fig. 6 for annular flow regime (j_2 >15 m/s), in the range from 0.93 to 1.27, are obtained with the two-fluid model, which is only composed of steam and water fluid streams, without a distinction between liquid film and droplets flows. These results show that the two-fluid model is not able to take into account the influence of the steam velocity on the intensity of droplets entrainment from the water film surface. The increase of the steam superficial velocity leads to more intensive droplets entrainment and liquid film depletion.

This process is taken into account by the present developed three-fluid model for local steam superficial velocity greater than 15 m/s, which corresponds to the onset of annular flow regime. The comparison of calculated and measured CHFs as well as the position of first Dryout within the bundle applying three-fluid model is shown in Fig. 7 with the range of error from 0.96 to 1.08.

The effect of coolant bundle inlet subcooling is modelled with excellent agreement. From Fig. 7 it is obvious that obtained disagreements appear to be a function of bundle inlet mass flow rate, similar to the case of two-fluid model [8]. Analyses have shown that this function reflects the influence of the local vapour velocity on the occurrence of Dryout. This is illustrated for both two-fluid and three-fluid models in Fig. 8 where the comparisons of results of the CP values in annular flow regime are shown as a function of vapour superficial velocity at location of maximum void fraction. The criteria used for critical liquid film thickness can be slightly improved with linear function of vapour local superficial velocity, presented also in Fig. 8. In this way corrected liquid film dry-out criteria provide agreements of calculated to measured CP values in the range from about – 2% to +4%. The mean of response (calculated to measured CP) variable is 1.0061 and estimated standard deviation of the model error equals to 0.0139. Compared to same values of two-fluid model (Fig. 8) this is significant improvement.

Finally, it has to be mentioned that higher disagreements of three-fluid model results and measured data shown in Fig. 8 for high bundle inlet mass flow rates could also be attributed to either hydrodynamic instability of the liquid film or to high relative steam velocity causing scrubbing out the liquid film from the heated surface. This practically means some kind of hydrodynamically caused dry patch rather than thermally induced. Both effects have not been currently taken into account but their influences on the CHF occurrence as well as the coupled effect of drag forces could be very important and are being analysed. Obtained results will be presented in near future.

CONCLUSION

A three-fluid model based on the porous media concept, suitable for the multidimensional simulation and analyses of nuclear fuel rod bundle thermal-hydraulics, is presented. Developed model is successfully applied to the simulation and analyses of the advanced nuclear fuel rod bundle thermal-hydraulics and to the CHF prediction. Proposed mechanistic models for dry-out occurrence are able to reliably predict CHF values for both churn and annular flow conditions. Improving mean value from 1.0889 (two-fluid model) to 1.0061 and reducing standard deviation from 0.0867 (two-fluid model) to 0.0139 successfully demonstrate the advantage of implementing third fluid stream in annular flow regime. Different radial and axial power distributions were used for three-fluid model verification with wide range of inlet mass flow rates (2 – 19 kg/s) and coolant inlet

subcoolings (25 – 185 kJ/kg) at the coolant pressure equal to 6.9 MPa.

Here presented multidimensional numerical method is an advantage in regard to the presently commonly used subchannel analyses methods for the nuclear fuel thermal-hydraulics. Subchannel analyses methods predict mass, momentum and energy exchange between neighbouring subchannels from single-phase mixing parameters and with more or less empirical correlations for two-phase flow multipliers. This could be very crude approximation in regard to the fully multidimensional three-fluid two-phase flow method presented in this paper.

REFERENCES

1. Stosic, Z. and Stevanovic, V., 2001, *An Advanced Numerical Method for Transient Multidimensional Two-Phase Flow Thermal-Hydraulics in Complex Geometry with Rod or Tube Bundles*, International Symposium on Advanced in Computational Heat Transfer, May 20-25, Palm Cove, Queensland, Australia.
2. Stosic, Z. and Stevanovic, V., 2001, *A Three-Dimensional Numerical Investigation of Two-Phase Flow Thermal-Hydraulics within Advanced Nuclear Fuel Rod Bundles, International Symposium on Advanced in Computational Heat Transfer*, May 20-25, Palm Cove, Queensland, Australia.
3. Stosic, Z., 1999, *Study on Thermal Performance and Margins of BWR Fuel Elements*, 7th Int. Conf. On Nuclear Engineering, April 19-23, Tokyo, Japan.
4. Stosic, Z. and Stevanovic, V., 2001, *Numerical Prediction of Void Fraction and Drift Velocity in Two-Phase Flow across Horizontal Tube Bundles, International Symposium on Advanced in Computational Heat Transfer*, May 20-25, Palm Cove, Queensland, Australia.
5. Stosic, Z. and Stevanovic, V., 2001, *A Numerical Approach to the Simulation of One-Phase and Two-Phase Reactor Coolant Flow around Nuclear Fuel Spacers*, 9th International Conference on Nuclear Engineering - ICONE 9, April 8-12, Nice, France.
6. Stosic, Z. and Stevanovic, V., 2001, *Analytical Investigation of the Influence of Spacer Geometry and Position on Turbulent Flow Structure and Parameters*, 9th International Conference on Nuclear Engineering - ICONE 9, April 8-12, Nice, France.
7. Stosic, Z. and Stevanovic, V., 2001, *Prediction of Thermal and Hydraulic Relaxation Length Behind Obstacle in Two-Phase Turbulent Coolant Flow*, 39th European Two-Phase Flow Group Meeting, June 17-20, Aveiro, Portugal.
8. Stosic, Z., Stevanovic, V. and Iguchi, T., 2001, *Three-Dimensional Porous Media based numerical Investigation of Spatial Power Distribution Effect on Advanced Nuclear Fuel Rod Bundles Critical Power*, 2nd International Conference on Computational Heat and Mass Transfer, October 22-26, Rio de Janeiro, Brazil.
9. Stosic, Z. and Stevanovic, V., 2001, *Schematisation of the Multi-Fluid Approach and Its Application to the CHF Prediction*, 4th International Conference on Multiphase Flow, May 27-June 1, New Orleans, Louisiana, USA.
10. Stevanovic, V. et al., 1995, *A Simple Model for Vertical Annular and Horizontal Stratified two-phase flows with liquid entrainment and phase transitions: one-dimensional steady state conditions*, Nuclear Engineering and Design, Vol. 154, pp. 357-379.
11. Saito, T., Hughes, E. D. and Carbon, M. W., 1978, *Multi-fluid Modelling of Annular Two-Phase Flow*, Nuclear Engineering and Design, Vol. 50, pp. 225-271.
12. Sugawara, S., 1988, *Droplet Deposition and Entrainment Modelling Based on the Three-Fluid Model*, Third International Topical Meeting on Nuclear Power Plant Thermal Hydraulics and Operation, Seoul, Korea, pp. A1-19-28.
13. Patankar, S., 1980, *Numerical Heat Transfer and Fluid Flow*, Hemisphere Publ. Co.
14. Noriyasu, K., Kumagai, K., Tsuji, Y., Kunugi, T., Serizawa, A., 2001, *Multi-dimensional Characteristics of Surface Waves on the Liquid Film Flow in a 3x3 Rod Bundle*, 4th International Conference on Multiphase Flow, May 27-June 1, New Orleans, Louisiana, USA.
15. Serizawa, A., 1983, *Theoretical Prediction of Maximum Heat Flux in Power Transients*, Int. J. Heat Mass Transfer, Vol. 26, No. 6, pp. 921-932.
16. Antal, S. P., Nagrath, S., Podowski, M. Z., 2001, *Multidimensional Simulations of Two-Phase Flows in Large Volumes with Injection Spargers*, 4th International Conference on Multiphase Flow, May 27-June 1, New Orleans, Louisiana, USA.

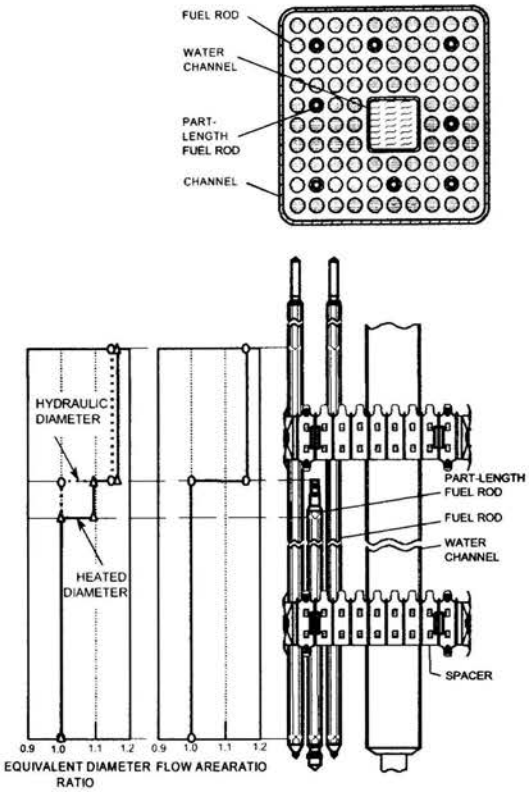

Fig. 1. ATRIUM™-10 Fuel Assembly and Axial Geometry Parameters as a Consequence of Part Length Fuel Rods

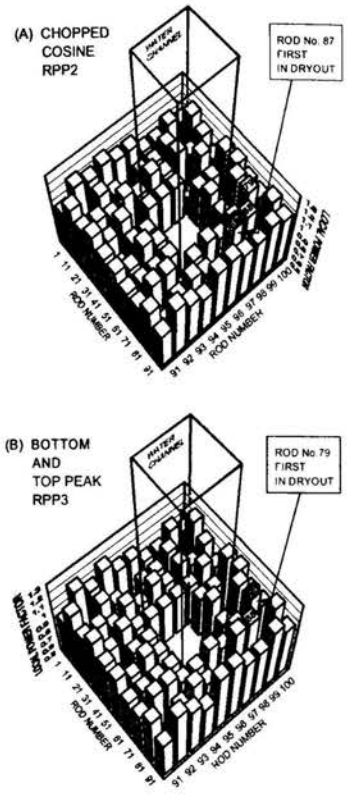

Fig. 2. Different Radial Peaking Pattern (RPP) of Test Bundle used for Model Verification

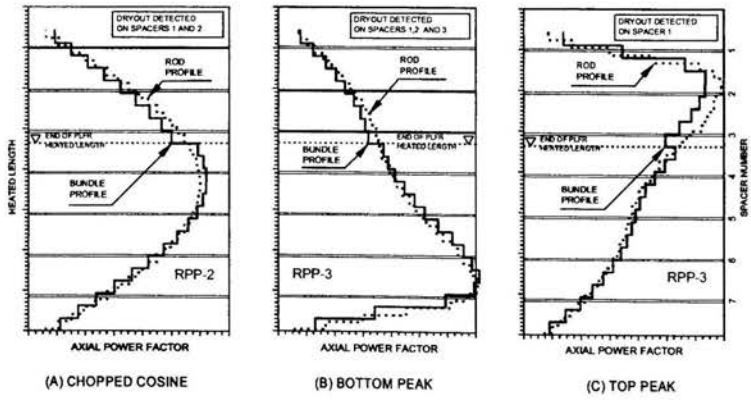

Fig. 3. Different Axial Peaking Pattern (APP) of Test Bundle used for Model Verification

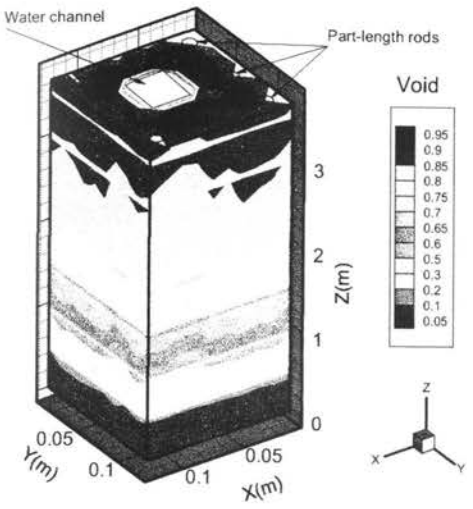

Fig. 4-a. Steam Void Fraction Distribution within the Test Bundle under the Dry-out Condition (Mass Flow Rate 16 kg/s, Inlet Subcooling 35.5 kJ/kg

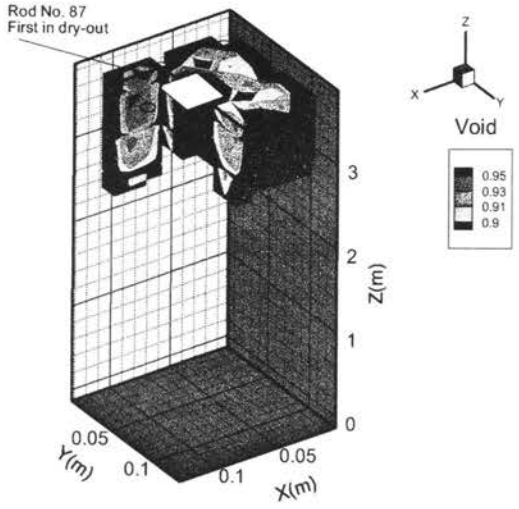

Fig. 4-b. Steam Void Fraction exceeds the Value leading to Dry-out at the Rod No. 87 (Mass Flow Rate 16 kg/s, Inlet Subcooling 35.5 kJ/kg)

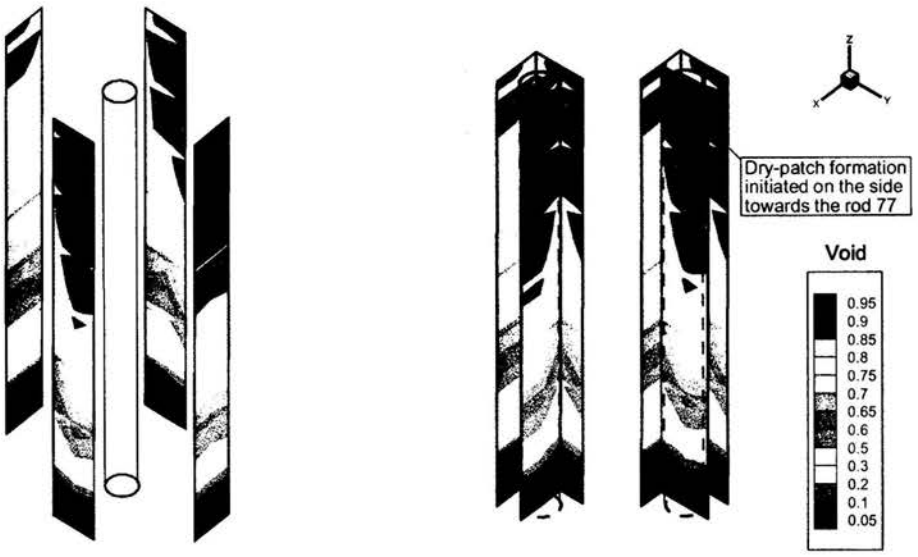

Fig. 5. Steam Void Fraction Distribution around Rod 87 which experienced Dry-out (left), and within Control Volumes that comprise Rod 87 (right). Test Bundle under the Dry-out Condition (Mass Flow Rate 16 kg/s, Inlet Subcooling 35.5 kJ/kg, Chopped Cosine Power Generation Profile)

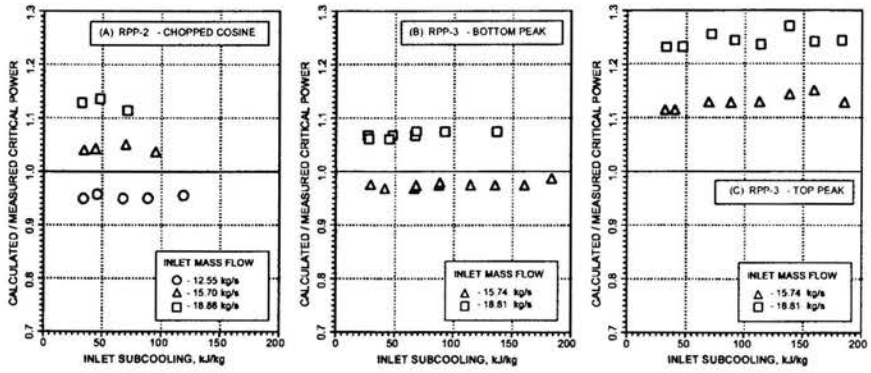

Fig. 6. 2-Fluids Model Results: Calculated to Measured Critical Bundle Power for Test Bundles with different Spatial Power Shapes

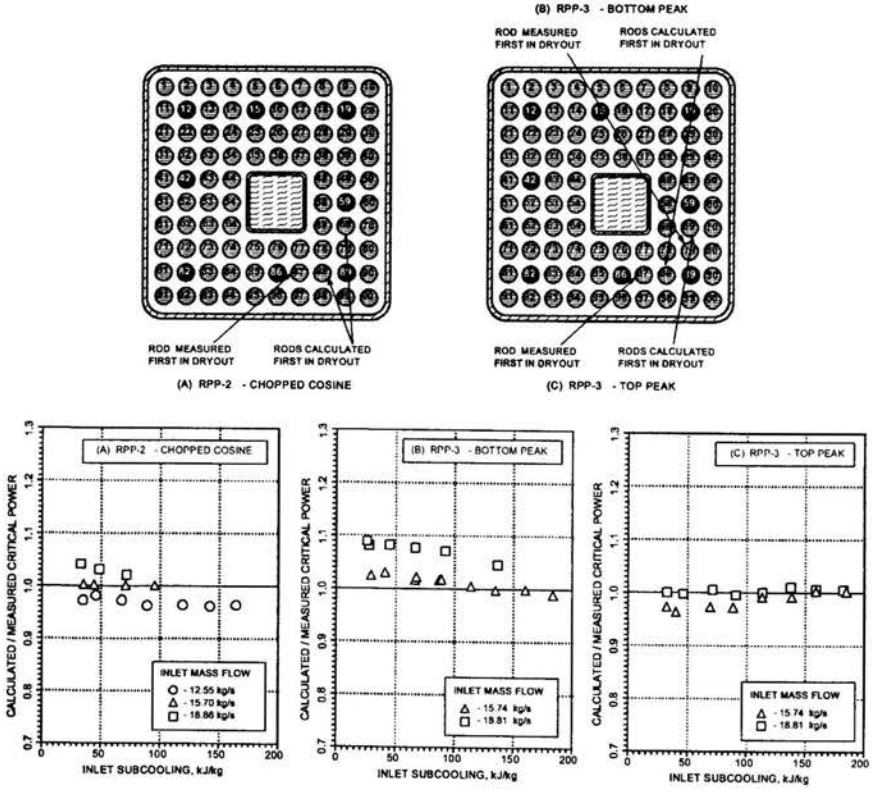

Fig. 7. 3-Fluids Model Results: Measured and Calculated Rods detecting first Dryout and Calculated to Measured Critical Bundle Power for Test Bundles with different Spatial Power Shapes

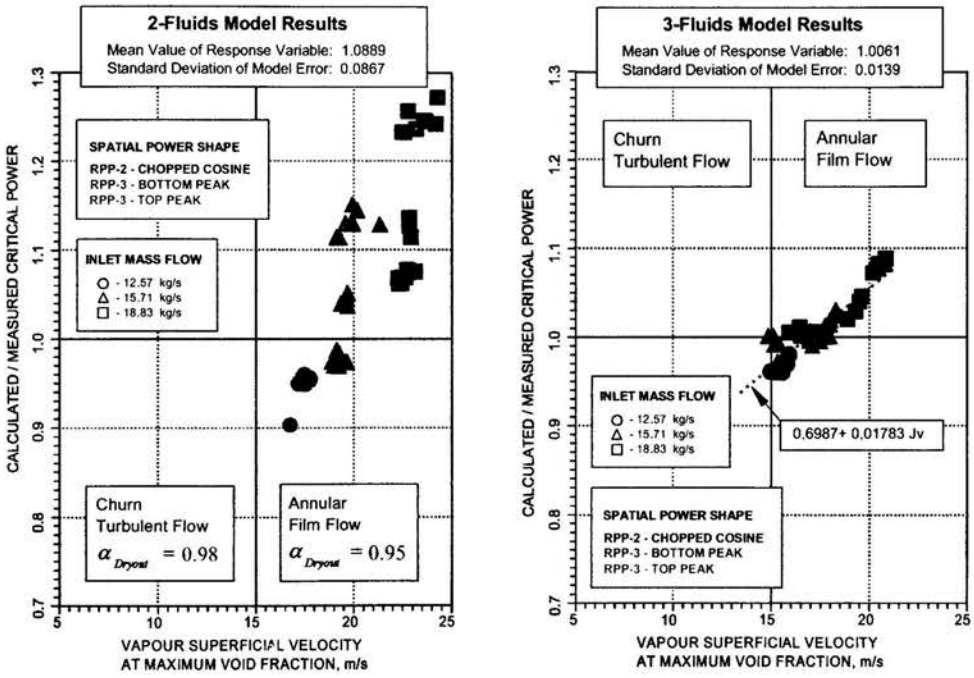

Fig. 8. 2-Fluid (left) and 3-Fluid (right) Model Calculated to Measured Critical Bundle Power for different Spatial Power Shapes

HEFAT2002
1st International Conference on Heat Transfer, Fluid Mechanics and Thermodynamics
8-10 April 2002, Kruger Park, South Africa
VG1

EXERGO-ECONOMIC ANALYSIS OF HEAT STORAGE SYSTEMS WITH PHASE CHANGING MATERIALS

G. Van den Branden*, W. D'haeseleer**
* Assistant, ** Professor
Division of Applied Mechanics and Energy Conversion
University of Leuven (K.U.Leuven)
Celestijnenlaan 300A
B-3001 Leuven, Belgium
william.dhaeseleer@mech.kuleuven.ac.be

ABSTRACT

This study evaluates the performance of large heat storage systems for power plants with a discontinuous power source such as nuclear fusion power plants. Emphasis is laid on the study of heat storage systems using latent heat storage, i.e., employing phase changing materials.

This evaluation is performed both from a thermodynamic point of view, inquiring whether the irreversibility of the system stays limited or not, and from an economic point of view, examining whether the system makes proper use of the heat storage capacity content present. It is shown that the operating conditions and the configuration of the phase changing material play an important role.

INTRODUCTION

When heat supply and heat demand are out of phase, a Heat Storage System (HSS) can provide a solution. In Van den Branden et al. (1999) the use of HSSs with a Phase Changing Material (PCM) has been studied for large HSSs.

HSSs with PCMs have also been studied by several authors: Adebiyi (1991, 1996), Aceves-Saborio (1994), Lim (1992) and Bejan (1998). Although they study the first and second law efficiencies in detail, they, unfortunately, do not investigate quantitatively whether the HSS makes efficient use of its heat capacity content; this is an important criterion, though, for the feasibility of large HSSs, as is shown is section 1.

Therefore, in contrast to previous studies, Van den Branden (1999) not only studied the second law efficiency but also the exergy capacity efficiency (for a definition see section 1) and found that HSSs with multiple PCMs were the best solution for large HSSs. This paper studies some typical parameters linked to the use of PCMs in HSSs.

NOMENCLATURE

c	heat capacity of the HSM (J/kg_K)
$\bar{c}_m$	$\Delta u_m/\Delta T$ average heat capacity of the HSM (J/kg_K)
$c_{m/f}$	$(\rho_m S_m c_m)/(\rho_f S_f c_{p,f})$ heat capacity ratio (-)
$c_{p,f}$	heat capacity at constant pressure of the fluid (J/kg_K)
h	heat transfer coefficient (W/m^2_K)
L	length of the HSS (m)
$\dot{m}$	mass flow (kg/s)
NTU	$(hPL)/(\dot{m}_f c_{p,f})$ number of transfer units (-)
P	heated perimeter (m)
T	temperature (K)
t	time (s)
S	cross-sectional area (m^2)
u_m	internal energy of the heat storage material (J/kg)
x	axial co-ordinate (m)

Greek Symbols

β_m	$\lambda_m/\Delta u_m$ latent heat fraction (-)
ΔT	$T_r - T_0$ maximum temperature difference (K)
Δu_m	$u_m(Tr) - u_m(T_0)$ maximum internal energy difference (J)
λ_m	latent heat (J/kg)
φ_m	$(u_m - u_{m,0}) / \Delta u_m$ dimensionless internal energy of the heat storage material (-)
θ	$(T-T_0)/\Delta T$ dimensionless temperature (-)
ρ	density (kg/m^3)
σ	$\Delta T / T_0$ temperature ratio (-)
η_2	second law efficiency (-)
η_C	exergy capacity efficiency (-)
τ	$t\dot{m}_f/(\rho_f S_f L)$ dimensionless time (-)
ζ	x/L dimensionless axial co-ordinate (-)

Subscripts

0	reference state
c	cold fluid coming from HSS
ch	charging
dis	discharging
f	fluid
h	hot fluid coming from HSS
m	heat storage material
r	hot fluid coming from reactor

Superscripts

L	liquid state
S	solid state

1 COST OF HEAT STORAGE

The total annual cost C_{an} (€/year) of a HSS that can store a net total amount of exergy A (J/year) consists of two contributions, the primary energy cost and the investment cost (Ter-Gazarian, 1994, Moran, 1989).

$$C_{an} = c_a A_{in} + c_M M_{HSS} \quad (1)$$

with c_a (€/J) the cost per unit exergy delivered by the heat source to the HSS, A_{in} (J/year) the yearly amount of exergy delivered by the heat source to the HSS, c_M (€/kg-year) the annualised investment cost per unit mass of the HSS installed and M_{HSS} the total installed mass of the HSS. The exergy A_{in} and the mass M_{HSS} of the HSS can be expressed as:

$$A_{in} = A/\eta_2 \quad (2)$$

$$M_{HSS} = A/(n_{an}\eta_C \Delta u_m) \quad (3)$$

with η_2 the second law efficiency of the HSS, n_{an} the number of cycles of the HSS per year, Δu_m the specific internal energy interval of the heat storage material in the temperature interval under consideration and finally, η_C the exergy capacity efficiency of the HSS. With this definition, η_C is the amount of exergy delivered by the HSS per cycle per unit heat capacity content of the HSS. Because n_{an} and A depend upon the application, the two remaining parameters that determine the cost of a particular HSS are η_2 and η_C. Consequently, these will be the two criteria studied for each HSS.

2 SYSTEM LAYOUT AND OPERATING CONDITIONS

The HSS studied operates in a cyclic steady-state mode. The HSS is consecutively charged and discharged. While charging, hot fluid is fed to the HSS at the hot side at a constant temperature T_r and a constant mass flow rate $\dot{m}_{ch}$ (see Figure 1). After it has deposited part of its energy content to the HSS, the fluid leaves the HSS at the cold side at a temperature T_c. The residual energy present in the exit fluid is regarded as waste, since it does not represent a contribution to the heat storage. In integrated systems, though, this heat could be used for other purposes.

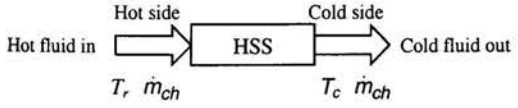

Figure 1: Heat storage system during charging

While discharging, the fluid flow through the HSS flows in the opposite direction and cold fluid is now fed to the HSS at the cold side at a constant temperature T_0 and a constant mass flow rate $\dot{m}_{dis}$ (see Figure 2). The fluid leaves the HSS at the hot side at a higher temperature T_h, as it has received heat from the HSS.

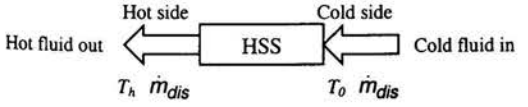

Figure 2: Heat storage system during discharging

To avoid excessive heat losses in the exiting fluid, the charging process finishes as soon as the temperature T_c of the fluid at the cold side rises above a certain prescribed value $T_{c,max}$. Similarly, the discharging process finishes as soon as the temperature T_h of the fluid at the hot side drops below a prescribed value $T_{h,min}$. Only low quality heat would be delivered afterwards. The above criteria, η_2 and η_C, are only based on the temperatures at the entrance and exit of the HSS: two observables of the system. No assumptions whatsoever concerning the geometry or the content of the HSS have been made. Therefore, these criteria permit us to compare different types of HSS under exactly the same working conditions.

3 MODEL DESCRIPTION

3.1 GOVERNING EQUATIONS

A HSS is governed by the energy-conservation equation of the fluid:

$$\rho_f S_f c_{p,f} \frac{\partial T_f}{\partial t} + \dot{m}_f c_{p,f} \frac{\partial T_f}{\partial x} = hP(T_m - T_f) \quad (4)$$

and the energy-conservation equation of the Heat Storage Material (HSM)

$$\rho_m S_m c_m \frac{\partial T_m}{\partial t} = hP(T_f - T_m) \quad (5)$$

Equations (4) and (5) are valid under the following conditions:

1. the flow of the fluid is one-dimensional,
2. no pressure losses,
3. no heat conduction in the fluid,
4. no axial heat conduction in the HSM,
5. infinite radial heat conduction in the HSM,
6. constant thermo-physical properties,
7. no heat losses to the environment.

The assumptions mentioned above might seem an oversimplification of the problem, but they have only a small impact on the principal results, as the aim of the study is to focus on the influence of the use and the configuration of the PCMs. Assumption 6 is not fulfilled, though, for PCMs as the heat capacity c_m becomes infinite during the phase transition. In that case, equation (5) has to be altered to:

$$\rho_m S_m \frac{\partial u_m}{\partial t} = hP(T_f - T_m) \quad (6)$$

3.2 DIMENSIONLESS FORMS OF THE GOVERNING EQUATIONS

For reasons of simplicity, equations (4) and (6) are cast into a dimensionless form.

$$\frac{\partial \theta_f}{\partial \tau} = -\frac{\partial \theta_f}{\partial \zeta} + NTU(\theta_m - \theta_f) \quad (7)$$

$$c_{m/f} \frac{\partial \varphi_m}{\partial \tau} = NTU(\theta_f - \theta_m) \quad (8)$$

The dimensionless temperatures θ and the dimensionless specific internal energy φ vary between 0 and 1.

3.3 STATE RELATIONSHIP OF THE HEAT STORAGE MATERIAL

The dependence of θ_m on φ_m is expressed by the state relationship of the HSM.

For a HSM with a constant heat capacity c_m the state relationship is trivial:

$$\theta_m = \varphi_m \tag{9}$$

For a HSM with phase changing at a temperature θ_γ, the state relationship is more complex (Adebiyi, 1991):

1. the HSM is solid

$$\theta_m = \frac{\bar{c}_m}{c_m^s}\varphi_m \quad \text{for} \quad \varphi_m \le \frac{c_m^s}{\bar{c}_m}\theta_\gamma \tag{10}$$

2. the HSM is partially melted / partially solid

$$\theta_m = \theta_\gamma \quad \text{for} \quad \frac{c_m^s}{\bar{c}_m}\theta_\gamma < \varphi_m < 1 - \frac{c_m^l}{\bar{c}_m}(1-\theta_\gamma) \tag{11}$$

3. the HSM is melted

$$\theta_m = 1 - \frac{\bar{c}_m}{c_m^l}(1-\varphi_m) \quad \text{for} \quad \varphi_m \ge 1 - \frac{c_m^L}{\bar{c}_m}(1-\theta_\gamma) \tag{12}$$

A parameter to characterise the HSM is β_m, defined as the ratio between the amount of heat λ_m that can be stored during the phase changing and the total amount of heat Δu_m that can be stored in the HSM.

$$\beta_m = \lambda_m / \Delta u_m \tag{13}$$

3.4 NUMERICAL SOLUTION

Equations (7) and (8) are transformed into a set of ordinary differential equations by a first order backwards difference scheme for the variable ζ (see equations (14) and (15)).

$$\frac{d\theta_{f,i}}{d\tau} = -\frac{\theta_{f,i-1} - \theta_{f,i}}{\Delta\zeta_i} + NTU(\theta_{m,i} - \theta_{f,i}) \tag{14}$$

$$c_{m/f}\frac{d\varphi_{m,i}}{d\tau} = NTU(\theta_{f,i} - \theta_{m,i}) \tag{15}$$

These equations, together with the state equations (9) or (10) to (12), are solved using a Runge-Kutta method of variable order from the matlab® library for a continuous set of cycles of charging and discharging using the stop criteria from section 2. As soon as the HSS is in regime, i.e. the stored energy during charging equals the released energy during discharging, the efficiencies defined by equations (2) and (3) are determined.

3.5 PARAMETERS USED

For the *NTU*-number a value of 200 is used. This may seem very high compared to the common *NTU* of heat exchangers but HSSs are normally much larger since at any moment only a fraction of the HSS length is active in transferring heat. The remaining part is inactive waiting to be (dis)charged.

For the heat capacity ratio $c_{m/f}$ a value of 50 is used. The results are rather insensitive, though, to the value of $c_{m/f}$ as long as it stays well above unity.

The value used for σ is 0.5, which is appropriate for high temperature heat storage (Van den Branden et al., 1999).

The moment of switching from charging to discharging is set by the switching parameter θ_α. The switching is assumed to be symmetrical so:

$$\theta_{c,max} = 1 - \theta_{h,min} = \theta_\alpha \tag{16}$$

4 RESULTS AND DISCUSSION

4.1 INFLUENCE OF THE NUMBER OF PCMs

The first and most important parameter to be studied is the number of PCMs. It has been shown in Van den Branden et al., (1999) that HSSs with a single PCM have poor efficiencies. In order to combine the particular advantage (compactness) of HSS with PCMs without suffering the accompanying disadvantages, different PCMs are combined into one HSS; see Figure 3.

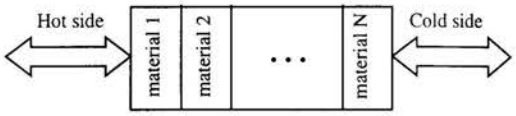

Figure 3: Configuration of PCMs in a HSS

The PCMs are ordered according to their phase-transition temperature with the PCM with the highest phase-transition temperature at the hot side and the PCM with the lowest phase-transition temperature at the cold side.

Three different HSSs are compared: HSS-1A with 1 PCM, HSS-3A with 3 PCMs and HSS-7A with 7 PCMs. HSS-0A with no PCM (only sensible heat storage) will serve as reference case for comparison. The melting temperatures of the PCMs are evenly spaced and the value of β_m is 50%. Further details can be found in Table 1.

Figure 4 shows the evolution of the second law efficiency and a scaled version of the exergy storage efficiency as a function of the switching parameter θ_α. We define the 'scaled exergy storage efficiency' as:

$$\eta_C^* = \eta_C \Big/ \left(1 - \frac{1}{\sigma}\ln(\sigma+1)\right) \tag{17}$$

	θ_γ	$\Delta\zeta$	θ_γ	$\Delta\zeta$	θ_γ	$\Delta\zeta$	θ_γ	$\Delta\zeta$
HSS-0A	-	1.0	-	-	-	-	-	-
HSS-1A	0.5	1.0	-	-	-	-	-	-
HSS-3A	0.75	0.33	0.5	0.33	0.25	0.33	-	-
HSS-7A	0.875	0.125	0.75	0.125	0.625	0.125	0.5	0.125
	0.375	0.125	0.25	0.125	0.125	0.125	-	-

Table 1: Parameters of HSS-0A, 1A, 3A and 7A

A general and important observation to be made is that the characteristics of a HSS depend to a large extent on the operating conditions, i.e., the switching parameter θ_α. When θ_α rises, the second law efficiency η_2 drops, because the average temperature leaving the HSS during discharging will be lower. At the same time the exergy capacity efficiency η_C rises because larger values of θ_α permit that the HSS is charged during a

longer period and thus better use is made of the heat storage capacity content present in the HSM.

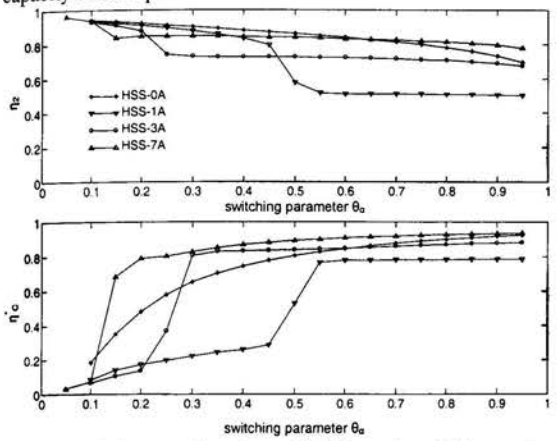

Figure 4: Influence of number of PCMs on the efficiency of a HSS

A first conclusion is that for HSSs with PCMs the exergy capacity efficiency, η_C , rises sharply when the value of the switch parameter exceeds the lowest melting temperature of the PCMs. According to the previous example, this occurs at the same moment that the second-law efficiency drops.

A second conclusion is that HSSs with multiple PCMs are superior to HSSs with a single PCM and even to HSSs without PCMs. The HSS with 7 PCMs (HSS-7A) has for the whole range of θ_α a second-law efficiency, η_2, that equals or exceeds the one of the sensible HSS. For the exergy capacity efficiency, η_C , the results are even more favourable. The superior behaviour of HSS-7A can be explained by looking at the temperature evolution and the temperature profiles for a cycle with $\theta_\alpha = 0.3$. Figure 5a shows that the exit temperature θ_h during discharging is high (high temperature heat is delivered) and the exit temperature θ_c during charging is low (only low temperature heat is discharged in the ambience) resulting in a high second-law efficiency, which is typical for small values of θ_α.

Figure 5b shows that notwithstanding the small value of θ_α most of the theoretical energy capacity content of the HSS is used. In this figure the temperature profile of the HSM is plotted at the end of the charging and at the end of the discharging period. The surface spanned between these two extreme temperature profiles gives an indication of the stored energy of the HSS during one cycle. Generally for larger θ_α, the two extreme temperature profiles will be wider apart resulting in a larger exergy capacity efficiency. For HSS-7A, even with the small value of θ_α, the temperature profiles span the melting temperatures of the PCMs (represented by the dots). The latent heat capacity content represents 50% (the value of β_m) of the total heat capacity content of the HSS. So, most of this heat capacity is used resulting in high values of the exergy capacity efficiency.

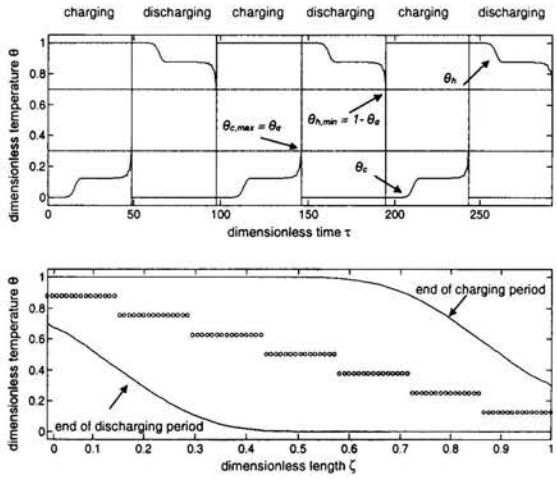

Figure 5: Temperature evolution and temperature profiles for HSS-7A with $\theta_\alpha = 0.3$

4.2 INFLUENCE OF THE LATENT HEAT CONTENT ON A HSS WITH MULTIPLE PCMS

As the use of PCMs improves the behaviour of the HSS it may seem interesting to augment the latent heat capacity of the PCMs, i.e. increase the value of β_m. Figure 6 shows the influence of β_m on the behaviour of the system for three different values of β_m: 0.75, 0.5 and 0.25. The other parameters are those of HSS-7A. Larger latent heat content means larger exergy capacity efficiencies but lower second law efficiencies. For large values of θ_α, though, HSSs with a large latent heat content, seem to be superior both for exergy capacity efficiency as for second law efficiency. The presence of a PCM with a high melting temperature, i.e. a temperature interval where a relatively large amount of heat is stored, causes an increase of the average temperature at which heat can be stored, resulting in a higher heat capacity efficiency and second-law efficiency.

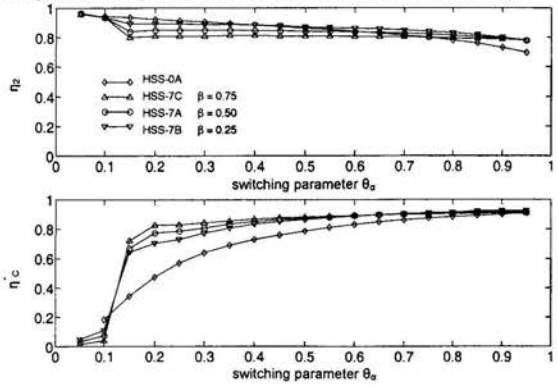

Figure 6: Influence of β on the efficiency of a HSS

4.3 INFLUENCE OF THE MELTING TEMPERATURES ON A HSS WITH MULTIPLE PCMS

Figure 4 showed that the exergy capacity efficiency sharply increases as soon as the switching parameter θ_α rises above the lowest melting temperature γ_N. Accordingly, it seems useful to lower this melting temperature. Figure 7 shows the efficiencies of HSSs with different melting temperature distributions. Each distribution is symmetrical around $\theta = 0.5$. Details of the HSSs can be found in Table 2.

	θ_γ	$\Delta\zeta$	θ_γ	$\Delta\zeta$	θ_γ	$\Delta\zeta$	θ_γ	$\Delta\zeta$
HSS-7D	0.98	0.125	0.82	0.125	0.66	0.125	0.5	0.125
	0.34	0.125	0.18	0.125	0.02	0.125	-	-
HSS-7E	0.8	0.125	0.7	0.125	0.6	0.125	0.5	0.125
	0.4	0.125	0.3	0.125	0.2	0.125	-	-

Table 2: Parameters of HSS-7D and 7E

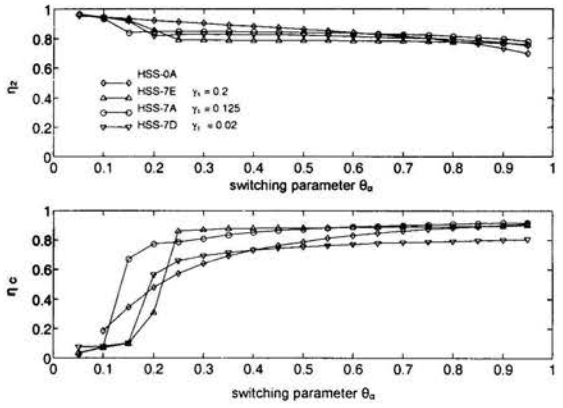

Figure 7: Influence of melting temperatures on the efficiency of a HSS

HSS-7E (HSS with the higher lowest melting temperature γ_N) has the expected behaviour. The exergy capacity efficiency rises when θ_α exceeds γ_N and at the same time the second law efficiency drops. HSS-7D (HSS with the lower lowest melting temperature γ_N) has a quite different behaviour. The exergy capacity efficiency rises only when θ_α exceeds γ_{N-1} (the second lowest melting temperature). This behaviour is explained by the temperature evolution and the temperature profiles of HSS-7D with $\theta_\alpha = 0.3$ as shown in Figure 8. At the end of the charging period the temperature of the first PCM equals its melting temperature, which means that this PCM is only partially melted. The internal energy profiles in Figure 8.c show that in fact only half of the potential heat capacity is used. This means that little heat is stored at high temperatures. Consequently, the outlet temperature during discharging drops rapidly (see Figure 8a) so that the cycle time is short compared with that of HSS-7A (see Figure 5a) resulting in a low exergy capacity efficiency. The PCM with the highest melting temperature, and by symmetry the one with the lowest melting temperature, can be omitted as both of them are hardly used at all.

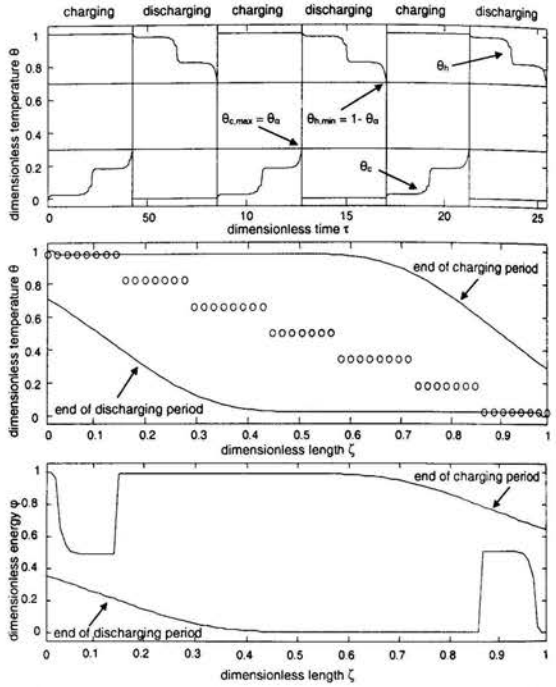

Figure 8: Temperature evolution, temperature profiles and internal energy profiles for HSS-7D with $\theta_\alpha = 0.3$

4.4 INFLUENCE OF THE DISTRIBUTION OF THE PCMS IN A HSS WITH MULTIPLE PCMS

Section 4.2 showed that increasing the latent heat content β increases the capacity to store heat at high temperatures. A way to increase the heat content of one particular PCM is to increase the relative length of that PCM in the HSS. This section focuses on the length of the first and last PCM, i.e. the ones with the highest and the lowest melting temperature. The lengths of both are varied in the same way to keep the problem symmetric. Figure 9 shows the influence of the length of those PCMs. Details of the HSSs can be found in Table 3.

	θ_γ	$\Delta\zeta$	θ_γ	$\Delta\zeta$	θ_γ	$\Delta\zeta$	θ_γ	$\Delta\zeta$
HSS-7F	0.875	0.083	0.75	0.167	0.625	0.167	0.5	0.167
	0.375	0.167	0.25	0.167	0.125	0.083	-	-
HSS-7G	0.875	0.222	0.75	0.111	0.625	0.111	0.5	0.111
	0.375	0.111	0.25	0.111	0.125	0.222	-	-

Table 3: Parameters of HSS-7F and 7G

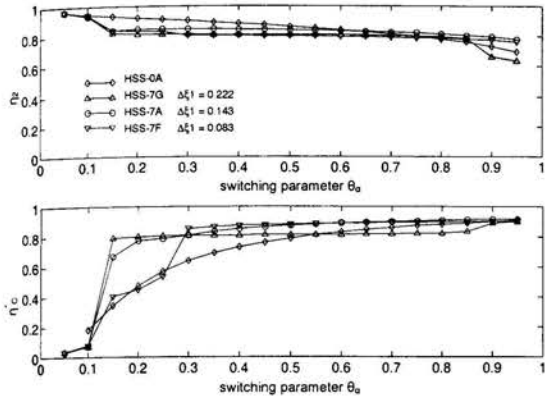

Figure 9: Influence of the length of the first and the last PCMs on the efficiency of a HSS

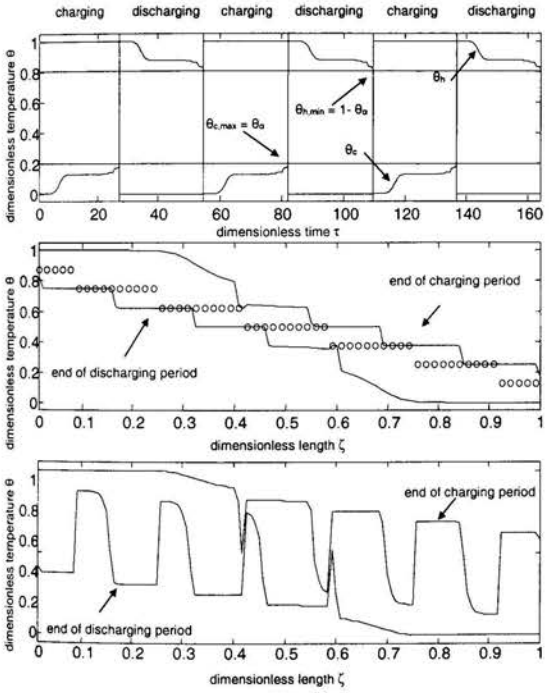

Figure 10: Temperature evolution, temperature profile and energy profile for HSS-7F with $\theta_\alpha = 0.2$

For HSS-7G (with a relatively large length of the first and last PCMs) the exergy capacity efficiency rises sharply as soon as $\theta_\alpha > \gamma_N$ because more heat capacity is present at the melting temperature γ_1 of the first PCM. The second law efficiency is somewhat lower than for HSS with evenly spaced PCMs, because the hot outlet temperature remains fixed at $\gamma_1 < 1$ for quite some time. The exergy capacity efficiency only rises to its maximal value, though, when $\theta_\alpha > \gamma_1$. The high temperature heat capacity present can apparently only be fully used when the charging time is large enough.

For HSS-7F (with relatively small lengths of the first and last PCMs) the exergy capacity efficiency rises sharply as soon as $\theta_\alpha > \gamma_N$ but not to its maximal value. This happens only when $\theta_\alpha > \gamma_{N-1}$. At first, the small length of PCM 1 is not sufficient to heat the fluid to the desired minimum temperature $(1-\theta_\alpha)$ for a long time, which results in small cycle lengths and partially used HSSs (see Figure 10). Only when this desired minimum temperature drops, the larger PCM 2 with melting temperature γ_2 can provide backup so that the exergy capacity efficiency reaches its maximum value.

5 CONCLUSION

This study has shown the influence of layout and characteristics of PCMs in HSSs on the second-law efficiency of the HSS, which is important for the fuel cost, and on the exergy capacity efficiency, which is important for the investment cost. To obtain an optimal HSS for a certain application, both parameters must be considered. For small HSSs, sensible heat HSSs without PCMs are probably the best solution. For large HSSs, latent heat HSS will be more useful because of their compactness. In the latter case, the PCMs (melting temperature, fraction latent heat) and their spatial distribution must be carefully chosen in order to obtain a high efficiency system.

REFERENCES

Adebiyi, G. A. (1991), 'A Second Law Study on Packed Bed Energy Storage Systems Utilizing Phase-Change Materials', *ASME Journal of Solar Energy Engineering*, **113**, 146-156.

Adebiyi, G.A., Hodge, B. K., Steele, W. G., Jalalzadeh-Aza, A., Nsofor, E.C., (1996). 'Computer Simulation of a High-Temperature Thermal Energy Storage System Employing Multiple Families of Phase-Change Storage Materials', *ASME Journal of Energy Resources Technology*, **118**, 102-111.

Aceves-Saborio, S., Nakamura, H., Reitad, G.M., (1994). 'Optimum Efficiencies and Phase Change Temperatures in Latent Heat Storage Systems', *ASME Journal of Energy Resources Technology*, **116**, 79-86.

Bejan, A. (1996). *Entropy Generation Minimization*, Boca Raton , CRC Press LLC.

Lim, J.S., Bejan, A., Kim, J.H., (1992). 'Thermodynamic Optimization of Phase-Change Energy Storing Using Two or More Materials', *ASME Journal of Energy Resources Technology*, **114**, 84-90.

Moran, M. J. (1989). *Availability Analysis*, New York, ASME Press.

Ter-Gazarian, A., (1994). *Energy storage for power systems*, IEE Energy Series 6, London, IEE.

Van den Branden, G., Hesius, M., D'haeseleer, W., (1999). 'Comparison of Heat Storage Systems Employing Sensible and Latent Heat', *Int. J. Energy Res.*, **23**, 605-624.

HEFAT2002
1st International Conference on Heat Transfer, Fluid Mechanics, and Thermodynamics
8-10 April 2002, Kurger Park, South Arfrica
YJ1

A STUDY ON THE FISSION PRODUCT RELEASE FROM A MOLTEN REACTOR CORE POOL AT HIGH PRESSURE

J. I. Yun*, K. Y. Suh**, C. S. Kang**
*Graduate Student, **Professor
Department of Nuclear Engineering, Seoul National University
San 56-1 Sillim-Dong, Kwanak-Gu, Seoul, 151-742, Korea
E-mail: kysuh@snu.ac.kr

ABSTRACT

Heat transfer and fluid flow in a molten pool are influenced by internal volumetric heat generated from the radioactive decay of fission product species retained in the pool. The pool superheat is determined based on the overall energy balance that equates the heat production rate to the heat loss rate. Decay heat of fission products in the pool was estimated by product of the mass concentration and energy conversion factor of each fission product. For the calculation of heat generation rate in the pool, twenty-nine elements were chosen and classified by their chemical properties. The mass concentration of a fission product is obtained from released fraction and the tabular output of the ORIGEN 2 code. The initial core and pool inventories at each time can also be estimated using ORIGEN 2. The released fraction of each fission product is calculated based on the bubble dynamics and mass transport. Numerical analysis is performed for the TMI-2 accident. The pool is assumed to be of a partially filled hemispherical geometry that does not change in shape during the numerical calculation. Results of the numerical calculation indicate that the temperature of the molten pool considerably decreases and most of the volatile fission products are released from the molten pool during the accident.

INTRODUCTION

A severe accident management concept known as "in-vessel retention" is based on the idea that the reactor vessel lower head can survive the downward relocation of a degraded core as much as it is sufficiently cooled by water. The lower head integrity can be maintained through removal of heat generated by radioactive fission products within the pool. As the reactor core material melts and relocates, the molten debris pool may be formed in the reactor vessel lower plenum or in the lower part of the core. If the fission product is released from the molten pool, heat source in the relocated material may be decreased appreciably. Results of the TMI-2 accident analysis [1] indicate that volatile fission products (e.g., I, Cs, Xe) can mostly be released from a molten pool. In the TMI-2 accident, a pool of molten core material was formed and grown within the consolidated region.

The chemical state of the fission products will depend on the temperature and the oxygen potential. During formation and growth of a pool, the release of the volatile fission products will be dominated by bubble dynamics as they all behave as gases. On the other hand the release of the non-volatile fission products will instead be controlled by mass transfer since they exist as condensed phases in the pool. The rate of fission product release is thus calculated using bubble dynamics and mass transfer. For the calculation of heat generation rate in the pool, twenty-nine (29) elements were chosen and classified (see Figure 1). The change of these fission products due to decay chain can be obtained from the tabular output of ORIGEN 2. The multidimensional flow in a molten pool is governed by natural convection with internal heat source. Heat transfer in the pool was treated with the lumped parameter model. The effect of fission product release on the pool temperature decrease was estimated with the energy balance. The energy balance, heat transfer and fluid dynamics within the molten pool are described in next section.

NOMENCLATURE

A	area of bubble surface (m^2)
A_{conv}	area for convection (m^2)
A_{down}	area for downward heat transfer (m^2)
A_{up}	area for upward heat transfer (m^2)
B	coalescence frequency function (m^3/s)
C	fission product concentration in the pool ($\#/m^3$)
c_p	specific heat capacity (J/kgK)
f	Fanning friction factor (= 0.004)
$f_{c,i}$	released fraction of species i before formation of the pool
f_p	released fraction of species i from the pool
H	depth of the pool (m)
k	thermal conductivity ($W/m \cdot K$)
k_m	mass transfer coefficient (m/s)
$\dot{m}$	rate of mass transport (kg/s)
m_c	mass of the core (kg)
m_p	mass of the pool (kg)
$M_{b,0}$	mass of volatile species in the initial bubbles (kg)
$M_{i,0}$	initial inventory of volatile fission product i in the pool (kg)
M_0	initial inventory of volatile species in the pool ($=\sum_i M_{i,0}$) (kg)
n	number density of bubble ($\#/m^3$)
ns_p	number of permanent nucleation sites ($\#$)
ns_t	number density of temperature-dependent nucleation sites ($\#/kg$)
$\dot{Q}$	volumetric heat generation rate (W/m^3)
p	pressure of the pool (_)

p_g pressure of gas bubble (Pa)
q average heat flux over a boundary (W/m^2)
R radius of bubble (m)
R_d radius of bubble at departure (m)
R_P radius of the molten pool (m)
T temperature of the pool (K)
ΔT superheat of the pool (K)
V_P volume of the pool (m^3)
v velocity of bubble (m/s)

Greek Letters

α thermal diffusivity (m^2/s)
β thermal expansion coefficient (K^{-1})
β_b growth constant of diffusion to a bubble
γ bubble-melt interfacial tension (N/m)
η heat generation per unit mass (W/kg)
ε Stefan-Boltzmann constant ($5.6\times10^{-8} W/m^2K^{-4}$)
ε_d eddy diffusivity (m^2/s^3)
κ gas constant (Boltzmann constant) (J/K)
θ_0 contact angle of nucleating bubble (°)
ν kinematic viscosity (m^2/s)
ρ_m density of the pool (kg/m^3)
μ viscosity of the pool ($N\cdot s/m^2$)

Subscripts

0 initial value or nominal value
∞ value in the bulk
coal coalescence
conv convection
diff diffusion
nucl nucleation
loss loss due to bubble rise
surf surface

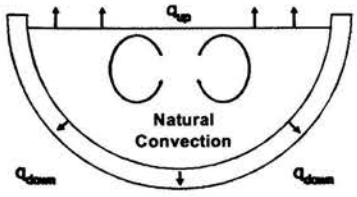

Figure 1: Heat Transfer and Fluid Flow in a Molten Pool

HEAT TRANSFER AND FLOW

The geometry of a molten pool is assumed to be a partially filled hemisphere. The molten material is the $(U,Zr)O_2$ eutectic with a melting point of ~2850 K. It is assumed that the pool is well mixed. Heat transfer and fluid flow in an oxidic pool shown in Figure 1 are induced by internal volumetric heat generated from the radioactive decay of fission product species retained in the pool. The pattern of flow in the pool having a heat-generating liquid is depicted by natural convection being governed by a Rayleigh number characterizing the relationship between the forces of buoyancy and viscous friction [2]. If the pool is deep enough, a stable natural-convection current can be formed. Kulacki and Goldstein [3] suggested that convective mixing of the fluid produces a temperature profile that is axially and radially uniform, except for thin laminar boundary layers at the top and at the bottom. Therefore, it is assumed that heat transfer in the pool can be treated with lumped parameter methods without introducing a significant error in the estimation of the pool temperature.

Natural convection phenomena can be scaled in terms of the Grashof (Gr) and Prandtl (Pr) numbers. The presence of volumetric heating necessitates use of the Dammköhler (Da) number. These numbers are expressed, respectively, as

$$Gr=\frac{g\beta(T_{\max}-T_i)H^3}{\nu^2},\quad Pr=\frac{\nu}{\alpha},\quad Da=\frac{\dot{Q}H^2}{k(T_{\max}-T_i)} \qquad (1)$$

The Rayleigh number is given by $Ra=Gr\cdot Pr\cdot Da$. The behavior of overall heat transfer can be characterized by a correlation in the form of

$$Nu=f(Gr,Pr,Da)=C_A Ra^{C_B} \qquad (2)$$

where C_A and C_B are empirically determined constants, and

$$Ra=\frac{\beta g\dot{Q}H^5}{\nu\alpha k} \qquad (3)$$

For the oxidic pool, the ranges of the Ra and Pr numbers are, respectively

$$10^{15}<Ra<6\times10^{15} \qquad Pr\sim0.6$$

Using the best-known correlations, the heat transfer is calculated at the top and the curved bottom of the pool as follows

$$Nu_{up}=0.36Ra^{0.23} \qquad (4)$$

$$Nu_{down}=0.54Ra^{0.2}(H/R_p)^{0.25} \qquad (5)$$

The schematic of the physical model is shown in Figure 2. The overall energy balance that equates the heat production rate to the heat loss rate may be written as

$$V_p\dot{Q}=A_{up}q_{up}+A_{down}q_{down} \qquad (6)$$

where A_{up} and A_{down} are the upper and lower surface areas of the partially filled hemisphere. In the partially filled hemisphere geometry, A_{up} and A_{dowun} can be determined as

$$A_{up}=\pi R_p^2(1-x^2) \qquad (7)$$

$$A_{down}=2\pi R_p^2\cos(\arcsin x) \qquad (8)$$

$$x=1-H/R_p \qquad (9)$$

Substituting Equations (4) and (5) into Equation (6) to eliminate q_{up} and q_{down}, the pool superheat ΔT may readily be calculated as

$$\Delta T=\frac{HV_p\dot{Q}}{k}[0.54A_{up}(Ra)^{0.2}(H/R)^{0.25}+0.36A_{down}(Ra)^{0.23}] \qquad (10)$$

Decrease of decay heat in the pool results from fission product release. The decay heat (i.e. heat source in the pool) of each species equals the product of mass and energy conversion factor. The total decay heat in the pool may be determined from

$$\dot{Q}=\sum_i M_i(t)\eta(i) \qquad (11)$$

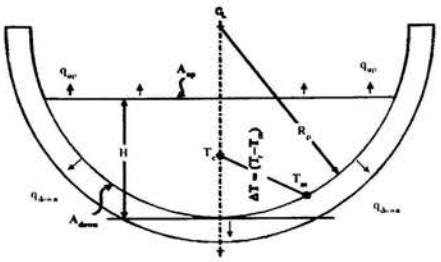

Figure 2: Schematic of the Physical Model

The heat generation rate in the pool is calculated for the twenty-nine (29) elements listed in Table 1. Note that the decay power fraction of the remainder of elements is less than 1 %. At time t, the initial mass concentration of fission product i in the pool can be obtained from

$$M_{i,0}(t) = [M_{i,j} + (M_{i,j+1} - M_{i,j})\frac{(t - t_j)}{(t_{j+1} - t_j)}](1 - f_c)(m_c / m_p) \quad (12)$$

In Equation (12), $M_{i,j}$ and t_j can be determined from the tabular output of the ORIGEN 2 code. Using ORIGEN 2, the initial core and pool inventories at each time can be estimated. With consideration of released fraction of fission product i at time t, the mass concentration of fission product i is estimated as

$$M_i(t) = M_{i,0}(t)(1 - f_p(t)) \quad (13)$$

Table 1: Radionuclide Elements and Classes

Class	Member Elements
1. Noble gases	Xe, Kr
2. Alkali metals	Cs, Rb
3. Alkaline earths	Ba, Sr
4. Halogens	I, Br
5. Chalcogens	Te, Se
6. Platinoids	Ru, Pd, Rh
7. Transition metals	Mo, Tc, Nb
8. Tetravalents	Ce, Zr, Np
9. Trivalents	La, Pm, Y, Pr, Nd
10. Uranium	U
11. More volatile metals	As, Sb
12. Less volatile metals	Sn, Ag

The thickness of the crust surrounding the molten pool can be roughly estimated by considering the steady-state molten pool and crust model illustrated in Figure 3.

The mini-ACOPO experiment [4] showed that the local heat flux varies considerably along the lower boundary of the molten pool. The local heat flux $q_{down}(\theta)$ is presented as a function of the angular position measured from the bottom in Figure 3. From the results of the minu-ACOPO experiment, the local heat flux $q_{down}(\theta)$ is obtained from q_{down} and the shape function as follows

$$\frac{Nu_{down}(\theta)}{Nu_{down}} = 0.1 + 1.08(\frac{\theta}{\varphi}) - 4.5(\frac{\theta}{\varphi})^2 + 8.6(\frac{\theta}{\varphi})^3 \quad (14)$$

when $0 \le \theta / \varphi \le 0.6$

$$\frac{Nu_{down}(\theta)}{Nu_{down}} = 0.41 + 0.35(\frac{\theta}{\varphi}) + (\frac{\theta}{\varphi})^2 \quad (15)$$

when $0.6 < \theta / \varphi \le 1.0$

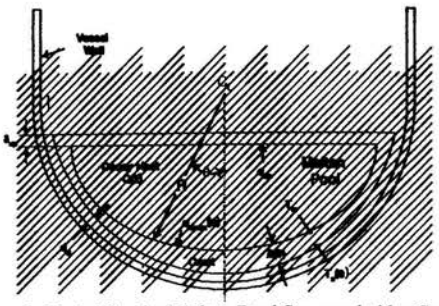

Figure 3: Model for the Molten Pool Surrounded by Crust

In Equations (14) and (15), φ signifies the maximum angle of the molten pool upper surface equaling $\cos^{-1}(H/R)$.

The local thickness of the crust $\delta(\theta)$ can be obtained by solving the one-dimensional conduction equation for the crust as

$$\frac{\dot{Q}\delta(\theta)}{2k_{cr}} + \frac{q_{down}(\theta)\delta(\theta)}{k_{cr}} = T_m - T_s(\theta) \quad (16)$$

where k_{cr} is the thermal conductivity of the crust. The heat loss from the outer surface of the crust is assumed to result mainly from thermal radiation neglecting potential presence of coolant in the gap between the crust and reactor vessel lower head. Therefore, a local energy balance can be given as

$$q_{down}(\theta) + \dot{Q}\delta(\theta) = q_{cr}(\theta) = \varepsilon\sigma T_s^4(\theta) \quad (17)$$

where ε is the emissivity of the surface of the crust and σ is the Stefan-Boltzmann constant. The local thickness of the crust can be calculated utilizing Equations (14) through (17).

FISSION PRODUCT RELEASE FROM THE POOL

The volatile fission products (Xe, Kr, Cs, I) are insoluble in liquid UO_2. Release of the volatile fission products is dominated by bubble dynamics because they all behave as gases in a molten debris pool. Bubble dynamics in the pool is thus characterized by bubble nucleation, coalescence, growth and rise. The time rate of change for the bubble concentration may be represented as follows

$$\frac{dn_i}{dt} = \frac{dn_{i,nucl}}{dt} + \frac{dn_{i,coal}}{dt} + \frac{dn_{i,diff}}{dt} - \frac{dn_{i,coal}}{dt} \quad (18)$$

The nucleated bubbles have very small sizes and follow the natural convection flows. Small bubbles coalesce into larger bubbles by turbulence and differential bubble rise in the pool. These bubbles will grow by diffusion of vapor molecules to bubbles. Bubbles may be released from the pool as they sufficiently grow up.

Nucleation of a Bubble

Heterogeneous nucleation of a volatile fission product species will occur when the vapor pressure of the species minus the pool pressure exceeds the surface tension in the bubble-liquid surface as given by

$$p_g - p_m > (\gamma / R) \quad (19)$$

The number of nucleation sites can be assumed to be proportional to the number of solid particles in the melt.

McClure *et al.* [5] proposed that the total number of nucleation sites could be represented by summation of temperature-dependent nucleation sites and permanent nucleation sites. The permanent nucleation sites were assumed to exist on temperature-independent surfaces. The number of solid particles in the molten material is assumed to be proportional to the pool mass. The number of sites may then be expressed as

$$s_n = (m_p s_{n,t} + s_{n,p}) \tag{20}$$

For small cavity sizes, the bubble size at departure is dictated mainly by a balance between the buoyancy and liquid inertial forces. But, for larger cavity sizes, the bubble size at departure is calculated by a balance of the surface tension and buoyant forces. A well-known equation was proposed by Fritz and Ende [6] as

$$R_F = 0.0104\theta_0\sqrt{\gamma / g(\rho_l - \rho_v)} \tag{21}$$

This agreed well with the experimental data at atmospheric pressure, but did not concur with the experimental data at super- and subatmospheric pressures. Cole and Shulman [7] found that, if $R_F = 0.5\sqrt{\gamma / g(\rho_l - \rho_v)}$ for a contact angle of 48°, $\overline{R}_d = R_d / R_F$ is a function of pressure. According to the experimental data, they obtained the following formula

$$\overline{R}_d = \frac{1000}{p} \tag{22}$$

where p is in mm Hg. The nucleation sites emit bubbles with a constant frequency. The frequency can be obtained by the time to grow to the departure diameter by diffusion. The time can be estimated by solving the multi-component diffusion equation. Scriven [8] proposed the following formulation for diffusion of a species to a sphere of changing radius

$$\frac{\partial C}{\partial t} = D\left(\frac{\partial^2 C}{\partial r^2} + \frac{2}{R}\frac{\partial C}{\partial r}\right) - \frac{R^2}{r^2}\frac{dR}{dt}\frac{\partial C}{\partial r} \tag{23}$$

Solution to Equation (23) is obtained by Martins and Szekely [9] as

$$\varsigma = -a\varphi(\beta_b)$$

$$\varphi(\beta_b) = 2\beta_b^3 \exp(3\beta_b^2) \times \int_{\xi}^{\infty} \xi^{-2} \exp(-\xi^2 - 2\beta_b^3\xi^{-1})d\xi \tag{24}$$

$$\zeta = \frac{C - C_m}{C_m} \quad \text{and} \quad a = D\frac{A}{C_m} \tag{25}$$

The growth constant β_b can be obtained from Scriven's useful expression for the solution to Equation (23)

$$\varphi(\beta_b) \sim \sqrt{(\pi/3)}[\beta_b - 4/9 + 0(\beta_b^{-1})] \tag{26}$$

Data of Scriven's tabulation are found to be incorrect for especially small values of $\varphi(\beta_b)$, however. This error is induced through the change of variable in the integral equation. In this study, new tabulation is obtained, as shown in Figures 4 and 5, by numerical integration of Equation (24) using Simpson's method. The results show that values of β_b for small $\varphi(\beta_b)$ are much smaller than those of Scriven's tabulation, and that values of β_b for large $\varphi(\beta_b)$ are close to half values of his tabulation.

Once β_b is known, the bubble detachment frequency can be calculated as

$$f_d = \frac{1}{t} = \frac{4\beta_b^2 D}{R^2} \tag{27}$$

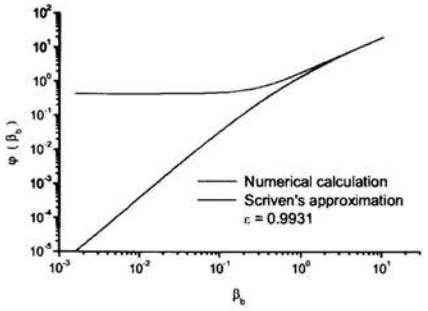

Figure 4: Function $\varphi(\beta_b)$ for Small Values of β_b

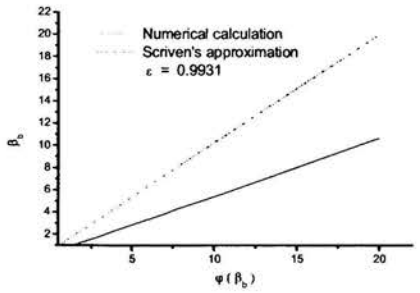

Figure 5: Results of β_b for Large Values of $\varphi(\beta_b)$

The product of the bubble detachment frequency and the number of nucleation sites determines the rate at which the bubbles are formed, viz.

$$\frac{dn_{i,nucl}}{dt} = f_d \cdot s_n \tag{28}$$

Diffusion to a Bubble

Diffusion to a bubble is governed by Equation (23) used to calculate nucleation rate of the bubble. The rate of change of the number density for bubble size R_i can be determined by the time to grow from bubble size R_{i-1} to size R_i. The rate of change of a discrete bubble radius R_i is the sum of loss term and production term. The loss term equals the number density of bubbles of size R_i divided by the time to grow from size R_i to size R_{i+1} and the production term is the number density of bubbles of size R_{i-1} divided by the time to grow from size R_{i-1} to size R_i. Therefore, the rate of change of the number density for bubble size R_i is represented as

$$\frac{dn_{i,diff}}{dt} = \frac{n_{i-1}}{t_i - t_{i-1}} - \frac{n_i}{t_{i+1} - t_i} \tag{29}$$

Coalescence of Bubbles

Bubbles interact due to their motion and grow by coalescence. The rate of coalescence of a bubble of radius R_k

is given by Olander [10] as

$$dn_k / dt = 0.5 \sum_{i+j=k} B_{ij} n_i n_j - \sum_{i=1} B_{ik} n_i n_k \quad (30)$$

The rate of change of number density for bubble size R_k can also be obtained by summation of production term and loss term. The production term is represented by the rate of formation of bubble size R_k due to collisions of bubbles of sizes R_i and R_j. The loss term is represented by the rate of disappearance of bubble size R_k due to coalescence with bubbles of other sizes. It is assumed that bubble coalescence is caused by two mechanisms, i.e. turbulence in the pool and differential rise velocity of bubbles. For the turbulence process, a correlation for aerosol agglomeration in turbulent pipe flow is used as presented by Friedlander [11]

$$B_{ij,turb} = 1.3(R_i + R_j)^3 (\varepsilon_d / \nu)^{1/2} \quad (31)$$

$$\varepsilon_d / \nu = (2/R_p)(f/2)^{1.5} v_{conv}^3 \quad (32)$$

The convective velocity in the pool can be obtained from an energy balance as given by

$$v_{conv} = 2Q / (\rho A_{conv} c_p \Delta T) \quad (33)$$

For coalescence due to differential bubble rise velocity, the frequency function is also given by Friedlander [11] as

$$B_{ij,rise} = \pi (R_i + R_j)^2 |v_i - v_j| \quad (34)$$

For all the fission product release calculations, the molten pool is assumed to be a partially filled hemisphere. The material is $(U,Zr)O_2$ with a melting point of ~2850 K. It is assumed that the pool is homogeneous.

Loss of Bubbles due to Bubble Rise

The rate at which bubbles leave the pool is proportional to the bubble number density and the rise velocity. The residence time of bubbles of size R_k is given by the pool height divided by the rise velocity. It is assumed that the rate at which bubbles leave the pool equals the number density of bubbles divided by the residence time in the pool. The rise velocity of a spherical gas bubble is found by balancing the drag and buoyant forces on the bubble. Hence,

$$v = 2\rho g R^2 / 9\mu \quad (35)$$

The rate of loss of bubbles due to buoyant rise may be determined by

$$\frac{dn_{i,loss}}{dt} = \frac{v_i n_i}{z} \quad (36)$$

Fission Product Release through Mass Transport

The less volatile fission products tend to remain as condensed phases in the melt because of their low vapor pressures. The chemical forms of the less volatile fission products in the melt are determined by the oxygen potential. It is assumed that mass transport governs release of the less volatile fission product from the pool. At high temperatures (>2850 K), rare earth elements such as europium and cerium exist as oxides, strontium is present as SrO, and ruthenium and antimony are present as metals immiscible in the molten pool as reported by Petti *et al.* [12]. The rate of mass transport of a species in a liquid is given by

$$\dot{m} = k_m A_{up} (C_\infty - C_{surf}) \quad (37)$$

The mass transfer correlations for the top of the pool can be obtained by means of a heat and mass transfer analogy

$$\Delta T = \frac{HV_p \dot{Q}}{k} [0.54 A_{up} (Ra)^{0.2} (H/R)^{0.25} + 0.36 A_{down} (Ra)^{0.23}] \quad (10)$$

RESULTS AND DISCUSSION

For all the fission product release calculations in this work, the main parameters were obtained from the analysis report of the TMI-2 accident [1]. The pool is assumed to be a partially filled hemisphere, 1.45 m in radius and 32,700 kg in mass. The change of pool geometry during the numerical calculation is neglected. The fission product inventories in the pool are about 24.5 % of the total core. The parameters used in the numerical calculations are listed in Table 2. The numerical analysis indicates that the height of the pool is 1.014 m and the peak temperature at the pool center exceeds 3000 K.

Table 2: Values and Ranges of Parameters used in Numerical Analysis

Parameter	Value
Pool mass, M_p (kg)	32,700
Pool radius, R_p (m)	1.45
Pool pressure, p (MPa)	0.1 ~ 10.0
Pool velocity, V_{conv} (m/s)	0.13
Number of permanent nucleation sites, ns_p (#)	100 ~ 1000
Number of temperature-dependent nucleation sites, ns_t (#/kg)	100 ~ 30,000
Diffusivity of fission product, α (m^2/s)	1×10^{-11} ~ 1×10^{-7}
Surface tension of liquid in the pool. γ (N/m)	0.5~1.6

The calculations were carried out with p=10 MPa, ns_t=5000, and the initial inventory = 100 %. For the cases of $M_{b,0}/M_0$=0 and 0.5, times to release 60 % of the total volatile gas inventory are about 4350 and 750 s as shown in Figures 6-(d) and 7-(d), respectively. From concentrations of the twenty-nine (29) elements in the pool, the total heat generation rate was obtained at time t. Figures 6-(a) and 7-(a) comparatively show the difference of volumetric heat generation rates between the volatile and non-volatile fission products. Figures 6-(b) and 6-(c) represent decrease of decay heat by fission product release and the peak temperature in the pool. When release of the fission products from the debris pool is considered, the peak temperature of the pool decreases from 3224 K to 3166 K at 4346 s as shown in Figure 6-(c). In Figure 7-(c), also, the peak temperature in the pool decreases from 3260 K to 3194 K at 745.5 s. Because the initial bubbles interact and rapidly grow by coalescence and diffusion to a bigger bubble, the peak temperature in the pool decreases faster when the bubbles in the molten core material existed prior to the formation of the pool.

When the thermal properties of the pool are taken to be: $k = 4\ W/mK$, $\alpha = 9.1 \times 10^{-7}\ m^2/s$, $\nu = 5.9 \times 10^{-7}\ m^2/s$, and $\beta = 9.1 \times 10^{-7}\ K^{-1}$, the pool Rayleigh number is in the range of $3 \sim 3.5 \times 10^{15}$. Table 3 presents the pool specific heat

and the average downward heat flux at the time to release 60 % of the volatile gas inventory. Under the condition of fission product release, the pool specific heat and average downward heat flux are sizably reduced by removal mechanism of the heat source. Therefore, the fission product release ought to be taken into account in order to realistically estimate the thermal load applied to the reactor vessel lower head.

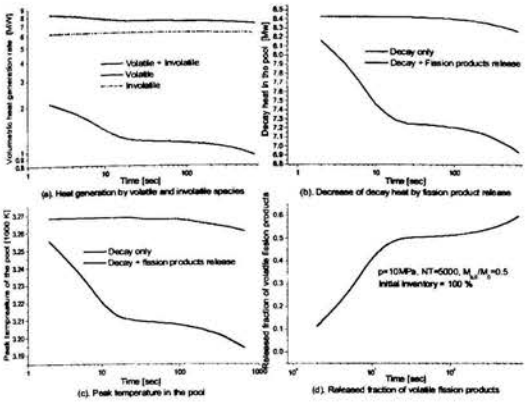

Figure 6: Heat Generation and Transfer for Mass Ratio of $(M_{b,0}/M_0) = 0.0$

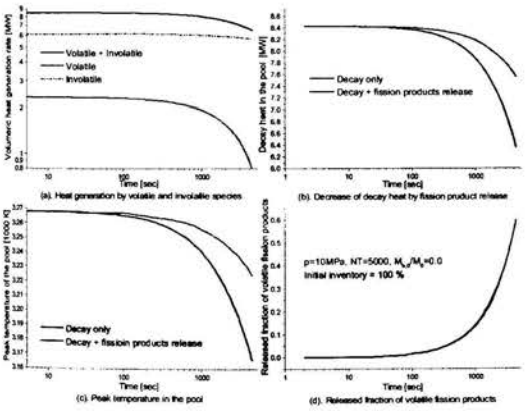

Figure 7: Heat Generation and Transfer for Mass Ratio of $(M_{b,0}/M_0) = 0.5$

Table 3: Pool Specific Heat and Heat Flux of the Pool

Mass Ratio	Release	Decay Heat Rate, $\dot{Q}$	Pool Specific Heat, ΔT	Heat Flux, q_{down}
0.0	No	7.55	374.5	9.34E5
	Yes	6.37	315.6	7.61E5
0.5	No	8.27	409.8	1.04E6
	Yes	6.93	343.7	8.42E5

CONCLUSION

When the fission products release from the molten pool, the heat source of the pool was estimated using twenty-nine (29) nuclide concentration data obtained from the ORIGEN 2 code. The heat flux, pool specific heat and peak temperature were calculated from the overall energy balance in the pool. It was numerically demonstrated that the heat generation rate decreases faster when the bubbles pre-existed in the pool due mainly to more effective release of the volatile fission products. The peak temperature considerably decreased by about 60 K as the fission products were released from the pool. For both cases with $M_{b,0}/M_0$ = 0.0 and 0.5, the heat flux was observed to be reduced by as much as 20 %. Results of the numerical analysis indicate that the fission product release must be credited in the best-estimate analysis of the reactor vessel lower head integrity when the debris has been relocated from the core.

REFERENCES

[1] Akers, D. C. *et al.*, 1989, "Three Mile Island Unit 2 Fission Product Inventory Estimates," Nuclear Technology, Vol. 87, pp. 205-213.

[2] Asfia, F. J., Frantz, B. and Dhir, V. K., 1994, "Experimental Investigation of Natural Convection in Volumetrically Heated Spherical Segments," Submitted for Publication in J. of Heat Transfer.

[3] Kulacki, F. A. and Goldstein, R. J., 1972, "Thermal Convection in a Horizontal Fluid Layer with Uniform Volumetric Energy Sources," J. Fluid Mech., Vol. 55, Part 2, p 271.

[4] Theofanous, T. G. *et al.*, 1994, "In-Vessel Coolability and Retention of A Core Melt," DOE/ID-10460.

[5] McClure, P. R., Leonard, M. T. and Razani, A., 1993, "A Model for Fission Product Release from Liquid-Metal Pools: Development and Sensitivity Investigation," Nuclear Science and Engineering., Vol. 114, pp. 102-111.

[6] Fritz, W. and Ende, W. , 1936, "Uber den Verdampfungsvorgang nach Kinematographischen Aufnahmen an Dampfblasen," Physik Zeitscher, Vol.37, pp. 391-401.

[7] Cole, R. and Shulman, H. L., 1966, "Bubble Departure Diameters at Subatmospheric Pressures," Chemical Engineers Progress Symposium Series 62, Vol. 64, pp. 6-16.

[8] Scriven, L. E., 1959, "On the Dynamics of Phase Growth," Chem. Eng. Sci., Vol. 10, pp. 1-13.

[9] Martins, G. P. and Szekely, J., 1969, "On Spherical Phase Growth in Multicomponent Systems," Transactions of the Metallurgical Society of AIME, Vol. 245, pp. 1741-1747.

[10] Olander, D. R. , 1976, "Fundamental Aspects of Nuclear Reactor Fuel Elements," TID-26711-P1, Department of Energy, Washington, DC, USA.

[11] Friedlander, S. K., 1977, "Smoke, Dust and Haze: Fundamentals of Aerosol Behavior," John Wiley and Sons, Inc., New York, NY, USA.

[12] Petti, D. A. *et al.*, 1989, "Analysis of Fission Product Release Behavior from the Three Mile Island Unit 2 Core," Nuclear Technology, Vol. 87, pp. 243-263.

HEFAT2002
1st International Conference on Heat Transfer, Fluid Mechanics, andThermodynamics
8-10 April 2002, Kruger Park, South Africa
ZT1

PINCH TECHNOLOGY AIDED DESIGN OF ECONOMISER SYSTEMS FOR FLEXIBILITY IMPROVEMENT OF INDUSTRIAL POWER STATIONS

T. Zhelev, Professor
Chemical Engineering Discipline
University of Durban-Westville
Private Bag, X54001, Durban 4000,
South Africa,
E-mail: zhelev@pixie.udw.ac.za

ABSTRACT

This paper reports intermediate results of an investigation in the area of energy efficiency improvement of industrial boilers accompanied with substantial ecological effect.

The hypothesis of possibility to maintain efficiency levels under disturbances such as fuel quality deterioration is based on known from years unit operation - the contact economiser. This unit is used for flue gas energy recovery and its design and operationutilises state of the art thermodynamic principles for energy and mass resources management realised with the help of expanded Pinch concept - the combination of thermal and water Pinch Analysis.

INTRODUCTION

In the light of recent decline in growth of nuclear power generation capacity the attention is focussing on conventional power plants as an energy resource of continuing importance. However, given the cost, scarcity and environmental implications of fossil fuels there is a strong incentive for continued improvement of fuel efficiency.

It is known from years that the major loss of energy in power production is through the flue gases. A thumb rule says that every 20°C decrease in flue gas temperature would improve the efficiency of the boiler by about one per cent. As it was proposed by Kolev [1] a family of contact economiser system can be deployed exploring the benefits of direct heat and mass transfer between the flue gas and circulating water taking the advantage of both sensible and latent heat and seeking additional environmental impact. An important problem in this case is to make available a simple procedure providing clear information about the maximum possible heat recovery and the maximum potential level of recovered heat, helping the decision making.

Second problem of practical interest is the information about maximum boiler flexibility improvement to be provided by the contact economiser system. The implementation of Pinch Principles for analysis of energy resources as suggested by Linnhoff et.al. [2 & 3] in mid 80-s had a big impact on the systematic energy management. The success of Pinch technology in hundreds of different industrial applications had provoked the implementation of same principles for management of a number of different resources. Our experience in the field (Zhelev & Semkov [4, 5]) led us to the logical idea to consider heat and mass resources management simultaneously being fully convinced that this will help us to solve the above-mentioned problems.

NOMENCLATURE

- C_i – calorific effect of the fuel
- RI – resilience index
- F_i – boiler's feed rate
- E_x – exergy
- Q – heat
- T_o – temperature
- ΔT_{LM} – log. mean temperature difference
- η_c - Carnot factor

CONTACT ECONOMISER SYSTEMS

In general, the systems of contact economisers are found quite suitable for heat utilisation from most gases generated by

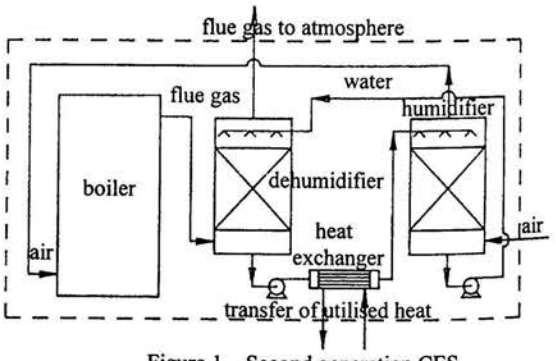

Figure 1. Second generation CES

various processes like coal and gas combustion, drying, etc.

The gains of the implementation of such systems are as follows:

- Flue gases energy recovery. Up to 12% boiler efficiency improvement.
- Reduction of harmful gases resulting from fuel combustion process (mainly CO_2 and NO_x)
- Substantial reduction of ash emission in the atmosphere.
- Production of substantial amount of water through dehumidification of stack gases that can lead to fresh water saving, etc.

The core of the contact economiser system is a classical packed-bed column providing high gas velocity and low pressure-drop. Difference between the first and the second-generation economiser systems is that part of the flue gas energy is used in the second system for preheating and controlled humidification of combustion air. The purpose of these additional processes is more efficient energy recovery. Controlled raise of combustion's air moisture content can have positive effect on boiler's efficiency. The three-atom molecule of water is associated with much higher radiation emissivity than the two-atom molecule of nitrogen, which is the major constituent of the air. Therefore, the introduction of additional water vapor with the combustion air will support the heat transfer in the radiation zone and compensate for the decrease of temperature caused by additional moisture. Our experience with 12 t/h boiler shows that the temperature in the radiation zone decreases by 150° when the moisture content of the combustion air is increased to 10%.

Controlled raise of moisture content in burners can have positive environmental effect too. It is known that some burner vendors use water steam injection into the flame zone for NOx reduction. Our experience with the 12 t/h boiler shows that the increased air humidity to 10% leads to decrease of the NOx concentration from 132 ppm to 38 ppm. In gas fired boilers at 10% air excess the beneficial extra moisture is in the range og 0.131 kg water wapour per kg dry gas. For coal fired boilers at coal moisture content of 7% this amount drops 3 times and is 0.433 kg/kg dry gas.

An obvious question arises – how one can target the optimal management of moisture and heat in complicated economiser system design.

PINCH ANALYSIS

The management of heat and mass transfer processes and the balance between humidification and dehumidification rates is proposed to be assisted by the extension of Pinch principles to simultaneous heat and mass transfer case. The complications to generalise such simultaneous analysis are apparent bearing in mind the large variety of mass transfer processes.

New composite curves are developed here to maintain optimal heat and mass transfer driving forces in packed bed columns. The composite curves are combined with reversed equilibrium curve in T/H presentation. The crossed over regions point out non-optimal processes. The equilibrium curve is to pass between the hot and the cold curves. The particular case presented in Fig.2 shows the way to manage the balance

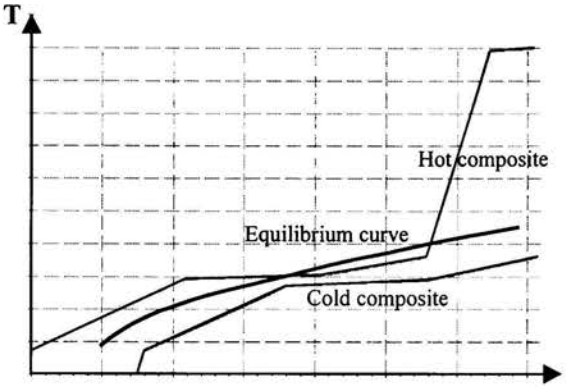

Figure 2. Combined composite-equilibrium curves

between the heat applied in the humidifier and that applied in the dehumidifier. Presented figure is constructed for a second-generation contact economiser system of parallel type comprising of three contact units (Fig. 3).

This system uses fraction of the heat recovered from the flue gas for partial preheating of combustion air and its humidification. The low potential heat supplied to the combustion air is recovered after the burner at much higher potential because of the higher wet bulb temperature (humidity) than in the first generation case. In such a way the second-generation economiser acts as a heat pump – taking the heat at lower level and raising the potential upstream. The question

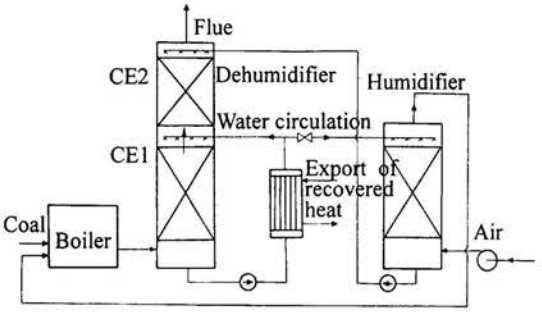

Figure 3. CES second generation of parallel type

arises what can be the maximum potential of recovered heat. The answer can be obtained from the Grant Composite Curve (GCC) - another tool of Pinch Technology (see Fig.4). The GCC allows to manage utilities and utility levels in the best way helping to minimise utility costs as shown by Linnhoff et.al. [2].

Our case study can be recognised as typical threshold problem, when one of utilities (hot or cold) is missing. The flue gas provides sufficient amount of energy restricted by its exit

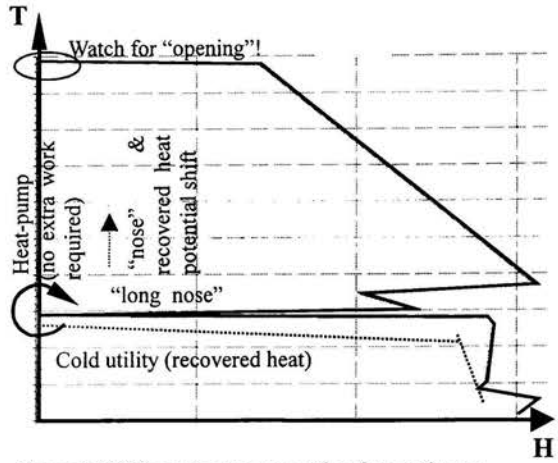

Figure 4. GCC and heat pump option for maximum heat potential

temperature, the dew point and natural draft ability of the stack. At the same time the GCC points out a heat-pump option characterised by a "long nose" at the diagram. The small temperature differences in this "nose" can be cost efficiently be overcomed by external work. The second generation contact economiser system acts just as a heat pump – takes some energy of the flue gas at low potential level transferring it to the combustion air in the humidifier and recovers it back after the burner at much higher potential level. The recovered heat can be transferred to the place of application through the water preheated in a plate heat exchanger. The amount and the potential of this energy can be found from the GCC (the dotted line). Any increase of the heat applied in the dehumidifier lifts the "nose" upwards and corresponding water (cold utility) temperature will increase. The maximum will be reached when the flue gas energy is not anymore sufficient and the upper part of the curve touching the ordinate opens.

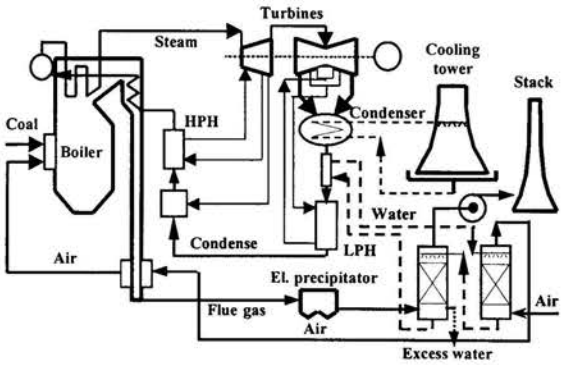

Figure 5. CES option in a typical power station flowsheet

APPLICATION

The low potential energy recovered from the flue gas through the contact economiser system is proposed to be applied for preheating of condensed water after the steam-condensers (Fig.5).

Because of the substantial decrease of flue gas density (dew to dehumidification) the increased pressure drop of installed contact economiser on the sucking line of the fan will be compensated and new, more powerful fan does not need to be installed. Raised moisture content of the flue gas would cause a negative effect on the efficiency of electrostatic precipitators, which will be compensated by the scrubbing feature of the first packed bed column. The laboratory experiment had shown very good washing ability of the packing preventing scaling and blocking.

These design changes will upset the bled streams and the overall thermal balance if applied to an industrial power station. This problem requires special attention.

REESTABLISHING THE BALANCE

A combined Pinch-Exergy analysis is proposed for reestablishment of the right thermal management including the thermal load of low-pressure heaters, high-pressure heaters and contact economiser heat exchangers.

The gain in efficiency through optimisation of bleed steam

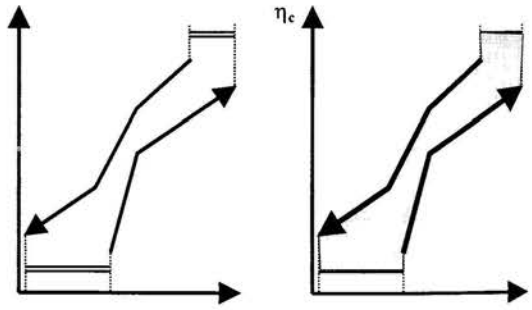

Figure 6. (a) Composite Curves and (b) Exergy composites

depends on the number of bleed levels used. In commercial power cycles the best return of additional capital cost is obtained with several bleed levels. The exact number depends on the economics of a given installation. The proper choice of bleed pressures and mass flowrates depends on well-established thermodynamic considerations. A systematic approach based on Pinch Technology was applied for first time for commercial power station by Linnhoff and Alanis [6]. The Combined Pinch and Exergy Approach to analyse thermal power station involving power was proposed by Dhole [7] and extended to design considerations by Dhole and Zheng, [8–11]. The basic tools used in this analysis are the Exergy Grant Composite Curves, the conventional composite

curves and the Grant Composite Curves. Combined analysis is able to describe the heat and power driving forces in one diagram.

The application of Pinch principles in combination with exergy analysis in order to address exergy losses and energy availability for mechanical work will help us to re-establish the right balance of energy in the system after the introduction of a new heat exchanger on the line of condensed steam (Fig.5).

For Q heat exchange over a linear temperature gradient (streams with constant flowrate and heat capacity) the exergy change is given as: $\Delta Ex = Q\ (1 - T_o/\Delta T_{LM})$. Both quantity and quality (temperature) of the heat are considered when assessing the exergy value. The thermodynamic limit associated with the shaft work equivalent to the heat used in an ideal Carnot machine is given by *Carnot factor*. Carnot efficiency is given by $(1 - T_o/T)$. Another words the extergy will be easily presented graphically in Carnot efficiency/enthalpy composite curve diagram through the surface between the hot and the cold composites (Fig.6b).

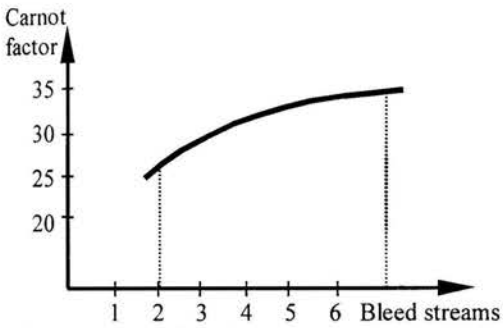

Figure 7. Improving efficiency (no account on capital)

The fuel acts as an exergy source for the whole system; one part of the exergy is lost in the boiler; the heat from the economiser system and the heat exchanger represents the exergy gain for power generation. For a fixed fuel consumption any reduction of the shaded area in Fig. 6b will result in increase of exergy gain and thus to increase of overall thermal efficiency. This approach powered with the combined pinch and exergy analysis would lead to best possible modifications of bleed streams level, flowrate and number, and will ensure the maximisation of boiler's efficiency (Fig.7).

The boiler's feed water heating Composite curve is presented in Fig. 8.

More comprehensive picture of energy management is shown in Fig.9.

It shows the cold streams composite curve matched against the flue gas heating abilities. It is used for targets setting and for consideration of thermodynamic constraints such as minimum temperature approach. The separate sections are representing different stages of flue gas energy recovery, i.e. combustion air preheating and condensate preheating in the contact economiser

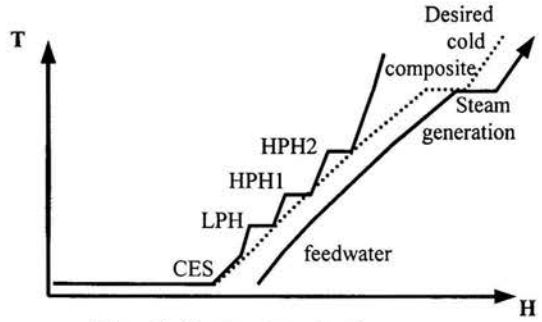

Figure 8. Condensate preheating

system, combustion air preheating in air preheaters, boiler's economiser, evaporation of water to steam and steam superheating. The minimum temperature approach in our case is set to 2°C (regenerative heat transfer is allowed).

To identify thermal inefficiencies and suggest design changes a thermodynamic analysis is used based on Exergy Composite Curve and Exergy Grand Composite Curves as suggested by Manninen and Zhu [12]. Combined Pinch and Exergy representation is shown in Fig. 10.

The combined Pinch/Exergy approach to flue gas energy recovery management comprises the following steps:

(1) Construct the Combined Power and Energy Representation.

(2) Obtain the minimum exergy loss through minimisation of area between the hot and cold composites. This is a typical mixed integer nonlinear optimisation problem and needs to be solved with the help of professional software (recommended GAMS). The number of bleed streams and the change of heat exchanger loads will modify the minimised area. The optimisation procedure should include consideration of final flue gas temperature accounting for the acid dew point of the gas and the effect of controlled combustion air humidity level.

(3) Design the heat exchanger system corresponding to the optimal heat recovery using Pinch Design Method [2, 3].

Presented principles can be applied to any power generation

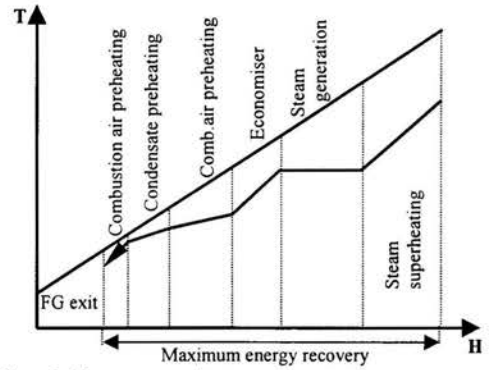

Figure 9. Flue gas composite curve

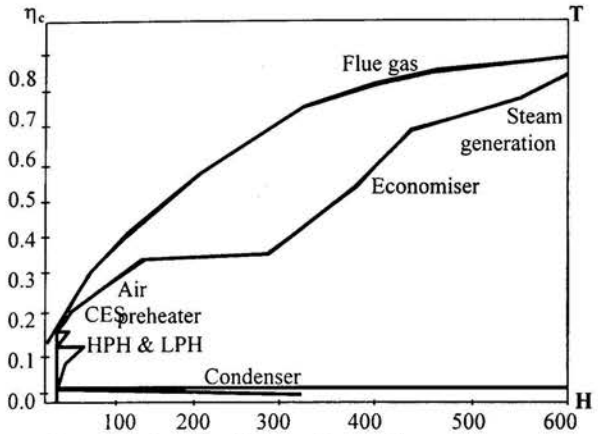

Figure 10. Combined Pinch - Exergy diagram

system (gas, liquid and coal fired industrial boilers). Combined Pinch-Exergy analysis was applied successfully for total site resources management. The targets can be set for site fuel, site co-generation, site emissions from fuel combustion, and site cooling. The approach can also be used to identify and evaluate design modifications in the processes or in the utility system.

FLEXIBILITY

Proposed energy recovery of the flue gas through contact economiser system brings the question about possible compensation of the lost of boiler efficiency related to constant deterioration of coal quality mined in South Africa. The degree of such compensation relates to an important system quality characteristic know as system flexibility. The importance of systems quality characteristics is apparent. Some quantitative characteristics of system's quality are to be monitored during design.

Resilience: A new system is said to be resilient if it is feasible for the whole disturbance range.

Flexibility is a static characteristic of system resilience, when dynamic resilience can be denoted as system *Controllability.* A resilient network can be achieved by selecting appropriate system topology and system reserves. *Flexibility objectives are:* (a) Feasibility analysis; (b) System reserves; (c) Path resilience; (d) Combined resilience; with final goal – debottlenecking. Flexibility is recognised as a static resilience in long time horizon.

One basic approach adopted in the literature for flexibility estimation is the *Parameter Ranges approach* [12]. This approach allows individual inlet parameters to vary over defined ranges between lower and upper bound.

Saboo and Morari [13] proposed the resilience index *(RI)* to characterise *the largest disturbance the system can tolerate*, remaining feasible. An efficient procedure for easy computation of flexibility index was introduced by Swaney and Grossmann [14]. The index is taken to be the minimum fraction over all parameter ranges for which the design is feasible.

The efficiency of the boiler is defined as energy turned into product (electricity or steam) over the total energy gained from the combusted fuel. If the calorific effect of current fuel is denoted as C_i and the coal quality at any moment in the future is C_i with the boiler feed rate in both cases given as F, then the resilience index (flexibility measurement) will be defined as $RI = maxF_i(C_i - C_i)$ compensating the lost efficiency with the improvement gained by the contact economiser system.

The maximum allowed coal quality variation (deterioration) is given by: $\left|\Delta C_i^s\right| \le \frac{RI}{F_i}$

BENEFITS

A preliminary calculation of the benefits of eventual implementation of the proposed approach is presented for one of the largest South African power station.

The preliminary calculations of the effect of an eventual application of contact economiser system for one of the six blocks at this power station are reported as follows:

- One block burns 340 t/h coal. A recovery of as much as *137 MW* of heat can be realised towards preheating the entire amount of condense of all six blocks of the station. The required quantity of heat can be obtained from the wasted flue-gases energy of just one of the 6 blocks by their cooling to *31°C*. This would improve the efficiency of the block by *7.6%* and respectively the entire station efficiency by *1.27%*. Considering the fact that three blocks are served by one stack, the expected decrease of the total stack-gas temperature would be minimal (decrease from *120* to *97.5°C*). This, as well as considering the insignificant concentration of SO_3 in the stack gases (not more than *10 ppm*) and the lowered stack gases' humidity, will exclude the danger of acid condensation and stack's corrosion. The coal savings would be 29.5 t/hour that is equivalent to $R9.42x10^6$ per year and corresponds to *57.8 MW* of extra electrical energy. The total effect of the proposed improvement would be $R29.5x10^6$ *per year*.
- The environmental impact of economisers application are as follows: (i) decrease of CO_2 emissions by *250,000 t/year*, and (ii) decrease of *NOx* emissions by *118 t/year*. The amount of water recovered from the flue gases would be approximately *15.03 kg/sec*. This represents *16.4%* of the fresh water consumption of the entire power station *(330 m^3/h)* and is approximately two times more than the boilers' make-up water for all *6* blocks of the station.
- Pay back periods are expected to be reasonably short (not exceeding 2.5 years).

EXPERIMENTAL SET-UP

First generation contact economiser was used as primary experimental set-up. It is expected to be upgraded to second generation shortly. Fluidised-bed burner: LPG start-up; 10 kg/h coal at maximum load.

Typical nominal parameters of the set-up:

- Coal feed rate for combustion - 10 kg/h
- Hot flue gases flowrate - 86.8 kg dry gas/h + 3.76 kg water vapor/h (if no additional steam is added into the combustion camera);
- Temperature of the gases at the cyclone exit ‹850°C;
- Temperature of the gases on the economiser's input 120°C;
- Temperature of the cooled gases - 30.6°C;
- Temperature of the heated water - 56.2°C;
- Temperature of the water at inlet to the economiser - 25°C;
- Flowrate of the circulation water - 208 l/h;
- Heat duty, utilised in the economiser - 8 kW.

Energy is recovered by the following processes:

(i) Condensation (latent heat of vaporization), Q_C = 1775.72 kJ
(ii) Cooling (Sensible heat), Q_S = 4217.56 kJ/kg.

The experiment focuses on several major goals: (1) The quality of the condensed water from the flue gas and possible application at power station site. (2) The condition of the packing after long service in substantial ash containing flue gas (around 27%). (3) SO_2 (SO_3) content in the flue gas and the acid dew point at flue gas exit. Verification of the contact economiser model and design calculation for future simulation purposes. (4) Maximum heat recovery in quantity and quality. (5) Maximum efficiency improvement and flexibility improvement under changeable fuel quality, etc.

CONCLUSIONS

The work confirms possibilities to furder utilise the sensible and latent heat of flue gases from coal fired industrial boilers. This opportunity is given by a contact economiser system of second generation that suceeds to decrease the danger of acid condensation in the stack by intensive simultaneous heat and mass transfer in a packed bed column. The flue gas is dried roughly by 50% as the temperature of the circulating water is kept below the acid dew point. The absorption of the SO_3 in the circulating water brings the PH of the water overflow to 2.9 level making it suitable for ash damp neutralisation. Additional environmental impact on NOx generation is realised through controlled combustion air humidity increase. The balance between the heat and mass transfer in all units of the economiser system is maintained with the help of new combined composite-equilibrium curves. The prior to design targeting of maximum possible heat recovery and the maximum level of recovered heat can be achieved through the standard Grant composite curves used for utility management and accounting for heat-pumps options. The final heat and power management including structural changes option and changeable bled streams flowrates and numbers can be successfully done through combined Pinch-Exergy analysis. Such analysis must be carried out if any change of condensate preheating is envisaged.

ACKNOWLEDGMENTS

We acknowledge and appreciate the strong support of ESKOM under its TESP progremme and NRF under THRIP programme for this research.

REFERENCES

1. Kolev, N., Darakchiev, R. & Semkov, K. (1993), "Systems containing contact economizers, Energy Efficiency in Process Technology", Elsevier, London & New York, 683.
2. Linnhoff, B. & Flower, J.P. (1978), "Synthesis of Heat Exchanger Networks: Part I & II", *AIChE J.*, **14**, 633-654.
3. Linnhoff, B, Townsend, D.W. et.al., 1982, "User Guide on Process Integration for Efficient Use of Energy", IChemE, Rugby, UK.
4. Zhelev, T.K., Semkov, K.A., 2001, "More Efficient Flue Gas Energy Recovery through Pinch Analysis", *PRES-01*, Florence, IT, 20-23 May, 235-240.
5. Zhelev, T., Bhaw, N., 2000, "Combined Water-Oxygen Pinch Analysis for Better Wastewater Treatment Management", Waste Management, Vol.20, 665-670.
6. Linnhoff, B & Alanis, F.J., 1989, "A Systems' Approach Based on Pinch Technology to Commercial Power Station Design", paper presented at ASME Winter Annual Meeting, San Francisco, Ca, USA, 10-15 December
7. Dhole, V. R., 1991, "Distillation Column Integration and Overall Design of Subambient Plants", PhD thesis, UMIST, Manchester, UK.
8. Dhole V. R. & Zheng, J., 1993, "Applying Combined Pinch and Exergy Analysis to Close Cycle Gas Turbine System Design", paper presented at ASME Cogen Turbo Power Conference, Bournemouth, UK, September 21-23.
9. Zheng, J., Dhole V. R., 1995, "Targeting for Efficiency Improvement in the Design of Comerrsial Power Stations", ASME Cogen Turbo Power'95, Vienna, Austria.
10. Manninen J.and Zhu, X.X., 1998, "Thermodynamic Analysis and Mathematical Optimisation of Power Plants, Comput.and Chem.Engng., Vol.22, s537-S544.
11. Sorin, M., Paris, J., 1997, "Combined Exergy and Pinch Approach to Process Analysis, Comput. And Chem.Engng., pp. S23-S28.
12. Swaney, R.E., I.E.Grossmann, 1985 ,"An Index for Operational Flexibility in Chemical Process Design. Part I: Formulation and Theory", AIChE J., 31, No.4, April, 621-630.
13. Saboo, A.K., M.Morari, 1985, "Design of Resilient Processing Plants-VIII. A Resilient Index for Heat Exchanger Networks", Chem. Eng. Sci., 40, No.8, 1553-1565.
14. Swaney, R.E., I.E.Grossmann, 1985, "An Index for Operational Flexibility in Chemical Process Design. Part II: Computational Algorithms", AIChE J., 31, No.4, April, 631-641.

HEFAT2002
1st International Conference on Heat Transfer, Fluid Mechanics, and Thermodynamics
8-10 April 2002, Kruger Park, South Africa
ZR1

COMPUTATIONAL AND EXPERIMENTAL THERMAL-HYDRAULIC STUDIES OF SUPERCONDUCTING MAGNETS FOR NUCLEAR FUSION APPLICATIONS

R.Zanino (*) and L.Savoldi (**)
(*) Professor; (**) Post-Doc
Dipartimento di Energetica, Politecnico, I-10129 Torino, Italy
E-mail: zanino@polito.it, savoldi@polito.it URL: http://www.polito.it/~zanino

ABSTRACT

We present an overview and some of the perspectives of the work performed by our group over the last few years in the field of thermal-hydraulic tests and modeling of superconducting magnets for fusion, with particular reference to the International Thermonuclear Experimental Reactor (ITER)-related activities.

INTRODUCTION

Superconducting magnets for fusion applications (see Fig.1) are based on low critical temperature (Tc) materials (e.g. Nb3Sn, NbTi, Nb3Al) because of the combined needs of high current density (several tens of kA to be carried) and magnetic field (up to 13T to be generated). In tokamaks, the magnet system is constituted by three subsystems: the toroidal field (TF) coils, which are DC and symmetrically located on vertical planes through the machine axis and guarantee the plasma stability; the central solenoid (CS), which is pulsed and provides the primary of a transformer for inducing a toroidal current in the plasma (secondary); the poloidal field (PF) coils, which are horizontal and are used to guarantee the equilibrium and shape of the plasma. Depending on their different functions and locations, different designs are required for the coils of different subsystems.

Magnets are wound in different topologies (layers, pancakes, one- or two-in-hand) using conductors (~ 100m long), which are then electrically connected through joints. Conductors are electrically in series and hydraulically in parallel. A peculiar aspect of the ITER cable-in-conduit conductors (CICC) is that the superconducting strands occupy only an annular (cable bundle) region around a central channel (hole) [1], i.e. they have a dual-channel topology (see Fig.2). The purpose of the hole is mainly to provide a low impedance path for the coolant and a pressure relief volume if local heating occurs in the bundle. Supercritical helium I in forced convection is used as a coolant to guarantee that the conductor safely operates below its current sharing temperature, above which a normal zone would be initiated, possibly evolving into a quench of the coil. Thermal hydraulics therefore becomes a central issue in design and operation.

Over the last few years a significant international R&D program has been pushed forward, starting from the test of single (subsize) conductors (e.g. the QUench Experiment on Long Length – QUELL – at PSI Villigen, CH, in 1998 [2]), through the test of joints (e.g. the Full-Size Joint Sample – FSJS [3,4] – of CEA Cadarache, F, and the US Prototype – USP [5,6] – at MIT, Cambridge, USA, in 1999), to the test of large coils (such as the Central Solenoid Model Coil, CSMC [7,8], at JAERI Naka, J, in 2000, and the Toroidal Field Model Coil, TFMC [9,10], at ForschungsZentrum Karlsruhe, D, in 2001-2002) and of full-size conductors (the so-called insert coils, e.g. the CSIC in 2000, the TFCI in 2001, the Nb3Al in 2002, the PFCI in 2004) to be inserted in the high-field (~ 13T) bore of the CSMC.

NOMENCLATURE

h heat transfer coefficient (W/m^2K)
Tc superconductor critical temperature (K)
Tcs superconductor current sharing temperature (K)

SINGLE-CONDUCTOR TESTS AND ANALYSIS

In strict correspondence with the evolving needs of the experiments, the topology of the ITER (single) conductors led us first to the development of a two-fluid code, Mithrandir [11], where different thermodynamic states of the helium in the two regions can be described. Two sets of coupled Euler-like equations model the transient compressible flow of helium in bundle and hole regions, which is coupled in turn to heat conduction in the strands and in the jacket, described by different temperatures. 1D geometry along the conductor axis is assumed, taking advantage of the widely separate length scales along and across (~ 0.01m) the CICC.

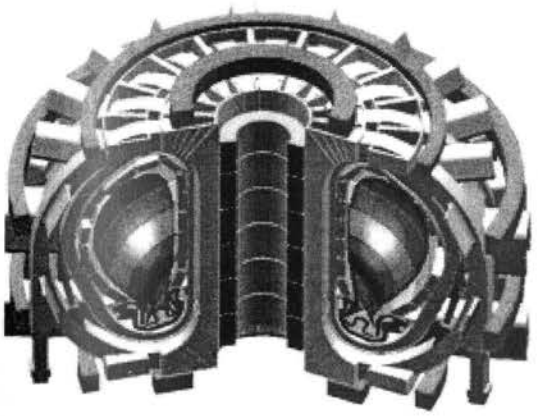

Figure 1 A sketch of the ITER tokamak project (major radius of the toroidal plasma column is ~ 6m)

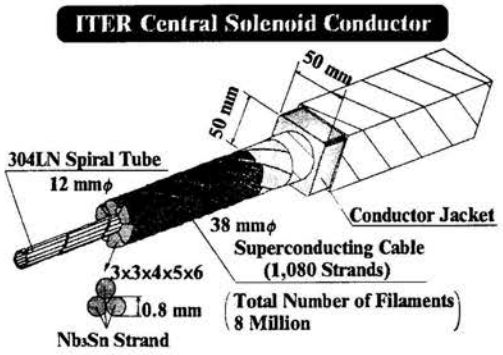

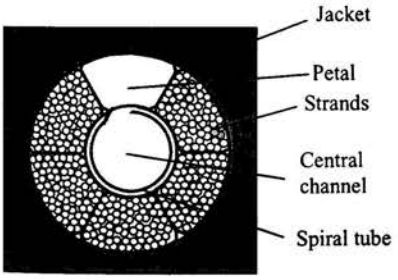

Figure 2 A sketch of the ITER CSMC conductor (notice the central cooling channel). (a) global view; (b) cross section.

The code has been validated against data from QUELL (1/6 of the total number of strands of a full-size conductor, i.e. a single "petal" without wrappings, see Fig.2), for the analysis of thermal-hydraulic transients (heat slug propagation and quench) [12-14]. The need of developing a *predictive* tool, independent of measured boundary conditions at conductor ends, led us eventually to the coupling between Mithrandir and the Flower code, which models fairly general cryogenic networks, resulting in the to-date most accurate simulations of quench propagation in a dual-channel CICC [15] (see Fig.3).

Finally, it may be worthwhile to mention at this stage that the Mithrandir model was also extended and validated to describe supercritical superfluid HeII [16], which appeared to be of interest for Superconducting Magnetic Energy Storage – a possible large-scale spin-off of fusion research.

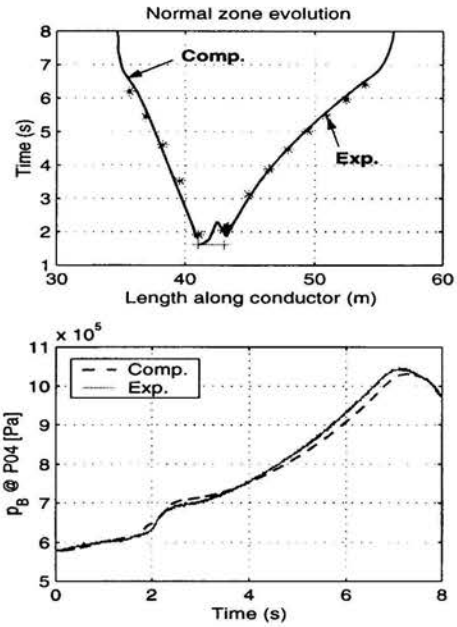

Figure 3 Comparison between experimental data and Mithrandir simulation of a quench propagation in QUELL

JOINT TESTS AND ANALYSIS

As seen above, the joints are the crucial link in order to build a magnet out of single conductors. Joints can have very different topologies (e.g. lap-type vs. butt-type, shaking hands vs. praying hands) but they all have in common the fact that in a joint current flows from the superconducting strands in one conductor, through contacts with a copper foil or sole, through the copper and finally into the strands of the other conductor, see Fig.4. This means that in the joint one always has Joule losses, although careful design (resistance ~ 1nΩ) can minimize their effect. From our point of view it should also be emphasized that the joints are, in a sense, the hydraulic gateway to a coil. In other words, since it is difficult and risky to have sensors or heaters *inside* an actual coil, any action or measurement from outside will have to be analyzed, including

the effect of the joint. As for the joints, the Mithrandir code was extended to allow for varying geometrical (e.g. helium flow area) and material properties along the length, and was validated against FSJS [17, 18] and USP [19] data.

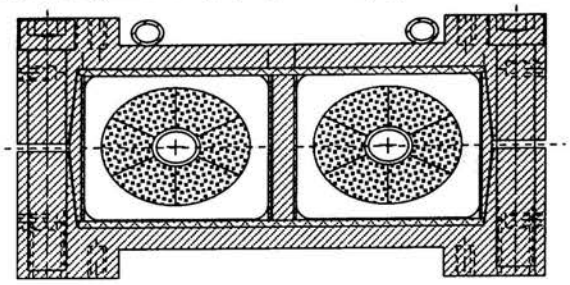

Figure 4 Cross section of the USP joint box

COIL TESTS AND ANALYSIS

The need for the treatment of a full coil, e.g. one of the ITER model coils, has required the evolution of the computational tools for the analysis of test results and for the design of new optimized conductors/joints/magnets.

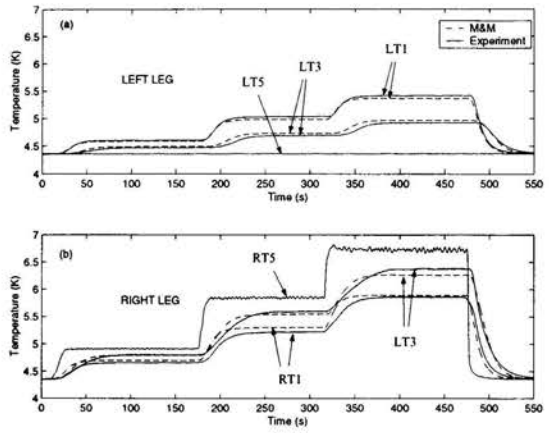

Figure 5 Comparison between experimental data and M&M simulation of the FSJS. Direct heating upstream of the right leg of the joint (as seen from the inlet temperature trace RT5) leads to heating (see downstream sensor traces LT1 and LT3) of the externally unheated (see LT5 trace) left leg, because of heat exchange through the copper sole.

Starting from Mithrandir, we have developed a new code, the Multiconductor Mithrandir (M&M) [20], for the analysis of thermal-hydraulic transients in superconducting magnets made by an arbitrary number of cables, which are hydraulically, thermally and electrically coupled together. The computational idea behind this tool is that the 3D problem of thermal-hydraulics in a coil [21] can be reduced to a series of (coupled) 1D problems for each of the conductors (defined here as the generic piece of coil between two joints). This is made possible by the widely separate time-scales for heat transfer along the conductors and across (i.e. between) conductors, the latter being much longer because of the presence of a relatively thick jacket and insulation (see Fig.2).

The validation of the novel tool has been performed first against experimental data coming from dedicated thermal-hydraulic tests that we performed on the FSJS in the SULTAN facility at PSI Villigen, CH [20], see Fig.5. Secondly, we did perform on the CSMC, see Fig.6, the first validation on a full coil, considering a part of the experimental campaign (in particular the so-called Tcs – current-sharing temperature – tests [22]), see Fig.7, which we also attended. This required the development and implementation of a rather complex model of the hydraulic circuit, see [22] for details. In all cases, it can be seen that the code shows a very good capability to simulate thermal-hydraulic transients with different time-scales in different topologies, capturing some effects that no other computational tool was previously able to reproduce, to the best of our knowledge.

The new code is also being applied in predictive fashion to the design and analysis of part of the test program of the TFMC [24].

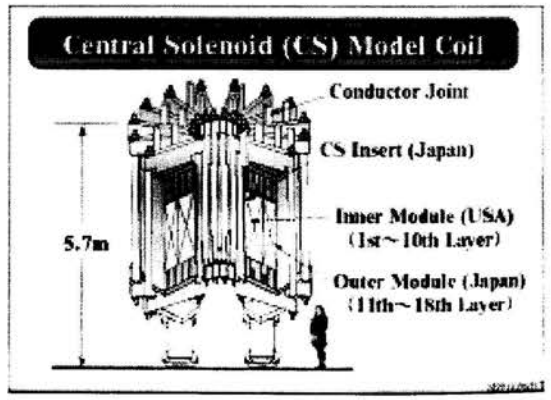

Figure 6 A sketch of the CSMC. The coil was tested in the year 2000 at JAERI Naka, J, within the frame of the ITER tokamak project, and set a number of world records for superconducting coils [23].

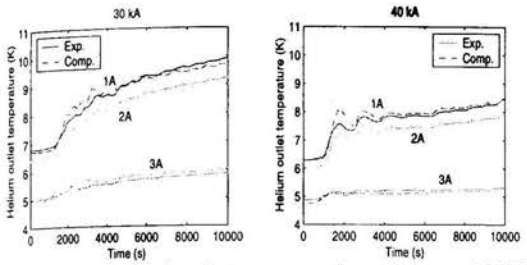

Figure 7 Comparison between experimental data and M&M simulation of the CSMC. Outlet temperatures from the innermost three layers of the coil are reported during the Tcs tests at 30kA and 40kA.

SOME OPEN PROBLEMS

Notwithstanding the relative success of the computational tools in reproducing, as reported above, a number of the experimental features in rather disparate situations, several problems are still open in the thermal-hydraulic modeling of superconducting magnets for fusion applications, and some of them will be briefly discussed here.

A number of uncertainties are present in the *friction factors and heat transfer coefficients* to be used in CICC. For friction in the central channel, correlations have been developed and tested (see, e.g., [25]) for different types of spirals delimiting the hole, while friction in the bundle region is treated as in a porous medium (pebble-bed) although the potentialities of this approach are far from being exhausted. However, analysis of recent experiments in the CSIC seems to indicate that, possibly because of Lorentz-force-induced deformation in the conductor, the mass flow rate prediction typically overestimates up to 10-20% the measured data in that case. As for the heat transfer mechanisms, a number of coefficients appear to be important in a CICC:

- Heat transfer between strands and helium ($h_{St,He}$)
- Heat transfer between jacket and helium ($h_{Jk,He}$)
- (Contact) heat transfer between strands and jacket ($h_{St,Jk}$)
- Heat transfer between helium in the bundle and helium in the central channel (h_{BH})

but none of these has been really measured up to now. Therefore, Dittus-Boelter correlations are typically used for the first two, and a fixed and somewhat arbitrary value for the third, while the last one is obtained by calibration of code results against experimental (usually heat slug propagation) data. This situation should be improved in the future both from the experimental and from the theoretical-modeling point of view.

More and more sophisticated *models of the whole cryogenic circuit* are necessary to adequately predict the behavior of a coil during transients. While this point was already assessed quantitatively during the CSMC validation [22], it might be of equal qualitative relevance. For instance, oscillations are predicted by M&M to appear in TFMC Tcs (heating) tests [24], but only a specifically dedicated portion of the experimental campaign will make clear in a few weeks if these oscillations are real or only an artifact of the still simplified model of the circuit.

A third, and very important area of present and future work is that of the *coupling of thermal-hydraulic and electromagnetic models of the conductor*. Here it should be emphasized that, while all of the modeling presented in this paper assumes a uniform distribution of the current among the strands, there is scattered evidence of non-uniform current distribution in present-day experiments. What this implies is that models are needed which can describe the evolution of the current distribution across the cable cross-section. However, this will depend on the resistances in the circuit, which in turn depend on the temperature distribution in the cable. On the other hand the evolution of the latter depends on the heat sources in the cable (e.g. AC losses), which could be adequately computed by the electromagnetic part of the model. While a few such hybrid models already exist at various levels of complexity (see e.g. [26,27]), our group is presently pursuing a systematic development effort within a multilateral collaboration of universities, ENEA and EFDA. As a first step in the direction of describing a current non-uniformity *among petals* we have already performed a thermal-hydraulic simulation of an experiment with M&M where just one of the petals was selectively heated, allowing for different thermodynamic states of the helium in each of the six petals [20].

Finally, it may be interesting to mention in closing another relevant spin-off of the present studies: we are applying the same approach to the thermal-hydraulic analysis as presented here to the study of transients in *high*-Tc conductors for power transmission applications, thanks to the fact that also there the (LN2 cooled) conductor has a dual-channel topology [28].

ACKNOWLEDGMENTS

The European Fusion Development Agreement (EFDA) and the Italian Ministry for University and Research (MURST) partially supported this work financially. LS is also recipient of a postdoctoral fellowship from Associazione per lo Sviluppo Scientifico e Tecnologico del Piemonte (ASP).

REFERENCES

[1] M.O.Hoenig, et al., "Supercritical-Helium Cooled 'Bundle-Bonductors' and their Applications to Large Superconducting Magnets", Proceedings of the 5th International Conference on Magnet Technology, 1975, 519.

[2] A.Anghel, et al., "The QUench Experiment on Long Length QUELL - Final Report", EPFL - CRPP, JAERI, MIT-PFC and SINTEZ-NIIEFA Report (1997).

[3] D.Ciazynski, et al., "Fabrication of the First European Full-Size Joint Sample for ITER", IEEE Trans. Appl. Supercond., Vol.9, pp. 648-651.

[4] D.Ciazynski, et al., "Test Results and Analysis of Two European Full-Size Conductor Samples for ITER", IEEE Trans. Appl. Supercond., Vol. 10, pp. 1058-1061.

[5] C.Y.Gung, et al., "Design and Manufacture of the US-ITER Pre Prototype Joint Sample", IEEE Trans. Appl. Supercond., Vol. 7, pp. 469-472.

[6] P.C.Michael, et al., "Qualification of Joints for the Inner Module of the ITER CS Model Coil", IEEE Trans. Appl. Supercond., Vol. 9, pp. 201-204.

[7] R.Jayakumar, et al., "Fabrication of ITER Central Solenoid Model Coil Inner Module", IEEE Trans. Appl. Supercond., Vol. 7, pp. 981-984.

[8] T.Ando, et al., "Fabrication of ITER Central Model Coil – Outer Module", IEEE Trans. Appl. Supercond., Vol. 9, pp. 628-631.

[9] E.Salpietro, "ITER Toroidal Field Model Coil (TFMC) design and construction", Fus. Technol., Vol. 34, 797.

[10] A.Ulbricht, et al., "The preparation for testing the ITER Toroidal Field Model Coil", Proceedings 20th SOFT, 1998, 739.

[11] R.Zanino, S.DePalo and L.Bottura, "A Two-Fluid Code for the Thermohydraulic Transient Analysis of CICC Superconducting Magnets", J. Fus. Energy, Vol. 14, pp. 25-40.

[12] R.Zanino, L.Bottura and C.Marinucci, "A Comparison between 1- and 2-Fluid Simulations of the QUELL Conductor", IEEE Trans. Appl. Supercond., Vol. 7, pp. 493-496.

[13] R.Zanino, L.Bottura and C.Marinucci, "Computer Simulation of Quench Propagation in QUELL", Adv. Cryo. Eng., Vol. 43, pp. 181-188.

[14] R.Zanino and C.Marinucci, "Heat Slug Propagation in QUELL. Part I: Experimental Setup and 1-Fluid GANDALF Analysis", Cryogenics, Vol. 39, pp. 585-593; Cryogenics, "Heat Slug Propagation in QUELL. Part II: 2-Fluid MITHRANDIR Analysis", Vol. 39, pp. 595-608.

[15] L. Savoldi, L. Bottura and R. Zanino, "Simulation of Thermal-Hydraulic Transients in Two-Channel CICC with Self-Consistent Boundary Conditions", Adv. Cryo. Eng., Vol. 45, pp. 697-704.

[16] R.Zanino, L.Bottura, L.Savoldi and C.Rosso, "Mithrandir+: a Two-Channel Model for Thermal-Hydraulic Analysis of Cable-in-Conduit Super-Conductors cooled with Helium I or II", Cryogenics, Vol. 38, pp. 525-531.

[17] R. Zanino, P. Santagati, L. Savoldi and C. Marinucci, "Joint + conductor thermal-hydraulic experiment and analysis on the Full Size Joint Sample using MITHRANDIR 2.1", IEEE Trans. Appl. Supercond., Vol. 10, pp. 1110-1113.

[18] R.Zanino and L.Savoldi, "Tests and Modeling of Heat Generation and Heat Exchange in the Full Size Joint Sample", Proceedings of the 18-th International Cryogenic Engineering Conference (ICEC18), pp. 363-366, Mumbai, India, 21-25 February, 2000.

[19] L.Savoldi, P.Michael and R.Zanino, "Tests and Simulation of Thermal-Hydraulic Transients in the US Prototype Joint Sample", Int. J. Mod. Phys. B, Vol. 14, pp. 3183-3188.

[20] L.Savoldi and R.Zanino, "M&M: Multi-Conductor Mithrandir Code for the Simulation of Thermal-Hydraulic Transients in Superconducting Magnets", Cryogenics, Vol. 40, pp. 179-189.

[21] R.Zanino and L.Savoldi, "Status and Perspectives of Thermal-Hydraulic Analysis of Superconducting Magnets for Nuclear Fusion Applications", presented at the 18th IAEA Fusion Energy Conference, Sorrento, Italy, October 4-10, 2000.

[22] L.Savoldi and R.Zanino, "Analysis of Tcs Measurement in Conductor 1A of the ITER Central Solenoid Model Coil using the M&M Code", Cryogenics, Vol. 40, pp. 593-604.

[23] H.Tsuji, K.Okuno, R.Thome, E.Salpietro, S.Egorov, N.Martovetsky, M.Ricci, R.Zanino, alii, L.Savoldi, W.Herz, A.Ninomiya, "Progress of the ITER Central Solenoid Model Coil Program", Nucl. Fusion, Vol. 41, pp. 645-651.

[24] L.Savoldi and R.Zanino, "Predictive Study of Current Sharing Temperature Test in the Toroidal Field Model Coil without LCT Coil using the M&M Code", Cryogenics, Vol. 40, pp. 539-548.

[25] R. Zanino, P.Santagati, L. Savoldi, A.Martinez and S.Nicollet, "Friction Factor Correlation with Application to the Central Cooling Channel of Cable-in-Conduit Super-Conductors for Fusion Magnets", IEEE Trans. Appl. Supercond., Vol. 10, pp. 1066-1069.

[26] S.A.Egorov, *et al.* "Up-grade of the CICC Stability Analysis Taking into Account a Current Imbalance Between Strands in Multistage Cables", IEEE Trans. Appl. Supercond., Vol. 10, pp. 1098-1101.

[27] N.Mitchell, "Modeling of Non-Uniform Current Diffusion Coupled with Thermohydraulic Effects in Superconducting Cables", Cryogenics, Vol. 40, pp. 637-653.

[28] T.Moore, "Powering up Superconducting Cable", EPRI Journal, Spring 1999, pp. 8-15.

HEFAT2002
1st International Conference on Heat Transfer, Fluid Mechanics, and Thermodynamics
8-10 April 2002, Kruger Park, South Africa
BC3

EXPERIMENTAL DATA OF THERMAL EXPANSION COEFFICIENT ON ARTISTIC GLASS

Cinzia Buratti* and Stefano Ortica**
* Researcher; ** PhD Student
Department of Industrial Engineering,
University of Perugia,
Via G. Duranti, 1/A-4, 06125 Perugia,
Italy
E-mail: cburatti@unipg.it

ABSTRACT
Building materials and components are often exposed to thermal stresses; in the long run this could be harmful. Effects on fragile materials such as glass could be significant, because they may break if subjected to quick or high fluctuations in temperature. It is a worrying problem if the glass is a work of art. The window surface, irradiated by sunlight, suffers different thermal stresses, depending on the color of the glass elements. Then daily thermal stresses of our typical climate have been evaluated and reproduced in a climatic room where ten glass samples, typically used for artistic window restoration, have been put inside and the thermal expansion coefficient has been evaluated.

INTRODUCTION
The conservation of artistic windows is very important due to the presence, especially in Italy, of numerous historical glasses in all the major Basilicas or Cathedrals of the world. These works of art play a dominant role in iconographical decoration. The causes of glass deterioration haven't only chemical origin; the glass is in fact subject to solar radiation, so they are subject to temperature stress on the surface, with different stress and strain in several points. Moreover the glass is embedded in its original chassis that doesn't allow for thermal expansion, causing the glass to bend until it breaks.
A quantitative evaluation of such phenomena is the aim of this paper; so measurements of thermal strain have been carried out on ten glass samples furnished by a restoration laboratory in Rome and the coefficients of linear thermal expansion have been calculated. An experimental apparatus and a measurement methodology of the deformations have been developed. The strain measurements have been carried out with electrical photoengraving strain gauges; the strain gauge is glued to the surface of a sample; when it is stressed, the correspondent strain is transmitted to the grid causing an electrical resistance variation. Two *twin* strain gauges have been employed for each measurement, one glued on to the sample, the other one on a reference material, the thermal expansion coefficient of which is known. In such a way, considering the difference between the thermal expansion of the sample and the one of the reference material, it is possible to eliminate any systematic error due to the thermal expansion of the strain gauge.
Some indications about the measurement methodology have been supplied by Technical Note TN 513-1 [1], others by ISO 7991 [2]; the measurement uncertainty evaluation conforms to UNI CEI ENV 13005 [3]. [1] has been used as a guide for the choice of the strain gauge, its connections, the preliminary operations before the strain measurements (such as the stability of the strain gauge signal, the elimination of the residual stresses, etc.); the characteristics and the precision of the measurement instrumentation, temperature uniformity in the climatic room and inside the samples have been also defined. [2] refers to the employment of the dilatometer, therefore it has been only employed to define the coefficient of the linear thermal expansion. When evaluating the measurement uncertainty [3], the *a priori* procedure calculation is employed, based on the uncertainties in the parameters measured for the calculation of the coefficient of linear thermal expansion.

NOMENCLATURE
F gain factor of the strain gauge (-)
L length (m)
R electrical resistance (Ω)
T temperature (°C, K)
T time (s, h)

Greek Letters
α coefficient of linear thermal expansion ($°C^{-1}$, K^{-1})
β_G thermal coeff. of resistivity of the grid material ($°C^{-1}$, K^{-1});
ΔL variation of length (m)
ΔR variation of electrical resistance (Ω)
ΔT variation of temperature (°C, K)
$\Delta\varepsilon$ strain variation between sample and reference material (-)
ε deformation (-)

Subscripts

G grid
R reference
S sample

EXPERIMENTAL METHOD

Facility

The experimental apparatus (Fig.1) is composed of a climatic room Mazzali mod. C33045, which allows control of temperature (-40 °C ÷ +150 °C) and relative humidity (15% ÷ 100%) in a volume of approximately 0.3 m^3; the glass samples with the electrical strain gauges are placed in the climatic room.

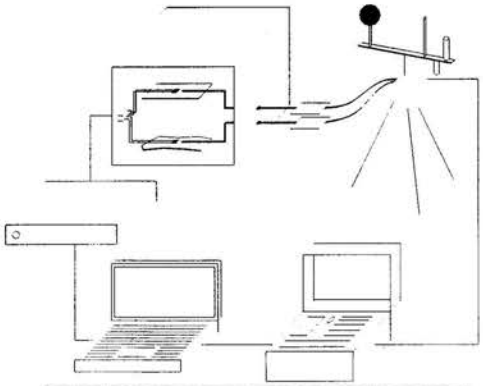

b)

Figure 1: Measurement facility: (a) scheme, (b) view. *1) Climatic room; 2) Multi-channel Transducer Spider 8; 3) PC; 4 and 5) Microclimate acquisition system TCR Tecora; 6) Reference bar with strain gauge and surface temperature probe; 7) glass sample with strain gauge and surface temperature probe.*

The strain-gauges are the Micro-Measurements type, series EA-06-125MG-120, produced by Measurements Group (Fig. 2). They are made up of a grid of laminated metal glued onto a support of plastic material; they are sensitive and precise in the temperature range -75°C ÷ +175°C. The number of fatigue cycles depends on the effort value that has been reached when measuring the deformation: 10^8 cycles at 1200 μm/m; 10^6 cycles at 1500 μm/m; 10^5 cycles at 1800 μm/m; 10^4 cycles at 2800 μm/mm for unidirectional solicitations of compression or traction. The gain factor, defined as the ratio between the electrical resistance variation $\Delta R/R$ and the correspondent variation of length $\Delta L/L$, is 2,045 ± 0.5% at 24°C; the cross-sectional sensitivity considers the lateral contraction of the grid and it is about +0,9 ± 0.2% at 24 °C.

In order to eliminate the error due to the thermal expansion of the strain gauge grid we employ two of them, one glued on to the sample, the other is glued on a reference material with a low value of α: a silica-titanium bar has been employed, with $\alpha = 0.03 \times 10^{-6}$ °C^{-1}. The two strain gauges are of the same type and are made by the same manufacturing processes. If high accuracy is required, *twin* strain gauges EA-06-125MG-120 are employed; they are sold coupled and are separated when employed (Fig. 2).

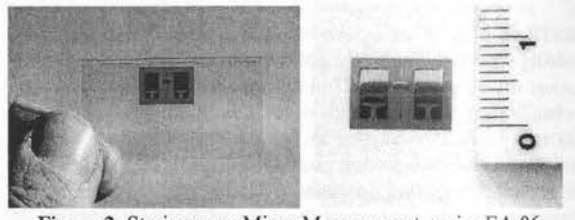

Figure 2: Strain gauge Micro Measurement, series EA-06-125MG-120

The strain gauge signal yields the value of Δε; it is recorded by a multi-channel transducer SPIDER 8, equipped with 8 channels for the acquisition of electrical resistance, current, voltage. It is connected to a Personal Computer for data storage and analysis by means of software Catman 2.1. At the same time, the surface temperatures of the sample and of the silica-titanium bar are measured by two NTC (Negative Temperature Coefficient) sensors (accuracy ± 0.04 °C); each one has a purposely realized electronic interface card and transmits the signal to a microclimate data acquisition system TCR Tecora, with optional channels for electrical signals (voltage up to 2500 mV). A tarature curve has been evaluated to transform the electrical voltage in the corresponding value of temperature. The sensors are connected to the sample and to the reference bar by a heat conducting paste. The data of surface temperature are stored and analysed by a PC.

Experimental Procedure

The first step of the experimental procedure is to verify the stability of the strain gauge signal. In the climatic room the temperature is kept constant (24 °C) for three hours, to promote thermal equilibrium between the sample and the air temperature; during the next three hours, the strain and the surface temperature of a glass sample and of the silica-titanium bar are recorded. In one of the first tests, the surface temperature of the reference bar varied between 23.7 °C and

23.8 °C; the surface temperature of the sample glass varied between 24.2 °C and 24.3 °C. The corresponding strains were in the range $-0{,}444 \cdot 10^{-6}$ and $+0.444 \cdot 10^{-6}$, with maximum instantaneous variations of $\pm\ 0{,}222 \cdot 10^{-6}$ (Fig. 3), so the strain gauge stability is verified. Such verification was periodically carried out during all the measurements.

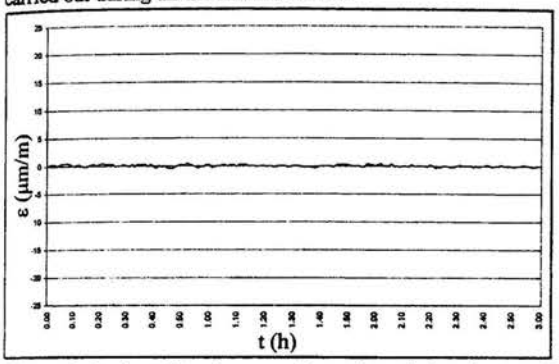

Figure 3: Strain of the glass sample vs. time during the test of strain gauge signal stability.

Temperature cycles, before the onset of the strain measurements have been executed to eliminate the residual stresses in all the components of the measurement system (glass samples, reference bar, strain gauges, wires, etc.); three cycles of temperature at least 5 °C above the maximum value and below the minimal value of the measure cycles have been realized, so the residual stress is eliminated and the possibility of repeating the test is guaranteed (normally this happens after the second or the third cycle). Three thermal cycles between 5 °C and 55 °C have been set, with a temperature gradient of 12,5 °C/h. The periods at T = constant = 5 °C and T = constant = 55 °C continue for 40 minutes; the periods with temperature gradient of 12,5 °C/h continue for 4 hours; so the total time of the three cycles is 28 hours. This temperature variation ($\Delta T = 50$ °C) is similar to the one to which glass in churches is subject; in fact the strain measurements have been carried out in the $10 \div 50$ °C temperature range. In the system calibration, the surface temperature of the silica-titanium bar varied within these ranges (Fig. 4):

I cycle: 5,1 °C - 54,5 °C ($\Delta T = 49{,}4$ °C)
II cycle: 5,1 °C - 54,0 °C ($\Delta T = 48{,}9$ °C)
III cycle: 5,2 °C - 53,6 °C ($\Delta T = 48{,}4$ °C)

The surface temperature of the glass sample varied within these ranges:

I cycle: 5,6 °C - 55,1 °C ($\Delta T = 49{,}5$ °C)
II cycle: 5,6 °C - 54,6 °C ($\Delta T = 49{,}0$ °C)
III cycle: 5,6 °C - 54,2 °C ($\Delta T = 48{,}6$ °C)

A comparison between the surface temperature of the samples and the air temperature in the climatic room shows a delay of some minutes of the sample temperatures: it is necessary for the samples to reach the thermal equilibrium with the air temperature.

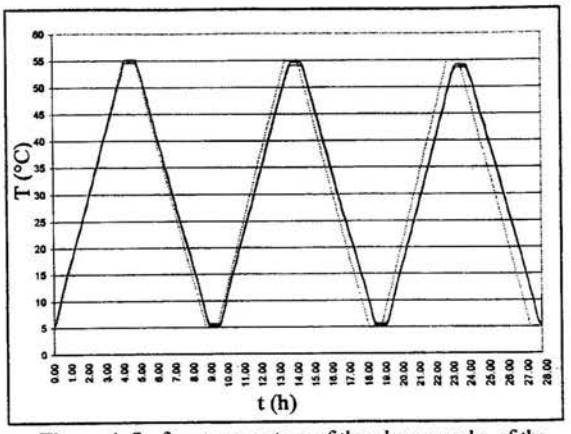

Figure 4: Surface temperature of the glass sample, of the reference bar (continuous lines) and of the air temperature in climatic room (dotted line) vs time, during the test of elimination of the residual stresses.

After verifying the strain gauge signal stability and the residual stress elimination, the measurements can begin.

A thermal cycle for the strain measurement has been chosen. It begins by maintaining the temperature at 10 °C, for 4 hours; then the temperature increases with a thermal gradient of 6,66 °C/hour, corresponding to 40 °C in 6 hours; another maintenance of the temperature at 50 °C, for 4 hours, and a decrease in temperature with a gradient of 6,66 °C/hour for 6 hours are then realized, until the temperature becomes 10 °C; finally a temperature maintainance at 10 °C for 4 hours is carried out. The cycle lasts 24 hours.

The measurement system has been tested measuring the strain of a *Saint Gobain* glass sample, with a known coefficient of thermal linear expansion (9.0×10^{-6} °C^{-1}). After eliminating the residual stresses, the strains were measured by setting up the described thermal cycle in the climatic room. Fig. 5 shows the Saint Gobain glass surface temperature vs. time; the temperature varies between 10,4 °C and 49,9 °C, so $\Delta T = 39{,}1$ °C. Fig. 6 shows the relative strain vs. time; the recorded data are:

$\Delta\varepsilon_{min} = -0{,}243 \times 10^{-6}$;
$\Delta\varepsilon_{max} = 352{,}798 \times 10^{-6}$;
$\Delta\varepsilon_{tot} = 353{,}041 \times 10^{-6}$.

The calculation procedure of the coefficient of thermal expansion of the Saint Gobain glass is carried out, by the procedure described in Data Elaboration, and a value of $9{,}054 \times 10^{-6}$ °C^{-1} is found. It coincides perfectly with the data given by the company.

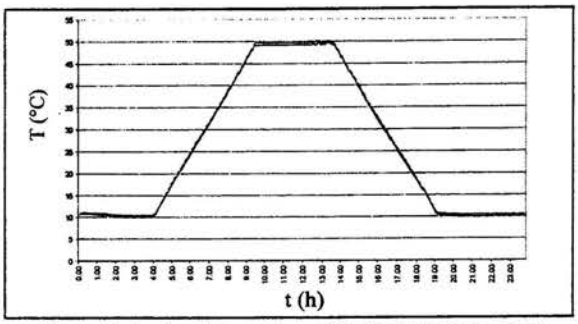

Figure 5: Surface temperature of the Saint Gobain glass (dotted line) and of the reference bar (continuous line) vs time during the strain measurements.

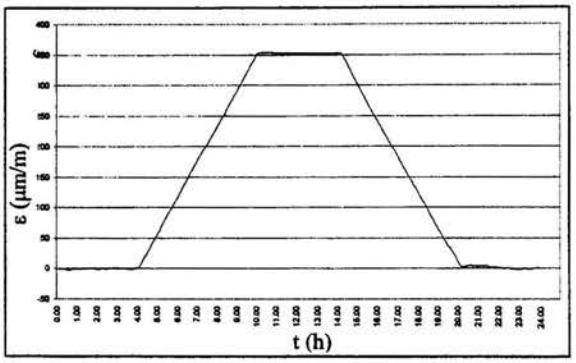

Figure 6: Saint Gobain glass strain vs time.

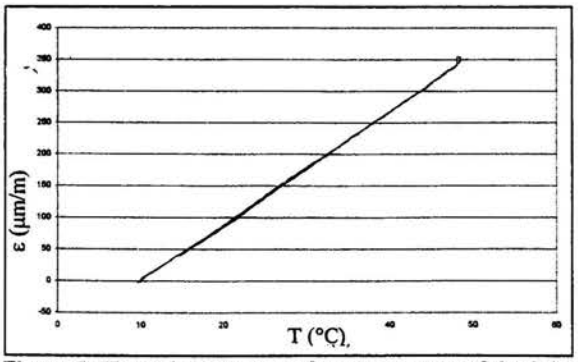

Figure 7: Thermal output vs surface temperature of the Saint Gobain glass, with increasing and decreasing temperature.

One final consideration has been made; in order to avoid measurements errors, the glass temperature must be uniform throughout the thickness of the sample or, at least, in the region where the strain gauge is glued. In order to control this temperature uniformity, the diagram of the stress vs temperature is sketched out for increasing and decreasing temperatures. The heating and cooling curves have to coincide; if the two parts of the curve are meaningfully separated to form a hysteresis loop, the temperature is not uniform in the sample thickness: in this case, two strain values correspond to the same temperature variation. Fig. 7 shows the results obtained for the Saint Gobain sample: it presents very good temperature uniformity in the thickness of the glass.

The choice of the temperature gradient in the measurement cycle is suggested by the ISO 7991: the maximum values are 300 ± 60 °C/h for increasing temperature and 120 ± 12 °C/h for decreasing temperature. A series of preliminary tests has been carried out, setting up various gradients, to evaluate the maximum gradient necessary to avoid the formation of hysteresis loops: 6.66 °C/h, 13.33 °C/h, 40 °C/h, 80 °C/h, all inferiors to those suggested by ISO 7991. Results show that with gradients over 6,66 °C/h there is a hysteresis loop between strain in the heating and the cooling; so this value of the temperature gradient has been chosen.

Data Elaboration

When a strain gauge is installed on the surface of a non stressed structure and the temperature of the material varies, the strain is transmitted to the grid of the sensor causing a variation in electrical resistance, proportional to the same deformation:

$$\frac{\Delta R}{R} = \frac{\Delta L}{L} F = \varepsilon F \qquad (1)$$

If the solicitation transmitted to the structure is a temperature variation ΔT, we can write:

$$\Delta L = \alpha L \Delta T \qquad (2)$$

From the previous two equations the following is obtained:

$$\frac{\Delta R}{R} = \alpha F \Delta T \qquad (3)$$

So the coefficient of thermal expansion of a sample (S) can be calculated simply by measuring the variation of specific electrical resistance $\Delta R/R$ and the difference of temperature ΔT, knowing the gain factor F of the strain gauge; this is due to the combination of two factors: the expansion of the glass sample and of the grid; therefore it is necessary to consider α_S, α_G, and the variation of resistivity of the grid material, by means of the term β_G. So:

$$\frac{\Delta R}{R} = [\beta_G + (\alpha_S - \alpha_G) F] \Delta T \qquad (4)$$

Combining equations (1) and (4) the following is obtained:

$$\varepsilon_{(G/S)} = [\beta_G / F + (\alpha_S - \alpha_G)] \Delta T \qquad (5)$$

in which $\varepsilon_{(G/S)}$ is the thermal output of the strain gauge glued over the sample. Using a second strain gauge glued to a reference bar, (5) can be rewritten:

$$\varepsilon_{(G/R)} = [\beta_G / F + (\alpha_R - \alpha_G)] \Delta T \qquad (6)$$

Subtracting member to member equation (6) from equation (5):

$$\alpha_S = \alpha_R + \Delta\varepsilon / \Delta T \qquad (7)$$

In equation (7) α_R is the coefficient of thermal expansion of the material that constitutes the silica - titanium bar, supplied by the Corning Glass Company (Corning NY 14831); in the range of temperatures -45 °C + 175 °C it is $0.03 \times 10^{-6} \pm 0.03 \times 10^{-6}$ °C^{-1}. ΔT is the measured value by surface temperature probes on the samples. The value of $\Delta\varepsilon$ is supplied directly by the acquisition system, which gives the electrical resistance variation as a strain; the measurement of the electrical resistance variation is carried out by a Wheatstone bridge electrical circuit, where two branches are constituted by the two *twin* strain gauges, whereas the others are simulated by the Spider 8.

RESULTS

The glass samples have been classified according to their surface characteristics; they are described in Tab. 1. Two of the samples (n. 9 and n.10) have been subjected to chemical analysis; the results show that, except for the calcium oxide absence, they can be considered sodium - calcium glasses. As an example, in Fig. 8 (a, b, c) the results related to the glass sample n. 4 are shown. In particular, in Fig. 8a) the surface temperature trend, in function of time, is shown: variation ΔT is about 38.1 °C. In Fig. 8b) the relative strain is reported: 381.6 μm/m. In Fig. 8c), finally, the strain trend vs the increasing and decreasing temperature are shown; there is no hysteresis loop, so the hypothesis of temperature uniformity throughout the thickness of the sample is verified. The calculation carried out with these data gives $\alpha_4 = 10{,}05 \times 10^{-6}$ °C^{-1}.

In order to verify the reliability and the possibility of repeating the results, two or three tests in the same conditions have been carried out; for every sample the final value of α is the average value of the different tests. For the sake of brevity, the extensive results relate to the other samples are not reported; a synthesis of all the measurements is reported in Tab. 1. The results show that the values of α vary between $8{,}4 \times 10^{-6}$ °C^{-1} and $10{,}3 \times 10^{-6}$ °C^{-1}. The higher values relate to glasses 5 and 6 (10.21×10^{-6} °C^{-1} and 10.29×10^{-6} °C^{-1}); it is due to the particularity of the two glasses: the red coloration of glass sample 5 is obtained in bath and not by adding metallic oxides in the paste; the brown color of glass sample 6 is due to a coloration only on one surface, realized with the technique called *grisaglia*.

The measurement uncertainty has been finally evaluated [3]; the measurement uncertainty of the different parameters has been estimated and the law of propagation of the uncertainty has been applied to equation (7). The uncertainty on α_R is equal to $\pm 0.03 \times 10^{-6}$ °C^{-1}, the one of ΔT is ± 0.84 °C, the one of $\Delta\varepsilon$ is approximately 0.08×10^{-6}. The measurement uncertainty obtained for α_s varies between 0.17 and 0.21×10^{-6} °C^{-1} for the different samples; it is in any case about 2% (Tab. 2). As regards the deformation measurements, the uncertainty is 0.02%.

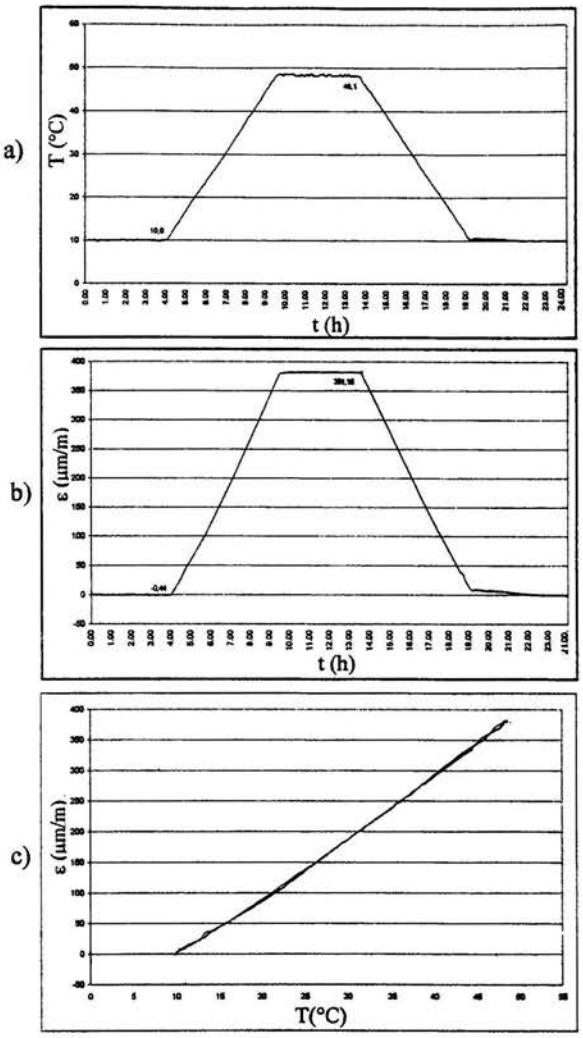

Figure 8: Surface temperature (a) and strain (b) vs time and strain vs temperature (c) of the glass sample n. 4.

CONCLUSION

The degradation of the artistic glass depends not only on the chemical actions due to air pollution and atmospheric agents, but is also due to the temperature stresses caused by solar radiation; they can be different from point to point of the glass, because of the

Table 1: Glass samples characteristics and experimental results.

Sample n.	*Colour*	*Thickness (mm)*	*ΔT (° C)*	*Δε*	*α (° C⁻¹)*
1	violet	2,71	38,1	$337{,}99 \times 10^{-6}$	$8{,}90 \times 10^{-6}$
2	transparent	2,71	38,1	$343{,}87 \times 10^{-6}$	$9{,}05 \times 10^{-6}$
3	violet	3,74	38,5	$326{,}92 \times 10^{-6}$	$8{,}50 \times 10^{-6}$
4	green	2,84	38,1	$381{,}60 \times 10^{-6}$	$10{,}05 \times 10^{-6}$
5	red	2,65	36,7	$373{,}50 \times 10^{-6}$	$10{,}21 \times 10^{-6}$
6	brown	1,96	36,7	$376{,}71 \times 10^{-6}$	$10{,}29 \times 10^{-6}$
7	blue	3,96	37,2	$322{,}67 \times 10^{-6}$	$8{,}70 \times 10^{-6}$
8	blue	3,39	37,4	$316{,}41 \times 10^{-6}$	$8{,}49 \times 10^{-6}$
9	yellow	3,52	36,7	$374{,}28 \times 10^{-6}$	$9{,}86 \times 10^{-6}$
10	violet	2,38	35,6	$348{,}85 \times 10^{-6}$	$9{,}84 \times 10^{-6}$

Table 2: Mean strain measurements, coefficients of thermal expansion and measurement uncertainties.

α (10⁻⁶° C⁻¹)	*Sample n.*	*Δε(10⁻⁶ m/m)*	*ΔT (° C)*	*Uncertainty*	
				(10⁻⁶°C⁻¹)	*(%)*
8	8	320	40	0.17	2
9	1, 2, 3, 7	360	40	0.19	2
10	4, 5, 6, 9, 10	400	40	0.21	2

glass colours and the relative absorption coefficients for solar radiation. The Laboratories of Thermotechnical and Environmental Controls of the Department of Industrial Engineering of the University of Perugia have been involved in the preservation of works of art for a long time. In a recent work [4] an analysis of the distribution of the surface temperature and of the relative thermal stress on an stained glass window in the Cathedral of Perugia has been carried out by means of a calculation program (Ansys 5.3); results show that the thermal stresses can cause a cracking of the glass.

In the present paper a methodology to measure the deformations due to temperature stresses and to calculate the coefficient of linear thermal expansion have been developed. Ten glass samples, employed in artistic glass restoration, have been subjected to thermal stress in a climatic room; the strains have been measured and the coefficients of thermal linear expansion have been calculated. The results of the measurements, carried out by means of electrical strain gauges, show values of the coefficients of thermal expansion within 8.4×10^{-6} °C^{-1} and 10.3×10^{-6} °C^{-1}. The measurement uncertainty has been estimated following the indications reported in [3]; it is 2% circa.

The obtained values are of the same order of magnitude of those classified in Literature as sodium - calcium glass; a chemical analysis, made on two of the ten samples, shows they can be considered sodium - calcium glass, a part a few chemical components. The higher values of the coefficients of thermal expansion have been obtained for the samples number 5 and number 6 ($10{,}2 \div 10{,}3 \times 10^{-6}$ °C^{-1}); their coloration is in fact obtained differently than in the other samples.

This methodology could be employed for the measurement of the thermal expansion of any kind of material. The obtained results can be employed for the simulation of the conditions of thermal stress on artistic windows with different geometrical configurations and spectral characteristics of the glasses, by means of adequate calculation programs. The same measurements, finally, can be repeated after having subjected the samples to accelerated aging in a climatic room, to estimate the influence of aging on the properties of thermal expansion of this kind of glass.

ACKNOWLEDGEMENTS

The authors wish to thank Prof.A.L. Materazzi (Department of Civil Engineering, University of Perugia) for having placed the multi channel transducer Spider 8 to their disposal.

REFERENCES

[1] Technical Note TN-513-1: "Measurement of Thermal Expansion Coefficient Using Strain Gages", North Carolina, USA, 1994.

[2] ISO 7991, "Vetro. Determinazione del coefficiente di espansione termica lineare", 1987.

[3] UNI CEI ENV 13005: "Guida all'espressione dell'incertezza di misura", UNI Ente Nazionale Italiano di Unificazione, July 2000.

[4] Buratti, C.: "Analysis of thermal stress and strain on Arrigo Fiammingo's artistic window in the Cathedral of Perugia", Journal of Heat Transfer, ASME, October 2001 (in course of publication).

[5] Gottardi, V.: "Il vetro. Appunti delle lezioni di Tecnologia dei materiali e chimica applicata ", PATRON EDITORE, Bologna, 1982.

[6] Rice, P. and Dutton, H.: "Il vetro strutturale ", TECNICHE NUOVE, 1990.

[7] Smith, F.W.: "Scienza e tecnologia dei materiali", McGRAW-HILL, Milano, 1993.

[8] Feodosev, V.I.: "Resistenza dei materiali", EDIZIONI MIR, 1991.

[9] Wellinger, K.: "Caratteristiche e prove dei materiali", Volume 3, PEM ROMA, 1967.

[10] Branca, F.P.: "Misure meccaniche", ESA, 1989.

[11] UNI 10593-2: "Vetro per edilizia. Vetrate isolanti. Prove di invecchiamento, misurazione della penetrazione del vapor d'acqua e requisiti ", UNI Ente Nazionale Italiano di Unificazione, July 1996.

HEFAT 2002
1st International Conference on Heat Transfer, Fluid Mechanics, and Thermodynamics
8-10 April 2002, Kruger Park, South Africa
DG4

PHYSICAL PROPERTIES OF NATURAL REFRIGERANTS

G.J. Doornbos*, C.H.M. Machielsen**, M. Janssen***
*Research & Development Department, Apparatenfabriek Helpman B.V.,
PO Box 44, 9700 AA Groningen, The Netherlands
**Delft University of Technology, Delft , The Netherlands; corresponding author
e-mail: c.h.m.machielsen@wbmt.tudelft.nl
***Re/Gent, Helmond, The Netherlands

ABSTRACT

In The Netherlands, a consortium of scientific institutes and companies has started a project to compile physical data of Natural Working Fluids, which include pure, mixed and secondary refrigerants. The information gathered contains data on thermodynamics (critical values, saturation properties, PVT functions), transport properties (e.g. viscosity, conductivity), heat transfer and pressure drop, and various info on the application (compatibility, safety).

The information will be presented in a digital format, to facilitate the engineering of refrigeration and heat pump systems. Generalised functions on all properties gathered will be available to use in computer programs. A ready-to-use cycle calculation will complete the comparison of the natural refrigerants available.

Key words: natural refrigerants, physical properties, environmental friendly

INTRODUCTION

The KANS initiative

Ever since the Montreal Protocol, a growing awareness is present to preserve the earth's atmosphere. Both worldwide and nationally, a common understanding has grown under scientists and engineers, that naturally available substances have less chance to degrade the earth's environment. Under the name KANS (Knowledge institute for Application of Natural working Substances), a group of Dutch people from companies and institutes (see list below) have joined to encourage the use of these natural working fluids.

Meanwhile, in the Netherlands, a governmental program ROB (Reduction of Greenhouse Gasses) was launched as a response to the Kyoto Protocol. Within this program, the KANS initiative deploys various projects, from children's awareness to testing facilities for refrigerants. One of the projects is described here: to compile available physical properties of natural refrigerants.

Compilation of properties of natural working fluids

It was noticed that various physical properties of natural refrigerants are not generally available. However, much information should exist, as these refrigerants were very important before the introduction of the CFC's in the 1930s. Apart from ammonia, which is only being applied by a restricted group of enterprises, the knowledge about natural refrigerants was not readily available anymore.

Now modern refrigerants, like CFC, HCFC's, HFC's, and their mixtures, are very well known, partly from the effective efforts of chemical companies, as they benefit from the sale of these halogenated hydrocarbons. Natural refrigerants however, have not been treated this way. This is exactly the purpose of this project: to ease the re-introduction of natural refrigerants by compiling the useful properties for the refrigeration industry in an easy and accessible way. Doing so, one of the obstacles in introducing the natural refrigerants in the general field of refrigeration industry is removed.

PROJECT DESCRIPTION AND LIMITATIONS

General objective

The general objective for this project is to facilitate the optimal engineering of refrigeration systems with natural refrigerants. To do this, the end result of this project consists of formulae for calculation of physical properties available as DLL files. Together with REFPROP data, these files can be used within a user defined EXCEL based program.

Beside this, a program is made to access physical, toxic and safety data. A simple cycle program for comparison of the various substances will complete the project.

Approach

The project was split up in 5 phases to ease the work as a team.

1. Quick Scan (to investigate in-house information available at all project partners),
2. Format (to decide the format in which the information will be presented),
3. Analysis (to analyse in-house and requested data and presenting it in the desired format),
4. Distribution (to distribute data to other partners)
5. Reports and publication

This approach worked fairly well, although the phase 3 (analysis) was underestimated in workload.

Selection of refrigerants

First, a choice had to be made for selecting the typical refrigeration systems. It was decided only to investigate compression (primary) systems and secondary systems. Absorption systems like ammonia/water have been skipped because of their complexity (one additional degree of freedom) and their (still) limited application.

Secondly, it had to be decided upon which refrigerants should be selected. The refrigerants have been selected by means of a ranking of all possible substances. After discussion it was decided to select the ones below on grounds of present use now (e.g. propane) or potential in the future (e.g. carbon dioxide). See the selected lists in table 1 and 2.

General data used

As there was no intention to produce any data that is already available in literature, it was decided to apply the data from REFPROP 6.0 (NIST 1998). However, some substances have (up to now) not been incorporated in this version. So REFPROP 5.1 was applied for the missing ones (e.g. dimethylether, n-pentane, iso-pentane). For the secondary fluids, the data of Melinder (Melinder 1997) was adopted, as this work contains already a lot of the most common brines. Other brines that were missing, were added with commercially available formulae and data (see list of contributers at the end of this article).

Constraints to the choices we made

To be able to compare different refrigerants, a simple DX cycle is calculated (see below). Heat transfer and pressure drop must be known within the cycle. For single phase flow, the commonly used Gnielinski model for heat transfer was used (VDI, 1988). For pressure drop, the Blasius model for friction in smooth tubes was taken.

For two-phase flow many (complicated) models are known. Nevertheless, only formulae have been selected, that have been developed for refrigerant formulation in terms of their physical properties. To reduce complexity (for the sake of this project), common models were accepted like the Gungor & Winterton model for heat transfer (Gungor and Winterton 1987). In the future, we hope to extend these fairly rough estimations.

Normally, it is sufficient to have only sub critical data of refrigerants. For CO2 however, many applications have been described that are super critical. However, for simplicity reasons in this project, this area is not covered up to now.

For secondary fluids, we have chosen so far not to incorporate mixtures of substances.

RESULTS

Gathered data

For each refrigerant several data are required. To have a good overview of all the data, each of the refrigerants have been assigned to one of the project partners. All gathered data from all the partners and other sources have been concentrated at the assigned partner. To do this, the partners have (in line with the "Quick scan") filled in a proceedings, software and book reference list of all information in their possession.

Once each partner had all the gathered information, the data had to be analysed to assess the usefulness. When the data are enough, a *function list* of that refrigerant property can be checked "Y" for enough. A completed *function list* for ammonia is given in table 3 as an example at the end of this article.

The *function list* is a set of functions applicable to each of the properties investigated. It is divided in groups concerning a general description (molar mass, CAS number, ODP, GWP etc.), application (flammability, toxicity, safety and compatibility), thermodynamic state properties (critical data, saturation, PVT functions, enthalpy and entropy) and transport data (specific heat, viscosity, conductivity and surface tension). To ease the calculation of heat transfer and pressure drop, the Reynolds, Prandtl and Nusselt number can be calculated. For the pressure drop the friction number (according to the Blasius equation) and the dynamic pressure head can be calculated.

Once each partner has completed all of his functions lists per refrigerant, a complete overview of the whole project can be made concerning the "white spots", or missing data. As by now (June 2001), the *Wight spot list* has the form as mentioned in table 4 at the end of this table.

Table 1. Selected primary refrigerants

Group	ASHRAE	Chemical name	NBP (°C)	$T_{crit.}$ (°C)
Pure	RE-170	Dimethyl-ether	-24,0	128,8
	R-290	Propane	-42,0	96,7
	R-600a	Iso-butane	-11,6	134,7
	R601x	Iso-pentane	27,8	187,4
	R-601 (NC5)	n-pentane	36,2	196,4
	R-717	Ammonia	-33,3	132,3
	R-744	Carbon dioxide	-78,4	31.1
	R-1270	Propylene	-47,7	92,4
Mixed	R-290/R-600a (50/50)	Propane/iso-butane	-33	115
	R-601/R-601a (50/50)	n-pentane/iso-pentane	-17	58
	R-170/R-290	Ethane/propane	-49	92

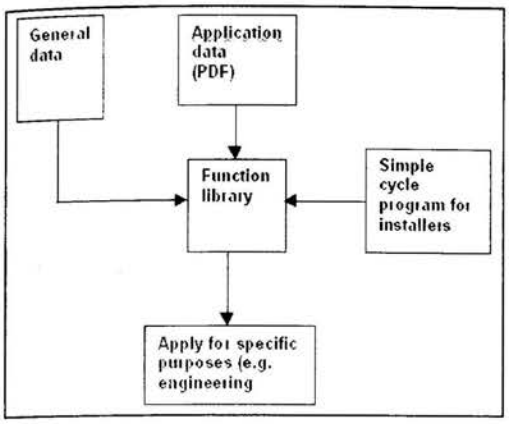

Fig. 1. Overview of the main units of the software program

Architecture of the software program

As the software program is the main output of this program, it contains all of the compiled data. To make this happen, the main architecture contains four units:

- A remote set of data from other sources, which is consulted by the function library.
- A library of help files, containing application data (i.g. safety and compatibility).
- A function library of all the data gathered in this project. This library can be consulted from an external user program (via DLL's), or by the program itself, when the user is searching particular data.
- A simple DX refrigeration cycle calculation program.

See figure 1 for an overview of the main units. By means of this architecture, the user may consult the function library, use the data within another user defined program, or is able to design a simple refrigeration system. The results can be compared between all the natural refrigerants with respect to pressures, temperatures, dimensions, energy consumption and environmental impact.

Layout of the program

To give an idea of the layout of the program, one of them is given in figure 2.

It can be observed that the program is easy to use, especially for the enterprises, which do not employ scientifically educated personnel.

Table 2. Selected secondary refrigerants

Group	Chemical	Brandnames
Aqueous	Ice slurry	
	Ethyl alcohol	
	Methyl alcohol	
	Glycerol	
	Ammonia	
	Ethylene glycol	Dowcal 10, Antifrogen N
	Propylene glycol	Dowcal 20, Antifrogen L
	Potassium carbonate	
	Potassium acetate	Tyfoxit 1, xx
	Potassium formate	Freezium, Hycool, Tyfoxit F, Antifrogen KF
	Sodium chloride	
	Magnesium chloride	
	Calcium chloride	
Non-aqueous	Diethyl benzene	Dowtherm j
	Hydrofluoroether	HFE7100
	Polydimethylsiloxan	Baysilon KT3, Sylthern XLT
	Terpene from citrus oil	D-limonene

Table 3. Function list of ammonia, as an example of all the refrigerants investigated

Functionlist Ammonia (NH_3)			
	Description	**Function call**	**Sources**
S	Molar mass	K_Molmas(Refr)	iiar92c, ammo7, llore94b, lind94
S	Freezing temperature (only secondary refr.)	K_Tfreezing(Refr, X)	ammo7, iiar92c
S	Brand names	K_BrandName(Refr)	
S	CAS number	K_CAS(Refr)	iiar92d (7664-41-7)
S	Chemical formula	K_ChemFormula(Refr)	NH3
S	Structural formula (or drawing)	K_Structural(Refr)	
	Flammability		
S	Lower flammability limit	K_LFL(Refr)	iiar92c, ammo7, lind94, carl96, iiar92d
S	Higher flammability limit	K_HFL(Refr)	iiar92c, ammo7, lind94, carl96, iiar92d
S	Ignition temperature	K_T_Ignition(Refr)	lind94, cpr13-2(pag22), iiar92c
	Toxicity		
S	Max allowable concentration (Mac-value)	K_MAC(Refr)	paul94a, ammo7,
S	General toxicity information	K_Toxicity(Refr)	cpr13-2, iiar92d, lind94
	General Safety		
S	Precautions in handling and storage	K_Handling(Refr)	CPR13-2,
S	Safety classification (A1..etc)	K_SafetyClass(Refr)	CPR13-2
	Compatibility		
S	General compatibility info	K_Comp(Refr)	CPR13-2, knab97, ammo-22, halo
	Critical values		iiar92c
	Critical temperature	K_tc(Refr)	iiar92c, ammo7, cpr13-2, lind94
	Critical pressure	K_pc(Refr)	iiar92c, ammo7, cpr13-2, lind94
	Critical specific volume	K_vc(Refr)	iiar92c,
	Saturation properties		
	Saturation pressure	K_psat(Refr, X, T, phase)	iiar92a, ammo8, refprop6.0,
	Saturation temperature	K_Tsat(Refr, X, p, phase)	iiar92a, ammo8, refprop6.0,
	PVT functions		
S	Specific volume,	K_v_Tp(Refr, X, T, p, phase)	refprop 6.0, iiar92a, ashr89.
	Temperature as f(p,v)	K_T_pv(Refr, X, p, v , phase)	refprop 6.0, iiar92a, ashr89.
	Pressure as f(T,v)	K_p_Tv(Refr, X, T, v, phase)	refprop 6.0, iiar92a, ashr89.
	Enthalpy functions		
	Enthalpy,	K_h_Tp(Refr, X, T, p, phase)	ashr89, refprop 6,0, ammo8.(tables)
	Temperature as f(p,h)	K_T_ph(Refr, X, p, h, phase)	ashr89, refprop 6,0, ammo8.(tables)
	Entropy functions		
	Entropy,	K_s_Tp(Refr, X, T, p, phase)	refprop 6.0, ash89,
	Temperature as f(p,s)	K_T_ps(Refr, X, p, s , phase)	refprop 6.0, (ash89 ?)
	Specific heat		
	Vapour heat capacity at constant volume	K_cv_Tp(Refr, X, T, p)	ashr89, refprop 6.0
S	Heat capacity at constant pressure	K_cp_Tp(Refr, X, T, p, phase)	ashr89, refprop 6.0
	Vapour velocity of sound	K_VS_Tp(Refr, X, T, p)	ashr89, refprop 6.0
	Transport properties		
S	Viscosity	K_Viscosity_Tp(Refr, X, T, p,phase)	ashr89, refprop 6.0, wiel72
S	Heat conductivity	K_Conductivity_Tp(Refr, X, T, p, phase)	ashr89, refprop 6.0, wiel72
	Surface tension of the liquid	K_SurfaceTension_T(Refr, X, T)	ashr89b, refprop 6.0
	Heat transfer and friction loss		
S	Reynolds number	K_Reynolds(Refr, X, T, p, u, d)	GUNGOR & WINTERTON
S	Prandtl number	K_Prandtl(Refr, X, T, p)	
S	Nusselt number	K_Nusselt (Refr, X, T, p, phase, Re, Pr)	ohad95, shah76, gung87, gung86
	Pdyn(rho, v) and Ksi		

Notes:

- X is composition of primary refrigerants or concentration for secondary fluids
- phase is the fluid state indication, 1 = liquid, 2 = vapour
- u is velocity of fluid
- All functions are related to primary refrigerants, the functions with an S in the first column also relate to the secondary refrigerants

Table 4. White spot list

White Spot List	ammonia	CO2	CARE-30	Pot.form	Pot.form/Pot.acet	Pot.acet	MgCl2	Pot.Carbonate	CaCl2	1,2-prop.glycol	Ethylene Glycol	Propane	Isobutane	NH3-Water	Polydimethylsiloxan	Glycerol-alcohol	Methyl-alcohol	Ethyl-alcohol	D-limonene	Hydrofluorether	Gilotherm d 12	Dowtherm J	Ice Slurry	Propylene	N-pentane	iso-pentane	dimethyl ether	n-pentane/iso-pentane
Description																												
$ Molar mass	Y	Y	Y	Y	Y	Y	Y	Y	Y	Y	Y	Y	Y	N	N	Y	Y	Y	Y	Y	N	N	Y	Y	Y	Y	Y	N
$ Freezing temperature (only secondary refr.)	Y			Y	Y	Y	Y	Y	Y	Y	Y	Y	Y	Y	Y	Y	Y	Y	Y	Y	N	Y	Y	Y				
$ Brand names	N	N	Y	Y	Y	Y	N		N	Y	Y	Y	Y	Y	Y	Y	Y	Y	Y	Y	N	Y	N	Y	N	N	Y	N
$ CAS number	Y	Y	Y	Y	Y	Y	Y	Y	Y	Y	Y	Y	Y	Y	Y	Y	Y	Y	Y	N	N	N	N	Y	Y	Y	Y	N
$ Chemical formula	Y	Y	Y	Y	Y	Y	Y	Y	Y	Y	Y	Y	Y	Y	Y	Y	N	Y	Y	Y	N	Y	Y	Y	Y	Y	Y	N
$ Structural formula (or drawing)	N		N	N	N	N	N	N	N	N	N	Y	N	Y	N	N	N	N	N	Y	N	Y	Y	Y	Y	Y	Y	N
Flammability																												
$ Lower flammability limit	Y	Y	Y	Y	Y	Y	Y	Y	Y	Y	Y	Y	Y	Y	Y	Y	Y	Y	Y	Y	N	Y	?	Y	Y	Y	Y	N
$ Higher flammability limit	Y	Y	Y	Y	Y	Y	Y	Y	Y	Y	Y	Y	Y	Y	Y	Y	Y	Y	Y	Y	N	Y	?	Y	Y	Y	Y	N
$ Ignition temperature	Y	Y	Y	Y	Y	Y	Y	Y	Y	Y	Y	Y	Y	Y	Y	Y	Y	Y	Y	Y	N	Y	?	Y	Y	N	Y	N
Toxicity																												
$ Max. allowable concentration (Mac-value)	Y	Y		N	N	N	N	N	N	N	N	N	Y	N	N	N	N	N	Y	N	N	N	?	Y	Y	N	Y	N
$ General toxicity information	Y	Y	Y	Y	Y	Y	Y	Y	Y	Y	Y	Y	Y	Y	Y	N	N	N	Y	Y	N	Y	?	Y	Y	Y	Y	N
General Safety																												
$ Precautions in handling and storage	Y	Y	Y	Y	Y	Y	Y	Y	Y	Y	Y	Y	N	Y	Y	N	N	N	Y	Y	N	Y	Y	Y	Y	N	N	N
$ Safety classification (A1 etc.)	Y	Y?	Y	Y	Y	N	Y	N	Y	Y	Y	Y	Y	N	N	N	N	N	Y	Y	N	N	N	N	N	N	N	N
Compatibility																												
$ General compatibility info	Y	Y	Y	Y	Y	N	N	Y	Y	Y	Y	Y	Y	Y	Y	N	N	N	Y	Y	N	Y	Y	Y	N	N	N	N
Critical values																												
Critical temperature	Y	Y	Y									Y	Y											?	Y	Y	Y	N
Critical pressure	Y	Y	Y									Y	Y											?	Y	Y	Y	N
Critical specific volume	N	Y	N									Y	Y											?	Y	N	Y	
Saturation properties																												
Saturation pressure	Y	Y	Y									Y	Y											?	N	N	N	N
Saturation temperature	Y	Y	Y									Y	Y											?	N	N	N	N
PVT functions																												
$ Specific volume,	Y	Y	Y									Y	Y											?	N	N	N	N
Temperature as f(p,v)	Y	Y	Y									Y	Y											?	N	N	N	N
Pressure as f(T,v)	Y	Y	Y									Y	N											?	N	N	N	N
Enthalpy functions																												
Enthalpy,	Y	Y	Y									Y	Y											?	N	N	N	N
Temperature as f(p,h)	Y	Y	Y									Y	Y											?	N	N	N	N
Entropy functions																												
Entropy,	Y	Y	Y									Y	Y											?	N	N	N	N
Temperature as f(p,s)	Y	Y	Y									Y	Y											?	N	N	N	N
Specific heat																												
Vapour heat capacity at constant volume	Y	Y	Y									Y	Y											?	N	N	N	N
$ Heat capacity at constant pressure	Y	Y	Y	Y	Y	Y	Y	Y	Y	Y	Y	Y	Y	N	Y	Y	Y	Y	Y	Y	N	N	Y	Y	N	N	N	N
Vapour velocity of sound	Y		Y									Y	Y											?	N	N	N	N
Transport properties																												
$ Viscosity	Y	Y	Y	Y	Y	Y	Y	Y	Y	Y	Y	Y	Y	N	Y	Y	Y	Y	Y	Y	N	Y	Y	Y	N	N	N	N
$ Heat conductivity	Y	Y	Y	Y	Y	Y	Y	Y	Y	Y	Y	Y	Y	N	Y	Y	Y	Y	Y	Y	N	Y	Y	Y	N	N	N	N
Surface tension of the liquid	Y	Y	Y									Y	Y											?	N	N	N	N
Heat transfer and friction loss																												
$ Reynolds number						Y	Y	Y	Y	Y	Y			Y	Y	Y	Y	Y	Y	Y	N	Y	Y	Y				
$ Prandtl number						Y	Y	Y	Y	Y	Y			Y	Y	Y	Y	Y	Y	Y	N	Y	Y	Y				
$ Nusselt number	Y	Y	Y	Y	Y	Y	Y	Y	Y	Y	Y	Y	Y	Y	Y	Y	Y	Y	Y	Y	N	Y	Y	Y				
Pdyn(rho, v) en Ksay((diverse formules y met Re, x, en coefficienten) ??																												

Notes
- x is composition of primary refrigerants or concentration for secondary fluids
- phase is the fluid state indication, 1 = liquid, 2 = vapour
- u is velocity of fluid
- All functions are related to primary refrigerants, the functions with an $ in the first column also relate to the secondary refrigerants

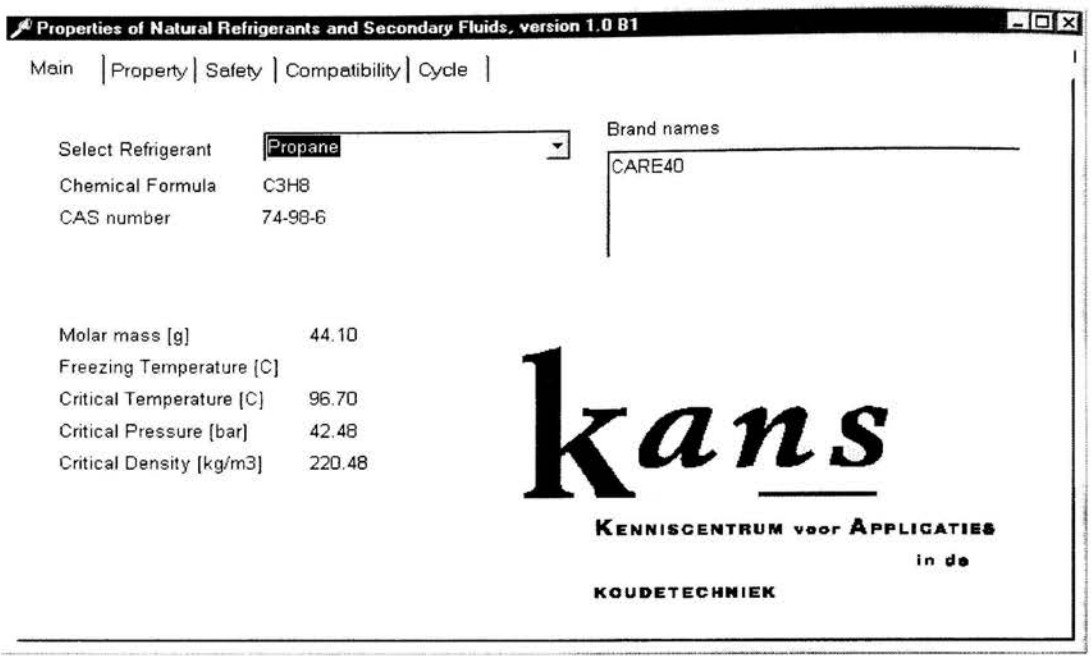

Fig. 2. Main screen of the software program

CONCLUSION AND OUTLOOK

A fairly complete compilation of data on natural refrigerants is needed. This project is now under progress, and should be ready in the spring of 2002. As it has not been finalised yet, any comments on the choices or any response in general are still welcome and can be incorporated.

Such a project encounters many difficulties. Many constraints and limitations must be accepted to keep the project manageable. Apart from this, many 'white spots' occur in the compilation, as (within the timeframe) it was not possible to find or measure missing information.

In a future project, this constraints, limitations and 'white spots' can be minimised. It would incorporate the super critical stages of CO_2, other heat transfer functions (e.g. to be able to dimension liquid coolers and liquid-cooled condensers), more elaborate airside heat transfer and mass transfer (moisture) and a safety design algorithm for hydro carbon systems (e.g. according to EN 378).

It might be necessary to include measurements when a thorough search in literature does not fully satisfy the need for information.

For secondary fluids, a mixing algorithm can be included to calculate mixtures as well. Examples of mixtures are brandnames as Temper and Pekasol (both potassium acetate and formate mixtures).

ACKNOWLEDGEMENTS

The authors would kindly thank their sponsor, Novem, for their contribution. Also the management role of the Dutch branch organisation, NVKL proved well for their encouraging guidance in this project. Not in the least, we are very grateful to individual researchers, brine manufacturers, universities and scientific institutes for their help, information and support for this project.

REFERENCES

[1] ASHRAE Handbook (1989), Fundamentals, ASHRAE Atlanta

[2] Doff, M. (2001), Waarom natuurlijke koudemiddelen? (dutch), Helpman B.V., Internal report

[3] Gungor K.E. and Winterton R.H.S., Simplified general correlation for saturated flow boiling in tubes and annuli, Chem Eng Res Des, March 65, Mars, pp 148-155

[4] Melinder Å (1997), Thermophysical properties of liquid secondary refrigerants, IIR Paris

[5] NIST (1998) Thermodynamic and Transport Properties of Refrigerants and Refrigerant Mixtures – REFPROP, Versions 5.0 and 6.01, U.S. Department of Commerce, Gaithersburg Maryland

[6] Pîrvu, C. M. (June 2001), Thermodynamic and Physical Properties of Natural Refrigerants, Delft University of Technology, Internal report KK1169,

ORGANISATIONS INVOLVED IN "KANS"

Apparatenfabriek Helpman BV*, Delft University of Technology *, Ecozone BV*, Grenco BV, Interko BV*, KoelCombi BV, Meko BV, Novem*, NVKL*, Re/Gent BV* and TNO.

The partners linked to this Properties Project have been marked with *

HEFAT2002
1st International Conference on Heat Transfer, Fluid Dynamics and Thermodynamics
8 – 10 April 2002, Kruger National Park, South Africa
MM4

THERMAL EMITTANCE OF THIN FILMS FOR MULTILAYER INSULATION SYSTEMS

M.Misale, C.Pisoni and G.Tanda

Dipartimento di Termoenergetica e Condizionamento Ambientale (DITEC)
University of Genoa
via all'Opera Pia 15/a
I 16145 Genova, Italy

ABSTRACT

Thermal radiation properties of solid films play an important role in many technological applications such as low-temperature insulation systems, solar collectors and thermal control of space vehicles. In this paper, an investigation of spectral normal and total normal emittance of thin coating layers on a metal substrate has been carried out on the basis of the electromagnetic theory. Various combinations of metallic (gold, rhodium, platinum) and non-metallic (silicon oxide and dioxide) coatings on a nickel substrate, with different values of the coating thickness, were investigated.

The aim of the work concerns the analysis of the substrate/coatings combinations that are suitable for the required performance (low emittance, low weight, low degradation of radiant properties in use) in different temperature ranges. Total normal emittance measurements were also performed on two samples and the results showed a good agreement with the theoretical calculations.

NOMENCLATURE

d thickness
n,k optical constants
T absolute temperature

Greek Letters

ε emittance
λ wavelength

Subscripts

1,2,3,..,N coating layer indexes
λ_n spectral normal
t_n total normal

INTRODUCTION

Interest for the thermal radiation properties of solid films has been stimulated by numerous technological applications such as low-temperature insulation systems, solar collectors, and thermal control of space vehicles. In this last field, insulation systems consisting of layers of closely spaced radiation shields are often employed to control surface

temperatures of a spacecraft. The shields are usually made of metallic foils with low emittance coatings. In fact, the thermal performance of multi-layer insulations (MLI) is strongly dependent on the emittance of the foils, which should be very low. The correct design of the shields (choice of materials, coatings, and thicknesses) should take into account many parameters such as: radiation properties of the employed materials, specific weight, operating temperatures range, occurrence of oxides rate or metallic diffusion, quality of the deposition processes, and costs.

Mylar polyester films are currently employed in most MLI shields when the operating temperatures are below 420 K. For wide operating temperature ranges (300 K to 1500 K) thin nickel and molybdenum foils (10-20 μm thick) are used [1]. Emittance of such metallic materials is very sensitive to the degree of surface oxidation. Coatings of low-emittance and oxidation-resistant materials (such as gold or platinum) can be applied. Gold has a very low emittance but it is soft without protection and its use greatly restricts the operating temperature range; platinum is quite refractory but difficult to apply. When both oxidation and heat resistance are required, rhodium coatings can be used.

Under severe environmental conditions, radiative properties degradation can be limited by using diffusion barriers (thin films of silicon oxide or dioxide), in order to prevent the diffusion of coating with substrate (which produces intermetallic compounds of low reflection), and/or using protective overcoatings (thin transparent oxide layers), to prevent abrasions and oxide growth [2].

For all the mentioned applications, it is important to know the radiant properties of the films employed as well as the influence exerted on the overall thermal performances by coating thickness and by surface temperature. This paper aims at giving a contribution on the subject, by presenting the emittance, theoretically evaluated, of numerous solid films as a function of the coating thicknesses and operating temperatures.

ANALYSIS

The calculation of the radiative properties of thin films can be performed by two different approaches: wave optics and geometric optics. Wave optics is based on superposition of the amplitudes of the electromagnetic fields, including interference phenomena [3-5]. Geometric optics is based on intensity superposition, excluding interference [6-7]. No quantitative criterion has been presented to characterise the range of applications for the two methods; the choice depends on the thickness of the film and of the degree of coherence [8].

In this paper the wave optics approach has been applied to predict the radiative behaviour of multi-layer systems: Figure 1

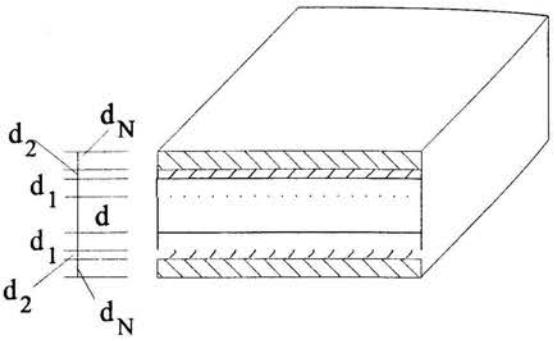

Figure 1: Scheme of a metallic foil (thickness d) coated on both sides by N-layers of thickness d_i (i=1, 2,.., N)

schematically shows N-absorbing non-scattering films, with optically smooth surfaces, deposited, on both sides, on a substrate. For this multi-layer system (radiation shield), bounded by air or vacuum, spectral and total normal emittance can be evaluated in terms of the optical constants n, k and the thickness of each homogeneous medium.

For instance, when N is equal to 1, (a single thin layer onto a thick substrate) the spectral normal emittance can be obtained by the following expression:

$$\varepsilon_{\lambda n} = 1 - (t_{12}^2 + u_{12}^2)/(p_{12}^2 + q_{12}^2) \qquad (1)$$

where:

$$\begin{aligned}
p_{12} &= p_2 + g_1 t_2 - h_1 u_2 \\
q_{12} &= q_2 + h_1 t_2 + g_1 u_2 \\
t_{12} &= t_2 + g_1 p_2 - h_1 q_2 \\
u_{12} &= u_2 + h_1 p_2 + g_1 q_2 \\
g_1 &= (n_0^2 - n_1^2 - k_1^2)/[k_1^2 + (n_0^2 + n_1^2)] \\
h_1 &= 2 n_0 k_1 /[k_1^2 + (n_0^2 + n_1^2)] \\
p_2 &= \cos\gamma_1 \exp(\alpha_1) \\
q_2 &= \sin\gamma_1 \exp(\alpha_1) \qquad (2) \\
t_2 &= (g_2 \cos\gamma_1 + h_2 \sin\gamma_1) \exp(-\alpha_1) \\
u_2 &= (h_2 \cos\gamma_1 - g_2 \sin\gamma_1) \exp(-\alpha_1) \\
g_2 &= (n_1^2 - n_2^2 + k_1^2 - k_2^2)/[(n_1^2 + n_2^2) + (k_1^2 + k_2^2)] \\
h_2 &= 2 (n_1 k_2 - n_2 k_1)/[(n_1^2 + n_2^2) + (k_1^2 + k_2^2)] \\
\alpha_1 &= (2\pi/\lambda)\, k_1\, d_1 \\
\gamma_1 &= (2\pi/\lambda)\, n_1\, d_1
\end{aligned}$$

In the above equations, n_0 is the air (or vacuum) refraction index taken equal to 1, while n_1, k_1 are the optical constants (refraction and extinction index) of the substrate and n_2, k_2 and d are the optical constants (refraction and extinction index) and the thickness of the thin layer.

emittance higher than 20% (owing to the combined radiant properties of Ni, SiO_2, and Au) while no significant influence is exerted for gold thicknesses greater than 0.05 μm. Besides, a SiO overcoating thinner than about 0.1μm does not significantly affect the total emittance of the system at 1073 K, for any gold coating thickness; if the temperature is reduced (273 K) the limiting SiO thickness can rise up to 0.2 μm.

Figs. 7 and 8 summarise the theoretical results obtained with 24 nickel foils with coatings of different composition and thickness. The film characteristics are given in Table 1: each combination investigated differs from the others not only in radiative properties but also in operating temperature range, degradation in use and manufacturing costs. Figure 7 gives the total normal emittance as a function of shield weight (for square meter) at 673 K. Each symbol and relevant code refer to the description (composition and thickness) of the foils reported in Table l. Densities of the investigated materials are taken from [10]. Figure 8 analyses the same parameters at 1073 K. Generally speaking, the figures show that the lowest emittance values are reached when weight and manufacturing complexity increase as a result of coating and overcoating applications. The most suitable configuration, however, results from a compromise choice of the described parameters, taking also into account costs and operating conditions.

EXPERIMENTAL RESULTS

Electromagnetic theory makes it possible to predict the radiant properties of multi-layer shields of different compositions; the results, however, may be affected by the restrictive hypotheses assumed by the theory. It is known, for instance, that the theoretical analysis used does not take into account surface effects (impurities, non-optically smooth geometry) that can greatly influence the radiative behaviour. Therefore, comparisons with experimental data are useful to verify the validity of the theoretical approach.

Total normal emittance has been measured for two metal foils by means of an apparatus, working on the radiometric method, described in the ref. [11]. Measurements are obtained by a comparison of radiances emitted by the test sample and a blackbody, maintained at the same temperature. Sample and blackbody are placed in a container (equipped with a vacuum-tight potassium bromide optical window) connected to a vacuum pumping system to perform measurements in air, vacuum or controlled atmosphere. Two separate DC power supplies maintain the sample and the blackbody at the same temperature (within ± 0.5 K). The sample and blackbody

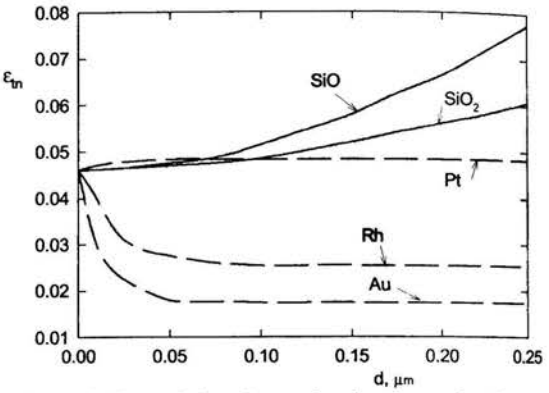

Figure 4: Theoretical total normal emittance as a function of the coating thickness, for various coating materials (T=673 K) on nickel substrates.

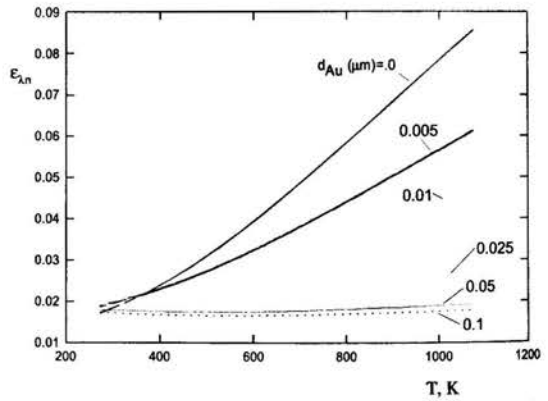

Figure 5: Theoretical total normal emittance of gold coated nickel foils against temperatures, with different coating thicknesses.

temperatures are measured by means of two thermocouples (type K, 0.5 mm-dia) placed inside the cavity of the blackbody and in a blind hole open on the back of the sample just below the emitting area (the distance between the top of the hole and the emitting surface is less than 0.2 mm). The two radiances coming from the sample and the blackbody are alternatively focused onto the detector through an optical path (plane mirrors S_1 and S_3, and spherical mirrors S_2 and S_4). A high-vacuum Hilger-Schwartz thermopile was used as detector and a lock-in

amplifier, operating on chopper frequency, was employed to measure the detector output. The experimental apparatus is periodically checked against normal emittance standard (platinum-rhodium, oxidised khantal, and oxidised inconel) supplied by the National Bureau of Standards (NBS). The difference between the measured and the certified total normal emittances of the three reference materials tested is within the standard deviations specified by NBS.

The first test sample consists of a nickel foil coated by a 0.1 μm SiO_2, layer and a 0.1 μm vapour-deposited gold film (code NSXG2). The second sample is a nickel foil coated by a 0.1 μm SiO_2, layer without gold overcoating (code NSX2).'The experimental results, carried out between 373 and 673 K, in air atmosphere as well as in vacuum, are reported in Fig.9 in comparison with theoretical calculations. It can be observed that computed and measured emittances are in good agreement, confirming the usefulness of the analysis based on the electromagnetic theory for practical calculations and proper design of low emittance radiation shields.·

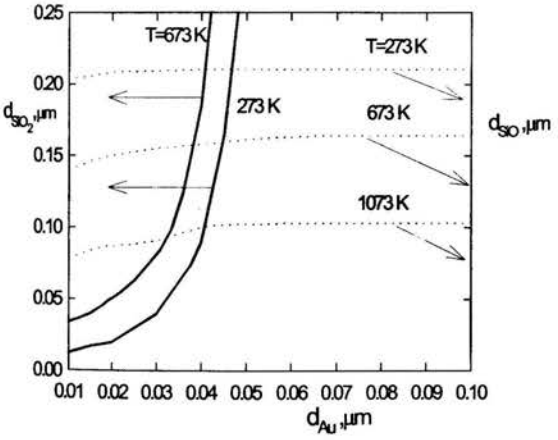

Figure 6: Limiting thickness of SiO_2 diffusion barriers and SiO overcoatings for Ni-Au systems in correspondence of which total emittance increases up to 20%. Influence of gold thickness and temperature.

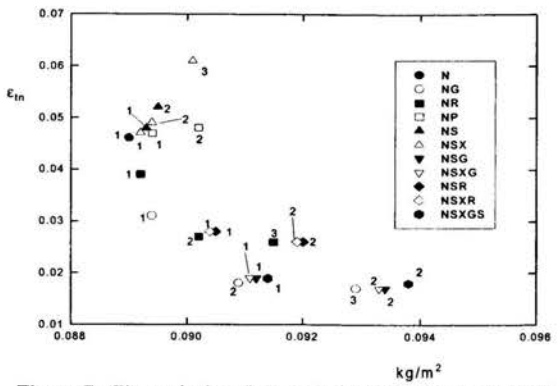

Figure 7: Theoretical total normal emittance as a function of weight (for square meter) for 24 nickel foils, at 673 K.

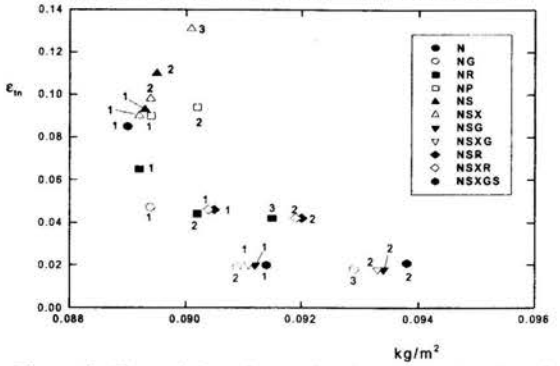

Figure 8: Theoretical total normal emittance as a function of weight (for square meter) for 24 nickel foils, at 1073 K.

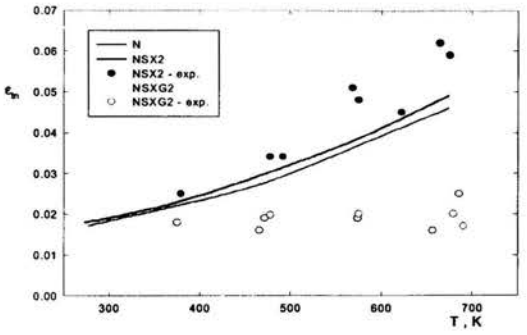

Figure 9: Computed and measured total normal emittances for two nickel foils.

Table 1: Composition (material and thicknesses) of 24 nickel foils.

Code	Substrate	d (μm)	Coat. (μm)	d1 (μm)	Coat. (μm)	d2 (μm)	Coat. (μm)	d3 (μm)
N1	Ni	10	-	-	-	-	-	-
NG1	Ni	10	Au	0.01	-	-	-	-
NG2	Ni	10	Au	0.05	-	-	-	-
NG3	Ni	10	Au	0.10	-	-	-	-
NR1	Ni	10	Rh	0.01	-	-	-	-
NR2	Ni	10	Rh	0.05	-	-	-	-
NR3	Ni	10	Rh	0.10	-	-	-	-
NP1	Ni	10	Pt	0.01	-	-	-	-
NP2	Ni	10	Pt	0.05	-	-	-	-
NS1	Ni	10	SiO	0.05	-	-	-	-
NS2	Ni	10	SiO	0.10	-	-	-	-
NSX1	Ni	10	SiO_2	0.05	-	-	-	-
NSX2	Ni	10	SiO_2	0.10	-	-	-	
NSX3	Ni	10	SiO_2	0.25	-	-	-	-
NSG1	Ni	10	SiO	0.05	Au	0.05	-	-
NSG2	Ni	10	SiO	0.10	Au	0.10	-	-
NSXG1	Ni	10	SiO_2	0.05	Au	0.05	-	-
NSXG2	Ni	10	SiO_2	0.10	Au	0.10	-	-
NSR1	Ni	10	SiO	0.05	Rh	0.05	-	-
NSR2	Ni	10	SiO	0.10	Rh	0.10	-	-
NSXR1	Ni	10	SiO_2	0.05	Rh	0.05	-	-
NSXR2	Ni	10	SiO_2	0.10	Rh	0.10	-	-
NSXGS 1	Ni	10	SiO_2	0.05	Au	0.05	SiO	0.05
NSXGS2	Ni	10	SiO_2	0.10	Au	0.10	SiO	0.10

CONCLUSIONS

In this work the radiation properties of thin films have been theoretically investigated by means of the wave optics theory.

Very thin layers of gold or rhodium coatings (about 0.1 μm thick) on nickel substrates were found to yield very low emittance values for the film in a large range of wavelengths. Morover, a coating of Au, Rh thicker than 0.1 μm eliminates the influence of the radiant properties of the substrate (Ni). Overcoatings of silicon oxide or dioxide layers (useful as a diffusion barrier and/or protection against abrasions and damages) up to 0.1 μm do not significantly increase the emittance levels of the Ni-Au (or Ni-Rh) films. An analysis including thermal properties and weight considerations has been presented in order to address the choice of most suitable film compositions for a given thermal duty.

Finally, theoretical total normal emittance results have been checked against measurements performed by means of a radiometric apparatus for two different thin films, in the 373-673 K range; the comparison between predicted and measured values showed a satisfactory agreement.

ACKNOWLEDGEMENTS

This research was supported by a grant from ASI (Agenzia Spaziale Italiana) through the project "Evaluation of radiant thermal properties of thin films".

REFERENCES

[1] E.S.A., 1979, "Spacecraft Thermal Control Design Data", Report TST-02, Issue n.1.

[2] Van Vliet,R.M., 1965, "Passive Temperature Control in the Space Environment", The Macmillan Company.

[3] Heavens, O.S., 1955, "Optical Properties of Thin Solid Films", Butterworths Scientific Publications.

[4] Brannon, R.R., Jr., and Goldstein, R.J., 1970, "Emittance of Oxide Layers on a Metal Substrate", ASME J. of Heat Transfer, Vol. 92, pp. 257-263.

[5] Phelan, P.E., Chen, G., Tien, C.L., 1992, "Thickness-Dependent Radiative Properties of Y-Ba-Cu-O Thin Films", ASME J. of Heat Transfer, Vol.114, pp.227-233.

[6] Siegel, R., and Howell, J.R., 1981, "Thermal Radiation Heat Transfer", Mc Graw-Hill.

[7] Tang, K., Kawka, P.A., Buckius, R.O., 1999, "Geometric Optics Applied to Rough Surface Coated with an Absorbing Thin Film", J. of Thermophysics and Heat Transfer, Vol.13, pp.169-176.

[8] Chen, G., and Tien, C.L., 1992, "Partial Coherence Theory of Thin Film Radiative Properties", ASME J. Of Heat Transfer, Vol.114, pp.636-643.

[9] Palik,E.D., 1985, "Handbook of Optical Constants of Solids", Academic Press.

[10] Goldsmith,A., Waterman,T.E., and Hirschhorn, H.J., 1961, "Handbook of Thermophysical Properties of Solid Materials" , The Macmillan Company.

[11] Misale,M., Pisoni,C., and Tanda,G., 1989, "Investigation of Total Emittance of Metals and Steels Subjected to Mechanical Surface Treatments", High Temperatures-High Pressures, Vol.21, pp.311-315.

HEFAT2002
1st International Conference on Heat Transfer, Fluid Mechanics and Thermodynamics
8-10 April 2002, Kruger Park, South Africa
SJ1

THE RHEOLOGICAL PROPERTIES OF ELECTRORHEOLOGICAL FLUIDS IN SQUEEZE FLOW UNDER IMPULSIVE LOADING

Ali K. El Wahed and John L. Sproston
Department of Engineering
University of Liverpool
Liverpool L69 3GH, U.K
E-mail:j.l.sproston@liverpool.ac.uk

ABSTRACT

This paper is concerned with an experimental determination of the rheological performance of an Electrorheological Fluid when subjected to time-dependent applied loads. The experimental facility was built as a squeeze cell in which the fluid is sandwiched between two electrodes, one fixed and the other moving, which permits the instantaneous measurement of the mechanical and electrical responses of the fluid. The transient rheological characteristics of the fluid were assessed for various mechanical force levels for constant field excitation of the fluid established by the use of a digital controller in conjunction with the high-voltage power supply to provide a time varying applied voltage proportional to the instantaneous electrode separation. Input and output stress levels across the fluid were monitored using a dedicated data acquisition system enabling the dynamic response of the fluid to be determined using a combination of displacement, force, velocity and acceleration transducers. A comparison of the experimental results was made with the results from a modified theoretical analysis, which employs a bi-viscous shear stress/shear strain characteristic of the electrically stressed fluid.

INTRODUCTION

Electrorheological (ER) fluids belong to the general class of smart materials whose rheological properties can be modified by applying an electric field. The first useful application of the ER fluid in vibration control was introduced by Bullough and Foxon (1978) when both Coulomb and viscous damping was achieved by means of an ER valve-operated vibration damper. The present ER fluids seem to meet the requirements of vibration control whilst the possibility of employing them commercially in different engineering devices such as clutches and brakes (Carlson and Duclos (1990)) is still not achievable. This is mainly due to the low value of yield stress that can be provided by the existing commercial ER fluids (Hartsock et al (1991)).

As a result, increasing attention has been devoted to the area of vibration control devices particularly in engine mounts (Petek et al (1988)) and primary shock absorbers (Nakano and Yonekawa (1997), and Wereley and Lindler (1999)) as well as in adaptive structures (Ehrgott and Masri (1993)).

These novel vibration control devices have been tested under slow transient loads applied to one of the electrodes or under low frequency steady vibration input. However, Maemori and Saito (1998) and Khusid et al (1999) have recently reported ER fluid shock absorbers that have been examined under fast loading, which corresponds to electrode velocities of the order of several cm/s.

Moreover, these studies employ the ER fluids in either flow mode or shear mode of operation when the fluid flow rate is controlled in the former whilst fluid shearing is controlled in the latter. Stanway et al (1992) invented an alternative means of generating variable damping forces of larger magnitude from ER fluids that are employed in the squeeze flow mode in which the fluid is subjected to compressive stress. It was then reported by Monkman (1995) that ER fluids under tension and compression provide a high yield stress, which is an order of magnitude higher than that in shear mode. This new fluid strength encouraged the authors and other researchers to carry out systematic investigations to evaluate the mechanical and electrical properties of ER fluids in squeeze flow, and as a result, improved design information in the area of vibration control has emerged (see for example, Sproston et al (1994a and 1994b), El Wahed et al (1995, 1998a, 1998b, 1999a and 2000), Jung and Choi (1995), Morishita and An (1996), Bonneau and Frene (1997)).

In general, it should be noted that many investigations have been conducted in the field of vibration isolation and control due to the rapid phase change of an ER fluid and hence the fast conversion of its physical properties. Stanway et al (1996) and Sims et al (1999) provide substantial reviews of the literature particularly in the classification of the modes of ER fluid operation and their potential engineering applications in vibration control.

The experimental and theoretical studies reported here are concerned with the application of an ER fluid device to the fixings of structural members subjected to blast or impact

loading. These devices could be employed to control the fast loading transmitted through the fixing or to control deformations (El Wahed et al (1998c and 1999b)). The transient characteristics of these field-controllable devices were assessed for various mechanical force levels, loading duration and electrical input. The experimental results are compared with the predictions of a theoretical model.

NOMENCLATURE

a	radius of electrodes
F_1	input force
F_2	output (or transmitted) force
G	dimensionless radial pressure gradient defined in equation (1)
h	initial separation of electrodes
M	mass of top (oscillating assembly)
p	local pressure
r	radial co-ordinate
S	dimensionless radial variable defined in equation (2)
t	time
x1, x2	maximum force amplitudes of two successive cycles
χ	dimensionless disk radius defined as the value of S at r = a
y	displacement of top electrode
$\dot{y}$	velocity of top electrode
$\ddot{y}$	acceleration of top electrode
γ	$= \eta/\eta_r$
η, η_r	post and pre-yield fluid viscosities
ξ	damping ratio
τ_1	fluid yield stress
ϕ	non-dimensional output force

EXPERIMENTAL ARRANGEMENT

Experimental Facility

The experimental arrangement shown in Figure 1 consisted of a vertically mounted rig capable of providing a transient input force to the upper assembly by means of a falling mass impacting on the striker plate. This force is subsequently transmitted across the ER device. The device consists of two superimposed, circular electrodes, 50 mm in diameter, the gap between which being filled with an ER fluid whose rheological characteristics can be changed by a change in the level of voltage applied across the fluid. The voltage applied was DC such that the fluid could be stressed by a constant applied field by employing a voltage controlling feedback device which increased or decreased the applied voltage in proportion to the instantaneous electrode separation (see El Wahed et al (1998a).

The upper assembly was attached rigidly to the striker plate by means of a Kistler (Model 9331A) piezoelectric force link whilst the lower surface of the lower assembly was rigidly attached to the supporting frame by means of a second identical force link.

For the experimental tests, a very light spring was incorporated in the experimental rig in order to support the top assembly. This fixture was designed to enable the adjustment of inter-electrode gap prior to impact. This experimental arrangement permitted the instantaneous measurement of the input and transmitted forces.

The instantaneous displacement of the upper electrode was determined using an RDP (Type D5-200HK) LVDT, the velocity using an RDP (Type 240A0500) self-induced velocity sensor and the acceleration using an Endevco (Type 7254-100) accelerometer, all three devices attached to the upper surface of the assembly. Electrical excitation of the ER fluid device was achieved by means of a Trek (Model 664) high voltage amplifier. Data acquisition and processing was achieved using a Measurement Group (Type ESAM) analogue to digital converter that is controlled by a Pascal program running on an IBM compatible personal computer. An additional Endevco accelerometer (Type 2251A-10) attached to the dropped mass was used to trigger the data logger just prior to the moment of impact.

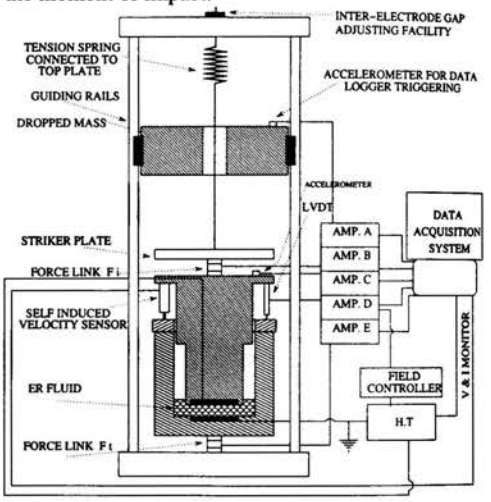

Figure 1. Experimental Arrangement

ER Fluids

In the present investigation, four different ER fluids were used which are as follows:

ER Fluid 1: A suspension of calcium alumina-silicate of size 0.5 to 5 μ m in silicone oil of viscosity 10 cSt.

ER Fluid 2: A suspension of agglomerated corn flour (supplied by Agglomeration Technology Ltd.) in silicone oil. The solid phase was supplied with an average diameter of 90 μ m, which was subsequently ground and sieved to produce particulates in the range 10 to 28 μ m (see El Wahed et al (1999a).

ER Fluid 3: A commercial fluid (ERF BA-1), which was supplied by Bridgestone Corporation (Bridgestone (1997)).

ER Fluid 4: A commercial fluid (Bayer RHEOBAY TP AI 3565) which consisted of a suspension of polyurethane of size 5 to 6 μ m in silicone oil of viscosity 5 cSt (Bayer AG (1994).

Experimental Procedure

The tests carried out consisted of the simultaneous measurement of the instantaneous values of the input force delivered to the upper assembly, its displacement, velocity and acceleration together with the transmitted force acting on the lower assembly across the ER fluid and the acceleration of the dropped mass. In addition, the applied voltage and the current drawn by the fluid were measured. The initial gap between the electrodes of the device was chosen as 2 mm, and the fluid was electrically excited by constant fields in the range 0 to 5

kV/mm. These measurements were collected at a sampling frequency of 10 kHz for three drop heights of the falling mass, namely 0.065, 0.115 and 0.165 m and for a mass ranging between 0.221 and 1.309 Kg. The device was tested under three different loading periods, namely 2 ms (system1), 50 ms (system2) and 70 ms (system3). These loading periods were achieved by incorporating compression springs with different stiffnesses between the striker plate and the upper force link.

THEORETICAL MODEL FOR ER DEVICE

The device in Figure 1 is modelled as an electrorheological fluid contained in the space between two parallel circular electrodes of radius a. The top electrode oscillates about its mean position with a displacement y (t) whilst the lower electrode is stationary. The theoretical modelling is directed towards the determination of the input force F_1 (t) and the transmitted force F_2 (t) from a set of experimental data for y (t), by application of the analysis reported earlier by Williams et al (1993). These forces can then be compared with the values taken from the experimental rig. The analysis (abbreviated here) assumes a quasi-static flow with a bi-viscous characteristic for the ER fluid in which the ratio γ represents the ratio of the viscosities in the 'yielded' to the 'unyielded' regions. ($\gamma = \eta / \eta_r$).

The non-dimensional pressure gradient G given by

$$G = -\frac{(h - y(t))}{2\tau_1}\left(\frac{dp}{dr}\right) \qquad (1)$$

is determined as a function of the non-dimensional radius S given by

$$S = -\frac{\dot{y}(t)\,\eta\, r}{(h - y(t))^2\,\tau_1} \qquad (2)$$

where h is the mean separation of the electrodes, τ_1 is the fluid yield stress, $\dot{y}$ (t) is the velocity of the top electrode and r is the radial co-ordinate. Integration over the upper electrode then gives the transmitted force F_2(t) in the form

$$F_2 = \frac{2\pi\tau_1 a^3 \phi(\chi)}{h - y(t)} \qquad (3)$$

where a is the radius of the electrodes, χ is the value of S at r = a, and the non-dimensional output force ϕ is

$$\phi = \frac{1}{108}\frac{\gamma}{\chi} + \frac{1}{\chi^3}\int_{s=\frac{\gamma}{3}}^{\chi} S^2 G\, dS \qquad (4)$$

The integration of equation (4), once G is determined (numerically) as a function of S, is evaluated using simple quadrature. When F_2 is obtained from equation (3) the input force F_1 is then calculated using Newton's second law applied to the top electrode in the form

$$F_1 - F_2 = M\,\ddot{y} \qquad (5)$$

where M and $\ddot{y}$ are the mass and acceleration of the top assembly.

RESULTS AND DISCUSSION

An extensive testing programme has been conducted in order to assess the characteristics of the device that could be used to relax the fixings of structural members such as blast resistant panels during an extreme loading event. This new technology would enable these components to be designed more efficiently and limit the loading transmitted to the primary structure, thus reducing the risk of progressive collapse.

The characteristics of the device were investigated when its initial inter-electrode gap was chosen at 2.0 mm. This represents almost half of the inter-electrode gap that was used by Khusid et al (1999) in their investigations.

The device (system 1), filled with ER fluid 4, is excited in advance with the required electric field and a signal from the accelerometer attached to the falling mass is used to trigger the data logger just before the moment of impact. For a falling mass of 0.221 kg and a drop height of 0.065 m, the variation in the input force (recorded by the top force link) and the transmitted force across the ER fluid (recorded by the lower force link) are shown in Figures 2 and 3 respectively as a function of time for the zero-field case. The variation of the input displacement of the upper assembly is also shown in both figures. It can be seen, Figure 2, that the device was subjected to a maximum force of about 300 N during a loading period of about 2 ms.

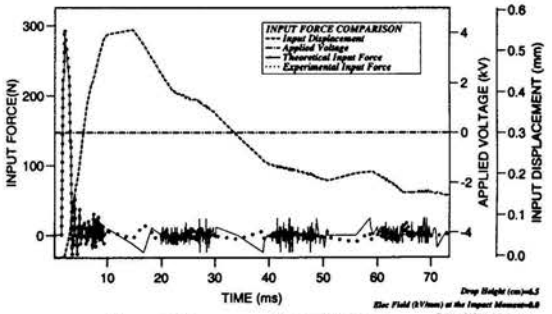

Figure 2. Response of ER Fluid Device

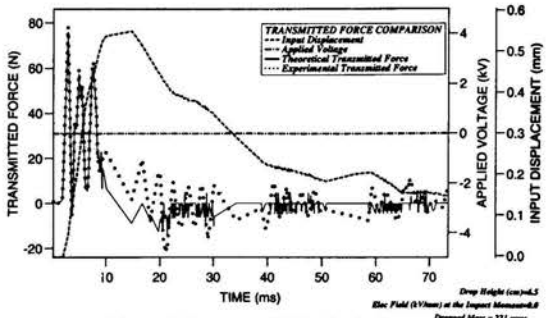

Figure 3. Response of ER Fluid Device

The top assembly travelled a maximum distance of about 0.55 mm after impact and this was reduced to about 0.15

mm after approximately 74 ms. The effect of applying a constant field of 3 kV/mm on the behaviour of the ER device can be seen clearly in Figures 4 and 5 where the input displacement and the transmitted force have maximum values nearly five times less and four times greater respectively than in the zero-field case. The initial peaks are followed approximately 60 ms later by secondary peaks caused by natural rebound of the falling mass. Moreover, the upper assembly was found to be displaced, after 74 ms, by an offset that was about three times less than for the zero-field case.

The performance of the electric field controller can be seen in Figure 4, where a decrease in the applied voltage was seen to correspond to a proportional decrease in the gap (see El Wahed et al (1998a). This was also found to be useful in order to prevent any discharge across the fluid gap when the electrodes become very close to each other.

The ER fluid behaviour in squeeze has been successfully predicted by Williams et al (1993) by a model which assumes a bi-viscous rheological fluid characteristic. This model has been verified by the authors when the ER device was subjected to steady vibrations and energised by either a DC (El Wahed et al (1998a)) or an AC field (El Wahed et al (2000)). In the present investigation, the same numerical technique has been tested when the ER device is subjected to impulsive loads.

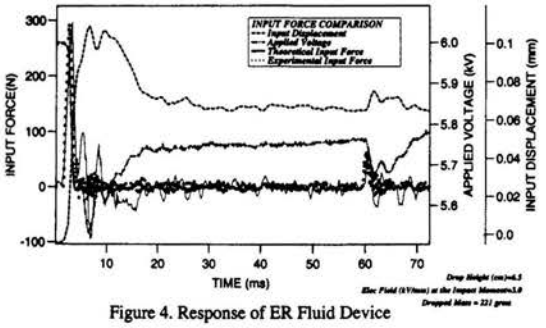

Figure 4. Response of ER Fluid Device

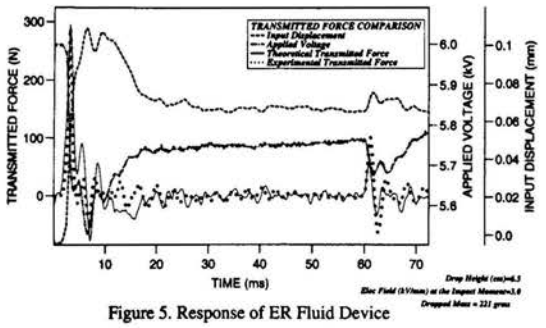

Figure 5. Response of ER Fluid Device

The results for the Newtonian case are shown in Figures 2 and 3 whilst the non-Newtonian case is shown in Figures 4 and 5. It can be seen that the predicted values of the transmitted force agree very well with the experimental results particularly when the change in the velocity of the upper assembly is high. This agreement is degraded when the transmitted force fluctuates about the zero value.

The predicted and the experimental values of the input force were also seen to be in good agreement although the former data becomes noisy after the initial hit. This could be partly ascribed to the noise imposed on the acceleration data that has been used to estimate the input force. However, the loading duration was successfully predicted since the temporal change in the predicted and experimental values of the input force seems to be in phase during the 2 ms period.

For an applied field of 3.0 kV/mm, the variation in transmitted force and drawn current is shown in Figure 6 and this shows a massive reduction in current level following the moment of impact, followed by an increase to its average value, which is about 175 μA. The reduction in current value is ascribed to the fact that chains of particulates already formed would be partially broken at the moment of impact. However, the response of the ER fluid is fast and this prompts a new fibrous structure to be formed hence resuming the same previous current level.

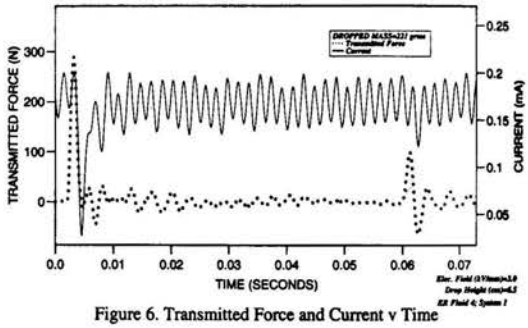

Figure 6. Transmitted Force and Current v Time

The results taken for the drop height of 0.065 m are compared with those for the two other heights of 0.115 and 0.165 m in Figures 7 and 8 in terms of the input displacement and force transmissibility (defined as the ratio of transmitted to input force) respectively, for a range of electric field strengths. The device is seen to exhibit increasing values of force transmissibility, accompanied by decreasing input displacement with field strength, reaching a transmissibility value equal to unity for the smallest drop height at a field strength of 3 kV/mm and at 5 kV/mm for the two larger heights.

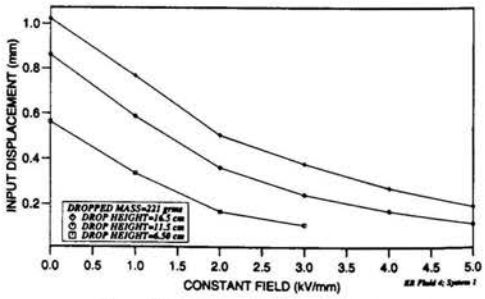

Figure 7. Input Displacement v Applied Field

This enhanced solid body characteristic which the fluid displays when excited by a sufficiently large electric field can

be seen in Figure 7 as the motion of the top assembly is almost arrested.

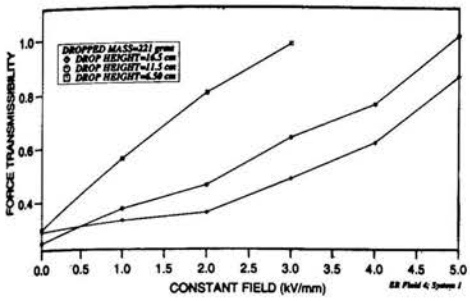

Figure 8. Force Transmissibility v Applied Field

The performance of the device was then assessed using the three further ER fluids, detailed earlier, and its characteristics are summarised in Figures 9 and 10 in terms of input displacement and force transmissibility respectively. It is clear that ER Fluid 4 (Bayer Fluid) produced the best system performance when solid body characteristics were seen to occur at 3 kV/mm whilst at least 5 kV/mm was required by the other fluids.

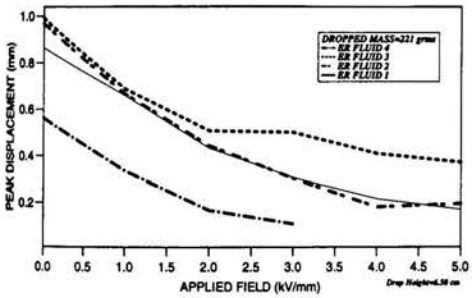

Figure 9. Input Displacement v Applied Field

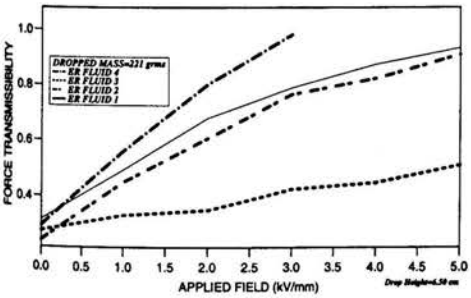

Figure 10. Force Transmissibility v Applied Field

Although, ER-Fluid 3 supplied by Bridgestone was reported (Niaura (1997)) to deliver 2.4 kPa when it was tested in a Couette cell and excited by 5.0 kV/mm, its performance during the present investigation is clearly disappointing since it produced a maximum value of 0.6 for force transmissibility under the same field conditions. It is recognised that the performance of the device would be enhanced further if an ER fluid with a higher yield stress was used as the Bayer fluid used here had a maximum yield stress of 3.0 kPa (see Bloodworth and Wendt (1996).

In order to test the device under different loading periods, the above system was then modified by the addition of a compression spring between the striker plate and the upper force link. As a result, the input load could be attenuated and the device was then assessed when a force surge applied to the upper assembly lasted for about 50 ms (system 2) and 70 ms (system 3) compared with 2 ms that was achieved using system 1. Figure 11 shows a comparison between the performance of systems 2 and 3 in terms of input displacement for a range of electric fields. It can be seen that System 3 was capable of reducing the input displacement from about 1.6 mm (zero field) to 0.054 mm (5.0 kV/mm field) for a drop height of 0.065 m. Despite using a mass of 1.309 kg (about six times bigger than that used with system 1) the ER device was seen to deliver high stiffness and damping that is required to suppress such fast loading.

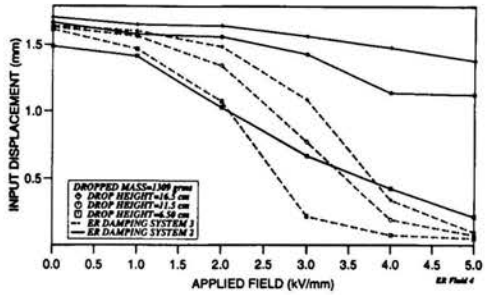

Figure 11. Input Displacement v Applied Field

CONCLUSIONS

In this work the performance of an ER fluid device subjected to various impulsive loading conditions has been investigated through a series of instrumented drop hammer tests. Of particular interest are the performance characteristics of the device under shock loading typical of blast conditions. The device was designed to work in squeeze flow mode and tested under various mechanical and electrical conditions. Experiments on four ER fluids showed that the device containing the Bayer fluid was capable of exhibiting sufficient electric field-induced damping forces under the imposed test conditions. The behaviour of this device was satisfactorily predicted by a theoretical model that assumes a bi-viscous fluid characteristic.

In terms of providing the type of adaptable structure fixing, which was the initiator of the present investigation, the tests have shown that ER fluid technology is capable of controlling forces and movements in structural components subjected to impulsive or dynamic loading conditions due to the fast response times of the fluids leading to rapid load attenuation. There is therefore potential for this technology to be applied to blast resistant panels as used on offshore structures, curtain wall glazing systems in the built environment and energy absorbing structures in transport systems. Under the conditions imposed on the present investigation, the device appears to meet these industrial

requirements by providing a more viable means of achieving fixing relaxation.

Further work will be conducted using an ER device with a larger electrode area in order to increase the capability of the device when subjected to rapid loading. The device is ultimately to be used to support either structural glazing panels or stiffened plates, which will be tested in a blast test facility recently developed in the University of Liverpool.

ACKNOWLEDGEMENT

This work is supported by EPSRC research grant GR/M25407.

REFERENCES

Bayer AG, 1994, Product Information on "Rheobay" ER Fluids and Damping Devices.

Bloodworth, R. and Wendt, E., 1996, Materials for ER fluids, *5th Int. Conf. ER Fluids, MR Suspensions and Associated Technology, Sheffield, 10-14 July 1995,* pp. 118-131.

Bonneau O and Frene J, 1997, Non-linear behaviour of a flexible shaft partly supported by a squeeze film damper, *Wear,* Vol. 206, No. 1-2, pp. 244-250.

Bridgestone Corporation, 1997, Product Information on Bridgestone's Electro-Rheological Fluids.

Bullough, W. A. and Foxon, M. B., 1978, A proportionate Coulomb and viscously damped isolation system, *J. Sound and Vibration,* Vol. 56, pp. 35-44.

Carlson, J. D. and Duclos, T. G., 1990, ER fluid clutches and brakes-fluid property and mechanical design considerations, *2nd Int. Conf. on Electrorheological Fluids, Technomic Publishing Co.,* pp. 353-367.

Ehrgott, R. and Masri, S., 1993, Experimental studies of electrorheological materials for application in adaptive structures, *3rd International Conference on Adaptive Structures, Technomic Publishing Co.,* pp. 161-175.

El Wahed A K, Sproston J L, Williams, E W and Stanway R, 1995, A vibration damper using electrorheological fluids in squeeze: experimental validation of theoretical models, *Symposium on Electrorheological Fluids III, ASME, San Francisco, November 1995*, Vol. 235, pp. 1-13.

El Wahed A K, Sproston J L and Stanway R, 1998a, The performance of an electrorheological fluid in dynamic squeeze flow under constant voltage and constant field, *J. Physics D: Applied Physics,* Vol. 31, pp. 2964-2974.

El Wahed A K, Sproston J L and Stanway R, 1998b, The dynamic performance of an electrorheological fluid in squeeze flow under AC excitation, *J. Intelligent Material Systems and Structures*, Vol. 9, No. 9, pp. 772-779.

El Wahed, A. K., Sproston, J. L. and Schleyer, G. K., 1998c, Electrorheological fluids applied to impulsive loads, *ASME Conf. Rheology and Fluid Mechanics of Nonlinear Materials,* FED-VOL. 246, Anaheim, USA, pp. 159-165.

El Wahed A K, Sproston J L and Stanway R, 1999a, The performance of electrorheological fluid in dynamic squeeze flow: the influence of solid phase size, *J. Colloid and Interface Science,* Vol. 211, pp. 264-280.

El Wahed, A. K., Sproston, J. L. and Schleyer, G. K., 1999b, A comparison between electrorheological and magnetorheological fluids subjected to impulsive loads, *7th Int. Conf. ER Fluids and MR Suspensions,* Hawaii, pp. 401-410.

El Wahed A K, Sproston J L and Williams, E. W., 2000, The effect of a time-dependent electric field on the dynamic performance of an electrorheological fluid in squeeze, *J. Physics D: Applied Physics,* Vol. 33, pp. 2995-3003.

Hartsock D L, Novak R F and Chaundy G J, 1991, Electrorheological fluid requirements for automotive devices, *J. Rheology,* Vol. 35, pp. 1305-1326.

Jung S Y and Choi S B, 1995, Analysis of a short squeeze-film damper operating with electrorheological fluids, *Tribology Transactions,* Vol. 38, No. 4, pp.857-862.

Khusid B, Acrivos A, Khodorkovsky Y and Beltran M, 1999, Electrorheological squeeze-flow shock absorber, *International Journal of Modern Physics B*, Vol. 13, Nos. 15&16, pp. 2143-2150.

Maemori, K. and Saito, T., 1998, New type of hydraulic shock absorber using electrorheological fluid (Countermeasures for electric current blocked), *JSME International Journal, Series C,* Vol. 41, No. 1, pp. 156-163.

Monkman G J, 1995, The electrorheological effect under compressive stress, *J. Physics D: Applied Physics*, Vol. 28, pp. 588-593.

Morishita S and An Y K, 1996, On dynamic characteristics of ER fluid squeeze film damper, *JSME International Journal, Series C*, Vol. 39, No. 4, pp. 702-707.

Nakano, M. and Yonekawa, T., 1997, Active damper using electrorheological suspension and its application to vibration control, *Noise and Vibration Worldwide,* Vol. 28, No. 8, pp. 21-29.

Niaura, W. S., 1997, *Private Communication*, Bridgestone/Firestone Inc., Akron, Ohio, USA.

Petek, N. K., Goudie, R. J. and Boyle, F. P., 1988, Actively controlled damping in electrorheological fluid-filled engine mounts, *SAE Technical Paper No. 881785.*

Sims, N. D., Stanway, R. and Johnson, A. R., 1999, Vibration control using smart fluids: A state-of-the-art review, *Shock and Vibration Digest,* Vol. 31, No. 3, pp. 195-205.

Sproston, J. L., Stanway, R., Williams, E. W. and Rigby, S. G., 1994a, The electrorheological automotive engine mount, *J. Electrostatics,* Vol. 32, pp. 253-259.

Sproston J L, Rigby S G, Williams E W and Stanway R, 1994b, A numerical simulation of electrorheological fluids in oscillatory compressive squeeze-flow, *J. Physics D: Applied Physics*, Vol. 27, pp. 338-343.

Stanway R, Sproston J L, Prendergast M J, Case J R and Wilne C E, 1992, ER fluids in the squeeze-flow mode: an application to vibration isolation, *J. Electrostatics,* Vol. 28, pp. 89-94.

Stanway R, Sproston J L and El Wahed A K, 1996, Applications of electrorheological fluids in vibration control: a survey, *J. Smart Materials and Structures*, Vol. 5, No. 4, pp. 464-482.

Wereley, N. M. and Lindler, J., 1999, Biviscous damping behaviour in electrorheological dampers, *ASME, Aerospace Division Publication AD, "Adaptive Structures and Material Systems",* Nashville, USA, Vol. 59, pp. 67-75.

Williams E W, Rigby SG, Sproston J L and Stanway R, 1993, Electrorheological fluids applied to an automotive engine mount, *J. Non-Newtonian Fluid Mechanics,* Vol. 47, pp. 221-238.

HEFAT2002
1st International Conference on Heat Transfer, Fluid Mechanics and Thermodynamics
8-12 April 2002, Kruger Park, South Africa
BJ2

PHYSICAL AND NUMERICAL MODELLING OF COMBUSTION PROCESSES AND FLOW PATTERNS IN INDUSTRIAL BOILERS AND FURNACES

Baranski J.*, Blasiak W.**, Stasiek J.***
* PhD Student, *** Professor, Department of Heat Technology,
Technical University of Gdansk, 80-952 Gdansk, Poland
E-mail: jbaransk@pg.gda.pl
** Associate Professor, Department of Metallurgy,
Royal Institute of Technology (KTH), 100-44 Stockholm, Sweden
E-mail: blasiak@metallurgi.kth.se

ABSTRACT

Physical modelling is an easy way to simulate combustion and flow patterns by visualisation in cold, isothermal models, [6]. This is done in steps beginning with a burner model to investigate the flame and continuing with a boiler model to visualise the flow pattern and combustion processes. These models must be used with certain similarity criteria to visualise real industrial processes properly. Together with mathematical modelling high accuracy in simulation will be achieved.

INTRODUCTION

Despite great advances, which have been made in combustion modelling over the last decades, its application to real combustion chambers is far from common practice, [4]. The real industrial combustion process is one of the most difficult to model. Much research has been devoted to developing simplified methods for the optimisation of combustion processes, which occur in furnaces or boilers, and very often represent a compromise between the accuracy of a model and the production of useful results. There is often a need for modifying and improving the quality of combustion to achieve a reduction of emissions and to get a more rapid and efficient mixing of reactants. This could be done by studying the flow pattern in the furnace and in the combustion zone in particular.

To model large-scale industrial units, like furnaces and boilers or burners the physical modelling technique is used. It is an efficient, cheap and rapid method to optimise or design modern boilers, burners and furnaces for implementation of low emissions of NOx, SOx, CO, soot and volatiles in real processes.

PHYSICAL MODELLING

Numerous studies in the field of heat and combustion technology have shown that physical modelling is a valuable experimental method involving small-scale water models for the study of aerodynamics of non-isothermal flow and combustion processes occurring in large-scale combustors. The technique makes it possible to visualise the movement and mixing of combustion air, fuel and exhaust gases. Assuming that combustion process is controlled by turbulent mixing, the shape of the turbulent diffusion flame can be studied and visualised by using acid-alkali technique. The basis of the physical modelling is similarity theory.

To physically simulate flow and mixing behavior in two- and three-dimensional, an isothermal water must meet a number of similarity criteria. These are necessary for qualitative and quantitative measurements in the model. By using dimensional analysis and differential equations, some dimensionless numbers of the physical model have the same values as the prototype. To obtain similar flow patterns in the model and in the real combustion chamber, kinematic and geometric similarities are necessary. This is usually done by keeping the Reynolds number the same in the model and the prototype, or, if the combustion process is controlled by turbulent mixing, by ensuring that the model is kept turbulent. To properly model the interaction between the hot furnace gases and the cooler air jets in a cold isothermal model, the thermal expansion of the jets is taken into account using so called equivalent dimensions principle (thermal similarity). To model mixing between fuel and combustion air it is necessary to create the same momentum ratios between each flow in the model as in the real combustion chamber.

There is a strong relationship between studying the flow pattern in order to obtain a better mixing of air, fuel and flue gases in the furnace room and having a decreased amount of different emissions of combustion products and an increased fuel saving. Therefore, it is interesting to investigate the flow pattern and by cheap means study what effects different changes will do to the boiler. Many times, physical modelling allows processes to be tested, which could never be examined, in a real plant because of the cost and the risk for damage to the plant. The model offers numerous possibilities such as changing the position of the burners or air inlet ports and the combustor shape

In practice it is not possible to maintain all similarity criteria at the same time – one is forced to choose. A problem then is to decide which criteria can be neglected. The choice must be based upon experience, comparative experiments, simple calculation and so one. This is one of the reasons why

modelling is sometimes referred to as an art rather than a science.

If possible a model investigation should be conducted in three steps:

1. experiments in a model of an existing plant under known conditions and comparison with experience from the plant – this will verify how well the model simulates real conditions;
2. the main experiments are carried out in a model of the planned plant, usually a newly proposed one;
3. when the new plant has been taken into operation works trials are conducted in order to verify the results of step 2 – in this way experience is continuously built up so that uncertainties of the model results become smaller and smaller.

The final design of the model is therefore often a compromise. Skills are required here in identifying the significant similarity criteria that need to be maintained. Once the model is built, a variety of experimental techniques are available to visualise the flows and obtain detailed measurements of required parameters.

Two-dimensional visualisation

The most commonly used physical model is the two-dimensional (2D) water table modelling technique. It is used primarily to provide qualitative information about combustion chamber performance.

In 2D modelling, water is used to represent the combustion gases or products and their mixing. The two-dimensional model is designed to visualise the flow pattern of the gas phase and simulates and visualises the non-isothermal combustion processes despite isothermal conditions in a physical model of plant by solids particles (e.g. aluminium powder) and colored dyes. The simplicity of this technique is its main advantage.

The two-dimensional model is a simple replica of the boiler's or furnace's vertical or horizontal cross section. The main dimensions of the model are scaled down whilst maintaining geometrical similarity, but dimensions of the inlets are increased according to and equivalent diameter concept. The concept is based on the Thring-Newby similarity criterion, which takes into consideration thermal expansion of the jet's cross-section when it enters the hot environment of combustion chamber. An original construction of a two-dimensional model allows easy changes to be made to the configuration and size in the working section of real boiler or furnace, which is made from aluminium plates in the water table. The 2-D model is arranged in a horizontal plane and placed in a water table, which allows observation and visualisation of the flow, Figure 1. Advanced digital video techniques are used so that the general flow patterns in a combustor can easily be seen and characterised depending on the combustor geometry and boundary conditions.

Simple 2-D modelling can be the answer to many questions regarding the malfunctioning of the real combustor at an early stage and before any 3-D modelling is performed. Information concerning the flow pattern helps to indicate the direction of the combustor and combustion process optimisation. Thus, 2-D modelling provides valuable information required to design a 3-D model, which is suitable for studies of e.g. different low-NOx combustion techniques or modifications in the design of a combustor.

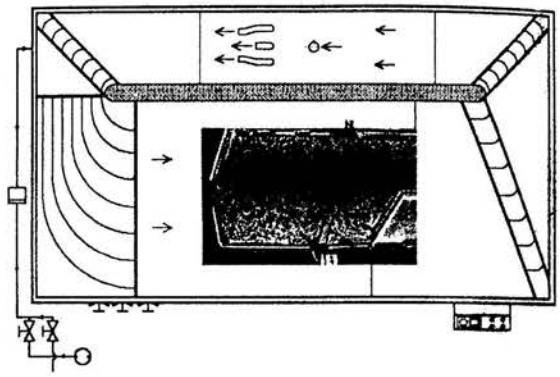

Figure 1. Two-dimensional visualization of the flow pattern performed during physical modelling in the two-dimensional (2D) water table, [11].

Three-dimensional visualization

The 3-D models are built of transparent materials, e. g. Plexiglas, on a scale of 1/30 - 1/50 and have usually a complex design, Figure 2. The geometrical similarity is maintained but as in the 2-D case, the concept of equivalent diameter is used to calculate all inlet dimensions.

The model need not be a full three-dimensional replica of the plant and in some examples only small sections of the equipment are simulated, often called partial modelling. An important feature in the design of the model is the facility of view its interior.

This technique is used, when it is necessary to simulate flame length and shape in a small-scale isothermal physical model in order to investigate the effects on a plants thermal performance of a change to the system geometry, fuel and air mixing arrangement or other operating parameters such as air excess factor. In this way the 3-D model allows processes to be tested which could never be examined in a real plant because of the cost and risk of damage to the plant.

The 3-D technique is used to visualise flow patterns in the gas phase and to simulate and visualise non-isothermal combustion processes in the isothermal conditions of the physical model. To simulate and visualise combustion in the water model "Neutralisation technique", sometimes called "Acid/alkali", is used. Due to the effectiveness and practical usefulness of this technique, it has been developed into an effective method for the study and design of complex, environmentally clean combustion processes. When used alongside computer simulations, it is a useful tool for the design of new and retrofitting of industrial combustion chambers. Of course, many assumptions and simplifications are made to allow the physical modelling of such complex chemical and non-isothermal processes.

The technique simulates the mixing in the flame by using dilute solutions of sulfuric acid and sodium hydroxide to represent combustion air and fuel respectively. The alkali contains colored indicator, which becomes clear on neutralisation

after mixing with diluted acid. The result is a visual representation of the diffusion flame. This method gives quantitative information that is directly related to the flame characteristics, but it is not appropriate for investigating the complex combustion and aerodynamic processes immediately in front of the burner.

The technique is developed around two basics concepts:

1. in a free, expanding turbulent jet, the concentration of entrained fluid as a function of axial distance only depends on the initial force (thrust) of the jet, it is independent of Reynolds number provided that fully turbulent flow exists;
2. the combustion rate in the turbulent diffusion flame is limited by fuel-air mixing and not by the rate of chemical reaction – the "mixed-is-burned" concept, hence better mixing produces more rapid combustion and thus shorter flames.

NUMERICAL MODELLING

Design requirements of high-performance boilers or furnaces are usually summarized as the achievement of time, temperature and turbulence, commonly called 3T.

Mathematical modelling methods have been very widely used tools for the design of a complicated boiler since 80s. With the rapid development of computer abilities recently the computational fluid dynamics (CFD) tools, such as FLUENT, STAR-CD or CFX, etc., have been successfully used for comprehensive simulation of different types furnaces or boilers.

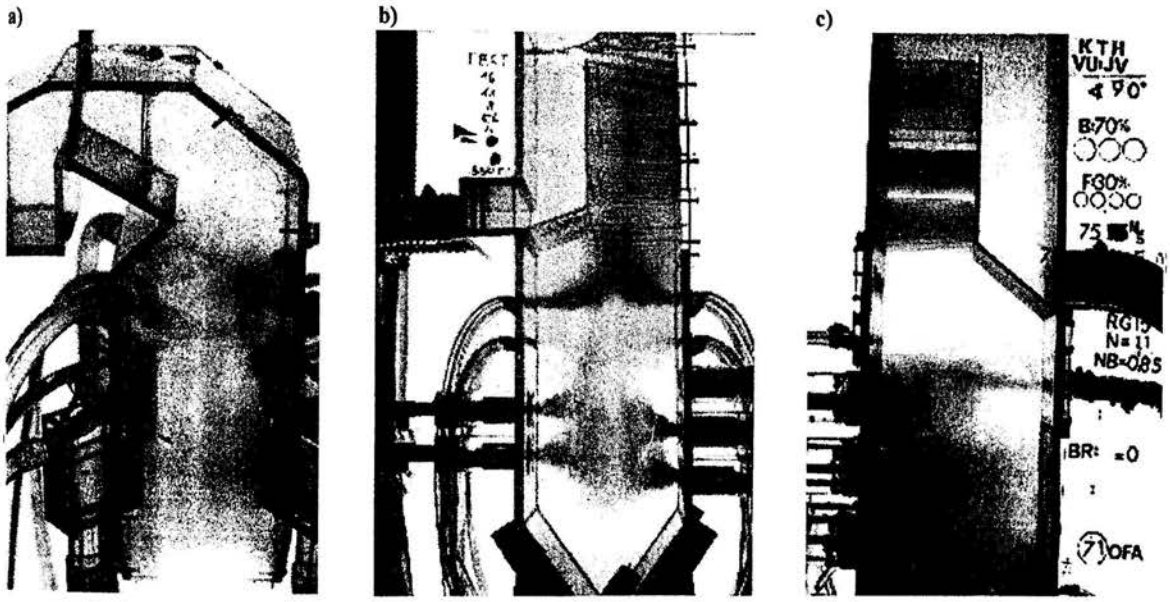

Figure 2. Examples of the three-dimensional (3D) visualization of the combustion processes performed during physical modelling in different types of boilers: a) tangentially coal and gas fired, [12]; b) wall coal and peat fired, [5]; c) oil fired, [9].

A similar process exists for turbulent alkali jet entraining and reaction with the acid. In this case it is the acid entrainment rate alone which determines the progress of neutralisation. The relative strengths of the acid and alkali should be arranged so that the ratio of the acid molarity to alkali molarity is equal to the stoichiometric air requirement on a mass basis. The reaction could be strong acid plus strong alkali resulting in neutral salt. As a result, complete neutralisation takes place when the two solutions are mixed in the same proportions, as that required for stoichiometric combustion; the product of acid flow rate and acid molarity is equal to the product of alkali flow rate and alkali molarity.

There are some indicators, which are colorless in acid solutions, e. g. thymolphthalein or phenolphthalein. A calibrated and reliable pH mater can been used to find the endpoint and burnout profiles precisely. Variation of pH values will then correspond to the degree of neutralisation and hence to the burnout.

CFD numerical method mainly consists of three parts. The first one is the physical models, which are a set of conservation of mass, momentum, energy and state equations turbulent equations, chemical reaction source term equations, etc. The second one is a series of solution approaches for solving these physical models, and the third one is the preprocessor of discretisation of computational domain and the postprocessor of visualisation of numerical results. The early versions of commercial CFD codes usually applied the structured grid, which made very difficult to deal with the industrial units, which have very complicated geometry. Recently the new generation CFD codes, such as FLUENT and STAR-CD, are based on the unstructured grid configurations, which make it possible to handle flexibly the very complicated geometry of real furnace or boiler.

Ideally, the whole system with combustion process could be simulated by using the solid fuel data and operating condi-

tions. Unfortunately, this kind of entire simulation tool has not reached the point where significant use is made in process development for combustion of solid fuels.

In the past, comprehensive numerical modelling of solid fuel combustion has been limited by lack of computer speed and capacity and by difficulties in describing essential physical model elements. However, with the in-furnace bed measurement data or a black-bed model, the entire simulation can focus on the processes of homogeneous gas phase in the simulating domain, then CFD technique becomes the strongest numerical tool to deal with it.

The CFD numerical simulations procedure for simulation of boilers and furnaces includes following steps:
- task analysis and physical models decisions;
- geometry configuration;
- discretization of computational domain – grid generation;
- bed data and boundary conditions;
- isothermal case – flow field and mixing pattern;
- combustion case;
- NOx postprocessor case;
- numerical results analysis.

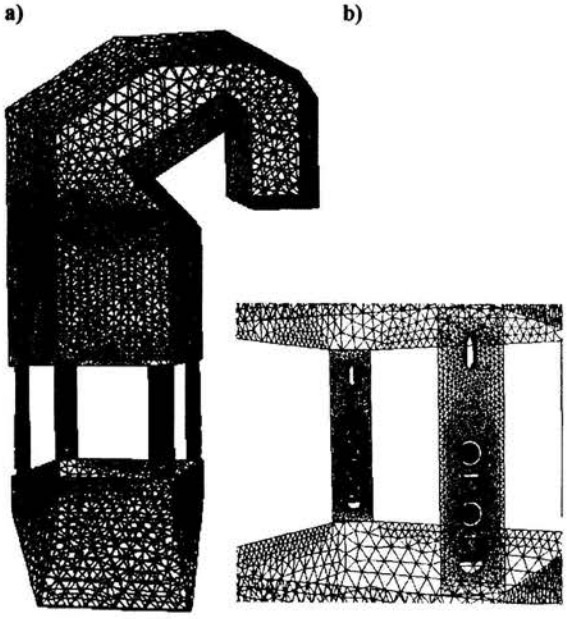

Figure 3. The examples of mesh: a) boiler's geometry, b) boiler's fuel and air nozzles.

APPLICATION OF PHYSICAL AND NUMERICAL MODELLING TECHNIQUES TO OPTIMISATIONS AND REDESIGN OF INDUSTRIAL BOILERS

Coofiring combustion system for wall-fired boiler, (5)

At the Firyskraft power station in Uppsala small solid particles (powders) of coal and peat are fired and the aim for the study of this plant was to develop and to apply by modelling the complicated combustion operations. The combustion system of a 400 MW_{el} pulverized-fired boiler, Figure 4, has been design for two types of fuels and was based on results of experimental, physical and numerical modelling, studies of the boiler furnace aerodynamics, effectiveness of mixing and combustion processes.

At the beginning of the boiler's retrofit, the burner model should be able to model representative flame shapes. In-furnace measures to reduce NOx emission as air and fuel staging and flue gas recirculation were studied taking into consideration the boiler furnace geometry and operating conditions.

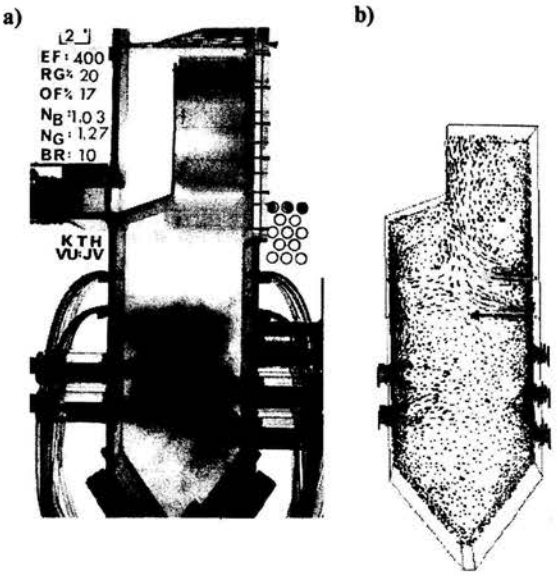

Figure 4. Modelling of wall coal-peat fired boiler by using: a) three-dimensional (3D) physical, b) numerical modelling techniques (mixing patterns).

Complete combustion process during under-stoichiometric conditions at the burner level was obtained when 20 – 30 % of the combustion air and 20 % recirculated flue gases were supplied via the OFA nozzles. Finally, the distribution of fuel between burner level was found to create even deeper under-stoichiometric conditions in the combustion chamber to reduce NOx.

Reburning system for tangentially-fired boiler

The complete combustion system of the Limhamn district heating plant 125 MW_{th} tangentially-fired boiler, Figure 5, with pulverized coal was redesigned based on results from mathematical and physical modelling experiments. The boiler was equipped in Low-NOx burners with an overfire air system OFA. The aim of the boiler modification was to reduce NOx emissions (about 250 ppm at 3 % O_2 in a waste gas) by installing reburn system. As a reburn fuel natural gas was to be used.

Primary in-furnace measures to reduce NOx as air staging and fuel staging were studied taking into account the boiler geometry and operating conditions.

On the other hand, the design of a new, Low-NOx combustion process was based on experimental (physical modelling) and theoretical (mathematical modelling) studies of the

boiler furnace aerodynamics, effectiveness of mixing and combustion processes.

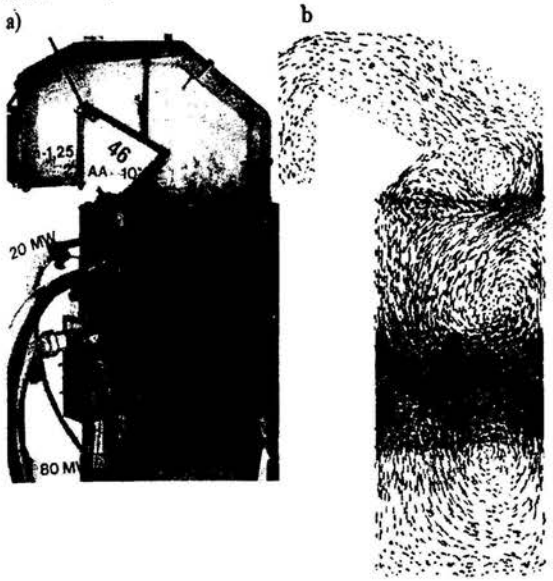

Figure 5. Modelling of tangentially coal-natural gas fired boiler: a) three-dimensional (3D) physical, b) numerical modelling techniques.

The experiments were conducted in a 1:40 scale model, equipped with nozzles that could be tilted in the vertical and horizontal directions in order to optimise the size and position of the natural gas nozzles and additional air ports. Before and after the retrofit extensive experiments were carried out.

It was found that the combustion and reduction of NOx could be efficiently influenced by the direction of the additional air nozzles, without recirculated waste gas. The direction of the natural gas ports had a little influence on NOx reduction. These results of the modelling were in good agreement with results of in-boiler experiments.

After installation and adjustment of the reburning equipment plant tests showed that low emission of the NOx, to about 120 ppm, have been achieved. This shows that reburning is an efficient way to reduce nitrous oxides.

EXPERIMENTAL RESULTS

In this work a combustion process has been simulated in a water models of a boilers' using weak solutions of acid (H_2SO_4) and base (NaOH), which represented fuel and air respectively. The local changes of the acid to base ratio inside the models were visualised using acid-base indicators, which alter the colour depending on the pH of the solution. The neutralisation process was recorded using the computer controlled video system.

The accuracy of simulation, using physical and numerical modelling techniques, depends on many factors like e. g. deep knowledge of the processes involved, great experience and quite a lot of scientific imagination and intuition and high quality of video system and high capability of computers.

SUMMARY

The physical modelling technique is an established method for the optimisation and redesign of industrial combustion chambers like boilers, furnaces or burners.

ACKNOWLEDGEMENT

Thanks to cooperation between Royal Institute of Technology, Stockholm, Sweden and Technical University of Gdansk, Poland J. Stasiek and J. Baranski from Department of Heat Technology are gratefully acknowledged for participation in researches conducted during visit in Heat and Furnace Technology Group, Department of Metallurgy at Royal Insitute of Technology (KTH), Stockholm, Sweden.

The financial assistance of the State Commiette of Research Science (KBN), Poland within Grant No **8T10B04615** is kindly acknowledged.

REFERENCES

[1] Someya T.;Advanced Combustion Science, Springer-Verlag, Tokyo 1993.

[2] Blasiak W., Collin R.; Large scale mixing in a recovery furnace, VI Congreso Latinoamericano De Celuloso y Papel, Torremolinos, Spain, 23-25 June 1992.

[3] Blasiak W., Vaclavinek J.; Modelling of grate fired incinerators, Eurotherm Seminar No.35, Compact Fired Heating Systems, Leuven, Belgium, May 26-27, 1994.

[4] Chomiak J.; Combustion: A study in theory, fact and application, Abacus Press, 1990.

[5] Olsson E., Blasiak W., Vaclavinek J., Landtblom M., Magnussen B., Grimsmo B.; Reduction of NO_x emissions from an industrial oil fired boiler. 4th European Conference on Industrial Furnaces and Boilers, Porto, Portugal, April 1-4, 1997.

[6] Rhine J.M., Tucker R.J.; Modelling of gas-fired furnaces and boilers, British Gas,1991.

[7] Spalding D.B.; The art of partial modelling, Ninth Symp. (intl.) on Combustion., pp 833-843, Academic Press, New York, 1963.

[8] Vaclavinek J.; Physical modelling of a fluidized bed incinerator - NO_x reduction, internal report, Dept. of Heat and Furnace Technology, Royal Institute of Technology, Stockholm, 1993.

[9] Vaclavinek J., Lidegran P., Helén C., Bång J., Blasiak W.; Physical modelling of Fyriskraft boiler, KTH, Div. of Heat and Furnace Technology, Stockholm, May 1997.

[10 Wei D., Helén C., Bång J., Blasiak W., Vaclavinek J.; Analysis of combustion processes in grate fired boiler at Braviken Paper Mill, Division of Heat and Furnace Technology, Royal Institute of Technology, Stockholm, 1997.

[11] Vaclavinek J., Baranski J., Helén C., Blasiak W.; Analysis of flow pattern in coal grate-fired boiler OSR-32, Division of Heat and Furnace Technology, Royal Institute of Technology, Stockholm, 1998.

[12] Bis Z., Blasiak W., Magnusson L., Collin R.; Reburning - injection methods, analytical and experimental study. Publications from nordic Gas Technology Centre. ISBN nr.: 87-89309-17-0.

HEFAT 2002
1st International Conference on Heat Transfer, Fluid Mechanics, and Thermodynamics
8-10 April 2002, Kruger Park, South Africa
CP1

FLAME STABILITY IN A SWIRL COMBUSTOR

P.C. Chisale [1]
The University of Zambia,
School of Engineering,
Department of Mechanical Engineering,
Box 32379, Lusaka, Zambia.
E-mail: P.C.Chisale@eng.unza.zm

T. Nakajima
Kobe University,
Faculty of Engineering,
Mechanical Engineering Department,
Ms-5 Research Unit, Rokko-dai, Nada-ku,
Kobe 657, Japan.

ABSTRACT

Two-dimensional velocity measurements, using a Laser Doppler Velocimetry (LDV) with a forward scattering mode, were conducted in a swirling cold flow model. Flow data was obtained by using light scattering micron-size particles seeded in the flow. 5000 samples, above 1 kHz, were collected in order to validate the results obtained.

Flame stability observation in a swirl combustor with preheated (combustion) air introduced in the combustor tangentially, was also studied. Fuel methane was introduced in the real model combustor axially. The geometric swirl number for the combustor was about 20. Experiments were conducted for air ratios ranging from 0.5 to 3.5 with and without pressure at the exit of the combustor.

Results included two dimensional mean velocity distributions in the entire flow, recirculation flow zones (r.f.z), and jet flow interaction. NOx well below 40 % corrected to 0 % oxygen, the current and anticipated regulatory levels, was measured at the exit of the combustor. Flame stability showed a strong dependence on pressure at the exit of the combustor due to mixture acceleration in the combustor. The flame observed at 800°C combustion inlet air temperature, and high pressure at the exit of the combustor, was mainly yellow and highly luminous, a characteristic strongly indicative of high combustion mixture velocity, a precursor for flame instability and extinction.

Keywords: Two-dimensional, velocity measurements, Laser Doppler Velocimetry, recirculation flow zones, jet interaction, flame stability, and NOx.

1. INTRODUCTION

This study is concerned with swirling flow measurements, in an isothermal model as well real combustor. The models used were of the same geometric configuration and meant for high temperature combustion. The need for high combustion efficiency and low NOx emission in industrial combustors stimulate a lot interest in developing techniques, for in-combustor flow controlling mechanism, that can sustain combustion and enhance flame stability at a given thermal load. Most industrial combustors use flame stabilizers, such as bluff bodies or flame holders, to stabilize the flames. Similarly, the use of swirl combustors, for flame stabilization, is well known due to their flexibility in adjusting reverse flow zones (r.f.z.), high shear mixing, and good combustion characteristics (1). The three-dimensionality nature, coupled with the spinning motion and difficulties associated with measurement techniques, make swirling flows in a combustor an interesting combustion topic to study.

[1] **Corresponding Author**

NOMENCLATURE

A_t	Area of the tangential inlet	MVf	Fuel jet momentum
D_e	Diameter of tangential inlets from the center of the combustor.	S_g	Geometric swirl number
D_o	Diameter of the exits	X	Measuring position along the X-axis
MVa	Air jet momentum	Y	Measuring position along the Y-axis

Many researchers such as Keith and Sonju (2), have focused their attention on investigating swirl decay, mixing, and pressure drop in vane generated swirl combustor.

However, in this study, swirl in the combustor was generated by introducing air tangentially, while fuel was introduced axially. Different behaviors of swirl flows, with high and low swirl numbers, have been reported by Weske and Shou (3), who noted that, the required axial and radial distances at which the fuel jet and swirling flows interacted varied with swirl intensities. At low swirl intensities, the axial and radial distances of fuel jet and swirling flow interaction was short. However, the opposite was true for high swirl numbers. It is, therefore, reasonable to deduce that, under the influence of high or low swirl intensities different mechanisms dictates swirl progression along the combustor axes.

Nevertheless, because of the uniqueness of almost every combustor installation, if only in regard to the associated ducting and surrounding, combustion and implicitly flame stability acceptability of a given installation, is often unpredictable on the basis of past performance of similar units. Specific information, on combustion stability of combustors, is not ordinarily available to the extent that unqualified predictions of flame stability can be made. Therefore, the present practice is to eliminate combustion instabilities by controlling heat release (1). Generally, flame stability in a gas-fired combustor, without the use of mechanical moving components, is influenced by the way energy is released. The combustor used in this study had no mechanical flame stabilizer (4). The thrust of this paper is, therefore, to bring to the fore some intricacies of flame stability in a preheated air swirl combustor.

To date many researchers are investigating preheated swirling flows, in low swirl number regimes, and conditions in tangentially injected swirl flows. Notable among the many results available are the works of Chang and Dhir (5).

2. EXPERIMENTAL SETUP

The experimental setup used, in cold flow studies, is shown in Fig. 1. Due to the difficulties associated with measuring the swirl number, experimentally, it was calculated according to Eq. 2.1, from the geometry of the swirl combustor assuming perfect mixing and conservation of momentum. The geometric swirl number in this case was about 20. In order to obtain velocity vectors at each measuring point, 5000 samples were averaged. To better visualize the flow characteristics the mean velocity values were plotted in the whole region of the reactor after establishing, experimentally, that the flow was axisymetric.

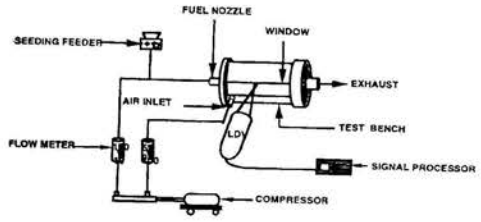

Fig. 1 Isothermal Experimental Model

$$S_g = \frac{\pi D_o D_e}{4 A_t}\left[\frac{Tangential\ \ flow}{Total\ \ flow}\right]^2 \qquad (2.1)$$

The experimental rig used to measure NOx, air inlet temperature, and observe flame stability is shown in Fig. 2. The experiments were carried using nozzle type 1. The nozzle used was made of high thermal resistance ceramic material (6,7) and had the same geometric configuration as the one used in the cold isothermal model. Air preheated to the required temperature of 800 °C was introduced in the combustor tangentially. Measurements of NOx and flame observation were conducted from the upper module at 320 and 400 l/min. air flow rates. For both flow regimes, cold air pressured to 6.7 MPa was either introduced at the exit of the combustor or not. The fuel flow rate was gradually adjusted to give the air ratios of 0.5 to 3.5.

Table 1. Isothermal Experimental Conditions

Test Condition	Burner Vel. [l/min]	Tangential Jet Vel. [l/min]
1-A	13	115
1-B	9	115
1-C	9	144

Three different flow conditions were investigated, in cold flow, as shown in Table. 1. The burner used had 8 holes of 0.6 mm diameter, set at 30 degrees angle to the edges of the burner (Type-1). Velocities were measured in five Y planes namely, 0, 10, 20, 30 and 40. The probe used was a backward scattering and manufactured by DANTEC. The specifications of the probe were as shown in Table.2.

Table 2. DANTEC LDV Specifications

Wave lenght [nm]	λ	500	500	514.5
Focal lenght [mm]	f	400	500	600
Beam separation [mm]	D	38	38	38
Beam waist [mm]	Din	1.35	1.35	1.35
Receiver aperture [mm]	Da	47	47	47
Fringe separation [μ m]	δ f	5.27	6.58	8.13
Diameter of focused laser beam [mm]	df	189	236	291
Measuring volume [mm]	dz	3.97	6.21	9.2
Fringe number	Nf	36	36	36

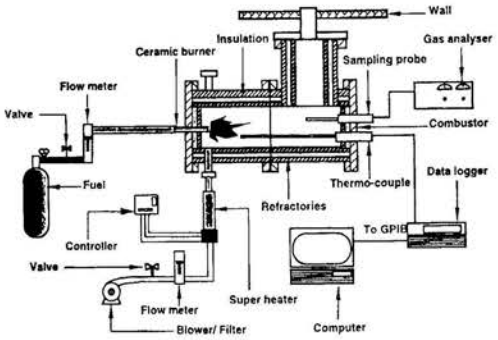

Fig.2 Real Model Experimental Setup

3. EXPERIMENTAL RESULTS

3.1 Condition 1-A

Under condition 1 -A, Fig. 3, an intensive type of r.f.z exited. The region of intensive reverse velocity (< -3 m/s) was located off the center line. The axial velocity ranged from -3 m/s minimum and 1.5 m/s maximum at Y = 0 mm and, 1.8 m/s to -3 m/s at Y = 40 mm. It was observed that the velocity profiles, at all Y positions, tended to rise towards the walls of the combustor. The fuel jet angle of attack region had a positive flow, which decreased with Y distances. This region represented the interaction zone between the fuel jet and the r.f.z. Positive flow in the direction of the fuel jet meant that, the fuel jet induced mixing was more predominant along the jet trajectory, compared to other swirling flow regions in the combustor. As for the decrease of the fuel jet velocity along Y-axis, it implied that the fuel jet disintegrated and lost its momentum along its trajectory, in the combustor upon interaction with the r.f.z. The r.f.z was pushed more towards the wall of the combustor, by the jet, at Y=10, 20 and 30 mm.

3.2 Condition 1-B

Under condition 1-B, Fig. 3, the region of positive velocity narrowed along the X-axis while the r.f.z was enlarged with less negative velocity (= -1.8m/s) in comparison to 1-A. In other words, less fuel volume flow rate meant little recirculation of the mass, from downstream to upstream region, in the combustor. Positive flow was noticed in the trajectories of the fuel jests. The maximum velocity, at Y= 0 mm in the trajectory of the fuel jet as a whole, was less than (= 1m/s) what was observed in condition 1-A (1.5 m/s). The point of maximum velocity was located close to the burner tip and remained unchanged for all positions along the Y-axis. The reason was that, by lowering the fuel volume flow while the air volume flow rate was kept constant, the fuel jet exit velocity was reduced and its prowess to disintegrate and enhance turbulence mixing was impaired. On the other hand, reduced fuel jet velocity meant less fuel jet ability to push the r.f.z further towards the wall compared to flow condition 1-A. In both flow conditions 1-A and 1-B there were prominent areas of positive velocity along the Y-axis of the combustor. However, fuel jet-r.f.z interaction in flow condition 1-B was not pronounced in X-axis compared to flow condition 1-A. Therefore, the region of intensive reverse flow velocity was short in flow condition 1-B compared to flow condition 1-A.

3.3 Condition 1-C

Under flow condition 1-C, Fig. 3, the tangential air flow rate was increased while, the fuel flow rate was kept constant compared to 1-B. The effects were such that the highest value of forward velocity (3.5 m/s) was at Y, X= 0 mm. This contrasted with axial velocities measured in flow conditions 1-A and 1-B. The region most affected extended up to Y = 10 mm. Otherwise, the axial velocity profiles and magnitudes at Y=20, 30 and 40 mm remained unchanged. The region of reverse flow, on both sides of the combustor axis, was relatively pushed far towards the walls of the combustor, as manifested by the location of the stagnation velocity (radial positions 18 and 28 mm at Y = 0 and 10 mm respectively). The maximum negative velocity value was about - 4 m/s at Y= 0 mm. This meant that, at higher tangential air flow rates the r.f.z rotated strongly and covered relatively a small area compared to flow conditions 1-A and 1-B. The steep profile trends, towards the combustor walls, in velocity noticed in conditions 1-A and 1-B were absent. It was, therefore, thought that the r.f.z was pushed more towards the walls of the combustor mostly due to the combined effects of centrifugal force and jet interaction. Only a small region of positive flow, very close X-axis, existed.

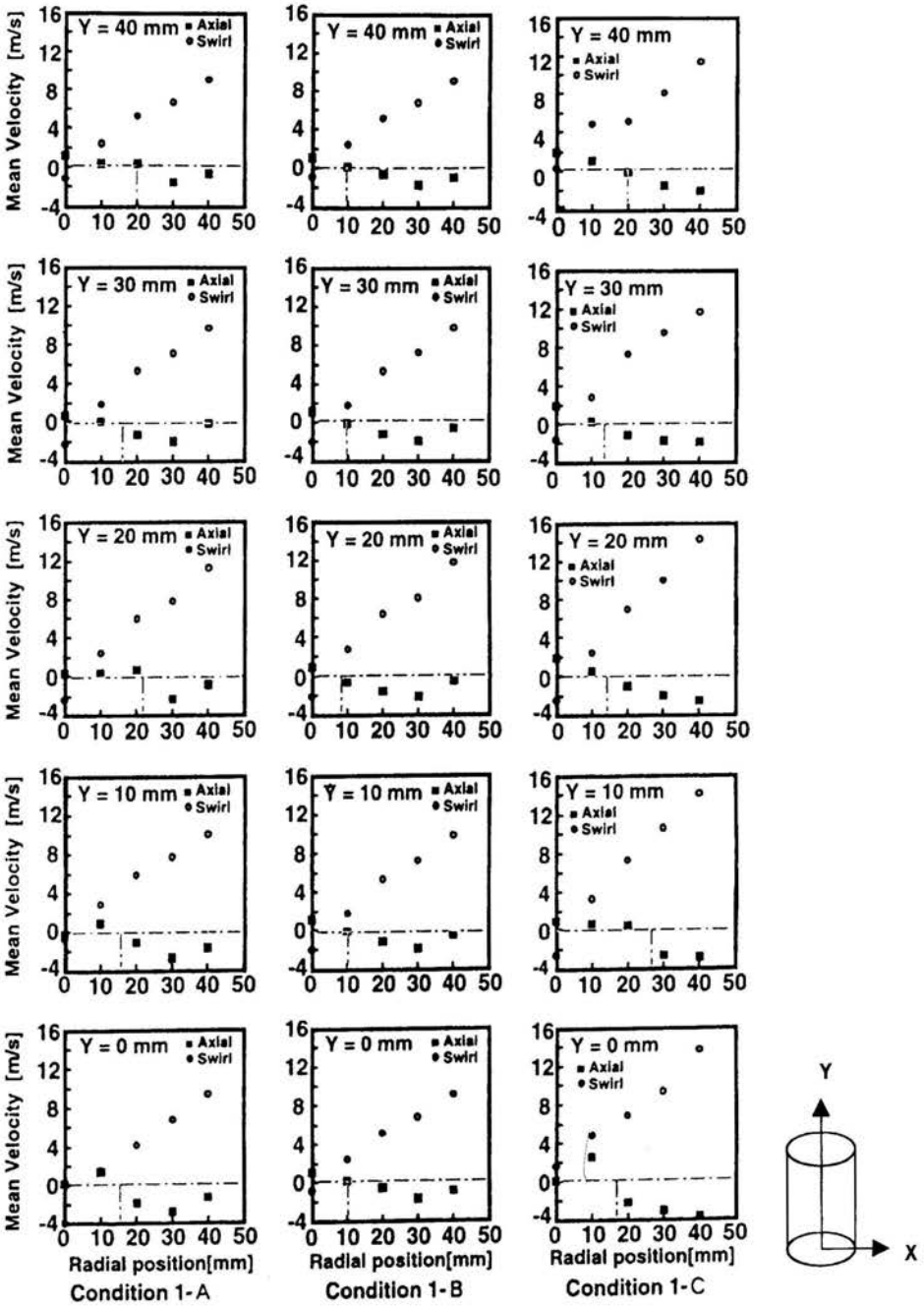

Fig. 3 Mean Axial and Swirl Velocity Profiles at Various Planes and Conditions

3.4 Swirl or Tangential Velocity

Swirl or tangential velocity profiles for conditions 1-A, 1-B and 1-C and Nozzle Type 1 are also depicted in Fig. 3. For all conditions the swirl velocity remained positive. In regions, ≈5 mm in axial direction close to the burner tip, swirl velocities were negative or close to negative and small in magnitude. However, at distances greater than 5 mm, from the burner tip in the axial direction, swirl velocities were positive and changed with radial distances. It was reasoned that the negative velocity values, at all Y positions and X ≈ 5 mm, may have been caused by miss alignment of the test rig with respect to the measuring LDV probe. A Precessing Vortex Core (PVC) was also thought to be probably one of the flow features, which may have led to negative velocity. However, swirl velocity increased in magnitude as the flow progressed along X and Y axes. Positive swirl flow velocities clearly meant enhanced fuel air mixing, in the combustor, by transporting the fluid from the center to the periphery of the combustor.

4. NO_X EMISSION

In terms of overall NO_X reduction, a comparison between Namazian et al (8) and the case of when a single hole exit plate was used in combination with a single hole burner, NO_X was reduced by 66 %. Namely, from 1200 to 180 ppm corrected to 0 % oxygen (Fig. 4).

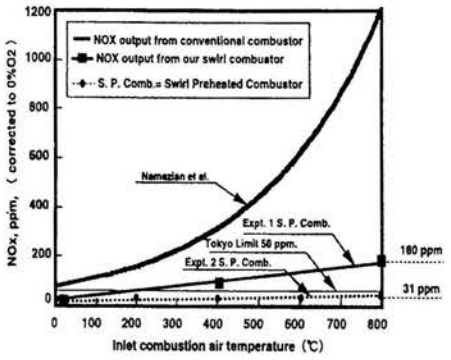

Fig. 4 Comparison of NO_X (ppm) at O% O_2

This reduction in NO_X is as result of improved fuel, air and hot vitiated products mixing due to the intensity of the recirculation created in the combustor (9). This phenomenon was, however, achieved at the expense of a very unstable flame described as a "Ball of Flame" (10). As combustion processed the color of the flame observed, in the combustor, changed from blue to blue-yellow and finally red. The yellowing and reddening of the flame was attributed to the gradual combustor lining temperature increase (Heat sink effect). On the other hand, temperature increase in the combustor was accompanied by increase in the flow velocity, which in turn shortened the residence time of the reactants and oxidants in the combustor. The short residence time led to improper mixing ratios and hence incomplete combustion. Kishimoto et al. (11) linked high temperature combustion flames to variations in oxygen quantities readily available for combustion. The colors of the flames observed in this study, as elucidated by Kishomoto et al., can be categorized as falling in the group of lean and near stoichiometric flames.

5. COMBUSTION STABILITY LIMITS

Stability limits of methane swirl combustion with preheated air, were studied under constant inlet air temperature and with and without pressure at the exit of the combustor. It was observed that, Fig. 5, introducing pressure at the exit of the combustor led to improved flame stability.

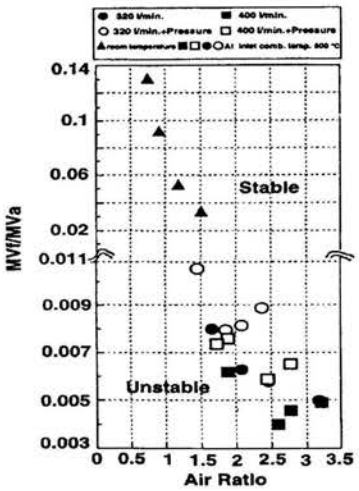

Fig.5 Stability Areas for Fuel-Air Momentum ratio Vs Various Air Ratios, with and without Pressure at the Combustor Exit.

This meant that accelerating mixture at the exit of the combustor led to improvement on the square root ratio of the maximum to minimum fuel pressure drop across the burner orifices. In other words the introduction of pressure down stream, at the combustor exit, served to act as a jet discharging in the combustor flow, therefore, inducing stagnation within the flow in the combustor that led to flame stabilization Fig.5. Stagnation of the combustion mixture downstream in the combustor improved combustion by creating high rate entrainment of the ambient fluid and hot vitiated products into the flame. Therefore, quick mixing took place in the vicinity of the burner nozzles and along the

In the case of a larger number of layers, the spectral normal emittance predicted by the electromagnetic theory is obtained through a more complicated expression [3], not reported here for the sake of brevity.

A calculation program, based on wave optics relationships, has been developed to compute spectral normal emittance $\varepsilon_{\lambda n}$ using the optical constants n and k (as a function of wavelength) for the investigated materials taken from [9]. Furthermore, the computed monochromatic values have been used to evaluate the total normal emittance ε_{tn} as a function of the surface temperature, according to the definition for ε_{tn}:

$$\varepsilon_{tn} = \int \varepsilon_{\lambda n} e_b d\lambda \,/\, \int e_b d\lambda \qquad (3)$$

where e_b is the Planck formula for the spectral blackbody radiation.

Numerous calculations were carried out, considering metal coatings (gold, platinum, rhodium), oxide coatings (silicon oxide and dioxide) and combinations of oxide/metal coatings on nickel substrates. The emittance of each system was computed by parametrically varying the thickness of the coating, in order to assess the deposition rate suitable to maintain or improve the thermal radiant properties of the base.

THEORETICAL RESULTS

In Fig.2, the computed monochromatic thermal emittance values are given for gold coated nickel foils, as the coating thickness varies. The curve with zero coating thickness refers to pure nickel: the shape of the other curves changes with the gold coating. Depositions exceeding 0.1 μm thickness do not appreciably improve the radiant characteristics of the system. The same considerations apply to rhodium-nickel systems, as shown in Fig.3. As a consequence, very thin layers of gold or rhodium coatings (about 0.1 μm thickness) can theoretically assure very low emittances of the system in a large range of wavelength. The total normal emittance as a function of the coating thickness, for various metallic and non-metallic depositions on nickel substrates, is reported in Fig.4, at 673 K. It can be observed that for metal coatings with thickness greater than 0.1μm the influence of nickel thermal properties on the emittance of the coating/ substrate system is eliminated. On the contrary, SiO and SiO_2. coatings are quite transparent if thickness is approximately less than 0.1 μm.

Gold coated nickel surfaces exhibit excellent radiative properties also in the presence of very thin film coatings: in particular, Fig.5 shows the total normal emittance of such foils against surface temperature for different thicknesses of the gold coating. As mentioned before, metallic diffusion barriers and/ or protective transparent overcoatings are required, in

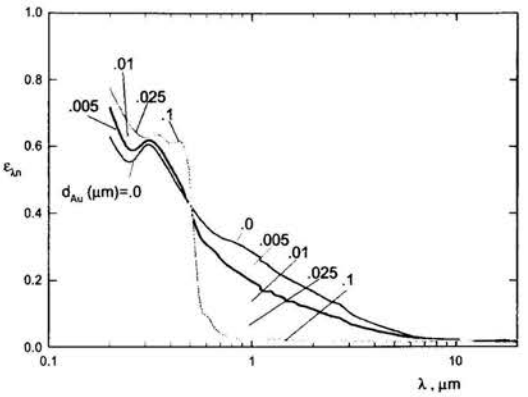

Figure 2: Theoretical spectral normal emittance for Ni-Au systems, with different coating thicknesses.

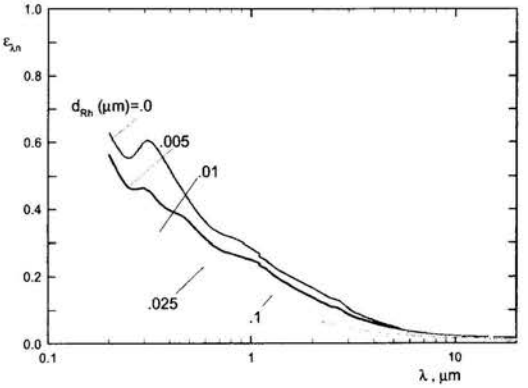

Figure 3: Theoretical spectral normal emittance for Ni-Rh systems, with different coating thicknesses.

systems involving gold coatings, to prevent degradation of radiative properties in operating conditions. The effect of diffusion barriers or protective overcoatings on total emittance of Ni-Au foils is depicted in Fig.6. A layer of SiO_2, placed between Au and Ni, and a SiO overcoating are considered separately. The curves reported in. Fig.6 correspond to the conditions for which a Ni-Au system exhibits a 20% increment in emittance owing to the presence of the SiO_2 barrier (left scale, continuous lines) or the SiO overcoating (right scale, dashed lines). As an example, at 673 K, a 0.1 μm SiO_2 layer between Ni and a 0.03 μm Au coating causes an increase in

HEFAT2002
1st International Conference on Heat Transfer, Fluid Mechanics, and Thermodynamics
8-10 April 2002, Kruger Park, South Africa
GA1

ICP and Microwave Plasma Torches and Gas Combustion Chamber with the Reverse Vortex Stabilization

A. Gutsol*, A. Fridman** and L. Kennedy**
*Research Scientist; **Professor
Department of Mechanical Engineering,
University of Illinois at Chicago,
842 West Taylor Street, Chicago, Illinois 60607-7022,
USA,
E-mail: agutsol@uic.edu, afridman@uic.edu, lkennedy@uic.edu

ABSTRACT

The recently developed method of Reverse-Vortex Stabilization (RVS) of plasma and flame is compared with the more traditional Forward-Vortex Stabilization (FVS) method Experimental calorimetric investigations and numerical simulations were performed with RVS and FVS comparing the energetic characteristics of Microwave and Radio Frequency inductive plasma torches The observed discrepancy between experimental and calculated results is sufficiently small t to conclude that the energy losses associated with the both types of vortex stabilization can be reliably predicted for the design of electrodeless plasma torches. . Calorimetric measurements were also performed comparison two gas combustion chambers using FVS and with RVS. Results of these investigations show that RVS is a very promising alternative for plasma technology and gas combustion chambers applications.

NOMENCLATURE

C_{NO}	concentration of nitrogen oxides
FVS	forward vortex stabilized (stabilization)
H_{10}	the main mode of MW energy propagation in the rectangular waveguide
ICP	inductively coupled plasma
J	energy input per unit mass of plasma gas
MW	microwave
RF	radio frequency
RSM	Reynolds Stress Model
RVS	reverse vortex stabilized (stabilization)
T_g	gas temperature after calorimetric tube
W_c	calorimetric power
W_d	power input into the discharge
W_g	gas heat power after calorimetric tube
W_j	plasma jet power
W_t	heat losses power
W_Σ	total power of gas burner
η	plasma torch efficiency
2*D*	two-dimensional

INTRODUCTION

Plasma sources are among the most powerful systems having relatively small dimensions; as such, heat transfer problems in such system are extremely important. To address the latter problem, a common method for insulating plasma-walls is by employing a vortex flow[1]. Due to buoyancy in the centrifugal force field, this results in the hot plasma fluid fixed on the axis of the system. In the usual vortex method of plasma stabilization / insulation, the vortex generator is placed upstream relative to the electric discharge and the outlet of the plasma jet is directed towards the opposite side; as such this method is termed Forward-Vortex Stabilization (FVS). In such systems with intensive flow rotation, the pressure minimum on the axis near the vortex generator is deeper than that which exits downstream. As a result a central reverse flow forms and transfers upstream the energy from the center of the vortex-stabilized plasma [2]. The hot reverse flow mixes with the incoming cold, direct vortex flow. In gas burners, this mixing results in ignition of the new gas reactants, high intensity and stability of the flame [3]. After mixing, the direct vortex of hot mixture or flame moves along walls of the plasma torch or gas burner and a significant portion of the thermal energy arrives at the device walls and becomes lost. This well-known phenomenon demands sufficient cooling of the device walls.

The idea of the Reverse-Vortex Stabilization (RVS) is to direct an outlet of the plasma or flame jet along the axis to the swirl generator side [4-6]. In this case, cold gas comes into the hot zone from all sides except the outlet side and no significant recirculation zone is formed [6, 7].

In this paper we present a review of experimental results obtained during investigation of Micro-Wave (MW) [5, 6] and Radio-Frequency (RF) [8, 9] Inductively Coupled Plasma (ICP) torches and gas combustion chamber [6, 10], together with the results of numerical simulations of investigated electrodeless plasma torches: MW [6, 7] and RF ICP [9, 11].

MICROWAVE PLASMA TORCH: EXPERIMENTS AND SIMULATION

Experiments were conducted with a microwave (MW) plasma generator with power input up to 5 kW. This plasma torch is a part of an experimental set-up for treatment of inorganic salt solutions [12]. A sketch of the MW plasma torch with the flow patterns of gas and plasma is shown in Fig. 1. The

quartz discharge tube (1) (r ID=4mm, length 140 mm) passes perpendicularly through two wave-guides (90×45 mm^2, not shown), which supply the H_{10} mode of MW energy (frequency 2.4 GHz) from two magnetrons. In the conventional FVS scheme (Fig. 1a) the plasma gas (air or nitrogen) enters the discharge chamber through four inlet openings of the original tangential vortex generator (2), resulting in stabilization of the plasma on the axis of the quartz tube 1 by the strong rotation of the gas. In the experimental plasma-chemical set-up, the MW plasma torch is joined to the uncooled massive steel reactor (4) by an uncooled connecting steel cone (5).

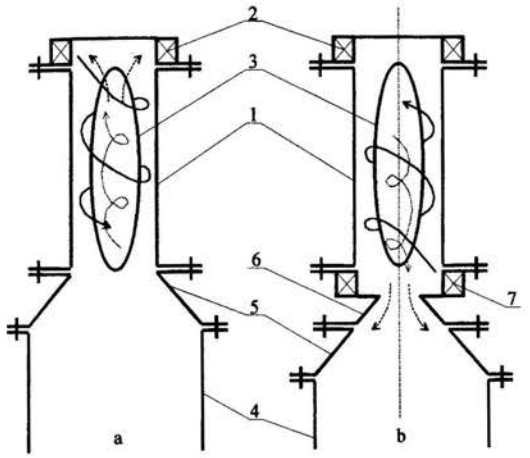

Figure 1: Scheme of the MW Plasma Torches with Supposed Flow Patterns of Gas and Plasma. (a) – FVS; (b) – RVS.

For experiments with RVS (Fig. 1b) an additional vortex generator (7) with a water-cooled diaphragm (6) (diameter 26 mm) was installed between the quartz tube and connecting cone. Calorimetric and electrical measurements permitted determining the MW power input W_d into the discharge and the heat losses W_t to the water-cooled parts of the plasma torch. Unfortunately it is not possible to use water cooling for the quartz tube of the MW plasma torch, but as this tube is surrounded by the water-cooled parts of the plasma torch almost on all sides, it was assumed that practically all the heat from the quartz tube ends up in the cooling system due to convection.

The experimental results are presented in Fig. 2 (dots with full curves) as function of J - the energy input into the discharge per unit mass of plasma gas consumption. The power input was approximately 3.5 kW; it varied a small amount due to the fact that changing the gas flow conditions also influences the discharge conditions. The dots of curve (1) were obtained for the FVS scheme (Fig. 1a) *without* the diaphragm and with the plasma-chemical reactor. Curve (2) corresponds to the same scheme, but *with* the diaphragm. Curve (3) corresponds to the RVS scheme (Fig. 1b) with the reactor. As the heat flux to the plasma torch walls from the reactor was significant, two additional series of experiments were made. The reactor was removed, the plasma torch was turned upside-down, and a hot plasma flow was directed upwards into ambient air. As the heat losses in the FVS scheme without the diaphragm were extremely large for all energy inputs, only the "new" scheme (Fig. 1b) was used in the additional experiments. Plasma gas

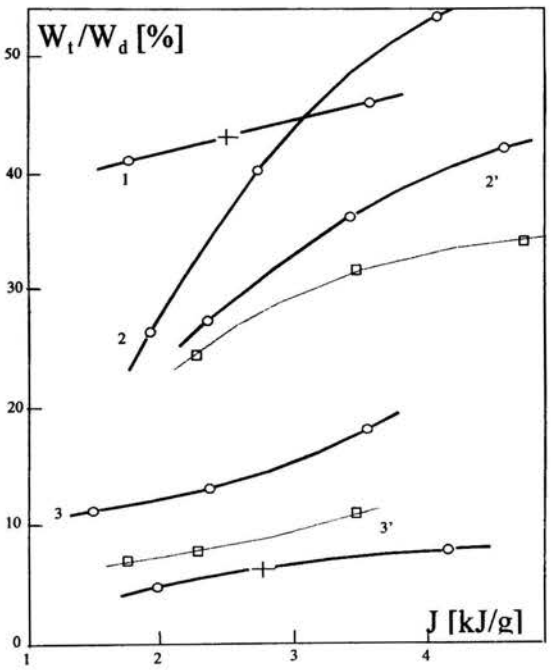

Figure 2: Heat Losses in the Microwave Plasma Generator.

might be supplied through the original vortex generator (2 in Fig. 1) for realizing the conventional FVS scheme, or through the additional vortex chamber (7 in Fig. 1) for realizing the *reverse vortex* scheme of plasma stabilization. Curves (2' and 3'inFig. 2) correspond to these two cases.

The experimental investigation showed that if the plasma was stabilized by the conventional vortex flow the energy loss to the plasma torch walls might exceed 30 %. With the RVS the energy loss was reduced to about 5 %. The heat loss in a simple system of this type corresponds to the low heat loss in plasma generators with a porous discharge chamber, which, however, is very complex and expensive to manufacture. More over, if the RVS is used, almost all of the plasma forming gas should pass through the discharge zone. Since the axial velocity in the "top" region of the reverse vortex should be quite low, discharge stability problems should not occur. As the flow direction should be constant throughout the axial region, it seems possible to inject additional gas or particles into the "top" of the reverse vortex. Tests with

ZrO_2+Y_2O_3 powder were made in the described MW facility. The introduction of the powder into the "top" of plasma torch with the RVS plasma ensures melting and spheroidization of particles up to 100 μm.

The numerical simulations flow and heat transfer of the MW plasma torch were made using FLUENT. In the 2D axisymmetric geometry the conservation equations for mass, energy and radial, axial and azimuthal momentum were solved simultaneously. To account for turbulence the Reynolds Stress Model was used. This model involves calculation of the individual Reynolds stresses and is more suitable for rotating flows than the usual k-ε model. In the near-wall region the program used the logarithmic law for velocity. The law-of-the-wall for temperature in Fluent comprises two different laws: a linear law for the thermal conduction sublayer and a logarithmic law for the turbulent region. The minimum size of the grid cell near the wall was about 0.3 mm. The heating of the plasma was assumed to take place in an idealized uniform heat generation zone in the central region of the rotating flow. The pre-described heating zone length was 120 mm. Its diameter was varied, but was usually 26 mm. The temperature of metallic parts of the plasma generator were assumed be 300 K. On the cylindrical wall, convective cooling with a heat transfer coefficient of 50 W m^{-2} K^{-1} and radiation cooling with an external emissivity of 0.8 were assumed. Test calculations showed that the most realistic flow pattern in the inlet regions was obtained in a 2D geometry when the discrete tangential gas inlet jets were simulated by fixing the rotating velocity in the cells next to the cylindrical wall and defining the appropriate mass sources for the same cells.

Figure (3a) shows the streamlines, profiles of axial velocity and the temperature distribution for the FVS scheme, and Fig. (3b) for the RVS scheme. In these two cases the heating zone (3.5 kW, length 0.14 m, diameter 44 mm) was in the center of the MW plasma torch quartz tube (1inFig. 1). Nitrogen gas enters tangentially into the discharge chamber (FVS scheme) or into the additional vortex chamber (RVS scheme). The initial velocity of the tangential gas jets was estimated from the measurements of the pressure drop and the gas consumption. In the two cases showed in Fig. (3a and 3b) the initial tangential velocities and the gas consumption are respectively 100 m s^{-1} (1 g s^{-1}) and 225 m s^{-1} (1.5 g s^{-1}),. It is easy to see (Fig. 3b) that the reverse vortex "compresses" the heat zone and protects the plasma torch walls from overheating. As it was initially supposed [4, 5], the main part of the plasma gas passes through the high temperature discharge zone and the size of recirculation zones are considerably reduced. Alternately, in the FVS scheme (Fig. 3a), , the main part of the incoming gas mixes with the hot recirculated flow and moves along the cylindrical quartz wall thus bypassing the discharge zone. The calculated energy losses for the appropriate cases are shown by the dots of the broken curves on Fig. 2 (curve 2' - for the FVS scheme, curve 3' - for the RVS scheme). While a discrepancy between experimental and calculated results occur due to the oversimplified description of the discharge zone, ; this discrepancy is sufficiently small to conclude that the energy losses can be reliably predicted for other electric discharges and flames by employing numerical simulation models.

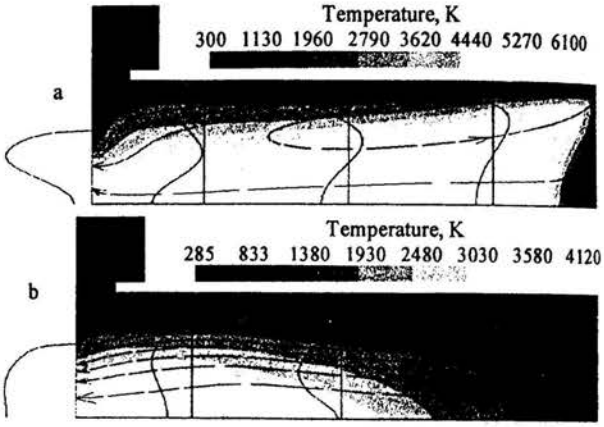

Figure 3: Temperature distribution, streamlines and profiles of axial velocity for three different cross-sections and for outlet of the MW plasma torches with FVS (a) and with RVS (b).

RADIO FREQUENCY (ICP) INDUCTIVELY COUPLED PLASMA TORCH: EXPERIMENTS AND SIMULATION

The scheme of the RF inductive plasma torch with the reverse vortex flow is shown on Fig.(4). Plasma gas enters the discharge volume through tangential swirler-2. The water-cooled nozzle-1 prevents the immediate exit of the plasma gas from the volume. On the left side of the scheme, the gas streamlines-5 are shown. The streamlines -7 of the gas and plasma in the radial plane are shown on the right side of the Fig (4). The discharge volume is restricted by the quartz tube -3. Water-cooled inductive coil-4 supplies RF electromagnetic energy, which is absorbed in the toroidal skin-layer -8 of the plasma fluid -9. Plasma leaves the discharge volume as a flow-6 through the nozzle-1.

There is one fundamental difference between microwave plasma and ICP. In a MW plasma there is a central hot zone with low flow velocity that acts as a stabilizing core producing active species and electrons. In ICP, the RF field energy is absorbed in a toroidal zone -8 around the center. The diameter of this zone determines the coupling efficiency of the energy transfer from the inductive coil -4 to the plasma-9. In the reverse vortex flow, there is a significant negative radial flow component over the entire length of the active region. This radial flow should compress the toroidal skin-layer zone-8 MW or flame. Therefore, the stability of this setup should be lower than in MW or flames.

Figure 4: Scheme of the RF ICP Torch with RVS.

Preliminary experiments [9, 13] show that it is possible to obtain stable ICP plasma with the reverse vortex flow

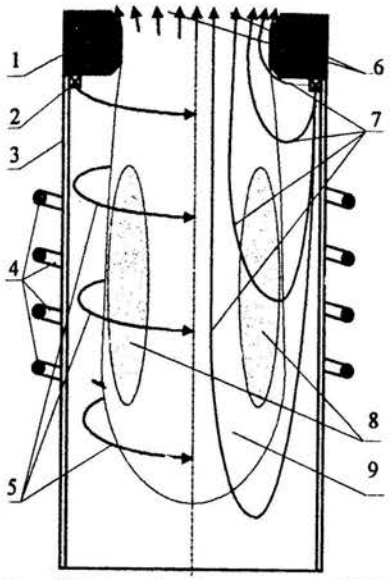

configuration. The experiments were accomplished using a common RF power supply with a frequency of 2 MHz. The quartz plasma chamber has ID= 75 mm. The 4-loop inductive coil has ID= 90 mm and length of 100 mm. The distance between the 50 mm nozzle and the inductive coil is 70 mm. Argon was principally used as the plasma gas. In some experiments the admixture of nitrogen was used.

To compare the efficiencies of the RVS ICP and FVS ICP torches of the same geometry as plasma jet generators, total calorimetric measurements and numerical simulations were made using atmospheric pressure argon plasma. The FVS ICP torch geometry differs from that normally used by the nozzle-(1in Fig 4)on the plasma exit end.

In the calorimetric measurements and simulations a nozzle of 43 mm length and 25 mm smallest ID, and a feeder with ID= 72 mm that has four circular tangential inlets of 2 mm diameter was used. The quartz tube length was 380 mm and the center of the inductive coil was at 130 mm from the feeder side of the nozzle. After a preliminary study [9,13] the plasma torch scheme was modified for the calorimetric measurements to provide water cooling of all surroundings including the quartz tube. The powers absorbed by the nozzle and the tube were separately measured. A stainless steel heat exchanger was mounted downstream of the plasma torch to measure the exhaust gas enthalpy. Measurement of the argon temperature after the heat exchanger indicated that heat loss after this point was negligible. The total radiation intensity at about 1.3 m distance from the plasma with a black-body surface absorber was measured and then the total radiation loss was calculated taking into account partial absorption by the non-transparent water-cooled parts of the plasma torch. The sum of all the measured losses (nozzle, tube, radiation and heat exchanger is equal to the total energy initially absorbed by the plasma from the inductive coil. The total discharge power W_d, measured with about 3% accuracy, was 55% - 75% of the plate power of the RF generator depending on the discharge regime and stabilization method. The plate power of the Soviet RF generator ВЧИ 11-60/1,76 was calculated by multiplying the anode voltage and anode current. The accuracy was poorer because of the low resolution of the monitoring devices. The repeatability of the discharge regime also was not very high, as the final adjusting of the generator-discharge system could be made only after the discharge ignition.

The experiments with a FVS ICP in the geometry with the contracted plasma exit have shown the extremely high stability of this discharge. It is possible to change the RF generator power by an order of magnitude with the same argon mass flow, retaining a stable discharge, only its brightness and volume change. The reason for the high stability becomes obvious from modeling [9,11]. The gas flows mostly around the discharge and cools it mainly through its "surface" (conductive cooling). The discharge absorbs energy from the electromagnetic field. When the RF power is increased, the stronger ampere force pulls more gas from the circumventing flow towards the skin region. Moreover, the plasma expands due to the increased power, and as a result the gas temperature in the circumventing flow increases and the gas expands thermally, partially mixing with the plasma. Thus, the result of an increased power increment is electromagnetic and thermodynamic "pumping" of gas through the plasma region (convective cooling).

The power characteristics of the FVS ICP, such as the dependence of the average plasma jet enthalpy on the plate power and the dependence of the plasma torch efficiency on the discharge power (Fig. 5) are typical.

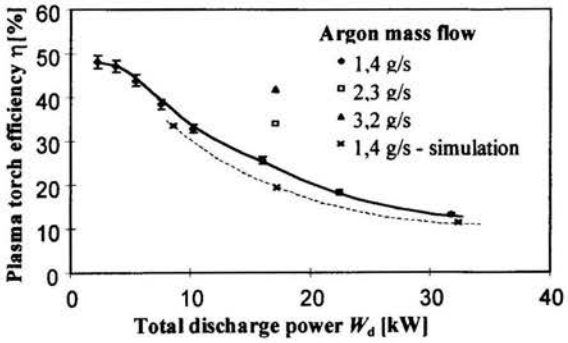

Figure 5: Argon FVS ICP. Dependence of η on W_d for Different Argon Mass Flow.

Here the plasma torch efficiency η is the ratio of the plasma jet power W_j (we assume that the power of the plasma jet is equal to the power absorbed by the heat exchanger) to the total discharge power W_d: $\eta = W_j/W_d$. Increasing plate power under a constant argon mass flow rate results in an increase of the average plasma jet enthalpy from 0.8 kJ/g to 3 kJ/g. An argon mass flow rate increase under a constant plate power results in a decrease of the average plasma jet enthalpy. The plasma torch efficiency drops with the growth of the discharge power and with the decrease of argon mass flow rate (Fig. 5). Thus, the FVS ICP is able to generate a high enthalpy plasma

jet with low efficiency or a low enthalpy plasma jet with rather high efficiency. The simulation results are in a reasonable agreement with the experimental ones (Fig. 5).

Considering the stability of the RVS ICP, the power threshold for its existence is much higher than for FVS ICP. The plasma torch efficiency for the RVS (Fig. 6) also drops with the growth of the discharge power and the gas flow rate decrease, though η reaches a higher level than in the FVS ICP.

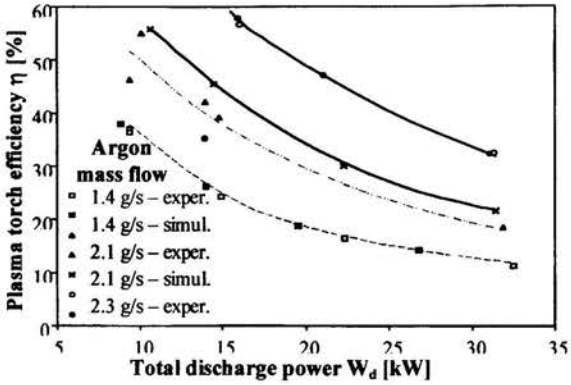

Figure 6: Argon RVS ICP. Dependence of η on W_d for Different Argon Mass Flow.

The average enthalpy of the argon plasma jet generated by the RVS ICP is higher than 2 kJ/g in all cases. It does not grow only with the plate power, but also with the argon mass flow rate, which is extremely unusual for any type of discharge. It is possible to understand the reason for this phenomenon from the result of the numerical simulation [9, 11] and flow pattern on Fig. 4. The gas flows mostly through the active discharge zone and after that its enthalpy rises to a very high and approximately constant level. An additional recirculation zone is formed in the closed part of the discharge tube due to the ampere force. Probably it is this recirculation that creates the plasma "tail", observed under some conditions during the preliminary study [9, 13], and results as additional heat and radiation losses. (The fraction of the radiation losses in the total energy balance of the RVS ICP torch varied in a wide range: from 8% to 32%.) The increase of the plasma gas flow results in shrinking of the additional recirculation zone and the plasma volume. This leads to a significant reduction of heat losses via the quartz tube and radiation, so the average plasma jet enthalpy increases. This phenomenon indicates that the RVS ICP torch is capable of generating a high enthalpy plasma jet with a high efficiency. This property is very useful in various applications. Fig. 6 also shows that the modeling results for the plasma jet generation efficiency of the RVS ICP torch was in good agreement with experiments. A large discrepancy between the experimental curve and the simulated result is only beyond the experimentally observed range of discharge stability (see data for the argon mass flow 3.2 g/s and 14 kW power).

The obtained plasma jet generation efficiency (up to 48 % for the FVS and 58 % for the RVS) of the studied argon RF plasma torches with a water-cooled nozzle was compared with reliable data for other argon ICP torches. The latter ranged from about 55% for the torch without a nozzle but with a water-cooled probe for material feeding [14]; up to 45% [15]; up to 37% in the papers cited in Ref.[16]. It becomes clear that the plasma jet generation efficiency of this RVS ICP torch is rather high. This is a promising property for those torches where the nozzle is a necessary design part, for example, in the sources of supersonic plasma jets [17].

From the application point of view, probably the most promising property of the reverse vortex flows is the possibility to inject an additional axial flow from the closed end of the system without substantially disrupting the flow pattern. Our experiments showed that the axial argon flow could be as strong as the main swirl argon flow without extinguishing the discharge. The calorimetric measurements of a similar regime gave the next results: at 49 kW plate power, 2.29 g/s argon mass flow through the tangential feeder and additional 0.85 g/s of nitrogen mass flow through the axial tube, the discharge absorbed 36.46 kW (74.4 % of plate power). With 48.4 % efficiency, it generates a plasma jet with average enthalpy of 5,62 kJ/g. This corresponds approximately to 6000K temperature for the given mixture of an argon and nitrogen. Therefore, it may be possible to insert large quantities of material (gaseous or disperse) for plasma treatment in the active zone. According to our insight [18] the treated products should not significantly interact with the plasma torch wall. This property may open new opportunities in plasma technology, as the lack of such properties in traditional RF discharges restricts their applications in plasma chemistry and technology [19].

EXPERIMENTAL INVESTIGATION OF THE GAS BURNERS

A comparative investigation was carried out for the experimental vortex gas burners with conventional FVS and with RVS. Schemes of the burners are presented in Fig. 7.

Propane-butane mixture was used as a fuel and air as oxidant. In all experiments consumption of fuel gas and air was constant and calculated power of the burner was 1800 ± 300 Wt. Energetic characteristics of the burners were examined using gas temperature measurements and a calorimetric water-cooled tube which was connected with the outlet of burner or acted for the burner side wall. These characteristics are presented in Table 1: gas temperature T_g and gas heat power W_g after the calorimetric tube, calorimetric power W_c, total power W_Σ and concentration of nitrogen oxides C_{NO}.

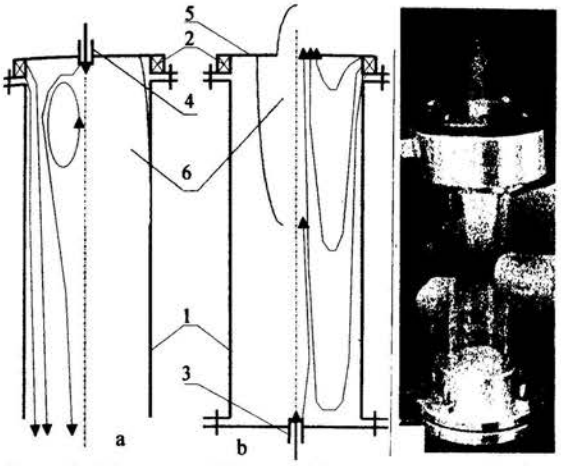

Figure 6. Schemes and Picture of the Gas Burners of 2 kW Power. (a) – with FVS; (b) and (c) – with RVS. 1 – quartz tube; 2 - tangential air feeder for swirl flow formation; 3 and 4 – fuel gas injection; 5 – diaphragm for flame jet exit.

Table 1. Energetic characteristics of the examined burners

Type of burner	W_c, Wt	T_g, K	W_g, Wt	W_Σ, Wt	C_{NO}, %
Reverse-vortex	1570±30	780±10	400±15	1970±40	0,35
Direct-vortex	1250±25	490±10	155±10	1405±30	0,41
Cooling direct vortex	100±30	560±10	215±10	1615±35	0,46

The quartz wall of the conventional direct vortex burner was heated to a red glow while the reverse vortex burner may be handheld without any special cooling (Fig. 6c). Hence, the heat loses to the wall of the reverse vortex burner cannot be more than 100 Wt.

CONCLUSIONS

Experimental investigations and numerical simulations show that RVS is very promising method for different high temperature applications. A discrepancy between experimental and calculated results is sufficiently small to conclude that the energy losses can be reliably predicted for the design of electrodeless plasma torches with the both types of vortex stabilization.

REFERENCES

[1] Goldshtik, M. A. (Editor), 1979, "Vortex Plasma Insulation", Nauka, Novosiborsk, USSR (In Russian).

[2] Dresvin, S. V., Donskoy, A. V., Goldfarb, V. M., et al., 1972, "Low-Temperature Plasma: Physics and Technology", Atomizdat, Moscow, USSR (In Russian).

[3] Gupta, A. K., Lilley, D. G. and Syred, N., 1984, "Swirl flows", Abacus Press, England.

[4] Gutsol, A. F., 1997, "Method for the flow system formation", Patent 2086812 RU, (Russia).

[5] Kalinnikov, V. T. and Gutsol, A. F., 1997, "A New Efficient Method of Insulating High-Temperature and Reacting Systems and the Ranque Effect", Physics - Doklady, Vol. 42, No. 4, pp. 179 - 181.

[6] Gutsol, A. F. and Kalinnikov, V. T., 1999, "Reverse-Flow Swirl Heat Insulation of Plasma and Gas Flame", High Temperature, Vol. 37, No. 2, 1999, pp. 172 - 179.

[7] Gutsol, A. and Bakken, J. A., 1998, "New Vortex Method of Plasma Insulation and Explanation of the Ranque Effect", J. Phys.D: Appl.Phys., Vol.31, No. 6, pp. 704-711.

[8] Gutsol, A., Larjo, J. and Hernberg R., 1999, "RF Inductive Plasma Torch with Reverse Vortex Flow Stabilization", Proc. of the 14th Int.l Symposium on Plasma Chemistry, Prague, August 2 - 6, 1999, Vol. 1, pp. 227 - 231.

[9] Gutsol, A., Larjo, J. and Hernberg, R., 2001, "Reverse-Flow Swirl Radio-Frequency Induction Plasmatron", High Temperature, Vol. 39, No. 2, pp. 169 - 179.

[10] Kalinnikov, V. T. and Gutsol, A. F., 1998, "Insulation of the gas flame in the reverse vortex", Physics - Doklady, Vol. 43, No. 5, pp. 302 - 305.

[11] Gutsol, A., Larjo, J. and Hernberg R., 1999, "The Effect of Turbulence Model on the Simulation of Gas Flow in ICP", Proceedings of the 14th Int Symposium on Plasma Chemistry, Prague, August 2 - 6, Vol. 1, pp. 275 - 280.

[12] Gutsol A. F., 1995, "Plasma processing of fluoride solutions of refractory rare metals", High Energy Chemistry, 1995, V.29, No.5, P.373-376.

[13] Gutsol, A., Larjo, J. and Hernberg R., 1999, "Reverse vortex flow stabilised ICP", Abstracts 2nd Int. Symp. Heat and Mass Transfer under Plasma Conditions, April 19-23, Tekirova, Antalya, Turkey, pp. 129-131.

[14] Merkhouf, A. and Boulos, M. I., 1999, "Experimental Validation for an Integrated Model of the Induction Plasma Generation System", Proc. 14th Int. Symp. Plasma Chemistry, Prague, August 2 - 6, Vol. 1, pp. 421-426.

[15] Reed, T. B., 1961, "Induction-Coupled Plasma Torch", Journal of Applied Physics, Vol. 32, pp. 821-823.

[16] Goykhman, V. Kh. And Goldfarb, V. M., 1977, "High-frequency inductive thermal discharge", In "Plasma Chemical Reactions and Processes", Nauka, Moscow, pp. 231-278 (In Russian).

[17] Hollenstein, M., Rahmane, M. and Boulos, M. I., 1999, "Experimental validation for an integrated model of the induction plasma generation system", Proc. of the 14th International Symposium on Plasma Chemistry, Prague, August 2 - 6, Vol. 1, pp. 257-262.

[18] Gutsol A. F., 1997, "The Ranque effect" Physics - Uspekhi, Vol. 40, No. 6, p. 639 - 658.

[19] McKelliget, J. W. and El-Kaddah, N., 1998, "The effect of coil design on materials synthesis in an inductively coupled plasma torch", Journal of Applied Physics, Vol. 64, No. 6, pp. 2948-2953.

HEFAT2002
1st International Conference on Heat Transfer, Fluid Mechanics and Thermodynamics
8-10 April 2002, Kruger Park, South Africa
KG1

Chemical Kinetic Formulations For Modeling Gas Phase Reactive Systems

Ghazi A. Karim
Mechanical Engineering, University of Calgary, Calgary, Canada, T2N 1N4
E-mail:karim@enme.ucalgary.ca

ABSTRACT

Gas phase combustion systems involve time dependent chemical reactions that release energy and change composition. To model the behavior of such systems, adequate account must be made of the chemical kinetics of the reactive medium. The paper presents with examples, some of the main procedures that have been followed to model successfully the events taking place in the combustion process in a variety of systems and to predict the temporal variations in the composition of all the important reactive species, temperature and the associated energy release. The limitations that need to be overcome are outlined.

Keyword: chemical kinetics, combustion modeling

INTRODUCTION

Combustion processes by definition involve chemical reactions that are exothermic and relatively fast. Accordingly, the proper modeling of such processes needs to define the type and sequence of chemical changes that take place and consider their consequent temporal changes in composition and properties of the system. This is no simple task since complex coupled non-linear differential equations would result with much of the key information about the mode of these reactions, their corresponding properties and the reactive species may be unknown. It is only relatively recently, with the continuing increase in the capacity and speed of computing facilities and the significant advances made in the solution of complex mathematical systems that extensive progress is achieved to satisfy these objectives with a considerable degree of success. This effort was prompted largely by the need to bring about substantial improvements to the performance of combustion systems to effect enhanced efficiencies, reduced emissions and a greater safety and reliability while burning a wide range of fuels.

The present contribution presents a concise review of some of the main procedures that have been followed to model successfully the combustion process in a variety of systems. These include practical heat and work producing devices. The limitations that still need to be overcome will be outlined. Throughout, much of the examples cited will be derived mainly for convenience from work the author and his associates have been involved with.

Modeling Combustion Systems

The computational modeling of combustion processes and systems has undergone rapid and major advances in recent years to contribute effectively to the continued development of improved designs coupled with improvement to our understanding of the complex processes involved. Such models serve both as design interpolative and explorative tools requiring only little support from experimental testing. They also serve as an analysis tool in the interpretation of the behavior and results of complex experiments while developing improvements to physical, chemical and numerical sub-models.

The combustion models can be classified according to their being either Diagnostic or Predictive. Those models that are mainly diagnostic aim through analysis and using some experimental input data, such as temperature or pressure-time variation, to derive additional information about the combustion processes such as the energy release rate, power output, efficiency and oxides of nitrogen formation. The quality of the derived results will depend very much on the experimental data utilized and the associated assumptions employed in their analysis. On the other hand, predictive models through formulations of the physical and chemical related equations describing the combustion system and making suitable assumptions with relevant boundary equations can predict some of the key combustion parameters without the need for input of experimental information. Of course, the extent of success achieved in modeling combustion is critically dependent

on the completeness of understanding its processes and the range of values of the variables over which the model is applicable. Experimental validation of the predicted results are, of course, always needed and expected.

The course of the combustion process can be followed and defined in a number of often-interdependent ways. Through chemical reaction, the concentrations of the different species of the system undergo rapid changes. These will have major influence on the overall and local properties of the system. Such changes will result in apparent energy release that is so important to applications. Accordingly, the rate of combustion can be defined in terms of the rate of change with time of the concentration of any of the reacting species; often the reactants or products. Or it may be through the consequent changes to some of the affected variables, such as mixture temperature, pressure and enthalpy or the net energy release. These variables, through proper modeling can be shown to be inter-related. In an application it would depend on the purpose of modeling to select a format of the combustion rate that is likely to provide more conveniently the answer needed.

Combustion models also can be broadly classified depending on how the combustion rate is defined. One of the simplest and widely established approaches is through specifying, whether arbitrarily or experimentally a function that describes the variation of the fraction of mass burned and the consequent energy release rate with time. These functions can vary very widely in form and often incorporate empirical constants that are made to vary depending on the system and operating conditions. Obviously, such approaches, although can be very simple to incorporate in comprehensive modeling procedures, are of very limited applicability unless experimental information about the behavior of the combustion system is available. The procedure is used primarily for interpolative or extrapolative purposes with a need for a full awareness of the limitations of the approach.

The combustion rate in turbulent combustion models is assumed related to the flame front area and the corresponding flame speed. The flame area is determined either experimentally or estimated from flow analysis considerations. The flame speed is often obtained from correlations that are derived either from experimental observations or a simple assumed theory. Such approaches have also their serious limitations, especially when the performance of practical devices such as engines, is modeled.

A third approach to modeling the combustion rate is through simulating the chemical reaction activity of the system. This can be done to varying degrees of detail depending on the objectives of the modeling activity, the extent of computational effort that is considered acceptable and above all whether the needed information about the reaction kinetics of the system is known with sufficient reliability. Such a modeling approach can be simplistic which considers hypothesized gross or global reactions that proceed during combustion to result in the conversion of the fuel-air mixture directly into products with the consequent release of energy. Obviously, this empirical approach has its serious limitations. The alternative is to formulate a comprehensive listing of the likely reacting species both stable and unstable and the corresponding combinations of sequential elemental reactions that may proceed at significant rates. The corresponding rate data for all these reactions need to be known with sufficient accuracy. This representation of the sequence of reactions during combustion should yield not only reliable energy release rates but also provide a detailed account of the composition of the reactive system and its temporal changes. Thus, it is the only approach to modeling that can provide reliably information about exhaust emissions. Such a detailed modeling becomes much too unwieldy, when considering the oxidation reactions of most practical fuel systems. Hence, reduced kinetic schemes may be formulated that tend to serve as a compromise between having fully detailed schemes and those of the simple gross type. The reduced formulation of kinetic schemes can vary widely in length and comprehensiveness depending on the system considered and the information required from using the model. Great care is equally needed in the derivation, selection and use of such abridged schemes.

Combustion models can be further classified broadly according to whether they are zero-dimensional single-zone or quasi-dimensional multi-zone models. Another group of models that is increasing in prominence is multi-dimensional that incorporate computational fluid dynamics, C.F.D.

Models Based on Energy Release Formulations

One of the simplest combustion models is the zero-dimension single-zone approach were the energy release is assumed to be time independent with the products of combustion in a state of chemical thermodynamic equilibrium. The resulting instantaneous bulk energy release then can be calculated from thermodynamic relations readily. The products are assumed to remain either frozen in composition, irrespective of the subsequent changes to the system or the Equilibrium State is retained. The consequent changes in composition and the corresponding bulk energy release determined can be determined accordingly. This is a simple approach that can be quite useful under some conditions such as those for highly reactive mixtures and under high temperature conditions. The composition of the products and the energy release calculated this way, however, can be grossly in error, especially when conditions depart significantly from the near-equilibrium state assumed. Moreover, during combustion only a partial state of equilibrium may be apparent, where some product species appear in near equilibrium concentrations while others do

not. Obviously, approaches that involve an assumption of thermodynamic equilibrium cannot be expected to predict well features and properties of time-dependent combustion processes.

An approach to combustion modeling of zero dimension single zone systems is through the use of empirically based combustion energy release functions that account for the gross energy changes due to combustion. This modeling approach effectively assumes combustion to be equivalent to an external heat transfer process with some adjustment made to the composition of the system due to the consequent changes in temperature. This approach has been used widely with some success in applications where sufficient information and experience are available about the combustion characteristics of the system and when only changes in gross performance parameters such temperature and pressure are needed. These heat release rate functions can be derived through simple thermodynamic analysis of existing experimentally obtained temporal variations in pressure or temperature. For example Figure (1) shows the energy release rate derived from the experimentally obtained pressure diagram of an engine operating on an autoigniting homogeneous mixture of n-heptane and air [6]. A similar approach has been used extensively by the diesel engine industry to develop pressure-time records and derive the consequent indicated power output and torque [1]. However, information about changes in composition due to combustion cannot be obtained reliably. Also, the charge in diesel engines is neither homogeneous nor has uniform properties. Such an approach, in principle, can be improved upon when dual or multiple combustion zones are assumed during the combustion phase [2]. For example, Figure (2) shows for a spark ignition engine the rate of burning fuel derived on the basis that the charge at any instant during combustion is made up of burned and unburned changing in size zones. Such an approach can produce a better representation of the energy release rate variation due to combustion than single zone models. From such information, generalized approaches can be developed that can represent the assumed temporal variation in the energy release due to combustion. These can be incorporated into fairly elaborate predictive engine performance models [3]. Such approaches have been shown to be quite useful in predicting changes in performance due to changes in operating and design conditions when formulated functions based on extension of experience with related practical systems are used.

Chemical Kinetic Combustion Modeling

It is assumed that the usual formulations for chemical kinetic relations are sufficiently well known that they need not be reproduced here. Only a selection of results that illustrate the different approaches to combustion modeling will be presented with typical examples of their applications presented and discussed.

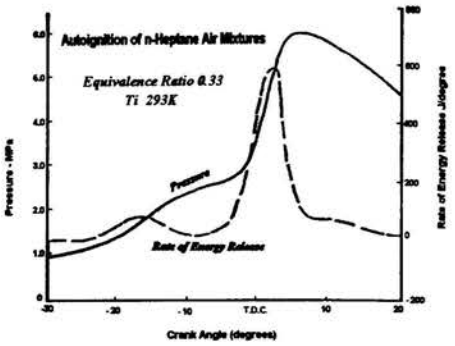

Figure (1) Rate of energy release variation with time derived from experimental pressure-time record for an engine operating on n-heptane air mixtures in the absence of external ignition [6].

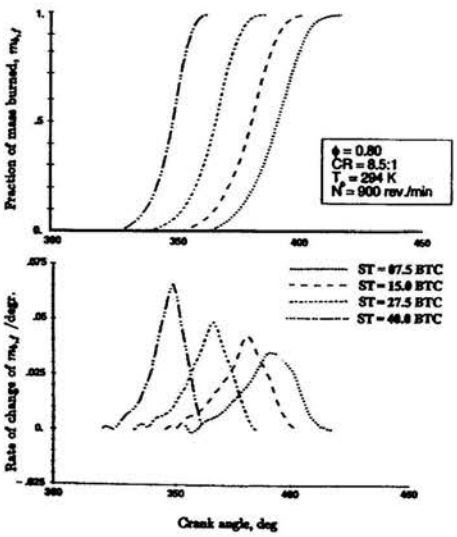

Figure (2) Variation of derived values of the mass of fuel burned and the energy released with time for a CFR engine operating on methane [10].

The reaction rate is commonly represented by the rate of change of the molar concentration of a reacting species, "i" with time, "dCi/dt". It is directly related to the product of the instantaneous concentrations of the species involved in the reaction and exponentially dependent on, "-E/RT"; where,"E" the activation energy of the reaction,"R" universal gas constant and "T" temperature. This relation is applicable strictly only to single step elementary reactions. However, mainly for convenience it

has been widely applied instead to the entire combustion process. A single-step gross overall reaction is assumed to take the fuel and oxygen directly to products without due regards to the multi-step nature and species of the combustion reactions. To have such a relation fit experimental observations; suitable empirical constants are derived. A resort to such an overall kinetic approach is empirical and can provide agreement with experiment over only the range of conditions that were used in the first instance to obtain the corresponding constants. Its application may be only viable for representing the energy release rate and changes in the fuel concentration over only a narrow range of the progress of reactions, such as during the preignition stage. For practical fuels and under certain operating conditions, even such a simple and approximate relation does not apply. For example, the pre-ignition reactions of a homogeneous mixture of n-heptane and air during the compression stroke in the absence of a deliberate external ignition source in an engine, shown in Figure (1), produces an apparent gross reaction rate that does not follow the Arrehenius format. Instead, it shows a multitude of activation energy values with some appearing to be even negative [6].

Of course, the combustion reactions of fuels in air increase in complexity with an increase in the size of the fuel molecule. Even for a relatively simple fuel such as hydrogen or methane numerous reaction species both stable and unstable are formed during the course of the reaction. These take part in a very large number of possible reaction steps. Each has its own rate, which varies with the instantaneous concentration of the corresponding species taking part and temperature. Accordingly, the prediction of the energy release and the local temporal changes in the system properties must take the rates of these reactions into account collectively.

There has been much progress in developing comprehensive schemes for the oxidation of common fuels in air. These vary widely in complexity, detail and accuracy. Obviously, when the transient and final concentrations of reacting species are required, such as often the case when the extent of exhaust emissions needs to be established, the use of a suitably comprehensive scheme is a must. For example, to consider the oxidation reactions of a mixture of common gaseous fuels such as that of natural gas, a scheme made up of around 150 reaction steps were used in predictive models relating to natural gas combustion [8]. For a higher hydrocarbon fuel such as n-heptane in air significantly larger size schemes are needed, especially when wide ranges of temperature, equivalence ratio and pressure are to be covered.

The use of comprehensive reaction schemes in predictive models is readily possible for zero-dimension single-zone systems. It can be applied often also to two-zone quasi-dimensional models. However, their incorporation in full into multi-dimensional CFD models remains a hurdle yet to be overcome. Much effort is expended in this direction with increasing prospects of success.

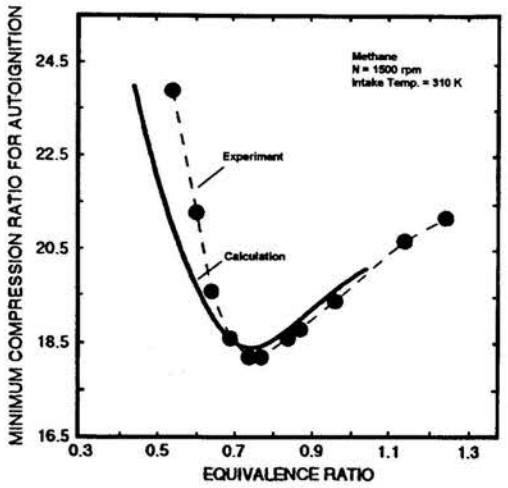

Figure (3) Calculated minimum compression ration required for autoignition of methane air mixtures over a range of equivalence ratios; Downs et al [5]; experimental results are also shown

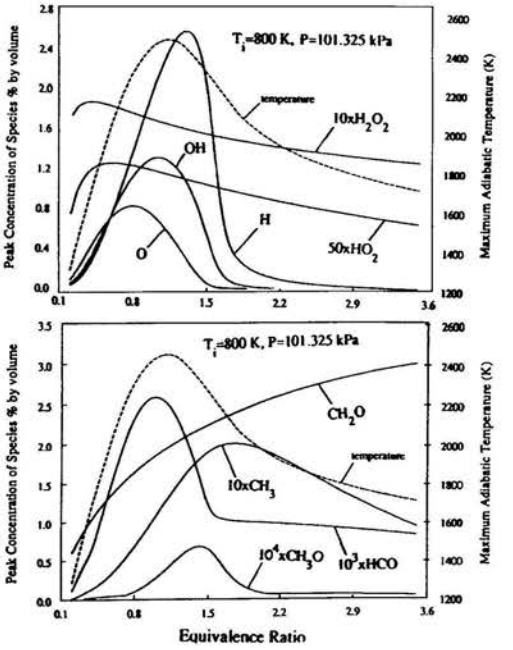

Figure (4) Variation of the concentrations of a selection of species taking part in the reaction of methane in air [10].

Some Examples

Liu and Karim [9] used a kinetic scheme for the oxidation reactions of methane in air made up of 138 reaction steps and 32 chemical species. They used it to predict the autoignition of methane in a variable compression ratio engine in the absence of an ignition source while considering the mixture to behave as a single zone and accounting for the effects of heat transfer and residual gases. Figure (3) shows very good agreement with the corresponding experimental results of Downs et al. [5]. Such approaches yield very comprehensive data about the concentration changes in the many species taking part in the reaction whether stable or unstable. Figure (4) shows typically for the case of adiabatic constant pressure reaction of methane initially at 800K, how the peak values of some of the key reactive species vary with equivalence ratio [10]. Some of these species have exceedingly low values while others (e.g. H, OH, O and CH3) do reach substantial concentrations during the course of the reaction. The corresponding peak value of temperature attained sometime during the reaction, which is also shown, can exceed the thermodynamic calculated values for rich mixtures.

Khalil et al. [7] used an extensive scheme of 1966 reaction steps and 380 species to describe the reactions of a higher hydrocarbon fuel such as n-heptane in air. Figure (5) shows the complex and changing nature of the combustion energy release under isothermal conditions of a stoichiometric mixture for a range of temperature values reflecting the multi-stage nature of its reaction. This cannot be represented adequately by a single gross reaction.

Until recently CFD modeling could not incorporate comprehensive detailed kinetics but incorporated mainly gross single step reactions. This invariably resulted in comprehensively detailed information of the flow characteristics while the chemical aspects often remain poorly represented. A number of approaches are being tried to remedy this situation. For example drastically reduced schemes are used. Another approach is to essentially decouple the two aspects of the calculation such that comprehensively detailed chemical scheme is used over a simplified corresponding condition with a zero dimensional system. Then, the results are used in a fitting procedure to obtain an apparent gross reaction rate functions that are reapplied into the CFD code to produce modified results. This way a quasi-combined CFD and detailed kinetics modeling is achieved [4].

For example, Figure (6) shows predicted pressure time development during the compression ignition of a H2/O2/Ar stoichiometric mixture both when using a single zone modeling with detailed kinetics and CFD modeling incorporating the varying activation energy function. Significant differences between the results of the two approaches and the corresponding experiment can be seen. These show that further research is needed to develop improved combustion models that account reliably for both the chemical and physical aspects of combustion.

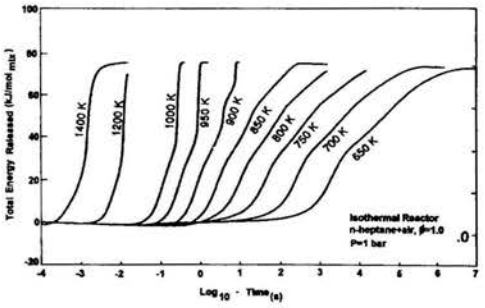

Figure (5) Variation of the calculated energy release rate for n-heptane-air mixtures for a range of temperatures [7].

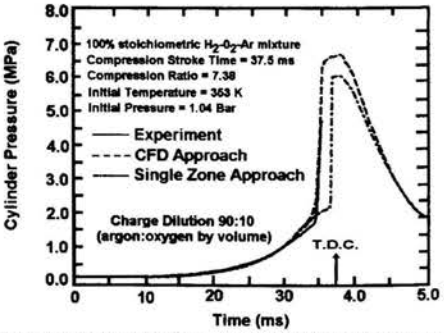

Figure (6) Comparison between experimental pressure-time record and those obtained using the single zone and CFD approaches for the compression ignition of hydrogen/ oxygen argon mixtures in a compression-expansion apparatus [4].

References

1- Austen, A. and Lyn, W.T., Proc. of CIMAC, P.1067, 1962.

2- Bade Shrestha, S.O. and Karim, G.A., SAE paper No.993482, October 1999.

3- Bade Shrestha, S.O. and Karim, G.A., Proc. Instn. Mech. Engnrs, Vol. 215, Part A, pp.63-74, 2001.

4- Chen, Kai, Karim, G.A. and Watson, H.C., ASME,ICE-Vol. 33-3, paper No. 99-ICE-235, 1999

5- Downs, D., Walsh, A.D. and Wheeler, R.W., Phil. Trans. Roy. Soc., Vol.243 (A-870), pp. 463-524, 1951.

6- Karim, G.A., Khan, M.O., and Moore, N.P.W., SAE Trans.,pp.164-177, Paper No. 700060, 1970.

7- Khalil,E., Samuel, P. and Karim, G.A., SAE Paper No. 961932, 1996

8- Liu, Zhigang, Ph.D. Thesis, University of Calgary, Mech.anical Engineering,1995.

9- Liu, Zhigang and Karim, G.A., SAE paper No.942039, 1994 .

10- Zhou, G., Ph.D. Thesis, University of Calgary, Mechanical Engineering, 1993.

Acknowledgement

The financial help of the Canadian Natural Sciences and Engineering Research council is acknowledged.

HEFAT2002
1st International Conference on Heat Transfer, Fluid Mechanics, and Thermodynamics
8-10 April 2002, Kruger Park, South Africa
SK1

DESIGN AND DEVELOPMENT OF HIGH PERFORMANCE COMBUSTOR TO CONTROL ATMOSPHERE IN GREENHOUSE

K. Sato*, Y. Chiba** and Y. Obara***
*Assistant Professor
Dept. of Intelligent System Engineering
**Professor
Dept. of Chemical Engineering
Ichinoseki National College of Technology
Ichinoseki City, Iwate, Japan 021-8511
***Representative
OBARA FLORA, Co., Ltd.
Tohwa-cho, Wagagun, Iwate, Japan 028-0115
E-mail:kaname@ichinoseki.ac.jp

ABSTRACT

For the efficient usage of energy resources, optimum design and development of new combustors are extremely important. Particularly, emission and energy efficiency are recently becoming very important considerations for our civilization.

Heating System including this newly developed combustor serves to supply warm air and moisture to control atmosphere in greenhouse to grow trees, vegetables, flowers etc. We developed the high performance combustor (80kw type) adapted fuel-air counter flow. With the cylindrical combustor, fuel oil is atomized from one side and bumps toward counter air supplied from another opposite side situated near the middle of combustor. The combusting flow go through along the periphery of inner wall of combustor and exhausts from the annular exit port provided at the opposite side of fuel inlet. The distance between fuel and air supply ports is very important for heat transfer efficiency and stable flame.

It is confirmed experimentally that the combustor attained to save 18% of fuel running cost, compared with current fuel-air conical supply combustor. The test was executed for hours from midnight to 8 a.m. to control at 14℃ setting of atmosphere in the greenhouse. The combustor design method and evaluation of performance are presented according to experimental data.

It is also revealed by CFD (Computer Fluid Dynamics) results that the periphery wall of the combustor is heated up by the high temperature combusting flow and therefore the heat transfer rate increased.

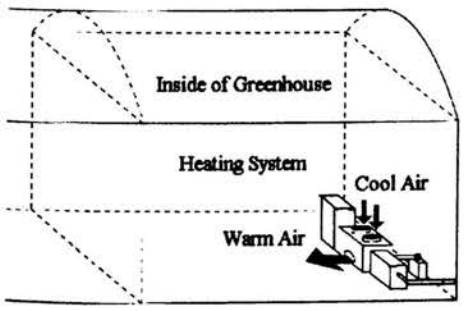

Fig. 1 Heating System arranged in Greenhouse

NOMENCLATURE

a	area (m^2)	Subscript	
C_p	specific heat (J/mole·℃)	1	start of measurement
H	enthalpy (kJ)	2	final of measurement
ΔH	heat formation (kJ)	A	heavy oil
n, N	flow rate (mole/s)	air	air
P	pressure (Pa)	ave	average
Q	heat(kJ)	B	accompany air flow
R	gas constance (Nm/mole·K)	C	counter air flow
t, T	temperature (℃), (K)	i	input
V	flow rate (m^3/s) or Volume	in	duct inlet
W	mass of economizer water	o	output
w	mass of vapor production	out	duct outlet
Greek Letters		p	warm air
α	heat efficiency	q	economizer
β	combustion efficiency	w	water
γ	specific latent heat of water	res	residual
η	performance factor	superscript	
θ	time (sec)	'	modification
χ	molecular fraction		

1. INTRODUCTION

Performance of heating system used to keep adequate temperature and moisture is very important not only for competition of price of product but also environmental problem. Generally, fuel and air are issued from dual annular nozzle in same direction for current combustors. It is probably that this combustion technology might be adapted in the original design without taking into the sufficient consideration such as efficiency and emission because of the ease of keeping the stable flames. Therefore, it has been thought that there might be the other better combustion technology or the improvement of the current combustors. However, no other ideas have been proposed up to date.

As venture, one engineer in OBARA FLORA, Co., Ltd., tried to bump the fuel into counter airflow. After several adjustments, combustion seemed to be emphasized because the warm airflow produced from the heating system, circulating in the greenhouse, became higher temperature. It was reported to our college (Ichionoseki National College of Technology) for the commission to the investigation. This research has been taken part to evaluate the combustion efficiency in actual proof for the

commission.

On the survey, reports for applications such as this heating system of combustor adapted the air-fuel counter flow combustion technology have never been published to date yet. Most of the papers on the basis of counter flow flame are concentrated on the basic research such as flame structure and extinction characteristics etc[1-3]. Therefore, we could not much refer the literatures.

This heating system is usually arranged in the green house as shown in Fig.1. Newly developed combustor is 80kW type.

2. APPARATUS

Newly developed heating system is shown schematically in Fig.2, including air-fuel counter flow combustor, fan to supply warm air and economizer. The parts of the combustor and the economizer are respectively shown in Photo.1 and Photo.2.

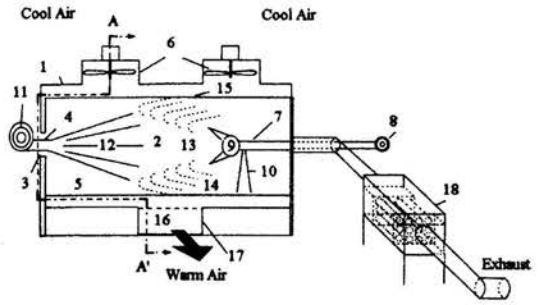

Fig. 2 Heating System with Counter Flow Combustor

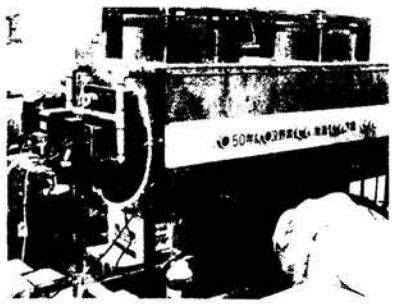

Photo 1 Air-Fuel Counter Flow Combustor 80 kW type

Photo 2 Economizer

In Fig. 2, the indices 1, 2, 3 and 4 respectively show the heater outer wall, combustion chamber, accompany air (secondary air) inlet and fuel nozzle. Here, we call the air in greenhouse the cool air and the air produced from the heating system the warm air. The indices 5, 6, 7, 8 and 9 are respectively inner wall of combustor periphery, blowers to supply cool air, blast pipe, ring blower and counter air flow supply nozzle. The indices 10, 11, 12 and 13 are the support stand, the burner with heavy oil atomizer, main flame and counter air spread The index 14 shows radiant heat flux from the flame against the periphery inner wall of the combustor. The index 15 is the heat transfer surface, which heats the cool air passing through the room surrounded by the combustor periphery outer wall and the heater inner wall The index 16 is the exhaust of the produced warm air, which go through index 17 (exhaust ducts; diameter 530mm) and then exhausts to atmosphere of greenhouse to control temperature, mixing with the cool air.

Combustor is cylindrical and the dimension is 500mm diameter and 2000mm length. The proper distance between fuel inlet and counter airflow nozzle is the range from 0.8m to 1.2m. This distance should be carefully adjusted to keep stable flame.

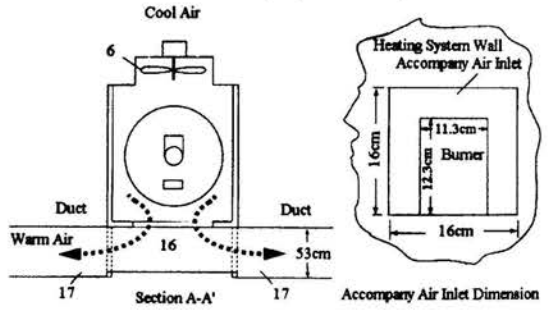

Fig. 3 Heating Part of Cool Air and Accompany Air Inlet

Section A-A' and the detail of the part of the accompany air inlet are shown in Fig. 3. The warm air passage is shown schematically with the arrows. Fuel accompany air (Secondary air) comes into the combustor through the inlet vent provided at the outside of the fuel nozzle device. This accompany air flow is important to serve to enhance combustion and keep stable flame.

The index 18 is economizer, which is heat exchanger as shown in detail in Fig.4. This serves to efficiently produce vapor from water heated by flue gas to give moisture to atmosphere in greenhouse. This device is constructed of pipe of 20 pieces of 50mm diameter tube. Index 19 is fan to blow an air to water surface to enhance the production of the vapor amount.

3. Theory

3.1 Material Balance Equations

Material balance block diagram is shown in Fig. 5. Here, we name this fuel oil "A", of which composition is uncertain. If fuel n_A mole, accompany airflow n_B mole, counter airflow n_C mole and flue gas n_D mole are respectively given, the material balance is as follows.

Reaction equation

$$C_{18}H_{38}(l)+(55/2)O_2(g)\rightarrow 19H_2O(g)+18CO_2(g) \quad (1)$$

Here, heavy oil formula is assumed $C_{18}H_{38}$.

inaccuracy of these approximate relations to the precise ones is negligible (in comparison with experimental setting of parameters k,n of a power-law model), these approximate relations do not include the parameter λ and with respect to their accuracy provide functional dependence of entry parameters in the resulting expression between flow rate and pressure gradient.

b) helical case

Rivlin [10], and Coleman and Noll [11] ranged among first who derived balance equations for the case of the rotating inner cylinder. A series of authors published papers dealing with various constitutive equations and experimental set-ups – e.g. Tanner [12,13], Dierckes and Showalter [14], Rea and Showalter [15], Rigbi and Galili [16], Winter [17], Wronski and Jastrebski [18,19], Garcia-Ramirez and Isayev [20], Dostal et al. [21]. This contribution shows that quasisimilarity behaviour described for non-helical case is possible to derive also for the helical one. Quasisimilarity analysis will be used to determination of the relation flow rate-pressure drop-torque.

PROBLEM FORMULATION

In the following we consider steady laminar isothermal helical flow of incompressible power-law fluids through a concentric annulus. We suppose that the outer cylinder is stationary, the inner one rotates under exerting of a constant torque M. The end effects are neglected, fluid is ejected into the annulus in the axial direction (purely axial pressure force).

Denoting velocity components

$$v_r = 0,\ v_\phi = r.W(r),\ v_z = U(r) \tag{1}$$

we can formulate balance equations in the form

$$\frac{dT_{rz}}{dr} + \frac{1}{r}\cdot T_{rz} = P,\ \frac{dT_{r\phi}}{dr} + \frac{2}{r}\cdot T_{r\phi} = 0,\ \frac{\partial p}{\partial r} = -\rho r W^2(r) \tag{2}$$

where

$$P \equiv \frac{\partial p(r,z)}{\partial z} = \frac{p(r,L) - p(r,0)}{L} < 0 \quad . \tag{3}$$

Boundary conditions fulfil

$$U(\kappa R) = 0,\ U(R) = 0,\ W(\kappa R) = \Omega,\ W(R) = 0 \quad . \tag{4}$$

Rate of strain tensor D and shear stress tensor T

$$D = \begin{vmatrix} 0 & r\frac{dW}{dr} & \frac{dU}{dr} \\ r\frac{dW}{dr} & 0 & 0 \\ \frac{dU}{dr} & 0 & 0 \end{vmatrix},\ T = \begin{vmatrix} 0 & T_{r\phi} & T_{rz} \\ T_{r\phi} & 0 & 0 \\ T_{rz} & 0 & 0 \end{vmatrix} \tag{5}$$

are related through the power-law model (η denotes viscosity)

$$D = \frac{1}{\eta}\cdot T,\ \eta = k^{\frac{1}{n}}\cdot (II_T)^{\frac{n-1}{2n}},\ II_T = T_{r\phi}^2 + T_{rz}^2 \quad . \tag{6}$$

The quasisimilarity solution will be derived in three consequent steps: derivation of a dimensional solution, its transformation to a non-dimensional form, and finally application of suitable scales to the resulting relations (obtaining of the 'universal' profiles).

First step

The solution is of the form

$$T_{rz} = \frac{\mathrm{Pr}}{2} + \frac{C_2}{r},\ T_{r\phi} = \frac{C_1}{r^2} \tag{7}$$

$$\eta = k^{\frac{1}{n}}\cdot\left(\frac{C_1^2}{r^4} + \left(\frac{\mathrm{Pr}}{2} + \frac{C_2}{r}\right)^2\right)^{\frac{n-1}{2n}} \tag{8}$$

$$U(r) = -\frac{P}{2}\cdot F_3(r) - C_2\cdot F_2(r),\ W(r) = -C_1\cdot F_1(r) \tag{9}$$

where

$$C_1 = -\frac{\Omega}{J_1},\ C_2 = -\frac{P}{2}\cdot\frac{J_3}{J_2} \tag{10}$$

$$F_i(r) = \int_r^R \frac{\bar{r}^{-2i-5}}{\eta(\bar{r})}\,d\bar{r},\ J_i = F_i(\kappa R) \quad (i = 1,2,3,4) \tag{11}$$

Consequently we obtain the relations for axial flow rate and torque

$$Q = -\frac{\pi P}{2}\cdot\left(J_4 - \frac{J_3^2}{J_2}\right) \quad ,\quad M = -\frac{2\pi L\Omega}{J_1} \tag{12}$$

Second step

To obtain dimensionless quantities we use the following coefficients to which the dimensionless transformations are related

physical quantity	coefficient	unit	dimensionless quantity
r,z,L	R	m	ξ,ζ,l
$T_{r\varphi}$, T_{rz}	-PR/2 (≡H)	Pa	$t_{\xi\varphi}$, $t_{\xi\zeta}$
U	$k^{-1/n}.R.H^{1/n}$	ms^{-1}	u
W, Ω	$k^{-1/n}.H^{1/n}$	s^{-1}	w, ω
Q	$k^{-1/n}.R^3.H^{1/n}$	m^3s^{-1}	q
η	$k^{1/n}.H^{1-1/n}$	Pa.s	η*
M	$R^3.H$	Nm	m
J_i, F_i	$k^{-1/n}.R.H^{-1+1/n}$	$N^{-1}m^{2i-2}s^{-1}$	j_i, f_i

From above we derive the non-dimensional form of the solution

$$t_{\xi\xi} = \frac{\lambda^2}{\xi} - \xi,\ t_{\xi\phi} = -\frac{\beta}{\xi^2} \tag{13}$$

$$\eta^* = \xi^{2\left(\frac{1}{n}-1\right)} \cdot \left(\beta^2 + \xi^2\left(\lambda^2 - \xi^2\right)^2\right)^{\frac{n-1}{2n}} \tag{14}$$

$$u(\xi) = f_3 - \lambda^2 \cdot f_2,\ w(\xi) = \beta \cdot f_1(\xi),\ \omega = \beta \cdot j_1 \tag{15}$$

where

$$f_i(\xi) = \int_{\xi}^{1} \frac{\bar{\xi}^{2i-5}}{\eta^*(\bar{\xi})} d\bar{\xi},\ j_i = f_i(\kappa R) \quad (i = 1,2,3,4) \tag{16}$$

$$\beta = \frac{\omega}{j_1},\ \lambda^2 = \frac{j_3}{j_2} \tag{17}$$

The relations for dimensionless axial flow rate and torque are of the form

$$q = \pi \cdot (j_4 - \lambda^2 j_3),\ m = 2\pi l \beta \quad . \tag{18}$$

Third step

The answer to a question how to obtain suitable scales transforming the dimensionless solutions for various entry parameters to a unique one is given by behaviour of the whole problem for the two limiting cases of a parameter β: $\beta \to 0$ and $\beta \to \infty$.

a) case $\beta \to 0$ (vanishing influence of rotation)
In this case we obtain

$$q \to q_0 = \frac{\pi n}{1+3n} \cdot \left(\left(1-\lambda^2\right)^{1+\frac{1}{n}} - \kappa^{1-\frac{1}{n}} \cdot \left(\lambda^2 - \kappa^2\right)^{1+\frac{1}{n}}\right),\ \omega \to 0 \tag{19}$$

where

$$j_i \to \int_{\kappa}^{1} \bar{\xi}^{2(i-2)-\frac{1}{n}} \cdot \left(\left(\lambda^2 - \bar{\xi}^2\right)^2\right)^{\frac{1-n}{2n}} d\bar{\xi} \quad (i = 1,2,3,4) \tag{20}$$

The relation for q_0 was derived by Hanks and Larsen [2].

b) case $\beta \to \infty$ (prevailing influence of rotation)
From the relations obtained in the second step it follows that

$$q \to q_\infty = \pi \cdot \left(a_4 - \frac{a_3^2}{a_2}\right) \cdot \beta^{\frac{1-n}{n}} \quad , \quad \omega \to \omega_\infty = a_1 \cdot \beta^{\frac{1-n}{n}} \tag{21}$$

where

$$j_i \to \beta^{\frac{1-n}{n}} \cdot \int_{\kappa}^{1} \bar{\xi}^{2\left(i-\frac{1}{n}\right)-3} d\bar{\xi} = \beta^{\frac{1-n}{n}} \cdot a_i \quad (i = 1,2,3,4) \quad . \tag{22}$$

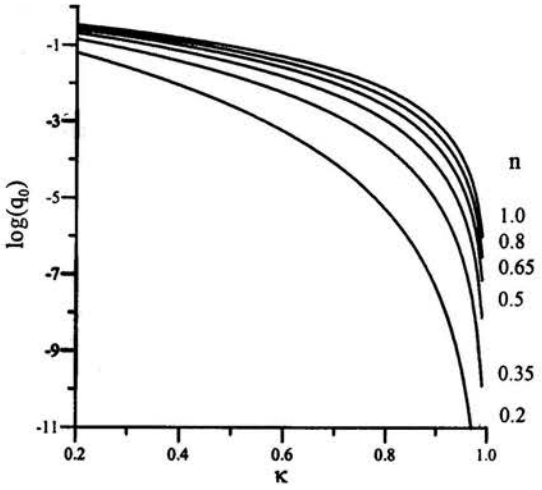

Figure 1: Dependence of q_0 on entry parameters n,κ. (individual curves correspond to values of n consecutively from top to bottom – as in Figs.2,3)

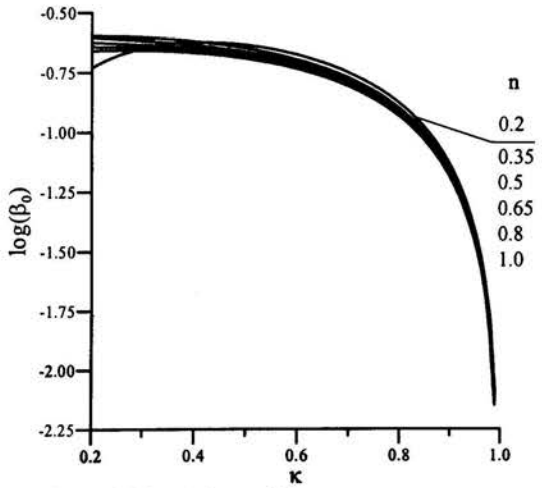

Figure 2: Dependence of β_0 on entry parameters n,κ.

The relations for q_0, q_∞ determine in the plots log(q) against log(β) two asymptotic straight lines intersecting at the point (q_0, β_0) where

$$q_0 = q_\infty \quad \Rightarrow \quad \beta_0 = \left(q_0 \cdot \left(\pi\left(a_4 - \frac{a_3^2}{a_2}\right)\right)^{-1}\right)^{\frac{n}{1-n}} \tag{23}$$

$$\omega_0 = a_1 \cdot \left(q_0 \cdot \left(\pi \left(a_4 - \frac{a_3^2}{a_2} \right) \right)^{-1} \right)^{\frac{1}{1-n}} \qquad (24)$$

These three quantities q_0, ω_0, β_0 represent the scales that enable to introduce the resulting transformations

$$q_r = \frac{q}{q_0}, \omega_r = \frac{\omega}{\omega_0}, \beta_r = \frac{\beta}{\beta_0} \qquad (25)$$

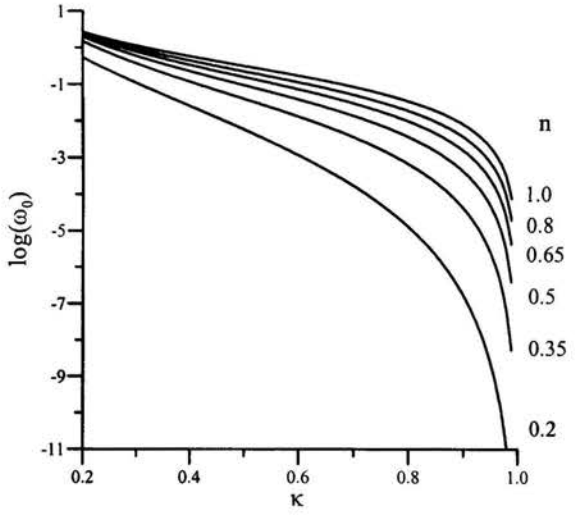

Figure 3: Dependence of ω_0 on entry parameters n,κ.

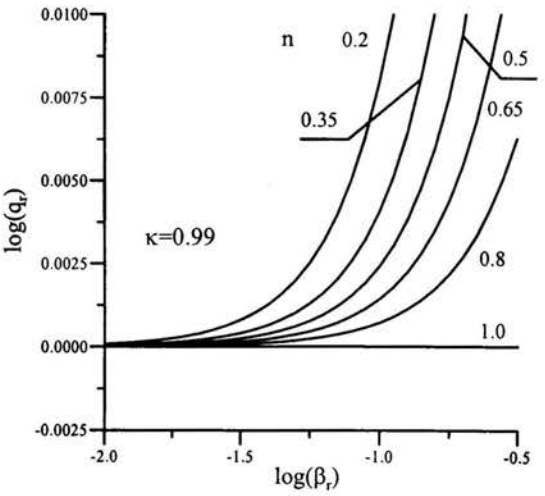

Figure 4: Dependence of q_r on n, β_r.

From above it follows that in the coordinate system $\log(q_r) - \log(\beta_r) - \log(\omega_r)$ there exist two asymptotic planes given by the relations

$$\lim_{\beta_r \to 0} \left(\frac{q_r \cdot \beta_r}{\omega_r} \right) = 1 \quad \Rightarrow \quad \log(q_r) + \log(\beta_r) - \log(\omega_r) = 0 \qquad (26)$$

$$\lim_{\beta_r \to 0} (\log(q_r)) = 0 \quad . \qquad (27)$$

It is evident that the straight line given by the intersection of these asymptotic planes represents all Newtonian cases. Moreover, and this is substantial for the whole quasisimilarity analysis, neither plane depends on flow behaviour index n and aspect ratio κ or any other entry parameters. This implies that it is possible to determine approximate resulting values of the whole problem from the following Figs.1-5 (where the value κ=0.99 was taken as a basis for a 'universal' profile). From the entry parameters we obtain the values q_0, ω_0, β_0, consequently the values q_r, ω_r, and from the above Table the resulting final values (as e.g. flow rate Q). If we restrict the quasisimilarity region by the conditions

$$\kappa \geq 0.4 \quad , \quad n \geq 0.2 \quad , \quad \beta \geq \frac{17}{2} \cdot \left(1 - \kappa^2\right) \cdot (1 + \kappa) \qquad (28)$$

then the inaccuracy of the approximate solution from the precise one does not exceed 2%.

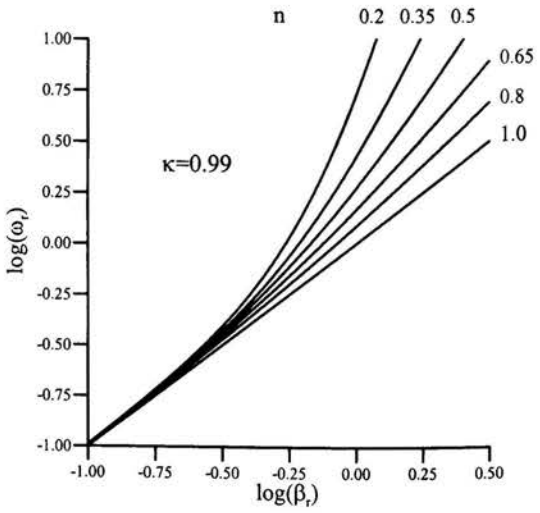

Figure 5: Dependence of ω_r on n, β_r.

CONCLUSIONS

Quasisimilarity of the problem studied enables determination of sufficiently precise solution flow rate-pressure

drop-torque in the broad region of entry parameters. This approach fully eliminates any numerical calculations and the results are immediately at hand using a few graphs depicting the individual transformations.

ACKNOWLEDGEMENT

The authors are grateful to the Grant Agency of the Academy of Sciences CR, Grant Project A2060004, for financial support of this work.

REFERENCES

[1] Fredrickson,A.G. and Bird,R.B.,1958, "Non-Newtonian Flow in Annuli," Ind.Eng.Chem., Vol.50, pp.347-352.

[2] Hanks,R.W. and Larsen,K.M.,1979, "The Flow of Power-Law Non-Newtonian Fluids in Concentric Annuli," Ind.Eng.Chem.Fundam., Vol.18, pp.33-35.

[3] Prasanth,N. and Shenoy,U.V.,1992, "Poiseuille Flow of a Power-Law Fluid Between Coaxial Cylinders," J.Appl.Polym.Sci., Vol.46, pp.1189-1194.

[4] Bird,R.B., Armstrong,R.C. and Hassager,O.,1987, Dynamics of Polymer Liquids. Vol.1:Fluid Mechanics. Wiley,New York, 649 pp.

[5] McKelvey,J.M.,1962, Polymer Processing. Wiley, New York, 409 pp.

[6] Worth,R.A.,1979, "Accuracy of the Parallel-Plate Analogy for Representation of Viscous Flow Between Coaxial Cylinders," J.Appl.Polym.Sci., Vol.24, pp.319-328.

[7] David,J. and Filip,P.,1995, "Relationship of Annular and Parallel-Plate Poiseuille Flows for Power-Law Fluids," Polym.-Plast. Technol. & Eng.J., Vol.34, pp.947-960.

[8] David,J. and Filip,P.,1994, "Quasisimilarity of Flow Behaviour of Power-Law Fluids in Concentric Annuli," Fluid Dyn.Res., Vol.14, pp.63-70.

[9] David,J. and Filip,P.,1996, "Explicit Pressure Drop-Flow Rate Relation for Laminar Axial Flow of Power-Law Fluids in Concentric Annuli," J.Pet.Sci.Eng., Vol.16, pp.203-208.

[10] Rivlin,R.S.,1956, "Solution of Some Problems in the Exact Theory of Visco-Elasticity," J.Rational Mech. Anal., Vol.5, pp.179-188.

[11] Coleman,B.D. and Noll,W.,1959, "Helical Flow of General Fluids," J.Appl.Phys., Vol.30, pp.1508-1512.

[12] Tanner,R.I.,1963, "Helical Flow of Elastico-Viscous Liquids. Part I. Theoretical," Rheol.Acta, Vol.3, pp.21-26.

[13] Tanner,R.I.,1963, "Helical Flow of Elastico-Viscous Liquids. Part II. Experimental," Rheol.Acta, Vol.3, pp.26-34.

[14] Dierckes,A.C. and Showalter,R.W., 1966, "Helical Flow of a Non-Newtonian Polyisobutylene Solution," Ind.Eng.Chem.Fundam., Vol.5, pp.263-271.

[15] Rea,D.R. and Showalter,R.W., 1967, "Velocity Profiles of a Non-Newtonian Fluid in Helical Flow," Trans.Soc.Rheol., Vol.11, pp.125-143.

[16] Rigbi,Z. and Galili,N.,1971, "Helical Flow of Some Non-Newtonian Liquids," Rheol.Acta, Vol.10, pp.473-478.

[17] Winter,H.H.,1973, "Helical Flow of Molten Polymers in a Cylindrical Annulus," Rheol.Acta, Vol.12, pp.1-12.

[18] Wroński,S. and Jastrzębski,M.,1990, "The Stability of the Helical Flow of Pseudoplastic Liquids in a Narrow Annular Gap with a Rotating Inner Cylinder," Rheol.Acta, Vol.29, pp.442-452.

[19] Wroński,S. and Jastrzębski,M.,1990, "Experimental Investigation of the Stability Limit of the Helical Flow of Pseudoplastic Liquids," Rheol.Acta, Vol.29, pp.453-461.

[20] Garcia-Ramirez,R. and Isayev,A.I.,1992, "Helical Flow of a Viscoelastic Fluid – An Approximation Towards the Analysis of Rotational Extrusion," J.Rheol., Vol.36, pp.1183-1211.

[21] Dostál,M., Žitný,R., Šesták,J. and Houška,M., 1993, "Helical Flow of Power-Law Fluids," AIChE J., Vol.39, pp.189-192.

HEFAT 2002
1st International Conference on Heat Transfer, Fluid Mechanics and Thermodynamics
8 -10 April 2002, Kruger Park, South Africa
HJ 1

EXPERIMENTAL STUDY OF THERMAL PROCESSES IN HYDRAULIC DESCALING

Jaroslav Horsky, Miroslav Raudensky
Brno University of Technology, Faculty of Mechanical Engineering,
Czech Republic
horsky@kinf.fme.vutbr.cz
http://ktermo41.fme.vutbr.cz/~heatlab

ABSTRACT

Experimental program for studying influence of parameters adjustable for hydraulic descaling by flat-water jet was prepared. Experimental work was concentrated on the study of descaling in relation to heat transfer. Influence of inclination angle and water pressure on heat transfer is discussed in this paper. The experimental work obtained physically realistic description of the mechanism of the heat transfer processes while removing oxides from the steel surface by high-pressure water jets. Heat transfer is described by heat transfer coefficients and by heat flux distribution. The knowledge of the boundary conditions allows using the numerical models for the computation of material temperature fields during descaling, the computation of heat losses and thermal stresses caused by high-pressure spraying.

INTRODUCTION

Hydraulic descaling is the process of removing oxides layer from a hot (typically steel) surface using high-pressure water jet. This process is essential in the hot rolling. Quality of descaling can strongly influenced final quality of rolled surface. The scale is formed during heating in a furnace (primary scale) and during rolling process (secondary scale). Both types of scale must be removed before entering rolls. High-energy water beam has two effects on a scale layer. The first one is a relatively intensive thermal shock depending on a set of parameters (water pressure, nozzle type, distance from the surface, inclination angle, speed of product moving). The second effect is mechanical caused by impingement pressure. There is no acceptable answer to the question – which effect is dominant? A suitable numerical model could give the answer to this question. Realistically working numerical model needs realistic boundary conditions. The knowledge of heat transfer coefficient (HTC) distribution and impingement pressure (IP) distribution is necessary.

EXPERIMENTS

The experimental conditions were prepared in the way, which is as close as possible to the real mill conditions. There are two basic conditions, which should be kept. The first is the initial temperature of tested sample and the second is the speed of sample motion. Speed is very sensitive parameter and should be kept with very good repeatability. A special experimental stand was developed for these tests.

EXPERIMENTAL STAND

The experimental stand was built to study the cooling of linearly moving objects. A six-meter-long girder carrying a movable trolley and a driving mechanism (Fig.1) forms the basic part of the experimental device. An electronic device measuring the instant position of the trolley is embedded in the trolley. The driving mechanism consists of an electric motor controlled by a programmable unit, a gearbox, two rollers and a hauling rope. The girder is divided into three sections. The marginal sections are used for the trolley's acceleration or deceleration. The velocity of the trolley is constant in the mid-section and it is here where the spray nozzles quench the measured sample. The experimental process can be seen at Photos 1 and 2.

PROCEDURE OF THE EXPERIMENT

- An electric furnace (heater) heats the test plate to an initial temperature of the experiment, (950°C was used here).
- The plunger water pump is switched on and the pressure is adjusted.

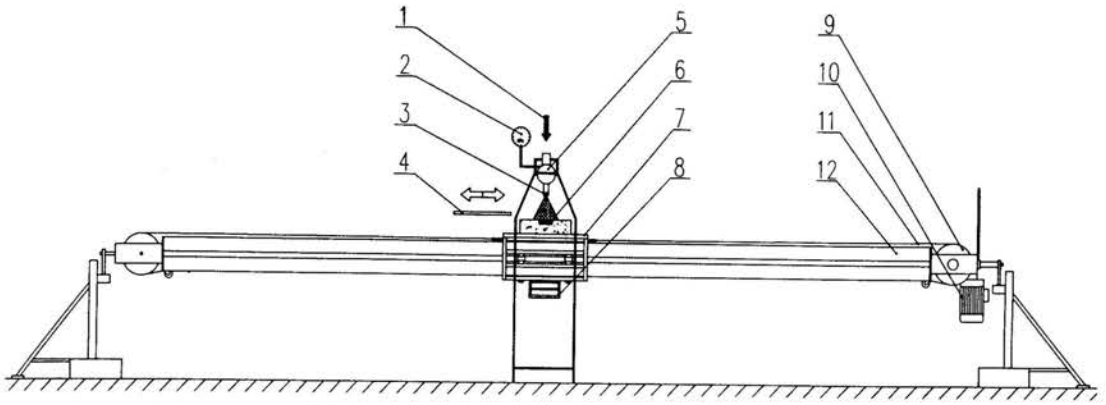

1. cooling medium supply
2. pressure gauge
3. nozzle
4. moving deflector
5. manifold
6. tested sample
7. moving trolley
8. data logger
9. roller
10. electric motor
11. hauling steel wire rope
12. girder

Figure 1: Principal scheme of the linear test bench

A driving mechanism moves the test plate under the spray. After recovering the temperature field in the plate, the movement of the plate under the spray is repeated.

- The sensor measures the temperature in nozzle axis position at a depth of 1 mm from the cooled surface and the temperature is recorded with a sampling frequency of 100 Hz.
- The positions of the test plate and the sensors (in the direction of movement) are recorded together with the temperature values. The record of instant positions is used for computation of instant velocities while moving under the spray.

A speed of 1 m/s was used for all experiments mentioned in this paper.

EXPERIMENTAL PROGRAM

High-pressure nozzles with flat-jet sprays were used for the experiments. The results published here are for the nozzle with a spray angle of 30° and a water flow of 0.75 l/s at 100 bar. The experiments were conducted for different pressures and the inclination angle at constant distances of 150 mm of the nozzle from the quenched surface.

Figure 2 shows schematically the tilting of the nozzle when studying the inclination angle.

The research program covers the angles from +30° to –30°, while the typical inclination, used in industry, is small and positive. The pressures used for experiments cover the range from 90 bar to 450 bar.

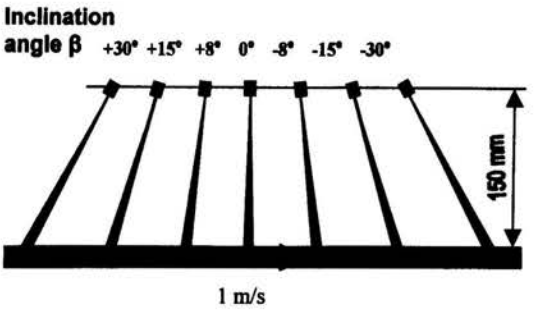

Figure 2: Scheme of nozzle positions

EXPERIMENT EVALUATION

The pass under the nozzle causes temperature drop in the material sample that is indicated by temperature sensor. An example of temperature record is plotted in Fig. 3. This information together with material properties and calibration characteristics of temperature sensor is used as input of inverse heat conduction task [3]. The results of computation are surface temperature, heat flux and heat transfer coefficient. An example of inverse computation output is in Fig. 3 (surface temperature) and Fig. 4 (HTC).

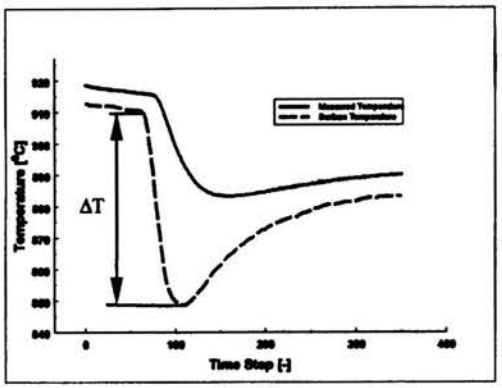

Figure 3: Measured and computed temperature drop – one path under the nozzle

The surface temperature drop ΔT under the jet was used as one of the parameters for comparing particular experiments. This was obtained as a difference between the temperature at the beginning of contact with spray and the lowest temperature after the spray (see Fig. 3).

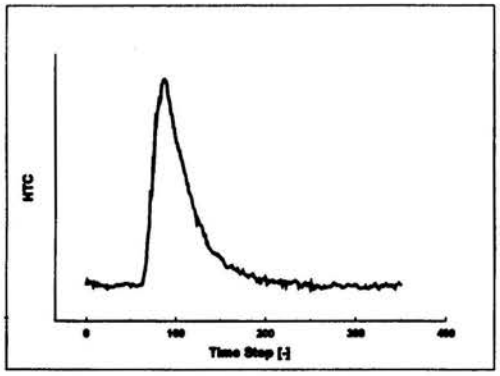

Figure 4: Computed HTC

Previous experience from experimental work shows that description of heat transfer must not be reduced to a single parameter – maximum of the heat transfer coefficient. The space distribution of HTC is important. If one parameter is necessary, the mean integral value of heat transfer coefficient is used. HTC history curve is integrated in the impact area and the mean value HTC^{mean} is computed.

INFLUENCE OF NOZZLE INCLINATION

Two computed parameters are used for investigation of inclination angle influence – temperature drops on the surface ΔT and HTC mean integral value HTC^{mean}. The relative values are plotted in Fig.5. The reference value of 100% is for inclination angle 0°.

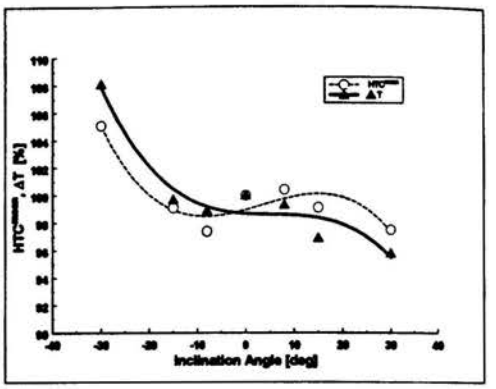

Figure 5: Influence of inclination angle

INFLUENCE OF WATER PRESSURE

Significant influence of water pressure on heat transfer intensity was expected. The minimum used pressure was 90 bar. This value is taken as reference for re-computation of cooling characteristics. The results are summarised in Fig.6.

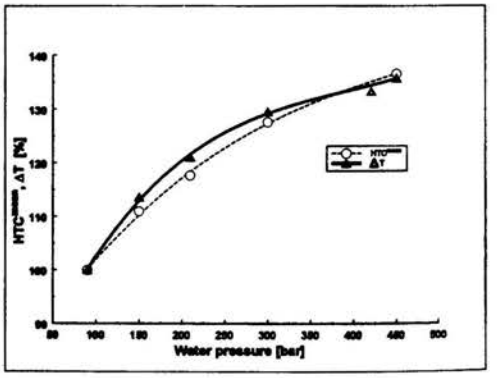

Figure 6: Influence of water pressure

MATHEMATICAL PROCEDURE FOR DATA GENERALISATION

The objective of the mathematical reduction of data was to obtain function HTC = $f(x,t)$ where x represents the position and t represents the surface temperature. The following formula satisfies these demands:

$$HTC(x,t) = \delta(t)\, e^{-\frac{(x-\mu)^2}{2\sigma^2(t)}} - l \qquad (1)$$

The Gaussian function $e^{\frac{(x-\mu)^2}{2\sigma^2(t)}}$ is used because of the high similarity to the computed data (see Fig.4) and the easy geometrical interpretation of coefficients σ and μ. As the shape of the function is asymmetrical to the impingement point μ the $\sigma(t)$ function is defined separately for $x < \mu$ and $x \geq \mu$.

Function $\delta(t)$ represents the maximum values of the HTC for surface temperature t. This function is important especially when the approximation function is used for a wide temperature range. It is expressed by formula

$$\delta(t) = \frac{a-b}{\pi} arctg\, c(t-d) + \frac{a+b}{2} \qquad (2)$$

Value a represents the maximum value of HTC for very low temperatures, value b represents the maximum value of HTC for very high temperatures. Value c represents the minimum value of the derivative $d\sigma/dt$. Value d represents temperature in which the minimum value of derivative is found, i.e. the temperature in which the highest decrease of the maximum HTC value is effected. The coefficient l in formula (1) is used to compensate the heat radiation. The value μ in formula (1) represents the position of the impingement point and it may be set to zero by defining the co-ordinate origin on the x-axis. The major advantage of the above numerical approximation is that it reduces the enormous number of data in the files to eight coefficients. Formula (1, 2) is easy to use in the numerical models.

CONCLUSION

The experimentally based study of water pressure and nozzle angle inclination on heat transfer intensity in water jet descaling process is presented. The experiments were conducted for one nozzle type and fixed speed of descaled surface 1 m/s.

The part of study, aimed to the influence of an inclination angle, showed small sensitivity of local values of the heat transfer coefficient to the impact angle. Non-negligible changes in heat transfer intensity were found for large inclination of +30° and –30°.

It should be stressed that the study of surface quality after descaling shows a significant role of the inclination of the nozzle. In the other words: Small sensitivity of local values of the heat transfer coefficient to the inclination does not mean small sensitivity of the quality of descaling to the inclination.

The pressure results, a related part of our study, give quantitative information on grows of the intensity of heat transfer with the growing pressure of descaling.

The generalisation formula for HTC data was designed. This formula can be used in the numerical models as a temperature boundary condition.

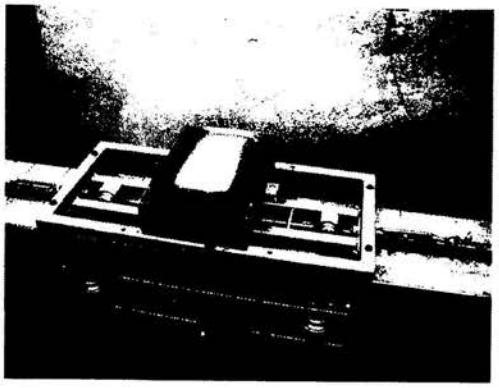

Photo 1: Hot test plate before experiment

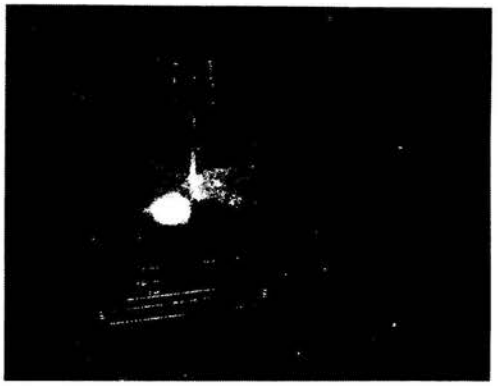

Photo 2: Test plate passing water jet

LITERATURE

[1] Marston, H.E.: Influence of Scale Structure on the Effectiveness of Descaling, Conf. Hydraulic Descaling in Rolling Mills, London, 1995

[2] Horský, J., Raudenský, M., Zela, L.: Experimental Study of Heat Transfer with Reference to Numerical Simulations in Hot Rolling, The 7th International Conference on Steel Rolling, Makuhari, Chiba, Japan, proc. published by The Iron and Steel Institute of Japan, pp. 216-220

[3] Raudenský,M.: Heat Transfer Coefficient Estimation by Inverse Conduction Algorithm, Int. J. Num. Meth. Heat Fluid Flow, vol 3, (1993), pp. 257-266.

ACKNOWLEDGEMENT

Theoretical work was done in the frame of the COST P3.60 project.

HEAFT2002
1st International Conference on Heat Transfer, Fluid Mechanics, and Thermodynamics
8-10 April 2002,Kruger Park, South Africa
JJ1

3-D HEAT TRANSFER ANALYSIS OF A BUILT-IN MOTORIZED HIGH SPEED SPINDLE WITH HELICAL COOLING CHANNEL

J. Y. Jang and C. H. Chien
Department of Mechanical Engineering
National Cheng Kung University
Tainan, Taiwan, 70101
E-mail: jangjim@mail.ncku.edu.tw

ABSTRACT

The purpose of this paper is to numerically analyze the three-dimensional heat conduction in a built-in motorized high-speed spindle with helical water cooling. The effects of different heat sources (q = 60 w, 120 w and 240 w), cooling water flow rate (0.4 L/min, 0.8 L/min and 1.2 L/min) and free convection heat transfer coefficient in atmosphere (h = 5 W/m^2 °C, 10 W/m^2 °C and 20 W/m^2 °C) on the temperature distribution are examined in detail. The numerical results indicate that without cooling liquid, the highest temperature of the spindle could be increased up to about 212 °C. The cooling liquid removes most of the heat produced by the motor. Even though the free convection heat transfer coefficient is increased up to 4 times, the temperature difference of the spindle is just within 1 °C only.

INTRODUCTION

High speed machining increases productivity and reduces production cost, and has been attracting interests of engineers for many years. Recently, the high-speed spindles are usually equipped with built-in motor, so that power transmission devices such as belts and gears are eliminated. However, the increase of the spindle also incurs adverse effects such as noise, chattering and heat generation of spindle bearing systems [1]. Therefore, how to solve the thermal behavior in a built-in motorized high spindle is becoming a very important topic.

Bossmanns and Tu [2, 3] presented a power flow mode for a more complete thermo-mechanical model of high-speed motorized spindles. This power flow model accounts for all major heat sources within the spindle system, such as (1) heat generation by angular contact ball bearings (2) heat generation by the electric motor (2) heat generation due to viscosity shear of air by the rotating components of the spindle. Later, Stein and Tu [4] proposed a dynamic mathematical model of the spindle system, which can be used as part of a model-based monitoring system for estimating the spindle bearing preload. The model is derived from physical laws of heat transfer and thermo-elasticity.

The purpose of the paper is to analyze the heat transfer in a built-in motorized high-speed spindle with helical water-cooling channel as shown in Figure 1. The spindle has a special bearing with 5~25 μm high-pressure gas layer between spindle and bearing. The temperature distributions for different values of heat sources, cooling water flow rate and free convection heat transfer coefficient are examined.

MATHEMATICAL ANALYSIS

Figure 2 is the physical model of the built-in motorized spindle with helical rectangular water-cooling channel. The heat generated per volume by the motor q is distributed in the middle of the inner housing with length 30 mm. The spindle is operated in an air-conditioned environment at temperature T_∞ = 20 °C. Therefore, the heat is removed both by the force convection of cooling water with convective heat transfer coefficient h_w and the natural convection of ambient air with convective heat transfer coefficien h_a. The following assumptions simplify the analysis:

1. The heat conduction is steady state.
2. The thermal conductivities k of the inner walls (material is copper, k = 386 W/m °C) and outer walls (material is AISI 302, k = 16.3 W/m °C) are isotropic and temperature independent.
3. The radiation effect is neglected.
4. Both the convective heat transfer coefficient of h_w and h_a are uniform over the solid surfaces.

Then the three-dimensional heat conduction using cylindrical coordinates (r , ϕ , z) is as follows:

$$\frac{1}{r}\frac{\partial T}{\partial r}+\frac{\partial^2 T}{\partial r^2}+\frac{1}{r^2}\frac{\partial^2 T}{\partial \phi^2}+\frac{\partial^2 T}{\partial z^2}+\frac{q}{k}=0 \qquad (1)$$

The corresponding boundary conditions are

1. At the inner walls with the heat source supplied,

$$-k\frac{\partial T}{\partial r}=q \qquad (2)$$

2. At the inner walls with no heat source, the adiabatic boundary condition is assumed.
3. At the surfaces of the helical water channel,

$$-k\frac{\partial T}{\partial r}=h_w(T-T_w) \qquad (3)$$

where T_w is the water temperature inside the helical channel, which is set to be 17 °C in the present study.

4. At the outer walls,

$$-k\frac{\partial T}{\partial r}=h_a(T-T_a) \qquad (4)$$

The forced convection heat transfer coefficient in the helical rectangular channel can be estimated from the experimental formula obtained by Abadzic [5]:

$$Nu=0.332(\mathrm{Re})^{0.6}(\mathrm{Pr})^{0.36} \qquad (5)$$

where Nu ($Nu = h_w D_h/k$) is Nusselt Number, Pr is the Prandtl Number of the cooling liquid (for water Pr = 5.38)and Re is the Reynolds number based on the hydraulic diameter.

NUMERICAL METHODS:

The governing equation (1) together with the boundary conditions were solved numerically. The three-dimensional elliptic partial differential equations are expressed in the finite difference forms by a second-order central difference scheme. The grid inside the computational domain was made by the elliptic generation methods. The whole grid system was divided into 3 blocks by the multi-block method. Figure 3 outlines the computational mesh used in this investigation, and the total number of grid points is approximately 48,103. Computations were performed on a Pentium III 700 personal computer and typical CPU times were 8~10 hours for each case.

RESULTS AND DISCUSSIONS

Figure 4 shows the temperature distribution of the spindle with heat source 120 W and no cooling water flowing in the channel. The heat dissipated is only by the natural convection with convective heat transfer coefficient h_a = 5 W/m^2 °C. It is seen that without cooling liquid, the highest temperature of the spindle could be increased up to about 212 °C. Figures 5 and 6 illustrate the temperature distribution of the spindle with heat source 120 W and 240 W, respectively, with cooling water volume flow rate FR = 0.8 L/min and h_a = 5 W/m^2°C. It is noted that for a flow rate FR = 0.8 L/min, the corresponding velocity and convective heat transfer coefficient are V = 0.475 m/s and h_w = 7143 W/m^2 °C, respectively. It is seen that the maximum temperatures are reduced significantly with helical water-cooling. In addition, the hot spots are almost concentrated near the center of the spindle. This is due to the fact that the wall thickness of the spindle is very thin compared to the spindle length. Thus, most of the heat is conduced along the radial direction compared with the axial direction. The temperature contour of the spindle with heat source 120W and cooling water flow rate 0.4L/min (V= 0.238 m/s, h_w = 4724 W/m^2 °C) and h_a = 5 W/m^2 °C is presented in Figure 7. One can see that the maximum temperature is increased slightly due to the decrease of the water flow rate from 0.8 L/min to 0.4 L/min.

Figure 8 shows the variation of the averaged temperature along the axial direction with different values of heat source (q = 60 W, 120 W and 240 W) with FR = 0.8 L/min and h_a = 5 W/m^2 °C. As expectedly, the temperature of the spindle is higher as the heat source is increased. Since The maximum temperature is less than 25°C even for q = 240 W, the present helical water cooling channel is a very efficient heat sink. Figure 9 presents the variation of the averaged temperature along the axial direction with different values of water flow rate (FR= 0.4, 0.8 and 1.2 L/min) with q = 120 W and h_a = 5 W/m^2 °C. For FR = 1.2 L/min, the corresponding velocity and convective heat transfer coefficient are V = 0.95 m/s and h_w = 10853 W/m^2 °C, respectively. The maximum temperature is reduced as the water flow rate is increased. Finally, Figure 10 illustrates the variation of the averaged temperature along the axial direction with different values of free convection coefficient (h_a = 5, 10 and 20 W/m^2 °C) with q = 120 W and FR = 0.8 L/min. The numerical results indicate that even though the free convection heat transfer coefficient is increased up to 4 times (from h_a = 5 to 20 W/m^2 °C) the temperature difference of the spindle is just within 1 °C. This confirms that most of heat is removed by the cooling water.

CONCLUSIONS

This paper presented the three-dimensional heat conduction in a built-in motorized high-speed spindle with force convection of cooling water and the natural convection of ambient air. The temperature distributions for different values of heat sources, cooling water flow rate and free convection heat transfer coefficient are shown. It is demonstrated that the hot spots are almost concentrated near the center of the spindle, and without cooling liquid, the highest temperature of the spindle could be increased up to about 212 °C. The temperatures rise can be reduced significantly with helical water-cooling. In addition, even though the free convection heat transfer coefficient is increased up to 4 times, the temperature difference of the spindle is just within 1 °C

ACKNOWLEDGEMENTS

Financial support for this work was provided by the National Science Council of Taiwan, under contract NSC 90-2212-E-006-125

REFERENCES

[1] Al-Shareeef, K. J. H. and Brandon, J. A., 1990, "On the Effects of Variations in the Design Parameters on the Dynamic Performance of Machine Tool Spindle Bearing System," International Journal of Machine Tools and Manufacture Vol., Vol. 30, pp. 43-439.

[2] Bossmanns, B. and Tu, J. F., 1998, "A Power Flow Model for High Speed Motorized Spindles- Heat Generation Characterization," International Mechanical Engineering Congress and Exposition, Anaheim, CA, U. S. A.

[3] Bossmanns, B. and Tu J. F., 1999, "A Thermal Model for High Speed Motorized Spindles," International Journal of Machine Tools and Manufacture Vol. 39, pp. 1345-1366.

[4] Stein, J. L. and Tu, J. F., 1994, "A State-Space Model for Monitoring Thermally Induced Preload in Anti-Friction Spindle Bearings of High-Speed Machine Tools," Transactions of the ASME, Vol. 116, pp. 372-386.

[5] Abadzic, E. E., 1974, "Heat Transfer on Coiled Turbular Matrix," ASME Winter Annual Meeting, ASME Paper 74-WA/HT-64.

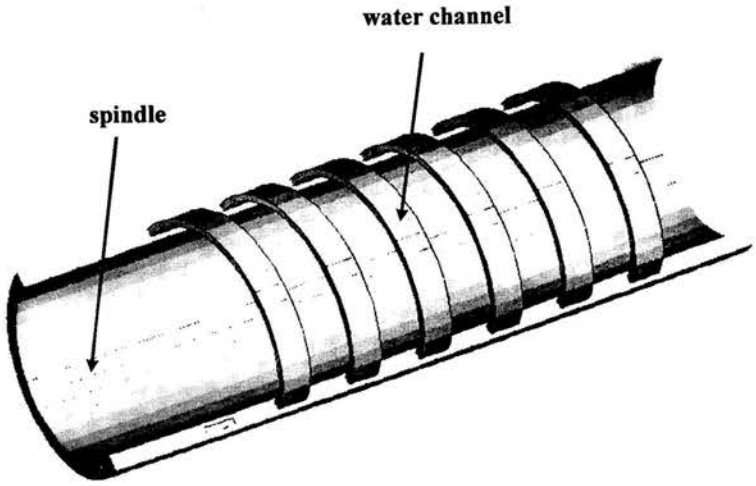

Figure 1: The built-in motorized high-speed spindle

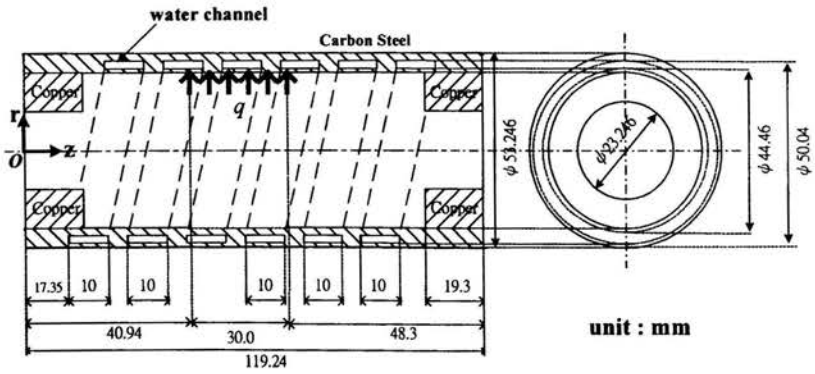

Figure 2: The physical model of the built-in motorized spindle with helical water-cooling channel

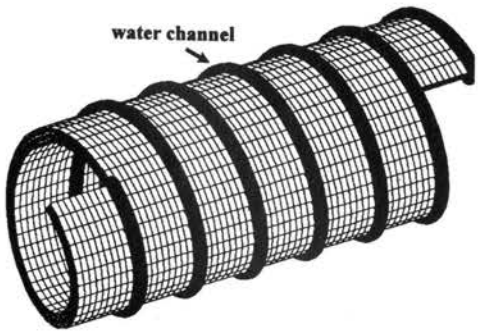

Figure 3: The computational grid system

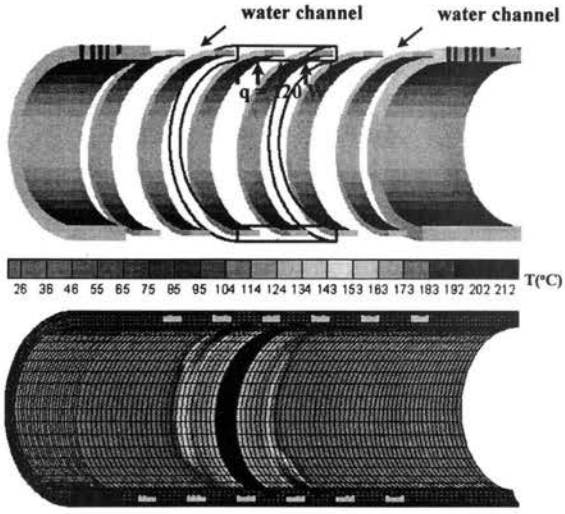

Figure 4: The temperature distribution with heat source 120W and no cooling liquid

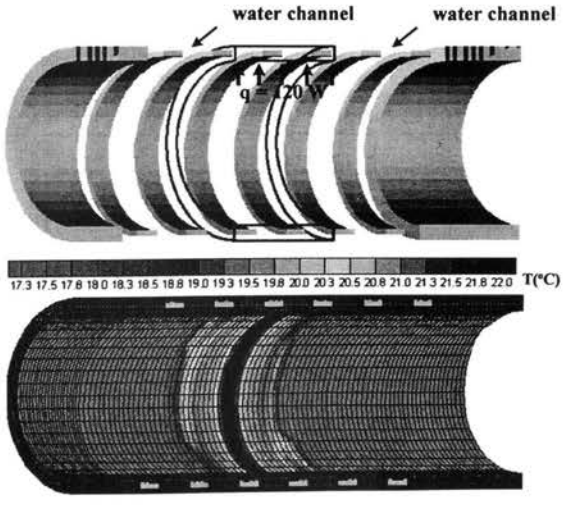

Figure 5: The temperature distribution with heat source 120W and cooling liquid 0.8L/min

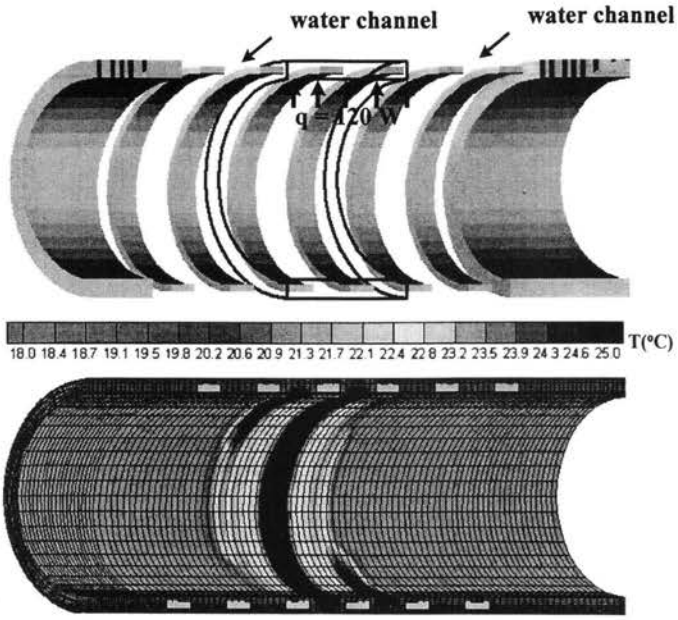

Figure 6: The temperature distribution with heat source 240W and cooling liquid 0.8L/min

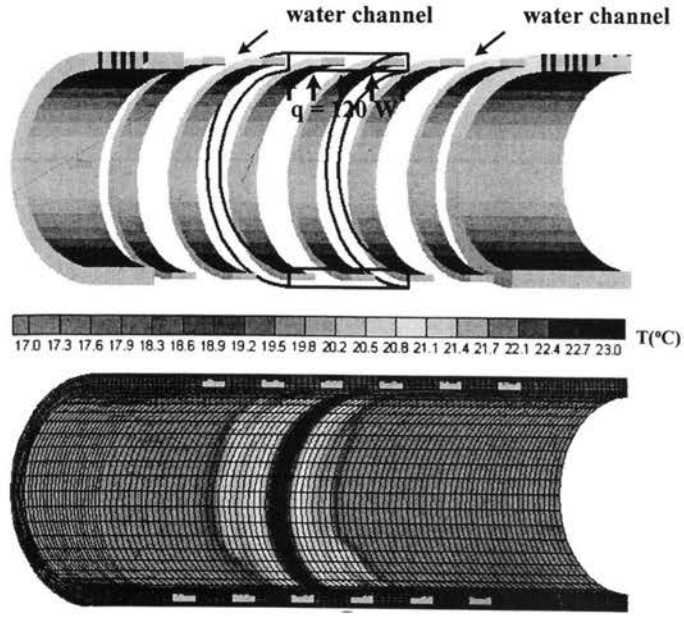

Figure 7: The temperature distribution with heat source 120W and cooling liquid 0.4L/min

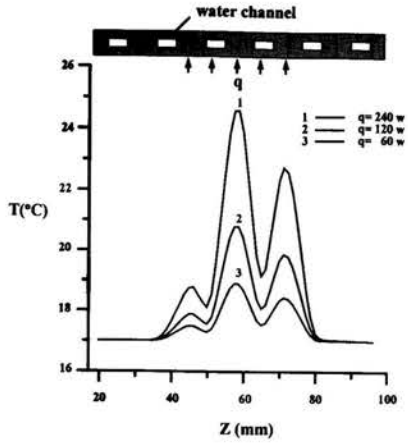

Figure 8: The variation of the averaged temperature along the axial direction with different q

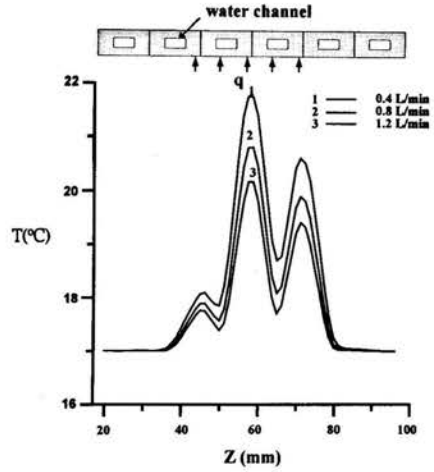

Figure 9: The variation of the averaged temperature along the axial direction with different FR

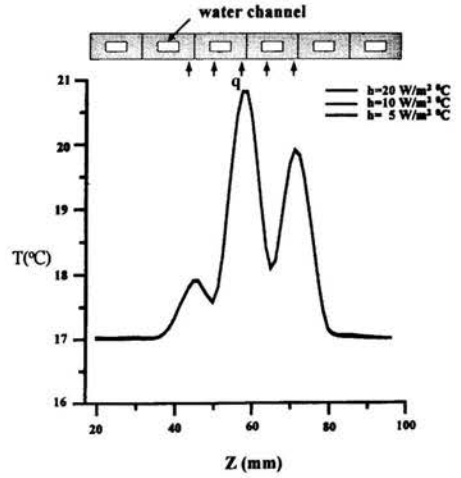

Figure 10: The variation of the averaged temperature along the axial direction with different h_a

HEFAT2002
1st International Conference on Heat Transfer, Fluid Mechanics, and Thermodynamics
8-10 April 2002, Kruger Park, South Africa
WP1

THE VARIATIONS OF DYNAMIC ELECTRICAL RESISTANCE DURING RESISTANCE SPOT WELDING

P. S. Wei and S. C. Wang
Professor and Graduate Student
Department of Mechanical and Electro-Mechanical Engineering
National Sun Yat-Sen University
Kaohsiung, Taiwan 80424
Republic of China
E-mail: pswei@mail.nsysu.edu.tw

ABSTRACT

This work quantitatively studies dynamic electrical resistance during resistance spot welding. A determination of dynamic resistance is necessary for predicting the transport processes and monitoring the weld quality during resistance spot welding. In this study, dynamic resistance is obtained by taking the sum of temperature-dependent bulk resistance of the workpieces and contact resistances at the faying surface and electrode-workpiece interface within an effective area corresponding to the electrode tip where welding current primarily flows. A contact resistance is composed of constriction and film resistances, which are functions of hardness, temperature, electrode force, and surface condition. The temperature is determined from the previous study in predicting unsteady, axisymmetric mass, momentum, heat, species transport, and magnetic field intensity with a mushy-zone phase change in workpieces, and temperature and magnetic fields in the electrodes of different geometries. The predicted nugget thickness and dynamic resistance versus time show quite good agreement with available experimental data. Excluding expulsion, the dynamic resistance curve can be divided into four stages. A rapid decrease of dynamic resistance in stage 1 is attributed to decreases in contact resistances at the faying surface and electrode-workpiece interface. In stage 2, the increase in dynamic resistance results from the primary increase of bulk resistance in the workpieces and an increase of the sum of contact resistances at the faying surface and electrode-workpiece interface. Dynamic resistance in stage 3 decreases, because increasing rate of bulk resistance in the workpieces and contact resistances decrease. In stage 4 the decrease of dynamic resistance is mainly due to the formation of the molten nugget at the faying surface.

INTRODUCTION

Resistance spot welding has been widely used in joining thin workpieces due to its light weight and easy manufacturing. Water-cooled copper electrodes apply a load to squeeze the workpieces. In addition to produce an intimate contact between workpieces to allow the current to flow, the electrode force also serves to break up any surface oxides or films on the faying surface. A voltage is applied across the ends of electrodes. In view of the induced current flow, electrical contact resistance at the faying surface results in the greatest heat generation and temperature near the interface. Melting begins at the faying surface either in the center of the contact patch or near the periphery. The molten nugget grows until current flow is terminated. The electrode force continues to be applied until cooling has been finished.

Evidently, electrical resistance is the most important factor affecting resistance spot welding. A rigorous study of electrical resistance is necessary not only for an understanding but also for a monitoring of the process to obtain good weld quality [1,2]. Aside from studying static electrical resistance affected by different electrode forces and workpieces in different thicknesses, Roberts [3] experimentally found that dynamic resistance cannot be considered as a constant during resistance spot welding. The dynamic resistance was equal to the sum of the bulk resistance of the two workpieces, and contact resistances at the faying surface and two electrode-workpiece interfaces. An initial drop of dynamic resistance was attributed to the rupture of the surface film. After the initial breakdown of contact resistance, the resistance increased slightly with time in welding aluminum using cleaned electrode tips, while the resistance tended to decrease in welding stainless steel and aluminum with contaminated electrodes. Dynamic resistance curves for welding low-carbon steel showed an increase and subsequent decrease after the breakdown of contact resistance. The rise in dynamic resistance after the breakdown of contact resistance was proposed to be due to the heating of the workpiece, and the subsequent fall after the maximum resistance has been reached may be attributed to two causes; the growth of the nugget diameter and the increasing penetration of the electrodes into the workpiece. Both produced increasing current carrying areas. At a given instant, the greater the welding current, the lower the resistance.

Bhattacharya and Andrews [4] obtained the similar dynamic resistance curve to monitor the quality of spot welds in mild steel, stainless steel and aluminum. In welding mild steel, the initial steep fall was followed by a trough and a distinct peak. Neither aluminum nor stainless steel showed this peak. Dynamic resistance can be divided into three stages. The decrease of dynamic resistance in Region I was due to the breakdown of contact insulation or fritting; in Region II the increase of dynamic resistance was attributed to the temperature coefficient of constriction resistance [5]; the diminishing dynamic resistance in Region III resulted from the growth of fused metallic bond. They proposed a detailed interpretation by using concepts of softening and melting voltages. In contrast to stainless steel and aluminum alloy and many other materials, the dynamic resistance curve for mild steel permitted correlation with nugget growth and offered a means of monitoring weld quality.

Savage et al. [6] extensively measured dynamic resistance curves for different welding currents, electrode forces, and material combinations of uncoated and galvanized auto-body steels with degreased or pickled surface conditions. The shape of the dynamic resistance curve differed markedly with the surface conditions and different material combinations. The typical dynamic resistance curves of steel-to-steel welds made from as-received stock agreed with the curves presented by Roberts [3]. Expulsion was found to occur for high welding current and time. If the nugget grows to a size such that it can no longer be contained by the surrounding solid metal under the compressive electrode force, expulsion will occur. The dynamic resistance curve of the plain carbon AK material interpreted by Dickinson et al. [7] can also be divided into five stages. Stage I reflects the breakdown of insulating layers or fritting. The contacts then become workpiece-workpiece contacts. In Stage II, contact resistance at the faying surface decreases due to the competition between the softening of contact spots and increases of bulk resistances in the surface film and workpieces with temperature. The increase of dynamic resistance in Stage III results from an increase of resistivity with temperature. The end of this stage corresponds to the local melting beginning to occur at the contact spots. Dynamic resistance in Stage IV results from a competition between the increased resistivity of bulk workpieces and decreased contact resistance at the faying surface from additional melting and softening. Stage V shows that contact resistance at the faying surface decreases due to the growth of the molten nugget and mechanical collapse. Variables including current level, electrode force, and material being welded can cause significant variations in the shape of the dynamic resistance curve.

Dynamic resistance is usually calculated by dividing the weld voltage by current. Most investigations measured the dynamic impedance rather than resistance, because a phase shift existed between voltage and current. At a small phase shift which is a function of resistance of the load and inductance, the impedance and resistance are nearly equivalent. To avoid the error induced by inductance, only one data point of dynamic resistance is available per half cycle. Applying a method to reduce the discrepancy, Gedeon and Eagar [8] and Gedeon et al. [9] found that the generalized dynamic resistance curve can be divided into four, six or eight stages depending on if the steels were uncoated, galvannealed , or hot-dipped. Weld quality thus can be more successfully monitored by using multiple sensors simultaneously measuring dynamic resistance, voltage, current, and electrode displacement.

Evidently, a quantitative and theoretical interpretation of the complicated dynamic resistance curve is needed to clarify the observed results. Holm [10] first pointed out that a constriction resistance will arise when current flows from one conductor of infinite extent to another through a finite area of perfect electrical contact. For a clean metal contact the contact resistance is simply a constriction resistances. If a film is present, the contact resistance consists of the constriction and film resistance. Greenwood [11] derived a general equation to find the constriction resistance of a cluster of contact spots. It was shown that the resistance may be regarded as the sum of the parallel resistance of contact spots. Although the theoretical analysis has been provided for a long time, a rigorous determination associated with experimental validification during resistance spot welding has not been found yet. This becomes the objective in this work.

In this study, a model including constriction and film resistances to determine dynamic resistance affected by hardness, temperature, electrode force, and surface conditions during resistance spot welding is presented [12]. The predicted results with the temperature obtained from the previous study [13] are compared with available experimental data. The significance and mechanism of dynamic resistance together with bulk and contact resistances therefore are revealed.

NOMENCLATURE

E^*	$r_0\tilde{R}_0\tilde{\sigma}_{liq}$
E_f	ε_f / r_0
g	volume fraction
H_v	hardness
I	welding current, amp
$\ell, \ell_1, \ell_2, \ell_3, \ell_4$	length, as illustrated in Fig.1
Lo	$I^2\mu_0\mu_{f\ell}/\tilde{\rho}_\ell\tilde{\alpha}_\ell^2$
n	total number of contact spots
Pr_m	magnetic Prandtl number = $\tilde{\eta}_\ell/\tilde{\alpha}_\ell$
R	r resistance
R_d	dynamic resistance, $R_d = \tilde{R}_d/\tilde{R}_0$
r_0	electrode radius, as illustrated in Fig. 1
$\tilde{R}_0$	electrical contact resistance at faying surface at T_0
s	film thickness
W	electrode force
δ	nugget thickness
ε_f	effective thickness of heat source at faying surface, m
$\tilde{\eta}_\ell$	magnetic diffusivity of liquid
σ	electrical conductivity, $\sigma = \tilde{\sigma}/\tilde{\sigma}_{liq} = g_\ell + g_s\sigma_{sol}$
Σ	$\tilde{\alpha}_\ell\tilde{\eta}_\ell/r_0^2h_f$
t	time, $\tau = t\tilde{\alpha}_\ell/r_0^2$

Superscript

~	dimensional quantity

Subscript

E	electrode
ℓ,liq	liquid and liquidus
s,sol	solid and solidus
w	water or coolant
0	ambient

SYSTEM MODEL AND ANALYSIS

Resistance spot welding is accomplished by the heat generated from temperature-dependent electrical contact resistance at the faying surface. Temperatures are obtained by solving axisymmetric, unsteady equations of mass, momentum, energy, species, and magnetic field intensity in the workpieces and electrodes [12,13]. Modeling electrical contact resistance is described as follows:

Electrical contact resistance. A local electrical contact resistance at the faying surface or electrode-workpiece interface can be simulated by

$$\tilde{R}_c = \frac{1}{2a\tilde{\sigma}} + \frac{\tilde{s}}{\pi a^2 \tilde{\sigma}_f} \qquad (1)$$

where the first and last terms on the right-hand side represent constriction and film resistances, respectively [10]. Each contact spot is considered as a circle with an effective radius

$$a = \sqrt{\frac{W}{\pi n \tilde{H}_v}} \qquad (2)$$

which shows that the size of a contact spot is a function of electrode force, hardness, and the total number of contact spots [10, 11, 14]. Temperature-dependent hardness indicates that contact area increases with time. In view of temperature-dependent electrical properties and hardness, the model presented by Eqs. (1) and (2) involves transient coupling between thermal-mechanical effects. In this work, the distribution of contact spots is considered to be uniform and the number of contact spots remains the same during the welding process. Considering a load W = 3000 N, hardness $\tilde{H}_v = 5\times10^9$ N/m^2 and choosing the number of contact spots $n_1 = 10$ implying the total number of contact spots n = 14940, Eq. (2) leads to an effective radius a = 3.6×10^{-6} m as a reasonable comparison to the electrode radius of $r_0 = 3.05\times10^{-3}$ m. Substituting Eq. (2) into Eq. (1), local contact resistance in a dimensionless form becomes

$$R_c = R_1\frac{\sqrt{nH_v}}{\sigma} + R_2\frac{snH_v}{\sigma_f} \qquad (3)$$

where dimensionless parameters governing constriction and film resistances are, respectively, defined as

$$R_1 \equiv \frac{1}{2\tilde{R}_0\tilde{\sigma}_{liq}}\sqrt{\frac{\pi\tilde{H}_{v0}}{W}}\,, \quad R_2 \equiv \frac{r_0\tilde{H}_{v0}}{W\tilde{R}_0\tilde{\sigma}_{liq}} \qquad (4)$$

In Eq. (3) temperature-dependent electrical conductivities of workpieces, surface film and hardness can be found by curve-fitting experimental data provided by Ono et al. [15], Boyer and Gall [16], Touloukian [17], and Grange et al. [18], respectively. Dimensionless temperature-dependent electrical conductivities and hardness from experimental data are as follows:

(a) Electrical conductivity of workpiece AISI 1008

Solid [16]

$$\sigma_s = \frac{1}{0.11 + 0.275(T-1)} \quad \text{for } 1 \le T \le 3.5 \qquad (5)$$

$$\sigma_s = \frac{1}{\frac{1}{\sigma_{sol}} + 0.07147(T - T_{sol})} \quad \text{for } 3.5 \le T \le T_{sol} \qquad (6)$$

Liquid [15]

$$\sigma_\ell = \frac{1}{1 + 0.034(T - T_{liq})} \quad \text{for } T \ge T_{liq} \qquad (7)$$

while electrical conductivity in the mushy zone $\sigma = g_\ell + g_s\sigma_{sol}$.

(b) Film electrical resistivity of iron oxide [17]

$$\frac{1}{\sigma_f} = 175483\, e^{-2.64301\,T} \qquad (8)$$

(c) Hardness of workpieces AISI 1026 [18]

$$H_v = 2.0657\, e^{-0.610487\,T} - 0.065 \qquad (9)$$

Resistance spot welding is analyzed by setting a cylindrical coordinate system with the origin on the intersection of the axisymmetric axis and bottom electrode-workpiece interface, as illustrated in Fig.1.

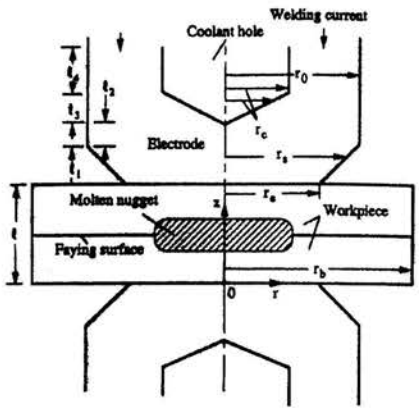

Fig. 1: Sketch for resistance spot welding and coordinate system.

Except for proposing more relevant and accurate electrical resistances to replace film resistance decreasing linearly with increasing temperature [19-22] , the major assumptions made are the same as those proposed by Wei et al [12] and Wang and Wei [13]. They are that the mushy zone is a porous medium in a local thermal and phase equilibrium. Mean values of properties within the temperature range considered are chosen and allowed to be distinct between phases. Solid diffusion is neglected.

Numerical method. Each of conservation equations as presented by the work of Wei et al. [13] and Wang and Wei [12] can be cast in the form

$$\frac{\partial\rho\phi}{\partial\tau} + \nabla.(\rho\mathbf{V}_m\phi) = \nabla.(\Gamma_\phi\nabla\phi) + S_\phi \qquad (10)$$

The control-volume, implicit finite-difference scheme with staggered grids [23] was used. A grid system 50 x 53 in workpieces and 27x72 in the electrode were selected. The axial direction is divided into uniform spaces while the spacing ratio in the radial direction is 0.95. A dimensionless uniform time step was 2 $\times10^{-5}$. The maximum deviation of the computed resistances by using grid systems of 50x53 and 72x75 is less than 1%. The convergence tolerances for global energy and velocity components and enthalpy, concentration, and magnetic intensity fields were 10^{-2} and 10^{-3}, respectively. If solutions converged, temperature distributions were used to calculate resistances. Number of iterations at each time were around 100. The global energy balance was that heat generation in the workpieces and electrodes should be equal to the total internal energy rise and heat convected to the electrodes, coolant hole, and surroundings. Considering 1500 time steps, the execution time by using an IBM RS6000 computer was about 4 hours.

RESULTS AND DISCUSSION

In this study, the unsteady variation of electrical resistance during resistance spot welding is quantitatively determined by incorporating in the previous work [12,13] predicting axisymmetric unsteady mass, momentum, energy, species and magnetic field intensity transport in the workpieces and electrodes. Electrical resistivity of the insulating surface film on a contact surface is much greater than that of the workpieces. An increase of temperature results in electrical resistivity of the surface film to decrease while bulk resistivity of the workpieces to increase. Hardness decreases with increasing temperature. The size of a contact spot on the contact surface is a function of the

electrode force, total number of contact spots, and hardness. Interactions between these factors affecting the change of electrical resistance during spot welding (see Eq. (3)) are therefore studied in the present work.

This model is confirmed from a good agreement with a measured relationship between nugget thickness and time provided by Gould [19] in welding AISI 1008, as shown in Fig. 2. In this case, solute concentration 0.32 wt% of Mn in a Fe-Mn alloy, total thickness of the two workpieces $\ell = 0.715$, electrode tip radius $r_e = 0.9$, dimensionless parameter governing welding current (or Lorentz force) $Lo = 6.17 \times 10^8$ and constriction and

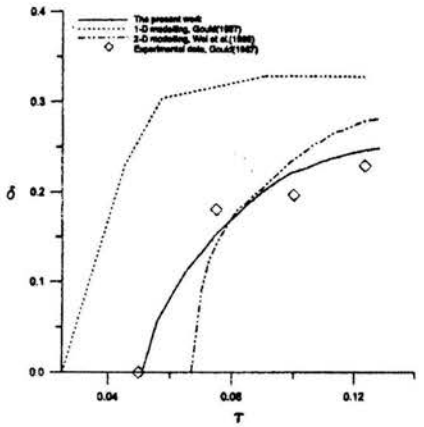

Fig. 2: Comparisons of dimensionless nugget thickness versus time in welding AISI 1008 steel between one- and three-dimensional predications from Gould [19], Wei et al. [12] and this work and the measurement from Gould [19].

film resistance parameters $R_1 = 100$ and $R_2 = 50$. This work shows a better agreement with the experimental result than the one-dimensional prediction from Gould [19] , and three-dimensional prediction from Wei et al. [6] . The former neglected heat transfer in the radial direction so that thicknesses of the nugget are overestimated. The latter assumed an inaccurate electrical resistances, where the film resistance decreases linearly with increasing temperature and bulk resistivity of the workpieces remains constant.

Fig. 3 shows that the predicted dimensionless dynamic resistance curve agrees quite well with the experimental result from Savage et al. [6] in welding uncleaned steels by choosing workpiece thickness of 0.89 mm, the number of contact points $n_1 = 10$, and $r_0 = 2.78$ mm, $Lo = 4.67 \times 10^8$, I = 8700 A, $R_1 = 40$, and $R_2 = 30$. The trend of the dynamic resistance curve also agrees with that presented by, for example, Roberts [3] , Bhattacharya and Andrews [4], and Dickinson et al. [7]. In this work, the dynamic resistance represents the total electrical resistance, which is the sum of bulk resistance in the workpieces, contact resistance at the faying surface and two times of contact resistance at the electrode-workpiece interface. After taking a sum of local resistances of grid points in series along the axial direction between the electrode tips for any given radius less than the electrode tip radius through which electric current primarily flows, the resulting resistances for all radii were added in parallel to give the total bulk resistance. The total contact resistance at the faying surface or electrode-workpiece interface was obtained by summing local contact resistances in parallel for all radii less than the electrode tip radius.

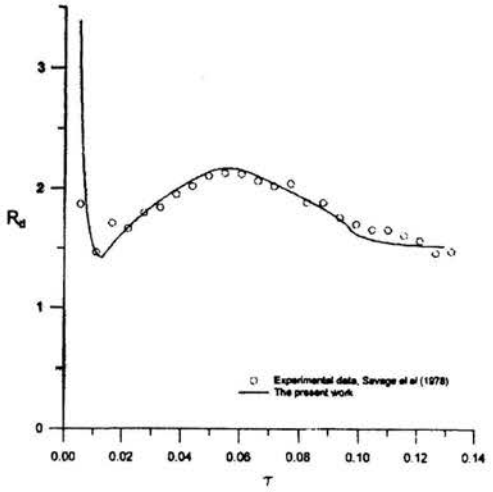

Fig. 3: A comparison of dimensionless dynamic resistance versus time between the measurement from Savage et al. [6] and prediction from this work in welding not cleaned steels with welding current of 8700 amps.

Typical values of dimensionless parameters estimated from pure iron and manganese and its alloy are listed in Table 1.

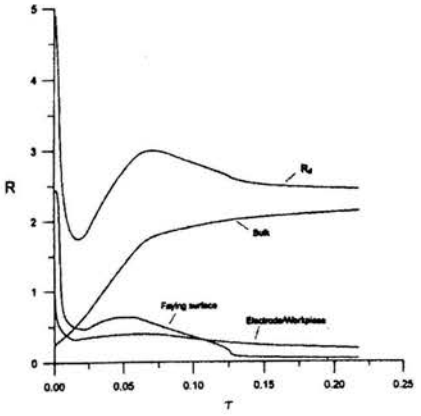

Fig. 4: Unsteady variations of dimensionless dynamic resistance, bulk resistance, and contact resistances at the faying surface and electrode-workpiece interface.

The variations of dimensionless bulk resistance in workpieces, contact resistances at the faying surface and electrode-workpiece interface, and the resulting dynamic resistance with time are shown in Fig. 4. It can be seen that contact resistance at the faying surface decreases rapidly in an early stage until the minimum value at a dimensionless time 0.02 is reached. Contact resistance then increases and reaches a local maximum value at a dimensionless time of 0.05. Thereafter, it decreases gradually and finds an inflection point at a dimensionless time of 0.125.

As can be seen from Eq. (3), contact resistance is composed of constriction and film resistances. The latter overrides the former in the early stage of welding. Because both electrical resistivity and hardness of the surface film on the contact surface decrease with increasing temperature, film resistance decreases in the early stage. The drop of contact resistance in the early stage therefore is a result of rapid decrease in film resistance. Since electrical resistivity of workpieces increases and hardness decreases with increasing temperature, constriction resistance or contact resistance at the faying surface exhibits a local maximum within a certain range of temperature in an intermediate stage. The inflection point of contact resistance at the faying surface at dimensionless time of 0.125 is due to an initiation of the molten nugget. A similar trend can be seen for the contact resistance at the electrode-workpiece interface. As welding time is large, contact resistance at the faying surface becomes lower than that at the electrode-workpiece interface. This is attributed to a more marked softening and earlier melting at the faying surface. It is also found that bulk resistance of the workpieces increases while the increasing rate decreases with increasing time or temperature.

The resulting dynamic resistance curve therefore can be divided into four regions. In the first stage, the rapid drop of dynamic resistance results from decreases in film resistances at the faying surface and electrode-workpiece interface. In the second stage, dynamic resistance increases with time. High increasing rate of dynamic resistance at the beginning of this stage is a result of increases in bulk resistance and contact resistances at the faying surface and electrode-workpiece interface. Near the end of this stage the reduction of increasing rate of contact resistance at the faying surface decreases the increase of dynamic resistance until the maximum is reached. In the third stage, dynamic resistance decreases as time proceeds.

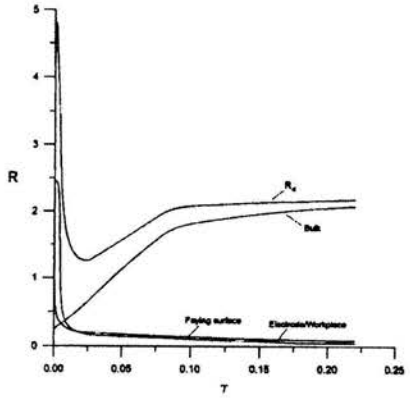

Fig. 5: Unsteady variations of dimensionless dynamic resistance, bulk resistance, and contact resistances at the faying surface and electrode-workpiece interface, $\sigma_s = \sigma_s(20^0C)$.

This is because the decreases in contact resistance at the faying surface and electrode-workpiece interface are greater than the increase in bulk resistivity. Decreases in contact resistances are due to an incessant increase in the soften area. The fourth stage starts from a marked drop accompanying with an inflection at a dimensionless time of 0.125, where the molten nugget initiates. It should be noted that the molten nugget takes place in this stage rather than the second region, as proposed by Dickinson et al. [8]. As time further increases, expulsion will take place. In view of mechanical collapse, expulsion cannot be treated in the present work.

Provided that bulk resistivity of the workpieces is a constant at the ambient temperature (namely, $\sigma = \sigma(20^0C)$, the predicted variations of dynamic resistance, bulk resistance in workpieces and resistances at contact surfaces with time are shown in Fig. 5. Instead of a local maximum within an intermediate stage as shown in previous figure (Fig. 4), contact resistances at the faying surface and electrode-workpiece interface monotonically decrease with time. This is due to the ignorance of the increase in bulk resistivity with temperature in constriction resistance. Contact resistances decrease solely from the reduction of hardness. Therefore, the local maximum of the dynamic resistance curve disappears and dynamic resistance becomes rather flat in the intermediate stage of welding time. Temperature-dependent bulk resistivity of the workpieces exhibits a significant effect on the shape of the dynamic resistance curve.

The surface contaminant and oxide layer can be removed by alkaline degreasing or acid pickling. In the case of a vanished film resistance or film thickness s = 0, rapid decreases of contact

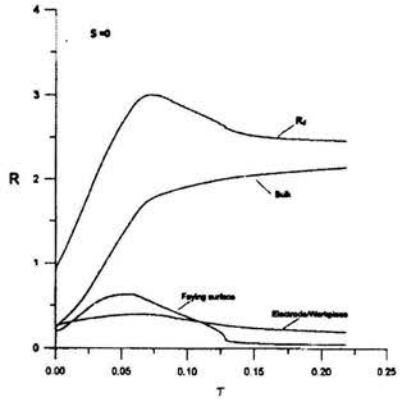

Fig. 6: Unsteady variations of dimensionless dynamic resistance, bulk resistance, and contact resistances at the faying surface and electrode-workpiece interface for vanished film resistance.

resistances and dynamic resistance in the early stage disappears, as shown in Fig. 6. Contact resistances at the faying surface and electrode-workpiece interface thus increase and then decrease with increasing time. The corresponding dynamic resistance curve increases with time until the maximum value is reached. Referring to Fig. 4, contact resistance at the faying surface exhibits a more pronounced rise.

CONCLUSIONS

The conclusions drawn are the following:

1. The predicted nugget thickness and dynamic resistance versus time agree quite well with available experimental data. Dynamic resistance is defined by summing the total bulk resistance in the workpieces and contact resistances at the faying surface and two electrode-workpiece interfaces within an effective area corresponding to the electrode tip where welding current primarily flows. The total bulk resistance is obtained by adding temperature-dependent resistance at each grid point in series for any given radius less than the electrode tip radius and then summing the resulting resistances of all radial locations in parallel. The total contact resistance at the faying surface or electrode-workpiece interface is determined by adding all local contact resistances in parallel within the electrode tip radius.

2. Contact resistance at the faying surface or electrode-workpiece interface is determined by taking the sum of

constriction and film resistances. A rapid drop of contact resistances in an early stage results from the decrease of film resistance, where both resistivity and hardness decrease as temperature increases. Contact resistance exhibits a local maximum in an intermediate stage, since constriction resistance can be increased or decreased by competing increased resistivity and decreased hardness with increasing temperature.

3. Without film resistance the rapid decrease of contact resistance in the early stage disappears. Provided that resistivity of workpieces is independent of temperature, the local maximum of contact resistance disappears.

4. Excluding expulsion, dynamic resistance versus time can be divided into four stages: Stage 1 is the decrease of dynamic resistance due to decreases in contact resistances at the faying surface and electrode-workpiece interface; an increase in dynamic resistance in stage 2 results from the primary increase of bulk resistance in the workpieces and an increase in the sum of contact resistances at the faying surface and electrode-workpiece interface; dynamic resistance in stage 3 decreases because the increasing rate of bulk resistance of workpieces and contact resistances decrease; in stage 4 the decrease of dynamic resistance is mainly due to a formation of the molten nugget at the faying surface.

REFERENCES

[1] Nied, H. A., 1984,"The Finite Element Modelling of the Resistance Spot Welding Process,"Welding J., Vol. 63, pp. 123-s-132-s.

[2] Tsai, C. L., Jammal, O. A., Papritan, J. C., and Dickinson, D. W., 1992,"Modeling of Resistance Spot Weld Nugget Growth," Welding J., Vol. 71, pp. 47-s- 54-s.

[3] Roberts, W. L., 1951,"Resistance Variations during Spot Welding," Welding J., Vol. 30, pp. 1004-1019.

[4] Bhattacharya, S., and Andrews, D. R., 1974, "Significance of Dynamic Resistance Curves in the Theory and Practice of Spot Welding,"Welding and Metal Fabrication, Vol. 42, pp. 296-301.

[5] Greenwood, J. A. and Williamson, J. B. P., 1958, "Electrical Conduction in Solids. II. Theory of Temperature-Dependent Conductors," Proc. Royal Soc. London, Vol. 246, pp. 13-31.

[6] Savage, W. F., Nippes, E. F., and Wassell, F. A., 1978, "Dynamic Contact Resistance of Series Spot Welds," Welding J., Vol. 57, pp. 43-s-50-s.

[7] Dickinson, D. W., Franklin, J. E., and Stanya, A., 1980, "Characterization of Spot Welding Behavior by Dynamic Electrical Parameter Monitoring,"Welding J., Vol. 59, pp. 170-s-176-s.

[8] Gedeon, S. A., and Eagar, T. W., 1986, "Resistance Spot Welding of Galvanized Steel: Part II. Mechanisms of Spot Weld Nugget Formation," Metallurgical Transactions B, Vol. 17B, pp. 887-901.

[9] Gedeon, S. A., Sorensen, C. D., Ulrich, K. T., and Eagar, T. W., 1987, "Measurement of Dynamic Electrical and Mechanical Properties of Resistance Spot Welds," Welding J., Vol. 66, pp. 378-s-385-s.

[10] Holm, R., 1967, Electric Contacts, Theory and Application, 4th edition, Springer-Verlag, New York.

[11] Greenwood, J. A., 1966, "Constriction Resistance and the Real Area of Contact," British J. Applied Physics, Vol. 17, pp. 1621-1632.

[12] Wang, S. C., and Wei, P. S., 2001, "Modeling Dynamic Electrical Resistance during Resistance Spot Welding," ASME J. Heat Transfer, Vol. 123, pp. 576-585.

[13] Wei, P. S., Wang, S. C., and Lin, M. S., 1996, "Transport Phenomena during Resistance Spot Welding," ASME J. Heat Transfer, Vol. 118, pp. 762-773.

[14] Crinon, E., and Evans, J. T., 1998, "The Effect of Surface Roughness, Oxide Film Thickness and Interfacial Sliding on the Electrical Contact Resistance of Aluminium," Materials Science and Engineering, Vol. A242, pp. 121-128.

[15] Ono, Y., Hirayama, K., and Furukawa, K., 1974, "Electric Resistivity of Molten Fe-C, Fe-Si, and Fe-C-Si Alloys," Tetsu-to-Hagan'e, Vol. 60, pp. 2110-2118.

[16] Boyer, H. E., and Gall, T. L., 1984, Metals Handbook, Desk Edition, ASM.

[17] Touloukian, Y. S., editor, 1967, Thermophysical Properties of High Temperature Solid Materials, Vol. 4: Oxides and Their Solutions and Mixtures, Macmillan Co, New York, pp. 214.

[18] Grange, R. A., Hribal, C. R., and Porter, L. F., 1977, "Hardness of Tempered Martensite in Carbon and Low-Alloy Steels,"Metallurgical Transactions A., Vol. 8A, pp. 1775-1785.

[19] Gould, J. F., 1987, "An Examination of Nugget Development During Spot Welding, Using Both Experimental and Analytical Techniques," Welding J., Vol. 66, pp. 1-s- 10-s.

[20] Wei, P. S., and Ho, C. Y., 1990, "Axisymmetric Nugget Growth during Resistance Spot Welding," ASME J. Heat Transfer, Vol. 112, pp. 309-316.

[21] Wei, P. S., and Yeh, F. B., 1991, "Factors Affecting Nugget Growth with Mushy-Zone Phase Change during Resistance Spot Welding," ASME J. Heat Transfer, Vol. 113, pp. 643-649.

[22] Khan, J. A., Broach, K., and Arefin Kabir, A. A. S., 2000, "Numerical Thermal Model of Resistance Spot Welding in Aluminum," J. Thermophysics and Heat Transfer, Vol. 14, pp. 88-95.

[23] Patankar, S. V., 1980, Numerical Heat Transfer and Fluid Flow, Hemisphere Publishing Corp., New York, Chapters 5 and 6.

Table 1 Typical values of dimensionless parameters

Constriction resistance parameter, R_1	30
Film resistance parameter, R_2	30
Electrical contact resistance, E^*	0.56
Thickness of surface film, E_f	10^{-3}
Thickness of heat source at contact surface, s	3.28×10^{-7}
Parameter governing welding current, Lo	3×10^{7}
Lengths for electrode, ℓ_2, ℓ_3, ℓ_4	0.5, 0.5, 1
Magnetic Prandtl number Pr_m	3×10^{4}
Maximum radius of coolant hole, r_c	0.5
Thermal-to-electrical property parameter, Σ	2.5×10^{-5}
Electrical conductivity ratios, σ_{sol} , σ_E	1.05, 6.5

HEFAT2002
1st International Conference on Heat Transfer, Fluid Mechanics, and Thermodynamics
8-10 April 2002, Kruger Park, South Africa
CH1

EXPERIMENTAL INVESTIGATION OF THERMAL RADIATIVE PROPERTIES FOR (Ba,Sr)TiO_3(BST) THIN FILMS

Hsin-Sen Chu* and Hsing-Chien Wang**
*Professor; **Graduate student
Department of Mechanical Engineering
National Chiao Tung University
Hsinchu 300, Taiwan, R.O.C.
E-mail: hschu@cc.nctu.edu.tw

Senpuu Lin***
***Associate Professor
Department of Mechanical Engineering
National Lien Ho Institute of Technology
Miaoli 360, Taiwan, R.O.C.
E-mail: spuulin@mail.nlhu.edu.tw

ABSTRACT

In this study, the transmittance and reflectance of (Ba,Sr)TiO_3 (BST) thin films for several different thickness deposited on the Fused-Quartz, MgO and silicon substrates are measured at room temperature using FTIR (Fourier Transform Infrared Spectrometer) from 0.64 μm to 19.6 μm. By Beer's law, the extinction coefficient of the BST films can be evaluated. Using the energy conservation law, the absorptance of the BST films sample can also be figured out. The results indicated that the transmittance and the extinction coefficient of the BST films are very high between 0.64 μm and 10 μm.

INTRODUCTION

Barium strontium titanate (Ba,Sr)TiO_3 (BST) thin films are being widely investigated as alternative dielectrics for ultra large scale integrated circuits (ULSIs) DRAM storage capacitors due to (1) its high dielectric constant, (2) low leakage current, (3) small dielectric loss, (4) lack of fatigue or aging problems, (5) high compatibility with device processes [1]. In addition, the thin films or multiplayer systems of BST can be used in nonlinear optical devices such as planar waveguides, optical switches with minimal optical propagation losses [2] or the sensor material for thermal imaging detector. However, whether or not BST films can be successfully applied largely depends on more thorough understanding the material's properties.

In the past, some investigations have focused on the dependence of optical properties and film structure on the deposition parameters of thin films deposited by various methods such as sputtering, sol-gel process, pulsed laser deposition and radio-frequency (RF) magnetron sputtering [2]. Tcheliebou et al. [3] stated that the films are polycrystalline with a strong reflection along the (111) plane. The refractive index and the absorption coefficient are determined at room temperature ranging from 0.382 to 0.8 μm by spectrophotometer measurements of the transmittance at normal incidence. Thielsch et al. [4] investigated the refractive index, absorption coefficient and the thickness of the BST films at near-normal incidence in the wavelength range 0.2-1.1 μm by measuring the optical reflection spectra with a double beam Perkin Elmer Lambda-2 spectrophotometer. Wang and Tseng [5] studied the structural and optical properties of BST films deposited on the transparent substrate at various temperatures of 350-650℃ and annealed at 450-650℃ in the spectral range 0.2-0.9 μm. Kuo and Tseng [6] determined the optical constants, refractive index and absorption coefficient, and the thickness of BST films by measuring optical reflection spectra in the wavelength 0.18-0.9 μm with Nikon n&k Analyzer 1200. Up to now, no detailed studies have elucidated the optical and thermal radiative properties related to the BST thin films in the infrared spectrum.

Fourier transform infrared (FTIR) spectroscopy is a major analytical technique that has widely been used by chemists [6, 7]. FTIR has brought additional merits such as high sensitivity, high precision, quickness of measurement, and extensive data processing capability. Ravindra et al. [8] studied the temperature-dependent emissivity of silicon-related materials and structures in rapid thermal processing using a emissometer, which consisted of a FTIR spectrometer designed specially to facilitate simultaneous measurements of surface spectral emittance and temperature. Recently, we [9] used FTIR spectroscopy to investigate the emission spectrum of some heating source in rapid thermal processing systems.

In this study, the transmittance and reflectance of BST thin films for several different thickness deposited on different substrates are measured using FTIR in the wavelength range from 0.64 to 19.6 μm. Then, the extinction coefficient of the BST films can be calculated by the Beer's law. Using the energy conservation law, the absorptance of BST thin-film samples can also be figured out from the transmittance and reflectance. Therefore the absorptive characteristics and optical properties will be known from these radiative properties, and are offered to be references in manufacturing and research.

NOMENCLATURE

d	thickness
k	absorption coefficient
n	refractive index

Greek symbols

λ	wavelength
σ_e	extinction coefficient (m^{-1})

Subscripts

e	extinction
f	film
s	substrate

EXPERIMENTAL METHOD

EXPERIMENTAL APPARATUS

A Bomem Micheson series MB-154 FTIR Spectrometer equipped with a deuterated triglycine sulfate (DTGS) detector (0.7-40 μm) or Silicon detector (0.64-1.2 μm), and a wide-band (0.7-20 μm) ZnSe substrate beam splitter was used. For the reflectance measurement, the Barnes Model 134 horizontal specular reflectance attachment is used. The angle of the incident

light beam was 11 deg from the normal to the BST thin film sample surface. Figure 1 shows the general arrangement of the instrument used in the present study. The spectrometer is a self-contained unit consisting of one sample compartment and a sealed interferometer compartment. The whole system contains a stabilized internal light source, a Michelson interferometer, an infrared-transmitting beam splitter, a Helium-Neon laser for measurement of the scan position, power supplies and electronic assembles. They are interfaced with a computer for data acquisition of the measured transmission and reflection. The cast aluminum compartment is sealed to prevent the entry of dusty and moist air, which could erode the beam splitter. It is noted that Bomem MB-154 spectrometer is a single substrate self-compensating beam splitter and a permanent alignment interferometer. Besides of the internal light source, there is an optional emission port for the external light source on Bomem MB-154 FTIR system. Instead of spatially separating the optical frequencies, the FTIR spectrometer modulates all wavelengths simultaneously with distinct modulation frequencies for each wavelength. This is done by means of a variable interference effect created by separating the incoming beam into two parts, then introducing a path difference, and finally recombining the beam. The resulting beam intensity recorded as a function of optical path difference is called "interferogram". Computing the Fourier transform of the interferogram yields the emission spectrum.

EXPERIMENTAL SPECIMENS

$(Ba_{0.7}Sr_{0.3})TiO_3$ (BST) thin films were prepared by sol-gel method on both Fused-Quartz and MgO (001) substrates with varying film thickness from 1 layer to 12 layers. While, the $(Ba_{0.5}Sr_{0.5})TiO_3$ (BST) thin films were deposited on the silicon substrate by the radio-frequency magnetron sputtering with varying thickness from 0.4437 to 0.6426 μm. These BST thin films were not deposited in-house—they were supplied through the courtesy of the Dr. Tseng, department of Electric Engineering of the National Chiao Tung University, Hsinchu, Taiwan, R.O.C.

The reflectance of the substrate with a thin film depends on the refractive indices of thin film and substrate, and on the path difference of the light rays in the film, i.e. on the thickness of the films. The film thickness could be calculated from the wavelength position and the interference order of the reflection maxima and minima [10]. The thickness for the thinner sample could be approximately obtained by multiplying the average 1 layer's thickness and the number of layer. The calculated thin films thickness and the substrate characteristics are listed in Table 1 in detail.

Table 1: The calculated films thickness of Samples.

Quartz/BST	sample A	sample B	sample C	sample D	sample E	sample F	sample G
d_s (mm)	1.3	1.3	1.3	1.3	1.3	1.3	1.3
d_f (μm)	0.0999	0.2939	0.4110	0.5109	0.7747	0.8621	0.9833
MgO/BST	sample H	sample I	sample J	sample K	sample L	sample M	sample N
d_s (mm)	0.5	0.5	0.5	0.5	0.5	0.5	0.5
d_f (μm)	0.0472	0.0945	0.1890	0.2413	0.3524	0.4922	0.6665
Si/BST	sample O	sample P	sample Q				
d_s (mm)	1.0	1.0	1.0				
d_f (μm)	0.4437	0.5898	0.6426				

EXPERIMENTAL PROCEDURE

When starting at room temperature, the spectrometer would need about an hour to allow its temperature to stabilize. In room-temperature experiments, the resolutions are $4cm^{-1}$, and the measurements were performed several times for each sample, ensuring the accuracy of measurements. The transmittance measurements are performed employing a typical FT-IR procedure. The incident beam is approximately normal to the sample plane and no accessory was need.

A gold mirror is used as the reference for the reflectance measurement. The spectral reflectance was determined by dividing radiation reflected from the sample at a given frequency by the radiation reflected from the gold mirror at the same frequency. Estimated reflectance of this gold mirror is about 99% for all wavelengths [11], which is used as a correction factor for the raw data. To enhance the signal-to-noise ratio, the number of scans is increased to 256.

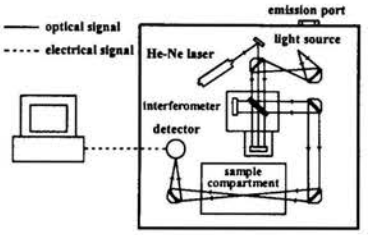

Figure 1: schematic diagram of the FTIR apparatus.

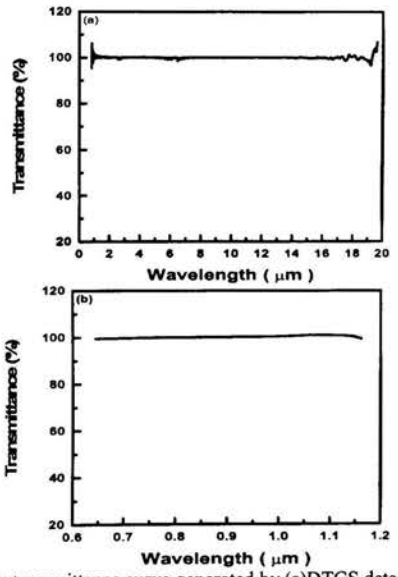

Figure 2: transmittance curve generated by (a)DTGS detector and (b) Silicon detector.

The calibrations were initiated by a self-calibrating system, which compensates for slight drifts in electronics. The procedure was done at the start of every working day. To test the validity of the transmittance curves generated by the Bomem attachment, the background spectrum is carried out twice continuously. The first scan was executed as background, and then the second scan was executed and divided by background. If the spectrometer measurement is accuracy, the exact transmittance should be 100%. Figure 2a shows the result of one divided by another, which is

generated by the DTGS detector. It is found that the transmittance is almost 100% in the spectral range from 1.0 to 17 μm. There are some error in the wavelength below 1.0 μm and the wavelength greater than 17 μm. As there are some errors below 1.0 μm the silicon detector is used to reduce the error below 1.5 μm generated by the DTGS detector. Figure 2b shows the transmittance curve generated by the silicon detector. It is found that the transmittance is almost 100% from 0.64 to 1.2 μm. Our experiments by the present instrument reasonably are in good performance on the measuring the radiative properties of the materials. In this study, the experiment data in the wavelength range from 0.64 to 1.0 μm is generated by the silicon detector and the experiment data in the wavelength range from 1.0 to 19.6 μm is generated by the DTGS detector.

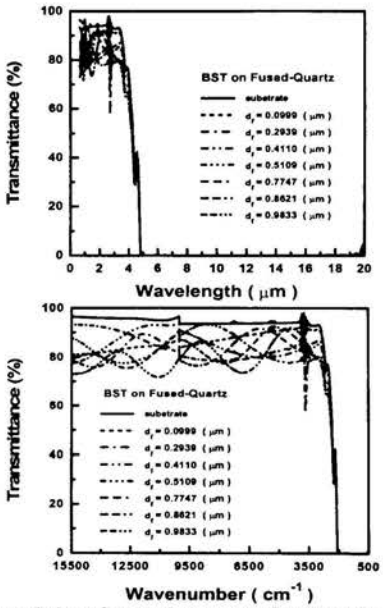

Figure 3: variation of transmittance as a function of wavelength for different thickness of the BST films deposited on the Fused-Quartz substrate.

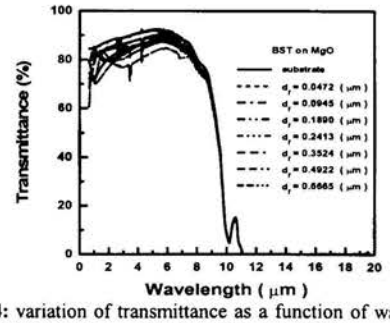

Figure 4: variation of transmittance as a function of wavelength for different thickness of the BST films deposited on the MgO substrate.

RESULTS AND DISCUSSION

The transmittance of the bare substrates and the BST thin films deposited on the Fused-Quartz and MgO substrates for various thickness are showed in figures 3 and 4, respectively. The bare MgO and Fused-Quartz substrates are double-side polished. The transmittance of bare Fused-Quartz substrate is about 95% in the wavelength range from 0.64 to 4.8 μm, and it is opaque at wavelength greater than 4.8 μm. The transmittance of bare MgO substrate is about 85% at wavelength smaller than 10 μm, and it is opaque at wavelength greater than 11 μm. The BST thin films will reduce the transmittance. Due to the interference between the air-film and film-substrate interfaces, there exist interference fringes where the thickness of thin films was approximately equal to the incident wavelength, e.g. smaller than 3.8 μm (greater than 2630 cm^{-1}) in figure 3.

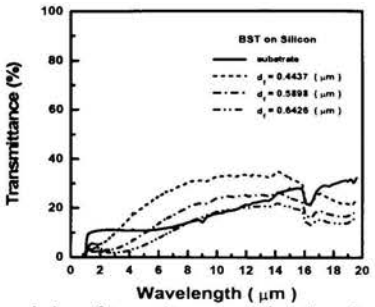

Figure 5: variation of transmittance as a function of wavelength for different thickness of the BST films deposited on the silicon substrate.

Figure 5 depicts the transmittance of the bare silicon substrate and the different-thickness BST thin films on it. The transmittance of bare silicon substrate is about 10-35% range from 1.08 to 19.6 μm, and it is opaque at wavelength smaller than 1.0 μm. It is apparent that the transmittances of the samples decrease with an increasing in thin films thickness.

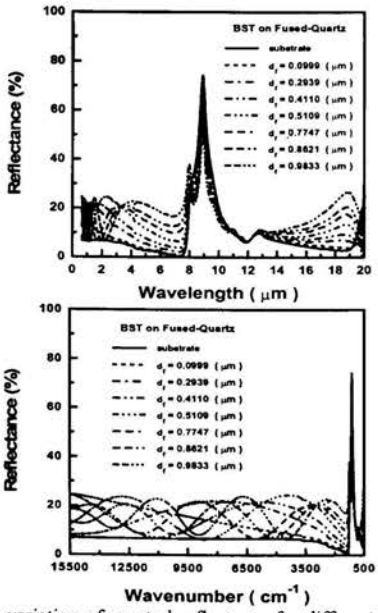

Figure 6: variation of spectral reflectance for different thickness of the BST films deposited on the Fused-Quartz substrate.

Figures 6, 7 and 8 show the reflectance of the BST thin films samples and bare Fused-Quartz, MgO and silicon substrates. There also interference fringes at the short wavelength as mentioned above. In figure 6, the reflectance of the BST/Fused-Quartz samples is higher than that of bare Fused-Quartz substrate in the spectral range 0.64-8 μm and 13-19 μm, respectively. The reflectance of the BST/Fused-Quartz samples increases with an increasing in BST film thickness. In figure 7, the reflectance of the BST/MgO samples is higher than that of bare MgO substrate in the spectral range 0.64-7 μm. From figures 6 and 7, the minimum reflectance of the BST/Fused-Quartz or BST/MgO samples at short wavelength is equal to the reflectance of bare Fused-Quartz or MgO substrate. In figure 8, the maximum reflectance of the BST/Si sample at short wavelength is equal to the reflectance of bare silicon substrate. The reflection period of BST samples vary with the BST thin films thickness. The thicker the BST thin film is, the larger the reflection period is.

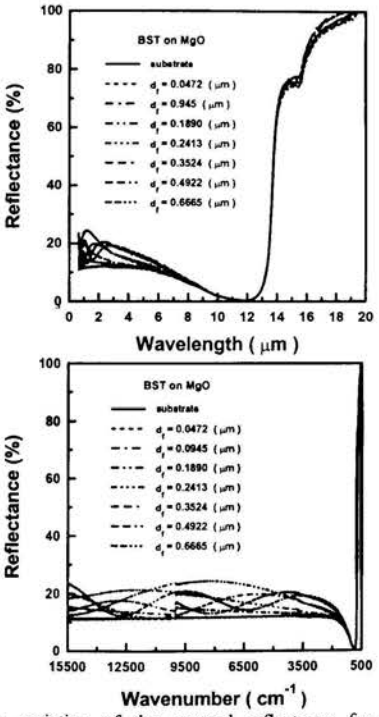

Figure 7: variation of the spectral reflectance for different thickness of the BST films deposited on the MgO substrate.

The experimental absorptance is determined by subtracting the sum of the reflectance and the transmittance from one. The spectral absorptance of different-thickness BST thin films is shown in figures 9, 10 and 11. In figure 9, the absorptance of the BST/Fused-Quartz samples decreases with an increasing in BST film thickness in the spectral range 5-7 μm and 13-19 μm, respectively. In figure 10, for the BST thin films deposited on the MgO substrate, a higher absorptance of above 90% appears from 9.5 to 14 μm. In figure 11, the absorptance of the BST/Si samples is higher than 60% in the range of 0.64 to 6 μm, and the absorptance of the samples inccreases with an increasing in BST film thickness in the spectral range 6-19.6 μm.

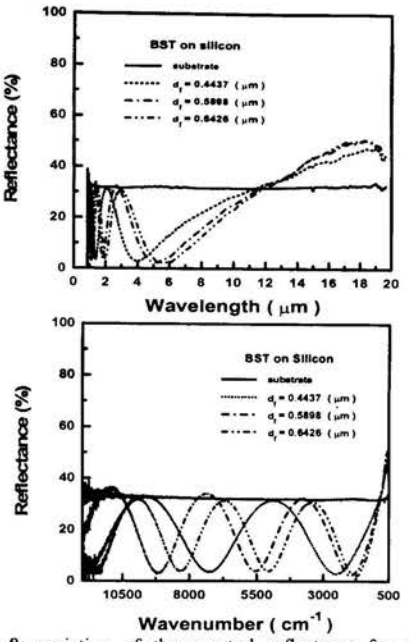

Figure 8: variation of the spectral reflectance for different thickness of the BST films deposited on the silicon substrate.

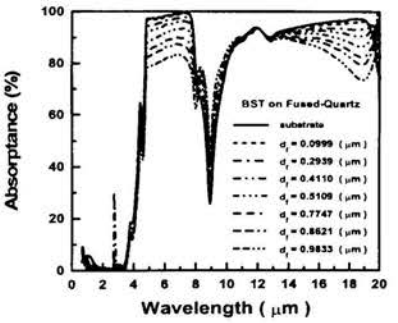

Figure 9: variation of the spectral absorptance for different thickness of the BST films deposited on the Fused-Quartz substrate.

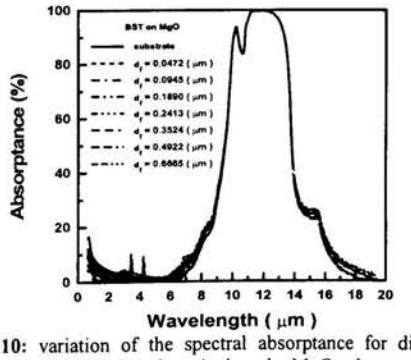

Figure 10: variation of the spectral absorptance for different thickness of the BST films deposited on the MgO substrate.

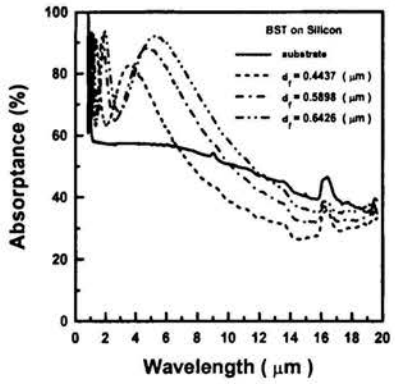

Figure 11: variation of the spectral absorptance for different thickness of the BST films deposited on the silicon substrate.

The spectral transmittance of the BST thin films could be determined by dividing the spectral transmittance of the film/substrate composite by the spectral transmittance of the substrate. Figures 12 and 13 show the transmittance of BST thin films for varying thickness deposited on the Fused-Quartz and MgO substrate, respectively. In figure 12, the BST thin films deposited on the Fused-Quartz substrate had a transmittance of above 75% in the spectral range from 0.64 μm to 4.1 μm. While, in figure 13, the transmittance of BST deposited on MgO was higher than 80% range from 0.7 to 11 μ m. Due to OH compounds on the Fused-Quartz substrate, there is an significant absorption at 2.7 μm in figure 12 [12, 13]. The transmittance of BST thin films decreased with increasing thickness at wavelength greater than 3 μm. As the spectral transmittance of the BST thin films were obtained, the extinction coefficient σ_e was calculated according to Beer's law [14]. Figures 14 and 15 show the extinction coefficient of BST films deduced according to the Beer's law from the transmittance of the BST films mentioned in figures 12 and 13. We noted that absorption of H_2O and CO_2 is very serious and this will have a seriously influence on the result of experiment data.

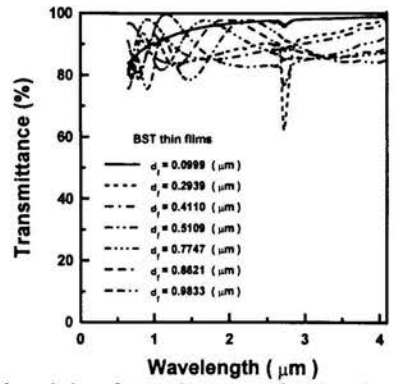

Figure 12: variation of transmittance as a function of wavelength for different thickness of the BST films deposited on the Fused-Quartz substrate.

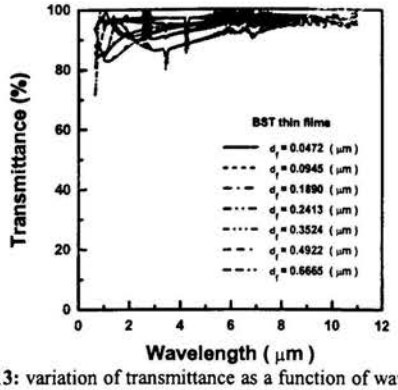

Figure 13: variation of transmittance as a function of wavelength for different thickness of the BST films deposited on the MgO substrate.

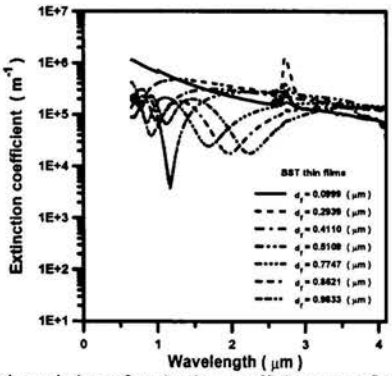

Figure 14: variation of extinction coefficient as a function of wavelength for different thickness of the BST films deposited on the Fused-Quartz substrate.

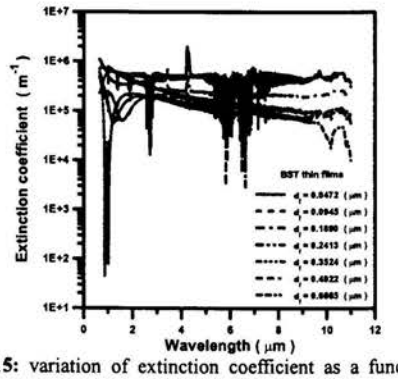

Figure 15: variation of extinction coefficient as a function of wavelength for different thickness of the BST films deposited on the MgO substrate.

The real and imaginary parts of the complex refractive index, n(λ) (refractive index) and k(λ) (absorption coefficient) of the BST films deposited on the silicon substrate were obtained from a Nikon n&k analyzer 1200. The spectral reflectance data were analyzed and fitting using the BST model built-in Nikon n&k Analyzer 1200. Figure 16 shows the refractive index n(λ) of

BST films deposited on the silicon substrate with different thickness in the wavelength range 0.18-0.9 μm. It reveals that the refractive index rises sharply toward the 0.3 μm wavelength, displaying the typical shape of a dispersion curve near an electronic interband transition. The strong increase in the refractive index is associated with the fundamental band gap absorption [2]. Figure 17 shows the absorption coefficient k(λ) of BST films deposited on the silicon substrate. It is found that the absorption coefficient of the BST films is decreasing with the increase wavelength from 0.3 μm to 0.9 μm and the value is very small.

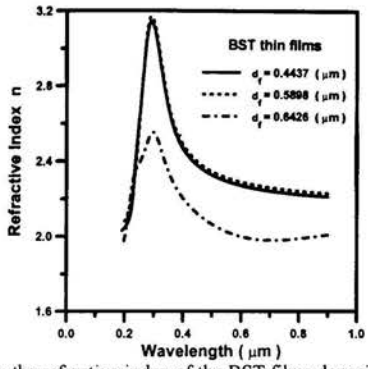

Figure 16: the refractive index of the BST films deposited on the silicon substrate for different thickness.

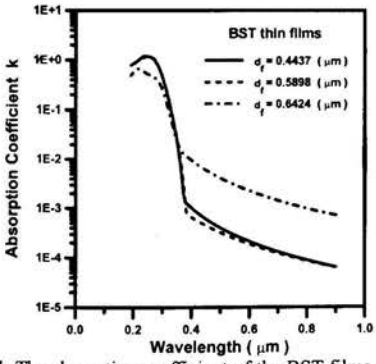

Figure 17: The absorption coefficient of the BST films deposited on the silicon substrate for different thickness.

CONCLUSION

The transmittance and reflectance of the BST films for several different thickness deposited on the Fused-Quartz, MgO and silicon substrates were measured at room temperature using FTIR from 0.64-19.6 μm. Using the energy conservation law, the absorptance of the BST films samples can also be figured out. The results indicated the absorptance of the BST/Fused-Quartz sample decreases with an increasing in BST film thickness in the spectral range 5-7 μm and 13-19 μm, respectively. For the BST thin films deposited on the MgO substrate, a higher absorptance of above 90% appears from 9.5 to 14 μm. The absorptance of the BST/Si samples is higher than 60% in the range of 0.64 to 6 μm, and the absorptance of the samples increases with an increasing in BST film thickness in the spectral range 6-19.6 μm. By Beer's law, the extinction coefficient of the BST films can be evaluated. The extinction coefficient of the BST films is high in the spectral range from 0.64 to 11 μm.

ACKNOWLEDGEMENT

This research was supported by the National Science Council of Taiwan, ROC. under grant NSC-89-2212-E-009-039.

REFERENCE

[1] Ezhilvalavan, S. and Tseng, T. Y., 2000, "Process in the Developments of (Ba,Sr)TiO_3 (BST) Thin Films for Gigabit era DRAMS," Materials Chemistry and Physics, Vol. 65, pp. 227-248.

[2] Kuo, Y. F. and Tseng, T. Y., November 1999, "Structure-Related Optical Properties of Rapid Thermally Annealed $Ba_{0.7}Sr_{0.3}TiO_3$ Thin Films," Materials Chemistry and Physics, Vol. 61, pp. 244-250.

[3] Tchelienou, F., Ryu, H. S., Hong, C. K., Park, W. S. and Baik, S., 1997, "On the Microstructure and Optical Properties of $Ba_{0.5}Sr_{0.5}TiO_3$ Films," Thin Solid Films, Vol. 305, pp. 30-34.

[4] Thielsch, R., Kaemmer, K., Holzapfel, B. and Schultz, L., 1997, "Structure-Related Optical Properties of Laser-Deposited $Ba_xSr_{1-x}TiO_3$ Thin Films Grown on MgO (001) Substrates," Thin Solid Films, Vol. 301, pp. 203-210.

[5] Wang, Y. P. and Tseng, T. Y., 1999, "Optical and Structural Properties of (Ba,Sr)TiO3 Thin Films Grown by Radio-Frequency Magnetron Sputtering," Journal of Materials Science, Vol. 34, pp. 4573-4578.

[6] Griffiths, P.R. and Haseth, J.A., 1986, Fourier Transform Infrared Spectroscopy, J. Wiley, New York.

[7] Ferraro, J.R. and Krishnan, K., 1976, Practical Fourier Transform Infrared Spectroscopy, Academic Press, Orlando.

[8] Ravindra, N.M., Abedrabbo, S., Chen, W., Tong, F.M., Nanda, A.K., and Speranza, A.C., 1998, "Temperature-Dependent Emissivity of Silicon-Related Materials and Structures," IEEE Transactions on Semiconductor Manufacturing, Vol. 11, No. 1, pp. 30-39.

[9] Chu, H.S., Lin, S.P., Chang, C.C., Su, C.C., Yen, C.C. and Tsau, J.C., 1999, "Emission Spectrum Measurement of the Rapid Thermal Processing Heating Source by Fourier Transform Infrared Spectroscopy." Submitted to J. Chinese Soc. Mech. Eng., pp. 553-562.

[10] Toscano, W. M. and Cravalho, E. G., 1976, "Thermal Radiation Properties of the Noble Metals at Cryogenic Temperatures," ASME Journal of Heat Transfer, Vol.98 pp. 438-445.

[11] Vasicek, A., 1960, "Optics of Thin Films," North-Holland Publishing Company, Amstredam Interscience Publishers Inc., New York., pp. 122-132.

[12] Roozeboom, F., 1996, "Advances in Rapid Thermal and Integrated Prpcessing," Boston: Kluwer Academic Publishers, pp. 6.

[13] Silverstein, Robert M. and Webster, Francis X., 1997, "Spectrometric Identification of Organic Compounds," Sixth Ed., John Wiley & Sons Inc., New York.

[14] Chu, H. S., Stretton, A. J. and Ten, C. L., 1988, "Radiative Heat Transfer in Ultra-Fine Power Insulations," International Journal of Heat and Mass Transfer, Vol. 31, No. 8, pp. 1627-1634.

Proceedings of HEFAT 2002
1st International Conference on Heat Transfer, Fluid Mechanics, and Thermodynamics
8 - 10 April 2002, Kruger Park, South Africa
HG 1

Influence of laser radiation on thermophysical and thermodynamic properties of non - transparent liquids.

Hikmet G. Hassanov
Azerbaijan State Oil Research and Project Institute (AzNSETLI);
Aga - Neymatullah str. 39, Baku 370033 - Azerbaijan
E - mail: hhassanov @ yahoo.com

Abstract : In research the heat structures arising under laser beam action on non - transparent liquids are theoretically investigated. It is known, that under strong laser radiation the temperature waves appear and propagate in liquid. These waves possess an information about thermophysical and thermo-dynamic properties of liquids. It is established by us, forms of the temperature waves depend greatly on physical properties of liquid involved. Moreover, on the base of these signals new optical method for investigation of thermophysical and thermodynamic properties of liquid is developed. Influence of laser parameters on thermophysical and thermodynamic properties of liquid is estimated.

Nomenclature : s - entropy, v_i - components of velocity vector, η and ξ - dynamic and volume viscosities respectively, $\langle \vec{s} \rangle$ - the falling wave Poynting vector averaged by the oscillation period of the electromagnetic radiation, I_0 - light intensity on the absorbing liquid boundary, R - radius of pipe, in which the liquid is acted by the laser, $f(t)$ - dimensionless function describing the dependence of light intensity on time, t_0 - laser radiation duration , P - acoustic pressure , l - length of liquid section under radiation, P_0 - initial pressure at $x = 0$, P_l - acoustic pressure amplitude on distance $x = l$ from liquid free boundary.

During nonresonance interaction of great laser radiation with non - transparent liquids various opto - thermophysical and opto - thermodynamic processes take place, which are connected with strong compression and heating the liquids. In propagating the laser radiation in absorbing medium (liquid) there are convection flows due to its heating. Increasing the laser generator power leads to transformation of laminar flow to turbulent one [1, 8]. Yarovaya et al [7] showed, that heating the liquid by laser radiation results in formation of gradient of various physical magnitudes, for example, refraction index $n(T)$, surface tension coefficient $\sigma(T)$ and so on.

Temperature waves propagating in liquid possess an information about the liquid physical properties. Using this information, i.e. the liquid temperature change by time, ones may find thermophysical and thermodynamic properties of medium. With connection to this fact, recently for investigation of kinetic coefficients of liquids the optical methods based on absorption and scattering of the light in liquids [2,5,6] are used.

In general form the differential equation of heat conductivity with account of absorbing the electromagnetic wave energy has a view:

$$\rho T\left[\frac{\partial s}{\partial t}+(\vec{v}\cdot\vec{\nabla})s\right]=div(\lambda\cdot\nabla T)+\frac{\eta}{2}\cdot\left(\frac{\partial v_i}{\partial x_k}+\right.$$

$$\left.+\frac{\partial v_k}{\partial x_i}-\frac{2}{3}\delta_{ik}\frac{\partial v_i}{\partial x_k}\right)+\xi\cdot(div\,v)^2-div\langle\vec{s}\rangle \quad (1)$$

The last summand in the equation (1) describes the energy density caused by absorption of the light wave.

On the base of theoretical calculations of Galich N.E. [1] it is established, if the laser radiation energy density is greatly less than the liquid internal energy, in other words, there is the condition $I << c\rho C_p T$ (herein c - sound velosity in medium, other indications are well - known), then the medium is weakly absorbing, and coefficient of transfer may be accepted to be constant. In this case mathematical model of the heat transfer is described by linear differential equation. However, if $I \approx c\rho C_p T$, then temperature of liquid already changes in wide area, and thermophysical and thermodynamic parameters of the liquid essentially alter by temperature, hence, for determining the kinetic coefficients it is necessary to use the nonlinear models.

It is proposed that absorption of the laser beam in liquid obeys Bouger'slaw, so the radiation intensity with penetration depth changes by well - known law

$$I(x,y,z,t)=I_0 f(t)\exp\left[-\frac{y^2+z^2}{R^2}-\alpha x\right] \quad (2)$$

Heat exchange with surrounding medium is defined by Newton law:

$$Q=\alpha_0(T)\cdot\left[T(x,y,z,t)-T_0\right] \quad (3)$$

For simplicity let's consider a case of one-dimensional heat propagation in liquid, when, before the laser action, temperature is the same everywhere and permanent. Under the laser radiation influence the liquid heats essentially, and the relaxation of temperature field takes place. It is of great interest to elucidate, how the laser power effects on thermophysical and thermodynamic properties of the liquid and , as a result, to handle technological processes by means of alternating electromagnetic waves.

The differential equation of heat conductivity accordingly to above may be represented in the following dimensionless form

$$\frac{\partial\theta}{\partial\tau}+Fo\frac{\partial^2\theta}{\partial\tau^2}+Pe\frac{\partial\theta}{\partial\zeta}=\frac{1}{C_p(\theta)\rho(\theta)}\frac{\partial}{\partial\zeta}\left(\lambda(\theta)\times\right.$$

$$\left.\times\frac{\partial\theta}{\partial\zeta}\right)+\frac{I_0\alpha(\theta)}{C_p(\theta)\rho(\theta)}\cdot\exp\left[-\int_0^{\zeta}\alpha(\theta)\,d\zeta\right]-$$

$$-2\frac{l}{R}Nu\frac{\alpha_0(\theta)}{C_p(\theta)\rho(\theta)}\cdot\theta \quad (4)$$

where the next abbreviations are introduced

$$I_0=\frac{I\cdot l}{\lambda_0\cdot T_0},\ Nu=\frac{\alpha_0 l}{\lambda_0},\ \theta=\frac{T-T_0}{T_0},\ \zeta=\frac{x}{l},$$

$$\tau=\frac{a\cdot t}{l^2},\ Fo=\frac{\tau_0 a}{l^2},\ Pe=\frac{vl}{a},\ a=\frac{\lambda_0}{C_0\rho_0}$$

Initial and boundary conditions are given like

$$\theta(\zeta,0)=0,\ \frac{\partial\theta(\zeta,0)}{\partial\tau}=0$$

$$\theta(0,\tau)=f(\tau),\ \theta(1,\tau)=\varphi(\tau) \quad (5)$$

Hence, problem of determining the laser radiation influence on thermophysical and thermodynamic properties of liquids is mathematically reduced to solving the inverse problem for the equation (4) under initial and boundary conditions (5).

It is taken, the heat conductivity due to convection is much more than that because of diffusion. Having neglected the diffusion summand in the equation (4), we have

$$\frac{\partial\theta}{\partial\tau}+Fo\frac{\partial^2\theta}{\partial\tau^2}+Pe\frac{\partial\theta}{\partial\zeta}=\frac{I_0\alpha(\theta)}{C_p(\theta)\rho(\theta)}\times$$

$$\times\exp\left[-\int_0^{\zeta}\alpha(\theta)\,d\zeta\right]-2\frac{l}{R}Nu\frac{\alpha_0(\theta)}{C_p(\theta)\rho(\theta)}\cdot\theta \qquad (6)$$

The equation (6) is nonlinear, so its solving is conjugated with serious mathematical difficulties. Nevertheless, under certain conditions ones may obtain correct analytical solution of the equation (6). If there is the following dependence

$$\alpha(\theta)=\theta\cdot\alpha_0(\theta)\cdot\exp\left[-\int_0^{\zeta}\alpha(\theta)\,d\zeta\right], \qquad (7)$$

then by using Laplace transformation solution of the equation (6) in images is expressed by the formula

$$\varphi^*(s)=f^*(s)\cdot\exp\left[\frac{1}{Pe}\left(I_0-2Nu\frac{l}{R}-s-\right.\right.$$

$$\left.\left.-Fo\cdot s^2\right)\right], \qquad (8)$$

where functions - images are defined by the next relationships, respectively

$$f^*(s)=\int_0^{\infty}f(\tau)e^{-s\tau}d\tau,\ \varphi^*(s)=\int_0^{\infty}\varphi(\tau)e^{-s\tau}d\tau$$

Having used the method of determinated moments for the equation (8), we acquire the next relationships for defining the thermophysical parameters of the liquid in dimensionless form, i.e. Pe , Fo and Nu

$$Pe=\frac{f_0}{f_1}\left(\frac{\varphi_0}{f_0}-\frac{\varphi_0}{f_1}\right)^{-1},\ Nu=\frac{R}{2l}\left[I_0-Pe\left(\frac{\varphi_0}{f_0}-1\right)\right]$$

$$Fo=Pe\cdot\frac{\varphi_2}{f_0}\left(\frac{\varphi_0}{f_0}-\frac{\varphi_2}{f_2}\right)-\frac{f_1}{f_0} \qquad (9)$$

During calculations, the moments of degree k for functions $f(t)$ and $g(t)$ are found by formulae

$$f_k=\int_0^{\infty}\left[f(t)-f(\infty)\right]\cdot\frac{t^k}{k!}dt,$$

$$\varphi_k=\int_0^{\infty}\left[\varphi(t)-\varphi(\infty)\right]\cdot\frac{t^k}{k!}dt \qquad ;$$

in the last relationships ones should use values of given functions $f(\tau)$ and $\varphi(\tau)$ at steady regime $t\to\infty$.

From the second formula in the relationships (9) we may conclude, increasing the laser power leads to increasing the Nusselt number, in other words, under the laser radiation action there is an intensification of the heat exchange with surrounding medium. Effect of the radiation intensity on values of Pe and Fo is expressed through f_k and φ_k.

By the same scheme ones can evaluate influence of the laser radiation on thermodynamic properties of liquids involved. In all existing investigations concerning interaction between laser beam and liquids, the lasts are taken as non - viscous, and influence of their viscosity and thermal conductivity on propagation and absorption of acoustic waves generated by laser action are neglected. Moreover, interaction of laser beam on heavy - viscous liquids, for example, oils and oil - products, drilling muds and cement slurries used for drilling wells are not studied in general.

For mathematical description we should take dimensionless function $f(t)$ in (2) in Gaussian form [4]

$$f(t)=(\pi)^{1/2}\cdot\exp\left[-\left(\frac{t}{t_0}\right)^2\right]$$

Restricting ourselves by parts of linear perturbations in motion equation, for determining an acoustic pressure ones have the following equation as it was made by Gusev V.E.and Karabutov A.A. in [4]

$$\frac{\partial^2 P}{\partial t^2} - c^2 \frac{\partial^2 P}{\partial x^2} - \left[\frac{1}{\rho_0}\left(\xi + \frac{4}{3}\eta\right) + \chi\left(\frac{C_p}{C_v} - 1 \right) \right] \frac{\partial^3 P}{\partial x^2 \partial t} = \frac{\alpha c^2 \beta I_0}{2C_p} f(t) e^{-\alpha x}, \qquad (10)$$

herein all the quantities are well - known. We consider linear variant of the problem, when all the liquid physical parameters insufficiently change under laser radiation action, and they may be proposed as permanent. The differential equation (10) should be resolved at zero initial conditions

$$P(x, t=0) = 0, \quad \frac{\partial P(x, t=0)}{\partial t} = 0 \qquad (11)$$

and boundary ones, that are given in accordance with involved phenomenon nature. Then, from additionally selected boundary condition effect of laser beam on liquid studied parameters is found by resolving the inverse problem.

For resolving the differential equation (10) under initial conditions (11) Laplace - transformation and the method of determinated moments are used again. After non - complex calculations ones have the following system of equations for determining required thermodynamic quantities

$$\left.\begin{aligned} \alpha &= \frac{2}{l}\left(1 + \frac{2C_p}{\beta I_0 l}\frac{\varphi_0}{f_0}\right), \\ \xi + \frac{4}{3}\eta + \rho_0 \chi\left(\frac{C_p}{C_v} - 1\right) &= -\rho_0 c^2 \frac{\varphi_1}{\varphi_0} + \\ + \frac{c^2 \beta I_0 \rho_0 l(\alpha l - 2)}{4C_p}\frac{f_1}{\varphi_0} &+ \frac{c I_0 \beta \rho_0 l}{2\alpha C_p}\frac{f_0}{\varphi_0} \end{aligned}\right\} \qquad (12)$$

Formulae (12) allow us to qualitatively estimate influence of laser radiation on liquid thermodynamic parameters. For this purpose it is necessary to represent informative part of the function $\varphi(\tau)$ in form

$$\varphi(\tau) = \varphi(\infty)\cdot\left(1 - e^{-k\tau}\right),$$

taken from obtained experimental data and to find all the ratios of type f_k / φ_k. On the base of available integrals values found by Gautschi W. [3] ones may write down

$$\left.\begin{aligned} \alpha &= \frac{2}{l}\left(1 + \frac{4\sqrt{2}C_p \varphi(\infty)}{\sqrt{\pi}\beta I_0 l k t_0}\right), \\ \xi + \frac{4}{3}\eta + \rho_0 \chi\left(\frac{C_p}{C_v} - 1\right) &= \rho_0 c^2 t_0 \times \\ \times\left[\frac{1}{2\sqrt{\pi}} - \frac{1}{k t_0} + \frac{\sqrt{\pi} I_0 \beta l k}{4\alpha C_p c \varphi(\infty)}\right] & \end{aligned}\right\} \qquad (13)$$

From the first formula in (13) it should be concluded, that absorption coefficient α depends on both liquid thermodynamic parameters, and the laser radiation characteristics. The second equation in (13) results in

$$\xi = \rho c^2 t_0 \left[\frac{1}{2\sqrt{\pi}} - \frac{1}{k t_0} + \frac{\sqrt{\pi} I_0 \beta l k}{4\alpha C_p c \varphi(\infty)}\right] - \frac{4}{3}\eta - \rho\chi\left(\frac{C_p}{C_v} - 1\right) \qquad (14)$$

Since volume viscosity ξ is exposed during expansion and compression of liquid only, i.e. when non - equilibrium processes take place in the liquid, so in the studied case (I_0 = const) laser radiation duration t_0 necessary for generating sufficiently non - equilibrium process should be defined as

$$t_0 \succ \left[\frac{\rho c^2}{k} + \frac{4}{3}\eta + \rho\chi\left(\frac{C_p}{C_v} - 1\right)\right] \times \left(\frac{\rho c^2}{2\sqrt{\pi}} + \frac{\rho c_0 \sqrt{\pi} I_0 \beta l k}{4\alpha C_p \varphi(\infty)}\right)^{-1}. \qquad (15)$$

From expression (14) it is also concluded, if the laser radiation intensity satisfies the condition

$$I_0 \le \left[\frac{4}{3}\eta + \rho\chi\left(\frac{C_p}{C_v} - 1\right) + \frac{\rho c^2}{\kappa} - \frac{\rho c^2 t_0}{2\sqrt{\pi}} \right] \times \times \frac{4\alpha C_p \varphi(\infty)}{\rho c_0 t_0 \sqrt{\pi}\, k\beta l} \quad , \qquad (16)$$

then arising non - stationary processes in liquid are not enough for volume viscosity.

As it was marked above, radiation absorption obeys Bouger's law, i.e. generated by laser radiation acoustic pressure amplitude is defined by

$$P = P_0 \cdot \exp\left[-\frac{2x}{l}\left(1 + \frac{4\sqrt{2}C_p\varphi(\infty)}{\sqrt{\pi}\beta I_0 l k t_0}\right)\right] \qquad (17)$$

Volume expansion coefficient β might be found from the last formula

$$\beta = \frac{4\sqrt{2}C_p\varphi(\infty)}{\sqrt{\pi}kt_0 I_0 l\left(\frac{1}{2}\ell n\frac{P_0}{P_1} - 1\right)} \qquad (18)$$

At last it should be noted, formula (18) is valid under condition $\alpha l > 2$ only, that is always satisfied for above case due to the first expression in (13). The formula (18) allows to qualitatively estimate influence of laser radiation parameters on volume expansion coefficient.

Conclusion

Convection variant of the problem (4) described in the paper corresponds to laminar regime of flow, when the last is characterized by small value of the Reynolds number. If the laser generator power value is less than certain critical magnitude evaluated by Galich N.E. [1] , then the convection is absent, and the problem should be solved without taking into account the summand proportional to the Peclet number.

Optoacoustic waves which arise in propagating the laser radiation within liquid can be applied for practical needs. Using these signals, we have developed the new method of determination of water - content in oil. Furthemore, technique of multiphase liquid separation on components by the laser radiation is recently found.

References

[1] Galich N.E. , 1980 , " Turbulence generated by laser radiation in liquid " , *Jour. of Tech. Phys.* , **50** , **№ 6** , pp. 1196 - 1199

[2] Gasanov G.T., Musayev M.A., 1994, " About optical method of determiation of liquids acoustic properties ", *Neft i gaz*, **2** , pp. 35 - 38

[3] Gautschi W., 1979 " Error function and Fresnel integrals ", in // Handbook on mathematical functions // , ed. by M. Abramowitz and I. Stegun , *Moskva , Nauka* , pp. 119 - 153

[4] Gusev V.E., Karabutov A.A., 1991, " Lazernaya optoakustika " , *Moskva , Nauka* , p. 63

[5] Hassanov H.G., Sadigova A.A. , 2000 , " New method of determining acoustic waves propagation velocity and coefficient of their absorption in liquids ", *Problemi energetiki* , **1** , pp. 92 - 94

[6] Viznyuk S.A. et al , 1990, " Using the coherent spectroscopy for measurement of heat conductivity of liquid ", *Jour. of Tech. Phys.* , **60** , **№ 7** , pp. 157 - 164

[7] Yarovaya R.T. et al , 1988, " Influence of laser radiation on gase bubbles motion in absorbing liquid ", *Jour. of Tech. Phys.* , **58** , **№ 7** , pp. 1375 - 1380

[8] Zuyev V.I. , 1986, " Experimental investigation of non - stability of convection caused by laser radiation ", *Jour. of Tech. Phys.* , **56** , **№ 2** , pp. 394 - 396

HEFAT2002
1st International Conference on Heat Transfer, Fluid Mechanics, and Thermodynamics
8-10 April 2002, Kruger Park, South Africa
SD2

EXPERIMENTAL AND ANALYTICAL INVESTIGATIONS OF SEMITRANSPARENT CYLINDRICAL RADIATION SHIELDS

D.A. Scott, S. Guers, M. Slanik, and B.R. Baliga
Department of Mechanical Engineering
McGill University
817 Sherbrooke Street West
Montreal, Quebec H3A 2K6, Canada

ABSTRACT

Experimental and analytical investigations of heat transfer between two concentric cylindrical tubes made of black anodized aluminum, with and without a concentric semitransparent cylindrical radiation shield in the annular space, are presented in this paper. The radiation shields were tubes made of Plexiglas (polymethylmethacrylate or acrylic), fused quartz, and Lexan (polycarbonate resin). The mathematical model of the radiation heat transfer was based on a diffuse-gray enclosure theory. In addition, it was assumed that the shields are opaque to thermal radiation emitted by surfaces with temperatures in the range 9 °C to 80 °C. In the experiments, the air inside the apparatus was evacuated to absolute pressures in the range 6 mbar to 10 mbar. At these values of air pressure, the natural convection heat transfer in the annular spaces between the inner and outer tubes is negligible. However, the conduction resistance through the residual air is significant, and it was accounted for in the proposed mathematical model. The calculated results deviate from the corresponding experimental data by less than ±11.8 %.

INTRODUCTION

Materials that are highly transparent to electromagnetic radiation with wavelengths in the range 0.1 μm < λ < 3.0 μm, and almost opaque for wavelengths longer than 3.0 μm, are commonly used in energy conversion, building, solar, thermal, and agricultural engineering, and also in heat transfer experiments. Examples and details of windows and radiation shields made of such materials can be found in the works of Sparrow and Cess (1970), Siegel and Howell (1972), Fuschillo (1975), Viskanta et al. (1978), Modest (1993), and Holman (1997). Additional references are available in Guers et al. (2001). Experimental and analytical investigations of heat transfer through semitransparent cylindrical radiation shields made of such materials are presented in this paper.

Specifically, this work deals with heat transfer between two concentric cylindrical tubes made of black anodized aluminum, with and without a concentric semitransparent cylindrical radiation shield positioned in the annular space. The inner tube was maintained at uniform temperatures in the range 30 °C to 80 °C. The outer tube was maintained at a uniform temperature of about 9.5 °C. The radiation shields were tubes made of Plexiglas (polymethylmethacrylate or acrylic), fused quartz, and Lexan (polycarbonate resin). The analytical model of the radiation heat transfer was based on a diffuse-gray enclosure theory. In addition, it was assumed that the semitransparent shields are opaque to thermal radiation emitted by surfaces with temperatures in the range 9 °C to 80 °C. In the experiments, the air inside the apparatus was evacuated to absolute pressures between 6 mbar to 10 mbar. At these values of air pressure, the natural convection heat transfer in the annular spaces between the inner and outer tubes is negligible. However, the conduction resistance through the residual air is significant, and it was accounted for in the proposed mathematical model.

Details of the experimental work are given in Guers et al. (2001). Nevertheless, a concise description of this aspect of the work is also included in this paper, for the sake of completeness. A mathematical model of the radiation heat transfer was also proposed by Guers at al. (2001), and their model is similar to that used in this paper. However, Guers et al. (2001) ignored conduction through the residual air, and concluded that errors in the predictions obtained with the diffuse-gray/opaque shield theory could be as high as ±38%. In this work, it is shown that with proper accounting of the heat conduction through the residual air, the diffuse-gray/opaque shield model yields results that are more accurate. The calculated results deviate from the corresponding experimental data by less than ±11.8%.

NOMENCLATURE

A_i	Area of surface i [m^2]
C	Thermal conductance [W/°C]
D_{inside}	Inside diameter of shield [m]
$D_{outside}$	Outside diameter of shield [m]
$e_{b,i}$	Blackbody emissive power of surface i [W/m^2]
F_{j-k}	Radiation shape factor from surface j to surface k

G	Irradiation or incident radiation flux [W/m^2]
I	Current input to heater [A]
J_j	Radiosity of surface j [W/m^2]
k_{air}	Thermal conductivity of air [W/m-°C]
k_{sh}	Thermal conductivity of shield material [W/m-°C]
k_{eff}	An effective thermal conductivity [W/m-°C]
L_{sh}	Effective length of the apparatus and shields [m]
$P_{in,calc}$	Calculated input power to the heater [W]
$P_{in,expt}$	Input power to the heater in the experiments [W]
q	Heat transfer rate [W]
q_{cond}	Conduction heat transfer rate [W]
q_{rad}	Radiation heat transfer rate [W]
r_i	Radius of surface i [m]
R_{cond}	Thermal conduction resistance [°C/W]
$R_{cond,\ adj}$	Adjusted conduction resistance, see Eq. (9), [m^{-2}]
R_{eff}	Effective resistances, see Eq. (10), [m^{-2}]
R_{eq}	Equivalent resistances, see Eq. (10), [m^{-2}]
$R_{sp,\ j\text{-}k}$	Space radiative resistance between surfaces j and k [m^{-2}]
$R_{surf,i}$	Surface radiative resistance of surface i [m^{-2}]
S	Heat conduction shape factor [m]
T_i	Temperature of surface i [°C]
$T_{abs,\ i}$	Absolute temperature of surface i [K]
V	Voltage input to heater [V]
ε_j	Total hemispherical emissivity of surface j
λ	Wavelength of radiation [μm]

SYNOPSIS OF THE EXPERIMENTAL SET-UP

The experimental set-up is shown schematically in Fig. 1. The outer diameter of the inner tube was 0.0381 m, and its effective length was 0.2743 m. The inner diameter of the outer tube was 0.1397 m, and it too had an effective length of 0.2743 m. These tubes were made of aluminum, and their surfaces were anodized (black).

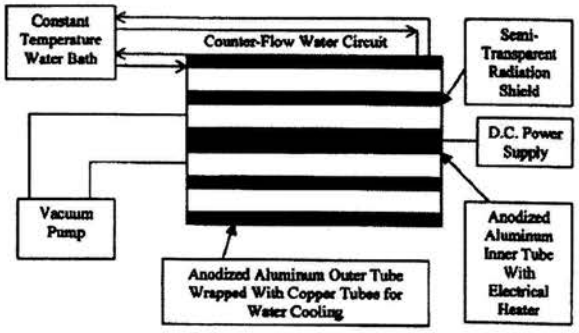

Figure 1: Schematic illustration of the experimental set-up.

The outer tube was tightly wrapped on its outer surface with a coil made of two (side-by-side) ¼-inch copper tubes. A paste of high thermal conductivity was used to minimize thermal contact resistance between the surfaces of the copper tubes and the outer surface of the outer tube. Water from a constant-temperature bath was circulated through the two copper tubes, in a counter-flow path, to maintain the outer tube at a desired uniform temperature (about 9.5 °C in this work). The inner tube was fitted with an electrical cartridge heater. This heater was supplied with dc power, which was adjusted to achieve steady, essentially uniform, inner tube temperatures in the range 30 °C to 80 °C. The voltage and current inputs to the heater were measured using high-accuracy digital multimeters.

Removable endplates made of Delrin (0.0191 m thick) and covered with aluminum foil were used to seal the openings between the concentric inner and outer tubes. During the experiments, the air in the annular space between the inner and outer tubes was evacuated and maintained at absolute pressures that were in the range 6 mbar to 10 mbar. Under these conditions, the density of the residual air is rather low, and hence the Rayleigh number for the annular gap is also low, so the natural convection in the annular space is negligible. However, conduction heat transfer through the residual air must be, and was, accounted for in the corresponding mathematical model. The thermal conductivity of the residual air at these absolute pressures was assumed to be essentially the same as that at one atmosphere absolute pressure.

Temperatures were measured at 12 locations both on the outer and the inner tubes, using 30-guage chromel-constant (Type E) thermocouples and an electronic digital readout. Using a calibrated quartz thermometer as a secondary reference, it was determined that this set-up yields temperature measurements that are accurate to within ± 0.1 °C.

The complete apparatus, consisting of the assembly of inner and outer tubes, semitransparent cylindrical radiation shield, and the Delrin endplates, was wrapped with about two layers of cotton and hydrogel (baby diapers) to insulate it and prevent moisture buildup on hot humid days. The entire apparatus was then enclosed in a large plastic box, filled with silica gel and paper insulation.

Three different Plexiglas tubes, three different fused quartz tubes, and one Lexan tube were used as the semitransparent radiation shields. These seven semitransparent radiation shields are denoted here as Shields # 1-7. Their inner and outer diameters are given in Table 1. A photograph of the test section loaded with the three fused quartz shields, and with the Plexiglas and the Lexan shields outside, is provided in Fig. 2.

Table 1: Details of the radiation shields used in this study

Material	Shield #	D_{inside}	$D_{outside}$
Plexiglas	1	0.04400 m	0.05057 m
	2	0.08800 m	0.09510 m
	3	0.10740 m	0.11360 m
Fused Quartz	4	0.04610 m	0.05052 m
	5	0.08030 m	0.08550 m
	6	0.11000 m	0.11480 m
Lexan	7	0.08935 m	0.09450 m

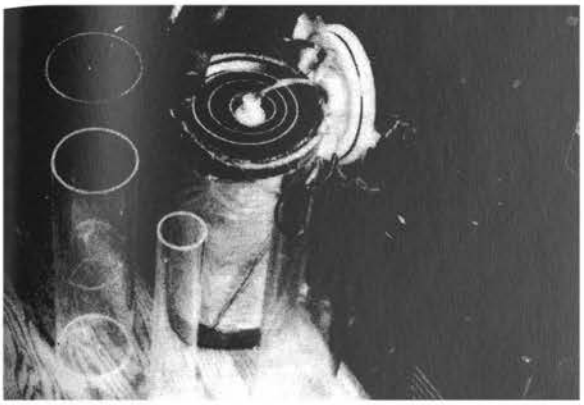

Figure 2: Photograph of the test section, shown here with one of the Delrin endplates pulled open.

ANALYTICAL CONSIDERATIONS

Heat Transfer in the Empty Test Section and Procedure for Estimating Heat Conduction Losses

Consider the schematic of the empty test section (the test section without any radiation shield) given in Fig. 3.

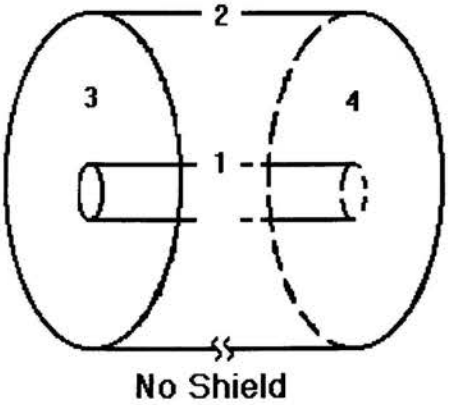

Figure 3: Schematic of the empty test section.

The outer surface of the inner tube is denoted as 1, the inner surface of the outer tube is denoted as 2, and 3 and 4 indicate the inner surfaces of the Delrin endplates. Each of these four surfaces is assumed to be isothermal and diffuse gray. The irradiation, G, and radiosity, J, for each of these surfaces are assumed to be uniform. Surfaces 3 and 4 are considered to be re-radiating surfaces and identical. With these assumptions, a diffuse-gray enclosure theory, as described by Holman (1997), for example, can be used to generate the equivalent resistance network given in Fig. 4.

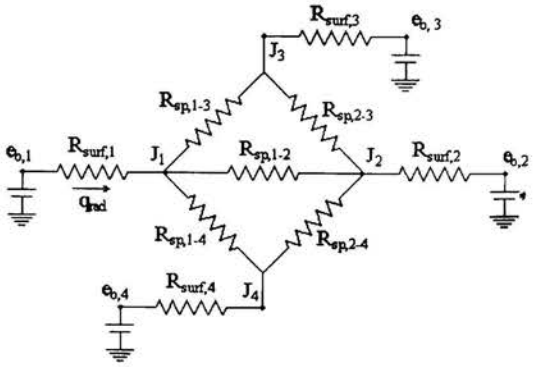

Figure 4: Equivalent resistance network representation of radiation heat transfer in the empty test section.

As surfaces 3 and 4 are re-radiating and identical, there is no *net* heat transfer to, from, or between them: $e_{b,3} = J_3 = e_{b,4} = J_4$. For any *diffuse-gray opaque* surface, j, the surface radiation resistance is:

$$R_{surf,j} = (1-\varepsilon_j)/(A_j\varepsilon_j) \tag{1}$$

where ε_j is the total hemispherical emissivity of the surface j, and A_j is its area. The space radiation resistance between any two *diffuse-gray opaque* surfaces, j and k, without any intermediate participating medium between them, is:

$$R_{sp,j-k} = 1/(A_j F_{j-k}) \tag{2}$$

where F_{j-k} is the corresponding shape factor. The total blackbody emissive power of any surface j is given by $e_{b,j} = \sigma(T_{abs,j})^4$. Using the equivalent resistance network, and with T_1 and T_2 as inputs, the net rate of radiation heat transfer from surface 1 to surface 4 can be calculated as follows:

$$\begin{aligned} R_{eqv,sp,1-2} &= \{1/R_{sp,1-2} + 2/(R_{sp,1-3} + R_{sp,2-3})\}^{-1} \\ q_{rad} &= (e_{b,1} - e_{b,2})/(R_{surf,1} + R_{eqv,sp,1-2} + R_{surf,2}) \end{aligned} \tag{3}$$

All required shape factors, F_{j-k}, were computed using well-established practices (Sparrow and Cess, 1970).

Under steady-state conditions, the power input to the heater embedded inside the inner tube is equal to the rate of heat loss from the inner tube to the outer tube by radiation and conduction:

$$P = q_{rad} + q_{cond,end\ plates,insl} + q_{cond,air} \tag{4}$$

The term, $q_{cond,\ end\ plates,\ insl}$, may be expressed in terms of the temperature difference ($T_1 - T_2$), a heat conduction shape factor, S, and an effective thermal conductivity, k_{eff}, that characterize the Delrin endplates *and* the insulation packed around the apparatus. Thus,

$$q_{cond,end\ plates,insl} = Sk_{eff}(T_1 - T_2) = C(T_1 - T_2) \tag{5}$$

where C is an effective heat conductance, given by

$$C = Sk_{eff} \tag{6}$$

The rate of heat conduction through the residual air in the annular space between the inner and outer tubes is given by:

$$q_{cond,air} = (T_1 - T_2)/\{\ln(r_2/r_1)/(2\pi k_{air} L)\} \quad (7)$$

In the experiments, the voltage and current inputs to the heater, V and I, respectively, and T_1 and T_2 were measured. These measurements were used to calculate the power input to the heater ($P = VI$), q_{rad}, and $q_{cond,\ air}$. In these calculations, it was assumed that the values of k_{air} at pressures around 1 mbar and one atmosphere are essentially the same. Then, using these calculated values, the effective heat conductance, C, for the apparatus was determined as follows:

$$C = (P - q_{rad} - q_{cond,air})/(T_1 - T_2) \quad (8)$$

For the empty test section, the following average value of C was determined: C = 0.0152 W/°C. This value was assumed to also apply in experiments with the radiation shields.

Heat Transfer in the Test Section Loaded With a Radiation Shield

A schematic representation of the test section loaded with a semitransparent radiation shield is given in Fig. 5.

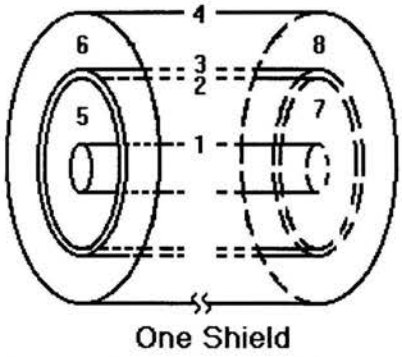

Figure 5: Schematic of the test section loaded with one shield.

Now, the outer surface of the inner tube is denoted as 1, the inner surface of the outer tube is denoted as 4, 2 and 3 indicate the inner and outer surfaces of the semitransparent shield, respectively, and 5, 6, 7, and 8 denote portions of the inner surfaces of the Delrin endplates. Each one of these surfaces was assumed to be isothermal, gray, and a diffuse emitter and reflector. In addition, the irradiation, G, and radiosity, J, for each one of these surfaces were assumed to be uniform. These assumptions were used as a starting point in the formulation of the mathematical model of radiation heat transfer in the test section loaded with one radiation shield.

In the mathematical model of the radiation heat transfer, it was assumed that the semitransparent shields used in this work are essentially opaque to thermal radiation emitted by gray surfaces with temperatures in the range 9 °C to 80 °C. Thus, the radiation heat transfer from the inner to the outer tubes goes through two finite-length annular spaces, as can be inferred from an examination of Fig. 5, each bounded by diffuse-gray opaque surfaces. The rate of heat transfer across each of the annular spaces is due to radiation exchange between diffuse-gray surfaces and conduction through the residual air, as described in the previous subsection. The heat transmission from one such annular space to the next one involves heat conduction through the wall of the intervening radiation shield. One-dimensional radial heat conduction was assumed through the wall of the radiation shield.

To facilitate an iterative solution of the governing equations, the integrated resistance network representation schematically shown in Fig. 6 was used.

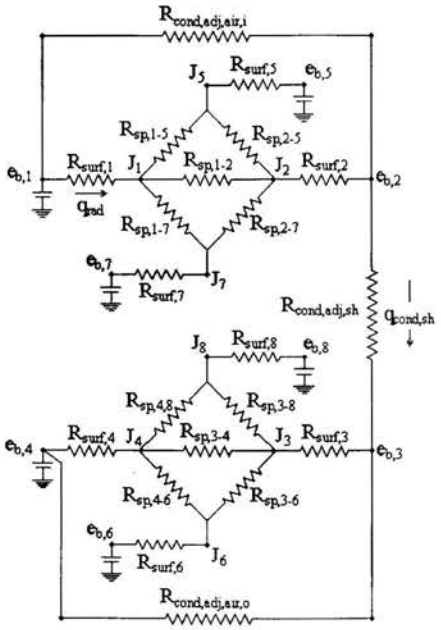

Figure 6: Integrated resistance network representation.

In this integrated resistance network, $R_{cond,adj,sh}$, $R_{cond,\ air,\ i}$, and $R_{cond,\ air,\ o}$ are adjusted conduction resistances of the shield, and air in the inner and outer annular spaces, respectively. They are defined as follows:

$$R_{cond,adj,sh} = \frac{(e_{b,2} - e_{b,3})}{(T_2 - T_3)/[\ln(r_3/r_2)/(2\pi k_{sh} L)]}$$

$$R_{cond,adj,air,i} = \frac{(e_{b,1} - e_{b,2})}{(T_1 - T_2)/[\ln(r_2/r_1)/(2\pi k_{air,i} L)]} \quad (9)$$

$$R_{cond,adj,air,o} = \frac{(e_{b,3} - e_{b,4})}{(T_3 - T_4)/[\ln(r_4/r_3)/(2\pi k_{air,o} L)]}$$

Here, surfaces 5 and 7 are assumed to be re-radiating and identical, as are surfaces 6 and 8. Thus, $e_{b,5} = J_5 = e_{b,7} = J_7$ and

$e_{b,6} = J_6 = e_{b,8} = J_8$. The blackbody emissive power of a surface j is $e_{b,j} = \sigma(T_{abs,j})^4$. The integrated resistance network given in Fig. 6 yields the following equations for $q_{rad} + q_{cond,\ air}$, transmitted through each of the two annular spaces in the test section loaded with one shield:

$$R_{eqv,sp,1-2} = [1/R_{sp,1-2} + 2/(R_{sp,1-5} + R_{sp,2-5})]^{-1}$$

$$R_{eqv,1-2} = R_{surf,1} + R_{eqv,sp,1-2} + R_{surf,2}$$

$$R_{eff,1-2} = [1/(R_{cond,adj,air,i}) + 1/(R_{eqv,1-2})]^{-1}$$

$$R_{eqv,sp,3-4} = [1/R_{sp,3-4} + 2/(R_{sp,3-6} + R_{sp,4-6})]^{-1} \quad (10)$$

$$R_{eqv,3-4} = R_{surf,3} + R_{eqv,sp,3-4} + R_{surf,4}$$

$$R_{eff,3-4} = [1/(R_{cond,adj,air,o}) + 1/(R_{eqv,3-4})]^{-1}$$

$$q_{rad} + q_{cond,air} = \frac{(e_{b,1} - e_{b,4})}{(R_{eff,1-2} + R_{cond,adj,sh} + R_{eff,3-4})}$$

Under steady-state conditions, $q_{cond,sh} = q_{rad} + q_{cond,air}$. The surface and space radiation resistances were calculated using Eqs. (1) and (2). Then, with experimentally measured values of T_1 and T_4 as inputs, Eqs. (9) and (10) were solved iteratively to obtain the corresponding value of $q_{rad} + q_{cond,air}$. This iterative procedure can be summarized as follows: 1) assign reasonable guess values for T_2 and T_3; 2) using Eq. (9), calculate $R_{cond,adj,sh}$, $R_{cond,\ adj,\ air,\ i}$, and $R_{cond,\ adj,\ air,\ o}$; 3) calculate $q_{rad} + q_{cond,\ air}$ using Eq. (10); 4) calculate T_2 and T_3; and 5) repeat steps 2) to 4) until convergence. In this work, the iterative solution procedure was assumed to have converged when the relative changes in the absolute values of T_2 and T_3, in successive iterations, were both less than 10^{-10}.

In principle, the radiation shield could be assumed to be semitransparent, for all wavelengths of radiation, and a numerical solution of the full radiative transfer equation (RTE) could be used to calculate the net radiation heat transfer from the inner tube to the outer tube [Siegel and Howell, 1972; Modest, 1997]. However, if scattering and emission of radiation within the shield material are considered negligible, then such calculations could be done using a relatively simple technique based on the net radiation method [Siegel and Howell, 1972; Siegel, 1973; Viskanta et al., 1978]. Using such an approach, in conjunction with a ray tracing procedure, an overall transmittance and an overall reflectivity of the shield to incident radiation from the inner tube could be worked out, and similar overall properties could also be worked out for radiation incident on the shield from the outer tube. As the radiation shields used in this work are cylindrical, the conditions of incidence on the shield for the radiation from the inner and outer tubes are different; thus, the corresponding values of overall transmittance and overall reflectivity would also be different. Appropriate values of these transmittances could be calculated from more basic radiation properties of the shield material and the surrounding media [Siegel and Howell, 1972; Siegel, 1973]. The development and implementation of such a detailed and sophisticated semitransparent model were not undertaken in this work; rather, they are suggested as possible extensions of this work. Here, the focus is on exploring the possibilities offered by the proposed model, in which a relatively simple diffuse-gray/opaque shield theory of the radiation heat transfer is used in conjunction with a model of one-dimensional radial conduction heat transfer through the residual air (at pressures between 6 mbar to 10 mbar) inside the experimental apparatus.

With the proposed mathematical model, and with the values of T_1 and T_4 (obtained from the experimental measurements) used as inputs, the power input to the electric heater inserted in the inner tube were calculated using the follows equations:

$$q_{cond,end\ plates,insl} = C(T_1 - T_4)$$

$$P_{in,calc} = q_{cond,end\ plates,insl} + q_{rad} + q_{cond,air} \quad (11)$$

Anodized Aluminum and Shield Material Property Data

The discussions and recommendations in Guers et al. (2001) pertaining to the emissivity of the anodized aluminum surfaces, and the emissivity and thermal conductivity of the shield materials, were followed here. Thus, for the anodized (black) aluminum surfaces with temperatures in the range 300 K to 400 K, the emissivity was obtained using the following equation:

$$\varepsilon_{al} = 0.82 - \{(0.82 - 0.76)/100\}(T_{abs} - 300) \quad (12)$$

For the shield materials, the emissivity and thermal conductivity data in Table 2 were used.

Table 2: Emissivity and thermal conductivity data for the shield materials.

Shield Material	ε_{sh}	k_{sh} [W/m-°C]
Plexiglas	0.88	0.18
Fused Quartz	0.90	1.40
Lexan	0.88	0.19

RESULTS, DISCUSSIONS, AND CONCLUSIONS

Data on V, I, T_1, and T_4 for 18 different experimental runs are presented in Table 3. For each run, these measurements were used to deduce the experimental value of the power input to the heater inserted in the inner tube as follows:

$$P_{in,expt} = VI \quad (13)$$

The proposed mathematical models of the radiation heat transfer, conduction heat transfer through the residual air and the radiation shield, and the conduction heat transfer through the Delrin endplates and the surrounding insulation were then used to *calculate* the corresponding values of the power input to the electric heater inserted in the inner tube ($P_{in,calc}$). Following that, the percentage deviations of the calculated values of the power input, $P_{in,calc}$, from the corresponding experimental values, $P_{in,\ expt}$, were determined using the following equation:

$$\%Dev = 100(P_{in,expt} - P_{in,calc}) / P_{in,expt} \qquad (14)$$

Table 3: Measured data and $P_{in,expt}$ values.

Run	Shield #	V [V]	I [A]	T_1 [°C]	T_4 [°C]	$P_{in,\,expt}$ [W]
A	1	34.18	0.2183	48.96	9.73	7.46
B	1	38.11	0.2432	57.45	9.72	9.27
C	1	42.10	0.2683	67.52	9.70	11.30
D	2	34.09	0.2147	51.33	9.59	7.32
E	2	42.02	0.2669	70.38	9.57	11.22
F	3	33.95	0.2177	48.67	9.64	7.39
G	3	38.06	0.2438	57.33	9.60	9.28
H	3	42.06	0.2692	66.25	9.66	11.32
I	4	34.00	0.2169	51.01	9.63	7.37
J	4	42.09	0.2676	71.98	9.59	11.26
K	4	38.11	0.2428	60.42	9.66	9.25
L	5	34.08	0.2186	55.48	9.68	7.45
M	5	42.06	0.2693	75.14	9.66	11.33
N	6	33.91	0.2174	50.64	9.63	7.37
O	6	38.03	0.2435	59.77	9.68	9.26
P	6	41.90	0.2681	68.76	9.63	11.23
Q	7	34.03	0.2183	53.48	9.69	7.43
R	7	42.03	0.2691	72.19	9.69	11.31

Table 4: Comparison of $P_{in,\,expt}$ and $P_{in,\,calc}$

Run	Shield #	$P_{in,\,expt}$ [W]	$P_{in,\,calc}$ [W]	%Dev
A	1	7.46	6.63	11.11
B	1	9.27	8.24	11.08
C	1	11.30	10.29	8.91
D	2	7.32	6.71	8.36
E	2	11.22	10.40	7.27
F	3	7.39	6.52	11.76
G	3	9.28	8.22	11.43
H	3	11.32	10.04	11.33
I	4	7.37	7.13	3.31
J	4	11.26	11.48	-1.90
K	4	9.25	8.99	2.88
L	5	7.45	7.60	-1.97
M	5	11.33	11.61	-2.48
N	6	7.37	7.11	3.61
O	6	9.26	8.96	3.20
P	6	11.23	10.91	2.90
Q	7	7.43	7.13	4.04
R	7	11.31	10.83	4.28

The results presented in Table 4 show that the proposed model, based on a simple diffuse-gray/opaque-shield theory of radiation heat transfer and a model of one-dimensional radial heat conduction through the residual air in the experimental apparatus, provides results that deviate from the experimental results by less than ±11.8 % in all cases considered here. In this context, it is worth noting that the calculated results of Guers et al. (2001), obtained using a similar diffuse-gray/opaque shield model, but ignoring conduction heat transfer through the residual air, deviated from the corresponding experimental data by as much as ±38%. Thus, the results presented in this paper clearly show that it is important to account for conduction heat transfer through the residual air, which, in all experimental runs, was at absolute pressures in the range 6 mbar to 10 mbar.

The results presented in Table 4 also show that the proposed diffuse-gray/*opaque-shield* model yields the most accurate results for the shields made of fused quartz. Thus, it may be concluded that of the three semitransparent materials examined in this study (ε_{sh} values almost equal), fused quartz provides the most effective shielding (it is essentially opaque) with respect to thermal radiation emitted by gray surfaces maintained at temperatures in the range 9 °C to 80 °C. The same conclusion can also be made purely on the basis of the experimental data given in Table 3.

ACKNOWLEDGMENTS

The authors gratefully acknowledge financial support of this work by the Natural Sciences and Engineering Research Council (NSERC) of Canada.

REFERENCES

Guers, S., Slanik, M., Scott, D.A., and Baliga, B.R. (2001), "A Study of Semitransparent Cylindrical Radiation Shields", Paper # IECEC2001-RE-22, *Proc. 36th Intersociety Energy Conversion Eng. Conf.*, Savannah, Georgia, July 29 – Aug. 2.

Fuschillo, N. (1975), "Semi-Transparent Solar Collector Window Systems", *Solar Energy*, Vol. 17, pp. 159-165.

Holman, J.P. (1997), *Heat Transfer*, 8th Ed., McGraw-Hill, New York.

Modest, M.F. (1993), *Radiative Heat Transfer*, McGraw-Hill, New York.

Siegel, R. and Howell, J.R. (1972), *Thermal Radiation Heat Transfer*, McGraw-Hill, New York.

Siegel, R. (1973), "Net radiation method for transmission through partially transparent plates", *Solar Energy*, Vol. 15, pp. 273-276.

Sparrow, E.M. and Cess R.D. (1970), *Radiation Heat Transfer*, Revised Ed., Brooks/Cole Publishing Co., Belmont, California.

Viskanta, R., Siebers, D.L., and Taylor, R.P. (1978), "Radiation Characteristics of Multiple-Plate Glass Systems", *Int. J. Heat Mass Transfer*, Vol. 21, pp. 815-818.

HEFAT2002
1st International Conference on Heat Transfer, Fluid Mechanics, and Thermodynamics
8-10 April 2002, Kruger Park, South Africa
PS1

EXPERIMENTAL STUDY AND COMPUTER SIMULATION OF HEAT TANSFER FOR HIGH FLUX COOLING APPLICATIONS WITH MICROCHANNELS IN MICRO-ELECTRO-MECHANICAL SYSTEM (MEMS)

Shuzhi Peng and Tilak T Chandratilleke
Department of Mechanical Engineering,
Curtin University of Technology,
GPO Box, Perth, U1987, Western Australia 6845,
Australia,
E-mail: pengsh@vesta.curtin.edu.au

ABSTRACT

The paper aims to apply experiment and computer simulation to investigate the heat transfer characteristics of different fluids through the microchannels with different geometries. An experimental apparatus with multi-functions, low uncertainties, high precision and temperature control was constructed. The experimental results are compared with the results of computer simulations and theoretical predictions from the conventional laminar flow theory. The flow rate, fluid temperature and pressure drop were measured at steady states to analyse the flow characteristics. It was concluded that the effect of allowance for machining of microchannels on heat transfer characteristics could be neglected under lower flow rate. The fluid mass flow rate, the inlet temperature of fluid, and the geometric parameters, particularly the hydraulic diameter and aspect ratio H/W_m in rectangular microchannels were found to have a significant influence on the fluid flow and heat transfer characteristics.

INTRODUCTION

Significant attention has been given to fluid flow in microchannels due to the development in micro-fluidic devices and systems. In 1981, Tuckerman and Peace [1] originally introduced the concept of the microchannel heat sinks. They demonstrated that the water-cooled microchannel heat sink is capable of dissipating high heat flux without a phase change. Wu and Litter [2] measured the fiction factor about the gas flow and heat transfer in a single microchannel. Their measurements indicated that the friction factors were above those obtained from the traditional Moody diagram. Peng and Wang [3-5] investigated the heat transfer characteristics of liquid flowing through microchannel structures. The forced convection of liquid in microchannels both with and without phase change was studied experimentally. They found that fully developed turbulent convection was initiated at Re from 1000 to 1500, and heat transfer behaviour in the laminar and transition regions was very unusual and complex and are affected by liquid temperature, velocity and microchannels. Tao and Mahulikar [6] investigated the effect of Brinkman number on heat transfer characteristics in microchannels. The experiment was carried out using a water tap to supply constant flow. Without the Data Acquisition System, and control of liquid flow and temperature, the experimental uncertainties were much larger. Wong [7] studied the heat transfer characteristics of a thermal microsystem. Without the control of fluid flow and temperature in his experimental apparatus, the unsteady state and uncertainty still affect his experimental results.

During the last decade, extensive studies both experiment and theory are carried out in the world. However, due to the lack of a clear fundamental understanding of the enhanced mechanics of microchannels, most of these results appear to be unclear or rather speculative and, therefore, have not gained a wide acceptance. This paper is focused on studying the heat and fluid flow characteristics in microchannels with different geometrical arrangements and a variety of conditions by evaluating channel pressure drop and distribution of temperature and velocity.

NOMENCLATURE

A_c	cross-sectional area (m^2)
D_H	dynamic diameter (m)
f	friction factor

$\overline{h_c}$	average heat transfer coefficient (W/ m^2 K)
H	height of microchannel (m)
k_f	thermal conductivity of fluid (W/K)
L	microchannel length (m)
$\dot{m}$	mass flow rate (kg/s)
n	number of microchannels
Nu	Nusselt number= $\overline{h_c} D_H/k_f$.
P_{in}	fluid absolute pressure at the inlet of microchannel (Z=L) (Pa)
P_{out}	fluid absolute pressure at the outlet of microchannel (Z=L) (Pa)
q	rate of heat flow (W)
q"	heat flux supplied to cooling liquid in microchannels (W/m^2)
Re	Reynolds number
T	temperature (K)
T_b	bulk fluid temperature (K)
ΔT_b	bulk fluid temperature difference (K)
T_w	surface temperature of microchannel wall (K)
T_{in}	temperature of fluid at the inlet of microchannel (Z=L) (K)
T_{out}	temperature of fluid at the outlet of microchannel (Z=L) (K)
$\overline{U}$	average fluid velocity (m/s)
$\dot{V}$	fluid volume flow rate (m^3/s)
W_m	width of microchannel [m]
X,Y,Z	Cartesian coordinates (m)

Greek Letters

μ	hydraulic viscosity (N/m^2)
ν	kinematic viscosity (m^2/s)
γ	aspect ratio of height to width =H/W_m
ρ_f	density of fluid (kg/m^3)
ΔT_b	temperature difference between the inlet and outlet of microchannel
Δp	pressure drop across the microchannels (Pa)

Subscripts

f	fluid
w	wall

EXPERIMENTAL APPARATUS

A schematic of the experimental apparatus used to investigate the fluid flow in rectangular microchannels is showed in Fig.1. This apparatus consists of four parts.

- **Water purification system**

It includes main water source, storage tank with temperature controller, micro-pump, and micro-metering valves. This purification system was used to provide the purified water as the working fluid. This pump has a flow rate range of 0.1–560±0.05 ml/min and can generate pressure up to 7×10^5Pa. The liquid temperature in the tank can be adjusted within the range of 20–70 ± 0.05°C by a temperature controller.

- **Flow visualization system**

The visualisation system includes a high-speed camera, two Ultra-violet lights and dye injection container. Through the patterns of fluid, fluid flow condition can be observed. A water-based dye is used to enhance the pattern quality.

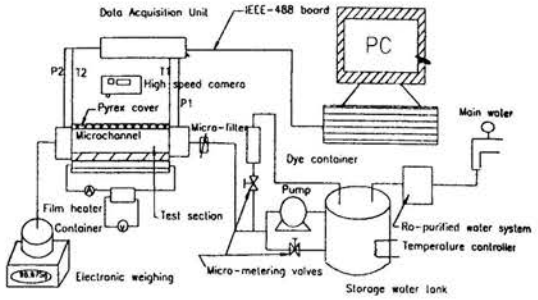

Figure 1: Schematic of experimental apparatus

- **Test section with microchannels and heating system**

This part consists of test sections with microchannels, differential pressure transducer, two thermocouples, film heaters, digital voltmeter, digital ammeter, variable transformer and insulation materials. The microchannels to be tested were machined on the copper plate with 18mm wide, 45mm long and 3mm high. To get the effects of different solid materials on the bulk temperature and pressure drop, aluminium and steel are used as the test materials. There are four microchannels in each plate. The microchannels in one plate have the same dimensions so that the flow through each channel is identical. CNC technique is used to process the microchannels. The double film heaters are designed to supply heat flux uniformly to the test section specimens, which is similar to the integrated circuit (IC) chips in MEMS. The fluid flow can be observed through the Pyrex cover.

- **Electronic weighing and Data Acquisition System (DAS)**

The volume flow of water flowing through the microchannels is measured by weighing method. The exiting fluid from microchannels is collected in a container on an electronic scale with an accuracy of ± 0.001g. Through measuring the accumulated liquid weight, the volume of the liquid can be calculated by dividing the fluid weight by its density. A 0.5μm micro-filter is installed in the entry of microchannels to decrease the block by bigger particles or bubbles. All the measurement devices are connected to DAS. During the measurement process, the micropump was set to keep a constant flow rate and pressure condition. Through setting up a record time, a series of data including the temperature, flow rate, pressure and pump rotate were transferred and kept in the PC to be analysed.

An uncertainty analysis of the experimental results was performed. The uncertainties in the microchannel sizes,

differential pressure and flow rate measurements were found to be less than ±1%. The maximum uncertainties for other parameters are as follows: average fluid velocity, ±1.5%, Reynolds number, ±2%, friction factor, ±3%, and pressure drop, ±1.5%.

Theoretical analysis and computer simulation

Considering the uniform structure, and thermodynamic condition including the similar boundary conditions, one three-dimensional microchannel with rectangular cross section was analysed and illustrated in Fig.2. It involves the determination of heat transfer and fluid flow for laminar forced convection in microchannels in the fully developed regime. A theoretical model is developed under the following assumptions:

1. The fluid is assumed to be Newtonian and incompressible
2. The flow is considered to be laminar
3. The material properties are independent with temperature
4. The effects of radiative heat transport are neglected.
5. The bottom of microchannel heat sink has a uniform heat flux

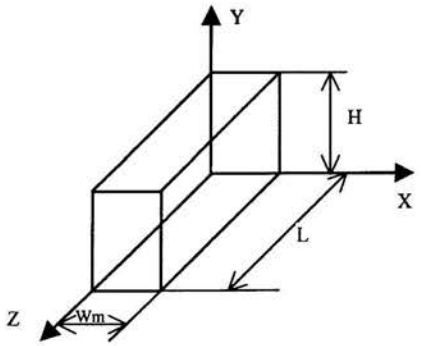

Figure 2: Schematic of microchannels

The heat transfer coefficient $\overline{h}_c$ can be calculated from the Nusselt number $\overline{h}_c D_H/k_f$. For flow in long microchannels, the significant length in the Nusselt number is the hydraulic diameter, D_H defined as

$$D_H = 4\frac{\text{flow cross}-\text{sectional area}}{\text{wetted perimeter}} \quad (1)$$

For a microchannel with rectangular cross-section, the hydraulic diameter can be calculated as follows:

$$D_H = 2\frac{W_m H}{(W_m + H)} \quad (2)$$

where W_m and H are the width and height of microchannel, respectively

The average heat transfer coefficient depends on the temperature of the fluid and wall surface. In forced convective heat transfer, the temperature of the fluid does not level out but varies both along the direction of mass flow and in the direction of heat flow. At a given cross-section of the microchannels, it is therefore a common practice, to use the average fluid bulk temperature, T_b, to replace T_f. At steady state, the heat generated from the bottom is totally removed by the fluid flowing through the microchannels owed to neglect the heat loss through the thermal insulation materials. From the energy conservation, q can be calculated by:

$$q = \dot{m} c_p \Delta T_b = c_p \dot{V} \rho_f [(T_w - T_{in}) - (T_w - T_{out})] = c_p \dot{V} \rho_f (T_{out} - T_{in}) \quad (3)$$

where $\dot{m}$ is mass flow rate; c_p is specific heat at constant pressure; ΔT_b *is* difference in average fluid bulk temperature between the inlet and outlet of microchannel; T_w is the surface temperature of wall; $\dot{V}$ is fluid volume flow rate, it can be calculated by the equation: $\dot{V} = n \overline{U} W_m H$, n is number of microchannels; W_m and H are single microchannel width and height, respectively; $\overline{U}$ is average fluid velocity; T_{in} and T_{out} are the fluid temperature at the inlet (Z=L) and the outlet (Z=0) of microchannel, respectively. If ΔT_b is small, it has good cooling effect under the same condition. In this paper twelve test sections with rectangular cross sectional geometries are investigated and listed in Table 1.

Table 1 Geometric parameters of the test sections

Test sections	W_m (mm)	H (mm)	L (mm)	D_H(mm)	Aspect ratio γ
1	0.1	0.6	45	0.1714	0.167
2	0.2	0.6	45	0.3	0.333
3	0.3	0.6	45	0.4	0.5
4	0.6	0.6	45	0.6	1
5	0.05	0.2	45	0.08	0.25
6	0.2	0.3	45	0.24	0.667
7	0.3	0.2	45	0.24	1.5
8	0.22	0.6	45	0.322	0.367
9	0.21	0.6	45	0.311	0.35
10	0.6	0.1	45	0.1714	6
11	0.3	0.1	45	0.15	3
12	0.2	0.1	45	0.1333	2

To simulate the practical condition, the film heater was supposed to produce heat flux $1\times10^4 W/m^2$. Deionized ultra filter water is used as the working liquid. Then oil, air and, methyl-alcohol are used as the working fluids to analyse the cooling effects. For a given fluid, more critical Nusselt number depends primarily on the flow conditions, which can be characterized by the Reynolds number, Re. For flow in long conduits the characteristic length in the Reynolds number, as in the Nusselt number, is the hydraulic diameter, and the velocity to be used is the average over the flow cross-sectional area, $\overline{U}$, or,

$$Re_{DH} = \frac{D_H \rho \overline{U}}{\mu} = \frac{D_H \overline{U}}{\nu} \quad (4)$$

According to above Equations, when n=4, the fluid flow rate and Re_{DH} can be calculated and given in Table 2 based on the medium water. In long ducts, where the entrance effects are not very important, the flow is laminar when the Reynolds number is below about 2100. In the range of Reynolds numbers between 2100 and 10000, a transition from laminar to turbulent flow takes place. The results of flow velocity, Reynolds number, friction factor and pressure drop between inlet and outlet of microchannel are calculated and given in Table 2. The flow friction factor f and pressure drop are expressed as follows

$$f=\frac{8\tau w}{\rho\bar{U}^2}=\frac{2D_H\Delta p}{\rho\bar{U}^2L} \quad (5)$$

$$\Delta p=P_{in}-P_{out}=\frac{f\rho\bar{U}^2L}{2D_H} \quad (6)$$

Table 2 The parameters of test sections with different cross-sectional areas

Test sections	D_H(mm)	A_c (m^2)	$\bar{U}$ (m/s)	Re_{D_H}	$\bar{U}$ (Re_{D_H}=2100) (m/s)	f	Δp(Pa)	Δp(Pa)(Re_{D_H}=2100)
1	0.1714	0.06	0.813	250.703	6.812	0.255	21896.15	183411.9
2	0.3	0.12	0.406	219.401	3.892	0.291	3574.286	34211.22
3	0.4	0.18	0.271	195.023	2.919	0.328	1340.357	14432.86
4	0.6	0.36	0.135	146.267	1.946	0.437	297.8571	4276.402
5	0.08	0.01	4.879	702.085	14.595	0.091	603160.7	1804107
6	0.24	0.06	0.813	351.042	4.865	0.182	11169.64	66818.78
7	0.24	0.06	0.813	351.042	4.865	0.182	11169.64	66818.78
8	0.322	0.132	0.369	214.082	3.626	0.298	2820.935	27671.36
9	0.311	0.126	0.387	216.615	3.754	0.295	3166.406	30697
10	0.1714	0.06	0.813	250.703	6.812	0.255	21896.15	183411.9
11	0.15	0.03	1.626	438.803	7.784	0.145	57188.57	273689.7
12	0.1333	0.02	2.439	584.925	8.759	0.109	108596.1	389882

COMPUTER SIMULATION AND EXPERIMENTAL RESULTS

A commercial Computational Fluid Dynamics (CFD) code was developed by FLUENT which was based on a boundary fitted finite volume control technique. All the computer simulations presented here were performed by using FLUENT 5.5.14 installed on a workstation. The QUICK discretization scheme was used to ensure at least second order spatial accuracy. Under-relaxation factors of pressure, momentum, energy and density are 0.3, 0.7, 1 and 1, respectively. Convergence criterions of continuity, x-velocity, y-velocity, z-velocity and energy are 1×10^{-6}, 1×10^{-6}, 1×10^{-6}, 1×10^{-6} and 1×10^{-9}, respectively. Computer simulations are focused on the effects of mass flow rate, fluid and solid materials, different geometries and processing tolerance on the pressure drop and fluid temperature.

- Effects of different D_H on the fluid bulk temperature and pressure drop when the mass flow rate and bottom heat flux are the constant
- Effects of fluid velocity on the fluid bulk temperature difference and pressure drop when the D_H and bottom heat flux are the constant.
- Effects of fluid materials on the fluid bulk temperature difference and pressure drop when the D_H, fluid velocity and bottom heat flux are the constant.
- Effects of solid materials on the fluid bulk temperature difference and pressure drop when the D_H, fluid velocity and bottom heat flux are the constant.
- Effects of processing tolerance on the fluid bulk temperature difference and pressure drop when the D_H, fluid velocity and bottom heat flux are the constant.

For all the test sections used in this study, the pressure drop, fluid bulk temperature difference and average flow velocity are plotted in Fig. 3, Fig. 4(a) and (b) as function of Dh when the working fluid is water, the material of test section is made of copper. The theoretical values of pressure drop, temperature and velocity are listed in Table 3. As seen in Fig. 3 and Fig. 4(b), for bigger channels there exists a good agreement both pressure drop and velocity among three curves. As Dh decreases, the pressure drop across the microchannel increases gradually. At the same time, the gap among these curves begins to increase. It can also be observed that pressure drop increased dramatically from about 1×10^5Pa at D_H=0.133mm to over 6×10^5Pa at D_H=0.08, which means that at a given flow rate, a higher pressure gradient is required to force the liquid to pass through the microchannels. As shown in Fig. 4(a), there does not appear to be a strong enhancement or decrease on the fluid bulk temperature when the mass flow rate is smaller. The temperature curves of computer simulation and experiment are lower than that of theoretical predictions.

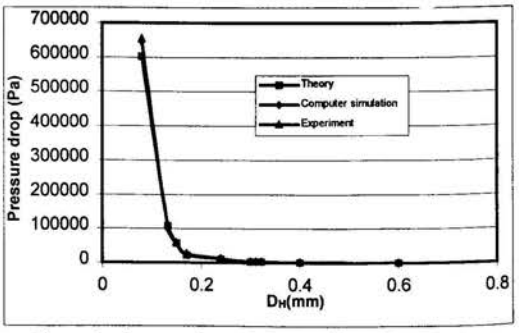

Figure 3: A comparison of experimental and computer simulation values of pressure drop vs. D_H with theoretical predictions

For the same fluid mass flow rate, the pressure gradient for smaller D_H is significantly higher than that required for larger D_H. However, the difference between bulk fluid temperature and wall temperature is less significant when

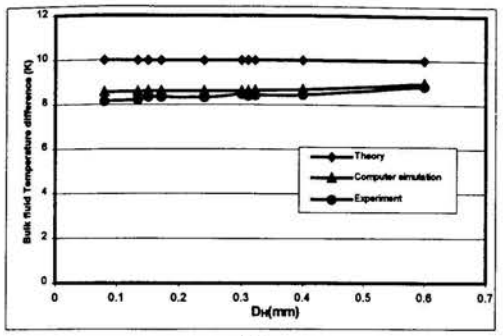

(a)

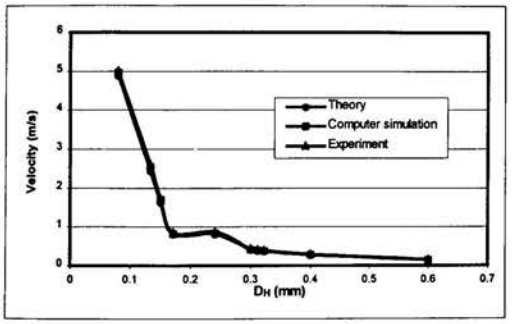

(b)

Figure 4: A comparison of experimental and computer simulation values of bulk fluid temperature difference and velocity vs. D_H with theoretical the predictions

D_H is above 0.24mm. To dissipate the high heat flux and keep the low wall temperature, it is clear that, if selected properly, the correct combination of mass flow rate and size of the microchannels can provide improvement in heat dissipation. As shown in Fig. 5, for test section 2, the curve of pressure drop by computer simulation is linear as expected from theoretical predictions. In Fig. 6, as the fluid flow velocity increases, the fluid bulk temperature and wall temperature of adjacent surface to fluid decrease smoothly. For solids with higher thermal conductivity, the effects of solid materials on the pressure drop and fluid bulk temperature can be neglected. Aluminium has the same cooling effect on wall surface temperature as copper. As shown in Fig. 8, the cooling effect of copper and aluminium are better than that of steel. Compared with solid materials, fluid materials have significant effects on the pressure drop and fluid bulk temperature. Among these liquid, air is the weakest cooling medium. Because oil has very high viscosity (1800 times than water), pressure gradient 7.5×10^6Pa is required to force oil to pass through the microchannels. Meanwhile, its cooling effect is lower than that of water. According to Fig. 9 and 10, considering both the pressure drop and cooling effect, water is one of the best cooling liquids.

For test section 1, 6, 7 and 10 with the same cross-sectional area 0.06mm^2, test section 1 has the same D_H as test section 10. Their results of pressure drop and bulk fluid temperature difference ΔT_b by computer simulation

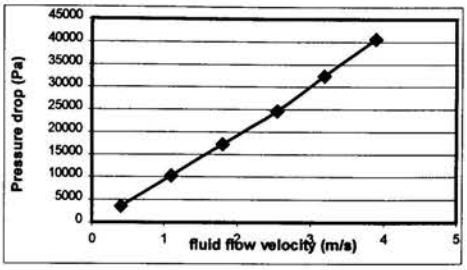

Figure 5: The effect of fluid flow velocity on pressure drop

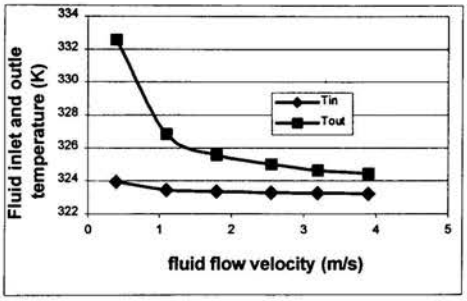

Figure 6: The effect of fluid flow velocity on fluid inlet and outlet temperature

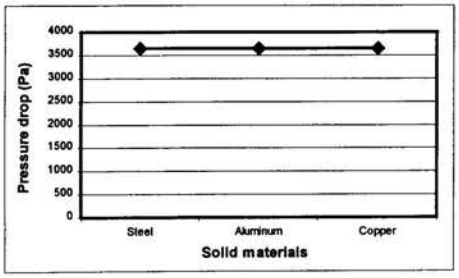

Figure 7: The effects of different solid materials on pressure drop

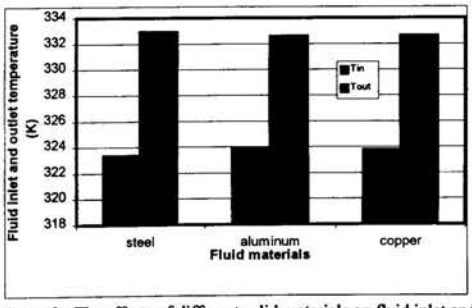

Figure 8: The effects of different solid materials on fluid inlet and outlet temperature

are given as follows: 25556Pa, 8.6K; 10069Pa, 8.6K;

9851Pa, 8.7K; 24886Pa, 8.9K, respectively. It is clear that the smaller aspect ratio γ is, the better cooling effect it has. D_H has a significant influence on pressure drop. Because the aspect ratio γ and D_H are the functions of size of microchannels, there exists an optimum between lower pressure drop and higher cooling capacity. For test sections 2, 8 and 9, the allowance for machining is 0mm, 0.01mm and 0.02mm, respectively. Their results of pressure drop and bulk fluid temperature difference ΔT_b

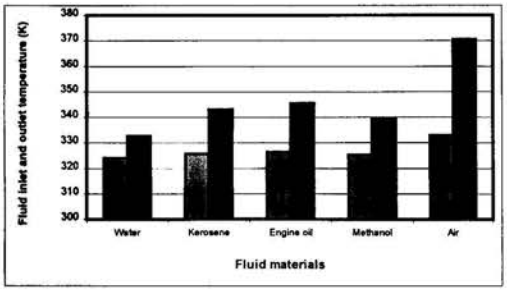

Figure9: The effects of different solid materials on fluid inlet and outlet temperature

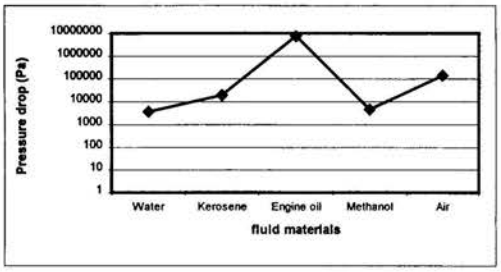

Figure 10: The effects of different fluid materials on pressure drop

by computer simulation are given as follows: 3651Pa, 8.6K; 3201Pa, 8.6K; 2827Pa, 8.6K, respectively. Allowance for machining affects the pressure drop more than bulk fluid temperature difference ΔT_b. Under lower mass flow rate, this influence can be neglected. For test section 10, 11 and 12, their results of computer simulation are given: 24886Pa, 8.9K; 57069Pa, 8.6K; 100142Pa, 8.6K, respectively. These results also confirm that the smaller aspect ratio γ is, the better cooling effect it has. Only tiny difference of D_H can cause a significant gap among the results of pressure drop.

CONCLUSIONS

Through giving theoretical predictions of pressure drop and fluid bulk temperature difference from conventional flow theory, laminar forced convection in microchannel heat sink with rectangular cross-section was investigated. For microchannels with large diameters, the results of experiment and computer simulation are in rough agreement with the theoretical predictions from the conventional flow theory. But, as D_H decreases, there is a significant increase in pressure drops and bulk fluid temperature difference compared to that predicted by conventional flow theory. The results indicate that fluid materials have more significant effects on heat transfer characteristics than solid materials of test section.

The results of theoretical prediction, computer simulation and experiment show that D_H is one of the most important parameters for the thermal-hydraulic performance. Mass flow rate has a significant influence on fluid cooling effect more than its pressure drop. Allowance for machining affects the pressure drop more than temperature. Under lower mass flow rate, this influence can be neglected. The aspect ratio is also an important factor for the heat transfer characteristics. It is undoubted that there exists an optimum among these variables. To optimise the geometry for microchnnel heat sink applications, further investigations are necessary.

ACKNOWLEDGEMENTS

The authors would like to greatly acknowledge the financial support of IPRS and CUPS scholarship from Curtin University of Technology. The authors also are grateful to the great help from National Centre Lab of Applied Optics, Changchun Institute of Optics and Fine Mechanics, Chinese Academy of Sciences.

REFERENCES

[1] Tuckerman, D.B. and Pease, R.F.W., 1981, "High-performance heat sinking for VLSI," IEEE Electron Device Letters, EDL2, Vol.5, pp. 126-129.

[2] Wu, P., and Little, W.A., 1983, "Measurement of friction factor for the flow of gases in very fine channel used for microminiature Joule-Thomson refrigerators," Cryogenics, Vol. 23, No. 5, pp. 273-277.

[3] Peng, X.F. and Wang, B.F., 1993, "Forced convection and flow boiling heat transfer for liquid flowing through microchannels, " International Journal of Heat and Mass Transfer, Vol. 36, pp. 3421-3427.

[4] Peng, X.F., Peterson, G.P., and Wang, B.F., 1994, "Frictional flow characteristics of water flowing through rectangular microchannels," Experimental Heat Transfer, Vol. 7, pp. 249-264.

[5] Wang, B.F., and Peng, X.F., 1994, "Experimental investigation on liquid forced-convection heat transfer through microchannels," International Journal of Heat and Mass Transfer, Vol. 37, pp. 73-82.

[6] Tao, C.P., and Mahulikar, S.P., 1998, "The use of the brinkman number for single phase forced convective heat transfer in microchannels," International Journal of Heat and Mass Transfer, Vol. 41, No. 12, pp. 1759-1769.

[7] Jiang, L.N., Wong, M. and Zohar, Y., 2000, "Unsteady characteristics of a thermal microsystem," Sensors and Actuators, Vol. 82, pp. 108-113.

HEFAT2002
1st International Conference on Heat Transfer, Fluid Mechanics, and Thermodynamics
8-10 April 2002, Kruger Park, South Africa
SM3

TRANSIENT THERMAL ANALYSIS OF A MICROPROCESSOR USING A HEAT SPREADER WITH VARIABLE THERMAL STORAGE CHARACTERISTICS

Mark E. Steinke
mark_steinke@hotmail.com

Satish G. Kandlikar
SGKEME@RIT.EDU

Mechanical Engineering Department
Rochester Institute of Technology
Rochester, NY 14623

ABSTRACT

The thermal performance of a heat spreader with Phase Change Material (PCM) is investigated experimentally under transient conditions. The transient thermal load generated by a microprocessor is obtained by running a variety of software applications commonly encountered in Personal Computer usage. The representative load cycle is used to simulate the chip with a variable heat source heater. Introducing PCM in selected pockets of the heat spreader modifies the heat spreader thermal characteristics. The heat dissipation characteristics of the air-cooling system mounted on the heat spreader are maintained constant for all of the experiments. The results indicate that modifying the thermal characteristics of the heat spreader improves the maximum heat dissipation rate under actual transient conditions encountered in PC operation.

INTRODUCTION

The thermal management of electronic devices has become an important topic in heat transfer. The power dissipation of the computer chips is rapidly increasing. The thermal management of these high power systems provides a complex challenge. Unfortunately, the heat transfer area is not increasing in line with the power dissipation. This results in an ever-increasing heat flux with higher power processors.

It becomes even more important to provide the proper cooling for these high power chips. In the most recent literature, new techniques have been developed to handle the demand for high power dissipation. New heat sink designs have new flow paths, increase in surface area, and heat transfer coefficient enhancements.

Microchannel heat sinks show a promising potential. In recent works, a microchannel has been applied to this problem. The small-scale enhancement of a microchannel gives and enhancement in the thermal performance of the heat sink. Yu et al. [1] used a microchannel heat sink for chip cooling. They found that the microchannel heat sink could provide an improvement.

Unfortunately, the majority of available literature does not take into account the transient nature of chip cooling. Most of the work has been done dissipating a steady state power load. However, the actual computer chip does not dissipate a steady state power. The highest power rating is still used as the design limit. However, the design limit is the maximum condition at 100% usage. An actual chip power will fluctuate with time. This is especially true for personal computers and small electronic devices. Therefore, the power output is directly dependent upon the percent CPU usage. This also allows the possibility of a momentarily higher than allowable surface temperatures.

The use of Phase Change Materials (PCM) is traditionally used in transient control of thermal systems. The PCM makes use of the latent heat of fusion to absorb heat. The addition of a PCM to a cooling scheme can add a better transient control.

Lu [2] modeled the transient performance of a high power electronics chip with PCM using FEM. Their results indicate the potential of a PCM in improving the transient performance. However, their results have employed very high temperatures, on the order of 5000 K, which do not have any practical significance. In another work, Weinstein [3] added a PCM to a handset mock up to provide transient control. They found that the PCM would allow for an increase in operation time. The present work explores the application of the PCM in PC chip cooling by conducting experiments with different void fraction ratios of the PCM in the heat spreader.

NOMENCLATURE

h_L	Average heat transfer coefficient, $W/m^{-2}K$
P	Power, W
t	Time, s
Δt	Time interval during transient power loading, s
T	Temperature, °C
v	Velocity, m/s
V	Volume, m^3
VF	Volume Fraction, dimensionless

GREEK LETTERS

θ Excess Temperature Percentage, $[(\Delta T/(T_b - T_a))*100]$

SUBSCRIPTS

a Air
b Base
i Inlet
o Outlet
s Surface
w Wax, used as PCM

OBJECTIVES OF THE PRESENT STUDY

The present work involves the use of phase change material in a heat spreader plate. The PCM is used to control the transient effect of chip loading. A typical power cycle is used to emulate the loading of a computer chip. The effect of the PCM on the transient thermal performance of the spreader plate is experimentally evaluated.

EXPERIMENTAL SET-UP

The experimental apparatus was developed to study the effect of PCM on the transient performance of a spreader plate. An electric heater is used to emulate the computer chip. The actual heater is a 1 cm x 1 cm flexible heater. The heater size is close to the actual dimensions of a chip. The heater is secured to a spreader plate using an adhesive. The power input is controlled to impose the desired loading conditions.

The spreader plate is manufactured from a plate of aluminum. The plate has the overall dimensions of 3 inches wide by 3 inches long and ¾ inch thick (76.2mm x 76.2mm x 19mm). The spreader plate is shown in Figure 1.

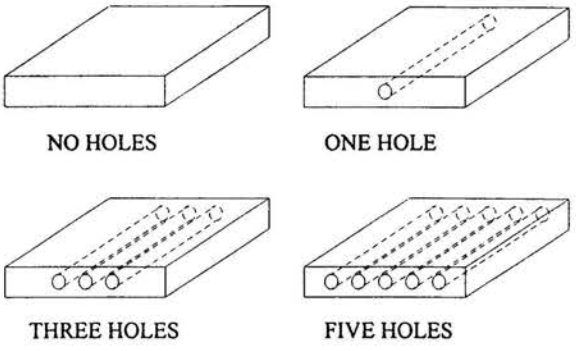

Figure 1: Aluminum Spreader Plates. The overall dimensions are 3"x 3"x ¾"thick and ¼ inch diameter holes. Four different volumes of PCM; 0.00 m^3, $2.413x10^{-6}$ m^3, $7.239x10^{-6}$ m^3, and $1.267x10^{-5}$ m^3.

The volume of the spreader plate is $1.1xE^{-4}$ m^3. Paraffin wax is used as a PCM. The spreader plate was altered to receive a varying volume of PCM. The three volumes of PCM material are $2.413x10^{-6}$ m^3, $7.239x10^{-6}$ m^3, and $1.267x10^{-5}$ m^3. The volume fraction, VF, is defined here as the volume of PCM divided by the volume of material. The respective VF for the PCMs are 0.02, 0.07 and 0.11. After completion of the first round of tests, a fifth spreader plate was constructed. Figure 2 shows the fifth plate. It has a wax volume of $2.17x10^{-5}$ m^3 and a VF of 0.20.

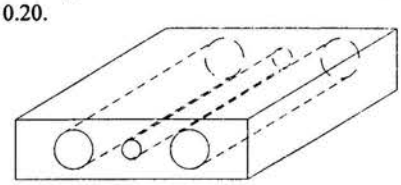

Figure 2: Modified Aluminum Spreader Plate. Overall dimensions are 3"x 3" x ¾" thick with one ¼" diameter hole and 2 ½" diameter hole. Volume of PCM = $2.17x10^{-6}$ m^3 and VF = 0.20.

Thermocouples are distributed in the spreader plate to determine surface temperatures. The base temperature is known. An array of surface temperatures on the cooling side is known. The temperature of the PCM is also known.

The spreader plates are placed in an identical air-cooling setup. A small wind tunnel is constructed to provide uniform airflow over the heat spreader as shown in Fig. 3. The air velocity is fixed at 4.00 ± 0.05 m/s. Each of the spreader plates is mounted in the same manner.

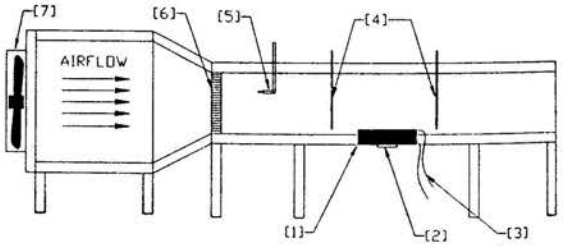

Figure 3: Air-cooling System. The miniature wind tunnel has a test section area of $5.806x10^{-3}$. The components are: [1] Spreader Plate, [2] Heater, [3] Thermocouples, [4] Air Thermocouples, [5] Pitot Tube, and [6] Fan.

The air-cooling system involves the use of a miniature wind tunnel made of Lexan as shown in Fig. 3. The Lexan is an optically clear polycarbonate. A variable speed fan controls the air velocity. The voltage is fixed to provide an air velocity of 4 m/s. The air passes through a set of flow straightener and enters the test section. The air velocity is measured using a pitot tube. The inlet and outlet air temperatures are measured using thermocouples. The thermocouples where calibrated to ±0.1°C. The inlet temperature varied slightly during the testing due to the changing ambient conditions. However, the temperature was within the range of 22.1°C to 23.1°C.

EXPERIMENTAL PROCEDURE

The spreader plates are mounted in the wind tunnel. The air velocity is held constant for each test. Four different volumes of PCM are tested. The four VF for these cases are 0, 0.02, 0.07, and 0.11. The air velocity is set at 4.00 ± 0.05 m/s. First, a steady state power load of 100 Watts is applied to the spreader plate. The temperatures are recorded for this case. The other cases involve a varying power load to emulate transient chip power usage. The thermal performance is reported for each testing condition.

RESULTS

The thermal performance of a spreader plate is found under several different power loading conditions. A spreader plate is used to distribute the heat from a small area into a larger base area. A variable electric heater is used to emulate a microprocessor. The maximum base temperature is limited to 62 °C. The reported melting temperature of the wax is 66°C. However, the actual melting temperature was experimentally determined to be considerably lower, around 50-55°C.

There are several different loading conditions that are presented. The thermal performance of each case is reported. The reference case for comparison is a spreader plate that has no PCM. It is the point of reference for all of the testing. This plate was tested first for each of the loading conditions. For reasons of clarity, only the spreader plate with a VF of 0.00, 0.07, and 0.11 will be presented. The spreader plate that has a VF of 0.02 has a similar performance as the plate with 0.00 VF PCM.

The first loading condition is a steady state power loading. The heater is set to deliver a constant power. The steady state temperatures are recorded.

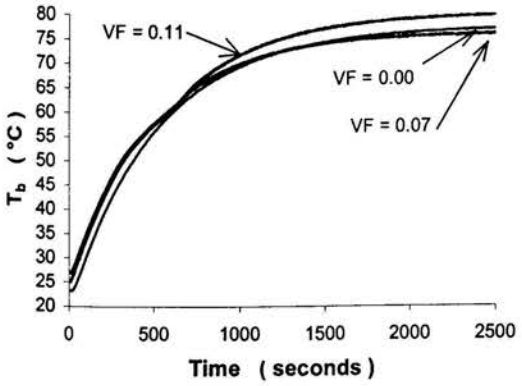

Figure 4: Base Temperature for Steady State Load of 40 Watts. The transient history of the Base Temperature for a steady state 40 watt loading of a spreader with varying PCM. VF = 0.00, 0.07, and 0.11.

Figure 4 shows the thermal performance for the constant load of 40 Watts. As seen in the figure, the temperatures reach a steady state value in approximately 2500 seconds. The average heat transfer coefficient, h_L, on the cooling side is calculated to be 28.8 W/m^{2}K. The spreader plate with no PCM reaches the lowest steady state temperature of 77.5 °C. The spreader plate with a VF of 0.07 reaches a steady state temperature of 76.1 °C. The spreader plate with the most PCM and a VF of 0.11 reaches the highest steady state temperature of 80.1 °C. This behavior makes sense because the increase in the PCM material results in a decrease in the thermal conduction paths. The base temperature for the plate with a VF of 0.11 shows a slight depression in the shape between 55 °C and 65 °C. This is due to the energy being consumed in the latent heat used to melt the PCM.

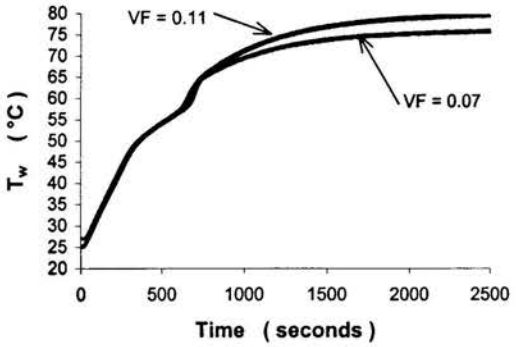

Figure 5: Wax Temperature for Steady State Loading of 40 Watts. The transient history of wax temperatures for each spreader plate cavity. The plate with VF=0.07 has 3 cavities. The plate with a VF=0.11 has five cavities. VF = 0.00, 0.07, and 0.11.

Figure 5 demonstrates the temperature history for the wax temperatures in the PCM under a constant load of 40 watts. The distinct temperatures are the temperatures of the wax in independent cavities. The spreader plate with a VF of 0.07 has three cavities. The spreader plate with a VF of 0.11 has five cavities. The effect of the PCM and latent heat can be seem by the flattening of the slop around the melting temperature of the PCM. This curve for each constant loading power input was useful in devcloping the transient loading.

Figure 6 shows the resulting base temperatures for the constant loading case. The steady state base temperatures are reported for the various spreader plates. Based upon this data, the variable loading case was developed.

The variable loading case uses two power inputs. The higher power input is the maximum power input. The lower power input is a percentage of the maximum or higher power input, typically 25% of the maximum value. The load is varied between these two power inputs with different time intervals. This loading scenario simulates the processor being loaded at 100% capacity and then at 25% capacity.

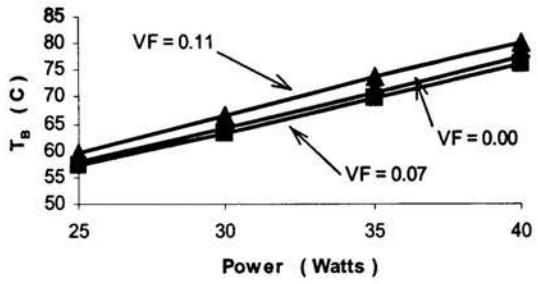

Figure 6: Base Temperature verses Power Input. The Base Temperature for a steady state loading verses the power input. VF = 0.00, 0.07, and 0.11.

The first variable loading case is shown in Figure 7. The first loading condition is using 40 watts as the maximum and 15 watts as the minimum. The time duration is 240 seconds at each power rating, starting at the maximum power.

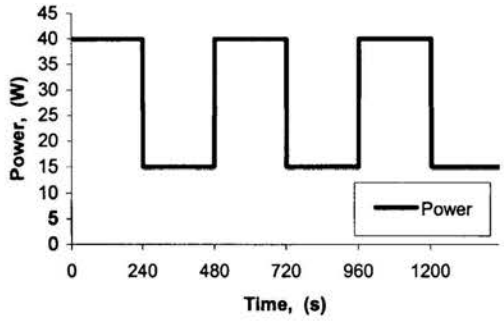

Figure 7: Power Curve for the First Variable Load. P_{max} = 40 W, P_{min} = 15 W, Δt = 240 s.

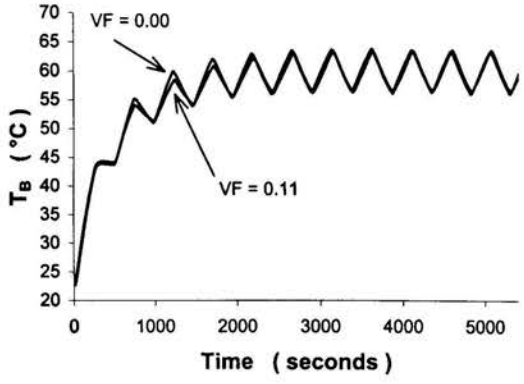

Figure 8: Base temperature versus time under variable loading – First Case. P_{max} = 40 W, P_{min} = 15 W, Δt = 240 s.

The first loading was applied to the spreader plates with a VF of 0.00 and 0.11. Figure 8 shows the results of the first transient load. The base temperature for the plate with VF = 0.00 varied between a maximum of 63.1 °C and a minimum of 56.9 °C. The plate with a VF of 0.11 varied between a maximum of 63.0 °C and a minimum of 57.5 °C. The two plates transient thermal performance is very close to each other. It is interesting to see that the only difference between these plates occurs in the early transients. Although, there is no discernable difference when the plates reach a steady state pattern.

The second variable loading case is shown in Figure 9. The second loading condition is using 30 Watts as the maximum and 7.5 Watts as the minimum. The time duration is 240 seconds at each power rating, starting at the maximum power.

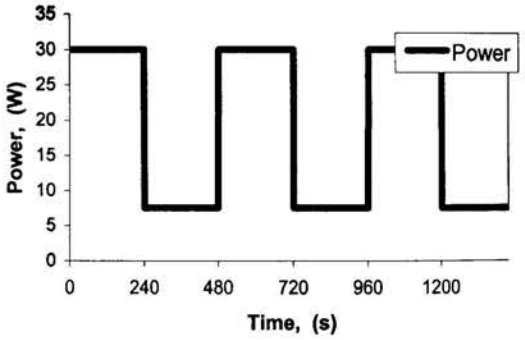

Figure 9: Power Curve for the Second Variable Load. P_{max} = 30 W, P_{min} = 7.5 W, Δt = 240 s.

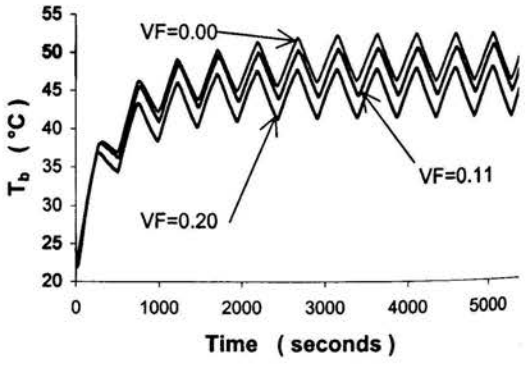

Figure 10: Base temperature versus time under variable loading – Second Case. P_{max} = 30 W, P_{min} = 7.5 W, Δt =240 s.

The second loading was applied to the spreader plates with VFs of 0.00, 0.11, and 0.20. Figure 10 shows the results of the second transient loading case. The base temperature for the plate with VF = 0.00 varied between a maximum of 52.5 °C and

a minimum of 46.7 °C. The plate with a VF of 0.11 varied between a maximum of 50.1 °C and a minimum of 44.5 °C. The plate with a VF of 0.20 varied between a maximum of 47.5 °C and a minimum of 42.0 °C. When the plates reach their steady state pattern, the spreader plate with PCM has a lower maximum surface temperature. The percent temperature excess, θ, for the VF of 0.11 is 8.0%. It seems that the VF of 0.11 is not absorbing enough energy to depress the base temperature for this loading. The plate with a VF of 0.20 begins to show a considerable improvement. The excess temperature for the VF of 0.20 is 16.7%.

The third variable loading case is shown in Figure 11. The third loading condition is using 30 Watts as the maximum and 7.5 Watts as the minimum. The time duration is now 120 seconds at each power rating, starting at the maximum power.

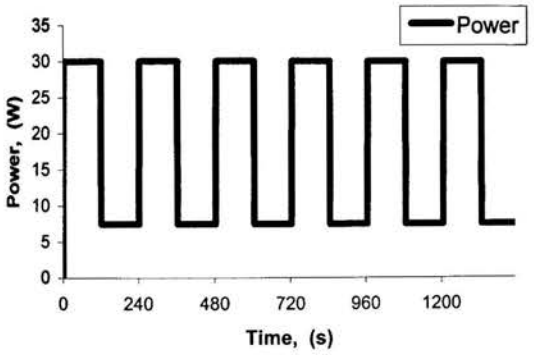

Figure 11: Power Curve for the Third Variable Load. P_{max} = 30 W, P_{min} = 7.5 W, Δt = 120 s.

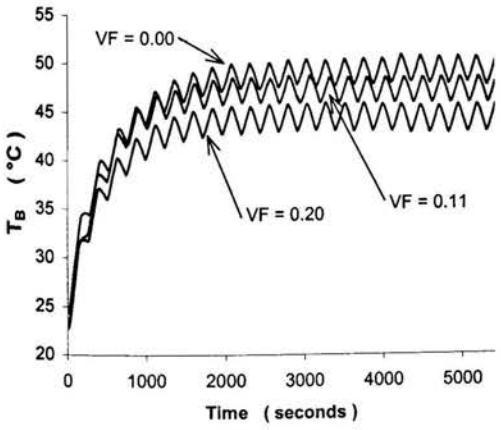

Figure 12: Base temperature versus time under variable loading – Third Case. P_{max} = 30 W, P_{min} = 7.5 W, Δt = 120 s.

The third loading was applied to the spreader plates with a VF of 0.00, 0.11, and 0.20. Figure 12 shows the results of this transient load. The base temperature for the plate with VF = 0.00 varied between a maximum of 50.74 °C and a minimum of 48.1 °C. The plate with a VF of 0.11 varied between a maximum of 48.5 °C and a minimum of 45.9 °C. The plate with a VF of 0.20 varied between 45.72 °C and 43.25 °C. When the plates reach their steady state behavior, the spreader plate with PCM has a lower maximum surface temperature. The percent temperature excess for a VF of 0.11 is 9.35%. The excess temperature for a VF of 0.20 is 17.2%.

The forth variable loading case is shown in Figure 13. The forth loading condition is using 35 watts as the maximum and 8.75 watts as the minimum. The time duration is now 120 seconds at each power rating, starting at the maximum power.

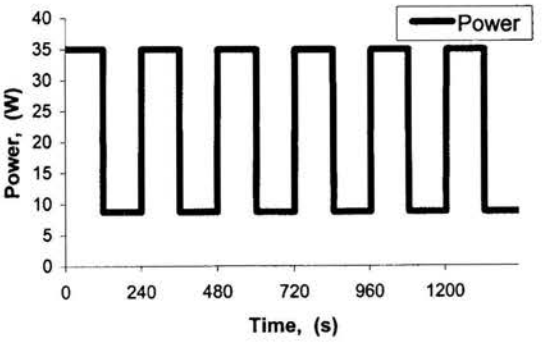

Figure 13: Power Curve for the Forth Variable Load. P_{max} = 35 W, P_{min} = 8.75 W, Δt = 120 s.

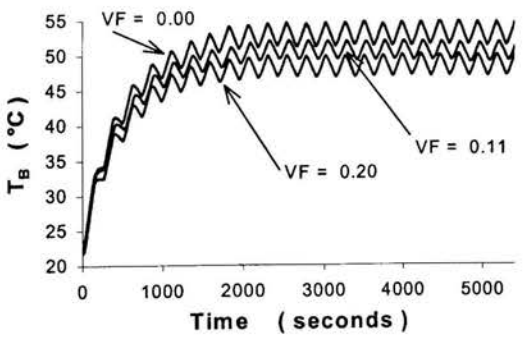

Figure 14: Base temperature versus time under variable loading – Forth Case. P_{max} = 35 W, P_{min} = 8.7, Δt = 120 s.

The forth loading was applied to the spreader plates with a VF of 0.00, 0.11, and 0.20. Figure 14 shows the results of this transient load. The base temperature for the plate with VF = 0.00 varied between a maximum of 54.8 °C and a minimum of 51.5 °C. The plate with a VF of 0.11 varied between a maximum of 52.0 °C and a minimum of 49.4 °C. The plate with a VF of 0.20 varied between 49.8 °C and 47.0 °C. When

the plates reach their steady state behavior, the spreader plate with PCM has a lower maximum surface temperature. The percent temperature excess for a VF of 0.11 is 10.1%. The excess temperature for a VF of 0.20 is 14.1%.

	Excess Temperature, θ, Percentage			
VF	**Case 1**	**Case 2**	**Case 3**	**Case 4**
0.00	0.0	0.0	0.0	0.0
0.11	0.0	8.0	9.35	10.1
0.20	0.0	16.7	17.2	14.1

Table 1: Excess Temperature, θ, Percentage for transient loading cases. VF = 0.00, 0.11, and 0.20.

Table 1 shows the results of the transient load testing for the five different spreader plates. The VF for each plate is 0.00, 0.11, and 0.20, respectfully. Case 1 is the first loading case of P_{max} = 40 watts, P_{min} = 15 watts, and Δt = 240 seconds. Case 2 is the second loading case of P_{max} = 30 watts, P_{min} = 7.5 watts, and Δt = 240 seconds. Case 3 is the third loading case of P_{max} = 30 watts, P_{min} = 7.5 watts, and Δt = 120 seconds. Case 4 is the forth loading case of P_{max} = 35 watts, P_{min} = 8.75 watts, and Δt = 120 seconds. As seen in the table, the largest q reached was 17.2 for Case 3 and a VF of 0.20. It can be seen that the increase in VF results in improved performance. However, an optimization for specific application is required.

CONCLUSIONS

The use of a phase change material in electronics cooling can provide an improvement in handling transient thermal management. The PCM has already proven useful in such applications as high heat fluxes [2] for high heat fluxes and in hand sets [3] to extend operation time. The use of PCMs in this application could possibly extend air-cooling of microprocessors. Some conclusions from this study are:

1. The PCM provides a lag in the very early transients as compared to the spreader plate without any PCM. The early stages of the loading have shown that the plates with PCM provide a more even ramp up in temperature. This would be valuable if the steady state behavior is not of concern.
2. The PCM does make a difference in the constant loading of the spreader plate. The PCM has the effect of augmenting the typical base temperature curve. The region of change denotes the operating region of the PCM. The transient design of the spreader plate should fall within this region. If the transient loading falls outside of this region, the PCM will be ineffective in producing the desired effect, as in Figure 7.
3. The PCM does provide a reduction in the maximum base temperature of the spreader plate as compared to the plate without any PCM. This behavior is seen in Figures 9, 11, and 13.
4. The volume of the PCM has a significant effect upon the transient performance. The volume for a specific loading must be optimized for the best performance. Table 1 also demonstrates this behavior. On the other hand, too much volume of PCM will cause a limiting effect in the conduction paths of the spreader plate. This will also cause a detrimental effect upon the base temperature and cause an increase in base temperature, as seen in Figure 3.

The use of a PCM in electronics could provide a much need extension of air-cooling. Unfortunately, the application of the PCM is very dependent upon the loading conditions. Further optimization is required to determine the proper PCM material type, PCM volume, and orientation. Further experiments are being planned with significantly higher volumes of PCM embedded in the heat spreader plate.

ACKNOWLEDGMENT

The experimental work was carried out in the Thermal Analysis Laboratory at the Rochester Institute of Technology, Rochester, NY, USA. The authors are grateful to their institutions for providing the necessary support in conducting this collaborative work. In addition, the authors would like to thank Jonathan P. Curry for his help in developing this concept.

REFERENCES

[1] Yu, S., T. Ameel, and M. Xin. "An Air-cooled Microchannel Heat Sink with High Heat Flux and Low Pressure Drop." 33rd Proceedings of National Heat Transfer Conference, Aug 1999, Albuquerque, NM. Paper # NHTD99-162. ASME Publications, 1999.

[2] Lu, T.J. "Thermal Management of High Power Electronics With Phase Change Cooling." International Journal of Heat and Mass Transfer, 43, (2000): 2245-2256.

[3] Weibstein, R.D., M. Hodes, and J.M. Piccini. "Improved Static and Transient Thermal Management of Handsets Using Heat Spreaders and Phase Change Materials (PCMS)." 35th Proceedings of National Heat Transfer Conference, June 2001, Anaheim, CA. Paper # NHTC2001-20026. ASME Publications, 2001.

[4] Incropera, F.P., and D.P. DeWitt. "Fundamentals of Heat and Mass Transfer." *John Wiley & Sons,* New York, 1996.

[5] Laouadi, A., and M. Lacroix. "Thermal Performance of a Latent Heat Energy Storage Ventilated Panel for Electric Load Management." *International Journal of Heat and Mass Transfer* 42, (1999): 275-286.

HEFAT2002
1st International Conference on Heat Transfer, Fluid Dynamics, and Thermodynamics
8-10 April 2002, Kruger Park, South Africa
TX1

LIQUID SUPERHEAT DURING FLOW BOILING IN MICROCHANNELS

X. Tu and P. Hrnjak

Department of Mechanical and Industrial Engineering
University of Illinois at Urbana-Champaign
1206 W. Green St., Urbana, Il 61801
USA
Xiaotu@uiuc.edu, pega@uiuc.edu

ABSTRACT

Experimental results have shown that it is very difficult to initiate boiling with refrigerant R134a flowing in microchannels with cross-section of 75 × 800 μm. The design of the test section made it possible to measure the bulk fluid temperature inside the microchannels non-intrusively. The bulk fluid was demonstrated to be in a metastable liquid state even under very high wall heat fluxes and superheat temperatures. The results suggest that bubble growth was suppressed (high wall superheats measured) for liquid R134a flow boiling in microchannel with hydraulic diameter (D_h) about 137μm.

INTRODUCTION

Recently, in various branches of industry, there has been a growing interest in developing miniaturized thermal systems and microscale devices. The increasing technological demands in various new areas require a comprehensive understanding of the fundamental phenomena that govern thermal transport in small scales. The boiling of liquids in microchannels is one of the most important topics, because of the potential applications in electronic cooling, micro thermal systems, and the like. Experimental data and theoretical work in the open literature reveal that the boiling process in micro scales is quite different from that in normal scales.

Lin *et al.* [1] could not generate bubble with static water, methanol, and FC43 liquids in microchannels that are 7.5 μm deep, 30 and 60 μm wide, until they raised the heater wall temperature to the proximity of the critical temperature. Jiang, *et al.* [2,3] observed that during the boiling process of water in microchannels with hydraulic diameters of 40 and 80 μm, the wall temperature increased almost linearly with the wall heat flux until the onset of critical heat flux (CHF) condition. No boiling plateau, which is associated with saturated nucleate boiling state, was observed in the boiling curves. The experimental results of Lin *et al.* [1] and Jiang *et al.* [2,3] indicated that the typical bubble generation and growth mechanisms commonly observed in macrochannels are suppressed in microchannels.

Peng and Wang [4,5] experimentally investigated water and methanol flow boiling in microchannels of cross-section from 200 × 700 μm to 800 × 700 μm. They noted that no vapor bubbles could be observed even in fully developed nucleate boiling regime. This behavior was termed as "bubble extinction". Two hypothetical concepts, "evaporating space" and "fictitious boiling", were proposed to explain this new behavior in microchannels [6]. "Evaporating space" is the critical liquid space less than which bubbles could not successfully form and grow. "Fictitious boiling" implies that the liquid has reached conventional nucleate boiling conditions, but internal evaporation and bubble growth have not yet been realized or there may exist countless micro-bubbles within the liquid that cannot be visualized by ordinary means. If the microchannel size is smaller than the "evaporating space", "fictitious boiling" can be induced, otherwise, normal nucleate boiling will occur.

Peng *et al.* [7] proposed semi-empirical correlations to predict the boiling conditions in the microchannels. The correlations demonstrated that decreasing the size of the microchannels resulted in dramatically high wall superheats for nucleation. Peng *et al.* [8] demonstrated experimentally that the correlation successfully described the superheats for nucleate boiling in microchannels. Peng *et al.* [9] investigated the role of perturbations on the dynamics of clusters, and developed the physical interpretation of "fictitious boiling". They also proposed a criterion for the occurrence of the fictitious boiling.

The literature review demonstrates that the boiling process in microchannels is quite different from that in conventionally sized channels. Bubble growth is suppressed when the channel size is below a critical value. However, this critical size is not the same for different fluids. For example, for water and methanol, it is difficult to generate bubbles in channels with diameter (D_h) smaller than 1 mm [7,8,9]; but bubbles can be produced easily within R-12 flow through channels with a hydraulic diameter of 0.7mm [7]. The theoretical work of Peng *et al.* [7] indicates that the critical channel size for refrigerants, such as R-12 and R134a, should be much smaller than that of

water. However, no experimental work has reported what the critical channel sizes should be when using refrigerants.

Shannon *et al.* [10] are developing a microscale cooling system in the size of 100 × 100 × 2.5 mm. The design of such a system needs to characterize heat transfer in channels as small as 75 × 800 μm (D_h = 137 μm). In the ongoing work of investigating evaporation heat transfer in microchannels, we found that two-phase flow is very difficult to be generated in microchannels with cross-section of 75 × 800 μm when heating the subcooled liquid R134a. This bulk refrigerant was determined to be in metastable liquid state even under very high wall heat fluxes and superheat temperatures. It is shown that hydraulic diameter of 137 μm is small enough to restrict bubble growth in R134a flow.

NOMENCLATURE

A	emp irical constant in equation (1)
D_h	hydraulic diameter (μm)
dP	pressure drop (kPa)
G	mass flux (kg/m^{2}s)
H	channel height (μm)
h_{lv}	latent heat (kJ/kg)
I	current (Amps)
m	mass flow rate (kg/s)
P	pressure (kPa)
q''	heat flux (kW/m^2)
T	temperature (°C)
ΔT_{sup}	minimum wall superheat in equation (1) (°C)
V	voltage (Volts)
v'	liquid specific volume at saturation (m^3/kg)
v''	vapor specific volume at saturation (m^3/kg)
W	channel width (μm)

Greek Letters

σ	surface tension (N/m)

Subscripts

bulk	bulk fluid
ei	test section inlet
eo	test section outlet
l	liquid phase
oi	orifice inlet
sat	saturation
v	vapor phase
wi	inner wall

EXPERIMENTAL METHOD

Facility

The experimental facility is shown schematically in Figure 1. It is an open-loop system consisting of a refrigerant supply tank, control valves, a test section, and a receiver tank for adjusting the flow rates and experimental conditions. The refrigerant tank contained saturated R134a, which was maintained at desired pressures (or temperatures) using an electric resistance heater and a variable transformer (variac). Liquid refrigerant was driven into the test loop by placing the supply pipe at the bottom of the refrigerant tank. The receiver tank was exposed to room temperature. A sufficiently large surface area of the tank wall provided a stable lower pressure. The flow rate and test section pressure were adjusted by two control valves.

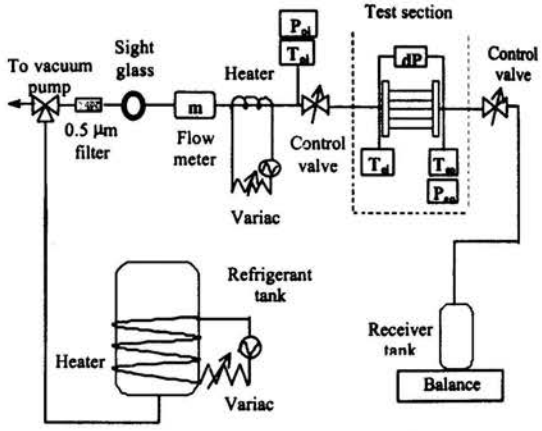

Figure 1: Microchannel test facility

In Figure 2, the test section is enlarged and shown in scale. It had four parallel channels 85 mm long, and a cross-section dimension of 75 × 800 μm. It was fabricated from four layers of Kapton® films with a total thickness of 250 μm. Two inner layers, with a thickness of 75μm each, were cut with channels and headers. The two outer layers were 50 μm thick each. The webs between the channels were 1000 μm wide. The fabrication process of such a heat exchanger has been reported by Selby *et al.* [11].

A Kapton® insulated heater was mounted above a 3mm thick aluminum block using high thermal conductive epoxy. Aluminum was used because its high thermal conductivity could provide uniform heating in the four channels. The aluminum block was then attached to the microchannels. The whole test section was insulated with rubber insulation 5 mm thick. The heater was supplied with DC, and the heating power was adjusted by a HP power controller. Twenty-five millimeters downstream of the heating section, four type-T fine-gage thermocouples (75 μm wire diameter, T_{ch1} ~ T_{ch4} in Figure 2) were mounted above the center of microchannels using high thermal conductive epoxy.

Heat leakage upstream and downstream was estimated to be negligible, because thermal conductivity of Kapton is low (~ 0.15 W/m °C) and the test section is very thin (250 μm). Therefore the heating effect was limited to the part mounted with heater only. This design is an improvement over others, where materials with high thermal conductivity were used; because of axial conduction, the boiling in the microchannels is mixed with that in the large inlet and exit headers [2,3].

Because the channel wall was very thin (50 μm) and it was insulated, the readings of the four thermocouples were just the bulk fluid temperature inside the specific channel. This new design for the test section permitted the bulk fluid temperature inside the microchannels to be measured non-intrusively.

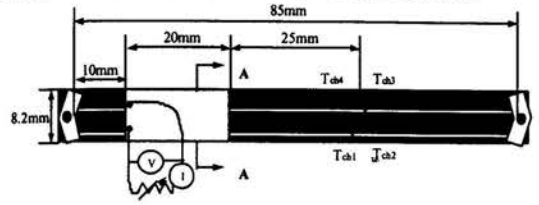

(a) Top view

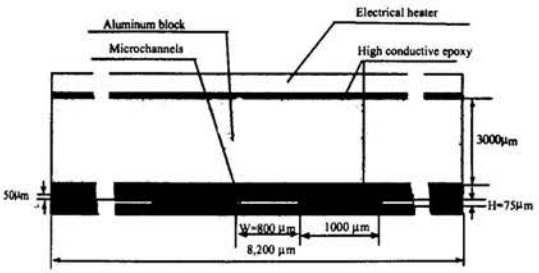

(b) Cross-section A-A

Figure 2: Test section

The fluid temperatures at the inlet and outlet were measured using two type-T thermocouples (T_{ei} and T_{eo} in Figure 1). A pressure transducer (Setra model 206, 0 ~ 1724 kPa, P_{eo} in Figure 1) was used to measure outlet pressure in the test section. The pressure drop across the test section, dP in Figure 1, was measured by using a differential pressure transducer (Setra model C230, 0 ~ 69 kPa). The mass flow rate was measured with a low-flow-rate meter (Rheotherm® model TU1/16), and double-checked by measuring the rate of mass accumulation in the collection tank. For all the experimental data, the differences between these two methods were within ±3%. The Rheotherm reading was used for data analysis.

Measurements were recorded with a Hewlett-Packard (HP) data logger and a microcomputer. The sampling interval was three seconds and all the data were recorded in Microsoft Excel for future processing. Errors associated with the thermocouples were estimated at less than ± 0.2°C. The uncertainty in flow rate measurements was estimated to be less than ± 3%. The uncertainty in pressure measurements was ± 0.2%; and in differential pressure measurements, less than ± 0.3%.

Experimental Procedure and Data reductioun

R134a was used as the working fluid. The liquid temperature was supplied at room temperature. The liquid subcooling varied from 0.5 to 5°C, by changing the test section pressures. The liquid mass flux raged from 100 to 330 kg/m²s. The first test procedure was to adjust the control valves in order to get the desired mass flux and pressure. When these values were stable, the heater was turned on and the heating power was increased step by step. At each power level, at least 6 minutes of data were taken, with the time depending on how long it took to reach a stable state. Data were taken continuously until liquid superheat disappeared, i.e., the readings of T_{ch1}-T_{ch4} were the same as saturation temperature corresponding to the test section pressure. During the experiments, the variation of mass flux was kept within ± 5%; inlet subcooling, within ± 0.2°C; and saturation temperature, within ± 1°C.

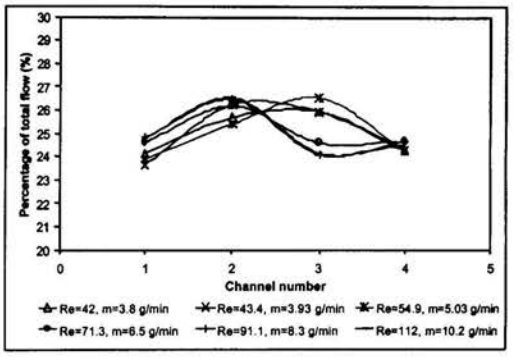

Figure 3: Water flow distribution in microchannels under different mass flow rates (Reynolds numbers)

The total heat generated by the electrical heater was calculated by multiplying the voltage and current across the heater. The test section was insulated with 5mm-thick rubber insulation. Heat losses to the environment were estimated as negligible. Axial heat conduction along the length of the tube was also negligible. The heat flux value was calculated by assuming that the same amount of heat had been added to each of the four channels. When subcooled liquid is heated, and especially when liquid superheat occurs, more heat will be added to the front part. Therefore, the calculated heat flux is the average over the entire heating section. Mass flux G was calculated assuming a uniform distribution among the four channels.

Auxiliary tests with water were preformed to evaluate the distribution, energy balance, and temperature measurements. After the heating section, the water bulk temperature was measured (T_{ch1}-T_{ch4} in Figure 2). The high thermal conductivity of the aluminum permitted the assumption of a uniform temperature heating condition. Therefore, the differences between T_{ch1}-T_{ch4} were attributed to maldistribution. The fraction of flow in each channel can be calculated, given the heating power, inlet temperature, as well as mass flow rate of the water. As shown in Figure 3 for Reynolds numbers ranging from 42 to 112, the percentage of total flow in each of the four channels was within 25% ± 1.5%, indicating good liquid flow

distribution. Since liquid refrigerant was supplied to the inlet-distribution header during the flow boiling test, this also indicated good distribution of R134a in the flow boiling experiments before the onset of nucleate boiling (ONB). The situation after ONB is quite complicated. An analysis of that is given later.

The energy balance of the test section was determined to be within ± 5% for all the six runs (Figure 3). Thus, the heat loss from the test section was rather small, and the test section was appropriate for our measurements.

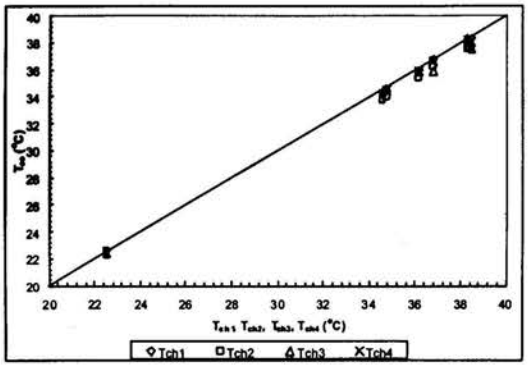

Figure 4: Comparison of T_{eo} with $T_{ch1} \sim T_{ch4}$ in water flow test

The effectiveness of thermocouples T_{ch1}-T_{ch4} in measuring bulk fluid temperatures was also evaluated by comparing the measurements of T_{ch1}-T_{ch4} with the exit temperature T_{eo}. As shown in Figure 4, T_{ch1}-T_{ch4} under-represent the bulk fluid temperature T_{eo} within 0 to −1 °C. This difference was attributed to heat loss from the test section into the environment.

RESULTS AND DISCUSSION

As described previously, the power level was increased from zero and data were taken continuously until liquid superheat disappeared. Figure 5 illustrates the experiment with a mass flux of 164 kg/m^{2}s, an inlet temperature of 23 °C (inlet subcooling of 5 °C), and a saturation temperature of 28 °C.

For the first 700 seconds (region I in Figure 5), the heater was turned off. All the temperatures remained the same and the pressure drop was low, which indicates that the fluid in and out of the channels was in liquid phase.

In region II of Figure 5, when the heating power was adjusted to 0.5W ($q'' \approx 5.5$ kW/m^2), the bulk fluid temperatures(T_{ch1}-T_{ch4}) increased to values higher than the saturation temperature. The outlet temperature (T_{eo}) was still a little bit lower than the saturation temperature, which was attributed to the heat loss of the metal T-junction used to insert the thermocouple. When the heater power level was increased to 0.7 W ($q'' \approx 8$ kW/m^2), the bulk fluid temperatures in all four channels were brought to about 32 °C; while the outlet temperature reached and remained at the saturation temperature of about 28°C. At the same time, vapor slugs (or plugs) were observed at the exit of the test section. Obviously, the fluid reached the boiling condition; but for some reason, boiling did not begin in the microchannels. So the fluid remained in a superheated liquid state. When the metastable superheated liquid reached the macroscale exit tube, boiling occurred and the superheat disappeared. This process continued for two power levels of 0.9 W and 1.3 W. Figure 5 (c) shows that the total pressure drop remained almost the same and at low values in regions I and II, which is another proof of liquid superheat state in region II.

When the power level was adjusted to 1.7 W ($q'' \approx 20$ kW/m^2), the bulk fluid temperatures in all four channels increased from 42°C to 46°C. Suddenly the temperatures dropped: channel four, to 29°C; channel three, to 33°C; and channel one and two, to 39 °C. These dropping temperatures were accompanied by a sudden increase in the total pressure drop, as shown in Figure 5 (c). After that, the measured bulk temperatures in region III exhibited a very strange behavior. The bulk temperatures increased and decreased alternatively, with enormous differences between various channels; while the measured total pressure drop increased monotonically.

The process that occurred in region III can be explained as follows. For some reason, boiling occurred earlier in channel 4 than in the others, and the bulk fluid temperature dropped to approximately saturation temperature. This point is taken as the onset of nucleate boiling (ONB). The bulk fluid temperature decreasing introduced more heat into this channel and increased the wall heat flux. Higher heat flux also, in turn, helped nucleation in this channel. The boiling introduced larger pressure drop to channel 4, which reduced the flow rate and caused the total flow to be redistributed among the channels. The channels with no or less boiling must have had a higher mass flow rate in order to balance the pressure drop. Therefore, the bulk fluid temperatures dropped to different values, and the total pressure drop went up. Because liquid superheat is a non-equilibrium metastable state, the boiling process may also be unstable and related to other factors such as heating time, history, etc. All these along with flow redistribution in parallel microchannels made the whole process a very complicated one, resulting in the strange behavior observed in region III.

Finally, in region IV, after the heater power was adjusted to 4.3 W ($q'' = 50$ kW/m^2) for 2 to 3 minutes, the bulk fluid temperatures in all four channels dropped to and remained at the saturation temperature. This process was also accompanied by a sudden jump in pressure drop. In region IV, boiling occurred in all four channels, and a stable two-phase flow was obtained. Therefore, energy balance could be used to estimate the vapor quality, which was determined to be about 70%.

Same experiments have been repeated for different mass fluxes (100 to 310 kg/m^{2}s), and inlet subcoolings (0°C to 5 °C). Similar liquid superheat phenomenon was recorded, and all four regions, as shown in Figure 5, were identified. However, the extents of superheat were different for different mass fluxes and inlet subcoolings.

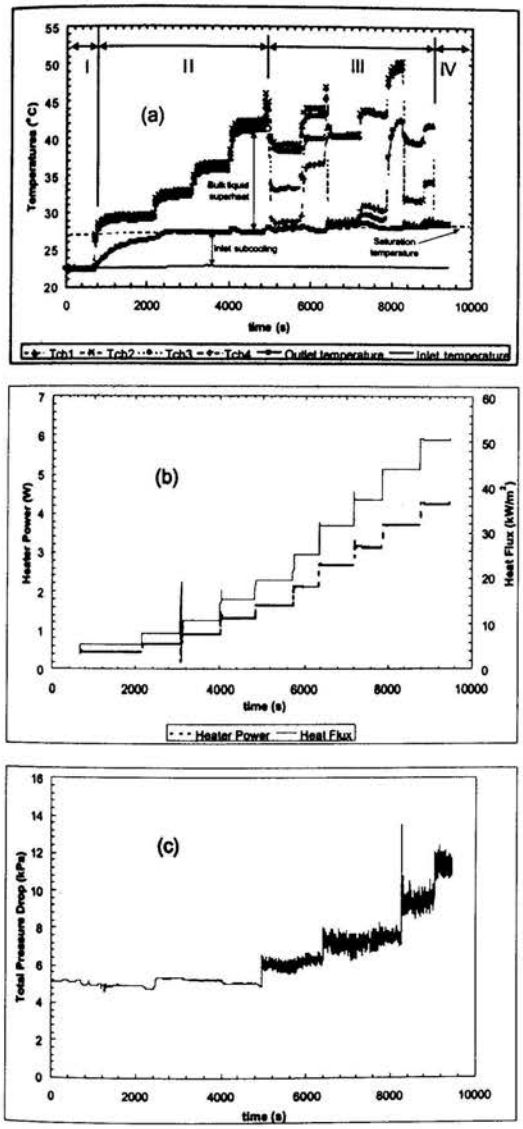

Figure 5: Flow boiling in microchannels, G = 164 ± 5 kg/m^{2}s, T_{ci} = 22.7 ± 0.2°C, T_{sat} = 28 ±1°C

When designing microchannel heat sinks with subcooled liquid flow boiling, great attention must be paid to the phenomenon of bulk liquid superheat. Normally, heat exchangers with phase change are preferred because they provide a relatively more uniform wall temperature and a higher heat transfer coefficient. However, when liquid superheat occurs, the evaporator performs in a fashion similar to single phase flow heat exchangers. Even worse, when bubbles form in the superheated liquid, the growth rate is very rapid; and the explosive formation of vapor is often a source of instability[13], as indicated in region III of Figure 5. Therefore, it is very important to understand the mechanism behind the bulk-liquid superheat phenomenon in the microchannels.

In Figure 5 region II, boiling did not begin in the microchannels until the measured bulk liquid superheat reached 18°C at a wall heat flux of about 20 kW/m^2. In fact, the wall superheat in the heating section $T_{wi} - T_{sat}$, which is of more interest for nucleation initiation, should be higher than the bulk liquid superheat $T_{bulk} - T_{sat}$, because the wall is heated from outside. Therefore, the bulk liquid superheat can be taken as a conservative estimation of the wall superheat $T_{wi} - T_{sat}$. So it is safe to say that ONB did not occur at wall superheat below 18°C. This wall superheat is much higher than what normally observed for heterogeneous nucleation boiling in macroscale channels.

In macroscale channels, the superheated liquid state owes its existence to an energy barrier that causes the vapor embryo to collapse, rather than lead to nucleation, if it is less than a critical size [11]. Typically, high liquid superheat before ONB occurs in the glass apparatus, where the range of active cavity sizes is severely restricted, or in well wetting fluids at low reduced pressures, such as nitrogen, R-12, and R-114 [13]. The surface roughness of the channel under investigation has been measured at 0.3 μm for upper and bottom walls. Kandlikar and Spiesman [14] reported that the difference in wall superheat for four surfaces with roughness of 0.188 μm to 3.06 μm is within 0-30%. Thus, surface roughness seems not to be the reason for the high liquid superheat reported. For sbucooled R134a flow boiling in macroscale annular ducts, Yin *et al.* [15] reported wall superheat as high as 18°C before ONB, but this is limited to very low saturation temperatures only (-5 ~ 1 °C), and the wall superheat decreased rapidly when saturation temperature increased. It looks like experimental results cannot be explained by macroscale nucleation theories.

In fact, the high bulk liquid superheat phenomenon in the current work revealed suppression of bubble growth by the confined wall of the microchannels. This is obvious because we observed that as soon as the superheated liquid exited into a larger tube, boiling occurred and liquid superheat disappeared instantly. Peng *et al.* [8] measured nucleation temperatures for static water, methanol, ethanol, and carbon tetrachloride boiling on a platinum wire confined in capillary tubes. Their results demonstrated that the bubble nucleation temperature increased markedly as the size of microchannel decreased. Their experimental results also support the theoretical work of Peng *et al.* [7], where they derived the correlation for bubble nucleation temperature in microchannels:

$$\Delta T_{sup} \geq \frac{4AT_{sat}(v''-v')\sigma}{h_{fg}D_h} \qquad (1)$$

where A is an empirically determined constant, with a suggested value of A = 280. Taking R134a at T_{sat} = 28°C as an

example, the calculated results were plotted according to decreases in the channel hydraulic diameter. As shown in Figure 6, the wall superheat needed for nucleation increases dramatically when the channel hydraulic diameter is reduced to about 100 μm. This is consistent with the current experimental results, suggesting that nucleation is very difficult to achieve in microchannels with hydraulic diameter of about 137 μm.

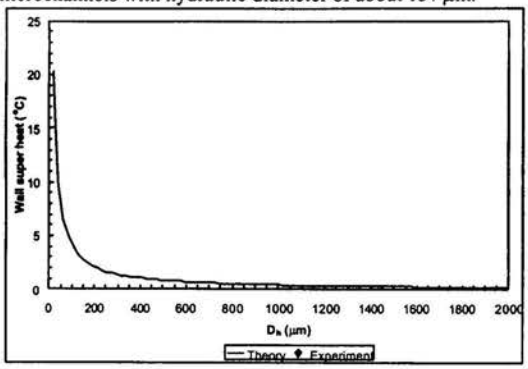

Figure 6: Comparison of measurement with the prediction of Peng et al. [7]

CONCLUSIONS

Metastable bulk liquid superheat phenomenon of R134a flow boiling in 75 × 800 μm microchannels was investigated experimentally. The specially designed test section provided a way to measure the bulk fluid temperature in microchannels non-intrusively. The bulk liquid superheat before the onset of nucleation boiling (ONB) was as high as 18 °C, at surface heat flux of 20 kW/m^2, saturation temperature of 28 °C, inlet subcooling of 5 °C, and mass flux of 164 kg/m^{2}s. The wall superheat was estimated to be even higher than the bulk liquid superheat before ONB. In addition, the bulk liquid superheat disappeared and two-phase flow was achieved when the fluid reached the conventional scale tubes. The experimental results indicate that the typical bubble growth mechanism observed in macrochannels is depressed for refrigerant R134a flow boiling in microchannels with hydraulic diameter close to 100 μm.

ACKNOWLEDGMENTS

This present work was supported under DARPA DSO, contract #DABT63-97-C-0069.

REFERENCES

[1] Lin, L., Udell, K.S. and Pisano, A.P., 1993, "Vapor bubble Formation on a Micro Heater in Confined and Unconfined Micro Channels," Heat Transfer on the Microscale ASME, Heat Transfer Division, Vol. 253, pp. 85-93

[2] Jiang, L., Wong, M. and Zohar, Y., 1999, "Micro-channel Heat Sink with Integrated Temperature Sensors for Phase Transition Study," Proceedings of the IEEE Micro Electro Mechanical Systems (MEMS), IEEE, Piscataway, NJ, USA, 99CH36291, pp.159-164

[3] Jiang, L., Wong, M. and Zohar, Y., 2000, 'Phase Change in Microchannel Heat Sink under Forced Convection Boiling," Proceedings of the IEEE Micro Electro Mechanical Systems (MEMS), pp.397-402

[4] Peng, X.F. and Wang, B.X., 1993, "Forced Convection and Flow Boiling Heat Transfer for Liquid Flow Through Microchannels," Int. J. Heat Mass Transfer, Vol.36, No. 14, pp. 3421-3427

[5] Peng, X.F. and Wang, B.X., 1994, "Liquid Flow and Heat Transfer in Microchannels with/without Phase Change," Proc. Int. Heat Transfer Conf., 10th, Vol.1, pp.159-177

[6] Peng, X. F. and Wang, B.X., 1994, "Evaporating Space and Fictitious Boiling for Internal Evaporation of Liquid," Science Foundation in China, 2(2), pp.55-59 (English)

[7] Peng, X.F., Hu, H.Y. and Wang, B.X, 1998, "Boiling Nucleation During Liquid Flow in Microchannels," Int. J. Heat Mass Transfer, Vol. 41, No.1, pp.101-106

[8] Peng, X.F., Tien, Y. and Lee, D.J., 2001, "Bubble Nucleation in Microchannels: Statistical Mechanics Approach," Int. J. Heat Mass Transfer, Vol. 44, pp.2957-2964

[9] Peng, X.F., Liu, D, Lee, D.J. Yan, Y. and Wang, B.X., 2000, "Cluster Dynamics and Fictitious Boiling in Microchannels," Int. J. Heat Mass Transfer 43 (23) pp. 4259-4265

[10] Shannon, M. A., Philpott, M. L., Miller, N. R., Bullard, C. W., Beebe, D. J., Jacobi, A. M., Hrnjak, P. S., Saif, T., Aluru, N., Sehitoglu, H., Rockett, A. and Economy, J., 1999, "Integrated Mesoscopic Cooler Circuits (IMCCS)," American Society of Mechanical Engineers, Advanced Energy Systems Division (Publication) Aes. v 39 pp. 75-82

[11] Selby, J.C., Philpott, M.L. and Shannon, M.A., 2001, "Fabrication of Mesoscopic Flexible, High Pressure, Microchannel Heat Exchangers (MHEx)," Transaction of NAMRI/SME, Volume XXIX

[12] Das, M., Chatterjee, B.K., Roy, B. and Roy, S.C., 2000, "How High can the Temperature of a Liquid be Raised without Boiling," Physical review E, vol.62, no. 4

[13] Collier, J.G. and Thome, J.R., 1996, "Convective Boiling and Condensation," Third edition, Oxford science publications

[14] Kandlikar, S.G. and Spiesman, P.H., 1998, "Effect of Surface Finish on Flow Boiling Heat Transfer," ASME HTD-Vol. 361-1, Proceedings of the ASME Heat Transfer Division

[15] Yin, C. P., Yan, Y.Y., Lin, T.F. and Yang, B.C., 2000, "Subcooled Flow Boiling Heat Transfer of R-134a and Bubble Characteristics in a Horizontal Annular Duct," International Journal of Heat and Mass Transfer, 43, pp.1885-1890

HEFAT2002
1st International Conference on Heat Transfer, Fluid Mechanics, and Thermodynamics
8-10 April 2002, Kruger Park, South Africa
BE1

PRESSURE DROP IN A PLATE EVAPORATOR FOR REFRIGERATORS

E. Björk
Dept. of Energy Technology
Div. of Applied Thermodynamics and Refrigeration
Royal Institute of Technology
SE-100 44 Stockholm, Sweden
E-mail: bjork@egi.kth.se

ABSTRACT

This study examines the two-phase refrigerant side pressure drop in a plate evaporator used in a refrigerator. The refrigerant was Isobutane (R600a). The refrigerant channel had a non-circular cross-section best described as a circular segment. It was found that the best estimation of the frictional pressure drop was with a homogeneous method and with a modified version of the separated Lockhart and Martinelli method.

INTRODUCTION

Despite the fact that domestic refrigerators and freezers are the most common application of the vapour compression cycle, not much can be found in the open literature on how to calculate the pressure drop in their evaporators. This two-phase pressure drop calculation is complicated by a winding refrigerant path with frequent bends and sometimes, as in the system studied in the present article, by a non-circular cross-section.

NOMENCLATURE

A	area (m^2)
B	constant
C	constant
C_f	skin-friction drag coefficient (-)
d	diameter (m)
d_h	hydraulic diameter (m)
F	force (N)
f	friction factor (-)
G	mass flux (kg/m^2s)
g	gravitational acceleration (m/s^2)
k	pressure drop coefficient (-)
L	length (m)
M	constant (-)
m	constant (-)
$\dot{m}$	mass flow (kg/s)
n	constant (-)
P	perimeter (m)
q	cooling capacity (W)
R	radius (m)
Re	Reynolds number (-)
t_1	condensing temperature (°C)
t_2	evaporation temperature (°C)
$\bar{u}$	average velocity (m/s)
x	quality (-)
z	length (m)

Greek

α	void fraction (-)
X	Martinelli parameter (-)
Δp	pressure difference (Pa)
ϕ^2	two-phase multiplier (-)
θ	inclination (°)
μ	viscosity (Ns/m^2)
$\bar{\mu}$	averaged viscosity (Ns/m^2)
ρ	density (kg/m^3)

Subscripts

l	liquid
v	vapour
lo	liquid only
vo	vapour only
tp	two-phase
h	hydraulic
e	entrance length

EXPERIMENTAL SET-UP

Experiments were conducted with a modified standard refrigerator (Electrolux ER8893C) under steady state conditions. It consisted (figure 1) of a piston compressor (Electrolux HL60AH), a wire on tube condenser using natural convection heat transfer, a capillary tube as expansion device (partly heat exchanged against the suction line) in series with a needle valve, and an evaporator also using natural convection heat transfer. Isobutane (R600a) was used as refrigerant. The system contained approximately 300ml mineral oil (standard charge) where most of the oil is hold-up in the compressor house. The evaporator studied (660mm*490mm) was positioned vertically, in the cabinet, at the back wall (cold wall evaporator). It was of plate type, which means two flat aluminium sheets embossed and bonded with a thin Zinc-layer, as to provide a path for the refrigerant flow between the two sheets. On the front side, pressure taps were attached on 16 positions along the refrigerant path (figure 1 and 2) with tubing leading upwards towards the transducer to avoid concentration of oil. A valve arrangement multiplexed the obtained pressure to a pressure difference transducer (Druck 0,35 bar). In this way a single pressure transducer was used to measure all the different pressure drops on the evaporator, stepwise addressing every position. Absolute pressure was measured on both the low (Druck 2,5 bar) and

the high-pressure side (Druck 16 bar). The refrigerant mass-flow was measured using a coriolis type meter (Micro Motion D6) positioned downstream the condenser. A hand-regulated needle valve was positioned just downstream the mass flow meter (and upstream the capillary tube). Thermocouples of type T were placed, on the surface, at different positions on the system. Inside the refrigerator cabinet a variable heat load was placed. The measurement data was collected with a logger (Agilent 34870A) and stored on an ordinary PC with HP VEE software. The software also controlled the valve arrangement via a relay output.

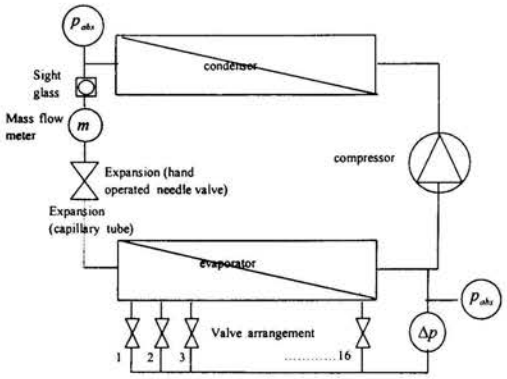

Figure 1: Experimental set-up.

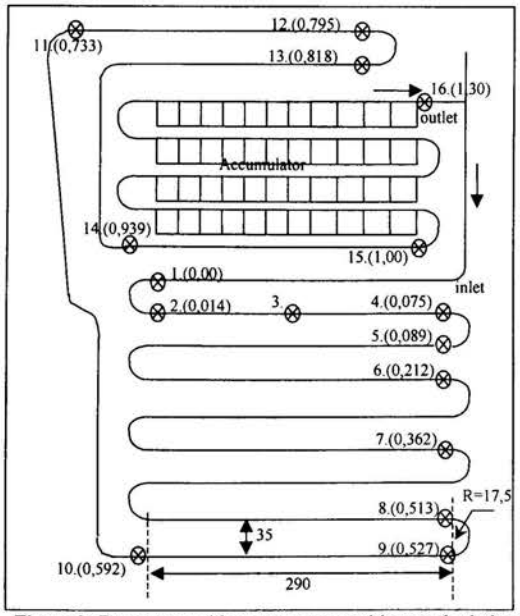

Figure 2: Evaporator with pressure tap positions and relative length.

MEASUREMENT PROCEDURE

All experiments were carried out in a climate chamber held at 25°C. By varying the heat load, inside the refrigerator cabinet, different cabinet air temperatures were achieved giving different evaporating temperatures and hence different refrigerant mass flows. After a heat load was set, the needle valve was adjusted so that superheat was achieved in the accumulator inlet as can be seen in figure 3 (i.e. vapour quality x=1 at relative length 1,0. See figure 2 for length scale). It was also checked through a sight glass, at the condenser side, that sub-cooled refrigerant entered the mass-flow meter. To achieve both these conditions the refrigerant charge had to be increased compared to the original charge (from 34g to approximately 55g). The pressure drop in the evaporator was measured 10 times at each position with a scan interval of about five seconds. This was repeated at least four times under steady state conditions giving no less than 40 measurement points at each position for every test condition. It was checked after a test series that no oil had concentrated in the tubing by simply turning off the cooling system while pressure measurement continued.

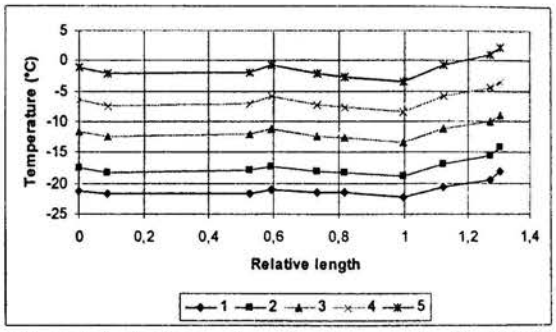

Figure 3: Surface temperatures along the evaporator. Superheating starting at accumulator inlet (Relative length 1,0)

DATA REDUCTION

Some disturbance at the measured pressure drop could be expected immediately after a shift in connected pressure tap positions. This could clearly be seen at the shift from position 16 to 1. Due to this, the first four scans at each position were discarded. The remaining data was averaged at every position over at least 24 measurement intervals.

EXPERIMENTAL RESULTS

Measurements were done under five test conditions as described by table 1. As can be seen the saturation temperature in the evaporator, calculated from pressure, differed somewhat from the measured surface temperature given in figure 3. This is likely the consequence of a boiling heat transfer resistance, a heat transfer resistance through the evaporator wall and perhaps some increase of the measured surface temperature due to ambient air heating through the thermocouple wire.

test nr	t_2 (°C)[1]	t_1 (°C)[2]	*mass flow* $\dot{m}$ (g/s)	*mass flux* G (kg/m²s)[3]	*inlet vapour quality* x (-)[4]	*cooling capacity* q (W)[5]
1	-23,1	39,5	0,280	20,34	0,136	94,1
2	-19,7	41,8	0,331	24,03	0,134	111,0
3	-14,0	45,3	0,428	31,10	0,126	143,0
4	-9,3	48,5	0,519	37,67	0,127	172,2
5	-4,3	51,9	0,627	45,50	0,132	205,8

Table 1: Test conditions.

Notes:

1) Saturation temperature from averaged pressure, position 1 to 15.
2) Saturation temperature from condenser pressure.
3) Mass flow divided by cross section area 13,774mm².
4) Calculated from enthalpy at condenser outlet minus enthalpy change over capillary-suction line heat exchanger.
5) Calculated as refrigerant mass flow times enthalpy change from evaporator inlet to outlet.

At test number one the heat load was turned off. In number two to five it was altered from 50 to 200W in steps of 50W. The measured mass flow and calculated cooling capacity were compared to compressor data and were found to be within 10%. As can be seen in figure 4 the pressure drop increases along the evaporator (the pressure drop along the evaporator is for simplicity considered as positive). From position 1 to 10 (relative length 0 to 0,6) the increase is somewhat lower compared to the rest of the evaporator. Also seen from the figure is, as expected, that a higher mass flow gives a higher pressure drop.

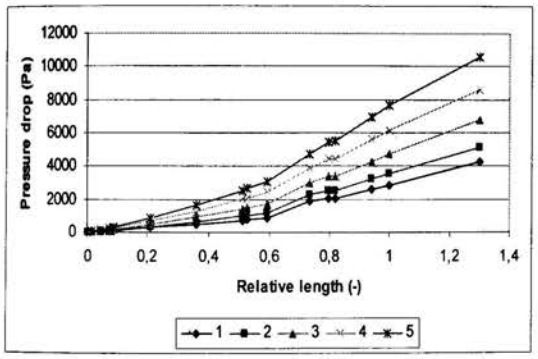

Figure 4: Measured pressure drop along the evaporator. Numbers referring to test (see table 1)

ANALYSIS

This analysis aims to find applicable correlations for calculating the two-phase flow pressure drop in the evaporator studied. Only the part of the evaporator with constant cross section (relative length 0,00 to 1,00 in figure 2) will be analysed. In the following it will be assumed that the flow is practically incompressible in the sense that the density of each phase is constant. This assumption simplifies separated flow calculations and is acceptably justified in this case since the pressure drop is small compared to the absolute pressure in the evaporator (4% to 6%). However local properties, including density of the vapour, will be used throughout the calculations. It is further assumed that the flow is steady, one-dimensional and that the two phases are in local thermodynamic equilibrium.

The total pressure drop can generally be subdivided into three components for a straight, constant cross section channel: the frictional, the change of momentum (or acceleration) and the elevation (or gravitational) component. Since the evaporator studied consists of a number of bends a separate deflection component for the bends is expected giving a total of four components.

$$\Delta p_{total} = \Delta p_{friction} + \Delta p_{acc.} + \Delta p_{grav.} + \Delta p_{bends} \qquad (1)$$

The friction pressure drop is often the largest component and will be given the largest attention in this article. First, however the other components will be treated and lumped together. It will be shown that they are a minor part of the total pressure drop.

Pressure drop from acceleration, gravitation and bends.

When calculating the acceleration and gravitational pressure drop, knowledge about the void fraction is necessary. It is also essential to know the quality along the evaporator (dx/dz). Here it will be assumed that the quality linearly approaches 1 with evaporator length. That is, the heat flux is evenly distributed. The influence of a distributed heat flux was also tested (but will not be shown here) where the local heat flux was proportional to the evaporator surface area. For instance the position 9 to 11 (figure 2) experienced a higher heat flux compared to position 1 to 8. Only a small difference in the calculated pressure drop, compared to the linear model, could be noted with this approach.

It was shown by Butterworth [3] that several of the available void fraction correlations could be cast in the general form:

$$\alpha = \left[1 + B\left(\frac{1-x}{x}\right)^{n_1}\left(\frac{\rho_v}{\rho_l}\right)^{n_2}\left(\frac{\mu_l}{\mu_v}\right)^{n_3} \right]^{-1} \qquad (2)$$

Where the constants from different models are given in table 2.

Correlation or model	B	n_1	n_2	n_3
Homogeneous	1	1	1	0
Zivi	1	1	0,67	0
Lockhart and Martinelli,tt	0,28	0,64	0,36	0,07
Thom	1	1	0,89	0,18
Baroczy	1	0,74	0,65	0,13

Table 2: Different void correlations

For comparison the CISE correlation as described by Whalley [15] was also used. Using local properties of Isobutane calculated from measurement data from test number 3 one gets the results in figure 5.

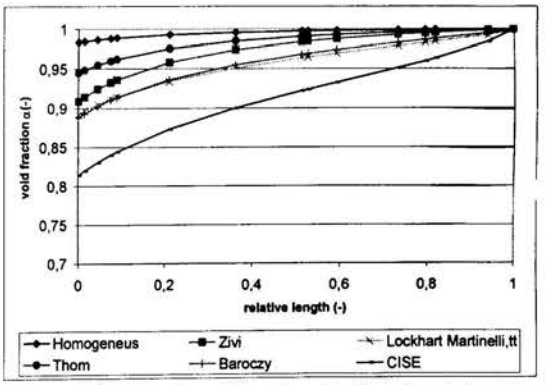

Figure 5: Void fraction, different models. Data from test number 3

As can be seen the void fraction increases with relative length. At relative length 0,0 the vapour fraction was approximately 0,2 in all tests while at relative length 1,0 it was 1. The CISE correlation gives the lowest void fraction, the homogeneous the highest. The void fraction of the homogeneous flow is showing some deviation from a straight line due to a change in the density ratio with pressure.

The acceleration and gravitational pressure drop can now be calculated according to Whalley [15]:

$$-\left(\frac{dp}{dz}\right)_{acc+grav} = G^2 \frac{d}{dz}\left[\frac{x^2}{\alpha\rho_v} + \frac{(1-x)^2}{(1-\alpha)\rho_l}\right] + \left[\alpha\rho_v + (1-\alpha)\rho_l\right]g \times \sin\theta \quad (3)$$

In this formula the first term represents the acceleration pressure drop and the second the gravitational pressure drop. The part $\sin\theta(\times dz)$ is replaced, in this analysis, with the discrete height value measured from the position with relative length 0. The underlying assumption here is that the flow can be considered as a liquid-gas column with a mean density to create a gravitational pressure. The acceleration pressure drop can be seen in figure 6, the gravitational in figure 7.

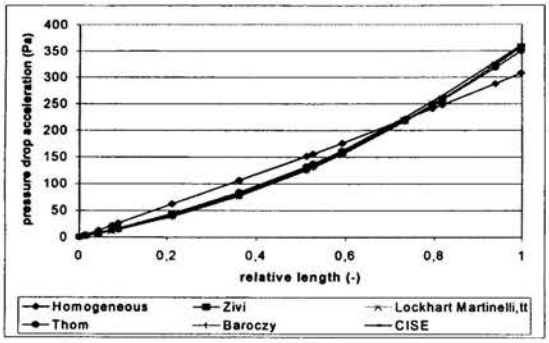

Figure 6: Acceleration pressure drop, different models. Data from test number 3.

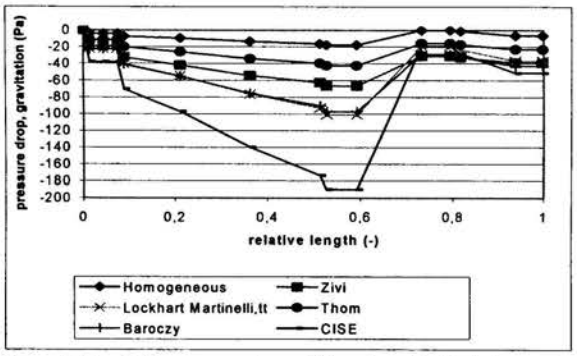

Figure 7: Gravitation pressure drop, different models. Data from test number 3.

As can be noted in figure 6 all the different void fraction models give similar acceleration pressure drop except the homogeneous. The results are consistent with the analysis given by Whalley [15] where it is shown that a homogeneous flow will give a linear acceleration pressure drop with quality while separated flow will give exponential shaped curves. As also can be seen, all the different curves, except the homogeneous, seem to follow the same line, despite different void fractions. This is due to a balancing effect of the ratio between quality and void in equation (3) levelling out each other for the different models. The calculated gravitational pressure drop (figure 7) is slightly more scattered, giving the highest pressure-increase at the lowest section of the evaporator with the CISE model. This is consistent with the lower void fraction as seen in figure 5.

For the calculation of pressure drop in bends the Chisholm [5] method was used. This method, which is of the two-phase multiplier type, assumes homogeneous flow through the bends. The pressure drop obtained is the deflection pressure drop, through the bend, and should be added to the frictional pressure drop through the bend (where the bend is considered as a straight channel).

$$\Delta p_b = \Delta p_{b,lo}\left[1 + \left(\frac{\rho_l}{\rho_v} - 1\right)(Bx(1-x) + x^2)\right] \quad (4)$$

where $\Delta p_{b,lo}$ is the deflection pressure drop obtained through the bend with single phase liquid only.

$$\Delta p_{b,lo} = k_{lo}\frac{G^2}{2\rho_l} \quad (5)$$

$$B = 1 + \frac{2{,}2}{k_{lo}(2 + \frac{R}{d})} \quad (6)$$

Entering these formulas with R/d=5,45 (Radius of bend divided by diameter) using the hydraulic diameter, and with the pressure drop coefficient k_{lo} =0,18 for a 90° bend circular tube of brass [16] and a pressure drop coefficient of k_{lo}=0,216 for a 180° bend using a correction factor of 1,2 [10]. The pressure drop for a bend positioned at a given relative length is shown in figure 8.

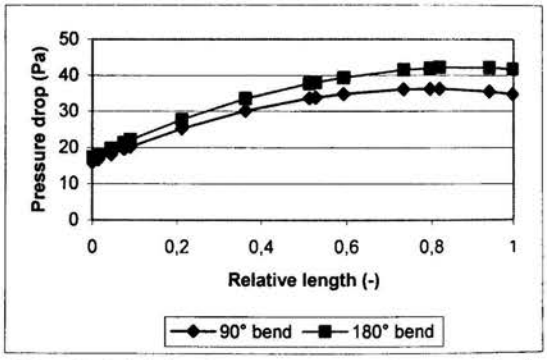

Figure 8: Calculation of pressure drop. Data from test number 3

Figure 8 shows that the pressure drop over a bend is larger, as expected, for a 180° bend compared to a 90° bend. Also seen in the figure is that the pressure drop for a bend increases with length (i.e. quality). Summing up all the different 90° and 180° bends, in the evaporator studied, the results of figure 9 are obtained.

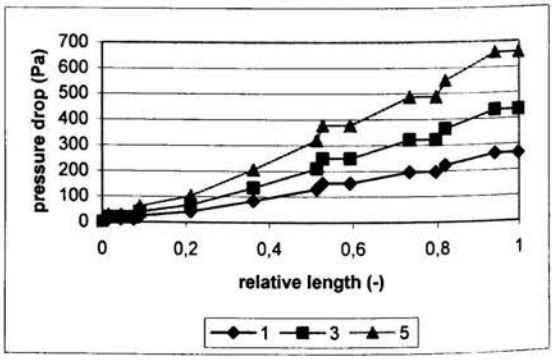

Figure 9: Pressure drop calculation due to bends integrated over length. Data from test number 1, 3 and 5.

Figure 9 shows that a higher mass flow gives a higher pressure drop. The pressure drop in the bends could not be verified experimentally. It is possible that local disturbances at the pressure tap positions upstream and downstream of the bends, as for instance described by Subbu et. al. [12], made it impossible to measure this small pressure differential. Finally putting together the pressure drop contribution from acceleration, gravitation and bends using the homogeneous void correlations one get the results in figure 10.

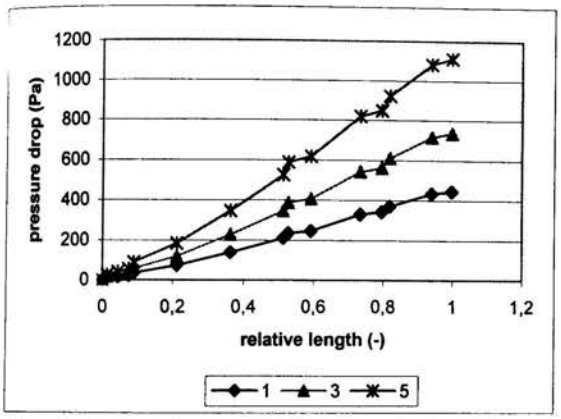

Figure 10: Pressure drop calculation due to acceleration, gravitation and bends. Data from test number 1, 3 and 5.

For comparison the Lockhart and Martinelli (turbulent-turbulent) void correlation was also tested with no significant change in the result. Figure 10 shows that the expected pressure drop for test number 5 is about 1100 Pascal. The measurement for this test number (figure 4) gave about 7600 Pascal and it can be concluded (assuming that the theoretical results are reasonably correct) that the major part of the total pressure drop comes from frictional forces.

Frictional pressure drop

Most correlations use the concept of a two-phase multiplier to calculate the two-phase frictional pressure drop. The single-phase pressure drop is calculated separately, in the ordinary way, using the friction factor and is multiplied with this multiplier as:

$$\Delta p_{friction,two-phase} = \phi^2 \times \Delta p_{friction,one-phase} \qquad (7)$$

where

$$\Delta p_{friction,one\_phase} = \frac{2 \times f \times G^2}{\rho \times d} \qquad (8)$$

Since the one-phase pressure drop can be calculated in different ways using the mass flux from liquid, the gas or local mass fluxes of liquid or gas different associated multipliers must be used. In the following analysis two methods will be described, the homogeneous [4] and the Lockhart Martinelli [4] method. First, however, some discussion about the non-circular cross section of the refrigerant channel in the evaporator studied.

As a consequence of the manufacturing process and the aesthetic demand of a flat surface, the refrigerant cross-section is not circular. It can best be described as a circular segment with a radius of 4 mm and a channel width of 2,5 mm. (figure 11). In the corners there is a small zinc deposition, from the manufacturing process (exaggerated in figure 11).

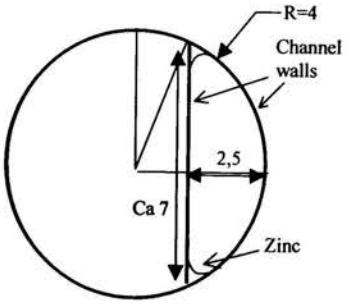

Figure 11: Refrigerant channel cross-section

One approximate way of treating a non-circular channel is to use the concept of a hydraulic diameter defined as:

$$d_h = \frac{4A}{P} \qquad (9)$$

A is here the cross section area and P the wetted perimeter. The hydraulic diameter, obtained with this equation, was 3,21 mm. The hydraulic diameter concept originates from the definition of the friction factor. A force balance over a circular tube gives [1]:

$$F = (2\pi RL) \times (\frac{1}{2}\rho\bar{u}^2) \times f \qquad (10)$$

where the first parenthesis is the surface area and the second the kinetic energy brought with the fluid. This force may also be described with the pressure difference over the length L (assuming horizontal flow):

$$F = \Delta p \times (\pi R^2) \qquad (11)$$

where the parenthesis is the cross section area. Elimination gives (with d=2R):

$$f = (\frac{1}{4}\frac{d}{L}) \times (\frac{\Delta p}{\frac{1}{2}\rho\bar{u}^2}) \qquad (12)$$

Here the first parenthesis is the ratio between the cross section area and the surface area. The numerical value 4 in the denominator, which is the scaling factor from conversion radius to diameter, explains the "4" in the definition of the hydraulic diameter (9). The condition that has to be met when using the hydraulic diameter concept for a non-circular duct is that the mean shear stress at the boundary is the same as for a circular cross section. In a circular tube contours of equal velocity are parallel to the perimeter giving a uniform shear stress. For a rectangular duct, however, the contours of equal velocity are not parallel to the surface, especially near the corners. In general, the less the cross section deviates from the circular the more reliable the concept with hydraulic diameter will be. It is known that for turbulent flow the shearing force is much more evenly distributed due to *turbulent secondary flow* [16] compared to laminar flow. For a rectangular duct with an aspect ratio of less than 8 [8] the concept with hydraulic diameter is reasonably justified for turbulent flow.

An experiment was performed on the cross section studied with single-phase gas. Using the definition of the friction factor (12) with the diameter calculated as (9) and experimental results of pressure drop, an experimental friction factor was obtained. This was compared

against a theoretical friction factor calculated with the well-known smooth-pipe, Blasius equation (13) also using the hydraulic diameter (9). In figure 12 it can be seen that the experimental friction factor is well fitted with the Blasius equation, using the hydraulic diameter calculated in the conventional way. It was found that with a diameter deviating from this value (3,21mm) the two different methods mismatched. This is a good indication that the hydraulic diameter concept is applicable for the cross section studied under turbulent conditions.

$$f = 0{,}079\left(\frac{Gd_h}{\mu}\right)^{-0{,}25} \qquad (13)$$

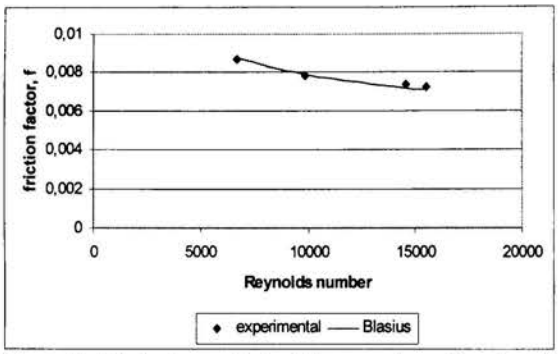

Figure 12: Friction factor calculated from experimental results with single-phase gas compared to Blasius equation.

In the case of laminar flow, where the shear force no longer can be assumed evenly distributed, analytical exact solutions can in principle be derived for every cross section. For the circular cross section an exact solution gives the classical:

$$f = \frac{16}{\mathrm{Re}} \qquad (14)$$

For the circular segment as described by figure 11 (neglecting the Zinc) an exact solution [9] gives:

$$f = \frac{15{,}75}{\mathrm{Re}_{d_h}} \qquad (15)$$

where Reynolds number is calculated using the hydraulic diameter (9) as characteristic length. This modest 1,6% decrease of the friction factor, compared to the circular tube, for the laminar case, is also an evidence that the concept of hydraulic diameter defined as (9) is valid in turbulent flow for the cross section studied. It has been shown [17] that a further improvement of the hydraulic diameter can be obtained for the turbulent case using the laminar duct solution:

$$d_{eff} = d_h \frac{16}{(C_f \mathrm{Re}_{d_h})_{\text{laminar}}} = d_h \frac{16}{15{,}75} = 1{,}016 d_h \qquad (16)$$

This equation holds in cross sections without unusually thin regions.

The hydraulic entrance length for single-phase flow can be calculated using the expression [16].

$$\frac{L_e}{d} \approx 0{,}06\mathrm{Re} \qquad \text{(laminar)} \qquad (17)$$

$$\frac{L_e}{d} \approx 4{,}4\mathrm{Re}^{\frac{1}{6}} \qquad \text{(turbulent)} \qquad (18)$$

The highest laminar Reynolds number used in the calculation was around 700 (liquid) giving an entry length of 0,13m. For the turbulent case Reynolds number lower than 22000 (vapour) were used giving an entry length of maximum 0,017m. In this entrance length the friction factor is slightly increased due to a sharper velocity gradient close to the walls.

In the following calculations the hydraulic diameter will be calculated using equation (9) neglecting the zinc joints in the corners. It will further be assumed that the flow is fully developed (no entrance length), and that no secondary flow exists as a result of the bends. In other words the single phase friction pressure drop will be calculated as a straight duct without entrance region. This assumption may seem crude but since the cross section is constant and the bends have fairly large radius of curvature it may be justified

In the homogeneous method two more assumptions are invoked: 1. The vapour and the liquid velocities are equal. 2. The two-phase flow behaves like a single phase having averaged two-phase fluid properties. With these assumptions it can be shown [4] that

$$\phi_{lo}^2 = \frac{f_{tp}}{f_{lo}}\left[1 + \left(\frac{\rho_l}{\rho_v} - 1\right)x\right] \qquad (19)$$

Where the friction factor for the two-phase flow is calculated as:

$$f_{tp} = M \times \left(\frac{Gd_h}{\bar{\mu}}\right)^{-m} \qquad (20)$$

M and m are respectively 0,079 and 0,25 for the turbulent case (Re>2000) and 15,75 and 1 for the laminar case. The mean viscosity is calculated as:

$$\frac{1}{\bar{\mu}} = \frac{x}{\mu_v} + \frac{1-x}{\mu_l} \qquad (21)$$

For the friction factor of liquid only (f_{lo}) the same equation (20) is used but with the viscosity taken as the liquids property.

In the Lockhart and Martinelli method [4], which is based on a separated model, the liquid and the vapour are no longer assumed to flow with equal velocities. In this method the two-phase multiplier is empirically correlated against the Martinelli parameter, defined as:

$$\mathrm{X} = \left[\frac{(dP/dz)_l}{(dP/dz)_v}\right]^{1/2} \qquad (22)$$

where (dp/dz) is the frictional pressure gradients for the liquid and the vapour as flowing alone in the pipe, respectively. The calculations of these gradients can be done as:

$$\left(\frac{dP}{dz}\right)_l = -\frac{2f_l G^2 (1-x)^2}{\rho_l d_h} \qquad (23)$$

$$\left(\frac{dP}{dz}\right)_v = -\frac{2f_v G^2 x^2}{\rho_v d_h} \qquad (24)$$

$$f_l = B \times \left(\frac{G(1-x)d_h}{\mu_l}\right)^{-n} \qquad (25)$$

$$f_v = B \times \left(\frac{Gxd_h}{\mu_v}\right)^{-n} \qquad (26)$$

B and n can for this cross section be taken as 15,75 and 1 in the laminar case (Re_l or Re_v < 2000) and as 0,079 and 0,25 for the turbulent case. Note that the product within the parenthesis of equation (25) and (26) are the Reynold numbers.

The empirical relations obtained for circular cross sections for the two-phase multipliers are:

$$\phi_l^2 = (1 + \frac{C}{X} + \frac{1}{X^2}) \quad (27)$$

$$\phi_v^2 = (1 + CX + X^2) \quad (28)$$

The recommended value of the constant C [4] is dependent of the flow regimes associated with the flow of the vapour and the liquid as flowing alone in the channel. Four combinations are possible (given in table 3).

Liquid	Vapour	Recommended value of C
Turbulent	Turbulent	20
Laminar	Turbulent	12
Turbulent	Laminar	10
Laminar	Laminar	5

Table 3: recommended values for the constant C

In these calculation the liquid was found to be laminar in all cases while the vapour was turbulent. Hence the constant C was taken to be 12. Whalley [15] showed that this constant assesses the interaction between the two phases. A higher value means larger interaction.

The comparison between calculated total pressure drop, including pressure drop from acceleration, gravitation and bends, and measured pressure drop is displayed in figure 13. Two other methods, the Pierre [11] and the Friedel [15] are also shown for comparison.

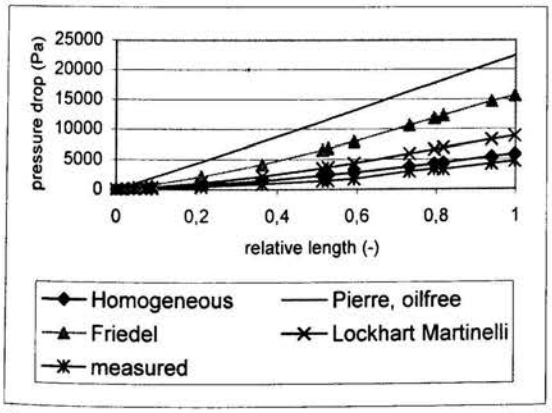

Figure 13: Comparison total calculated pressure drop, test number 3

The homogeneous method is using the homogeneous void fraction for calculating acceleration and gravitational pressure drop, the Lockhart Martinelli method and the Friedel method are using the Lockhart and Martinelli,tt (turbulent-turbulent) void fraction. All of the methods predict higher pressure-drop than measured. The homogeneous method predicts the closest values. It may seem odd that the homogeneous method, which assumes a high interaction between the two phases, gives a lower value than the Lockhart and Martinelli method with a low interaction constant. One must however remember that the two-phase multipliers as given by equation (27) or (28) and (table 3) are empirical and suited for a circular cross-section with fully developed two-phase flow. It is not known, to the knowledge of this author, how the non-circular cross-section and the influence from frequent bends change the correlation. If one assumes that the concept with a two-phase multiplier correlating against the Martinelli parameter still is applicable during these conditions the interaction constant C can be modified, using the obtained experimental data, for better pressure drop estimations. Using C=1 for Reynolds (liquid only)<500 or mass fluxes <34kg/(m²s) and C=3 above those limits a reasonable fit to measured data are achieved as shown in figure 14.

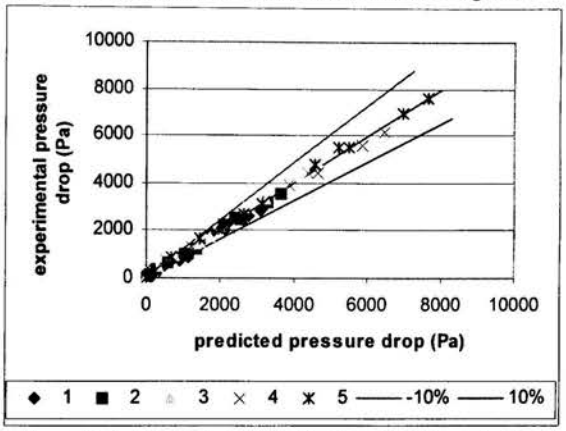

Figure 14: Lockhart Martinelli method (modified C constant) vs. experimental data. Test number 1 to 5.

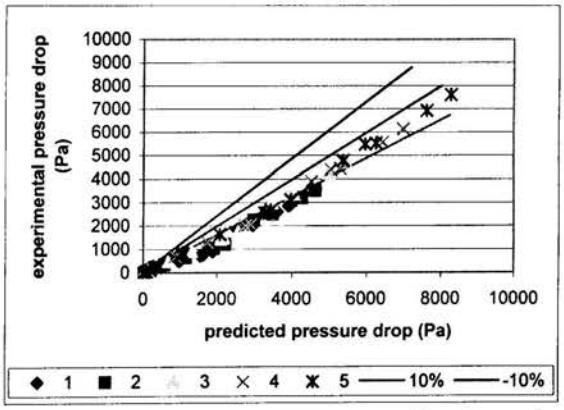

Figure 15: Homogeneous method vs. experimental data. Test number 1 to 5

The homogeneous method, as can be seen in figure 15, overestimates the pressure drop, especially at the more upstream part of the evaporator and at lower mass fluxes. It may be due to lower gas velocity at the upstream part of the evaporator and a lower interaction between the two phases with lower mass flux.

Using the Taitel and Dukler [13] flow map for horizontal flow (figure 16) one can see that the flow pattern is predicted to entirely be in the annular region. But as noted by for instance Hoogendoorn [7] the upstream conditions (bends etc) can produce different flow maps. It was found by Björk [2] that bends could act as slug generators during similar conditions. Further, the cross section studied is expected to modify the flow pattern map. Numerous evidence are also testifying

that these borderlines should be considered as the middle of a broad band.

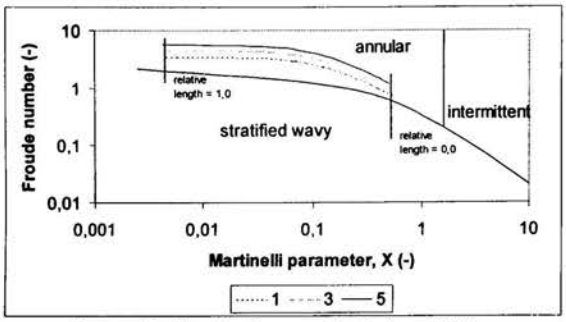

Figure 16: Flow regime map. Taitel and Dukler

CONCLUSIONS

It has been shown that best fit to data for calculating two-phase pressure drop in the evaporator studied was with a slightly modified version of the Lockhart Martinelli separated method. The interaction constant C = 1 is recommended for Re_{lo}<500 or a mass-flux less than 34 kg/m²s. Over those limits it is recommended as C = 3. This method can only be recommended at similar conditions in terms of mass-flux and cross-section. More experiments are needed with other kind of plate evaporators, with different cross-sections and refrigerant path to create a more general method. Another robust method seems to be the homogeneous method predicting slightly higher pressure drop than measured. The concept with hydraulic diameter seems to be useful in the cross section studied.

ACKNOWLEDGEMENT

The Swedish National Energy Administration and Electrolux AB supported this work.

REFERENCES

[1] Bird, R.B., Stewart, W.E., Lightfoot, E.N. Transport Phenomena (New York: John Wiley & Sons, Inc., 1960)

[2] Björk, E. 2001, "Slug formation in a domestic refrigerator with plate evaporator.", ICMF-2001 4th Int. Conf. On Multiphase Flow, New Orleans, USA.

[3] Butterworth, D., A comparison of some void-fraction relationships for co-current gas-liquid flow, Int. J. Multiphase Flow, vol. 1, pp. 845-850, 1975.

[4] Carey, Van P., Liquid-Vapor Phase Change Phenomena. 1992. Hemisphere Publishing corporation, ISBN 1-56032-074-5

[5] Chisholm, D. Two-Phase Flow in Bends. Int. J. Multiphase Flow 1980 pp. 363-367.

[6] Collier, J. G., Convective boiling and condensation. McGraw-Hill Book Company (UK), 1972.

[7] Hoogendoorn, C.J. (1959). Gas-Liquid flow in horizontal pipes, Chem. Eng., Sci. 9, 205.

[8] Massey, B.S. Mechanics of Fluids, sixth edition, 1994, Chapman & Hall.

[9] Olson, R.M., Wright, S.J. Essentials of Engineering Fluid Mechanics. Fifth edition, Copyright 1990 by Harper & Row, Publishers, Inc.

[10] Peterson, Folke 1984 Värmesystem (konventionella och lågtemperatur), tredje upplagan. Uppvärmnings och ventilationsteknik, KTH Stockholm.

[11] Pierre, B., 1964 Flow resistance with boiling refrigerants, part 1 and 2, ASHRAE Journal, September and October 1964.

[12] Subbu, S.K, Das, S.K., Biswas, M.N., Mitra, A.K. Pressure drop in U-bends for Air-Water flow. Int. J. Eng. Fluid Mech. 1990, 3, 239-248.

[13] Taitel, Y., and A.E. Dukler. 1976. "A model for predicting flow regime transition in horizontal and near-horizontal gas liquid flow." American institute of Chemical Engineering Journal. 22(1): 47-55

[14] Tong, L.S. Boiling Heat Transfer and Two-Phase Flow. Second printing, November, 1966 (New York: John Wiley & Sons, Inc)

[15] Whalley, P.B. Boiling, Condensation and Gas-Liquid Flow. Oxford Science Publication. 1987.

[16] White, F.M. Fluid Mechanics. Third edition, International edition. McGraw-Hill, 1994.

[17] White, F.M. Viscous Fluid Flow, 1991 McGraw-Hill.

HEFAT2002
1ST International Conference on Heat Transfer, Fluid Mechanics, and Thermodynamics
8-10 April 2002, Kruger Park, South Africa
CI1

FRICTIONAL PERFORMANCE OF SMALL DIAMETER RETURN BEND

Ing Youn Chen*, Yung-Wei Yang*, Bing-Chwen Yang+, and Chi-Chung Wang+√

+Energy & Resources Laboratories,
Industrial Technology Research Institute,
Hsinchu, 310, Taiwan,
E-mail : ccwang@itri.org.tw

*Graduate School of Engineering Science &Technology,
+National Yunlin University of Science and Technology, Taiwan 640
E-mail: cheniy@flame.yuntech.edu.tw

ABSTRACT

Experimental investigations of air and water single-phase flows in 180° return bends were conducted. A total of nine 180° return bends has been tested for the present study. The test tubes are made of glass tube having inner diameter (D) of 3.0, 4.95, and 6.9 mm with dimensionless tube curvature ratio (2R/D) of 3, 5 and 7, where R is the radius of center line of bend. Test range of the Reynolds number for water and air is about $400 < Re_D < 10000$. The calculated bend friction loss includes the loss in bend and the loss caused by the distorted flow in the downstream straight tube of the bend. This leads to the definition of the equivalent friction factor, f_c. For both laminar and turbulent flow the bend friction factor increases when the curvature ratio (2R/D) is reduced. However, for a given curvature ratio, the effect of tube diameter on the bend friction factor is not significant. Based on the present f_c data, correlations for laminar and turbulent friction factors for 180° return bend are proposed.

INTRODUCTION

Flow in curved channel finds a lot of applications in engineering practice. For example, the helically coiled pipes are largely used for heat exchangers such as steam generators and superheaters in nuclear power plant. The design of air-cooled heat exchangers requires the knowledge of heat transfer and frictional loss. For typical air-cooled coils, use of hairpin is very common. As expected, the hairpin that contains the 180° return bend (U bend) will cause higher pressure drops than the corresponding straight tube. In addition, the higher pressure drops of return bend may significantly affect the refrigerant distribution in the design of circuitry. As a consequence, the frictional performance of a return bend is very important for accurate estimation of the performance of an air-cooled heat exchanger. Reported data of the friction factor and therefore the pressure drop, for flow in bends and curved pipes, were shown to be greater than for flow in straight tubes for laminar flow [1] and for turbulent flow [2]. In curved pipes, the centrifugal force drives the more rapid fluid in the concave part of the curve channel while the fluid in the convex parts is slowing down. Dean was the first to point out that the occurrence of a secondary flow at right angle to the main flow is due to the centrifugal force [3]. The magnitude of such secondary flows obviously reduces with an increase of bend radius, and with a decrease of fluid velocity. Dean also proposed a parameter to consider the dynamic similarity for steady laminar flow in a curved tube, which is now called the Dean number ($D_N = Re_D (2R/D)^{0.5}$). Furthermore, when the Dean number exceeds a critical value, a secondary vortex pair with counter-rotating circulation is found near the outer wall [4].

√Corresponding author

There are some investigations relevant to this subject, but most of the previous studies were associated with helical coil and wavy pipe. For investigation to the 180° return bend, the investigations by Ito [2,5] are probably the most informative. However, his reported data were mainly applicable for larger diameter tubes (D > 10 mm). In the application of HVAC&R, small diameter tubes may be more preferable [6]. This is because of less refrigerant inventory and smaller air-side drag are likely. Therefore it is the purpose of this study to investigate the frictional performance of 180° return bend having small diameter tubes subjected to various radius of curvature. In this study, air and water are used as the working fluids because air and water have diverse difference of physical properties.

NOMENCLATURE

D	internal diameter of tube (m)
D_N	Dean number $[Re(2R/D)^{0.5}]$
f_c	friction factor for a bend
f_s	friction factor for a straight tube
L	tube length (m)
ΔP_s	pressure drop across the straight test section (Pa)
ΔP_{total}	total pressure drop across the test section (Pa)
Q	2R/D
R	radius of center line of bend (m)
Re_D	Reynolds number ($\rho U_m D/\mu$)
U_m	mean axial velocity (m/s)

Greek Letter

ρ	density (kg/m^3)
μ	viscosity (Ns/m^2)

Subscripts

d	downstream
s	straight tube
u	upstream

EXPERIMENTAL METHOD

Test Facility

The test rig is designed to be capable of conducting tests for the air-water two-phase mixtures or for the single-phase flows of air and water alone, as shown in Figure 1. Air is supplied from an air-compressor and then stored in a compressed-air storage tank. Airflow through a pressure reducer and, depending on the mass flux range, is measured by three mass flow meters. The water flow loop consists of a variable speed gear pump that delivers water. The mixer is designed to provide better uniformity of the flow stream. The inlet temperatures are near 25 °C. Three very accurate magnetical flowmeters with different applicable flow ranges are installed at the downstream of the gear pump. The accuracy of the air and water flowmeters is within ±0.2% of the test span. The test tubes are made of glass tube having inner diameters (D) of 3.0, 4.95, and 6.9 mm. A total of nine tubes are used for testing. Each tube has a upstream straight test tube of 100D and the total tube length including bend, upstream and downstream straight tubes is 340D+πR as shown in Figure 1. Further relevant geometries like radius of the return bend (R), curvature ratio (2R/D) are tabulated in Table 1.

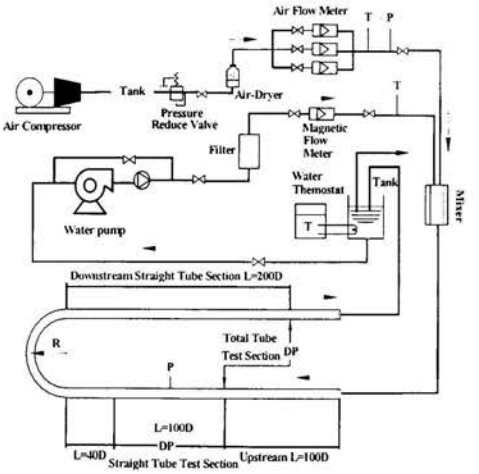

Figure 1: Schematic of the test facility

Table 1 Geometrical parameters of the test tubes.

D (diameter mm)	R (center to center)	2R/D
3	9.6	3.2
	15	5
	21	7
4.95	15	3.03
	25	5.05
	35	7.07
6.9	21	3.04
	35	5.03
	49	7.1

The pressure drop for air and water single-phase flows was measured by a differential pressure transducer having an adjustable span of 1300 to 13000 Pa. The pressure taps are drilled vertically to the test tubes with a hole diameter of 0.5 mm. Resolution of this pressure differential transducer is 0.3% of the measurements.

Tests of the single-phase flow for air and water are individually conducted in the loop. Leaving the test

section, the air is vented and the water is re-circulated by an open water tank. The air and water temperatures were measured by resistance temperature device (Pt100Ω) having a calibrated accuracy of 0.1 K. Test range of Reynolds number for water and air is about $400 < Re_D < 10000$.

The distorted flow condition by the secondary flow induced in bend was observed to persist at a downstream distance more than 50 D by Ito [2] for single-phase flow and 70 D by Cheng and Yuen [4] for two-phase flow. Therefore the flow resistance in this disturbed distance is increased. To have a fully developed flow condition for measurement, a straight entrance length, 100D, is located at the upper stream of the straight test section, which has a length of L_s=100D, to serve as a reference for comparison of the pressure gradient between the bend and the straight tube. Also, a straight length of 200D is directly connected to the bend outlet for flow recovery. A differential pressure transducer is used to measure the pressure drop across the upstream straight test section (ΔP_s), and another differential pressure transducer is utilized to measure the total pressure drop (ΔP_{total}) which includes the loss of the bend and the loss from the straight portions of the upstream (L_u = 140D) and downstream (L_d = 200D) straight tubes.

Data Reductions

The pressure drop of the return bend is calculated by subtracting the equivalent straight tube pressure drop having the length, L_u+L_d, from the measured total pressured drop (ΔP_{total}). This leads to the definition of the equivalent friction factor, f_C. Thus,

$$f_c = \frac{\left(\Delta P_{total} - \frac{4(L_u + L_d)}{D} f_s \frac{\rho U_m^2}{2}\right)}{\frac{4L_c}{D}\frac{\rho U_m^2}{2}} \qquad (1)$$

where $L_C = \pi R$ is the axial length of the 180° return bend, R is the radius of center line of bend, U_m is the mean axial velocity in the tube, ρ is the fluid density, and the frictional factor for the straight tube, f_s, is calculated as

$$f_s = \frac{\Delta P_s}{\frac{4L_s}{D}\frac{\rho U_m^2}{2}} \qquad (2)$$

The aforementioned approach is similar to that by Ward-Smith [7]. To verify the instrumentation and the measurement results, single-phase pressure drops for air and water alone were measured and a plot for friction factor versus the Reynolds number ($Re_D = \rho U_m d/\mu$) is shown in Figure 2, where μ is the fluid viscosity. The base line is the Blasius friction factor equation for laminar and turbulent flow in smooth straight tube $f_s = 16/Re_D$ and $f_s = 0.0791/Re_D^{0.25}$, respectively. As seen, the single-phase data for air and water agree favorably with the base lines. The good agreements shown in Figure 2 substantiate the accuracy of the instrumentation and the experimental apparatus.

RESULTS AND DISCUSSION

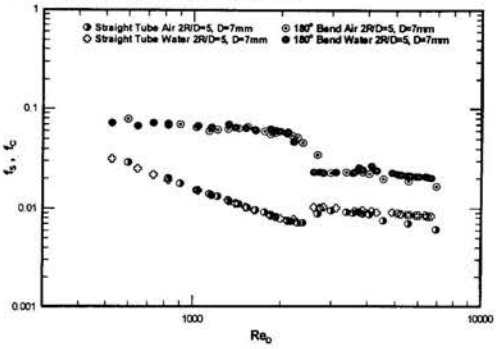

Figure 2: Straight tube and U bend friction factors for air and water

The pressure losses in U bends are presented in a form of friction factor as calculated by Equation (1). Test results for D = 7 mm are shown in Fig. 2. Data are plotted as friction factor vs. Reynolds number. The U bend friction factors (f_c) are obviously greater than the straight Tube friction factors (f_s) for the same Reynolds number shown in Figure 2. This difference is mostly caused by the secondary flow which increase the disturbance in flow. For turbulent flow the ratio of f_c/f_s is about 2 to 2.5, but for laminar flow much higher values of f_c/f_s up to 10 have been observed. The value of this ratio in laminar flow increases with Re_D and reachs its high values just before the transition to turbulent flow. Notice that the exponent dependence of the friction factor is quite different from that of straight tube. Furthermore, the slope is roughly the same in both laminar and turbulent region with a slope of –0.25. Test results indicate that the difference in property (either air or water) has a very negligible influence on friction factor and may eliminate the effect of Prandtl number.

Figure 3 and Figure 4 are friction factor (f_c) versus Reynolds number (Re_D) for water and air, respectively. The tube diameter is 7 mm with the influence of curvature ratio (2R/D) shown in the figures. For both laminar and turbulent flow, the bend friction factor increases with decrease of the curvature ratio 2R/D.

This trend is also observed for flow in curved tubes in the literature.

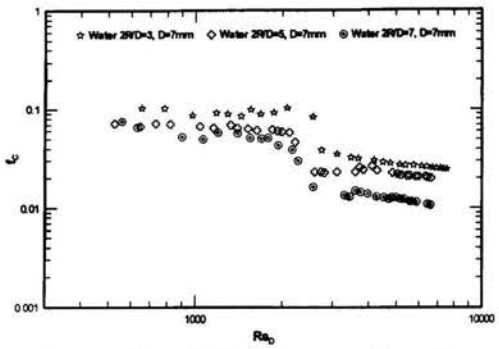

Figure 3: Water friction factor versus Reynolds number with the effect of curvature ratio.

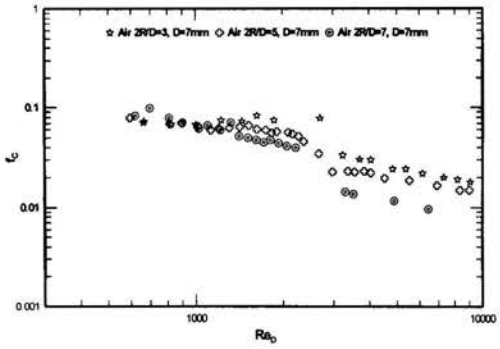

Figure 4: Air friction factor versus Reynolds number with the effect of curvature ratio.

Figure 5 and Figure 6 are friction factor (f_c) versus Reynolds number (Re_D) subjected to the effect of tube diameter for water and air, respectively. Although there is a little difference for various tube diameters in the frictional f_c data at $Re_D < 800$, however, this phenomenon does not prevail at higher Reynolds number region.

In this study a smooth transition from laminar to turbulent region in the friction factor versus Reynolds number plot, typical for curved pipe flow, is not observed in this study. An opposite trend to the transition from laminar to turbulent for straight tube has been seen in the plot of f_c versus Re_D. The large ratio (approximately 97 ~ 227) of straight tube length to curved tube length forces the calculated friction factor of the U bend to become the opposite trend of the straight tube. This is because the pressure drop of the return bend is calculated by subtracting the calculated pressure drop for the total length of the upstream and downstream straight tubes from the measured total pressured drop as shown in Equation (1). There is an uncertainty for using the calculated f_c in the range of $2000 < Re_D < 3000$. Therefore, the bend friction factor data are then correlated with the effects of Dean number (D_N), Reynolds number (Re_D) and curvature ratio (2R/D) for 113 laminar flow data ($Re_D < 2000$) and 143 turbulent flow data ($Re_D > 3000$), respectively.

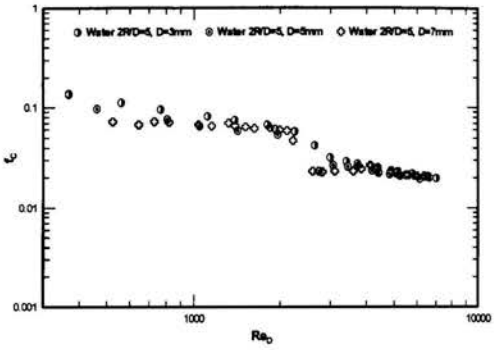

Figure 5: Water friction factor versus Reynolds number with the effect of tube diameter.

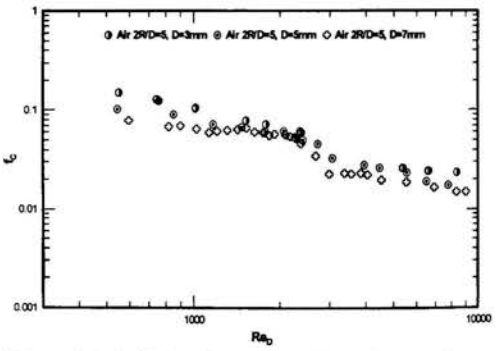

Figure 6: Air friction factor versus Reynolds number with the effect of tube diameter.

The following empirical correlations were deduced from the calculated f_c data by Equation (1):

Laminar for $Re_D < 2000$

$$\frac{f_c}{f_s} = (0.21D)e^{\frac{-6}{Q}}\left(\frac{16}{Re_D}\right)^{\frac{-3.44}{Q}} Q^{0.66} \qquad (3)$$

Turbulent for $Re_D > 3000$

$$\frac{f_c}{f_s} = (0.0317D)e^{\frac{-35.3}{Q}}(Re_D)^{\frac{34.72}{Q}} Q^{-0.25} \qquad (4)$$

where Q = 2R/D is the curvature ratio. The comparisons of the f_c data and the predictions of the bend friction factor using Equations (3) and (4) for laminar and turbulent flows are shown in Figures 7 and 8, respectively.

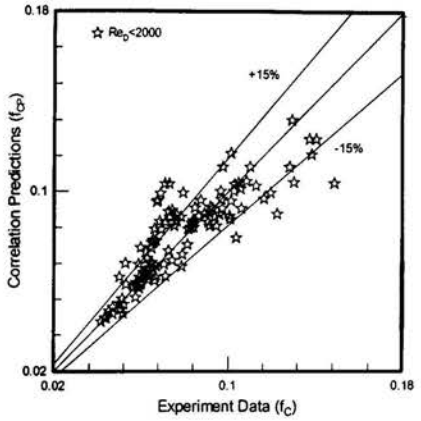

Figure 7: Comparison of the laminar f_c data with predictions by Equation (3).

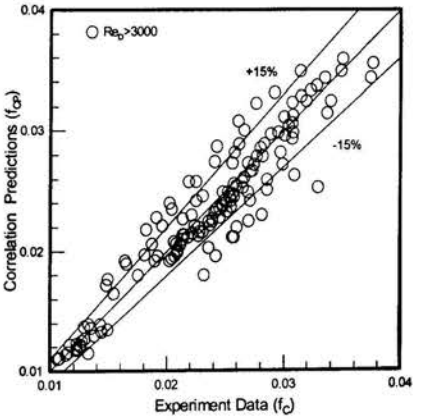

Figure 8: Comparison of the turbulent f_c data with predictions by Equation (4).

Fair agreements of data and predictions are observed in Figures 7 and 8. The mean deviations for the comparisons with predictions are 10.1% for the laminar data and 6.73% for the turbulent data.

CONCLUSION

1. For both laminar and turbulent flow the bend friction factor increases with decrease of the curvature ratio (2R/D).
2. However, for a given curvature ratio, the effect of tube diameter on the bend friction factor is rather small.
3. Since f_c data were reduced from Equation (1) instead of utilizing the measured pressure drop directly across U bends, a smooth transition typical for curved pipe flow, from laminar to turbulent region in the friction factor versus Reynolds number plot, is not observed in this study.
4. Based on the present f_c data, correlations for laminar and turbulent friction factors for 180° return bend with the effects of the curvature ratio, Dean number and Reynolds number were proposed.
5. The mean deviations for the comparisons with predictions are 10.1% for the laminar data and 6.73% for the turbulent data.

ACKNOWLEDGEMENTS

The authors would like to acknowledge the finical supports by the Energy Commission of the Ministry of Economic Affairs and National Science Council (NSC 89-2212-E-224-007), Taiwan, R. O. C.

REFERENCES

[1] Manlapaz, R. L. and Churchill, S. W., 1980, "Fully Developed Laminar Flow in a Helical Coiled Tube of Finite Pitch," Chemical Engineering Communications, Vol. 7, pp. 57-58.

[2] Ito, H, 1960, "Pressure Losses in Smooth Pipe Bends," ASME J. of Basic Engineering, Vol. 82, No. 1, pp. 131-143.

[3] Dean, W. R., 1927, "Note on the Motion of Fluid in a Curved Pipe," Phil' Mag. 4, pp. 208-695.

[4] Cheng, K. C., and Yuen, F. P., 1987, "Flow visualization studies on secondary flow patterns in straight tubes downstream of a 180 deg bend and in isothermally heated horizontal tubes," ASME J. of Heat Transfer, Vol. 109, pp. 49-61.

[5] Ito, H, 1987,"Flow in Curved Pipes," JSME Int. J., Vol. 30, No. 262, pp. 543-552.

[6] Chen, I. Y., Yang, K. S., Chang, Y. J. and Wang, C. C., 2001, "Two-Phase Pressure Drop of Air-Water and R-410A in small Horizontal Tubes," Int. J. Multiphase Flow, Vol.27, pp. 1293-1299.

[7] Ward-smith, 1980, "Internal Fluid Flow, the Fluid Dynamics of Flow in Pipes & Ducts," Clarendon press, Oxford.

HEFAT2002
1st International Conference on Heat Transfer, Fluid Mechanics, and Thermodynamics
8-10 April 2002, Kruger Park, South Africa
CJ1

DISCREPANCY BETWEEN CALCULATED AND MEASURED SUPERHEATED AREA IN AN EVAPORATOR PLATE HEAT EXCHANGER

J. Claesson‡, B. Palm
Div. of Energy Technology
Dept. of Applied Thermodynamics and Refrigeration
Royal Institute of Technology
SE-100 44 Stockholm, Sweden
‡E-mail: claesson@egi.kth.se

ABSTRACT

The use of compact brazed plate heat exchangers as evaporators in refrigerating units has increased during the last few years, due to their compactness and high performance, and it is important to be able to accurately predict this performance. Numerous articles have been published concerning the heat transfer and pressure drop characteristics for one-phase flows. The main task still to solve is to present a general theory for the performance of the plate heat exchanger in one-phase applications. However, satisfactory accuracy is obtained with existing correlations for each geometry over a large range of Reynolds numbers. For the use of plate heat exchangers as evaporators in refrigerating systems, no general methods for the calculation of the heat transfer and/or pressure drop have been presented in the open literature, even though some correlations do exists. In the evaporator, two main regions are present - boiling region and superheating region. When predicting the performance of the evaporator, these two regions have to be treated individually. First the area of each region must be determined. With a given superheat and mass flows of both fluids known, the superheating area is readily calculated since both fluids are in single phase, i.e. single phase correlations can be used. The remaining heat transfer area would then be used to evaporate the refrigerant. However, some indications suggest that this "backwards calculating procedure" overestimate the overall heat transfer coefficient in the superheating region, i.e. the superheating area is underestimated. The present article investigates this described discrepancy between the "backwards" calculated superheating area and the observed superheating area. From simultaneous measurements of superheating area and temperature, mass flows and so forth, the discrepancy is readily calculated. The superheating area is measured with Thermochromic Liquid Crystals (TLC), a temperature sensitive paint, and an ordinary CCD-camera.

INTRODUCTION

In a current research program, sponsored by the STEM (Swedish National Energy Administration), high efficiency heat pump systems are investigated. As a part of that program, a project dealing with efficient evaporators in heat pumps for domestic use is carried out. A large majority of the evaporators in heat pumps on the Swedish market are compact brazed plate heat exchangers (CBE). The CBE has a small internal volume compared to the heat transfer area. Also almost all the material in the CBE is used for the heat transfer area. Further, it has a small external volume, hence it is easy to install in narrow spaces.

Extensive research have been reported on the single-phase heat transfer in chevron-plate heat exchangers. Worth mentioning is the work by Martin [1] who extended the Lévêque-analogy for simultaneous developing flows into the turbulent region. Claesson et al. [2] found good agreement between experimentally developed correlations (eq. 3) and the approach by Martin.

Research concerning two-phase flows in chevron-plate heat exchangers is rather scarce. However, adiabatic two-phase flows in corrugated geometries has been investigated by some researchers [3-8]. Further, research has been conducted on the use of plate heat exchangers as evaporators in refrigerator systems [9-28]. The focus in most of these has been the overall performance of the evaporator, with little attention on the separate regions in the evaporator.

When evaluating the boiling heat transfer coefficient in a CBE, it is necessary to determine the heat transfer areas of the boiling and superheating regions. Perhaps the most common way is to use the single-phase heat transfer correlation on both sides in the superheating region. The area of the superheating region is then obtained and the boiling area and the boiling

heat transfer coefficient can be determined. However, Claesson et al. [2] found that this approach did not provide consistent results. The boiling heat transfer coefficients were expected to be a function of the boiling heat flux, as found in a previous investigation [29]. However, the resulting heat transfer coefficient displayed a considerable scatter. The reason for this scatter was not clear and a comparison between the measured area for superheat in Claesson & Palm [29], and the predicted area for superheat in Claesson et al. [2], showed a considerable deviation. It must, however, be kept in mind that the former investigation was done on a three plate CBE with only one refrigerant channel heated from one side whilst the latter test was on a commercial CBE with 40 plates. It is the aim of the present investigation to explore this observed discrepancy using the data from Claesson & Palm [29].

NOMENCLATURE

A_{sup}	Area used for superheating the refrigerant (m^2)
b	Pressing depth (m)
C_{Nu}	Constant in expression for Nusselt number (-)
d_e	Equivalent diameter (m)
$\dot{m}_{ch}$	Mass flow per sub-channel (kg/s)
n	Exponent on Reynolds number in expression for Nusselt number (-)
N_{sup}, N_{Re}, $N_{q''}$	Exponent(s) in eq. (9)
Nu	Nusselt number (-)
q"	Heat flux (=Q / A), (W/m^2)
$\dot{Q}_{sup}$	Heat load in superheating region (W)
Re	Reynolds number (-)
t	Temperature (°C)
u_m	Mean flow velocity (m/s)
U_{sup}	Overall heat transfer coefficient in the superheating region ($W/m^2 \cdot K$)
W	Width of plate (m)
Greek	
α	Heat transfer coefficient ($W/m^2 \cdot K$)
Δt_{sup}	Superheat (°C)
δ_{plate}	Plate thickness (m)
$\vartheta_{m,sup}$	Logarithmic mean temperature difference in the superheating region (°C)
λ	Thermal conductivity ($W/m \cdot K$)
μ	Viscosity ($Pa \cdot s$)
ρ	Density (kg/m^3)
Subscripts	
0	Reference case
evap	Evaporating region
H_2O	Water side
in	Inlet condition in the heat exchanger
Measured	Measured value
out	Outlet condition in the heat exchanger
Predicted	Predicted value
refr	Refrigerant side
sup	Superheating region
tot	Total heat exchanger
w	Fluid at the wall

COMPACT BRAZED PLATE HEAT EXCHANGERS

The CBE investigated is of the chevron-plate type. It has an almost sinusoidal corrugation pattern and the corrugations are formed in a V-shape. Every second plate is rotated, see figure 1, giving a complex flow geometry, which promotes an early transition to turbulent flow.

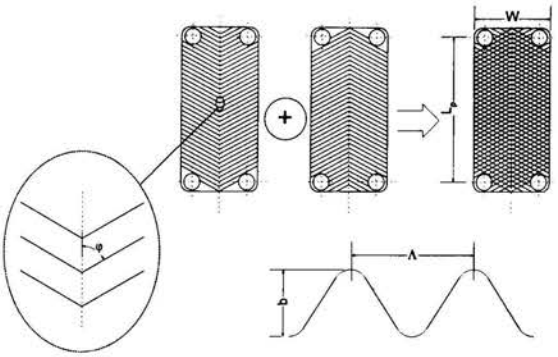

Figure 1: Schematic picture of the assembly of plates and the corrugation pattern.

The chevron angle φ is defined as the angle between the direction of the channel formed by the corrugation and the centerline of the heat exchanger. Several different definitions of the characteristic numbers can be encountered in the open literature, due to the complex flow geometry. In this work, the equivalent diameter is defined as twice the corrugation depth, b. Subsequently, the Reynolds and the Nusselt numbers are based on this diameter, i.e.:

$$Re = \frac{\rho \cdot u_m \cdot d_e}{\mu} = \frac{2 \cdot \dot{m}_{ch}}{W \cdot \mu} \quad (1)$$

and

$$Nu = \frac{\alpha \cdot d_e}{\lambda} \quad (2)$$

The one-phase heat transfer is predicted by a Dittus-Boelter type of equation, developed experimentally by the manufacturer on this specific geometry.

$$Nu = C_{Nu} \cdot Re^n \cdot Pr^{f_{Pr}(Pr)} \cdot \left(\frac{\mu}{\mu_w}\right)^{f_\mu(Re)} \quad (3)$$

The heat exchanger used in the experiments only had three plates, forming two channels. Hence, each channel was heated from one side only. Eq (3) was developed for a heat exchanger with several channels, each being heated from both sides. To compensate for this difference, the heat transfer coefficients calculated by eq. (3) were adjusted according to Petukhov & Roizen [30].

More information on the respective functions for the exponents can be found in Bogaert & Bölcs [31].

MEASUREMENT OF SUPERHEATING AREA

The experiments were carried out on a simple refrigerating system, with R-22 as the refrigerant, containing only the most important items, see figure 2. The evaporator had three plates, i.e. two channels, and no cover plate on the backside. Hence, the heat was transferred through only one plate, the other plate being near adiabatic. To ensure that the plate painted with TLC did not participate in the heat exchange, the ambient air was kept near the saturation temperature of the refrigerant flowing inside the evaporator.

The system was run with four different heat loads, four different superheats and four different secondary refrigerant flows, with a total number of measuring points exceeding 50. The temperatures were measured with thermocouples of T-type. The mass flow of the refrigerant was measured with a Coriolis flow meter from Micro Motion. The water flow on the secondary side was measured with a calibrated positive displacement flow meter. The water flow in the condenser was not measured.

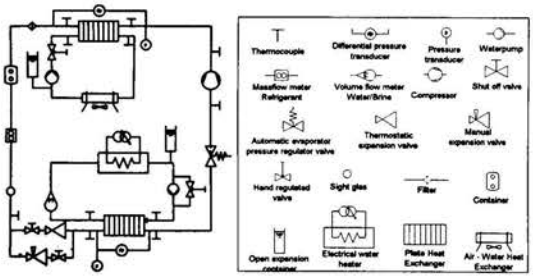

Figure 2: Flowchart of test equipment.

The superheating area was measured with a CCD-camera observing the colorplay of Thermochromic Liquid Crystals (TLC), which were painted on the outside of the corrugated surface of the refrigerant channel. A schematic picture of the setup is shown in figure 3.

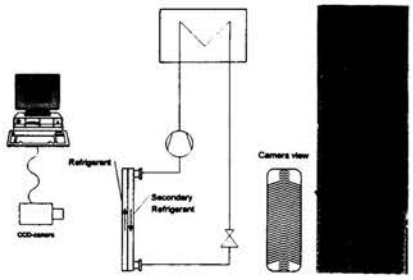

Figure 3: Measurement of the superheating area.

All of the measured data were recorded by a HP 34970A Data Acquisition/Switch Unit and stored on the hard-drive of the computer. The colorplay in the pictures were transformed into area by calculating how many pixels that had a certain color. This procedure was carried out in Optimas 6.0. As can be seen in figure 3, a rather sharp transition occurs from the boiling region into the superheating region. Note that the entire heat exchanger is not displayed in this figure. It might also be interesting to note that there seems to be almost no maldistribution inside the channel, which was characteristic for almost all of the measured points.

CALCULATION OF SUPERHEATING AREA

The simplest way to find the heat transfer area for the superheating region as well as the evaporating region is to assume that the single-phase correlations for the heat transfer coefficient holds in the superheating region. For a performance evaluation process the backwards-calculating procedure is outlined as follows:

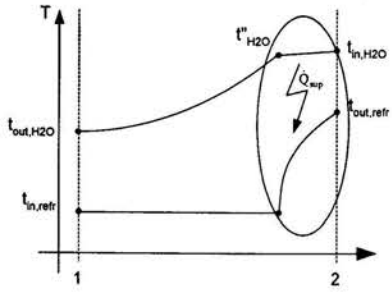

Figure 4: Temperature profile in the evaporator, superheating region highlighted.

In the superheating region, highlighted in figure 4, from measured mass flow, temperatures and pressures on both sides, eq. (3) is used for calculation of the heat transfer coefficients. Then the overall heat transfer coefficient is calculated according to

$$\left(\frac{1}{U_{sup}}\right)_{pred} = \left(\frac{1}{\alpha_{sup,refr}}\right)_{pred} + \frac{\delta_{plate}}{\lambda_{plate}} + \left(\frac{1}{\alpha_{sup,H_2O}}\right)_{calc} \quad (4)$$

In the experiment carried out the secondary refrigerant was water and thus denoted in eq. (4) as H_2O.

From the measured heat load in the superheating region, the area required to transfer that heat is readily calculated.

$$A_{sup,pred} = \frac{\dot{Q}_{sup}}{U_{sup,pred} \cdot \vartheta_{m,sup}} \quad (5)$$

where

$$\vartheta_{m,sup} = \frac{\left(t''_{H_2O} - t_{in,refr}\right) - \left(t_{in,H_2O} - t_{out,refr}\right)}{\ln\left(\frac{t''_{H_2O} - t_{in,refr}}{t_{in,H_2O} - t_{out,refr}}\right)} \quad (6)$$

is the logarithmic mean temperature difference over the superheating region. It is assumed that no pressure drop occurs in the evaporator.

The heat load is calculated by taking the enthalpy difference times the mass flow on respective side. Comparison between the two different heat loads obtained from respective fluid side shows a total energy balance better than 10% for almost all measurements. The losses to the surrounding from the un-insolated surface are calculated to less than one watt. The total heat load used in the calculations is taken as the arithmetic mean. The mass flow of each fluid side is then adjusted to match the averaged heat load.

The evaporating heat transfer area is the total heat transfer area minus the required superheating area calculated.

HEAT TRANSFER COEFFICIENT FROM MEASURED SUPERHEATING AREA

The heat transfer coefficients predicted by eq. (3) were compared to values based on the measured data. The calculations are quite straightforward and are briefly shown here. As for the calculation of the superheating areas described in the previous section the heat transfer coefficient on the water side is calculated by eq. (3). From measured heat load, heat transfer area and logarithmic mean temperature in the superheating region, the overall heat transfer coefficient is determined by

$$U_{sup,meas} = \frac{\dot{Q}_{sup}}{A_{sup,meas} \cdot \vartheta_{m,sup}} \quad (7)$$

The measured heat transfer coefficient on the refrigerant side is then calculated as

$$\left(\alpha_{sup,refr}\right)_{meas} = \frac{1}{\frac{1}{U_{sup,meas}} - \frac{\delta_{plate}}{\lambda_{plate}} - \left(\frac{1}{\alpha_{sup,H_2O}}\right)_{calc}} \quad (8)$$

The uncertainty in the heat transfer coefficient calculated in eq. (8) is estimated by propagation of error to be ± 11 % for low superheat and ± 6 % for high superheat.

RESULTS

The outlined procedure is used to calculate the superheating area in all tests with the three plate heat exchanger. The result is presented in figure 5 together with the experimentally determined superheating areas. It can be seen that at low superheats, the absolute discrepancy is not large, but at larger superheats the discrepancy becomes significant. Also the predicted area required for superheat flattens out at these larger superheats. A few of the calculated values agree well with the measured areas.

Comparison between the predicted and the measured heat transfer coefficients as a function of the Reynolds number in the refrigerant flow is shown in figure 6. It is clear that the Reynolds number is not by itself responsible for the deviation. The predicted heat transfer coefficient, eq. (3), seems to be an upper limit to the measured heat transfer coefficient in the superheating area.

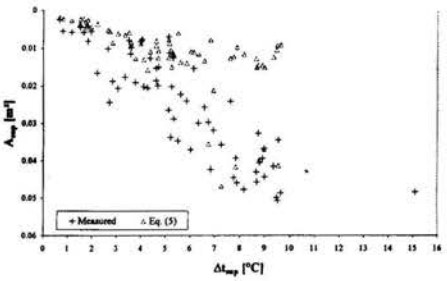

Figure 5: Area required for superheating.

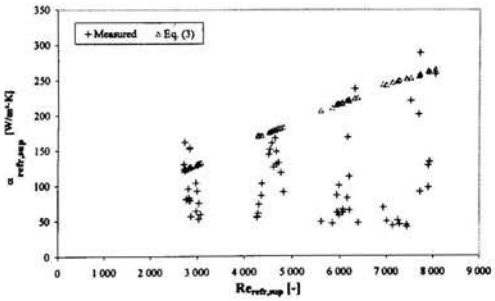

Figure 6: Measured and predicted heat transfer coefficient as a function on Reynolds number.

It is assumed that the deviation is dependent on the refrigerant side only and that the waterside is appropriately modeled. Using eq. (3), it can easily be shown that the heat transfer coefficient on the waterside is more than an order of magnitude larger than the refrigerant heat transfer coefficient in the superheating region, so no significant error is introduced by this assumption.

DISCUSSION

The reasons for the observed discrepancies are not clear, and no parameter(s) fitting the behavior could be found. It might be that the superheating area determined with Thermochromic Liquid Crystals (TLC) is not the correct one.

The reason for this may be if dry-out of the wall occurs before all the liquid have evaporated, as may be the case in tube flow. However, as there exists a large swirl flow in the PHE (Claesson [32], Mehrabian [33]), it is believed that any droplets existing in the gas-core would be thrown onto the wall, hence re-wetting the wall. A distinct transition from wetted wall to pure gas flow with no entrained droplets in the gas core have indeed been visually observed (Pelletier [34]). Also, no correlation between the discrepancy and the predicted dry-out quality (Sthapak et al. [35]) could be found. Sthapak et al. developed their correlation for 6.55 mm diameter horizontal tube. Further, the nonequilibrium factor as defined by Katsaounis [36] is very close to one, indicating that thermodynamic equilibrium prevails near the dry-out point. Yan & Lin [28] found that mist flow occur at higher vapor qualities. This contradicts the finding of Pelletier [34]. However, the mass fluxes were higher in Yan & Lin than in the present investigation and the saturation pressures were substantially higher. It is also stated that the "...mist flow results in a substantial rise in the heat transfer coefficient. The high-speed turbulent mist flow continuously wets the heat transfer wall...". Thus, even if entrained droplets exist in the vapor core, the heat transfer is not reduced and the wall temperature is maintained. From the discussion above, it is suggested that the error made in measuring the superheated area is small.

Another possible reason for the discrepancy might be that the longitudinal heat transfer in the wall is important. The reason for this could be that the wall temperature just upstream of the boundary between the boiling and superheating region is lower than predicted by traditional logarithmic mean temperature difference procedure, due to the high upstream boiling heat transfer coefficient. To explore this possibility, a simple finite difference scheme was employed.

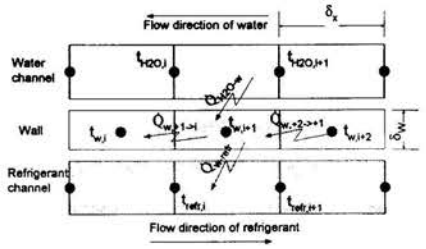

Figure 7: Finite difference scheme.

The calculation scheme starts at the position were the superheat begins. The corresponding water temperature is calculated through a heat balance in the superheating region and the wall temperature is set to the arithmetic mean of the refrigerant and the water temperatures, i.e. assuming equal heat transfer coefficients on the water and refrigerant sides in the boiling region. The heat transfer area of each cell is set to a fixed value, ΔA_w, and the total heat transfer area required to heat the refrigerant to the known leaving temperature of the heat exchanger is the total sum of the ΔA_w. At the exit of the heat exchanger, the longitudinal heat transfer in the wall is set to zero, i.e. $\left.{}^{dt_w}/_{dx}\right|_{x=L} = 0$.

Now, consider a small section of the heat exchanger, see figure 7. The energy balance on the water side is constructed of three equations. The first is delivered heat from the water to the wall.

$$\dot{Q}_{H_2O\to w} = \alpha_{H_2O} \cdot \Delta A_w \cdot \left(\frac{t_{H_2O,i+1} + t_{H_2O,i}}{2} - t_{w,i+1} \right) \tag{9}$$

We thus have a decrease of water temperature over the section

$$\dot{Q}_{H_2O} = \dot{m}_{H_2O} \cdot c_{p_{H_2O}} \cdot \left(t_{H_2O,i+1} - t_{H_2O,i} \right) \tag{10}$$

The amount of these two should equal, hence

$$\dot{Q}_{H_2O\to w} = \dot{Q}_{H_2O} \tag{11}$$

On the refrigerant side, the same principle is used, thus

$$\dot{Q}_{w\to refr} = \alpha_{refr} \cdot \Delta A_w \cdot \left(t_{w,i+1} - \frac{t_{refr,i+1} + t_{refr,i}}{2} \right) \tag{12}$$

$$\dot{Q}_{refr} = \dot{m}_{refr} \cdot c_{p_{refr}} \cdot \left(t_{refr,i+1} - t_{refr,i} \right) \tag{13}$$

$$\dot{Q}_{w\to refr} = \dot{Q}_{refr} \tag{14}$$

The equations over the wall are

$$\dot{Q}_{w,+1\to i} = \lambda_w \cdot W \cdot \delta_w \frac{t_{w,i+1} - t_{w,i}}{\delta_x} \tag{15}$$

$$\dot{Q}_{w,+2\to+1} = \lambda_w \cdot W \cdot \delta_w \frac{t_{w,i+2} - t_{w,i+1}}{\delta_x} \tag{16}$$

and finally the energy balance over a small segment of the wall

$$0 = \dot{Q}_{H_2O\to w} + \dot{Q}_{w,+2\to+1} - \dot{Q}_{w\to refr} - \dot{Q}_{w,+1\to i} \tag{17}$$

The complete set of equations along with the boundary conditions is set up and calculated in MS-Excel. Eq. (3) is used for the heat transfer coefficients on respective fluid side. The calculations show, even though up to more than 10% of the heat leaving the water is not retained on the refrigerant side but transported along the wall into the boiling region, that the effect of longitudinal heat transfer in the wall is not responsible for the deviation between eq. (3) and the measured heat transfer coefficient. The main influence the longitudinal heat transfer will have on the superheating region is that the water entering into the superheating region will have somewhat lower temperature than calculated by an energy balance between water and refrigerant only. However, the changes in the water temperature due to the increase of heat

leaving the water side is quite small since the heat capacity rate of water is quite large.

Yet another phenomenon that might play a role for the discrepancies are the maldistribution of the superheated gas. As seen in figure 3, the boiling region seems to have no, or very little, maldistribution, thus the gas leaving the boiling region is evenly distributed. If the superheat is low, i.e. the onset of superheat is near the outlet port, the gas is in good contact over a large part of the superheating region. However, if the superheat increases, the gas is flowing towards the outlet port, creating a relatively larger portion of the heat transfer area in which the mass flow is low, hence decreasing the average heat transfer coefficient.

The possibility that the maldistribution affect the degeneration of the area averaged heat transfer coefficient in the superheating region should be further investigated.

Figure 8: Moderate and low superheat, heat transfer area not well used market in the right figure.

Finally, the discrepancy between the measured and calculated areas necessary for superheating could be caused by the fact that the experimentally determined areas were measured in a three-plate heat exchanger with heating of each channel from one side only, and that the correction made for this through the use of the thermal diameter is not correct. Further tests determining the superheating area in channels with double sided heating would be needed. This, however, is an experimentally challenging task.

INFLUENCE ON SUPERHEATING AREA FROM CONTROLLED EXPERIMENTAL PARAMETERS

In the experiments, three parameters were independently controlled, namely the amount of superheat, the mass flow on the water side and the total heat load in the CBE. In figure 9, the influence on the temperature profiles of a change in the operating parameters of the system are shown.

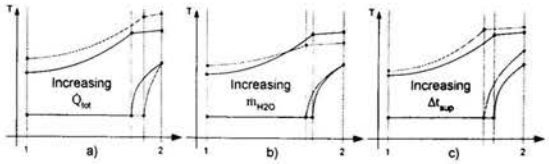

Figure 9: Different temperature profiles depending on the changes made on the refrigerant system.

In figure 9a, the superheat and the mass flow of water is kept constant while the total refrigerating heat load is increased. The increase in total heat load leads to, beside the increase of the mass flow on the refrigerant side, an increase of the logarithmic mean temperature difference in the boiling region. The temperature level of the waterside is increased, thus also increasing the logarithmic mean temperature difference in the superheating region. To keep a constant superheat (which is taken care of by the expansion device), the heat transfer area of the superheating region will decrease. Hence, an increase in the total heat load yields a smaller superheating area.

In figure 9b, the superheat and the total heat load is kept constant and the mass flow on the waterside is increased. The temperature profile on the waterside will flatten out with the incoming water temperature at a somewhat lower value, lowering the logarithmic mean temperature difference in the superheating region. To compensate, the superheating heat transfer area is increased. Hence, an increase of the water flow yields a larger superheating area.

In figure 9c, the total heat load and the mass flow on the waterside is kept constant and the superheat is increased. The increase of superheat increases the heat load in the superheating region. The overall heat transfer coefficient will remain about the same, so a larger surface area will be needed in the superheating region to transfer the larger heat load.

To quantify the impact on the area required for superheat of the different parameters discussed, a simple regression analysis was conducted, based on eq (18).

$$\frac{A_{sup}/A_{tot}}{A_{sup,0}/A_{tot,0}} = \left(\frac{\Delta t_{sup}}{\Delta t_{sup,0}}\right)^{N_{sup}} \cdot \left(\frac{Re_{H_2O}}{Re_{H_2O,0}}\right)^{N_{Re}} \cdot \left(\frac{q''_{tot}}{q''_{tot,0}}\right)^{N_{q''}} \quad (18)$$

where

$A_{sup,0}/A_{tot,0} = 0.316$, $\Delta t_{sup,0} = 3.8$ °C, $Re_{H_2O,0} = 428$, $q''_{sup,0} = 5\,467$ W/m², $N_{sup} = 0.97$, $N_{Re} = 0.5$ and $N_{q''} = -0.23$.

Table 1: Range of validity of eq. (18)

	(A_{sup}/A_{tot}) / $(A_{sup,0}/A_{tot,0})$	$\Delta t_{sup}/\Delta t_{sup,0}$	$Re_{H2O}/Re_{H2O,0}$	$q''_{tot}/q''_{tot,0}$
Max	2.673	2.550	2.200	2.818
Min	0.129	0.174	0.452	0.998

The exponents were determined by multiple nonlinear regression analysis using the software Statistica, ver 4.5. Figure 10 shows the agreement between the calculated heat transfer area and the measured heat transfer area, and it can be seen that the agreement is fairly good.

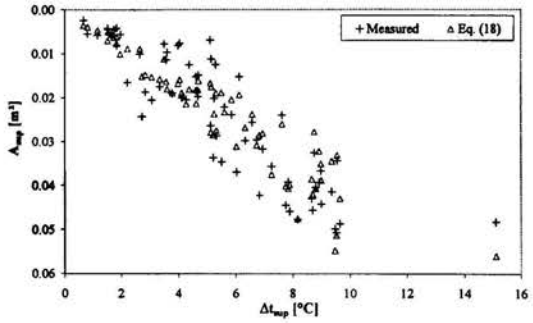

Figure 10: Comparison between predicted and measured heat transfer area in the superheating region.

CONCLUSION

The present article investigates the observed difference between the measured and the predicted heat transfer area required for superheating the refrigerant in a Compact Brazed Plate Heat Exchanger used as evaporator in a small refrigerating unit. The cause of the difference is not quite understood. However, an attempt is made to empirically correlate the ratio of the measured and the predicted heat transfer area and fairly good agreement was obtained.

A finite difference scheme was also employed, showing that the longitudinal heat transfer can not explain the discrepancies. Also the possibility that maldistribution of the superheated gas affect the discrepancy has been discussed. Finally, the correction for single sided heating may not be the correct one and more studies will be needed for more accurate predictions on the heat transfer coefficient in single sided heating.

ACKNOWLEDGEMENTS

The authors gratefully acknowledge the funding receiveo from STEM (Swedish National Energy Administration), SWEP International AB and Thermia Värme AB.

REFERENCES

[1] Martin H., 1996, "A theoretical approach to predict the performance of chevron-type plate heat exchangers", Chemical Engineering and Processing, Vol. 35, No. 4, pp. 301-310.

[2] Claesson J, Palm B., Pelletier O., 2001, "On the influence of geometry on evaporation in compact brazed plate heat exchangers", ICMF-2001 4th International Conference on Multiphase Flow, E.E. Michaelides ed., May 27 to June 1, 2001, New Orleans, Louisiana, USA, paper 156.

[3] Bai X., Newell T.A., 2000, "An investigation of two-phase flow characteristics in chevron-style flat plate heat exchangers", 8th Int. Refrigeration Conf., Purdue University, West Lafayette, IN, USA.

[4] Kreissig G, Müller-Steinhagen H.M., 1992, "Frictional pressure drop for gas/liquid two-phase flow in plate heat exchangers", Heat Transfer Engineering, Vol. 13, No. 4, pp. 42-52.

[5] Tribbe C., 1998, "Gas/liquid flow in cylindrical and corrugated channels" Ph.D. thesis, University of Surrey, UK.

[6] Tribbe C., Müller-Steinhagen H.M., 1997, "The hydrodynamics of gas-liquid two-phase flow in a plate heat exchanger", The 1997 Jubilee Research Event, IchemE, University of Nottingham, UK, pp. 357-360.

[7] Tribbe C., Müller-Steinhagen H.M., 2001, "Gas/liquid flow in plate-and-frame heat exchangers – Part 1: Pressure drop measurements", Heat Transfer Engineering, Vol. 22, No. 1, pp. 5-11.

[8] Tribbe C., Müller-Steinhagen H.M., 2001, "Gas/liquid flow in plate-and-frame heat exchangers – Part 2: Two-phase multiplier and flow pattern analysis", Heat Transfer Engineering, Vol. 22, No. 1, pp. 12-21.

[9] Baskin E., 1991, "Applicability of plate heat exchangers in heat pumps", ASHRAE Transactions, Vol. 97, Pt. 2, pp. 305-308.

[10] Boccardi G, Celata G.P., Cumo M., Gerosa A., Donati F.M., Zorzin A., 2000, "R22 replacement aspects in compact heat exchangers for air conditioning", Int. J. Heat Exchangers, Vol. 1, No. 1, pp. 77-91.

[11] Boccardi G, Celata G.P., Cumo M., Geroza A., Giuliani A., Zorzin A., 2000, "The use of new refrigerants in compact heat exchangers for the refrigeration industry", Heat Transfer Engineering, Vol. 21, No 4, pp. 53-62.

[12] Dutto T., Blaise J.C., Benedic T., 1991, "Performance of brazed plate heat exchanger set in heat pump", (in French), Proc. 18th Int. Congr. Refrigeration, Vol, III, pp. 1284-1288, Montreal, Quebec, Canada.

[13] Gray R.M., 1984, "The design and use of plate heat exchangers in boiling and condensing applications" IchemE Symp. Ser., Vol 1, Pt. 86, pp. 685-694.

[14] Haseler L.E., Butterworth D., 1995, "Boiling in compact heat exchangers / Industrial practice and problems", 1st Int. Conf. Convective Flow Boiling, Banff, Canada, pp. 57-70.

[15] Hickson D.C., 1999, "Boiling and condensation heat transfer coefficients in a plate heat exchanger", ImechE Conference Transactions, "6th UK National Conf. on Heat Transfer", Paper C565/077/99, pp. 133-139.

[16] Kedzierski M.A., 1995, "Effect of inclination on the performance of a compact brazed plate heat condenser and evaporator", NISTIR 5767, National Institute of Standards and Technology, Gaithersburg, USA.

[17] Kumar H., 1993, "Evaporation in plate heat exchangers", AIChE Symp. Ser. 295, Vol. 89, "Heat Transfer – Atlanta 1993", ed. B.G. Volintine, pp. 211-228.

[18] Palm B., Thonon B., 1999, "Thermal and hydraulic performances of compact heat exchangers for refrigeration systems", 2nd Engineering Conf. on "Compact Heat Exchangers and Enhancement Technology for the Process Industries", Banff, Canada.

[19] Palmer S.C., Payne II W.V., Domanski P.A., 2000, "Evaporation and condensation heat transfer performance of flammable refrigerants in a brazed plate heat exchanger", NISTIR 6541, National Institute of Standards and Technology, Gaithersburg, USA.

[20] Pelletier O., 1998, "Propane as refrigerant in residential heat pumps", Engineering Licentiate Thesis, Div. of Applied Thermodynamics and Refrigeration, Dept. of Energy Technology, Royal Institute of Technology, Stockholm, Sweden, Trita REFR No 98/24, ISSN 1102-0245.

[21] Polat S., Manglik R.M., Wilkins R.L., 1993, "Forced convective boiling of a non-Newtonian liquid in a multipass plate heat exchanger" AIChE Symp. Ser. 295, Vol. 89, "Heat Transfer – Atlanta 1993", ed. B.G. Volintine, pp. 229-235.

[22] Sterner D., 1999, "Experiments and analysis of performance of plate heat exchangers as evaporators in refrigerator systems", Engineering Licentiate Thesis, ISRN LUTMDN/TMHT-99/2007--SE, Div. of Heat Transfer, Dept. of Heat and Power Engineering, Lund Institute of Technology, Lund, Sweden.

[23] Sterner D., Sundén B,, 1997, "Performance of some plate-and-frame heat exchangers as evaporator in a refrigeration system", ImechE Conference Transactions, "5th UK National Conf. on Heat Transfer".

[24] Thonon B., Feldman A., Margat L., Marvillet C., 1997, "Transition from nucleate boiling to convective boiling in compact heat exchangers", Int. J. Refrigeration, Vol. 2, No. 8, pp. 592-597.

[25] Thonon B., Mercier P., 1996, "Plate heat exchangers : Ten years of research at GRETh – Part 2. Sizing and flow maldistribution" (in French), Rev Gén Therm, Vol. 35, pp. 561-568.

[26] Thonon B., Vidil R., Marvillet C., 1995, "Recent research and developments in plate heat exchangers", J. Enhanced Heat Transfer, Vol. 2, No. 1-2, pp. 149-155.

[27] Usher J.D., 1970, "Evaluating plate heat exchangers", Chemical Engineering, Vol. 77, No. 4, pp. 90-94.

[28] Yan Y.-Y., Lin T.-F., 1999, "Evaporation heat transfer and pressure drop of refrigerant R-134a in a plate heat exchanger", ASME J. Heat Transfer, Vol. 121, No. 1, pp. 118-127.

[29] Claesson J., Palm B., 1999, "Boiling mechanism in a small compact brazed plate heat exchanger (CBE) determined by using thermochromic liquid crystals (TLC)", Refrigeration into the third millennium, 20th International Congress of Refrigeration, September 19 - 24, 1999, Sydney, Australia, paper 117.

[30] Petukhov B.S., Roizen L.I., 1964, "Generalized relationships for heat transfer in a turbulent flow of gas in tubes of annular section", High Temperature 2, pp. 65 – 68.

[31] Bogaert R., Bölcs A., 1995, "Global performance of a prototype brazed plate heat exchanger in a large Reynolds number range", Experimental Heat Transfer, Vol. 8, pp. 293-311.

[32] Claesson J., 1996, "Numerisk simulering av värmeöverföring och strömning i plattvärmeväxlare med CFDS-FLOW3D 3.3", (Numerical simulation of heat transfer and fluid flow in a plate heat exchanger using CFDS-FLOW3D 3.3), in Swedish, Master of Science Thesis 96/2, Division of Heat Transfer, Lunds Institute of Technology.

[33] Mehrabian M.A., Poulter R., 2000, "Hydrodynamics and thermal characteristics of corrugated channels: computational approach", Applied Mathematical Modelling, Vol. 24, No. 5-6, pp. 343-364.

[34] Pelletier O., 1999, Personal communication.

[35] Sthapak B.K., Varma H.K., Gupta C.P., 1975, "Mass vapour fraction at the onset of dryout in a horizontal tube evaporator", Progress in Refrigeration Science and Technology, 14th International Congress of Refrigeration, Moscow, 1975, published 1978, Vol. 2, paper B1.39, pp. 318-324.

[36] Katsaounis A., 1993, "Post-dryout heat transfer during forced convection", 1st English Edition, VDI Heat Atlas, VDI Verlag, ISBN 3-18-400915-7, section Hbd.

HEFAT2002
1st International Conference on Heat Transfer, Fluid Mechanics, and Thermodynamics
8-10 April 2002, Kruger Park, South Africa
DG2

MODELLING THE THERMAL PERFORMANCE OF ROTARY REGENERATIVE BOILER AIR HEATERS

GB de Klerk, TJ Sheer, HH Jawurek
School of Mechanical, Industrial and Aeronautical Engineering,
University of the Witwatersrand, Johannesburg
Private Bag 3
Wits 2050
South Africa

ABSTRACT

A simulation model for predicting the thermal performance of rotary regenerative boiler air heaters is presented. The model is based on an energy balance for a flow channel element from within a pair of plates of different thicknesses. The proposal for using plates of different thicknesses is due to the finding that one plate of a repeating pair used in a pack erodes faster than the other. Thus making the faster eroding plate thicker should extend the life of the pack. Previous work has shown that the thermal performance of a pack of alternating-thickness plates lies between that of a pack made up of either the thicker or the thinner plates and that erosion does not significantly affect performance. Hence the potential advantage of extended life is preserved. A case study is presented whereby an air heater is simulated with equal and then alternating-thickness packs. The results show very little change in thermal performance, but an increase in the mass and the life with alternating thickness packs. The increase in mass results in an increase in capital cost, but an economic analysis shows that the alternating-thickness pack is probably more cost effective. In addition to simulating the thermal performance of packs of different thickness plates, the air heater model is capable of simulating the effects of leakage, blockage, varying pack characteristics in the matrix and non-uniform velocity distributions. Verification of the model is discussed.

NOMENCLATURE

β - Thickness Ratio (a/b)
λ - Conduction Parameter ($k.A_{cond}/(m.C_f.L)$)
θ - Dimensionless Time ($m.C_f.t/(M.C_s)$)
ρ - Density of the solid [kg/m^3]
a - Half the corrugated plate thickness [m]
A - Area [m^2]
b - Half the undulated plate thickness [m]
C - Specific heat capacity [kJ/kg K]
FG - Flue gas
h - Convective heat transfer coefficient [W/m^2 K]
i - Enthalpy [kJ/kg]
k - Conductivity of the Solid [W/m K]
L - Length of the plates [m]
m - Mass flowrate [kg/s]
M - Mass of Solid [kg]
Ntu - Number of transfer units ($h.A_{conv}/(m.C_f)$)
SA - Secondary air
t - Time [s]
T - Temperature [°C]
T^* - Dimensionless T ($(T-T_{cold\ inlet})/(T_{hot\ inlet}-T_{cold\ inlet})$)
W - Width of the plates [m]
x - Distance from leading edge [m]
z - Dimensionless distance from the leading edge
subscripts :
f - Fluid
s - Solid
cond- Conduction
conv - Convection

INTRODUCTION

Rotary regenerative air heaters are used in fossil-fuelled power stations to preheat boiler combustion air by means of the exhaust flue gas. A matrix of steel plates rotates relative to the flue gas and air streams so that the plates are alternately heated and cooled. The result is a net transfer of energy from the flue gas to the combustion air.

Ljungstrom air heaters are of the rotating matrix type. The ductwork is fixed and directs the flow through packs of plates housed in a moving rotor as shown in figure 1. They are mainly used to heat secondary air, although a variation known as a Ljungstrom Tri-sector air heater has an extra sector for heating primary air.

In a Rothemühle air heater, double winged hoods rotate on either side of a fixed matrix located in the flue gas duct to direct a flow of secondary air through packs of plates. In this case, the matrix is known as a stator. Besides the standard Rothemuhle air heater, another important type used in South African power stations is the Twinflow air pre-heater which employs separate hoods for heating primary air. The primary air hoods are located in the center section of the main secondary air hoods. The advantage of this type of design is that a separate primary air heater is not required. (The ratio of secondary to primary air flow rates is typically 8:1).

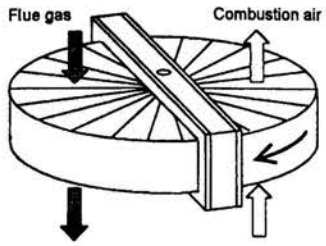

Figure 1 : Regenerative air heater rotor – Ljungstrom type

In both Rothemuhle and Ljungstrom air heaters, the flue gas and air streams are arranged in counterflow. The axis of rotation is usually vertical, although some horizontal axis heaters exist. Two 50% duty air heaters per boiler are used, located directly after the boiler in the flue gas ducting. The flue gas inlet side of the air heater matrix (the top or boiler side) is known as the hot end while the lower (outlet) side is known as the cold end.

Typically, the temperature of the flue gas at inlet is 320°C. The outlet temperature is limited by the acid dewpoint of the flue gas and should be higher than approximately 120°C depending on the sulphur content of the coal (typically 1.3 % for South African power coal). The inlet combustion air enters at close to ambient temperature (5-50°C) and leaves at roughly 300°C. Recirculation of the combustion air and bypass around the air heater can be used to control the temperatures.

By heating the combustion air in this manner the boiler efficiency is improved. Leakage occurs in regenerative heat exchangers as a result of the rotation of the matrix between streams and direct leakage from higher-pressure to lower-pressure streams. Seals are used to minimize direct leakage, but air heaters operate with losses of combustion air (which is at a higher pressure than the flue gas) of 7% and more. This results in higher fan power requirements for a given outlet flow.

Pressure drop is another important consideration when dealing with overall plant efficiency. The lower the pressure drop across the regenerative air heater, the lower the fan power required. Thus the matrix needs to be packed with corrugated plates giving low resistance to flow but high heat transfer rate to keep the matrix compact and cost effective.

The matrix consists of a structural framework packed with repeating pairs of steel plates, the two plates in a pair having different geometries. The plates are produced by rolling sheet metal with corrugated rollers to produce a corrugated surface. One plate with corrugations parallel to the flow is known as the corrugated or notched plate while the second plate, with corrugations at an angle to the flow, is known as the undulated plate. The corrugated and undulated plates are conventionally made from material of equal thickness.

The packs are arranged in multiple layers in the matrix. A matrix may consist of a hot end layer, an intermediate layer or layers and a cold end layer. The characteristics of the plate profiles are chosen depending on the most likely failure mode in each layer.

Two modes of failure of packs exist in South African power stations - blockage and erosion. Erosion is the mechanical removal of plate material due to ash particle impingement. This can be a major problem in South Africa owing to ash contents of coal that can be as high as 38% by mass. Different plate configurations have different blockage and erosion characteristics. Blockage mainly occurs at the cold end of the matrix when metal temperatures drop below the acid dewpoint temperature. Water vapour condenses on the plates and dissolves oxides of sulphur to form sulphuric acid. This can result in an agglomeration of fly ash. Without effective sootblowing (the practice of cleaning plates by directing jets of steam into the packs) the build-up worsens to the point where the packs become blocked and must be replaced. Corrosion occurs in conjunction with the above two modes of failure.

Erosion gradually takes place throughout the matrix and results in failure at approximately 40% mass loss when the plates lose structural integrity. Erosion studies (Gruen et al, 2000; Crookes, 2000) have identified that the undulated plate of each repeating pair in a pack eroded at a higher rate than the corrugated plate. Making the faster-eroding undulated plate thicker should thus extend the life of that pack in applications in South Africa where erosion is a problem (Wilson et al, 1998).

The School of Mechanical Engineering at the University of the Witwatersrand and Eskom TSI are jointly carrying out research into the thermal and erosion performance of air heaters. A simulation model (Habbitts et al, 1998) was developed to predict air heater thermal and pressure drop performance for optimisation purposes.

In order to investigate the thermal performance of an air heater packed with plates of alternating thickness, the model of Habbitts was extended as outlined below.

THE AIR HEATER MODEL

To develop the equations necessary for analysis of an air heater, consider an element within a pair of parallel plates. The element consists of two metal sections of half the respective plate thicknesses and a fluid region of the same width as the flow passage between two plates (Figure 2).

The following assumptions are made :

- Steady flow into and out of the fluid region.
- The width and number of plates are sufficient to reduce the problem to essentially one dimension.
- Finite thermal conduction in the solid parallel to the direction of fluid flow, with no transverse temperature gradients.
- Finite convection from the solid regions to the fluid region, represented by an average heat transfer coefficient, h.
- Fluid thermal heat capacity is negligible in comparison with solid thermal heat capacity.

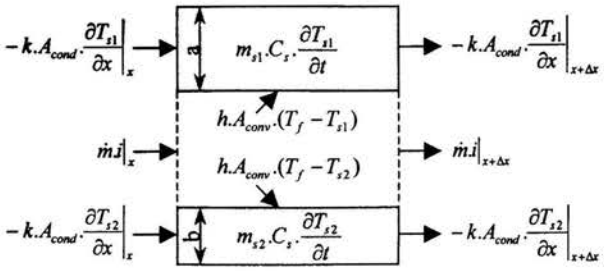

Figure 2 : Basic plate / channel element

An energy balance for the fluid region gives :

$$\frac{\partial T_f}{\partial x} + \frac{h.W}{\dot{m}.C_f}(2T_f - T_{s1} - T_{s2}) = 0 \qquad (1)$$

while that for each of the solid regions gives :

$$\frac{\partial T_{s1}}{\partial t} = \frac{k}{\rho_s.C_s}.\frac{\partial^2 T_{s1}}{\partial x^2} + \frac{h}{\rho_s.C_s.a}\left(T_f - T_{s1}\right) \qquad (2)$$

and

$$\frac{\partial T_{s2}}{\partial t} = \frac{k}{\rho_s.C_s}.\frac{\partial^2 T_{s2}}{\partial x^2} + \frac{h}{\rho_s.C_s.b}\left(T_f - T_{s2}\right) \qquad (3)$$

Equations (2) and (3) differ only in the last term where the half plate thicknesses, *a* and *b* affect the conduction areas in the solid. The equations are now converted to dimensionless form where a plate thickness ratio, β is introduced and applied together with the conventional dimensionless groups.

$$\frac{\partial T_f^*}{\partial z} + Ntu\left(T_f^* - \frac{T_{s1}^* + T_{s2}^*}{2}\right) = 0 \qquad (4)$$

$$\frac{\partial T_{s1}^*}{\partial \theta} = \lambda\frac{\partial^2 T_{s1}^*}{\partial z^2} + \frac{Ntu}{2}\left(1+\frac{1}{\beta}\right)\left(T_f^* - T_{s1}^*\right) \qquad (5)$$

$$\frac{\partial T_{s2}^*}{\partial \theta} = \lambda\frac{\partial^2 T_{s2}^*}{\partial z^2} + \frac{Ntu}{2}(\beta+1)\left(T_f^* - T_{s2}^*\right) \qquad (6)$$

Equations (4), (5) and (6) are the same as those used by Habbitts et al(1998) if the thickness ratio is unity. They are solved using the numerical technique of Mullisen and Loerke (1986). The plates are divided into elements and the equations are applied in finite difference form. The forward finite difference approximation is used for the fluid temperature equation, while the Crank-Nicholson implicit method is used in conjunction with the forward finite difference approximation for the two solid region equations.

$$\frac{T_f^*(i,n) - T_f^*(i-1,n)}{\Delta z} + Ntu\left(T_f^*(i,n) - \frac{T_{s1}^*(i,n) + T_{s2}^*(i,n)}{2}\right) = 0 \qquad (7)$$

$$\frac{T_{s1}^*(i,n+1) - T_{s1}^*(i,n)}{\Delta\theta} = \lambda(X+Y) + \frac{Ntu}{2}\left(1+\frac{1}{\beta}\right)\left(T_f^*(i,n) - T_{s1}^*(i,n)\right)$$

Where

$$Y = \frac{T_{s1}^*(i+1,n) - 2T_{s1}^*(i,n) + T_{s1}^*(i-1,n)}{2\Delta z^2}$$

$$X = \frac{T_{s1}^*(i+1,n+1) - 2T_{s1}^*(i,n+1) + T_{s1}^*(i-1,n+1)}{2\Delta z^2} \qquad (8)$$

The finite difference equation for solid region 2 is similar to equation 8, but differs by the (1+1/β) term being replaced by (β+1) and the temperatures being replaced by those of solid 2. The numbers in brackets represent the element number, i and the time interval, n, respectively. The equations are applicable for 2<i<m-1 and n>0 where i and n are integers and m is the number of elements along the plate. At the ends of the plate, an insulated end approach is implemented by setting the temperature of a fictitious element before and after the plate to the temperature of the end elements (i.e. $T_{s1}^*(0,n)=T_{s1}^*(1,n)$ and $T_{s1}^*(m,n)=T_{s1}^*(m+1,n)$; Similarly for solid region 2).

Equation (8) results in m simultaneous equations for each of the two half plates which are solved at each time interval using matrix methods (Mullisen and Loerke, 1986).

To model a pack of corrugated/undulated plate pairs, a 'stretched length' is used to modify the surface area available for convection and the cross sectional area available for conduction. The convective heat transfer coefficient is determined experimentally in a previously built thermal test facility (Caby, 1996). The facility uses the single blow transient testing technique (Cheng and Huang, 1994), whereby a computer simulation model of the test pack is set up and using the input and output temperature histories, the heat transfer coefficient is iteratively determined.

The thermal test facility produces a correlation for the thermal and pressure drop performance of a sample pack. The data is represented by a power relationship of Colburn-j factor versus Reynolds number and Fanning friction factor versus Reynolds number respectively (Figure 3).

To model the entire air heater, the face of the matrix is divided into a number of sectors. Each sector has a stream of fluid and a pack arrangement associated with it depending on its location within the matrix and its current position relative to the ducting. Once all the parameters of a sector are known, the air heater model is applied together with a heat transfer coefficient to determine the temperatures of the fluid and the solid in the particular sector for one layer. The next layer can then also be calculated, using the outlet fluid temperature of the first layer as the inlet fluid temperature for the next layer. Once all the temperatures in a sector have been found, the algorithm moves on to calculate the temperatures of the next sector.

Owing to the regular periodic variation of the temperatures within the air heater, it is not sufficient to calculate the temperatures once. Rather, the temperatures for

each sector are calculated in an ordered fashion and repeated as though the matrix were moving relative to the streams until convergence on the steam outlet temperatures is achieved.

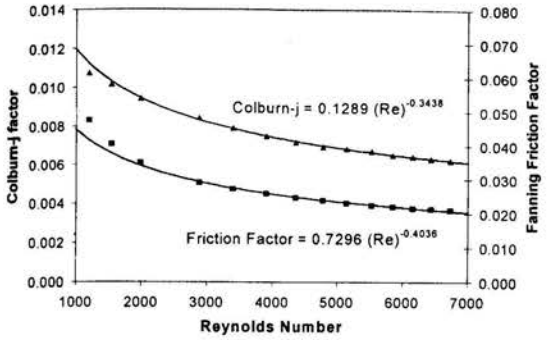

Figure 3 : An example of experimental heat transfer and pressure drop correlations

The fluid properties are predicted for each sector during the calculation. For the air streams, the values are predicted by interpolation of tabulated data. The properties of the flue gas are dependent on composition, temperature and pressure. To simplify the problem, the gas is assumed to consist of oxygen, nitrogen, carbon dioxide, and water vapour. The specific thermal capacity is then predicted based on the mass fractions of these components. To account for the effect of ash, the heat capacity of the ash particles is used to modify the gas value based on a mass fraction.

The viscosity and conductivity of the flue gas are calculated by the semi-empirical formula of Wilke (1950). The similar formula of Wassiljewa (1904) is used to calculate the conductivity of the fluid. The ash burden of the flue gas is ignored when finding the viscosity and conductivity.

Leakage is accounted for by assuming that it takes place at the cold end only. This is due to the larger pressure difference between the combustion air and flue gas streams at the cold end of the air heater. The air stream flowrates are modified prior to the calculation and the leakage quantity is mixed into the flue gas stream once the outlet temperatures have been determined.

To account for blockage, the cross sectional area available for flow is reduced, i.e. the velocity of the flow is increased. This is used to represent the obstruction to flow caused by the matrix framework or blockage due to ash buildup. Blockage is specified as a percentage for the entire layer in the matrix. Blockage in a particular sector can be specified by a defining a different pack for that sector.

The velocity distribution is described by a velocity factor which is specified for each sector. The velocity factor is then used to modify the flow rate through the sector before the calculation begins. The stream flow rate remains unaffected as the velocity factors are corrected to maintain an average of unity.

The calculation is deemed to have converged once the difference in the stream outlet temperatures for each revolution is less than a defined tolerance. If a different pack type is specified for a particular region of a layer, the above method of determining convergence fails. This is due to the different thermal performance of a different pack, which periodically changes the outlet temperature as it rotates through a stream. To accommodate this situation, two revolutions are simulated before the temperature versus time profiles for each revolution are compared. The difference between any two temperatures one revolution apart is then monitored until each difference falls below the convergence tolerance specified.

The air heater model is written to simulate Ljungstrom, Ljungstrom Tri-sector, Rothemuhle and Rothemuhle Twinflow air preheaters. A maximum number of 6 layers can be simulated. The number of time steps, distance steps and radial divisions are unlimited, but require more processing time for more divisions. A typical simulation with uniform velocity distribution, performed on an Intel Pentium 3 300Mhz machine, required 25 seconds to process.

THERMAL TEST FACILITY RESULTS

The thermal and pressure drop performance characteristics of eroded packs have been investigated in a previous study (Gruen et al, 1998). It was concluded that the thermal performance was not significantly affected by erosion.

Packs with plates of alternating thickness have also been tested in the thermal test facility. A new computer program for finding the heat transfer coefficient by the single blow transient test method (Cheng and Huang, 1994) was written, based on the heat transfer model for packs with alternating-thickness plates. It was found that the performance of the alternating-thickness pack lay between those of a pack made up of the thinner plates and one made up of the thicker plates.

Hence, the advantage of increased life with similar thermal performance of the alternating-thickness pack is preserved throughout the life of the pack.

VERIFICATION OF THE MODEL

As mentioned earlier, air heaters are conventionally packed with equal thickness plates. Thus no data exist for an actual air heater operating with alternating-thickness packs and the model cannot be verified directly against measured plant data.

To verify the calculation procedure, the results of the air heater simulation model may be compared with the results produced by the program of Habbitts for the same input data. The packs simulated must be of equal thickness plates and hence the thickness ratio is set equal to unity in the present air heater model. The program of Habbitts has been adequately verified by comparison with measured plant data from Matimba power station (Habbitts et al, 1998).

Obtaining reliable plant data for direct verification is difficult. The uncertainty in power station measurements is high. The flow rate measurements, for example, can have an uncertainty of 10 %. The simulation model is, however, useful in design and investigation work where the temperatures of different simulations can be compared.

Two comparative simulations are considered for verification of the present model, one for a Rothemuhle type and the other for a Ljungstrom type. In both cases, the geometry and estimated inlet conditions were specified to approximate real air heaters. The outlet conditions and the difference in the values between the two simulation programs are presented in Table 1.

The difference in the temperatures is small and can be attributed to the way in which the many outlet temperatures for each sector are reduced to one stream outlet temperature. The program of Habbitts uses an average temperature calculated on an area basis while the present model uses an energy balance. The methods are similar because the specific heats of the fluid are almost constant under all conditions within the air heater and the mass flow rate through each sector is constant.

Table 1 : Comparison of simulated temperatures.

	Model Habbitts Et al (1998)	Model Present Study	Difference
Simulation of a Ljungstrom type :			
FG out T [°C]	119.17	120.07	0.92
SA out T [°C]	270.67	269.84	-0.83
Simulation of a Rothemuhle type :			
FG out T [°C]	143.19	143.87	0.68
SA out T [°C]	285.45	285.39	-0.06

Entrained leakage is also calculated differently in the two programs. (Entrained leakage is that amount of fluid that is transferred from one stream to the next by the relative rotation of the matrix.) The prediction of density in both programs is calculated by the ideal gas law which depends on temperature and pressure. The current simulation program uses the average of the inlet and outlet values whereas the program of Habbitts used the values at outlet.

Based on the outlet temperatures and the aforementioned differences in the simulation programs, the calculation procedure of the present model can be accepted as being the same as the model of Habbitts. Because the model of Habbitts has been verified against measured plant data, the calculation procedure and implementation of the present model is thus also verified.

The question arises as to the validity of the case where the thickness ratio is not unity. The thermal test facility predicts an outlet temperature using an estimated heat transfer coefficient and then compares this temperature to that measured. Depending on the error, the heat transfer coefficient is modified and the process is repeated to minimize the difference between the two temperatures. For the difference to reduce to an appreciably small value, the heat transfer model must be valid.

For the tests carried out using the alternating plate thickness heat transfer model, the error between the measured and the simulated temperature versus time profiles were sufficiently small to conclude that the heat transfer model is valid.

Hence, the air heater simulation model is verified, firstly by checking the calculation procedure against a verified simulation program and secondly by predicting the correct temperature versus time profile for the thermal tests of a sample pack with plates of alternating thickness.

PERFORMANCE OF AN AIR HEATER PACKED WITH PLATES OF ALTERNATING THICKNESS

A fictitious air heater similar to the Rothemuhle secondary air pre-heaters at Matimba Power Station was chosen for comparative simulations. The geometry and input conditions of the air heater were set identical to those of the real air heaters. The packs used in the simulations were different from those at Matimba due to the pack types at Matimba not having been tested for their thermal and erosion performance.

The first simulation used packs of plates of 0.5 mm thickness, whilst the second simulation replaced the packs with packs of alternating thickness plates. The plate thicknesses were 0.5 and 0.8 mm for the corrugated and undulated plates respectively. The volume occupied by the packs remained constant for the two simulations, as this is most likely to be the case in reality due to the similar thermal performance of the two cases.

The erosion life for each simulation was predicted using the experimental data and method of Crookes (2000). Although Crookes only considers packs of plates with equal thicknesses, the percentage mass loss to failure can be modified to predict the life of an alternating-thickness pack. Two assumptions are made, firstly that the erosion rate of the undulated plate is double that of the corrugated plate (this is a typical finding from previous work (Gruen et al, 2000, Crookes, 2000)) and secondly, that failure occurs once the average thickness of the corrugated plate is the same as for a pack with equal thickness plates at 40% mass loss. The point of failure for the 0.5/0.8 mm pack is predicted to be at 46 % mass loss.

Table 2 shows a summary of the results. The thermal performance remains effectively unchanged, but the pressure drop has decreased by a small amount. This is due to the increased gap between the plates of the alternating thickness pack. On the other hand, the increased thickness of a plate pair reduces the number of plates per unit volume, with the result of slightly decreased thermal performance.

The minimum plate temperatures for the two simulations have also been calculated to check if there are any detrimental effects due to the thinner plate attaining a lower temperature. As is shown, the average cold end plate temperature has increased by 1°C. The thinner the plate, the greater the temperature fluctuations for a given rotational speed of the air heater. Thus, if the alternative of reducing the corrugated plate thickness instead of increasing the undulated plate thickness is used, the average cold end temperature would decrease. This must be considered for air heaters with already low flue gas outlet temperature as the possibility of sulphuric acid condensing on to the plates is increased.

Table 2 : Simulated comparison of equal versus alternating thickness plates on air heater performance

	Equal thickness plates	Alternating thickness plates	Difference
FG out T [°C]	129.28	130.7	1.42
SA out T [°C]	278.06	277.44	-0.62
FG ΔP [kPa]	0.802	0.746	-0.056
SA ΔP [kPa]	0.548	0.510	-0.038
Min Plate T [°C]	80.96	80.85	-0.11
Ave Cold end T [°C]	101.34	102.26	0.92
Pack mass [ton]	259.2	325.0	65.8
Predicted Life [yrs]	11.7	17.2	5.5

The predicted erosion life of the alternating-thickness pack is 5.5 years longer than the pack with equal thickness plates. This amounts to an increase of almost 50% in the life of the pack.

The cost of a pack is essentially proportional to the mass of steel used and this makes up the capital cost. Thus the above simulation comparison shows that the capital cost of the alternating-thickness pack is approximately 65 tons of steel more expensive than the pack with equal thickness plates. (The relative costs of the supporting structures are not considered here.)

The increase in capital cost is offset by the longer life of the alternating-thickness pack. Using pack lives of 12 and 18 years for the equal and alternating-thickness packs respectively, a net present value study of the above situation shows that the alternating-thickness pack would be more cost effective in certain circumstances. With an interest rate of 10 % p.a. and an inflation rate of 3 % p.a. over a time period of 36 years, the net present costs of both methods are equal. Increasing the inflation rate causes the alternating-thickness pack to become more cost effective, while increasing the interest rate causes the equal-thickness pack to become more cost effective.

Another economic advantage of the alternating-thickness pack is the reduced pressure drop which then requires less fan power to achieve the same flow rates through the air heater.

CONCLUSIONS

A regenerative air heater simulation model has been developed for predicting the thermal performance of air heaters packed with plates of alternating thicknesses. The model is also capable of predicting the effects of leakage, blockage, varying pack characteristics in the matrix and non-uniform velocity distributions. The model has been verified by comparison with the model of Habbitts et al (1998) and prediction of outlet temperatures from a thermal test facility.

A case study of the economic implications of replacing the equal thickness plates in a particular air heater with alternating-thickness packs showed that the alternating-thickness packs are likely to be more cost effective.

ACKNOWLEDGEMENT

The authors would like to thank Eskom for permission to publish this paper and the Eskom Resources and Strategy Group Research Division for providing the funding. Particular thanks are due to Mr M Lander for his invaluable assistance.

REFERENCES

Caby MJ (1996) *Experimental Investigation of heat transfer in Regenerative Heat Exchangers*, MSc(Eng) dissertation, University of the Witwatersrand, Johannesburg.

Cheng CH and Huang CS (1994) Extended Model for Single Blow Transient Testing Method in Evaluating Thermal Performance of Heat Transfer Surfaces, *Int. Communications in Heat and Mass Transfer*, Vol. 21, pp. 53-63.

Crookes RA (2000) *Erosion by Fly Ash of Regenerative Air Pre-heater Elements in Power Stations*, MSc(Eng) dissertation, University of the Witwatersrand, Johannesburg.

Gruen K, Jawurek HH, Sheer TJ and Lander M (2000) Erosion Patterns on Heating Plates for Regenerative Air Pre-Heaters, *Proc. 12th International Symposium on Transport Phenomena*, Istanbul, pp. 1-9.

Habbitts SA, Sheer TJ, Jawurek HH, Lander M and Schmitz W (1998) Simulation and Measurement of the Thermal Performance of Regenerative Air Pre-heaters, *Proc. 11th International Heat Transfer Conference*, Kyongju Korea, Vol. 6, pp. 45-50.

Mullisen RS and Loerke RI (1986) A Transient Heat Exchanger Evaluation Test for Arbitrary Fluid Inlet Temperature Variation and Longitudinal Core Conduction, *Journal of Heat Transfer*, Vol. 108, pp. 370-376.

Wilke CR (1950) *Journal of Chemistry and Physics*, Vol. 18 pp. 517.

Wilson RW, Sheer TJ, Jawurek HH (1998) Erosion Prediction in Rotary Regenerative Air Preheaters, *Proc. 2nd South African Conference on Applied Mechanics*, Rondebosch South Africa, Vol. 2, pp. 1127-1137.

Wassiljewa A (1904) *Physik. Z.*, Vol. 5, pp. 737.

HEFAT2002
1st International Conference on Heat Transfer, Fluid Mechanics and Thermodynamics
8-10 April 2002, Kruger National Park, South Africa
DM1

THREE DIMENSIONAL TIME ACCURATE UNSTRUCTURED FINITE VOLUME TECHNIQUE FOR MODELLING GROUND-COUPLED HEAT EXCHANGERS

Michel De Paepe
Department of Flow, Heat and Combustion Mechanics
Ghent University
Sint-Pietersnieuwstraat 41
B 9000 Gent, Belgium
Email: Michel.Depaepe@rug.ac.be

ABSTRACT

Ground-coupled heat exchangers can be used to reduce energy consumption in building ventilation systems. The idea is to preheat air in winter and precool air in summer using the thermal capacity of the soil. To do this concrete or plastic tubes are put underground. Through these tubes the ventilation air is drawn. Due to the temperature difference between ground and air, the ventilation air is cooled or heated. The scope of this paper is to describe and develop a three-dimensional unstructured finite volume model for the calculation of the ground-coupled heat exchanger. The model solves the conduction through the soil (including radiation and convection on the top layer) and the convective heat transfer with the air flowing through the pipe, using the unstructured finite volume solver of FLUENT. Time stepping is introduced to take the seasonal variations into account. The model is validated with measurements done on an existing ground-coupled heat exchanger and then used to study the performance of the ground-coupled air heat exchanger in the Belgian climate situation. Calculations are made with the Test Reference Year (TRY) data of Uccle (Belgium). It is shown that in summer the air can be cooled with about 9 ^oC at sufficient depth (3 m) and tubes of about 50 m. In winter heating of 7 ^oC can be realised. It is also shown that a good control strategy is important.

NOMENCLATURE

a thermal diffusivity (m^2/s)
A heat transfer area (m^2)
c_p heat capacity (J/kgK)
d tube diameter (m)
h convection coefficient (W/m^2K)
L tube length (m)
$\dot{m}$ mass flow rate (kg/s)
Nu Nusselt number (-)
Pr Prandtle number (-)
$\dot{q}$ heat flux (W/m^2)
Re Reynolds number (-)
t time (s)
T temperature (K)
u wind speed (m/s)

Greek Letters

λ conductivity (W/mK)
ρ density (kg/m^3)
ξ friction factor $(-)$

Subscripts

air air
face calculation face in a segment
i tube segment number
m average in tube segment
sur surface
w tube wall

INTRODUCTION

In order to reduce energy consumption of buildings, several passive techniques are nowadays being introduced in HVAC-installations. In most cases solar energy is directly or indirectly used to supply heat or electrical energy. Sometimes solar gains inside the building are avoided to keep down the size of the air-conditioning unit. The soil absorbs heat from the sun and thus accumulates heat in summer. In winter the heat is released to the surrounding structures and air. Furthermore,

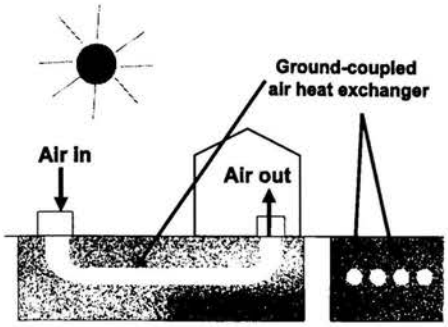

Figure 1. GROUND-COUPLED HEAT EXCHANGER

the soil has a big thermal inertia. Because of the aforementioned phenomena the temperature of the soil (at a sufficient depth) is lower than the surrounding air in summer and higher in winter. This effect can be used to supply a building with energy. One of the interesting techniques is to put tubes into the ground, through which air is drawn (see Figure 1). The air is cooled in summer and is heated in winter. These systems are called ground-coupled air heat exchangers. In several European countries this technique is used for private houses and office buildings. Recent examples are found in Germany (Schuler, 1999) and Switzerland (Zimmerman, 1998). In Belgium only two buildings exist where a ground coupled heat exchanger is used. The first one is the Zenit-house, a private house (Lievens, 1999), the second one is the Oxfam building in Ghent (Cenergie, 2000), an office building in which several advanced passive technologies are used. In both cases no special care was taken for the design of the ground tube. In the Zenit-house one tube is used at a depth of 0.6 *m*. In the Oxfam building also one tube is used, put at a depth of 0.5 *m*. Neither of these systems gives good performance (De Paepe et al., 2001). At this moment two new office buildings are under construction in Belgium, using a more advanced ground coupled heat exchanger. These were designed using the CAPSOL software and a 1 dimensional model developed at the Ghent University (De Paepe et al., 2001). In the near future measurement results of the performance of these buildings will be published. Up till now no thorough analysis was made of the possibilities of the ground-coupled air heat exchanger in the Belgian climate. In this paper a three-dimensional model is developed to study the performance of the ground coupled heat exchanger. The conduction through the ground and the heat transfer at the ground-air surface are taken into account. This model is coupled to weather data for Uccle (Belgium). The model allows to analyse the performance of the ground-coupled air heat exchangers in the Belgian climate.

LITERATURE REVIEW

In the literature several calculation models for ground coupled heat exchangers are found. Tzaferis et al. studied eight models (Tzaferis et al., 1992). Six of the models use a one-dimensional description of the pipe. A relation between inlet and outlet temperature of the tube is derived. For al these models no influence of thermal capacity of the earth can be taken into account. Secondly the influence of different pipes on each other cannot be studied. In one algorithm the ground is divided into coaxial cylindrical elements. The thermal resistance of the ground is considered to be time-dependent. The pipe is divided in segments. In each segment the exit temperature is determined. In an other algorithm the steady-state heat balance is solved between a point in the ground and the tube. Mihalakakou et al. (Mihalakakou et al., 1994) present a model in which the ground surrounding the pipe and the pipe itself are described in polar co-ordinates. In this model temperature and moisture profiles are included in the equations. The influence of the ground surface temperature is modelled by the superposition of the algebraic solution of the undisturbed temperature field caused by the surface air temperature and the temperature field caused by the pipe. The authors claim the importance of including the moisture content in the soil. They show good comparison of calculations and measurements. The model is solved in the TRNSYS environment. In this model it is not possible to solve the influence of several pipes on each other. Bojic et al. (Bojic et al., 1997) developed a model in which the soil is divided into horizontal layers. It is assumed that the temperature of each layer is uniform. Al the pipes are placed in one layer. The heat transported from the air to the soil is modelled by solving the heat balance between entrance and exit of the pipe and taking the temperature difference between the temperature at the pipe wall and the average air temperature between entrance and exit of the pipe. This model is a 2 dimensional model, so no influence of pipes on each other can be detected. The temperature variation through the pipe cannot be studied with this model. No validation is given. None of the aforementioned models is capable of directly predicting the fully transient three-dimensional heat transfer in a multiple pipe ground-coupled air heat exchanger. Gauthier et al. (Gauthier et al., 1997) describe a fully three-dimensional model. A Cartesian co-ordinate system is used. To be able to do this, the round pipes are replaced with square pipes of equivalent areas. In this model the influence of different layers in the soil, concrete foundations and insulation can be added. Validation of the model is discussed In this paper the last approach is further refined. In order to be able to calculate any type of geometry a unstructured grid is used. This enables the use of round tubes, without any further constraint. Furthermore the size of the grid can be varied to give more detail around the pipes and reduce calculation time where the precision is not needed.

A comparable model with modelling of the condensation/evaporation in the tubes was recently presented by Hollmuller and Lachal (Hollmuller et al. 2001). The model uses the same assumptions as (Gauthier et al., 1997) and is adapted to TRNSYS. It is validated with data from (Zimmerman, 1998).

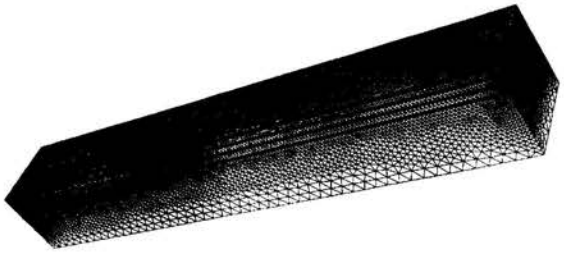

Figure 2. THE UNSTRUCTURED CALCULATION GRID

PHYSICAL MODEL AND NUMERICAL PROCEDURE

A typical calculation grid is shown in Figure 2. The calculation grid is considered to be a rectangular block in which cylindrical holes are drilled representing the buried pipes. The upper side of the rectangular block is the outside air surface. Here an extra layer can be added to take slabs, insulation, etc. into account. The lower side is considered to be at great distance (infinity) from the tubes. It is at a distance of at least 20 times the diameter of the tubes. The left-hand and right-hand side of the calculation domain are considered to be adiabatic and at a sufficient distance from the tubes. The front and rear sides contain the inlet and outlet of the tubes. The calculation domain is divided in finite tetrahedral volumes. For each volume the temperature is constant and the conduction equation is solved. The mesh spacing near the surface and the tubes is more refined than at the boundaries of the grid. The airflow inside the tubes is coupled with the calculation grid through he boundary conditions at the tube wall. The tubes are divided in equal segments. The number of segments can be varied to obtain more accuracy, but is always taken big enough to have a good resolution. Figure 3 illustrates the principle. In each segment the temperature is taken to be constant. The temperature of the previous segment and the heat flux through the wall are used to calculate the temperature in a given segment.

The heat transfer model is based on the following assumptions :

1. Conduction heat transfer is transient and fully three dimensional in the soil and other materials.
2. The thermophysical properties of the soil and other materials are constant.
3. Heat transfer by moisture gradients in the soil is neglected.
4. Heat transfer in the pipe is dominated by convection. It is however coupled with the temperature field of the surrounding soil by the boundary conditions at the pipe surface

Assumption 3 is justified by the fact that heat transfer processes take place over periods of 24 h and involve temperature differences of less than 10 K. Gauthier (Gauthier, 1994) showed that the maximal influence of the moisture gradients on heat transfer is below 0.1% of the total heat transfer in the soil. Puri (Puri, 1986) also reached the conclusion that moisture movement has little effect on heat transfer. The thermal

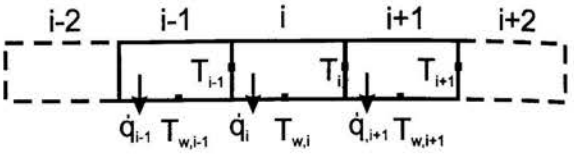

Figure 3. THE SEGMENTS FOR CALCULATIONS OF THE TUBES

conductivity of the soil increases with water content, but so does in a similar proportion the heat capacity.

The governing equations for the conduction in the soil may be stated as :

$$\rho c_p \frac{\partial T}{\partial t} = \lambda \nabla T \tag{1}$$

The boundary conditions for the underground lateral external surfaces of the computational domain are assumed to be adiabatic, i.e. :

$$\frac{\partial T}{\partial n} = 0 \tag{2}$$

where n is the unit vector normal to the surface.

A constant and uniform temperature for the horizontal plane deep underground is imposed. For all the calculations this was set to 10 C.

At the ground surface the heat flux from the outside air to the surface and the solar radiation is calculated by :

$$\lambda \frac{\partial T}{\partial z} = h_{sur}(T_{soil} - T_{sur}) + \dot{q}_{sur} \tag{3}$$

where T_{sur} is the temperature of the surrounding air and $\dot{q}_{sur}$ the net radiation heat flux on the surface due to solar radiation and radiation to the sky. This can be a constant value or a time dependent function. h_{sur} is the convection coefficient determined by the empirical correlation (Mihalakakou et al., 1997):

$$h_{sur} = 0.5 + 1.2u^{0.5} \tag{4}$$

where u is the wind speed above the ground surface. The T_{sur}, u and $\dot{q}_{sur}$ are taken from experimental data or the Test Reference Year (European Communities, 1985). Not all the solar radiation is absorbed. Depending on the type of ground surface a absorption coefficient is defined. There is also a radiative loss from the surface to the sky. For summer this is taken to be 100 W/m^oC, in winter 50 W/m^oC and in between 75 W/^oC.

For the air flow inside the tubes the following equations are solved (see Figure 3) :

$$\dot{q}_i = h_{tube}(T_{i,m} - T_{w,i}) \tag{5}$$

$$\dot{q}_i A_i = \dot{m}_{air} c_{p,air}(T_i - T_{i+1}) \tag{6}$$

where A_i is the inside surface area of the tube segment, $\dot{q}_i$ the heat flux over it. Equation (6) is the energy balance for the air flow. The convection coefficient h_{tube} is determined by the Gnielinski correlation for turbulent flow (VDI, 1994):

$$Nu = \frac{\frac{\xi}{8}(Re-1000)Pr}{1+12.7\sqrt{\frac{\xi}{8}}\left(Pr^{\frac{2}{3}}-1\right)} \quad \xi = (1.82\log Re - 1.64)^{-2} \quad (7)$$

and for laminar flow :

$$Nu = \left[3.66^3 + 0.7^3 + \left(1.615\left(RePr\frac{d}{L}\right)^{\frac{1}{3}} - 0.7\right)^3\right]^{\frac{1}{3}} \quad (8)$$

Finally the heat flux is calculated by equation (5). Here the driving force is the temperature difference between the wall temperature and the average temperature of the air in the segment :

$$T_{i,m} = \frac{T_i - T_{i-1}}{2} \quad (9)$$

The wall temperature is calculated by taking the weighted average over the surface of the segment's faces :

$$T_{w,i} = \frac{1}{A_i}\Sigma_{faces} A_{face} T_{face} \quad (10)$$

The entrance temperature of the tube is taken to be the air temperature at the surface and can be varied with time. The boundary condition at the tube surface is thus for each segment:

$$\lambda\frac{\partial T}{\partial z} = \dot{q}_i \quad (11)$$

The calculation grid is generated with the GAMBIT grid generation software (Fluent, 1998). The conduction equations are solved with FLUENT 3D (Fluent, 1998). The routines for the boundary conditions of the tubes have been added by user defined subroutines to the Fluent environment.

Time stepping was set in the Fluent solver as the second order implicit method. Time steps are set to 1000 s in real time, in the simulations.

VALIDATION OF THE MODEL

One-dimensional conduction

In a first test case the solution of the conduction equations is validated. The problem of a semi-infinite solid onto which at one side a temperature is imposed is calculated. As there is no heat flux in x and y directions (sideways) this problem can be analytically solved as a one-dimensional conduction problem.

The surface temperature is :

$$T(t,0) = T_s \quad (12)$$

And the initial value of the ground temperature is

$$T(0,z) = T_\infty \quad (13)$$

The analytical solution is given by :

$$T(t,z) = T_s + (T_\infty - T_s)\,erf\left(\frac{z}{12\sqrt{at}}\right) \quad (14)$$

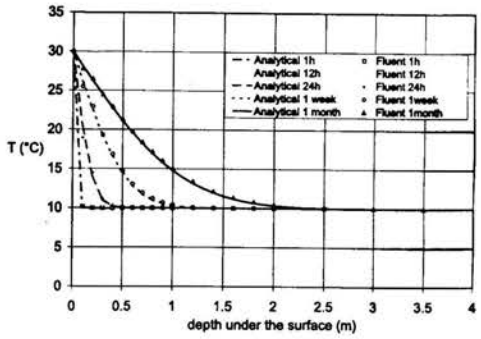

Figure 4. NUMERICAL VERSUS ANALYTICAL SOLUTION

where $a = \frac{\lambda}{\rho c_p}$.

Simulations were done with ρ = 1800 kg/m^3, λ = 0.5 W/mK, $c_p = 2000\ J/kgK$.

In Figure 4 the analytical solution is shown for time steps of 1 h, 12 h, 24 h, 1 week and 30 days, with initial value of $T_\infty = 10\ ^oC$ and $T_s = 30\ ^oC$. The abscissa shows a variation of depth from $z = 0\ m$ to 4 m. In the same Figure the numerical results are shown for the simulation with the same values. A good correspondence is found. It is also shown that temperature influence at a depth of more than 3 m is not important.

Ground-coupled air heat exchanger

Secondly measurement data provided by Tzaferis et al. (Tzaferis et al., 1992) were used to validate a real simulation of a ground tube. In Figure 5 the input data are shown. These were realized by placing a heater in front of the tube to control the inlet air temperature. The ground temperature at 1.1 m depth is nearly constant and is 23 ^oC. The tube has a diameter of 0.15 m and a length of 14.8 m and is placed at a depth of 1.1 m. A air mass flow rate at 4.5 m/s is circulated continuously through the pipe during 9 days. Calculations were made with the same values for the soil characteristics as in the previous section. In Figure 5 the measured outlet temperatures and

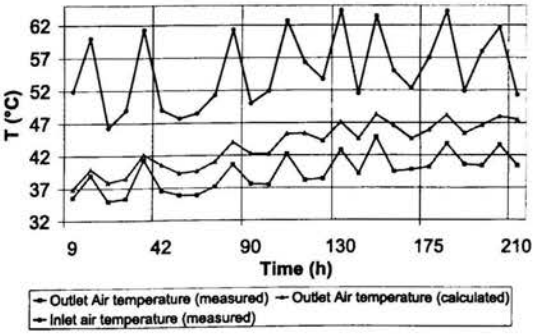

Figure 5. VALIDATION WITH MEASUREMENTS

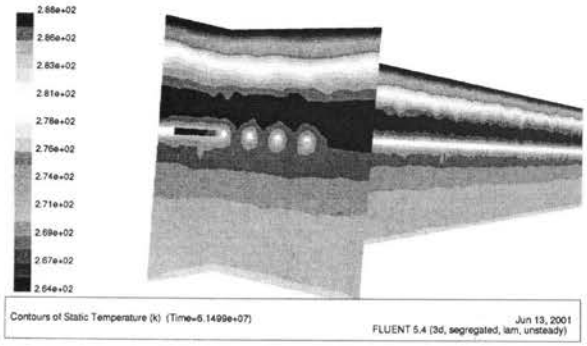

Figure 6. A CUT THROUGH THE CALCULATION DOMAIN

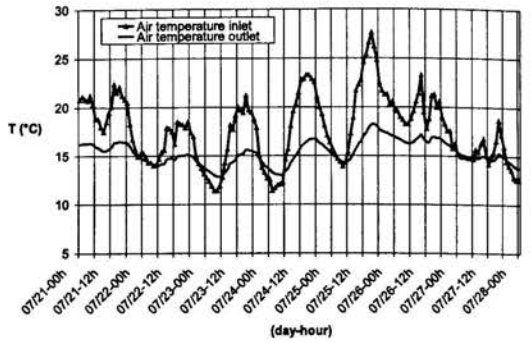

Figure 7. TEMPERATURES FOR WEEK FROM 21/7 TO 28/7

the calculated outlet temperatures are shown. The calculations follow the same trend as the measurements. The model underpredicts the cooling by approximately 2 ^oC to 5 ^oC on average. This is caused by the fact the exact composition of the soil and thus the characteristic values for heat capacity and thermal conductivity are not known.

PERFORMANCE IN THE BELGIAN CLIMATE

Scope

The described model was used to study the behaviour of a ground-coupled air heat exchanger in the Belgian climate situation. Therefore the weather data of the Test Reference Year of Uccle (Belgium) were added to the simulation (European Communities, 1985). The absorption coefficient of the soil was set to 0.8. The radiative losses were to the values mentioned earlier. With these data the whole year was simulated twice tot damp out the transient phenomena. The obtained solution was used as basis for the simulation of a real year. The problem of four tubes with a diameter of 0.2 m and a length of 50 m was solved as a reference case. A total air flow rate through the tubes of 3000 m^3/h is assumed, resulting in and air velocity of 6.6 m/s inside the tubes. The tubes are placed at a depth of three meter under the ground surface. The distance between the tubes is 1 m. These data were chosen in accordance with the rules of thumb for the design of ground-coupled heat exchangers given by Santamouris et al. (Santamouris et al., 1996). Although these figures relate to increased summer ventilation rates for cooling, they were here assumed to be constant over the whole year.

With the aforementioned assumptions the heat exchangers were calculated for the whole year. First some general aspects will be discussed. Secondly a typical summer week in the Belgian climate is studied. Finally a typical winter week is analyzed.

General aspects

Figure 6 shows two planes cutting through the calculation domain, one along the length of a tube, and one perpendicular to it. The case shown here are data for the winter situation. One can see that the top layer of the soil is frozen (below 0 ^oC). At a depth of about 1 m the temperature starts to rise to about 15 ^oC at 2.5 m. This high temperature zone is strongly influencing the top side of the tubes.

In the surroundings of tubes a clear temperature drop in the soil can be detected up to 3 diameters from the tubes. This zone is seen along the whole length of the tubes. Due to the use of the 3-dimensional model, this can be clearly calculated. The tube spacing of 1 m is not sufficient to damp out the influence of the tubes on each other.

A typical summer week

Figure 7 shows the inlet air temperature (i.e. the outside air temperature) as defined by the TRY and the calculation results for the week from July 21 to July 28.. At a maximum air temperature of 27.6 ^oC cooling to 18.2 ^oC is possible, which is a temperature difference of 9.4 ^oC. In general the calculations show that the ground-coupled tubes used here, damp out the variations in air temperature. This is mainly caused by putting them at a depth of 3 m and by sufficient length of the tube. Secondly a phase shift between the tube exit temperature and the inlet temperature can be detected. The response of the tubes is about 1 hour slower then temperature at the exit. Figure 7 also shows that during the night the air temperature is lower then the temperature leaving the ground-coupled heat exchanger. This clearly shows that a good control strategy is needed when a ground-couples heat exchanger is connected to a building. By-passing of the tubes, and thus taking air directly from the surroundings of the building, might be necessary. As the summers in the Belgian climate are moderate, the ground-coupled heat exchanger has potential to supply a building with low temperature air. By doing this cooling installations can be reduced in capacity or even omitted.

A typical winter week

In figure 8 the results are shown for the week from December 21 to December 28. During cold days the air can be heated from -2.7 ^oC to 4.3 ^oC, yielding a temperature difference of

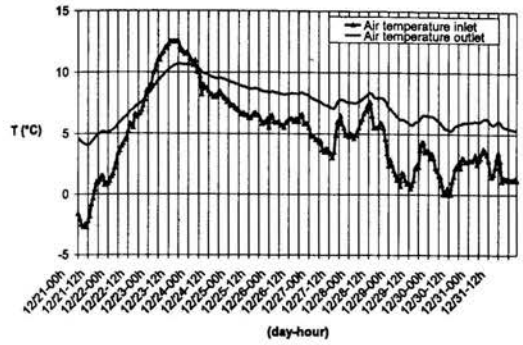

Figure 8. TEMPERATURES FOR WEEK FROM 21/12 TO 28/12

7.0 ^oC. The same phase shift can be detected as in summer. During warmer winter days the air is not heated but cooled by the ground tubes. This is a situation that is not allowable. This again confirms the fact that at all times it is necessary to monitor the outside air temperature and the exit temperature of the ground-coupled heat exchanger. For the Belgian winters the ground-coupled heat exchanger can reduce the power needed for heating, but heating cannot be avoided.

CONCLUSION

In this paper a fully three-dimensional unstructured conduction model is presented, which is coupled to the convection problem of air flowing through tubes buried in the soil. This model can be used for studying ground-coupled air heat exchangers. The model is validated with two different test cases. The model is used to study the use of ground-coupled air heat exchangers in the Belgian climate situation.

It is shown that the influence of the pipe on the temperature of the surrounding soil is detected to a distance of twice the diameter of the tube. To make optimal use of the thermal capacity of the soil and to eliminate the influence of the outside air, the tubes have to be buried below 2.5 m.However, this thermophysical optimum should be compared to less drastic lay-outs and carefully be weighted against financial aspects (excavation costs).

Finally typical summer and winter weeks have been simulated. It is shown that the ground-coupled air heat exchangers have great potential. Cooling with 9 ^oC or heating with 7 ^oC is possible. Due to the moderate winters in Belgium, it is important to apply a good control strategy when a ground-coupled air heat exchanger is used. This has to allow bypassing the heat exchanger.

REFERENCES

Bojic, M., Trifunovic, N., Papadakis, G., Kyritsis, S., Numerical simulation, technical and economic evaluation of Air-to-earth heat exchanger coupled to a building, Energy, Vol. 22 No 12, pp 1151-1158, 1997.

Cenergie, Research report 069 of the research program with BBRI, Ghent University, Wenk St-Lucas, supported by the Flemish Regional Government (IWT), 2000.

De Paepe M., Mlecnik E., de Bruyn G., Govers K., Van Dyck T., Bossaer A., Baert K., Earth-air Heat Exchangers in the Belgian Climate : First Practical Experience, 22e AIVC confrence, Bath, United Kingdom, 2001.

European communities, Test Reference Years, TRY. Weather data sets for computer simulations of solar energy systems and energy consumption in buildings, Directorate General XII for Science, Research and Development, 1985.

Fluent, Fluent Incorporated, Centerra Resource Park, 10 Cavendish Court, Lebanon, NH 03766, 1998.

Gauthier, C., Transfer de chaleur et d'hulit dans le sol. Internal report, Group de recherche THEMAUS. Dpartement de gnie mchanique, Universit de Sherbrooke, 1994.

Gauthier, C., Lacroix, M., Bernier, H., Numerical simulation of soil heat exchanger-storage systems for greenhouses, Solar energy, Vol 60 No 6 pp 333-346, 1997.

Hollmuller, P., Lachal, B., Cooling and preheating with buried pipe systems : monitoring, simulation and economic aspects, Energy and Buildings, Vol 33 No 5, pp. 509-518, 2001.

Lievens, W., Zenith , het 'andere' huis van de toekomst. de Koevoet, juli 99, pp 26-28, 1999 (in dutch).

Mihalakakou, G., Santamouris, M., Asimakopoulos, D., Modelling the thermal performance of earth-to-air heat exchangers, Solar Energy, Vol. 53, No. 3 pp. 301-305, 1994.

Mihalakakou, G., Santamouris, M., Lewis, J., Asimakopoulos, D., On the application of the energy balance equation to predict ground temperature profiles., Solar Energy, Vol. 60, No. 3/4 pp. 181-190, 1997.

Puri, V. 1986. Feasiblity and performance curves for intermittent earth tube heat exchangers. AM. Soc. Agricul. Eng. Vol 29, pp. 526-532, 1986.

Physibel, Capsol versie 3.3 computerprogramma voor het berekenen van multizonaal dynamisch warmtetransport - Physibel Document M-CP-A-N05, Belgium, 1999 (in dutch).

Santamouris, M., Asimakopoulos, D. Passive cooling of buildings, James & James London, 1996.

Schuler, M., Design for Daylighting and Energy in Ingolstadt, Advanced Building Newsletter 23/24, pp. 18-23, 1999.

Tzaferis, A., Liparakis, D.,Santamouris, M., Argiriou, A. Analysis of the accuracy and sensitivity of eight models to predict the performance of earth-to-air heat exchangers, Energy and Buildings, Vol. 18 pp 35-43, 1992.

VDI, Wärmeatlas, Springer Verlag, 1994.

Zimmermann, M., The Schwerzenbacherhof Office and Industrial Building Swerzenbach, Switzerland, Ground Cooling (Air), IEA Low Energy Cooling Demonstration 15/1-15/8, 1998.

HEFAT2002
1st International Conference on Heat Transfer, Fluid Mechanics, and Thermodynamics
8-10 April 2002, Kruger Park, South Africa
ES1

METHODS FOR ASSESSMENT OF HEAT TRANSFER COEFFICIENT IN A 180°-BEND BY MEANS OF CFD FOR ENGINEERING APPLICATIONS

*S. Etemad, **E. Celik, ***M. Ewaldsson and ****B. Sundén
*Lic. Eng.; ***M. Eng.
Thermodynamic Analysis
Dept. 92591 HB2S
Volvo Car Corporation
SE-405 31 Gothenburg
Sweden
**M.Eng.; ****Professor
Division of Heat Transfer
Lund Institute of Technology
Box 118
SE-221 00 Lund
Sweden
E-mail: setemad@volvocars.com

ABSTRACT

The local turbulent heat transfer coefficient in a U-shaped bend was assessed by means of applied CFD. Both heat-momentum analogy methods and a direct or conventional method were used. The experimental data show an increasing heat transfer coefficient from the inner part of the bend to the outer part in all cross sections along the bend. This trend was captured by all methods except for Reynolds analogy, which predicted a nearly constant value at each cross-section.

The analogy methods over-predicted the lowest values and under-predicted the highest values of Nusselt number in most positions along the bend. When using the analogy methods, various linear and non-linear k-ε turbulence models and k-ε-RNG were used to solve the flow field.

The direct method showed better agreement with experimental data (although under-predicted). In addition to the standard k-ε and k-ε-RNG, an Algebraic Stress Model, ASM, was used. The trends were generally best captured with ASM. It is obvious that the analogy methods (combined with detailed flow simulations) such as Reynolds analogy are incapable of predicting the variation of the Nusselt number in cross sections of the bend. However, predicted values of the mean Nusselt number in each cross section were reasonable.

INTRODUCTION

The development of CFD in recent years has made it possible to carry out pre-design analyses for industrial applications. There is a desire to come closer to the so-called virtual sign-off for instance in automotive, aerospace and process industry. This has forced the CFD-specialists on development of new methods for more accurate prediction of important flow and heat transfer properties. In thermodynamic machines such as reciprocating engines and gas turbines, the rate of heat transfer has a great impact on the fluid properties and the temperature field of the structure. This in turn influences the efficiency of the machines and their mechanical property. Thus, accurate and reliable prediction methods for local heat transfer coefficients in passages such as the cooling passages in gas turbine blades or coolant jacket in the internal combustion engines are highly desirable. Modern passenger car engines with aluminium alloys and increasingly higher power output, require ever more advanced cooling. These coolant passages have usually complex geometrical shapes with curvature, converging-diverging sections, and also flow separation and re-attachment regions are present.

The methods available today for prediction of heat transfer coefficients for these applications are, however, inaccurate or expensive. There is therefore a great need for investigation of

the validity of the existing methods, identification of their weaknesses and if necessary development of better methods should be attempted for.

NOMENCLATURE

C_F shear stress coefficient = $2\tau_w / \rho u^2$
c_p specific heat [J/kgK]
$C_{1\varepsilon}$ =1.44, empirical coefficient
$C_{2\varepsilon\varepsilon}$ =1.92, empirical coefficient
C_μ =0.09, empirical coefficient
D tube diameter [m]
f friction coefficient $=\Delta p/(L/D)(\rho U^2/2)$
h heat transfer coefficient [W/m^{2}K]
k turbulent kinetic energy [m^2/s^2]
L tube length [m]
Nu Nusselt number = hD/λ
Pr laminar Prandtl number $=\mu c_p / \lambda$
Pr_t turbulent Prandtl number [-]
q_w local heat flux (per unit area) [W/m^2]
Re Reynolds number = UD/ν
r bend radius [m]
St Stanton number; $h / \rho c_p u$
t time averaged fluid temperature [°C]
t_b fluid bulk temperature [°C]
t_w wall temperature [°C]
U mean velocity in the pipe [m/s]
u time averaged flow velocity parallel to wall [m/s]
v time averaged flow velocity perpendicular to wall [m/s]
y normal distance to the wall [m]

Greek Letters

Δp pressure drop [Pa]
ε turbulent dissipation [m^2/s^3]
λ fluid thermal conductivity [W/mK]
μ molecular viscosity [Pa s]
μ_t turbulent viscosity [kg/ms]
ν kinematic viscosity [m^2/s]
ρ density [kg/m^3]
σ_k =1.00, empirical coefficient
σ_ε =1.30, empirical coefficient
τ_w wall shear stress [Pa]
Φ angle in tube cross section, 0=inside of bend, 180=outside of bend (see Fig. 1)
Ω bend angle, 0= start of bend, 90=mid-bend (see Fig 1)

Superscripts

' fluctuating properties (time dependent)
- time averaged properties

Subscripts

D diameter-based numbers
i, j tensorial indices

THEORY

Analogy methods

Due to its simplicity, Reynolds analogy or other similar temperature-independent calculation methods are popular for prediction of the heat transfer coefficient for above-mentioned applications. Assuming that both Pr and Pr_t are equal to 1, for a two-dimensional case, according to Incropera and Dewitt [2], Reynolds analogy reads:

$$h = \tau_w c_p / u \quad (1)$$

or

$$St = C_F/2 \quad (2)$$

which thereby assumes analogy between the temperature profile and velocity profile (heat-momentum analogy).

If Pr can not be assumed equal to 1, then the modified Reynolds analogy or Colburns analogy can be used instead:

$$St \cdot Pr^{2/3} = C_F/2 \quad (3)$$

Petukhov and Popov [3] proposed another analogy for tube flow with constant heat flux through the wall:

$$St = \frac{Nu_D}{Re_D Pr} = \frac{\frac{f}{8}}{1.07 + 12.7\sqrt{\frac{f}{8}}\left(Pr^{\frac{2}{3}} - 1\right)} \quad (4)$$

where

$$f = C_F/4 \quad (5)$$

Another analogy method, known as Gnielinskis equation [8], is verified by measurements for $2300<Re<10^6$ and $0.5<Pr<2000$.

$$Nu = \frac{\frac{f}{8}(Re - 1000)Pr}{1 + 12.7\sqrt{\frac{f}{8}}\left(Pr^{\frac{2}{3}} - 1\right)} \quad (6)$$

As these analogies are applied, the friction factor has to be known by , e.g., a CFD calculation of the corresponding flow field. This is the way the analogies are used in this paper.

Direct method

Both the momentum equation as given by White [7] and the energy equation as given by Eckert & Drake [3] have to be solved in the direct method. The temperature gradient at the wall is then used in the conventional way, as described by Eckert & Drake, to deduce the local heat flux, q_w, through a unit area normal to y, at the wall.

$$q_w = -\lambda \frac{\partial t}{\partial y} + \rho c_p \overline{t'v'} \quad (7)$$

For the engineering applications, the heat transfer coefficient, h, is then calculated by:

$$q_w = h(t_w - t_b) \qquad (8)$$

The first term in eq. (7) accounts for molecular conduction and the second term is caused by turbulent convection. As eq. (7) suggests, both temperature field and flow field are necessary for the direct method. This means that the CFD methods have to solve one additional equation compared to the analogy methods. In addition, thermal boundary conditions have to be defined. In many engineering applications the thermal boundary conditions are not well known. This is another reason for the popularity of the analogy methods.

Turbulence models

The basic or reference turbulence model used in this work was the standard k-ε model. The Reynolds stresses are modelled using the Boussinesq formula which links the Reynolds stresses to the mean rates of deformations:

$$\tau_{ij} = -\rho\overline{u_i' u_j'} = \mu_t\left(\frac{\partial U_i}{\partial x_j} + \frac{\partial U_j}{\partial x_i}\right) - \frac{2}{3}\delta_{ij}\rho k \qquad (9)$$

where μ_t is the eddy viscosity:

$$\mu_t = \rho C_\mu \frac{k^2}{\varepsilon} \qquad (10)$$

The turbulent kinetic energy, k, and the turbulent dissipation, ε, are given by Versteeg, & Malalasekera, [5], as

$$\rho U_j \frac{\partial k}{\partial x_j} = \tau_{ij}\frac{\partial U_i}{\partial x_j} + \frac{\partial}{\partial x_j}\left[\left(\mu + \frac{\mu_t}{\sigma_k}\right)\frac{\partial k}{\partial x_j}\right] - \rho\varepsilon \qquad (11)$$

and

$$\rho U_j \frac{\partial \varepsilon}{\partial x_j} = C_{\varepsilon 1}\frac{\varepsilon}{k}\tau_{ij}\frac{\partial U_i}{\partial x_j} - C_{\varepsilon 2}\rho\frac{\varepsilon^2}{k} + \frac{\partial}{\partial_j x_j}\left[\left(\mu + \frac{\mu_t}{\sigma_\varepsilon}\right)\frac{\partial \varepsilon}{\partial x_j}\right] \qquad (12)$$

The values of the constants are: $C_\mu = 0.09$, $\sigma_k = 1.00$, $\sigma_\varepsilon = 1.30$, $C_{1\varepsilon} = 1.44$ and $C_{2\varepsilon} = 1.92$.

Also non-linear k- ε turbulence models, quadratic and cubic models as well as k-ε-RNG were used in this work. The non-linear models take into account the anisotropy in the flow for instance near the wall. They are more suitable for separating flow and secondary flow. The RNG model has an extra term in the ε-equation and is known to give better predictions of flows by curved surfaces.

An algebraic stress model, ASM, was also applied. ASM accounts for the anisotropy of Reynolds stresses and might be regarded as a simplified full Reynolds stress model (RSM) without being as CPU-demanding. This is because the convection and diffusion terms are either removed or modelled. For details, see Versteeg, & Malalasekera, [5].

GEOMETRY DESCRIPTION

It was found appropriate to use the same geometry as the one investigated by Baughn *et al.* [1]. They used a 76-mm diameter circular tube with a 180° bend, in a U-shape, with 50 diameter long inlet and outlet pipe legs. The tube was heated so that the wall temperature was 20 °C above the ambient temperature. Ambient air entered a bell-mouth with a 16:1 area contraction, passed the inlet pipe leg, the U-bend and the exit pipe leg before it was routed to a sucking fan and back to the ambient. The bend mean radius was 3.375 times the pipe diameter. The Reynolds number was 60000.

The temperature and velocity profiles at 2 pipe diameters upstream the bend were measured and presented by Baughn *et al.* [1]. In the present work, the measured velocity and temperature profiles were applied as inlet boundary conditions at the above-mentioned position. This reduced the size of the CFD models. Figure 1 shows the geometry and explains the geometry-related definitions.

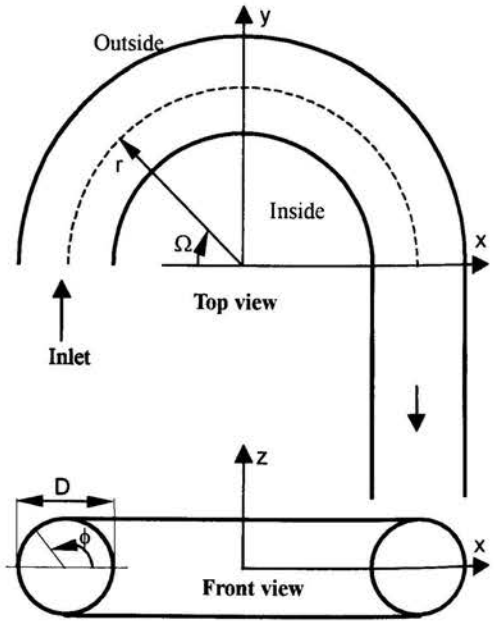

Figure 1: Schematic description of the U-bend geometry and the coordinates.

CFD MODELS

Two CFD cases were studied. For Case 1 and Case 2 the commercial codes CFX and STAR-CD were used, respectively.

The model in Case 1 consisted of 34686 cells and 36860 vertices. Reynolds analogy as well as Colburns analogy, Petukhov-Popov analogy and Gnielinskis equation were used.

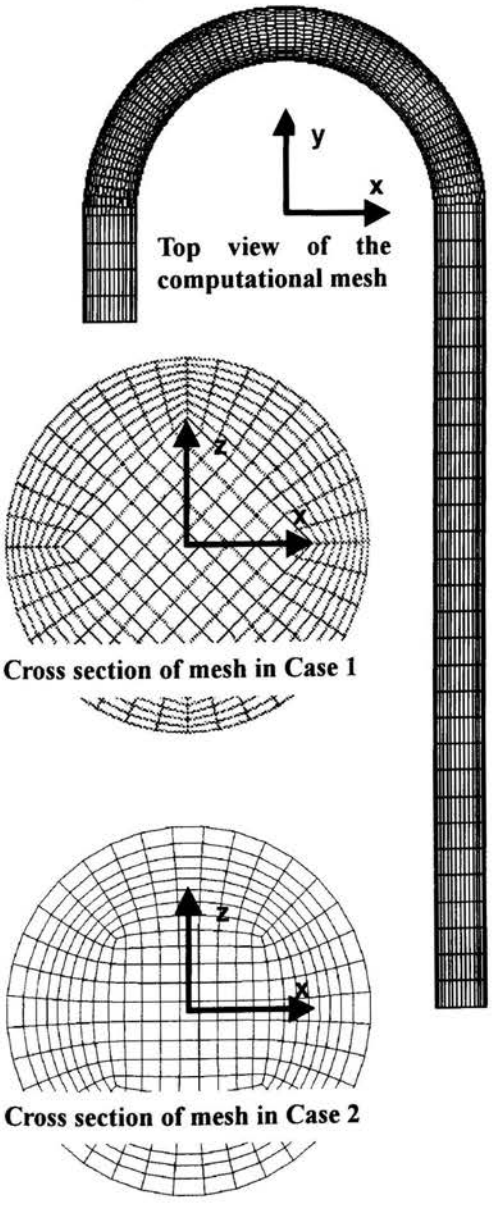

Figure 2: Computational mesh used for Cases 1 and 2

The turbulence models used were standard k-ε, k-ε–RNG, and Algebraic stress model, ASM. Turbulent steady state air-flow at Re=60000 was assumed. The physical constants for air at 300°K were used. The wall temperature was set to 20°C higher than the inlet air temperature.

In Case 2 the model consisted of 36162 cells and 38412 vertices. The tube cross-section mesh and also the mesh density in the flow direction were slightly different from that used in Case 1. Reynolds analogy was used. Standard as well as quadratic and cubic k-ε and k-ε–RNG, were used. In one case the two-layer model was used with a Norris-Reynolds one-equation low-Re [4] k-ε in the sub-layer. The Norris-Reynolds model is more suitable for boundary layers without pressure gradient [6]. In the log-law layer a standard high-Re k-ε was used. The boundary layer was modelled by the computational mesh so that the sub-layer was resolved by at least 15 cell layers. Most cases were run both with Upwind difference scheme and MARS. MARS was used because it is a second order scheme and therefore predicts the flow characteristics better than a first order scheme like UD. This allows to study the influence of cells further up-stream than UD. The boundary conditions were the same as for Case 1. Figure 2 shows the used computational mesh for the two cases.

RESULTS

The results were processed in various cross sections along the U-bend at Ω = 15, 55, 90, 125 and 165 degrees, and at 6 diameters downstream the bend. At each cross section, values were read at five Φ values, namely Φ = 15, 152.5, 90, 127.5 and 165 degrees, i.e. upper half of the bend as shown in Figure 1. At 6D only the locations Φ = 0, 45, 135 and 180 degrees were considered. These are the positions chosen in the experiments by Baughn *et al.* [1]. In the present work, however, only the results for the mid-bend cross section, i.e. at Ω=90 degrees, are presented. It is important to mention that Baughn *et al.* assessed the heat transfer coefficient by measuring the local heat flux and the difference between the temperature in the centre of the cell and the wall temperature. Thus the same method was used in the CFD-post processing. Figures 3 and 4 show the results at Ω=90° obtained for Case 1 and Case 2, respectively.

Case 1-results

As can be seen in Figure 3, non of the analogy methods could predict the correct value at the outer part of the bend. They all seem to predict a similar trend, which fails to predict the continuously increasing Nusselt number from inner to outer part of the bend.

The direct methods captured the above mentioned trend much better. ASM is the most successful one in the outer region. The standard k-ε and k-ε-RNG display very small difference.

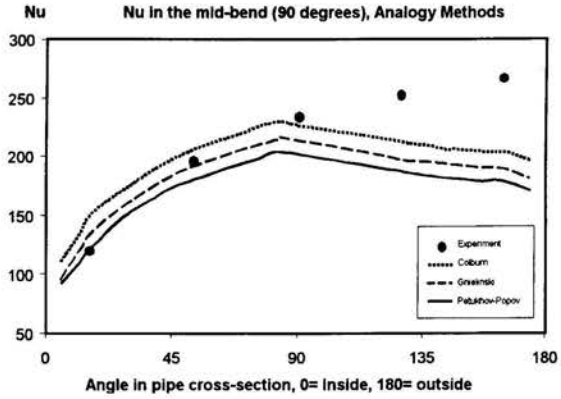

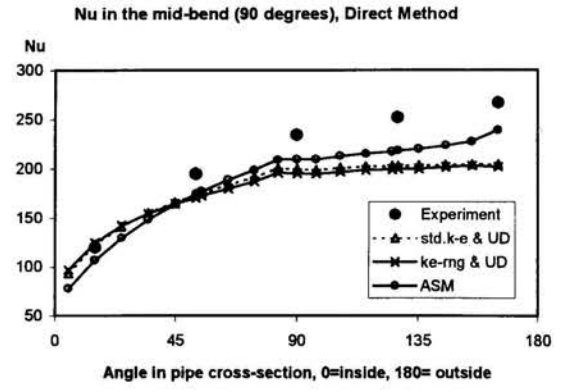

Figure 3: Computed Nusselt number for Case 1 at Ω=90°, in the middle of the bend.

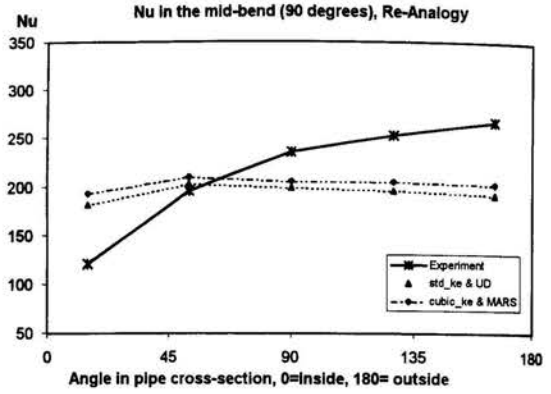

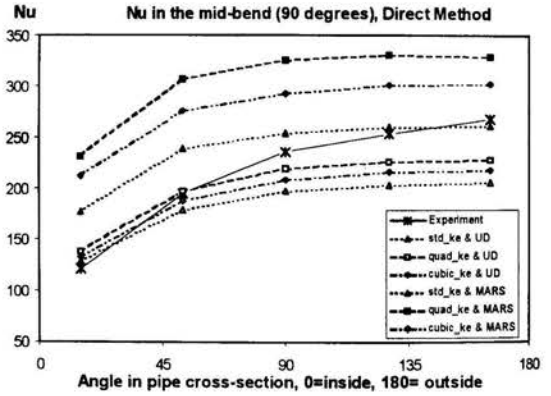

Figure 4: Computed Nusselt number for Case 2 at Ω=90°, in the middle of the bend.

Case 2-results

Figure 4 shows the results for Case 2. Note that the scale and the legend are different from Figure 3. All the k-ε models gave very similar results. Only the two extreme results, standard k-ε with upwind difference scheme and cubic k-ε with MARS scheme are plotted. Obviously they have all completely failed to predict the trend. Almost a constant value is predicted. Also in Case 2 the direct method has captured the trend better.

The results from the two-layer model were between the results from cubic and standard k-ε model. By shifting from Upwind difference scheme to MARS scheme, the level of Nusselt number increased dramatically, but the trend remained unchanged.

DISCUSSION AND CONCLUSIONS

The results presented here are similar to those for other cross sections of the bend. The analogy methods fail to predict the correct local Nusselt number. Nevertheless, they manage to predict a value, which is close to the mean value. This might be useful when only the transferred amount of heat is of greatest interest.

To understand the mechanism which governs the Nusselt number, the flow field in the cross-section at Ω=90°, shown in Figure 5, can be studied. It can be seen that the secondary flow transports hot fluid from outside of the bend to the inside of the bend. This causes cold fluid to continuously impinge on the hot wall of the outer bend. Thereby a high rate of heat transfer with high Nusselt number is achieved in the outer bend, i.e., near Φ=180°. On the inner bend, near Φ=0° the fluid temperature is closer to the wall temperature than at Φ=180°. This is due to the transfer of heat from the wall to the fluid during its motion from the outer bend to the inner bend next to the hot wall. Hence, the Nusselt number has its lowest values near Φ=0°. These effects are captured when the temperature field is known.

When using analogy methods, the Nusselt number is determined only based on the flow field. The highest secondary flow velocity and the highest shear stress occur near Φ=60°. This explains why Reynolds analogy has its highest values around Φ=60°. Other differences between the results from analogy methods in Cases 1 and 2 are probably due to the difference in the way the shear stress is assessed in the two cases.

It is concluded that solving the temperature field for determination of Nusselt number is vital when local values are desired. It is also important to investigate why MARS scheme over-predicts the Nusselt number and which impact other turbulence models have.

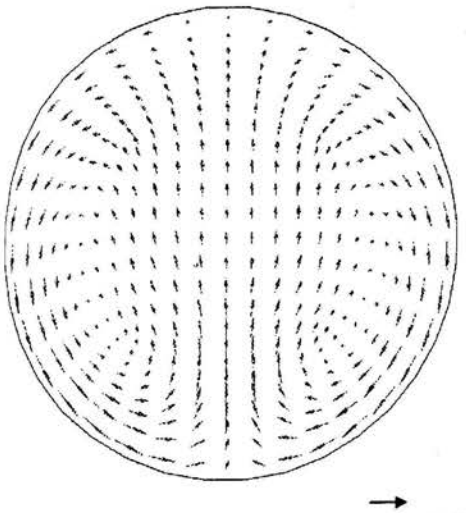

Figure 5: Velocity field at Ω=90°, in the middle of the bend. The velocity scale is given by the arrow above, indicating 12.5 m/s = Mean velocity in the pipe.

ACKNOWLEDGEMENTS

Mr. Hans Agardh, Computational Dynamics-Sweden and Mr. Martin Janson, Volvo Car Corporation are gratefully acknowledged for their valuable contributions to this work.

REFERENCES

[1] Baughn, J.W., Iacovides, H., Jackson, D.C. and Launder, B.E., 1987, "Local Heat Transfer Measurements in Turbulent Flow around a 180-Deg Bend", ASME J. Heat Transfer, Vol.109, pp. 43-48.

[2] Incropera, P.F. and DeWitt, D.P., 1996, "Fundamentals of Heat and Mass Transfer", Fourth Edition, John Wiley & Sons.

[3] Eckert E.R.G. & Drake R.M. Jr., 1972, "Analysis of Heat and Mass Transfer", McGraw-Hill Kogakusha Ltd

[4] STAR-CD, 1999, "Methodology v3.10", Computational Dynamics Limited, London, UK

[5] Versteeg, H.K. & Malalasekera, W., 1995, "An Introduction to Computational Fluid Dynamics", Longman Group Ltd.

[6] W. Rodi, 1991, "Experience with Two-Layer Models Combining the k-ε Model with a One-Equation Model Near the Wall", AIAA 91-0216.

[7] White, F.M., 1994, "Fluid Mechanics", McGraw-Hill Inc.

[8] Ghariban, N., Haji-Sheikh, A., You, S. M., 1995, Pressure Drop and Heat Transfer in Turbulent Duct Flow: A Two-Parameter Variational Method, ASME J. Heat Transfer, Vol. 117/No2, pp. 289-295

HEFAT2002
1st International Conference on Heat Transfer, Fluid Mechanics and Thermodynamics
8-10 April 2002, Kruger Park, South Africa
GA3

COMPACT HEAT EXCHANGERS BASED ON FINNED HEAT PIPES

A. Gershuni, A. Nishchik, Ye. Pysmennyy
National Technical University of Ukraine, Pr. Peremogy, 37, Kyiv, Ukraine, 252056.
G. Polupan, F. Sanchez-Silva, I. Carvajal-Mariscal
National Polytechnic Institute, SEPI-ESIMEZ, Av. IPN, UPALM, 07738, Mexico D.F.
polupan@maya.esimez.ipn.mx

ABSTRACT

Heat exchangers based on finned heat pipes have been designed and investigated. The heat pipe consists on a steel tube with an outside spiral aluminium fins. The distilled water with some impurities is used as a heat transfer medium in heat pipes.

The method of the calculation of thermo-technical performances of heat exchangers based on heat pipes has been developed. It is offered to use designed heat exchangers as a recuperator of heat with low power boilers.

The improvement of the boiler thermal efficiency is 5-10 % and the diminution of ambient medium thermal pollutions has been achieved, using designed heat exchangers as water economizers and air-heaters in gas-fired boilers.

The questions, connected with improving boiler parameters, decreasing of the fuel consumption, dropping down of the heat exchanger mass and overall dimensions have been discussed also.

A complex of scientific investigations, design-experimental and technological-experimental works is carried out with the aim to creation the high effective heat pipe exchangers of a "gas-gas" type. These exchangers are intended for recovering of ejected heat flows behind the fuel and energy using equipment. The main characteristics of heat exchangers for different equipments and their advantages in comparison with traditional constructions are given.

NOMENCLATURE

$Q_{air\text{-}heater}$ - a heat flow transmitted in air-heaters;
B - rate of a fuel flow for boilers with air-heaters;
$I_{gas}^{esc.boiler}$, $I_{gas}^{esc.air-heater}$ Enthalpy of combustion products escaping a boiler and combustion products escaping of air-heaters;
$I_{air}^{ent.air-heater}$, $I_{air}^{esc.air-heater}$ - air enthalpy at an air input and escaping of an air-heater;
Q_{boiler} - useful thermal power of the boiler;
q_3, q_4, q_5 - heat loses in the boiler;
α - coefficient of air-excess;
I_{air}^{0} - enthalpy of theoretically calculated the air quantity needed for burning;
$\Delta T_{air-heater}$ - medial temperature flow in air-heaters;
$n_{h.pipe}$ - Number of heat pipes in an air-heater;
ΣR_i - medial value of an aggregate thermal resistance of heat pipes;
ϑ, t - temperatures of the combustion products and air;
$\Delta\eta_{boiler}$ - magnification of boiler thermal efficiency at the using of an air-heater;
Q_L^w - a lowest heat value of the fuel;
N, η_{eq} - Additional power of the drive unit of a draft - blast equipment;
V_{gas}, V_{air} - volumes of the air and combustion products at inlet temperature in draft - blast equipment;
Δp_{gas}, Δp_{air} - aerodynamic resistivity of the air-heater for combustion products and air.

INTRODUCTION

The complex research and design works are held in the field of the development of heat pipes - evaporative - condensation systems, as well as devices and an inventory on their base. The high priority direction is the making and implementation of effective heat exchangers to recovering of ejected heat flows with the aim to solve of the energy saving problems.

The major reserve of saving and rational using of fuels and energy resources, as well as improving of ecological

state of the surrounding medium, is the recovering of ejected heat flows for different fuel-using inventories. The analysis of the temperature of such heat flows is held. The temperature analysis has shown, that for industrial boiler using natural gas, the temperature of ejected gases compounds 180 - 250 °C and above. For industrial furnaces using natural gas the temperature of ejected gases achieves 400 - 600 °C. For drying installations, the temperature of air-drying agent compounds 100 - 200 °C. At the development and designing of fuel-using inventories such high temperatures of ejected gases had the feasibility base. Using of low-temperature heating surfaces (water economizers and air-heaters) of traditional constructions gives the mass-clearance performances of heat exchangers commensurable with mass and overall dimensions of the main equipment.

However at the requirement of energy saving and at the ecological crisis in the world such thermal exhausts are intolerable. Our calculation shows the temperature of exhausts at incineration of natural gas should not exceed of 100-130 °C.

It is possible to provide an effective heat salvage and saving of fuels and energy resources with the help of heat exchangers based on heat transfer devices of evaporative - condensation types as heat pipes - two-phase hot-water thermo-siphons.

The heat exchangers based on heat pipes are effective and perspective type of the heat exchange inventory with diversified applications [1, 2]. They are intended for effective heat transfer between the flows of different matters, as well as for a salvage of power resources. At the efficiency estimation of their application as a recover of ejected heat flows it is necessary to remember, that such kettles are the most effective, when heat-exchanging mediums are gas flows. Thus, key problem is the rational using of heat recovers. The most effective is following applications of heat exchangers based on heat pipes as, for example, the air-heaters of boilers, furnaces, heat generators, propulsion systems and etc. It gives direct rising of the thermal efficiency of heat-using inventories due to delivery in fuel-combustion devices of the air, heated by the leaving combustion products.

RESULTS

We fulfilled operations connected with making and implementation of heat exchangers based on heat pipes [3, 4]. These exchangers were intended as air-heaters of boilers with the thermal power of 0,7 MW and more, using the natural gas (fig.1).

The creation of such air-heaters included a complex of research, development and design operations:

I) Development and examination of effective constructions of heat transfer devices - heat pipe exchangers;

2) Settlement analysis of the thermal engineering performances of heat exchangers and analysis of the influence of these performances on technical and economic parameters of the inventory, equipped with heat exchangers;

3) Creation and development of the technology of a heat exchanger manufacture;

4) Manufacture of the prototype and carring out of heat-technical and life cycle tests in the composition of inventories.

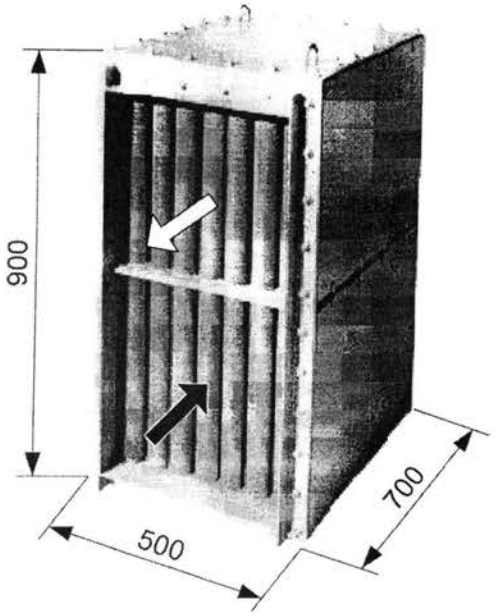

Fig.1. Heat exchangers for industrial boilers based on heat pipes

At the first stage the effective, reliable and technological constructions of heat pipes and two-phase thermo-siphons based on the tubes, created from carbon steel with spiral aluminium fins and water as heat transfer medium, have been designed.

It is known the combination of steel and water in heat pipes gives the formation of uncondensible gas - hydrogen blocking a part of condensation zones, that aggravates the performance of heat pipes and heat exchangers. Within of a complex research the study of physicochemical processes of compatibility of steel - water pairs in heat pipes is carried out. The long-time life cycle test of such heat pipes is held. The thermal properties of corrosion products and waste heat transfer medium [5, 6] are explored. On the basis of the analysis of these examinations the additives to water for killing a process of hydrogen emission at the operation of heat pipes are proposed. The life cycle test of heat pipes with water and designed additives is held. The trials were carried out during several thousand operation hours. They have shown the stability and invariance of heat pipe performances in investigated external environment. Moreover, the additives to water averting a

freezing of heat transfer medium are proposed. It prevents the depressurization of heat pipes at their storage or transportation in composition of heat exchangers at negative temperatures. Indicated additives to water are safe in operation, have inappreciable concentrations in heat transfer medium and do not slash the intensity of heat exchange processes in evaporation and condensation zones.

The complex of thermal engineering examinations was held with the purpose of an information deriving about the heat transfer performances and thermal resistance of heat pipes. The contribution of contact thermal resistance between the aluminum fins and steel tubes in blanket thermal resistance was spotted for relevant heating environments. The examinations have shown, that despite of essential distinctions of material expansion temperature coefficients for steel and fins, the value of contact thermal resistance R_{cont} practically self-similar concerning the temperature in contact zone up to 180 °C. The obtained experimental values of R_{cont} are $(2\text{-}3)\cdot10^{-4}$ m^{2}K / W.

The relevant part of the development is the settlement analysis of air-heater heat-technical performances as well as analysis of the influence of air-heater technical performances on technical and economic performances of the inventory. Such analysis is grounded on the solution of combined equations described the heat balances for air-heater, inventory with air-heater, as well as the heat transfer in air-heater, pinch of profitability of inventory, padding operational energy expenses and so on.

$$Q_{air\text{-}heater} = B\,(I_{gas}^{esc.boiler} - I_{gas}^{esc.air-heater}) \quad (1)$$

$$Q_{air\text{-}heater} = B\,(I_{air}^{ent.air-heater}, I_{air}^{esc.air-heater}) \quad (2)$$

$$(Q_{boiler} / B) + I_{gas}^{esc.boiler} =$$

$$= \left(1 - \frac{q_3 + q_4 + q_5}{100}\right) Q_L^w + \alpha\, I_{air}^0 \quad (3)$$

$$Q_{air\text{-}heater} = (\Delta T_{air-heater} / \Sigma R_i)\, n_{h.pipe} \quad (4)$$

$$I_{gas} = f_{gas}(\vartheta, \alpha) \quad (5)$$

$$I_{air} = f_{air}(t) \quad (6)$$

$$\Delta\eta_{boiler} = Q_{air\text{-}heater} / B\; Q_L^w \quad (7)$$

$$N = B\,(V_{air}\,\Delta p_{air} + V_{gas}\,\Delta p_{gas}) / \eta_{eq} \quad (8)$$

The joint solution of combined equations allows to receive expressions for finding of next parameters: t_{esc}, ϑ_{esc}, $Q_{air\text{-}heater}$, B, $\Delta\eta_{boiler}$. The numerical analysis allows, for example, to reveal the ranges of next parameter t_{esc}, ϑ_{esc}, $Q_{air\text{-}heater}$, Δp_{gas}, Δp_{air} changes in dependence on escaping gas temperature (ϑ_{esc}), fuel parameters, air-heater design parameters.

On the basis of numerical analysis, the calculation results for heat exchangers, as well as the design and fabrication documentations were created. Thus, the new solutions of the series of actual problems are found and implemented:

- The original fastening of heat pipes in a tubal board is offered;
- The method of cleaning of heat exchange surfaces from contamination is designed;
- The reliability and operation resource of heat exchanger with additives in heat transfer medium are estimated;
- The cycle operation technology of filling and potting of heat pipes is designed.

During whole operations of the constructed heat exchangers a lot of changes have been made, directed to improving of the adaptability to manufacture arrangement, dropping of metal consumption, rising mass-clearance performances and aerodynamic drag, perfecting of ergonomic parameters. The basic performances of designed heat pipe exchangers used as the boiler air-heaters (boiler evaporation capacity 1-50 t/h), the hot water boiler (with a heating capacity up to 10 MW) and in drying installations are following:

- Temperature range of hot gases at the inlet of heat exchanger - 100-315 °C;
- Temperature range of heated air at outlet of air-heater 70-230 °C;
- Range of recover heat flows of 24-3300 kW;
- The reached performances of the compactness and specific material consumption - up to 300 kW/m^3 and up to 3,0 kg / kW accordingly.

The performances for some designed and implemented heat exchangers based on heat pipes are given in the table 1.

Heat exchangers successfully operated in many plants of different industrial branches. The term of the operation of first models has reached of 10 years. For example, as the air-heaters of the boiler they used:

1) As additional tail heat exchangers (poses. 1, 2, 5, 6 in the table 1), that give a pinch of thermal efficiency of boiler up to 6-8 % at inappreciable magnification of mass and overall dimensions of boiler installation as a whole;

2) As the air-heaters, which substitute the regular tubular air-heaters (poses. 4);

3) As the air-heaters, which substitute the regular rotary air-heaters (poses. 3).

Using designed heat exchangers as the regular air-heaters (poses 3, 4) gives a considerable technical and economic effects from a drop of capital outlays on acquisition and installation of inventory and from a drop of

fuel operational expenditures, electrical power and service time.

CONCLUSION

The development and trial result analysis, as well as the experience of implementation and operation of heat exchangers based on heat transfer devices of an evaporative - condensation type in industrial conditions allow to make the following basic deductions:

1. Heat exchangers ensured the pinch on 5-10 % of inventory energy efficiency and the diminution of harmful thermal exhausts. The economic benefit of heat exchanger implementation, for example, as air-heaters of industrial boilers working on natural gas, is 0,4-0,6 US dollars per 1 t of steam produced.

2. Mass-clearance performances and specific material consumption for heat exchangers based on heat pipes in 5-7 times lesser than in heat exchangers of traditional "gas – gas" types.

3. The rather small aerodynamic resistance of heat exchangers allows equipping by them of the boilers and to use as the regular draft - blast equipment.

4. The designed heat exchangers are characterized by the high performance reliability and stability at long-lived operations.

REFERENCES

1. Vasilev L.L. Heat exchangers based on heat pipes. - Minsk: Science and technique, 1981, 144 p.

2. Vasilev L.L., Kiselev V.G., Matveev U.N., Molodkin F.F. Heat exchangers based on heat pipes for heat recovery.- Minsk: Science and technique, 1987, 200 p.

3. Semena M.G., Gershuni A.N., Rudenko A.N. The performances of two-phase thermo-siphons as devices for heat exchangers. J. Industrial energetic. –1988, N 4, p. 41-44.

4. Zaripov B.K., Gershuni A.N., High performance unobstructive: a heat exchanger based on heat pipes for heat recovery. J. Industrial Energetic, 1989, N 1, pp. 37-39.

5. Rudenko A.N., Gershuni A.N., Kalabina L.V., Semena M.G. About compatibility of steel with water in two-phase hot-water thermo-siphons, J. Protection of Metals, 1989,v. 25, N 6, pp. 958-961.

Table 1. Characteristics of air heaters for low and middle power boilers.

	Heat exchangers based on fining heat pipes	Rate of the gases, nm^3/s	Rate of the air, nm^3/s	Temperature of the escaping gases, oC		Temperature of the air, oC		Using heat flows, kW	Aerodyn. resistance of duct of Gas / Air Kg / m^2	Dimensions (width x length x height), m; weight, kg
				inlet	outlet	inlet	outlet			
1	Air heater of the boiler of 1 ton/h	0.3	0.25	250	120	30	170	44	200/100	0.5 x 0.7 x 0.9; 200
2	Air heater of the boiler of 2.5 ton/h	0.75	0.625	220	120	30	155	100	310/340	0.8 x 0.8 x 0.9; 450
3	Air heater of the boiler of 50 ton/h	19.3	15.5	310	180	50	220	3330	1060/700	4.0 x 1.3 x 2.6; 10400
4	One section of air heater of the boiler	4.85	3.93	265	135	30	205	900	665/745	1.3 x 1.3 x 2.6; 3600
5	Air heater of the hot water boiler 7.5 MW	2.9	2.0	160	100	20	113	243	440/390	1.0 x 0.7 x1.8; 1000
6	Air heater of the hot water boiler 9.65 MW	3.5	2.8	190	124	30	121	364	100/60	1.6 x 0.4 x 3.0; 1500

HEFAT2002
1st International Conference on Heat Transfer, Fluid Mechanics, and Thermodynamics
8-10 April 2002, Kruger Park, South Africa
GJ1

ANALYSIS OF STAGGERED TUBE BANK HEAT TRANSFER IN CROSS FOAM FLOW

J. Gylys*, M. Jakubcionis**, S. Sinkunas*** and T. Zdankus****
*Professor; **M. Sc.; ***Assoc. Professor; ****M. Sc.
Department of Thermal and Nuclear Energy
Kaunas University of Technology
Donelaicio 20, Kaunas, LT-3006
Lithuania
E-mail: jonas.gylys@mf.ktu.lt

ABSTRACT

In this paper experimental results of heat transfer of staggered bundle of tubes to static stable foam flow are presented. The experiments were performed on the model of heat exchanger. The cellular foam flow as heat transfer agent was used in this model. The experiments were provided for the middle and the side lines of the tube bank consisting of the three lines. The results of investigation are discussed from the standpoint of the influence of tube position in the line. The experimental results were described by dependence between Nusselt and Reynolds numbers.

INTRODUCTION

In many technological processes, which deal with heat and mass transfer, two-phase flow consisting of liquid and gas are exploited. These two phases may be in different state and that depends on hydrodynamic state of the whole system.

The foam state is one of the possible existence forms of gas-liquid system.

Let us consider a structure of the vertical upward two-phase flow generated from the detergent solution (Fig. 1). A structure of two-phase system varies depending on the height of a flow channel. Directly on the plate exists a bubble or so called barbotage regime. Near the plate a regime of dynamically stable foam can be checked, which consists of the turbulent mixture of the gas and liquid flows. Dynamically stable foam is very unstable two-phase system. It exists during the gas barbotage only. If the delivering of gas stops, the turbulent foam immediately destroys into pure liquid and gas (if a foam is generated from the pure liquid) or in the case of the detergent solution it turns into the statically stable foam (SSF). Statically stable foam flow is generated when gas and liquid with admixtures comes into contact. Statically stable foam (cellular foam) consists of gas bubbles, which have a shape of regular polygons, separated each from other by the thin liquid films. Without gas delivering SSF can live quite a long period of time (from seconds to years).

The apparatus, based on foam, are used in evaporation, concentration, drying, burning processes and in a lot of technological systems of waste water treatment or utilization systems [1].

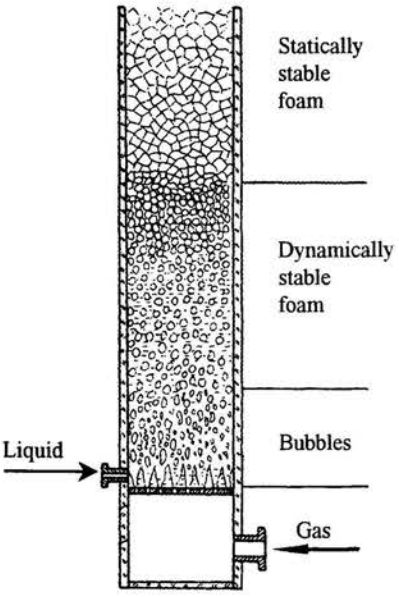

Figure 1: Foam Generation Scheme

Use of static stable foam flow in heat transfer apparatus may be very perspective deal from the economic and engineering point of view. Investigations showed that heat transfer apparatus, which use static stable foam as heat transfer agent, have a lot of merits: small quantities of liquid are needed, heat transfer rate is relatively high (lower than of water but much higher than of gas), low energy consumption for foam delivery into heat transfer zone.

A lot of data related to the hydrodynamics, heat and mass transfer processes, which take place in the dynamically stable foam system, can be found in literature. At the same time there are very little data about the analogical processes related to the statically stable foam [3, 4]. Heat transfer of single tube and single line of tubes to foam flow was investigated in previous works of authors [2, 5]. But these investigations can not completely reveal processes and factors, which make influence on heat transfer between heated units and cellular foam flow.

In order to make deeper investigation of heat transfer in foam flow bundle of tubes was investigated experimentally. In this case it is possible to reveal influence of tube position in bundle and in experimental channel on heat transfer intensity.

It must be stated here that structure of foam flow depends not only on height of experimental channel. It highly depends on flow velocity as well.

NOMENCLATURE

d_b	external diameter of the foam bubble (m)
d_e	external diameter of the tube (m)
F	cross section area of channel in free part (m^2)
G	volumetric flow rate (m^3/s)
$\overline{Nu}$	average Nusselt number $[\alpha d_e / \lambda_f]$
q	heat flux density (W/m^2)
$\overline{Re}$	average Reynolds number $[w d_e / \nu_g]$
s	spacing among tubes (m)
SSF	static stable foam
T	temperature (K)
$\overline{\Delta T}$	average temperature difference $[(T_w - T_f)]$
$\overline{w}$	mean velocity (m/s)

Greek Letters

$\overline{\alpha}$	average coefficient of heat transfer ($W/K\ m^2$)
β	volumetric void fraction
λ	thermal conductivity (W/K m)
ν	kinematic viscosity (m^2/s)
σ_o	surface tension of a pure liquid (without detergents) (N/m)
$\overline{\sigma}$	minimal value of a surface tension for given liquid (N/m)
σ	current value of a surface tension for a given liquid (with detergents) (N/m)

Subscripts

b	value referred to the foam bubble
e	value referred to the tube
f	value referred to the foam flow
g	value referred to the gas
l	value referred to the liquid
t	value referrred to the tube
w	value referred to the wall

STATIC STABLE FOAM FLOW REGIME

Statically stable foam (SSF) can be produced from the solutions, which have a reduced surface tension in comparison with the pure liquid. Even small concentration of detergents causes an intensive SSF generation during the barbotage processes. For different kinds of detergents and various liquids there exists a minimal concentration of detergents, above which any limited volume of liquid can be transformed to the SSF flow [6]. Experiments showed that such minimal (critical) concentration of detergent is equal to 0.1 ÷ 0.3 % of the solution mass. The exact value of the critical concentration depends on gas velocity and on a foam channel height. It was noticed that above the average gas velocities, which approximately are equal to $(0.7 \div 1.0)\ 10^{-1}$ m/s, a regime of foam flow slowly changes to the emulsion regime with a very small size of bubbles. A flow of SSF is very original due to the liquid flow rate dependence on the gas flow rate in a foam channel. Increase of mean gas velocity generates more foam bubbles, which carry upwards more liquid. The drainage of liquid through Plateau channels is comparatively slow process. The fast foam flow carries much more liquid than the slow one, where an influence of the drainage is much more significant.

Investigations [7] showed that there are four main regimes of SSF upward flow in the vertical channel: laminar flow regime $\overline{Re} = 0 \div 600$, transition flow regime $\overline{Re} = 600 \div 1500$, turbulent flow regime $\overline{Re} = 1500 \div 1900$, emulsion flow regime $\overline{Re} > 1900$.

Influence of Reynolds number for gas ($\overline{Re}_g$) and surface tension (σ_o, $\overline{\sigma}$, and σ) in calculation of Reynolds number for liquid ($\overline{Re}_l$) in the vertical foam channel have been obtained by Gylys and Udyma [7]:

$$\overline{Re_l} = 1.576 \cdot 10^{-4}\, \overline{Re_g}^{2.24} \cdot \left[0.644 - \frac{\sigma_o - \sigma}{\sigma_o (\overline{\sigma} - \sigma)} \right] \qquad (1)$$

In practice sometimes it is difficult to know the exact values of $\overline{\sigma}$ and σ. In such cases we can use a simplified expression:

$$\overline{Re_l} = 3.3 \cdot 10^{-5}\, \overline{Re_g}^{2.24} \qquad (2)$$

or

$$\overline{w}_l = 0.075\overline{w}_g^{2.24} \quad (3)$$

The Eqs. (1), (2) and (3) are valid for the range of mean gas velocity $\overline{w}_g = (0 \div 10.0)\cdot 10^{-3}$ m/s, which corresponds to the all regimes of the statically stable foam flow.

EXPERIMENTAL METHOD

Facility

The experimental arrangement consisted of the following: foam generation (experimental) channel, two regulating valves for gas and liquid, two rotameters for gas and liquid respectively, two reservoirs for liquid storage and constant liquid level keeping, air fan, transformer and stabilizer for electric current.

Experimental channel consisted of the following: riddle at the bottom of the channel and experimental part. The whole experimental channel was made of glass in order to observe optically foam flow regimes and the size of foam bubbles. The cross section of the channel was equal to (0.14 x 0.14) m^2. The height of experimental channel was 1.8 m. Foam flow was generated on riddle. The liquid with admixtures from reservoir was delivered on riddle, while gas flow was delivered through riddle. When gas and liquid came into contact, foam flow was created. Liquid in experiment was used only once and was not supplied back to reservoir.

A riddle of the foam generator was made of stainless steel plate with thickness of 2 mm. The diameter of holes was 1 mm and spacing among centers of holes was 5 mm. Holes were arranged in staggered order.

Schematic view of experimental section can be seen in Fig. 2.

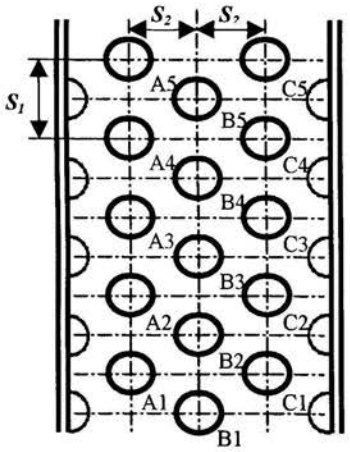

Figure 2: Experimental Section of Foam Channel

The bundle of tubes consisted of three vertical rows with five tubes in each. Spacing among centers of tubes $s_1 = s_2 =$ 0.035m. All tubes had an outside diameter of 0.02 m. The heated tube was made of copper and had an outside diameter of 0.02 m also. The endings of tube were sealed and insulated to prevent heat loses through them. The tube was heated electrically. The electric current value was measured by ammeter and voltage by voltmeter.

The temperature of foam flow was measured by two calibrated thermocouples: one in front of the bundle and one behind it. The temperature of heated tube surface was measured by eight calibrated thermocouples. Six of them were placed around central part of heated tube and two of them were placed in both sides of tube at the 50 mm distance from the central part.

The water solution was used in experiments. Concentration of detergents was kept constant and it was equal 0.5 %.

Experimental procedure

Investigation of tube heat transfer in the bundle consisted of three series of experiments. The experiments were provided for different values of mean volumetric void fractions β = 0.996, 0.997 and 0.998. The volumetric void faction can be expressed by equation

$$\beta = G_g / (G_g + G_l) \quad (4)$$

The foam flow rate can be written as

$$G_f = G_g + G_l \quad (5)$$

Gas and liquid mean velocities were changeable by changing gas and liquid flow rates respectively

$$\overline{w}_g = G_g / F \quad (6)$$

$$\overline{w}_l = G_l / F \quad (7)$$

The temperature of the tube surface and the foam flow, electric current and voltage were measured and recorded during the experiments. These values were registered not earlier than 90 s after the latest change of foam flow rate or electric current. The investigations showed that the foam flow regime at 35 mm distance from the riddle becomes stable after 90 s. After registration of electric current and voltage the heat flux density on the tube surface q_w was calculated.

After registration of heated tube surface and foam flow temperature by means of thermocouples, the temperature difference $\overline{\Delta T}$ between the mean temperature of the foam

flow T_f and the mean temperature of the tube surface T_w was calculated. The average heat transfer coefficient was calculated as

$$\bar{\alpha} = q_w / \overline{\Delta T} \quad (8)$$

The thermal conductivity of the foam flow was determined as follows

$$\lambda_f = \beta\lambda_g + (1-\beta)\lambda_l \quad (9)$$

In order to avoid possible errors during the work all the experiment series were done and repeated three times.

RESULTS

Experimental results of heat transfer for B4 tube in the middle line of tube bundle are presented in Fig. 3. The experimental results have shown that the heat transfer rate depends both on the mean gas velocity and on the mean volumetric void fraction β of the foam flow. It was noticed that heat transfer intensity increases with increase of gas velocity and decrease of volumetric void faction. With increase of gas velocity foam flow becomes more vortex and more intensive destruction of laminar boundary layer on heated tube takes place. Influence of volumetric void fraction reduction on heat transfer intensity is more significant at bigger gas velocities. When these two factors (bigger gas velocity and reduced void fraction) are combined, effect of foam flow vortex is much bigger. The character of dependencies is the same for all tubes of the bank.

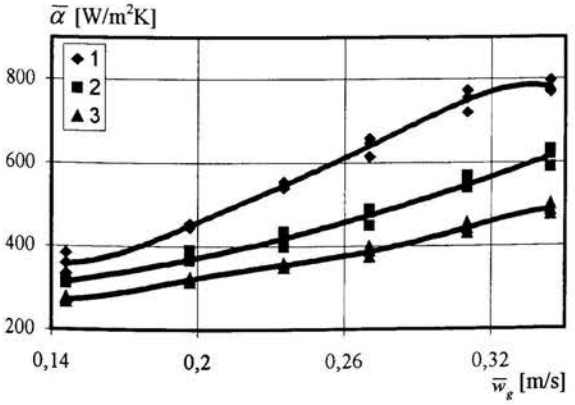

Figure 3: Heat Transfer of the Fourth Tube in the Middle Tube Line of the Bundle
β : 1 - 0.996; 2 – 0.997; 3 – 0.998

In Fig. 4 experimental results of the heat transfer for middle line of the tube bank are plotted against gas velocity. Fig. 4a and 4b represents heat transfer results for the middle tube line when volumetric void fraction β = 0.996 and 0.998 respectively.

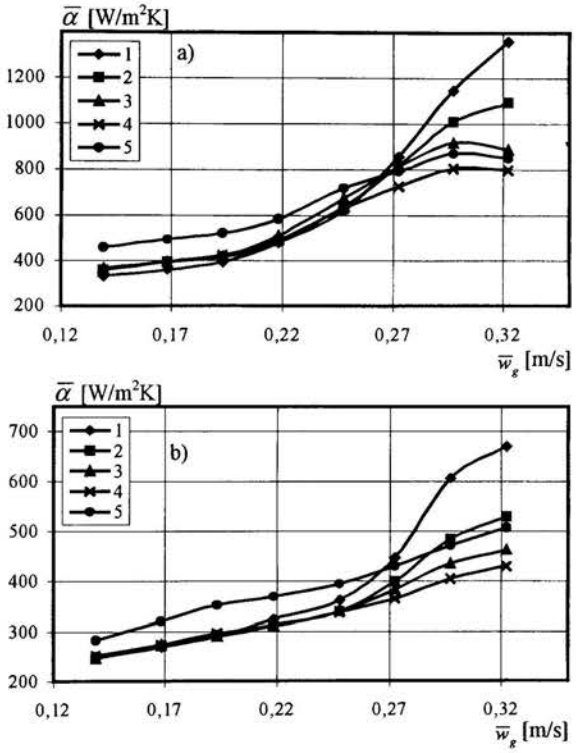

Figure 4: Heat Transfer of the Middle (B) Line of the Tube Bundle
a): β = 0.996; b): β = 0.998
1, 2, 3, 4, 5 - B1, B2, B3, B4, B5 Tube Correspondingly

It was noticed that when the foam flow is wetter (β = 0.996) in initial period of gas velocity augmentation influence of tube position in the line on heat transfer intensity is insignificant. Only the heat transfer intensity of the fifth i.e. last tube of the tube bank is different than of other tubes. In case of dryer foam (β = 0.998) heat transfer intensity of the fifth tube in the line of tube bundle is significantly different than of other four tubes also. When gas velocity is higher (starting at 0.24 ÷ 0.25 m/s) influence of tube position becomes more significant, especially for the first tube of the line of tube bundle.

During investigation of a single line of tubes in vertical cannel [2] it was noticed that the highest heat transfer intensity is of the first tube of line. It was noticed that heat

transfer intensity starting from the fourth tube of a single line becomes stable i.e. values of heat transfer coefficient are the same for fourth, fifth and the following tubes. In case of bundle of tubes situation is different. In the initial part of gas velocity augmentation the highest heat transfer intensity can be observed for fifth (last or the highest) tube of bundle. Only at the highest gas velocity heat transfer of the first tube is the most intensive. This phenomenon can be explained due to influence of the next lines of the bundle tubes and of the walls of foam channel on hydrodynamics of foam flow. For lower gas velocities the first tube of the bundle is in contact with foam flow consisting of large size (d_b = 8 ÷ 14 mm) bubbles. In such a case smaller amount of liquid fraction of foam flow gets into contact with the heated tube surface and conditions of heat transfer becomes worse.

The large bubbles of foam flow passing through the bundle of tubes are destroyed into small bubbles (d_b = 2 ÷ 5 mm). It means that fifth tube is wetted by the foam flow with more homogenous structure and liquid fraction of foam flow can access surface of heated tube more easily. For this reason the conditions of heat transfer become better.

When gas velocity is higher foam flow becomes more vortex and laminar boundary layer on the wall of tube is destroyed more effectively. Due to it heat transfer rate of frontal tube increases. At the same time size of the foam bubbles becomes smaller in the initial part of bundle of tubes. That has influence on intensification of heat transfer of frontal tubes also. Conditions of heat transfer of fourth and fifth tubes do not change at the higher gas velocity and heat transfer intensity becomes lower than of frontal tubes.

In Fig. 5 and 6 experimental results of heat transfer of tubes in the tube bundle are plotted against mean gas velocity. Fig. 5 represents comparison of heat transfer intensity of the first tube in the side (A1 and C1) and in the middle line (B1). In Fig. 6 comparison of heat transfer intensity of the fifth tube in the side (A5 and C5) and in the middle line (B5) can be seen.

It can be seen (Fig. 5) that wall of foam generator makes positive influence on heat transfer of the first tube of the bundle. It should be noted that such observation is valid for a case of low and average gas velocity. When values of gas velocity becomes bigger, the heat transfer intensity of the tube in the middle line (B1) exceeds heat transfer intensity of that in the side line (A1 and C1). It can be explained in such a way. When gas velocity is lower part of draining liquid is directed under the influence of the first tube of the bundle into the side zone of experimental channel. Because of that foam around first tube of the side line carries more liquid and heat transfer rate increases. When gas velocity is higher draining liquid is not directed into side zone from central zone of the channel. Foam flow becomes more vortex around the first tube of the middle line and heat transfer rate of it becomes higher than of tube in side line.

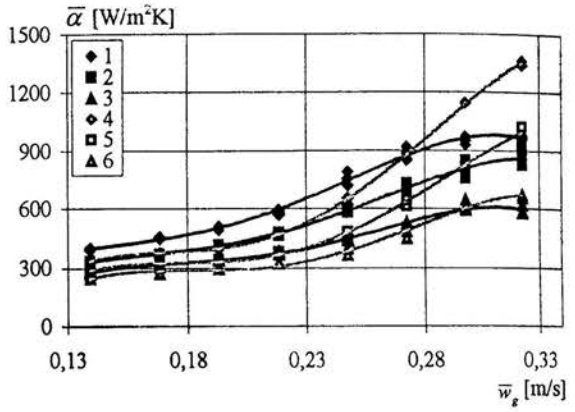

Figure 5: Heat Transfer of First Tube in Side (A1 and C1) and Middle Line (B1)
1, 2, 3 – A1 and C1 tubes; 4, 5, 6 – B1 tube
β : 1, 4 - 0.996, 2, 5 – 0.997; 3, 6 – 0.998

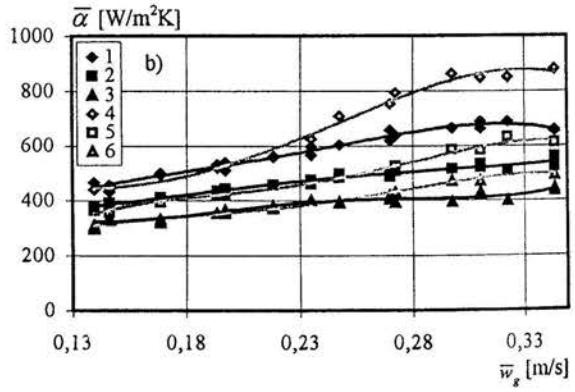

Figure 5: Heat Transfer of Fifth Tube in Side (A5 and C5) and Middle Line (B5)
1, 2, 3 – A5 and C5 tubes; 4, 5, 6 – B5 tube
β : 1, 4 - 0.996; 2, 5 – 0.997; 3, 6 – 0.998

For the fifth tube in a middle and in a side line (A5, B5 and C5) situation is slightly different. At low gas velocity the influence of tube position is negligible. At high gas velocity (especially for foam flow with β = 0.996) heat transfer rate of tube in a middle line becomes higher than for the tube in the side line. It can be explained so that gas velocity becomes lower after the bundle of tubes in comparison with gas velocity inside the bundle of tubes. The bigger amount of liquid comes from walls of foam bubbles due to this drop of velocity. This draining liquid flows down from the tubes of a side line (these tubes stand at the highest level of the bundle) to the fifth tube of a middle line. For this reason foam around the fifth tube of a middle line is much wetter and heat transfer rate increases.

HEAT TRANSFER GENERALIZATION

The experimental results of heat transfer were generalized using dependence between Nusselt and Reynolds numbers. This relationship can be written as follows:

$$Nu_f = c\, Re_g^{\,n} \qquad (10)$$

Values of coefficients c and n are presented in Table 1.

Table 1: Values of coefficients c and n in Eq. 10

Tube pos.	$\beta = 0.996$		$\beta = 0.997$		$\beta = 0.998$	
	$Re_g = 190 \div 320$					
	c	n	c	n	c	n
A1	3,2	0,85	4,2	0,77	6,3	0,66
A(2÷3)	12,02	0,61	19,8	0,49	18,4	0,47
A(4÷5)	23,4	0,49	23,9	0,47	31,8	0,385
B(1÷4)	1,4	0,97	6,6	0,66	9,5	0,56
B5	7,0	0,72	13,9	0,555	10,05	0,58
	$Re_g = 320 \div 450$					
A1	0,35	1,25	0,08	1,48	0,2	1,26
A2	0,49	1,16	0,2	1,27	0,7	1,03
A3	5,77	0,74	1,1	0,98	2,8	0,79
A4	31,4	0,45	10,5	0,6	15,7	0,5
A5	189,6	0,14	45,8	0,35	45,8	0,32
B1	$8 \cdot 10^{-6}$	3,06	0,0001	2,59	0,002	2,03
B2	0,0017	2,14	0,0004	2,33	0,008	1,77
B3	0,12	1,43	0,03	1,59	0,47	1,08
B4	2,04	0,92	0,07	1,43	0,89	0,97
B5	1,25	1,03	0,3	1,21	1,13	0,95

In Fig. 7 experimental results of heat transfer and results of calculation by Eq. 10 are compared.

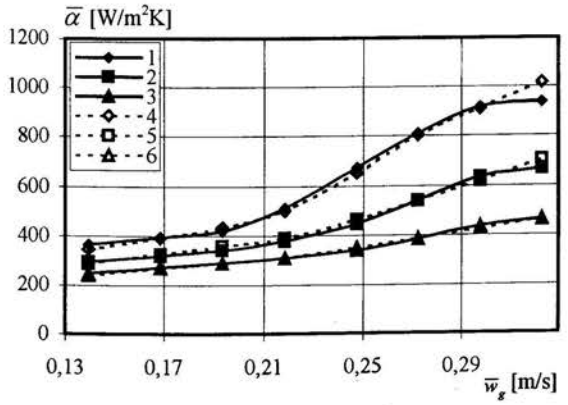

Figure 7: Experimental and Theoretical Heat Transfer Results for the Third tube of the Middle line (B3)
1, 2, 3, - Experiment; 4, 5, 6, - Theoretical results (Eq. 10)
β : 1, 4 - 0.996; 2, 5 – 0.997; 3, 6 – 0.998

CONCLUSION

1. Heat transfer rate increases with increase of mean gas velocity and with decrease of volumetric void fraction.
2. The highest heat transfer rate can be observed for the fifth tube of the bundle in the case if a gas velocity is low and average (w_g = (0.14 ÷ 0.26) m/s). When gas velocity is higher (w_g > 0.14 m/s) the highest heat transfer rate is in a case of the first tube of the bundle.
3. At high gas velocity heat transfer distribution in line of the bundle is similar to the one observed in the case of single line of tubes, i.e. the highest heat transfer rate is in case of the first tube of the line. At low gas velocity situation is different. In this case the highest heat transfer rate is of the fifth tube of the line.
4. Heat transfer of the tube in the side line is higher than of tube in the middle line in initial part of the bundle at lower gas velocity. When gas velocity is high and volumetric void fraction is low the higher heat transfer rate is in a case of the tube in the middle line.
5. Influence of tube position is negligible for the last tubes of the bundle at lower gas velocity. When gas velocity is high the highest heat transfer rate is for the middle line tube.
6. Heat transfer results were generalized by using dependence between Nusselt and Reynolds numbers $Nu_f = f(Re_g)$.

REFERENCES

[1] Tichonov V., 1983, "Foams. Theory and Practice of Foam Generation and Destruction", Chimija, Moscow.

[2] Gylys J., 1998, "Hydrodynamics, Heat and Mass Transfer Under the Cellular Foam Systems", Technologija, Kaunas.

[3] Krotov V., 1981, "Theory of Foam and Concentrated Emulsions Drainage", Colloid Journal, Vol. 6 (42), pp. 1081 – 1089.

[4] Desai D., Kumar R., 1982, "Flow Through a Plateau Border of Cellular Foam", Chemical Engineering Science, Vol. 9, pp. 1361 – 1370.

[5] Gylys J., Daugele A., Jakubcionis M., Sinkunas S., 1999, "Heat Transfer Under the Static Stable Foam Flow", Proceedings of the Third Baltic Heat Transfer Conference, pp. 667 – 673.

[6] Gylys J., 1977, "Investigation of the Hydrodynamics and Heat – and Mass Transfer Processes in the Foam Evaporators", Ph.D. thesis, MEI, Moscow.

[7] Gylys J., Udyma P. G., Montvilas R., 1989, "The Volumetric Void Fraction of the Foam", Energetika, Vol. 6, pp. 73 – 77.

[8] Gylys J., Jakubcionis M., Sinkunas S., 2000, "Heat Transfer of Tubes in Cross Foam Flow", Advanced Computational Methods in Heat Transfer, Southampton, Boston, pp. 637 – 646.

HEFAT2002
1st International Conference on Heat Transfer, Fluid Dynamics, and Thermodynamics
8-10 April 2002, Kruger Park, South Africa
HP1

HEAT TRANSFER IN SINGLE PHASE SECONDARY REFRIGERANTS AT LOW TEMPERATURES: EFFECTS OF LONG THERMALLY DEVELOPING REGION IN STRAIGHT PIPE AND HORIZONTAL U BEND

P. Hrnjak and S. H. Hong
Department of Mechanical and Industrial Engineering
University of Illinois at Urbana-Champaign
1206 W. Green St., Urbana, Il 61801, USA
pega@uiuc.edu

ABSTRACT

The paper presents experimental results and analysis of heat transfer in thermally developing region of round pipes for three fluids typically used as low temperature coolants (secondary refrigerants). The experiments were performed at low Re and high Pr numbers that are typically found in secondary loop conditions at low temperatures. Effect of horizontal U bend is presented and compared to available experimental data in the open literature.

It is shown that positive effect of thermal development (high Nu number) last long thanks to technically significant length of thermally developing region. Secondary flow developed in and after U bend is so important that it has almost identical effect as thermal development at the pipe entrance. That is the reason for extremely good performance of the heat exchangers with secondary refrigerant in laminar flow regime.

INTRODUCTION

Indirectly refrigerated systems for commercial and industrial refrigeration applications (with secondary loops) have attracted significant attention lately. The objective of one of research programs at the Air Conditioning and Refrigeration Center (ACRC), University of Illinois was to analyze these systems and compare them to conventional DX systems. Experimental program was focused to performance of the low temperature display case. It was demonstrated that the display case operated better when served with secondary refrigerant than in the baseline mode with R404A as a refrigerant, Mao et al. (1998, 1997). Beside obvious drawbacks of secondary loop systems (added pumping power and temperature difference associated with additional heat exchanger), Hrnjak (1997, 1997a) several advantages of secondary systems were identified: better frost distribution, higher heat transfer rates, quicker defrost and pool-down after defrost, more uniform product temperature during defrost, etc... Real surprise for many was better heat transfer. That was the reason to look closer into heat transfer issues.

There is a limited number of acceptable single-phase secondary refrigerants that are environmentally friendly, non-toxic, nonflammable, and with reasonably good thermophysical properties at low temperatures. Almost all of them operate in laminar flow regime in refrigeration mode. Many engineers in "back of the envelope" calculations assume fully developed laminar flow in the heat exchanger pipes in comparative studies. In typical refrigeration conditions these fluids have high Prandtl number $Pr = \mu C_p/k = \nu/\alpha$ resulting in long thermally developing regions. These lengths are technically significant (even up 0.5 to 2 m). That fact indicates potential for underprediction of heat transfer if developing region is neglected. Prandtl numbers in currently available and acceptable secondary refrigerant candidates at low temperatures (-30 to -40°C) are in the range 70-120. It is well known that in thermally developing region heat transfer coefficients on refrigerant side have very high values, sometimes in few orders of magnitude higher than in fully developed region. It is also known that U bends have significant role in mixing and restarting flow development. It will be shown that U bend has effect of almost fully restarting developing region. That fact could be the explanation for unexpectedly high refrigerant side heat transfer coefficient experimentally determined. Heat transfer in transition region that follows the U bend is less explored but has significant effect on heat exchanger performance.

In developing laminar flow of heated fluid in the horizontal tube the core is colder and thus heavier than annulus closer to heated walls. Due to that effects fluid in the central zone sinks and generates secondary flow that moves upward in vicinity of vertical heated walls. The effects of the denser central zone are even more significant in fluid turning, like in U bends or elbows. Greater inertial force impinges the stream to the bend or elbow

wall causing stronger **secondary flows** and significant mixing. That effectively increases **heat transfer** bringing central cold stream in contact with the walls.

NOMENCLATURE

A	area
Cp	specific heat
Farr	Farr correlation
fd	fully developed
Gn	Gnielinski correlation
h	heat transfer coefficient
D	diameter
ID	inside diameter
k	conductivity
L	length
m	mass flow
Nu	Nusselt number
OD	outside diameter
PA	potassium acetate
PG	propylene glycol
PF	potassium formate
Re	Reynolds number
Pr	Prandtl number
Q	heat transfer
R	resistance
T	temperature
x	local length
x*	dimensionless length

Greek Symbols

μ	viscosity

Subscripts

b	bulk
h	heating fluid
H	constant heat flux
i	inlet
in	inside
m	mean
meas	measured
o	outlet
out	outside
pred	predicted
r	refrigerant
x	local
T	constant temperature
w	wall

EXPERIMENTAL FACILITY

A schematic of the experimental facility is shown in Figure 1. Details could be found in Hong and Hrnjak (1999). The facility provides secondary refrigerant (fluids that are studied) and heating fluid (water in this case) at required measured flow rates and at required uniform temperatures. The fluids measured are propylene glycol (PG) - 35% by volume, potassium acetate (PA) - 47.5 % by weight, and potassium formate (PF) - 46% by weight. Thermophysical properties are defined in Hong and Hrnjak (1999).

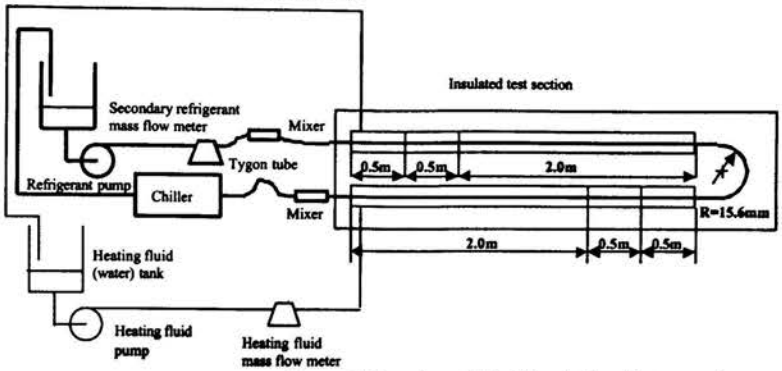

Figure 1. Experimental facilities for local heat transfer measurements

The test heat exchanger consists of a pair of 3 meters long annular coaxial heat exchanger tubes placed side by side in horizontal plane connected with a return U-bend. Secondary refrigerant flows through the inner (copper) tube of the heat exchanger. Heating fluid, which is water, flows through the outer annular spacing between copper and PVC tubes. Flow through the annulus is articulated with a spiral insert. Each heat exchanger tube has three test sections: 0.5 m, 0.5 m, and 2 m long. A schematic of the test coaxial heat exchanger is shown in Figure 2. Details of the test sections could be found in Hong and Hrnjak (1999). The lengths of the first two sections of coaxial heat exchangers are designed shorter than the last sections because their local heat transfer coefficients are expected to be higher at the inlets but decrease rapidly down to the asymptotic value by the last sections. Therefore shorter sections are used to capture rapidly changing high heat transfer coefficient near the inlet. The two annular coaxial heat exchangers before and after the U-bend are identical in construction. The only difference is their function. Inlet to the upstream heat exchanger section has a uniform cross section temperature profile. The uniform profile is obtained by a long adiabatic section in the hose leading to the heat exchanger and one static mixer before the inlet. The heat exchanger functions as a test section to measure local heat transfer coefficient of a thermally developing region. The other identical heat exchanger is positioned downstream of the U-bend to measure the effect of the bend on local heat transfer coefficient. The data collection from a side-by-side setup of the heat exchanger sections allows direct comparison of the effect of the horizontal U-bend to a uniformly temperature distributed thermally developing inlet regime.

The inner copper tube diameter is ID = 9.53mm. Dimensions of the U-bend used in the coaxial heat exchanger are ID = 9.14mm while radius of curvature (center to center) is 15.6 mm.

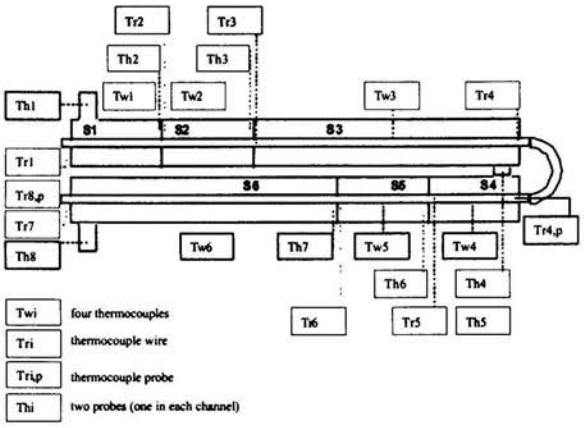

Figure 2: Schematic of the test section

EXPERIMENTAL RESULTS

Heat transfer in straight section preceding and following the U bend

The goal of the experiments with the coaxial heat exchanger that are presented in this paper is to experimentally determine the local heat transfer coefficient of refrigerant flow in the straight section before and after U-bend and to determine the effect of the U-bend. Parameters needed to determine local heat transfer coefficients are: 1) temperature readings at the inlet and the outlet of each test section, 2) wall temperatures, and 3) mass flow readings of the refrigerant and heating fluids given its specific heat value. At this point we will not go in details of discussion of the experimental uncertainty but just say that it is between 3% at higher Nu to 8% at lower values of Nu number. Detailed analysis and uncertainty tables for each data taken is presented in Hong and Hrnjak (1999).

Table 1: Range of operating parameters

	$T_{r,i}$ [°C]	$T_{h,i}$ [°C]	V_r [m/s]
Propylene Glycol	-2.1 to -8.5	25 - 17	0.27 – 0.95
Potassium Acetate	-20 to –23	24 - 20	0.17 – 0.61
Potassium Formate	-20 to –23	24 - 19	0.17 – 0.61

Values of heat transfer coefficient (h_r) were determined based on measured data and than converted to dimensionless Nusselt number ($Nu=h_r * ID/k$) based on inner tube diameter ID and refrigerant conductivity k (bulk). Then Nu is plotted versus number (length) x^* ($x^*=x/(ID_{in}*Re*Pr)$), a dimensionless number incorporating length (x), Reynolds number Re, and Prandtl number Pr as accepted for heat transfer in developing region, Shah and London (1978), Kakac et al. (1987), Gnielinski (1983, 1987).

For the cases when thermophysical properties are significantly different within a cross section (which happens in almost every real application) certain additional corrections should be made. Among others Sieder and Tate (1936), and Popovska (1975) have proposed correction factors to take into account effects of changed thermophysical properties close to the walls. The classic correction given by Sieder and Tate for flow of viscous oils described their own data for vertical tubes and data of other investigators for horizontal tubes uses exponent 0.14 as shown in the equation given below.

$$\left(\frac{Nu}{Nu_{cp}}\right)=\left(\frac{\mu_b}{\mu_w}\right)^{0.14}$$

When data are obtained, they are plotted, and a regression analysis is performed. A general form of the curve-fit equation was taken from Gnielinski's (1997) correlation for thermally developing flow. Assuming the same effect of variable thermophysical properties one would expect that results for all three fluids would fall on top of each other. However Figure 3 shows some variation among fluids. Potassium formate has the highest Nu number while propylene glycol and potassium acetate are more or less on top of each other. There are three lines in the graph. The one in the middle is the correlation shown in the graph as an equation. That equation has R^2 = 0.951. Two other lines show the narrow range of 99 % probability confidence interval.

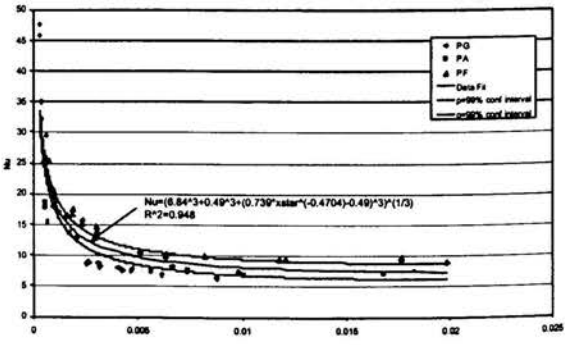

Figure 3. Local Nusselt number versus x^* preceding U-bend

The same procedure is repeated for the data points after the U-bend. The plot below, Figure 4, gives a 99% confidence interval and R^2 for the data-fit curve of data after the U-bend. Its standard deviation is 3.64.

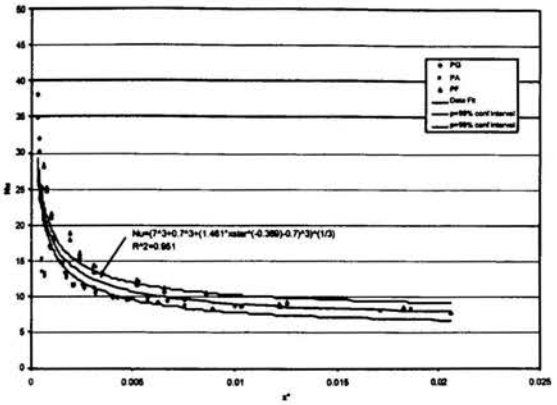

Figure 4. Nu versus x* in straight section following U-bend for all three fluids examined

Figure 5 helps in comparing the results of these experiments to published correlations. It shows the correlation developed here (solid line) with two of Gnielinski's correlations - one is constant temperature (T):

$$Nu_{x,T} = (3.66^3 + 0.7^3 + (1.077x^{*-1/3} - 0.7)^3)^{1/3}$$

while the other is constant heat flux correlation (H) correlation:

$$Nu_{x,H} = (4.364^3 + 1 + (1.302x^{*-1/3} - 1)^3)^{1/3}$$

The actual boundary condition in this experiment lies somewhere between the two extreme boundary conditions of the correlations. Therefore the Nu of experimental data is expected to be bounded by the two correlation curves. However the plots show Nusselt number of data to be higher than both of the correlations. In addition Gnielinski's correlations have been adjusted with Sieder and Tate's temperature dependent viscosity ratio. The correction factor brings up the Nu of the correlations from constant physical property assumption to a more accurate variable property case. Following Figure 6 shows a maybe more "engineer friendly" plot of heat transfer coefficient development for potassium formate because it gives the heat transfer coefficient along the pipe with fluid velocity as a parameter. Similar graphs for propylene glycol and potassium acetate could be found in Hong and Hrnjak (1999). It has two groups of lines: solid lines are curve fits of the experimental data while dotted lines are results of the correlation presented in McAdams, 1954:

$$Nu = 1.86 \cdot x^{*-1/3}$$

The lines are presented for three typical fluid velocities inside the tubes, which give very low Re numbers. Graphs demonstrate strong effect of velocity in thermally developing region and weak effect in developed zones. It is also interesting to see that heat transfer coefficients could be well above 1000 W/m^2°C in first 0.5m. This fact indicates that it location of the twisted strip enhancers (or similar) would make sense in the second part of the tube. It looks like there is no reason to put them close to the inlet because it is less reasonable to spend pumping power (generate pressure drop) for enhancing already high heat transfer coefficients.

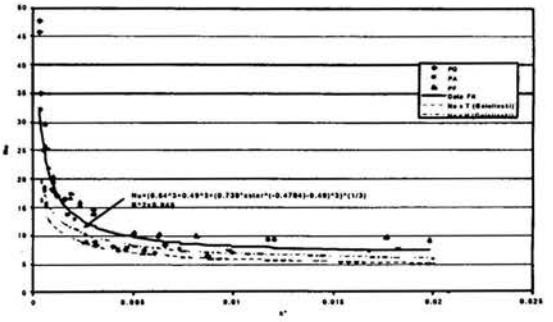

Figure 5. Comparison of experimental data for all three fluids in the straight pipe preceding the return U bent to Gnielinski correlation

Effect of the U bend on the heat transfer in straight section preceding and following it

To get a better measure of the difference between the two test sections, a ratio between a curve-fit of data points for a straight section before the U-bend to that of after the U-bend for all three fluids is determined. As can be seen from Figure 7 the ratio shows that Nusselt number after U-bend is slightly less than before the U-bend for x* less than 0.0011 but becomes greater after that point. At large value of x* the ratio reaches an asymptotic value near 1. One striking fact is how similar the two curves of Nu after and before the U-bend are.

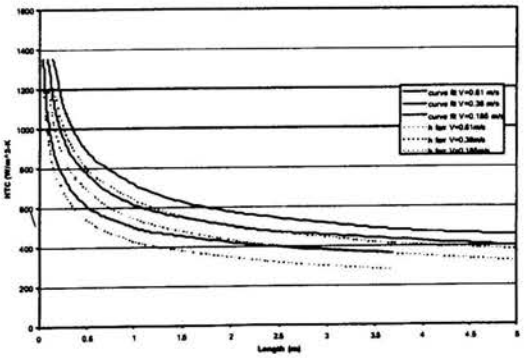

Figure 6 Local heat transfer coefficient inside the tube for potassium formate. Prediction is made at −29°C

This result clearly shows that even a smooth U-bend will have an effect of remixing the thermal stratification of a laminar flow sufficiently well that essentially a thermally developing flow occurs after the U-bend. Moreover, the ratio is very close to one - it is in the range 0.9 to 1.11. It is very close to experimental uncertainty.

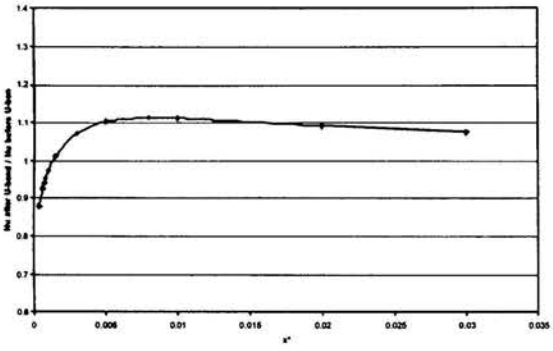

Figure 7: Averaged ratio of Nusselt number preceding and following U-bend for all three fluids

COMPARISON TO OTHER EXPERIMENTS TO DETERMINE EFFECT OF THE U BEND

For laminar flow through a U-bend Mehta and Bell (1981) have reported extensive experimental data. Their objective was to investigate radial temperature distribution after the U-bend as a consequence of secondary flow. The experimental setup is a coaxial heat exchanger type similar to this work, but the heat exchanger was electrically heated thus had a different boundary condition than the coaxial heat exchanger tested in this case, so direct comparison should be made with caution. The other significant difference between this project and Mehta and Bell's is that their U-bend is on a vertical plane with its outlet on top in contrast to this which is horizontal..

Since their test section is electrically heated, the appropriate boundary condition is that of constant heat flux. On the other hand, the actual boundary condition of the coaxial heat exchanger in this project is predicted to be between constant heat flux condition and constant wall temperature. The coaxial heat exchanger would reach the constant heat flux boundary case (as is the case if it were electrically heated like Mehta and Bell's apparatus) if the capacities of refrigerant and heating fluid are equal, and it would reach the constant wall temperature case if the capacity of the heating fluid becomes infinite.

Even with the above mentioned and other differences between Mehta and Bell's experiment and this coaxial heat exchanger setup, comparison of the results between the two experiments are conducted to aid in the understanding of thermally developing flow.

Mehta and Bell were less interested in the development of heat transfer coefficient along the tube, and so they have not reduced data into Nusselt number versus x^*. Therefore appropriate dimensionless variables were extracted from their raw data and compared to data in theis experiment.

Figure 8 shows Mehta and Bell's data points preceding a U-bend in filled symbols. Open symbols are data obtained in this project for each individual fluid. At the higher x^* values the Nu number for developed region as reported by Ede (1966) is shown. Solid and dotted lines are Gnielinski's correlations. In the figure Mehta and Bell's experimental results show a relatively constant value and do not show a significantly higher value of Nusselt number at its entry region.

The comparison shows qualitatively better correlation of current results to Gnielinski correlation. The difference in offset may come from the effect of different thermophysical properties at the wall and in the center of the flow and phenomena associated with secondary flow induced by this effect. Nevertheless, Mehta and Bell's results indicate slightly different change in heat transfer coefficient with x^* as expected and found here. Values are less or more unaffected by x^*. The data shown by solid circles are calculated from original data based on average values in circumferential direction to fit into the Nu vs. x^* variables. Experimental values reported by Ede in sketchy form agree with the data obtained in this project.

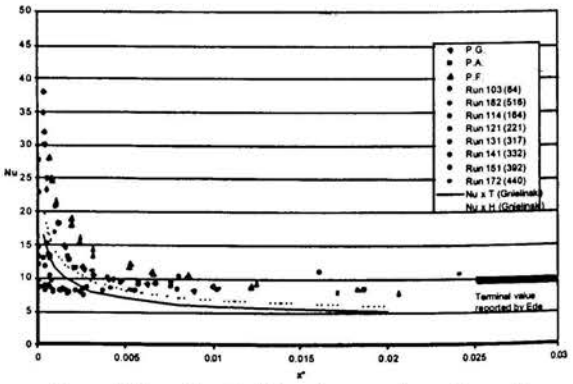

Figure 8: Preceding the U-bend - comparison of several experimental results: Mehta and Bell (solid circles), Ede, this project (open symbols)

Figure 9 plots the data for locations after the U-bend. A steep asymptotic curve at the region right after the U-bend is clearly evident in Mehta and Bell's result. However the effect of the U-bend is evident at much smaller value of the parameter x^* than found in this project with the coaxial heat exchanger or what Gnielinski correlation would predict.

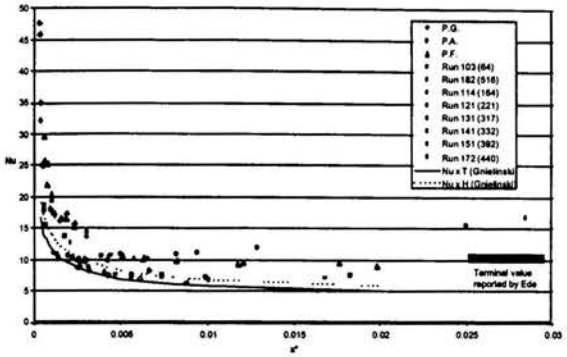

Figure 9: Heat transfer in the coaxial heat exchanger experimental results following the U-bend - comparison of several experimental results: Mehta and Bell (solid circles), Ede, this project (open symbols)

CONCLUSIONS

The results of heat transfer experiments in laminar flow with three fluids that are the leading candidates for the secondary refrigerants: propylene glycol at temperatures 0 to –10°C, potassium acetate at temperatures -20 to –40°C and potassium formate at temperatures -20 to –40°C are presented.

Measured values show good qualitative agreement in thermally developing region in straight pipe with existing correlations and with Gnielinski's in particular. Nevertheless experimental values show slightly higher values than correlations predict. The difference is approximately in the range 20-40%.

Effects of return U bend are extremely positive for heat transfer due to mixing in laminar regime. The heat transfer is increased almost to the level of restarted thermal development for lower values of x^* and even beyond it at higher x^*.

Due to very high Pr numbers thermally developing flow length is technically significant (0.5 to 1.5 m) and that affects the performance of the real heat exchangers.

ACKNOWLEDGMENTS

Results presented are obtained in laboratories of ACRC (Air Conditioning and Refrigeration Center) University of Illinois at Urbana-Champaign with funding and in-kind support of US EPA, Kemira OY, Hydro Chemicals, Heatcraft, Hussmann Corporation, Tyler Refrigeration Corporation, Hill-Phoenix, Alfa Laval, and Standard Refrigeration. Their help is greatly appreciated.

REFERENCES

[1] Ede, A.J. 1966. The Effect of a 180° Bend on Heat Transfer to Water in a Tube, 3d Int. Heat Transfer Conf., Vol. 1, pp. 99-103

[2] Gnielinski, V. 1983. Heat Exchanger Design Handbook, Chap. 2, Hemisphere Publishing Co.

[3] Gnielinski, V. 1997. VDI-Waermeatlas, Springer-Verlag, Berlin

[4] Hong, S. H., P. Hrnjak. 1999. Heat Transfer in Thermally Developing Flow of Fluids with High Prandtl Numbers Preceding and Following U-Bend, ACRC report CR-24, Urbana, IL

[5] Hrnjak, P. 1997. Benefits and Penalties Associated with the Use of Secondary Loops, Proceedings NIST - ASHRAE Conference Refrigerants for the 21st Century, pp. 85-95, Gaithersburg, MD, October 6-7

[6] Hrnjak, P. 1997a. Secondary Loops - Is it the only option for some natural refrigerants?, Proceedings IEA Annex 22: Natural working fluids for compression refrigeration systems, pp. 197-206, Gatlinburg, TN, October 2-3.

[7] Kakac, S., Shah, R.K., Aung, W. 1987. Handbook of Single-Phase Convective Heat Transfer, Chap 10, John Wiley and Sons, New York

[8] Kays, W. M., Crawford, M.E. 1993. Convective Heat and Mass Transfer. 3rd Ed., McGraw-Hill, New York

[9] Mao, Y., W. J. Terrell, R. C. Reef, P. S. Hrnjak. 1997. New Coolant for Indirect Refrigeration Based on Potassium Formate, ACRC report, Urbana, IL

[10] Mao, Y., W. Terrell, and P. S. Hrnjak. 1998. Performance of a Display Case At Low Temperatures Refrigerated With R404a and Secondary Coolants, Proceedings RTSRD, International Institute of Refrigeration, Refrigeration Science and Technology Proceedings, Cambridge, UK, pp. 181-188

[11] Mao, Y., W. Terrell, and P. S. Hrnjak. 1997. Tests of Supermarket Display Cases when Operating with Secondary Refrigerants, Proceedings of International Conference on Ozone Protecting Technologies, pp. 176-186, Baltimore, MD

[12] McAdams, W. H. 1954. Heat Transmission. 3d Ed., McGraw-Hill, New York

[13] Mehta, N.D., Bell, K.J. 1981. Laminar Flow Heat Transfer in a Tube Preceded by a 180° Bend, Heat Transfer - Sov. Res., Vol. 13, No. 6, pp. 71-80

[14] Shah, R.K., London, A.L. 1978. Laminar Flow Forced Convection in Ducts. Academic Press, New York

[15] Sieder, E.N., Tate, G.E. 1936. Heat Transfer and Pressure Drop of Liquids in Tubes, Industrial and Engineering Chemistry, Vol. 28, pp. 1429-1435

HEFAT2002
1st International Conference on Heat, Fluid Mechanics, and Thermodynamics
8-10 April 2002, Kruger Park, South Africa
HP2

EXPERIMENTAL INVESTIGATION OF MIXED ANGLED PLATE HEAT EXCHANGERS

P.J.Heggs and C.Walton
Department of Chemical Engineering
UMIST
PO Box 88, Manchester, M60 1QD, UK
E-mail: p.j.heggs@umist.ac.uk

ABSTRACT

A mass transfer analogy experimental procedure (the diffusion limited current technique) has been employed to measure local mass transfer coefficients within plate heat exchanger channels with pure and mixed corrugation angles. A pressure drop study has also been performed on these same corrugation angle channels. The integral results reveal that both the mixed 90°/0° and the 60°/30° channels have very similar hydraulic and mass transfer characteristics to the pure 45° channel. However, although the overall average performance of the mixed channel is similar to that of the pure 45° channel, the individual mass transfer coefficients within the channel are quite different. In an actual exchanger therefore, the two sides of a mixed angle channel will have quite different film heat transfer coefficients.

INTRODUCTION

Although there are now many different plate geometries for the main heat transfer area of a plate exchanger, by far the most commonly reported pattern is the herringbone or chevron corrugation. The channel formed from these patterns is such that the corrugations on adjacent plates are arranged so that they point in opposing directions. This produces a very complicated flow area for the fluid to pass through. Although the corrugated design is by no means a new concept, it is still unclear exactly how the fluid flow effects both heat transfer and pressure drop.

The aim of the designer of a plate heat exchanger is to try to match the specifications of both the duty and the available pressure drop. However, the designer has only a limited number of different plate geometries available, due to the cost of the presses for the manufacture of the plates. As such it is not possible to have any combination of duty and pressure drop. One of the two following situations must therefore occur.

1. Although the duty is matched, the achieved pressure drop is too high. More plates are added to reduce the pressure drop and this causes a reduction in the velocity in each channel.
2. The duty is matched, but the available pressure drops are not fully utilised.

The above summary does very much simplify the problem. For example, it should be remembered that there are two streams to consider in the design. This may seem very obvious, but design approaches often only mention the pressure drop for one stream. While it is quite possible that the designer could match both the duty and the pressure drop for one stream, they are unlikely to be able to match the pressure loss for both streams. So in that situation the design would have to be based around the stream with the limiting pressure drop. Selecting the stream that is pressure drop limiting is not a simple decision. The choice of the stream with the limiting pressure drop would depend on both the flow rate and the allowable pressure drop of each stream.

This problem apart the designer still has the difficulty of a limited number of plate designs with which to match the duty and the pressure drop. One way of increasing the number of options available is to combine plates with different *theta* values. So a high *theta* plate may be combined with a low *theta* plate to generate a channel with intermediate characteristics. The most commonly reported way of achieving this is to combine plates with different corrugation angles. Such a channel is often termed a mixed angle channel.

Now while overall performance data for pure angle channels is not particularly common, data for mixed angle channels is even scarcer. There are a just a couple of studies in the literature. Manglik and Muley (1995 and 1997) presented both the overall thermal and hydraulic performance for a chevron type channel with angles of 30° and 60°. Test fluids used were water and vegetable oil for a Reynolds number range of 2 to 6000. However, results were only reported for this one particular channel type. As such the data does not provide any information that has not already been derived from the performance plots for pure angle channels.

Really there are two questions that immediately arise when considering mixed angle channels. The first problem is to

consider how the designer would go about calculating the performance of a mixed angle channel. Clearly the designer could just use a correlation that has been derived from experimental data, in much the same way that Manglik and Muley did for the 60°/30° channel. But some authors have suggested that the average angle can be used to approximately represent the performance of a mixed angle channel [Heavner *et al.* (1993), Edwards *et al.* (1984)]. For example the performance of the 60°/30° channel used by Manglik and Muley would be roughly equivalent to that of a pure 45° channel. Presumably then the performance of a mixed angle channel can be calculated by interpolating between the performances for two pure angle channels. This then leads into the second question concerning mixed angle channels, and that is how do mixed angle channels compare to the performance of pure angle channels? The statement that the average angle can be used to represent the performance of a mixed channel is quite commonly reported. However, there is almost no evidence to support this statement.

The only previous study to examine the performance of both mixed and pure angle channels was presented by Heavner *et al.* (1993). A total of five different combinations were tested: 45°/0°, 67°/0°, 45°/45°, 45°/67° and 67°/67°. This resulted in five average corrugation angles of 22.5°, 33.5°, 45°, 56° and 67°. The test fluid used was water over a Reynolds number range of 300 to 10,000. They presented both the thermal and hydraulic performance as a function of the Reynolds number with the corrugation angle as a parameter. Note that they were not able to directly compare the performance of a mixed angle channel with a pure angle channel. For example they were unable to compare the performance of a 45°/0° channel with that of a pure 22.5° channel.

NOMENCLATURE

A_e	electrode surface area		(m^2)
b	plate gap		(m)
c_b	concentration of reacting species		(kmol/m^3)
d_e	effective diameter		(m)
D	ionic diffusivity		(m^2/s)
F	Faraday's constant	96,487	(C/equiv)
f	friction factor		
g	acceleration due to gravity		(m^2/s)
I_L	diffusion limited current		(A)
L	projected plate length		(m)
Re	Reynolds number		
Sc	Schmidt number		
Sh	Sherwood number		
t	plate thickness		(m)
u	average channel velocity		(m/s)
U	overall heat transfer coefficient		(W/m^2 K)
V	volumetric flow rate		(m^3/h)
W	plate width		(m)
z	valence change in electrochemical reaction		

Greek Symbols

α	film heat transfer coefficient	(W/m^2 K)
β	corrugation angle	(°)
Δh	height difference in manometer legs(m)	
ΔP	pressure drop	(N/m^2)
λ	thermal conductivity	(W/m K)
μ	fluid viscosity	(kg/m s)
θ	thermal length	
ρ	fluid density	(kg/m^3)

Subscripts

c	cold
C	contributions to apparatus pressure drop
h	hot
m	mercury
var	varying pressure drop
T	total
w	wall

EXPERIMENTAL METHODS

In this study, local mass transfer coefficients have been obtained in a single simulated heat exchanger channel by an electrochemical methodology: the diffusion limited current technique. The technique involves subjecting an electrolytic solution to a potential gradient, resulting in ions being consumed at the electrode surface. Under certain conditions the flux of ions can be described by a Fickian relationship, and the mass transfer coefficient can be expressed as a local Sherwood number according to:

$$Sh = \frac{I_L d_e}{zFA_e Dc_b} \qquad (1)$$

A potassium ferrocyanide/ferricyanide redox couple was chosen as the reactive electrolyte with potassium carbonate as a supporting electrolyte.

The results of the mass transfer studies and the description of the experimental technique and the equipment for have been described previously by Heggs *et al.* (1997) and Heggs and Walton (1999). In summary, the most important parts of the equipment are the test plates and the electrodes. Hence a brief description of their design is provided below, and a diagram of one of the test plates is presented in Figure 1. The anode and cathode are each mounted on one half of a simulated plate heat exchanger channel. These two electrodes can be turned to give results at various corrugation inclination angles: 90°, 60°, 30° and 0° normal to the direction of flow. The perspex test plates are profiled with sinusoidal corrugations of depth 5.3 mm and pitch of 21.0 mm. The dimensions of these plates were selected to provide a uniform flow distribution and to develop the flow regime prior to the electrolyte reaching the test area. To provide a uniform flow distribution a relatively high aspect ratio (ratio of plate length to breadth) of three to one was

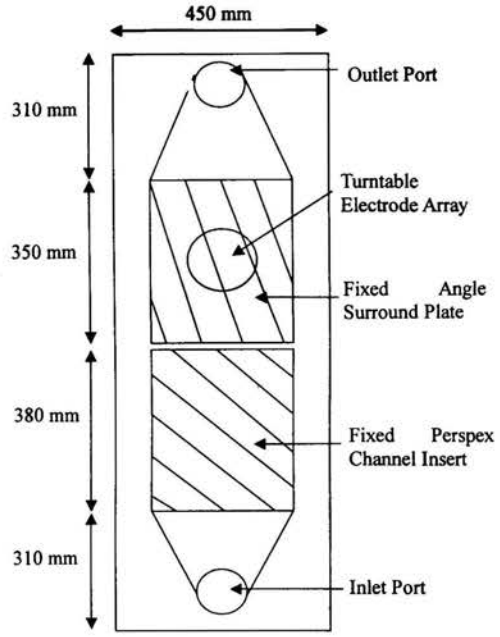

Figure 1. Schematic drawing of the bottom plate of the experimental apparatus.

chosen. In addition, the electrode pair are positioned inside a matching angled surround plate. Thus for each corrugation angle tested, a separate fixed angle surround plate was manufactured. This not only helped to provide a uniform flow distribution, but it also helped to develop the flow regime prior to the electrode section. To record values of local mass transfer coefficients within a single corrugation, a grid of 99 nickel plated brass micro-electrodes are embedded in the central corrugation of the principal cathode. This grid of micro-electrodes is termed the working electrode. The anode is of the same shape and overall dimensions of the substrate cathode, but the ridges of the corrugation crests were insulated to prevent short-circuiting. A typical unit cell within the channel is pictorially illustrated in Figure 2.

In a pure angle channel this working electrode can be placed on either side of the channel, because the profiles of mass transfer in each plate are identical. In a mixed angle channel however, the two sides of the channel have different mass transfer characteristics. Therefore to gain a full understanding of the performance of a mixed channel it is necessary to run different experiments in which the working electrode has been positioned in both sides of the channel. A mixed angle channel will thus generate two different mass transfer profiles.

More recently Walton (2001) has used the apparatus also to measure the pressure drop over the various pure and mixed angle channels for which mass transfer results have been reported. The pressure drop was recorded using a mercury manometer connected to the inlet and outlet legs of the exchanger apparatus. (see Figure 3)

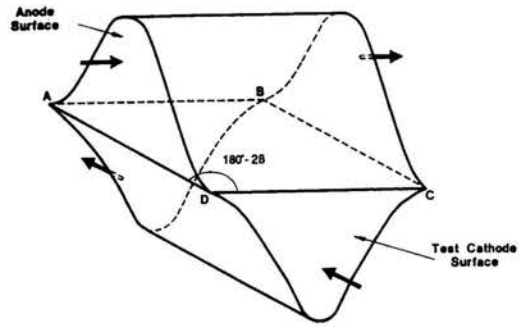

Figure 2. The unit cell arrangement.

This preserves the integrity of the perspex channel. The problem with this approach is that the measured pressure drop is not due solely to the corrugated section. There are additional contributions to the pressure drop from: friction in the connecting pipe work, bends in the connecting pipe work, expansion and contraction losses at the entrance and exit of the plate channel and finally, losses in the top 380 mm of the channel containing the fixed 45° section.

The area of interest is the pressure drop across the variable angle section that surrounds the electrodes. So it is necessary to calculate the pressure drop due to these additional losses and then subtract this contribution from the measured pressure drop. To establish the pressure drop due to the additional losses, it was decided to first operate the rig with a 90°/90° combination in the variable angle section. This combination results in a set of parallel ducts with a constant cross-sectional area. The total pressure drop across the exchanger (ΔP_T) can then be written as the sum of the pressure drop across the 90° section (ΔP_{var}) plus the pressure drop due to the additional contributions (ΔP_C).

$$\Delta P_T = \Delta P_{var} + \Delta P_C \qquad (2)$$

By calculating the pressure drop across these sine ducts and subtracting this contribution from the measured pressure drop, then it is possible to obtain a value for the pressure loss due to all the additional contributions. Focke *et al.* (1985) gave the following expression for the friction factor across a 90°/90° channel.

$$f = 0.552 Re^{-0.263} \qquad (3)$$

The friction factor is defined as

$$f = \frac{2\Delta P d}{\rho u^2 L} \qquad (4)$$

It should be noted that Focke *et al.* used the three dimensional definition of the effective diameter. The ratio of the developed to projected area for the channel is 1.157 giving an effective

diameter of 9.16×10^{-3} m. The length term in equation (4) is the length of the variable angle section, which is 380 mm. The pressure drop across the 90°/90° section is therefore given by

$$\Delta P = 39.34\rho^{0.737}\mu^{0.263}u^{1.737} \quad (5)$$

The fluid velocity in the channel can be obtained from the volumetric flow rate according to

$$u = \frac{V}{Wb} \quad (6)$$

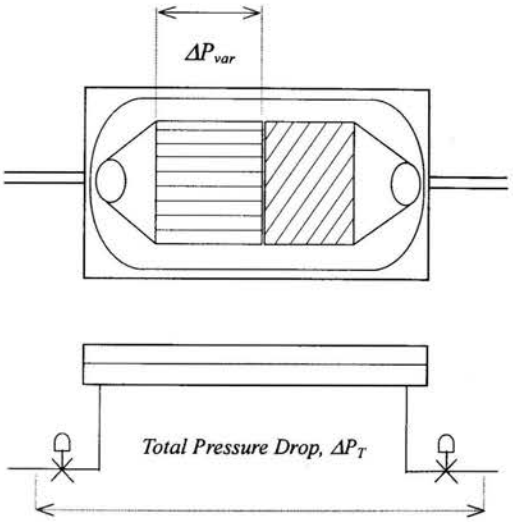

Figure 3. Pressure drops over the exchanger apparatus.

The final task is to relate the manometer readings to the pressure drop across the exchanger rig. The manometer consists of a glass U-tube of length 1m containing mercury as the measuring fluid and water as the operating fluid. (Water was chosen as the operating fluid primarily for reasons of safety.) The height of the mercury was recorded using a 1mm divided scale. It is essential that any air bubbles are fully purged from the rig and the exchanger prior to operation so that the water sits directly on top of the mercury surface. For this reason both legs of the manometer are connected to a vent. By denoting the height difference of the mercury in the two arms of the manometer as Δh, then the pressure difference may be written as:

$$\Delta P = (\rho_m - \rho_{water})g\Delta h \quad (7)$$

where ρ_m represents the density of the mercury. It is now possible to calculate the pressure drop across the exchanger rig and across the 90°/90° section. By subtracting the pressure drop due to the pure 90° section from the total pressure loss, then it is possible to obtain the drop in pressure due to all the additional contributions as a function of the channel flow rate. This data is illustrated in Figure 4.

Note that the friction factor correlation presented by Focke had an associated Reynolds number range of 5000 – 56,000. Clearly this correlation has been applied to much lower values of the Reynolds number in this study. There are two reasons why this correlation has been applied to a wider Reynolds number range. Firstly the pressure drop due to the 90° section was found to be considerably smaller than the contribution due to the additional losses. Indeed the largest contribution from the 90° section only accounted for 4.5% of the total recorded pressure drop. Secondly, the total pressure drop results across the apparatus including the 90° section revealed no sharp transition region. It may be that the large contribution to the total pressure drop from the additional losses has tended to

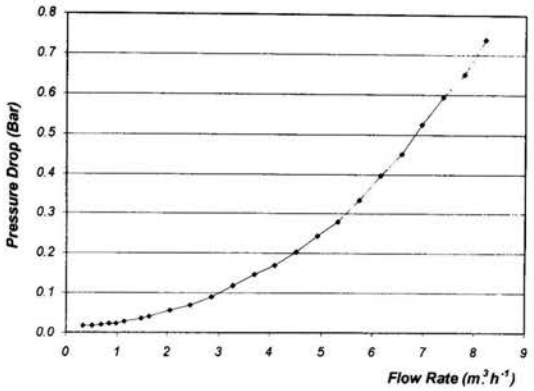

Figure 4. Pressure Drop Due to the Additional Apparatus Contributions.

dampen any transitional regions. Also recall however, that a fixed 45° corrugated section is situated above the 90° section. It is quite possible that the flow patterns generated in the 45° section would affect the fluid motion within the 90° corrugations. This may well account for the lack of a transition. However, because the pressure drop within the 90° section accounted for only 4.5% of the total pressure drop, it was concluded that an acceptable error would be introduced by applying Focke's correlation beyond the stated Reynolds number range.

A second error is introduced through the manometer scale. Notice from the results presented in Figure 4 that the pressure drop across the rig encompasses a wide range of values. At the top end of the scale, the pressure drop is equivalent to approximately one metre of mercury. At this end of the scale the mercury level was observed to fluctuate between ± 2.5 cm, resulting in an error of ± 2.5%. It contrast at the lower end of the scale the pressure drop is equivalent to only 1 cm of mercury. Clearly with a graduated scale of 1 mm a much larger error of ± 10% is introduced even though the mercury level was observed to be very steady at this location. Assuming an error of ± 4.5% in the estimation of the 90° pressure drop the total error varies between ± 5.2% to ± 11.0%.

PRESSURE DROP RESULTS

It is common to find pressure drop data for plate heat exchangers presented as a logarithmic plot of the friction factor. While this is useful for calculating the pressure drop over a range of physical properties, it does not necessarily help to explain what occurs during the experiment. It is more helpful to plot the pressure drop versus the flow rate on a linear scale. In the first instance this reflects what actually occurs during the experiment, in that the flow rate was varied to produce a deviation in the pressure drop. The linear scale also makes it a little simpler to interpret the data.

The pressure drop curves for both the mixed angle channels and the pure angle channels are presented in Figure 5. Interestingly, the two mixed angle arrangements show very similar characteristics to the pure 45° channel. It would seem that the pure 45° channel presents a slightly lower hydraulic resistance than the two mixed angle channels (particularly in the flow rate range of 3.2 – 5.8 m^3/h). However, in comparison to the range of pressure drops covered by the pure 30° and 90° channels, this difference is very small. Again this is a particularly surprising result for the mixed 90°/0° channel. The geometry of this mixed 90°/0° channel is somewhat different to the geometry found in the pure angle channels. It is conceivable that the available cross-sectional area in the 90°/0° channel is only half that of the other channels. Certainly the fluid velocity in the 90° plate should be higher than the velocity in both the 60°/30° channel and the pure 45° channel. Despite these differences however, the 90°/0° channel reveals very similar characteristics to the pure 45° channel.

It was not possible to correlate the various sets of data by the usual friction factor and Reynolds number type correlation due to the random scatter at the low flow rates. The data at the lower flow rate range needs to be repeated using a more sensitive measuring device. Time did not permit this during the studies.

It is interesting to note that the unit cells for the pure angle 45° channel and the mixed angle channels 30°/60°and 90°/0° will have streams crossing the crests of the corrugations at right angles (see Figure 2 cross section ABCD). However in the 90°/0° channel, fluid will not be flowing in the 0° corrugation. The mass transfer results did reveal that the fluid trapped in the 0° corrugation had a secondary motion caused by the crossing flow from the 90°corrugation.

INTEGAL MASS TRANSFER RESULTS

The previously reported integral mass transfer data were not correlated and now have been correlated by the following equation:

$$Sh = \sigma Re^{n} Sc^{1/3} \qquad (8)$$

The power of one third on the Schmidt number is almost universally accepted. It is possible to examine this dependence of the Sherwood number on the Schmidt number by varying the electrolyte temperature. Although the fluid temperature did vary between experiments, these variations were relatively small with a maximum temperature change of around 5°C. (There was also no direct control over the fluid temperature. The variations

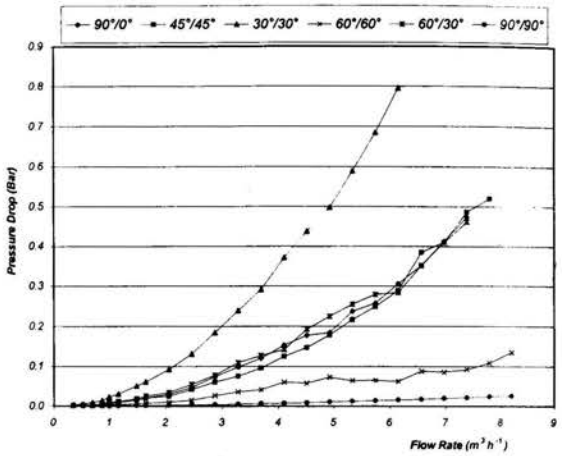

Figure 5. Pressure Drop Curves for the Mixed Angle Channels.

were principally due to atmospheric conditions.) Considering the relatively small temperature changes it was decided not to try and estimate the exponent on the Schmidt number.

The correlation coefficients obtained by linear regression are presented in Table1. Note that the first angle for the mixed angle correlations refers to the side of the combined angle channel. In general as the corrugation angle is reduced, the exponent on the Reynolds number tends to increase. The lowest exponent of 0.351 was obtained for the pure 90° channel and the highest exponent of 0.463 was obtained for the 90°/0° case. As expected the pure 45° correlation and the 60°/30° correlation are almost identical. Note also that the 30°/60° case appears to have a slightly different correlation to these two arrangements. This would seem a slightly surprising result, but note that the Reynolds number range is much narrower for the 30°/60° correlation and there are also far fewer data points. (There were some short-circuiting problems associated with the 30°/60° arrangement at low values of the Reynolds number.)

Angles	σ	n	*Re range*	*Data*	R^2 *Value*
90/0	2.148	0.463	220-8770	14	0.996
30/30	3.385	0.409	210-8070	12	0.992
45/45	3.189	0.405	210-8150	12	0.991
60/30	3.237	0.403	220-9650	11	0.996
30/60	1.846	0.475	1550-9320	6	0.999
0/90	1.642	0.451	230-9650	11	0.995
60/60	3.269	0.389	220-9650	14	0.992
90/90	2.838	0.351	210-8070	12	0.992

Table 1. Correlation Coefficients for the Integral Mass Transfer Results.

CONCLUSIONS

The results presented in these studies have demonstrated how the two sides of a mixed angle channel generate different mass transfer rates. Therefore in a heat exchanger it would seem that the two sides of the channel would present quite different thermal resistances. This presents an interesting problem when considering the quantity of heat that is transferred between each channel. For example consider the overall heat transfer coefficient describing the transfer of heat across a single plate. Ignoring any fouling resistances the overall coefficient may be written as

$$\frac{1}{U} = \frac{1}{\alpha_h} + \frac{t}{\lambda_w} + \frac{1}{\alpha_c} \qquad (9)$$

The correlations describing the film coefficients α_h and α_c will be identical. However the actual values of the film coefficients will be different, because of the different physical properties of the hot and cold streams. Now in a pure angle channel the correlations describing the film coefficients will be identical for every plate in the pack. In contrast a mixed angle channel must have a separate thermal correlation for each plate type in the pack. As an example, recall that a mixed 60°/30° channel generated two different mass transfer rates on the two sides of the channel. Also recall that a 30° plate gives a different performance in a mixed 60°/30° channel to its pure angle arrangement. So the pure angle correlation would not describe the performance of a plate in a mixed channel. An interesting problem for the future then is to consider how the individual film coefficients in a mixed channel may be evaluated.

It has also been demonstrated how the 90°/0° channel presents the widest variation in mass transfer performance between the two plates. This is not perhaps surprising considering the differences in the fluid velocity between the two sides of the channel. What is surprising however, is that the 90°/0° channel appears to show a similar mass transfer performance to the pure 45° channel.

The pressure drops in a mixed 90°/0° and 60°/30° channels are very similar in magnitude to the pressure drops in a pure 45° channel.

ACKNOWLEDGMENTS

C. Walton thanks EPSRC for his Research Studentship and UMIST for his Graduate Research Scholarship.

REFERENCES

Edwards, M.F., Changal Vaie, A.A. and Parrott, D.L., 1974, Heat transfer and pressure drop characteristics of a plate heat exchanger using Newtonian and non–Newtonian liquids, The Chemical Engineer, 285: 286-288.

Focke, W.W., Zachariades, J. and Olivier, I., 1985, The effect of the corrugation inclination angle on the thermo-hydraulic performance of plate heat exchangers, Int. J. Heat Mass Transfer, 28: 1469-1479.

Heavner R.L., Kumar, H. and Wanniarachchi, A.S., 1993, Performance of an industrial plate heat exchanger: effect of chevron angle, AIChemE Symposium Series No. 295, 89: 262-267.

Heggs, P.J., Sandham, P., Hallam, R.A. and Walton, C., 1997, Local transfer coefficients in corrugated plate heat exchanger channels, Trans. IChemE, 75: Part A, 641-645.

Heggs, P.J. and Walton, C., 1999, Local transfer coefficients in corrugated plate heat exchanger channels with mixed inclination angles, 6th.UK Heat Transfer Conference on Heat Transfer, IMechE Conference Transactions 1999-7, 39-44.

Manglik, R.M. and Muley, A., 1995, Thermal-hydraulic behaviour of a mixed chevron single-pass plate-and-frame heat exchanger, National Heat Transfer Conference, HTD Vol. 314: 89-96.

Manglik, R.M. and Muley, A., 1997, Enhanced heat transfer characteristics of single-phase flows in a plate heat exchangers with mixed chevron plates, Enhanced Heat Transfer, 4: 187-201.

Walton, C., 2001, Flow and heat transfer in corrugated plate heat exchanger channels, PhD Thesis, UMIST, UK.

HEFAT2002
1st International Conference on Heat Transfer, Fluid Mechnics and Thermodynamics
8-10 April 2002, Kruger Park, South Africa
MM2

CONTRIBUTIONS TO THE STUDY OF COMPACT HEAT EXCHANGERS ASSEMBLIES OBTAINED BY DIFFERENT CONNECTION OF MODULES

M. Muresan*, N. Serbanoiu* and V.B. Ungureanu**
*Professor, **Associate Professor
Department of Mechanical Engineering,
University TRANSILVANIA of Brasov,
B-dul Eroilor 29, Brasov, 2200
Romania,
E-mail: virbung@unitbv.ro

ABSTRACT

An analytical method is presented for thermal performances determination of compact heat exchangers assemblies by different connection modes of a variable number of modules.

The computed results for assemblies composed of four modules, compared with the experimental results obtained on the stand, confirm the validity of the proposed method.

The method allows finding the optimal arrangement from the thermal point of view, of an assembly consisting of a given number of modules.

INTRODUCTION

The variety of heat exchangers used in industry requires a great number of different constructive solutions. This number can be diminished by developing standard modules, with superior performances, that can be linked in series, parallel or mixed connections, in order to obtain the assemblies with heat rates and dimensions corresponding to some practical situations.

The study of heat exchanger assemblies obtained by using different types of connections has represented the main subject of several specialty works, [1], [2], [3] and [4]. The present paper analyses, yet by another method, all the possible arrangements of a number of four modules, establishing, also, the best arrangement.

NOMENCLATURE

Q_1	the heat rate transferred by a module (W)
T_{i1}, T_{i2}	temperatures of the fluid 1 at the input and output of the module i (K)
T_{i1}, T_{i2}	temperatures of the fluid 2 at the input and output of the module i (K)
S	heat transfer surface of a module (m^2)
c_{p1}, c_{p2}	specific heats at constant pressure of fluids 1 and 2 ($Jkg^{-1}K^{-1}$)
m_1, m_2	mass flows of fluids 1 and 2 ($kg\,s^{-1}$)
k	overall heat transfer coefficient $W\,m^{-2}\,K^{-1}$
η	the restraint coefficient of the heat in the heat exchanger

PRESENTATION OF THE PROBLEM

The series, parallel or mixed connection can be approached using as main criterion the primary (fluid 1) or the secondary (fluid 2) fluid circulation. For the case of line connection of the modules, the four possible arrangements, studied in [4], are presented in figure 1.

Considering the modules as identical and the flows of the two heat carriers as constant for each module, the heat rate of the assembly has been determined depending on the transmitted flow of module and the exit temperatures of two fluids.

The assemblies dimensions, obtained as a result of the connections presented in figure 1, can be, in certain conditions, unfavorable, and subsequently the modules will be disposed as in figure 2, thus obtaining compact assemblies. In this case, fluid 2 circulates through two series connected and two

parallels connected modules as for the circulation of fluid 1 there are three possibilities (figure3):

- it flows successively through the four modules (arrangements I... VI);
- it flows successively through the groups of two modules (arrangements VII...IX);
- it flows separately through the four modules (arrangement X).

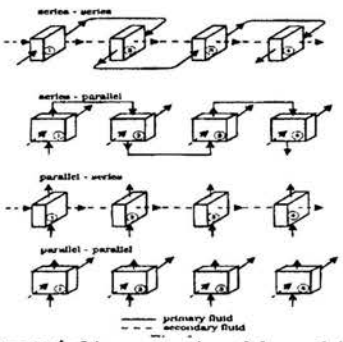

Figure 1: Line connection of the modules.

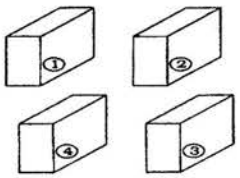

Figure 2: Compact arrangement of the modules.

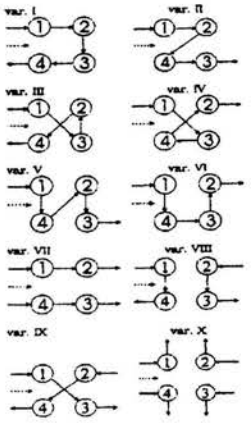

Figure 3: Arrangements for connection of modules.

FUNDAMENTAL RELATIONS FOR A MODULE

It is known, [5], that for a cross-flow heat exchanger, (figure 4), the heat rate and the exit temperatures of the two fluids are given by the following relation:

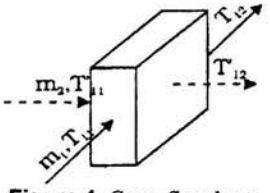

Figure 4: Cross-flow heat exchanger.

$$Q_1 = \alpha \cdot (T_{11} - T'_{11}); \tag{1}$$

$$T_{12} = \beta \cdot (T_{11} - T'_{11}) + T'_{11}; \tag{2}$$

$$T'_{12} = \gamma \cdot (T_{11} - T'_{11}) + T'_{12}; \tag{3}$$

the notations being:

$$\alpha = \eta m_1 c_{p1} \frac{1 - \exp\frac{(\varphi - 1)kS}{\eta m_1 c_{p1}}}{1 - \varphi \exp\frac{(\varphi - 1)kS}{\eta m_1 c_{p1}}}; \tag{4}$$

$$\beta = \frac{(1 - \varphi)\exp\frac{(\varphi - 1)kS}{\eta m_1 c_{p1}}}{1 - \exp\frac{(\varphi - 1)kS}{\eta m_1 c_{p1}}}; \tag{5}$$

$$\gamma = \frac{\varphi\left[1 - \exp\frac{(\varphi - 1)kS}{\eta m_1 c_{p1}}\right]}{1 - \varphi \exp\frac{(\varphi - 1)kS}{\eta m_1 c_{p1}}}; \tag{6}$$

$$\varphi = \eta \frac{m_1 c_{p1}}{m_2 c_{p2}}. \tag{7}$$

ARRANGEMENTS IN WICH THE FLUID CIRCULATES SUCCESSIVELY THROUGH THE FOUR MODULES

Considering the notations from figure 5 and using relations (1), (2) and (3) for modules two, three and four respectively, follows:

- module two

$$Q_2 = \alpha(T_{12} - T'_{12}); \tag{8}$$

$$T_{22} = \beta \cdot (T_{12} - T'_{12}) + T'_{12}; \tag{9}$$

$$T'_{22} = \gamma \cdot (T_{12} - T'_{12}) + T'_{12}; \tag{10}$$

- module three:

$$Q_3 = \alpha(T_{22} - T'_{42}); \tag{11}$$

$$T_{32} = \beta \cdot (T_{22} - T'_{42}) + T'_{42}; \tag{12}$$

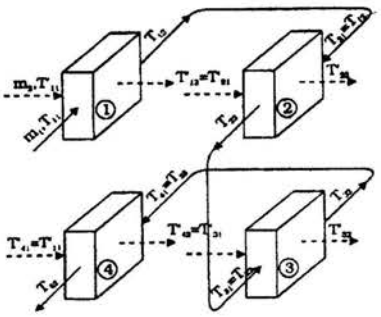

Figure 5: Fluid flows successively

$$T'_{32} = \gamma \cdot (T_{22} - T'_{42}) + T'_{42}; \quad (13)$$

- module four:

$$Q_4 = \alpha \cdot (T_{32} - T'_{11}); \quad (14)$$

$$T_{42} = \beta \cdot (T_{32} - T'_{11}) + T'_{11}; \quad (15)$$

$$T'_{42} = \gamma \cdot (T_{32} - T'_{11}) + T'_{11}; \quad (16)$$

In the above mentioned relations the specific conditions for each arrangement were taken into consideration: $T_{21} = T_{12}$; $T_{31} = T_{22}$; $T_{41} = T_{32}$; $T'_{21} = T'_{12}$; $T'_{41} = T'_{11}$ and $T'_{31} = T'_{42}$.

By solving the system consisting of equations (2), (3), (9), (10), (12), (13), (15) and (16) the temperatures of the two fluids at the exit of the modules will be determined, and, by replacing them in the expression of heat rates, we obtain:

$$Q_2 = (\beta - \gamma) Q_1; \quad (17)$$

$$Q_3 = \frac{(1-\gamma)[\beta(\beta-\gamma)-\gamma]}{1+\gamma(\beta-1)} Q_1; \quad (18)$$

$$Q_4 = \frac{\beta[\beta(\beta-\gamma)+\gamma]}{1+\gamma(\beta-1)} Q_1. \quad (19)$$

The total flow transmitted by the assemble, for the first arrangement will be:

$$Q_I = Q_1 + Q_2 + Q_3 + Q_4, \quad (20)$$

or:

$$Q_1 = \frac{(1+\beta^2)(1+\beta-\gamma)}{1+\gamma(\beta-1)} Q_1. \quad (21)$$

For the other arrangements of the same type, (the fluid 1 circulating successively through the modules), there results:

- for the arrangement II:

$$Q_2 = (\beta - \gamma) Q_1; \quad (22)$$

$$Q_3 = (\beta - \gamma)[\beta(\beta-\gamma)+\gamma] Q_1; \quad (23)$$

$$Q_4 = [\beta(\beta-\gamma)+\gamma] Q_1; \quad (24)$$

$$Q_{II} = (1+\beta-\gamma)[1+\beta(\beta-\gamma)+\gamma] Q_1; \quad (25)$$

- for arrangement III:

$$Q_2 = \frac{\beta^2 - \gamma^2(\beta-1) - \gamma}{1+\beta\gamma(\beta-1)} Q_1; \quad (26)$$

$$Q_3 = \frac{\beta(1-\beta\gamma) + \gamma^2(\beta-1)}{1+\beta\gamma(\beta-1)} Q_1; \quad (27)$$

$$Q_4 = \frac{\beta^3 - \gamma(\beta-1)}{1+\beta\gamma(\beta-1)} Q_1; \quad (28)$$

$$Q_{III} = \frac{\beta^3 + \beta^2 + \beta(1-2\gamma) + 1}{1+\beta\gamma(\beta-1)} Q_1; \quad (29)$$

- for arrangement IV

$$Q_2 = \frac{\beta^3 + \gamma^3 - \beta\gamma^2 - \gamma}{1+\gamma(\beta-1)} Q_1; \quad (30)$$

$$Q_3 = \frac{\beta(1-\gamma)}{1+\gamma(\beta-1)} Q_1; \quad (31)$$

$$Q_4 = \frac{\beta^2}{1+\gamma(\beta-1)} Q_1; \quad (32)$$

$$Q_{IV} = \frac{\beta^3 + \gamma^3 + \beta^2 + \beta + 1 - 2\gamma - \beta\gamma^2}{1+\gamma(\beta-1)} Q_1; \quad (33)$$

- for arrangement V:

$$Q_2 = (\beta^2 - \gamma) Q_1; \quad (34)$$

$$Q_3 = (\beta - 2\beta\gamma + \gamma) Q_1; \quad (35)$$

$$Q_4 = \beta Q_1; \quad (36)$$

$$Q_V = (\beta^3 + \beta^2 + \beta + 1 - 2\beta\gamma) Q_1; \quad (37)$$

- for arrangement VI:

$$Q_2 = (\beta^3 - \beta^2\gamma + \beta\gamma - \gamma) Q_1; \quad (38)$$

$$Q_3 = \beta(\beta - \gamma) Q_1; \quad (39)$$

$$Q_4 = \beta Q_1; \quad (40)$$

$$Q_{VI} = (1 + \beta + 2\beta^2 - \beta^2\gamma - \gamma) Q_1. \quad (41)$$

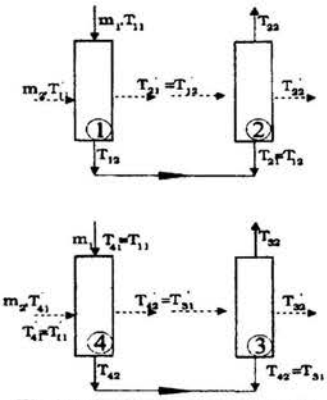

Figure 6: Fluid 1 flows through groups of two modules.

ARRANGEMENTS IN WHICH FLUID 1 CIRCULATES THROUGH GROUPS OF TWO MODULES

One of the arrangements in which the fluid 1 flows through groups of two modules (arrangement VII) is shown in figure 6.

Considering the presented scheme we obtain:

$$Q_2 = \beta Q_1 ; \quad (42)$$

$$Q_3 = \beta Q_1 ; \quad (43)$$

$$Q_4 = Q_1 ; \quad (44)$$

$$Q_{VII} = 2(1+\beta)Q_1 ; \quad (45)$$

and for the other arrangements:

- for arrangement VIII:

$$Q_2 = (1-\gamma)Q_1 ; \quad (46)$$

$$Q_3 = (\beta+\gamma-2\beta\gamma)Q_1 ; \quad (47)$$

$$Q_4 = \beta Q_1 ; \quad (48)$$

$$Q_{VII} = 2[1+\beta(1-\gamma)]Q_1 ; \quad (49)$$

- for arrangement IX:

$$Q_2 = (1-\gamma)Q_1 ; \quad (50)$$

$$Q_3 = [\beta-\gamma(\beta-\beta\gamma+\gamma)]Q_1 ; \quad (51)$$

$$Q_4 = (\beta-\beta\gamma+\gamma)Q_1 ; \quad (52)$$

$$Q_{IX} = (1+2\beta-\beta\gamma+\beta\gamma^2-\gamma^2)Q_1 . \quad (53)$$

ARRANGEMENT IN WHICH FLUID 1 CIRCULATES SEPARATELY THROUGH EACH MODULE

For the last possible connecting arrangement (arrangement X) of four modules, (figure 7), fluid 1 flowing separately through each module, we have:

$$Q_2 = Q_3 = (1-\gamma)Q_1 ; \quad (54)$$

$$Q_4 = Q_1 ; \quad (55)$$

$$Q_X = 2(2-\gamma)Q_1 . \quad (56)$$

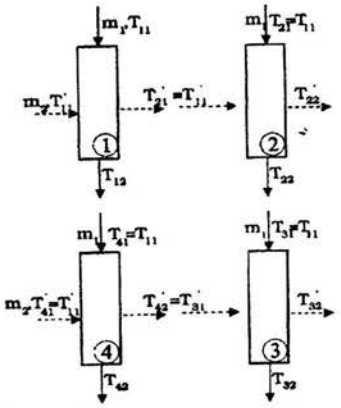

Figure 7: Fluid 1 flows separately through each module.

ARRANGEMENTS OF SERIES AND PARALLEL CONNECTION

For a compared study of all the possible arrangements, the series and parallel connection arrangements shown in figure 1 (scheme given in figure 8) and deat with in study [4]. So,

- both fluids flow in series (arrangement XI):

$$Q_{XI} = \frac{1-(\beta-\gamma)^4}{1-(\beta-\gamma)} Q_1 , \quad (57)$$

- fluid flows in series and fluid 2 in parallel (arrangement XII):

$$Q_{XII} = \frac{1-\beta^4}{1-\beta} Q_1 , \quad (58)$$

- fluid 1 flows in parallel and fluid 2 in series (arrangement XII):

$$Q_{XII} = \frac{1}{\gamma}\left[1-(1-\gamma)^4\right] Q_1 , \quad (59)$$

- both fluids flow in parallel (arrangement XIV):

$$Q_{XIV} = 4Q_1 . \quad (60)$$

CONCLUSIONS OF THE THEORETICAL STUDY

Considering as a basic module, a water-air heat exchanger, for $m_1 = 0.0166$ kg/s, $m_2 = 0.1$ kg/s, $c_{p1} = 4187$ J/kg K, $c_{p2} = 1004.65$ J/kg K, $k = 20.46 \text{W/m}^2\text{K}$ (experimentally determined), $S = 2.65\text{m}^2$, $\eta = 0.95$, using the above determined formulae, are obtained the data presented in table 1.

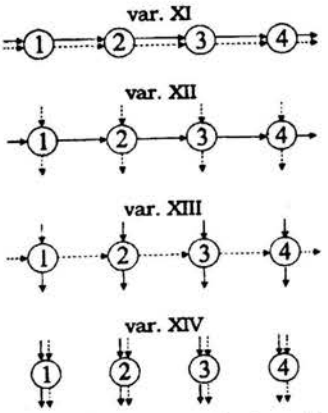

Figure 8: Schemes of series and parallel connection.

Table 1: Comparison of the arrangements.

arrangement	Q/Q_1	arrangement	Q/Q_1
I	1.7889	VIII	2.6997
II	1.6965	IX	1.8148
III	1.7242	X	3.3595
IV	1.4865	XI	1.2396
V	1.5863	XII	1.9159
VI	1.6394	XIII	2.4559
VI	3.0290	XIV	4.0000

Considering all the arrangements presented in this study, the best is the XIVth, in which both fluids flow in parallel. If we take into account only the compact arrangements, in which the modules are placed as well as in figure 2, we obtain:

- of all the arrangements in which fluid 1 circulates successively through groups of two modules, the biggest heat rate is transmitted by arrangement 1;
- of the arrangements in which the fluid 1 circulates successively through group of two modules, the best is the arrangement VII;
- the arrangement in which fluid 1 flows separately through each module (arrangement X yields a heat rate of $Q_X = 3.3595 \cdot Q_1$.

THE EXPERIMENTAL INSTALLATION

The results previously obtained were checked, also, experimentally. The experimental stand developed for water/air heat exchanger testing (vehicle radiators) is presented in figure 9.

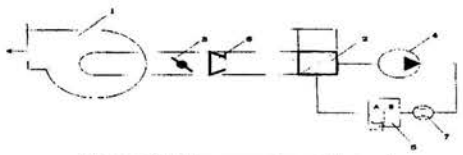

Figure 9: The experimental stand.

The centrifugal fan 1 aspirates the air from an allaying tank, on which the tested heat exchanger 2 is fitted, and releases it into the environment. On the suction line an air throttle 3 is placed, that allows adjustment of the aspirated air. The water circuit consists of a pump 4 that aspirates the water from the radiator and releases it into a two room (A and B) tank 5. The water overfills from room B into room A where it is electrically heated and then it is lead to the radiator. A thermo/adjusting circuit maintains a hot water constant temperature.

In order to perform the measurements, the installation has been endowed with the following measurement devices: diaphragm 6 for air flow measurement; thermocouples for air flow measurement; electromagnetic flow-meter 7 for water flow measurements; thermocouples for water temperature measurement at air the radiator entrance and exit.

COMPARISON BETWEEN THE EXPERIMENTAL AND THEORETICAL RESULTS

In order to check experimentally the previous obtained theoretical results, on the stand presented above the following arrangements have been tested:

- series connection of two, three and four modules (arrangement XI);
- parallel connection of two, three and four modules (arrangement XII);
- mixed connection of four modules (arrangements I, IV and IX).

The experimental results obtained for these arrangements will be compared with the theoretical results, as follows.

Thus the figure 10 presents the variation of the ratio of the heat rates exchanged by the assemblies made of two, three or four modules, series connected, and the heat rate transmitted by one module varying with φ. There is a good correspondence between the experimental and the theoretical results.

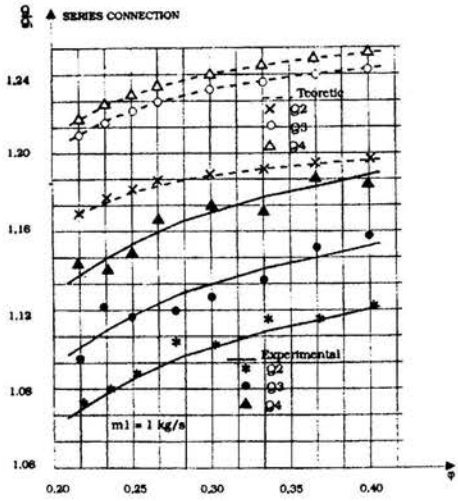

Figure 10: Heat rates exchanged by one, two, three and four modules series connected

The same stands for figure 11, where the arrangement of a parallel connection of two, three and four modules is presented.

The figure 12 presents the same dependence in the case of four modules in mixed connection, experimentally tested. The best is arrangement IX, followed by arrangements I and IV, the order being kept as in the case of the theoretical study.

CONCLUSIONS

The small discrepancies between the experiment and the above mathematical model are due to the small variation of the overall heat transfer coefficient of each module connected given the situation when it is isolated.

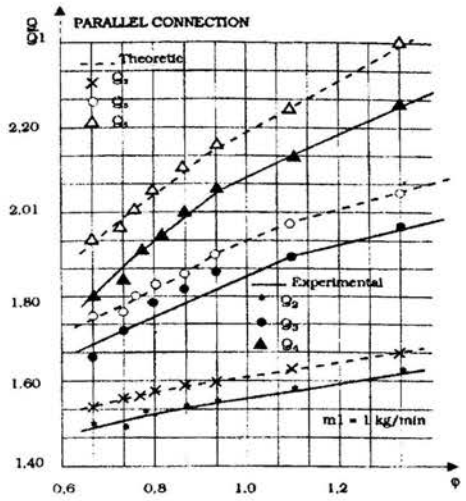

Figure 11: Heat rates exchanged by two, three and four modules parallel connected

In conclusion, the experimental results confirm the validity of the theoretical study, and therefore, also for other configurations, the theoretical calculus can be used in order to establish the optimum arrangement.

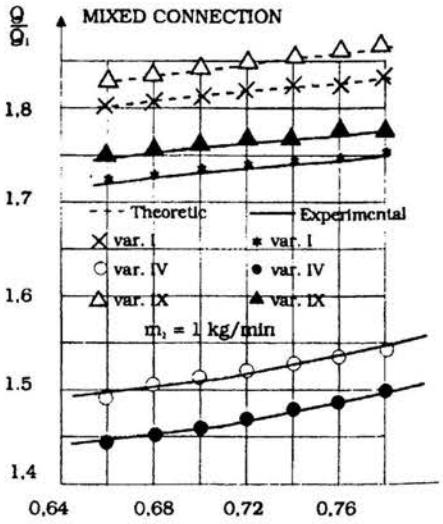

Figure 12: Heat rates exchanged by four modules mixed connected.

REFERENCES

[1] Domingos, I.D., 1969, "Analysis of Complex Assembles of Heat Exchangers", Int. Heat and Mass Transfer, vol. 12, p.p. 537-548.

[2] Serbanoiu, N., Muresan, M., Hrimiuc, C., 1992, "Methode de determination des performances thermiques des radiateurs de vehicules automobiles comportant des modules montes en serie ou en parallele", Bulletin of the Transilvania University of Brasov, serie A, vol. XXXIV, p.p. 101-110.

[3] Serbanoiu, N., Muresan, M., Sora, G., 1995, "Verallgemeinerte Gleichungen zur Ermittlung des Warmeflusses und der Flussigketstemperatur beim Austritt aus modulaufgebauten Kuhlern", B.W.K, no. 3, p.p. 97-99.

[4] Korpela, T., 1977, "Die rechnerische Behandlung von Warmeubertragergruppen", B.W.K., no. 10, p.p. 419-423.

[5] Leonachescu, N., 1974, "Termotehnica", Editura Didactica si Pedagogica", Bucuresti.

[6] El Quamia, Lacroix, M. 1998, "Modelisation d'un echangeur de chaleur compact a courant croises separes par des couches de materiau a changement de phase". Revue Generale de Thermique.

[7] Rousse, D., 2000, "Numerical Predictions of Two-Dimensional Conduction, Convection and Radiation Heat Transfer". Int. J. Thermal sciences, vol. 39, nov. 3, pp. 332-353.

[8] Hewitt, G.F., 1998, "Heat Exchanger Design Handbook". Begel House.

HEFAT2002
1st International Conference on Heat Transfer, Fluid Mechanics, and Thermodynamics
8-10 April 2002, Kruger Park, South Africa
WS4

EXPERIMENTAL AND THEORETICAL INVESTIGATION OF HEAT TRANSFER AND PRESSURE DROP IN A PLATE-TYPE EVAPORATOR

S. Wellsandt* and L. Vamling**
*PhD student; **Professor
Department of Heat and Power Technology,
Chalmers University of Technology,
SE-412 96 Gothenburg, Sweden
Phone: +46-31-7723013, Fax: +46-31-821928
E-mail: Sven.Wellsandt@hpt.chalmers.se
E-mail: Lennart.Vamling@hpt.chalmers.se

ABSTRACT

The purpose of the work reported here was to determine heat transfer and pressure drop in a plate-type evaporator both experimentally and theoretically. An experimental facility was built to provide the means for detailed measurements at different conditions. Subsequently, a calculation method was developed to simultaneously calculate heat transfer and pressure drop in a variable number of steps along the evaporator. Results from measurements and calculations are compared and discussed. In the investigated range the calculation method overestimates heat transfer by between 1-8% and underestimates pressure drop by between 7% and, at very high outlet vapour fractions, 30%.

INTRODUCTION

Background

High-temperature heat pumps are of considerable interest for Swedish district heating systems, where about 20 large (25 MW) heat pumps using R22 are installed. These heat pumps utilise plate-type heat exchangers as evaporators with around thousand plates each. One such plate taken, from the plant, was investigated. The evaporator is of the self-circulation type, i.e. after the expansion valve there is a gas-liquid separator, where the liquid is led down to the inlet of the evaporator. The outlet is connected to a separator, from which the gas proceeds to the compressor inlet.

According to Swedish regulations for HCFCs, there is a ban on refilling R22 in the year 2002, which raises the problem of finding appropriate substitutes. The most probable substitute currently is R134a since the application requires condensation temperatures around 80°C and flammable fluids must not be used due to the central location of the plant. However, at normal compressor inlet conditions, the density of R134a is about 30% lower than when using R22, which results in a lower flow. Gabrielii [1] states that this leads to a heating capacity 35% lower than for a R22 heat pump and consequently to a decrease in evaporator duty, which per se could affect the heat transfer.

The aforementioned makes it clear that in order to support the conversion process from R22 to a new working fluid, detailed measurements as well as the development of a calculation method was desirable.

Why a vertical plate-type evaporator?

The horizontal shell and tube evaporator is the most commonly used type of water chiller due to its compactness, high efficiency and low cost. However, when used for water source heat pumps it has some disadvantages. Exit water temperatures below 2°C (refrigerant in tubes) to 3°C (water in tubes) are normally not recommended. Such limits may exclude the use of many natural sources in a northern climate. Particularly cold water calls for an evaporator design, which permits ice formation on the surface without risk of damage to the evaporator. The plate-type evaporator satisfies this requirement.

In terms of flow direction it is important to point out that the heat transfer efficiency in evaporators with horizontal flow channels often suffers as a result of drying out due to separated flow. Liquid will contact only the lower part of the surface, leaving perhaps the major part of it dry and rather inefficient. The described effect is evidently more pronounced when material thermal conductivity is low, as in the case of stainless and high alloy steels. According to Haukås [2], the best way to acquire complete wetting of the walls is to use vertical flow direction. The channels should be rather short in order to keep the elevation pressure drop for high-density refrigerants at an acceptable level. At the same time, the mass rate of flow and average refrigerant vapour fraction should be high to secure efficient convective heat transfer. These conditions can best be achieved by using channels where the ratio of circumference to cross-section area is high, which means narrow ducts with a rectangular cross-section.

NOMENCLATURE

a	heat diffusivity (m^2/s)
cp	specific heat (J/kgK)
D	diameter (m)
g	gravitational acceleration (m/s^2)
h	heat transfer coefficient (W/m^2K)
i	enthalpy (J/kg)
Δi_{lg}	latent heat of evaporation (J/kg)
k	thermal conductivity (W/mK)
m	mass flow (kg/s)
Nu	Nusselt number
n	circulation number ($1/x$)
Pr	Prandtl number
Δp	pressure drop (Pa)
Q	heat duty (W)
Re	Reynolds number
r_{cr}	critical radius (m)
T	temperature (K)
ΔT	temperature difference (K)
U	overall heat transfer coefficient (W/m^2K)
x	vapour fraction

Greek Letters

ν	kinematic viscosity (m^2/s)
η	dynamic viscosity (Ns/m^2)
Φ	heat flux (W/m^2)
ρ	density (kg/m^3)
σ	surface tension (N/m^2)

Subscripts

acc	accelerational
bub	bubble point
conv	convective
fo	liquid only
fric	frictional
g	gas
grav	gravitational
h	hydraulic
i	inner
l	liquid
NcB	nucleate boiling
in	inlet
out	outlet
R	refrigerant
sat	saturation
sp	single-phase
TP	two-phase
w	water

EXPERIMENTAL METHOD

Facility

The experimental set-up consists of a refrigerant and a water loop, of which the latter is an open system since the water is employed as a falling film on the outside of the evaporator plate. Desired water inlet temperatures are established by utilizing an electrical heater. Water flow from each side of the panel is collected separately and its temperature is measured. This enables the detection of maldistribution between the two sides of the plate. Water flow and water inlet temperature are the two parameters that can be controlled on the water side. The use of tap water was found to be reasonable, since the full-scale evaporator is fed with brackish seawater with a very low salt content.

The refrigerant loop consists of the evaporator plate, a separator as well as a condenser and can be operated at either natural or forced circulation. When the latter is applied, a bypass with a pump is interposed and in this way the refrigerant flow can be controlled. At natural circulation, the refrigerant flow can be varied by using a valve positioned at the plate inlet. Since measurements were mainly to be carried out at natural circulation, a flow meter that does not introduce pressure drop exceeding that in the tubing was required. This demand led to the use of a straight-flow coriolis-type flow meter.

A cooling machine where the compressor has a variable speed drive controls the pressure in the separator and thereby the evaporation pressure and temperature. Refrigerant inlet and outlet temperatures are measured by means of type T thermocouples and a pressure difference transducer gauges pressure drop over the panel.

Evaporator

The evaporator plate, as seen in Fig. 1, is made of stainless steel and is 3000 mm high, 500 mm wide and, at channel centre, 5 mm thick. The wall thickness is about 1 mm. Two steel sheets are attached by means of 1287 point-weldings creating 13 vertical flow channels. The application of point-weldings of course involves the possibility of fluid exchange between the different channels. It is also obvious that the effective heat transfer area results from the total plate area reduced by the area of all point-weldings. The effective heat transfer area is about 2,75 m^2.

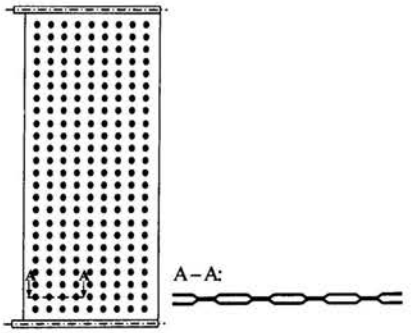

Figure 1: The plate-type evaporator (not to scale)

Experimental Procedure and Data Reduction

Test conditions were downscaled from those encountered at the full-scale evaporator. This led to a water flow of 2.45 kg/s, water inlet temperatures between 2°C and 6°C, and evaporator duties between 12 and 20 kW.

The evaporator duty was determined on the water side by measuring inlet and outlet temperatures and mass flow $(Q = m_w cp \Delta T)$. Since the refrigerant is normally leaving the plate at two-phase condition, it was not possible to double-check the internal evaporator duty. However, a few measurements at superheat conditions were performed. Even though the refrigerant flow tended to be less stable at superheat conditions, the energy balance error was below 2%. With the evaporator duty it was possible to calculate the overall heat transfer coefficient (U-value) from Eq. (1).

$$U = \frac{Q}{A\,T_{LMTD}}, \qquad (1)$$

where the logarithmic mean temperature difference is defined on the basis of water temperatures in and out, refriger-

ant bubble point temperature at inlet pressure and refrigerant temperature at the evaporator outlet

$$T_{LMTD} = \frac{(T_{W,\,in} - T_{R,\,out}) - (T_{W,\,out} - T_{R,\,bub})}{\ln \frac{(T_{W,\,in} - T_{R,\,out})}{(T_{W,\,out} - T_{R,\,bub})}}. \qquad (2)$$

The above definition of T_{LMTD} was chosen, because the enthalpy change over the subcooled region is negligibly small. Using the refrigerant inlet temperature would mean an overestimation of the temperature driving force, whereas applying the bubble point temperature instead closer reflects the actual temperature profile.

Two different kinds of experiments were conducted. First the effect of a change in temperature driving force was investigated. This was done by keeping the water inlet temperature constant (at 2°C and 6°C) and changing the evaporation pressure. The second series of measurements was aimed at the influence of various refrigerant flows on heat transfer. For this purpose the evaporation pressure and water inlet temperature were held constant and the refrigerant flow was varied by throttling.

All experiments were conducted at natural circulation.

CALCULATION METHOD

For the theoretical approach a preliminary decision upon a possible simplification of the plate's complex channel geometry had to be made. It was decided to divide the plate into 13 separate flow channels, i.e. to neglect possible fluid exchange between channels, and to use a constant hydraulic diameter along one channel. This hydraulic diameter was chosen to double the channel height (D_h = 2 x 3mm = 6 mm), which is the hydraulic diameter of the largest cross-section in one channel. Between point-weldings the hydraulic diameter varies and is about 4.15 mm at the smallest cross-section (Fig. 1). The chosen hydraulic diameter is of course larger than a mean hydraulic diameter, which, however, is not known due to unknown exact channel geometry. The effect of a smaller hydraulic diameter is discussed further below.

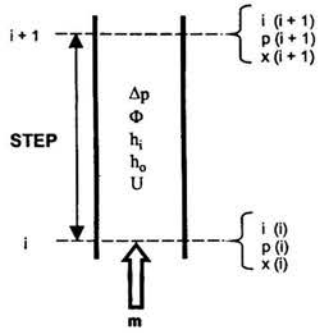

Figure 2: Channel step with parameters included in the calculation method.

Since the temperature profile over the channel is dependent on pressure drop, enthalpy and pressure were calculated simultaneously in a stepwise manner from evaporator inlet to outlet. As seen in Fig. 2, for each step, heat transfer coefficients, heat flux and pressure drop were determined according to step inlet and outlet conditions (enthalpy, pressure and vapour fraction).

Heat Transfer

Water Side

The water side heat transfer coefficient was calculated according to a recommendation by the VDI-Wärmeatlas [3] for falling film heat transfer. The following three dimensionless numbers describe the heat transfer:

$$Nu \equiv \frac{h}{k}\left(\frac{\nu^2}{g}\right)^{1/3}, \qquad \mathrm{Re} \equiv \frac{m}{\eta}, \qquad \mathrm{Pr} \equiv \frac{\nu}{a} \qquad (2)$$

Reynolds numbers were about 1600, which indicated turbulent flow (Re > 400); the recommended expression is then:

$$Nu = 0.0136 Re^{2/5}\ Pr^{0.344}. \qquad (3)$$

Refrigerant side

On the refrigerant side, a general application boiling correlation was applied, as proposed by Steiner and Taborek [4] for boiling in vertical tubes with upward (and downward) flow. The Steiner-Taborek model is arranged so that one can utilize all of it or substitute one's own correlations or data for various parts of it. Collier and Thome [5] state that from initial indications, it is the most accurate vertical tube correlation that is currently available.

The two-phase heat transfer coefficient is calculated from a power law type model, which combines the nucleate boiling and convective boiling coefficients as shown in Eq. (4).

$$h_{TP} = \left[\left(h_{NcB,o} F_{NcB}\right)^3 + \left(h_{fo} F_{TP}\right)^3\right]^{1/3} \qquad (4)$$

Eq. (4) is an asymptotic approach since the magnitude of h_{TP} tends to the larger of the two values.

$h_{NcB,o}$ is the local normalized nucleate flow boiling coefficient at a standard condition of heat flux and reduced pressure. It was obtained by the Gorenflo [6] procedure, which uses a 'base' pool boiling heat transfer coefficient predicted by the physical properties-based method of Stephan and Preusser [7].

F_{NcB} is the nucleate boiling correction factor that accounts for the difference between pool and flow boiling, as calculated by Steiner-Taborek.

h_{fo} is the local liquid-phase forced convection coefficient based on the total flow as liquid. The Gnielinski [8] correlation valid for both the transition and fully turbulent regimes was used.

F_{TP} is the two-phase multiplier that accounts for the enhancement of convection in a two-phase flow. It is a function of the vapour fraction and the liquid/vapour density ratio. This was calculated according to Steiner-Taborek.

Since the refrigerant enters the evaporator subcooled, the calculation method also accounts for subcooled boiling. This is done by comparing the heat flux for onset of nucleate boiling, Eq. (5), and the actual heat flux.

$$\Phi_{ONB} = \frac{2\sigma T_{sat} h_{fo}}{r_{cr} \rho_g \Delta i_{lg}} \quad (5)$$

Eq. (5) was developed in evaluation of the Karlsruhe data bank [9] and is recommended by Steiner-Taborek. Spindler, Shen and Hahne [10] reported experimental results of subcooled boiling heat transfer in vertical tubes, which were compared with different correlations given in literature. They came to the conclusion that the recommendation by the VDI-Wärmeatlas (Steiner and Taborek) showed best agreement with measured results.

Pressure Drop

The pressure drop was determined according to a recommendation by the VDI-Wärmeatlas [11,12], where the total pressure drop is divided into frictional, gravitational and accelerational pressure drop, see Eq. (6).

$$\Delta p = (\Delta p)_{fric} + (\Delta p)_{grav} + ((\Delta p)_{acc})_{TP} \quad (6)$$

Due to space restrictions the method is not described in more detail and the reader may refer to VDI-Wärmeatlas.

RESULTS AND DISCUSSION

Experimental results

Effect of temperature driving force variation

An increasing temperature driving force means an increasing evaporator duty as long as superheat conditions are avoided. As can be seen in Fig. 3, the U-value is decreasing towards lower duties which could be due to decreasing outlet vapour fractions (70% → 30%) and thereby a deterioration of convective heat transfer. At the same time lower duties mean lower heat fluxes and hence less nucleate boiling heat transfer.

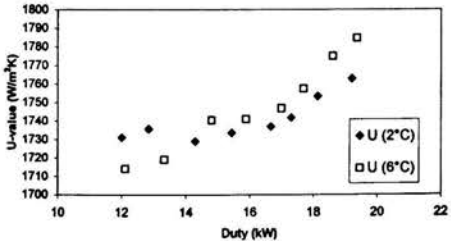

Figure 3: U-values as a function of duty at typical water temperatures (natural circulation)

Apparently there is a water temperature dependency as the U-value falls slightly more for 6°C water temperature (4%) than for 2°C water temperature (2%).

Effect of flow variation

Fig. 4 shows the evaporator duty and U-value for changing flow.

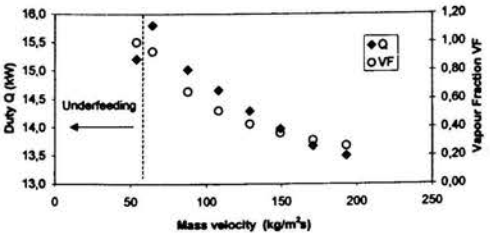

(a)

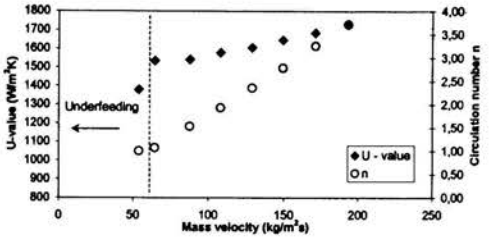

(b)

Figure 4: Evaporator performance at changing flow.
(a) Evaporator duty and vapour fraction,
(b) U-value and circulation number.
3°C water inlet temperature. 2.7 bar evaporator outlet pressure.

Particular attention may be paid to the fact that the evaporator duty increases up to high outlet vapour fractions (93%), i.e. a circulation number approaching unity. At the same time the U-value decreases with higher vapour fractions, which is a fact that necessitates further explanation. Considering Eq. (1), apart from the area, none of the parameters are constant. The temperature driving force T_{LMTD} increases towards lower flows (pressure drops) since the bubble point temperature decreases more than the water outlet temperature (water inlet and refrigerant outlet temperatures are constant). The above described underlines, that it is important to choose a T_{LMTD} definition, that as close as possible reflects the real temperature profile over the plate. A constant evaporation temperature would not account for pressure drop and thus overestimate the U-value.

In Fig. 4 it is clearly seen that at superheat conditions, described as underfeeding, the evaporator duty and U-value drop significantly.

Calculation results

Heat Transfer

The contribution from different types of heat transfer mechanisms for refrigerant heat transfer is illustrated in Fig. 5.

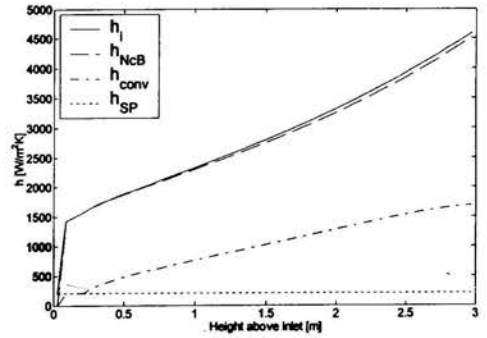

Figure 5: Calculated heat transfer coefficients on refrigerant side. Outlet vapour fraction 68%.

The convective part is represented by the dash dotted line and is a result of the local liquid-phase forced convection coefficient (lower horizontal dotted line) enhanced by the two-phase multiplier. Its rather low value is due to a relatively low flow rate. The nucleate boiling coefficient

(dashed line), on the other hand, has a much larger value since it is a function of the heat flux, which is increasing significantly from inlet to outlet. Due to the asymptotic nature of the correlation, it is the nucleate boiling coefficient that dominates the total inner heat transfer (solid line). However, with increasing flow rate, the forced convection coefficient *will* have an influence on the total heat transfer. This means that at the same evaporator load, a higher flow rate will lead to a lower outlet vapour fraction and thereby to a higher single-phase convection coefficient but a lower two-phase enhancement factor.

A correction factor ε_U is used to describe the deviation between calculations and experiments. The U-value in every step is multiplied with ε_U, which is iteratively adjusted to yield a given evaporator duty. A correction factor close to unity indicates a good agreement with measured data, whereas a value lower and higher than one means an over- and underestimation of heat transfer respectively. Fig 6 and 7 show the correction factors for the different measured conditions.

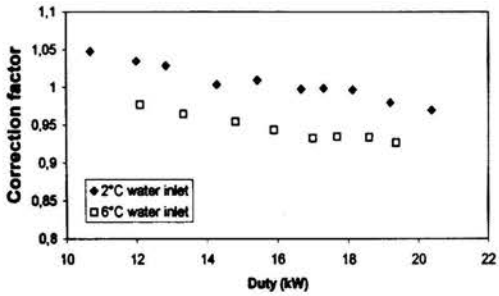

Figure 6: Correction factors – temperature driving force variation

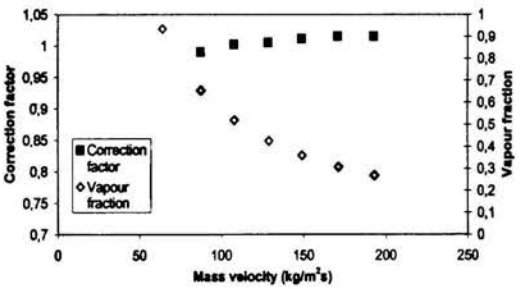

Figure 7: Correction factors – flow variation

As seen in Fig. 7, correction factors for flow variation measurements are very close to unity and rather constant over the entire flow range. Correction factors in Fig. 6 decrease towards higher duties, which means that according to the calculation method, the U-value should be even more dependent on the evaporator load than what the measurements showed. Correction factors for 6°C water inlet temperature are about 5% lower than values for 2°C water inlet temperature. This fact might indicate the existence of a further parameter that could alter results according to different measurement conditions.

Pressure drop

A general picture of how the different types of pressure drop contribute to the total pressure gradient is depicted in Fig. 8.

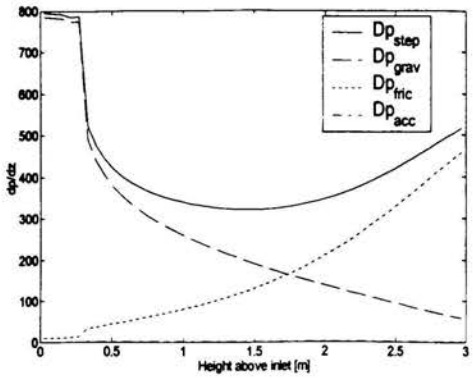

Figure 8: Calculated pressure drop along the evaporator plate. Outlet vapour fraction 68%.

The gravitational pressure drop (dashed line) dominates at one-phase flow, but drops drastically as soon as two-phase flow exists and decreases gradually with higher vapour fractions. Conversely, the frictional pressure drop (dotted line) increases towards higher vapour fractions and governs the total pressure drop in the upper part of the plate. Consequently, in most cases the lowest pressure gradient occurs neither at plate inlet nor at plate outlet but rather somewhere in the middle part of the evaporator. The accelerational pressure drop is so low that it is not even visible in Fig. 8.

Calculated and measured pressure drops for the different experimental cases are shown in Fig. 9 and 10.

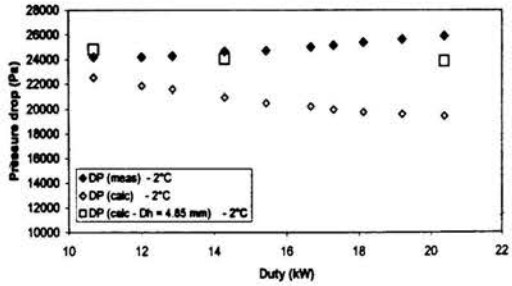

Figure 9: Calculated and measured pressure drop – varying temperature driving force

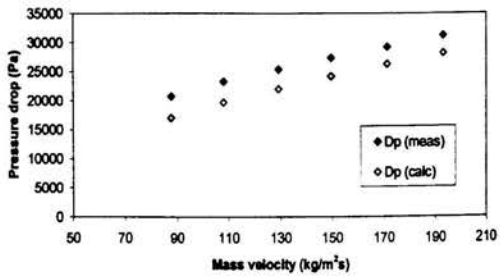

Figure 10: Calculated and measured pressure drop – flow variation

In Fig. 9, the calculated and the measured pressure drop differ from each other progressively more towards higher duties (vapour fractions). Whilst the measured values increase with higher duties, calculated values decrease. Since values for 2°C and 6°C water inlet temperature follow the same trend, for reasons of clarity, results are exclusively

shown for 2°C water inlet temperature. For flow variation, measured and calculated values show the same tendency but there is an increasing discrepancy towards lower mass velocities (higher vapour fractions).

There are several possible causes for the underestimation of the pressure drop. First, the hydraulic diameter chosen is at the upper end of the range of possible values. The effect of using a lower value is illustrated in Fig 9. By choosing the hydraulic diameter to Dh=4.85 mm, the calculated pressure drops will be close to the experimental ones, but there is still some kind of dependence on evaporator duty. Reducing the hydraulic diameter does, however, result in an overestimate of heat transfer (about 8% in error factor).

Another likely reason is the assumption that the plate can be approximated as a number of vertical channels. The flow area variation due to the point weldings is very likely to give additional pressure drop, similar to the situation for tube banks.

The above discussed causes might be even more distinct at higher vapour fractions (flow velocities), i.e. in Fig. 9 towards higher duties and in Fig. 10 towards lower flows. It is clearly seen that the deviation between measured and calculated values increases in the respective direction.

CONCLUSIONS

An experimental set-up was built to enable heat transfer and pressure drop measurements for a vertical plate-type evaporator. Experiments were conducted at different temperature driving forces as well as varying flow rates.

Measurement results were compared to calculated values from a proposed calculation method. From results and their discussion, the following conclusions can be drawn:

(1) For measurements at different temperature driving forces, a decrease of U-values towards lower duties was recognised. Calculation results agree with measured values (correction factors close to unity) but suggest an even more distinct dependency of the U-value on the evaporator duty.

(2) In a second series of measurements, the refrigerant flow was varied at constant evaporation pressure and water inlet temperature. At up to rather high vapour fractions the evaporator duty increased, whereas the U-value decreased.

U-value correction factors from calculations were very close to unity and rather constant over the entire range of flow rates.

(3) According to the proposed calculation method, nucleate boiling heat transfer is dominating the heat transfer on the evaporation side for conditions investigated.

(4) The comparison of measured and calculated pressure drops show deviations between 7% and at very high vapour fractions 30%.

(5) The general level of the calculated pressure drop is determined by the choice of the hydraulic diameter. A smaller hydraulic diameter than the one applied in this work would lead to better pressure drop but a poorer heat transfer calculation.

(6) The flow area variation due to the point-weldings might introduce an additional pressure drop, which is not taken into account by the proposed calculation method. These effects are probably more distinct at high vapour fractions/flow velocities.

ACKNOWLEDGMENTS

Financial support from the Swedish National Energy Administration and from Birka Energi AB is gratefully acknowledged.

REFERENCES

[1] **Gabrielii, C.**, HFC Mixtures as Replacement for HCFC-22 in Large-Scale Heat Pumps and Chillers, *Doctor Thesis*, 2000.

[2] **Haukås H.T.**, Design of a plate-type evaporator for heat pumps, *International Journal of Refrigeration*, Volume 7, Number 1, pp. 59-63, January 1984.

[3] **Schnabel, G.**, Wärmeübergang an senkrechten berieselten Flächen, Sect. Md, in *VDI Wärmeatlas*, Springer-Verlag Berlin, 1998.

[4] **Steiner, D., Taborek, J.**, Flow Boiling Heat Transfer in Vertical Tubes Correlated by an Asymptotic Model, Heat Transfer Engineering, vol. 13, no. 2, pp. 43-69, 1992.

[5] **Collier, G., Thome, R.**, Convective Boiling and Condensation, third edition, chapt. 7.4.4, Oxford Science Publications, 1999.

[6] **Gorenflo, G.**, Behältersieden, Sect. Ha, in *VDI Wärmeatlas*, Springer-Verlag Berlin, 1988.

[7] **Stephan, K., and Preusser, P.**, Wärmeübergang beim Behältersieden, Chem. Ing. Tech., vol. 51, pp. 649-679, 1979.

[8] **Gnielinski, V.**, Forced Convection in Ducts, in *Heat Exchanger Design Handbook (HEDH)*, vol. 2, sec. 2.5.1, Hemisphere, New York, 1983, suppl. 1989; *Hemisphere Handbook of Heat Exchanger Design*, Hemisphere, New York, 1990.

[9] **Steiner, D.**, Strömungssieden gesättigter Flüssigkeiten, Sect. Hbb, in *VDI Wärmeatlas*, Springer-Verlag Berlin, 1998.

[10] **Spindler, K., Shen, N., Hahne, E.**, Vergleich von Korrelationen zum Wärmeübergang beim unterkühlten Sieden, in *Wärme- und Stoffübertragung*, Springer-Verlag Berlin, 1990.

[11] **Kast, W.**, Druckverlust bei der Strömung durch Rohre, Sect. Lb, in *VDI Wärmeatlas*, Springer-Verlag Berlin, 1998.

[12] **Chawla, J. M.**, Druckverlust in durchströmten Verdampferrohren, Sect. Lga, in *VDI Wärmeatlas*, Springer-Verlag Berlin, 1998.

HEFAT 2002
1st International Conference on Heat Transfer, Fluid Mechanics and Thermodynamics
8-10 April 2002, Kruger Park, South Africa
WS5

HEAT TRANSFER MEASUREMENTS FOR AN EVAPORATOR PLATE – DISCUSSION OF HYSTERESIS AND ICE FORMATION PHENOMENA

S. Wellsandt* and C. Gabrielii**
*PhD student; ** Dr
Department of Heat and Power Technology,
Chalmers University of Technology,
SE-412 96 Göteborg, Sweden
sven.wellsandt@hpt.chalmers.se
cecilia.gabrielii@hpt.chalmers.se

ABSTRACT

The aim of this paper is to investigate ice formation and the possible occurrence of hysteresis phenomenon in a plate-type evaporator, used in for example district heating heat pumps. Detailed heat transfer and pressure drop measurements are carried out for both pure fluids and zeotropic mixtures.

Experimental results, together with some simulation results, are used to discuss the ice formation phenomenon. One result is that the refrigerant temperature at start of ice formation differs between refrigerants, especially between pure fluids and mixtures.

The evaporator duty is observed to depend on start-up conditions. An explanation based on a boiling hysteresis phenomenon is suggested.

INTRODUCTION

The background to this investigation is the international regulation of the ozone-depleting substance HCFC22, which is used as working fluid in many district heating heat pumps. The most probable replacement fluid today is HFC134a, which can however decrease the heating capacity up to 35%. In an earlier work based on simulations of a heat pump plant, some zeotropic HFC-mixtures were identified as possible substitutes. [1]. However, there exist some uncertainties with the use of these mixtures, which had to be investigated further.

In a Nordic climate, the use of sea water as heat source fluid implies a risk for ice formation on the evaporator plates. Due to the non-isothermal evaporation of zeotropic mixtures (the so called temperature glide), there is possibly a larger risk for ice formation when using a mixture compared to a pure fluid. Since this might severely limit the capacity of the heat pumps, it is of high interest to study it in more detail.

In order to investigate the ice formation phenomenon, a test facility with one evaporator plate was constructed and detailed measurements of heat transfer as well as pressure drop were carried out.

During measurements another interesting phenomenon was observed, namely an evaporator performance depending on start-up conditions. To find explanations to this behaviour was of importance since it might be taken advantage of when operating the full-scale evaporator.

NOMENCLATURE

HCFC	hydrochlorofluorocarbons
HFC	hydrofluorocarbons
LMTD	logarithmic mean temperature difference
ΔP	pressure drop [Pa]
Q	heat duty [W]
T	temperature [°C]
$\Delta T_{subcool}$	amount of subcooling [°C]
U	overall heat transfer coefficient [W/m^2,°C]

Subscripts

refr	refrigerant

EXPERIMENTAL

The evaporator consists of one evaporator plate taken from a full-scale heat pump plant. The plate consists of thirteen vertical narrow flow channels with an hydraulic diameter between 4.2 and 6.0 mm. The channels were created by attaching two sheets by means of point weldings (see *Figure 1*). It is 3000 mm high, 500 mm wide and, at channel centre, 5 mm thick. The wall thickness is about 1 mm.

The evaporator works with natural circulation of the working fluid, and water is employed as a falling film on the outside of the plate. By measuring inlet and outlet water temperatures and water flow, the heat input can be calculated. Pressure drop over the plate is measured as well as inlet refrigerant temperature. Wall temperatures are measured at twelve locations at four levels on the plate by means of T-type thermocouples which were soldered to the plate.

For a complete description of the facility the reader is referred to Wellsandt et al. [2].

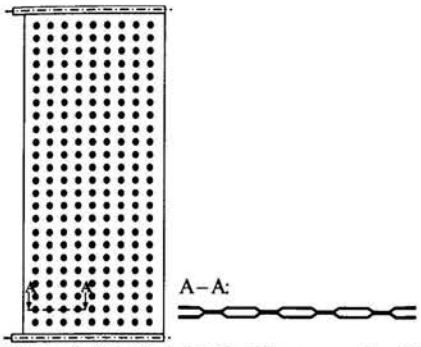

Figure 1: Principal sketch of the evaporator plate

Measurements were carried out for two pure fluids - HCFC22 and HFC134a - and three zeotropic mixtures – Mix1 (96% HFC134a + 4% HFC32), Mix2 (67% HFC134a + 17% HFC125 + 16% HFC143a) and Mix3 (30% HFC134a + 29% HFC125 + 41% HFC143a) having a temperature glide during evaporation of around 2.1°C, 3.6°C and 3.1°C respectively.

PART I – ICE FORMATION

Theory

In the actual heat pumps the inlet sea water temperature can be as low as 2°C, which means an obvious risk for ice formation on the evaporator plates. To prevent ice formation, the heat pumps are controlled by a lower limit on the evaporator pressure. If not controlled in this way, an increasingly thicker ice-film on the plates resulting in a successive decrease in heating capacity might occur. The pressure is controlled by the compressor speed and, thus, this pressure limit might lead to a volume flow into the compressor which is lower than the maximum flow possible, which, in turn, leads to a decrease in capacity. When investigating alternatives to replace HCFC22 it is important to have an accurate value of this pressure limit since it can largely affect the capacity output of the heat pump in winter-time [1].

The risk for ice formation might be larger for mixtures than for pure fluids, due to the difference in temperature profile between pure fluids and zeotropic mixtures, as shown principally in *Figure 2*. Before discussing this figure it should be mentioned that the working fluid enters the evaporator at the bottom, where the pressure is higher than the outlet pressure, due to gravitational and frictional pressure drop. This means that the working fluid enters as a subcooled liquid.

In *Figure 2* an equal evaporator area, heat duty, heat transfer coefficient and pressure drop are assumed for all fluids. This also means an equal mean temperature difference for the evaporation process. As seen, the inlet temperature is therefore lower for a zeotropic mixture than for a pure fluid, i.e. a larger glide means a lower inlet temperature.

Note that the actual size of the glide is depending on the outlet vapour fraction / circulation number. For actual values of the circulation number, and its variation with evaporator duty the reader is referred to Wellsandt et al. [4].

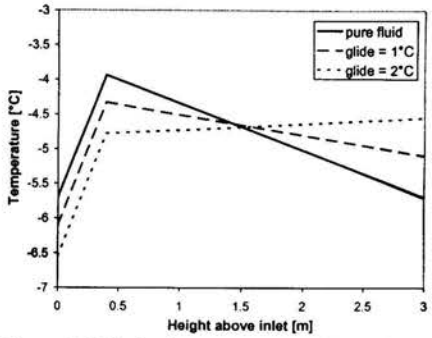

Figure 2: Principal temperature profile in the evaporator for a pure fluid and mixtures with a temperature glide. Calculated data.

Traditionally, the limit on evaporator pressure to prevent ice formation corresponds to this inlet temperature, i.e. the subcooled temperature of the working fluid. The reason is that both the water and refrigerant have their lowest temperature at the refrigerant inlet, i.e. the bottom of the plate. However, whilst the water temperature has its minimum at the very bottom, the wall temperature might not. Further, seen from a practical point of view, the start of ice-formation is defined as the point when the ice layer causes a drastic decrease in evaporator duty. This point might not correspond to the minimum wall temperature but instead to a certain combination of wall and water temperature. For these reasons, it is possible that the pressure limit should not correspond to the inlet refrigerant temperature.

RESULTS AND DISCUSSION

In order to investigate the ice formation phenomenon, measurements were carried out at a water inlet temperature of 2°C. The presented results are mainly experimental, but as a help to find explanations some simulation results are discussed.

As previously mentioned, whether or not an ice layer causing a drop in capacity will occur at a certain point is determined by a combination of water and wall temperature. These temperatures are dependent on the refrigerant temperature profile which in its turn is influenced by heat transfer, pressure drop, inlet subcooling, and – for zeotropic mixtures – the temperature glide.

In *Table 1*, inlet refrigerant temperature, number of degrees subcooling, pressure drop, overall heat transfer coefficient (U-value) and duty are shown for the different fluids. When carrying out these measurements it was very difficult to physically see the exact start of ice formation. The values presented in *Table 1* were taken when a sudden decrease of evaporator duty occurred, indicating the existence of ice on the plate (see *Figure 3*). Before this drop in duty, there might

have been a thin ice layer somewhere on the plate. However, as discussed above, the 'practical definition' for the start of ice formation, that is used in this paper, corresponds to a drop in duty.

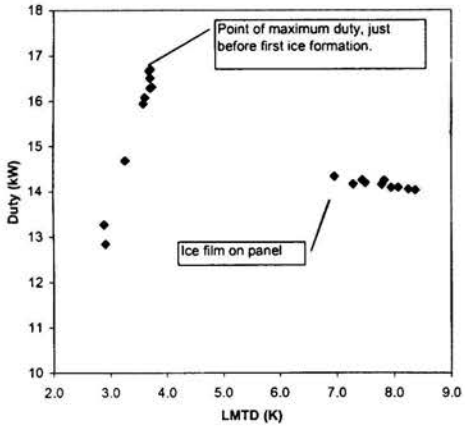

Figure 3: Evaporator duty during the process of ice formation

Table 1: Measured values at start of ice formation

Fluid	$T_{in,refr}$ [°C]	$\Delta T_{subcool}$ [°C]	ΔP [kPa]	U [W/m^2,K]	Q [kW]
HCFC22	-3.15	0.97	24.7	1647	16.9
HFC134a	-3.74	1.93	25.4	1642	16.7
Mix1	-4.02	1.78	24.3	1542	15.8
Mix2	-4.76	1.69	25.8	1474	16.3

As seen in *Table 1*, the inlet refrigerant temperature at start of ice formation varies between different fluids. Below a discussion of probable reasons for these differences is given.

Starting with the two pure fluids, it is seen that they have almost the same U-value and duty, i.e. the same mean temperature difference. The pressure drop differs with less than 1 kPa between these fluids, but due to differences in their temperature-pressure relationship, the difference in saturation temperature between inlet and outlet is around 1°C higher for HFC134a. This also means that the inlet subcooling is about 1°C higher for HFC134a. Since the subcooled part is very small, it only affects the mean temperature difference marginally and is therefore neglected. The difference in saturation temperature between inlet and outlet however affects the refrigerant temperature profile. Since this temperature difference is larger for HFC134a and the two fluids have the same mean temperature difference, the bubble point temperature is higher (0.4°C) for HFC134a. However, since the subcooling is 1°C higher for HFC134a, the inlet temperature is still lower for this fluid. Thus, for a fluid with a large subcooling pressure drop the temperature limit can be set to a lower value.

For both mixtures the inlet temperature at start of ice formation is lower than for HFC134a despite a smaller subcooling for the mixtures. As also seen in *Table 1*, the U-value is lower for the mixtures, especially for Mix2. A decrease in heat transfer affects the wall and water temperature profiles, and thus the point where ice formation starts to occur. The main reason for the lower inlet temperatures is however the difference in temperature profile for mixtures compared to pure fluids. For a mixture, the increasing temperature at evaporation compensates to different extents for the temperature decrease due to pressure drop. Therefore, for the same mean temperature difference the bubble point is lower compared to a pure fluid, followed by a lower inlet refrigerant temperature (for the same subcooling). The glide is largest for Mix2, and consequently it has the lowest inlet temperature.

From this discussion it was concluded that one cannot use the same temperature limit for all fluids. The results also indicate that the start of ice formation is not at the very bottom of the plate, thus it does not occur at the lowest refrigerant temperature. The reason is that for the same outlet water temperature and similar heat transfer the inlet refrigerant temperature would be the same for all fluids if the ice formation started at the inlet. From the values presented in *Table 1*, it is difficult to draw any conclusion about where the ice formation starts to occur. Therefore, temperature profiles were evaluated both from experiments and simulations.

Measured temperature profiles

Wall temperatures were visualized in a graphical manner, a so called thermogram. For reasons discussed by Gabrielii et al. [3], the measured wall temperatures represents a temperature midway between the refrigerant temperature and the wall temperature. Temperatures between the twelve measured points were interpolated by using MATLAB. Observed in these thermograms is that the mixtures have a more uniform temperature over the plate, and that there seems to be a somewhat unequal flow distribution for all fluids. Otherwise it is hard to draw any firm conclusions since the temperatures at the inlet and outlet were not measured. Hence, temperature profiles from simulations were evaluated as well.

Calculated temperature profiles

Simulations of experimental data were carried out with a detailed step-wise calculation method. The model by Steiner-Taborek was used to predict the heat transfer, and for pressure drop a method proposed in VDI-Wärmeatlas was used. This simulation model is described by Wellsandt et al. [4]. As shown there, both heat transfer and pressure drop calculations are in good agreement with experimental values. Therefore, the temperature profiles obtained from calculations can approximately represent the actual temperature profiles over the plate. These profiles are shown for R134a and Mix1 in *Figure 4*.

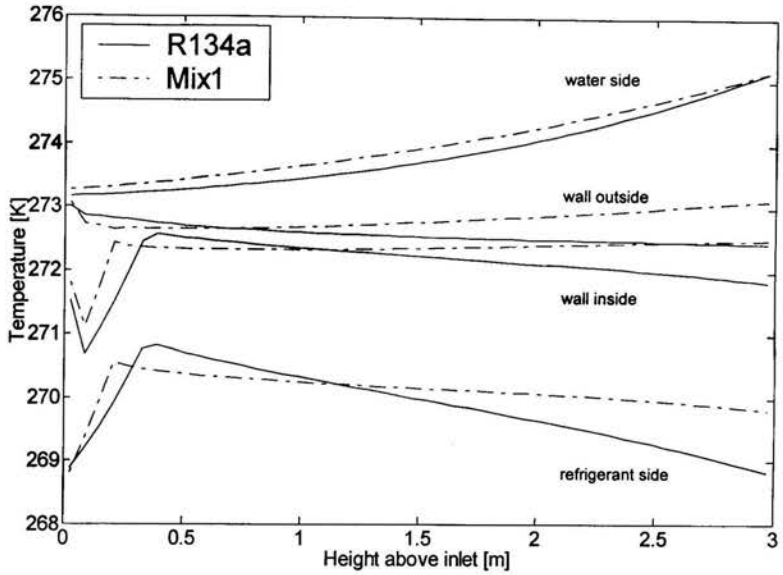

Figure 4: Calculated temperature profiles

The drop in wall temperature, seen in *Figure 4*, happens at the onset of subcooled boiling, due to the sudden increase in heat transfer. Furthermore, the water temperature gradient is very small in this region since the heat transferred in the subcooled part is very small. Thus, it is most probable that the start of ice formation occurs at the onset of subcooled boiling, which is around 200 mm above inlet.

It is also seen that the inlet wall temperature and the shape of water and wall temperature profiles are different for the different working fluids, possibly implying differences in the point where ice formation occurs. As previously discussed, reasons for this difference in temperature profiles are differences in heat transfer, pressure drop, subcooling and temperature glide.

Summarizing the results, it is difficult to give any exact recommendation on how to set the temperature / pressure limit. However, it has been shown, that for a fluid with a large subcooling/pressure drop it is possible to use a somewhat lower temperature limit. For a mixture with a large glide, but the same subcooling/pressure drop, an even lower limit can be used. This is an important result, since the use of the same limit for a mixture and a pure fluid implies that the mixture will give a lower capacity.

PART II - HYSTERESIS

The other topic discussed in the present paper is a possible hysteresis effect such that the evaporator performance depends on start-up conditions.

Theory

In the search for explanations to this behaviour, a literature review were made concerning investigations where a dependence on start-up conditions was observed. All investigations found are carried out applying constant heat flux or wall temperature over the evaporator plate/tube. However, in the actual experiments both heat flux and wall temperature vary over the plate, which implies that the onset of nucleate boiling occurs at different times at different levels. Below a brief summary of the literature review is given as an introduction to the boiling hysteresis phenomenon.

Boiling hysteresis was recognised in 1950 by Corty and Foust [5]. Studies concerning hysteresis have than gained increased importance, especially for cooling of electronic systems by highly-wetting fluids. Traditionally, hysteresis was connected to boiling incipience, which means that the superheat required for incipience is much higher than the one required at normal boiling conditions. The theory behind this is described by for example Shi et al. [6] and Bräuer et al. [7]. Shi et al. [6] point out that there are experiments indicating two different boiling hysteresis characteristics. They state that hysteresis can exist also after boiling has been initiated, i.e. in the transitional region between partial and fully developed nucleate pool boiling. Maracy et al. [8] have also experienced hysteresis in the transition boiling, with higher heat transfer

rates if the transition region is approached from the nucleate boiling side instead of from the film boiling side. This kind of boiling hysteresis has not been clearly understood, and may possibly be the reason for uncertainties for boiling heat transfer data and irregularities in boiling curves. As discussed below this kind of boiling hysteresis might be an explanation to the results observed in the present study.

As discussed by Shi et al. [6], the main factors influencing boiling hysteresis are surface conditions, thermal properties of the fluid and the wall, system pressure, the thermal history of the wall and the heating procedure, i.e. anything that affects the fluid/surface combination

The hysteresis effect is larger for enhanced than for smooth surfaces, as reported in several publications [6,9,10,11]. There are also indications that the hysteresis phenomenon is larger for mixtures than for pure fluids [9,12].

RESULTS AND DISCUSSION

In *Figure 5* the dependence on start-up conditions, in form of different start-up water temperatures, are shown. As seen, the steady-state duty can differ as much as 15% depending on the inlet water temperature at start-up, and the dependence is larger for the mixture than for the pure fluid.

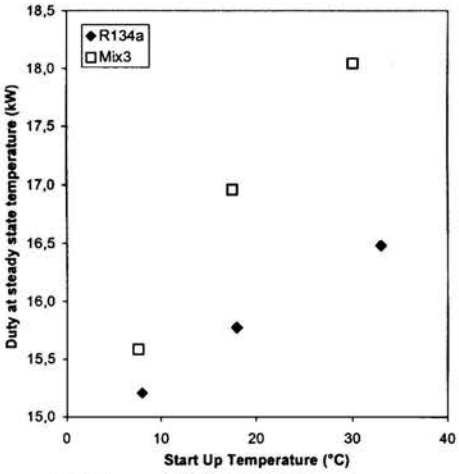

Figure 5 Effect of different start-up temperatures on the steady-state evaporator duty.

When trying to explain these results it is of course important to clarify what the consequences are of having different water temperatures at start-up. Most often the start-up temperature of the water is higher than the desired steady-state inlet water temperature. Thus, during start-up, by means of the evaporator plate, the water is cooled down until steady-state is reached. Furthermore, after a period of inactivity, the refrigerant has to be cooled down from room temperature to the set pressure (temperature). It was observed that the cooling of refrigerant seems to be faster than the cooling of the water. Hence, at start-up there is a larger temperature difference between refrigerant and water compared to steady-state conditions. This could mean, as mentioned above and discussed by Shi et al. [6] and Maracy et al. [8], depending on the temperature difference at start-up one reaches different steady-state duties - the higher the start-up temperature the higher the duty. This is principally illustrated in *Figure 6*.

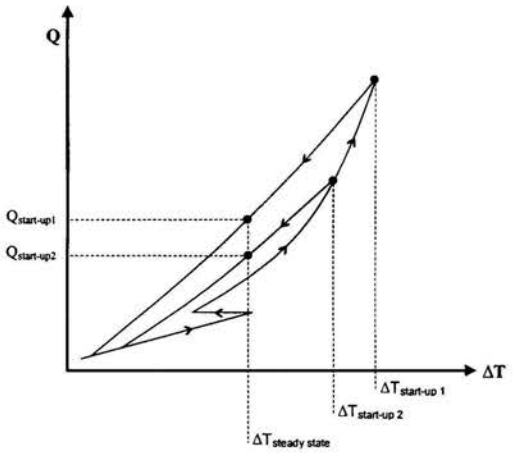

Figure 6 Principal illustration of nucleate boiling hysteresis

Before a deeper discussion is made concerning a possible boiling hysteresis phenomenon it is important to establish if the heat transfer mechanisms over the plate are such that boiling hysteresis can occur. Since the flow is rather low and vertical, it is most probable that nucleate boiling dominates over forced convection. This is confirmed by simulations of the evaporator plate [4]. Thus, there might be a boiling hysteresis phenomenon. Next, the problem of how to investigate its occurrence in more detail is discussed.

As already addressed, the temperature difference between refrigerant and water is higher at start-up than at steady state. It would be of interest to get measured values during the process before steady-state. However, in the actual facility, dynamic measurements cannot be carried out. Therefore, some additional experiments were performed with the aim of investigating if the boiling curve is different when increasing the temperature difference compared to when decreasing it. A constant steady-state inlet water temperature was used. First, the steady-state evaporator pressure was set to a value giving a small temperature difference. Then it was successively decreased, implying an increasing temperature difference and duty. When reaching the maximum possible duty at this water inlet temperature, the evaporator pressure was successively increased, i.e. the temperature difference and duty decreased. In *Figure 7*, the duty at increasing and decreasing temperature difference is shown. A clear hysteresis effect can be observed.

Note that since the evaporator works with natural circulation, a change in duty implies changes in flow and vapour fraction. There are, however, only minor differences in

vapour fraction and flow between the experiments at increasing and decreasing duty. It can be stated that these differences cannot explain the differences in boiling curve seen in *Figure 7*.

An important question now is if the results presented in *Figure 7* can explain the dependence on start-up conditions, seen in *Figure 5*. The two figures are not entirely comparable since the temperature difference at high start-up temperatures in *Figure 5* are probably somewhat larger than the maximum steady-state temperature difference in *Figure 7*. What can be stated is that the differences in duty between the curve at increasing and decreasing temperature difference seen in *Figure 7* are as large as the difference in duty between different start-up conditions seen in *Figure 5*. Thus, there are strong indications that the observed dependence on start-up conditions can be explained by a boiling hysteresis phenomenon.

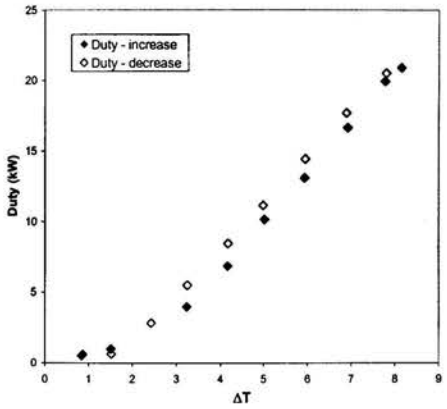

Figure 7 Measured duties at increasing and decreasing temperature differences. 6.6 °C water inlet temperature.

CONCLUSIONS

An investigation on hysteresis and ice formation phenomena, occurring in a plate-type evaporator, was carried out. From measurements of heat transfer and pressure drop, together with some simulation results, the following conclusions were drawn:

(1) The start of ice formation, causing a drastic drop in duty, seems to occur at the onset of subcooled boiling. At start of ice formation, the refrigerant temperature differs between different refrigerants, especially between mixtures and pure fluids. This is explained by deviations in temperature profiles, due to differences in heat transfer, pressure drop, subcooling and temperature glide.

(2) The evaporator duty was shown to depend on the water temperature at start-up. Measurements show differences in duty if experiments are carried out at increasing or decreasing temperature difference. A hysteresis phenomenon that occurs after boiling incipience can be the probable explanation.

ACKNOWLEDGMENTS

Financial support from the Swedish National Energy Administration and from Birka Energi AB is gratefully acknowledged.

REFERENCES

1. Gabrielii C., Vamling L. Replacement of R22 in heat pumps used for district heating, *Proc. Int. Refrigeration Conf.* July 25-28 **2000**, Purdue University, West Lafayette, USA, pp.449-456

2. Wellsandt S, Vamling L. Heat Transfer of R-22 and Alternatives in a Plate-Type Evaporator *Proc. Int. Refrigeration Conf.* July 25-28 **2000**, Purdue University, West Lafayette, USA, pp.161-168

3. Gabrielii C., Wellsandt S., Karlsson T., Ingvarsson P. New Refrigerant Blends to Replace R22 *Klimat 21 report* Jun **2000**, Chalmers University of Technology, Gothenburg, Sweden

4. Wellsandt S., Vamling L. Experimental and Theoretical Investigation of Heat Transfer and Pressure Drop in a Plate-Type Evaporator *Proc. 1st Int. Conf. On Heat Transfer, Fluid Mechanics, and Thermodynamics* 8-10 April **2002**, Kruger Park, South Africa

5. Corty C., Foust A.S. Surface variables in nucleate boiling, *Chem Engng Prog. Symp.* **1955** Ser. 51, nr. 16, pp. 1-12

6. Shi M.-H., Ma J., Wang B-X., Analysis on hysteresis in nucleate pool boiling heat transfer, *Int. J. Heat Mass Transfer* **1993** vol. 36, no. 18, pp. 4461-4466

7. Bräuer H., Mayinger F., Onset of nucleate boiling and hysteresis effects under forced convection and pool boiling *Proc. Engineering. Foundation Conference on Pool and External Flow Boiling ASME* March 22-27 **1992** Santa Barbara, USA

8. Maracy M., Winterton R. H. S., Hysteresis and contact angle effects in transition pool boiling of water *Int. J. Heat Mass Transfer* **1988** vol. 31, no. 7, pp. 1443-1449

9. Hsieh S-S., Weng C-J. Nucleate pool boiling from coated surfaces in saturated R-134a and R-407C *Int. J. Heat Mass Transfer* **1997** vol. 40, no. 3, pp. 519-532

10. Tekhver Y. K. Hysteresis phenomena with boiling on porous coatings, *Thermal Engineering* **1990** vol. 37 no. 12, pp 625-627

11. Pinto A. D., Caplanis S., Sokkol P., Gorenflo D. Variation of hysteresis phenomena with saturation pressure and surface roughness, *Proc. Engineering. Foundation Conference on Pool and External Flow Boiling ASME* March 22-27 **1992** Santa Barbara, USA

12. Thome, J.R., Shock R.A.W., Boiling of Multicomponent Liquid Mixtures, *Advances in Heat Transfer*, **1984** vol.16 Academic Press Inc.

HEFAT2002
1st International Conference on Heat Transfer, Fluid Mechanics and Thermodynamics
8-10 April 2002, Kruger Park, South Africa
WM1

LIQUID CRYSTAL THERMOGRAPHY FOR HEAT TRANSFER INVESTIGATION IN A FIN-TUBE HEAT EXCHANGER ELEMENT

M. Wierzbowski*, J. Stasiek**
*Ph.D. Student; **Professor
Department of Heat Technology, Technical University of Gdansk
G. Narutowicza 11/12, 80-952 Gdansk, Poland
E-mail: (*) rwierzbo@pg.gda.pl , (**) jstasiek@pg.gda.pl

ABSTRACT

The use of thermochromic liquid crystal technique (LCT) and true-colour image processing system in heat transfer modelling is described. Experimental procedure, led on rig at Technical University of Gdansk, cover full-field flow patterns in heat exchanger element (flat plate with fine-tubes in-line, staggered and with vortex generators) describing local heat transfer coefficient and Nusselt number on the surfaces. Also the dependence of average heat transfer and pressure drop on Reynolds number and geometrical parameters is investigated.

INTRODUCTION

For the last decade liquid crystals (LC) has been successfully used in many experimental works. Aerodynamics, Fluid Mechanics, Heat Exchange or Aeronautics are the most important fields where LC's were used. The experimental technique, used by numerous experimentalists in heat transfer problems) is interesting and promising [3, 4, 5, 6].

Liquid crystals are highly anisotropic fluids that exist between the boundaries of the solid phase, and the conventional, isotropic liquid phase. Since the colour change is reversible and repeatable, they can be calibrated accurately with proper care and used in this way as temperature indicators. They can be painted on a surface or suspended in a fluid and used to indicate visibly the temperature distribution. Nowadays, colour image processing has become an integral part of many scientific and industrial applications. A great majority of applications that use colour image processing do so because colour is the most important and obvious feature of the images they are examining. These new tools (liquid crystals, computers and image processing) have come together during the past few years to produce a powerful new examination technique: true-colour digital processing of liquid crystal images to yield full-field temperatures, velocity and heat transfer coefficient distributions [1, 2, 3]. Now, new and more incisive experiments are being settled in conventional situations, while those which have been previously intractable can also be studied. In this paper a novel approach is suggested to calculate heat transfer coefficient. The method is based on counting the number of pixels and their corresponding values of measured quantity. This method has been illustrated on examples of complex geometrical configurations.

EXPERIMENTAL APPARATUS

The experimental apparatus used in this study is the same as that presented before [7]. A brief description of the test section is presented here for clarification. The experimental study is carried out using an open low-speed wind tunnel consisting of entrance section with fan and heater, large settling chamber and then mapping and working sections. Air is drawn through the tunnel using a fan able to provide Reynolds numbers between 500 and 10 000 and the heater, which can adjust air temperature T_f between 25 and 60 °C. The major construction material of the wind tunnel is Perspex. Local and mean velocity are measured using conventional Pitot tubes and DISA hot-wire velocity probe.

Test section is of 7 mm height, 320 mm width and 350 mm length. Pipes are of 30 mm diameter, while winglets

are 14 mm long and distanced 2 mm from the tube (Fig. 2). The alternative effects of constant wall temperature and constant heat flux boundary conditions are obtained using a water bath. Photographs of liquid crystal patterns are taken using a colour video-camera and a true-colour image processing technique. It is possible, thanks to a special by-pass installed, to measure using both steady state and transient technique (Fig. 1). Local heat transfer measurements are carried out for Reynolds number based on the centreline inlet velocity along the main flow direction. Local heat transfer coefficient and Nusselt number maps, derived from local wall-temperature distributions as indicated by LC's for different Reynolds number are reported below. False colour isotherm representation of local Nusselt number was made automatically by GLAB software of Data Translation Inc [8]. The experiment is reported for fin-tube heat exchanger elements, both in-line and staggered. Air flows around the tubes and heat transfer between the fluid and the plate is determined by the flow structure.

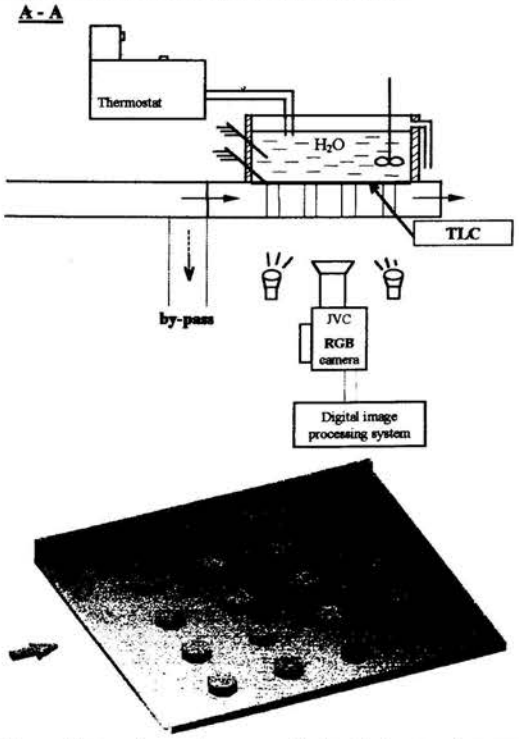

Figure 1 Experimental set-up and tube-fin heat exchanger model for in-line arrangement.

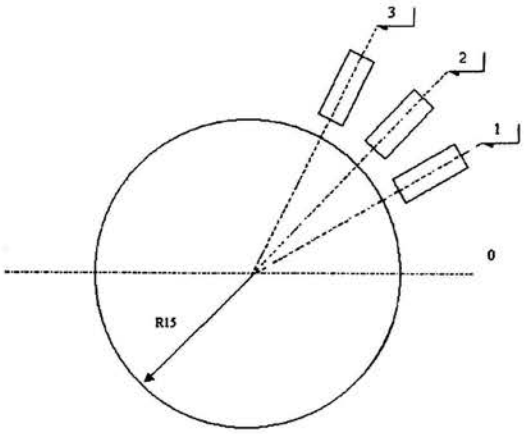

Figure 2 Position of the winglet behind the tube (1- 30 deg, 2- 45 deg, 3- 60 deg)

PERFORMANCE PARAMETERS

Heat Transfer

The heat transfer coefficient is a defined quantity, calculated from the surface heat flux and the difference between the surface temperature and some agreed reference temperature. This is usually the far field temperature, the mixed mean temperature or the adiabatic surface temperature. In the experiment described here, liquid crystals were used to determine the distribution of surface temperature and heat flux. This allows evaluation of the local heat transfer coefficient and Nusselt number. The temperature recorded from the liquid crystal sheet was held at yellow-green for image processing.

The local convective heat transfer coefficient h_l is derived from the fact that the conductive heat flux q_k in either working section is equal to the convective heat flux from air to the surface in the steady state:

$$h_l = \frac{k_t}{\delta_t}\frac{\left(T_1 - T_b\right)}{\left(T_a - T_1\right)} \qquad (1)$$

The experimental results are presented in terms of a local Nusselt number:

$$Nu_i = h_l H/k_a \qquad (2)$$

The Nusselt number value requires the test plate thermal conductance to be evaluated. It can be measured by

imposing a one-dimensional conductive heat flux across a sample having the composition and thickness as the test plate and measuring the extent of the heat flux and the temperature drop between the opposite sides. The measurement was performed by use of thermal conditions occurring in the liquid crystal experiment. From thermal conductance thermal conductivity of the test plate can be deduced, which turned out to be k_t = 0.202 W/m K.

With the temperature difference between the air and liquid crystal isotherm fixed, different heat transfer coefficient (Nusselt number) contours are determined by varying the heat flux values. The contours of constant heat transfer coefficient are not directly equivalent to the isotherms, as measured from the images. They are determined after taking into account thermal conduction in the plate, radiation from the surface and other corrections, the most important of which is the lateral conduction. This correction is typically about 4 % of the net flux [1, 2].

The liquid crystal colour temperature T_l is 35.5 °C some 9.5 °C below the air temperature (T_a=45 °C) for these experiment. Ten to sixteen isotherms (each corresponding to a different heat flux) are photographed by RGB camera to record the local contours under an oblique Reynolds number. The location of each isotherm was digitised involving colour scale representation of the several video images of the heat transfer coefficient distribution into a single image using the Global Lab software of Data Translation Inc.[8] as described in [3, 7].

Average Nusselt numbers can be estimated as weighted mean values of the local Nusselt numbers obtained from the relationship:

$$Nu_{av} = \frac{\sum_{i=1}^{n} Nu_i r_i}{\sum_{i=1}^{n} r_i} \qquad (3)$$

By using Eq.(1) - (3) and the image combination technique capabilities of Global Lab, colour images like that in figures below were obtained.

Pressure Drop

The second most relevant performance parameter of the heat exchange matrix is the pressure drop per unit length. The pressure drop can be made dimensionless by defining the equivalent friction factors coefficient:

$$f = \frac{2\Delta PH}{\rho L U^2} \qquad (4)$$

The experimental results are summarised in Figs 2 and 3. Reynolds number values were calculated as:

$$Re = \frac{U \cdot H}{\upsilon} \qquad (5)$$

Both friction factor and Reynolds number are related to mean velocity U and height of the tunnel H,. which can correlate f=f(Re).

EXPERIMENTAL RESULTS

Channel Averaged Pressure Drop

Figures of friction factor versus Reynolds number show the comparison of the different layout of the test section (in-line or staggered). It is easily to find out that in both applications insert of wings angled 60 degrees causes less pressure drop than the other positioning.

It is clear to find hydraulic jump at the transitional region of Reynolds number 1 000 – 2 500 both for 30 and 45 degrees positioned winglets.

Local Nusselt Number Maps

Photographs are taken using a video-camera and a true-colour image processing technique. Usually several isotherms (each corresponding to a different heat flux) are taken by camera to record the local Nusselt contours under an unique Reynolds number.

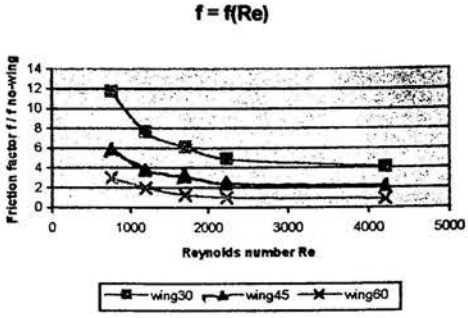

Figure 3. Friction factor relation for in-line arrangement of working section.

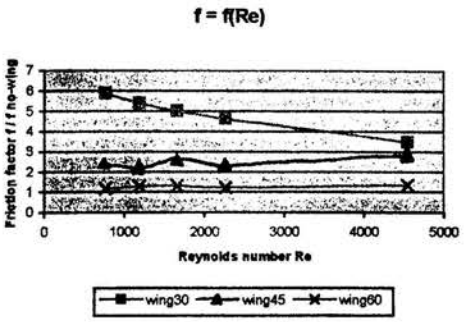

Figure 4. Friction factor relation for staggered arrangement of working section.

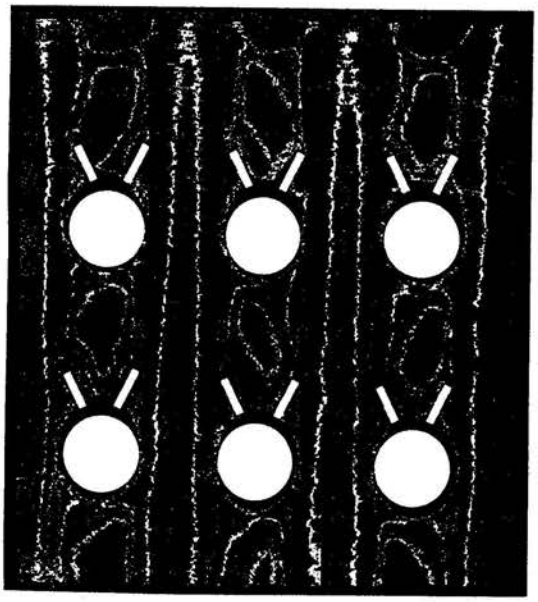

Figure 5. False image for in-line arrangement. *Re*=1 200; Nusselt number: red – 5.44; blue – 7.99; green – 10.77; violet – 18.7

The locations of each isotherm and colour (adjusted to each Nusselt number) are digitised following a projection of the false colour image on a digitising image respectively. Figures 5 - 8 shows colour-scale representation of Nusselt number distribution around in-line and staggered configuration of cylinders in experimental section.

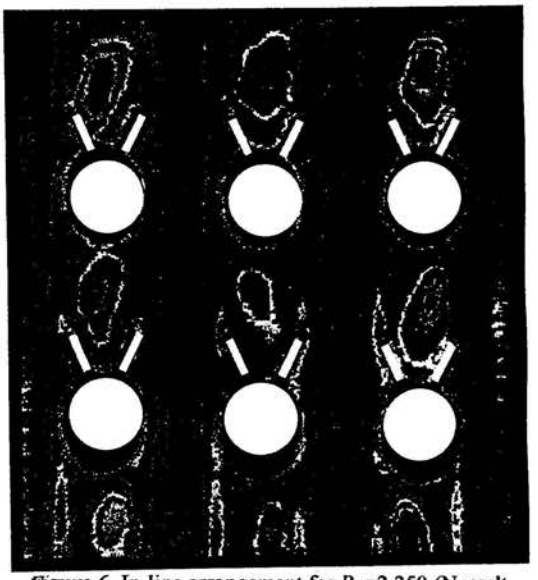

Figure 6. In-line arrangement for *Re*=2 250 (Nusselt number: red – 5.01; brown – 7.46; blue – 11.33; violet – 17.72; green – 27.76)

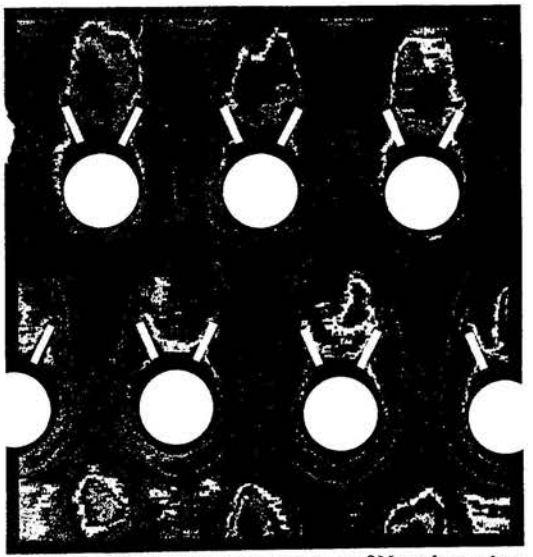

Figure 7. Colour-scale representation of Nusselt number for staggered cylinders. *Re*=1 600 (Nusselt number: red – 5.27; green – 7.99; blue – 15.38; violet – 19.17)

The maximum error of the air temperature is 0.1 °C and 0.025°C for the water bath. The uncertainty of thermal conductivity measurements for plate – liquid crystal package is about 0.005 W/m K. The most important factor seems to be the temperature difference between the water bath and liquid crystal layer temperature. When the difference is small the error significantly increases.

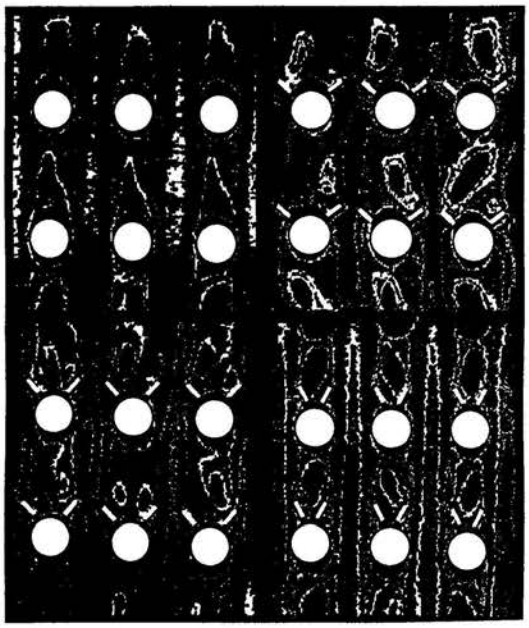

Figure 8. In-line working section for different wing's experimental arrangement. *Re*=1 200 (clock-wise: no wing, wing 30 deg, wing 60 deg, wing 45 deg).

CONCLUSIONS

LC technique is fairly new and powerful. With no doubts we can agree that new powerful technique has been established for obtaining local heat transfer conditions in complicated geometries, which can be useful for developing of different areas of heat transfer research. This technique is especially good for investigation of complex geometry heat transfer problems.

ACKNOWLEDGEMENT

Work reported were sponsored by State Committee of Research Science grant No.8T10B01814.

NOMENCLATURE

- H - height of the channel [m]
- k_a - conductivity of the air [W/m K]
- k_t - mean conductivity of the liquid crystal package and plate [W/m K]
- L - the length of the channel in the main flow direct. [m]
- ΔP - pressure drop [Pa]
- r_i - Hue ratio coefficient (ratio of number of pixels for the hue range considered) [dimensionless]
- T_a - temperature of air [K]
- T_b - temperature of plate from water side [K]
- T_l - temperature of surface (liquid crystal yellow-green isotherm temperature) [K]
- U - inlet mean velocity [m/s]
- δ_t - thickness of the liquid crystal package and plate [m]
- ρ - air density [kg/m^3]
- υ - viscosity of the air [m^2/s]

REFERENCES

[1]. Hollingsworth D.K., Boehman A.L., Smith E.G. and Moffat R.J.: Measurement of temperature and heat transfer coefficient distributions in a complex flow using liquid crystal thermography and true-colour image processing. *ASME Heat Transfer*, vol. 123, pp. 35-42, 1989.

[2]. Stasiek J.A.: Experimental studies of heat transfer and fluid flow across corrugated-undulated heat exchanger surfaces. *Int. J. Heat Mass Transfer*, Vol. 41, Nos. 6-7, pp. 899-914, 1998.

[3]. Stasiek J., Collins M.W.: The use of liquid crystals and true-colour image processing in heat and fluid flow experiments. *Atlas of Visualization*, Vol. 2, CRC Press Inc., USA, 1996

[4]. Baughn J.W., Yan X.: Liquid crystal methods in experimental heat transfer. *Proceedings of 32nd Heat Transfer and Fluid Conference*, pp.15-40, 1991

[5]. Jones T.V., Wang Z., Ireland P.T.: The use of liquid crystals in aerodynamic and heat transfer experiments. *Proceedings of 1st ImechE Seminar on Optical Methods and Data Processing in Heat and Fluid Flow*, pp.55-65, 1992

[6]. Moffat R.J.: Experimental heat transfer. *Proceedings of the 9th International Heat Transfer Conference*, Vol. 1, pp. 308-310, 1991.

[7]. Wierzbowski M., Barański J., Stąsiek J.: Local heat transfer measurement in heat exchanger elements. *X Symposium of Heat and Mass Transfer*, Vol. II, pp. 868-874, 1998

[8]. Data Translation Inc.: *Image Processing Handbook*, 1991.

AUTHOR INDEX

B & D Printers (011) 837-3888